



Proceedings
PRO 128

Proceedings of the International Conference on Sustainable Materials, Systems and Structures (SMSS2019)

Durability, Monitoring and Repair of Structures

Edited by
Ana Baričević
Marija Jelčić Rukavina
Domagoj Damjanović
Maurizio Guadagnini

RILEM Publications S.A.R.L.

**International Conference on Sustainable
Materials, Systems and Structures
(SMSS 2019)**
Durability, Monitoring and Repair of Structures

Published by RILEM Publications S.A.R.L.
4 avenue du Recteur Poincaré 75016 Paris - France
Tel : + 33 1 42 24 64 46 Fax : + 33 9 70 29 51 20
<http://www.rilem.net> E-mail: dg@rilem.net
© 2019 RILEM – Tous droits réservés.
ISBN: 978-2-35158-217-6, Vol 3. 978-2-35158-225-1
e-ISBN: 978-2-35158-218-3

Publisher's note: *this book has been produced from electronic files provided by the individual contributors. The publisher makes no representation, express or implied, with regard to the accuracy of the information contained in this book and cannot accept any legal responsibility or liability for any errors or omissions that may be made.*

All titles published by RILEM Publications are under copyright protection; said copyrights being the property of their respective holders. All Rights Reserved.

No part of any book may be reproduced or transmitted in any form or by any means, graphic, electronic, or mechanical, including photocopying, recording, taping, or by any information storage or retrieval system, without the permission in writing from the publisher.

RILEM, The International Union of Laboratories and Experts in Construction Materials, Systems and Structures, is a non profit-making, non-governmental technical association whose vocation is to contribute to progress in the construction sciences, techniques and industries, essentially by means of the communication it fosters between research and practice. RILEM's activity therefore aims at developing the knowledge of properties of materials and performance of structures, at defining the means for their assessment in laboratory and service conditions and at unifying measurement and testing methods used with this objective.

RILEM was founded in 1947 and has a membership of over 900 in some 70 countries. It forms an institutional framework for co-operation by experts to:

- optimise and harmonise test methods for measuring properties and performance of building and civil engineering materials and structures under laboratory and service environments,
- prepare technical recommendations for testing methods,
- prepare state-of-the-art reports to identify further research needs,
- collaborate with national or international associations in realising these objectives.

RILEM members include the leading building research and testing laboratories around the world, industrial research, manufacturing and contracting interests, as well as a significant number of individual members from industry and universities. RILEM's focus is on construction materials and their use in building and civil engineering structures, covering all phases of the building process from manufacture to use and recycling of materials.

RILEM meets these objectives through the work of its technical committees. Symposia, workshops and seminars are organised to facilitate the exchange of information and dissemination of knowledge. RILEM's primary output consists of technical recommendations. RILEM also publishes the journal *Materials and Structures* which provides a further avenue for reporting the work of its committees. Many other publications, in the form of reports, monographs, symposia and workshop proceedings are produced.

International Conference on Sustainable Materials,
Systems and Structures – SMSS 2019
Durability, Monitoring and Repair of Structures

Rovinj, Croatia
20-22 March 2019

Edited by
Ana Baričević
Marija Jelčić Rukavina
Domagoj Damjanović
Maurizio Guadagnini

RILEM Publications S.A.R.L.

RILEM Publications

The following list is presenting the global offer of RILEM Publications, sorted by series. Each publication is available in printed version and/or in online version.

RILEM PROCEEDINGS (PRO)

PRO 1: Durability of High Performance Concrete (ISBN: 2-912143-03-9); *Ed. H. Sommer*

PRO 2: Chloride Penetration into Concrete (ISBN: 2-912143-00-04);
Eds. L.-O. Nilsson and J.-P. Ollivier

PRO 3: Evaluation and Strengthening of Existing Masonry Structures (ISBN: 2-912143-02-0);
Eds. L. Binda and C. Modena

PRO 4: Concrete: From Material to Structure (ISBN: 2-912143-04-7); *Eds. J.-P. Bournazel and Y. Malier*

PRO 5: The Role of Admixtures in High Performance Concrete (ISBN: 2-912143-05-5);
Eds. J. G. Cabrera and R. Rivera-Villarreal

PRO 6: High Performance Fiber Reinforced Cement Composites - HPFRCC 3
(ISBN: 2-912143-06-3); *Eds. H. W. Reinhardt and A. E. Naaman*

PRO 7: 1st International RILEM Symposium on Self-Compacting Concrete (ISBN: 2-912143-09-8); *Eds. Å. Skarendahl and Ö. Petersson*

PRO 8: International RILEM Symposium on Timber Engineering (ISBN: 2-912143-10-1);
Ed. L. Boström

PRO 9: 2nd International RILEM Symposium on Adhesion between Polymers and Concrete
ISAP '99 (ISBN: 2-912143-11-X); *Eds. Y. Ohama and M. Puterman*

PRO 10: 3rd International RILEM Symposium on Durability of Building and Construction Seal-
ants (ISBN: 2-912143-13-6); *Eds. A. T. Wolf*

PRO 11: 4th International RILEM Conference on Reflective Cracking in Pavements
(ISBN: 2-912143-14-4); *Eds. A. O. Abd El Halim, D. A. Taylor and El H. H. Mohamed*

PRO 12: International RILEM Workshop on Historic Mortars: Characteristics and Tests
(ISBN: 2-912143-15-2); *Eds. P. Bartos, C. Groot and J. J. Hughes*

PRO 13: 2nd International RILEM Symposium on Hydration and Setting (ISBN: 2-912143-16-0); *Ed. A. Nonat*

PRO 14: Integrated Life-Cycle Design of Materials and Structures - ILCDES 2000
(ISBN: 951-758-408-3); (ISSN: 0356-9403); *Ed. S. Sarja*

PRO 15: Fifth RILEM Symposium on Fibre-Reinforced Concretes (FRC) - BEFIB'2000
(ISBN: 2-912143-18-7); *Eds. P. Rossi and G. Chanvillard*

PRO 16: Life Prediction and Management of Concrete Structures
(ISBN: 2-912143-19-5); *Ed. D. Naus*

PRO 17: Shrinkage of Concrete – Shrinkage 2000 (ISBN: 2-912143-20-9);
Eds. V. Baroghel-Bouny and P.-C. Aïtcin

PRO 18: Measurement and Interpretation of the On-Site Corrosion Rate (ISBN: 2-912143-21-7);
Eds. C. Andrade, C. Alonso, J. Fulla, J. Polimon and J. Rodriguez

- PRO 19:** Testing and Modelling the Chloride Ingress into Concrete (ISBN: 2-912143-22-5); *Eds. C. Andrade and J. Kropp*
- PRO 20:** 1st International RILEM Workshop on Microbial Impacts on Building Materials (CD 02) (e-ISBN 978-2-35158-013-4); *Ed. M. Ribas Silva*
- PRO 21:** International RILEM Symposium on Connections between Steel and Concrete (ISBN: 2-912143-25-X); *Ed. R. Eligehausen*
- PRO 22:** International RILEM Symposium on Joints in Timber Structures (ISBN: 2-912143-28-4); *Eds. S. Aicher and H.-W. Reinhardt*
- PRO 23:** International RILEM Conference on Early Age Cracking in Cementitious Systems (ISBN: 2-912143-29-2); *Eds. K. Kovler and A. Bentur*
- PRO 24:** 2nd International RILEM Workshop on Frost Resistance of Concrete (ISBN: 2-912143-30-6); *Eds. M. J. Setzer, R. Auberg and H.-J. Keck*
- PRO 25:** International RILEM Workshop on Frost Damage in Concrete (ISBN: 2-912143-31-4); *Eds. D. J. Janssen, M. J. Setzer and M. B. Snyder*
- PRO 26:** International RILEM Workshop on On-Site Control and Evaluation of Masonry Structures (ISBN: 2-912143-34-9); *Eds. L. Binda and R. C. de Vekey*
- PRO 27:** International RILEM Symposium on Building Joint Sealants (CD03); *Ed. A. T. Wolf*
- PRO 28:** 6th International RILEM Symposium on Performance Testing and Evaluation of Bituminous Materials - PTEBM'03 (ISBN: 2-912143-35-7; e-ISBN: 978-2-912143-77-8); *Ed. M. N. Partl*
- PRO 29:** 2nd International RILEM Workshop on Life Prediction and Ageing Management of Concrete Structures (ISBN: 2-912143-36-5); *Ed. D. J. Naus*
- PRO 30:** 4th International RILEM Workshop on High Performance Fiber Reinforced Cement Composites - HPFRCC 4 (ISBN: 2-912143-37-3); *Eds. A. E. Naaman and H. W. Reinhardt*
- PRO 31:** International RILEM Workshop on Test and Design Methods for Steel Fibre Reinforced Concrete: Background and Experiences (ISBN: 2-912143-38-1); *Eds. B. Schnütgen and L. Vandewalle*
- PRO 32:** International Conference on Advances in Concrete and Structures 2 vol. (ISBN (set): 2-912143-41-1); *Eds. Ying-shu Yuan, Surendra P. Shah and Heng-lin Lü*
- PRO 33:** 3rd International Symposium on Self-Compacting Concrete (ISBN: 2-912143-42-X); *Eds. Ó. Wallevik and I. Nielsson*
- PRO 34:** International RILEM Conference on Microbial Impact on Building Materials (ISBN: 2-912143-43-8); *Ed. M. Ribas Silva*
- PRO 35:** International RILEM TC 186-ISA on Internal Sulfate Attack and Delayed Ettringite Formation (ISBN: 2-912143-44-6); *Eds. K. Scrivener and J. Skalny*
- PRO 36:** International RILEM Symposium on Concrete Science and Engineering – A Tribute to Arnon Bentur (ISBN: 2-912143-46-2); *Eds. K. Kovler, J. Marchand, S. Mindess and J. Weiss*
- PRO 37:** 5th International RILEM Conference on Cracking in Pavements – Mitigation, Risk Assessment and Prevention (ISBN: 2-912143-47-0); *Eds. C. Petit, I. Al-Qadi and A. Millien*
- PRO 38:** 3rd International RILEM Workshop on Testing and Modelling the Chloride Ingress into Concrete (ISBN: 2-912143-48-9); *Eds. C. Andrade and J. Kropp*
- PRO 39:** 6th International RILEM Symposium on Fibre-Reinforced Concretes - BEFIB 2004 (ISBN: 2-912143-51-9); *Eds. M. Di Prisco, R. Felicetti and G. A. Plizzari*

- PRO 40:** International RILEM Conference on the Use of Recycled Materials in Buildings and Structures (ISBN: 2-912143-52-7); *Eds. E. Vázquez, Ch. F. Hendriks and G. M. T. Janssen*
- PRO 41:** RILEM International Symposium on Environment-Conscious Materials and Systems for Sustainable Development (ISBN: 2-912143-55-1); *Eds. N. Kashino and Y. Ohama*
- PRO 42:** SCC'2005 - China: 1st International Symposium on Design, Performance and Use of Self-Consolidating Concrete (ISBN: 2-912143-61-6); *Eds. Zhiwu Yu, Caijun Shi, Kamal Henri Khayat and Youjun Xie*
- PRO 43:** International RILEM Workshop on Bonded Concrete Overlays (e-ISBN: 2-912143-83-7); *Eds. J. L. Granju and J. Silfwerbrand*
- PRO 44:** 2nd International RILEM Workshop on Microbial Impacts on Building Materials (CD11) (e-ISBN: 2-912143-84-5); *Ed. M. Ribas Silva*
- PRO 45:** 2nd International Symposium on Nanotechnology in Construction, Bilbao (ISBN: 2-912143-87-X); *Eds. Peter J. M. Bartos, Yolanda de Miguel and Antonio Porro*
- PRO 46:** ConcreteLife'06 - International RILEM-JCI Seminar on Concrete Durability and Service Life Planning: Curing, Crack Control, Performance in Harsh Environments (ISBN: 2-912143-89-6); *Ed. K. Kovler*
- PRO 47:** International RILEM Workshop on Performance Based Evaluation and Indicators for Concrete Durability (ISBN: 978-2-912143-95-2); *Eds. V. Baroghel-Bouny, C. Andrade, R. Torrent and K. Scrivener*
- PRO 48:** 1st International RILEM Symposium on Advances in Concrete through Science and Engineering (e-ISBN: 2-912143-92-6); *Eds. J. Weiss, K. Kovler, J. Marchand, and S. Mindess*
- PRO 49:** International RILEM Workshop on High Performance Fiber Reinforced Cementitious Composites in Structural Applications (ISBN: 2-912143-93-4); *Eds. G. Fischer and V.C. Li*
- PRO 50:** 1st International RILEM Symposium on Textile Reinforced Concrete (ISBN: 2-912143-97-7); *Eds. Josef Hegger, Wolfgang Bramehuber and Norbert Will*
- PRO 51:** 2nd International Symposium on Advances in Concrete through Science and Engineering (ISBN: 2-35158-003-6; e-ISBN: 2-35158-002-8); *Eds. J. Marchand, B. Bissonnette, R. Gagné, M. Jolin and F. Paradis*
- PRO 52:** Volume Changes of Hardening Concrete: Testing and Mitigation (ISBN: 2-35158-004-4; e-ISBN: 2-35158-005-2); *Eds. O. M. Jensen, P. Lura and K. Kovler*
- PRO 53:** High Performance Fiber Reinforced Cement Composites - HPFRCC5 (ISBN: 978-2-35158-046-2); *Eds. H. W. Reinhardt and A. E. Naaman*
- PRO 54:** 5th International RILEM Symposium on Self-Compacting Concrete (ISBN: 978-2-35158-047-9); *Eds. G. De Schutter and V. Boel*
- PRO 55:** International RILEM Symposium Photocatalysis, Environment and Construction Materials (ISBN: 978-2-35158-056-1); *Eds. P. Baglioni and L. Cassar*
- PRO56:** International RILEM Workshop on Integral Service Life Modelling of Concrete Structures (ISBN 978-2-35158-058-5); *Eds. R. M. Ferreira, J. Gulikers and C. Andrade*
- PRO57:** RILEM Workshop on Performance of cement-based materials in aggressive aqueous environments (e-ISBN: 978-2-35158-059-2); *Ed. N. De Belie*
- PRO58:** International RILEM Symposium on Concrete Modelling - CONMOD'08 (ISBN: 978-2-35158-060-8); *Eds. E. Schlangen and G. De Schutter*

PRO 59: International RILEM Conference on On Site Assessment of Concrete, Masonry and Timber Structures - SACoMaTiS 2008 (ISBN set: 978-2-35158-061-5); *Eds. L. Binda, M. di Prisco and R. Felicetti*

PRO 60: Seventh RILEM International Symposium on Fibre Reinforced Concrete: Design and Applications - BEFIB 2008 (ISBN: 978-2-35158-064-6); *Ed. R. Gettu*

PRO 61: 1st International Conference on Microstructure Related Durability of Cementitious Composites 2 vol., (ISBN: 978-2-35158-065-3); *Eds. W. Sun, K. van Breugel, C. Miao, G. Ye and H. Chen*

PRO 62: NSF/ RILEM Workshop: In-situ Evaluation of Historic Wood and Masonry Structures (e-ISBN: 978-2-35158-068-4); *Eds. B. Kasal, R. Anthony and M. Drdácý*

PRO 63: Concrete in Aggressive Aqueous Environments: Performance, Testing and Modelling, 2 vol., (ISBN: 978-2-35158-071-4); *Eds. M. G. Alexander and A. Bertron*

PRO 64: Long Term Performance of Cementitious Barriers and Reinforced Concrete in Nuclear Power Plants and Waste Management - NUCPERF 2009 (ISBN: 978-2-35158-072-1); *Eds. V. L'Hostis, R. Gens, C. Gallé*

PRO 65: Design Performance and Use of Self-consolidating Concrete - SCC'2009 (ISBN: 978-2-35158-073-8); *Eds. C. Shi, Z. Yu, K. H. Khayat and P. Yan*

PRO 66: 2nd International RILEM Workshop on Concrete Durability and Service Life Planning - ConcreteLife'09 (ISBN: 978-2-35158-074-5); *Ed. K. Kovler*

PRO 67: Repairs Mortars for Historic Masonry (e-ISBN: 978-2-35158-083-7); *Ed. C. Groot*

PRO 68: Proceedings of the 3rd International RILEM Symposium on 'Rheology of Cement Suspensions such as Fresh Concrete (ISBN 978-2-35158-091-2); *Eds. O. H. Wallevik, S. Kubens and S. Oesterheld*

PRO 69: 3rd International PhD Student Workshop on 'Modelling the Durability of Reinforced Concrete (ISBN: 978-2-35158-095-0); *Eds. R. M. Ferreira, J. Gulikers and C. Andrade*

PRO 70: 2nd International Conference on 'Service Life Design for Infrastructure' (ISBN set: 978-2-35158-096-7, e-ISBN: 978-2-35158-097-4); *Ed. K. van Breugel, G. Ye and Y. Yuan*

PRO 71: Advances in Civil Engineering Materials - The 50-year Teaching Anniversary of Prof. Sun Wei' (ISBN: 978-2-35158-098-1; e-ISBN: 978-2-35158-099-8); *Eds. C. Miao, G. Ye, and H. Chen*

PRO 72: First International Conference on 'Advances in Chemically-Activated Materials – CAM'2010' (2010), 264 pp, ISBN: 978-2-35158-101-8; e-ISBN: 978-2-35158-115-5, *Eds. Caijun Shi and Xiaodong Shen*

PRO 73: 2nd International Conference on 'Waste Engineering and Management - ICWEM 2010' (2010), 894 pp, ISBN: 978-2-35158-102-5; e-ISBN: 978-2-35158-103-2, *Eds. J. Zh. Xiao, Y. Zhang, M. S. Cheung and R. Chu*

PRO 74: International RILEM Conference on 'Use of Superabsorbent Polymers and Other New Additives in Concrete' (2010) 374 pp., ISBN: 978-2-35158-104-9; e-ISBN: 978-2-35158-105-6; *Eds. O.M. Jensen, M.T. Hasholt, and S. Laustsen*

PRO 75: International Conference on 'Material Science - 2nd ICTRC - Textile Reinforced Concrete - Theme 1' (2010) 436 pp., ISBN: 978-2-35158-106-3; e-ISBN: 978-2-35158-107-0; *Ed. W. Brameshuber*

PRO 76: International Conference on ‘Material Science - HetMat - Modelling of Heterogeneous Materials - Theme 2’ (2010) 255 pp., ISBN: 978-2-35158-108-7; e-ISBN: 978-2-35158-109-4; *Ed. W. Brameshuber*

PRO 77: International Conference on ‘Material Science - AdIPoC - Additions Improving Properties of Concrete - Theme 3’ (2010) 459 pp., ISBN: 978-2-35158-110-0; e-ISBN: 978-2-35158-111-7; *Ed. W. Brameshuber*

PRO 78: 2nd Historic Mortars Conference and RILEM TC 203-RHM Final Workshop – HMC2010 (2010) 1416 pp., e-ISBN: 978-2-35158-112-4; *Eds J. Válek, C. Groot, and J. J. Hughes*

PRO 79: International RILEM Conference on Advances in Construction Materials Through Science and Engineering (2011) 213 pp., e-ISBN: 978-2-35158-117-9; *Eds Christopher Leung and K.T. Wan*

PRO 80: 2nd International RILEM Conference on Concrete Spalling due to Fire Exposure (2011) 453 pp., ISBN: 978-2-35158-118-6, e-ISBN: 978-2-35158-119-3; *Eds E.A.B. Koenders and F. Dehn*

PRO 81: 2nd International RILEM Conference on Strain Hardening Cementitious Composites (SHCC2-Rio) (2011) 451 pp., ISBN: 978-2-35158-120-9, e-ISBN: 978-2-35158-121-6; *Eds R.D. Toledo Filho, F.A. Silva, E.A.B. Koenders and E.M.R. Fairbairn*

PRO 82: 2nd International RILEM Conference on Progress of Recycling in the Built Environment (2011) 507 pp., e-ISBN: 978-2-35158-122-3; *Eds V.M. John, E. Vazquez, S.C. Angulo and C. Ulsen*

PRO 83: 2nd International Conference on Microstructural-related Durability of Cementitious Composites (2012) 250 pp., ISBN: 978-2-35158-129-2; e-ISBN: 978-2-35158-123-0; *Eds G. Ye, K. van Breugel, W. Sun and C. Miao*

PRO 85: RILEM-JCI International Workshop on Crack Control of Mass Concrete and Related issues concerning Early-Age of Concrete Structures – ConCrack 3 – Control of Cracking in Concrete Structures 3 (2012) 237 pp., ISBN: 978-2-35158-125-4; e-ISBN: 978-2-35158-126-1; *Eds F. Toutlemonde and J.-M. Torrenti*

PRO 86: International Symposium on Life Cycle Assessment and Construction (2012) 414 pp., ISBN: 978-2-35158-127-8, e-ISBN: 978-2-35158-128-5; *Eds A. Ventura and C. de la Roche*

PRO 87: UHPFRC 2013 – RILEM-fib-AFGC International Symposium on Ultra-High Performance Fibre-Reinforced Concrete (2013), ISBN: 978-2-35158-130-8, e-ISBN: 978-2-35158-131-5; *Eds F. Toutlemonde*

PRO 88: 8th RILEM International Symposium on Fibre Reinforced Concrete (2012) 344 pp., ISBN: 978-2-35158-132-2, e-ISBN: 978-2-35158-133-9; *Eds Joaquim A.O. Barros*

PRO 89: RILEM International workshop on performance-based specification and control of concrete durability (2014) 678 pp, ISBN: 978-2-35158-135-3, e-ISBN: 978-2-35158-136-0; *Eds. D. Bjegović, H. Beushausen and M. Serdar*

PRO 90: 7th RILEM International Conference on Self-Compacting Concrete and of the 1st RILEM International Conference on Rheology and Processing of Construction Materials (2013) 396 pp, ISBN: 978-2-35158-137-7, e-ISBN: 978-2-35158-138-4; *Eds. Nicolas Roussel and Hela Bessaies-Bey*

PRO 91: CONMOD 2014 - RILEM International Symposium on Concrete Modelling (2014), ISBN: 978-2-35158-139-1; e-ISBN: 978-2-35158-140-7; *Eds. Kefei Li, Peiyu Yan and Rongwei Yang*

PRO 92: CAM 2014 - 2nd International Conference on advances in chemically-activated materials (2014) 392 pp., ISBN: 978-2-35158-141-4; e-ISBN: 978-2-35158-142-1; *Eds. Caijun Shi and Xiadong Shen*

PRO 93: SCC 2014 - 3rd International Symposium on Design, Performance and Use of Self-Consolidating Concrete (2014) 438 pp., ISBN: 978-2-35158-143-8; e-ISBN: 978-2-35158-144-5; *Eds. Caijun Shi, Zhihua Ou, Kamal H. Khayat*

PRO 94 (online version): HPFRCC-7 - 7th RILEM conference on High performance fiber reinforced cement composites (2015), e-ISBN: 978-2-35158-146-9; *Eds. H.W. Reinhardt, G.J. Parra-Montesinos, H. Garrecht*

PRO 95: International RILEM Conference on Application of superabsorbent polymers and other new admixtures in concrete construction (2014), ISBN: 978-2-35158-147-6; e-ISBN: 978-2-35158-148-3; *Eds. Viktor Mechtcherine, Christof Schroefl*

PRO 96 (online version): XIII DBMC: XIII International Conference on Durability of Building Materials and Components (2015), e-ISBN: 978-2-35158-149-0; *Eds. M. Quattrone, V.M. John*

PRO 97: SHCC3 – 3rd International RILEM Conference on Strain Hardening Cementitious Composites (2014), ISBN: 978-2-35158-150-6; e-ISBN: 978-2-35158-151-3; *Eds. E. Schlangen, M.G. Sierra Beltran, M. Lukovic, G. Ye*

PRO 98: FERRO-11 – 11th International Symposium on Ferrocement and 3rd ICTRC - International Conference on Textile Reinforced Concrete (2015), ISBN: 978-2-35158-152-0; e-ISBN: 978-2-35158-153-7; *Ed. W. Brameshuber*

PRO 99 (online version): ICBBM 2015 - 1st International Conference on Bio-Based Building Materials (2015), e-ISBN: 978-2-35158-154-4; *Eds. S. Amziane, M. Sonebi*

PRO 100: SCC16 - RILEM Self-Consolidating Concrete Conference (2016), ISBN: 978-2-35158-156-8; e-ISBN: 978-2-35158-157-5

PRO 101 (online version): III Progress of Recycling in the Built Environment (2015), e-ISBN: 978-2-35158-158-2; *Eds I. Martins, C. Ulsen and S. C. Angulo*

PRO 102 (online version): RILEM Conference on Microorganisms-Cementitious Materials Interactions (2016), e-ISBN: 978-2-35158-160-5; *Eds. Alexandra Bertron, Henk Jonkers, Virginie Wiktor*

PRO 103 (online version): ACESC'16 - Advances in Civil Engineering and Sustainable Construction (2016), e-ISBN: 978-2-35158-161-2

PRO 104 (online version): SCS'2015 - Numerical Modeling - Strategies for Sustainable Concrete Structures (2015), e-ISBN: 978-2-35158-162-9

PRO 105: 1st International Conference on UHPC Materials and Structures (2016), ISBN: 978-2-35158-164-3, e-ISBN: 978-2-35158-165-0

PRO 106: AFGC-ACI-fib-RILEM International Conference on Ultra-High-Performance Fibre-Reinforced Concrete – UHPFRC 2017 (2017), ISBN: 978-2-35158-166-7, e-ISBN: 978-2-35158-167-4; *Eds. François Toutlemonde & Jacques Resplendino*

PRO 107 (online version): XIV DBMC – 14th International Conference on Durability of Building Materials and Components (2017), e-ISBN: 978-2-35158-159-9; *Eds. Geert De Schutter, Nele De Belie, Arnold Janssens, Nathan Van Den Bossche*

PRO 108: MSSCE 2016 - Innovation of Teaching in Materials and Structures (2016), ISBN: 978-2-35158-178-0, e-ISBN: 978-2-35158-179-7; *Ed. Per Goltermann*

PRO 109 (2 volumes): MSSCE 2016 - Service Life of Cement-Based Materials and Structures (2016), ISBN Vol. 1: 978-2-35158-170-4, Vol. 2: 978-2-35158-171-4, Set Vol. 1&2: 978-2-

35158-172-8, e-ISBN : 978-2-35158-173-5; *Eds. Miguel Azenha, Ivan Gabrijel, Dirk Schlicke, Terje Kanstad and Ole Mejlhede Jensen*

PRO 110: MSSCE 2016 - Historical Masonry (2016), ISBN: 978-2-35158-178-0, e-ISBN: 978-2-35158-179-7; *Eds. Inge Rörig-Dalgaard and Ioannis Ioannou*

PRO 111: MSSCE 2016 - Electrochemistry in Civil Engineering (2016), ISBN: 978-2-35158-176-6, e-ISBN: 978-2-35158-177-3; *Ed. Lisbeth M. Ottosen*

PRO 112: MSSCE 2016 - Moisture in Materials and Structures (2016), ISBN: 978-2-35158-178-0, e-ISBN: 978-2-35158-179-7; *Eds. Kurt Kielsgaard Hansen, Carsten Rode and Lars-Olof Nilsson*

PRO 113: MSSCE 2016 - Concrete with Supplementary Cementitious Materials (2016), ISBN: 978-2-35158-178-0, e-ISBN: 978-2-35158-179-7; *Eds. Ole Mejlhede Jensen, Konstantin Kovler and Nele De Belie*

PRO 114: MSSCE 2016 - Frost Action in Concrete (2016), ISBN: 978-2-35158-182-7, e-ISBN: 978-2-35158-183-4; *Eds. Marianne Tange Hasholt, Katja Fridh and R. Doug Hooton*

PRO 115: MSSCE 2016 - Fresh Concrete (2016), ISBN: 978-2-35158-184-1, e-ISBN: 978-2-35158-185-8; *Eds. Lars N. Thrane, Claus Pade, Oldrich Svec and Nicolas Roussel*

PRO 116: BEFIB 2016 – 9th RILEM International Symposium on Fiber Reinforced Concrete (2016), ISBN: 978-2-35158-187-2, e-ISBN: 978-2-35158-186-5;

PRO 117: 3rd International RILEM Conference on Microstructure Related Durability of Cementitious Composites (2016), ISBN: 978-2-35158-188-9, e-ISBN: 978-2-35158-189-6; *Eds. Changwen Miao, Wei Sun, Jiaping Liu, Huisu Chen, Guang Ye and Klaas van Breugel*

PRO 118 (4 volumes): International Conference on Advances in Construction Materials and Systems (2017), ISBN Set: 978-2-35158-190-2, Vol. 1: 978-2-35158-193-3, Vol. 2: 978-2-35158-194-0, Vol. 3: ISBN:978-2-35158-195-7, Vol. 4: ISBN:978-2-35158-196-4, e-ISBN: 978-2-35158-191-9; *Ed. Manu Santhanam*

PRO 119 (online version): ICBM 2017 - Second International RILEM Conference on Bio-based Building Materials, (2017), e-ISBN: 978-2-35158-192-6; *Ed. Sofiane Amziane*

PRO 120 (2 volumes): EAC-02 - 2nd International RILEM/COST Conference on Early Age Cracking and Serviceability in Cement-based Materials and Structures, (2017), Vol. 1: 978-2-35158-199-5, Vol. 2: 978-2-35158-200-8, Set: 978-2-35158-197-1, e-ISBN: 978-2-35158-198-8; *Eds. Stéphanie Staquet and Dimitrios Aggelis*

PRO 121 (2 volumes): SynerCrete18: Interdisciplinary Approaches for Cement-based Materials and Structural Concrete: Synergizing Expertise and Bridging Scales of Space and Time, (2018), Set: 978-2-35158-202-2, Vol.1: 978-2-35158-211-4, Vol.2: 978-2-35158-212-1, e-ISBN: 978-2-35158-203-9; *Ed. Miguel Azenha, Dirk Schlicke, Farid Benboudjema, Agnieszka Knoppik*

PRO 122: SCC'2018 China - Fourth International Symposium on Design, Performance and Use of Self-Consolidating Concrete, (2018), ISBN: 978-2-35158-204-6, e-ISBN: 978-2-35158-205-3

PRO 123: Final Conference of RILEM TC 253-MCI: Microorganisms-Cementitious Materials Interactions (2018), Set: 978-2-35158-207-7, Vol.1: 978-2-35158-209-1, Vol.2: 978-2-35158-210-7, e-ISBN: 978-2-35158-206-0; *Ed. Alexandra Bertron*

PRO 124 (online version): Fourth International Conference Progress of Recycling in the Built Environment (2018), e-ISBN: 978-2-35158-208-4; *Eds. Isabel M. Martins, Carina Ulsen, Yuri Villagran*

PRO 125 (online version): SLD4 - 4th International Conference on Service Life Design for Infrastructures (2018), e-ISBN: 978-2-35158-213-8; *Eds. Guang Ye, Yong Yuan, Claudia Romero Rodriguez, Hongzhi Zhang, Branko Savija*

PRO 126: Workshop on Concrete Modelling and Material Behaviour in honor of Professor Klaas van Breugel (2018), ISBN: 978-2-35158-214-5, e-ISBN: 978-2-35158-215-2; *Ed. Guang Ye*

PRO 127 (online version): CONMOD2018 - Symposium on Concrete Modelling (2018), e-ISBN: 978-2-35158-216-9; *Eds. Erik Schlangen, Geert de Schutter, Branko Savija, Hongzhi Zhang, Claudia Romero Rodriguez*

RILEM REPORTS (REP)

Report 19: Considerations for Use in Managing the Aging of Nuclear Power Plant Concrete Structures (ISBN: 2-912143-07-1); *Ed. D. J. Naus*

Report 20: Engineering and Transport Properties of the Interfacial Transition Zone in Cementitious Composites (ISBN: 2-912143-08-X); *Eds. M. G. Alexander, G. Arliguie, G. Ballivy, A. Bentur and J. Marchand*

Report 21: Durability of Building Sealants (ISBN: 2-912143-12-8); *Ed. A. T. Wolf*

Report 22: Sustainable Raw Materials - Construction and Demolition Waste (ISBN: 2-912143-17-9); *Eds. C. F. Hendriks and H. S. Pietersen*

Report 23: Self-Compacting Concrete state-of-the-art report (ISBN: 2-912143-23-3); *Eds. Å. Skarendahl and Ö. Petersson*

Report 24: Workability and Rheology of Fresh Concrete: Compendium of Tests (ISBN: 2-912143-32-2); *Eds. P. J. M. Bartos, M. Sonebi and A. K. Tamimi*

Report 25: Early Age Cracking in Cementitious Systems (ISBN: 2-912143-33-0); *Ed. A. Bentur*

Report 26: Towards Sustainable Roofing (Joint Committee CIB/RILEM) (CD 07) (e-ISBN 978-2-912143-65-5); *Eds. Thomas W. Hutchinson and Keith Roberts*

Report 27: Condition Assessment of Roofs (Joint Committee CIB/RILEM) (CD 08) (e-ISBN 978-2-912143-66-2); *Ed. CIB W 83/RILEM TC166-RMS*

Report 28: Final report of RILEM TC 167-COM 'Characterisation of Old Mortars with Respect to Their Repair (ISBN: 978-2-912143-56-3); *Eds. C. Groot, G. Ashall and J. Hughes*

Report 29: Pavement Performance Prediction and Evaluation (PPPE): Interlaboratory Tests (e-ISBN: 2-912143-68-3); *Eds. M. Partl and H. Piber*

Report 30: Final Report of RILEM TC 198-URM 'Use of Recycled Materials' (ISBN: 2-912143-82-9; e-ISBN: 2-912143-69-1); *Eds. Ch. F. Hendriks, G. M. T. Janssen and E. Vázquez*

Report 31: Final Report of RILEM TC 185-ATC 'Advanced testing of cement-based materials during setting and hardening' (ISBN: 2-912143-81-0; e-ISBN: 2-912143-70-5); *Eds. H. W. Reinhardt and C. U. Grosse*

Report 32: Probabilistic Assessment of Existing Structures. A JCSS publication (ISBN 2-912143-24-1); *Ed. D. Diamantidis*

Report 33: State-of-the-Art Report of RILEM Technical Committee TC 184-IFE 'Industrial Floors' (ISBN 2-35158-006-0); *Ed. P. Seidler*

Report 34: Report of RILEM Technical Committee TC 147-FMB 'Fracture mechanics applications to anchorage and bond' Tension of Reinforced Concrete Prisms – Round Robin Analysis and Tests on Bond (e-ISBN 2-912143-91-8); *Eds. L. Elfgren and K. Noghabai*

Report 35: Final Report of RILEM Technical Committee TC 188-CSC 'Casting of Self Compacting Concrete' (ISBN 2-35158-001-X; e-ISBN: 2-912143-98-5); *Eds. Å. Skarendahl and P. Billberg*

Report 36: State-of-the-Art Report of RILEM Technical Committee TC 201-TRC ‘Textile Reinforced Concrete’ (ISBN 2-912143-99-3); *Ed. W. Brameshuber*

Report 37: State-of-the-Art Report of RILEM Technical Committee TC 192-ECM ‘Environment-conscious construction materials and systems’ (ISBN: 978-2-35158-053-0); *Eds. N. Kashino, D. Van Gemert and K. Imamoto*

Report 38: State-of-the-Art Report of RILEM Technical Committee TC 205-DSC ‘Durability of Self-Compacting Concrete’ (ISBN: 978-2-35158-048-6); *Eds. G. De Schutter and K. Audenaert*

Report 39: Final Report of RILEM Technical Committee TC 187-SOC ‘Experimental determination of the stress-crack opening curve for concrete in tension’ (ISBN 978-2-35158-049-3); *Ed. J. Planas*

Report 40: State-of-the-Art Report of RILEM Technical Committee TC 189-NEC ‘Non-Destructive Evaluation of the Penetrability and Thickness of the Concrete Cover’ (ISBN 978-2-35158-054-7);
Eds. R. Torrent and L. Fernández Luco

Report 41: State-of-the-Art Report of RILEM Technical Committee TC 196-ICC ‘Internal Curing of Concrete’ (ISBN 978-2-35158-009-7); *Eds. K. Kovler and O. M. Jensen*

Report 42: ‘Acoustic Emission and Related Non-destructive Evaluation Techniques for Crack Detection and Damage Evaluation in Concrete’ - Final Report of RILEM Technical Committee 212-ACD (e-ISBN: 978-2-35158-100-1); *Ed. M. Ohtsu*

Report 45: Repair Mortars for Historic Masonry - State-of-the-Art Report of RILEM Technical Committee TC 203-RHM (e-ISBN: 978-2-35158-163-6); *Eds. Paul Maurenbrecher and Caspar Groot*

Report 46: Surface delamination of concrete industrial floors and other durability related aspects guide - Report of RILEM Technical Committee TC 268-SIF (e-ISBN: 978-2-35158-201-5); *Ed. Valérie Pollet*

Conference Chairs

Marijana Serdar, Faculty of Civil Engineering, University of Zagreb, Croatia

Ivana Banjad Pečur, Faculty of Civil Engineering, University of Zagreb, Croatia

Honorary president of scientific committee

Dubravka Bjegović, Faculty of Civil Engineering, University of Zagreb, Croatia

International Scientific Committee of segment: Durability, Monitoring and Repair of Structures

Mark Alexander

Arkadiusz Kwiecien

Miguel Azenha

Mirjana Laban

Yunus Ballim

Damir Lazarević

Ana Baričević

Maria Giuseppina Limongelli

Farid Benboudjema

Barbara Lubelli

Piotr Berkowski

Mirjana Malešev

Hans Beushausen

Kyriacos Neocleous

Lars Böstrom

Ivanka Netinger Grbeša

Jorge Branco

Takafumi Noguchi

Matthieu Briffaut

Jan Olek

Alvaro Cunha

Vagelis Papadakis

Christian Christodoulou

Ioanna Papayianni

Meri Cvetkovska

Alejandro Perez Caldentey

Gianmarco De Felice

Kypros Pilakoutas

Geert De Schutter

Giovanni Plizzari

Domagoj Damjanović

Juraj Pojatina

Emmanuel Denarie

Meera Ramesh

Guido De Roeck

Pierre Rossi

Josée Duchesne

Inge Rörig-Dalgaard

Ivan Duvnjak

Aljoša Šajna

Berhard Elsener

Jay Sanjayan

Eduardo M.R. Fairbairn

Ana Skender

Miguel Ferreira

Mohammed Sonebi

Raoul Francois

Irina Stipanović Oslaković

Josip Galić

Merima Šahinagić-Isović

Christoph Gehlen

Ivana Štimac Grandić

International Conference on Sustainable Materials, Systems and Structures (SMSS 2019)
Durability, Monitoring and Repair of Structures
20-22 March 2019 – Rovinj, Croatia

Mette Geiker

Branko Glisic

Arlindo Gonçalves

Kei-ichi Imamoto

Marija Jelčić Rukavina

Jin Wei-Liang

Harald Justnes

Agnieszka Klemm

Joško Krolo

Luping Tang

Michael Thomas

Jean-Michel Torrenti

François Toutlemonde

Thanasis Triantafillou

Tamon Ueda

Johan Vyncke

Dunja Vla

Børge Johannes Wigum

Organizing Committee of the segment:
Durability, Monitoring and Repair of Structures

Ana Baričević, Faculty of Civil Engineering, University of Zagreb, Croatia

Marija Jelčić Rukavina, Faculty of Civil Engineering, University of Zagreb, Croatia

Domagoj Damjanović, Faculty of Civil Engineering, University of Zagreb, Croatia

Maurizio Guadagnini, Department of Civil and Structural Engineering, University of Sheffield, United Kingdom

Contents

Preface	XXIV
<i>Ana Baričević, Marija Jelčić Rukavina, Domagoj Damjanović, Maurizio Guadagnini</i>	

Keynote lectures

Field survey on re-bar corrosion of carbonated existing concrete buildings in Japan	2
<i>Kei-ichi Imamoto</i>	
Practical Applications of Non-Destructive Testing in Assessment and Repairs of Structures	10
<i>Predrag L. Popovic</i>	

Durability of construction materials

Chemo-poro-mechanical modeling of cementitious materials (diffusion-precipitation-cracking)	23
<i>Adrien Socié, Frédéric Perales, Frédéric Dubois, Yann Monerie</i>	
Magnesium silicate hydrate formation at the surface of hydrated cements	31
<i>Barbara Lothenbach, E. Bernard, W. Kunther, K. de Weerd</i>	
Formation and stability of U-phase in cementitious materials under sulphate attack	39
<i>Yogarajah Elakneswaran, Li Chuang, Tomohiro Kajio, Eiji Owaki, Yuka Morinaga, Toyoharu Nawa</i>	
Air permeability, water penetration and water absorption to specify durability of ECO-friendly concrete	47
<i>Joachim Juhart, Rok Bregar, Gheorge David, Markus Krüger</i>	
A correlation between vapour diffusion coefficient and oxygen permeability coefficient of concrete	48
<i>Rakesh Gopinath, Mark Alexander</i>	
Suitability of impedance surface moisture meter to complement air-permeability tests	56
<i>Roberto Torrent, Veronica Bueno, Fabrizio Moro, Albert Jornet</i>	
The intrinsic coefficient of concrete permeability subjected to cyclic water freezing	64
<i>Alicja Wieczorek, Dalia Bednarska, Marcin Koniorczyk</i>	
Non equilibrium molecular dynamics simulation of the hydrodynamics in crystalline calcium silicate hydrates nanopores	72
<i>Tulio Honorio, Kamilia Abahri</i>	

Fundamental study on waterproof performance and evaluation of repair agent filling level of self-repairing system for cracked concrete <i>Hiroto Tanaka, Keiichi Imamoto, Chizuru Kiyohara</i>	78
Long-Term Mechanical and Shrinkage Properties of Cementitious Grouts for Structural Repair <i>Md Shamsuddoha, Götz Hüskens, Wolfram Schmidt, Hans-Carsten Kühne, Matthias Baeßler</i>	86
Influence of recycled fibre reinforcement on plastic shrinkage cracking of cement-based composites <i>Ida Bertelsen, L. M. Ottosen, G. Fischer</i>	87
Identification of drying, creep and shrinkage constitutive laws for concrete at 20°C and 40°C, application to VeRCoRs mock-up <i>Laurent Charpi, Jessica Haelewyn, Jean-Philippe Mathieu</i>	95
Shrinkage and bond behaviour of one-part alkali-activated mortars <i>Patrick Sturm, Gregor Gluth, H. J. H. Brouwers, Hans-Carsten Kühn</i>	103
Tensile behaviour of natural fibre textile-reinforced mortar <i>Niki Trochoutsou, Matteo Di Benedetti, Kypros Pilakoutas, Maurizio Guadagnini</i>	111
Mechanical characterization of lime cement mortars: E-modulus and fracture energy <i>Meera Ramesh, Miguel Azenha, Paulo Lourenço</i>	119
Experimental study on durability and sustainability of concrete with limestone and dolomite fillers <i>Moetaz El-Hawary, K. E. Nouh</i>	127
New generation of lime-based renders with the addition of ultrafine waste material from dolerite quarries <i>Ioannis Rigopoulos, Loucas Kyriakou, Ákos Török, Theodora Kyratsi, Ioannis Ioannou</i>	135
<i>Avoiding alkali aggregate reactions</i>	
RILEM Technical Committee: TC 258-AAA (Avoiding Alkali Aggregate Reactions in Concrete - performance based concept: current activities and achievement) <i>Børge Wigum, Jan Lindgård</i>	144
Optimization of concrete prism test for ASR expansion by alkali-wrapping and a new approach assessing the alkali reactivity of concrete for nuclear facilities <i>Kazuo Yamada, Yuichiro Kawabata, S. Ogawa, K. Shibuya, J. Etoh, A. Teramoto, G. Igarashi</i>	152
A new performance test method for alkali-silica reaction <i>Edward Moffatt, Michael Thomas, Michael Laskey</i>	160
Strategies for quantification of alkali metal release from aggregates in concrete <i>Klaartje De Weerd, Mette Geiker, Gilles Plusquellec, Jan Lindgård, Jose Duschene, Benoit Fournier</i>	168

Influence of the mineral composition of cement binder on the ACR reaction in concrete	176
<i>Petra Štukovnik, Violeta Bokan Bosiljkov, Marjan Marinšek</i>	
Alkali-silica reaction in alkali-activated concretes: the tempering effect of fly ash in slag/fly ash systems	184
<i>Alexandre Rodrigue, Josée Duchesne, Benoit Fournier, Benoit Bissonnette</i>	
AAR in concrete: Russian experience	192
<i>Vyacheslav Falikman, Nikolai Rozental, Alexandr Rozental</i>	
The effects of different cementitious binders on expansion induced by alkali silica reaction	200
<i>Taehwan Kim, Dinesh Arachchige, Quang Dieu Nguyen, Mohammad Khan, Arnaud Castel</i>	
An ambt study on the effect of limestone on ASR mitigation: ground limestone vs. interground limestone in cements	201
<i>Marie Joshua Tapas, Kirk Vessalas, Paul Thomas, Vute Sirivivatnanon</i>	
Synthesis and characterization of alkali-silica reaction products	208
<i>Z. Shi, B. Lothenbach, A. Leemann</i>	
Microstructural analysis of ASR in concrete - accelerated testing versus natural exposure	214
<i>Andreas Leemann, Ingmar Borchers, Mahdieh Shakoorioskooie, Michele Giffa, Christoph Müller, Pietro Lura</i>	
Analytical modelling to describe alkali-aggregate reaction (AAR) induced expansion	222
<i>N. Goshayeshi, L. F. M. Sanchez, A. C. D. Santos, R. Gorga</i>	
Numerical simulation of the expansion behavior of field-exposed concrete blocks based on a modified concrete prism test	230
<i>Y. Kawabata, K. Yamada, S. Ogawa, Y. Sagawa</i>	
<i>Reinforcement corrosion</i>	
Study on non-uniform corrosion of steel bars in concrete	239
<i>Yuxi Zhao, Xiaowen Zhang, Wang Kun, Chen Ju, Hailong Wang</i>	
Evolving performance based environmental classifications for chloride exposure	247
<i>B S Dhanya, Manu Santhanam, Santosh Cheriyan</i>	
Influence of the bars position in the reinforced concrete for the prediction of the chloride concentration in the layer steel-concrete	255
<i>Fabiano Tavares, Carmen Andrade</i>	
Damage parameters of rebars in marine environment and fatigue life	263
<i>Charis Apostolopoulos, Konstantinos Koulouris, Maria Basdeki</i>	

The reliability of corrosion detection with regard to chosen grid size <i>Sylvia Keßler</i>	271
Chloride ingress in concrete exposed to a Swedish road environment for over 20 years <i>Luping Tang, Dimitrios Boubitsas, Peter Utgenannt</i>	278
New mechanism of stress corrosion cracking: fracto-surface mobility mechanism <i>Javier Sanchez, E. Torres, Nuria Rebolledo, Alvaro Ridruejo</i>	286
Diffusion coefficient of H in Fe: first principles calculation <i>P. de Andres, J. Sanchez, A. Ridruejo</i>	292
Crack propagation rate by hydrogen embrittlement in high strength steels: trap-controlled diffusion <i>A. Ridruejo, J. Sanchez, E. Torres, N. Rebolledo</i>	300
<i>Carbonation of concrete with SCMs</i>	
X-ray diffraction study of carbonation rate of C-S-H(i) with different Ca/Si ratio <i>Bei Wu, Guang Ye</i>	309
Difference in carbonation behavior at 0.04%, 1% and 10% CO₂ for High-Volume Fly Ash (HVFA) mortar: effect on internal humidity and resistivity <i>Philip Van den Heede, Nele De Belie</i>	317
Thermodynamic modelling of the carbonation process of alkali-activated slag cements <i>Xinyuan Ke, Susan Bernal, John Provis</i>	325
Traditional coatings as protection of portland cement concrete against carbonation <i>Rui Reis, Aires Camões, Manuel Ribeiro</i>	333
Investigations of corrosion due to calcium leaching <i>Stefanie von Greve-Dierfeld, Yves Schiegg, Fritz Hunkeler</i>	341
Reaction products formed in early age cement pastes with granulated blast furnace slag exposed to accelerated CO₂ ingress <i>Hanne Vanoutrive, Azzlem Cizer, Peter Minne, Ilse Van de Voorde, Elke Gruyaert</i>	349
Natural and accelerated carbonation rates of alkali-activated slag/fly ash blended concretes <i>Susan Bernal, Jannie van Deventer, John Provis</i>	357
Accelerated carbonation of recycled aggregate concrete <i>Andreas Leemann, Roman Loser</i>	365
On the determination of carbonation in cementitious materials <i>Charlotte Thiel, Christoph Gehlen</i>	373

Construction and demolition waste as an addition in new cements. effect on carbonation	381
<i>Caesar Medina Martinez, Isabel Fuencisla Sáez del Bosque, Eloy Asensio de Lucas, Moisés Frías Rojas, María Isabel Sánchez de Rojas Gómez</i>	
Influence of exposure environments on the carbonation resistance of concrete structures	389
<i>A. S. AL-Ameeri, M. I. Rafiq, O. Tsioulou</i>	
The influence of cracks and carbonation level on the salt scaling resistance of natural and recycled aggregate concrete	397
<i>Ivan Ignjatović, Vedran Carević</i>	
Accelerated carbonation of recycled concrete aggregates: the FastCarb project	405
<i>Jean Michel Torrenti</i>	
Development of durable and structural lightweight concrete	413
<i>Maria Stratoura, Theofilos-Marios Zavras, Efstratios Badogiannis, Kosmas Sideris, Vagelis Papadakis</i>	
C/S ratio influence on the carbonation of cementitious material using designed model systems	421
<i>Ekoé Kangni-Foli, Stéphane Poyet, Patrick Le Bescop, Emilie L'Hôpital, Alexandre Dauzères, Thibault Charpentier, Jean-Baptiste d'Espinose de Lacaillerie</i>	
Influence of biomass fly ash on hydration and carbonation of cementitious materials	428
<i>Elisabete Teixeira, Aires Camões, Fernando Branco</i>	
Coupling effect and durability in cement pastes and concretes with supplementary cementitious materials	436
<i>Mickael Saillio, Matthieu Bertin, Veronique Baroghel-Bouny</i>	
<i>Influence of high temperatures</i>	
Numerical investigations on post-fire bond performance of reinforcement in concrete	445
<i>Arunita Das, Josipa Bošnjak, Sharma Akanshu</i>	
Effects of rehydration conditions on the mechanical recovery and the properties of portland cement paste subjected to high temperature	446
<i>Heongwon Suh, Taehoon Park, Hyeonseok Jee, Bumyeon Cho, Sungchul Bae</i>	
High-temperature behavior of heavy-weight concretes	454
<i>Flora Faleschini, Raissa Njinwoua, Anne-Lise Beaucour, Prosper Pliya, Albert Noumowe, Carlo Pellegrino</i>	
Predicting the fire rating of reinforced concrete columns: effect of load induced thermal strains (LITS)	462
<i>Hitesh Lakhani, Joško Ožbolt, Batsuuri Boldbaatar</i>	

Explosive spalling potential of ultra-high performance concrete prepared by a novel approach	470
<i>Xu-Jing Niu, G.F. Peng, Ya-Jie Shang, Xi-Wang Chen, Hong Ding</i>	
Multiaxial behaviour of fibre reinforced mortar for masonry strengthening subjected to high temperatures	478
<i>João Almeida, Eduardo Pereira, Hernán Xargay, Paula Folino, Joaquim Barros</i>	
Numerical model of an experimentally tested timber-concrete composite slab exposed to fire	486
<i>Cvetanka Chifliganec, Meri Cvetkovska, Ljupco Lazarov, Ana Tormbeva Gavriloska</i>	
 <i>Condition assesment and monitoring of structures</i>	
Durability of reinforced concrete structures – An overview of past and current re-search achievements in Croatia	495
<i>Dubravka Bjegović, Marijana Serdar, Ana Baričević</i>	
Factors affecting durability of concrete repairs	503
<i>Dunja Vla, Predrag Popovic</i>	
Mistakes in design and building of concrete structures - practice examples	511
<i>Jure Galić, Željko Lebo</i>	
Investigation works and structure condition of sewerage pipe under Heinzlova street in city of Zagreb	519
<i>Jure Galić, Ivana Banjad Pečur</i>	
Preliminary analysis of durability related field inspection of reinforced concrete bridge	527
<i>Dita Vořechovská, Petr Konečný, Martina Šomodíková, Pavla Rovnaníková</i>	
The renewal of multi-storey prefabricated residential buildings	534
<i>Mirjana Laban, Radomir Folic, Vlastimir Radonjanin, Mirjana Malešev</i>	
Investigation and repair of stone building facades	542
<i>Dunja Vla</i>	
Reconstruction of a family villa in Zagreb city center	550
<i>Angela Čuljak</i>	
Influence of pounding on seismic performance of existing buildings in the city of Zagreb, Croatia	556
<i>Jakov Oreb, Božen Mušterić, Marta Šavor Novak, Josip Atalić</i>	
Fundamental study on detecting internal defect of timber due to termite and its mechanical improvement with resin	564
<i>Akiko Ohtsuka, Kei-ichi Imamoto, Chizuru Kiyohara</i>	

Advances in durability monitoring of concrete structures <i>Ueli Angst</i>	572
Development of a multifunctional concrete with carbon sensor <i>Paulo Cachim, Emanuel Pereira</i>	580
Modal identification of a double-curvature concrete arch dam under natural excitation: analysis of the accuracy achieved with different types of accelerometers <i>Sergio Pereira, Filipe Magalhães, Carlos Moutinho, Álvaro Cunha</i>	587
Design for durability of reinforced concrete structures under the hot desert climate of the Arabian peninsula <i>Sotiris Demis, Vagelis Papadakis</i>	595
Evaluation of service life of reinforced concrete in the middle east eight years of testing <i>Mohamad Nagi, Jessi Meyer, Nizar Marjaba</i>	603
8-year performance of cathodic protection systems in reinforced concrete slabs and life-cycle cost benefits <i>Deepak Kamde, Naveen Krishnan, Radhakrishna Pillai, George Sergi, Dhruvesh Shah, Rajendran Velayudham</i>	611
Organic corrosion inhibitors - bio based technology to extend durability of concrete for new build and existing structures performance <i>Ivana Lipošćak, Jessi Meyer, Boris Mikšić</i>	619
 <i>Lime-based historic repair</i>	
Testing properties governing the durability of lime-based repair mortars <i>I. Papayianni, J. Válek, J. Alvarez, V. Bokan Bosiljkov, P. Faria, L. Ferrara, C. Groot</i>	628
Durability of lime based renders: a review of some degradation mechanisms and assessment test methods <i>Rosario Veiga, Ana Velosa, Kristin Balksten, José I. Alvarez, Cristiana Nunes, Magdalini Theodoridou, Paulina Faria, Ioanna Papayianni, Rob van Hees</i>	629
Microstructure aspects related to durable lime mortars <i>Maria Stefanidou</i>	637
Durability aspects related to repointing of historic mortars with lime based mortar <i>Caspar Groot, Rob van Hees, Ioanna Papayianni</i>	644
Self-healing lime mortars: an asset for restoration of heritage buildings <i>Cristina De Nardi, Claudia Brito de Carvalho Bello, Liberato Ferrara, Antonella Cecchi</i>	652
Evaluation of lime-based mortars used for repairing the Galerius Palace (4th century AD) during Restoration project (1994-2006) <i>Ioanna Papayianni, Maria Stefanidou, Vasiliki Pachta, Stavroula Konopisi, Fani Athanasiou, Maria Sarantidou</i>	660

Material properties of heritage masonry buildings from 19th century <i>Davor Grandić, Paulo Šćulac, Natalija Bede</i>	668
Structural and material diagnostics of historical industrial buildings <i>Piotr Berkowski, Grzegorz Dmochowski</i>	676
Optimising in-situ testing for historic masonry structures: a case study <i>Miroslav Sykora, Dimitris Diamantidis, Jana Markova, Maria Masciotta</i>	684
Thermal behavior of rigid and flexible composite-to-substrate strengthening <i>Bogusław Zajac, Arkadiusz Kwiecień</i>	692
A probabilistic approach to investigate the physical compatibility between bedding and re-pointing mortars <i>Cristina Tedeschi, Elsa Garavaglia</i>	700
Seismic retrofitting of masonry walls with textile reinforced mortar composites <i>Gianmarco de Felice, Stefano De Santis</i>	708
 <i>High-performance repair</i>	
Experimental investigation on RC beams strengthened with bottom or side NSM FRP bars <i>Thanongsak Imjai, Monthian Setkit, Navapadol Khumthong, Kornrit Keeratithanikkul, Reyes Garcia</i>	717
Use of NSM FRP for the strengthening of a bridge deck - a case study <i>Alejandro Perez Caldentey</i>	724
Effect of corner radius on the axial behavior of FRCM-confined concrete members <i>Jaime Gonzalez-Libreros, Flora Faleschini, Mariano Angelo Zanini, Carlo Pellegrino</i>	732
Rehabilitation of an old steal railway bridge using UHPFRC - material characteristics and casting technology <i>Aljoša Šajna, Irina Stipanović Oslaković, Henar Martín-Sanz, Domagoj Damjanović</i>	740
Experimental investigation of a steel railway bridge strengthened with UHPFRC deck slab <i>Domagoj Damjanović, Sandra Škarić Palić, Irina Stipanović Oslaković, Henar Martín-Sanz, Janko Koščak, Ivan Duvnjak, Uroš Bohinc</i>	748
Experimental investigations of UHPC, steel fibres and embedded steel fibres under cyclic tensile loading <i>Martin Empelmann, Vincent Oettel, Jan-Paul Lanwer</i>	756
Upgrading the concept of UHPFRC for high durability in the cracked state: the concept of ultra high durability concrete in the approach of the H2020 project ReSHEALience <i>Pedro Serna, Francesco Lo Monte, Eduard Mezquida-Alcaraz, Estefania Cuenca, Viktor Mechtcherine, Michaela Reichardt, Alva Peled</i>	764

High-performance and durable fiber concrete made of recycled carbon fibers <i>Magdalena Kimm, Thomas Gries</i>	772
Shear behavior of fiber reinforced concrete beams <i>Marta Kosior-Kazberuk, Julita Krassowska, Piotr Berkowski</i>	780
Analysis of Steel Fibers Distribution and Orientation in Hybrid-Fibers Reinforced High-Performance Concrete Column Using Micro-Computed Tomography <i>Taehoon Park, Heongwon Suh, Jaeyeon Park, Bumyeon Cho, Seyoon Yoon, Sungchul Bae</i>	788
Towards the development of damage tolerant engineered cementitious composites with super-elastic reinforcement <i>Dario Mirza, Eduardo Pereira, João Almeida, Vitor Cunha</i>	796
Tests on strengthening fasteners in riveted steel structures - fit bolts and weld studs <i>Janusz Hołowaty, Bernard Wichtowski</i>	804
Methodology of numerically aided optimisation of consolidants for surface treatments of mortars <i>Janez Perko, Li Yu, Diederik Jacques, Eddie.A.B. Koenders, Neven Ukrainczyk, Anna Varzina, Pagona-Noni Maravelaki, Ioannis Arabatzis</i>	812

Preface

RILEM International Conference on Sustainable Materials, Systems and Structures (SMSS 2019) is a conference organised by Faculty of Civil Engineering University of Zagreb as a supporting event of RILEM Spring Convention from in Rovinj, Croatia. Both are organised in the year Faculty of Civil Engineering in Zagreb is celebrating 100 years from its establishment, making 2019 a perfect year for hosting such an important international event. The scope of the conference was to gather scientists, practitioners, members of technical committees and users of technical recommendations, to jointly at the same place discuss and envision the future sustainable development of materials, systems and structures in a holistic, global way.

SMSS 2019 conference has gathered participants from 50 countries, from Argentina to United States of America, who will exhibit a total of 290 papers. The conference was sponsored by 10 international industrial partners, supported by 6 international organisations of scientists and practitioners and organised under the patronage of 4 governmental bodies. A total of 450 contributions which arrived was reviewed by more than 150 prominent reviewers from different fields. Event was organised by 16 members of the local organising committee and 6 invited international members of organising committee.

As part of the ***RILEM SMSS 2019 conference***, segment ***DURABILITY, MONITORING AND REPAIR OF STRUCTURES*** has consisted of 107 scientific papers which cover durability aspects of construction material in a variety of structures and harsh environments, maintenance and management of civil infrastructure and sustainable repair, rehabilitation and retrofitting. Among the others, the topics addressed are characterization of innovative and traditional durable materials, diagnosis of structures including service life design, seismic safety assessment, fire resistance, repair and conservation of heritage structures, advanced materials for structural rehabilitation, strengthening methods and case studies.

Editors wish to thank the authors for their efforts at producing and delivering papers of high standard. We are sure that this Proceedings will be a valued reference of research topics in this important field and that it will together with the other volumes from SMSS conference form a suitable base for discussion and suggestions for future development and research.

Ana Baričević (University of Zagreb, Croatia)
Marija Jelčić Rukavina (University of Zagreb, Croatia)
Domagoj Damjanović (University of Zagreb, Croatia)
Maurizio Guadagnini (University of Sheffield, United Kingdom)

**International Conference on Sustainable
Materials, Systems and Structures
(SMSS 2019)**
Durability, Monitoring and Repair of Structures

Keynote lectures

FIELD SURVEY ON RE-BAR CORROSION OF CARBONATED EXISTING CONCRETE BUILDINGS IN JAPAN

Kei-ichi Imamoto (1), Manabu Kanematsu (1), Chizuru Kiyohara (1), Hitoshi Hamasaki (2), Toru Kinose (3), Kouji Teranishi (4), Takafumi Noguchi (5)

(1) Department of Architecture, Tokyo University of Science, Japan

(2) Division of Architecture, Shibaura Institute of Technology, Japan

(3) General Building Research Corporation of Japan, Japan

(4) Department of Architecture, Meijo University, Japan

(5) Department of Architecture, Tokyo University, Japan

Abstract

This paper reports re-bar corrosion of existing concrete buildings based on field survey. Twenty-one buildings ranging in age from 42 to 100 years were surveyed in 2017. The survey results indicated that the re-bar was corroded only in cases of poor cover thickness. Re-bar corrosion of concrete at low relative humidity was quite minor although carbonation had significantly progressed. This might indicate that not only carbonation but also moisture is key to cause re-bar corrosion. It was found that a relative humidity of approximately 80% and re-bar with thin cover thickness strongly affect the corrosion in a carbonated concrete structure. At an appropriate cover thickness layer, the relative humidity of the concrete was stable. On the other hand, concrete carbonation progress was not significant due to a high moisture content under relative humidity of 80% or more, which prevented CO₂ ingress from the outer zone. The truth of carbonation induces re-bar corrosion, given a sufficient cover thickness under relative humidity of 80% or more, should be discussed in the future.

Keywords: existing RC building, carbonation, re-bar corrosion, relative humidity

1. INTRODUCTION

Carbonation-induced steel corrosion is one the dominant factors affecting the life span of reinforced concrete (RC) structures. In 1928, Minoru Hamada, emeritus professor of Tokyo University, found that carbonation progresses according to the square root of time based on the diffusion theory of CO₂ in concrete. This means that the life span of an RC structure can be quantitatively evaluated by estimating both the progress of carbonation and the cover thickness of the re-bar in concrete. In 1956, his finding was adopted into Japanese Architectural Standard Specification for Reinforced Concrete Work “JASS 5”. After that, carbonation has been an

important basis of the grade of concrete manufacturers and an economical reference service for the life of a building.

Steel corrosion of carbonated concrete have studied by C. Andrade from the view point of moisture and these researches are bases of this study [2],[3]. A research working group on “Investigation of Material Deterioration of Existing Reinforced Concrete Buildings” chaired by Prof. Noguchi at Architectural Institute of Japan was established and field surveys of existing RC buildings were performed. This paper reports on the investigation of the relationship between re-bar corrosion and carbonation of concrete.

2. OUTLINE OF SURVEY

Twenty-one RC buildings were surveyed and the outlines of these buildings are summarised in Table 1. As shown in the table, the ages of buildings ranged from 27 to 100 years old. Blast furnace slag cement was used as structural concrete of No. 8. Concrete sampling points were selected considering the effects of water pouring and the inner/exterior zone. Test items are shown in Table 2. Not only carbonation depth but also moisture content and relative humidity of the concrete at the re-bar cover zone were measured. The re-bar corrosion rate was estimated based on criteria shown in Figure 1 as proposed by the Japan Concrete Institute “Guidelines for Assessment of Existing Concrete Structures 2014” [4]. Corrosion rates of 4 and 5 are significant and those of 1, 2, and 3 are slight.

Table 1 : Outlines of the buildings

No.	Function	Years of construction (Age)	Level	Finishing	Location
1	Warehouse	1914 (100)	2	M	Hiroshima
2	Warehouse	1918 (97)	2	U	Tokyo
3	Office	1926 (90)	2	M, P	Gifu
4	House	1929 (84)	4	M, F, S	Tokyo
5	School	1935 (81)	3	U, M, F	Tokyo
6	Lab.	1935 (81)	2	M, P	Tokyo
7	Lab.	1937 (80)	2	M, P	Tokyo
8	Arena	1958 (58)	5	U, M, F	Tokyo
9	Museum	1959 (55)	3	U, M, F	Tokyo
10	Radio tower	1962 (53)	2	M, F	Ibaraki
11	Office	1962 (54)	8	M, F	Tokyo
12	Radio tower	1963 (52)	1	M, F	Nagano
13	House	1965 (44)	4	U, M, P	Tokyo
14	House	1965 (44)	5	M, F	Tokyo
15	Office	1966 (51)	8	M, P	Tokyo
16	School	1967 (50)	3	M, P	Tokyo
17	School	1968 (47)	6	U, M, P	Aichi
18	School	1968 (49)	2	U, M, P, T	Chiba
19	House	1970 (42)	7	M, F	Tokyo
20	House	1971 (43)	13	U, M, P	Tokyo
21	Radio tower	1972 (44)	2	M, F	Gifu

U:Exposed concrete, M:Mortar, P:Paint, F:Multi layer, T:Tile, S:Stucco

Table 2: Test items

Test Item	Test method
Carbonation depth	JIS A 1152 with core in diameter with 80mm
Relative humidity of concrete	Embedded moisture sensor in concrete at reinforcing bar
Moisture content of concrete	Measurement by drying of core with drilled under dried condition
Cober thicknes	Direct measurements with concrete chipping
Steel corrosion	Visual inspection based on corrosion grade






Grade	Corrosion condition	Example
1	No corrosion	
2	Partial slight corrosion	
3	Partial corrosion	
4	Overall corrosion	
5	Serious defect of section	

Figure 1: Re-bar corrosion rate [4]

3. SURVEY RESULTS

Figure 2 shows the distribution of the core concrete strengths. As shown in the figure, the strength of many of the cores ranged from 20 to 30 MPa which meet a service life of 65 years according to JASS5.

Figure 3 shows the distribution of the carbonation progress. It can be seen that the carbonation of concrete without a water pouring zone was greater than that with a water pouring zone.

Figure 4 shows the distribution of the steel corrosion rates. It can be seen that the steel corrosion rate was slight although the carbonation reached to the steel bar and no significant corrosion was confirmed at the concrete without a water pouring zone. This might indicate that moisture strongly affects the steel corrosion of existing RC structures.

Figures 5 and 6 show the cover thickness and the cover thickness minus carbonation depth (carbonation rest) versus the steel corrosion rate, respectively. Significant re-bar corrosion was observed only at a poor cover thickness less than 30 mm and a carbonation rest of less than 10 mm. Many surveyed re-bar with sufficient cover thickness were deemed quite sound.

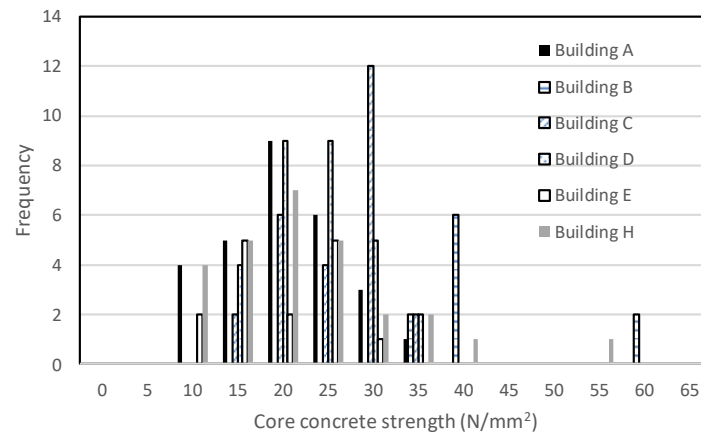


Figure 2: Distributions of core concrete strengths (to be prepared)

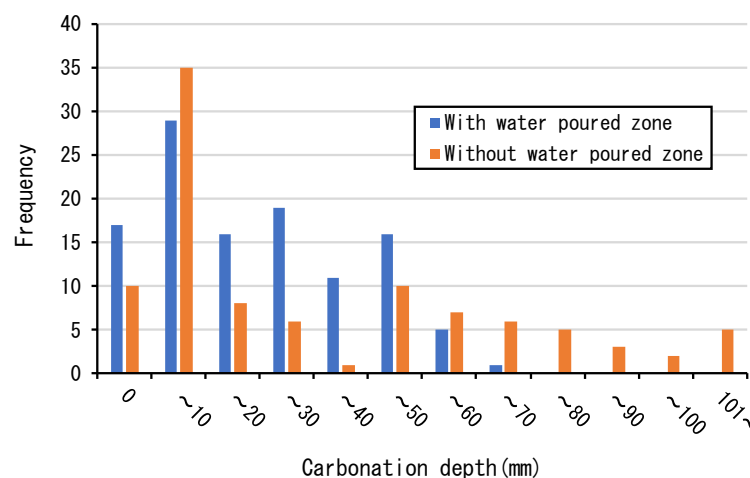


Figure 3: Distributions of carbonation progress

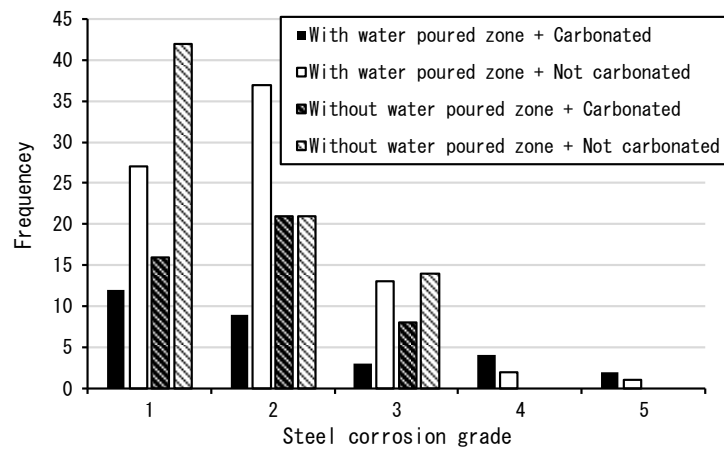


Figure 4: Distributions of steel corrosion rates

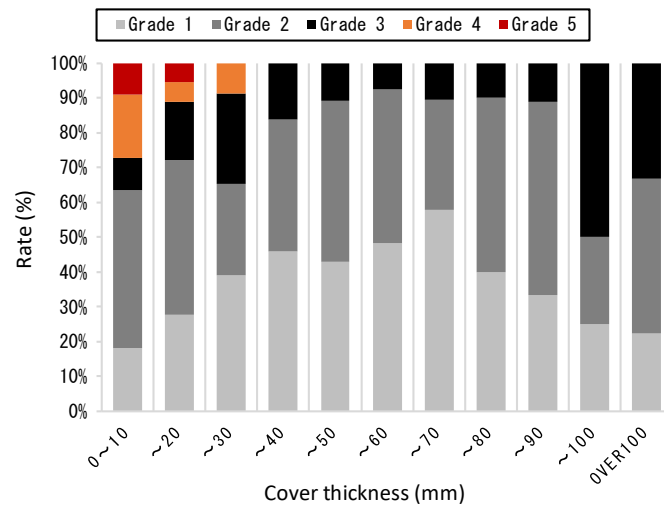


Figure 5: Cover thickness and steel corrosion rate

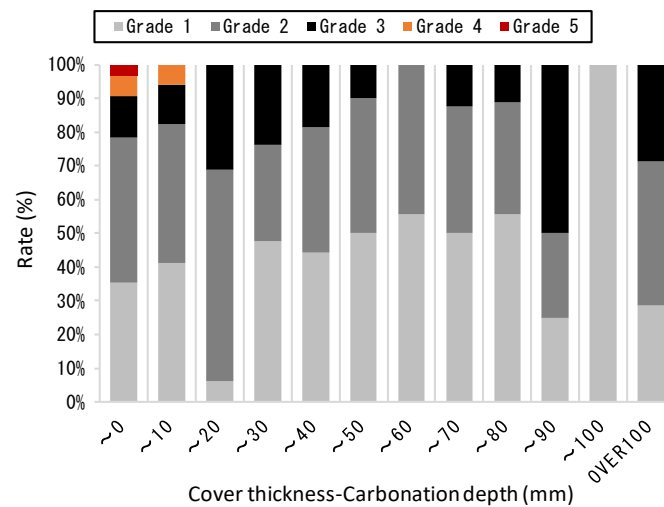


Figure 6: Cover thickness minus carbonation depth and steel corrosion rate

4. MOISTURE CONDITION AND ITS RELATION TO RE-BAR CORROSION

4.1 Electro-chemical mechanism of steel corrosion and observation of re-bar corrosion of carbonated concrete

Moisture and oxygen contribute to steel corrosion in terms of an electro-chemical mechanism as schematically shown in Figure 7. Figure 8 shows the relationship between moisture film thickness and steel corrosion rate under a stabilised relative humidity. It can be seen that a peak of the steel corrosion rate occurs at 10 nm in thickness of the moisture film formed under an 80% relative humidity (R.H.) condition [5], as shown in Table 3 [4]. Oxygen can reach the steel bar throughout the moisture film and sufficient moisture causes steel corrosion. At R.H. < 80%, moisture content is not sufficient to cause steel corrosion and, on the other hand, sufficient oxygen cannot reach the steel bar above 80% R.H.

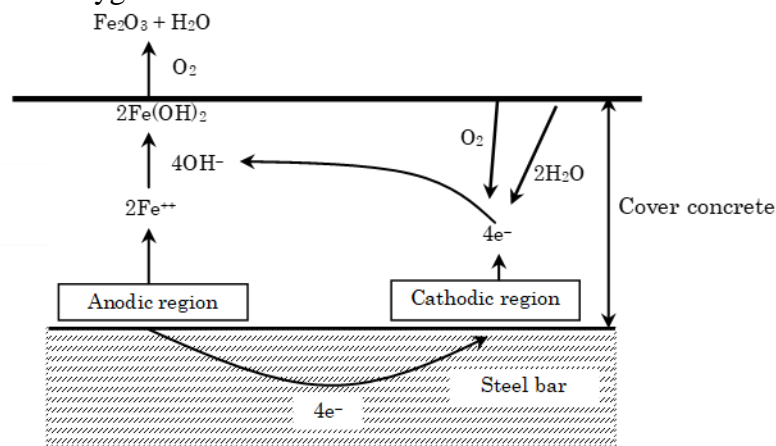


Figure 7: Schematic re-bar corrosion mechanism

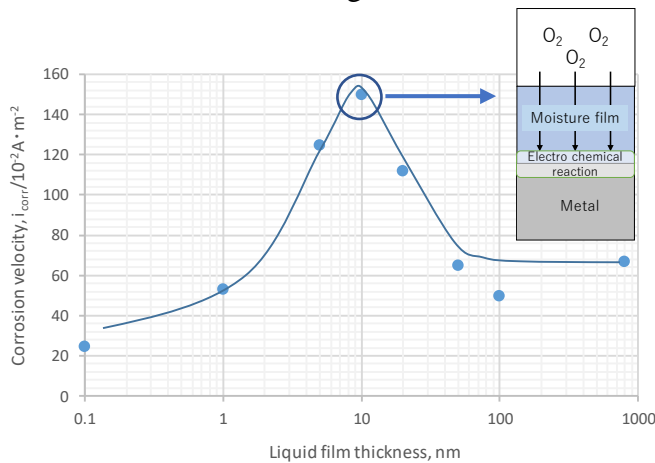


Table 3: R.H. and moisture film thickness

R.H.	Moisture film thickness (nm)
60% R.H.	0.5
90% R.H.	1
80% R.H.	10
100% R.H.	10^3
結露	10^4
Rain	10^5

Figure 8: Moisture film thickness and steel corrosion rate [5]

4.2 Moisture condition of cover concrete in existing RC building

The moisture conditions of cover concrete of existing RC building over 40 years old were investigated. The outline of the building is summarised in Table 4. R.H. sensors were embedded at 10, 30, and 50 mm depth from the concrete surface. Figure 9 shows changes in the R.H. in the concrete. It can be seen that the change in R.H. at 10 mm was remarkable because of the

change in the atmospheric R.H. and that at 50 mm was stable. The result shown in Fig. 8 was obtained under a stabilised R.H. laboratory condition and, in the case of the actual condition of the RC building, the R.H. of the surface concrete was variable. Based on these measurements, the following assumptions were considered regarding re-bar corrosion of the existing RC buildings.

1. Moisture less than 70% R.H. would be insufficient to corrode re-bar.
2. Both moisture and oxygen would be supplied at a stable 80% and a greater than 80% cyclic R.H. condition would cause re-bar corrosion.
3. The aforementioned cyclic R.H. change occurs only at the thin cover layer.

Table 4: Outline of the building

Building type	RC structure
Year of construction (Age)	1968 (49)
Finishing	Exposed and Mortar
Location	Chiba Pref.

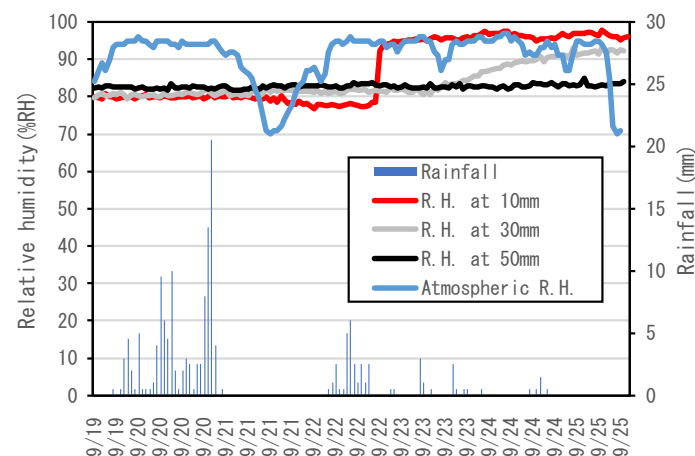


Figure 9: Changes in R.H. in concrete

4.3 Moisture content and its relation to carbonation progress

Figure 10 shows the relationship between R.H. and the moisture content of the concrete. It shows the apparent moisture sorption isotherm of the concrete. It can be seen that a R.H. of 80% on the concrete corresponds to approximately 35% relative mass moisture content. Figure 11 shows the relationship between moisture content and carbonation progress of the concrete in the existing concrete structures. The pore structure of concrete would be a pathway for CO_2 . It can be seen that carbonation progress decreases with an increase in moisture content of the concrete because of the saturation of the pores. The relative mass moisture content of 35% also corresponds to approximately $3.5 \text{ mm/year}^{0.5}$ of carbonation verbosity. The value of $3.5 \text{ mm/year}^{0.5}$ means approximately 24.7 mm in the progress of carbonation depth at 50 years old based on the square root time theory. If the concrete member has a regulated cover thickness greater than 40 mm, more than 80 years would be needed for the carbonation to reach the re-bar.

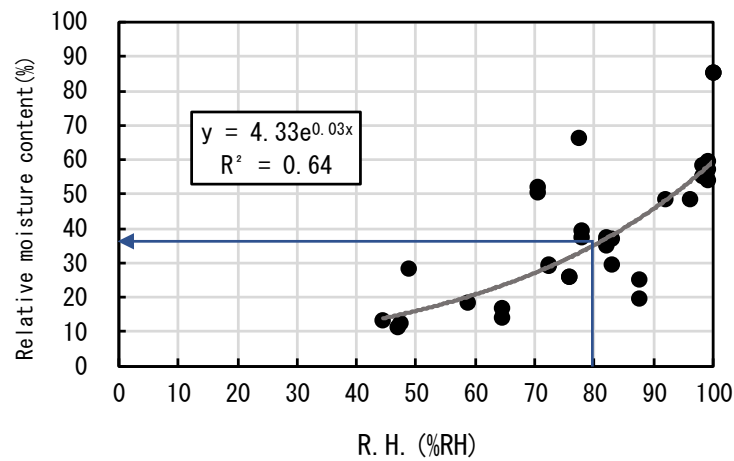


Figure 10: Relationship between the R.H. of concrete and the moisture content

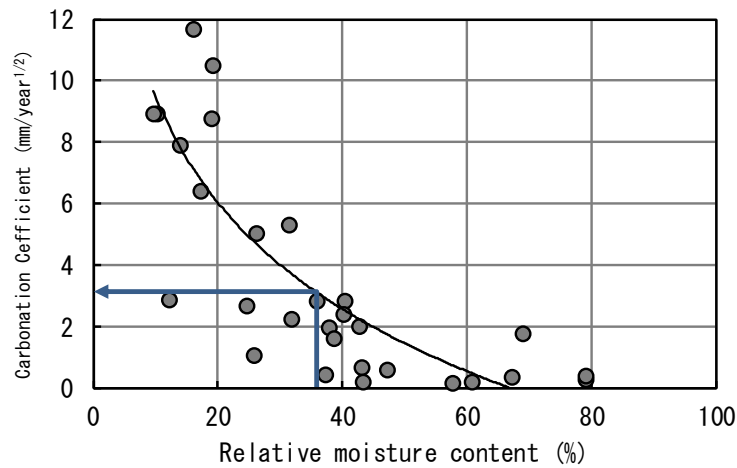


Figure 11: Relationship between the moisture content and the carbonation progress of the concrete

Figure 12 shows relationship between the relative humidity of the concrete and the re-bar corrosion rate. R.H. without a water pouring condition tended to be distributed in a lower humidity area and that with water pouring was more common in a higher humidity area. No re-bar corrosion was observed under a “without water pouring” condition, i.e. a drying condition such as indoors. It was remarkable that re-bar corrosion was not observed in the case of a 0-mm cover thickness in carbonated concrete as indicated by the arrow on the left side of Figure 12. It can be seen that the peak of the steel corrosion rate was observed at approximately 80% R.H. with a water pouring condition (the right side of Figure 12). As indicated in the figure, corrosion rate 4 and 5 in the carbonated concrete had a poor cover thickness of less than 30 mm. As indicated in Figure 9, these layers have cyclic R.H. that provide both oxygen and moisture, causing re-bar corrosion.

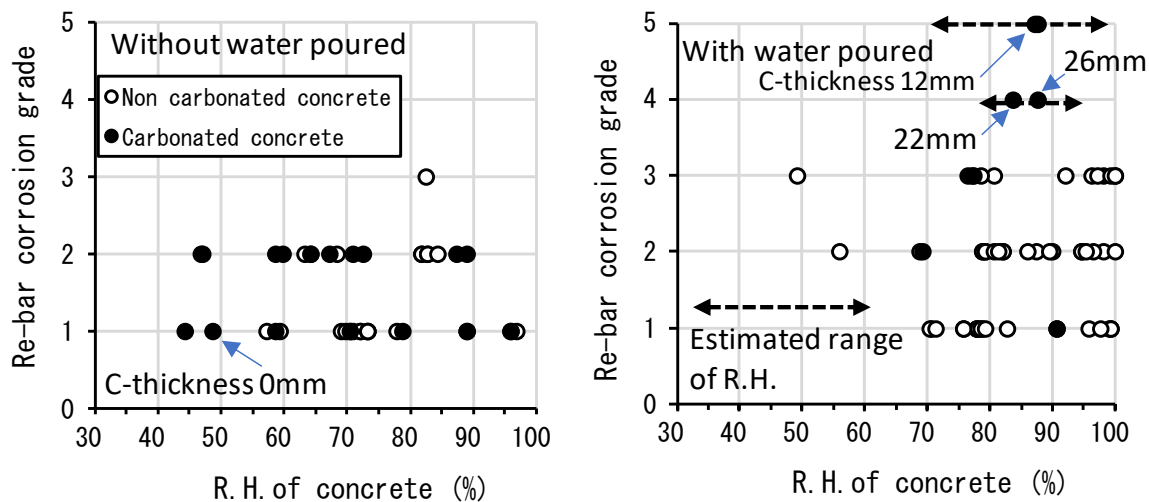


Figure 12: R.H. of concrete and re-bar corrosion rate

5. CONCLUSIONS AND FUTURE OVERVIEW

Regarding carbonation-induced re-bar corrosion, the following conclusion could be obtained through our field survey of existing concrete structures:

- Re-bar corrosion of concrete at low relative humidity was quite minor although carbonation had significantly progressed. This might indicate that not only carbonation but also moisture is key to cause re-bar corrosion.
- Poor cover thickness with cyclic relative humidity around 80% caused serious re-bar corrosion in a carbonated concrete structure.
- The re-bars with appropriate cover thickness were sound at 50 to 80 years old buildings. The truth of carbonation induced re-bar corrosion, with sufficient cover thickness in a water pouring condition, would be mysterious because carbonation itself did not reach to re-bar in all cases.

REFERENCES

- [1] Architectural Institute of Japan: Japanese Architectural Standard Specification for Reinforced Concrete Work: JASS 5, 2015.
- [2] J.A. Gonzalez, S. Algaba and C. Andrade: Corrosion of Reinforced Bars in Carbonated Concrete, Br. Corros. J., pp.135-139, Vol.15, No.3. 1980.
- [3] A.A. Sagues, E.I. Moreno, W. Morris, R.G. Powers and M.C. Andrade: Field and Laboratory Investigation of Concrete Carbonation in Florida Highway Structures, Conference on Understanding Corrosion Mechanisms in Concrete, July 1997, Massachusetts Institute of Technology, USA.
- [4] Japan Concrete Institute: Guidelines for Assessment of Existing Concrete Structures 2014, 2014.
- [5] H. Nagano, T. Doi and M. Yamashita: Materials Science Forum, Vols. 289–292, pp.127–134, 1998.

PRACTICAL APPLICATIONS OF NON-DESTRUCTIVE TESTING IN ASSESSMENT AND REPAIRS OF STRUCTURES

Predrag L. Popovic, P.E., S.E.(1)

(1) Vice President, Wiss, Janney, Elstner Associates, Inc., Northbrook, IL, USA

Abstract

Non-destructive testing is an essential tool in assessment and repairs of structures. Different techniques used in several actual projects are reviewed and presented in this paper.

Keywords: non-destructive testing, impact echo, ground penetrating radar, tomography

1. INTRODUCTION

An important component in the assessment and repair of structural systems is an understanding of the as-built conditions present during and after construction, the cause and extent of subsequent deterioration and distress, and evaluation of the performance of repairs. Nondestructive evaluation (NDE), also referred to as nondestructive testing (NDT), is the practice of assessing critical aspects of structural components and materials without causing significant damage. The practice of NDE combines sophisticated tools, analysis, and experience to provide information about existing conditions which may otherwise be hidden from view. Continued research, technological advances in hardware and software, the need for comprehensive and efficient evaluation of structural systems, and increased specification of testing for quality assurance have led to a gradual increase in the use of NDE worldwide.

Nondestructive evaluation techniques are employed in the assessment of common structural building materials, including concrete, steel, stone, masonry, and wood. Testing methodologies and associated testing techniques for the assessment of structural concrete include reflective ultrasonics (impact-echo (IE), shearwave tomography), through-transmission ultrasonics (ultrasonic pulse velocity (UPV), cross-hole sonic logging), and geophysical/electromagnetic methods (ground-penetrating radar (GPR), conventional and digital radiography (XRay), infrared thermography (IR)). These techniques can be used to identify and assess a variety of internal conditions, including embedded elements (reinforcing steel, prestressing strand, conduit, etc.), internal flaws or distress, material degradation, support conditions, repair and overlay integrity, and member dimensions. Although this article is not intended to provide a comprehensive list or thorough description of each technique, several techniques are introduced in the project examples provided below.

For the evaluation of steel bridge components, NDE techniques are used to detect fracture, fatigue cracking and other distress, and to measure member and coating thicknesses. Magnetic particle, dye penetrant, eddy current, and reflective and through-transmission ultrasonic testing methods are commonly employed. ASTM International and the American Society for Nondestructive Testing (ASNT) provide reference documents and testing standards for a range of methods used in the evaluation of structural steel and steel connections.

The various NDE techniques, due to their particular natures, may lend themselves especially well to certain applications and be of little or no value in other applications. Therefore, choosing the correct method and technique is an important part of the performance of NDE. Additionally, testing typically requires proper calibration and correlation with known conditions at selective locations. For concrete assessment, visible conditions at a limited number of inspection openings and core locations can provide the necessary information to properly evaluate NDE testing results throughout the tested area. Laboratory testing of mock-up test samples with known internal conditions or trial testing performed in the field can also provide the necessary correlation results. The testing of steel components for thickness measurement or flaw detection is typically corroborated with the testing of standards blocks, test samples with known conditions and of similar materials.

Even though some NDE techniques described above have been developed for evaluation of concrete and steel structures, they have been successfully adapted and used in evaluation of stone facade components in high-rise buildings and in other types of structures.

2. APPLICATIONS OF NDT METHODS

2.1 Water Treatment Plant Precast Roof Tees: Investigation and Repair

The project included the assessment and repair of the concrete roof system of a water treatment plant which consisted of cast-in-place concrete framing supporting precast, prestressed concrete double-tee roof beams. The double tees spans measured up to seventy-two feet (22 m) over open water tanks in the treatment areas. Early in the service life of the plant, routine inspections identified wide, diagonal shear cracking in the webs of the double tees at the ends of numerous beams (Figure 1). Additionally, horizontal cracks were observed near the bottom of the stems. The most severe diagonal cracking measured approximately 50 to 100 mils (0.050 to 0.100 in.) wide and extended through the entire web thickness.



Figure 1: Diagonal shear cracking and longitudinal cracking in stem



Figure 2: Tensile bond testing of the applied FRP

Nondestructive testing utilizing ground penetrating radar (GPR) was used to locate and document as-built reinforcing steel, including prestressing strands, conventional reinforcing bars in the dap region, and welded wire (WWR) shear reinforcement in the tee stems.

Ground-Penetrating Radar also known as pulsed radar, is a geophysical nondestructive testing technique for the evaluation of structural elements and materials. The method involves using electromagnetic waves to assess the internal characteristics of the material. GPR surveys performed on structural concrete elements allow for the detection and location of embedded objects, assessment of member geometry, and identification of internal conditions (such as poor consolidation and flaws). The technique involves the use of a high-frequency radar antenna that transmits electromagnetic radar pulses along a discrete longitudinal scan at the surface of the element. Electromagnetic signals are reflected from material interfaces of differing dielectric properties. Signals are collected by the antennae, amplified, and displayed for subsequent interpretation. An example of a horizontal GPR scan collected on the lateral face of a stem along with an elevation view of the stem showing the embedded reinforcing is provided in Figure 3. Structural calculations confirmed that shear reinforcing was required and the beams were under-strength. GPR was a cost-effective, reliable, nondestructive approach that not only identified the problem, but helped define the scope of required repairs.

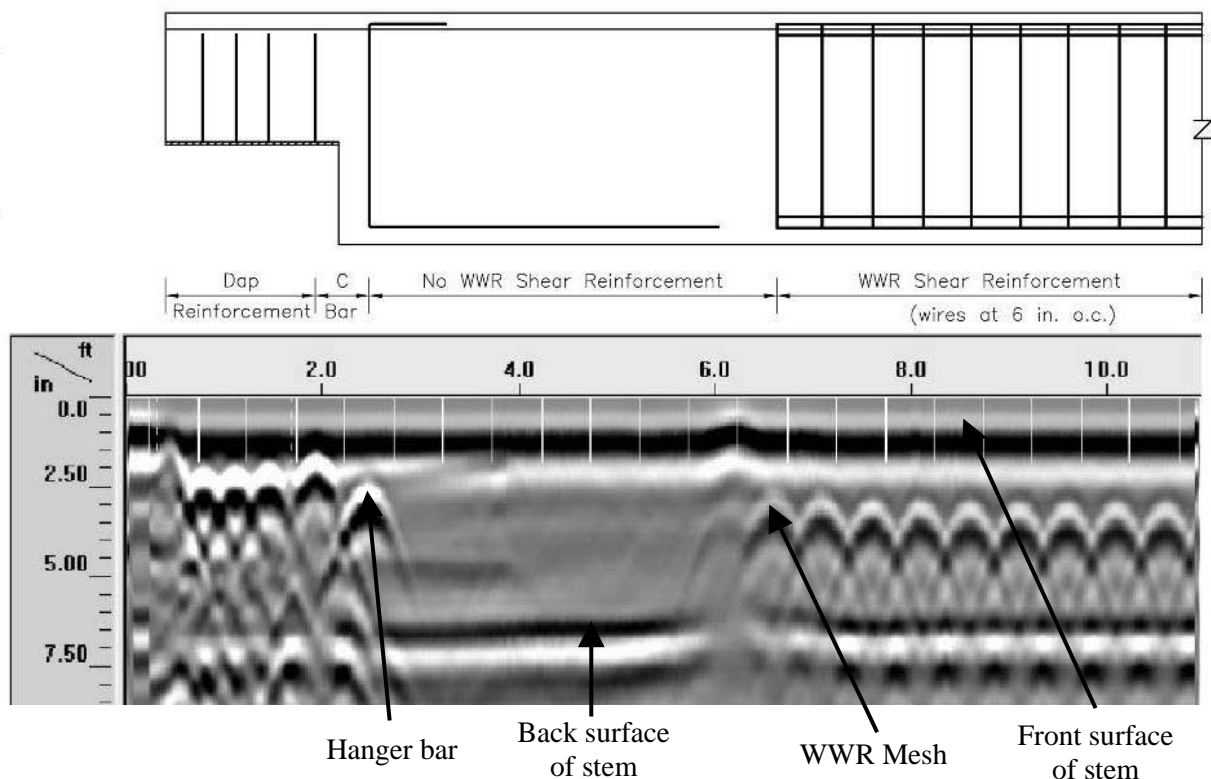


Figure 3: Elevation view of double tee stem and as-built reinforcing (top) and longitudinal GPR scan

The selected repair concept for the double tee stems involved installing vertically-oriented, bonded carbon fiber sheets (FRP) to the sides of the stems to supplement the shear capacity.

This repair approach provided a lightweight, economical solution which allowed for completion of repairs while the plant remained operational.

During the construction phase of the project, each double tee stem was evaluated with GPR ahead of repairs to confirm as-built location of reinforcement and define the required length of FRP repair. Various conventional nondestructive evaluation techniques were used to ensure the quality of the FRP application during and after completion of the repairs. Concrete surface preparation quality was evaluated by tensile pull-off testing prior to FRP installation, ensuring that the surfaces were adequate to properly bond the FRP and result in fully composite structural behavior. Tensile bond strength testing is a commonly used and accepted practice for evaluating the placement of concrete repairs, structural overlays, bonded strengthening materials, and cementitious toppings. Adhesion of the applied FRP was evaluated by acoustic hammer sounding all surfaces of the applied FRP. Unbonded areas of the FRP were injected with additional epoxy saturant to provide adequate bond. The quality control program also included tensile bond strength testing of the bonded FRP (Figure 2).

2.2 Court Complex Parking Garage and Plaza: Investigation, Repair and Load Testing

For large-scale concrete repair projects, NDE can provide useful information during the initial assessment phase, during the construction process, and post-construction for quality control purposes. Several NDE methods were used during various phases of a recent structural concrete repair project at a large court complex. The court complex included an attached parking garage which provided over 7,300 sq m of parking on two underground levels, and an above ground plaza supported by the roof slab of the garage. The slab systems were designed as conventionally-reinforced, two-way flat slabs with drop panels at each column. Less than three years after completion of the garage, widespread cracking was reported throughout the elevated slabs supporting the second level of the garage and the exterior plaza level.

An assessment into the extent and causes of the distress included comprehensive visual surveys, delamination surveying using chain-dragging and hammer sounding audible sounding techniques, and nondestructive testing to determine the as-built conditions of the slabs and drop panels. High-frequency GPR testing was performed on the top and bottom surfaces of each bay to determine the depth and spacing of the reinforcing and to determine the as-built thickness of the slabs and drop panels. Results of the testing and subsequent finite-element structural analysis identified widespread deficiencies in top reinforcing placement and drop panel thicknesses in the slabs resulting in flexural and shear capacity deficiencies of up to 45%.

An economical repair approach incorporating supplemental concrete column capitals and drop panels at each column and strengthening of selected slab spans using FRP was selected. The conventionally-reinforced square capitals and supplemental drop panels were doweled into the top of the existing columns and were poured using a concrete mix design which allowed the repair material to be pumped into the forms from below the existing slab. Photographs of a supplemental column capital prior to and after concrete placement is shown in Figure 4.



Figure 4: Column capital prior to and after concrete placement

In order to assess contact and ensure adequate load transfer between the existing slabs and drop panels and the supplemental column capitals and drop panels placed below, nondestructive testing was used extensively during the construction phase of the repair. Reflective ultrasonic testing using the Impact-Echo method was performed at each repair location to assess the repair interface and identify areas at which contact was not adequate. Impact-echo (IE) testing is a nondestructive evaluation method based on the spectral analysis of reflected waves. IE testing of concrete elements can detect the presence and approximate depth of internal flaws, such as honeycombing, delamination, planar cracking and cold joints, or to measure overall member thickness. The method involves introducing mechanical energy, in the form of a short pulse, on the surface of a structural element using a small steel impactor.

For repair locations where the top surface of the slab was accessible, IE testing was performed from the top surface on a 15 cm testing grid incorporating the entire repaired areas below. Signals were collected and analyzed at each test grid location to identify signal reflections from the original bottom surface of the slab (areas that were not well bonded to the repair capital) and those reflected from the bottom surfaces of the new capital beyond. For repair location beneath the plaza, where the top surface was not accessible, testing was performed on the diagonal faces of the new capitals. The test locations with inadequate contact with the existing slab are shaded and the areas to be epoxy injected are indicated by the black dots in Figure 5. Coring was performed to the repair interface at selected locations to confirm the results of the nondestructive testing. Areas that were identified as having inadequate contact at the repair interface were injected with a low-viscosity epoxy. Upon completion of this process, additional quality control testing using IE was performed at selected locations to confirm that the epoxy injection provided adequate contact at the repair interface.

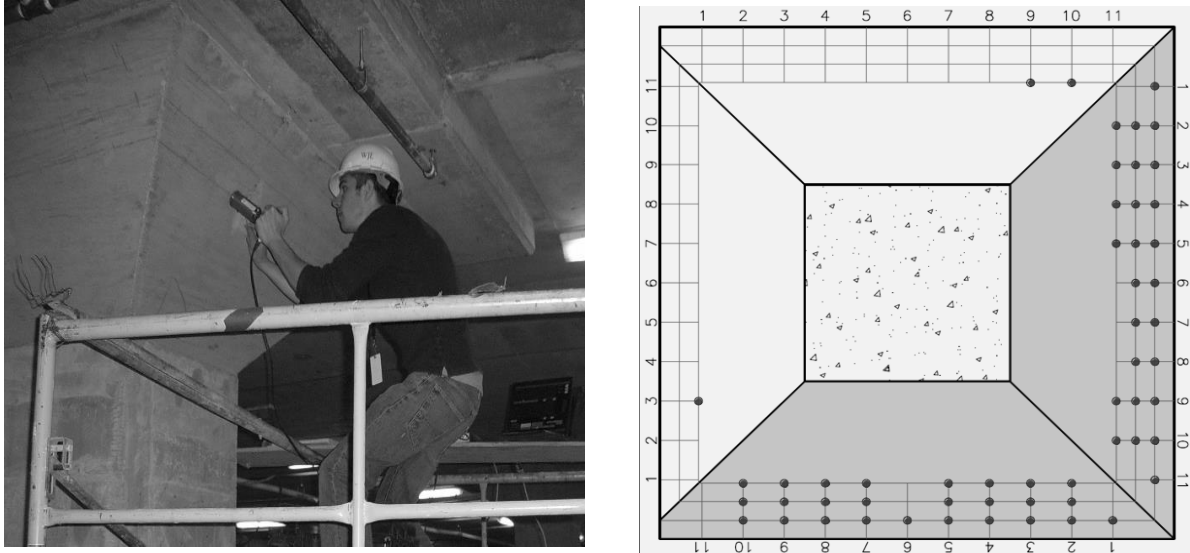


Figure 5: Impact echo testing of the supplemental column capital

Load testing of structural elements and systems can provide for an immediate indication of the structural capacity of system to support maximum anticipated loads. At the completion of the garage repairs, a load test was performed in a selected bay to confirm that the repair provided the required capacity to support gravity loads. The load test was performed in accordance with the code requirements. A load test set-up and load-deflection plot at one of the gage locations during this load test is shown in Figure 6. Results of the load test indicated that the maximum measured deflections and the recovery of the system were within applicable deflection limits.

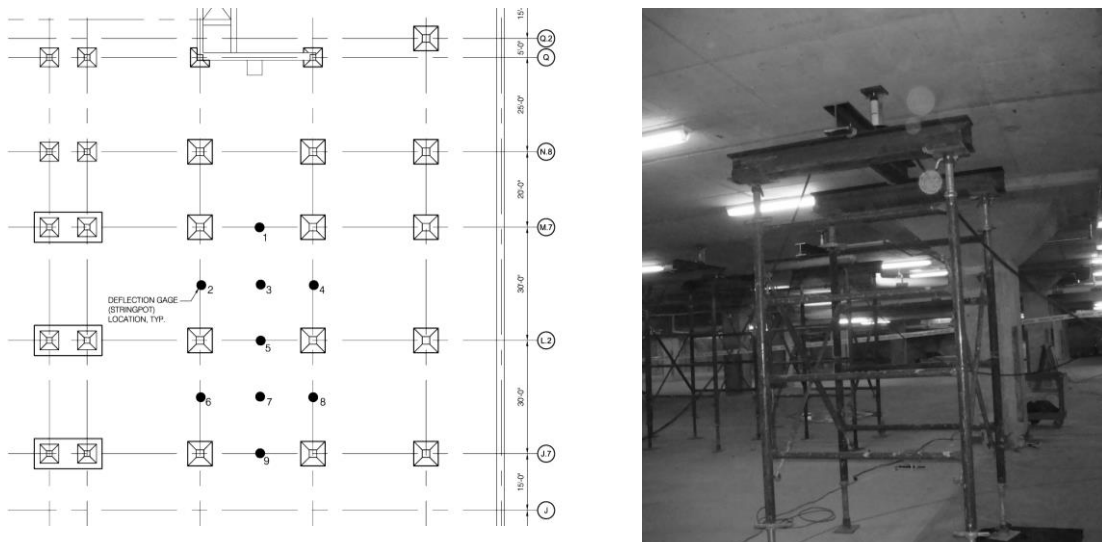


Figure 6: Load test set-up and load-deflection results after completion of slab repairs

2.3 Assessment of Post-Tensioned Bridge Elements

Nondestructive testing methods are commonly used for condition assessment of bridge components. Recent efforts have been focused on the use of NDE methods to evaluate post-tensioned tendon systems within precast and cast-in-place concrete box girders, pre-cast concrete bulb tees, and concrete bridge decks. The primary concern with respect to the post-tensioning tendons is voiding due to incomplete grouting and separation of water from the grout mix. The discovery of failed post-tensioning tendons in four bridges in Florida between 1999 and 2000, and earlier post-tensioned bridge failures in Europe, brought to light deficiencies in grouting procedures and materials for this class of bridge. The effectiveness of traditional corrosion assessment methods such as half-cell potential and corrosion rate measurement are limited due to encasement and shielding of the tendons within the ducts.

A promising technology based on the principles of reflective ultrasonic tomography may provide the means to assess internal grout conditions within tendon duct systems without the need for extensive destructive testing. Several new devices have been developed which utilize arrays of ultrasonic transducers to produce 3-D tomographic images of the internal conditions within concrete elements. In contrast to conventional reflective ultrasonic techniques, these new devices integrate multiple piezoelectric transducers which emit and receive ultrasonic shearwaves. The most promising of these new testing devices is the MIRA Tomographer system. The MIRA system consists of a transducer array incorporating forty (40) spring-loaded, dry-point contact (DPC) piezoelectric transducers. Each transducer emits shear waves at the surface of the test element at a specified central frequency of 30-100 kHz. Reflected shear waves received by the array are processed by the controlling console. A synthetic aperture focusing technique data processing method is then performed to generate 2-D and 3-D images of the concrete element. The reconstructed images are displayed as a plan view, cross-section, or isometric view. Testing can be performed and interpreted at discrete testing locations or can be collected as a series of individual tests combined and interpreted as scans. The system can be used to measure approximate member thicknesses and to detect embedded elements, internal voids, planar cracking and delaminations, and poorly-consolidated concrete.

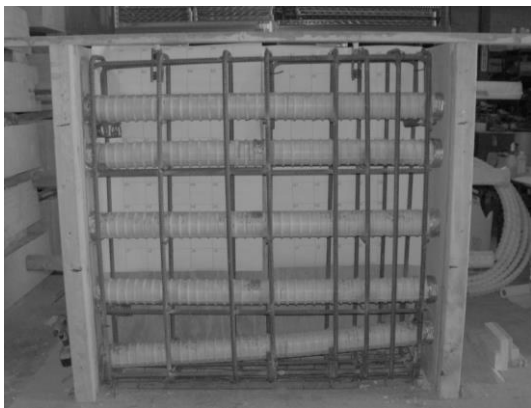


Figure. 7: Mock-up tendon duct wall sample prior to concrete placement



Figure 8: View from below of a post-tensioned cast-in-place box girder bridge

A recent investigation of the post-tensioning tendon systems at four bridges on the island of Oahu in Hawaii combined visual assessment, nondestructive evaluation, targeted inspection

openings, and material sampling. The four bridges and their primary superstructures consisted of a 1,560 m bridge comprised of precast I-girders bridged with haunched piers, a 190 m bridge employing prestressed and post-tensioned concrete I-girders; a 1,680 m cast-in-place segmental box girder bridge (Figure 8), and a 2,075 m precast segmental box girder bridge. Post-tensioning tendons totaling four hundred miles (640,000 m) were used in the construction of these four bridges.

To aid in the development of nondestructive testing methodologies to be employed during field assessment, several mock-up wall samples were designed, constructed, and trial tested in a laboratory setting. The wall samples incorporated a variety of features from the actual bridge structures, including variable wall thicknesses, variable mild reinforcing placement, embedded plastic and steel tendon ducts, and most importantly, variable grouting conditions and strand exposure conditions within the tendon ducts. Trial testing of NDE methods can be an effective way in evaluating the capabilities and limitations of various techniques under controlled conditions to determine the most effective and efficient field evaluation methods.

Field assessment of the bridges comprised of a targeted inspection and testing program focused on evaluating the conditions of the grout and tendons at high points and anchorages within the tendon systems, locations at which there is a higher probability of grout voiding, and water intrusion and corrosion of the post-tensioning strand. Ground-penetrating radar was used to locate the embedded ducts within the walls or girders and to identify relative high points within the duct system (Figure 9). Shearwave ultrasonic testing using an early version of the MIRA Tomographer device was performed along selective lengths of the tendon duct in order to identify possible voiding within the ducts (Figure 10). The test method was able to detect significant voids within the steel tendon ducts embedded within the stem walls of precast I-girders.



Figure 9: Location of embedded post-tensioning



Figure 10: View from below of a post-tensioned cast-in-place box girder bridge

2.4 Assessment of Fatigue Damage in Steel Bridges

During fatigue inspections, a variety of tools can be employed to assist with verifying or locating crack locations. Visual inspection is the most common tool used during inspections. In addition to visual inspection, nondestructive test methods including liquid penetrant, magnet particle, ultrasonics, radiography, and eddy current testing are increasingly being used.

Liquid penetrant and magnetic particle test methods are the most common tools used to examine steel structures for surface cracks. Liquid penetrant requires no power source, is economical, and can be used with limited training. It produces a flaw indication that is much larger and easier for the eye to detect than the flaw itself by providing a high level of contrast between the indication and the background. Liquid penetrant can be messy and difficult to use on a weld toe that is rough.

Magnetic particle testing (MT) utilizes a yoke to generate an electromagnetic field. A crack or defect oriented perpendicular to the flux field produces a discontinuity in the field causing iron filings sprinkled on the surface to highlight the crack or defect location. Figure 11 shows a crack highlighted by MT. MT is only applicable to ferromagnetic materials with defects greater than 3x surface roughness and approximately 0.5 mm long. It also requires more training to properly use and interpret than liquid penetrant.

In a typical inspection, each detail of concern is thoroughly cleaned and visually inspected under a bright light. Paint is removed from around welds if any crack-like indications are observed or if thick paint prevents effective visual inspection. Locations requiring additional examination are then re-inspected using a nondestructive test method such as magnetic particle testing. If a crack-like indication is detected, the weld is typically ground using a die-grinder with a carbide burr or a disk grinder with a sanding disk. After grinding the suspect weld is nondestructively tested again to verify if a defect exists. If possible, shallow weld defects including small cracks, weld overlap conditions, porosity, and slab inclusions may be removed by additional grinding. The welds are then painted using a rust inhibitive paint. Figure 12 shows MT of welded cover plate termination.



Figure 11: Highlighted fatigue crack in web gap using MT method

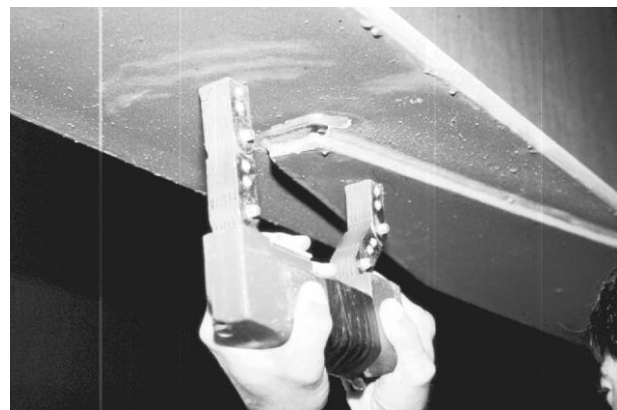


Figure 12: Magnetic particle testing of welded cover plate terminations

Typical cross sections of a structure at locations can be instrumented with strain gages to determine the effective stress range experienced by the structure under normal traffic conditions. This information, when used in conjunction with historical traffic data, is used to estimate remaining fatigue life for the bridge. Details with measured effective stress ranges

above established stress range thresholds suggests with a certain reliability that fatigue crack growth may occur.

Instrumentation and field testing of fatigue-sensitive details to evaluate out-of-plane distortion is a reliable method of determining the potential for crack growth. Test set-ups using linear variable displacement transducers (LVDT) and strain gages can be used to measure small gap distortion and stresses. Field measurements of these test set-ups are usually made using control truck passages. Data is recorded under dynamic load conditions.

As an example, at girder web gaps where the vertical connection plate is not welded to the girder top flange, a LVDT can be used to measure the relative movement of the girder top flange to the girder web gap. Displacement measurements of as little as 0.05 mm provide an indication that web gap cracking is possible. Strain gradient gages or single element strain gages placed on opposite sides of the girder web adjacent the web gap can provide measurements of the magnitude of bending forces occurring in the web place at the web gap.

Instrumentation and field testing can also be used to measure the stresses adjacent to an installed retrofit, as shown in Figure 11. Information from these studies can be used to assess the performance of the retrofit and the retrofit to extend its fatigue life.

2.5 Evaluation of Unbonded Post-Tensioned Structures

During the assessment and repairs of unbonded post-tensioned concrete structures, various non-destructive evaluation techniques are used. Ground penetrating radar or some magnetic device is usually used to locate the post-tensioned tendons before beginning concrete removal.

Prior to repairs, it is sometimes of interest to determine the remaining amount of tensioning force in the tendon. There is a simple method that involves pulling the tendon perpendicular to its length over a distance of about 30 cm and comparing the pulling force with the tendon displacement (Figure 13). Comparing these two values, the tension force in the tendon can be estimated without cutting the tendon.

When the tendon is already cut and spliced during the repair, the question is how to measure the force in the spliced tendon. In some cases, retensioning can be achieved by using a calibrated torque wrench (Figure 14).



Figure 13: Tendon pull test



Figure 14: Calibrated torque wrench

In the tendon splice coupler, a hexagonal nut is turned which brings two sides of the tendon together and increases tension in both sides of the spliced tendon. The number of turns corresponds to a certain tension force which could be recorded.

2.6 Use of Non-Destructive Techniques in Other Applications

Some of the non-destructive techniques originally developed for evaluation of concrete or steel structures have been successfully adapted and used in the evaluation of stone and concrete cladding of the high-rise building facades.

Impact-echo and impulse response testing was performed to identify debonding and separation of a concrete architectural mix that had been integrally cast with structural back-up (Figure 15). In a different facade evaluation project, insitu evaluation of the existing bond and contact between sandstone panels was performed. This evaluation included visual inspection, impact echo, and ultra-shear wave tomography (Figure 16). Using this approach, evaluation was performed of the existing bond and contact for approximately 3,050 panels on the building facade in about 1-1/2 days. It was determined that about 15% of the panels evaluated had inadequate bond or contact to the substrate, and that about 50 of the panels evaluated had no bond or contact and could fall from the building.



Figure 15: Impact echo test of facade panels

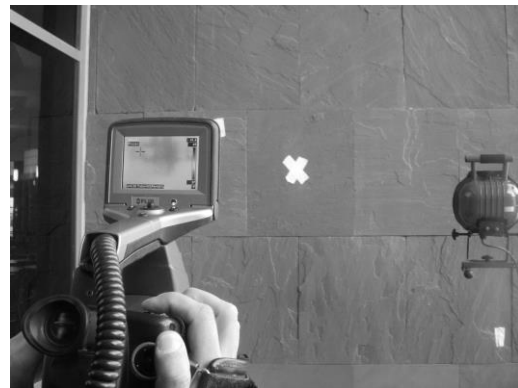


Figure 16: Shear wave tomography used on facade panels

During the exhumation of the remains of King Petar II to be transported to Serbia for state burial, GPR and MIRA systems were used to determine the thickness of the marble panel over his grave as well as to assess the thickness of the concrete slab under the marble panel (Figure 17). This information was used to determine the best method to access and recover the coffin with his body (Figure 18).



Figure 17: Determining the thickness of stone with GPR



Figure 18: Use of vacuum chamber to lift the stone

3. SUMMARY

Non-destructive testing has become integral and a very important tool in the assessment of existing structures as well as during the process of repairs of the structure. Through several examples of projects which involved assessment and repairs of structures of reinforced concrete, precast concrete, post-tensioned concrete, steel, and natural stone materials, use of different non-destructive techniques and equipment were presented in this paper.

REFERENCES

- [1] ACI 228.2R-98, Nondestructive Test Methods for the Evaluation of Concrete in Structures (ACI Committee 228, 1998).
- [2] ICRI Technical Guideline 210.4-2009, Guide for Nondestructive Evaluation Methods for Condition Assessment, Repair, and Performance Monitoring of Concrete Structures (International Concrete Repair Institute, 2009)
- [3] ASTM D6432 Standard Guide for Using the Surface Ground Penetrating Radar Method for Subsurface Investigation, 2011.

**International Conference on Sustainable
Materials, Systems and Structures
(SMSS 2019)**
Durability, Monitoring and Repair of Structures

Durability of construction materials

CHEMO-PORO-MECHANICAL MODELING OF CEMENTITIOUS MATERIALS (DIFFUSION-PRECIPITATION-CRACKING)

A. Socié^a(1,3), F. Perales (1,3) F. Dubois (2,3) and Y. Monerie (2,3)

(1) Institut de Radioprotection et de Sûreté Nucléaire (IRSN), PSN/SEMIA/LPTM, Saint-Paul-Lez-Durance, France

(2) LMGC, Univ. Montpellier, CNRS, Montpellier, France

(3) MIST, Univ. Montpellier, CNRS, IRSN

Abstract

The present work focuses on the impact of the chemical degradations of cementitious materials such as Delayed Ettringite Formation (DEF) on the overall material properties. DEF is an endogenous pathology due to the crystallization of ettringite within voids and cracks. The crystallization pressure in the porous cement paste induces swelling and cracking by differential expansion. The study aims to characterize the evolution of effective material properties (diffusion coefficient, apparent tenacity) with respect to DEF. A non-linear chemo-mechanical modeling is proposed where the entire diffusion-precipitation-pressurization-crack process is solved in a staggered approach. The diffusion-precipitation mechanism is translated by a rough chemical model. The resulting local volume fraction of ettringite is estimated by a finer micro-mechanical-based model using the effective elastic properties of the cement paste. The crack initiation and propagation is estimated with a dedicated cohesive zone model including pressure effect. Some applications of the model are presented.

Keywords: delayed ettringite formation, poromechanics reactive transport, cracking, cohesive zone model, analytical homogenization

1. INTRODUCTION

1.1 Context

In context of the lifetime extension of nuclear power plants, the French “Institut de Radioprotection et de Sûreté Nucléaire” (IRSN) leads research on the ageing of cementitious materials. Previous works dealt with chemo-thermo-mechanical at early age and hydro-mechanical modifications on the long term; these works induce delayed strain and degradation of concrete [1]. Since few years, IRSN has been interested in swelling reactions as alkali silica reaction and Delayed Ettringite Formation (DEF) [2]. The present work focuses on the impact of the DEF on the overall material properties at the aggregate scale (mesoscale), mainly on the diffusion coefficient and on the apparent tenacity of the concrete.

1.2 Delayed Ettringite Formation physics

DEF is an endogenous pathology due to early age chemical reactions. Some elevated thermal conditions induce dissolution of primal ettringite and later on due to moisture environment ettringite can precipitate again within voids and cracks. The ettringite crystallization pressure in the porous cement paste induces both swelling and cracking by differential expansion. These cracks are preferred location for ion diffusion and further ettringite precipitations [3]. It is commonly admitted that DEF and associated swelling depend on:

- Temperature:
 - At early age, depending on the kinetic and the maximum value of heat treatment, swelling varies [4]. It seems that these variations are induced by the quantity of aluminum available [5]
 - During the lifetime of the material, the temperature seems also to play an indirect role (via various chemo-diffusion processes) both on the swelling rate and on the maximum swelling [6]
- Humidity environment: DEF only develops in an environment with a high relative humidity [2]
- Cement composition: water-cement ratio [7], the cement paste fineness and the alkali proportions modify the chemical processes leading to DEF [8]
- Microstructure of aggregates: nature [3] [9], size effect and volume fraction [2] also play a role in the chemo-mechanical coupling that leads to ettringite-induced swelling.
- The experimental swelling depends on chemical reactions (moisture environment leads to alkalis leaching that induces sulfate desorption) and on the material properties. To model this phenomenon, it is necessary to consider coupled chemical reaction, transport of ions, and mechanical response.

1.3 Delayed Ettringite Formation modeling

At least, two types of modeling exist to represent the impact of swelling in a cemented structure:

- Hydro-mechanical coupling: these models couple drying and swelling. The swelling depends on saturation threshold and maximum strain [4] [10]. The work of [10] depicts the difficulty to obtain these values due to a strong dependence on material properties.
- Chemo-mechanical coupling: some models are based on thermodynamic chemistry to evaluate the quantity of ettringite which precipitates and its mechanical impact [5] [6]. Recently a semi empirical chemo-mechanical modeling [11] was proposed to exhibit intelligible results for structure applications [12]

As previously reported by several authors [5] and [10], a strongly coupled modeling should improve predictions of swelling kinetics. To our knowledge, there exists no modeling with a strong coupling between transport properties and mechanical balance applied to DEF. The aim of the study is to characterize the degradation of material properties by crystallization pressure, with a coupled diffusion model within cracks and to estimate the overall mechanical response.

2. CHEMO-PORO-MECHANICAL MODEL

The strongly coupled phenomena suggest a chemo-mechanical modeling. In our model, the entire diffusion-precipitation-pressurization-crack process is solved in a staggered approach.

Before performing a simulation, the cement composition is estimated with a chemical model [13] and the mortar poro-mechanical and diffusion properties are evaluated by analytical homogenization. The chemical model does not take into account alkali and thermal impact. The goal is to estimate the influence of clinker composition and water-cement ratio on effective properties. The steps of the simulation are (Figure 1):

- First, compute the transport of the chemical species. This model follows the framework of [15] and the crack have a resistive impact on crack normal flow, decreases when the crack density increases,
- Second, knowing the ions in solution, the amount of volume of the precipitate is evaluated by a chemical system,
- Third, a local overpressure is calculated to feed the poro-mechanical model and the pressure in the cracks. The crack initiation and propagation are based on a dedicated cohesive zone model [14].

The associated numerical framework is Xper [14]. This software allows to simulate the fracture dynamics of heterogeneous materials, from crack initiation to non-smooth frictional post-fracture.

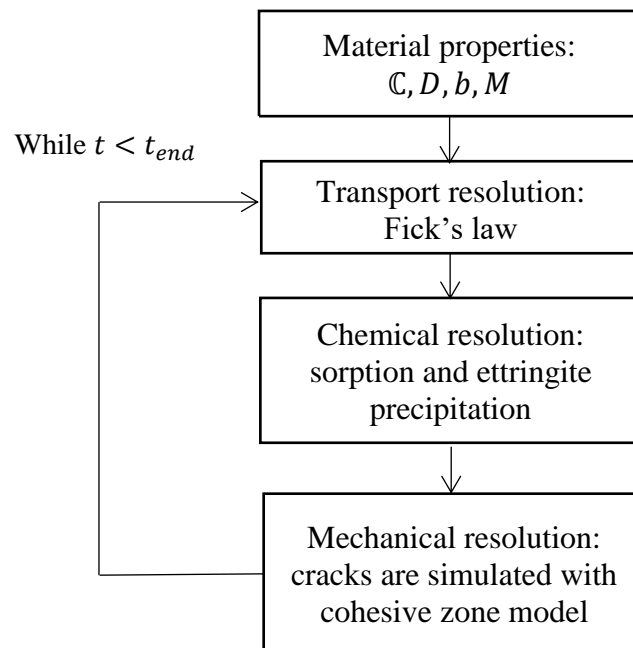


Figure 1: Diagram of the model

2.1 Analytical homogenization

The retained homogenization schemes follow recommendations of the literature [16] [17]:

- Cement paste: Mori-Tanaka for poro-mechanical properties, Maxwell for effective diffusion coefficient
- Mortar: generalized self-consistent scheme for poro-mechanical and effective diffusion properties

2.2 Transport resolution

The concrete is assumed to be immersed. Fick's law is used to solve the transport phenomena:

$$\frac{\delta \phi C_i}{\delta t} = \nabla \cdot (D \nabla C_i) + r_i + \varphi_t \quad (1)$$

where ϕ is the porosity, C_i is the ion concentration, D is the effective diffusion coefficient, r_i is the chemical source term and φ_t is the transversal flux through the crack [15]. The transversal flux depends on diffusion coefficients of the crack D_{crack} , and on the concentration difference between the crack lip:

$$\varphi_t = D_{crack} \frac{\Delta C}{lc} \quad (2)$$

where lc is a characteristic length for the gradient estimate. The transversal flux has a resistive impact on the concentration field. It is assumed that the diffusivity increases with the crack opening $[u_N]$, until the critical value $[u_{cri}]$ is reached [18]. Once this threshold is reached, the diffusivity is the same as in water, $D_0 \approx 10^{-9} \text{ m}^2 \cdot \text{s}^{-1}$:

$$\text{if } u_N < u_{cri} = 100 \text{ } \mu\text{m} \text{ then } D_{crack} = D_0 \frac{[u_N]}{[u_{cri}]} \quad (3)$$

else $D_{crack} = D_0$

2.3 Chemical resolution

The chemical model takes into account sulfate desorption by alkali leaching and ettringite precipitation. We use the desorption model from [5]:

$$C_{(SO_4^{2-})_{ad}} = k C_{SO_4^{2-}} (C_{Na^+})^{0.2} \quad (4)$$

where k depends on temperature and on C-S-H concentration in the solid. The model is restricted to sulfate and aluminate ions.

2.4 Mechanical resolution

The dynamic fracture of heterogeneous materials is studied through a micromechanical multibody modelling. The modelling consists in introducing Frictional Cohesive Zone Model [14] between each adjacent elements of a finite element mesh:

- The bulk behaviour is described with a visco-poro-mechanical model without any damage,
- A frictional cohesive zone model is inserted at element interfaces to take into account cracking and post pressure impact.

2.4.1 Bulk behaviour: visco-poro-mechanical model

The visco-poro-mechanical model describes the impact of the precipitation on the porous viscoelastic matrix. The viscoelasticity is described through a Zener rheological model (Figure 2). This viscoelastic constitutive law is equivalent to a Pointing Thompson model usually used to describe primary creep [1] [12]:

$$\underline{\underline{\sigma}} = \mathbb{C} : \underline{\underline{\varepsilon}} + \mathbb{V}_M : (\mathbb{C} + \mathbb{C}_M) \underline{\underline{\dot{\varepsilon}}} - b P \underline{\underline{I}} \quad (5)$$

where \mathbb{C} , \mathbb{C}_M , and \mathbb{V}_M are respectively elasticity fourth order tensor, Maxwell elasticity tensor and Maxwell viscous tensor. The internal stress is defined by the hydrostatic pressure P and the Biot coefficient b . The pressure law considers only positive value [5] [11] [12]:

$$P = M \langle V_{ett} - \langle V_0 + b \operatorname{tr}(\underline{\underline{\varepsilon}}) \rangle_+ \rangle_+ \quad (6)$$

where $\langle X \rangle_+ = 0$, if $X \leq 0$ and $\langle X \rangle_+ = X$, if $X > 0$, M is the bulk Biot modulus of ettringite, V_{ett} is the volume of ettringite, and V_0 is a connected pore volume threshold.

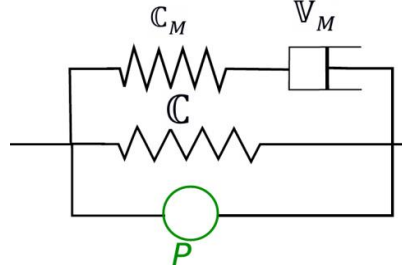


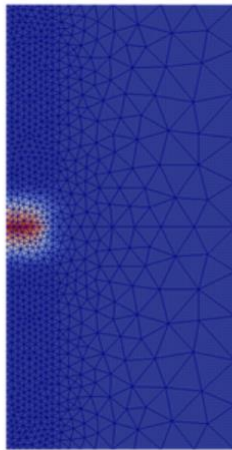
Figure 2: Rheological scheme of the model (Zener model with poro-mechanical)

2.4.2 Interface model: frictional cohesive model with post cracking pressure

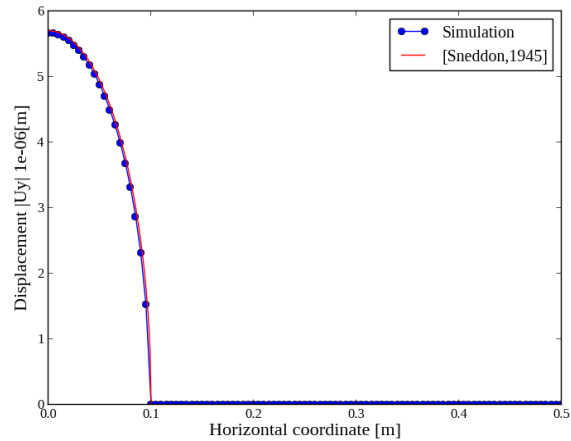
The cohesive model is based on [14] and [19], and considers post cracking pressure. The model takes into account normal and tangential components of the displacement jump through the crack lips $[\underline{u}]$ and gradually introduces a post-rupture pressure $P(t)$, see equation (5). For a crack of normal n , the cohesive stress vector $\underline{\sigma}_{adh}$ depends on a surface damage described by β ($\beta = 1$: healthy interface, $\beta = 0$: broken interface) and on a damageable surface elastic tensor $\underline{\underline{K}}(\beta)$:

$$\underline{\sigma}_{adh} = \underline{\underline{K}}(\beta)[\underline{u}] - (1 - \beta)^\alpha P(t)n \quad (5)$$

where $\alpha > 0$. The implementation of this new cohesive law with progressive transition resistance-damage-swelling is validated on a cubic elemental volume ellipsoidal pressure [20] (Figure 3). The pressure is only taken into account in the mechanical part of the model and evolves with respect to time.



a)



b)

Figure 3: Study of crack opening pressured in an impermeable matrix a) displacement field, only one quarter of cube simulate and b) comparison with analytical solutions [20]

3. APPLICATION

The stress-free swelling of a concrete sample (11 x 22 cm) is studied. The sample has an aggregate volume fraction of 0.3, with radius of 6 mm. The mortar is composed of 50 % of sand and the cement is a CEM I with water-cement-ratio of 0.3. Diffusion boundaries conditions take place only for alkali ions. The sample is immersed in a solution without alkali: an homogeneous Dirichlet boundary condition is applied on all boundaries. Initial concentrations of adsorbed sulfate by C-S-H and free aluminates are assumed. An axial displacement is prescribed along the longitudinal direction. The system is solved in 2D under plane strain assumption. The poro-mechanical and diffusion parameters are estimated by an analytical homogenization technic with a cement composition described in [17]. Viscoelastic properties are evaluated by means of value in the literature (ratio of Young modulus and Kelvin's modulus, and characteristic time). The cohesive parameters are described in [15]. The sample is initially without crack.

The first results show diffuse cracking due to DEF mostly at the interface between mortar and granulates, which seems to agree with experimental observations [4] (Figure 4 a). Ettringite precipitates in the entire sample (Figure 4 b). The localization of precipitation depends strongly on the microstructure: diffusion coefficient aggregates and cracks. The longitudinal displacement field depends on crack localization and boundary conditions (Figure 4 c). The swelling is thus not homogenous in the sample.

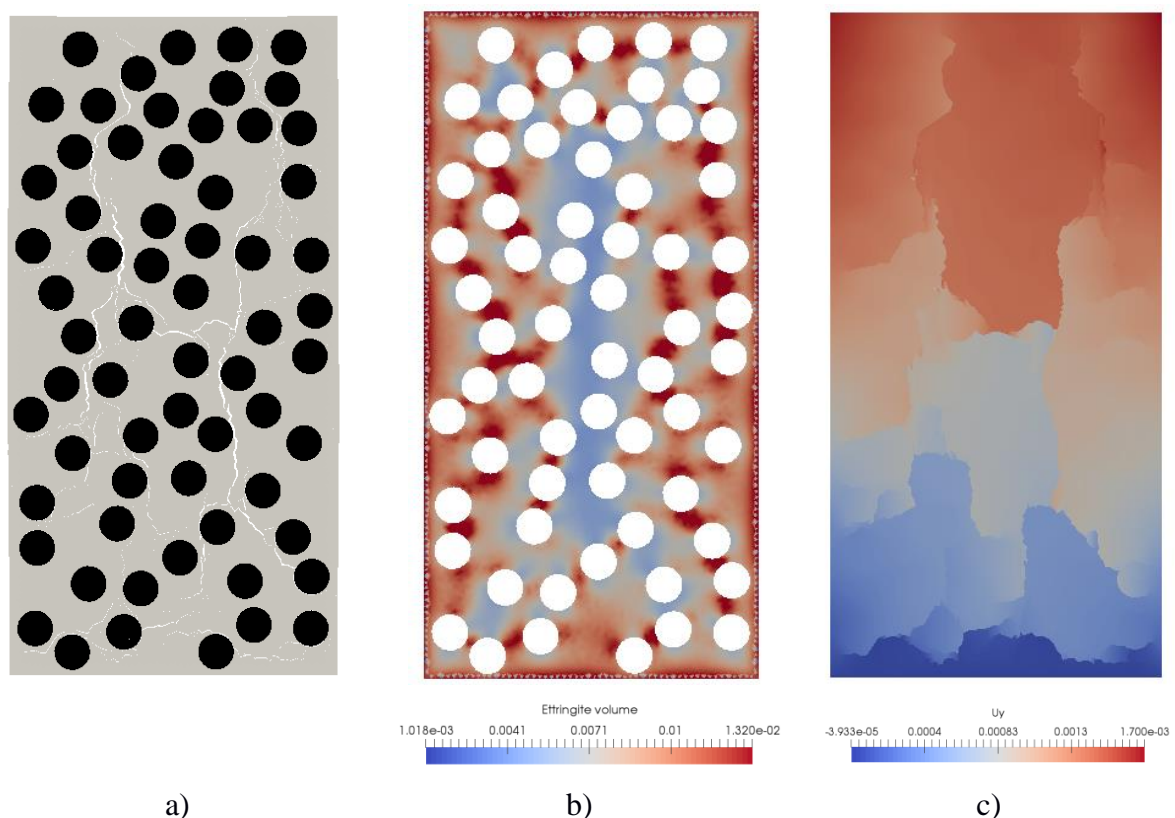


Figure 4: a) cracking profile (crack in white, mortar in gray and granulates in black), b) ettringite volume field [m^3] (granulates in white) and c) longitudinal displacement [m]

The numerical macroscopic expansion (Figure 5 a) is less than in the reported average experimental results of [4]. Initial aluminates concentration and adsorbed sulfate should not be present in enough quantities. Since, in this simulation the cohesive zone model was not coupled to the chemical reaction, the post cracking pressure law is not take into account. At last, the Figure 5 b shows the evolution of the crack density with the macroscopic volumetric strain. It is observed that the density increases abruptly for a value of 0.4%. These cracks could have a real impact on the diffusion properties which can not be neglected. This could be explained by the fact that we do not have a real sigmoid curve for the expansion curve.

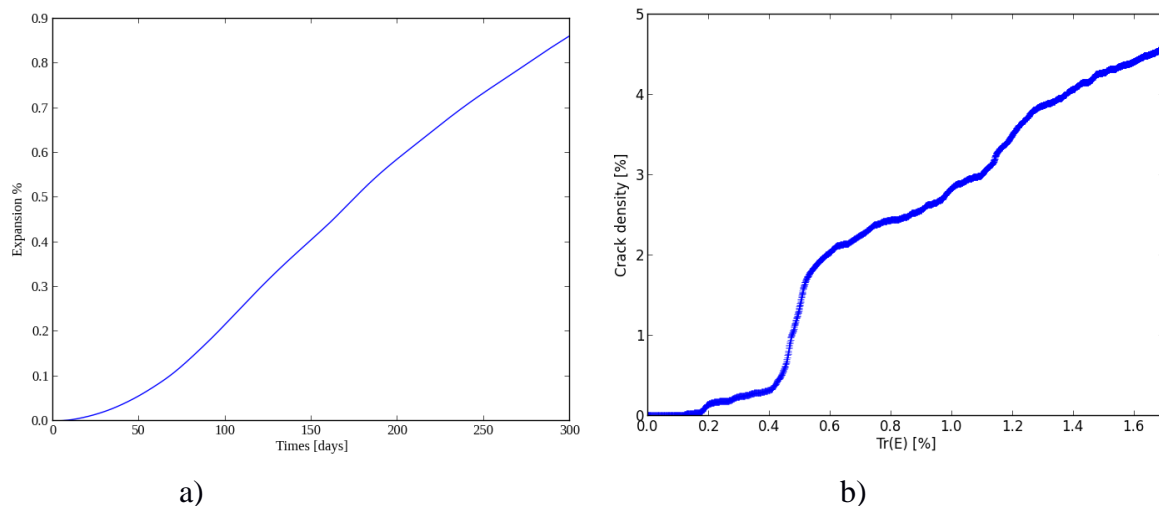


Figure 5: First coupling test, a) expansion measured on the left side of the numerical sample and b) evolution of crack density with volumetric strain

To model the impact of cracks on the macroscopic swelling kinetic, the reactive transport through the crack needs to be modeled as well as the link between chemistry and post cracking pressure law.

REFERENCES

- [1] Hilaire, A., 'Study of delayed strains for concrete in compression and in tension from early age to long term', *PhD thesis Ecole Normale Supérieure de Cachan* (2014).
- [2] Al Schamaa M., 'Study of risk of developing a delayed ettringite formation and its consequences in concrete of nuclear structures', *PhD thesis Université Paris-Est* (2012).
- [3] Brunetaud X., 'Study of the influence of various parameters and their interaction on the kinetics and the amplitude of the internal sulfate attack on concrete', *PhD thesis Université Paris-Est* (2005).
- [4] Kchakech B., 'Effect of temperature and curing duration of early and late heat treatments on the risk of expansion associated with Delayed Ettringite Formation', *PhD thesis Université Paris-Est* (2016).
- [5] Salgues M., 'DEF structural effects modeling : application to concrete dams', *Thèse de Doctorat Université Paul-Sabatier Toulouse III Sabatier* (2013).
- [6] Flatt R.J. and Scherer G.W., 'Thermodynamics of crystallization stresses in def', *Cement and Concrete Research*. **38** (2008) 325-336.
- [7] Leklou N., 'Contribution to the knowledge of internal sulfate reaction', *PhD thesis Université Paul-Sabatier Toulouse III* (2008).

- [8] Pavoine A., Brunetaud X. and Duvet L. The impact of cement parameters on delayed ettringite formation. *Cement and Concrete Composites* **34** (2012) 521-528.
- [9] Malbois M., Divet L., Lavaud S. and Torrenti J.M., 'Experimental study on effects of aggregates mineralogical composition and preservation conditions on def in concrete', Proceedings of an International Conference, Chambéry, June, 2017 (Sweeling Concrete in Dams and Hydraulic Structures, 2017) 106-117
- [10] Martin R.P., Metalssi O.O. and Toutlemonde F., 'Importance of considering the coupling between transfer properties, alkali leaching and expansion in the modelling of concrete beams affected by internal swelling reactions', *Construction and Building Materials* **49** (2013) 23-30.
- [11] Sellier A. et Multon S., 'Chemical modelling of delayed ettringite formation for assessment of affected concrete structures', *Cement and Concrete Research* **108** (2018) 72-86.
- [12] Morenon P., 'Modelling of concrete internal swelling reactions with poro-chemo-mechanical couplings', *PhD thesis Université Paul-Sabatier Toulouse III Sabatier* (2017).
- [13] Thierry M., Platret G., Massieu E. Villain G. and Baroghel-Bouny V., 'Un modèle d'hydratation pour le calcul de la teneur en portlandite des matériaux cimentaires comme donnée d'entrée des modèles de carbonatation', Proceedings of an International Conference, Lyon, April, 2005 (Journées Ouvrage d'Art du réseau des L.P.C).
- [14] F. Perales and S. Bourgeois and A. Chrysochoos and Y. Monerie., 'Two field multibody method for periodic homogenization in fracture mechanics of non linear heterogeneous material', *Engineering Fracture Mechanics*, **75** (2008) 3378 - 3398
- [15] Bichet L., 'Taking into account the transport mechanisms in the fracture of heterogeneous materials : application to the nuclear power plant aging', *PhD thesis Université de Montpellier II* (2017)
- [16] Tognevie A., 'Multi-scale modelling and simulation of the thermo-hydro-mechanical behavior of concrete with explicit representation of cracking', *PhD thesis École Normale Supérieure de Cachan* (2012)
- [17] Bary B. and Beajoui S., 'Assessment of diffusive and mechanical properties of hardened cement paste using a multi-coated sphere assemblage model', *Cement and Concrete Research* **36** (2006) 245-258
- [18] Idiart A.E., 'Coupled analysis of degradation processes in concrete specimens at the meso-level', *PhD thesis Universitat Politècnica de Catalunya* (2009).
- [19] Bisoffi-Sauve M., 'Study of stone masonry building with discrete element method : Caracterization and modeling of themortar joints cohesive behavior', *PhD thesis Université de Bordeaux*, (2016).
- [20] Sneddon I.N., 'The distribution of stress in the neighbourhood of a crack in an elastic solid', *The Royal Society* **187** (1946) 229-258

MAGNESIUM SILICATE HYDRATE FORMATION AT THE SURFACE OF HYDRATED CEMENTS

B. Lothenbach (1,2), E. Bernard (1,3), W. Kunther (4) and K. de Weerd (2)

(1) Empa, Laboratory Concrete & Construction Chemistry, 8600 Duebendorf, Switzerland

(2) NTNU, Faculty of Engineering, 7491 Trondheim, Norway

(3) University of Berne, 3000 Bern, Switzerland

(4) Technical University of Denmark, Department of Civil Engineering, 2800 Kgs. Lyngby, Denmark

Abstract

At the interaction zone of hydrated cements with seawater or with clayey rocks, leaching, carbonation, decalcification of C-S-H as well as the formation of magnesium silicate hydrates (M-S-H) is observed. The formation of M-S-H is related to the relatively high magnesium concentrations (3-60 mmol/L) in seawater as well as in the interstitial solution of clayey rocks and the lowering of the pH at the leached surface of the cement. Leaching and carbonation decrease the pH at the surface and destabilise C-S-H, which accelerates M-S-H formation. The direct study of the properties of M-S-H at surface of hydrated concrete in contact with seawater or clays is complicated by the very poor crystallinity of M-S-H and the presence of other minerals.

Detailed studies on synthetic M-S-H indicated that M-S-H has a sheet silica structure similar to clay minerals and contains in addition to magnesium, silica, and water also some aluminium, calcium and alkalis. Thermodynamic modelling indicated that conditions which favour leaching of C-S-H ease the formation of M-S-H at the surface of mortars and concretes. Thermodynamic modelling was able to highlight the sequence of chloride, sulfate and magnesium accumulation observed at the surface of mortar exposed to seawater.

Keywords: magnesium silicate hydrate (M-S-H), deterioration, leaching, seawater

1. INTRODUCTION

At the interaction zone of hydrated cements with seawater [1-3] or with clayey rocks [4, 5], leaching, carbonation, decalcification of C-S-H as well as the formation of magnesium silicate hydrates (M-S-H) is observed. The formation of M-S-H is related to the relatively high magnesium concentrations (3-60 mmol/L) in seawater as well as in the interstitial solution of clayey rocks and the lowering of the pH at the leached surface of the cement [5, 6]. Magnesium from the seawater or clay interstitial solution reacts with silica from the cement leading to the

formation of M-S-H. The direct study of the properties of M-S-H at the surface of hydrated concrete in contact with seawater or clays is complicated by the very poor crystallinity of M-S-H and the presence of other minerals. Detailed studies of synthetic M-S-H indicated that M-S-H has a sheet silica structure similar to clay minerals [7, 8]. Electron microprobe and SEM/EDS and TEM studies have recently suggested that M-S-H is a tri-octahedral 2:1 phyllosilicate containing not only magnesium, water and silica, but also some aluminium, calcium and iron comparable to smectites [1, 9]. This paper summarises investigations on the structure of synthetic M-S-H and C-S-H, of M-S-H observed in simple model systems and at the surface of hydrated concrete.

2. MATERIALS AND METHODS

M-S-H and C-S-H phases were synthesized as detailed in [7, 10]. MgO, CaO, and SiO₂, were directly mixed with ultrapure water to obtain C-S-H or M-S-H with different Ca/Si and Mg/Si ratios and equilibrated for several months before filtration and drying.

Mortar bars based on PC and PC-slag cements were cured for 28 days before exposure to solutions containing either 4.2 g MgSO₄/l (35 mM Mg) [11] or to seawater (56 mM Mg) [12] as detailed in [11] and [12]. After several months interaction-time the changes in the composition were investigated by SEM/EDS using polished thin sections. Elemental EDS maps of the surface near region of a selection of samples are presented.

The heavily leached zone on marine exposed concrete is often only about 100 µm thick [1] and it is therefore challenging for the performance of bulk measurements. Thus, a set-up was developed which simulated aggravated leaching of concrete in contact with seawater. About 50 g ground cement paste was leached by 100 l of seawater over 6 weeks as detailed in [2].

Thermodynamic modelling of the experiments was carried out using the Gibbs free energy minimization program GEMS. The thermodynamic data for aqueous species as well as for SiO₂, brucite and portlandite were taken from the PSI-GEMS thermodynamic database [13], general cement data from [14] including the data for the M-S-H from [8].

3. RESULTS AND DISCUSSION

3.1 Properties of synthetic M-S-H

For M-S-H prepared from mixing magnesium oxide and silica in water, Mg/Si ratios ranging from ~0.8 to ~1.3 are observed after long equilibration times [7, 8]. ²⁹Si NMR data (see Figure 1) indicate that the silica is arranged in tetrahedral sheets which are attached to octahedral sheets containing magnesium oxides. M-S-H has thus a structure comparable to phyllosilicates such as saponite or hydrated talc. M-S-H, however, has a higher surface area and very small coherent areas, is poorly ordered and contains significant amounts of water and hydroxide groups. TEM pictures of pure M-S-H (see Figure 1) illustrate the homogeneous layered structure of M-S-H [5]. Due to its poorly ordered structure, the XRD shows only very broad humps, which make identification of M-S-H by XRD possible in synthetic samples but very difficult within the complex matrix of cement or mortar samples [5]. The partial deprotonation of the surface hydroxide groups of M-S-H result in a negative surface charge, which becomes even more negative with increasing pH. This charge is compensated by the presence of exchangeable Mg²⁺

ions on the surface of M-S-H. In the presence of alkali and calcium, the exchangeable Mg^{2+} can be replaced by Ca^{2+} , Na^+ or K^+ [15, 16].

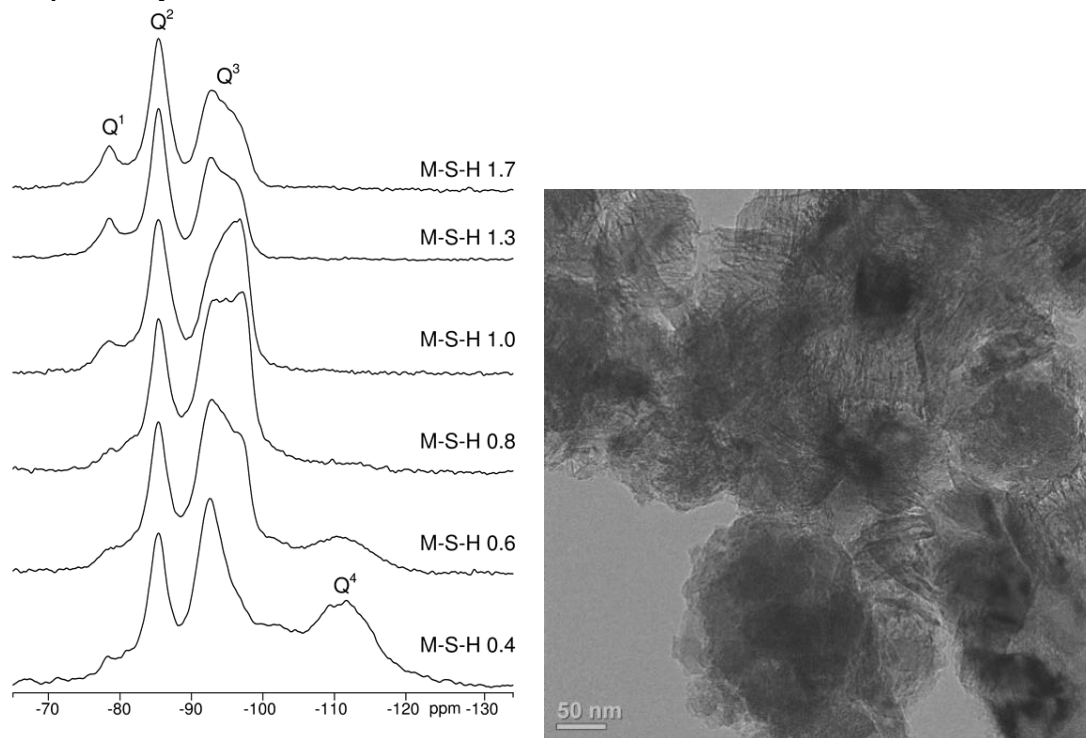


Figure 1: ^{29}Si MAS NMR spectra (9.4 T, $\nu_R = 4.5$ kHz) and TEM (Mg/Si = 0.8) of the synthesized M-S-H samples with total Mg/Si ratios ranging from 0.4 to 1.7. Effective Mg/Si in C-S-H ranged from 0.8 to 1.3 due to the formation of brucite at high Mg/Si and the persistence of silica at low Mg/Si. Reproduced from [8] and [5].

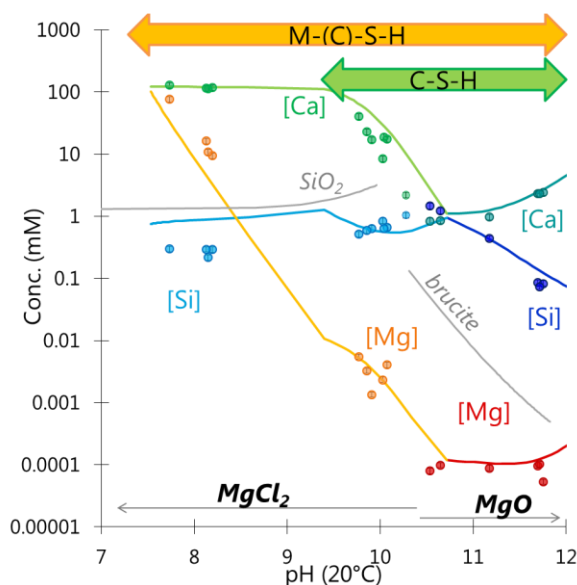


Figure 2: Effect of pH on the measured silicon, magnesium, and calcium concentrations at 20°C. The solubility of M-S-H, C-S-H (solid lines), brucite and amorphous silica (grey lines) were calculated using thermodynamic modelling. Adapted from [10].

Low Ca/Si C-S-H, as present in blended fly-ash or slag cements, is destabilised in the presence of Mg^{2+} , while M-S-H is formed [10]. This process, however, is very slow, particularly at pH values above 10, such that initially often also brucite is formed, which limits the availability of magnesium. If the pH is increased, e.g. by the addition of MgO, very low Mg concentrations result, as shown in Figure 2, while both M-S-H and C-S-H are stable. If the pH is decreased, e.g. by the addition of MgCl_2 , MgSO_4 or in the presence of seawater, a much faster destabilisation of C-S-H as well as relatively fast formation of M-S-H is observed, together with a strong increase of the dissolved Mg concentrations [15]. C-S-H has been observed to be completely destabilised at pH values below 10, as also indicated in Figure 2. This destabilisation of C-S-H at lower pH values in the presence of magnesium and the formation of M-S-H agrees with the observation of M-S-H at the leached interaction zone of hydrated cements with seawater [1] or with clayey rocks [4, 5].

3.2 M-S-H at surface of cements exposed to magnesium sulfate

The formation of M-S-H has been observed at the surface of concrete exposed to seawater, to magnesium sulfate solutions, at the interface with clay minerals and M-S-H is also present as the main hydrate in magnesium silicate cements.

M-S-H formation is observed mainly at the surface of blended cements [5, 11, 17] as shown below in Figure 3 for CEM III/B exposed to magnesium sulfate solutions, while Portland cements with their higher pH values are less affected and rather brucite than M-S-H is observed.

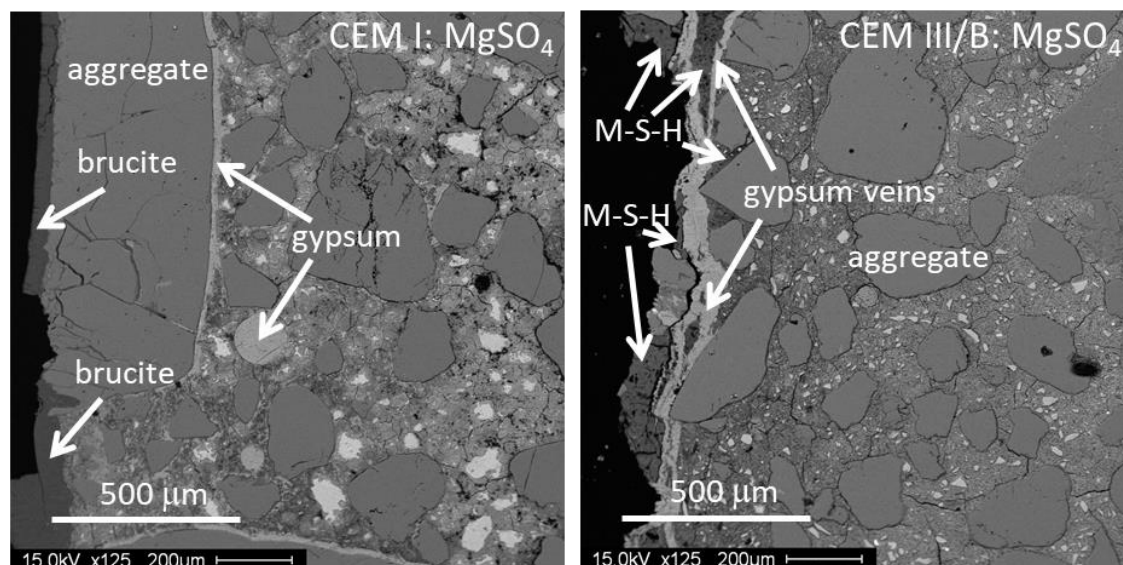


Figure 3: BSE micrographs of CEM I and CEM III/B mortar bars exposed to MgSO_4 solution (4.2 g MgSO_4 /l (35 mM Mg) for 2 years. Adapted from [11].

Thermodynamic modelling has been used to predict the effect of MgSO_4 solution on Portland cement (CEM I) and on cements containing blast furnace slags (CEM III/B). The interaction of the cement with the MgSO_4 solution is mimicked by assuming that the inner part of the specimen “sees” no or very little of the magnesium sulfate solution (as shown on the left hand side of the graphs in Figure 4), while the surface “sees” much more of the magnesium

sulfate solution. Such a simplified modelling approach reproduces well the changes caused by the interaction with the solution, although time and distance cannot be derived.

The modelling indicates that near the surface ettringite and also gypsum formation is expected and in the outermost area, in addition brucite and M-S-H can be present for CEM I, where the Portland cement imposes a pH above 10.5. For CEM III/B, where a low Ca/Si C-S-H is present, only M-S-H is predicted, in agreement with the experimental observations as shown in Figure 3 and in [11]. Both modelling and experimental data indicate that more M-S-H is formed in the case of the CEM III/B, where the lower pH prevents brucite formation. In addition, M-S-H formation is expected to occur faster at lower pH values such as in the case of CEM III/B cements than at the higher pH of imposed by CEM I cements, as the batch experiments discussed above have indicated a faster M-S-H formation at lower pH values.

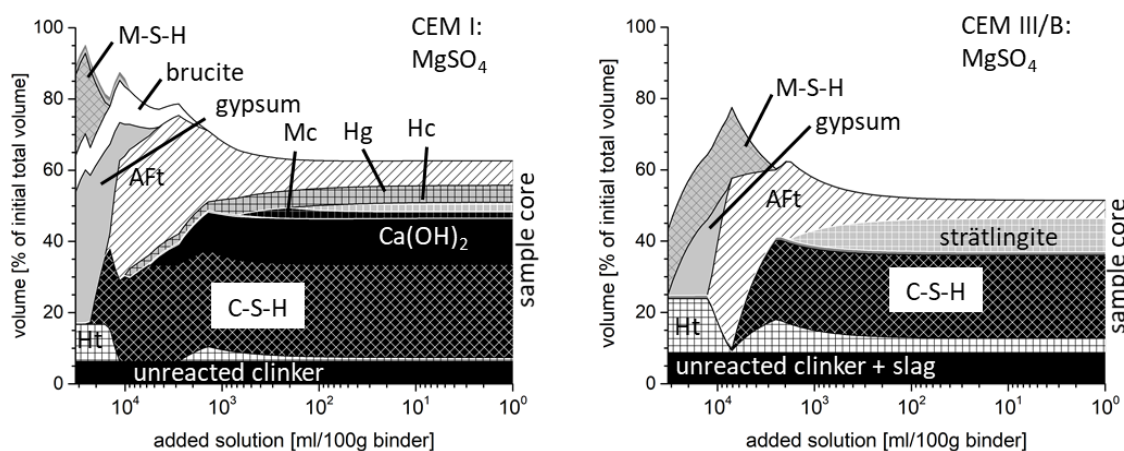


Figure 4: Thermodynamic predictions of the phases changes of Portland cement and blended cements exposed to magnesium sulfate solutions. Adapted from [11].

3.3 M-S-H at surface of cements exposed to seawater

In the presence of seawater, which contains in addition to NaCl also significant amounts of sulfate, carbonates and magnesium, a sequence of changes can be observed near the surface as detailed in [1, 2, 12]. SEM/EDS and microscopic observations of seawater exposed samples have shown a zonation where Friedel's salt is formed at some distance to the surface, followed by ettringite while on the outermost zone M-S-H, brucite and calcium carbonate can be observed [1]. This behaviour can be well reproduced with thermodynamic modelling as shown in Figure 5.

M-S-H formation has been observed at the surface of samples exposed to seawater [1, 2, 12]. Figure 6 shows as an example the BSE image and Mg, Ca and Si EDS-maps of a concrete surface exposed to seawater for 16 years [3]. The Mg enriched zone at surface is about 20-30 μm thick and contains M-S-H. The crack in the middle of the image is filled with brucite and calcium carbonate.

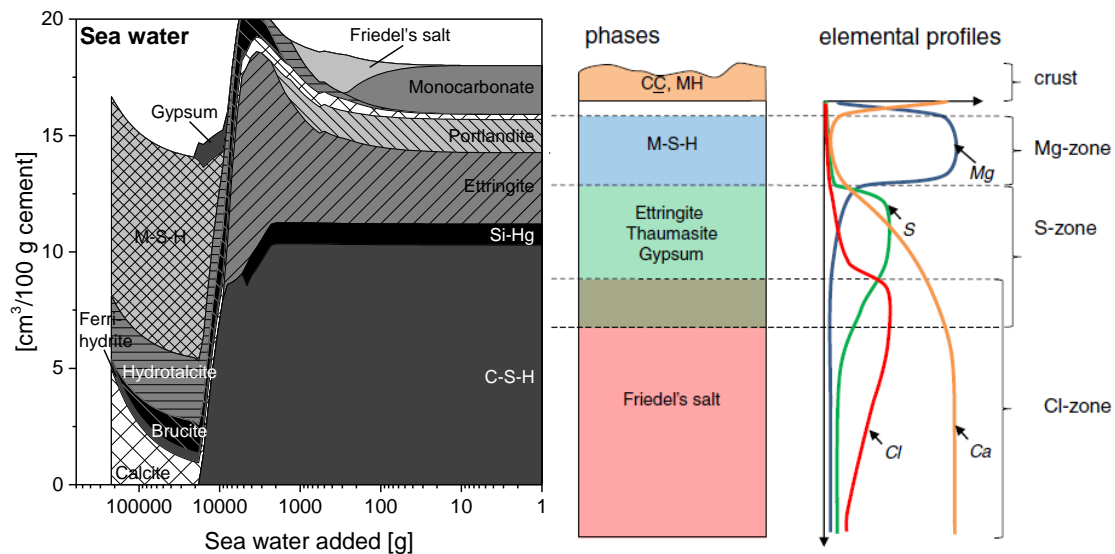


Figure 5: Thermodynamic predictions of the phase changes of Portland cement exposed to seawater (56 mM Mg, 580 mM Cl, 500 mM Na, 20 mM sulfate) reproduced from [12] and observed changes in samples exposed for two years to seawater adapted from [1].

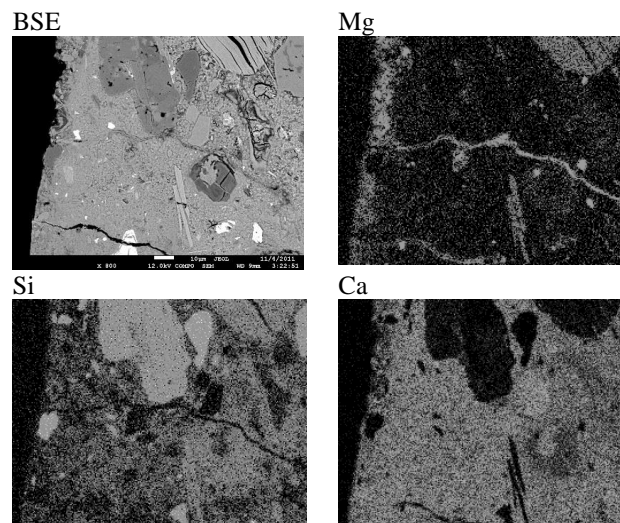


Figure 6: BSE image and Mg, Si and Ca EDS maps of the outermost zone in concrete exposed to seawater for 16 years. The exposed surface is at the left and the white scale in BSE image indicates 10 µm. The Mg and Si rich zone at the surface contains M-S-H. After [3].

M-S-H formed due to seawater exposure was investigated in further detail on a crushed cement paste sample (50 g) which was leached by 100 l of seawater over 6 weeks [2]. The BSE image and SEM-EDS maps of the leached sample are shown in Figure 7. The Mg- and Si-rich particles consist of M-S-H. Note that the M-S-H also contains Al, Ca, Cl and Na which is in agreement with observations on synthesized M-S-H in [15, 16]. Besides M-S-H, the leached sample also contained decalcified C-S-H, calcite, gypsum, brucite and some precipitated NaCl.

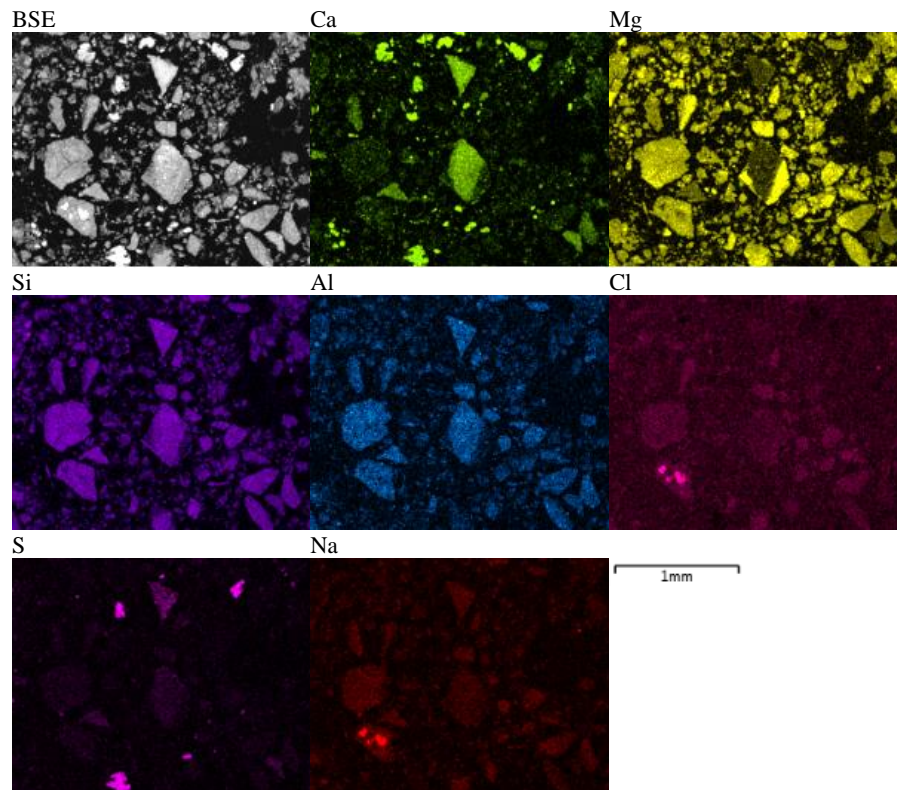


Figure 7: BSE image and EDS maps of cement paste leached with seawater. The scale indicates 1 mm. The Mg and Si rich particles contain M-S-H. After [2].

The observed sequential changes of the hydrates formed upon seawater exposure (see Figure 5) affect also the ability of the cement paste to bind chloride as well as the porosity and thus indirectly the rate of chloride ingress. A recent study which compared chloride ingress in NaCl and seawater exposed samples, however, observed little difference in the measured chloride ingress although different phases were present at the surface [12].

4. CONCLUSIONS

Magnesium silicate hydrates (M-S-H) can form at the interaction zone of hydrated cements with magnesium containing solutions such as seawater or interstitial solution of clayey rocks, often together with leaching, decalcification of C-S-H and carbonation. M-S-H is composed of silica sheets and MgO sheets arranged similar as in phyllosilicates such as saponite or hydrated talc but less ordered. It has a higher surface area and contains significant amounts of water and hydroxide groups. M-S-H formation has been observed by SEM-EDS on the surface of mortars exposed to MgSO_4 and to seawater; its formation could also be reproduced by thermodynamic modelling.

Thermodynamic modelling indicated that conditions which favour leaching of C-S-H ease the formation of M-S-H at the surface of mortars and concretes and highlighted the sequence of chloride, sulfate and magnesium accumulation observed at the surface of mortar exposed to seawater.

ACKNOWLEDGEMENTS

The authors would like to IRSN for the funding of E.B.

REFERENCES

- [1] U.H. Jakobsen, K. De Weerd, M.R. Geiker, Elemental zonation in marine concrete, *Cem Concr Res*, 85 (2016) 12-27.
- [2] K. De Weerd, H. Justnes, The effect of sea water on the phase assemblage of hydrated cement paste, *Cem Conc Comp*, 55 (2015) 215-222.
- [3] K. De Weerd, H. Justnes, M.R. Geiker, Changes in the phase assemblage of concrete exposed to sea water, *Cem Conc Comp*, 47 (2014) 53-63.
- [4] A. Jenni, U. Mäder, C. Lerouge, S. Gaboreau, B. Schwyn, In situ interaction between different concretes and Opalinus clay, *Phys Chem Earth*, 70-71 (2014) 71-83.
- [5] A. Dauzères, G. Achiedo, D. Nied, E. Bernard, S. Alahrache, B. Lothenbach, Magnesium perturbation in low-pH concretes placed in clayey environment—solid characterizations and modeling, *Cem Concr Res*, 79 (2016) 137-150.
- [6] E. Bernard, A. Dauzères, B. Lothenbach, Magnesium and calcium silicate hydrates, Part II: Mg-exchange at the interface “low-pH” cement and magnesium environment studied in a C-S-H and M-S-H model system, *Appl Geochem*, 89 (2018) 210-218.
- [7] E. Bernard, B. Lothenbach, D. Rentsch, I. Pochard, A. Dauzères, Formation of magnesium silicate hydrates (M-S-H), *Phys Chem Earth*, 99 (2017) 142-157.
- [8] D. Nied, K. Enemark-Rasmussen, E. L'Hôpital, J. Skibsted, B. Lothenbach, Properties of magnesium silicate hydrates (M-S-H), *Cem Concr Res*, 79 (2016) 323-332.
- [9] C. Lerouge, S. Gaboreau, S. Grangeon, F. Claret, F. Warmont, A. Jenni, V. Cloet, U. Mäder, In situ interactions between Opalinus Clay and Low Alkali Concrete, (2017), *Physics and Chemistry of the Earth* 99 (2017) 3-21.
- [10] E. Bernard, B. Lothenbach, F. Le Goff, I. Pochard, A. Dauzères, Effect of magnesium on calcium silicate hydrates (C-S-H), *Cem Concr Res*, 97 (2017) 61-72.
- [11] W. Kunther, B. Lothenbach, Improved volume stability of mortar bars exposed to magnesium sulfate in the presence of bicarbonate ions, *Cem Concr Res*, 109 (2018) 217-229.
- [12] K. De Weerd, B. Lothenbach, M.R. Geiker, Comparing chloride ingress measurements from seawater and NaCl solution, *Cem Conc Res*, submitted.
- [13] T. Thoenen, W. Hummel, U. Berner, E. Curti, The PSI/Nagra Chemical Thermodynamic Database 12/07, PSI report 14-04, Villigen PSI, Switzerland, (2014).
- [14] B. Lothenbach, D. Kulik, T. Matschei, M. Balonis, L.G. Baquerizo, B.Z. Dilnesa, G.D. Miron, D. Myers, Cemdata18: A thermodynamic database for hydrated Portland cements and alkali-activated materials, *Cem Concr Res*, (2018) submitted.
- [15] E. Bernard, B. Lothenbach, C. Cau-Dit-Coumes, C. Chlique, A. Dauzères, I. Pochard, Magnesium and calcium silicate hydrates, Part I: Investigation of the possible magnesium incorporation in calcium silicate hydrate (C-S-H) and of the calcium in magnesium silicate hydrate (M-S-H), *Appl Geochem*, 89 (2018) 229-242.
- [16] E. Bernard, B. Lothenbach, C. Cau-Dit-Coumes, I. Pochard, Alkali binding by magnesium silicate hydrates, *J Am Ceram Soc*, submitted.
- [17] W. Kunther, B. Lothenbach, K. Scrivener, Deterioration of mortar bars immersed in magnesium containing sulfate solutions, *Mater Struct*, 46 (2014) 2003-2011.

FORMATION AND STABILITY OF U-PHASE IN CEMENTITIOUS MATERIALS UNDER SULPHATE ATTACK

Yogarajah Elakneswaran (1), Li Chuang (1), Tomohiro Kajio (1), Eiji Owaki (2), Yuka Morinaga (1), Toyoharu Nawa (3)

(1) Division of Sustainable Resources Engineering, Faculty of Engineering, Hokkaido University, Kita 13, Nishi 8, Kita-ku, Sapporo, 060-8628, Japan

(2) Civil Structure and Material Research Section, Civil Engineering Research Institute Technology Centre, Taisei Corporation, Japan

(3) Hokkaido University, Kita 8, Nishi 5, Kita-ku, Sapporo, 060-0808, Japan

Abstract

Cementitious materials have been considered as main component for low- and intermediate-level radioactive waste disposal facilities. The liquid wastes are partially evaporated and solidified with cementitious materials, which leads high concentration of salts such as sodium sulphate (higher than 25 wt %) in the solidified waste. A critical concern of highly concentrated sodium sulphate nuclear waste with co-hydrating of cementitious materials is the degradation of the materials by chemical interaction of sulphate with cement hydrates and crystallisation of sodium sulphate as well as the deterioration due to external sulphate attack. A very high concentration of sodium sulphate solution could induce to form U-phase $[(\text{CaO})_4(\text{Al}_2\text{O}_3)_{0.9}(\text{SO}_3)_{1.1}(\text{Na}_2\text{O})_{0.5}:16\text{H}_2\text{O}]$ and this may cause deterioration to the solidified material. However, the stability of formed U-phase in cementitious materials expose to service aqueous environments has not well understood. In this study, U-phase formation in hydrating white Portland cement (WPC) and slag-blended cement (42 % of cement replacement) and its degradation in water and sodium and magnesium sulphate solutions were examined. The experimental results show that U-phase coexists with ettringite in hydrating both WPC and its slag-blended case in 15% of Na_2SO_4 . Furthermore, the hydration reaction and replacement of slag increase the U-phase formation. The WPC and slag-blended WPC were hydrated in 13% of Na_2SO_4 solution for 28 days before exposure to water and 1300 mmol/L of Na_2SO_4 and MgSO_4 for one month. Solid phases in the specimens from the exposure surface to its core were quantified by XRD/Rietveld analysis. The type of exposure solution and the replacement of slag influence the dissolution of U-phase and consequent formation of ettringite. The diffusion of ions from pore solution to exposure solution destabilises the U-phase in cementitious materials and the degradation.

Keywords: U-phase, sulphate attack, leaching, sodium sulphate low-level waste, XRD

1. INTRODUCTION

Sulphate attack is one of severe durability problems for the cementitious materials in sulphate bearing groundwater or soil. Sulphate ions penetrate the materials and chemically react with cement hydrates form expansive products such as ettringite, gypsum, and thaumasite. The deleterious phases cause deterioration and eventual failure of concrete structures. The sulphate attack has been studied over the past couple of decades and many factors affect the ingress of sulphate ions into the cementitious materials and associated degradation mechanism [1]. The external sulphate attack causes the dissolution and decalcification of cement hydrates due to the leaching of calcium and hydroxide ions from the pore solution upon ingress of sulphate ions. Sodium sulphate crystallisation is another form of sulphate attack called physical sulphate attack, which induces degradation due to formation of mirabilite ($\text{Na}_2\text{SO}_4 \cdot 10\text{H}_2\text{O}$) and thenardite (Na_2SO_4) or their phase changes (mirabilite to thenardite or vice versa) [2]. But, the physical sulphate attack does not involve any chemical interaction with cement hydrates.

Cementitious materials are the key component of low- and intermediate level nuclear waste repositories because of their high-quality performance in service environments to retard the transport of radioactive elements from the barrier to environments and also the low-cost of the materials. A number of studies have been conducted to evaluate the cementitious materials for immobilisation of nuclear waste [3-5]. Sulphate attack is an important durability problem for the cementitious material in nuclear waste repositories. In many nuclear powerplants, seawater has been used a cooling water and the precipitates in the pipes such as NaCl has been removed by sulfuric acid. The liquid wastes are partially evaporated to reduce the volume before solidified with cementitious materials at elevated temperature [6-7]. The use of sulfuric acid and evaporation cause very high concentration of sodium sulphate, more than 25% by weight, in the liquid waste. Therefore, it is necessary to investigate the chemical interaction of sodium sulphate with co-hydrating cementitious materials as well as the performance of solidified waste in service environments.

It has been reported that U-phase $[(\text{CaO})_4(\text{Al}_2\text{O}_3)_{0.9}(\text{SO}_3)_{1.1}(\text{Na}_2\text{O})_{0.5} \cdot 16\text{H}_2\text{O}]$ could form in cementitious material at very high concentration of sodium sulphate [8]. However, to the best of author's knowledge, a very few studies have reported about the U-phase in cementitious materials [7-10]. The conditions in which U-phase form and stable in cementitious materials are not yet well understood. Authors' recent research has determined the thermodynamic properties of U-phase as function of temperature [11]. In this paper, the amount of U-phase formed in hydrating cement and slag-blended cement with sodium sulphate is quantified as function of hydration time. Furthermore, stability of U-phase in the cementitious materials, which is exposed to water and sodium and magnesium sulphate solution, is studied. Finally, the U-phase degradation mechanism and the influencing parameters are discussed.

2. EXPERIMENTAL

2.1 Materials and sample preparation

White Portland cement (WPC) and blast furnace slag were used for experiments. The summary of sample preparation and exposure conditions is given in Table 1.

Table 1: Experimental outline

Cement	WPC	
Slag replacement ratio (%)	0	42
Mixing solution	* Pure water * 13 % Na_2SO_4 solution	
Water to binder	0.6	
Curing condition	Sealed curing for 28 days at 50 °C	
Exposure solution	* Pure water * 1300 mmol/L Na_2SO_4 * 1300 mmol/L MgSO_4	
Exposure period	1 month	
Exposure solution to solid ratio	3:1	

2.2 Experiments

After the curing, the cylindrical specimens were sealed with epoxy resin except the bottom of circular surface which will face to exposure solution. The sealed specimens were exposed to pure water and sulphate solution for one month (**Table 1**). The epoxy resin of the specimen was removed after the exposure period, and the specimen was ground using file from the exposure surface in 2 mm depth. The collected powder was used for XRD measurement to determine mineralogical composition including U-phase. In another experiment, WPC and slag-blended WPC (42 % of slag replacement) were mixed with 15 % of Na_2SO_4 solution with water to binder ratio of 0.6 to determine the amount of U-phase formed as a function of curing period. After the curing, the specimens were ground to fine powders and analysed by XRD. In the Rietveld analysis, clinkers, ettringite, monosulfate, portlandite, calcite, hydrotalcite, and thenardite were used as targets. The known amount of synthesised U-phase was mixed with the hydrated WPC and XRD patterns were obtained to draw the calibration curve for the intensity of U-phase. The amount of U-phase in hydrates was calculated by the ratio of intensity of XRD pattern.

3. RESULTS AND DISCUSSION

3.1 U-phase formation in the hydration of cement with Na_2SO_4

The XRD patterns of hydrating WPC in Na_2SO_4 solution show the presence of U-phase in the hydration products, and Rietveld analysis was used to determine its amount. **Figure 1** shows the XRD/Rietveld analysis of hydrating WPC and slag-blended WPC (42 % of slag replacement). The presence of Na_2SO_4 in the solution could influence the hydration of clinker minerals and the reaction of slag. The addition of Na_2SO_4 in the hydrating solution results in the formation of U-phase and thenardite in addition to the main hydration products such as calcium silicate hydrate (C-S-H) (given as amorphous), portlandite, and ettringite, and the addition limits monosulfate formation. The results show the evidence of U-phase formation,

consistent with previous studies [7, 9], in highly concentrated Na_2SO_4 environments. The U-phase never forms in the hydrating Portland cement in water [7]. Although the types of hydration products are the same in both hydrating WPC and slag-blended WPC, the reaction of slag modifies its amount. The results obtained in this study show that both U-phase and ettringite were existed together with hydration time, but this may be destabilised when exposed to service environments. The amount of produced U-phase as a function of hydration time is shown in **Figure 2** for both WPC and slag-blended cement. The hydration of cement and slag reaction increases the formation, and a partial replacement of Portland cement by slag promotes the U-phase formation at later age.

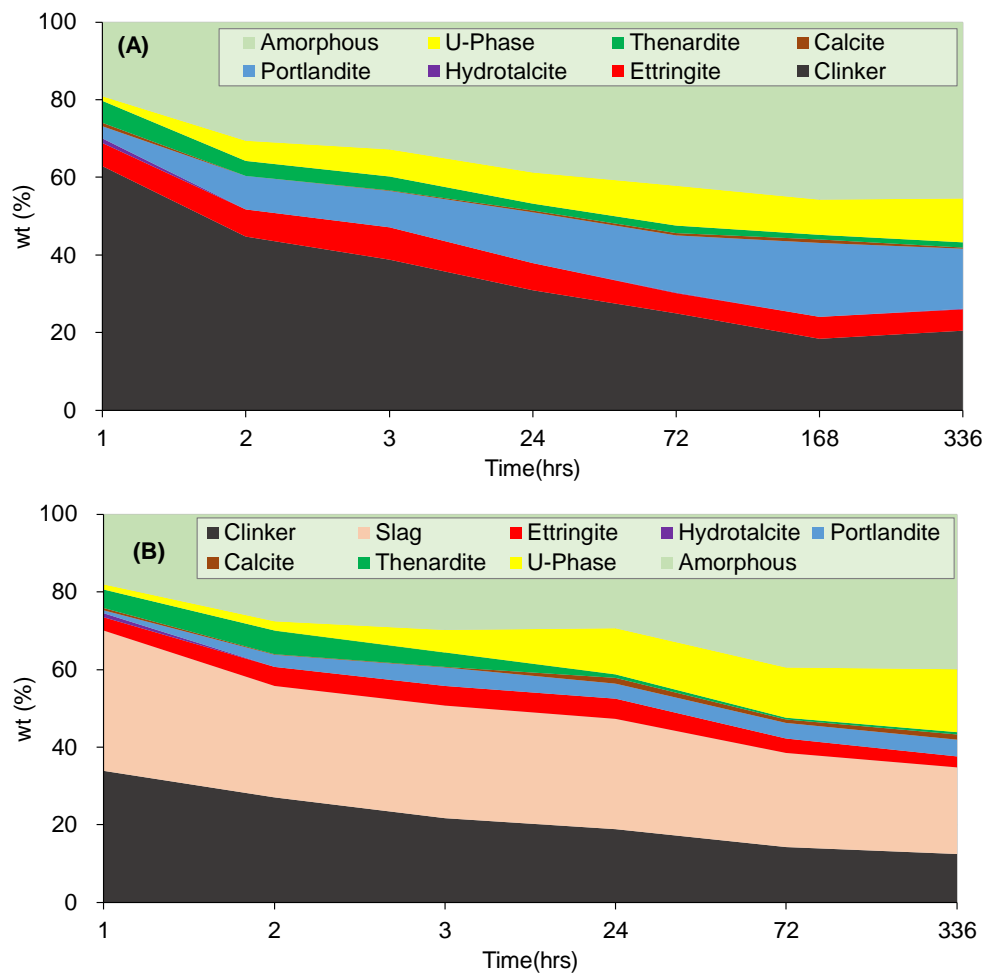


Figure 1: Phase distribution of hydrating, (A) WPC; (B) slag-blended WPC, in 15% of Na_2SO_4 solution

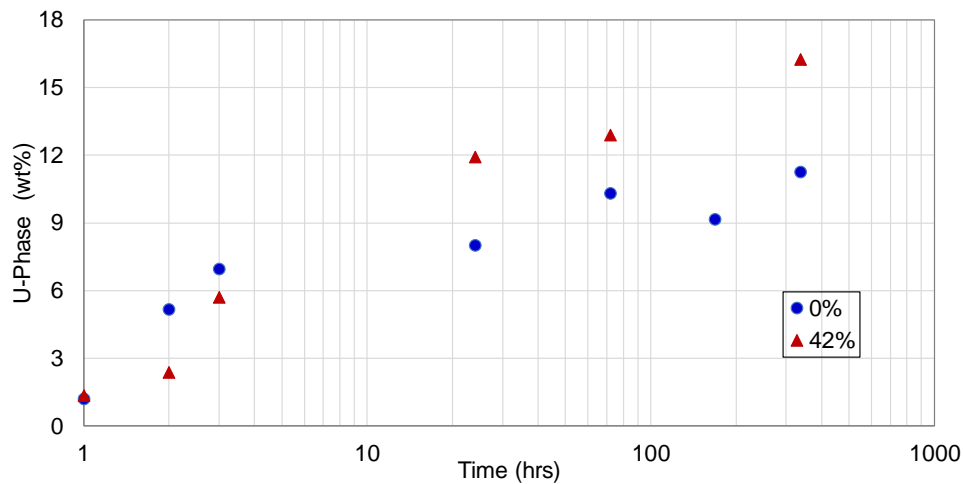


Figure 2: The amount of U-phase in hydrating WPC (0%) and slag-blended WPC (42%) in 15% of Na_2SO_4 solution

3.2 Influence of exposure solution on the stability of U-phase

The quantified solid phase changes in terms of weight percentage in the hydrated WPC and slag-blended WPC, which were hydrated in 13% of Na_2SO_4 solution for 28 days, immersed in water and sulphate solutions for one month are shown in **Figures 3 and 4** as a function of the depth. Similar to the results given in **Figure 1**, C-S-H (indicated by amorphous in WPC, but amorphous given in slag-blended WPC results of C-S-H and un-reacted slag), portlandite, ettringite, and U-Phase are the main hydration products. The replacement of WPC by slag modifies the mineralogy of hydration products as well as their amount during the hydration reaction with sodium sulphate solution. Although a visual damage on the surface could not be observed in both WPC and slag-blended WPC, a significant phase change was obtained at the exposure surface. The dissolution of C-S-H, portlandite, and U-phase and the formation of ettringite and gypsum were observed close to the surface. In the slag-blended WPC, the formation of gypsum could not be observed at the exposure surface due to the small amount of portlandite in the hydration product because of its consumption for the slag reaction, and the portlandite is dissolved completely at the exposure surface.

The U-phase is not stable as the hydrated paste is exposed to water or sulphate solution; it dissolves and transforms to ettringite during the exposure. The type of exposure solution significantly influences the U-phase dissolution and thus ettringite formation. The samples immersed in water show higher instability of U-phase than those exposed to sulphate solution. The diffusion of ions from pore solution to external solution causes the instability of U-phase as it is in equilibrium at very high sodium and sulphate solution [11]. Although the associated cations such as sodium or magnesium in the sulphate do not affect the U-phase instability or ettringite formation, it notably influences portlandite and C-S-H dissolution and gypsum formation. The rate of U-phase dissolution and consequent formation of ettringite is relatively high in slag-blended WPC as compared to WPC.

The formation of U-phase and its degradation mechanism are similar in both WPC and its slag-blended case. However, the high amount of U-phase formation in the hydration products of slag-blended WPC shows comparatively its high dissolution and thus ettringite formation.

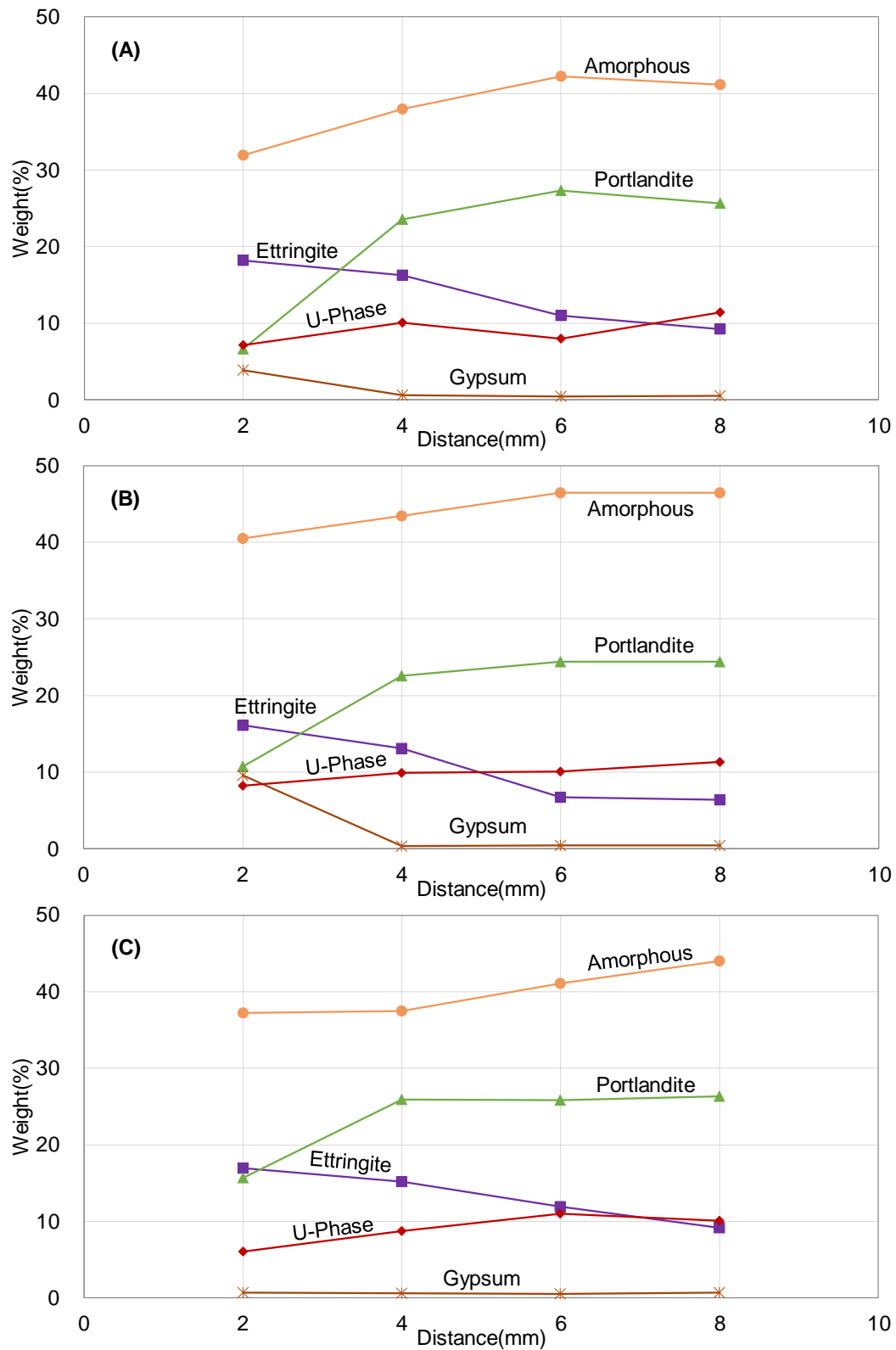


Figure 3: Spatial distribution of solid phases deduced by XRD/Rietveld analysis in WPC exposed to: (A) 1300 mmol/L Na_2SO_4 ; (B) 1300 mmol/L MgSO_4 ; (C) water for one month

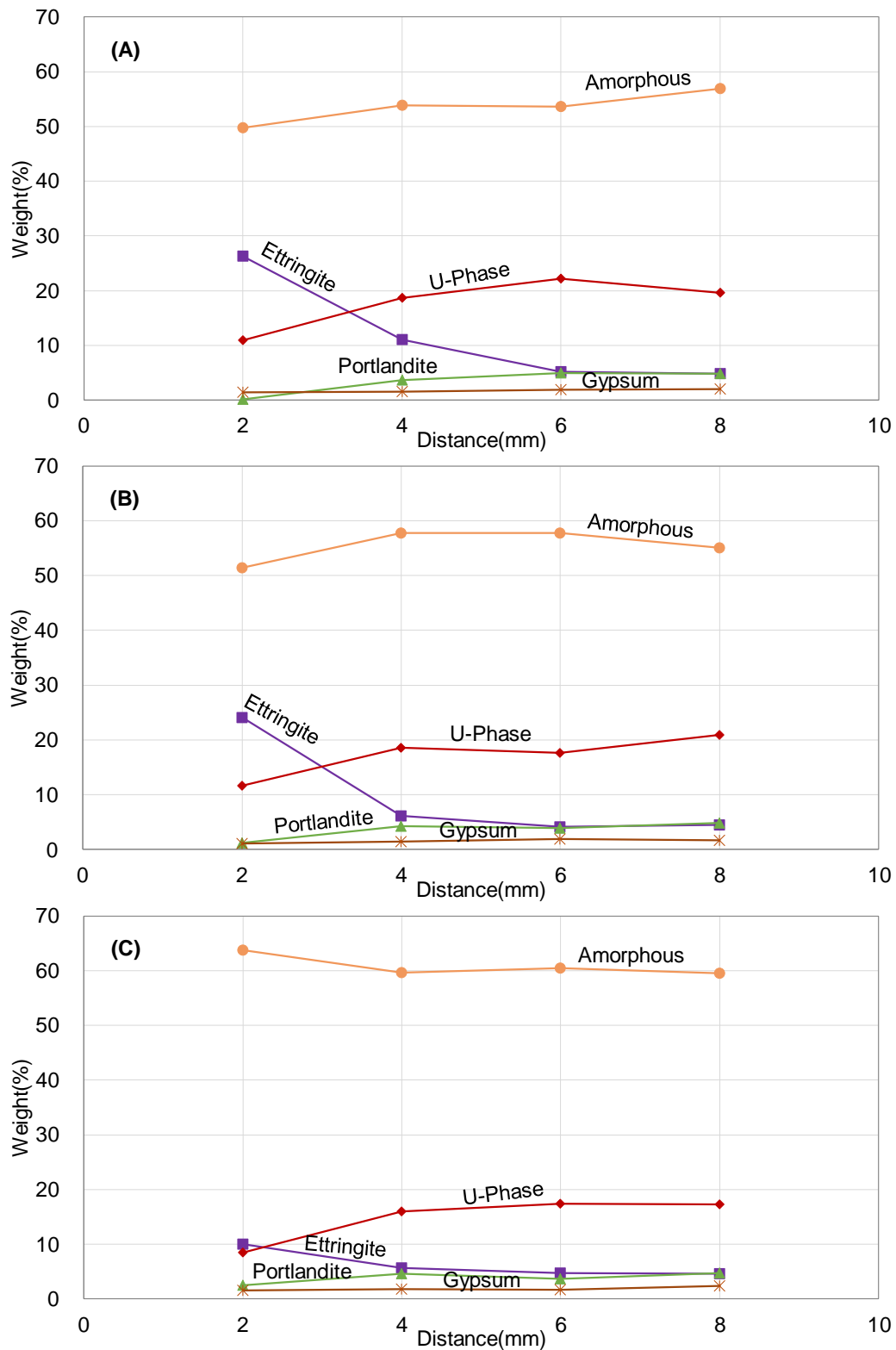


Figure 4: Spatial distribution of solid phases deduced by XRD/Rietveld analysis in slag-blended WPC exposed to: (A) 1300 mmol/L Na_2SO_4 ; (B) 1300 mmol/L MgSO_4 ; (C) water for one month

4. CONCLUSIONS

U-Phase formation in cementitious materials and its degradation when the U-phase containing materials expose to water and sulphate solutions have been studied. The formation of U-phase was identified in the hydrating WPC and slag-blended WPC at high concentration of Na_2SO_4 solution. Both U-phase and ettringite exist together in the materials, and the amount of U-phase increases with the hydration and the replacement of WPC by slag. Spatial distribution of phases in the hydrated WPC and its slag-blended case immersed in water and 1300 mmol/L of Na_2SO_4 and MgSO_4 for one month were determined by XRD/Rietveld analysis. The U-phase is dissolved and converted to ettringite during the exposure period. Exposure to water destabilises U-phase higher than that occurs in sulphate solution due high concentration gradient for diffusion of pore solution ions. A considerable influence of the type of associated cation with sulphate on U-phase dissolution and ettringite formation could not found. The degradation mechanism in both WPC and slag-blended cement is similar.

ACKNOWLEDGEMENTS

A part of this study financially was supported by JSPS KAKENHI Grant No: 18K0429708.

REFERENCES

- [1] Scrivener, K. and J. Skalny, International RILEM Workshop on Internal Sulfate Attack and Delayed Ettringite Formation. Proceeding, *RILEM publications*, (2004)
- [2] Rodriguez-Navarro, C., Doehne, E. and Sebastian, E. How does sodium sulfate crystallize? Implications for the decay and testing of building materials. *Cement and Concrete Research*. (2000) 30(10):1527-1534.
- [3] IAEA, 'Near Surface Disposal of Radioactive Waste', *IAEA Safety Standards Series, Requirements* (1999)
- [4] Lovera, P et al., 'Physico-chemical transformations of sulphated compounds during the leaching of highly sulphated cemented wastes', *Cement and Concrete Research*, **27**, (1997)1523-1532.
- [5] Atkins, M., Glasser, F.P., 'Application of portland cement-based materials to radioactive waste immobilization'. *Waste Manag.* **12 (2-3)**, (1992) 105-131.
- [6] Owaki, E et al., 'Effect of curing temperature on cement paste containing sodium sulfate', *Proceeding of JSCE Annu. Meet*, (2012) 57-58.
- [7] Li, G et al., 'The U Phase formation in cement-based systems containing high amounts of Na_2SO_4 ', *Cement and Concrete Research*, **26**, (1996) 27-33.
- [8] Li, G et al., 'Synthesis of the U phase ($4\text{CaO} \cdot 0.9\text{Al}_2\text{O}_3 \cdot 1.1\text{SO}_3 \cdot 0.5\text{Na}_2\text{O} \cdot 16\text{H}_2\text{O}$)', *Cement and Concrete Research*, **27**, (1997) 7-13.
- [9] Li, G et al., 'Expansion mechanism associated with secondary formation of the U phase in cement based systems containing high amounts of Na_2SO_4 ', *Cement and Concrete Research*, **26**, (1994) 195-201.
- [10] Champenois, J. B. et al., 'Influence of sodium borate on the early age hydration of calcium sulfoaluminate cement' *Cement and Concrete Research* **70** (2015) 83-93.
- [11] Kajio, T et.al, 'Characterization of U-Phase and its prediction in cementitious materials', NUWCEM, October 2018

AIR PERMEABILITY, WATER PENETRATION AND WATER ABSORPTION TO SPECIFY DURABILITY OF ECO-FRIENDLY CONCRETE

Joachim Juhart, Rok Bregar, Gheorghe Alexandru David, Markus Krüger

Institute of Technology and Testing of Building Materials, Graz University of Technology,
Graz, Austria

Abstract

The durability of eco-friendly, clinker reduced concrete is a key factor of its performance. In the presented study, different durability indicators of a newly developed eco-concrete composition (ECO) are tested versus standard normal concrete as reference (REF). The tested durability indicators are open porosity, water penetration depth, rate of water absorption by capillarity and two different methods of measuring air permeability (PermeaTORR AC device versus Testing bubble counter). The ECO mix and in particular its cementitious matrix is designed by a combined filler concept substituting Portland cement partially by properly selected limestone fillers of different grain sizes. The approach is based on a combination of particle packing optimization techniques and the reduction of water demand for certain flowability of the paste. Cement content is below the limits of traditional standards while w/c-ratio exceed such limits. While the performance of the eco-concrete in terms of workability and strength is at least equivalent to the standard mix, ecological impact indicators as global warming potential and embodied energy are substantially improved. Durability indicators overall show nearly equivalent performance of ECO and REF. In detail, the resulting air permeability coefficient tested with a bubble counter differs significantly from the coefficient tested by PermeaTORR.

Keywords: sustainable concrete, durability testing, air permeability, equivalent performance

This work was invited for publication in the open access journal *RILEM Technical Letters*. You can visit the journal and benefit from the full open access to the published articles at: letters.rilem.net.

A CORRELATION BETWEEN VAPOUR DIFFUSION COEFFICIENT AND OXYGEN PERMEABILITY COEFFICIENT OF CONCRETE

Rakesh Gopinath(1,2) and Mark Alexander (2)

(1) Department of Civil Engineering, Central University of Technology, South Africa

(2) Department of Civil Engineering, University of Cape Town, South Africa

Abstract

Durability of reinforced concrete structures is governed, inter alia, by the microstructure and the transport characteristics of the concrete. The “Durability Index” (DI) approach has been developed in South Africa, in order to improve the durability performance of reinforced concrete structures. The South African Oxygen Permeability Index (OPI) test is a DI test based on permeation, and can be used to address deterioration mechanisms such as carbonation of concrete. However, carbonation of concrete also depends on the humidity condition in the concrete pore structure in the range of 50% - 80%. Therefore, it is important to characterise moisture conditions and transport properties in concrete, in order to predict the rate of carbonation of concrete. The paper addresses these issues. For the experimental work, eighteen different concretes were produced by varying the water to binder ratio, curing conditions, and by using fly ash and slag as cement replacements. The specimens were exposed to constant relative humidity (RH) in the laboratory, and the RH profile of the concrete was measured at different time intervals. Idealizing the moisture movement as an evaporation–diffusion process, a correlation between the permeability coefficient based on the OPI test and the water vapour diffusion coefficient was established.

Keywords: Durability, Diffusion, Oxygen Permeability Index (OPI), Carbonation

1. INTRODUCTION

Most of the deterioration mechanisms related to the durability of concrete are governed by the pore structure and transport properties of concrete. A ‘Durability Index’ (DI) approach, based on different test methods to measure the transport-related properties of cover concrete, has been developed in South Africa, aimed at improving durability design of reinforced concrete structures. Each durability index test is based on a particular transport mechanism relevant to a specific deterioration process. (Alexander et al., 2008; Ballim et al., 2009) For example, the South African OPI test is a durability index test based on permeation, and can be

used to address the deterioration mechanism of carbonation of concrete. Details regarding the OPI test procedure and apparatus can be obtained from the UCT Durability Index Testing Procedure Manual (Ver 4.5.1, April 2018).

(https://docs.wixstatic.com/ugd/5586b6_07c436992a6d4768ba2ae42d86a0a88f.pdf)

Moreover, the OPI test method is sensitive to material factors such as choice of material and mix proportions etc., construction factors such as placing, degree of compaction, curing techniques, and environmental factors. The OPI test is also able to assess micro-voids and cracks, presence of bleed voids and channels, and the degree of interconnectedness of the pore structure, all of which influence concrete permeability (Ballim et al., 2009). Studies by Mackechnie and Alexander (2002) showed good correlation between OPI values recorded at 28 days and the depth of carbonation under natural conditions. Furthermore, a carbonation model was developed using the oxygen permeability coefficient (from the OPI test) as a key variable (Gopinath et al., 2017). However the model, in its basic form, is not able to address the impact of drying and wetting cycles, and thus overestimates the depth of carbonation of concrete exposed to rain.

Therefore a moisture model needs to be coupled with the carbonation model in order to address the influence of drying and wetting cycles on the rate of carbonation. Since the OPI can provide permeation characteristics of the concrete, a moisture model with oxygen permeability coefficient as key variable would be very useful to address the influence of drying and wetting cycles. In the present work, an experimental program to measure the moisture profile in terms of RH was developed. Using the test results, a correlation between the oxygen permeability coefficient based on the OPI test and the water vapour diffusion coefficient was established.

2. CONSTITUENT MATERIALS AND EXPERIMENTAL DETAILS

Concrete mixes with different combinations of cement extenders and a range of water:binder ratios (w/b) under varying curing conditions were designed for the present study. The materials used were cement (CEM I 52.5 N, the normal EN 52.5 grade cement); cement additions such as low calcium fly ash (FA) at 30% replacement, and ground granulated blast furnace slag (GS) at 50% replacement; and a constant water content of 170 L/m³. Details of the mix constituents and proportions of the mixes are shown in Table 1.

Table 1: Mix proportions (kg/m³) and permeability coefficient of concrete

w/b	Mix Designation	CEM I 52.5N	FA (30%)	GGBS (50%)	Crusher Sand	Dune sand	13mm Granite	Permeability coefficient (k) from OPI test		
								Curing-X	Curing-Y	Curing-Z
								(m/s)		
0.45	PC	377	0	0	512	341	1000	4.23E-11	7.28E-11	5.47E-11
	PC+30% FA	264	113	0				3.59E-11	8.34E-11	1.13E-10
	PC+50%GS	189	0	189				1.31E-11	8.90E-11	1.19E-10
0.65	PC	262	0	0	581	387	1000	5.77E-11	1.41E-10	2.92E-10
	PC+30%FA	183	79	0				9.86E-11	2.94E-10	6.06E-10
	PC+50%GS	131	0	131				3.56E-11	3.50E-10	5.71E-10

A total of six different concrete mixes were developed, using two different w/b (0.45 and 0.65) and three different binder combinations. Superplasticizer at varying dosage for each mix was used in order to maintain the slump in the range of 90-120 mm. Three different curing regimes (Curing-X, Curing-Y and Curing-Z) were adopted to achieve OPI values in the range of 9.0-10.8 (log scale) at 28 days after casting. Curing-X is the standard 28-day water curing in water bath maintained at a temperature of 23 - 25°C. For Curing-Y; after 1 day of casting, the specimens were covered with plastic for 6 days and thereafter stored in a laboratory environment (20-22°C and 60-70% RH) until 28 days after casting. Curing-Z was adopted to replicate harsh curing practices on site, where the demoulding was done after 1 day of casting and the concrete was left to cure in air, in a laboratory environment (20-22°C and 60-70% RH), until 28 days.

3. TESTING DETAILS

3.1 Oxygen Permeability Index Test

The oxygen permeability index (OPI) test was done as per the UCT Durability Index Testing Procedure Manual (Ver 4.5.1, April 2018). Four concrete discs with 70 ± 2 mm diameter, 30 ± 2 mm thickness are needed. The specimens were acquired by coring a sample beam (cast with the mix proportions given in Table 1) perpendicular to the casting direction at the age of 28 days. Slices of 5 mm on either end of the core were cut off and discarded to avoid any wall effect. From the remaining core, two concrete discs of required thickness (30 ± 2 mm) were cut, one from each end, and the rest of the core was discarded.

Directly after cutting, the specimens were conditioned by placing them in oven at $50 \pm 2^\circ\text{C}$ for 7 days \pm 4 hours. This was followed by cooling the specimens to $23 \pm 2^\circ\text{C}$ in the desiccator for a period of between 2 - 4 hours. The specimen was then placed and clamped on the top of the test chamber and the testing was commenced by introducing oxygen gas in the test chamber of the oxygen permeability index testing apparatus. The test chamber was initially maintained at a pressure of 100 ± 5 kPa and the subsequent pressure drop with time was noted. The D'Arcy coefficient of permeability was then calculated for each specimen from the data obtained. The OPI is expressed as the negative log of the average of the coefficients of permeability of the four specimens (details of the test and calculation: see UCT Durability Index Testing Procedure Manual (Ver 4.5.1, April 2018))

3.2 Moisture Profile Measurement Details

Different techniques are available for moisture profile measurements in concrete. In the current study, the moisture condition of concrete was expressed in terms of relative humidity (RH). The measurement was done using a modified version of the method used by Parrott (1998), on concrete prisms of dimensions 100x100x150 mm, cast using a specially designed mould which contained seven removable steel pins, 7 mm diameter and 80 mm long, with a PVC collar 20 mm diameter and 16 mm long at one end (which was embedded in the concrete after casting) as shown in Figure 1. The pins were arranged parallel to each other and at a distance of 4, 8, 12, 20, 30, 50 and 80 mm from the bottom of the mould. Once the concrete hardened, the steel pins were removed by unthreading them from the PVC collar, leaving a cavity of 7 mm diameter and 80 mm long inside the concrete. The specimens were then demoulded and the cavity sealed by inserting a silicon button (with a small slit in the middle) in the collar and covered with a hollow PVC cap. The specimens were subjected to different

curing conditions as discussed above. For the specimens cured in the water bath, the steel pins were inserted back into the specimen after demoulding till the end of curing period. Thereafter the surface of the specimen was coated with epoxy except the bottom face in the casting direction. This was done to ensure that moisture and water vapour movement took place unidirectionally (see Figures 1 & 2).

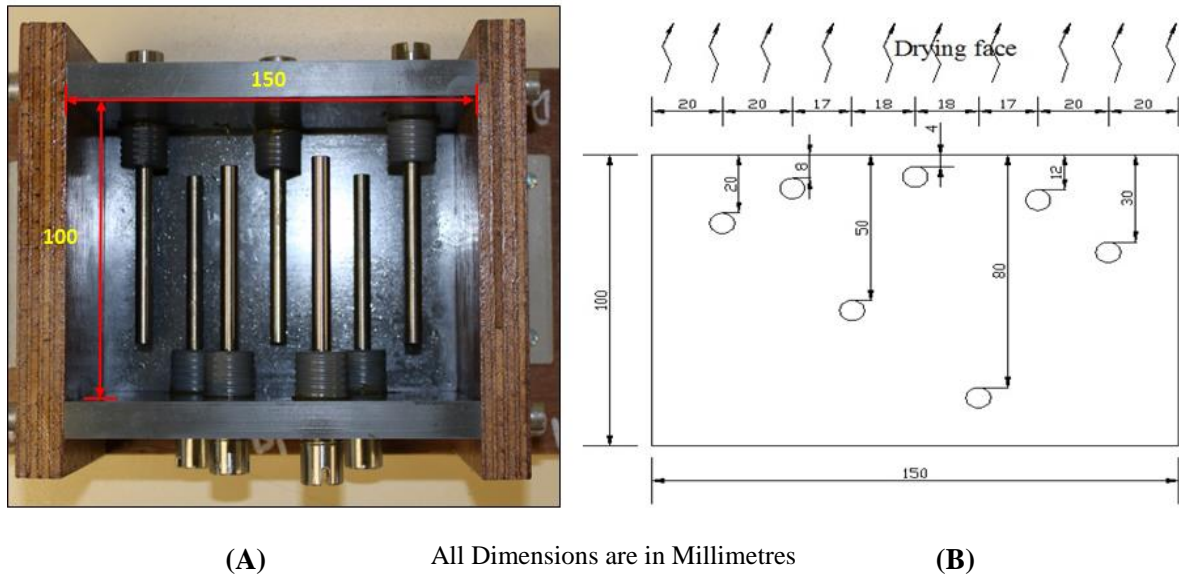


Figure 1: Arrangement of Cavities in Concrete Prism (A) Plan View of Mould used for Casting Concrete Specimens for Moisture Measurement, (B) Cross Section



Figure 2: Experimental program for RH measurement

After coating the specimen with epoxy, the initial moisture reading at different depths from the exposed surface was taken. The measurement was done using a 5 mm diameter humidity probe (HC2-P05 from Rotonic Measurement Solutions with measurement range: -40 to 85°C / 0 to 100 % RH) attached to a digital hygrometer (HygroPalm 23-A from Rotonic

Measurement Solutions with measurement range: -10 to 60°C / 0 to 100 %RH) as shown in Figure 2. After the initial measurement was taken, the concrete samples were then exposed to controlled environmental conditions in the laboratory, where the temperature and RH was maintained at 20-22°C and 50% respectively, and the moisture profile of the concrete was measured at intervals.

4. OXYGEN PERMEABILITY INDEX TEST RESULTS

The OPI test was performed on eighteen different concretes. The OPI values are represented as the negative logarithms of the coefficient of permeability (k) values (see Table 1), as shown in Figure 3. The test results show that OPI values reduce with increase in w/b , indicating a higher permeability coefficient. This can be attributed to the increase in porosity and interconnectivity of the pore structure due to an increase in w/b . Similar trends of decrease in OPI values (i.e. an increase in permeability) with increase in w/b were also observed by Salvoldi (2010), and Alhassan (2014).

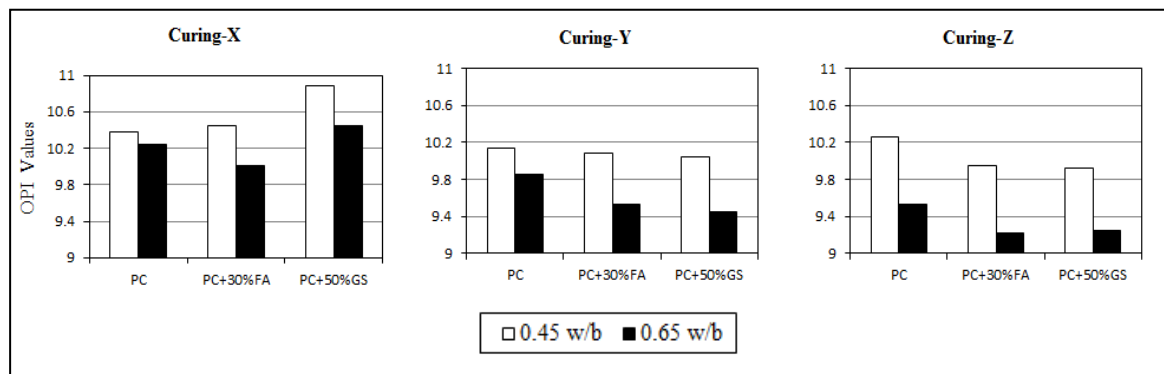


Figure 3: OPI test result of concrete at 28 days - Curing-X, Curing-Y and Curing-Z

The influence of curing on the permeability of concrete can be assessed from Figure 3. Specimens subjected to standard water curing (Curing-X) show better permeability characteristics because of the development of denser microstructures due to proper hydration, resulting in higher OPI values. On the other hand, poor curing conditions (Curing-Z), result in lower OPI values indicating higher permeability. This can be attributed to the poor microstructure developed because of inadequate conditions for cement hydration. It can be observed that the samples with Curing-Y show better performance when compared with the samples with Curing-Z, due to the better curing conditions where the samples are covered with plastic for six days before exposing to the laboratory conditions. This resulted in more favourable conditions for the cement hydration, and development of a denser microstructure when compared to specimens subjected to Curing-Z. In general it can be summarised that along with other factors, curing regime dictates the permeability characteristics of concrete. Similar trends of increase in permeability or reduction in OPI with poor curing were noted in previous studies by other researchers (Martin (2012)).

The influence of cement additions such as low calcium fly ash (FA) and ground granulated blast furnace slag (GS) on the permeability can also be observed from the OPI test results. Figure 3 shows that, when subjected to Curing-X, the concrete with FA and GS gives higher OPI values when compared PC. The increase in OPI values can be attributed due to the denser microstructure because of further hydration and pozzolanic activity. Similar trends were also

observed by other researchers (Ballim et al., 2009; Salvoldi, 2010; Alhassan, 2014). Among all the concrete specimens with Curing-X, for the same w/b, the concrete with GS shows the lowest permeability (high OPI values). A similar trend was also observed by Salvoldi (2010). As discussed above, curing has a major influence on the permeability performance of concrete, especially in the case of concrete with cement FA and GS. Improved permeability performance of concrete with cement additions over PC concrete is mainly observed in the case of Curing-X. Figure 3 clearly depicts this phenomenon, where, for the same w/b ratio, the OPI values of concrete with FA and GGBS are observed to be lower than the PC concrete for all curing regime other than Curing-X. Similar trends were also observed by Martin (2012).

5. CORRELATION BETWEEN PERMEABILITY COEFFICIENT AND WATER VAPOUR DIFFUSION COEFFICIENT

The RH profiles of the concrete specimens measured after 16-17 months of drying (at 20-22°C and 50% ambient RH) are shown in Figure 4. It can be observed that moisture equilibrium was not achieved under uniaxial drying for a 100 mm deep specimen even after 16-17 months of drying for all the specimens. Similar trends were observed by Parrott (1998). Furthermore, a sharp variation in RH was observed up to a depth of 20-30 mm from the drying surface.

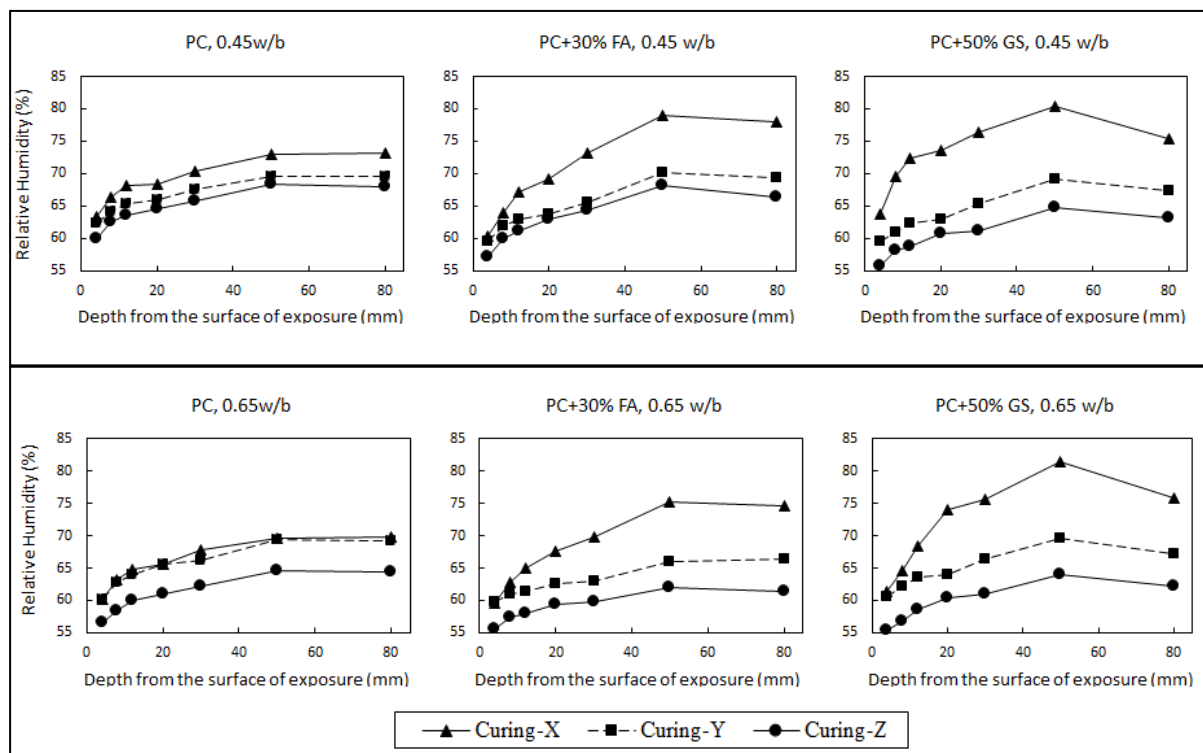


Figure 4: RH profile after 16-17 months of drying (at 20-22°C and 50% ambient RH)

The influence of curing was clearly reflected in the drying capacity of the concrete. All concrete mixes with Curing-Z shows the lowest relative humidity throughout the depth of the concrete, which is in agreement with the lower OPI values as discussed earlier. Similar to the

higher OPI values of the concrete with FA and GS with Curing-Z, a low rate of drying can be observed for the corresponding concrete specimens, irrespective of the w/b, indicating a dense microstructure. Therefore it can be inferred that a strong link exists between concrete microstructure, which can be characterised in terms of its permeability coefficient, and the drying capacity of the concrete.

During drying, the concrete is exposed to the ambient RH which is lower than the RH at the gas-liquid interface, resulting in a vapour concentration gradient between the interface and the concrete surface. The concentration gradient therefore induces diffusion of vapour from the interface to the concrete surface. Considering drying of concrete as a one-dimensional evaporation-diffusion process, and based on the measured moisture profile data, the vapour diffusion coefficient in the concrete pore structure (D_v) was calculated from the following equation proposed by Li et al. (2009)

$$h - h_0 = \frac{h_s - h_0}{\text{erf}(\lambda)} \times \text{erf}\left(\frac{x}{2 \times \sqrt{D_v \times t}}\right) \quad (1)$$

Where, h_s = relative humidity at the interface; h_0 = relative humidity at the concrete surface; 'h' is the relative humidity at depth 'x' from the surface at time 't' and λ = drying front coefficient, which can be calculated from Li et al. (2009). The vapour diffusion coefficient (D_v) based on Equation (1) was plotted against the permeability coefficient (k) based on the OPI test, as shown in Figure 5.

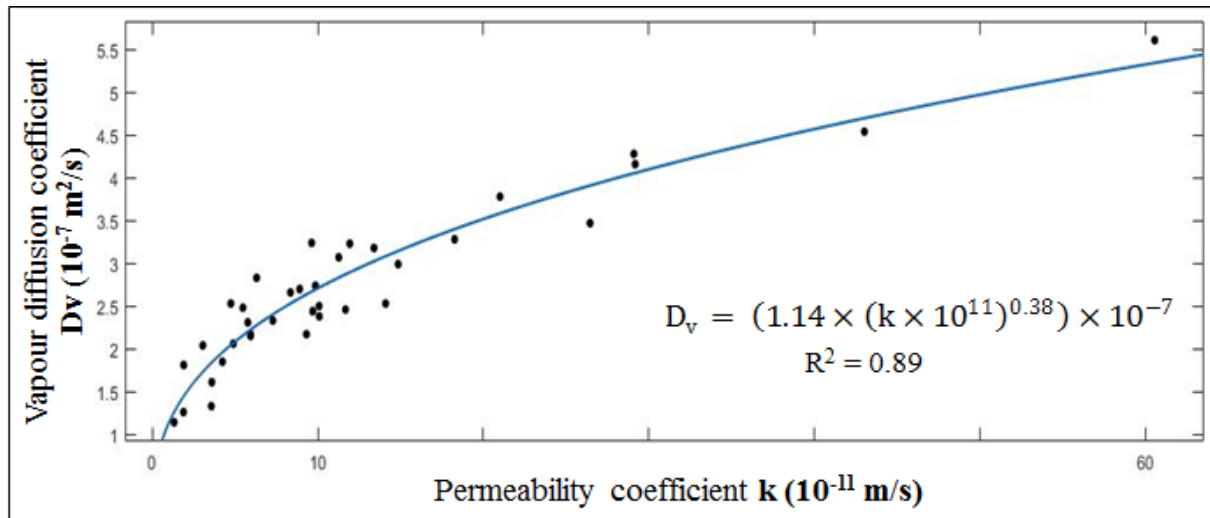


Figure 5: Correlation between vapour diffusion coefficient and permeability coefficient

Based on a regression analysis, a power relationship between effective vapour diffusion coefficient and permeability coefficient from the OPI test after 28 days of curing for a range of concrete mixes and curing conditions was established (see Figure 5). The moisture profile of concrete therefore can be predicted using the permeability coefficient of concrete based on the above correlation and using Equation (1). Furthermore the above correlation can be

coupled with a carbonation model to incorporate the influence of drying and wetting cycles on the rate of carbonation.

11. CONCLUSIONS

- The influence of water: binder ratio, cement additions such as fly ash (FA) and granulated blast furnace slag (GGBS) and curing regime were reflected in both OPI test results and in the moisture profile (in terms of RH) after 16-17 months of drying.
- A correlation between the permeability coefficient based on the OPI test and the water vapour diffusion coefficient in concrete pore structure was established.

ACKNOWLEDGEMENTS

The authors wish to acknowledge with gratitude the financial support over the period of this work received from: The University of Cape Town, The Concrete Institute, The National Research Foundation (NRF), Sika (SA) Pty Ltd., PPC Ltd, AfriSam, The Tertiary Education Support Programme (TESP) of ESKOM, and the Water Research Commission (WRC).

REFERENCES

- [1] Alexander, M.G., Ballim, Y. and Stanish, K., 'A framework for use of durability indexes in performance-based design and specifications for reinforced concrete structures', *Materials and Structures*. 41 (2008) 921-936.
- [2] Ballim, Y., Alexander, M. & Beushausen, H. Durability of concrete. In *Fulton's concrete technology*. G. Owens, Ed. (2009)
- [3] UCT, 'Durability Index Testing Procedure Manual' (Ver 4.5.1) April (2018). https://docs.wixstatic.com/ugd/5586b6_07c436992a6d4768ba2ae42d86a0a88f.pdf
- [4] Mackechnie, J.R. and Alexander, M.G., 'Durability Predictions Using Early-Age Durability Index Testing', '9th International Conference on Durability of Building Materials and Components', Rotterdam (Netherlands), 2002
- [5] Gopinath, R., Alexander, M.G. and Beushausen, H., 'Predicting depth of carbonation of concrete for varying climatic conditions', '2nd International RILEM/COST Conference on Early Age Cracking and Serviceability in Cement-based Materials and Structures - EAC2', Belgium, September, 2017 515-518.
- [6] Parrott, L.J., 'Moisture profiles in drying concrete', *Advances in Cement Research* 1 (1988).164-170.
- [7] Salvoldi, B.G., 'Modeling the carbonation of concrete using early age oxygen permeability index tests', (M.S. thesis, University of Cape Town, South Africa, 2010).
- [8] Alhassan, Y.A., 'The effect of materials and micro-climate variations on predictions of carbonation rate in reinforced concrete in the inland environment', (PhD. thesis, University of Witwatersrand, South Africa, 2014).
- [9] Martin, M., 'The influence of curing techniques and chemical admixtures on the properties of concrete', (M.S. thesis, University of Cape Town, South Africa, 2012).
- [10] Li, K., Li, K. and Chen, Z., 'Influential depth of moisture transport in concrete subject to drying-wetting cycles', *Cement and Concrete Composites* 31 (2009).693-698.

SUITABILITY OF IMPEDANCE SURFACE MOISTURE METER TO COMPLEMENT AIR-PERMEABILITY TESTS

R. Torrent (1), V. Bueno (2), F. Moro (3) and A. Jornet (4)

(1) Materials Advanced Services SRL, Buenos Aires, Argentina

(2) Materials Advanced Services Sagl, Coldrerio, Switzerland

(3) LafargeHolcim, Lyon, France

(4) Istituto Materiali e Costruzioni, DACD, SUPSI, Lugano, Switzerland

Abstract

The coefficient of air-permeability kT , measured non-destructively by the so-called "Torrent Method", has gained acceptance as a suitable durability indicator of the as-built cover concrete and has been standardized in Switzerland (Standard SIA 262/1:2013 Annex E). The standard adopted the ND electrical impedance method to control the moisture of site concrete, requiring that the latter should not exceed 5.5% for making meaningful readings of kT .

This paper presents data of moisture changes, assessed gravimetrically (H) and by ND Impedance (m) of concrete cubes dried naturally in the lab (during ≈ 3 years) and in an oven at 50°C (during ≈ 5 months). The changes in H , m and air-permeability kT were monitored regularly. Data of 17 concrete mixes, made with 9 different cement types (produced from 2 clinkers), are presented and discussed. A monotonic decrease of m and increase of kT was observed along the drying process, with reasonable continuity between natural and oven dried specimens. The results confirm that the impedance-based surface moisture meter is a suitable instrument to monitor the changes in humidity of drying concrete and an essential complement when measuring kT . The results obtained are very useful for establishing a preconditioning process prior to kT tests in the lab and offer solid ground for developing a correction factor of kT as function of m , when the latter is outside the range 4.5% - 5.5%.

Keywords: moisture, drying, air permeability, non destructive, impedance

1. INTRODUCTION

The coefficient of permeability to gases of the concrete cover has been acknowledged as a suitable and practical durability indicator [1].

It is well known that the moisture content in the concrete strongly affects the results of a gas-permeability test, due to its blocking effect on the flow of gas through the pore system of

the material. To avoid this problem, laboratory samples (cast specimens or drilled cores) are preconditioned by a controlled drying process before measuring gas-permeability [2-4].

The Swiss Code 262 [5] prescribes: “The impermeability of the cover concrete shall be checked by means of permeability tests (e.g. air permeability measurements) on the structure or on core samples taken from the structure”.

Measuring the air-permeability of concrete structures on site poses the problem of the virtual impossibility of artificially preconditioning the measuring area. The tests have to be conducted on a concrete, the moisture content of which is usually unpredictable and unknown, raising doubts on the validity of the test results.

The new version (1st August 2013) of the Swiss Standard SIA 262/1 [6], which describes in Annex E how to conduct the site air-permeability test, prescribes:

1. The moisture of the concrete shall be measured by an electrical impedance-based instrument
2. The moisture content of the concrete at the point where the coefficient of air-permeability kT is to be measured should not exceed 5.5%

Preliminary results of an investigation to better understand the meaning of the surface moisture readings, based on Electrical Impedance Method and their relation with kT were presented in [7]. This paper presents new results totalling 17 mixes made with 9 binders produced from 2 different clinkers.

2. OBJECTIVE OF THE INVESTIGATION

The objective of this investigation was twofold:

- To check the suitability of Electrical Impedance to monitor the surface moisture of drying concrete
- To develop a pre-conditioning procedure to measure kT in the laboratory

3. EXPERIMENTAL

3.1 Mixes, Specimens, Curing and Storage

Each pair of mixes (w/c=0.40 and 0.65) was prepared with a different binder, covering a wide range of compositions, as described in Table 1.¹

In Table 1, the first letter of the code indicates the clinker used to produce the cements (H: Höver, Germany; M: Merone, Italy). The values in brackets indicate the content and type of mineral additions originally included in the cement (MIC). When a mineral addition was added separately as Supplementary Cementitious Material (SCM) into the concrete mix, the content and type is indicated in italics².

Two 150 mm cubes of each mix were cured in a moist room (20°C, > 95% RH) for around 3 months. The long curing period was deliberately established to ensure a high degree of hydration, so as to minimize further hydration during the drying period.

After completion of the moist curing period, one cube of each mix was exposed to natural laboratory drying (stored in a room with still air at 18-23 °C and 50-65% RH) during 3 ± 0.2 years. The companion cubes were kept in a ventilated oven at 50°C during 4 to 6 months

¹ For cement M0, only the mix with w/c 0.65 was tested.

² Mixes are described with the cement code - w/c ratio (%); e.g. H0-40; M31FL-65.

(tests of the oven-dried cubes were performed after 24 ± 2 hour cooling in the laboratory dry room). After the tests were completed, the cubes were immediately returned to the oven.

Table 1. Binders used in the Concrete Mixes

Code	Brand (MIC) + SCM	EN Class
H0	Holcim Pur-5N	CEM I 52.5 N
H8M	92 % Holcim Pur-5N + 8% <i>Silica Fume</i>	CEM II/A-D
H22S	Holcim Ferro 4 (22% GBFS)	CEM II/B-S 42.5 R
H41S	Holcim Duo 4 (41% GBFS)	CEM III/A 42.5 N
H68S	Holcim Aqua 4 (68% GBFS)	CEM III/B 42.5 L
M0	I 52,5 R	CEM I 52.5 R
M26L	II/B-LL 32.5R (26% Limestone Filler)	CEM II/B-LL 32.5 R
M31FL	IV/A 32,5 R (27% Fly Ash + 4% LF)	CEM IV/A 32.5 R
M40FL	87% IV/A 32,5 R + 13% <i>Fly Ash</i>	CEM IV/B 32.5

3.2 Test Methods and Instruments

Figs. 1 and 2 show the instruments used and a sketch of the location of the testing points. At intervals, the following NDT and (Instruments) were applied on the cubes (Fig. 1):

- Mass M (10 kg/0.1 g *Kern Scale*)
- Moisture by impedance method m (*CMExpert*). The instrument's scale goes from 0.0 to 6.9 % [8]
- Wenner Electrical resistivity ρ (*RESI*). These results are not discussed here, as the new results confirm that ρ is not a useful indicator of concrete moisture, as already discussed in [7]
- Air-Permeability kT (*PermeaTORR*). The instrument measures values of $kT \geq 0.001 \cdot 10^{-16} \text{ m}^2$

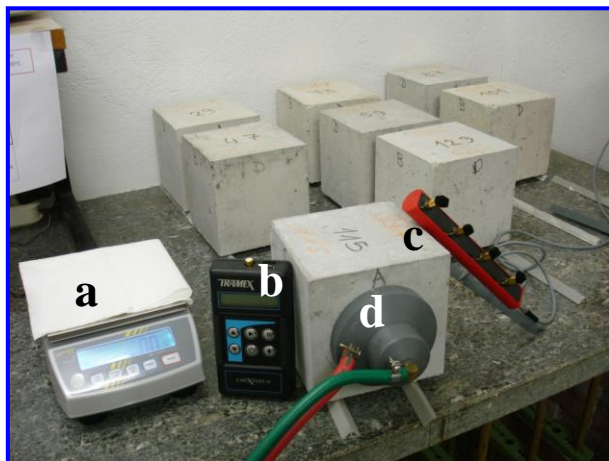


Fig. 1 - Cubes and instruments used

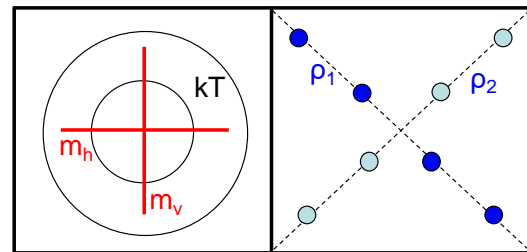


Fig. 2 - Sketch of the location of testing points

Reported value m is the average of 4 readings on each cube; reported value of kT is the geometric mean of both values measured on each cube. For more details, see [7].

When the 50°C oven-dried specimens had completed at least 4 months of drying, they were weighed and dried at 105 °C till constant weight, recording the mass M_{105} , and measuring kT and m . Then, the samples were submerged under water at 20°C until constant weight, recording the saturated mass M_s . This allowed converting the values of mass M of all

the cubes into bulk moisture H (%) and degree of saturation S_d (-), using (1) and (2), respectively.

$$H = (M - M_{105}) / M_{105} \cdot 100 \quad (1)$$

$$S_d = (M - M_{105}) / (M_s - M_{105}) \quad (2)$$

4. TEST RESULTS AND DISCUSSION

4.1 Relation between m and H

Figs. 3 and 4 show the relation between the surface moisture m (impedance test) and the gravimetric bulk density H , see Eq. (1), for Höver and Merone mixes, respectively. The framed symbols correspond to results obtained on oven-dried cubes.

For Höver mixes, Fig. 3, the results are balancedly scattered around the equility line $m = H$, with a trend of m overestimating H for mixes with $w/c = 0.40$ (blue symbols) and underestimating it for $w/c = 0.65$ (red symbols). For values of $m \leq 3\%$, the estimate of H is quite accurate, but not for $m > 3\%$; in particular, the $w/c = 0.40$ mixes show a marked non-linear behaviour for $m > 4\%$.

For Merone mixes made with M0 (OPC) and M26L (26% limestone filler), Fig. 4, m grossly overestimates H along the whole range of humidities, whilst for binders containing fly-ash, m estimates H quite accurately.

It has to be mentioned that m measures the moisture content of a surface layer 15-20 mm thick [9], whilst H measures the bulk moisture of the whole cube. Due to the expected moisture gradient, more severe for the oven-dried cubes, the surface moisture should be lower than the average (bulk moisture). The results of Figs. 3 and 4 suggest that m is, in most cases, overestimating the true surface moisture of concrete.

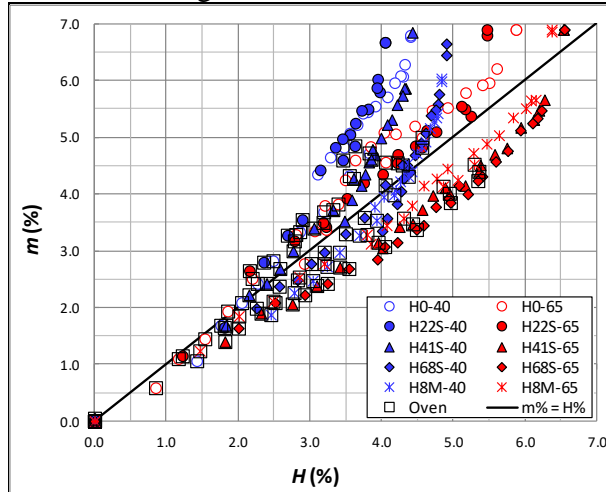


Fig. 3 - Relation between m and H (Höver)

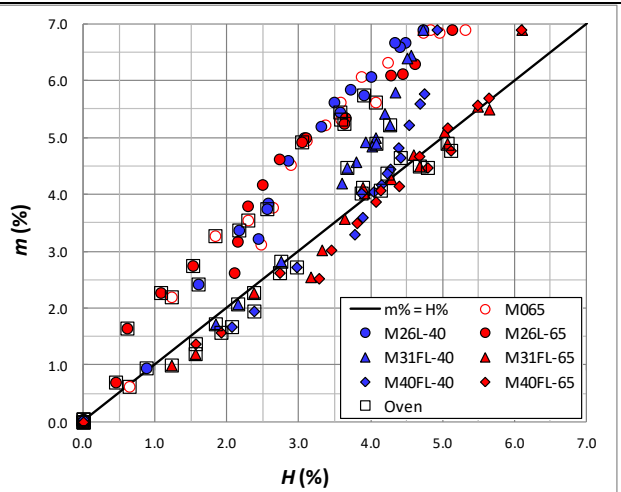


Fig. 4 - Relation between m and H (Merone)

4.2 Relation between m and S_d

Figs. 5 and 6 show the relation between surface moisture m and bulk saturation degree S_d , see Eq. (2) for the cubes made with Höver and Merone clinkers, respectively.

All specimens' results are plotted in the charts, including those under laboratory and oven drying, the latter identified by the framed symbols. It is worth mentioning that all the cubes showed that: - after 105°C drying to constant mass ($S_d = 0.0$) $\rightarrow m = 0.0\%$ (bottom of instrument's scale)

- after water saturation to constant mass ($S_d = 1.0$) → $m = 6.9\%$ (top of instrument's scale)

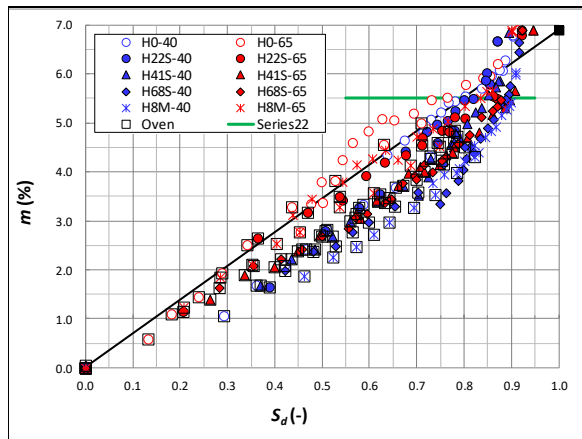


Fig. 5 - Relation between m and S_d (Höver)

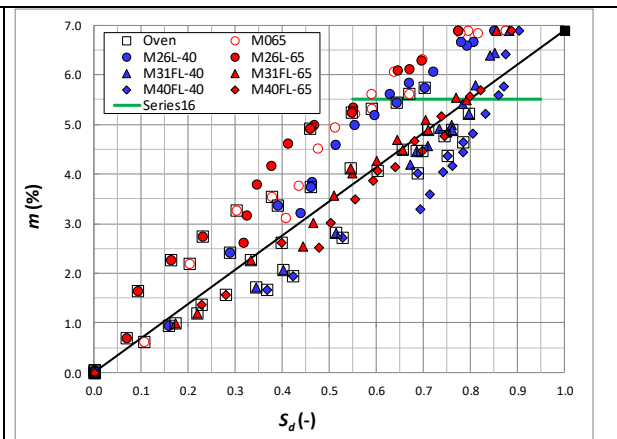


Fig. 6 - Relation between m and S_d (Merone)

This situation is indicated by the solid black line (indicative only) joining the extreme black squares.

Figs. 5 and 6 show the monotonic relation existing between S_d and m along the whole drying process, with the oven-dried samples showing reasonable continuity with the lab dried.

Comparing Figs. 5 and 6, it can be concluded that the binder type, in particular the clinker type, exerts a significant influence on the S_d vs. m relationship. Indeed, for the same m values, the S_d obtained on the cubes made with Merone clinker (Fig. 6) show a larger scatter with a tendency towards lower S_d values than Höver's (Fig. 5). It can also be observed that, for the same m , concretes made with H0 and M0 (OPC) and M26L (26% limestone filler), show lower values of S_d than those containing hydraulic MIC and/or SCM.

In both Figs. 5 and 6 a segment with $m = 5.5\%$ (maximum value admitted by Swiss Standard SIA 262/1 [6] for performing air-permeability test kT on site) corresponds to S_d within 0.75-0.90 for Höver samples and 0.60-0.90 for Merone samples.

4.4 Relation between kT and m

Figs. 7 and 8 show the relation between the coefficient of air-permeability kT and the surface moisture m , for Höver and Merone cubes, respectively. Results measured on cubes under both lab and oven drying are plotted, the latter indicated by the framed symbols. The values of $kT < 0.001 \cdot 10^{-16} \text{ m}^2$ are not accurate, being below the limit of sensitivity of the instrument, as indicated by the red box at the bottom of both Figs. Therefore, the values inside the box, calculated from the pressures recorded by the instrument, should be taken with caution. The limit value of $m \leq 5.5\%$, stipulated by Swiss Standard SIA 262/1 [6] for measuring kT on site, is indicated by a vertical green line in both Figs. Given the wide range of kT results, a logarithmic scale is used in Figs. 7 and 8.

There is a monotonic increase in kT as concrete gets drier, with the highest kT value corresponding to the cubes subjected to the drastic final drying at 105°C ($m = 0\%$).

At first sight, the relation $\ln(kT)$ vs. m presented in Figs. 7 and 8 show some linearity and parallelism for the different mixes, particularly for values of m within the range 1.0 - 5.5%.

This opens the way for attempting a correction of kT when the m values are too low (e.g. indoors elements), to be presented in a future communication.

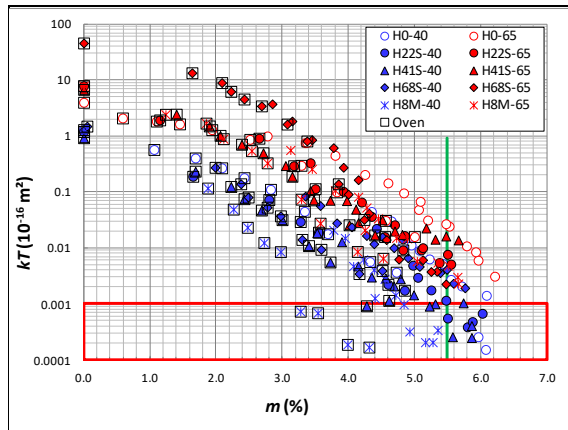


Fig. 7 - Relation between m and kT (Höver)

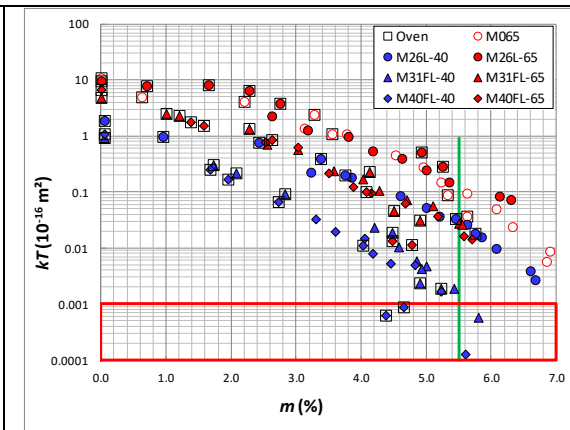


Fig. 8 - Relation between m and kT (Merone)

4.5 Drying conditions for kT laboratory tests

In [10], guidelines are given for testing kT in the laboratory, which is not covered by Swiss Standard SIA 262/1 [6] which refers exclusively to site testing. Regarding pre-conditioning of the samples, [10] specifies the following procedure: "Place the specimens in the ventilated oven at $50^\circ \pm 2^\circ\text{C}$, making sure that hot air can circulate freely over the faces to be tested (a free distance of at least 20 mm should be left between the test faces of adjacent specimens and/or the oven's walls and floor. After 3 days, remove the samples from the oven and let them cool down in a laboratory room (relatively dry) at 20 to 23°C for 6 ± 2 hours.

Apply the Surface Moisture Meter on the surfaces where kT is to be measured, making 2 readings at 90° per test area, and check that their average is within the range 4.0 - 5.5%. Under normal circumstances, 3 days in the oven should suffice to reduce the surface moisture to the required level. If not, repeat the drying and cooling procedure until the moisture falls within the specified range."

This criterion has been applied to the data recorded in this investigation, with the result shown in Fig. 9.

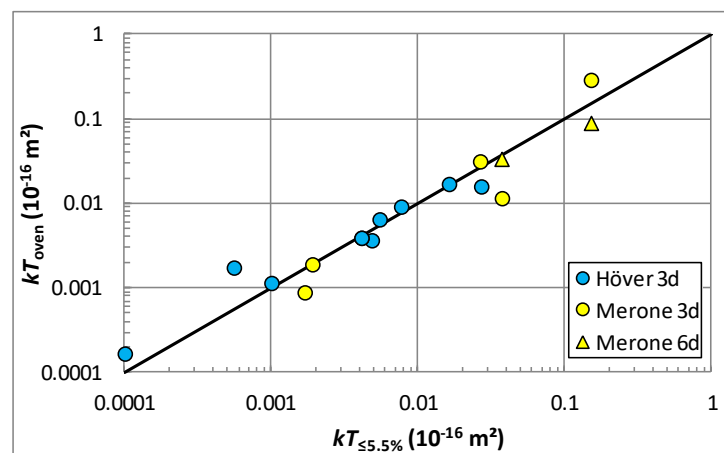


Fig. 9 - Relation between oven-dried (3 or 6 d.) and lab-dried (until $m \leq 5.5\%$) kT values

Fig. 9 shows the kT values obtained for the 17 mixes reported, in abscissas for laboratory drying until $m \leq 5.5\%$ and in ordinates after 3 days in the oven at 50°C to reach a surface moisture $4.0\% \leq m \leq 5.5\%$; if not achieved, the value obtained after 6 days in the oven was taken. It has to be mentioned that, in the case of Mix H0-40, after 3 days of oven-drying, the moisture dropped already to 3.8% . Only for mixes M0-65 and M26L-40, was it necessary to dry the specimens 6 days to reach $m \leq 5.5\%$, indicated by triangles in Fig. 9.

Fig. 9 shows that the criterion works well in that the kT values obtained according to the oven-drying procedure prescribed in [10] leads to very similar values to those obtained in lab-drying until reaching $m \leq 5.5\%$.

Fig. 10 shows the kT values obtained on the 17 mixes tested under: lab-drying till $m \leq 5.5\%$ (blue bars); oven-drying at 50°C till $m \leq 5.5\%$ (yellow bars); oven-drying at 105°C till constant mass (red bars).

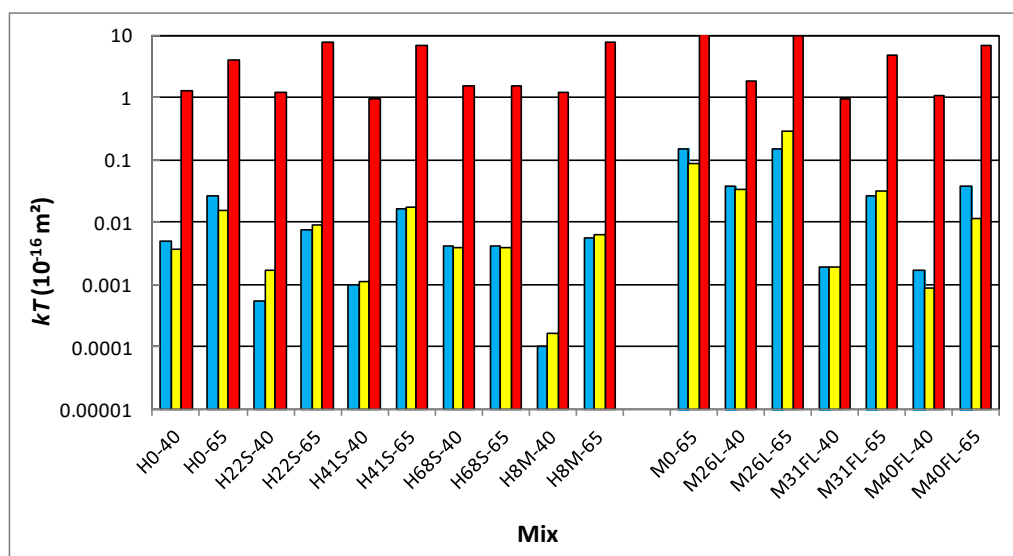


Fig. 10 - kT values of 17 mixes after three different drying regimes

The results presented in Fig. 10 show the inconvenience of drying the samples at 105°C (as applied in [11,12]), because the kT values obtained after such drastic drying are several orders of magnitude higher than those expected for surface moisture $4.0\% \leq m \leq 5.5\%$ and, therefore, not representative of normal field conditions. Moreover, the difference between kT of mixes H8M-40 and M0-65, which is three orders of magnitude for lab-drying and 50°C oven-drying, is reduced to just one order of magnitude after 105°C oven-drying.

5. CONCLUSIONS

- The impedance method is a good NDT to follow the effect of drying on the surface moisture of concrete m ; 105°C oven-dried specimens have $m = 0.0\%$ (bottom of scale) and water saturated samples have $m = 6.9\%$ (top of scale)
- For each mix, m relates well with the bulk moisture H and saturation degree S_d , with continuity between laboratory and oven-dried specimens, although the relations vary with the type of mix and binder.

- c) The impedance method is suitable to monitor the effect of surface moisture on air permeability coefficient kT test results.
- d) The *PermeaTORR* and the *CMExpert* instruments followed well the evolution of kT and m under drying conditions, during 3 years (good stability and repeatability).
- e) The limit established in the Swiss Standards for surface moisture ($m \leq 5.5\%$) seems adequate and corresponds, in terms of measured kT , to 3 days drying at 50°C in the oven used in this investigation.
- f) This is acceptable for new structures (28-91 days of age), to which the Standard applies (where m is typically within the range 4.5%-5.5%), but not to old structures where m can be considerably lower.
- g) The 'parallelism' of the relation $\ln(kT)$ vs m for the different mixes opens a way to correct the measured values of kT when the moisture meter reading m is out of the usual range 4.5% - 5.5%
- h) For lab applications, oven-drying at 50°C and checking that the surface moisture m is within 4.0-5.5%, may be a robust and realistic conditioning procedure for lab specimens to be tested for kT . On the contrary, strong drying at 105°C is not recommended.

ACKNOWLEDGMENT

To Dr. Christian Paglia, Director of Istituto Materiali e Costruzione (SUPSI) for the support provided to this investigation.

REFERENCES

- [1] "Performance Criteria for Concrete Durability", Kropp J. and Hilsdorf, H. K. (Eds.), RILEM Report No. 12, 1995.
- [2] RILEM TC 116-PCD, "Recommendations: Tests for Gas Permeability of Concrete", Materials and Structures, v. 32, 1999, 174-178.
- [3] Spanish Standard UNE 83966, "Acondicionamiento de probetas de hormigón para los ensayos de permeabilidad al aire y capilaridad", Julio 2008, 5 p.
- [4] Alexander, M.G., Ballim, Y. and Mackechnie, J. R., "Concrete durability index test manual", Research Monograph No. 4, Univ. of Cape Town and Witwatersrand, South Africa, 1999, 16 p.
- [5] Swiss Standard SIA 262:2013, "Concrete Construction".
- [6] Swiss Standard SIA 262/1:2013, "Concrete Construction - Complementary Specifications".
- [7] Torrent, R., Moro, F. and Jornet, A., "Coping with the Effect of Moisture on Air-Permeability measurements", Intern. Workshop on Performance-based Specification and Control of Concr. Durability, Zagreb, Croatia, 11-13 June 2014, 489-498.
- [8] Tramex, "CEMEXPERT II User guide", <https://www.radtke-messtechnik.com/wp-content/uploads/2015/09/Bedienungsanleitung-TRAMEX-CMEX.pdf>
- [9] Ashworth, J., Tramex, Personal communication, 19 June 2013.
- [10] Torrent, R., "Guidelines for applying the *PermeaTORR* in the Laboratory". Materials Advanced Services, V2.3, Buenos Aires, Argentina, December 2015, 15 p.
- [11] Baroghel-Bouny, V., "Durability indicators: relevant tools for performance-based evaluation and multi-level prediction of RC durability". RILEM PRO 047, 2006, 3-30.
- [12] AFPC-AFREM, "Durabilité des Bétons, Méthodes recommandées pour la mesure des grandeurs associées à la durabilité". Compte-rendu des journées techniques de l'AFPC-AFREM, 11 et 12 décembre, Toulouse, France, 1997, 284p.

THE INTRINSIC COEFFICIENT PERMEABILITY OF CONCRETE SUBJECTED TO CYCLIC WATER FREEZING

Dalia Bednarska (1), Alicja Wieczorek (1) and Marcin Koniorczyk (1)

(1) Lodz University of Technology, The Department of Building Physics and Building Materials, Poland

Abstract

The parameters characterizing inner structure of the cement-based materials, such as porosity or permeability, determine risk of degradation of cement matrix due to aggressive environment. The paper concerns the influence of frost degradation on transport properties of water saturated concrete in accelerated durability tests and their resistance to cyclic water freezing. The experimental study is focused on the examination how the frost-induced damage affects the intrinsic coefficient of concrete permeability. The measurements have been performed on concrete specimens with two type of Portland cement (CEM I 42,5N/NA and CEM I 42,5R) with different water-cement ratio ($w/c=0.4\div0.5$) without air-entraining admixtures. In order to analyse the frost degradation of the material, which is characterized by the permeability evolution (measured by means of Cembureau permeability test), two methods of sample preparation have been proposed. In the first method, the measurements of gas permeability are performed before samples are subjected to repeating freeze-thaw cycles. In this case specimens cut off from the central part of the cylindrical sample have been considered. Subsequently, the discs are placed in the climatic chamber and undergone an assessment of their resistance to frost. Once the assumed number of freezing-thaw cycles is achieved, the oxygen permeability test is conducted again. The analysis of the process of frost destruction in the second proposed procedure is slightly different. In case of the next experimental method, after cyclic water freezing, the concrete cylindrical samples have been cut into smaller specimens and then the oxygen permeability test is conducted. The proposed research procedures, apart from the advantages, are also associated with some restrictions, which are described in detail in the report. The choice of the method is important and influences the obtained results.

Keywords: concrete, oxygen permeability test, elastic modulus, freeze-thaw cycles, frost deterioration

1. INTRODUCTION

The knowledge about porous material property changes caused by environmental conditions is necessary for a more profound understanding of damage phenomena and vital for development of more durable materials and accurate prediction models. It is acknowledged that due to the frost-induced damage mechanical properties are considerably reduced, what has been highlighted also in recent investigations [1,2,3]. Furthermore, frost-induced damage have an impact on the material transport properties. Investigations on the deterioration of cement-based materials exposed to freeze-thaw cycles reveal a reduction of mechanical properties such as compressive strength or elastic modulus and an increase of gas permeability, which are associated with the changes of microstructure [3,4]. Chung et al. [5] investigated the influence of freeze-thaw cycles on the coefficient of chloride ion diffusivity of fly ash and silica fume concretes. It was found that this parameter increased due to the cyclic freezing. It is also acknowledged that gas permeability of concrete measured on the basis of chloride transport, increased under repeated freeze–thaw cycles [6]. Consequently, material was more vulnerable to the subsequent water penetration and the ice-induced degradation. It is established that water transport occurs through a continuous network of pores, which exists in the solid skeleton of concrete [7,8]. An air-entraining admixture is one of the most commonly used additives in order to obtain high frost-resistance of cementitious composites [9, 10], which is why we intentionally rejected the application of AEA. Our purpose is to investigate the impact of cyclical changes of temperature on the mechanical and transport properties of cement-based materials without air-entraining admixtures and their microstructure.

2. MATERIALS

The experimental research concerns the concrete, which has been prepared using the Portland cement CEM I 42.5N-NA and CEM I 42,5R with different water to cement ratios. The concrete compositions are presented in Table 1 and Table 2. There are two different examination procedures applied, which are described in detail in the consecutive section.

Table 1: Concrete compositions – Method 1.

Mix ingredients (kg/m ³)	B1	B2
CEM I 42,5R	390	360
Water	156	162
Coarse aggregate, 8-16mm	575	581
Medium aggregate, 2-8mm	668	675
Sand, 0-2mm	612	620
Plasticizer	3.12	1.98
w/c	0.40	0.45

Table 2: Concrete compositions – Method 2.

Mix ingredients (kg/m ³)	C1	C2
Cement CEM I 42.5N-NA	425	425
Water	212	170
Coarse aggregate, 8-16mm	524	556
Medium aggregate, 2-8mm	648	686

Sand, 0-2mm	576	612
Plasticizer	-	2.12
w/c	0.50	0.40

3. METHODS

3.1 Freeze and thaw cycles

At the beginning one has to subject the studied samples to frost damage. The temperature changes are imposed by the freeze-thaw climatic chamber according to [11]. The freezing of the specimens during the test is carried out at -20°C for 4 h, while the thawing is performed in water at +20°C and continues at least 2 h. As soon as all the freeze-thaw cycles are finished, all the samples are removed from water. The concrete specimens are removed from the freezing chamber after 50, 100 and 150 cycles, accordingly.

3.2 Oxygen permeability

Due to a gas pressure gradient, which is induced between two opposite surfaces of a sample located in the measuring chamber, a one-dimensional gas flow is imposed. Apparent gas permeability, k_a , is calculated at a given pressure according to the Hagen-Poiseuille equation for laminar flow under steady-state conditions [12]:

$$k_a = (2 \cdot p_o \cdot Q_i \cdot L \cdot \mu) / [A \cdot (p_i^2 - p_o^2)] \quad (1)$$

where p_i and p_o are the inlet and outlet pressure, Q_i is the volumetric flow rate, L is the sample thickness in the direction of the gas flow, A is the area of the sample cross-section, and μ is the viscosity of oxygen. Before the measurements, steady state flow has to be established. This condition is verified by taking two measurements separated by 10 minute time interval. It is assumed, that if two values differ by less than 3% the steady state flow condition is achieved.

To consider Knudsen flow an intrinsic coefficient of permeability, k_v , is calculated using Klinkenberg relationship [14]:

$$k_a = k_v [1 + (b / p_m)] \quad (2)$$

where b is the Klinkenberg coefficient and $p_m = (p_i + p_o) / 2$ is the mean gas pressure. The intrinsic permeability of concrete subjected to a laminar gas flow can be given by a linear regression of the apparent permeabilities to the infinite average pressure.

Gas permeability tests for concrete samples are performed using Cembureau method, which is recommended by RILEM [12,13].

3.3 Elastic modulus

Tested samples are loaded under axial compression and the stresses and strains are recorded. The mean value of compressive strength is used to define the stress level. The elastic modulus is calculated from stress-strain experimental curves obtained at the end of three loading-unloading cycles for a stress varying between 0.5MPa and 1/3 of the compressive strength [15].

3.4 Method 1

In case of the first approach three discs of 48mm in thickness are cut off from the central part of the cylindrical specimen with a diamond saw. Then the lateral sides of the discs are sealed with silicon in order to ensure one-dimensional gas flow. Firstly samples are oven-dried

at 60°C as long as sample mass changes less than 0.1% of initial mass within 24 hours. Such a procedure in the extreme case lasts 3 months. Then the gas permeability test is conducted. Afterwards they are entirely saturated and put inside the climatic chamber and when the assumed number of freeze-thaw cycles is achieved, the samples are oven-dried at 60°C until solid masses are obtained according to aforementioned procedure. Then the samples are examined in gas permeability test once more. The measurements of the elastic modulus are conducted for normalized samples (Ø150mmx300mm), which have been subjected to the same freezing-thawing procedure. This method regards to B1 and B2 concrete.

3.5 Method 2

In case of the second approach the initial specimens (Ø150mmx300mm) are fully saturated and subjected to freeze-thaw cycles. Subsequently, after drying at 60°C until solid mass is obtained, three discs of 48mm in thickness are cut off from the central part of the cylindrical specimen with a diamond saw and lateral sides of the discs are sealed with silicon. After drying process, oxygen permeability test is conducted on damaged and undamaged (reference) concrete samples. Additionally the measurements of the elastic modulus are conducted for normalized samples (Ø150mmx300mm), which have been subjected to the same freezing-thawing procedure. This method regards to C1 and C2 concrete.

4. RESULTS AND DISCUSSION

The damage of the material is characterized by the reduction of elastic modulus as well as the increasing gas permeability value.

4.1 Method 1

Table 3 presents the elastic modulus changes during the rising number of freeze-thaw cycles. The test is conducted on three specimens of each series after 150 as well as 300 freeze-thaw cycles. The presented results are the average of three measurements. The elastic modulus is equal to about 32.5GPa for B1 reference samples and 30.6 for B2 reference samples. There is not any significant decrease of elastic modulus observed after 150 and 300 freeze-thaw cycles.

Table 3: The values of elastic modulus of concrete specimens after the freeze-thaw cycles and reference samples.

	Number of freeze-thaw cycles		Reference samples
	150	300	
Concrete	Elastic modulus [GPa]		
B1 [w/c=0.4]	31.6 ± 0,6	31.8 ± 0,8	32.5± 0,9
B2 [w/c=0.45]	29.8 ± 0,8	29.1 ± 1,5	30.6 ± 1,1

The oxygen permeability test has been conducted after 0, 50, 100, 150 freeze-thaw cycles in case of B1 concrete and after 100, 150, 200, 250 freeze-thaw cycles in case of B2 concrete. The obtained results are presented in Table 4. The presented gas permeability is an average value of six samples cut out from the central part of two cylinders. The relation between intrinsic permeability and number of freeze and thaw cycles for B1 and B2 concrete is presented in Figure 1a, b.

For B1 concrete there can be noticed significant increase of intrinsic coefficient of permeability especially after 50 and 100 freeze-thaw cycles. The permeability of analyzed specimens after the 50th cycle is 23.9 times higher than the reference permeability, at the end of the 100th cycle is approximately 66 times higher. For B2 concrete the intrinsic permeability coefficient increases slightly only after 50 and 100 cycles and afterwards remains almost constant. Hence, it can be assumed that is no any relation between the number of freeze-thaw cycles and permeability in case of B2 concrete.

Table 4: Intrinsic coefficient of permeability after n freeze-thaw cycles, k_{vn} – the permeability of the samples which are subjected to 50, 100, 150, 200, 250 freeze-thaw cycles, coefficient of variation, c_v (ratio of the standard deviation and the mean value of permeability).

$k_{vn} [10^{-17} \text{ m}^2] \pm c_v [\%]$						
	Number of freeze-thaw cycles					
n	REF	50	100	150	200	250
B1; w/c=0.40	1.7 ($\pm 11\%$)	38.0 ($\pm 86\%$)	128.4 ($\pm 102\%$)	109.9 ($\pm 148\%$)	-	-
B2; w/c=0.45	1.8 ($\pm 26\%$)	-	22.8 ($\pm 162\%$)	11.8 ($\pm 133\%$)	11,9 ($\pm 148\%$)	8,4 ($\pm 55\%$)

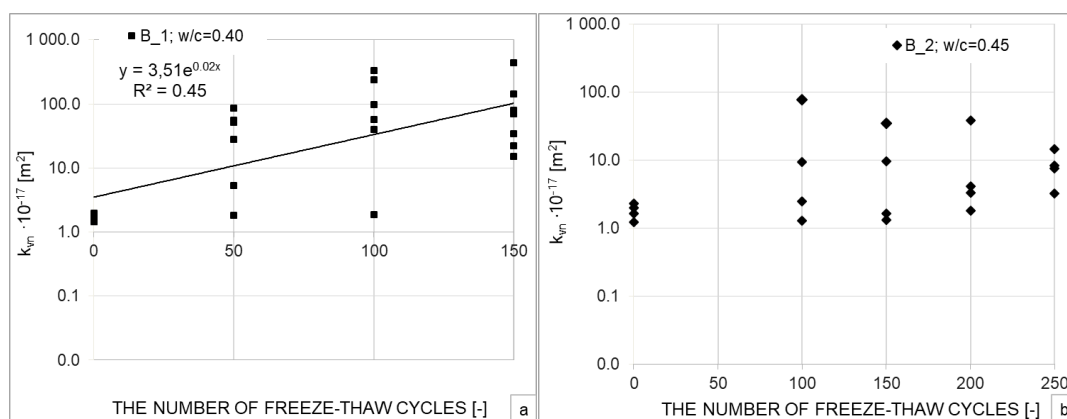


Figure 1: Intrinsic permeability of concrete without air-entraining admixtures after n freeze-thaw cycles: a) B1 concrete, w/c=0.4 and b) B2 concrete, w/c=0.45

4.2 Method 2

Table 5 presents the elastic modulus changes during the rising number of freeze-thaw cycles. The test is conducted on three specimens of each series and each number of freeze-thaw cycles. The presented results are the average of three measurements. The elastic modulus is equal to about 31.7GPa for C1 reference samples. Its value decreases 40% after 100 f-t cycles and 50% after 150 f-t cycles. For samples made of C2 concrete, the parameter does not change significantly and is on the stable level of about 32GPa.

Table 5: The values of elastic modulus of concrete specimens after the freeze-thaw cycles and reference samples.

	Number of freeze-thaw cycles			
	50	100	150	Control samples
Concrete	Elastic modulus [GPa]			
C1 [w/c=0.5]	31.3 ± 0.3	19.1 ± 4.8	15.8 ± 3.2	31.7 ± 0.2
C2 [w/c=0.4]	32.5 ± 0.2	32.3 ± 1.0	31.7 ± 1.0	33.3 ± 0.5

Change of the intrinsic coefficient of permeability is presented in Tab. 6. The presented gas permeability is an average value of six samples cut out from the central part of two cylinders. The number of discs for C1 series is increased to nine, because of visible destruction after 100 and 150 freeze and thaw cycles. The relation between intrinsic permeability and number of freeze and thaw cycles for C2 and C1 concretes is presented in Figure 2a, b.

For C1 concrete, significant increase of intrinsic coefficient of permeability can be observed between 50 and 100 freeze-thaw cycles. The permeability of analyzed specimens after the 50th cycle is 1.5 times higher than the reference permeability, at the end of the 100th cycle is approximately 40 times higher and at the end of the test it is 80 times higher than the permeability of undamaged specimens. In case of C2 concrete the permeability coefficient remains at the same level independently of the freeze-thaw cycle number. Hence, it can be assumed there does not occur any significant deterioration induced by freezing in case of C2 concrete.

Table 6: Intrinsic coefficient of permeability after n freeze-thaw cycles, k_{vn} – the permeability of the samples which are subjected to 50, 100 and 150 cycles, coefficient of variation, c_v (ratio of the standard deviation and the mean value of permeability).

$k_{vn} [10^{-17} \text{ m}^2] \pm c_v [\%]$				
Number of freeze-thaw cycles				
n	REF	50	100	150
C-1; w/c=0.50	3.2 (±21%)	4.7 (±35%)	132.6 (±50%)	256.2 (±43%)
C-2; w/c=0.40	1.0 (±11%)	0.9 (±20%)	1.0 (±20%)	1.1 (±16%)

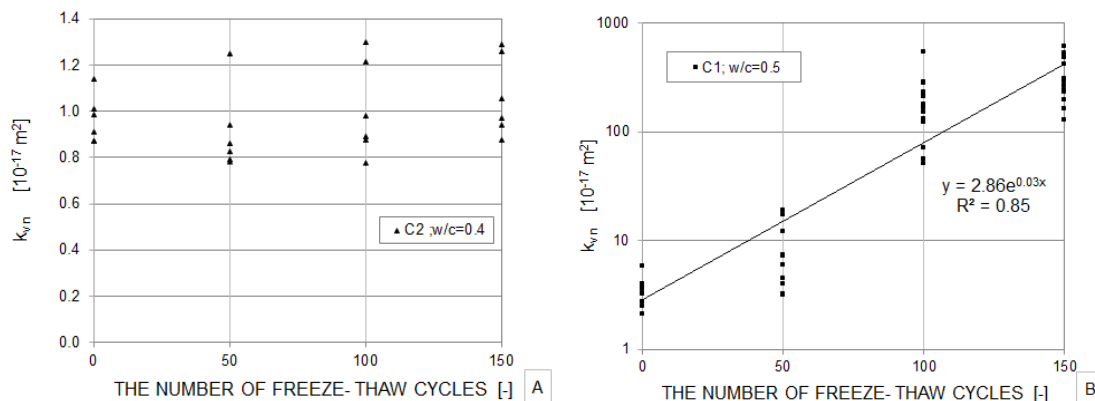


Figure 2: Intrinsic permeability of concrete without air-entraining admixtures after n freeze-thaw cycles: a) C2 concrete, $w/c=0.4$ and b) C1 concrete, $w/c=0.5$

5. CONCLUSIONS

The following conclusions can be drawn:

- Frost action induces often irreversible microstructure damages of the cementitious matrix. An increase of water volume during freezing causes appearance of numerous microcracks, which causes the growth of intrinsic permeability coefficient value. Hence, it has to be claimed that gas permeability is strongly affected by microstructure changes.
- In case of method 1 it is observed that significant increase of intrinsic coefficient of permeability especially after 50 and 100 freeze-thaw cycles occurs for B1 concrete, whereas for B2 concrete the intrinsic permeability coefficient increases slightly and after 100 cycles remains at almost constant level.
- According to results obtained for concrete C1 and C2 (method 2) high value of water to cement ratio ($w/c=0.5$) leads to significant increase of intrinsic coefficient of permeability. For this case the permeability of analyzed specimens after 50 cycles is 1.5 times higher than the reference permeability and at the end of 100 and 150 cycles is approximately 40 times and 80 times higher than the permeability of undamaged specimens. In case of $w/c=0.40$ one can observe no further destruction. To sum up the registered results reveal significantly different relations between permeability and number of freeze-thaw cycles for each type of analysed concrete. Such a situation is caused primarily by applying two different research procedures as well as differences in values of water to cement ratio.
- The visible reduction of elastic modulus is accompanied by an increase of transport properties of cement-based materials actually only in case of the C2 concrete. In case of other samples the elastic modulus remains at almost constant level, which may be caused by the fact that frost action is associated mainly with the development of microcracks in the cement matrix. This pore size redistribution can be observed easily by the growing value of intrinsic permeability, whereas mainly bigger cracks cause the elastic modulus reduction. This leads to the conclusion, that intrinsic permeability coefficient is the parameter, which describes sample destruction more thoroughly than elastic modulus.
- Two proposed analysis approaches are significantly different. In case of method 1 studied samples are oven-dried two times, which influences specimens microstructure. In case of

second method samples have been dried only once. On the other hand only the first method allows to examine the gas permeability before subjecting samples to cyclic freezing, which enables to determine actual change of gas permeability coefficient. However, the research conducted according to method 1 takes much more time in comparison with method 2. Moreover multiple drying and significantly smaller dimensions of freezing samples in method two lead to much faster deterioration process, which is why the second method is chosen as more appropriate one to analyse the ice-induced deterioration of cement-based materials.

6. REFERENCES

- [1] M. Pigeon, R. Pleau, Durability of concrete in cold climates. Modern Concrete Technology Series. Taylor & Francis, 1995
- [2] G. Wardeh, A.S.M. Mohamed, E. Ghorbel, Analysis of concrete internal deterioration due to frost action, *Journal of Building Physics* 35 (1) (2010) 54-82
- [3] Z. Wang, Q. Zeng, Y. Wu, L. Wang, Y. Yao, K. Li. Relative humidity and deterioration of concrete under freeze-thaw load. *Construction and Building Materials* 62 (2014), 18-27
- [4] P. Soroushian, M. Elzafraney, Damage effects on concrete performance and microstructure, *Cement and Concrete Composites* 26 (7) (2004), 853-859
- [5] C. W. Chung, C.S. Shon, Y.S. Kim, Chloride ion diffusivity of fly ash and silica fume concretes exposed to freeze-thaw cycles, *Construction and Building Materials* 24 (9) (2010), 1739-1745
- [6] M. Saito, M. Ohta, H. Ishimori, Chloride permeability of concrete subjected to freeze-thaw damage, *Cement and Concrete Composites* 16 (4) (1994), 233-239.
- [7] T.C. Powers, T. L. Brownyard, Studies of the physical properties of hardened Portland cement paste. Part 7. Permeability and absorptivity, *American Concrete Institute Journal Proceedings* 43 (9) (1947), 845-880.
- [8] E.J Garboczi, Permeability, diffusivity, and microstructural parameters: a critical review. *Cement and Concrete Research* 20 (4) (1990), 591-601.
- [9] M. Pigeon, J. Marchand, R. Pleau, Frost resistant concrete. *Construction and Building Materials* 10 (5) (1996) 339-348
- [10] ACI Committee 201, Guide to Durable Concrete, American Concrete Institute, Farmington Hills, Michigan, 1991, pp. 1-41
- [11] PN-B-06250:1988. Polish Standard: Normal Concrete (in Polish)
- [12] RILEM Technical Committee 116-PCD.1999. Permeability of Concrete as a Criterion of Its Durability. *Materials and Structure* 32 (217), 163-173
- [13] J. J. Kollek, The determination of permeability of concrete to oxygen by the Cembureau method – a recommendation. *Materials and Structures* 22 (3) (1989), 225-230
- [14] L. J. Klinkenberg, The permeability of porous media to liquids and gasses. *Drilling and Production Practice*. American Petroleum Institute (1941), 200-213
- [15] EN 12390-13.2014-02. Testing hardened concrete. Part 13. Determination of secant modulus of elasticity in compression

NON EQUILIBRIUM MOLECULAR DYNAMICS SIMULATION OF THE HYDRODYNAMICS IN CRYSTALLINE CALCIUM SILICATE HYDRATES NANOPORES

Tulio Honorio (1), Kamilia Abahri (1)

(1) LMT, ENS Cachan, CNRS, Université Paris-Saclay, 94235 Cachan, France

Abstract

The processes associated with the hydrodynamics in calcium silicate hydrates nanopores are crucial to durability and confinement performance of concrete. We report Non Equilibrium Molecular Dynamics (NEMD) simulations of forced flows in crystalline calcium silicate hydrates nanopores. For slit pores larger than 4 nm, Poiseuille flow is observed for an imposed force parallel to both orthogonal directions of the basal plane. This result shows that Navier-Stokes, which is *a priori* restricted to the realm of continuum mechanics, can provide, even for nanopores, a reasonable description of the flow provided the adequate boundary conditions are employed. This observation goes towards a better comprehension of water and aqueous solution transport phenomena in cement-based materials.

Keywords: Non Equilibrium Molecular Dynamics; Viscosity; Slip Boundary Conditions; Poiseuille flow.

1. INTRODUCTION

The understanding of the physical phenomena governing the dynamics of water at the nanometric scale is crucial to predict the behaviour of micro- and meso-porous materials such as calcium silicate hydrates. Regarding cement-based materials, water transport phenomenon is critical to performance specifications related to the durability and the confinement capacity of the material.

Nanopores are one of the main pore size classes in cement-based materials. Water confined in nanometric pores is recognized to exhibit a different behaviour from bulk water due to adsorption and depletion forces resulting from the interaction with the solid surfaces, alters the structure and dynamics of confined.

Molecular simulations have been extensively used to assess the particularities of confined water within various nanoporous materials [1–3], including calcium silicate hydrates [4–6]. Water ordering adjacent to solid surfaces that is pore-size dependent is observed in crystalline

calcium silicate hydrates [7]. Also, as for other nanoporous materials [2,8], confinement is recognized to deaccelerate water dynamics leading to a sub-diffusion behaviour and heterogenous diffusion [9].

On the other hand, hydrodynamics under forced flow at the nanoscale may exhibit the characteristics of (“macroscopic”) Poiseuille flow, i.e. parabolic velocity profiles, in some nanoporous materials such as clays [10].

In this work, the hydrodynamics in calcium silicate hydrates under forced flow is studied using Non Equilibrium Molecular Dynamics (NEMD). To the best of the author’s knowledge, this is the first time NEMD is used to assess forced flow in calcium silicate hydrates nanoporous. Velocity and density profiles are computed for 4 pore sizes. The viscosity of the fluid is computed using two approaches. The results are validated against experimental and simulation data concerning the viscosity of water. These results contributes to a better understanding of water transport in calcium silicate hydrates.

2. MOLECULAR MODELS AND METHODS

We consider the atomic structure of Hamid 11 Å Tobermorite with a Ca/Si ratio of 1, which corresponds to the structural formula $[\text{CaO}][\text{SiO}_2][\text{H}_2\text{O}]_{0.5}$. The species in the system interact via CSHFF empirical force field [11]. Slit pores are constructed as detailed by Honorio [7] and filled with water via Grand Canonical Monte Carlo (GCMC) simulations for a system in equilibrium with an external water reservoir at 300 K and under 1 atm for pore sizes up to 4.2 nm. Figure 1(a) shows the snapshot of an equilibrium configuration obtained by GCMC simulations of tobermorite with a pore size of $H = 0.8$ nm. For pores sizes exceeding 1 nm, the number of water molecules scales linearly with the pore size (Fig. 1(c)), which allows extrapolating the water content of pores larger than nm. Figure 1(b) shows the equilibrium configuration of the $H = 8$ nm pore.

To simulate forced flow in tobermorite nanopores, NEMD simulations are performed. These simulation consist in applying a constant force $F = 0.75 \times 10^{-3}$ (kcal/mol)/Å = 5.21×10^{-5} nN to each fluid atom in the direction of the flow. We test both orthogonal direction of the basal plane (named here x and y). Similar simulation protocol and simulation parameters have been employed to study clays [10]. The temperature of 300 K was ensured via the rescaling of velocities and the thermostating was performed taking only the in-plane direction orthogonal to the forced flow into account. SHAKE algorithm was used to rigidify SPC water molecules. Periodic boundary conditions are applied. Ewald summation with a precision of 10^{-5} in forces was used to account for long-range electrostatic interactions.

We performed the simulations with LAMMPS code [12] using a 1 fs time step. Velocity and density profiles were computed per chunks defined by binning along the thickness of the slit pore and averaged during 0.1 ns blocks. A simulation not exceeding 2 ns was enough to reach steady state flows for the pore sizes considered here. Then, the system was sampled during at least 5 ns in order to get the velocity and density profiles.

3. RESULTS AND DISCUSSION

Figure 2 shows the velocity and density profiles for both orthogonal direction of the basal plan according to the four pore sizes studied. The velocities profiles obtained for both in-plane orthogonal directions are equivalent for all pore sizes. This result shows that the anisotropic surface roughness of tobermorite does not affect water dynamics, even for pores as small as

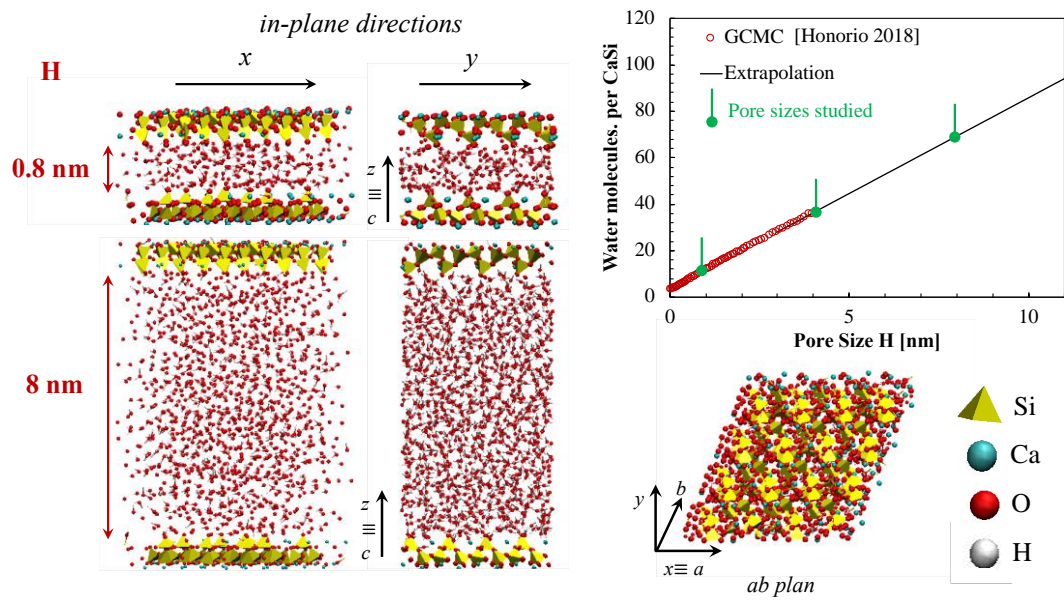


Figure 1: At the left, snapshots of equilibrium configurations of nanoporous tobermorite-water system with pore sizes $H = 0.8$ nm and $H = 8$ nm. At the top right, water isotherm at 300 K and under 1 atm of nanoporous tobermorite as a function of the pore size: GCMC simulations and extrapolation.

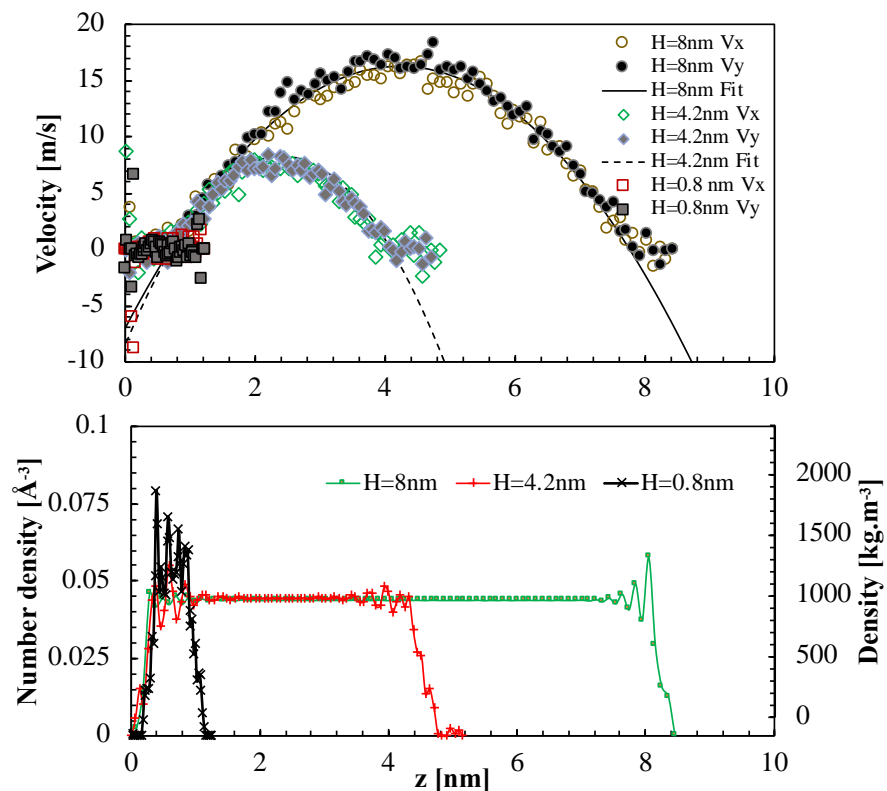


Figure 2: Velocity and density profiles for tobermorite-water system with pore sizes $H = 0.8$, 4.2 and 8 nm.

0.8 nm, which roughly corresponds to a three water layer according to the definitions of interfaces in [7].

Poiseuille flows (i.e. parabolic velocity profiles) are observed for the pores sizes of 4.2 and 8 nm. NEMD simulations on clays show that Poiseuille flows can be identified from pores larger than 3 nm [10]. Confinement effects significantly affects the hydrodynamics in 0.8 nm nanopores so that no parabolic velocity profiles are observed for this pore size. Density profiles of 0.8 nm nanopores shows denser packing of water molecules when compared to larger pore sizes.

The density profiles exhibit a marked oscillatory feature in the vicinity of the solid surfaces. These oscillations are due to water ordering adjacent to these surfaces as discussed in Honorio [7]. At distances z exceeding 1 nm from the solid surface, these effects are not significant and the water reach a density closer to the density of bulk water at 300 K and under 1 atm (approximately 1000 kg/m³). In the portions of the pore the pores that are distances larger than 1 nm from the solid surface, velocity profiles are parabolic.

An estimation of the water viscosity η can be obtained from these velocity and density profiles using the expression [10]:

$$\eta = -F\rho_V \left(\frac{d^2v}{dz^2} \right)^{-1} \quad (1)$$

where ρ_V is the number density. The estimations of water using this expression are compared with the viscosity of SPC water and experimental viscosity of water at 300 K and 1 atm in Table 1. Our results are consistent with the values reported in the literature, which corroborates the validity of the results in Fig. 2.

Table 1: Viscosity of water: comparison against data from the literature

	Viscosity η [cP]	Reference
This work (Eq. 1)	0.79 (H = 4.2 nm) 1.1 (H = 8nm)	-
SPC water	0.58	[13]
SPC/E water	0.67	[10]
Experimental	0.85	[13]
SPC/E water in clay nanopores	0.70 (H = 4.5nm) 0.68 (H = 6nm) 0.709 (H = 8 nm) 0.685 (H = 10 nm)	[10]

The usual *stick* boundary conditions, which corresponds to a zero velocity at the interface fluid-solid, does not apply to the studied system, as can be readily seen from Fig. 2. In this context, a slip boundary condition can be defined based on the specific position z_I of the fluid-solid interface and a slip length b :

$$b = \pm V(z_I) \left(\frac{dV}{dz} \right)^{-1}_{z_I} \quad (2)$$

Different theoretical approaches can be employed to determine z_I [10]. The simplest one is to set z_I as the distance from the fluid-solid interface in which the fluid can be considered as

behaving like a bulk fluid, that is the distance of approximately 1 nm as discussed above. Using $z_l = 1$ nm, the slip length $b = 2.8$ Å ($H = 4.2$ nm) and 2.5 Å ($H = 8.0$ nm). These values are larger than the slip length of 2.1 Å computed to clays using different theoretical approaches to determine z_l [10]. Since the roughness of tobermorite solid surface is larger than the roughness of swelling clays (montmorillonite), the slip length of tobermorite it is expected to be larger than the slip length of clays.

4. CONCLUSIONS

Non Equilibrium Molecular Dynamics simulations were performed to study the hydrodynamics in crystalline calcium silicate hydrates nanopores. We conclude:

- Poiseuille flow is observed in slit pores larger than 4 nm for an imposed force parallel to the basal plane. In smaller pores, due to interface effects and water ordering, density and viscosity are not constant. This is also true to the first nm from the fluid-solid interfaces for all pore studies here.
- Regarding the pore allowing Poiseuille flows, the velocity profiles in both in-plane orthogonal direction are equivalent. Therefore, the anisotropic roughness of tobermorite surface does not affect significantly the flow within slit pores larger than 4 nm.
- Stick boundary conditions are not adapted to describe the Poiseuille flow observed in larger tobermorite nanopores. Slip boundary conditions with a slip length of approximately 2.65 Å can be used to correctly describe this Poiseuille flow.
- These results show that the simplest form of Navier-Stokes equation (i.e. with a homogeneous fluid fully characterized by its bulk viscosity and density) can provide a reasonable description of the flow provided the adequate boundary conditions are employed. This observation is particularly interesting because it points out the transferability of continuum fluid mechanics results to the nanoscale.

The perspectives of this work includes developing homogenization strategies that allows upscaling the hydrodynamics information from the nanoscale up to the scale of industrial applications of concrete.

REFERENCES

- [1] T. Honorio, L. Brochard, M. Vandamme, Hydration Phase Diagram of Clay Particles from Molecular Simulations, *Langmuir*. 33 (2017) 12766–12776. doi:10.1021/acs.langmuir.7b03198.
- [2] T. Honório, T. Lemaire, D.D. Tommaso, S. Naili, Anomalous water and ion dynamics in hydroxyapatite mesopores, *Comput. Mater. Sci.* 156 (2019) 26–34. doi:10.1016/j.commatsci.2018.08.060.
- [3] B. Coasne, C. Alba-Simionesco, F. Audonnet, G. Dosseh, K.E. Gubbins, Adsorption, structure and dynamics of benzene in ordered and disordered porous carbons, *Phys. Chem. Chem. Phys.* 13 (2011) 3748–3757. doi:10.1039/C0CP02205E.
- [4] P.A. Bonnaud, Q. Ji, B. Coasne, R.J.-M. Pellenq, K.J. Van Vliet, Thermodynamics of Water Confined in Porous Calcium-Silicate-Hydrates, *Langmuir*. 28 (2012) 11422–11432. doi:10.1021/la301738p.
- [5] P.A. Bonnaud, C. Labbez, R. Miura, A. Suzuki, N. Miyamoto, N. Hatakeyama, A. Miyamoto, K.J.V. Vliet, Interaction grand potential between calcium-silicate-hydrate nanoparticles at the molecular level, *Nanoscale*. 8 (2016) 4160–4172. doi:10.1039/C5NR08142D.

- [6] M. Youssef, R.J.-M. Pellenq, B. Yildiz, Glassy Nature of Water in an Ultraconfining Disordered Material: The Case of Calcium–Silicate–Hydrate, *J. Am. Chem. Soc.* 133 (2011) 2499–2510. doi:10.1021/ja107003a.
- [7] T. Honorio, Monte Carlo Molecular Modeling of Temperature and Pressure Effects on the Interactions between Crystalline Calcium Silicate Hydrates Layers, Pre-Print <https://bit.ly/2z0T0KZ>. (2018).
- [8] R. Metzler, J.-H. Jeon, A.G. Cherstvy, E. Barkai, Anomalous diffusion models and their properties: non-stationarity, non-ergodicity, and ageing at the centenary of single particle tracking, *Phys Chem Chem Phys.* 16 (2014) 24128–24164. doi:10.1039/C4CP03465A.
- [9] M.J.A. Qomi, M. Bauchy, F.-J. Ulm, R.J.-M. Pellenq, Anomalous composition-dependent dynamics of nanoconfined water in the interlayer of disordered calcium-silicates, *J. Chem. Phys.* 140 (2014) 054515. doi:10.1063/1.4864118.
- [10] A. Botan, B. Rotenberg, V. Marry, P. Turq, B. Noetinger, Hydrodynamics in Clay Nanopores, *J. Phys. Chem. C.* 115 (2011) 16109–16115. doi:10.1021/jp204772c.
- [11] R. Shahsavari, R.J.-M. Pellenq, F.-J. Ulm, Empirical force fields for complex hydrated calcio-silicate layered materials, *Phys. Chem. Chem. Phys.* 13 (2010) 1002–1011. doi:10.1039/C0CP00516A.
- [12] S. Plimpton, Fast Parallel Algorithms for Short-Range Molecular Dynamics, *J. Comput. Phys.* 117 (1995) 1–19. doi:10.1006/jcph.1995.1039.
- [13] P.E. Smith, W.F. van Gunsteren, The viscosity of SPC and SPC/E water at 277 and 300 K, *Chem. Phys. Lett.* 215 (1993) 315–318. doi:10.1016/0009-2614(93)85720-9.

FUNDAMENTAL STUDY OF A CRACKED CONCRETE SELF-REPAIRING SYSTEM: EVALUATION OF WATERPROOFING PERFORMANCE AND FILLING LEVEL OF REPAIR AGENT

Hiroto Tanaka (1), Keiichi Imamoto (1) and Chizuru Kiyohara (1)

(1) Tokyo University of Science, JAPAN

Abstract

This study aims at prevention of reinforcement corrosion due to water leakage through concrete cracks. The authors propose a self-repairing system for cracked concrete. A glass tube containing a repair agent is embedded near a steel bar. When concrete cracks occur and rupture the glass tube, the repair agent enters the cracks and repairs them. This research presents an investigation of the capability of such a system using several kinds of concrete specimens. Water permeability testing was carried out to investigate the waterproofing performance of the system. Additionally, ultrasonic testing was conducted to confirm that the repair agent filled the cracks in the concrete specimens. It was found that the performance of the repair agents depended on their viscosities, wherein specimens with ultralow-viscosity repair agent exhibited best performance to prevent water penetration. Furthermore, analysis of the specimens using such a system showed that the repair agent filled the concrete cracks as well as the area around the reinforcing bars. The experimental results suggested that the system successfully prevents corrosion of reinforcement due to water leakage through cracks in concrete.

Keywords: glass tube, self-repairing system, repair agent, ultrasonic testing

1. INTRODUCTION

In recent years, Japan has witnessed an increasing requirement for long-term reinforced concrete (RC) structures. It is unclear that how long RC structures may be safely used. Generally speaking, even if the RC structure undergoes carbonation, unless steel bars are corroded, the RC structures can continue being used as intended. However, some investigations of RC structures showed water seeping through concrete cracks caused by the local corrosion of steel bars even though neutralization had not reached the steel bars [1]. An example of local corrosion of a reinforcement bar in a non-neutralized area of RC is shown in Figure 1.

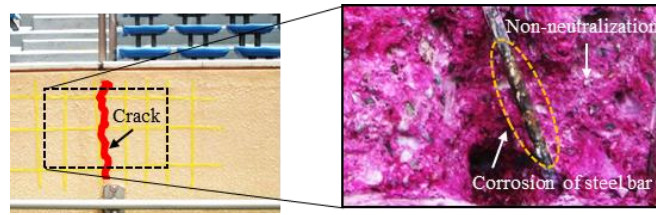


Figure 1: Local corrosion of reinforcement bar within a non-neutralized area of RC [1]

In order to maintain the durability of RC structures, therefore, appropriate treatment is necessary in zones where minimal cracks are expected to occur, especially those in which water is expected to penetrate. However, regular inspection and repair work on RC structures require considerable labor and enormous amounts of time. In recent years, therefore, many studies have focused on introducing self-repairing systems for concretes [2].

This study introduces a self-repairing system (glass tube system) for cracked concrete as shown in Figure 2. A glass tube containing a repair agent is embedded near a steel bar inside the RC structure. When concrete cracks occur to cross the glass tube, the repair agent is automatically filled into the cracks and repairs them in order to prevent local corrosion of the surrounding steel bars due to water seepage through the concrete cracks.

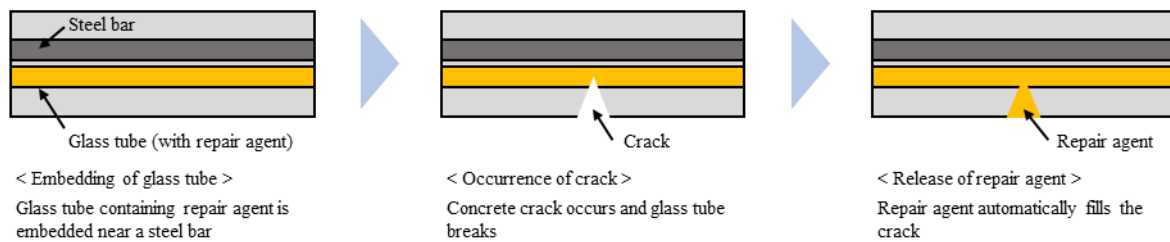


Figure 2: Schematic of a self-repairing system comprising a glass tube filled with a repair agent

In this paper, two series of tests were carried out to investigate the capability of the glass tube system to repair concrete specimens with cracks. Firstly, a water leakage testing was carried out on the cracked RC specimens containing the glass tube system to investigate the waterproofing performance of the glass tube system. These experiments are labelled as Series 1. Secondly, an additional set of experiments (labelled as Series 2,) involved ultrasonic testing to confirm the filling level of the repair agent in the cracks.

2. SERIES 1 EXPERIMENTS

Table 1, Table 2, and Figure 3 show the mix proportion of concrete, materials used in the concrete, and shape of the specimens in the Series 1 experiments, respectively. In every specimen, the concrete placing surface is defined as the lower surface and the opposite surface is defined as the upper surface. The size of all the specimens was $100 \times 100 \times 360$ mm, and a deformed steel bar (D10, length: 740 mm) was set at the center of each specimen. A borosilicate glass tube (length: 400 mm, outer diameter: 15 mm, wall thickness: 1.2 mm) was embedded near the deformed steel bar. Furthermore, notches (depth: 15 mm, thickness: 20 mm) were arranged at both sides at the center of the specimen, where a crack was positioned.

Table 1: Mix proportion of concrete (Series 1)

W/C [%]	s/a [%]	Unit content [kg/m ³]					Slump [cm]	Air [%]
		W	C	S	G	AE [×%]		
55.0	45.5	170	309	808	991	3.09	18.0	4.5

Table 2: Materials used in concrete (Series 1 and Series 2)

Material	Properties	Density [g/cm ³]	F.M. and solid content
Cement: C	Ordinary Portland Cement	3.16	-
Fine aggregate: S	Pit sand	2.58	2.57
Coarse aggregate: G	Crashed stone (Gmax:20 mm)	2.65	62.7 [%]
Air-entraining and water-reducing admixture: AE	Lignin sulfonic acid	-	-

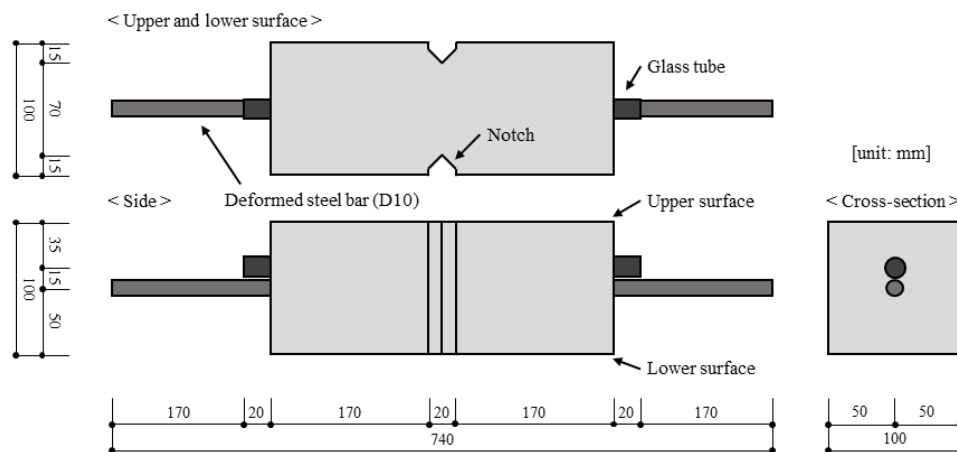


Figure 3: Shape and dimensions of the specimens (Series 1)

The experimental parameters of the concrete specimens are shown in Table 3. Eighteen specimens were prepared, and each of them was classified into 4 types according to kinds of repair agents used.

The repair agent used in Series 1 was a one-pack type epoxy resin that reacts with moisture in the air. The underlying epoxy resin was defined as Epoxy A (viscosity: 150 mPa·s). Epoxy B (viscosity: 500 mPa·s) and Epoxy C (viscosity: 1500 mPa·s) were made by adding ultrafine particulate special aggregate as filler to Epoxy A, and thus had different viscosities. In addition, all the repair agents were colored blue for visual confirmation of discharged resin from the glass tube.

The target crack mouth opening displacement (CMOD) of all types was to be 0.2 ± 0.1 mm. In order to generate a crack in the notch of each specimen, a tensile force was applied to the steel bar by using a universal testing machine. Once a crack exceeding the target CMOD was generated, metal plates (thickness: 20.2 mm) were inserted into the notches on the side of the specimen, and the target CMOD was generated by unloading [3]. Simultaneously, the CMOD of each specimen surface was controlled by utilizing π -type displacement gauges. The CMOD of each specimen was measured with a crack scale. These measurements were conducted at 5 points on each surface of the specimens (Figure 4), and the value of the CMOD of each surface was taken as the average CMOD at the upper and lower surface of each specimen.

Table 3: Experimental parameters of concrete specimens (Series 1)

Type	Description of repair agents	Viscosity [mPa·s]	Target CMOD [mm]	Number of specimens
No. 1	None	-	0.2 ± 0.1	5
No. 2	Epoxy A	150	0.2 ± 0.1	9
No. 3	Epoxy B	500	0.2 ± 0.1	2
No. 4	Epoxy C	1500	0.2 ± 0.1	2

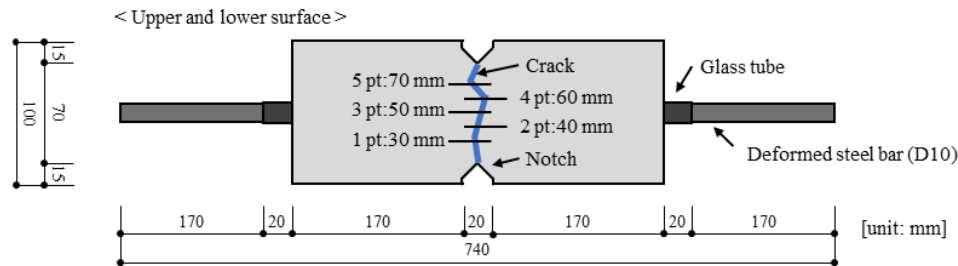


Figure 4: Measurement positions for CMOD (Series 1 and Series 2)

After creating the cracks, the water leakage test was carried out to confirm the waterproofing performance of the glass tube system (Figure 5). An acrylic pipe (outer diameter: 50 mm, inner diameter: 44 mm) was attached at the center of the upper surface of the specimen, and a funnel (inner diameter: 60 mm) was attached at the center of its lower surface. Water was poured until the water head of 100 mm was reached. Then, the changes in the amount of water leakage and water head were measured for 30 min. Water leakage from points other than the funnel was prevented by sealing the cracks outside the acrylic pipe and funnel with a silicone sealant.

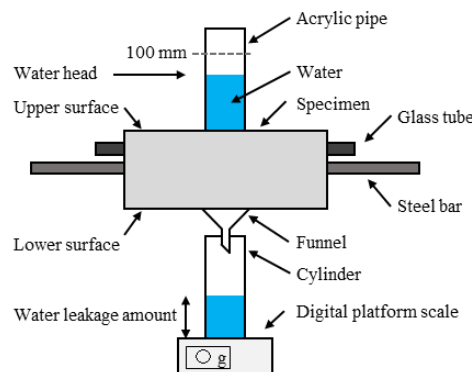


Figure 5: Water leakage test

3. RESULTS AND DISCUSSION: SERIES 1

Table 4 shows the measurement results of the average CMOD of the upper and lower surfaces and amount of water leakage per minute (water leakage rate) for each specimen. Here, the water leakage per minute, from 30 to 60 s after the test started, is defined as the water leakage rate in this study. The water leakage rate of each specimen equipped with the repair agent was compared to a reference specimen without the repair agent in order to confirm the waterproofing performance of the glass tube system.

Table 4: Average CMOD of the upper and lower surfaces and the water leakage rate

Type	Name	Average CMOD [mm]		Water leakage rate [mL/min]
		Upper	Lower	
No. 1	1-1	0.45	0.44	80
	1-2	0.53	0.45	100
	1-3	0.16	0.40	24
	1-4	0.19	0.14	40
	1-5	0.12	0.05	4
No. 2	2-1	0.05	0.20	0
	2-2	0.61	0.63	104
	2-3	0.27	0.27	10
	2-4	0.25	0.50	28
	2-5	0.25	0.12	0
	2-6	0.26	0.31	40
	2-7	0.35	0.29	52
	2-8	0.15	0.53	22
	2-9	0.20	0.13	16
No. 3	3-1	0.18	0.50	34
	3-2	0.29	0.83	80
No. 4	4-1	0.13	0.29	12
	4-2	0.22	0.25	30

Figure 6 shows the relationship between the water leakage rate and the CMOD of the upper surface. The CMOD of the upper surface was compared because the correlation between the CMOD of the upper surface and water leakage rate was higher than that of the other surface. The curve shown in Figure 6 is an approximate curve obtained from the relationship between the water leakage rate and the CMOD of upper surface of reference specimen of No. 1 (total of 5 bodies). In this study, the curve is defined as a criterion to confirm waterproofing performance. The experimental result shows relatively low waterproofing performance than expected. This might be because that it was difficult to inject the repair agent into the all parts of internal cracks in this system. However, Figure 6 shows that all specimens of No. 2 are plotted below the regression curve of No. 1. That means that overall performance would be improved by this system. In particular, water leakage did not occur in the specimens that released Epoxy A to the outside (Figure 7). On the other hand, No. 3 and No. 4 failed to exhibit waterproofing performance. Thus, it was surmised that it is difficult to impregnate concrete cracks with the high viscosity repair agent.

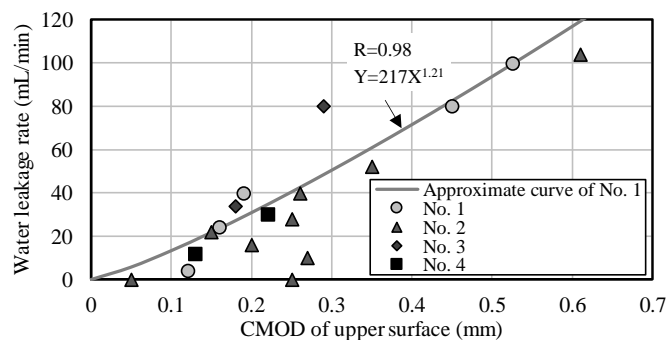


Figure 6: Relationship between water leakage amount per minute and CMOD of the upper surface



Figure 7: Release of repair agent outside the specimen

4. SERIES 2 EXPERIMENTS

Table 5 shows the mix proportions of the concrete used in the Series 2 experiment. The materials used in the concrete are the same as those for Series 1. The Series 2 specimens were almost the same as the Series 1 counterparts, the only change being that of the steel bar. The steel bar was changed to an M12 steel bolt with a length of 600 mm, and a center of 50 mm, and a diameter of 8 mm.

Table 5: Mix proportion of concrete (Series 2)

W/C [%]	s/a [%]	Unit content [kg/m ³]					Slump [cm]	Air [%]
		W	C	S	G	AE [%]		
65.0	48.5	178	274	864	941	2.19	18.0	4.5

The experimental parameters of the concrete in Series 2 are shown in Table 6. Five specimens were prepared, and each specimen was classified into two types according to whether they contained a repair agent or not. Given the results of Series 1, Epoxy A was used as the repair agent in Series 2. The target CMOD of all types was the same as in Series 1. Using a universal testing machine, a tensile force was applied to the steel bolt to generate cracks in the notch. A special jig was used on one side to relax the force that was generated when the specimen was attached to the testing machine. The influence of eccentricity caused by glass tube was minimized using a universal joint on the other side. The CMOD was controlled and measured using π -type and a crack scale, respectively, as in Series 1.

Table 6: Experimental parameters of concrete (Series 2)

Type	Description of repair agent	Viscosity [mPa·s]	Target CMOD [mm]	Number of specimen
No. 5	None	-	0.2 ± 0.1	2
No. 6	Epoxy A	150	0.2 ± 0.1	3

After creating the cracks, the ultrasonic test was carried out to confirm that the repair agent filled the cracks in the concrete specimens. A transmitting ultrasonic probe and a receiving ultrasonic probe with a diameter of 50 mm were placed on the same surface. The propagation time of the ultrasonic waves between the measurement positions on the upper and lower surfaces (Figure 8) was measured. Thereafter, the change rate of the propagation time was calculated using the following equation (1).

$$T_c = T_b \div T_a \quad (1)$$

where, T_c : The change rate of the propagation time [-], T_b : The propagation time after the crack occurs [μ s], T_a : The propagation time before the crack occurs [μ s]

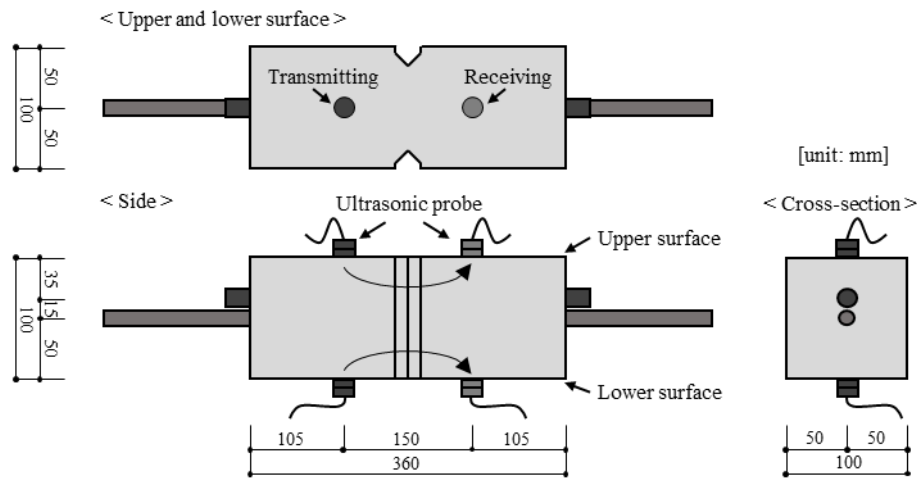


Figure 8: Measurement positions of ultrasonic waves

5. RESULTS AND DISCUSSION: SERIES 2

Table 7 shows the measurement results of the average CMOD, the release condition of the repair agent, and the change rate of the propagation time. The repair agent was not released in 6-1, but it was released in 6-2 and 6-3. The change rate of the propagation time for No. 5 is approximately 0.8, both for the upper and lower surfaces. This is because the ultrasonic wave faced interferences due to the occurrence of the cracks. Therefore, the propagation time after the occurrence of the cracks was longer than in the initial condition. For No. 6, a difference in the change rate of propagation time, depending on whether or not the repair agent was released, was confirmed. For 6-1, both change rates of propagation time (for each surface) were almost the same as those for No. 5. On the other hand, for 6-2 and 6-3, both change rates of propagation time for each surface were higher than those for No. 5. This is because the repair agent filled the cracks sufficiently and prevented ultrasonic wave interference due to the cracks. The change rate of the propagation time for the upper surface of No. 6 was close to that of No. 5 after the occurrence of cracks as the repair agent was hardly discharged to the upper surface because the lower surface of the specimen faced downward. These results suggested that the refilling condition of the repair agent could be confirmed by measuring the propagation time of the concrete cracks when the repair agent is released outside specimens.

Table 7: Measurement results of average CMOD, release condition of repair agent, and change rate of propagation time

Type	Name	Release condition of repair agent	Average CMOD [mm]		Change rate of propagation time [-]	
			Upper	Lower	Upper	Lower
No. 5	5-1	-	0.18	0.24	0.80	0.77
	5-2		0.34	0.42	0.81	0.82
No. 6	6-1	No-Release	0.12	0.13	0.89	0.79
	6-2	Release	0.32	0.12	0.87	0.93
	6-3	Release	0.32	0.35	0.87	0.91

It was considered that the repair agent filled the cracks of the specimen without being released outside it. The split test was carried out to confirm the internal condition of 6-1. The result confirmed the release of the repairing agent into the area around the steel bolt (Figure 9).

Although, at this stage, all that has been shown is some limited crack healing mechanism, this result suggested that it is possible to prevent reinforcement bars from corroding due to water leakage through concrete cracks even if the repair agent could not be released at the outside of the specimen. As the scope of application for the thought is limited to this experiment, it requires further verification.

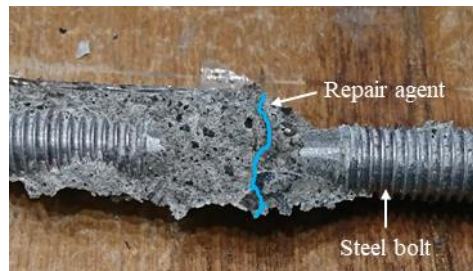


Figure 9: Repair agent released in the area around the steel bolt

6. CONCLUSIONS

- The one-pack type epoxy resin with extremely low viscosity was the most suitable repair agent for this glass tube system.
- Most specimens with extremely low viscosity repair agents confirmed good waterproofing performance in the water leakage test of this study. Moreover, when the repair agent was sufficiently discharged to the outside of the specimen, water leakage did not occur at all.
- It was possible to confirm the filling condition by ultrasonic testing for the specimens in which the repair agent was discharged to the outside. On the other hand, except for the former, it was difficult to confirm the filling condition using ultrasonic testing.
- As the filling of the repair agent around the steel bar inside the specimen was confirmed, in this experiment, it is suggested that the glass tube system proposed in this paper can prevent reinforcement bars in RC structures from corroding due to water leakage through concrete cracks.

REFERENCES

- [1] Kohtatsu Katsumata, et al.: Investigation on Building Materials of the Former National Stadium, Tokyo No.10 permeability coefficient and corrosion of Steel, Summaries of Technical Papers of Annual meeting, Architectural Institute of Japan, pp.435-436, 2015.9
- [2] Japan Concrete Institute: Report of the technical committee on self-healing / repairing technology in cement-based materials (in Japanese), 2011.6
- [3] Kyo Kobiyama, et al.: A study of control method of crack width and evaluation method of initial water flow reduction (in Japanese), Japan Concrete Institute, pp.1439-1444, 2001.3

LONG-TERM MECHANICAL AND SHRINKAGE PROPERTIES OF CEMENTITIOUS GROUTS FOR STRUCTURAL REPAIR

Md Shamsuddoha, Götz Hüsken, Wolfram Schmidt, Hans-Carsten Kühne, and Matthias Baeßler

Bundesanstalt für Materialforschung und -prüfung (BAM), Unter den Eichen 87, 12205 Berlin, Germany

Abstract

Grouts are particularly favoured in rehabilitation of structures due to penetrability and convenience of application. Grouts for repair applications typically require high-performance properties such as rapid strength development and superior shrinkage characteristics. Sometimes industrial by-products referred as supplementary cementitious materials (SCM) are used with neat cement due to their capabilities to provide binding properties at delayed stage. Micro silica, fly ash and metakaolin are such SCMs, those can modify and improve properties of cement products. This study aims at investigating long-term mass loss and linear shrinkage along with long-term compressive and flexural strength for grouts produced from ultrafine cement and SCMs. A series of mixtures were formulated to observe the effect of SCMs on these grout properties. Properties were determined after 365 days of curing at 23°C and 55% relative humidity. The effect of SCMs on the properties are characterised by statistical models. Response surfaces were constructed to quantify these properties in relation to SCMs replacement. The results suggested that shrinkage was reduced by metakaolin, while micro silica and fly ash had positive effects on compressive and flexural strength, respectively.

Keywords: grout, long-term shrinkage, micro silica, fly ash, metakaolin

This work was invited for publication in the open access journal *RILEM Technical Letters*. You can visit the journal and benefit from the full open access to the published articles at: letters.rilem.net.

INFLUENCE OF RECYCLED FIBRE REINFORCEMENT ON PLASTIC SHRINKAGE CRACKING OF CEMENT-BASED COMPOSITES

I. M. G. Bertelsen (1), L. M. Ottosen (1) and G. Fischer (1)

(1) Department of Civil Engineering, Technical University of Denmark, Brovej 118, 2800 Kgs. Lyngby, Denmark

Abstract

Recycled polyethylene (R-PE) fibres from discarded waste fishing nets are used as fibre reinforcement in cement-based mortars for control of plastic shrinkage cracking. A thin, fresh mortar overlay is cast directly on top of a restraining concrete substrate and placed under controlled environmental conditions. Mortar overlays with the addition of R-PE fibres up to 2.0 vol% were tested and compared to mortar overlays with a 0.2 vol% addition of commercially available PP fibres. The cracking behaviour is monitored using a digital image correlation (DIC) technique allowing measurements of strain and displacement fields on the overlay surface. The R-PE fibres were successful in controlling the plastic shrinkage cracking of restrained mortar overlays for fibre fractions of 2.0 vol%.

Keywords: plastic shrinkage, crack detection, plastic waste fibres, digital image correlation

1. INTRODUCTION

The amount of marine plastic litter that have been entering the marine environment has accelerated in the last two decades of the 20th century [1]. Among these are lost or otherwise discarded fishing nets one of the most troublesome fractions due to their large volume and their ability to continue to “ghost fish” while floating around [2]. It is, therefore, important to create incentives for reusing these materials. In this study, we show how recycled polyethylene (R-PE) fibres processed by mechanical cutting of discarded fishing nets can be used for controlling plastic shrinkage cracking in cement-based materials. Plastic shrinkage is the volumetric contraction of cementitious materials and occurs within the first few hours after casting, thus it happens when the material is still in a plastic state [3]. Cracking induced by plastic shrinkage deformations may occur if the tensile stresses generated in the material exceed the strength of the fresh material. A laboratory-scale test method comprising of a fresh overlay cast on top of restraining concrete substrates has been used by [4,5] for evaluation of restrained plastic shrinkage cracking of cement-based materials. The addition of low-modulus synthetic fibres to cement-based materials susceptible to plastic shrinkage cracking is a well-known technique for

controlling the formation of this type of surface cracking [4]. The fibres have the ability to improve the strain capacity of the fresh material and to provide bridging forces across the cracks. Also, polymeric fibres from different types of waste fractions have shown positive results in controlling plastic shrinkage cracking [6–10]. The degree of surface cracking induced by plastic shrinkage is most frequently evaluated based on techniques such as manual microscopic measurements, which are commonly resulting in semi-quantitative measures of the degree of surface cracking; or image-based techniques such as digital image correlation (DIC) enabling more quantitative results [11,12]. In this study, a 2D-DIC technique has been used to analyse the degree of surface cracking of restrained mortar overlays and thereby to evaluate the influence of recycled and virgin fibres.

2. MATERIALS AND METHODS

The test method used for evaluation of restrained plastic shrinkage behaviour of cement-based mortar overlays using DIC was developed at the Technical University of Denmark as described in [13,14]. Each shrinkage test comprised of a concrete substrate and a fresh, thin mortar overlay with the addition of fibres.

2.1 Materials

Substrate bases measuring approximately 50 x 95 x 420 mm³ as shown in Figure 1 were produced in accordance with UNI/EN 1339 [15] and the surface was prepared to a desired roughness using a needle hammer. The compressive strength of the substrate material was tested in accordance with UNI/EN 12390-3 [16] on cylinders and was found to 35.5 ± 6 MPa. At the time of testing, the substrate bases were wetted with tap water and placed inside moulds measuring 60 x 95 x 420 mm³, whereupon a fresh mortar overlay with a thickness of 10 mm was poured on top of the substrate bases directly after mixing. The mixture proportions for the mortar overlay are given in Table 1. The test was carried out with three replicates of each specimen type. Two types of fibres were added to the fresh mortar overlay during the mixing process; 1) commercially available polypropylene (PP) fibres of the type Fiberflex with a diameter of 19.5 µm and a length of 12 mm; and 2) recycled polyethylene (R-PE) fibres obtained from discarded waste fishing nets with a length of 15 ± 9 mm and a diameter of 280 ± 30 µm. The geometrical variations were due to an “uncontrolled” mechanical cutting operation of the waste fishing nets. The recycled R-PE fibres were provided by a Danish recycling company, Plastix A/S that collects, sorts, washes and reprocesses waste fishing nets of difference material fractions. The fishing nets were collected from national and international harbours. The compressive strength and secant modulus of the material used for the mortar overlays was tested on cylinders measuring 60 x 120 mm (three replicates) with the two fibre types at different curing times in accordance with UNI/EN 12390-2 [16] and -13 [17].

Table 1: Mixture proportions for mortar overlay				
	CEM I	Sand 0-4 mm	Water	Fibres (V _f)
	kg/m ³	kg/m ³	kg/m ³	
Mortar overlay	700	980-1032	350	REF: 0% PP: 0.2% R-PE: 0.2-2.0%



Figure 1: Geometry of substrate bases and mortar overlay; R-PE fibres; and PP fibres

2.2 Methods

The shrinkage test was carried out inside a climate-controlled chamber (Figure 2) and the specimens were monitored using DIC. The procedure for the shrinkage tests was as follows:

Time	Procedure
t = 0 min	Mixing procedure included first dry-mixing of cement and sand, whereupon water was gradually added under continuous mixing. If fibres were added, they were added to the wet mixture. “Time zero” (t = 0 h) was being defined as the time when water was added to the dry mixture.
t = 10-15 min	Casting and vibration of the fresh mortar overlay on top of substrate bases.
t = 20-45 min	Specimens were left at ambient temperatures of 20 ± 3 °C.
t = 45 min	Specimen surfaces were covered with a white layer of chalk-based spray paint and subsequently spray painted with black dots of chalk-based paint for the DIC analysis. The chalk-based paint type was more diffusion open than other paint types such as acrylic paint and was, therefore, not affecting the water evaporation rate [13].
t = 55 min	Specimens were transferred to a climate-controlled chamber with a temperature of 32.0 ± 1.5 °C and a relative humidity of $33.5\% \pm 5\%$. Electrical fans were placed in front of the specimens to ensure a wind flow resulting in a maximum water evaporation rate of ~ 0.5 kg/m ² /h. A constant light source was ensured by LED panels and high-resolution optical cameras were fixed parallel to the specimen surfaces as shown in Figure 2.
t = 1 h	The DIC monitoring was initiated by capturing the first image of the specimen surface at t = 1 h, and subsequently every 15 min until t = 25 h. The technique enabled continuous monitoring of in-plane strain and displacement fields.
t = 25 h	Test finished and images imported to DIC software for processing.

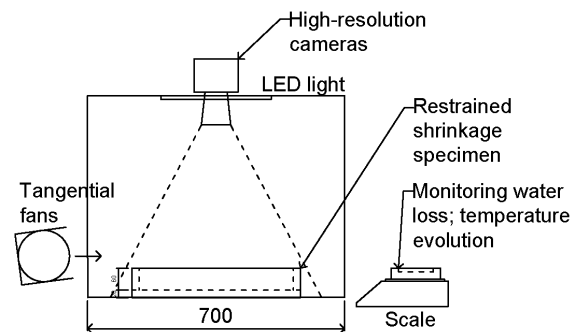


Figure 2: Plastic shrinkage test setup using DIC

After the test, the high-resolution images of the specimen surfaces were modified in ImageJ to improve the brightness and contrast and subsequently analysed using the DIC software, GOM Correlate Professional 2016. A region of interest (ROI) was defined for each specimen in the DIC software and was virtually meshed into a grid with overlapping subset elements. The subset elements were defined to have a size of 20 x 20 pixels and a point to point distance of 15 pixels with a pixel length corresponding to 0.080 mm/pixel. Finally, the DIC data was exported for further analysis and visualisation in Matlab, see also [13,14].

3. RESULTS AND DISCUSSION

3.1 Study of surface cracking using DIC

The DIC software is capable of providing information about the in-plane surface displacement and strain in each subset element, thus the plastic shrinkage behaviour of restrained mortar overlays was evaluated based on this data. The specimens tested included mortar overlays with addition of PP fibres (0.2%), R-PE fibres (0.2-2.0%) or no fibres (REF, 0%). First, we observe one of the reference overlays, REF (A), because this mixture design was expected to be susceptible to plastic shrinkage cracking under the given environmental conditions. The principal strain data in the (x,y)-directions is good for a visual presentation of the surface cracking since peaks in strain (dark colours) represent the crack locations, see Figure 3(a), which illustrates the strain level at the end of the test ($t = 25$ h). From this figure, it is observed that the crack openings mainly appeared in the x-direction (x-direction defined as being parallel to the longer side of the specimens of 420 mm), which is considered due to the geometry of the specimen and the wind flow in the x-direction. Actual crack widths are calculated based on the displacement data [18], which is only given for the x-direction since the main cracks appeared in this direction, see Figure 3(b). Section A-A is going through the centreline of the specimen surface parallel to the x-direction and shows the surface displacement (dotted blue line) and principal strain (red line) along the section surface; see Figure 3(c). Sudden drops in surface displacement correspond well with the opening of an actual surface crack [18] (marked with red and blue circles). For the reference specimen, REF (A), the crack widths along the selected section A-A at $t = 25$ h are for example 102, 317, 327, 83, 189, 51, 72 and 31 μm , which corresponds well with microscopy measurements.

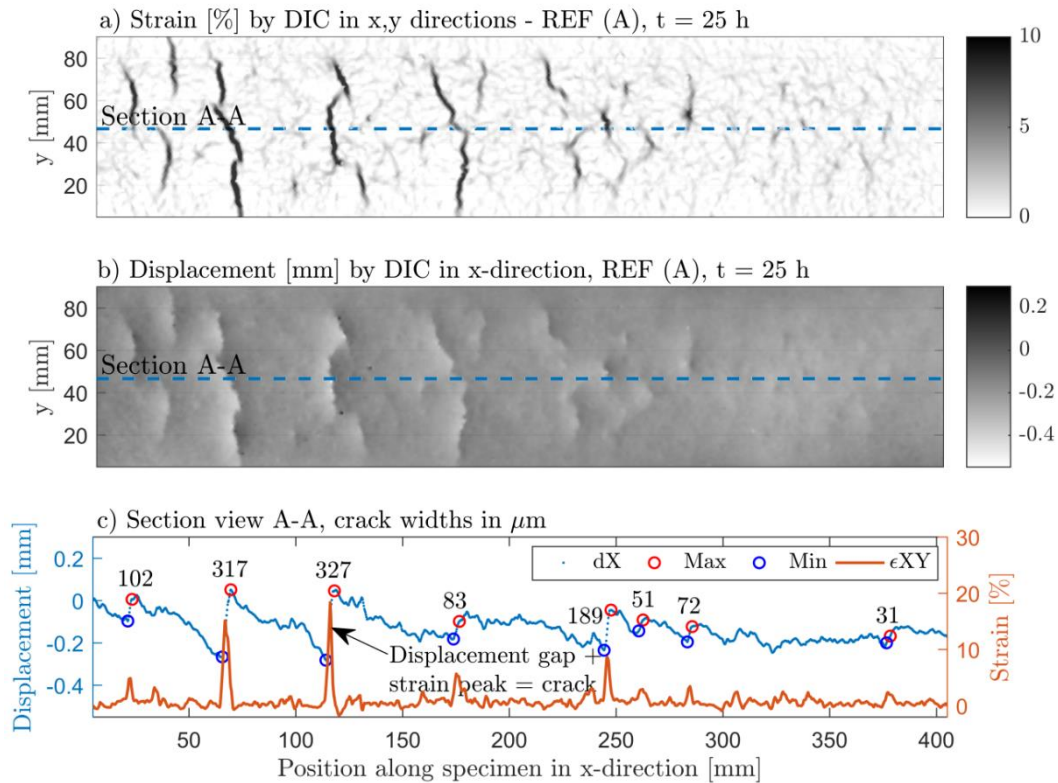


Figure 3: REF (A) specimen at $t = 25$ h. a) Principal surface strain in the (x,y)-direction by DIC; b) Surface displacement in the x-direction by DIC; c) Section A-A going through specimen showing surface displacement in x-direction and principal strain

3.2 Influence of fibres

The surface strains in (x,y)-direction are given for all tested specimens in Figure 4. By visual observations, it is obvious that the addition of fibres had a positive effect on the cracking behaviour of the restrained overlays. As expected, the commercially available PP fibres performed well in controlling the plastic shrinkage surface cracking when added in volume fractions as low as 0.2%. Only very few and fine cracks were visible on the specimen surface and the DIC also revealed areas with increased strain but yet not any visible cracks. Similar results with the use of PP fibres in similar fibre fractions added to restrained cementitious materials were obtained in other studies [4,5]. With respect to the R-PE fibres, which have a diameter that is approximately 15 times coarser than the PP fibres, the influence was not expected to be as good as for the PP fibres. No reduction in surface cracking was observed for the specimens added 0.2% R-PE fibres. For additions of larger fibre fractions such as 0.5% and 1.0% some improvements with respect to the amount and size of cracks were observed, and when 2.0% of R-PE fibres were added to the overlay, only very few visible surface cracks were observed. Despite the fact that 2.0% is a very high volume fraction to add to the material, it was seen that the fibres have a good effect in controlling the plastic shrinkage cracking of the restrained overlays. These results are also in agreement with other studies testing the influence of recycled fibres or fibres with similar coarse diameter, where volume fraction up to 1.5% have been studied [6–8,10,19]. For more elaborated results, please see [14].

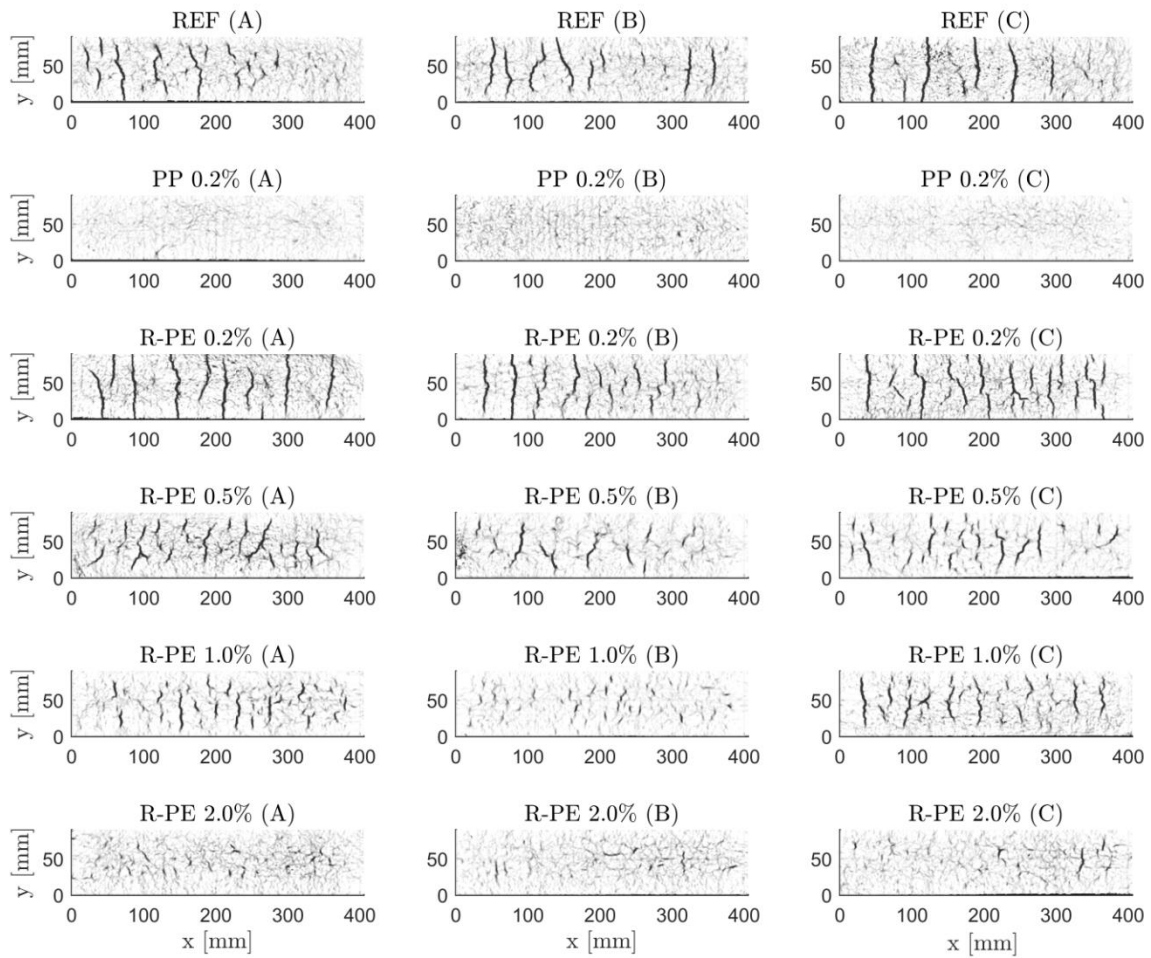


Figure 4: Principal strain for specimens at $t = 25$ h. White colour represents uncracked area with strain $\epsilon_{x,y} = 0\%$; Black colour represents surface cracks with strain $\epsilon_{x,y} = 5\%$.

3.3 Mechanical properties of mortar mixtures

As observed in Figure 4, the necessary addition of R-PE fibres for achieving a satisfactory reduction in surface cracking is 2.0% compared to only 0.2% for the commercially available PP fibres. The compressive strength and secant modulus were tested for three different mixture designs similar to the ones used for the fresh mortar overlays; A reference mortar (no fibres); 0.2% PP fibres; and 2.0% R-PE fibres, with the results being illustrated in Figure 5. The REF specimens achieved the highest compressive strength at all curing times, followed by the 0.2% PP specimen and finally by the 2.0% R-PE specimen. The development of compressive strength and secant modulus followed the same curve shape for all specimen types. The 28-days compressive strength was 52.5 MPa for the reference specimens, 49.0 MPa for the 0.2% PP specimens, and 47.1 MPa for the 2.0% R-PE specimens. These results show that the addition of 0.2% PP fibres decreased the compressive strength with 6%, while the much larger amount of 2.0% R-PE fibres decreased the 28-days compressive strength with 10%. Similar tendencies with respect to the influence of fibres were observed for the secant modulus.

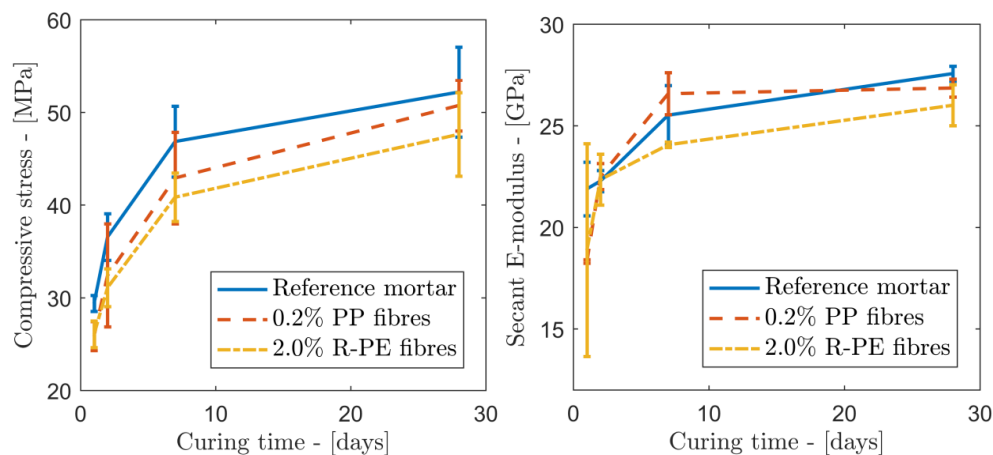


Figure 5: Compressive strength and secant modulus of mixtures used for the mortar overlay in the plastic shrinkage test. Age of wet-curing: 1 day, 2 days, 7 days and 28 days.

4. CONCLUSION

The plastic shrinkage cracking of restrained mortar overlays cast on top of concrete substrates was studied with the aim of evaluating the influence of two fibre types; commercially available PP fibres and recycled polyethylene (R-PE) fibres obtained by mechanical cutting of waste fishing nets. The surface cracking was studied by using a DIC technique enabling the detection of surface strains and displacements. The results showed that the addition of 0.2% PP fibres was successful in controlling the plastic shrinkage surface cracking, while 2.0% of R-PE fibres were necessary to add to the overlay for achieving comparable results.

ACKNOWLEDGEMENTS

The study is part of the project Circular Ocean, which is funded through the ERDF Interreg VB Northern Periphery and Arctic (NPA) Programme 2014-2020 (Grant no. 21). The R-PE fibres were kindly provided by Plastix A/S.

REFERENCES

- [1] C.J. Moore, Synthetic polymers in the marine environment: A rapidly increasing, long-term threat, *Environ. Res.* 108 (2008) 131–139. doi:10.1016/j.envres.2008.07.025.
- [2] J. Brown, G. Macfadyen, Ghost fishing in European waters: Impacts and management responses, *Mar. Policy.* 31 (2007) 488–504. doi:10.1016/j.marpol.2006.10.007.
- [3] P.N. Balaguru, S.P. Shah, *Fiber Reinforced Cement Composites*, McGraw-Hill, 1992.
- [4] N. Banthia, R. Gupta, Influence of polypropylene fiber geometry on plastic shrinkage cracking in concrete, *Cem. Concr. Res.* 36.7 (2006) 1263–1267. doi:10.1016/j.cemconres.2006.01.010.
- [5] A.E. Naaman, T. Wongtanakitcharoen, G. Hauser, Influence of different fibers on plastic shrinkage cracking of concrete, *ACI Mater. J.* 102.1 (2005) 49–58.
- [6] N. Pešić, S. Živanović, R. Garcia, P. Papastergiou, Mechanical properties of concrete reinforced with recycled HDPE plastic fibres, *Constr. Build. Mater.* 115 (2016) 362–370. doi:10.1016/j.conbuildmat.2016.04.050.
- [7] J.H.J. Kim, C.G. Park, S.W. Lee, S.W. Lee, J.P. Won, Effects of the geometry of recycled PET fiber reinforcement on shrinkage cracking of cement-based composites, *Compos. Part B Eng.* 39.3 (2008) 442–450. doi:10.1016/j.compositesb.2007.05.001.

- [8] R.P. Borg, O. Baldacchino, L. Ferrara, Early age performance and mechanical characteristics of recycled PET fibre reinforced concrete, *Constr. Build. Mater.* 108 (2016) 29–47. doi:10.1016/j.conbuildmat.2016.01.029.
- [9] M. Serdar, A. Baričević, M. Jelčić Rukavina, M. Pezer, D. Bjegović, N. Štirmer, Shrinkage Behaviour of Fibre Reinforced Concrete with Recycled Tyre Polymer Fibres, *Int. J. Polym. Sci.* 2015.3 (2015) 1–9. doi:10.1155/2015/145918.
- [10] B.S. Al-Tulaian, M.J. Al-Shannag, A.R. Al-Hozaimy, Recycled plastic waste fibers for reinforcing Portland cement mortar, *Constr. Build. Mater.* 127 (2016) 102–110. doi:10.1016/j.conbuildmat.2016.09.131.
- [11] S. Ghourchian, M. Wyrzykowski, L. Baquerizo, P. Lura, Susceptibility of Portland cement and blended cement concretes to plastic shrinkage cracking, *Cem. Concr. Compos.* 85 (2018) 44–55. doi:10.1016/j.cemconcomp.2017.10.002.
- [12] P. Zhao, A.M. Zsaki, M.R. Nokken, Using digital image correlation to evaluate plastic shrinkage cracking in cement-based materials, *Constr. Build. Mater.* 182 (2018) 108–117. doi:10.1016/j.conbuildmat.2018.05.239.
- [13] I.M.G. Bertelsen, C. Kragh, G. Cardinaud, L.M. Ottosen, G. Fischer, Quantification of plastic shrinkage cracking in mortars using digital image correlation, *Submitt.* 2018.04.28. (n.d.).
- [14] I.M.G. Bertelsen, L.M. Ottosen, G. Fischer, Quantitative analysis of the influence of synthetic fibres on plastic shrinkage cracking using digital image correlation, *Constr. Build. Mater.* 199 (2019) 124–137. doi:10.1001/archinte.168.13.1371.
- [15] UNI/EN-1339, Concrete paving flags - Requirements and test methods, (2003).
- [16] UNI/EN-12390-3, Testing hardened concrete – Part 3 : Compressive strength of test specimens, (2012).
- [17] UNI/EN-12390-13, Testing hardened concrete – Part 13: Determination of secant modulus of elasticity in compression, (2013).
- [18] T. Mauroux, F. Benboudjema, P. Turcry, A. Aït-Mokhtar, O. Deves, Study of cracking due to drying in coating mortars by digital image correlation, *Cem. Concr. Res.* 42.7 (2012) 1014–1023. doi:10.1016/j.cemconres.2012.04.002.
- [19] H. Najm, P. Balaguru, Effect of large-diameter polymeric fibers on shrinkage cracking of cement composites, *ACI Mater. J.* 99.4 (2002) 345–351.

IDENTIFICATION OF DRYING, CREEP AND SHRINKAGE CONSTITUTIVE LAWS FOR CONCRETE AT 20°C AND 40°C, APPLICATION TO VERCORS MOCK-UP

Laurent Charpin (1), Jessica Haelewyn (2) and Jean-Philippe Mathieu (1)

(1) EDF R&D MMC, EDF Lab Les Renardières, France

(2) EDF R&D ERMES, EDF Lab Paris-Saclay, France

Abstract

This article presents a part of EDF's efforts to understand and model the aging of double wall concrete containment buildings of its nuclear power plants. These concrete walls are prestressed walls which must remain leak-tight during the service life of the structure. As a part of this effort a 1/3 mock-up called VeRCoRs has been built for experimental purpose.

Creep and shrinkage induce a decrease of the leak-tightness which must be understood and modeled. Therefore, drying creep and shrinkage constitutive laws are used to model the CBBs. In this paper the identification of these constitutive laws in a non-isothermal context is detailed, and an example of application is shown on the mock-up inner wall.

Keywords: VeRCoRs, concrete containment building, drying, creep, shrinkage

1. INTRODUCTION

Electricité de France (EDF) operates 58 nuclear power plants (NPP) in France. On each plant, the final barrier against accidental release of radioactive fission products to the environment consist in a prestressed concrete containment building (CCB). This structure is not replaceable, and the issue of ageing management has to be addressed with specific care for Long Term Operation.

The prestressing forces are supposed to provide adequate resistance to withstand to a design basis accident, implying an internal pressure of 4.25 bars and a temperature around 140°C. Then, the containment strength and subsequent leaktightness depends on the remaining forces of the prestressing tendons at the end of operation time. However, as for any other civil prestressed structure, these tendons forces decrease slowly with time, due to the effects of the relaxation of the steel tendons and to the shrinkage and creep in concrete.

In addition, for the CCB without steel liner (24 units in EDF French fleet), containment leak tightness seems to be closely linked to the available prestressing forces if the internal pressure rises.

Therefore drying, creep of shrinkage of CCBs need to be carefully addressed in order to predict the remaining service life of structures.

In this work it is shown how the parameters of drying, shrinkage and creep constitutive laws can be identified in a non-isothermal context using laboratory experiments coming from different labs, but on the same concrete: VeRCoRs concrete. The VeRCoRs mock-up is a 1/3 scale mock-up of a CCB aiming at progressing on the understanding and modelling of the mechanical behavior and the evolution of leaking of CCBs [8].

First the constitutive laws used are presented, then the identification process is detailed and finally an example of a simulation on the VeRCoRS mock-up is shown.

2. PRESENTATION OF THE DRYING MODEL

The drying model used in this study is available in Code_Aster under the name SECH_GRANGER (see https://www.code-aster.org/V2/doc/v14/en/man_r/r7/r7.01.12.pdf, [1] and [2]). A non-linear diffusion equation governs the evolution of the water concentration C (L/m³). It writes $\partial C / \partial t = \text{div}[D(C, T) \text{grad} C]$. In non-isothermal conditions, the effect of temperature on the drying kinetics is taken into account by the following temperature dependence of the diffusion coefficient: $D(C, T) = A \exp(BC) \frac{T}{T_0} \exp \left\{ -\frac{Q}{R} \left(\frac{1}{T} - \frac{1}{T_0} \right) \right\}$. Parameter A governs the kinetics while B governs its dependence on the water concentration. Other important parameters are the boundary condition C_{eq} which is imposed as a fixed water concentration at the boundary and represents the water concentration of the concrete at the relative humidity of the test room as well as the initial water concentration C_i . The Q factor plays the role of an activation energy for drying.

3. PRESENTATION OF THE MECHANICAL MODEL

The mechanical model was originally developed for EDF R&D by [1]. It was then modified in order to better represent long term basic creep according to [10], and implemented as a Code_Aster law and then in MFront (www.tfel.sourceforge.net). It is based on an additive decomposition of the strain in four main contributions: elastic strain, drying shrinkage strain, basic creep strain, and dessication creep strain. A detailed description can be found in https://www.code-aster.org/V2/doc/v14/en/man_r/r7/r7.01.35.pdf.

The strain decomposition takes into account drying shrinkage strains, elastic strains, basic creep strains and drying creep strains (the bold font denotes second order tensors): $\boldsymbol{\varepsilon} = \boldsymbol{\varepsilon}^{shr} + \boldsymbol{\varepsilon}^{el} + \boldsymbol{\varepsilon}^{bc} + \boldsymbol{\varepsilon}^{dc}$

Drying shrinkage. The drying shrinkage rate is assumed proportional to the water concentration rate following $\dot{\boldsymbol{\varepsilon}}^{shr} = k^{shr} \dot{C} \mathbf{1}$ where $\mathbf{1}$ is the second order identity tensor. Parameter k^{shr} is the proportionality factor.

Elasticity and basic creep. The combination of elastic and basic creep strains is formed as a Burgers rheological model. Elasticity and basic creep are isotropic and hence, the Burgers model is duplicated in deviatoric and spherical chains (“d” relates to deviatoric while “s” relates to spherical). For each chain the strain is composed of elastic strain (ε_s^{el} and ε_d^{el}), reversible basic creep modeled by the Kelvin-Voigt element (ε_s^{rbc} and ε_d^{rbc}) and irreversible basic creep

modeled by the Maxwell element by using a viscosity which is not constant in time and dependent on the current state of strain (ε_s^{ibc} and ε_d^{ibc}).

The equations related to this Burgers model are now recalled for the spherical chain (the deviatoric can be obtained by replacing “s” by “d” and using tensors instead of scalars).

The elastic strain is simply proportional to the stress: $\varepsilon_s^{el} = \sigma_s / (3k^{el})$.

The basic creep strains are assumed proportional to the water concentration. The reversible basic creep is governed by the equation $h\sigma_s = k^{rs}\varepsilon_s^{rbc} + \eta^{rs}\dot{\varepsilon}_s^{rbc}$ while the irreversible basic creep follows the equation $h\sigma_s = \eta^{is}\dot{\varepsilon}_s^{ibc}$. The viscosity of the irreversible contribution is assumed to be dependent on the current state of irreversible strains following the equation: $\eta^{is} = \eta_0^{is} \exp\{\|\varepsilon_m^{ibc}\|/\kappa\}$ where $\|\varepsilon_m^{ibc}\| = \max\{\|\varepsilon_m^{ibc}\|, \sqrt{\varepsilon^{ibc}:\varepsilon^{ibc}}\}$. This feature induces non-linearity in the creep model.

The model is also thermo-activated by adding a temperature dependence to the parameters of the previous equations. Parameters k^{rs} , k^{rd} , η^{rs} , η^{rd} , η_0^{is} and η_0^{id} have the following temperature dependence exemplified on $k^{rs}(T) = k_0^{rs} \exp\left\{\frac{E_{ac}}{R}\left(\frac{1}{T} - \frac{1}{T_0}\right)\right\}$. Also, $\kappa = \kappa_0 / \exp\left\{\frac{E_{ac}}{R}\left(\frac{1}{T} - \frac{1}{T_0}\right)\right\}$.

Where E_{ac} is the activation energy for creep.

Therefore, a large number of parameters is introduced. However, assuming that the basic creep Poisson's ratio is constant and equal to the elastic Poisson's ratio ν^{el} , the number of independent parameters can be reduced. Using this assumption the basic creep parameters can be related through the equations $\eta^{is}/\eta^{id} = \eta^{rs}/\eta^{rd} = k^{rs}/k^{rd} = (1 + \nu^{el})/(1 - 2\nu^{el})$.

Desiccation creep Finally, the desiccation creep is computed according to a modified version of a law called Bažant's law, relating the excess of strain rate during drying to the rate of change of the water concentration [3]. It is supposed in this version of the model that desiccation creep occurs with a zero Poisson's ratio and that its rate is proportional to the absolute value of the relative humidity rate: $\dot{\varepsilon}^{fdess} = |\dot{h}|/\eta^{fd} \sigma$. The zero Poisson's ratio assumption has been discussed elsewhere but is still used in the present paper [4].

4. IDENTIFICATION OF THE PARAMETERS

Different labs at EDF and elsewhere have performed experiments on VeRCoRs concrete under EDF funding or through the MACENA program. In this article a selection of these tests is used in order to calibrate the parameters of the drying and mechanical models. In this section a brief explanation of how the parameters were identified and the results obtained is given. The tests used come from 3 labs:

- EDF DI TEGG (Aix en Provence, France): mass-loss, drying shrinkage, basic creep and drying creep at 20°C/50% RH on cylindrical samples with diameter 16 cm and length 100 cm
- EDF R&D MMC (Ecuelles, France): desorption isotherm at 25°C, mass loss at 25°C/58% RH on cylindrical samples with diameter 11 cm and thickness 3 cm
- LMDC (Toulouse, France): mass-loss, drying shrinkage, basic creep, drying creep at 20°C/50% RH and 40°C/50%RH on cylindrical samples with diameter 11cm and length 22 cm [11].

Other tests have been performed but will not be mentioned further in this paper such as tests at higher temperatures. The calibration of the constitutive laws on such tests will be the focus of future work.

4.1 Drying

The identification of the drying law is performed using different kinds of experimental data:

- Porosity measurements performed on different samples of VeRCoRs concrete made on the construction site or in the lab according to the same mix give the porosity for each type of concrete. The porosity is taken equal to 16.1% for TEGG tests, 16.3 for MMC tests and 15.5 for LMDC tests. For these tests saturation is performed under vacuum and the dry mass is determined after drying at 105°C.
- Density measurements were also performed. The density is taken equal to 2357 kg/m³.
- The initial saturation has also been measured on samples from DI TEGG. It is taken equal to 88.17% for concrete sealed before the beginning of the drying phase (LMDC and TEGG) and equal to 100% for concrete resaturated before the tests (MMC).
- The desorption isotherm has been measured at MMC at 25°C. It is given in Table 1 where the columns at 100% and 0% have been deduced from porosity tests.

Table 1: Desorption isotherm at 25°C. The water content is computed assuming a porosity equal to 16.3%.

HR (%)	100	97	92	84	75	58	43	23	0
S (%)	100	86.7	79.4	67.5	53.6	37.2	25.5	15.2	0
C (L/m ³)	163	141.3	129.4	110.0	87.4	60.6	41.6	24.8	0

Once these measurements taken into account, the unknown parameters are the A and B kinetics coefficients concerning the ambient temperature (the initial water concentration and boundary water concentration are known assuming that the desorption isotherm at 20°C is identical to the one at 25°C). Concerning the temperature behaviour, the activation energy term Q/R and the boundary condition (i.e. the water content corresponding to 40°C/50%RH at equilibrium) are unknown. These 4 parameters are identified in two phases, making use of the tests at 20°C in the first stage and those at 40°C in the second one. A specificity is the samples in MMC for which an exchange condition at the boundary had to be assumed for consistency with the other tests, where a fixed water concentration has been used, introducing a new parameter h_{MMC} also identified in the first stage. The comparison between experiment and simulation is presented on Figure 1. The values of the parameters are $A = 4.87 \cdot 10^{-15} \text{ m}^2/\text{s}$, $B = 0.08$, $h_{MMC} = 2.26 \cdot 10^{-9} \text{ m/s}$, $S_{eq}^{40^\circ\text{C}/50\%} = 9.97\%$, $Q/R = 7147.7\text{K}$ and the reference temperature used is $T_0 = 15^\circ\text{C}$.

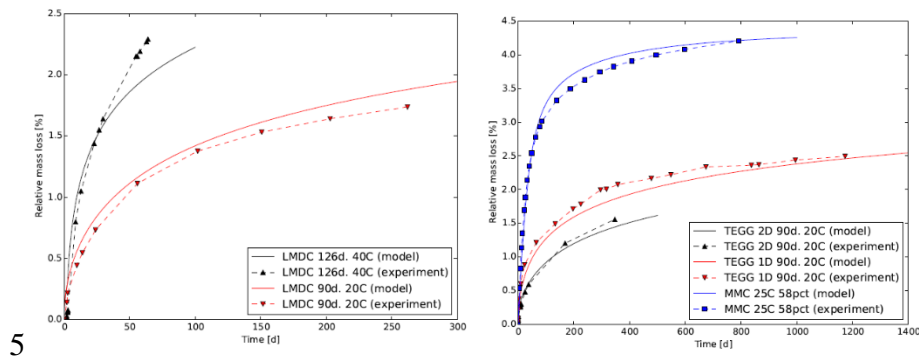


Figure 1: Identification of drying. Left: LMDC tests. Right: MMC and TEGG tests.

Discussion:

- The need for using an exchange coefficient for MMC tests comes from the fact that compared to TEGG and LMDC tests, drying of the MMC samples always seems slower. Different explanations can be proposed. First, the MMC tests are performed in dessiccators while other tests are performed in large air conditioned rooms or large climate chambers. The ventilation conditions might have been different. However a test has been performed comparing drying in dessiccators with or without a fan, and this explanation has been ruled out. A second explanation could be related to the long underwater conservation experienced by the MMC samples. However since the porosity values are the same, it is unlikely that large evolutions of the porosity network has occurred. Finally, the exposed surface of the MMC sample is a sawed surface, while for other tests it is a molded surface. A tests to quantify the influence of this fact is under progress. It has been reported earlier that sawed samples dry slower that molded ones [1].
- For the identification at 20°C the boudary condition has not been identified since the equilibrium water concentration at 20°C and any RH is known using the desorption isotherm. However at 40°C it is not the case and hence, the boundary condition has been identified. This is a rather uncomfortable situation in the case where the mass-loss curve used does not reach equilibrium. The knowledge of the desorption isotherm at 40°C would be very beneficial. Work is under progress to measure it and hence know the isotherm at various temperatures, making use of models such as the one presented in [5].
- The identification of the kinetics parameters of the drying law is ill-posed when the experimental data used is only mass-loss at the same RH [6]. Work is under progress to use water content profiles to overcome this difficulty.

4.2 Mechanics

Some mechanical parameters have been measured independently from these tests such as the Young's modulus. The Young's modulus is taken equal to 34 GPa and the Poisson's ratio 0.248. The conversion from the water concentration to relative humidity needed for the mechanical model is performed using the desorption isotherm at 25°C.

Different identification steps are performed to identify all the parameters. First, the drying shrinkage parameter is identified on TEGG and LMDC drying shrinkage test at 20°C, see Figure 2.

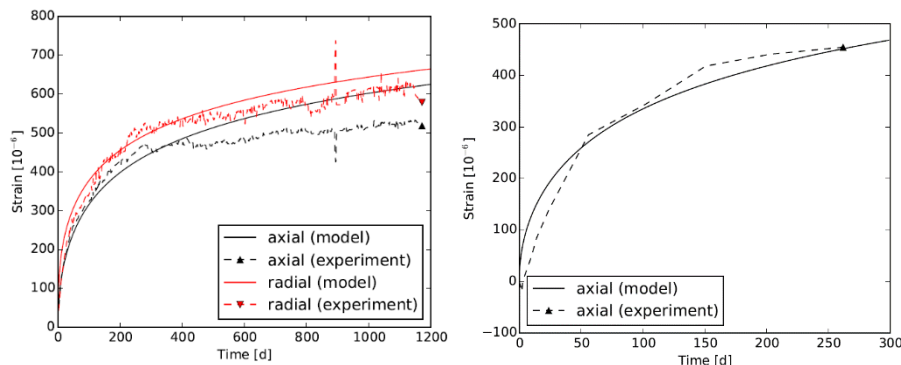


Figure 2: Identification of the drying shrinkage parameter. Left: TEGG. Right: LMDC.

Second, it is verified that the model is capable of reproducing shrinkage at 40°C and the thermal dilation coefficient is identified (Figure 3 Left).

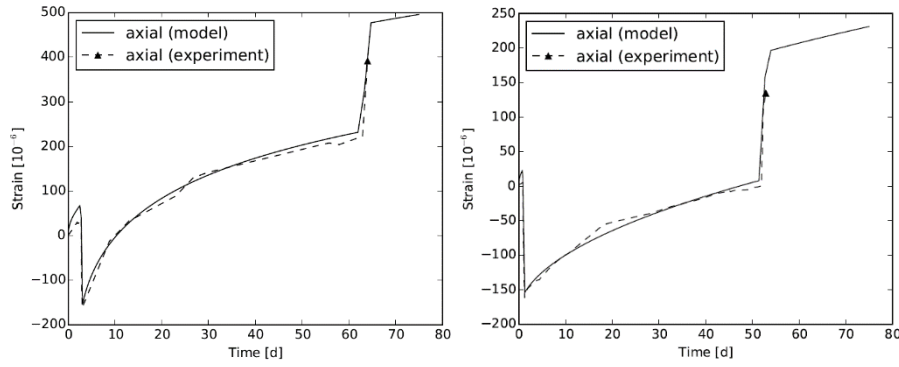


Figure 3: Left: LMDC drying shrinkage at 40°C. Right: LMDC autogenous shrinkage at 40°C

Then, a parasite mass-loss parameterized function is identified for the 40°C autogenous shrinkage test which has undergone important leakage (Figure 3 Right). The parasite mass-loss at the end of the test identified in the simulation is consistent with that measured on the real samples (0.6% of the total mass).

In the next step the parameters of the creep model (basic and drying creep) are identified on TEGG tests at 20°C (Figure 4). The radial strains in the basic creep tests are not well reproduced, but this might be related to an instrumentation problem since the measurement on these small strains is not very accurate on the sealed tests due to small leaks occurring at the measurement location [7].

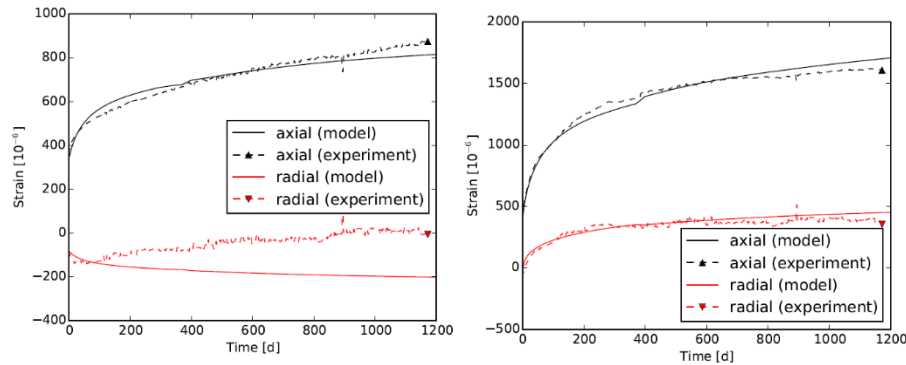


Figure 4: Identification of creep parameters at 20°C. Left: TEGG basic creep. Right: TEGG drying creep.

Then the activation energy for creep is also identified on the LMDC 40°C tests (Figure 5). Eventually all the parameters can be summarized: $k^{shr}=1.03 \cdot 10^{-5} \text{ m}^3/\text{kg}$, $\alpha_{ther}=9.2 \cdot 10^{-6}/\text{K}$, $k^{rd}=1.70 \cdot 10^{11} \text{ Pa}$, $\eta^{rd}=5.04 \cdot 10^{17} \text{ Pa.s}$, $\eta^{id}=1.48 \cdot 10^{17} \text{ Pa.s}$, $\kappa=1.03 \cdot 10^{11}$, $\eta_0^{fd}=7.39 \cdot 10^9 \text{ Pa.s}$, $E_{ac}/R=5181 \text{ K}$, with the reference temperature $T_0=20^\circ\text{C}$.

Discussion:

- This set of parameters induced a temperature-dependent creep kinetics. The temperatures sometimes fall below 20°C in the VeRCoRs experiment (down to 5°C). It could be interesting to verify that this thermal behavior is valid for such low temperatures.
- In some cases (e.g. TEGG tests) it seems that sealed creep tests loose less water than sealed shrinkage tests, perhaps due to a confinement effect of the sealing aluminum foil under loading. This assumption has been used here but must be verified.

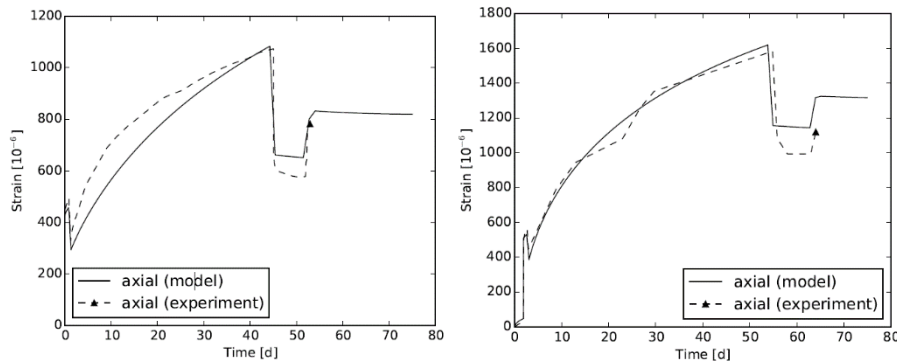


Figure 5: Identification of the creep activation energy at 40°C. Left: LMDC basic creep. Right: LMDC drying creep.

5. APPLICATION TO THE VERCORS MOCK-UP

The VeRCoRs mock-up is shown on Figure 6 Left. The mock-up is used to understand the mechanical behavior and the evolution of leak-tightness of containment buildings.

The computations performed on the full mock-up have been described in reference [8] and will not be detailed. A finite element model of the full containment including concrete, prestress and other details is used for thermal, hydric and mechanical simulations (Figure 6 Middle). The thermohydric boundary conditions are prescribed from the measurements of the ambient temperatures and humidities. The simulations starts before prestress and takes into account pressure tests performed every year on the mock-up. The comparison between simulations and experiment is here focused on a single strain measurement (vibrating wire gage). As can be seen on Figure 6 Right, the simulation in green corresponding to the present set of parameters reproduces correctly the strain measures on the mock-up during the ageing phases and also during the periods where heating is stopped in order to perform the pressure tests.

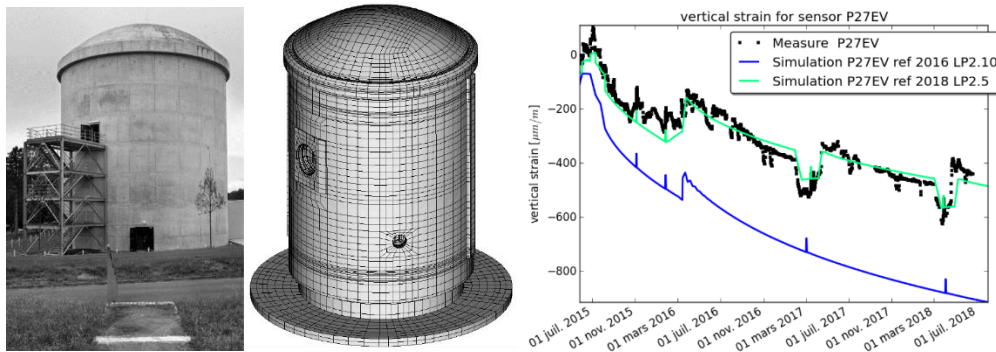


Figure 6 - Left: VeRCoRs mock-up. Middle : FE mesh. Right: results comparison

6. CONCLUSION

Simulating the behaviour of concrete structures requires the proper identification of the parameters of the constitutive laws. In this article, the process of such an identification of parameters for drying and mechanical laws is detailed for the VeRCoRs mock-up.

The parameters are successfully identified on drying, creep and shrinkage tests coming from different laboratories but on the same concrete, at 20°C and 40°C.

Finally, an example of application on the real structure is shown.

ACKNOWLEDGEMENTS

Different teams performing the experiments are acknowledged. At DI TEGG: F. Guijarro, E. Coustabeau and O. Brémond. At R&D MMC: P. Sémété and R. Thion. At LMDC: T. Vidal, V. N. Nguyen and H. Cagnon. IFSTTAR (J.-M. Torrenti) and ANRT are also acknowledged as well as the team working on the VeRCoRs at EDF: A. Legrix, A. Courtois, B. Masson, M. Corbin, G. Boulant, C. Toulemonde, F. Hamon, S. Michel-Ponnelle, F. Taillade, J.-M. Hénault.

RÉFÉRENCES

- [1] Granger L., *Comportement différé du béton dans les enceintes de centrales nucléaires : analyse et modélisation*, Ecole Nationale des ponts et Chaussées, 1996.
- [2] Mensi R., Acker P. and Attolou A., 'Séchage du béton: analyse et modélisation', *Materials and Structures*, vol. 21, n° 13, pp. 3-12, 1988.
- [3] Bazant Z. and Chern J., 'Concrete creep at variable humidity: constitutive law and mechanism', *Materials and Structures*, vol. 18, n° 11, pp. 1-20, 01 1985.
- [4] Charpin, L., Sow, T., d'Estève, X., Hamon, F. and Mathieu, J.-P., 'Numerical simulation of 12 years long biaxial creep tests. Efficiency of assuming a constant Poisson's ratio,' 6th BIOT conference, Champs sur Marne, France.
- [5] Poyet, S. and Charles, S., 'Temperature dependence of the sorption isotherms of cement-based materials: Heat of sorption and Clausius–Clapeyron formula', *Cement and Concrete Research*, 2006.
- [6] Charpin, L., Courtois, A., Taillade, F., Martin, M., Masson, B. and Haelewyn, J., 'Calibration of Mensi/Granger constitutive law: evidences of ill-posedness and practical application to VeRCoRs concrete', TINCE 2018, Paris-Saclay, France, 2018.
- [7] Charpin, L., Le Pape, L., Coustabeau, E., Toppani, E., Heinfli, G., Le Bellego, C., Masson, B., Montalvo, J., Courtois, A., Sanahuja, J. and Reviron, N., 'A 12 year EDF study of concrete creep under uniaxial and biaxial loading', *Cement and Concrete Research*, pp. 140-159, 2017.
- [8] Mathieu, J.-P., Charpin, L., Sémété, P., Toulemonde, C., Boulant, G., Haelewyn, J., Hamon, F., Michel-Ponnelle, S., Hénault, J.-M. and Taillade, F., 'Temperature and humidity-driven ageing of the VeRCoRs mock-up', Euro-C conference, Austria, 2018.
- [9] Benboudjema, F., *Modélisation des déformations différées du béton sous sollicitations biaxiales. Application aux enceintes de confinement de bâtiments réacteurs des centrales nucléaires*, Doctoral dissertation, Université de Marne la Vallée, 2002.
- [10] Sellier, A. and Buffo-Lacarrière, L., 'Toward a simple and unified modeling of basic creep, shrinkage and drying creep for concrete', *European Journal of Environmental and Civil Engineering*, vol. 10, 2009.
- [11] Nguyen, V.N., Cagnon, H., Vidal, T., Torrenti, J.-M., Sellier, A., 'Effet des couplages Thermo-Hydro-Mécanique sur le comportement différé du béton précontraint', Congrès Français de Mécanique, Lille, 2017

SHRINKAGE AND BOND BEHAVIOUR OF ONE-PART ALKALI-ACTIVATED MORTARS

P. Sturm (1), G. J. G. Gluth (1), H. J. H. Brouwers (2) and H.-C. Kühne (1)

(1) Bundesanstalt für Materialforschung und -prüfung (BAM), 7.4 Technology of Construction Materials, Unter den Eichen 87, 12205 Berlin, Germany

(2) Technische Universiteit Eindhoven, Department of the Built Environment, P.O. Box 513, 5600 MB Eindhoven, The Netherlands

Abstract

Mortars for application on concrete, e.g. repair mortars or protective coatings, need to have a durable bond to the substrate. This bond is determined by the adhesion between the two materials and by the differential deformations of the mortar and the substrate. In the present contribution, the hygric deformations (shrinkage/expansion) of novel one-part alkali-activated mortars and their bond to concrete substrates are studied. Shrinkage of the mortars was studied at 50 % r.H., while expansion was studied on mortars stored over an open water surface (> 99% r.H.). The bond behaviour was studied by pull-off tests according to DIN EN 1542 and by optical microscopy.

The alkali-activated mortars exhibit hygric deformations much lower than the deformations of an established, commercial mortar for sewer maintenance that was tested as reference in parallel with the alkali-activated mortars. The bond behaviour of the alkali-activated mortars depends strongly on their mix-design and curing. Optical microscopy showed that in the mortars with lower bond strength, cracks developed in the mortar during curing. Mortars with appropriate mix-design and curing did not exhibit cracking, and their pull-off strength (up to > 3 MPa) conformed to the requirements of relevant standards.

Keywords: alkali-activated materials, repair mortars, shrinkage, bond behaviour, durability

1. INTRODUCTION

Alkali-activated materials (AAMs) have been reported numerous times to exhibit a high resistance against acid attack [1-6]. This makes them promising candidates for application as sewer repair mortars, where high resistance against biogenic sulfuric acid is required [7,8]. Very recently, one-part alkali-activated mortars, which do not require storage and employment of alkaline activator solutions, thus providing significant easier handling, were developed and shown to exhibit excellent resistance against sulfuric acid attack [5]. Their high acid resistance was found to be caused by precipitation of silica gel during acid attack at the solution-mortar interface, which inhibited further degradation [5].

Besides acid resistance, the bond to the concrete substrate is of major importance for the suitability of repair systems such as sewer repair mortars. The bond, in turn, is determined by the hygric deformations (*i.e.* drying shrinkage and swelling), creep/relaxation as well as evolution of Young's modulus and tensile strength. In general, AAMs have been found to provide a good bond behaviour on concrete [9-11], but often exhibit considerable deformations due to drying [12, 13]. However, because the materials differ in chemical and mineralogical composition, these previous results are not necessarily valid for the one-part activated mortars under study. Thus, in the present contribution, we have studied their shrinkage and swelling as well as their bond behaviour.

2. MATERIALS AND METHODS

2.1. Mortar mix-designs and mixing

Solid binders were produced from silica (rice husk ash or microsilica) and sodium aluminate, mixed in proportions to yield specified $\text{SiO}_2/\text{Al}_2\text{O}_3$ ratios. For specific formulations the binder was exchanged with ~22 wt.% ground granulated blast furnace slag (SL) to provide a total CaO content of 10 wt.% in the dry binder mass. The chemical compositions of the starting materials can be found in Ref. [5]. The mortars were produced with CEN standard sand with a maximum grain size of 2 mm. The designations and compositions of the mortars are given in Table 1.

Mixing of the fresh mortars for the deformation measurements (shrinkage and swelling) was done with a rotating pan Zyklos mixer with additional fixed paddles. Binder and sand were dry-mixed for 2 minutes at a rotation speed of 70 min^{-1} . Subsequently the water was added and the mortars were mixed for further 5 minutes. The mortars for the investigation of the bond strength were produced with an Eirich Intensive Mixer (Type RV02) at rotation speed 1 with additional rotating paddles (400 min^{-1}). Binder and sand were homogenized by dry-mixing for 2 minutes. Subsequently the mixing water was added, and the fresh mortars were mixed for further 5 minutes.

Table 1: Composition of the one-part alkali-activated mortars

Mortar	$\text{SiO}_2/\text{Al}_2\text{O}_3$ (mol/mol)	w/b (g/g)	Paste content (wt.%)	$\text{Na}_2\text{O}/\text{CaO}$ (mol/mol)	$\text{H}_2\text{O}/(\text{Na}_2\text{O}+\text{CaO})$ (mol/mol)
<i>MS_6</i>	6.03	0.40	37.4	10.66	11.44
<i>MS_6_SL</i>	6.31	0.38	30.0	0.80	6.74
<i>RHA_6</i>	6.05	0.40	37.6	12.40	11.30
<i>RHA_6_SL</i>	6.38	0.38	38.2	0.80	6.67

A commercially available repair mortar for sewer maintenance was used as reference material (denoted REF). The mortar binder was based on calcium aluminate cement (CAC), but in addition contained significant amounts of Portland clinker phases as shown by XRD measurements.

2.2. Deformation measurements

The measurement of the deformations of the mortars at ambient temperature was performed on standard mortar prisms ($40 \text{ mm} \times 40 \text{ mm} \times 160 \text{ mm}$) in accordance with DIN EN 12617-4:2002, using a Heidenhain MT12 (D-K-17552-01-00) measuring device. The alkali-activated mortars were heat-cured either at $80^\circ\text{C}/80\% \text{ r.H.}$ (mortars without slag) or at $60^\circ\text{C}/80\% \text{ r.H.}$ (mortars with slag) for 24 h. Immediately after that period, the specimens were removed from the moulds, measurement pins glued to the prisms using a two-component adhesive and the

initial lengths recorded (at an age of ~24.5 h). Subsequently, the prisms were exposed to either 23 °C/50% r.H. (shrinkage) or at 23 °C in closed boxes above water (swelling; relative humidity measured to be > 99 % r.H.). The REF mortars for the shrinkage measurement were cured at 23 °C in the moulds above water for 1 day and subsequently treated like the alkali-activated mortars. The deformations, *i.e.* shrinkage or expansion, were recorded up to 91 days.

2.3. Pull-off tests

The determination of the bond strength was carried out by pull-off tests based on DIN EN 1542:1999 with minor adjustments. The mortars were applied on standard MC 0.40 (w/b = 0.40) concrete specimens in accordance with DIN EN 1766:2017. The fresh mortars were applied with a thickness of 8 mm; no bridging agents were used. For samples marked with “1”, the mortars were applied horizontally; for samples marked with “2”, the mortars were applied vertically. If no number is given in the figures below, only the horizontally oriented specimens are reported. After a time of 2–4 hours the formwork was removed and the specimens were either heat-cured at 60 °C or 80 °C for 24 h and then at 23 °C for 2 days, or cured at 23 °C covered with a plastic film for 3 days. Subsequently, the specimens were stored at 23 °C and a relative humidity of 50 % or 65 % until a mortar age of 28 days. The REF mortars for the investigation of the bond behaviour were cured and stored at 23 °C like the alkali-activated mortars without initial heat-curing. The detailed curing and storage conditions for each specimen are given together with the results in the figures below.

The pull-off tests were performed at a mortar age of 28 days, using a F15D EASY M2000 device (1.5–15 kN range) at a loading rate of 100 N/s (~0.05 MPa/s) until failure occurred.

Optical microscopy was performed on cut pieces from undisturbed regions of selected specimens after pull-off testing, using an Olympus SZX 16 stereo microscope with an integrated ultraviolet (UV) mode. Before microscopy, samples were embedded in epoxy resin (Conpox Resin BY 158; Conpox Hardener HY 2996) under vacuum. An UV fluorescent resin (EPODYE) was added to the epoxy, thus, areas of low density, *e.g.* cracks or pores, appear brighter in the micrographs when recorded under UV light.

3. RESULTS AND DISCUSSION

3.1. Hygric deformation behaviour

Figure 1 shows the hygric deformations of the mortars. In all cases, except shrinkage of RHA_6, the deformations had reached a plateau before the end of the measurements, *i.e.* the values recorded at the end of the measurements can be regarded as final deformations. The fact that the shrinkage of RHA_6 did not plateau within the measurement period may have been caused by a slower development of the mechanical strength of that mortar (*cf.* the development of the pull-off strengths, Section 3.2).

The REF mortar exhibited the highest shrinkage of all mortars at all measurement times. After 91 days a final shrinkage of 1.9 mm/m was recorded, and during the measurements cracks occurred at the surface of the specimens. The drying shrinkage of the alkali-activated mortars was significantly lower, with the largest value of 0.9 mm/m observed for MS_6. Notably, the final shrinkage values of RHA_6 and RHA_6_SL were less than 0.001 mm/m, *i.e.* negligible.

A very similar picture emerged for the swelling of the mortars. While the REF mortar exhibited the highest values at all times (1.1 mm/m after 91 days), the swelling of the alkali-activated mortars was low or even negligible. MS_6 underwent 0.1 mm/mm expansion (last measurement after 56 days) and MS_6_SL exhibited an expansion of only 0.04 mm/m after 91 days. The expansion under moist conditions was negligible for the RHA_6 and RHA_6_SL.

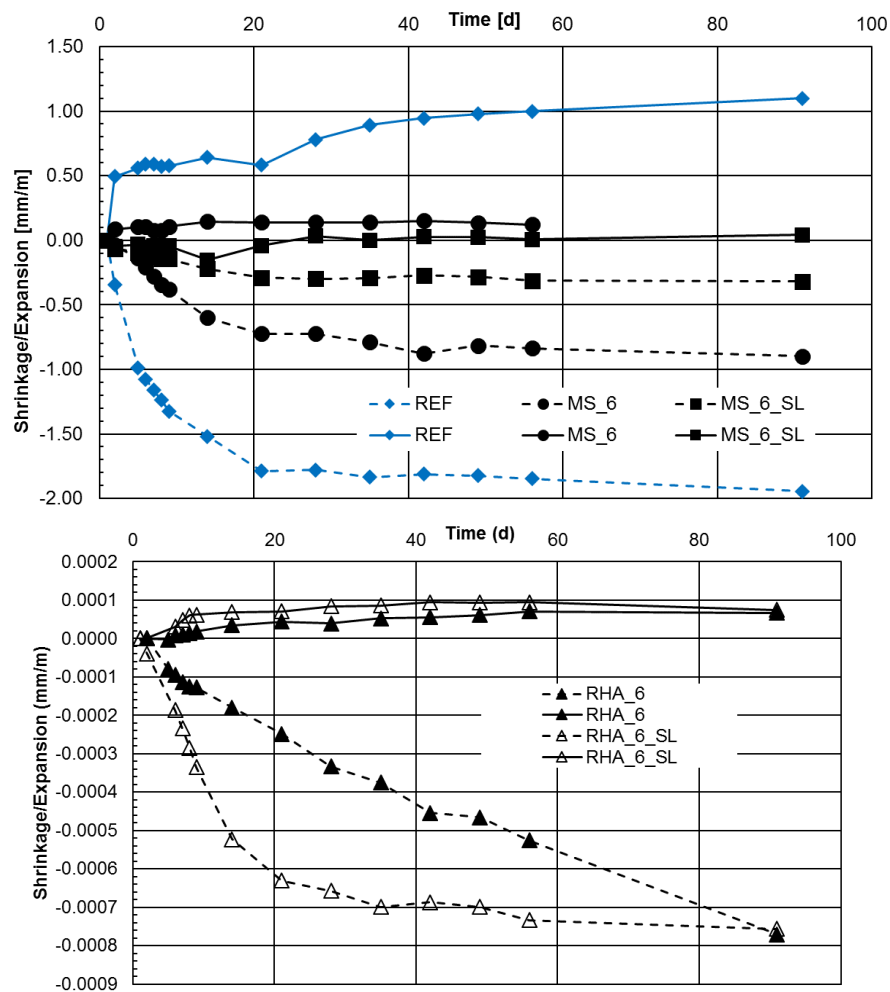


Figure 1: Hygic deformations at 23 °C/50 % r.H. (shrinkage; dashed lines) and at 23 °C/> 99 % r.H. (expansion; full lines). **Top:** MS-based one-part alkali-activated mortars and the REF mortar. **Bottom:** RHA-based one-part alkali-activated mortars.

All tested alkali-activated mortars conformed to the shrinkage requirements of the German guideline „*Richtlinie für die Prüfung von Mörteln für den Einsatz im Siedbau*“ for mortars in sewer repair applications (shrinkage < 0.9 mm/mm after 28 days at 23 °C/50 % r.H.), the requirements of the German guideline *DAfStb Richtlinie* „*Schutz und Instandsetzung von Betonbauteilen*“ (*Rili-SIB*) (shrinkage < 0.9 mm/mm after 28 days at 21 ± 2 °C/60 ± 10 % r.H.) as well as the requirements for various repair mortars of DIN 19573 „*Mortars for construction and rehabilitation of drains and sewers outside buildings*“ (shrinkage ≤ 2 mm/mm to ≤ 4 mm/mm, depending on the specific application, after 91 days at 23 °C/50 % r.H.).

Regarding swelling too, all alkali-activated mortars conformed to the requirements of *Rili-SIB* (expansion < 0.3 mm/mm after 28 days at 20 °C/65 % r.H.).

Though the hygric deformations of the alkali-activated mortars were significantly lower than those of the REF mortar, their mass changes at the end of the measurements were higher (Fig. 2). The final recorded values for the REF mortar were ~1.5 % on exposure to >99 % r.H. and approx. -2.5 % on drying, while for the alkali-activated mortars were ~3 % on exposure to >99 % r.H. and approx. -4 % on drying.

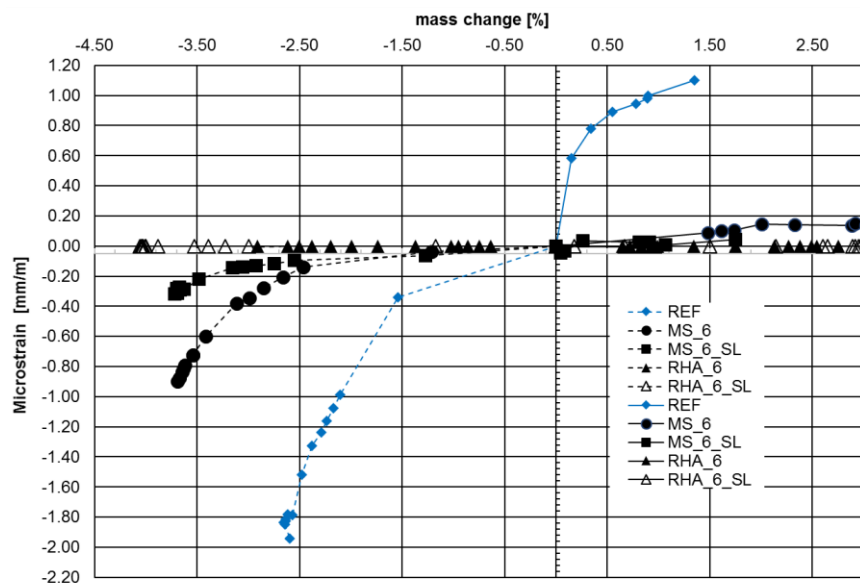


Figure 2: Hygric deformations at 23 °C/50 % r.H. (shrinkage; dashed lines) and at 23 °C/> 99 % r.H. (expansion; full lines) *versus* mass change.

The lower shrinkage, but higher mass loss, of the alkali-activated mortars under the dry conditions suggests that they had a coarser pore structure than the REF mortar, as drying shrinkage at the applied relative humidity is largely determined by loss of physically bound water from pores and the corresponding development of drying stresses [14]. In addition, since the alkali-activated mortars were heat-cured, it is likely that their Young's moduli, *i.e.* their resistance against deformations caused by the drying stresses, were higher than for mortar REF. Another contributing factor was the comparatively low paste content of the alkali-activated mortars (≤ 38 wt.%), because the aggregates (quartz) of the mortars do not undergo hygric deformations and thus act as inert fillers. In an analogous manner, the lower paste content of MS_6_SL has probably contributed to its better shrinkage performance compared to MS_6.

The same mechanisms as for drying shrinkage should be responsible for the better performance of the alkali-activated mortars as regards expansion at high humidity. However, the very low expansions observed indicate that additional factors, *e.g.*, the absence of AFm and other phases that can take up interlayer water (contrary to REF), may play a role. Verification of this and the above assumptions will require detailed microstructural analyses in future studies.

3.2. Bond behaviour

Fig. 3 shows the results of the pull-off tests. In most of the cases, failure occurred in the mortars, *i.e.* the bond strengths between the mortars and the concrete substrate were higher than the tensile strength of the mortars in these cases. Exceptions from this general trend were RHA_6, cured at 80 °C (failure mainly in the interface between mortar and concrete), and MS_6_SL, cured at 23 °C (failure mainly in the concrete). These mortars and MS_6, cured at 23 °C, exhibited the highest pull-off strengths, *viz.* ~ 2 MPa for RHA_6 and ~ 3 MPa for MS_6 and MS_6_SL; these values were significantly higher than the pull-off strengths obtained for mortar REF.

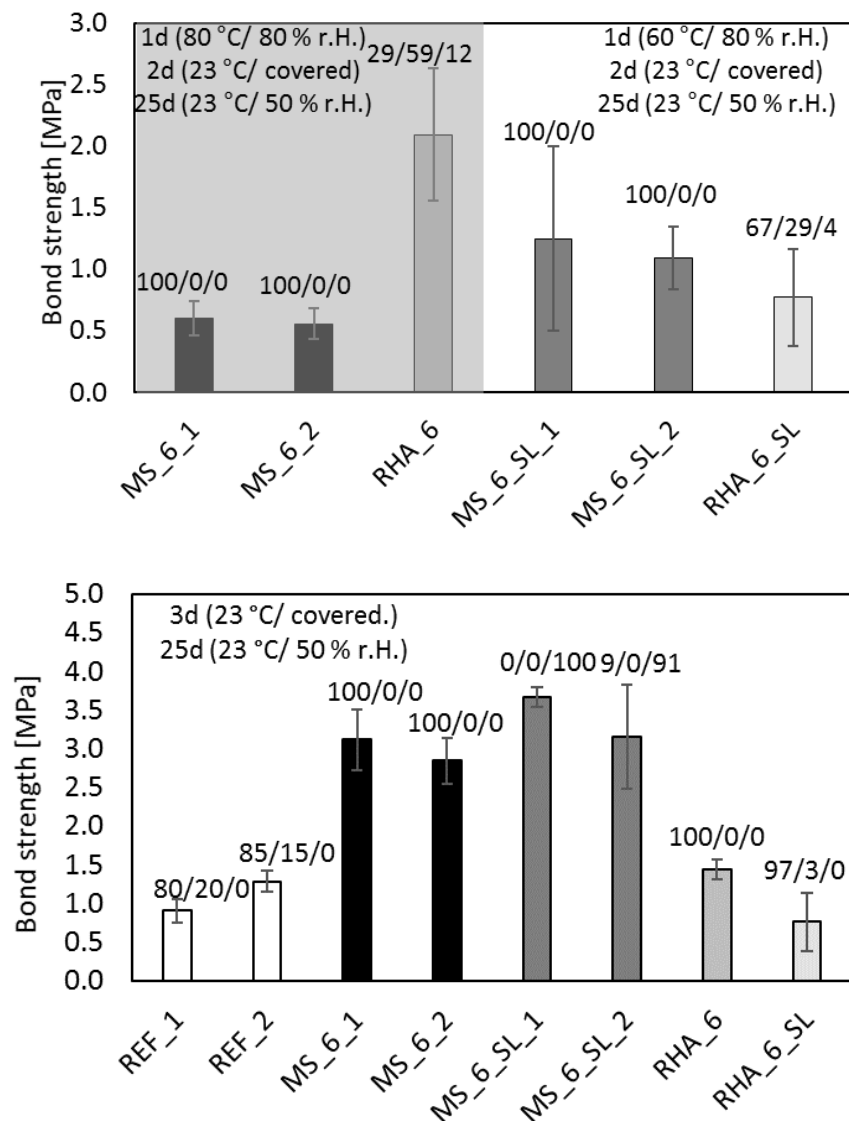


Figure 3: Results of the pull-off tests of mortars on MC 0.40 concrete substrate with initial heat-curing (**top**) and cured without heat-curing (**bottom**). The values X/Y/Z on top of the columns refer to the percentage of the failure in X = mortar, Y = between X mortar and concrete, Z = concrete). Each column represents the average of four pull-off tests and error bars represent one standard deviation in each direction.

All MS-based mortars cured only at 23 °C (*i.e.* without heat-curing) provided excellent bond strength in line with previous reports in the literature [9-11] and conformed to the requirements of DIN 19573 for repair mortars (class B2), coating mortars (class B1 and B2) and injection mortars. Also, the bond strengths requirements of *Rili-SIB* for all exposition classes (M2, M3) were met. However, the heat-cured MS-based mortars failed to achieve required pull-off strengths.

Fig. 4 shows micrographs of the region around the mortar/substrate interface of mortar MS_6 after two different curing procedures. Only limited cracking was observed in the specimen that was not heat-cured, while the sample that was heat-cured for 1 day at 80 °C exhibited numerous horizontal cracks in the mortar. It is very likely that this cracking is the reason for the significantly lower pull-off strengths of MS_6 and MS_6_SL mortars after heat-

curing. The cause of the cracking is presumably expansion of the mortar due to hydrogen-releasing reactions of silicon impurities in the microsilica during heat-curing, as was deduced previously for related pastes [15].

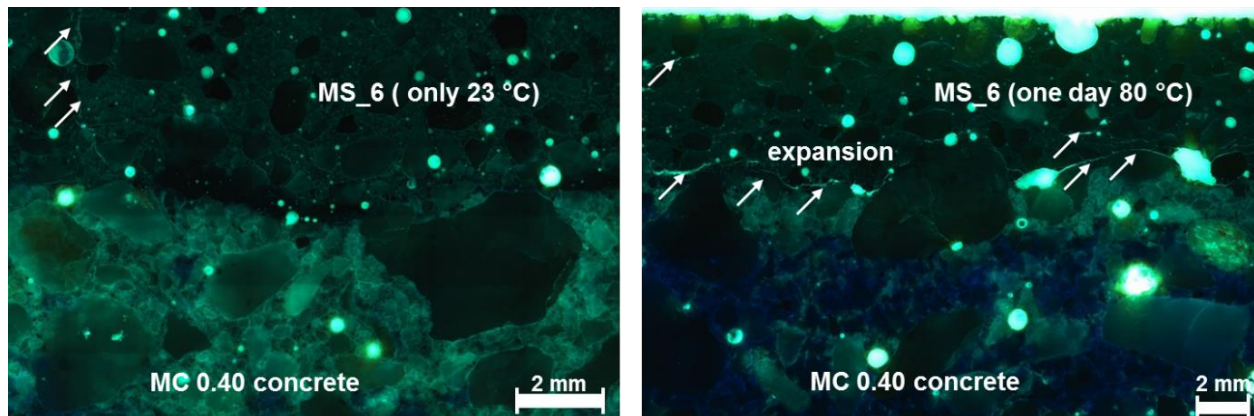


Figure 4: Micrographs of MS_6 mortars on MC 0.40 concrete substrate without heat-curing (**left**) and after initial heat-curing at 80 °C/80 % r.H. (**right**). Arrows indicate cracks.

Contrary to what was observed for the MS-based mortars, the pull-off strength of RHA_6 was generally lower when no heat-curing was applied, compared to the heat-cured specimens. When no heat-curing was applied, failure occurred usually in the mortar. This behaviour is tentatively attributed to a slower hardening, and thus slower development of tensile strength, in the RHA-based mortars without heat-curing.

4. CONCLUSIONS

The low hygric deformations, the satisfactory bond behaviour (when cured appropriately) and the previously demonstrated [5] excellent resistance against sulfuric acid attack of the one-part alkali-activated mortars studied here, make these materials promising candidates for applications in sewer repair. It is noted that the temperature/r.H. conditions required for rapid hardening of the mortars can be created by passing hot air (with adjusted r.H. where necessary) into sections of the sewer structure.

Future microstructural analyses should be conducted to confirm the hypotheses regarding the improved shrinkage and swelling behaviour of the alkali-activated mortars, compared to the commercial reference mortar, to explain the differences between the shrinkage behaviour of the MS-based and the RHA-based mortars and, most importantly, to better understand the mechanisms that determine the strength of the bond of the mortars to a concrete substrate. In addition, further studies are required to evaluate the durability of the mortar-substrate bond under real-world conditions for long periods of time.

ACKNOWLEDGEMENTS

This work was supported by the German Federal Ministry for Economic Affairs and Energy and HERMES Technologie GmbH & Co. KG (Schwerte, Germany) *via* the program ‘MNPQ-Transfer’ (project No. 21/14). The authors are grateful to R. Hermes (HERMES Technologie) for valuable discussions.

REFERENCES

- [1] Blaakmeer, J. Diabind: an alkali-activated slag fly ash binder for acid-resistant concrete. *Adv. Cem. Based Mater.* **1**, 275-276 (1994).

- [2] Fernandez-Jimenez, A., García-Lodeiro, I. & Palomo, A. Durability of alkali-activated fly ash cementitious materials. *J. Mater. Sci.* **42**, 3055-3065 (2007).
- [3] Montes, C. & Allouche, E. N. Evaluation of the potential of geopolymer mortar in the rehabilitation of buried infrastructure. *Struct. Infrastruct. Eng.* **8**, 89-98 (2012).
- [4] Koenig, A., Herrmann, A., Overmann, S. & Dehn, F. Resistance of alkali-activated binders to organic acid attack: Assessment of evaluation criteria and damage mechanisms. *Constr. Build. Mater.* **151**, 405-413 (2017).
- [5] Sturm, P., Gluth, G. J. G., Jäger, C., Brouwers, H. J. H. & Kühne, H.-C. Sulfuric acid resistance of one-part alkali-activated mortars. *Cem. Concr. Res.* **109**, 54-63 (2018).
- [6] Aiken, T. A., Kwasny, J., Sha, W. & Soutsos, M. N. Effect of slag content and activator dosage on the resistance of fly ash geopolymer binders to sulfuric acid attack. *Cem. Concr. Res.* **111**, 23-40 (2018).
- [7] Sand, W. & Bock, E. Concrete corrosion in the Hamburg sewer system. *Environ. Technol. Lett.* **5**, 517-528 (1984).
- [8] Grengg, C. et al. The decisive role of acidophilic bacteria in concrete sewer networks: a new model for fast progressing microbial concrete corrosion. *Cem. Concr. Res.* **101**, 93-101 (2017).
- [9] Alanazi, H., Yang, M., Zhang, D. & Gao, D. Bond strength of PCC pavement repairs using metakaolin-based geopolymer mortar. *Cem. Concr. Compos.* **65**, 75-82 (2016).
- [10] Zhang, H. Y., Kodur, V., Qi, S. L. & Wu, B. Characterizing the bond strength of geopolymers at ambient and elevated temperatures. *Cem. Concr. Compos.* **58**, 40-49 (2015).
- [11] Song, L., Li, Z., Duan, P., Huang, M. & Hao, X. Novel low cost and durable rapid-repair material derived from industrial and agricultural by-products. *Ceram. Int.* **43**, 14511-14516 (2017).
- [12] Lee, N. K., Jang, J. G. & Lee, H. K. Shrinkage characteristics of alkali-activated fly ash/slag paste and mortar at early ages. *Cem. Concr. Compos.* **53**, 239-248 (2014).
- [13] Ma, Y. & Ye, G. The shrinkage of alkali activated fly ash. *Cem. Concr. Res.* **68**, 75-82 (2015).
- [14] Scherer, G. W. Theory of drying. *J. Am. Ceram. Soc.* **73**, 3-14 (1990).
- [15] Sturm, P., Gluth, G. J. G., Simon, S., Brouwers, H. J. H. & Kühne, H.-C. The effect of heat treatment on the mechanical and structural properties of one-part geopolymer-zeolite composites. *Thermochim. Acta* **635**, 41-58 (2016).

TENSILE BEHAVIOUR OF NATURAL FIBRE TEXTILE-REINFORCED MORTAR

Niki Trochoutsou (1), Matteo Di Benedetti (2), Kypros Pilakoutas (1) and Maurizio Guadagnini (1)

(1) Department of Civil and Structural Engineering, The University of Sheffield, UK

(2) Multidisciplinary Engineering Education, The University of Sheffield, UK

Abstract

Natural fibre Textile-Reinforced Mortar (NTRM) systems, comprising open mesh fabrics embedded in inorganic matrices, could potentially provide a sustainable and low-cost solution for the rehabilitation and strengthening of structures in developing countries. Current understanding of their tensile characteristics, however, is still very limited.

This paper examines the feasibility of using NTRM systems for strengthening unreinforced masonry structures and investigates the degree of composite action that can be developed between different types of natural fibres and lime-based mortars. The mechanical properties that are required for design are determined from direct tensile tests on both bare flax yarns and flax-TRM composites. The parameters investigated include: a) textile geometry; b) number of TRM layers (from one to three) and c) layer thickness.

Smaller yarn diameter textiles are shown to perform better in TRM composites than larger diameter textiles with yarn strength up to 380 MPa and elastic modulus up to 76 GPa.

Keywords: TRM, tensile tests, bond, natural fibres, strengthening

1. INTRODUCTION

The seismic vulnerability of unreinforced masonry (URM) buildings, in particular those built in developing countries, has been identified in numerous past earthquakes. This highlights the need for new strengthening systems that are effective and resilient, as well as economic and easily applicable to meet the requirement of less favoured economies, and environmentally friendly to meet pressing sustainability requirements.

Owing to their high specific mechanical properties, chemical/mechanical compatibility with masonry substrates, vapour permeability and reversibility [1], strengthening systems comprising high-strength fibre-grids embedded in inorganic matrices (Textile-Reinforced Mortars, TRM, or Fabric-Reinforced Cementitious Matrices, FRCM) are attracting the interest

of the research community. TRM systems have been shown to be valid alternatives to FRP systems and can be applied successfully for in-plane and out-of-plane strengthening as well as confinement of brick, tuff and adobe masonry elements. However, many synthetic fibres currently used in commercially available TRM composites (e.g. carbon, PBO etc.) have very high stiffness and strength compared to the masonry substrate and their tensile strength cannot be fully exploited as their failure mode is generally governed by debonding of the reinforcing fibres [2]. These fibres are also expensive to manufacture and can cause environmental and disposal problems [3]. The cement-rich mortars that are predominantly used as inorganic matrices also contribute to environmental pollution, due to the high carbon dioxide emissions during cement production.

This study investigates the use of natural-fibre grids embedded in lime-based mortars (Natural-Fibre TRM - NTRM) to develop more efficient yet cost-effective retrofitting solutions for masonry structures and contribute to a “greener” and more sustainable development. Natural fibres are renewable, biodegradable, recyclable and carbon neutral, hence are environmentally friendly [4-6]. Furthermore, their light weight and low cost, combined with good specific mechanical properties, make natural-fibre composites systems potentially suitable for such applications, even when compared to the cheapest commercially available solutions using glass fibre reinforced composites [7, 8]. The proposed systems can be easily implemented in developing countries, where natural fibres are readily available and abundant [9]. As inorganic matrices, lime-based mortars are preferable to cement-based solutions for three main reasons: a) lower alkalinity, b) sustainability and c) better compatibility with masonry substrates [10]. The alkaline environment provided by the cementitious matrices would eventually lead to degradation of the natural fibres and significant loss in strength [11]. On the contrary, lime-based products have minimal effects on the tensile properties of natural fibres [12].

Although the performance of chopped natural fibres in inorganic environments has been examined in previous studies [e.g. 13-15], their behaviour in the form of grids in externally bonded strengthening systems is still unknown. The use of natural fibre based systems is limited mainly due to: a) the lack of a comprehensive understanding on the bond between the constituents of the composite system and b) the difficulty in assessing their mechanical properties based on existing testing methodologies. An experimental program was designed to address these challenges and investigate the stress-transfer mechanisms between fibres and matrix through tensile tests on flax-TRM composites with different textile geometries, number and thickness of TRM layers. This paper summarises the overall experimental methodology and presents the preliminary results followed by a discussion on the effect of the examined parameters. The present study is part of a larger experimental program on bond between NTRM and masonry.

2. EXPERIMENTAL PROGRAM

2.1 Materials

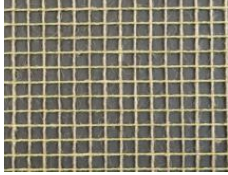

Two types of flax grids are examined:

- i. F1: high linear density flax grid of 14-mm orthogonal mesh size (centre-to-centre yarn)
- ii. F2: less fine and denser grid of 4-mm orthogonal mesh size.

Both grids are balanced bidirectional (i.e. equal number of plies and strength properties in the two directions) and their characteristics are reported in Table 1.

A commercially available lime-based mortar was chosen as inorganic matrix. Its mechanical properties were experimentally determined, after carrying out flexural and compression tests, according to EN 1015-11 [16]. The mean values of the flexural and compressive strength at 28 days were found to be 2.8 MPa (CoV:15%) and 7.7 MPa (CoV:15%), respectively.

Table 1: Grid characteristics (supplied by the manufacturer).

Property		
	F1	F2
Mesh size (mm)	14	4
Weight (gsm)	215	300
Linear density (tex)	1500	324
Bulk density (kg/m ³)	1350	1500

2.2 Specimen Preparation

Direct tensile tests were carried out on fibre yarns to assess their mechanical properties. Twenty yarns with a free length of 300 mm were extracted from each grid type and tested in tension until rupture according to EN ISO 2062 [17].

Thirty-six NTRM coupons (six replicates for each grid type) were cast in plexiglass formworks. The specimens were 600 mm long, 50 mm wide and their thickness varied from 6 to 12 mm, depending on the number of grid layers (1 to 3). Mortar overlays were 3-mm thick. Four additional specimens with one layer of F1 grid were manufactured using 5-mm thick overlays to investigate the effect of mortar thickness. F1 and F2 coupons comprised three and twenty (10x2) longitudinal yarns per layer, respectively. After casting, specimens were cured for 28 days (under wet conditions) and then stored in laboratory conditions for at least one month prior to testing. A random speckle pattern was applied manually to the surface of the specimens to enable the use of digital image correlation (DIC) analyses and obtain full-field displacement measurements, which will be presented in future publications.

2.3 Experimental Setup

Tensile tests on yarns and NTRM coupons were conducted in a universal testing machine of 10 kN capacity in displacement control. The loading rate was equal to 300 mm/min for yarns, whilst the NTRM composites were load at 0.2 mm/min up to the occurrence of the first crack and 1 mm/min thereafter.

Clamping of the yarns in the machine was achieved by wrapping the ends of the yarns twice around a 25-mm diameter disc, placed in the grips of the machine, and by securing them on the side by means of bolts or by tying a knot (Fig. 1a).

Aluminium tabs with a length of 150 mm were epoxy bonded to the NTRM coupon ends (Fig. 1b). Clevis-type grips were used, according to AC434 [18] (Fig. 1c).

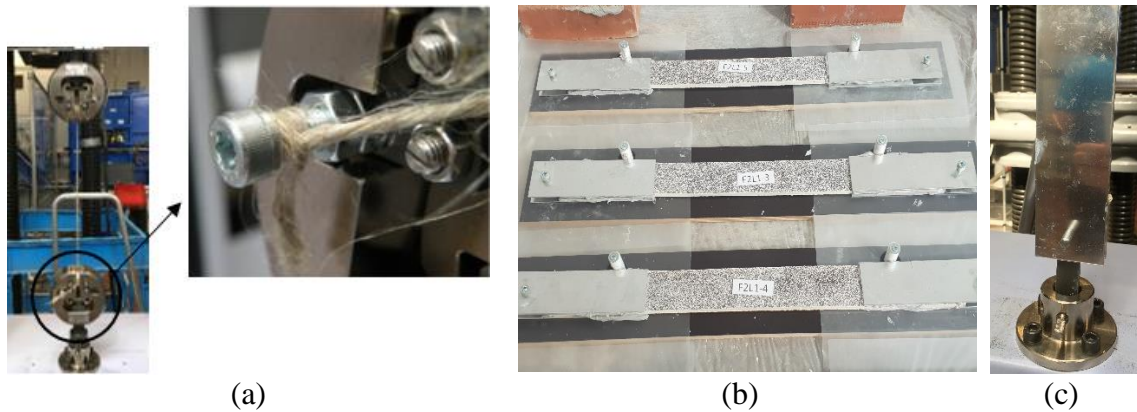


Figure 1: a) Test setup for yarns; b) NTRM coupons; c) clevis-type grips

3. EXPERIMENTAL RESULTS

3.1 Yarns

The results of the tests on the yarn specimens are summarised in Table 2 in terms of maximum load and strength, elongation and elastic modulus (average values with coefficient of variation are shown in parentheses). The yarn area was calculated as the ratio of linear density over bulk density. Fig. 2 shows a representative stress-strain behaviour for each flax type and a typical failure mode. All specimens were characterised by an initial inelastic branch, followed by an almost linear behaviour up to rupture. The apparent initial hardening is due to realignment of the single filaments and is not taken into account for the estimation of the elastic modulus. A more progressive failure was observed for F1 yarns, possibly due to their larger diameter and more pronounced shear lag effect.

Table 2: Single yarn properties.

Specimen	Area (mm ²)	Max. Load (N)	Tensile Strength (MPa)	Elongation (%)	Elastic Modulus (GPa)
F1	1.1	233.9 (9%)	212.6 (9%)	6.71 (10%)	53.9 (12%)
F2	0.2	81.6 (7%)	377.9 (7%)	9.17 (5%)	76.1 (7%)

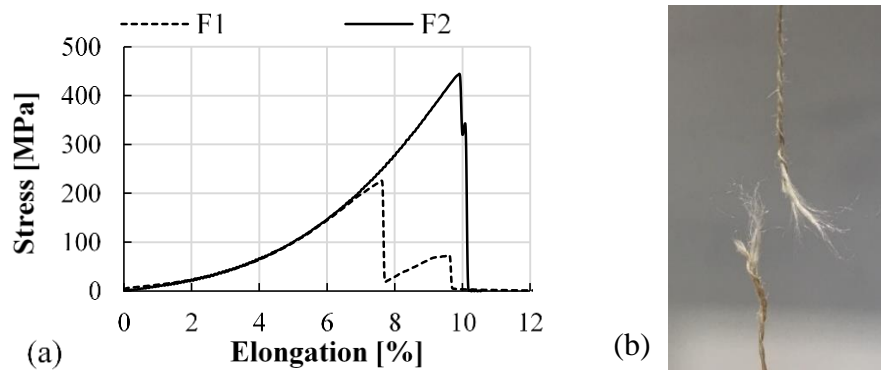


Figure 2: a) Typical stress-strain response of F1 and F2 yarns; b) rupture of a yarn (F2)

3.2 NTRM composites

The average values of the results obtained from the tensile tests on NTRM coupons are presented in Table 3 in terms of maximum load (P_u), ultimate strength (f_{fu}), ultimate strain (ϵ_{fu}) and stiffness during uncracked (E_f^*) and cracked stage (E_f), along with the corresponding CoV values. The stresses were computed by dividing the load by the cross-sectional area of the textile taken as 3.34 mm^2 and 4 mm^2 for F1 and F2, respectively. The specimen ID uses the notation XY.Z-n, where X is the fibre type (F1 or F2), Y the number of TRM overlays (L1, L2 or L3), Z if present indicates a thickness of 5 mm per each mortar layer and n is the replicate number. The reinforcement ratio for each specimen (ρ_f) is also indicated in Table 3.

Table 3: Tensile properties of NTRM coupons. CoV is given in parentheses.

Specimen ID	ρ_f (%)	P_u (N)	f_{fu} (MPa)	ϵ_{fu} (%)	E_f^* (GPa)	E_f (GPa)
F1L1	1.1	274 (16%)	82 (16%)	2.25 (29%)	-	20 (17%)
F1L1.5	0.7	192 (8%)	57 (8%)	1.47 (4%)	1328 (35%)	19 (10%)
F1L2	1.5	553 (12%)	82 (12%)	2.90 (9%)	-	24 (16%)
F1L3	1.7	892 (17%)	89 (17%)	3.60 (22%)	-	27 (25%)
F2L1	1.3	768 (14%)	192 (14%)	5.21 (20%)	1942 (15%)	40 (30%)
F2L2	1.8	1805 (9%)	225 (9%)	5.44 (15%)	1038 (10%)	44 (15%)
F2L3	2.0	2657 (5%)	221 (5%)	5.27 (9%)	722 (16%)	40 (8%)

Fig. 3a shows the load-displacement curves for F1L1 and F2L1 coupons. For a similar reinforcement ratio (1.2% for one layer), F2 is characterised by higher ductility and by the formation of multiple cracks in the lime-based mortar matrix, along with superior mechanical properties. All F2-TRM specimens presented the typical three-stages of tensile behaviour exhibited by currently established TRM systems (i.e. pre-cracked, crack development and post-cracking stage [19]) (Fig. 4a), indicating a good stress transfer mechanism, hence good bond, at the fibre/mortar interface, despite the higher density of the mesh. On the contrary, the response of F1L1-TRM specimens included the formation of one single crack due to the lower reinforcement ratios. In addition, problems during curing and handling were more pronounced for this type of fabric, with micro-cracks forming prior to testing. These issues may be attributed to the larger diameter and possibly increased moisture absorption of the fibre yarns. As a result, most of these specimens were already cracked prior to testing and it was not possible to estimate their corresponding uncracked stiffness. In case of multiple F1 layers, more cracks were observed (Fig. 4b), confirming the need of a minimum reinforcement ratio required to activate the reinforcement and to work compositely with the mortar. Comparing F1L1 specimens (Fig. 3b), a thicker overlay led to an overall reduction of the final strength and strain of the NTRM composite. However, a thick overlay facilitated the manufacturing of more robust specimens, which were more easily handled.

In terms of mechanical properties, the increase of TRM layers did not alter significantly the stress-strain response of either flax types.

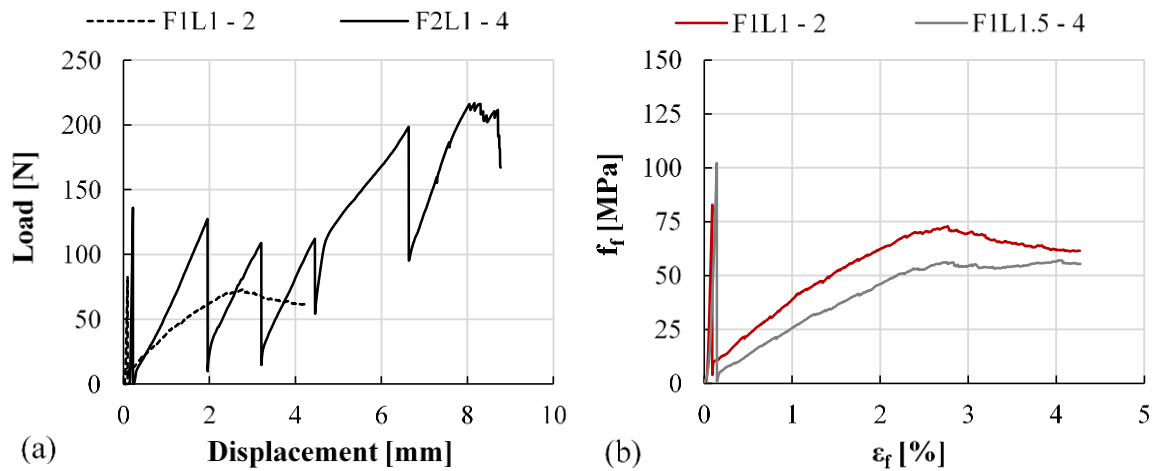


Figure 3: (a) Load-displacement curves for single-layered F1- and F2-TRM coupons;
 (b) Effect of overlay thickness for F1L1

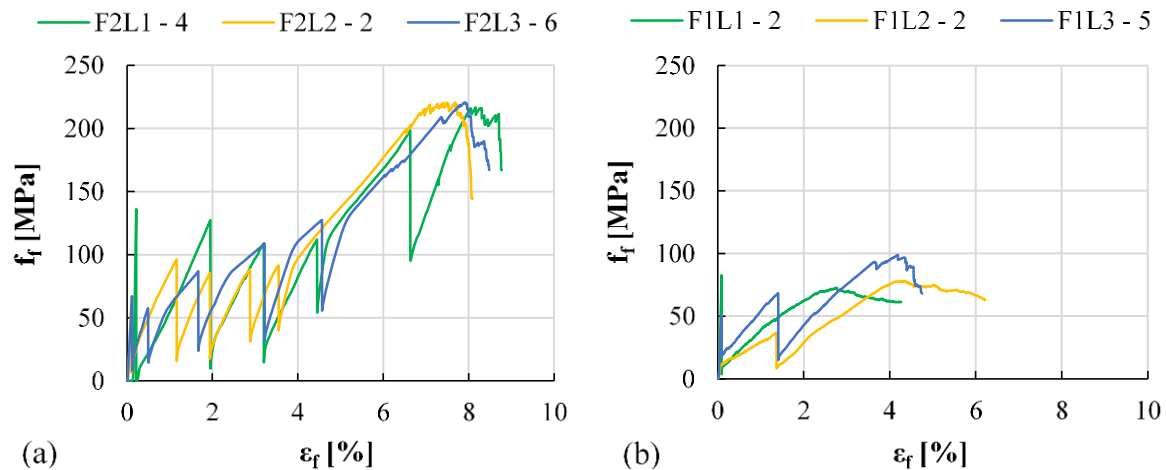


Figure 4: Stress-strain response curves for representative specimens of one, two and three NTRM layers; (a) F2 and (b) F1

In terms of failure mode, all F1-TRM specimens failed due to slippage of the reinforcement within the mortar matrix having developed few cracks located away from the clamps (Fig. 5a), while the F2-TRM counterparts failed progressively due to fibre tensile rupture (Fig. 5b), with cracks distributed along the whole free length (Fig. 5c).

Although special care was taken during casting and curing to position the grids within the specimen with a high degree of accuracy and produce specimens with a constant thickness, geometrical imperfections were unavoidable and may have affected the overall tensile behaviour at varying degrees.

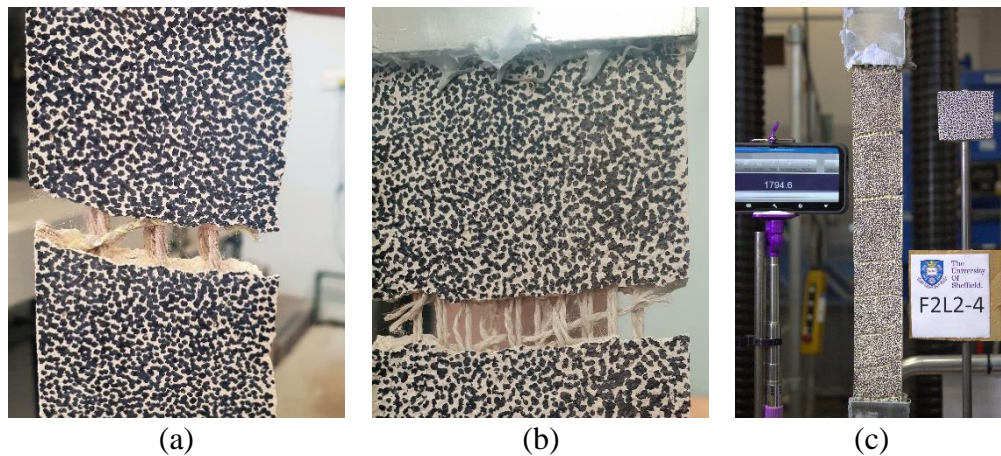


Figure 5: (a) F1-TRM at failure (slippage); (b) F2-TRM specimen at failure (rupture);
(c) typical crack pattern on F2-TRM specimens

4. CONCLUDING REMARKS

This paper presented the results obtained from direct tensile tests on two types of flax yarns and flax-reinforced TRM composites.

- Both flax type yarns are deformable (up to 9%), with good values of strength (up to 380 MPa) and stiffness (up to 76 GPa).
- The larger diameter yarn does not perform as well as the small diameter one, possibly due to impregnation issues.
- An increase of NTRM layers does not affect significantly the ultimate stress in the textile and strain in the composite.
- Though a thicker mortar overlay enables the manufacturing of more robust specimens, it leads to the reduction of post-cracking mechanical properties.

Flax grids embedded in lime-based mortar appear to be a promising solution for externally bonded systems. Their flexibility, along with their reasonably good strength and excellent environmental credentials, make them ideal candidates for the strengthening of masonry structures.

ACKNOWLEDGEMENTS

The authors gratefully thank Vimark S.r.L for providing the strengthening mortar matrix and Kerakoll S.p.a. for the epoxy adhesive. Special thanks to Lisa Barilli for her assistance in the experimental program.

REFERENCES

- [1] Triantafillou, T.C., and Papanicolaou, C., 'Shear Strengthening of Reinforced Concrete Members with Textile Reinforced Mortar (TRM) Jackets'. *Mater. Struct.* **39** (2006) 93-103.
- [2] Dittenber, D. B., and Gangarao, H. V. S., 'Critical review of recent publications on use of natural composites in infrastructure'. *Compos. Part A Appl. Sci. Manuf.* **43** (8) (2012) 1419-1429.
- [3] Yan, L., Kasal, B., and Huang, L., 'A review of recent research on the use of cellulosic fibres, their fibre fabric reinforced cementitious, geo-polymer and polymer composites in civil engineering'. *Compos. Part B Eng.* **92** (2016) 94-132.

- [4] Silva, F.D.A., Mobasher, B., and Filho, R.D.T., 'Advances in Natural Fiber Cement Composites: A Material for the Sustainable Construction Industry', in 'Textile Reinforced Structures', Proceedings of the 4th Colloquium on Textile Reinforced Structures, Dresden, January, 2009 (Eigenverlag) 377-388.
- [5] Salit, M.S., 'Tropical Natural Fibre Composites, Properties Manufacture and Applications', (Springer, Singapore, 2014) 15-38.
- [6] Fan, M., 'Future scope and intelligence of natural fibre based construction composites', in 'Advanced High Strength Natural Fibre Composites in Construction', (Woodhead Publishing, Duxford, 2017) 545-556.
- [7] Joshi, S. V., Drzal, L. T., Mohanty, A. K., and Arora, S., 'Are natural fiber composites environmentally superior to glass fiber reinforced composites?'. *Compos. Part A Appl. Sci. Manuf.* **35** (3) (2004) 371-376.
- [8] Dunne, R., Desai, D., Sadiku, R. and Jayaramudu, J., 'A review of natural fibres, their sustainability and automotive applications'. *J. Reinf. Plast. Compos.* **35** (13) (2016) 1041-1050.
- [9] Sen, T., and Jagannatha Reddy, H.N., 'Strengthening of RC beams in flexure using natural jute fibre textile reinforced composite system and its comparative study with CFRP and GFRP strengthening systems'. *Int. J. Sustain. Built Environ.* **2** (1) (2013) 41-55.
- [10] de Felice, G., De Santis, S., Garmendia, L., Ghiassi, B., Larrinaga, P., Lourenço, P. B., Oliveira, D.V., Paolacci, F., and Papanicolaou, C.G., 'Mortar-based systems for externally bonded strengthening of masonry'. *Mater. Struct.* **47** (12) (2014) 2021-2037.
- [11] Wei, J., and Meyer, C., 'Degradation mechanisms of natural fibre in the matrix of cement composites'. *Cem. Concr. Res.* **73** (2015) 1-16.
- [12] Olivito, R.S., Cevallos, O.A., and Carrozzini, A., 'Development of durable cementitious composites using sisal and flax fabrics for reinforcement of masonry structures'. *Mater. Des.* **57** (2014) 258-268.
- [13] Pereira, M. V., Fujiyama, R., Darwish, F., and Alves, G. T., 'On the Strengthening of Cement Mortar by Natural Fibers'. *Mater. Res.* **18** (1) (2015) 177-183.
- [14] Pacheco-Torgal, F., and Jalali, S., 'Cementitious building materials reinforced with vegetable fibres: A review'. *Constr. Build. Mater.* **25** (2011) 575-581.
- [15] Ardanuy, M., Claramunt, J., García-Hortal, J. A., and Barra, M., 'Fiber-matrix interactions in cement mortar composites reinforced with cellulosic fibers'. *Cellulose* **18** (2011) 281-289.
- [16] BS EN 1015-11:1999, 'Methods of test for mortar for masonry - Part 11: Determination of flexural and compressive strength of hardened mortar', (BSI, London, 2006).
- [17] BS EN ISO 2062:2009, 'Textiles-Yarns from packages - Determination of single-end breaking force and elongation at break using constant rate of extension (CRE) tester', (BSI, London, 2009).
- [18] ICC Evaluation Service, 'AC434-1011-R1 Acceptance Criteria for Masonry and Concrete Strengthening Using Fibre-reinforced Cementitious Matrix (FRCM) Composite Systems', (ICC Evaluation Service LLC, Birmingham, 2011).
- [19] Arboleda, D., Carozzi, F. G., Nanni, A., and Poggi, C., 'Testing Procedures for the Uniaxial Tensile Characterization of Fabric-Reinforced Cementitious Matrix Composites'. *J. Compos. Constr.* **20** (3) (2016) 1-13.

MECHANICAL CHARACTERIZATION OF LIME CEMENT MORTARS: E-MODULUS AND FRACTURE ENERGY

Meera Ramesh (1), Miguel Azenha (1) and Paulo B. Lourenço (1)

(1) University of Minho (ISISE), Guimarães, Portugal

Abstract

In masonry constructions, the choice of mortar composition is usually guided by requirements of the final application, which could range from new constructions to conservation projects. Often, lime and cement are combined together, to overcome their individual shortcomings and consequently serve as a suitable binder in masonry mortars. Depending on their proportion in the mixture, it may be possible to obtain a desired range of characteristics in different mechanical properties like strength and stiffness. However, existing studies exploring this subject are scarce. Therefore, this work aims at adopting a systematic approach to studying the effect of different lime-cement ratios on the mechanical properties of masonry mortars, specifically targeting a discussion on E-modulus and fracture energy. Three distinct mixes with quantities of lime varying from 25% to 67% (by volume) have been studied. The benefits and trade-offs associated with substitution of different quantities of cement with lime in mortars, have been explored with regard to resistance to crack propagation.

Keywords: Lime-cement mortars, E-modulus, Fracture energy, Shear modulus, mechanical strength

1. INTRODUCTION

To understand the mechanical behaviour of masonry as a system, it is important to be aware of the mechanical performance of its individual components namely, unit and mortar. For the latter, two of the most common binder materials involve air lime and cement which in the recent few years have been increasingly often mixed together [1]. Multiple works of research have studied different mechanical properties of lime-cement blended mortars, in an attempt to overcome the individual shortcomings of either type of binder [1-4]. It has been fairly well established that an increase in the quantity of cement in the binder leads to an increase in mechanical strength of the mortar [5-8]. Workability and permeability, on the other hand have been reported to improve with increase in quantity of lime in the mortar [8][9]. Other parameters, such as drying shrinkage, ultrasound velocity and static E-modulus,

were found to have been studied but past works were focussed on discussing other issues and only coincidentally addressing different lime-cement proportions [6,10-11]. Especially with regard to static E-modulus, values were found to vary widely, ranging from 3 GPa to 24 GPa as a function of binder content and composition [12-13]. Furthermore, no work discussing the shear (or G-) modulus or fracture energy of lime-cement mortars could be found in literature. Scattered data on important mechanical properties makes it difficult to consolidate requisite information for characterization of any material. In general, it is difficult to make direct comparisons of experimental data from any two works of different sources, due to differences in more than one variable: type of air lime or cement employed, the proportions used, nature and quantity of aggregate employed, the amount of water used and the workability targeted. These observations make ample room for a systematic experimental campaign which explores the evolution of mechanical properties of mortar as a function of the proportions of different constituents in its binder.

This work aims at a discussion of important mechanical parameters such as E-modulus, G-modulus, fracture energy and mechanical strength of blended mortars, as a function of the quantity of lime or cement in the mortar. The paper studies the evolution of the above mentioned parameters at ages of 7, 28 and 90 days of curing age. The goal is to facilitate the choice of an appropriate mortar in conjunction with the chosen unit, for better performing masonry construction.

2. RESEARCH PROGRAM

2.1 Materials

Air lime, type CL-90S and cement, type CEM I – 42.5 R were used to compose the binder of all the mixes. Despite the fact that CEM II is the cement used more often in field applications, CEM I was chosen to ensure consistency and repeatability of properties in the experimental campaign, as well as to facilitate interpretation of the mechanisms at stake (since the cementitious binder chosen would result in a simpler set of reactions). The binding materials were pre-conditioned at 20°C temperature and 65% relative humidity for up to 7 days prior to casting of the mixes. In accordance with the standard BS 1200-1976, sand with customized particle size range of 0/4 mm, was employed as the aggregate [11]. Before each casting, the aggregates were oven dried at 105°C and cooled down to room temperature, for the sake of consistency in their moisture content.

2.2 Mortar composition

Three different mix compositions were selected with a binder-aggregate ratio of 1:3 by volume. The binder consisted of air lime replacing cement in different proportions by volume, namely 25%, 50% and 67%.

The notations used (Table 1), indicate the proportion of the constituents of the mix, i.e. cement, lime and sand, for instance 1C1L6S denotes a mix ratio of 1:1:6 in the sequence of cement, lime and sand. Additionally, all notations have been supplemented with quantity of lime in the binder in parenthesis, to facilitate comprehension of the reader. Apparent density was employed to convert the proportions from volume to mass. Following EN 1015-3, a flow value of 175 ± 10 mm was targeted for all mixes, to ensure adequate workability with regard to application of mixes on field [14]. Water-binder ratios were determined accordingly (Table 1). The standard EN 1015-11 was used to decide curing conditions for the specimens:

temperature was maintained at 20°C up to the point of testing, with relative humidity maintained at 95% for the first seven days and 65% thereafter [15]. The specimens were demoulded either two or five days after casting, based on the lime content in the binder being less or greater than 50% by mass, respectively as per standard EN 1015-11.

Table 1: Mortar composition – For every 1 m³ of mortar produced

Nomenclature of mixes		Cement: Lime: Sand (Ratio by volume)	Cement (kg)	Lime (kg)	Water (kg)	Water-Binder ratio (By weight)
Notation	Lime in binder (Volume %)					
3C1L12S	25	3:1:12	262.7	33.4	295.6	1.00
1C1L6S	50	1:1:6	175.1	66.8	303.1	1.25
1C2L9S	67	1:2:9	116.8	89.0	325.0	1.58

2.3 Specimens and experiment specifications

Tests of unconfined uniaxial compression, three point bending (flexural strength), fracture energy, unconfined cyclic compression (static E-modulus) and Poisson's ratio were performed for all three mixes at curing ages of 7, 28 and 90 days. According to standard EN 1015-11, three point bending test was performed on prismatic specimens of size 40×40×160 mm [15]. Displacement control was used at 0.006 mm/s with a preload of 150 N and values were averaged from three specimens. Subsequently, the broken halves were used to measure compressive strength, for which load was applied at the rate of 50 N/s.

In this work, fracture energy has been defined and measured according to RILEM recommendation 50 FMC [16]. It was measured using prismatic specimens of size 40×40×160 mm (Fig 1), with a trapezoid shaped precast notch; 5 mm in depth, equal length of non-parallel sides inclined at an angle of 15° and the shorter parallel side being 2.5 mm in length [16]. Displacement control was used at 0.006 mm/s with a preload of 50 N. Static E-modulus was measured using the conventional unconfined cyclic compression test (Fig 2) with procedures adapted from concrete testing practices [17]. Cylindrical specimens were used, with a height to diameter ratio of 2, and diameter of 60 mm. Load was applied in four continuous loading and unloading cycles, employing a 25 kN hydraulic actuator, and a preload of 50 N. To ensure constant duration of each loading cycle, pre-determined at 60 seconds, the loading rate was calculated for each case. Maximum load of each cycle was fixed at approximately one-third of the maximum compressive strength of the mortar at that age. Exactly the same cyclic loading was used to measure lateral deformation in the same cylindrical specimens, in order to calculate Poisson's ratio. A metallic ring with a hinge was fastened at the centre of the specimen with an LVDT attached in the horizontal direction (Fig 3). Results obtained for flexural strength, E-modulus, Poisson's ratio and fracture energy were all averaged from measurements of three specimens each and have been presented with error bars calculated using standard error of the mean value (Standard deviation divided by square root of the number of specimens). Compressive strength was obtained from an average of six measurements from three specimens, i.e. six halves of the three samples used for the flexure test.

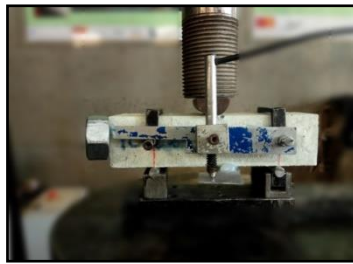


Figure 1: Set-up of fracture energy



Figure 2: Set-up of static E-modulus



Figure 3: Set-up of Poisson's ratio

3. RESULTS AND DISCUSSION

Results obtained for compressive strength (Fig 4) and flexural strength (Fig 5) exhibit expected trends, with the increase in the quantity of cement in the mix leading to higher values of mechanical strength in the mortar. In the case of compressive strength (Fig 4), the mixes with greater quantities of lime, continue to gain strength between 28 and 90 days of curing age with mix 1C2L9S (67%) exhibiting a gain in strength of 2%, and the mix 1C1L6S (50%) exhibiting a gain in strength of almost 30%. This difference in behaviour needs to be investigated further. It may be observed (Fig 4) that the mix 3C1L12S (25%), with the least amount of lime does not demonstrate any increase in strength in the period between 28 and 90 days of curing age. In the case of flexural strength (Fig 5), all mixes exhibit a continued gain in strength up to 90 days of age. One of the reasons for decreasing mechanical strength of mixes with increasing quantities of lime has been attributed to higher specific area of lime compared to cement, which leads to an increase in demand for water of the mix, for the same workability [3, 8]. Additionally, since cement hydration contributes significantly to early gain of strength in blended mixes, a reduction in the weight of cement used in the mixes will cause a drop in strength of the mixes [1]. On the other hand, the presence of lime in the mix, which endures carbonation that induces relevant hardening of this binder, leads to a continued gradual increase in values of mechanical strength which is not observed in mixes consisting of only cement, up to the age of 90 days [2]. Change in mechanical strength of blended mortars has been observed by other authors as well and appears to be adequately validated [3].

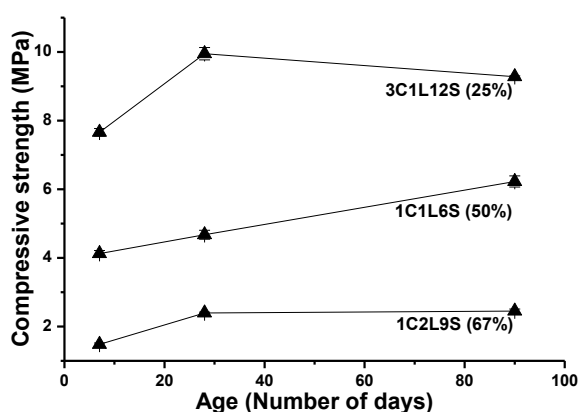


Figure 4: Evolution of compressive strength

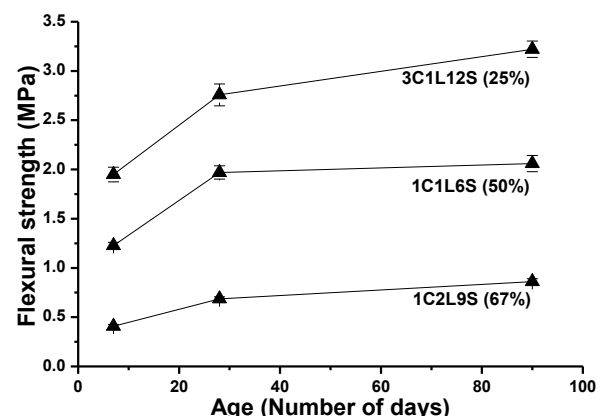


Figure 5: Evolution of flexural strength

Evolution of static E-modulus as a function of lime content in the binder of the mix has been recorded, and shown in Fig 6. It may be observed that the greater the quantity of lime in the mix, the lower is the stiffness of the mortar. While stiffness of all the mixes is observed to evolve with time, the mixes with greater quantities of cement in them seem to gain most of their stiffness in the first 7 days (Fig 6). The increase in stiffness of the mixes between day 7 and day 90 is found to be 7%, 19% and 27% for the mixes 3C1L12S (25%), 1C1L6S (50%) and 1C2L9S (67%) respectively. One may therefore conclude that greater the amount of lime in the binder of the mix more is the continued increase in stiffness, up to the age of 90 days. The most plausible explanation for this increase in stiffness over time may be attributed to stiffening induced by carbonation of the lime, since hydration processes are expected to have been almost completed by 28 days of curing age [3].

Fracture energy exhibits an interesting trend (Fig 7). The mix with the maximum amount of lime, 1C2L9S (67%) shows a continued increase in fracture energy while, the other two mixes, show an increase up to 28 days of age, followed by a drastic decrease in value at 90 days of curing age. This pattern deserves further investigation, especially due to differences in trends observed on comparison with flexural strength (Fig 5) which was measured using the same method of three-point bending. Regardless, it is possible to conclude that greater the quantity of lime in the mix, lower is the energy required for crack propagation through the mortar.

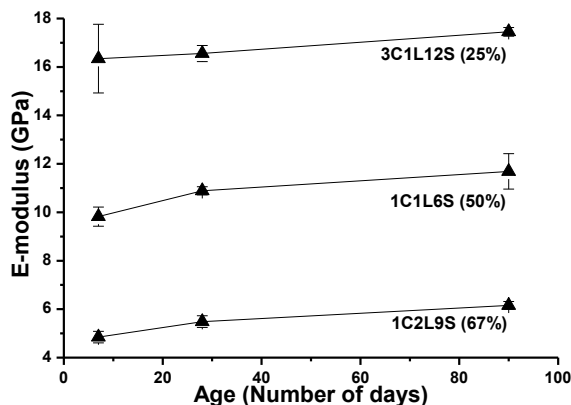


Figure 6: Evolution of E-modulus

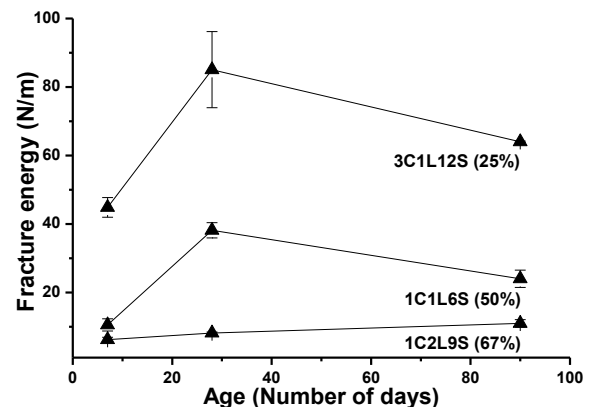


Figure 7: Evolution of fracture energy

Table 2: Evolution of poisson's ratio and shear modulus

Property	Poisson's ratio (COV %)			Shear modulus (GPa)		
Mix/Age (Days)	1C2L9S (67%)	1C1L6S (50%)	3C1L12S (25%)	1C2L9S (67%)	1C1L6S (50%)	3C1L12S (25%)
7	0.12 (17.3)	0.13 (21.4)	0.11 (13.5)	2.16	4.36	7.36
28	0.11 (5.9)	0.09 (8.2)	0.12 (9.7)	2.47	5.00	7.36
90	0.11 (16.7)	0.08 (0.2)	0.13 (14.2)	2.77	5.39	7.70

Poisson's ratio was recorded for the different mixes and has been displayed along with the percentage of variation of each measurement, adjacent to it (Table 2). No specific pattern

could be discerned, and almost all values were observed to be in the same range (0.08-0.13). For this reason, shear modulus (G) for each of the mixes was calculated using the average value of E-modulus (E) and Poisson's ratio (ν) measured (Equation 1).

$$G = \frac{E}{2(1+\nu)} \quad (1)$$

It was possible to observe that the greater the quantity of lime in the mix, the lower was the value of shear modulus obtained (Table 2). It may also be noted that the value of shear modulus increased with time for all mixes, regardless of binder content. However, the quantity of lime in the binder of the mix was found to influence the extent of increase in values of shear modulus recorded. For instance, between day 7 and day 90 of curing age, shear modulus was found to increase by 28%, 24% and 5% in the mixes 1C2L9S (67%), 1C1L6S (50%) and 3C1L12S (25%) respectively. However, it is worth noting that Poisson's ratio is a parameter that is difficult to measure very accurately and tends to have high values of dispersion, due to the precision and sensitivity of the set up and instrumentation involved. Hence, values of Poisson's ratio were averaged for different mixes regardless of the age at which they were measured (i.e. 7, 28 and 90 days) and it was found that the values were very close; 0.12, 0.10 and 0.12 for the mixes 1C2L9S (67%), 1C1L6S (50%) and 3C1L12S (25%) respectively. Therefore, G-modulus was once again calculated (using Equation 1) for all mixes using one common Poisson's ratio value, 0.11 which resulted from an average of all values (Table 3). It was found that the values of G-modulus did not change much. Rather, the trend of G-modulus increasing with time only became more evident for all lime-cement mixes, at all ages. It may thus be concluded that the greater the quantity of lime in the binder of the mix, the lower is the rigidity or stiffness of the mortar with regard to shear strains.

Table 3: Shear modulus values for lime-cement mixes with averaged value of poisson's ratio

Property	Shear modulus (GPa) with poisson's ratio equal to 0.11 for all mixes		
Mix/Age (Days)	1C2L9S (67%)	1C1L6S (50%)	3C1L12S (25%)
7	2.18	4.42	7.36
28	2.47	4.90	7.46
90	2.77	5.27	7.86

4. CONCLUSIONS

The aim of this paper has been to facilitate the choice of mortar for construction or repair of masonry, such that its behaviour together with the corresponding unit is appropriate for the masonry system. To do so, it is not only important to know the absolute values of different mechanical properties that may be obtained from different combinations of lime and cement in a mortar, but also to be aware of the trends that may be obtained from changing the proportions of constituents of the binder of the mortar. Values of E-modulus, fracture energy and shear modulus have been discussed as a function of lime content in the binder resulting in the following conclusions:

- Compressive strength and flexural strength of the mortar decrease with increasing quantities of lime in the binder of the mix. However, the presence of lime was found to lead to a more gradual increase in strength especially between 7 and 90 days of age.

- Static E-modulus was found to decrease with increase in quantity of lime in the binder of the mix. Increased quantities of lime in the mixes, led to a continued gain in stiffness of the mortars up to 90 days of curing age.
- Fracture energy was found to be a function of lime content in the binder of the mix with an inversely proportional relationship. Only the mix with maximum amount of lime in the binder 1C2L9S (67%) displayed a continued increase in fracture energy, with time. The other two mixes initially exhibited increase in values of fracture energy up to 28 days of age, followed by a sharp decrease at the age of 90 days. This phenomenon requires further investigation.
- Evolution of Poisson's ratio with time was found to result in values ranging from 0.08 to 0.13 for different lime-cement mixes. Values of shear modulus, on the contrary showed a consistent increase up to the curing age of 90 days for all the mixes. Mixes with greater amount of lime in the binder, displayed lower values of shear modulus.

ACKNOWLEDGEMENTS

The authors gratefully acknowledge European Lime Association for funding this project. Funding provided by the Portuguese Foundation for Science and Technology (FCT) to the Research Project PTDC/ECM-EST/1056/2014 (POCI-01-0145-FEDER-016841), as well to the Research Unit ISISE (POCI-01-0145-FEDER-007633) is also gratefully acknowledged.

REFERENCES

- [1] Smith, A., Verhelst F., Denayer, C. and Givens, R., 'Quantifying the benefits of lime additions in cement based mortars', in '9th International Masonry Conference', Proceedings of an International conference, Guimarães, July, 2014 (International Masonry Society).
- [2] Arandigoyen, M. and Alvarez, J. I., 'Pore structure and mechanical properties of cement-lime mortars', *Cem. Concr. Res.* **37** (5) (2007) 767–775.
- [3] Cizer, O., Balen, K.V., Gemert, D.V. and Elsen, J., 'Blended lime-cement mortars for conservation purposes: microstructure and strength development', in '6th Structural Analysis of Historic Constructions', Proceedings of an International conference, London, July, 2008 (Taylor and Francis group) 965–972.
- [4] Gulbe, L., Vitina, I. and Setina, J., 'The Influence of Cement on Properties of Lime Mortars', Proceedings of an International conference, Vilnius, May, 2016 (Procedia Engineering) 325–332.
- [5] Jaafri, R., Aboulayt, A., Alam, S.Y., Roziere, E. and Loukili, A., 'Influence of lime on the properties of cement-based materials', in '10th RILEM ICCM', Proceedings of an International conference, Montreal, October, 2017, (American Concrete Institute, SP 320) 586–597.
- [6] Pozo-Antonio, J.S., 'Evolution of mechanical properties and drying shrinkage in lime-based and lime cement-based mortars with pure limestone aggregate', *Constr. Build. Mater.* **77**, (2015) 472–478.
- [7] Tate, M., 'The most important property of cement-lime mortar in masonry construction is', in 'International Building Lime Symposium', Proceedings of an International Conference, Orlando, March, 2005 (NLA Building Lime Group).
- [8] Mosquera, M.J., Silva, B., Prieto, B. and Ruiz-Herrera, E., 'Addition of cement to lime-based mortars: Effect on pore structure and vapor transport', *Cem. Concr. Res.* **36** (9) (2006) 1635–1642.
- [9] Hendrickx, R., 'The adequate measurement of the workability of masonry mortar', PhD thesis (KU Leuven, October, 2009).

- [10] Palomar, I. and Barluenga, G., 'Assessment of lime-cement mortar microstructure and properties by P- and S- ultrasonic waves', *Constr. Build. Mater.* **139** (2017) 334–341.
- [11] Haach, V.G., Vasconcelos, G. and Lourenço, P.B., 'Assessment of Compressive Behavior of Concrete Masonry Prisms Partially Filled by General Mortar', *J. Mater. Civ. Eng.* **26** (10) 04014068.
- [12] Singhal, V. and Rai, D.C., 'Suitability of Half-Scale Burnt Clay Bricks for Shake Table Tests on Masonry Walls', *J. Mater. Civ. Eng.*, **26** (4) (2014) 644–657.
- [13] Mohamad, G., Fonseca F.S., Roman H.R., Vermeltfoort, A.T. and Rizzati, E., 'Behavior of mortar under multiaxial stress' in '12th North American Masonry Conference', Proceedings of an International Conference, Denver, May, 2015 (The Masonry society).
- [14] European Standard, EN 1015-3, '*Methods of Test for Mortar for Masonry, Part 3: Determination of consistence of fresh mortar (by flow table)*', 2006.
- [15] European Standard, EN 1015-11, '*Methods of Test for Mortar for Masonry, Part 11: Determination of Flexural and Compressive Strength of Hardened Mortar*', 2006.
- [16] RILEM Recommendation (50 FMC), 'Determination of the fracture energy of mortar and concrete by means of three-point bend tests on notched beams', *Mater. Struct.*, **18** (6) (1985) 484.
- [17] European Standard, EN 12390:2013, '*Testing hardened concrete, Part 13: Determination of secant modulus of elasticity in compression*', 2013.

EXPERIMENTAL STUDY ON DURABILITY AND SUSTAINABILITY OF CONCRETE WITH LIMESTONE AND DOLOMITE FILLERS

M.M.El-Hawary (1) and K. E. Nouh (1)

(1) Kuwait University, Kuwait

Abstract

Investigating efficient new methods and techniques to improve concrete sustainability is one of the main concerns of researchers in the field of concrete technology. The utilization of a cheap filler as partial replacement of the Portland cement which is a high energy consuming material. The use of fillers is more beneficial in the case of high strength concrete where both water and space are limited to achieve full hydration of cement.

In this work the behavior, properties, durability and sustainability benefits of concrete produced using different ratios of fillers (0,10,20,30%) as partial replacement of Portland cement are investigated. Two types of fillers are utilized, crushed limestone and crushed dolomite. In general, it was found that the introduction of up to 30% of limestone or dolomite as cement replacement will greatly improve sustainability with tolerable effects on concrete properties or durability. The use of 10% fillers improve sustainability, shrinkage resistance, chloride penetration, alkali silica resistance while slightly reduce compressive strength and increase absorption. Results were found to depend on the type of filler. Tensile strength, for example, was found to increase due to the use of 10% limestone and decrease when using 10% dolomite. It is expected, however, that the penetration will be reduced and mechanical properties will improve with the increase in filler fineness.

Keywords: Durability, Sustainability, Fillers, Concrete, Dolomite

1. INTRODUCTION

The production of Portland cement leads to the release of a huge amount of carbon dioxide (CO₂) which is one of the greenhouse gases. The production of one ton of cement results in the release about 0.9 ton of CO₂ into the environment. Greenhouse gases are the main cause of the currently experienced global warming. Due to its deleterious effects, it is necessary to reduce the CO₂ release into environment. Several methods to reduce cement utilization have been investigated. One of those methods is the partial replacement of Portland cement with a 'green' material [1]. The utilization of high strength concrete is becoming a common practice. The utilization of some types of fillers is gaining popularity as a method to achieve a cheaper, more sustainable concrete, especially with high strength concrete with low water to cement ratio, where no enough water or space are available for full cement hydration. Limestone is the most common type of filler. Dolomite is another promising type of filler that is considered in the current research investigation due to its availability in Kuwait. Portland Limestone cement (PLC) may be defined as cement containing ground limestone as a partial replacement

for Portland cement (PC). It is produced by blending Portland cement and limestone or intergrinding Portland cement clinker, limestone, and calcium sulphate [2]. The ASTM and CSA specifications both limit the amount of limestone in Portland Limestone Cement to 15%. The purpose of using limestone is to reduce the amount of cement consumption, and to achieve sustainable concrete [3]. Dolomite and limestone are considered carbonate rock. Using dolomite as a partial replacement of cement to produce Portland Dolomite Cement (PDC) decreases the amount of cement which in turn reduce the CO₂ emissions [4]. Its use is not as common as limestone and research studies on the properties of dolomite as a partial cement replacement are limited [5]. The use of 5% limestone filler was also found to increase the rate of cement hydration [6]. Mortars with up to 20% limestone filler and 30% natural pozzolana were tested [7], where the maximum strength was found to be at 10% limestone filler. In another investigation [8], where up to 30% dolomite filler was used, the maximum compressive strength of mortar was found to take place at 25% dolomite.

The scope of this research is to investigate the properties and examine the performance of concretes produced using fine ground dolomite and limestone as partial replacements of Portland cement. Strength and durability properties such as compressive strength, tensile strength, shrinkage, permeability, absorption and Alkali-Silica Reaction are determined and compared. Sustainability of the resulting concrete is also investigated.

2. MATERIALS AND MIX DESIGNS

Portland cement Type I was provided by Kuwait cement company (KCC) in accordance with (ASTM C150). Fine ground dolomite was obtained from National Industries Company of Kuwait (NIC). Fine Aggregates are natural sand, acquired from local quarries in Kuwait.. The natural coarse aggregates utilized are crushed stone (Gabbro) with three different sizes of 19.0 mm (3/4"), 12.7 mm (1/2") , and 9.5 mm (3/8 "), obtained from the United Arab Emirates. KUTPLAST SP-400 superplasticizing admixture was used in all concrete mixes, meeting the requirements ASTM C494 Type F. Concrete mix was designed for a compressive strength of 50 MPa with low water cement ratio of 0.35. The mix proportions are shown in table 1. Dolomite and limestone fillers were introduced as partial cement replacement of 0%, 10%, 20% and 30% , by weight, rendering four different concrete mixes. Mixes were designed for a target slump range of 50 – 100mm and a target air content range between 2-2.4%.

3. MIXING AND SAMPLES PREPARATION

The concrete mixes and samples were prepared according to ASTM C192. A 1200 kg rotating mixer was used to mix concrete. Concrete was cast and compacted using a vibrator and vibrating table. After 24 hours and were transferred to water tank for curing. The sample sizes cast are 150 mm cubes and 150x300mm cylinders for compressive strength tests; 100x200mm cylinders for the split test; 395mm outer diameter, 215mm inner diameter x 150mm height rings for the shrinkage test; 200x200x120mm prisms for water permeability test ; 75x75x280 mm prisms for Alkali Silica test .

4. CONCRETE TESTING AND PROPERTIES

4.1 Fresh and Mechanical Properties

Slump and air content for all mixes were determined and found to be within target design ranges. Unit weight tests were performed at the age of 28 days. Three samples were tested for

each property, averages are reported. Compressive strength test was performed according to ASTM C 39. Cubes were also tested and reported as they are more common in Kuwait. Compressometer and dial gauges were used to determine the modulus of elasticity as per ASTM C469. Modulus of elasticity was determined as the slope of stress strain curve when the stress reaches approximately 45% of the compressive strength. Stress strain relationships for the four mixes were also evaluated. The compressive strength variation with the filler percentage is shown in figure 1. The split tensile strength was evaluated according to ASTM C 496. The compressive strength and the modulus of elasticity and tensile strength are shown in table 2.

Table 1: Concrete mix proportions

Constituent Material	Value
w/c	0.35
Cementitious materials (kg/m ³)	410
Water (kg/m ³)	143.5
Sand (kg/m ³)	705
SSD Coarse Aggregate 3/8" (kg/m ³)	500
SSD Coarse Aggregate 1/2" (kg/m ³)	340
SSD Coarse Aggregate 3/4" (kg/m ³)	260
Super-plasticizer Dosage (L/100Kg CM)	2-2.5

4.2 Durability Properties

4.2.1 Restrained Ring Test

Concrete volume changes due to cement hydration and subsequent cement paste drying. The reduction of the amount of cement will, therefore, result in the reduction of concrete shrinkage and hence the delay and reduction in shrinkage cracking which in turn increase concrete durability. Shrinkage was evaluated using the restrained ring test according to ASTM C 1581. The steel ring is used to restrain concrete from moving, which leads to an increase in the tensile stress. When tensile stress exceeds the concrete resistance, cracking occurs. Concrete samples were cast in a steel ring having wall thickness of 8 mm, an outer diameter of 395 mm and a height of 150 mm as shown in figure2. Two electrical strain gauges (Type FLA 10-11, gauge factor of $2.11 \pm 0.3\Omega$, and transverse sensitivity of -0.5 %) were bonded at mid height on the interior surface of the steel ring opposite to each other. Within 10 minutes of casting, samples were transferred to the place of testing, strain gauges were connected to the device and initial strains were recorded. Samples were covered in wet burlap and polyethylene sheet for 24 hours after which they were removed and top surface of each test specimen were coated with concrete curing wax to seal the top surface and to make sure that the test specimen will dry only through the outer circumferential surface. The relative humidity and ambient temperature were recorded every day, while the deformation was recorded each 6 hours. The sudden decrease of the strain indicates that the specimen had cracked. The relations between the average measured strain and time for the Limestone and Dolomite mixes are shown in figure 3.

4.2.2 Water Permeability (Penetration) Test

As water is generally the common factor in concrete deterioration, water penetration is an important measure of durability. In this test the depth of water penetration into hardened

concrete is determined according to BS EN 12390-8. Three samples of sizes 200x200x120mm were cast, covered by wet burlap and polyethylene sheet for 24 hours before being demoulded and cured in water tank for 28 days. Samples were removed from the curing tank and left in air at $20 \pm 2^\circ \text{C}$ for 72 hours before testing. Samples were then placed in the penetration cell under water pressure of 0.5 Mpa for 72 hours. Concrete samples were then placed in the compression test machine where two steel rectangular bars were placed to split the specimen into two pieces. Just after splitting, the maximum water depth was marked for each sample. The more the of water penetration depth, the less the durability of concrete. The relation between the water penetration and the filler percentage is shown in figure 4.

Table 2: Mechanical properties of concrete

Property	Designation						
	OPC	PDC 10	PDC 20	PDC 30	PLC 10	PLC 20	PLC 30
Cube Compressive Strength at 28 Days (MPa)	50.8	45.4	44.0	37.6	45.8	43.5	36.9
Modulus of elasticity (GPa)	35.2	34	32.66	32.72	34.79	34.78	32.02
Split tensile strength (MPa)	3.5	3.5	3.2	2.7	3.7	3.3	2.9

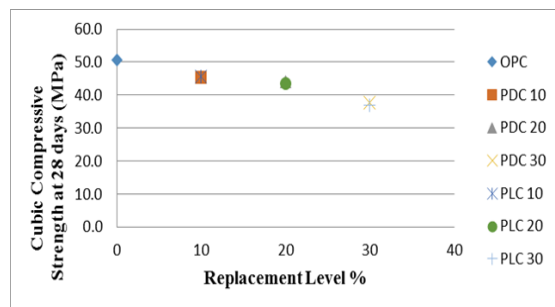


Figure 1: Variation of cube compressive strength with filler percentage



Figure 2: Ring samples

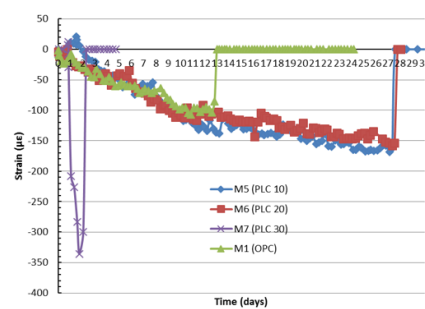
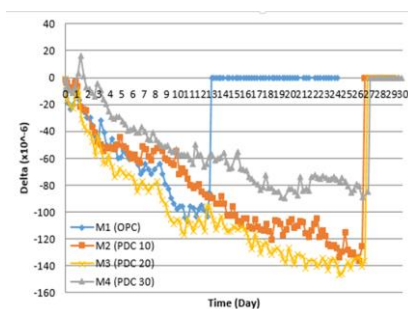


Figure 3: Relations between strain and time for ring samples for dolomite (left) and Limestone (right)

4.2.3 Absorption Test

Absorption was determined according to ASTM C 642. Three cubes of size 150mm were cast and cured for 28 days. 150mm height x 70mm diameter core was taken from each cube. Cores were oven dried for 72 hours at temperature of 100°C , specimens dried in air and

weighed (A) , immersed in water at 22°C for half an hour and weighed again (B) and then boiled in water at 100°C for $3\frac{1}{2}$ hours and weighed (C). Although in practice, water is not boiled, reporting results for both boiled and not boiled water is a requirement according to ASTM C 642. The absorption was calculated as: Absorption after immersion, % = $[(B - A)/A \times 100]$, and Absorption after immersion and boiling, % = $[(C - A)/A \times 100]$. The absorptions after boiling for the four mixes are shown in figure 5.

4.2.4 Chloride Due to Seawater Penetration

Chloride concentration in concrete cubes immersed in seawater was investigated. Three cubes 150 mm were cast and cured for 25 days under water and 3 days in air. Samples were then coated twice from five sides with an elastomeric membrane waterproofing (Type II) at 0.96 m²/ liter per coat allowing 48 hours between each coat. The dry film thickness was 3 mm on all five faces. Samples were then immersed in seawater tanks for 35 days after which they were saw cut in 15 mm layers parallel to the uncoated face. Each layer of concrete was then grounded and powdered. 50ml of distilled water was added to 2 g of each sample in a beaker, mixed and stirred for one hour and left to stand for two hours. The filtrate was filtered using 0.45 µm syringe driven filter unit. The filtered samples were then analyzed using (IC-MS Metrohm 850) instrument device ion chromatograph. The chloride concentration of the concrete was determined and plotted against the corresponding depth. The chloride concentrations for the first two layers (0-15 and 15-30mm) for the four concrete mixes are shown in figure 6.

4.2.5 Alkali Silica Reaction (ASR)

The ASR test was performed according to ASTM C 1260. Prisms of size 75x75x280 mm were cast and cured for 28 days. Prisms were immersed in water for 24 hours at 80° C, and zero readings were taken. 1N NaOH solution was prepared by dissolving 40 g of NaOH in 1000 mL of distilled water; such that the volume proportions of the solution was 4 times the volume of concrete prisms. All the prisms were then immersed in the solution at room temperature (20±1°C). Samples were removed one at a time from the solution and one reading was taken daily for 30 days. The prism expansion measurements are shown in figures 7.

5. DISCUSSION AND ANALYSIS

The average cube compressive strengths of mixes (PDC 10), (PDC 20), (PDC 30), were 10.5, 13.2 and 25.8 % lower, respectively, than that for normal concrete. For mixes (PLC 10), (PLC 20), (PLC 30), the compressive strength was found to be 9.8, 14.3 and 27.3% lower than that for normal concrete, respectively. In this research, dolomite and limestone available in the Kuwaiti market were introduced. Both fillers have fineness moduli slightly higher than that of cement. Results, however, may be improved by increasing the filler fineness. Slight reductions in module of elasticity were also noticed. Reduction of 3.4, 7.1 and 7.1% were measured for mixes (PDC 10), (PDC 20), (PDC 30), respectively, and 1.1, 1.1, 9% for the limestone mixes, in the same order. Reduction in the ultimate strain was also noticed. The split tensile strengths of PDC were also lower than those of conventional concrete. The reductions for concrete containing 10%, 20% and 30% dolomite were found to be 0, 8.6 and 22.9 %, in order. For limestone mixes an increase of 5.7% was noticed for the 10% mix, while a reduction of 5.7 and 17.1% were noticed for the 20% and 30% mixes, respectively. The main advantage of introducing fillers and reducing cement, beside the sustainability benefits,

is the reduction in shrinkage and associated cracking. The restrained shrinkage test was conducted for all mixes. Within the first 12 hours a slight expansion was observed due to the heat of hydration followed by gradual shrinkage. The cracking for mixture (OPC) was observed after 12.6 days with strain value $-103.5 \mu\epsilon$. The times of cracking for the three dolomite mixtures (PDC 10, PDC 20 and PDC 30), were (26.25, 26.38 and 26.67 days, respectively, with strain values of 136, 140 and $89 \mu\epsilon$, in the same order. Cracking, therefore, was delayed for the dolomite mixes by 108.3%, 109.4% and 111.7% for the 10%, 20% and 30% dolomite mixes, respectively.

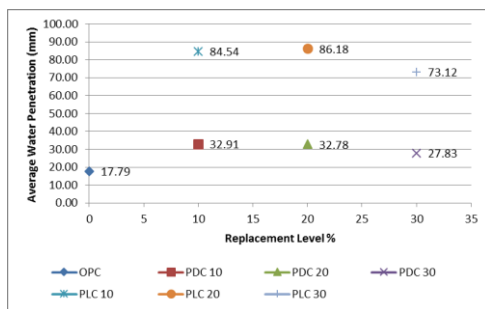


Fig.4: Relation between water penetration depth and the for the four mixes

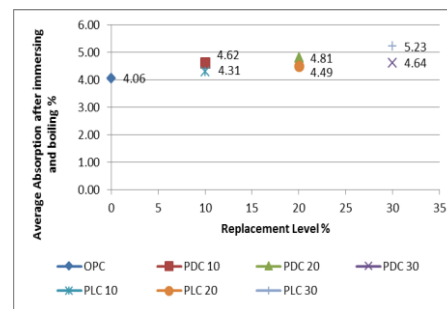


Figure 5: Absorption after boiling filler percentage

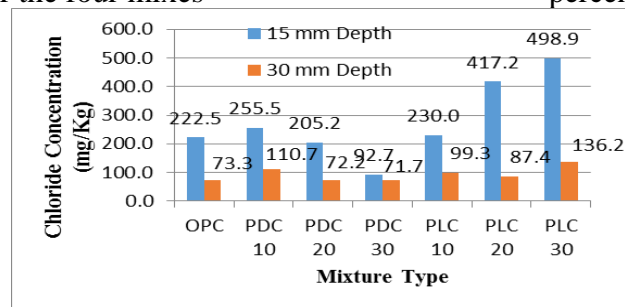


Figure 6: Chloride concentration due to seawater penetration for the four mixes.

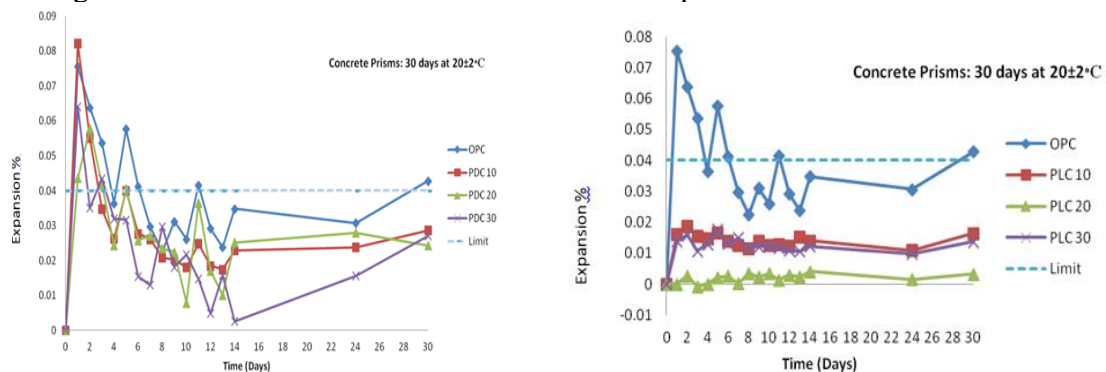


Figure 7: Relations between prism expansions and time for dolomite(left) and Limestone (right)

The strain tolerance (strain at cracking) for the two practical mixes of 10% and 20% dolomite was increased by 32% and 36%, in order. The delay in cracking and increase in strain tolerance are expected to greatly improve durability of mixes containing dolomite filler. The same trend was noticed for the limestone mixes where cracking was delayed by 115.4 and 117% for the 10 and 20% lime mixes, respectively. A problem occurred for the 30% lime mix

during this test. The strain tolerance was increased by 62.3 and 52.7% for the 10% and 20% lime mixes, in order.

The water penetration test is another method to verify concrete durability. The introduction of dolomite filler as partial cement replacement was found to increase the water penetration. The increase in water penetration was 85 %, 84.26 %, and 56.4 % for the 10, 20 and 30% dolomite mixes, respectively. The water penetration was much higher for the limestone mixes. It is expected, however, that the penetration will be reduced and mechanical properties will improve with the increase in filler fineness. Similar results were observed for the absorption tests where average water absorption after immersion for mixtures (PDC 10), (PDC 20), and (PDC 30) was increased by 12.41%, 30.34 %, and 48.96 % respectively when compared with the (OPC) mixture. Almost a similar result was observed after boiling for (PDC 10) where the average water absorption was found to increase by 13.79 %. For (PDC 20), and (PDC 30) , however, better results were observed after boiling where the absorptions were found to increase only by 18.47 %, and 14.28%, respectively, compared to conventional concrete without fillers. The increase for lime mixes was found to be 6.2, 10.6 and 28.8% for the 10, 20, 30% lime mixes, respectively. Durability was also assessed through the chloride penetration test. Chloride concentration was found to increase for (PDC 10) compared to ordinary concrete at both 15 and 30mm depth. The increase is 14.8% at 15mm and 52.4% at 30mm. For (PDC 20) and (PDC 30), however, lower chloride concentrations, indicating durability improvement, were noticed. The chloride concentrations were 7.8% and 58.3% less than OPC at 15mm and 1.4% and 2.2% less at 30mm depth, at the same order. The increase due to the use of limestone filler are 3.4, 87.5 and 124.2% at 15mm and 35, 19.2 and 86% at 30mm for the 10, 20, 30% lime, respectively.

Alkali-silica reaction is common locally due to the high temperature marine environment. Resistance to this type of deterioration, therefore, is of great importance. As the reduction of cement will reduce alkalinity, the introduction of fillers is expected to reduce the alkali-aggregates reaction. The prism expansions for 0, 10, 20 and 30% dolomite were found to be 0.043, 0.029, 0.024 and 0.027%, respectively, after 30 days. The reductions in expansion due to the introduction of dolomite as cement replacement are 32.5, 44.2 and 37.2% for (PDC 10), (PDC 20) and (PDC 30), respectively. The reductions in expansion due to limestone after 30 days are 62.8, 93 and 70% in the same order.

The introduction of dolomite as a partial replacement of cement will result in the reduction of cement and hence reduction in the CO₂ by the same percentage,[9]. The sustainability benefits also include the reduction cost due to the difference in price between cement and crushed dolomite and the benefit of the utilization of indigenous materials. As the introduction of fillers will result in reduction in cracks and durability improvement, sustainability will also improve due to the prolonged service life of structures.

6. CONCLUSIONS

In this paper, the mechanical and durability properties of concrete incorporating dolomite and limestone filler as partial replacement of cement were investigated. The benefits of introducing such filler were determined. The following were concluded:

- The introduction of ground dolomite or limestone as a concrete filler resulted in reductions in both compressive and split tensile strengths. Reductions in the modulus of

elasticity and ultimate strain were also noticed. Reduction increase with the increase in the filler percentage. Mechanical properties may be improved by increasing the filler fineness.

- The utilization of either filler as partial replacement of cement resulted in great delay in shrinkage cracking of more than 100% for all investigated filler percentage. A large increase in strain tolerance was also observed.
- The Chloride concentration due to sea water penetration test was found to increase at low filler percentage and decrease at higher percentages. Same results were observed at all tested concrete depths.
- Resistance to Alkali-Aggregates reaction was significantly improved due to the introduction of fillers. The resistance increase with the increase in filler percentage.
- The use of filler as partial cement replacement reduces energy consumption in cement production and CO₂ emission by the same ratio. Concrete sustainability also improve due to the increased service life resulting from increased durability.
- The use of 10% dolomite will not affect tensile strength, reduce cube compressive strength by 10.5%, increase water penetration by 85%, increase water absorption by 12.4%, increase chloride penetration by 14.8%, reduce ASR by 32.2%, delay shrinkage cracking by 108.3% and increase strain tolerance by 32%. In addition, the use of dolomite will result in sustainability benefits such as energy reduction, cost reduction, gas emission reduction, use of indigenous materials and possible increase in service life.
- The introduction of 10% crushed limestone improved tensile strength by 5.7%, reduced compressive strength by 9.8%, delayed cracking by 115.4%, improved strain tolerance by 62.3%, increased chloride concentration at 15mm by only 3.4% and reduced expansion due to ASR by 62.8%, in addition to the sustainability benefits.

REFERENCES

- [1] El Mostafa, M. "The life cycle assessment of concrete manufacturing in Kuwait" ,Doctoral dissertation, Massachusetts Institute of Technology, (2013).
- [2] Thomas, M. "Field trials of concretes produced with Portland limestone cement". Concrete international, 35, (2010).
- [3] Ramezaniapour, A.M. "Sulfate Resistance and Properties of Portland-limestone Cements" , Doctoral dissertation, University of Toronto, (2012).
- [4] Preethi,G. & Prince,G. "Effect of replacement of cement with dolomite powder on the mechanical properties of concrete", International Journal of Innovative Science, Engineering and Technology, 2(4), (2015), 1083-1088.
- [5] Szybalski, M. & Nocuń-Wczelik,W. "The Effect of Dolomite Additive on Cement Hydration", Procedia Engineering, 108, (2015),193-198.
- [6] Bonavetti, V., Donza, H., Menendez, G., Cabrera, O., & Irassar, E. F. "Limestone filler cement in low w/c concrete: a rational use of energy". Cement and Concrete Research, 33(6), (2003).
- [7] Ghrici, M., Kenai, S., & Said-Mansour, M." Mechanical properties and durability of mortar and concrete containing natural pozzolana and limestone blended cements". Cement and Concrete Composites, 29(7), (2007),542-549.
- [8] Mikhailova, O., Yakovlev, G., Maeva, I., & Senkov, S."Effect of dolomite limestone powder on the compressive strength of concrete", Procedia Engineering, 57, (2013),775-780.
- [9] El-Hawary, M. & Terro, M. "Sustainability and Energy Saving Though Proper Construction Practices and Materials Selection", International Journal of Chemical, Environmental and Biological Sciences 1(2) (2013).

NEW GENERATION OF LIME-BASED RENDERS WITH THE ADDITION OF ULTRAFINE WASTE MATERIAL FROM DOLERITE QUARRIES

I. Rigopoulos (1), L. Kyriakou (1), Á. Török (2), T. Kyratsi (3), and I. Ioannou (1)

(1) Department of Civil and Environmental Engineering, University of Cyprus, 1678 Nicosia, Cyprus

(2) Department of Engineering Geology and Geotechnics, Budapest University of Technology and Economics, Budapest 1111, Hungary

(3) Department of Mechanical and Manufacturing Engineering, University of Cyprus, 1678 Nicosia, Cyprus

Abstract

The sustainable use of quarry wastes for the development of environmentally friendly building materials could ameliorate the anthropogenic impact on the environment. This study focuses on traditional lime-based composites, the slow setting/hardening reactions of which are considered as the main burden for their broader application in construction. Here, we present new data about the performance of hydrated lime renders modified by the addition of different amounts (5% and 15% w/w as a replacement of lime) of ultrafine waste material from dolerite quarries. The ball milling process was applied to produce this ultrafine quarry waste. The results reveal that the addition of the latter at 5% w/w results in composites with a denser microstructure due to the nano-filler effect and an enhancement of the carbonation reactions. A further enhancement of the degree of carbonation, in combination with a significant increase of the compressive strength, were observed by increasing the amount of nanoscale waste material from 5% to 15% w/w. The results demonstrate that this approach could result in significant economic benefits for the quarrying and building industries, providing at the same time a measurable carbon offset associated with the production of lime.

Keywords: ball milling, carbonation, dolerite, lime renders, nanomaterial, quarry waste

1. INTRODUCTION

Over the past decade, the influence of various nano-additives on the performance of building materials has attracted the interest of many researchers [1-6]. Most of these studies have shown that the engineering behaviour of composite building materials can be notably enhanced due to

the addition of specific nanomaterials. Nevertheless, limited research has been performed on the use of nano-additives that are based on waste rock materials [7].

Here, we focus on the development of novel, environmentally-friendly lime-based renders, through the addition of waste material (quarry fines) produced in dolerite quarries. This type of quarry waste material was selected due to the worldwide abundance of similar mafic rock quarries, as well as due to the high reactivity of mafic rocks towards CO₂. The studied waste material was added to the composites as a replacement to the lime binder, following the application of the ball milling process. The latter is commonly used for the development of nano-sized powders and is very efficient in increasing the reactivity of mafic/ultramafic rocks with CO₂ [8,9].

2. MATERIALS AND METHODS

2.1 Selection of suitable quarry fines and development of ultrafine powders

A sample of waste material was collected from a dolerite quarry, located in the Troodos ophiolite complex (Cyprus). This quarry waste was selected due to the fact that it is less altered, compared to similar waste materials from other quarries operating in the Troodos ophiolite (for further details see Rigopoulos et al. [10]). Furthermore, dolerites are considered as high-quality aggregate materials for the construction industry; hence significant quantities of quarry fines are produced worldwide during their extraction and processing.

Ball milling was performed on the aforementioned quarry waste to further reduce its original particle size (<63 µm) to the nanoscale range and increase its reactivity towards CO₂. The optimum milling conditions for this specific waste material were applied (i.e. 20 h of wet ball milling with 50 wt% ethanol as milling liquid), based on the experimental results reported by Rigopoulos et al. [10]; these led to a significant enhancement of the CO₂ uptake of the studied waste material by a factor of ~120 (from 0.8 to 96.9 µmol g⁻¹). Based on transmission electron microscopy (TEM) studies [10], the majority of the particle sizes in the ball-milled samples ranged between 30 and 50 nm. The aforementioned milling procedure was applied to produce a sufficient quantity of ultrafine quarry waste to be used as additive (in partial replacement to lime) during the preparation of lime-based renders.

2.2 Mix design and preparation

Three mix designs were prepared using calcareous fine (0-2 mm) aggregates and lime (CL80-S) as binder (Table 1). For comparison purposes, the binder/aggregate ratio (1/3) and the workabilities (165±5 mm; EN 1015-3 [11]) of all mix designs were kept fixed. The waste nanomaterial was added at 5% and 15% w/w with respect to the total binder (i.e. lime+nanomaterial) content.

Table 1: Mix design of laboratory composites (REF: reference composite, NW5: composite with 5% w/w waste nanomaterial, NW15: composite with 15% w/w waste nanomaterial).

Sample code	Binder (Lime+Nanomaterial)/ Aggregate	Workability (mm)	Water/Binder	Nanomaterial (% w/w of binder)
REF	1/3	163	0.90	-
NW5	1/3	167	0.93	5
NW15	1/3	162	1.03	15

Initially, lime and sand were dry-mixed in a laboratory mixer, whilst the ultrafine quarry waste was added to the composite mixtures following sonication in water for 15 min. Additional water was added in order to acquire a homogeneous mixture with the required workability. The fresh renders were placed in prismatic steel moulds (40×40×160 mm) and compacted in two layers using a jolting table. Following hardening, all specimens were cured in a room with stable temperature (25 ± 2 °C) and relative humidity ($50\pm 5\%$) for at least 90 days.

2.3 Test methods

Powder X-ray diffraction (PXRD) analyses were performed on the quarry waste material before and after ball milling using a Bruker D8 Advance system. PXRD patterns were also obtained for the reference and nano-modified composites in order to study potential mineralogical transformations that might have occurred after 7, 28 and 90 curing days. The analyses were carried out with a continual rotation of the sample, using a step scan of $1^\circ/\text{min}$ within the $3\text{--}80^\circ$ 2θ angle range. The ICDD PDF 2 database was used for the qualitative identification of the constituent minerals.

Differential thermal and thermogravimetric analyses (DTA/TG) were also performed on the studied composites using a Shimadzu DTG-60H. These measurements were also carried out after 7, 28 and 90 days of curing, aiming to highlight differences in the carbonation mechanism among the reference and nano-modified renders. The analyses were conducted from 35 to 1200 °C, at a heating rate of 5 °C/min.

The microstructural features of the composites were also determined after 28 and 90 curing days using a JEOL, JSM-6610 LV scanning electron microscope (SEM), equipped with a BRUKER type QUANTAX 200 energy dispersive X-ray spectrometer (EDXS).

Additionally, the average pore diameter of the composites was determined using a Micromeritics (AutoPore IV 9520) mercury intrusion porosimeter (MIP). This porosimeter has a low pressure upper limit of 50 psia, while in the range of high values it generates pressures up to 60,000 psia. The open porosity and apparent density were measured by vacuum saturation using water as the wetting liquid.

Last but not least, the flexural strength (three-point bending test) was determined for each mixture using three prismatic specimens (40×40×160 mm), according to the procedure described in EN 1015-11 [12]. The mean uniaxial compressive strength of each mixture was also determined using the six half prisms acquired from the three-point bending test. The aforementioned mechanical parameters were determined after 28 and 90 curing days.

3. RESULTS AND DISCUSSION

3.1 Powder X-ray diffraction (XRD)

PXRD analysis of the initial quarry waste material indicated that its mineralogical composition included augite, anorthite, chlorite, actinolite, epidote, albite, quartz, calcite and magnetite [10]. Some of these minerals (mainly augite and anorthite) are rich in the divalent cations Ca^{2+} , Mg^{2+} and Fe^{2+} , which are the necessary components for mineral carbonation.

Additionally, PXRD patterns were obtained for the reference and nano-modified renders after 7, 28 and 90 curing days, demonstrating that the content of portlandite decreases with the addition of ultrafine waste material (Figure 1). This suggests that the added ultrafine waste material contributes towards the setting/hardening reactions of the mortars under investigation.

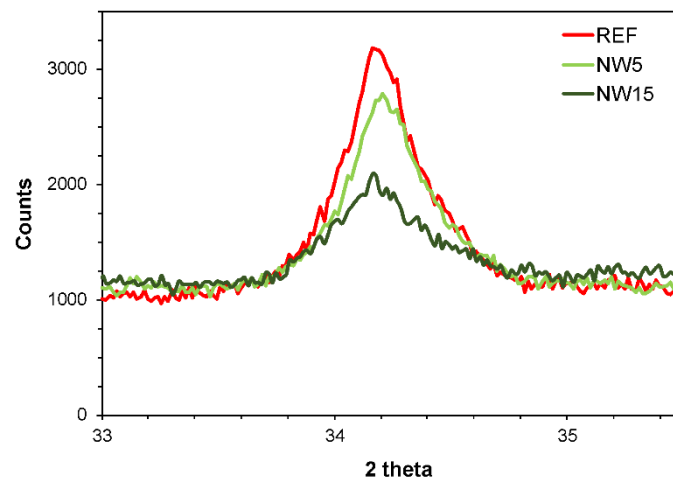


Figure 1: Evolution of the main XRD peak of portlandite after 28 curing days (REF: reference composite, NW5: composite with 5% w/w waste nanomaterial, NW15: composite with 15% w/w waste nanomaterial).

3.2 Thermal analyses

The results of thermal analyses further indicated a significant reduction of the content of portlandite in the nano-modified renders compared to the reference one (Table 2). This was much more evident in the composite with 15% w/w waste nanomaterial, which showed signs of early-stage (before 7 curing days) portlandite reduction. Regarding the composite with 5% w/w milled quarry waste, the reduction of its portlandite content was significantly enhanced between 7 and 28 curing days (reduction by 47%) compared to the reference composite (reduction by 23%) (Table 2). These results are consistent with the observations acquired by the PXRD studies (see Figure 1), indicating that the studied ultrafine quarry waste material can accelerate the setting/hardening process of lime-based renders by enhancing their carbonation reactions.

Table 2: Content of portlandite (%) for the studied composites estimated via thermal analyses (REF: reference composite, NW5: composite with 5% w/w waste nanomaterial, NW15: composite with 15% w/w waste nanomaterial).

Sample code	Portlandite content %		
	Curing days		
	7	28	90
REF	1.60	1.23	1.05
NW5	1.35	0.72	0.77
NW15	0.27	0.27	0.14

3.3 Scanning electron microscopy (SEM)

SEM studies were also carried out on the reference and nano-modified composites after 28 and 90 curing days. Detailed observations were performed on fragments from both the surface and the centre of the specimens, showing that the microstructure of the composites under study

has become denser and more homogeneous after the addition of ultrafine quarry waste (compare Figure 2a with 2b).

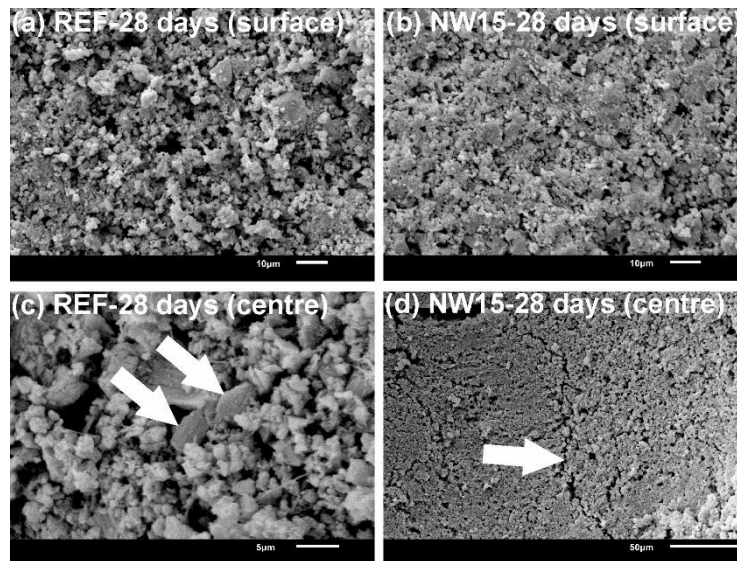


Figure 2: SEM images of the studied composites after 28 curing days (REF: reference composite, NW15: composite with 15% w/w waste nanomaterial).

The SEM/EDXS analyses also revealed that the reference specimens contain a significant amount of portlandite crystals after 28 curing days (see arrows in Figure 2c). In contrast, portlandite crystals become rare after the addition of ultrafine quarry waste, indicating that the latter has notably enhanced the carbonation reactions of lime-based renders; this observation is also supported by the results of the PXRD studies and thermal analyses (see sections 3.1 & 3.2).

Furthermore, the SEM observations revealed that the nano-modified renders contain sporadic microcracks (Figure 2d), the formation of which is probably assigned to excess drying shrinkage induced by the use of increased water/binder ratios in the presence of nano-additives [13,14].

3.4 Physico-mechanical properties

MIP studies were performed after 7, 28 and 90 curing days. The results showed a considerable reduction of the average pore size diameter in the composites containing ultrafine quarry waste, irrespective of the curing age (Table 3). It should be underlined that after 90 curing days, this decrease was much more evident in the composite containing 15% w/w waste nanomaterial, despite the presence of microcracks. This confirms that the nano-filler effect becomes more evident when using a larger quantity of nanomaterial. The smaller average pore size diameter of the nano-modified composites is consistent with the denser microstructure of the latter observed by SEM (see Figure 2b). These findings are also supported by the PXRD studies and thermal analyses (see Figure 1 and Table 2), which showed that the addition of ultrafine quarry waste promotes carbonation in the composites hereby studied.

Table 3: Physico-mechanical properties of the studied composites (REF: reference composite, NW5: composite with 5% w/w waste nanomaterial, NW15: composite with 15% w/w waste nanomaterial).

Sample code	Curing days	Physical properties			Mechanical properties	
		¹ Average pore diameter (nm)	² Open porosity (%)	² Apparent density (kg m ⁻³)	Compressive strength (MPa)	Flexural strength (MPa)
REF	7	250	33.41	1743	-	-
	28	321	33.33	1756	1.57	1.16
	90	339	26.54	1753	2.64	1.39
NW5	7	199	33.90	1733	-	-
	28	276	33.72	1745	1.62	0.98
	90	304	29.17	1752	2.65	1.45
NW15	7	154	32.57	1732	-	-
	28	209	30.55	1742	2.93	0.77
	90	196	27.86	1771	3.10	1.04

¹: measured by MIP, ²: measured by vacuum saturation.

Despite the smaller average pore size diameter of the nano-modified composites, the open porosity and apparent density values of the latter do not show significant differences compared to the reference composite (Table 3). This is presumably attributed to the presence of sporadic microcracks in the nano-modified renders, as confirmed by SEM (see Figure 2d).

Regarding the mechanical properties of the studied renders, the results showed that the composite containing 5% w/w ultrafine waste material has similar compressive strength with the reference one, irrespective of the curing age (Table 3). A notably higher compressive strength was obtained for the composite with 15% w/w ultrafine waste. This improvement was obvious even after 28 curing days (see Table 3), implying the positive effect of a higher quantity of the studied waste nano-additive, even at early curing times. Similarly, Duran et al. [13] mentioned a significant increase in the early-age compressive strength of lime-based mortars modified by the addition of nanosilica (6% to 20% w/w as a replacement of the lime binder). Additionally, Alvarez et al. [15] mentioned that the addition of 3% w/w of nanosilica (with respect to lime) increased the compressive strength of air lime-based mortars. In the current work, the results of the PXRD studies and thermal analyses, in combination with the MIP measurements and SEM observations, suggest that the higher compressive strength in the composite with 15% w/w waste nanomaterial is attributed to the enhancement of the carbonation reactions, in combination with the nano-filler effect.

The flexural strength did not show any significant changes due to the addition of 5% w/w waste nanomaterial (Table 3). However, an increase of the quantity of ultrafine waste from 5% to 15% w/w generally resulted in a reduction of the flexural strength (Table 3). This is probably attributed to the fact that the higher proportion of waste nano-additive resulted in an increased water/binder ratio (see Table 1). Subsequently, this promoted the formation of microcracks in the nano-modified composite with 15% w/w nano-additive, as confirmed by SEM (see Figure 2d). These results are consistent with Pérez-Nicolás et al. [14], who noted that the greatest flexural strengths were acquired for nanosilica-free mortars, due to the fact that nanosilica

increased the water demand of the mixture. Similarly, Stefanidou and Papayianni [16] mentioned that the flexural strength of cement pastes with 5% w/w nanosilica is lower than that of reference specimens.

4. CONCLUSIONS

The current experimental study revealed that lime-based renders modified by the addition of ultrafine waste material from dolerite quarries (in partial replacement to lime) show a denser and more homogeneous microstructure compared to the reference render. This is primarily attributed to the nano-filler effect, in combination with the enhancement of the carbonation reactions after the addition of the aforementioned ultrafine waste material. The composites containing 15% w/w waste nanomaterial showed a considerably higher degree of carbonation and compressive strength compared to those with 5% w/w waste nanomaterial. In contrast, a reduction of the flexural strength was observed in the composites with 15% w/w ultrafine quarry waste. This is attributed to the increased water/binder ratio after the addition of a higher proportion of waste nano-additive, which subsequently resulted in the formation of microcracks.

The results clearly demonstrate that the proposed approach could provide an effective option for the sustainable management of solid wastes generated from quarrying processes, with great economic benefits for the quarrying and building industries. The fact that the ball-milled quarry waste was added as a replacement to the lime binder could notably contribute to the reduction of the CO₂ emissions associated with the production of lime worldwide. Further research is needed to quantify the carbonation process in these nano-modified composites and determine if this approach could potentially comprise an efficient CO₂ sequestration technology.

ACKNOWLEDGEMENTS

The authors would like to acknowledge financial support from the Republic of Cyprus and the European Committee through the Cyprus Research Promotion Foundation (Project KOINA/M-ERA.NET/0316/04) and from Hungary through the National Research, Development and Innovation Office (Project NKFI/M-ERA.NET2/127023). Additional support was provided (IR) by the CO2NOR project, which has received funding from the European Union's Horizon 2020 Research and Innovation Programme under the Marie Skłodowska-Curie Grant Agreement No 654091.

REFERENCES

- [1] Lin, D.F., Lin, K.L., Chang, W.C., Luo, H.L. and Cai M.Q., 'Improvements of nano-SiO₂ on sludge/fly ash mortar', *Waste Manage.* **28** (2008) 1081-1087.
- [2] Zygantidis, I., Stefanidou, M., Kalfagiannis, N., Logothetidis, S., 'Nanomechanical characterization of cement-based pastes enriched with SiO₂ nanoparticles', *Mater. Sci. Eng. B* **176** (2011) 1580-1584.
- [3] Maravelaki-Kalaitzaki, P., Agioutantis, Z., Lionakis, E., Stavroulaki, M., Perdikatis, V., 'Physico-chemical and mechanical characterization of hydraulic mortars containing nano-titania for restoration applications', *Cem. Concr. Compos.* **36** (2013) 33-41.
- [4] Polat, R., Demirboğa, R., Khushefati, W.H., 'Effects of nano and micro size of CaO and MgO, nano-clay and expanded perlite aggregate on the autogenous shrinkage of mortar', *Constr. Build. Mater.* **81** (2015) 268-275.

- [5] Theodoridou, M., Charalambous, E., Maravelaki-Kalaitzaki, P., Ioannou, I. 'Amelioration of crushed brick-lime composites using nanoadditives', *Cem. Concr. Compos.* **68** (2016) 77-87.
- [6] Kong, D., Huang, S., Corr, D., Yang, Y., Shah, S.P., 'Whether do nano-particles act as nucleation sites for C-S-H gel growth during cement hydration?', *Cem. Concr. Compos.* **87** (2018) 98-109.
- [7] Rigopoulos, I., Török, Á., Kyratsi, T., Delimitis, A., Ioannou, I., 'Sustainable exploitation of mafic rock quarry waste for carbon sequestration following ball milling', *Resour. Policy* (2018), <https://doi.org/10.1016/j.resourpol.2018.08.002>.
- [8] Rigopoulos, I., Petallidou, K.C., Vasiliades, M.A., Delimitis, A., Ioannou, I., Efstathiou, A.M., Kyratsi, Th., 'Carbon dioxide storage in olivine basalts: effect of ball milling process', *Powder Technol.* **273** (2015) 220-229.
- [9] Rigopoulos, I., Vasiliades, M.A., Ioannou, I., Efstathiou, A.M., Godelitsas, A., Kyratsi, Th., 'Enhancing the rate of ex situ mineral carbonation in dunites', *Adv. Powder Technol.* **27** (2016) 360-371.
- [10] Rigopoulos, I., Petallidou, K.C., Vasiliades, M.A., Delimitis, A., Ioannou, I., Efstathiou, A.M., Kyratsi, Th., 'On the potential use of quarry waste material for CO₂ sequestration', *J. CO₂ Util.* **16** (2016) 361-370, <https://doi.org/10.1016/j.jcou.2016.09.005>.
- [11] European Committee for Standardization, Methods of Test for Mortar for Masonry – Part 3: Determination of consistence of fresh mortar (by flow table), EN 1015-3, 1999.
- [12] European Committee for Standardization, Methods of Test for Mortar for Masonry. 'Determination of Flexural and Compressive Strength of Hardened Mortar', EN 1015-11, 1999.
- [13] Duran, A., Navarro-Blasco, I., Fernández, J.M., Alvarez, J.I., 'Long-term mechanical resistance and durability of air lime mortars with large additions of nanosilica', *Constr. Build. Mater.* **58** (2014) 147-158.
- [14] Pérez-Nicolás, M., Duran, A., Navarro-Blasco, I., Fernández, J.M., Sirera, R., Alvarez, J.I., 'Study on the effectiveness of PNS and LS superplasticizers in air lime-based mortars', *Cem. Concr. Res.* **82** (2016) 11-22.
- [15] Alvarez, J.I., Fernández, J.M., Navarro-Blasco, I., Duran, A., Sirera, R., 'Microstructural consequences of nanosilica addition on aerial lime binding materials: influence of different drying conditions', *Mater. Charact.* **80** (2013) 36-49.
- [16] Stefanidou, M., Papayianni, I., 'Influence of nano-SiO₂ on the Portland cement pastes', *Compos. Part B* **43** (2012) 2706-2710.

**International Conference on Sustainable
Materials, Systems and Structures
(SMSS 2019)**
Durability, Monitoring and Repair of Structures

Avoiding alkali aggregate reactions

RILEM TECHNICAL COMMITTEE; TC 258-AAA (AVOIDING ALKALI AGGREGATE REACTIONS IN CONCRETE – PERFORMANCE BASED CONCEPT); CURRENT ACTIVITIES AND ACHIEVEMENT.

Børge J. Wigum (1, 2), Jan Lindgård (3)

(1) Norwegian University of Science and Technology. Sem Sælands veg 1, N-7491 Trondheim, Norway

(2) HeidelbergCement Northern Europe - Lilleakerveien 2B, 0283 Oslo, Norway

(3) SINTEF Building and Infrastructure, Pb 4760 Torgarden, 7465 Trondheim, Norway

Abstract

Since 1988, several consecutive RILEM TCs have been seeking to establish universally applicable test methods for assessing the potential alkali-reactivity of aggregates and concrete mixtures; TC 106 (1988–2001), TC 191-ARP (2001–2006) and TC 219-ACS (2006–2014). The major recommendations, focusing on test methods for aggregates, were published in 2016.

In 2014, TC 258-AAA (2014-2019) was established, concentrating on performance-based assessment. The TC includes four Work Packages (WPs); WP1 aims to develop one or more concrete performance tests (CPTs). Currently, a Round Robin Test (RRT) is being carried out with the draft procedure for the 38°C "RILEM AAR-10" CPT. More accelerated CPTs are also under development. WP2 is dealing with the link between results from laboratory testing and field. In 2015, about 80 monitored concrete cubes were prepared and distributed at 10 field exposure sites in Europe and North America. Drilled cores from about 20 field cubes cast in 2004 are also being analysed. WP3 primarily aims to develop a method for measuring the (maximum) potential alkali release from aggregates, while the main goal of WP4 is to compile results from laboratory testing, exposure sites and concrete structures to assess the “true” level of alkali released from various aggregates.

Keywords: RILEM, Alkali-Aggregate Reactions, Concrete

1. INTRODUCTION

Alkali-Silica Reaction (ASR) is a serious deterioration mechanism of high socio-economic importance for concrete structures. Basically, ASR is a chemical reaction between alkali metals (sodium and potassium) in the high pH pore solution and certain minerals in the aggregate. ASR

essentially starts as a dissolution reaction where silica (SiO_2) is dissolved from "alkali-silica reactive" aggregates. Sorption of water by the produced hygroscopic alkali-silica gel causes swelling and expansion of the concrete. Expanding structural elements may cause constraining forces and displacement of adjacent elements, which may lead to unexpected load redistribution, operational issues and problems with the structural capacity.

The expansion will further lead to internal tensile stresses and cracking, which will gradually result in significant reduction in tensile strength and Young Modulus of elasticity. In addition to the structural consequences of ASR induced expansion and cracking of the concrete, subsequent deterioration mechanisms may enhance the overall distress, such as freeze/thaw degradation, delayed ettringite formation (DEF) and chloride ingress/steel corrosion. ASR might thus strongly influence the structural safety and reduce the service life. The incubation time needed before ASR damage starts ranges from a few months to several decades, much depending on aggregate type, binder type and exposure climate.

2. RILEM ACTIVITIES ON AAR SINCE 1988 – BRIEF HISTORY

Development and assessments of universally test methods for avoiding deleterious Alkali Aggregate Reaction (AAR) in concrete have been the focus of consecutive RILEM Technical Committees (TCs) for 3 decades (*in addition to ASR, AAR also includes possible Alkali-Carbonate Reaction, ACR*). The first TC was established in 1988 as TC 106, with Dr Philip Nixon from the Building Research Establishment (BRE) in the UK as the Chairman and Dr Ian Sims from Sandberg, UK (now with RSK Environment Ltd) as the secretary. The TC was proposed by Micheline Regourd-Moranville. The formation of this TC was reported at the 8th International Conference on Alkali Aggregate Reaction (ICAAR) in Kyoto (1989), where also the 2nd and 3rd TC meetings were arranged. The primary objective of the TC was to develop test methods for aggregate reactivity that could form the basis for internationally agreed test methods (Nixon & Sims [1]).

TC 106 also performed a survey of national specifications for avoiding AAR damage and carried out an assessment of reports of any AAR damage to structures made with low alkali cements or containing fly ash or ground granulated blast-furnace slag (ggbfs). In 1993, TC 106 presented an interim report on the progress of the work (Nixon & Sims [2]). In 1996, participants from 21 countries were members of the TC, including virtually all those countries which at that time were regarded as having significant AAR problems. The TC also conducted a survey of test methods in use in these countries (Nixon & Sims [3]). Following trials to demonstrate effectiveness in differentiating reactive and non-reactive aggregate combinations worldwide, TC 106 published two expansion tests in 2000; an 80°C accelerated mortar-bar test (AMBT, "RILEM AAR-2" [4]) and a 38°C concrete prism test (CPT, "RILEM AAR-3" [5]). The methods were presented by Nixon and Sims [6] at the 11th ICAAR in Québec City (2000). The CPT [5] was considered reliable for most aggregate combinations, and the AMBT [4] was in many cases found suitable for predicting behaviour in the concrete prism test.

The work of TC 106 culminated in 2000 in an integrated assessment scheme, presented by Sims & Nixon in 2001 [7]. After having considered a wide range of methods for assessing aggregates with respect to potential alkali-aggregate reactivity, TC-106 proposed a three steps procedure:

- 1) Petrographic examination ("RILEM AAR-1") [8]
- 2) 80°C Accelerated mortar-bar expansion test ("RILEM AAR-2") [4]

3) 38°C Concrete prism expansion test ("RILEM AAR-3") [5]

The subsequent TC 191-ARP ("Alkali-Reactivity & Prevention – assessment, specification and diagnosis"), formed in 2000, continued working on aggregate test methods. They introduced an accelerated 60°C CPT ("RILEM AAR-4") and a specialised procedure (80°C AMBT) for carbonate aggregates ("RILEM AAR-5"). TC 191-ARP also had a widened scope to seek international consistency in approaches to diagnosis and appraisal of AAR damage on concrete structures ("RILEM AAR-6.1") and specifications for avoiding AAR ("RILEM AAR-7"). The TC also initiated work on a test method for measuring the potential alkali release from aggregates ("RILEM AAR-8"). The overall progress of TC 191-ARP was presented by Sims et al. [9] and Nixon et al. [10] at the 12th ICAAR in Beijing (2004). Following discussions at the 11th and the 12th ICAAR conferences, TC 191-ARP developed the basis of a specification to avoid AAR damage to concrete worldwide (Sims & Nixon [11] and Nixon & Sims [12]).

The 3rd RILEM TC on AAR, TC 219-ACS ("Alkali aggregate reaction in Concrete Structures: performance testing and appraisal") was established in 2007. Most of the issues included in the former TC proceeded, but a few new topics were added. The progress and new achievements were presented at the 14th ICAAR in Austin (2012) [13]. One main new activity initialised in the new TC was performance testing of concrete, i.e. how to safely use alkali-reactive aggregates. Several documents and recommendations were prepared within, or in conjunction with, TC 219-ACS; Lindgård et al. [14], [15], [16] and Godart et al. [17]. Early in 2014, the TC terminated its activities and concluded the work of the three TCs chaired by Dr Nixon with Dr Sims as the secretary for 25 years (Figure 1).



Figure 1: Honoured after 25 years of heading of the three RILEM TCs on AAR since 1988; Dr Philip Nixon - Chairman (left), and Dr Ian Sims – Secretary (right). Professor Børge Johannes Wigum (middle) is the Chairman of the current RILEM TC 258-AAA.

The full set of RILEM Recommendations were finally published in 2016 (Nixon & Sims [18]). This State-of-the-art Report contains five recommended test methods for aggregates (designated "RILEM AAR-1 to AAR-5") and an overall recommendation which describes how these test methods should be used to enable a comprehensive aggregate assessment ("RILEM AAR-0"). The report also includes two Recommended International Specifications for concrete ("RILEM AAR-7.1 & 7.2") and a Preliminary International Specification for dams and other hydro structures ("RILEM AAR-7.3"), which describe how the aggregate assessment can be combined with other measures in the design to produce a concrete with a minimised risk of developing damage from AAR.

Within the TC, considerable effort was put on publishing a petrographic atlas with overview of alkali reactive aggregates (Fernandes et al. [19]). This "RILEM AAR 1.2" Atlas is complementary to the petrographic method described in "RILEM AAR 1.1" [8]. It is designed and intended to assist in the identification of alkali-reactive rock types in concrete aggregate by thin-section petrography.

3. ACTIVITIES IN RILEM TC 258-AAA (2014-2019)

The present 4th RILEM TC on AAR (TC 258-AAA) was established in October 2014. It is chaired by Professor Børge Johannes Wigum (*HeidelbergCement Northern Europe, Norway*) and the secretary is Dr Jan Lindgård (*SINTEF, Norway*).

The main purpose of this on-going TC, including four Work Packages (WPs), is to develop and promote a performance-based testing concept for the prevention of deleterious ASR in concrete (the issue Alkali Carbonate Reaction (ACR) is not included). Emphasis is also put on implementing the RILEM methods and recommendations as national- and international standards.

RILEM TC 258-AAA has a wide international membership which helps to promote the eventual international use of RILEM methods and recommendations. Physical meetings twice a year are still the centre of the TC's activities (Figure 2), but whenever possible the meetings are co-ordinated with major relevant international conferences to facilitate attendance. Members around the world that are not able to travel to the meetings are following the discussions through the extended minutes of the meetings. All relevant documents, including the minutes from the meetings, are available for TC members at the RILEM internal website.



Figure 2: Group photo taken at the 9th TC meeting in Reykjavik, Iceland.

A Norwegian R&D project ("KPN-ASR", funded by the Norwegian Research Council), dealing with the same topics as TC 258-AAA, has provided valuable input to the TC work and partly funded some joint activities. Moreover, the R&D project has also enabled fruitful co-operation with leading researchers in Northern America and with LNEC in Portugal.

3.1 WP1 - Performance testing and accelerated testing in the laboratory

By implementing performance test methods one can derive advantage from the mitigating effect of supplementary cementitious materials (SCMs) such as fly ash, silica fume and ggbfs, and of low alkali cements. By using such mitigating measures, a much wider selection of aggregates can be safely used while increasing the sustainability of the concrete and aggregate industry. The performance testing concept includes applications for performance assessment of combinations of aggregates and cement/binders at varying or fixed alkali contents. In some countries, for example Norway and Canada, concrete performance tests have been used for decades. By assessing existing methods and new findings in various national research projects, WP1 of TC 258-AAA, headed by Dr Terje F. Rønning (*HeidelbergCement Northern Europe, Norway*), aims to develop one or more concrete performance test methods. Draft procedures have been prepared, but there is still a necessity to finalize and validate these procedures, including arranging international inter-laboratory trials (Round-Robin Tests, RRTs). As soon as the necessary validation is finished, it is the intention to publish these methods as RILEM Recommendations.

The main concrete performance test method being developed in WP1 is a 38°C Concrete Prism Test (CPT), labelled "RILEM AAR-10". To reduce the sources of error, where alkali leaching from the concrete prisms during the exposure period has been documented to be the most important one (Lindgård et al. [20]), relatively large prisms are used (100 x 100 x 400 mm³). The 38°C CPT method published by the former RILEM TC ("RILEM AAR-3" [18]) use smaller prisms (75±5 x 75±5 x 250±50 mm³). However, that method is only intended used for testing of the potential alkali-reactivity of aggregates (*Note: In this pure aggregate testing, a CEM I cement is used with a fixed high alkali content [18]. Even though the extent of alkali leaching is higher when using smaller prisms, for most alkali-reactive aggregates enough alkalis are present in the concrete pore water for ASR to develop*).

The principles and test setup for the 38°C "RILEM AAR-10" concrete performance test has been agreed. During 2018, a RRT was initiated based on the agreed draft test procedure. However, the RRT was conducted within the framework of the Norwegian "KPN-ASR" projects, addressing a limited number of laboratories. The test results will then be offered to the TC for inclusion of precision data in the test document. Publication of the RRT as such will of course acknowledge all participating parties, but it will not constitute a RILEM TC activity.

A more accelerated 60°C concrete performance test (labelled "RILEM AAR-11" and "RILEM AAR-12"; without and with alkali supply) is under development. Still, the principles and test setup for this possible alternative test procedure are being discussed within the TC.

A Japanese approach based on the Japanese test procedure "TC-Draft of JCI-TC115FS-2013" (using alternative storage conditions) has been presented and might also be included as "RILEM AAR-13". The "main question", still discussed within the TC, is how to reliably calculate the alkali content of the alkali wrapping that corresponds to the alkali concentration in the concrete pore water (that normally will vary over time if SCMs are applied).

3.2 WP2 - Performance testing and laboratory vs. field; Exposure sites

An important tool for validating the performance testing concept is to assess the link between accelerated results from laboratory testing and behaviour of these concrete mixtures in field, either on field exposed blocks or on real structures. An extensive State-of-the-art (STAR) report on the laboratory/field correlation is currently being prepared.

One key objective of WP2 is to establish a link between outdoor exposure sites dedicated to AAR investigations and located in different parts of the world, and thereby generating an international database on the effect of environmental conditions on the kinetics of AAR. A paper [21] giving an overview of field exposure sites world-wide has recently been presented by Professor Benoît Fournier (*Université Laval, Québec, Canada*) that is heading WP2.

The initial work of WP2 included preparation of about 80 monitored concrete cubes ($300 \times 300 \times 300 \text{ mm}^3$) for outdoor storage at 10 different exposure sites in Europe and North America (Portugal, France, Germany, Norway, Iceland, Canada & USA). The concrete mixtures included ordinary Portland cement and addition of fly ash (20 & 30%), along with control mixtures (highly reactive and non-reactive). These cubes will be measured once or twice a year for at least ten years, preferably longer.

The EU PARTNER project (2003-2006) produced identical monitored concrete cubes ($300 \times 300 \times 300 \text{ mm}^3$) from 13 aggregate combinations (all with a high alkali Portland cement) that were distributed to eight field exposure sites across Europe. In 2017, the laboratory of LNEC in Portugal shipped about 80 cores drilled from about 20 selected PARTNER cubes after 12 years of field exposure to laboratories taking part in the post-documentation program being part of WP2.

3.3 WP3 - Performance testing; Assessment of detailed alkali inventory in concrete, including internal alkali release from aggregates, recycling of alkali and external alkali supply

One important “missing link” with respect to testing methods for ASR is how to reliably measure the potential (maximum) amount of alkalis that might be released from various types of aggregates in the laboratory, under accelerated conditions. The main aim of WP3, headed by Dr Esperanza Menéndez Méndez (*Institute of Construction Science, “Eduardo Torroja” (CSIC), Spain*), is to prepare and validate a test method for measuring this potential alkali contribution from aggregates. A draft test method labelled “RILEM AAR-8” has been prepared. As soon as the necessary validation is finished, it is the intention to publish this method as a RILEM Recommendation. A RRT with the draft “RILEM AAR-8” methods has already been completed, revealing some important issues to be reviewed in the testing procedure. Hence, a new RRT has recently been initiated.

As part of the literature review report (STAR) also being prepared within WP3, it is in addition important to evaluate the potential internal alkali recycling in the concrete which in some instances have been reported, in addition to assess any alkali contribution from external sources.

3.4 WP4 - Verification of alkalis released from aggregates

Results from measured (maximum) alkali release from aggregates in accelerated laboratory tests need to be verified and calibrated to what actually will be released to the concrete pore water in real concrete structures. The main aim of WP4, headed by Dr Klaartje De Weerd (*Norwegian University of Science and Technology, Norway*), is to compile results from

exposure sites and concrete structures worldwide to assess the “true” level of alkali released from various aggregates. This WP was initiated in 2016, mainly to assess results from WP3.

A Post-doc study in the Norwegian "KPN-ASR" project developed an efficient and assumed accurate test method to determine the alkali level in the concrete pore water facilitating activities to verify the level of potential alkali release from aggregates in real concrete structures (Plusquellec et al. [22]). This procedure will be used frequently in the planned project activities in WP4, including the following actions:

1. How much of the total alkali from the cement is available in the concrete pore solution?
2. Comparing methods to determine free alkali content? What is their accuracy?
3. Gathering results from on-going verification tests.
4. Propose reference non-releasing aggregate for future studies.

4. CONCLUDING REMARKS

We have struggled to understand, control and prevent damage due to AAR in the past 75 years since it was first reported in concrete. In addition to the international ICAAR conferences initialized in 1974, the continuing series of RILEM Technical Committees have helped to harness international co-operation in this struggle for the last 30 years. The RILEM work has recently achieved some significant milestones regarding recommendations to prevent damage by AAR in new concrete structures.

The work in the current TC 258-AAA will continue until the end of 2019, with particular focus on the performance-based testing concept. It is our anticipation to increase the input from all parties all around the world, enabling the implementation of the RILEM methods and recommendations as national- and international standards.

REFERENCES

- [1] Nixon, P.J. and Sims, I., 'RILEM TC106 Alkali Aggregate Reaction – Accelerated tests. Interim Report and Summary of Survey of National Specifications', in 'Proceedings of the 9th International Conference on Alkali-Aggregate Reactions in Concrete (ICAAR)', (London, 1992) 731-738.
- [2] Nixon, P.J. and Sims, I., 'RILEM TC106 Alkali Aggregate Reaction – accelerated tests', *Interim report. BRE Client Report CR* (1993) 130/93.
- [3] Nixon, P. and Sims, I., 'Testing aggregates for alkali-reactivity. Report of TC-106', *Materials and Structures*, Vol. 29, (July 1996) 323-334.
- [4] RILEM, 'AAR-2 - Detection of potential alkali-reactivity of aggregates — the ultra-accelerated mortar bar test', *Materials and Structures* 33 (2000) 283-289.
- [5] RILEM, 'AAR-3 - Detection of potential alkali-reactivity of aggregates — method for aggregate combinations using concrete prisms', *Materials and Structures* 33 (2000) 290-293.
- [6] Nixon, P. and Sims, I., 'Universally accepted testing procedures for AAR. The progress of RILEM Technical Committee 106', in: Bérubé, M.A., Fournier, B. and Durand, B. (Eds.), *Proceedings of the 11th International Conference on Alkali-Aggregate Reactions in Concrete (ICAAR)*, Quebec, Canada (2000) 435-444.
- [7] Sims, I. and Nixon, P., 'Alkali-reactivity – a new international scheme for assessing aggregates', *Concrete*, (January, 2001) 36-39.
- [8] RILEM, 'AAR-1 - Detection of potential alkali-reactivity of aggregates — Petrographic method', *Materials and Structures* 36 (2003) 480-496.

- [9] Sims, I., Nixon, P.J. and Marion, A-M., 'International collaboration to control Alkali-Aggregate Reaction: The successful progress of RILEM TC 106 and TC 191-ARP', in Tang, M., Deng, M. (Eds.), *Proceedings of the 12th International Conference on Alkali-Aggregate Reaction in Concrete (ICAAR)*, (Beijing, 2004) 41-50.
- [10] Nixon, P., Hawthorn, F. and Sims, I., 'Developing an international specification to combat AAR. Proposals of RILEM TC 191-ARP', in Tang, M., Deng, M. (Eds.), *Proceedings of the 12th International Conference on Alkali-Aggregate Reaction in Concrete (ICAAR)*, (Beijing, 2004) 8-16.
- [11] Sims, I. and Nixon, P.J., 'Assessment of Aggregates for Alkali-Aggregate Reactivity Potential: RILEM International Recommendations', in Fournier, B. (Editor) *Proceedings of the Marc-André Bérubé Symposium on Alkali-Aggregate Reactivity in Concrete*, (Montreal, 2006) 71-91.
- [12] Nixon, P. and Sims, I., 'An International Specification to Combat AAR. Proposals of RILEM TC 191-ARP', in Fournier, B. (Editor) *Proceedings of the Marc-André Bérubé Symposium on Alkali-Aggregate Reactivity in Concrete*, (Montreal, 2006) 195-215.
- [13] Sims, I., Nixon, P. and Godart, B., 'Eliminating Alkali-Aggregate Reaction from long-service structures, in: Drimalas, T., Ideker, J.H., Fournier, B. (Eds.), *14th International Conference on Alkali-Aggregate Reactions in Concrete (ICAAR)*, Austin, Texas, (2012).
- [14] Lindgård, J., Nixon, P.J., Borchers, I., Schouenborg, B., Wigum, B.J., Haugen, M. and Åkesson, U., 'The EU Partner project – European standard tests to prevent alkali reactions in aggregates', *Cement & Concrete Research* 40 (2010) 611-635.
- [15] Lindgård, J., Andiç-Çakır, Ö., Borchers, I., Broekmans, M.T.A.M., Brouard, E., Fernandes, I., Giebson, C., Pedersen, B. Pierre, C., Rønning, T.F., Thomas, M.D.A. and Wigum, B.J., 'RILEM TC219-ACS-P: Literature survey on performance testing', *COIN project report 27*, ISBN: 978-82-536-1209-6, Trondheim (2011) 164 pp.
- [16] Lindgård, J., Andiç-Çakır, Ö., Fernandes, I., Rønning, T.F. and Thomas, M.D.A., 'Alkali-silica reactions (ASR): Literature review on parameters influencing laboratory performance testing', *Cement and Concrete Research* 42 (2012) 223-243.
- [17] Godart, B. de Rooij, M. and Wood, J.G.M. (Eds.), 'Guide to Diagnosis and Appraisal of AAR Damage to Concrete in Structures. Part 1 Diagnosis (AAR 6.1)', *Springer Series: RILEM State-of-the-Art Reports*, Vol. 12 (2013) 91 pp.
- [18] Nixon, P.J. and Sims, I. (Eds.), 'RILEM Recommendations for the Prevention of Damage by Alkali-Aggregate Reactions in New Concrete Structures', *Springer Series: RILEM State-of-the-Art Reports*, Vol. 17, 1st ed. (2016), XVI, 168 pp.
- [19] Fernandes, I., Anjos Ribeiro, M., Broekmans, M.A.T.M. and Sims, I., 'Petrographic Atlas: Characterisation of Aggregates Regarding Potential Reactivity to Alkalis. RILEM TC 219-ACS Recommended Guidance AAR-1.2, for use with the RILEM AAR-1.1 Petrographic Examination Method', *Springer*, 1st ed. (2016), XI, 191 pp.
- [20] Lindgård, J., Thomas, M.D.A., Sellevold, E.J., Pedersen, B., Andiç-Çakır, Ö., Justnes, H. and Rønning, T.F., 'Alkali-silica reaction (ASR) - Performance testing: Influence of specimen pre-treatment, exposure conditions and prism size on alkali leaching and prism expansion', *Cement and Concrete Research* 53 (2013) 68-90.
- [21] Fournier, B., Lindgård, J. and Wigum, B.J., 'Outdoor exposure site testing for preventing Alkali-Aggregate Reactivity in concrete – a review', Presented at ICCRRR, Cape Town, Nov. 2018.
- [22] Plusquellec, G., Geiker, M.R., Lindgård, J., Duchesne, J., Fournier, B. and De Weerd, K., 'Determination of the pH and the free alkali metal content in the pore solution of concrete: Review and experimental comparison', *Cement and Concrete Research* 96 (2017) 13-26.

OPTIMIZATION OF THE CONCRETE PRISM TEST FOR ASR EXPANSION BY ALKALI-WRAPPING AND A NEW APPROACH ASSESSING THE ALKALI REACTIVITY OF CONCRETE FOR NUCLEAR FACILITIES

K. Yamada (1), Y. Kawabata (2), S. Ogawa (3), K. Shibuya (3), J. Etoh (4), A. Teramoto (5), Go. Igarashi (6) and I. Maruyama (7)

(1) National Institute for Environmental Studies, JAPAN

(2) Port and Airport Research Institute, JAPAN

(3) Taiheiyo Consultant, Co. Ltd., JAPAN

(4) Mitsubishi Research Institute, JAPAN

(5) Hiroshima University, JAPAN

(6) Tohoku University, JAPAN

(7) Nagoya University, JAPAN

Abstract

There are many testing methods to evaluate the alkali reactivities of aggregates. However, the expansion of concrete by the alkali-silica reaction (ASR) is determined by many factors other than the characteristics of the aggregate, and the acceptable level of expansion and design life depends on the type of structure in which the concrete is used. Therefore, a performance evaluation or a quantitative expansion estimate of the concrete mixture that takes into account environmental conditions is required. The concrete prism test is a promising method for a reliable test procedure; however, the traditional test suffers from alkali loss from the test prism, known as alkali leaching, and insufficient moisture supply during the test. These problems may be avoided by wrapping concrete prisms with a wet cloth containing an alkaline solution, whose pH is close to that of pore solution in the concrete. This process is called AW-CPT. In order to assess the alkali reactivity of concrete, especially for nuclear facilities, not only AW-CPT but also the holistic procedure is required. A new approach was proposed combining petrographic observations, an accelerated mortar bar test at 80 °C, and an AW-CPT at 60 and 40 °C depending on the reactivity of aggregate.

Keywords: ASR, alkali wrapping, concrete prism test, alkali leaching, nuclear facilities.

1. INTRODUCTION

There are several techniques to evaluate the risk of the alkali-silica reaction (ASR) of aggregates. These techniques must take into account many factors, including not only the characteristics of the aggregate, but also the pessimum effects due to aggregate mix proportions and size, alkali content, curing temperature, evaluation age, etc. In addition to these material properties and the properties of the test procedure, there are environmental factors that must also be considered when determining the risk of ASR in the performance of concrete members and structures. Among these factors are temperature changes, humidity, and precipitation (moisture supply). The geometric features and profile of the concrete members, their location in the concrete structure, thickness, and constraints in terms of free expansion are factors that affect expansion characteristics and evaluating expansion due to ASR. The various factors that affect the expansion potential by ASR and the aging effects of ASR are presented in Figure 1. Simple aggregate tests are thus insufficient to assess quantitatively the expansion by ASR for concrete structures over their design life. Instead, performance testing should provide basic data for long-term expansion estimates.

Several Japan Concrete Institute (JCI) technical committees have researched ASR diagnosis and performance testing [1-3]. A particular area of concern is in nuclear power plants, where ASR damage has been found in some facilities. The former Japan Nuclear Energy Safety Organization (JNES) published a report on a series of projects on ASR with the aim of introducing a new procedure for the prevention of ASR [4]. This report, with consideration of advanced standards such as the RILEM AAR series and Canadian Standards, provided three new flow procedures: aggregate testing flow for ASR potential, diagnostic flow for ASR in concrete structures, and selection flow for countermeasures against ASR. The report also provided a summary of remaining issues requiring additional investigation. An investigation, based on this report and the research conducted by the JCI, was carried out between 2014 and March of 2017 to address the remaining issues.

Based on the outlined research activities in Japan, a new approach for assessing the alkali reactivity of concrete based on an optimized concrete prism test (CPT) for ASR expansion by alkali-wrapping (AW), or AW-CPT, is proposed and detailed here.

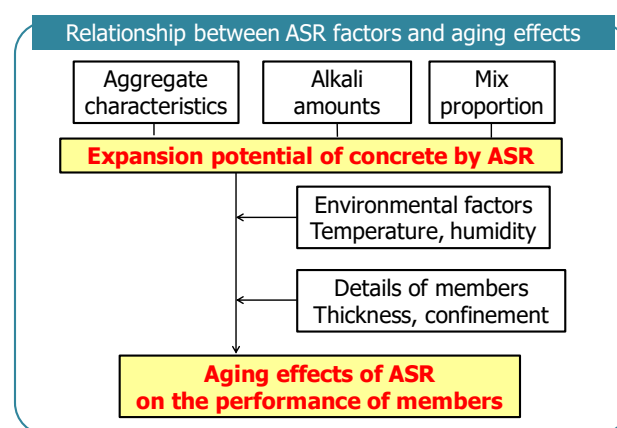


Figure 1: Relationship between various factors affecting the performance of concrete members over time (translated from [5]).

2. ALKALI-WRAPPED CONCRETE PRISM TEST, AW-CPT

While the most reliable assessment of alkali-silica reactivity comes from field experience and exposure testing, the accurate reproduction of certain environments is challenging. One such example is the thick bio-shield concrete of a nuclear reactor, which may see temperatures of up to 60 °C, and has a design life of 60-80 years. Thus, accelerated laboratory testing is required, with the alkali boosted CPT being a promising method. However, even when the same concrete mix is used, expansion of field-exposed blocks is much larger than in the laboratory test [6], with the loss of alkalis, known as alkali leaching, from the test prism in the accelerated test condition considered as the major contributing factor [7, 8]. A second problem with the accelerated CPT arises from the moisture supply during the test. In general, during acceleration tests, concrete prisms are placed in a humid chamber containing water in the bottom. However, there is a significant difference in moisture supply between this humid curing and direct contact with water. This variance in moisture supply is a significant detraction of the accelerated test, and outweighs that of the alkali leaching [9].

A new test method was introduced to overcome these two problems [10]. The concrete test prism from the traditional CPT is modified by overwrapping a wet cloth, containing an alkaline solution with a pH close to that of the concrete pore solution. This modification results in the alkali-wrapped concrete prism test, AW-CPT, as shown in Figure 2. For samples with boosted alkalis, the pH of the alkaline solution is modified accordingly. In particular, for assessing ASR, controlling the alkali contents of the concrete is critical, as the alkali-silica reaction consumes alkalis to form the alkali silica gel that causes the expansion, and when all alkalis are consumed, the reaction terminates. If there are excess alkalis supplied by the solution, the reaction is prolonged and the expansion may be overestimated. The alkali content in the wrapping cloth is controlled to prevent this. Finally, water is consumed by the alkali-silica reaction, so additional water is supplied periodically. This matches external environmental conditions, where additional water is supplied continuously from the environment and no additional alkalis are supplied.



Figure 2: Examples of alkali-wrapping of concrete prisms.

Figure 3 presents a comparison between traditional CPTs, such as RILEM AAR-4, and AW-CPT, comparing expansion, mass gain, and alkali leaching. Rapid expansive andesite (TO) and late reactive hornfels (WI) were used as the aggregates, with alkali amounts boosted to 5.5 kg/m³. The rapid expansive andesite, which has a pessimum proportion of 30% (coarse aggregates are 70% non-reactive pure limestone, fine aggregates are 100% non-reactive pure limestone), demonstrated rapid expansion followed by saturation in the relatively early test stage. The addition of the AW yielded similar results. However, for the late expansive hornfels no expansion was observed for the traditional CPT case, while a slowed but continuous expansion was found for the AW-CPT. From the mass loss during the curing

process and the alkali leaching of 20% at 26 weeks (see Figure 3), it is likely that a limited moisture supply and alkali leaching are responsible for the lack of expansion. When the AW was applied, the alkali leaching was effectively suppressed.

It is possible to optimize the acceleration conditions depending on the reactivity of the aggregate. For some highly reactive aggregates that show in-field expansion with 2.5 kg/m³ of alkalis, the acceleration condition of 60 °C and 5.5 kg/m³ of alkalis is too great. In such a condition, many parts of formed alkali silica gel are extruded from the prisms without generating expansive pressure. For late expansive aggregate, this type of severe condition is preferable to obtain the results in a reasonable testing time. Additional study is required to determine optimal acceleration conditions depending on the type of aggregate.

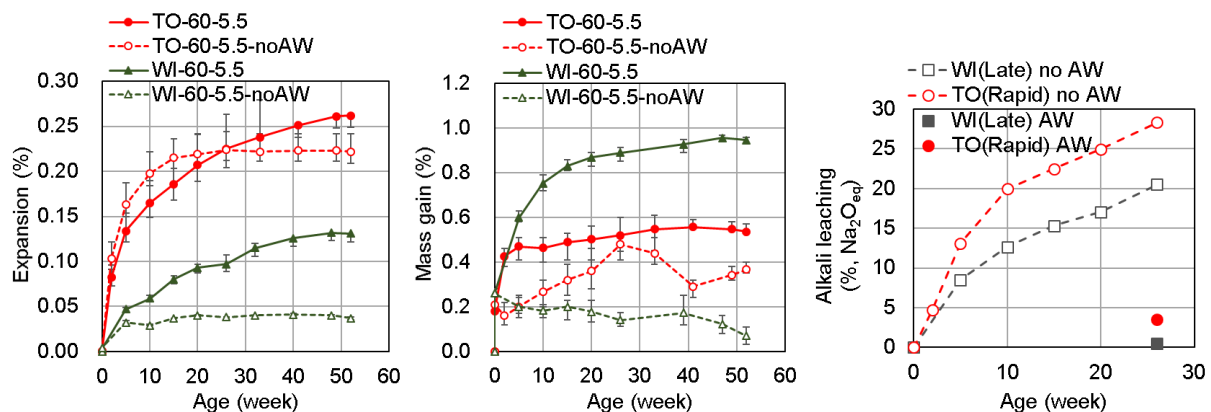


Figure 3: Comparison of traditional CPT and AW-CPT for expansion (left), mass gain (middle), and alkali leaching (right). Legend: Aggregate type - Test temperature – AW [5].

3. PROPOSED ASSESSMENT FLOW OF ALKALI REACTIVITY OF CONCRETE

In the new project that was performed by the NRA on ASR prevention, an aggregate selection flow procedure was used with AW-CPT being part of that selection process. This is because AW-CPT tests a specific mix, and is not an aggregate test. Presented in Figure 4 is the proposed holistic flow for assessing the alkali reactivity of concrete [5]. In this flow, petrographic evaluation by polarized microscope is carried out before the AW-CPT, done in order to find the presence of reactive minerals and rock types that are associated with reactive minerals. After petrographic observation, an accelerated mortar bar test is carried out. The accelerated mortar test has a severe testing condition of 80 °C, which may cause some “false positives”, i.e. non-reactive aggregates being found as reactive, and some “false negatives”, i.e. some reactive aggregates such as highly reactive chert containing chalcedony may be found as non-reactive. However, the accelerated mortar test is just that, accelerated, providing temporal results within two weeks and thus may be useful for quality control.

After the petrographic observation, if the aggregate is determined not to be rapid expansive, an accelerated AW-CPT is performed at 60 °C. This is because this test may allow for a quicker judgment or evaluation of the aggregate as the results are obtained relatively quickly as compared to the normal AW-CPT at 40 °C. If the aggregate is determined unsuitable after the accelerated test, then the normal AW-CPT at 40 °C, which would follow,

is therefore avoided and the selection process restarts. The final decision about acceptability of the aggregate for use in the concrete mixture is made after the test at 40 °C. For rapid expansive aggregate, the accelerated AW-CPT at 60 °C is not performed, as it is too severe for the rapid expansive aggregate and would result in a lower predicted expansion (a “false negative”).

At this moment, some methods for quantitative estimation of expansion are under research and development. Some examples will be presented in a separate paper in this conference. Because AW-CPT is a “job mix” test as mentioned before, reselection of aggregate is not always necessary when a result of harmful expansion was obtained by AW-CPT. Controlling total alkali amounts in concrete under some value or the addition of supplemental cementitious materials, SCMs are typical suppressing method of ASR. AW-CPT can evaluate the effects of both countermeasures by modifying total alkali amounts and by adding SCMs in concrete mixture evaluated by AW-CPT for controlling alkali amounts and the performance testing of SCMs, respectively. In this procedure, it is important to understand the acceleration ratio of AW-CPT of ASR compared to the environments where concrete is used. In general, alkali boosting and higher temperature of AW-CPT are combined accelerating factors. However, when concrete is used in 60 °C like bio-shield concrete in NPP, AW-CPT at 60 °C cannot be an accelerated test. In such condition, alkali boosting is the only accelerating factor. Besides, it is easy to imagine that faster expansion is expected in hot and humid climate than cold and dry climate even if the same concrete is used. Therefore, the threshold value judging acceptable or not must be determined domestically but it is difficult to show a universal value. From this kind of viewpoint, a quantitative estimation method for ASR expansion considering climate conditions based on the results of AW-CPT is strongly required.

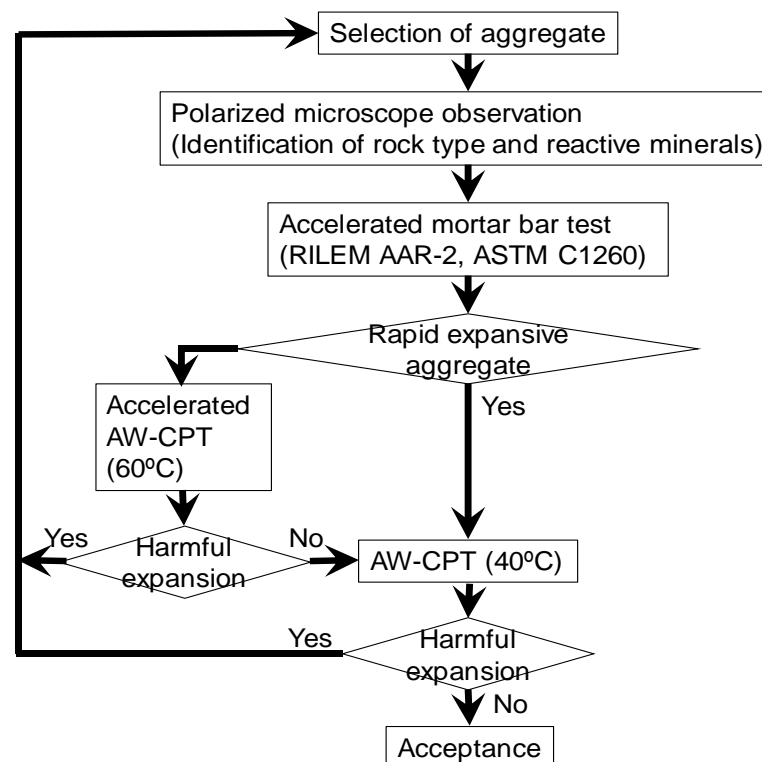


Figure 4: Proposed flow assessing the reactivity of concrete [5].

4. COMPARISON BETWEEN AW-CPT AND FIELD EXPOSURES

Significant discrepancies have been found between laboratory tests and field exposures in terms of ASR expansion. In particular, in-field ASR expansions of concrete block having bigger size have been found to be significantly larger than those obtained by traditional CPTs. It is important to compare expansion behaviors between in-field exposures and AW-CPT. For example, this discrepancy was examined for coarse aggregate with 30% being highly reactive, comparing the results between a AW-CPT at 38 °C with a total alkali content of 5.25 kg/m³ and field exposure of a 1 x 1 x 0.5 m block [11]. In this investigation, various suppressing measures against ASR such as Li salt, fly ash, and blast furnace slag were examined. The correlation between the expansions for the field samples at four years and the AW-CPT at two years is shown in Figure 5. Field expansions were approximately 0.05% smaller than AW-CPT, indicating a reasonable correlation. The acceleration effects of the AW-CPT may account for this difference.

In a separate investigation, a numerical estimation of expansion was performed, based on experimental data from three-year field exposures in three different climate conditions of several blocks with the same concrete mixtures and a corresponding AW-CPT performed for one year [12]. AW-CPT was performed at different temperatures at 20, 40, 60 °C. In this investigation, the climate condition, daily temperature change, and precipitation at three different locations were considered, with annual average temperatures of 7.7, 18.8, and 24.3 °C and annual precipitations of 941, 1016, and 2108 mm, respectively. The different climate conditions had a significant effect on the expansion behavior, and the proposed model was found to be capable of successfully reproducing these effects.

Thus, due to the reasonable correlation between the AW-CPT and the corresponding field exposures, and due to the successful reproduction of field expansion by numerical modeling based on the AW-CPT, the AW-CPT can be considered as a meaningful test to assess the reactivity of a concrete mixture. This reactivity can be quantitatively assessed in terms of expansion over time considering environmental conditions, and AW-CPT can be combined with a numerical model for long-term performance evaluation.

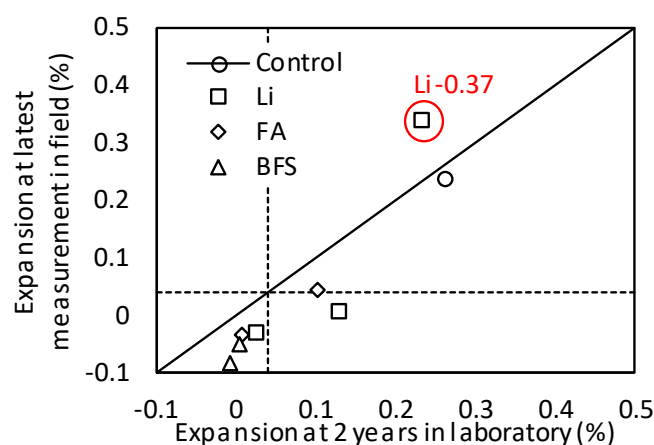


Figure 5: Correlation between field expansion and AW-CPT [11]

5. CONCLUSIONS

- The concrete prism test is necessary for the assessment of potential ASR in concrete and the corresponding expansions. CPT is the only potential method for estimating quantitatively the expansion of concrete due to ASR.
- Alkali-leaching and an insufficient supply of moisture are problems associated with the application of the traditional CPT. By applying a wrapping paper to the test prism, in which there is an alkaline solution with a pH close to that of a concrete pore solution, these problems may be avoided.
- A new assessment flow of ASR of concrete is proposed. This flow is composed of a petrographic evaluation, an accelerated mortar bar test at 80 °C, and AW-CPT at 40 and 60 °C for rapid and late expansive aggregates, respectively.
- A comparison was made between field exposures and laboratory AW-CPT. The AW-CPT was found to be a useful test for determining quantitative long-term ASR expansions.
- A numerical model combined with the AW-CPT can be a valuable performance evaluation tool.

ACKNOWLEDGEMENTS

Part of this work was financially supported by the Japan Society for the Promotion of Science (JSPS, No. 16H04393, No. 17H03292). Some parts of this study have been carried out as part of a NRA project for advanced aging management technical evaluation of concrete structures in nuclear power plants. The information presented in this paper is the sole opinion of the authors and does not necessarily reflect the views of the sponsoring agencies.

REFERENCES

- [1] Torii, K., Yamada, K., Kog, H., Kubo, Y. and Yamaji, T., 'Committee Report: JCI-TC062A Technical committee on mitigation and diagnosis of alkali silica reaction considering the action mechanisms', Technical Committee Reports, Japan Concrete Institute (2008) 47-66.
- [2] Yamada, K., Kawabata, Y., Kubo, Y., Goda, H., Sagawa, Y. and Hirono, S., 'Committee Report: JCITC115FS Technical committee on Diagnosis of ASR-affected structures', Technical Committee Reports, Japan Concrete Institute (2014) 1-17.
- [3] Yamada, K., Yamamoto, T., Sagawa, Y., Ueda, N., Kubo, Y. and Ogawa, S., 'Committee Report: JCI-TC152A Technical committee on performance based design and maintenance scenario with controlling ASR deterioration', Technical Committee Reports, Japan Concrete Institute (2017).
- [4] Nakano, M., 'Proposal of investigation methods of alkali aggregate reaction on concrete for nuclear power plant', Japan Nuclear Energy Safety Organization, JNES-RE-2013-2050 (2014) (In Japanese).
- [5] Mitsubishi Research Institute, Inc, "Project report of enhancing ageing management technical assessment FY2016 (Research on soundness evaluation of concrete structures in long-term with respect to the Alkali Aggregate Reaction)", Nuclear Regulatory Commission annual report (2017) (in Japanese).
- [6] Ideker, J.H., Bentivegna, A., Folliard, K. and Juenger, M., 'Do current laboratory test methods accurately predict alkali-silica reactivity?', *ACI Mat. J.* 4(2012) 395-402.
- [7] Rogers, C. and Hooton, R.D., 'Reduction in mortar and concrete expansion with reactive aggregates due to alkali leaching', *Cem. Con. Agg.* 13(1991)42-49.

- [8] Lindgard, J., Thomas, M.D.A., Sellevold, E.J., Pedersen, B., Andic-Cakir, O., Justnes, H. and Ronning, T.F., 'Alkali-silica reaction (ASR) – performance testing influence of specimen pre-treatment, exposure conditions and prism size on alkali leaching and prism expansion', *Cem. Concr. Res.* 53(2013)68-90.
- [9] Kawabata, Y., Yamada, K., Ogawa, S., Martin, R-P., Sagawa, Y., Seignol, J.-F. and Toutlemonde, F., 'Correlation between laboratory expansion and field expansion of concrete: Prediction based on modified concrete expansion test', *Proceedings of 15th International Conference on Alkali-Aggregate Reaction in Concrete* (2016)034.
- [10] Kawabata, Y., Yamada, K., Sagawa, Y. and Ogawa, S., 'Alkali-wrapped concrete prism test (AW-CPT) – New testing protocol toward a performance test against alkali-silica reaction -, *J. of Advanced Concrete Technology* 64(2018)441-460.
- [11] Kawabata, Y., Someya, N., Tanaka, Y. and Kawamura, N., Comparison of the preventive measures against alkali-silica reaction between laboratory and field-exposure tests, In: *Proceedings of 73rd JSCE Annual Meeting* (2018)675-676 (in Japanese).
- [12] Kawabata, Y., Yamada, K., Ogawa, S. and Sagawa, Y., 'Numerical simulation of expansion behavior of field-exposed concrete block on the basis of modified concrete prism test', *Proceedings of SMSS 2019* (in submission).

A NEW PERFORMANCE TEST METHOD FOR ALKALI-SILICA REACTION

Edward (Ted) Moffatt (1), Michael Thomas (2) and Michael Laskey (3)

(1) Department of Civil Engineering, Queen's University, Kingston, Ontario, Canada

(2) Department of Civil Engineering, University of New Brunswick, Fredericton, New Brunswick, Canada

(3) Stresscon Inc., Saint John, New Brunswick, Canada

Abstract

Current standardized tests methods for identifying alkali-silica reactive aggregates cannot be used as performance tests to determine the risk of damaging reaction of a specific combination of materials or “job mixture”. This paper presents data for a new test that aims to provide a continuous supply of external moisture without either augmenting or reducing the alkalis in the concrete (job) mixture under test. Concrete cylinders are stored in cylindrical containers with a slightly larger diameter such that there is a small annulus of 1 to 2 mm around the concrete specimen. This annulus is filled with a “model pore solution” which is determined based on the composition of the binder in the job mixture. The sealed containers are then stored at either 38°C or 60°C and the length-change of the specimens is measured periodically. Results are shown for a wide series of mixtures using combinations of materials that have been previously used to produce concrete blocks for storage on outdoor-exposure sites; consequently there are long-term field-performance data for the mixes under test. The results show that the new test method is better able to predict the performance of the job mixtures than existing tests. A number of modifications are proposed for future testing.

Keywords: alkali-silica reaction, durability, performance test method

1. INTRODUCTION

Since its discovery in 1940, alkali-silica reaction (ASR) is second to corrosion as the leading cause of premature deterioration of concrete structures [1]. Deterioration of concrete as a result of ASR is typically a long-term process and is influenced by a number of factors including type of reactive aggregate, level of alkalis and source of moisture (i.e. sea water or rain water). Fortunately, there are numerous ways in which ASR can be prevented primarily through the use of supplementary cementing materials (SCMs) [2], lithium-based admixtures,

and restricting the alkali concentration from the portland cement (in addition to other sources such as aggregates and deicing salts) [3].

Currently there are a number of test methods used to predict the efficiency of supplementary cementing materials, natural pozzolans, slag or lithium-based admixtures in mitigating expansion due to ASR [4]. However, these tests have been known to produce varying results in terms of the threshold amount of pozzolan and/or slag required to mitigate ASR to an acceptable level. Using the performance of concrete structures in the field to evaluate the efficiency of preventive measurements is certainly the most reliable tool; however, limited long-term data exist on the effectiveness of preventative measures in mitigating ASR.

Determining a satisfactory level of supplementary cementing materials (SCMs), lithium or cement content for a particular aggregate requires the use of a suitable performance tests. There currently exist numerous performance test methods, however, their performance has been shown to vary widely, which has been the motivation by many to produce a rapid, reliable and relevant test method to better predict the rate of ASR and the capability of testing “job” mixtures [3, 4]. At the moment, all test methods require a set combination of mixture proportions resulting in the inability to test a specific mix that is to be used in the field. These test methods also require the augmentation of alkali level (by directly adding alkalis to the mixture or submerging specimens in a highly alkaline soak solution).

This paper begins with a brief description of alkali-silica reaction, followed by current and existing test methods used for preventing expansion due to alkali-silica reaction. Thereafter, a new proposed test method is presented which compares the performance of a number of mixtures to the concrete prism test (CPT, ASTM C1293, CSA A23.2-14A and RILEM AAR-3).

2. BACKGROUND

Alkali-silica reaction (ASR) results from a reaction between reactive silica minerals found in certain aggregates with alkali hydroxides provided by the portland cement. Following its discovery, Stanton suggested that using low-alkali cement, which he defined as anything less than 0.60% Na_2O_e , would be effective in mitigating ASR [1]. It is now well established that controlling the alkali content of the concrete is more appropriate [5].

Test methods for evaluating the efficiency of preventative measures and correctly identifying reactive aggregates have evolved since Stanton developed the mortar bar test, which resulted in the creation and adoption of ASTM C227. However, this test was recently removed as a standard as it was ineffective in identifying certain types of reactive aggregate especially slowly reactive rocks such as certain gneisses, greywackes, argillites, quartzites and meta-volcanics [3, 6, 7].

Perhaps the most widely used test methods for evaluating aggregate reactivity are the Accelerated Mortar Bar Test (AMBT, ASTM C1260, CSA A23.2-27A and RILEM AAR-2) and the Concrete Prism Test (CPT, ASTM C1293, CSA A23.2-14A and RILEM AAR-3). The CPT was originally developed in 1950s based on issues associated with ASTM C227. The currently version of the test, published in 1994, requires a cementitious content of 420 kg/m^3 (708 lb/yd^3) with the cement alkalis raised to 1.25% Na_2O_e through the addition of NaOH to the mix water. Concrete prisms ($75 \times 75 \times 275 \text{ mm}$ [$3 \times 3 \times 11 \text{ in.}$]) are stored over

water in sealed containers at 38°C (100°F) and are measured for length change. An expansion limit of 0.04% at 1 year (ASTM C1778) is used to identify reactive aggregate and the same limit at 2 years is used to evaluate preventative measures. Unfortunately, issues related to alkali leaching from specimens stored over water has been found by many and originally reported by Blanks and Meissner [8]. This work motivated the increase in alkali content by adding NaOH to the mixing water (total alkali content of 1.25%) and has been found to correlate reasonably well with exposure blocks following 10 years of natural exposure, however, the test still takes a significant amount of time [9].

One of many issues facing the industry now is the development of a rapid, reliable and relevant test method to better predict the effect of ASR is a challenge. The test must not only be inexpensive and rapid, but should mirror the long-term (i.e. 50 years) field performance of concrete structures [10]. Finally, the test must have the possibility in testing “job” mixes with identical aggregate and concrete composition that will be used in actual projects.

3. EXPERIMENTAL BACKGROUND

3.1 Materials

Three ASTM C150 Type I portland cements (OPC), were used as a part of this study. The chemical composition of all cementitious materials was determined using x-ray florescence (XRF) and is presented in Table 1. These cements were selected based on their range in equivalent alkali contents (Na_2O_e).

Table 1: Chemical composition of cementitious materials

Chemical composition (%)	PC-1	PC-2	PC-3
SiO_2	20.61	20.84	18.72
Al_2O_3	4.93	5.07	5.82
Fe_2O_3	3.51	2.14	2.71
CaO	64.15	64.83	61.32
MgO	0.72	2.97	2.74
SO_3	2.81	2.42	4.01
Na_2O	-	0.23	-
K_2O	-	0.32	-
Na_2O_e	0.36	0.43	0.92
LOI	2.44	1.61	2.13

Three reactive siliceous aggregates were used to study the performance of the new test method. These aggregates include a fine aggregate from El Paso, Texas (designated as Jobe) and two coarse aggregates including Springhill, a greywacke from Fredericton, New Brunswick, Canada and Spratt, a siliceous limestone from Spratt, Ontario, Canada. All aggregates were paired with non-reactive fine or coarse aggregate.

In this study, seventeen concrete mixtures were prepared at a range of alkali contents (0.36-1.25% Na_2O_e) in order to match replicate mixtures from exposure site blocks in addition to current concrete structures deteriorating from ASR (i.e. Mactaquac Dam, portland cement

Na₂O_e = 0.70). Table 2 presents the range of alkali contents prepared with respect to one or more reactive aggregates.

Table 2: Concrete mixtures

Alkali Content (% Na ₂ O _e)	Jobe	Springhill	Spratt
0.36	x		
0.41	x	x	x
0.43	x		
0.49		x	x
0.52	x		
0.70	x	x	
0.90		x	x
0.92	x		
0.95	x		
1.25	x	x	x

3.2 Test Methods and Procedures

The University of New Brunswick Concrete Cylinder Test (UNBCCT) consists of casting concrete “job” mixtures into custom made concrete molds (145 mm diameter x 280 mm) as presented in Figure 1a and 1b. Figure 1a also demonstrates the process employed to cast gauge pins into the top and bottom of the specimens. The casting process begins by placing the bottom plate in the mold with a gauge pin screwed into its centre. Concrete is cast in three layers after which the top plate, also with an embedded screw, is secured to the top of the mold and agitated in order to ensure concrete completely consolidates around the embedded screw (see Figure 1c). Specimens are then covered in wet burlap and plastic for 24 hours at room temperature (22±2°C) after which they are demoulded. Following the removal of the top and bottom plates, the gauge pin is embedded in the concrete as presented in Figure 1d. At this point, initial length change measurements are completed using a standard length comparator. Specimens are then placed in a plastic 150 mm diameter x 300 mm standard laboratory mold where the annulus between the concrete and the mold is filled with a “model pore solution” which is determined based on the composition of the binder in the job mixture (see Figure 2a and 2b). The level of equivalent alkalis in the host solution was determined using the assumption the pore solution is 0.7 mol/L per 1% equivalent alkalis in the cement, as conducted by Diamond and Penko [11]. Three specimens from each mixture were then placed in ovens at both 38 and 60°C in order to study the effect of temperature on rate of expansion.

In order to determine the validity of the UNBCCT, concrete prisms (75 x 75 x 230 mm) were also cast and cured in accordance with ASTM C1293 from the same mix as those used to cast the UNBCCT. Unlike the standard, concrete prism test which requires NaOH to be added to the mixing water in order to boost the mixture to 1.25%, the alkalinity matched that of the UNBCCT mixture as presented in Table 2.



Figure 1: (a) Custom made mold with top and bottom plates holding embedded studs, (b) Concrete mold with bottom plate prior to casting, (c) Installing top plate with gauge pin, (d) embedded gauge pin following curing

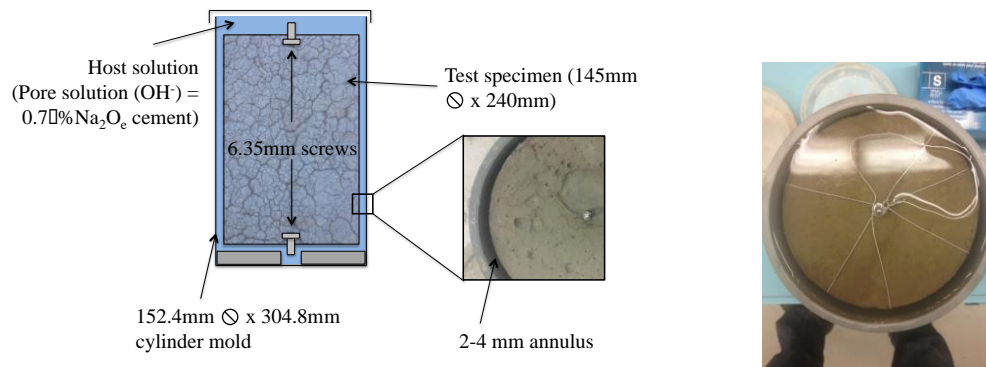


Figure 2: (a) Diagram of UNBCCT setup and, (b) Model pore solution surrounding specimen

4. RESULTS AND DISCUSSION

Figure 1 presents the expansion results of all non-SCM mixtures containing Jobe aggregate for both the new UNBCCT and the concrete prism test (ASTM C1293) stored at 38°C (100°F). The majority of these mixtures (0.41, 0.52, 0.95, 1.25% Na_2O_e) were selected as they have shown to fail in the field (University of Texas at Austin concrete exposure site), but in certain cases have passed the concrete prism test (ASTM C1293).

Following almost 950 days, the UNBCCT is shown to be effective in producing expansion in mixtures containing an alkali content in excess of 0.70% Na_2O_e compared to the CPT, which results in little if not any expansion at this level. The marked reduction observed in the concrete prism test (CPT) is of the many shortfalls of this test and the significant permissible

alkali leaching, which occurs during the duration of this test.

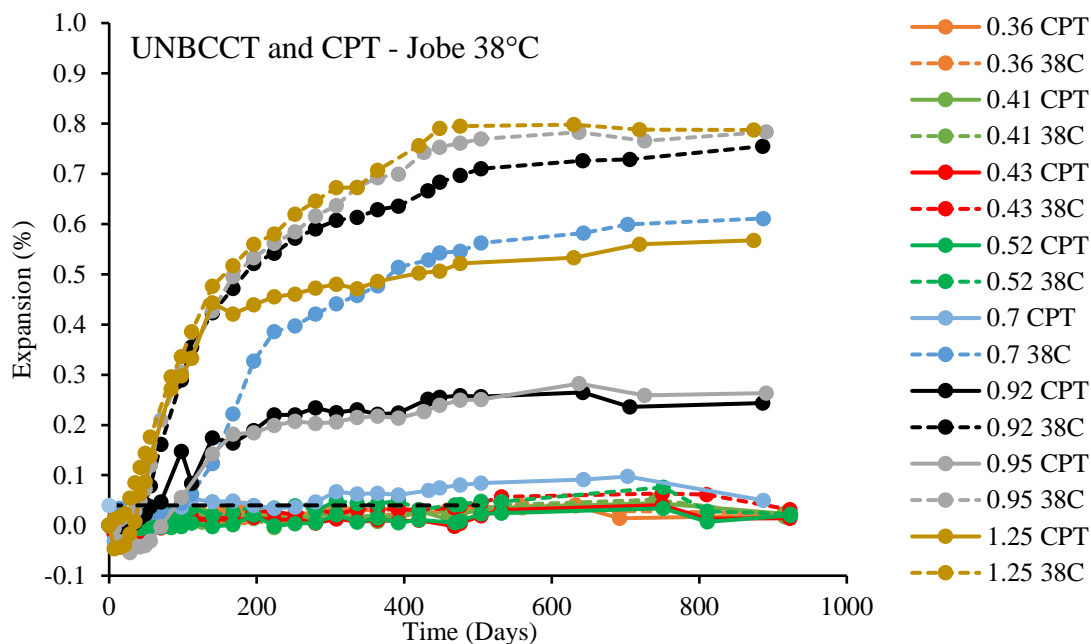


Figure 3: UNBCCT and ASTM C1293 expansion results using Jobe aggregate at 38°C.

Figure 4 presents the same mixtures in Figure 3, however, exposed to 60°C, where the rate of expansion is shown to be much faster. Specimens exposed to the elevated temperature are shown to reach final expansion in approximately half the time. The elevated temperature also results in the expansion of low-alkali binders that did not show any signs of expansion at 38°C. Expansion is found in specimens with as low as 0.41% Na_2O_e , which was also found to expand in the field after approximately 7 years.

It is interesting to note that a number of high alkali-content mixtures (i.e. 0.95 and 1.25% Na_2O_e) produced long-term expansions lower than 0.70 and 0.92% mixtures. Further research is needed to validate the test method and determine whether or not leaching occurs, however, it is anticipated that since the pore solution was mixed with only NaOH and not KOH as well, potassium could be leaching out of the specimens resulting in the underestimation of the true expansion.

5. FUTURE RESEARCH

Current work is underway in determining the validity of the test method by casting control specimens with non-reactive aggregate and measuring the transport of alkalis relative to time. It is also intended to explore the use of embedded strain gauges so that specimens can be monitored without periodic removal from containers. There is concern that partial carbonation and evaporation of the solution in the container may be occurring during this period and the cumulative impact of this over many measurements may reduce the OH concentration and, hence, the pH of the host solution. In certain cases, the addition of distilled water is needed to account the evaporation, which may also be diluting the host solution.

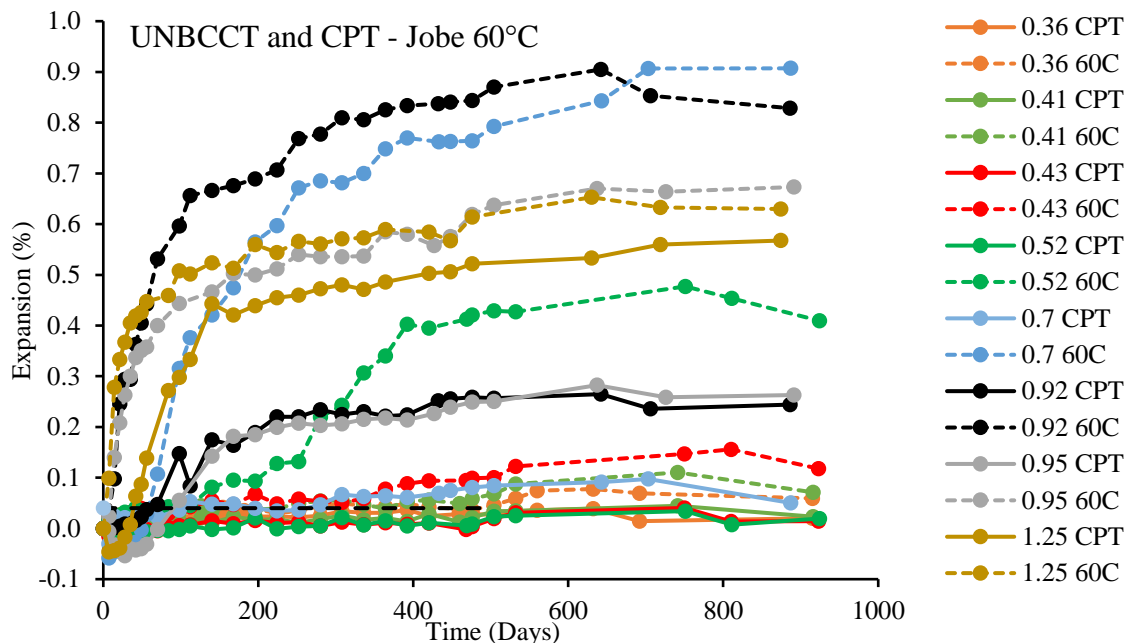


Figure 4: UNBCCT and ASTM C1293 expansion results using Jobe aggregate at 60°C.

6. CONCLUSIONS

Based on the results presented here, the following conclusions can be made:

- The UNBCCT is capable of evaluating the contribution of cement alkalis rather than requiring the addition of alkalis to the mixing water and was found to be more reliable than the CPT.
- Although, the UNBCCT was ineffective in mirroring long-term exposure data, the test successfully identified aggregates and alkali contents that failed in the field.
- Specimens exposed to higher exposure temperatures resulted in an accelerated rate of expansion and were capable of identifying expansion in low-alkali mixtures.
- Further research and validation is needed to ensure alkali leaching is eliminated while also accelerating the rate of expansion.

REFERENCES

- [1] T.E. Stanton, 'Expansion of concrete through reaction between cement and aggregate', Proceedings of the American Society of Civil Engineers, 1940, 66 (10)1781–1811.
- [2] Thomas, M. (2011). The effect of supplementary cementing materials on alkali-silica reaction: A review. Cement and Concrete Research. 41, pp. 1224-1231.
- [3] Thomas, M., Fournier, B., Folliard, K., Ideker, J and Shehata, M. (2006). Test methods for evaluating preventive measures for controlling expansion due to alkali-silica reaction in concrete. Cement and Concrete Research, 36, pp. 1842-1856.
- [4] Lingard, J., Andic-Cakir, P., Fernandes, I., Ronning, T.F., Thomas, M.D.A., 'Alkali-silica reactions (ASR): Literature review on parameters influencing laboratory performance testing', (Cement and

- Concrete Research, 2012) 42, 223-243.
- [5] Thomas, M.D.A., Fournier, B. and Folliard, K.J. 'Alkali-Aggregate Reactivity (AAR) Facts Book', (U.S. Department of Transportation – Federal Highway Administration), 2013.
 - [6] C.A. Rogers, P.E. Grattan-Bellew, R.D. Hooton, J. Ryell, M.D.A. Thomas, Alkali-aggregate reactions in Ontario, Canadian Journal of Civil Engineering 27 (2000) 246–260.
 - [7] D. Stark, Alkali–silica reactions in concrete, in: P. Klieger, J. Lamond (Eds.), Significance of Tests and Properties of Concrete and Concrete-Making Materials, ASTM STP 169C, American Society for Testing and Materials, Philadelphia, PA, 1994, pp. 365–371.
 - [8] R.F. Blanks, H.S. Meissner, The expansion test as a measure of alkali-aggregate reaction, Journal of the American Concrete Institute 17 (5) (1946) 517–539.
 - [9] B. Fournier, P.-C. Nkinamubanzi, R. Chevrier, Comparative field and laboratory investigations on the use of supplementary cementing materials to control alkali–silica reaction in concrete, in: Tang Mingshu, Deng Min (Eds.), Proc. 12th Int. Conf. Alkali-Aggregate Reaction in Concrete, vol. 1, Beijing, 2004, pp. 528–537.
 - [10] Lingard, J., Nixon, P.J., Borchers, I., Schouenborg, B., Wigum, B.J., Haugen, M. and Akesson, U., (Cement and Concrete Research, 2010), 40, 611-635.
 - [11] Diamond, S and Penko, M. (1992). Alkali Silica Reaction Processes: The Conversion of Cement Alkalis to Alkali Hydroxide. ACI Special Publication, 131, 153-168.

STRATEGIES FOR QUANTIFICATION OF ALKALI METAL RELEASE FROM AGGREGATES IN CONCRETE

Klaartje De Weerdt (1), Mette Geiker (1), Gilles Plusquellec (2), Jan Lindgård (3), Josee Duchesne (4), Benoit Fournier (4)

(1) Norwegian University of Science and Technology, NTNU, Norway

(2) RISE CBI, Sweden

(3) SINTEF, Norway

(4) Laval University, Canada

Abstract

Alkali silica reaction (ASR) is one of the major deterioration mechanisms for concrete. ASR takes place when the aggregates contain reactive silica, the concrete is exposed to moisture and sufficient alkali metals are available for the reaction.

The main source of alkali metals in concrete is the cement. However, recent studies have indicated that the aggregates can release alkali metals. Due to the high volume share of aggregates in concrete even a relatively small release of alkali metals from aggregate could affect the free alkali metal content in the concrete considerably.

Accelerated leaching methods are being developed to determine the potential release of alkali metals from aggregates. However, these methods might overestimate the actual released alkali metals in the concrete. There is a need to quantify the release of alkali metals from aggregates in concrete, and thereby verify the applicability of the proposed accelerated leaching methods.

This paper gives an overview of different strategies and their limitation to investigate the alkali metal release by aggregates in concrete.

Keywords: ASR, alkali metals

1. INTRODUCTION

Alkali silica reaction (ASR) is a deleterious reaction which leads to expansion and cracking of concrete structures. The reaction requires: 1. the presence of reactive siliceous aggregates, 2. high alkali metal concentration in the pore solution of the concrete, and 3. humid conditions.

The main source of free alkali metals in concrete has been considered to be cement. However, recent studies have indicated that the aggregates can potentially also release alkali metals over time [1]. Due to the high volume share of aggregates in concrete, even a relatively

small release of alkali metals from the aggregate could affect the free alkali metal content in the concrete considerably. This phenomenon can explain why ASR has been observed in concrete made with binders with low alkali content [1]. The fines and sand fraction potentially contribute with more alkali metals compared to the coarse aggregate fraction due to their larger exposed surface [2].

Accelerated leaching methods are being developed to determine the potential release of alkali metals from aggregates, for example the RILEM AAR-8 method [3] developed within the RILEM TC 258-AAA (2014-2019). However, such accelerated aggregate test methods might overestimate the alkali contribution from aggregates to the pore solution. Drolet, et al. [2] suggested for example an overestimation of about 30%. The implementation of such test methods in regulations could on one hand lead to unnecessary exclusion of certain aggregate types and on the other hand unrealistic requirements for the alkali metal content of the cement. Hence, there is a need to quantify the release of alkali metals from aggregates in concrete, and thereby verify the applicability of the proposed accelerated aggregate leaching methods.

This paper gives an overview of different strategies and their limitation to investigate the alkali metal release by aggregates in concrete.

2. ALKALI INVENTORY

To determine the alkali release from aggregates, one needs to have an overview over the different sources and sinks for alkali metals in concrete i.e. the alkali inventory. The alkali inventory sketched in Figure 1 illustrates the different factors influencing the free alkali metal content in the pore solution of ASR affected concrete.

Alkali inventory

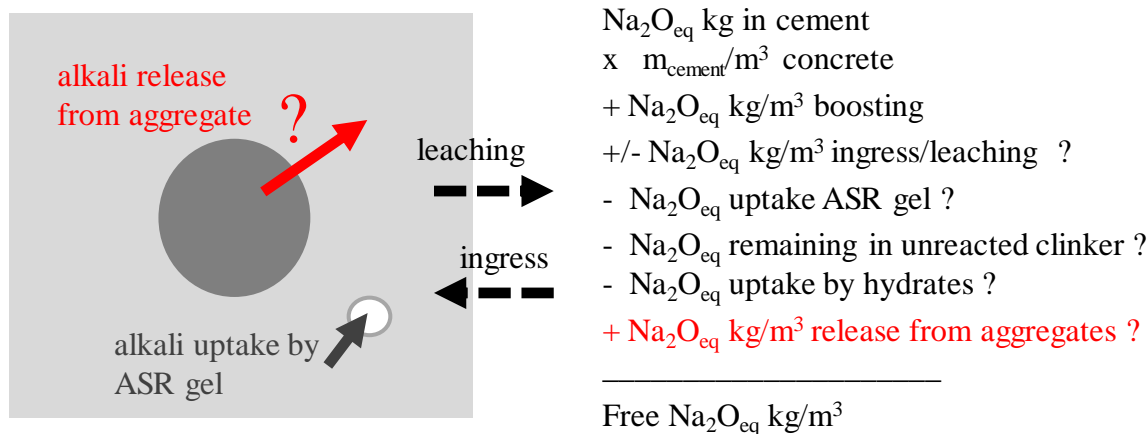


Figure 1: Sketch illustrating the alkali inventory in ASR affected concrete.

One of the major sources of alkali metals in concrete is the binder, meaning the **cement** and potential **supplementary cementitious materials**. Part of the alkalis in cement are present as easy soluble sulfate salts, such as K_2SO_4 or Na_2SO_4 [4]. They dissolve in the pore solution during the first minutes after the addition of water. The concentration of alkalis in the pore solution will then increase over time due to the decrease of the amount of free water (hydration

process) and due to the release of the remaining alkali in cement which are incorporated in the silicate and aluminate phases of the clinker [4].

In case of laboratory ASR performance testing additional NaOH can be added to the concrete to accelerate the expansion, but also to compensate for later modification of concrete composition or changes in alkali contribution from its constituents, or to account for alkali leaching during the exposure period. This is referred to as alkali **boosting**.

The environmental exposure conditions of the concrete also play a role: part of the alkali metals can leach out from the concrete when it is exposed to high humidity or water, while in other cases also ingress of alkali metals can occur for example due to exposure to de-icing salts. Alkali **leaching** can have a non-negligible impact on ASR, both on samples from performance testing and on real structures [1, 5].

A fraction of the dissolved alkali ions will in turn be sorbed on **hydration products** such as C-S-H (calcium silicate hydrate) [6]. The amount of sorbed species is dependent of the C-S-H structure, which varies according to the binder type (structural changes leading to different surface charges). For example, an OPC paste can fix approx. 0.06 mmol K/g C-S-H, while a paste with the same OPC but a 15% replacement by silica fume leads to a fixation of 0.42 mmol K/g C-S-H [7].

ASR-gel is, similarly to decalcified C-S-H, able to sorb considerable amounts of alkali metals [8].

The proportion of alkalis metals that are free in the pore solution is thus depending on numerous parameters, such as: the original alkali content of the cement, the presence of supplementary cementitious materials, the hydration degree, the water-to-binder ratio of the mix, the exposure conditions and the aggregate type used.

3. METHODS FOR DETERMINATION OF FREE ALKALI METALS

In order to determine the free alkali metals content in concrete, one needs to analyse the pore solution composition.

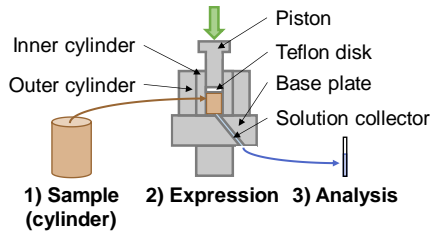
The most common method to determine the pore solution composition is **pore water expression (PWE)**. This method consists of compressing a sample under a high pressure (e.g. 200 MPa) in order to extract the pore solution (Figure 2). It has to be noted that the use of PWE to determine the alkali metal content of the concrete, expressed in for example [kg Na₂O_{eq}/m³ concrete], requires that the amount of free water of the concrete is known [9]. In some cases, it can be challenging to obtain sufficient pore solution for analysis due to the low pore solution content of the concrete caused by low w/b ratio, high aggregate-to-binder ratio or long term cured concrete.

The **cold water extraction method (CWE)** has been found to be a relatively easy and quick method to determine the free alkali content of laboratory and field samples. CWE consists of grinding a sample (paste, mortar or concrete) to a particle size below 80 µm, mixing the obtained powder with deionized water (liquid-to-solid ratio of 1) for 5 min in order to extract the free ions, filtrate the suspension and finally analyse the filtrate for Na and K (Figure 2). The ions that are bound on hydration products are not being released during the process [10]. Compared pore water expression, CWE is applicable on concretes with a low water content and allows to determine profiles as only a small amount of powdered material is required [11, 10].

It should be noted that there are several alternative versions of CWE such as Espresso method [12] and hot water extraction [13]. The use of pure water for extraction can cause

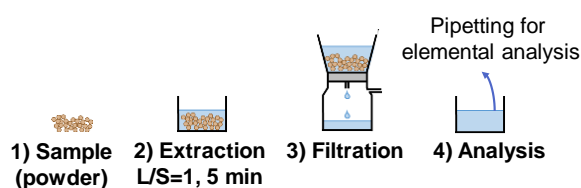
hydrates to decompose, alternatively one could use alkaline solutions and longer equilibration times [8].

PWE (Pore water expression)



- Not applicable on relatively dry samples or old concrete
- Need to know the free water content to convert to $[\text{Na}_2\text{O}_{\text{eq}} \text{ kg/m}^3]$

CWE (Cold water extraction)



- Dissolution of solids (mainly portlandite): can only be used for Na and K.
- Potential release of Na and K by the aggregates

Figure 2 : Sketch illustrating two methods to determine the free alkali metal content in concrete.

4. STRATEGIES FOR DETERMINATION OF ALKALI RELEASE FROM AGGREGATES

Determining alkali release from aggregates from a concrete core extracted from a field structure is not straightforward. Figure 3 and Figure 4 give a schematic overview of strategies to determine the alkali release of aggregates on concrete samples extracted from the field.

From Figure 3 it can be seen that the strategy depends on the method applied to determine the alkali metal content in the concrete.

If the alkali metal content is determined by cold water extraction (CWE), the results are expressed in $[\text{mmol/g}]$ which upon knowledge of the density of the concrete can be easily converted to $[\text{Na}_2\text{O}_{\text{eq}} \text{ kg/m}^3 \text{ concrete}]$. It has to be noted that during CWE of fine ground concrete, the fine ground aggregates might also release alkali metals. One could correct the CWE result of the concrete by subtracting the alkali metals determined by CWE on the aggregate only. However, if non-exposed aggregates are used, this might lead to an overcorrection as part of the alkali metals extracted from the aggregates might have been released already in the pore solution of the concrete.

If the alkali metal concentration (free $\text{Na}_2\text{O}_{\text{eq}}$) is determined by pore water extraction (PWE), the results will be expressed in $[\text{mmol/L}]$. In order to determine the free $\text{Na}_2\text{O}_{\text{eq}} \text{ kg/m}^3 \text{ concrete}$, one has to know the volume of the pore solution in the concrete $[\text{L/m}^3]$. This can be done by determining the mass loss upon drying until constant mass at e.g. 50 or 100 °C. However, this is only correct if the moisture content is homogeneous over the entire sample. It should be noted that a temperature of 100 °C induces a decomposition of C-S-H and ettringite, resulting in a slight overestimation of the volume of the pore solution.

If one has a reference concrete with a non-releasing and non-reactive aggregate (e.g. pure limestone), same mix design and with similar exposure, it is possible to check the potential alkali metal release by the aggregates by comparing the alkali metal concentrations in the pore

solution of both concretes independent of whether CWE or PWE is used. In the case one wants to quantify the release by aggregates (e.g. in $\text{Na}_2\text{O}_{\text{eq}}$ kg/m^3 concrete), the pore solution content in the concrete is needed if PWE is used.

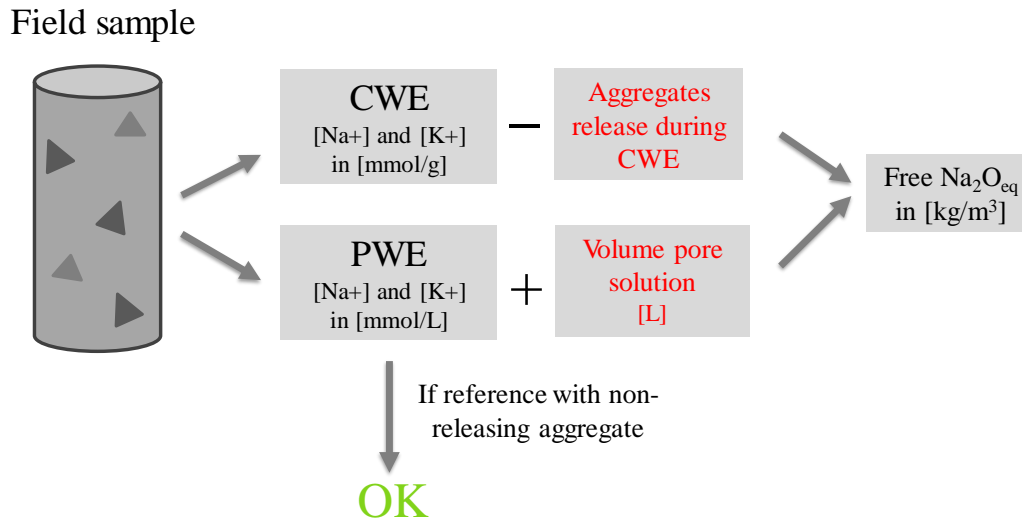


Figure 3 : Strategies for determination of alkali release from aggregates in concrete.

If the free alkali metal content of the concrete is obtained according to one of the strategies in Figure 3 but one does not have a reference concrete with non-releasing aggregates, the alkali release by the aggregates can be determined as shown in Figure 4. The idea is then to compare the free alkali metal content in the investigated sample with the one we would theoretically expect based on the concrete recipe and cement composition if there is no release, ingress, leaching or ASR.

However, only a part of the total alkali metal content of the concrete is free in the pore solution, as part of the alkali metals might still be found in unhydrated clinker phases and part might be sorbed by phases such as C-S-H. The free fraction of the total alkali metal content which is referred to as k_{free} . k_{free} is mainly dependent on the cement type and the resulting hydrates that are formed. The theoretical free $\text{Na}_2\text{O}_{\text{eq}}$ in the cement paste of the investigated concrete can thus be obtained by multiplying the total $\text{Na}_2\text{O}_{\text{eq}}$ in the cement paste with k_{free} .

The theoretical value of the free $\text{Na}_2\text{O}_{\text{eq}}$ (i.e. with no release, ingress, leaching or ASR) can be calculated, but it requires the knowledge of the cement content and the $\text{Na}_2\text{O}_{\text{eq}}$ of the cement used. This might be challenging for cores taken from field structures without documentation of the concrete.

If the investigated aggregate is reactive, the inventory will be complicated as the ASR gel will be able to take up alkali metals. Validation experiments will therefore preferably be performed on non-reactive releasers aggregates or one should at least try to take into account potential uptake by the ASR gel.

Similarly, the results can be blurred by potential ingress or leaching of alkali metals. Therefore, preferentially cores unaffected by leaching or ingress are used. In order to ensure that the part of the core investigated has not been influenced by alkali leaching one can determine alkali metal profiles with either CWE or μXRF [14].

The difference between the measured free $\text{Na}_2\text{O}_{\text{eq}}$ and the theoretical $\text{Na}_2\text{O}_{\text{eq}}$ content based on the concrete recipe enables us to verify the alkali metal release by aggregates in the pore solution.

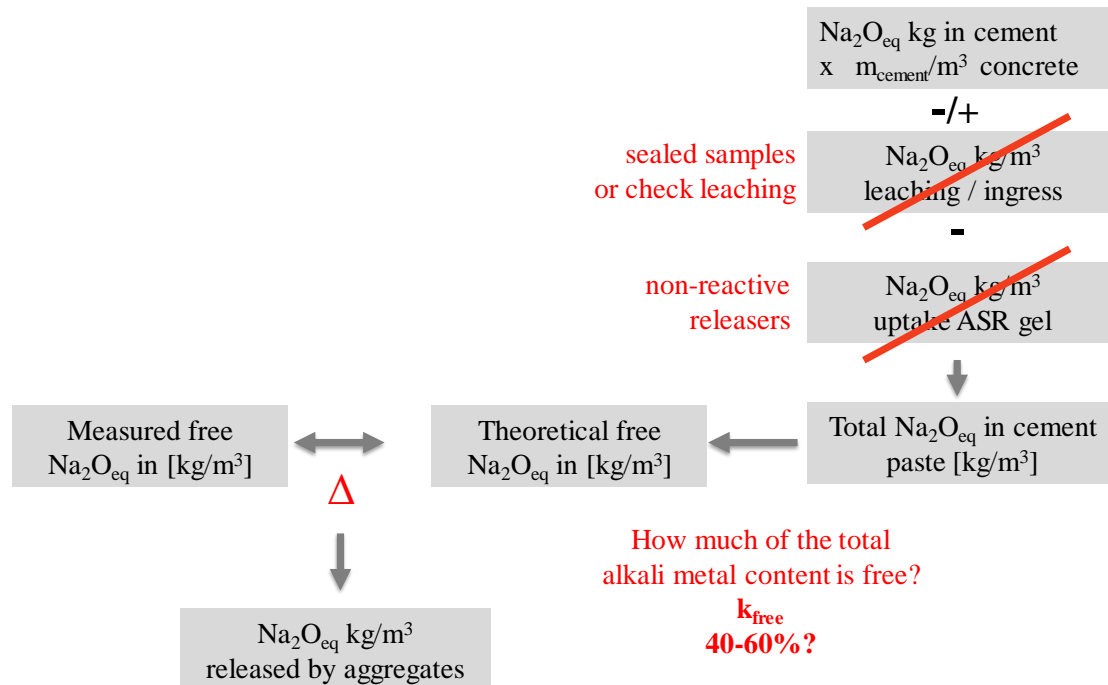


Figure 4 : Strategies for determination of alkali release from aggregates in concrete.

5. IMPORTANCE OF k_{free}

A brief literature review [15] showed that k_{free} can vary between 40-70% depending on, amongst other, the binder type, w/b ratio and exposure time. Plusquellec, et al. [9] measured the free alkali content of mortar samples after 28 days by using the cold water extraction method (CWE). One mortar was made from a pure OPC (CEM I) and the other one has a 30% replacement by fly ash (CEM II/B-V). The sand used is a non-releaser. For the CEM I, approx. 51% and 61% of the Na and K originating from the cement were present in the pore solution. For the CEM II/B-V mortar, approx. 44% and 39% of the Na and K content originating from the composite cement were found in the pore solution.

Drolet, et al. [2] measured the free alkali content of concrete samples made with a non-releasing aggregates (high purity limestone) and two cements, one with a high content and one with a low alkali content. The measurements were done using the hot water extraction method after one year. For the high alkali cement, 54% of the total Na_2O and 52% of the total K_2O of the cement were measured in the pore solution. For the low alkali cement, 59% of the total Na_2O and 46% of the total K_2O were measured in the pore solution.

The importance of knowing k_{free} for the determination of the alkali release from aggregates was demonstrated in a study of an ASR-affected dam [11]. The measured free alkali content in the bulk (area not affected by leaching) was compared with the theoretical value of the free alkali content as shown in Figure 4. k_{free} needs to be known in order to calculate this theoretical total alkali content. A variation of k_{free} from 50 to 70% resulted in a difference in the calculated alkali metal release from aggregates between 0.2 and 1.1 kg/m^3 $\text{Na}_2\text{O}_{\text{eq}}$. This is a large

difference if one considers that the alkali metal threshold in concrete containing potentially reactive aggregates in Norway is set to $2.5 \text{ kg/m}^3 \text{ Na}_2\text{O}_{\text{eq}}$ [16].

Hence, the determination of k_{free} is crucial for an accurate determination of the alkali metal release by aggregates. Accurate determination of k_{free} requires the determination of the free alkali metal content on a parallel reference concrete sample with a similar concrete composition as the investigated concrete except for the aggregates which should be non-reactive non-releasing aggregates (e.g. pure limestone). Preferably the reference sample is sealed to ensure that no leaching or ingress can occur.

6. RECOMMENDATIONS

Alkali metal release from aggregates is a slow process, hence there is a need for long-term investigations for verification. The recommended strategies described in Figure 3 were implemented by Drolet, et al. [2]. In this study the release from a series of ASR-reactive and/or releasing aggregates was investigated in mortar and concrete samples. The reference samples were prepared with non-releasing and non-reactive fine and coarse pure limestone aggregates. Even though the experiments were performed at elevated temperatures (38 and 60 °C) to accelerate the alkali metal release by the aggregates, the alkali release of the investigated aggregates was too low (except for an extreme releaser, phonolite) to be detected within the time frame of the investigation, i.e. 1 year. This study also indicated that the potential alkali release from the sand fraction is considerably larger than from the coarse aggregate fraction. Hence release verifications studies should focus on the sand fraction.

7. OUTLOOK

There is a need for large scale and long-term investigations to verify the potential contribution of aggregates to the free alkali metals in the pore solution of concrete. This paper presents potential strategies for verification of alkali metal release from aggregates.

Sealed reference samples containing non-reactive and non-releasing aggregates should be included in future large scale field and laboratory experiments on alkali metal release by aggregates. These samples will function as a reference for the free alkali metals originating from the cement, to which the samples containing aggregates to be investigated can be compared in order to determine potential alkali release. This is independent of the method applied for the determination of the free alkali metal content.

Pure limestone is suggested as reference sand and aggregate.

ACKNOWLEDGEMENTS

The authors acknowledge the financial support from the project 236661/O30 “Alkali–silica reaction in concrete – reliable concept for performance testing”, managed by SINTEF Building and Infrastructure and supported by the Norwegian Research Council and industrial partners: Norcem, NorStone, Norsk Stein, Hydro Energy, Axion, and the Norwegian Public Roads Administration.

REFERENCES

- [1] M.-A. Bérubé, J. Duchesne, J. F. Dorion and M. Rivest, Laboratory assessment of alkali contribution by aggregates to concrete and application to concrete structures affected by alkali–silica reactivity, *Cement and Concrete Research*, 32 (2002), pp. 1215-1227.

- [2] C. Drolet, J. Duchesne and B. Fournier, Validation of the alkali contribution by aggregates to the concrete pore solution, *Cement and Concrete Research*, 98 (2017), pp. 10-23.
- [3] RILEM Recommended Test Method AAR-8, Determination of Alkalies Releasable by Aggregates in Concrete. In preparation by RILEM TC 258-AAA, Draft 2018, in preparation.
- [4] I. Jawed and J. Skalný, Alkalies in cement: A review I. Forms of Alkalies and their effect on clinker formation, *Cement and Concrete Research*, 7 (1977), pp. 719-729.
- [5] J. Lindgård, M. D. A. Thomas, E. J. Sellevold, B. Pedersen, Ö. Andiç-Çakır, H. Justnes and T. F. Rønning, Alkali-silica reaction (ASR)—performance testing: Influence of specimen pre-treatment, exposure conditions and prism size on alkali leaching and prism expansion, *Cement and Concrete Research*, 53 (2013), pp. 68-90.
- [6] E. L'hôpital, B. Lothenbach, K. Scrivener and D. A. Kulik, Alkali uptake in calcium alumina silicate hydrate (C-A-S-H), *Cement and Concrete Research*, 85 (2016), pp. 122-136.
- [7] T. Chappex and K. Scrivener, Alkali fixation of C-S-H in blended cement pastes and its relation to alkali silica reaction, *Cement and Concrete Research*, 42 (2012), pp. 1049-1054.
- [8] M. Thomas, The role of calcium hydroxide in alkali recycling in concrete, *Materials Science of Concrete Special* (2001), pp. 225-236.
- [9] G. Plusquellec, M. R. Geiker, J. Lindgård, J. Duchesne, B. Fournier and K. De Weerd, Determination of the pH and the free alkali metal content in the pore solution of concrete: Review and experimental comparison, *Cement and Concrete Research*, 96 (2017), pp. 13-26.
- [10] K. De Weerd, G. Plusquellec, A. Belda Revert, M. R. Geiker and B. Lothenbach, effect of carbonation on the pore solution of mortar, Submitted to *Cement and Concrete Research* (2018).
- [11] G. Plusquellec, M. R. Geiker, J. Lindgård and K. De Weerd, Determining the free alkali metal content in concrete – Case study of an ASR-affected dam, *Cement and Concrete Research*, 105 (2018), pp. 111-125.
- [12] B. Fournier, L. Sanchez and S. Beauchemin, Outils d'investigation de la réactivité alcalis-granulats dans les infrastructures en béton, Rapport Final, Ministère des transports du Québec, Canada, 2015.
- [13] M.-A. Bérubé, J. Frenette, M. Rivest and D. Vézina, Measurement of the alkali content of concrete using hot-water extraction, *Cement, concrete and aggregates*, 24 (2002), pp. 28-36.
- [14] J. Lindgård, T. Østnor, B. Fournier, Ø. Lindgård, T. Danner, G. Plusquellec and K. De Weerd, Determining alkali leaching during accelerated ASR performance testing and in field exposed cubes using cold water extraction (CWE) and μ XRF, ICCRRR, Cape Town, 2018.
- [15] G. Plusquellec and K. De Weerd, Alkali metals in concrete, RILEM TC 258-AAA – Stockholm – 11 & 12 May 2017 (2017).
- [16] Norwegian Concrete Association, Durable concrete with alkali reactive aggregates, NB21, Oslo, 2017.

INFLUENCE OF THE MINERAL COMPOSITION OF CEMENT BINDER ON THE ACR REACTION IN CONCRETE

P. Štukovnik (1), V. Bokan Bosiljkov (1) and M. Marinšek (2)

(1) University of Ljubljana, Faculty of Civil and Geodetic Engineering, Slovenia

(2) University of Ljubljana, Faculty of Chemistry and Chemical Technology, Slovenia

Abstract

The paper presents a study about differences and similarities in alkali-carbonate reaction (ACR) process inside concrete prepared with the same carbonate aggregate and different cement binders. Used aggregate is typical Slovenian late diagenetic dolomite. The first cement binder is pure Portland cement (CEM I) and the second one is Blastfurnace cement (CEM III). The study of the ACR progress was carried out under accelerated conditions simulated by the 1 M aqueous NaOH solution at 60°C, up to 1 year. Analyses on the micro level were carried out using a petrographic microscope and scanning electron microscopy with X-ray microanalysis (SEM/EDS). On the macro level, measurements of specimens' length and mass changes as well as compressive and flexural tests were carried out parallel to the microscopic investigations.

The first results of the study show that the ACR process is slower in concrete with Blastfurnace cement. However, for both compositions the same products that are results of the ACR are formed. We can conclude that the replacement of the CEM I cement with the CEM III cement does not hinder the initialisation and progress of the ACR. It only shifts the formation of the reaction products to a later time.

Keywords: dolomite aggregate, Portland cement CEM I, Blastfurnace cement CEM III, alkali carbonate reaction

1 INTRODUCTION

In Slovenia, the main sources of crushed stone aggregates for the concrete production are limestone and dolomite rocks. Until recently, when alterations of concrete microstructure were detected and analysed for certain type of typical Triassic age late diagenetic dolomite (from the northern part of Slovenia) in wet concrete [1], both types of aggregates were considered as inert part of the concrete mixtures. On the macro level, these alterations resulted in increased compressive strength of concrete. Later studies that involved other sources of dolomite aggregates, from southern and south-eastern part of Slovenia, confirmed the first observations on the micro level and enabled further description of chemical reactions in concrete, as a consequence of the alkali carbonate reaction (ACR) [2]. However, for these dolomite aggregates substantial increase in the compressive strength of concrete was not observed, which

indicates that the strengthening process was parallel result of the ACR only for one type of dolomite aggregate studied so far.

Some authors [3, 4] consider the solubility rate of dolomite crystals in alkaline solutions to be low. On the other hand, results of a very recent study indicate that dolomite aggregates used in concrete are less stable at strongly alkaline conditions than previously though [5] and that dedolomitisation considerably increases the concrete's microporosity, which helps different ions (also those causing concrete deterioration) to infiltrate in the altered concrete.

In this work we focus on the progress of ACR in concrete prepared by silica free dolomite aggregate and two types of cement binder, pure Portland cement (CEM I) and Blastfurnace cement (CEM III), under accelerated conditions. Accelerated ageing took place in 1 M aqueous NaOH solution at 60°.

2 EXPERIMENTAL STUDY

2.1 Materials and methods

Tests were carried out on mortar mixtures that represent mortar level of concrete mixtures under consideration. Dolomite rock used as source of the crushed aggregate in this investigation was middle age Triassic dolomite (T₂₊₃) from south-eastern part of Slovenia. This type of dolomite is often of light to dark grey colour, with coarse grained crystals [6]. To prepare the mortars, aggregate fraction 0/4 mm was used. The water absorption of the aggregate is 0.2 %, and its density is 2810 kg/m³. The result of mineralogical quantitative X-ray analysis showed that dolomite represents 98.1% of the mineral content in the used aggregate, and calcite represents ~1.9 %.

As first binder, the Portland cement CEM I 52.5 R (EN 197-1) with the Blain specific surface area 4770 cm² g⁻¹ and density 3.11 g cm⁻³ was used. As second binder, the Blastfurnace cement CEM III/B 32.5N-LH/SR (EN 197-1) with density 2.92 g cm⁻³ and the Blain specific surface area 4680 cm² g⁻¹ was applied.

The chemical composition of both cements and GGBFS used for the CEM III production are given in Table 1.

Table 1: Chemical composition of cements and GGBFS

Oxide (%)	SiO ₂	CaO	MgO	Al ₂ O ₃	Fe ₂ O ₃	SO ₃	Na ₂ O	K ₂ O	Cl
CEM I	19.5	62.3	1.6	4.6	3.0	3.4	0.3	0.8	/
CEM III	30.3	44.8	6.1	9.0	1.6	2.4	0.3	0.6	/
GGBFS	31.91	36.34	7.32	11.04	0.57	2.41	/	/	0.22

The mortar samples (40 x 40 x 160 mm) were prepared according to the EN 196-1 standard, with the water-to-cement ratio 0.45. The mortar bars were cured for 28 days in an environment with a relative humidity above 90 % and temperature of 20 ± 1 °C. At the age of 28 days, they were exposed to accelerated ageing, simulated by 1 M aqueous solution of NaOH at 60 °C. After 1, 3 and 6 months, and 1 year of accelerated aging, the samples were submitted to microstructural characterisation. Parallel tests on macro level were carried out more frequently.

The denotation of samples consists of a letter and a number, e.g. C1 or C3, for the CEM I or CEM III, respectively.

2.1.1 Methods

Microstructure characterizations of the samples were first performed by optical microscopy (a polarizing optical microscope with transmitted light, Zeiss AxioImager Z1). The samples - thin sections (15-20 μm) - were prepared from the mortar bars in accordance with the descriptions in [7, 8]. Next, electron microscopy was carried out using FE-SEM Zeiss Ultra Plus microscope equipped with EDS Oxford X-Max SDD 50 mm² 106 detector and INCA 4.14 5 X-ray microanalysis software.

Flexural (3 parallel samples) and compressive (6 parallel samples) strength of the mortar bars was determined according to the EN 1015-11 standard, by using testing machine with a capacity of 100 kN and 500 kN, respectively.

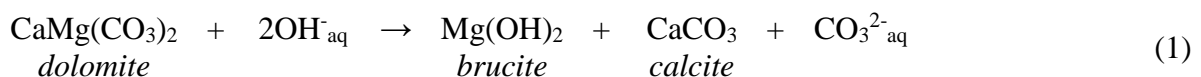
Change in weight of the bar specimens with time was measured using balance with a capacity of 4200 g and resolution of 0.01 g. Length change of mortar bars was measured by length comparator consisting of a high-grade dial micrometre with a measuring range of 0-12.5 mm and resolution of 0.001 mm. An Invar® reference bar (40x40x160 mm) was used for checking the measuring device, before and after each set of readings.

3 RESULTS AND DISCUSSION

3.1 Mineralogical observations

The optical and SEM microscopy was conducted on samples exposed to the accelerated ageing for 0, 1, 3 and 6 months, and 1 year. The progress of ACR is demonstrated in Figure 1. Two apparent features may be unambiguously observed in the aged samples: 1) areas of changed colour of cement paste at the vicinity of aggregate/paste boundary, and 2) areas of reaction rims in aggregates, as a result of dedolomitisation. In the optical micrographs the reaction rims are shown as alteration of the original grey colour of sparite crystals to brownish appearance of the secondary products. Changes in cement binder are shown as dark zones close to dedolomitised aggregate grains. Under the SEM, dedolomitisation is visible as characteristic myrmekitic texture [9].

The reaction of dedolomitisation requires humid environment and involves mobile ionic species. Therefore, it is best represented when written as an ionic equation (Eq. 1).



Progressing dedolomitisation reaction causes also the formation of secondary calcium carbonate, often also named carbonate halo or “Ca-halo”. The formation of the Ca-halo (Figure 1) follows Eq.2 and can be observed close to aggregate/cement phase boundary. During the dedolomitisation, some of the liberated CO_3^{2-} ions not consumed by the calcite formation inside the aggregate grains migrate toward the cement paste, where they meet portlandite and precipitate as Ca-halo.



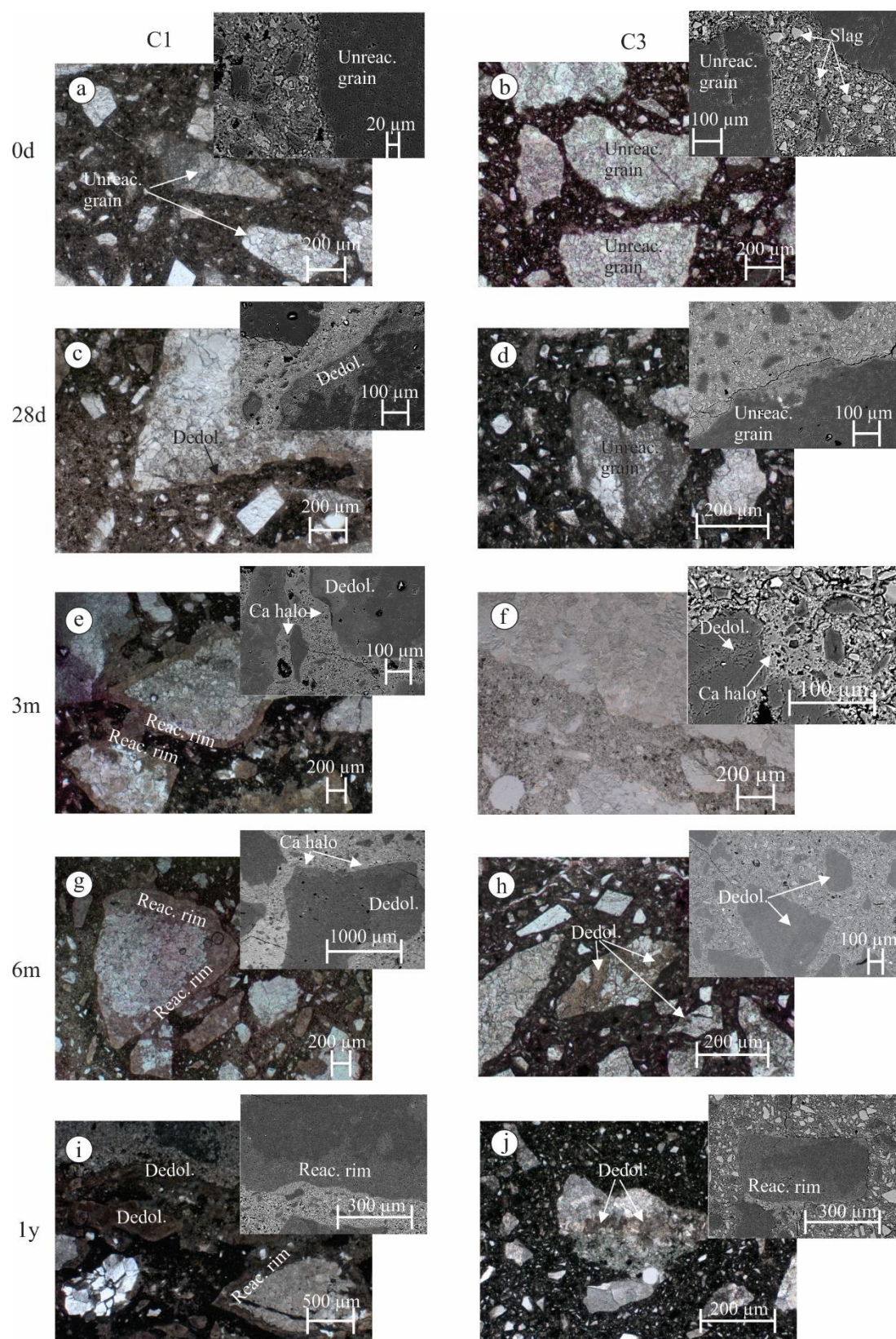


Figure 1: Progress of dedolomitisation and formation of Ca-halo with time.

Processes of dedolomitisation and formation of Ca-halo are progressive with time for both cements used in the study (Figure 1). However, microstructural alterations are faster for the C1 composition, where dedolomitisation was detected already after 28 days of the accelerated ageing, and reaction rims were visible after 3 months. In the C3 samples, on the other hand, dedolomitisation and Ca-halo were detected after 3 months (Figure 1f) and reaction rims are clearly visible only after 1 year (Figure 1j).

The ACR process results also in the formation of “new phases”. These phases are gradually replacing dolomite aggregate grain, from its edge towards its centre. The new phases are a consequence of precipitation of Al and Si ions from cement binder (Figure 2).

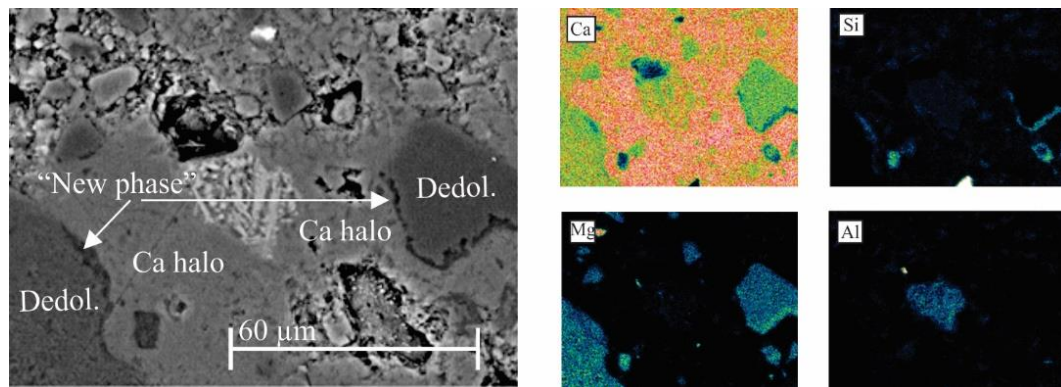
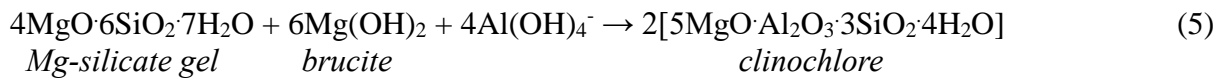
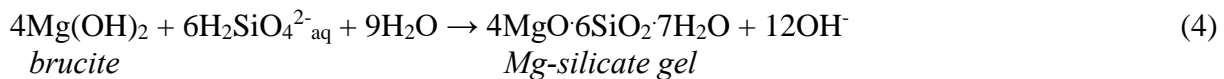
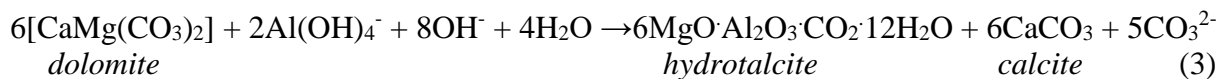


Figure 2: Formation of “Ca-halo” and “new phase” after 1 year in sample C1.

Formation of Al- and/or Si-involving phase may be chemically described with bellow equations (Eq. 3-5).



Chronologically, Mg-Al phase is observed after 3 months of accelerated ageing for sample C1, and Mg-Si phase after 1 year of its ageing (Figure 2). In sample C3, on the other hand, the formation of Al- or Si-involving phases has not yet been detected.

3.2 Physical properties

The mass end length changes of the mortar bars were measured up to 16 months of exposure to the accelerated ageing conditions, on 3 parallel samples for each cement type. Results in Figure 3a show that during the whole test period the mass of each specimen stayed in interval ± 2 g from its mean mass. For the C1 bars, the mass stayed approximately constant up to 16 months of measurements. For the C3 bars, however, slight but steady increase of mass with time could be observed. Changes in length of the mortar bars are given in Figure 3b. From

Figure 3b it is obvious that the ACR under consideration results in shrinkage of specimens. It seems that the shrinkage is lower for the C3 specimens until about 280 days of exposure, compared to that of the C1 specimens. After that the shrinkage intensity of the C3 specimens started to increase considerably, compared to the C1 specimens. However, also for the C1 specimens the shrinkage intensity increased after 6 months of exposure. The observed behaviour can result in the formation of microcracks in the concrete structure.

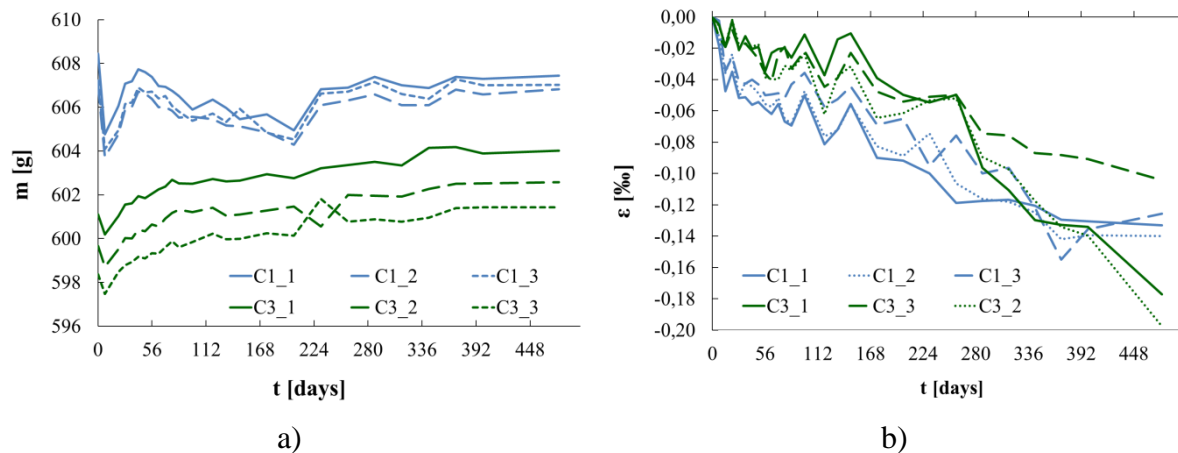


Figure 3: Results of mass (a) and change of length (b) measurements.

3.3 Mechanical properties

The compressive and flexural strengths of the mortar bars were measured up to about 11 months of their exposure to the accelerated ageing conditions. Figure 4 presents the compressive strength results, as mean value and standard deviation of 6 results (6 specimens) for each exposure time, for the C1 and C3 compositions.

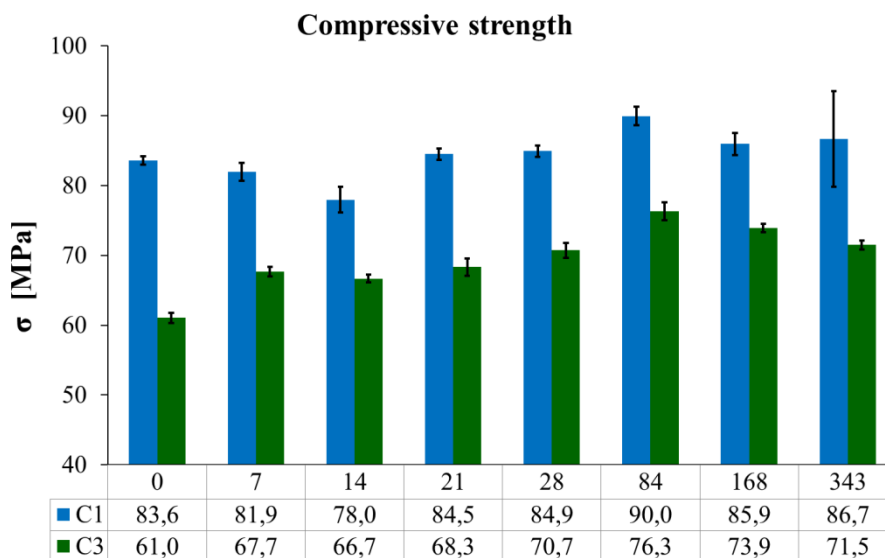


Figure 4: Compressive strength of samples C1 and C3.

As expected, the compressive strengths of the C3 specimens are considerably lower, compared to those of the C1 specimens, due to the type of cement used. The C1 specimen results show slight decrease of compressive strength for the first 14 days of exposure, which can be related to the initiation of the ACR. After that, the compressive strength starts to increase, up to 3 months of exposure. At this time, microscopic analyses revealed the formation of the “new phase” for the C1 specimens. Average compressive strength at about 6 and 11 months of exposure is again lower. However, there is still no clear sign of compressive strength reduction with time.

Figure 5 presents the flexural strength results, as mean value and standard deviation of 3 results (3 specimens) for each exposure time, for the C1 and C3 compositions. We can see that despite much lower compressive strength of the C3 specimens, compared to that of the C1 specimens, flexural strength of the C3 specimens is higher than at the C1 composition already after 14 days of exposure. The slag grains in the binder are responsible for higher flexural strength. Flexural strength is more sensitive to the formation of potential microcracks in the specimens than compressive strength. Thus, considerable reduction in the flexural strength of the C1 specimens at about 6 and 11 months of exposure can be related to the presence of shrinkage microcracks in the specimens. Much lower decrease in flexural strength for the C3 specimens after 28 days of exposure can be related to lower shrinkage measured for this composition and also to the continuous dissolution of the slag grains and consequent increase in flexural strength. These two opposite effects on the flexural strength could be responsible for the measured constant flexural strength of the C3 specimens at 84, 168 and 343 days of the exposure.

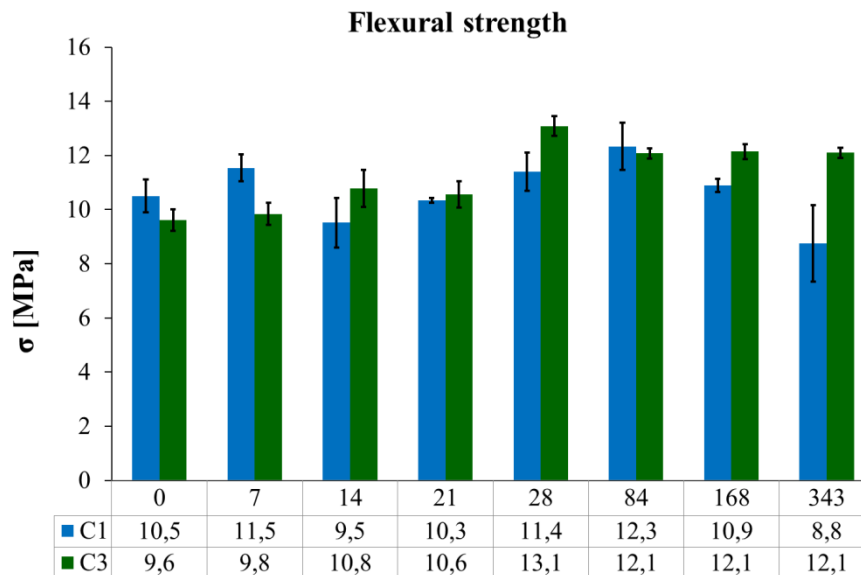


Figure 5: Flexural strength of samples C1 and C3.

4 CONCLUSIONS

The first results of the study show that the ACR process in concrete prepared with silica free dolomite aggregate is slower for the composition with the Blastfurnace cement. However, for

both compositions the same products that result from the ACR are formed. We can conclude that by replacing the CEM I cement with the CEM III one the initialisation and the progress of the ACR are not hindered. It only shifts the formation of the reaction products to a later time. This conclusion is supported by results of the length change measurements, which reveal continuous shrinkage of the specimens exposed to accelerated ageing. Shrinkage deformations are lower for the composition with the Blastfurnace cement until about 9 months of the exposure. Formation of shrinkage microcracks is plausible explanation for the flexural strength decrease of the C1 mortar. It means that also the type of the ACR under consideration can be responsible for cracking of concrete, such as the expansive type of the ACR. Therefore, the definition in [10] that allows to use the ACR denotation only for reactions in carbonate aggregate concrete accompanied by deleterious expansion should be rewritten.

ACKNOWLEDGEMENTS

This work was financially supported by the Slovenian Research Agency, through Programme Groups P1-0175 and P2-0185, and Research Project J2-9196.

REFERENCE

- [1] Prinčič, T., Štukovnik, P., Pejovnik, S., De Schutter, G., Bokan Bosiljkov, V. 'Observations on dedolomitization of carbonate concrete aggregates, implications for ACR and expansion', *Cem.Concr.Res.*, 54, 0: (2013) 151-160.
- [2] Štukovnik, P., Bokan Bosiljkov, V., Marinšek, M. 'Microstructural changes in cement mortar due to alkali-carbonate reaction', *Mater.Techn.* (2018) (to be published).
- [3] Appelo, C.A.J., Postma, D. 'Geochemistry, Groundwater and Pollution', 2nd Edn (A.A.Balkema Publisher, Amsterdam, 2007).
- [4] Pokrovsky, O.S., Schott, J. 'Kinetics and mechanism of dolomite dissolution in neutral to alkaline solutions revised', *Am. J. Sci.* 301 (2001) 597-626.
- [5] Mittermayr, F. et al. 'Environmental controls and reaction pathways of coupled de-dolomitization and thaumasite formation', *Cem.Concr.Res.*, 95 (2017) 282-293.
- [6] Plenicar, M. et al. 'Geological map of SFRJ. L33-79, Novo mesto [map]. 1:100.000' (Zvezni geoloski zavod, Beograd, 1975).
- [7] Poole A.B., Sims, I. *Concrete Petrography: 'A Handbook of Investigative Techniques'*, 2nd Edn (CRC Press, 2015)
- [8] Ingham, J. 'Geomaterials Under the Microscope', (London, Mason Publishing, 2011)
- [9] Katayama, T., Jensen, V., Rogers, C.A. 'The enigma of the "so-called" alkali-carbonate reaction'. *Constr. Mater.*, 169(CM4): (2016) 223-232.
- [10] Godart, B., de Rooij, M., Wood, J.G.M. (ed.) 'Guide to diagnosis and appraisal of AAR damage to concrete in structures. Part 1 Diagnosis (AAR 6.1)', RILEM STAR (2013).

ALCALI SILICA REACTION IN ALKALI-ACTIVATED CONCRETES: THE TEMPERING EFFECT OF FLY ASH IN SLAG/FLY ASH SYSTEMS

Alexandre Rodrigue (1), Josée Duchesne (1), Benoit Fournier (1), Benoit Bissonnette (2)

(1) Department of geology and geological engineering, Université Laval, Canada

(2) Department of civil engineering, Université Laval, Canada

Abstract

Alkali-silica reaction in concrete can result in severe cracking and lead to loss in serviceability of the affected infrastructures. To occur, the reaction needs alkali ions in the pore solution, reactive silica in the aggregates and high relative humidity. Alkali-activated systems require high pH activators to dissolve the aluminosilicates used as binders and could represent an aggravating factor to ASR. Dimensional changes of prismatic concrete specimens were monitored over time for a range of alkali-activated concrete mixtures prepared with slag, fly ash and slag/fly ash binders. Extremely reactive, highly reactive and non-reactive aggregates were used. Different fly ash contents (20, 30 and 40%) were investigated in slag/fly ash concretes prepared with the same aggregates and with a moderately reactive aggregate. With slag as unique binder, concrete prism expansions of 0.12% and 0.15% were recorded after two years for extremely and highly reactive aggregates, respectively. With fly ash as unique binder, expansions of -0.01% and 0.02% respectively were obtained after 2 years. For slag/fly ash mixtures, increasing the fly ash replacement level results in decreasing expansions for all tested aggregates. After one year of testing, only specimens from the mixtures with 20% fly ash and extremely reactive aggregates exceeded the 0.040% limit.

Keywords: alkali-activated concretes, slag, fly ash, ASR, alkali-silica reaction

1. INTRODUCTION

Alkali-silica reaction (ASR) is well known in portland cement-based concretes and mortars. The ASR-induced damage will develop when three conditions are met: sufficient humidity (80% and more), high alkalinity level in the concrete pore solution and the presence of reactive silica phases within the aggregate particles [1]. The reaction produces a silico-calco-alkaline gel which absorbs water and expands [2]. The internal pressures thus generated result in expansion and microcracking when the tensile strength of the paste is exceeded. Calcium plays

an important role as it allows the recycling of the alkalis to the pore solution by substitution in the expansive gel [3]–[5]. Ca^{2+} ions play an active role in the formation of reaction rims around the reactive minerals. These rims would allow the penetration of alkali hydroxide from the pore solution into the affected aggregate but would prevent alkali silicate gel to exit the particles, thus increasing pressure in the particle and, ultimately, cracking of the rim and of the surrounding paste [6].

Alkali-activated concretes need a high alkaline solution to dissolve the aluminosilicate precursor, thus allowing the formation and hardening of the paste. Therefore, the effect of such high alkaline solution on aggregates that contain reactive siliceous phases must be investigated. Many authors conclude that mortars and concretes using fly ash as single precursor show expansion levels that are inferior to what is observed for mortars and concretes using a type I low alkali portland cement [7-8]. Williamson and Juenger showed that activation solutions with higher alkali concentrations result in higher alkali concentrations in the pore solutions of alkali-activated fly ash systems [9]. Fernandez-Jimenez and al. suggested that the type of activator can also have a strong influence on ASR; for instance, the use of sodium silicate in combination with 12.5M sodium hydroxide ($\text{SiO}_2/\text{Na}_2\text{O}=0.16$) resulted in expansion levels in mortars which were higher than that of OPC mortars [8]. Diverging behaviors were observed in slag-based alkali-activated mortars and concretes. Puertas and al. [11] indeed observed expansion levels 4 times lower for alkali-activated slag mortars made with sodium silicate alone when compared to OPC mortars. Inversely, after 50 days and 22 months of testing, Bakharev and al. [12] obtained higher expansions for slag concretes activated with a sodium hydroxide/sodium silicate solution ($\text{SiO}_2/\text{Na}_2\text{O}=0.75$) than for OPC concretes (0.03 and 0.1% respectively).

The main objective of this research was to evaluate the behavior of alkali-activated materials in presence of alkali-silica reactive aggregates. The alkali-activated concretes used in this study were cement-free systems based on slag, fly ash and a slag/fly ash combination.

2. EXPERIMENTAL PROGRAM

2.1 Materials and concrete mixture proportionings

Table 1. Blast furnace slag and class F fly ash precursors in major oxides %

Oxides, wt. %	SiO_2	Al_2O_3	CaO	MgO	Fe_2O_3	Na_2O	K_2O	TiO_2	LOI
Slag Gr. 80	37.74	10.75	36.20	12.62	0.50	0.41	0.49	0.91	-0.8
Class F Fly Ash	56.72	24.07	9.29	1.05	3.14	2.50	0.64	0.65	1.2

The Blaine fineness for the blast furnace slag and class F fly ash are of 479 and 334 m^2/kg , respectively. Table 2 shows the main properties of the aggregates including their bulk density and absorption. Concrete mixtures were manufactured in two separate phases. All phase I mixtures used single fly ash or slag precursors at a 400 kg/m^3 dosage, as well as a constant aggregate proportioning; in phase II concrete mixtures also used a precursor content of 400 kg/m^3 (20, 30 & 40% fly ash combined with 80, 70 and 60% slag, respectively) but the aggregate proportioning was adjusted to an equivalent volume (Table 3). The alkaline activator was a mixture of a sodium silicate solution (28.7% SiO_2 , 9% Na_2O , 62.3% H_2O) combined with

an 8M sodium hydroxide solution at a sodium silicate to sodium hydroxide ratio (Ss/NaOH) of 0.5 for the slag and slag/fly ash concretes. The fly ash concretes were activated with an 8M sodium hydroxide solution. A fixed activator to binder ratio of 0.35 was used.

Table 2. Physical Properties and Characteristics of the Coarse Aggregates

Aggregates	Bulk density, kg/m ³	Absorption, %	Type	Lithologies	ASR reactivity level
High purity limestone (HP)	2716	0.19	Crushed aggregate	Limestone	Non-reactive
Spratt (Sp)	2675	0.43	Crushed aggregate	Siliceous limestone with traces of chert	high
New Mexico (NM)	2534	1.52	Natural gravel	Andesite, quartzite, granite, granitic gneiss and rhyolite	Extreme
Sudbury (Su)	2687	0.50	Natural gravel	Siltstone, granite, claystone, greywacke, quartzite sandstone	moderate

Table 3. Coarse aggregate proportions

Aggregates	Aggregate Proportions, kg/m ³ (phase I/phase II)			
	14-20 mm	10-14 mm	5-10 mm	Total
High purity limestone (HP)	416/425	312/319	312/319	1040/1063
Spratt (Sp)	416/419	312/314	312/314	1040/1047
New Mexico (NM)	416/397	312/298	312/298	1040/992
Sudbury (Su)	-/421	-/316	-/316	-/1052

2.2 Curing and making of test specimens

Three concrete prisms, 75 x 75 x 300 mm in size, were made from each concrete mixture. After casting, the fly ash-based concrete specimens were heat cured while being kept in their molds for 24 hours at 80°C in sealed containers at a relative humidity of 100%. All the other concrete specimens were cured at 23°C and 100% relative humidity before demolding.

2.3 Expansion testing of Concrete

The expansion was evaluated in accordance with the CSA A23.2-28A Standard Practice with some adjustments. The precursor contents were kept at 400 kg/m³, instead of 420 kg/m³ as required in the Standard Practice; also, no additional alkalis were added to the concrete mixtures due to the already strong alkalinity of the activators. After their initial curing, reference length measurements were made on the test prisms in the laboratory at 23°C. All specimens were then

stored in hermetic plastic containers at 38°C and 100% RH, while expansion readings were made at selected ages over one to two-year periods. Prior to length change measurements, the plastic containers were removed from the high-temperature room and stored for 16 ± 4 hours at 23°C. An expansion greater than 0.040% at years indicates “reactive” system.

3. RESULTS

3.1 Expansion of slag-based concretes – Phase I

Figure 1 shows a plot of the expansion as a function of time for slag concretes incorporating NM, Sp and HP aggregates. Test prisms made with NM and Sp aggregates exceeded the 0.040% expansion limit before reaching the 20th week of testing, with two-year expansions of 0.116% and 0.151%, respectively. Figure 2 shows the aspect of the NM and Sp prisms at the completion of testing. In both cases, cracking and exudation products are visible on the surface of the specimens.

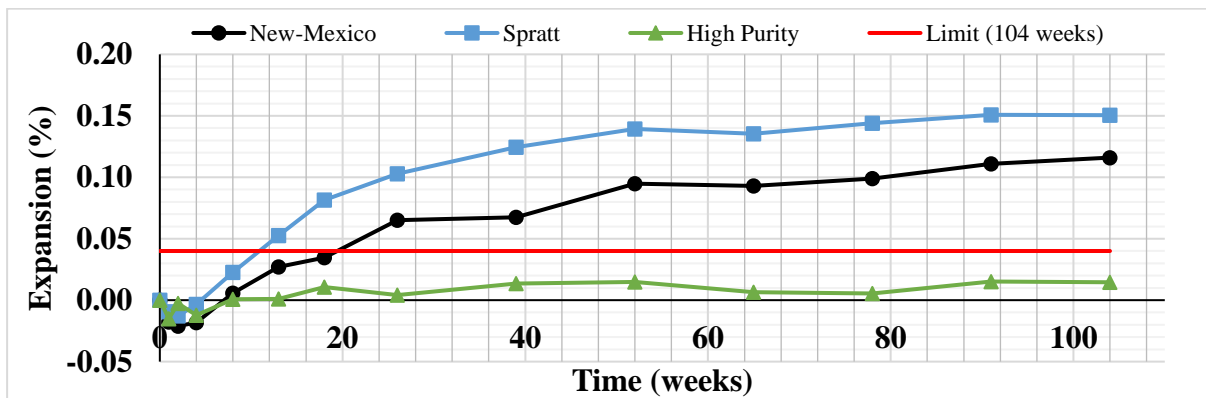


Figure 1. Expansion (ASR) of Alkali-Activated Slag Concrete Mixtures with Reactive (NM and Sp) and Non-reactive (HP) Aggregates

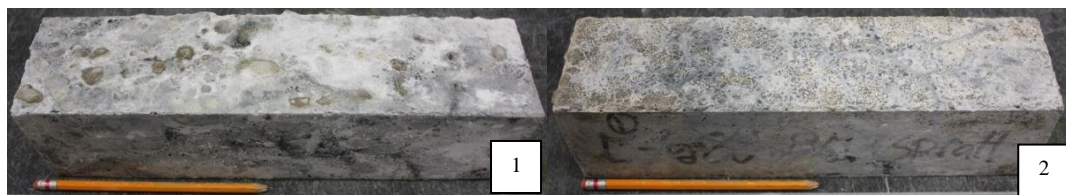


Figure 2. Visual Aspect of Slag-Based Concrete Prisms after 2 Years of Expansion Testing with NM Aggregates (1) and Sp Aggregates (2)

3.3 Expansion of fly ash-based concretes – Phase I

Figure 3 shows the expansion trends for fly ash concretes using NM, Sp and HP aggregates. In all cases, no deleterious expansion was observed, with two-year expansions $<0.015\%$. No cracking or exudation products were observed on the specimens.

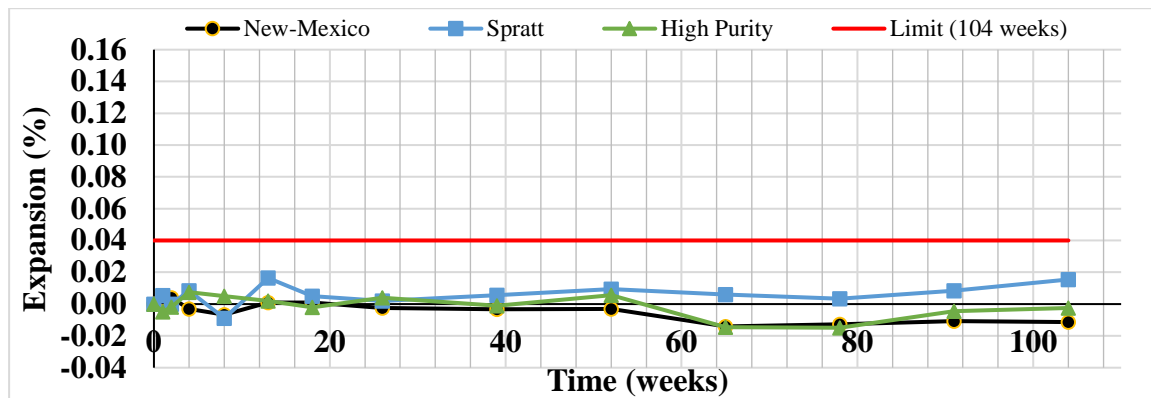


Figure 3. Expansion (ASR) of Alkali-Activated Fly Ash Concrete Mixtures with Reactive (NM and Sp) and Non-reactive (HP) Aggregates

3.3 Expansion of combined slag and fly ash-based concretes – Phase II

Figure 4 shows the expansion curves of all slag/fly ash concretes tested with NM, Sp, Su and HP aggregates throughout the first year of testing (completed to date). In all cases, it can be noticed that increasing the fly ash content resulted in decreasing expansions at any given time and for all the tested aggregates. The concrete specimens made with the NM aggregate and 20% and 30% fly ash are the only systems that reached the 0.040% expansion level before or at one year of testing. Slag/fly ash-based concretes tested with Sp aggregates showed a maximum expansion of 0.024% (20% fly ash) at one year. The maximum one-year expansion for Su-bearing slag/fly ash concretes was -0.004%.

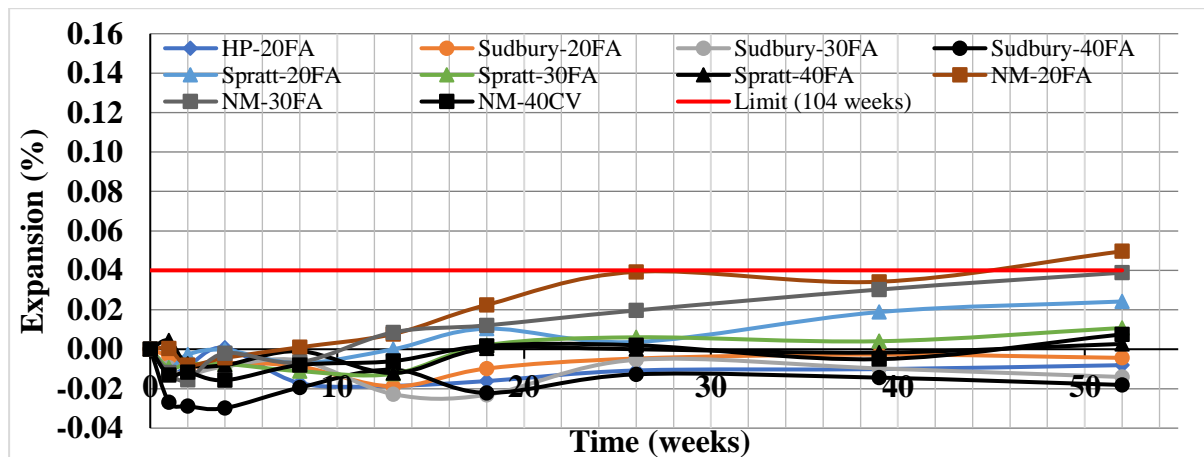


Figure 4. Expansion (ASR) after One Year of Alkali-Activated Slag/Fly Ash Concrete Mixtures with 20, 30 and 40% Fly Ash Contents and NM, Sp, Su and HP aggregates

Figure 5 shows the typical aspect of the slag/fly ash concrete specimens after one year of testing. In the case of the NM-bearing concretes, the 20% fly ash specimens show localized exudation while those with 30 and 40% fly ash show traces of exudation products but no visible surface cracking. The Sp specimens with 20% fly ash show surface exudation but low cracking, while those with 30 and 40% fly ash show no exudation or cracking. Slag/fly ash-based concrete specimens using the Su and HP aggregates show no exudation or cracking.

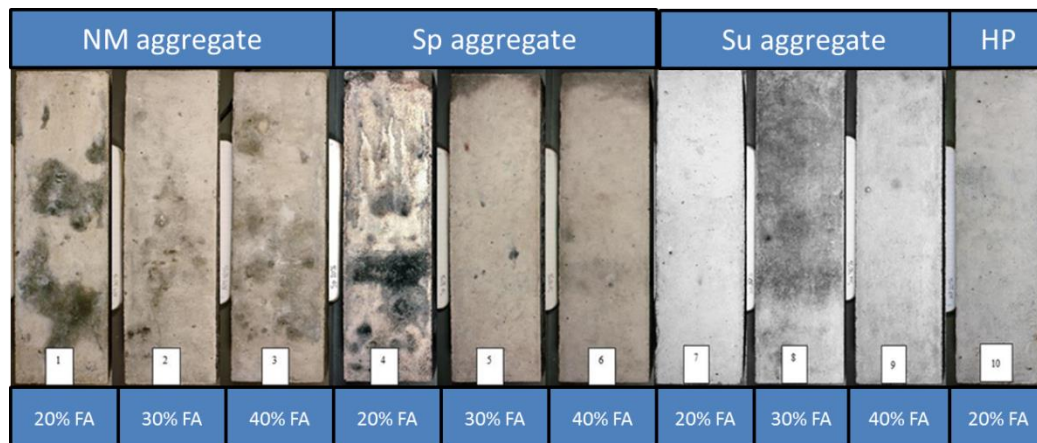


Figure 5. Visual aspect of slag/fly ash concrete prisms after 1 year of testing

4. DISCUSSION

The results obtained in this study showed that the use of fly ash in alkali-activated concretes was effective in reducing or even eliminating expansion when reactive aggregates are used. With fly ash as a single precursor, no expansion was observed for specimens that incorporated highly reactive aggregates (NM and Sp) after 2 years of testing. On the other hand, with slag as a single precursor, high expansion occurred with the same highly-reactive aggregates. The higher calcium content in slag can potentially explain these significant differences where it could participate in alkali recycling as previously observed in OPC concretes facing ASR [5]. However, these systems are already highly alkaline and concerns arise in regards of the importance of this phenomenon to reduce significantly the alkalinity of the pore solution. Fly ash alone or combined with slag in alkali-activated systems will form C-A-S-H and N-A-S-H gels incorporating sodium in replacement of calcium thus making sodium less available for gel formation [13]–[16]. By retrieving the alkalis and binding them into the N-A-S-H gels, fewer alkalis should be available to participate in ASR and since calcium must be completely consumed before alkali intake, alkali recycling could be potentially reduced significantly.

Water availability also seems to represent an important factor to ASR in these systems. Hybrid N-C-A-S-H gels show more tightly bound water and higher degrees of crosslinking resulting in smaller pores capable of holding water [15]. Water supply being essential to ASR, paste permeability is thus also a factor to consider with these systems. These alkali-activated systems show early-age microcracking which increase absorption and volume of permeable voids [17] and thus, increasing the overall paste permeability to water. Increasing fly ash contents have shown to decrease overall microcracking therefore cutting out additional external water supply for ASR gels. The slower reaction rates at ambient temperature for paste formation when fly ash is used could explain the lower observed cracking whereas the lower stiffness of the matrix at early-ages could accommodate the volume variations that are inherent to paste formation.

5. CONCLUSION

The main conclusions from this research are as follows:

- Alkali-activated slag concretes with highly to extremely-reactive aggregates (Sp and NM) show expansions that exceed the 0.040% limit before 20 weeks of standard testing. These concretes show abundant surface cracking and exhibit exudation products.
- Alkali-activated fly ash concretes with highly to extremely-reactive aggregates (Sp and NM) show expansions below the 0.040% limit after two years of standard testing.
- Increasing the fly ash content in alkali-activated slag/fly ash concretes from 20 to 30 and 40% results in decreasing expansions for all the tested aggregates (NM, Sp and Su).

ACKNOWLEDGEMENTS

The authors would like to thank the National Science and Engineering Research Council of Canada (NSERC) and the *Fonds de Recherche du Québec – Nature et Technologies* (FRQ-NT) for their financial support.

REFERENCES

- [1] M.D.A. Thomas, B. Fournier, & K.J. Folliard, Alkali-Aggregate reactivity (AAR) facts book. Report No. FHWA-HIF-13-019, U.S. Department of Transportation, Federal Highway Administration. 211 pp. 2013.
- [2] M.-A. Bérubé and B. Fournier, "Les produits de la réaction alcalis-silice dans le béton; étude de cas de la région de Québec." *The Canadian Mineralogist* **24**(2): 271-288, 1986.
- [3] E. Grimal, "Caractérisation des effets du gonflement provoqué par la réaction alcali-silice sur le comportement mécanique d'une structure en béton," PhD thesis, Université Paul Sabatier, Toulouse, France, 2007.
- [4] A. Sellier, E. Bourdarot, S. Multon, M. Cyr, and E. Grimal, "Combination of structural monitoring and laboratory tests for the assessment of AAR-swelling: application to a gate structure dam," *ACI Mater. J.*, vol. 106, no. 106, pp. 281–290, 2009.
- [5] F. Rajabipour, E. Giannini, C. Dunant, J. H. Ideker, and M. D. A. Thomas, "Alkali-silica reaction: Current understanding of the reaction mechanisms and the knowledge gaps," *Cem. Concr. Res.*, vol. 76, pp. 130–146, 2015.
- [6] T. Ichikawa, "Alkali-silica reaction, pessimum effects and pozzolanic effect," *Cem. Concr. Res.*, vol. 39, no. 8, pp. 716–726, 2009.
- [7] I. García-Lodeiro, a. Palomo, and a. Fernández-Jiménez, "Alkali-aggregate reaction in activated fly ash systems," *Cem. Concr. Res.*, vol. 37, no. 2, pp. 175–183, Feb. 2007.
- [8] a. Fernandez-Jimenez, I. García-Lodeiro, and a. Palomo, "Durability of alkali-activated fly ash cementitious materials," *J. Mater. Sci.*, vol. 42, no. 9, pp. 3055–3065, Dec. 2007.
- [9] T. Williamson and M. C. G. Juenger, "The role of activating solution concentration on alkali-silica reaction in alkali-activated fly ash concrete," *Cem. Concr. Res.*, vol. 83, pp. 124–130, 2016.
- [10] K. Kupwade-Patil and E. Allouche, "Impact of alkali silica reaction on fly ash-based geopolymer concrete," *J. Mater. Civ. ...*, no. January, pp. 131–139, 2012.
- [11] F. Puertas, M. Palacios, a. Gil-Maroto, and T. Vázquez, "Alkali-aggregate behaviour of alkali-activated slag mortars: Effect of aggregate type," *Cem. Concr. Compos.*, vol. 31, no. 5, pp. 277–284, May 2009.
- [12] T. Bakharev, J. G. Sanjayan, and Y. B. Cheng, "Resistance of alkali-activated slag concrete to alkali-aggregate reaction," *Cem. Concr. Res.*, vol. 31, pp. 331–334, 2001.
- [13] C. Shi, a. F. Jiménez, and A. Palomo, "New cements for the 21st century: The pursuit of an alternative to Portland cement," *Cem. Concr. Res.*, vol. 41, no. 7, pp. 750–763, Jul. 2011.

- [14] I. Garcia-Lodeiro, a. Palomo, a. Fernández-Jiménez, and D. E. MacPhee, “Compatibility studies between N-A-S-H and C-A-S-H gels. Study in the ternary diagram Na₂O-CaO-Al₂O₃-SiO₂-H₂O,” *Cem. Concr. Res.*, vol. 41, no. 9, pp. 923–931, Sep. 2011.
- [15] I. Ismail, S. a. Bernal, J. L. Provis, R. San Nicolas, S. Hamdan, and J. S. J. van Deventer, “Modification of phase evolution in alkali-activated blast furnace slag by the incorporation of fly ash,” *Cem. Concr. Compos.*, vol. 45, pp. 125–135, 2014.
- [16] H. Ye and A. Radlińska, “Fly ash-slag interaction during alkaline activation: Influence of activators on phase assemblage and microstructure formation,” *Constr. Build. Mater.*, vol. 122, pp. 594–606, 2016.
- [17] A. Rodrigue, J. Duchesne, B. Fournier, and B. Bissonnette, “Influence of added water and fly ash content on the characteristics, properties and early-age cracking sensitivity of alkali-activated slag/fly ash concrete cured at ambient temperature,” *Constr. Build. Mater.*, vol. 171, 2018.

AAR IN CONCRETE: RUSSIAN EXPERIENCE

Vyacheslav R. Falikman (1), Nikolay K. Rozental (2) and Alexander N. Rozental (2)

(1) International Academy of Engineering, Russia

(2) Scientific Research Center “Construction”, Russia

Abstract

Statistics give the output of aggregates in Russia as 508.9 million m³ including 223.9 million m³ of gravel and crushed rock aggregate and 244.2 million m³ of sand. The total explored reserve of stone is estimated for the European region of the Federation to be 15.7 billion m³. In Russia, requirements for aggregates test methods are regulated by several standards. All the Russian standards are of a prescriptive nature. If the soluble silica quantity exceeds the specified, then the accelerated method is used with fine grained concrete specimens to give a deformation (expansion) measurement. Many of the tests undertaken in Russia have shown that accepted chemical criterion is not a reliable indicator. The results obtained with the long-term method based on concrete specimens tests over one year should be considered as the most reliable. Attention to “internal corrosion” in Russia is increasing every year, because its consequences are rather serious, and the causes of structural damage are intensifying. Practical examples of structural damage caused by AAR and their preventions are given. At present, AAR deterioration processes and the appropriate protection methods of concrete have been studied in detail, which has allowed for the active use of reactive rock in concrete.

Keywords: concrete, durability, alkali aggregate reaction, deterioration processes

1. INTRODUCTION

Production of non-metallic building materials (primarily, crushed stone obtained from natural rock quarrying, gravel and sand) in the Russian Federation is spread over than 1080 major, medium and minor companies. Sand and gravel represents over 20% of the total output of these materials.

According to [1], the resource potential of the raw sand-gravel materials (SGM) in the RF is represented by over 2400 deposits with total reserves of 10.9 bln m³. Of them, designated material is estimated as 45.9% of deposits with 5.3 bln m³ of reserves, while the unappropriated stock is estimated as 54.1% with 5.5 bln m³ of reserves. Sand deposits for building works number over 2 thousand with industrial grade reserves of 7.1 bln m³. The proportions of these

in the designated stock are 53.7% with 3.4 bln m³ of reserves, while those in the non-designated stock are 46.3% with 3.7 bln m³ of reserves.

In Russia, the rock comprising the minerals capable to interreact with alkalis is widely spread [2]. They include different magmatic rock – granites and granodiorites with deformed lattice quartz and mouldy feldspar inclusions; rhyolites, dacites, andesites, trachyandesites and basalts comprising silicate and basalt glass devitrificated in various degrees as well as some tridymite, cristobalite, opal; obsidian, cinerites, retinites, silica-rich glass, often with microcracks; gneisses and glists characterized by open grain contacts and the deformed lattice quartz content, microquartz, feldspar and micaceous minerals. From metamorphic rock the hazardous ones are quartzites, sandstone rock and hornblendes comprising opaline cement and secondary microquartz, microcrumpling quartz as well as quartz schists, greywackes and silicites including opal, phyllite minerals and microcrystalline quartz. To potentially reaction-hazardous sedimentary rock one also refers limestones, dolomitic limestones and dolomites comprising chalcedony, opal in the form of intermediate layers, micrograins or diffusedly distributed in the lattice. To the rock comprising potentially reactive silica one refers sandstones in the middle Volga region, flint stone comprising gravel and sand deposits (Urals, East Siberia, and North-West of the country's European part). In the Far East, in the Maritime Territory, Sakhalin Island and Kamchatka some acid rock (andesites, scorias, etc.) are potentially reactive.

The great igneous rock reserves are in the Leningrad Region, Karelia, and the Urals Region. The gravel-sand and sand deposits are located mainly in the RF European part and unavailable in the most Siberian areas [3].

According to [4], production of non-metallic materials (NMBM) in 2017 was 508.9 mln m³. Over 44% of NMBM output are referred to pebble stone, gravel and crushed stone. 48% comes to sand and 8% - to other NMBM. In the recent years, the NMBM production structure is sufficiently constant and has not underwent essential changes.

The expected growth of long-term requirements for non-metallic building materials encourages increasing quarrying in all Russian regions. The analysis shows that the reserves of the RF unappropriated stock fit for development will be about 3.9 bln m³ of the sand-gravel material and 2.6 bln m³ of sand for building works. This can meet the economics' demands up to 2040-2050. To create reserves for the next periods it is necessary to increment them in the majority of Federal Districts (FD), and in the first turn, in individual regions of the Central, Volga, Southern and North Caucasus FD.

In the former USSR, the AAR studies were described for the first time by V.M. Moskvin and G.S. Royak in 1962 [5]. Their book summarizes the research results obtained in the USSR up to 1962. Further on this issue was considered in a number of other domestic studies on concrete and reinforced concrete durability [6]. V.M. Moskvin, S.M. Royak and G.S. Royak, F.M. Ivanov, A.M. Viktorov, G.V. Lyubarskaya, N.K. Rosental, G.V. Chekhny, Z.B. Entin, B.E. Yudovich, M.L. Nisnevich, M.I. Lopatnikov, N.S. Levkova, T.A. Zatvornitskaya and others studied individual aggregates and interaction processes of cement alkalis and additives with reactive aggregates, and identified the list of reactive rock and estimated the raw material base. At present, the processes caused by AAR and protection methods have been adequately studied; this allows actively using reactive rock for manufacture and use of aggregates from them in concrete.

2. TECHNICAL REGULATION, SPECIFICATIONS AND AAR TEST METHODS

In Russia, requirements to aggregates are regulated by standards for coarse aggregate – GOST 8267 [7] and sand GOST 8736 [8]. The test methods for AAR are specified in GOST 8269.0 [9]. When updating the latter standard, the RILEM recommendations [10-12] and ASTM C 1260 [13] were used in addition to the domestic findings.

According to [9], rock, crushed stone (gravel) are referred to potentially reactive ones, if the petro graphic analysis finds the presence of one or several varieties of minerals comprising reactive silica in the amounts equal to or exceeding the values given in Table 1.

Table 1: Potentially reactive rock

Mineral and silica type	Types of potentially reactive rock	Content of mineral, %, by mass.
Opal	Basalts and other lavas. Limestones, hornfels, opal-like shale	0.25
Crystalline cristoballite, tridymite	Silica-comprising melts (materials obtained by melting)	1.0
Deformed mouldy quartz	Quartz vitrophyres, quartzites, sandstones, volcanic and metamorphic acid rock	3.0
Amorphous acid glass	Vitreous-based obsidians, perlites, liparites, andesite-dacites, andesites, tuffs and these rock analogues	3.0
Cryptomicrocrystalline chalcedony	Flint stones, limestones, dolomites, sandstones with opal-chalcedony and chalcedony-quartz cement, jaspers, hornfels	5.0

Russian standards permit using overburden and enclosing rock, ore and non-metallic mineral processing wastes.

All standards have a prescriptive nature. If the soluble silica quantity exceeds the specified value – not more than 50 mmol/l of alkali-soluble silica – the accelerated mortar-bar test method is used.

The accelerated method is based on relative deformations determination of fine-grained concrete (mortar) samples made on cement and crushed aggregates from rock or gravel containing more than 50 mmol/l of soluble silica in the established terms (no more than 1 month). Tests are carrying out on the bar samples with size 25x25x254 mm. Composition of fine-grained concrete should be 1:2.25 by weight. Cone flow when tested on the flow table should be 106 - 115 mm. Amount of mixing water has to be determined previously.

The deformation of the sample should be determined by measuring the length of the control beam and testing samples before and after their daily exposure in a 1M solution of sodium hydroxide at a temperature of (80±1)°C. Exposure of samples and deformations measurements should be repeated at least eleven times.

Aggregates are considered to be non-reactive to alkalis, if during the test the expansion deformations of the samples in sodium hydroxide solution are less than 0.1%, provided that the last (eleventh) test result differs from the three previous measurement results by no more than 15%. If the deformation exceeds these values, the rock, gravel are considered potentially reactive with alkalis, and the possibility of using them as aggregates has to be determined by the test of concrete samples.

The long-term test method is based on the determination of the relative deformations of concrete samples in a time (within one year). Tests are carrying out on beams samples with size 70x70x280 mm. The concrete mixture composition for samples should be 1: 1.4: 2.6 (Portland cement with a given composition: natural non-reactive sand with Abram's fineness modulus over 2.0 to 2.5: reactive coarse aggregate) by weight. The workability of the fresh concrete determined by slump shall not exceed 2 to 4 cm. If the monthly elongation of the samples in each test does not exceed 0.04 %, the test shall be carried out during one year, each time comparing the result with the previous one. Rock, gravel refers to the non-reactive, if the last (twelfth) value of the relative elongation does not exceed 0.04 %.

The test methods set forth in the standard are generally coordinated with the methods developed by RILEM [10-12]. The only difference is that the accelerated method additionally accounts for deformation variation dynamics at the test end. The value obtained in the last measurement shall not exceed the values in three preceding measurements by more than 15%.

It should be noted that the performed tests have shown that the criterion assumed in the chemical method is not a reliable indicator. In a number of cases the specimen expansion was observed when the soluble silica content was less than 50 mmol/l; at the same, time the aggregates with essentially higher than 50 mmol/l quantity of soluble silica were revealed, but no above-level concrete deformations were observed. Basing on these results, the conclusion was made that the specimen tests with deformation measurements are mandatory.

With account of RILEM recommendations, the accelerated tests with specimen expansion deformation measurements were conducted at 80°C in different environments: distilled water, sodium chloride solution and alkali solution. The tests in water and in 1M sodium chloride solution have not revealed advantages as compared to the tests in the alkali solution.

The basic requirements to concrete protection against AAR are specified in the Code [14]. The Code envisages prevention procedures also. For example, when reactive silicon dioxide is present in aggregates, it is not allowed to introduce sodium and potassium salts as admixtures into concrete.

In practice such recommendations as cement consumption reduction, use of cements with low alkali contents, non-use of aggregates comprising alkali-reactive silica, in many cases are hardly feasible. In a number of regions, the basic commercial cement comprises great alkali quantities. In the same regions, a number of aggregates comprise increased quantities of potentially reactive silicon dioxide (quarries on the basis of fluvioglacial sediments in the north-west of Russia's European part, sand-gravel sediments at the Kama River, fluvial sediments and volcanic rock of Siberia, etc.).

The above-mentioned regulatory documents have served a basis for numerous tests conducted by different researchers.

3. AGGREGATES WITH ACTUAL OR POTENTIAL HAZARD FOR AAR. LAST STUDIES IN RUSSIA

In the recent decades, the Research Institute for Concrete and Reinforced Concrete (NIIZhB) more that 50 different aggregates (crushed stone, gravel, sand) with the content of alkali-soluble SiO_2 from 20 to 1100 mmol/l were studied [15].

Considering the data on amounts of aggregates supplied to Moscow precast concrete plants, four deposits have been studied in detail: Abramovo, Akademicheskoye, Vyazemskoye, Oreshkinskoye. At the plants using aggregates from the above deposits the representative samples of crushed stone from gravel and sand were taken to chemically determine alkali-soluble silicon dioxide (Table 2). The majority of the aggregates presented have shown high contents of alkali-soluble silicon dioxide – over 50 mmol/l. For a number of aggregates the tests were many times repeated in different years [16].

Taking into account the chemical analysis results, it was considered for a long time that the crushed stones from Vyazemsky quarry are capable to AAR. Reactivity of them was studied at NIIZhB in different years for 12 lots of crushed stone. The soluble SiO_2 content was 141.9 to 682.4 mmol/l. The twelfth sample was prepared intentionally by the Vyazemsky quarry administration by flint stone grain sampling using a microscope. The soluble SiO_2 content in this sample was 782.0 mmol/l. The accelerated tests of all samples have shown deformation values 0.03 to 0.069%; this being less than 0.1% specified by [9]. The year-long tests were conducted with two lots of crushed stone with the soluble SiO_2 content of 363.9 and 437.2 mmol/l. Deformation values after 12 months of tests were 0.024 and 0.016% accordingly; this being less than 0.04% specified by [9]. Thus, the crushed stone from Vyazemskoye deposit was recognized as non-reactive with cement alkalis. Laboratory tests are also confirmed by the long-term experience of using the Vyazemskoye deposit crushed stone in construction.

Table 2: Results of alkali-soluble silicon dioxide quantity determination

Deposit and aggregate type	Grain size, mm	Soluble SiO_2 content, mmol/l
Abramovo (crushed stone from gravel)	5-10	294; 250
	10-20	274
Akademicheskoye (crushed stone from gravel)	5-10	230
	10-20	377; 465
Vyazemskoye (crushed stone from gravel)	5-10	339; 361; 364
	10-20	142; 302; 406; 437; 508; 533; 594; 682
Oreshkinskoye (crushed stone from gravel)	5-10	120; 144; 137; 338;
	10-20	201; 241; 255; 261; 684
Vyazemskoye (sand)	0-5	21; 52

The integrated studies of a wide range of aggregates by all three methods were conducted according to [9]. Portland cements from three cement plants (Belgorodsky, Voskresensky, and Maltsovsky) were used in concrete testing with the alkali content from 0.6 to 1.1%. The accelerated test results identified 13 aggregates containing over 50 mmol/l of alkali-soluble SiO_2 , but these aggregates proved to be non-reactive. While out of five aggregates comprising less than 50 mmol/l of soluble SiO_2 , three aggregates were reactive [15].

In a joint RF – UK research project, similar procedures were used to test the gravel from Listvennichnoye deposit (SiO_2 : 20.5 mmol/l) and the sand from Okhotskoye deposit (SiO_2 : 46.7 mmol/l). By the expansion test measurements both in the RF and the UK the aggregates were recognized as reactive, though the alkali-soluble SiO_2 content in samples was less than 50 mmol/l.

The tests of 12 aggregates by the accelerated and long-term methods have shown in 10 cases the same evaluation of their reactivity. By the accelerated test results, the crushed stone from Oreshkinskoe deposit gravel gave an expansion value of 0.125% and was evaluated as reactive, though the long-term test results indicated that it is non-reactive. The crushed stone from Ryboretskoye deposit has shown expansion of 0.07% (less than specified 0.1%) in accelerated tests, but the increment of the latter result was 16%, i.e., higher than the specified value of 15%. However, since the key method is the year-long test, when the concrete test for this crushed stone gave an expansion of 0.019% (less than the 0.04% criterion), the crushed stone from the Ryboretskoye deposit was recognized as non-reactive.

In the course of numerous studies, reactive sands from different deposits have been identified. These sands are characterized by a crystalline structure, the weathering degree, availability of amorphous silica and the presence of various impurities. The sand comprised metamorphic rock containing quartz, veined quartz, acid volcanic rock and quartz with a disturbed crystalline structure. It has been found that reactivity is inherent for sands from deposits at Okhotskoye, Vyazemskoye and Malkinskoye.

NIIZhB has conducted also tests of crushed stone from dolomitic limestone of Dankovskoye and Zubtsovskoye deposits. The carbonate content in the Dankovskoye deposit crushed stone was 41.07% of CaCO_3 and 35.91% of MgCO_3 . The content of alkali-soluble SiO_2 was 0.85 mmol/l. In the Zubtsovskoye deposit crushed stone the CaCO_3 content was 38.98%, MgCO_3 – 42.44%, alkali-soluble SiO_2 – 28.36 mmol/l. The accelerated tests were performed by AAR-5 method [17] developed by RILEM for carbonate rock studies with the specimen deformation measurements in the course of storing in 1M NaOH solution at 80°C. Deformations were measured during one month every 7 days (Table 4).

In conformance with [17], the aggregate from dolomitic limestone is considered reactive, if specimen deformation by the moment of test completion (28 days) equals to 0.1% and more. By the accelerated test results the aggregates from dolomitic limestone of Dankovskoye and Zubtsovskoye deposits are recognized as non-reactive with cement alkalis.

Table 3: Deformations of dolomitic limestone-based mortar-bar specimens in 1 M NaOH solution at 80°C.

Deposit	Deformations, %, after tests during ... days				
	3	10	17	24	30
Dankovskoye	0.011	0.015	0.019	0.026	0.030
Zubtsovskoye	0.017	0.020	0.032	0.037	0.046

The long-term tests of crushed stone from dolomitic limestone of Dankovskoye and Zubtsovskoye deposits were performed according to GOST 8269.0 with concrete specimens at 38°C with the alkali content in concrete 1.5% in terms of Na_2O of the cement mass. The concrete composition was Cement : Sand : Crushed stone = 1:1.4:2.6; slump was 1.5-3 cm. Crushed stone grain size was 5-20 mm.

As seen from the Table 4, the decisive are long-term tests (12 months). By the accelerated and long-term test results the crushed stone from Dankovskoye deposit dolomitic limestone is evaluated as non-reactive with cement alkalis. By the long-term test results the crushed stone from Zubtsovskoye deposit dolomitic limestone is evaluated as reactive with cement alkalis.

Table 4: Deformations of dolomitic limestone-based concrete specimens in long-term tests at 38°C

Deposit	Cement content kg/m ³	W/C	Bulk weight, kg/m ³	Deformations, %, after tests during...					
				months					
				2	4	6	8	10	12
Dankovskoye	341	0.50	1875	0.027	0.023	0.023	0.022	0.019	0.019
Zubtsovskoye	325	0.62	1828	0.028	0.037	0.036	0.040	0.04	0.040

4. CASES OF DAMAGE

In Russia and the former USSR, the cases of damage of house footing structures, railway sleepers, concrete elements in a number of public and industrial buildings and structures, port facilities are well-known. In some cases there appeared visible signs of concrete degradation – crack network, white jelly-like blooms - in a few months or even years after manufacture of structures. The chemical analysis showed the presence of great quantities of SiO₂ and alkali metals – sodium and potassium – in the blooms. These damages in humid conditions being most favorable for concrete strength retaining and even gaining in the long-term periods were gradually developing and the structural concrete was deteriorating. Such corrosion processes occurred within concrete without environmental components, except the necessary presence of moisture.

The detailed field inspections of concrete pile foundations of high-rise residential buildings in the city of Novgorod, conducted by NIIZhB in 1998–2002, disclosed indicators of alkali-aggregate reactivity, and have resulted in development of similar recommendations providing for the secondary protection of structures using special impregnating compounds.

In 2004, there were in Russia cases of mass-scale deterioration of under-rail concrete structures manufactured in 2001 [18]. The deterioration was accompanied by appearance of cracks with various opening widths. Core samples drilled out from under-rail structures show coarse aggregate grains that deteriorated with gel release, being one of the characteristic features of the alkali-silica reaction. Of the similar nature were failures of transmission tower footings of the USSR railway overhead system after 3 years of service [19].

Quite a few cases are known, when internal corrosion was explained by damages due to other causes (low frost-resistance, technological defects, concrete composition etc.). The fact that a concrete damage was a result of internal corrosion could be established only by a thorough analysis when the alkali content in cement and reactive silica presence in aggregates are determined. Correct detection of internal corrosion is very important, since the initiated process of concrete deterioration can be stopped only by creating dry operation conditions, this being unfeasible in most cases.

5. CONCLUSIONS

Attention to internal corrosion in Russia is increasing every year, because its consequences are rather serious, and the causes of structural damage are intensifying. First of all, the alkali

content in cements increases as a result of dust collection and recovery improvements; the dust comprises the increased quantities of alkali metal compounds sublimated in cement clinker calcinations. Simultaneously the alkali content rises in the raw materials for cement production, while in some cases the alkalis are components of raw materials and alkali-comprising wastes – aluminum plant nepheline tailing, some fly ash types from thermal power plants.

REFERENCES

- [1] Bekrenev I.V. Investigation of specific development of the non-metallic building materials market in Russia. Mining Information Analysis Bulletin (GIAB), 6, 2013, P. 340-348.
- [2] Ivanov F. M. Internal corrosion of concrete. *Beton i zhelezobeton* (Concrete and reinforced concrete). - 1992. - No. 8. -P. 8-10.
- [3] Buyanov Yu.D., Kharo O.Ye., Butkevich G.R., Levkova N.S. Prospects of improving concrete aggregate qualities. Proceedings of the 2nd All-Russian (International) Conference on Concrete and Reinforced Concrete (in 5 volumes). V. 3, P. 236-241, 2005.
- [4] Annual report on the market of non-metallic building materials in Russia in 2017. CMPro, 125 p., 2018.
- [5] Moskvina V.M., Royak G.S. Concrete corrosion under interaction of cement alkalis and the aggregate active silica – M.: Gosstroyizdat, 1962. – 164 pp.
- [6] Moskvina V.M., Ivanov F.M., Alekseev S.N., Guzeev E.A. Corrosion of concrete and reinforced concrete, their protection methods. M., Stroyizdat, 1980, 536 p.
- [7] GOST 8267-93. Crushed stone and gravel from dense rock for construction works. Specifications.
- [8] GOST 8736-93. Sand for construction works. Specifications.
- [9] GOST 8269.0-97. Crushed stone and gravel from dense rock and industrial wastes for construction works. Physical and mechanical test methods.
- [10] RILEM Recommended Test Method AAR-0 'Detection of potential alkali-reactivity in concrete' Outline guide to the use of RILEM methods in assessments of alkali-reactivity potential.
- [11] RILEM Recommended Test Method AAR-1 'Detection of potential alkali-reactivity aggregates'. Petrographic method.
- [12] Recommendations of RILEM TC 106-AAR: Alkali aggregate reaction A. TC 106-2 - Detection of potential alkali-reactivity of aggregates -The ultra-accelerated mortar-bar test B. TC 106-3 - Detection of potential alkali-reactivity of aggregates - Method for aggregate combinations using concrete prisms.
- [13] ASTM C 1260 (2001). Standard Test Method for Potential Alkali Reactivity of Aggregates (Mortar-Bar Method).
- [14] SP 28.13330.2017 Protection of building structures against corrosion. Moscow, Standartinform, 110 p., 2017.
- [15] Rosental N.K., Lyubarskaya G.T.V., Rosental A.N. Test of concrete with reactive aggregates. *Concrete and reinforced concrete*, No.5, 2014
- [16] Rosental N.K., Chekhny G.V., Lyubarskaya G.V., Rosental A.N. Internal corrosion protection of concrete with reactive aggregate. *Building materials*, No.3, 2009, P. 68-71.
- [17] RILEM TC 191-ARP 'Alkali-reactivity and prevention - Assessment, specification and diagnosis of alkali-reactivity' AAR-5: Rapid preliminary screening test for carbonate aggregates.
- [18] Petrova T. M., Sorvacheva Yu. A. Internal corrosion of concrete as a factor of the durability decreasing of the objects of transport construction. Science and Transport. *Transport construction*. No. 4, 2012, pp. 56 – 60.
- [19] Petrova T. M., Sorvacheva Yu. A. The reasons for development of internal corrosion and fall of concrete sleepers' durability. Bulletin of PGUPS. No. 2, p.p. 87 – 92, 2012.

THE EFFECT OF DIFFERENT CEMENTITIOUS BINDERS ON EXPANSION INDUCED BY ALKALI SILICA

Taehwan Kim (1), Dinesh Habaragamu Arachchige (1), Quang Dieu Nguyen (1), Mohammad Khan (1), Arnaud Castel (1), and Pre de Silva (2)

(1) Centre for Infrastructure Engineering and Safety (CIES) Civil and Environmental Engineering, UNSW Sydney, NSW 2052, Australia

(2) Chemistry, Australien Catholic University, North Sydney NSW 2060, Australia

Abstract

Different types of cementitious materials have been developed and investigated to construct and restore infrastructure in an economical, durable, and sustainable manner while reducing carbon footprint. However, the durability of concrete using these alternative cementitious materials has yet to be fully investigated and the results are still controversial. This paper presents the effect of different binders on alkali silica reaction (ASR). It is expected that each binder involves different chemical reactions, consequently, resulting in different mortar systems for ASR to occur.

Six different mortar mixtures were prepared using a highly reactive aggregate, including: a) one portland cement mixture, b) three geopolymer mixtures (9, 4, and 1 of fly ash to ground granulated blast furnace slag (GGBFS) ratios), and c) two limestone calcined clay cement (LC3) mixtures (20% and 30% of replacement rates). The accelerated mortar bar tests were performed for an extended period. ASR phases of different mixtures were investigated using Scanning electron microscopy with energy dispersive X-ray spectroscopy (SEM-EDS) at different exposure time in NaOH solution. Dissolution behaviors of the reactive aggregate were monitored in four different NaOH solutions.

The expansions of three geopolymer mortars showed initial delay (about 20 days). It implies that the geopolymer system requires an extended test period to assess the ASR expansion. The higher content of GGBFS in geopolymer binder caused the greater expansion, which indicates the calcium content is associated with the expansion induced by ASR. ASR gels observed from SEM-EDS also supported the effect of calcium on the expansion. The LC3 mortars significantly reduced the expansion of mortar bars at all ages. 30% OPC substituted by calcined clay and limestone restricted the expansion of mortar bars below the 10-day limit and 21-day limit, which can prevent the potential ASR in concrete structure using reactive aggregate.

Keywords: cementitious materials, alkali silica reaction, reactive aggregate

AN AMBT STUDY ON THE EFFECT OF LIMESTONE ON ASR MITIGATION: GROUND LIMESTONE VS. INTERGROUND LIMESTONE IN CEMENTS

Marie Joshua Tapas (1), Kirk Vessalas (1), Paul Thomas (2), Vute Sirivivatnanon (1)

(1) School of Civil and Environmental Engineering, University of Technology Sydney

(2) School of Mathematical and Physical Sciences, University of Technology Sydney

Abstract

This study reports on the effect of cement limestone addition on alkali-silica reaction (ASR) induced expansion for binder systems with and without supplementary cementitious materials (SCMs) using accelerated mortar bar test. Two (2) approaches were carried out to obtain the desired amount of limestone in the binder: one by adding ground limestone to 0% Limestone General Portland cement (LC) and another by combining 17% LC (interground limestone source) with 0% LC to get desired limestone content. The combined effect of limestone and SCMs was also evaluated by replacing part of the cement with nominated percentages of fly ash and ground granulated blast furnace slag. AMBT expansion results show that regardless of limestone source (ground or interground), limestone does not influence the efficacy of SCMs in ASR mitigation. Further, it shows that there is no difference in expansion regardless of limestone content in specimens with and without SCMs suggesting that limestone has no mitigating effects. Thermogravimetric analysis (TG) results however show that portlandite content decreases with respect to increasing limestone content consistent with cement dilution. As there was no observable difference in expansion corresponding to limestone content, this suggests that the effect of cement dilution maybe beyond the capacity of AMBT. Additional work however needs to be done to verify the hypothesis.

Keywords: alkali-silica reaction; limestone; fly ash; slag; mitigation

1. INTRODUCTION

Cement based construction materials are the world's largest manufactured product by mass [1]. Cement production, however, involves calcination of limestone which releases carbon dioxide (CO₂) into the atmosphere and hence contributes to global warming. Using limestone mineral addition as a partial substitution for cement has the potential to help mitigate the carbon footprint of concrete [2, 3]. The current allowable limestone mineral addition in Australian Standard AS 3972 for general purpose Portland cement (GP) is 7.5%

but there are current efforts to increase the mineral addition limit to 12% to align with international limits [3, 4].

While the impact of increasing limestone on mechanical performance has been widely studied, its effect to alkali-silica reaction (ASR) and ASR mitigation methods is less explored. ASR can occur when high alkali pore solution of the concrete reacts with certain silica phases in the aggregate. Silica dissolves in high alkali environments and once in solution, they react with calcium (Ca^{2+}) and alkali ions (Na^+ , K^+) in the system to form the ASR product (calcium alkali silicate hydrate gel) which can induce pressure build up, resulting in expansion, and, potentially, cracking of the concrete.

The role of limestone in ASR mitigation is currently uncertain, specifically on the effect of ground limestone and interground limestone on ASR. Limestone addition has variously been reported to have an insignificant effect on ASR [2, 5], or to have a mitigation role through dilution effects [6, 7]. In order to investigate the role of limestone mineral addition on ASR, this study reports AMBT data for mortar bars with and without SCMs and a parallel paste study where the degree of reaction is monitored through the proportion of calcium hydroxide present using thermogravimetric analysis (TG) [8].

2. MATERIALS AND METHODOLOGY

The cements (0%LC, 17%LC), ground limestone, ground granulated blast furnace slag (slag) and fly ash (FA) used in this study were all sourced locally. The compositions of the raw materials as determined by X-Ray Fluorescence (XRF) are listed in Table 1. Based on the XRF data and the mass loss data using thermogravimetric analysis (TG), the ground limestone is estimated to be 98% CaCO_3 , containing circa 1.3% silica, hence easily conforming to AS 3972 definition of a limestone mineral (Table 1, Figure 1(a)). XRD analysis of the limestone confirmed the predominance of limestone with trace proportions of quartz present (Figure 1(b)). The XRF data coupled with TG analysis demonstrates that the 0% LC used does not contain CaCO_3 mineral addition. The 17% LC showed approximately 7.5% weight loss from TG which corresponds to the decomposition of about 17% CaCO_3 content Figure 1(a)).

Table 1: XRF Data of Raw Materials

Oxide Wt. %	0% Limestone Cement	17% Limestone Cement	Ground Limestone	Slag	Fly Ash
SiO_2	20.36	19.40	1.30	34.12	59.21
TiO_2	0.30	0.22	0.04	0.87	1.11
Al_2O_3	5.25	4.26	0.43	14.37	28.11
Fe_2O_3	2.99	2.63	0.21	0.30	3.68
Mn_3O_4	0.06	0.04	0.02	0.36	0.11
MgO	1.41	1.14	0.36	5.31	0.53
CaO	64.36	58.31	55.11	41.59	2.48
Na_2O	0.41	0.25	0.14	0.35	0.63
K_2O	0.43	0.41	0.06	0.26	1.18
P_2O_5	0.22	0.17	0.02	0.01	0.41
SO_3	2.25	2.51	0.02	2.83	0.16

L.O.I.	1.34	10.34	42.99	0.35	1.05
--------	------	-------	-------	------	------

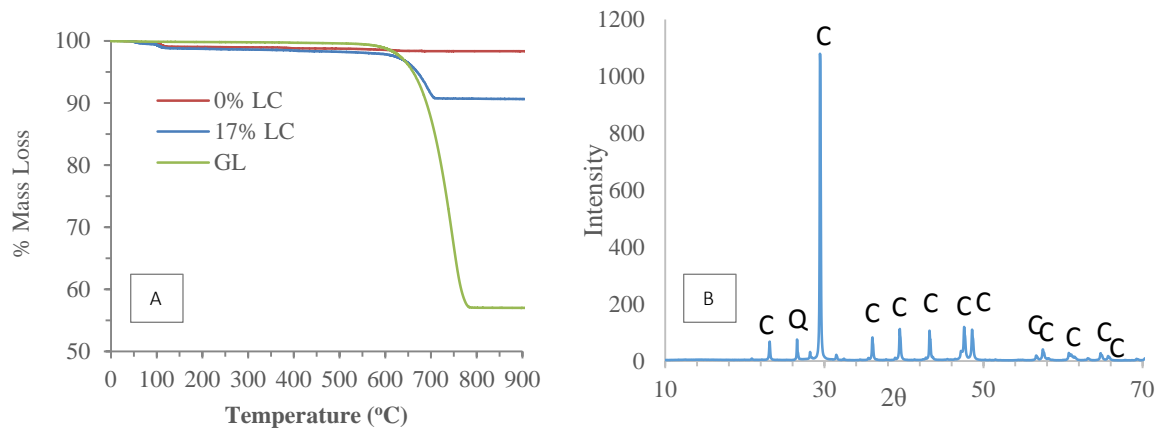


Figure 1: a) TG curves of 0% and 17% Limestone cement (LC) and Ground Limestone (GL) and b) XRD pattern of the ground limestone where C=calcite, CaCO_3 and Q=quartz

Table 2 provides particle size data of the cements and ground limestone. A slight difference in particle size is notable with the ground limestone having higher $d(90)$ than 0% LC and 17% LC.

Table 2: $d(10)$, $d(50)$ and $d(90)$ for the cements and ground limestone

Material	$d(0.1)$	$d(0.5)$	$d(0.9)$
0% LC	3.81	15.56	37.69
17% LC	2.06	17.36	69.94
Ground Limestone	3.07	19.66	157.92

2.1 Accelerated Mortar Bar Test (AMBT)

AMBT specimens were prepared in accordance to AS 1141.60.1. Mortar bars are composed of 1 part of cement to 2.25 parts of graded aggregate by mass (440g cement per 990g of aggregate) and water to cement ratio equal to 0.47 by mass.

For mixes with ground limestone addition, the limestone content was added by replacing 0% limestone cement with 8%, 12% and 17% ground limestone by mass of cement. For the interground limestone mixes, to obtain the 8% limestone cement, 0% and 17% limestone cements were blended to required ratio.

For mixes with SCMs, the SCMs replaced part of the cement at a nominated percentage (15% and/or 25% for fly ash; 35% and/or 65% for slag) and water to cementitious binder ratio was maintained at 0.47 by mass. SCM dosages used are typical dosage requirements to mitigate ASR in Australia [9]. All mortar specimens used reactive greywacke aggregate. Expansion measurements were obtained up to 28 days.

2. 2 Thermogravimetric Analysis

Blended pastes containing GP cement with 0, 7.5, 12, and 17% limestone by mass of cement were prepared by mixing cement, ground limestone and water (0.47 water-to-cementitious material ratio). The paste specimens were cured for one day in 90%RH and 25°C oven and after stored in 1M NaOH 80°C for 28 days. Pure cement paste (OPC) was also prepared to serve as a reference (i. e., control). TG was used to measure the portlandite ($\text{Ca}(\text{OH})_2$) content at 1 day and after 28 days.

3. RESULTS AND DISCUSSION

3.1 Accelerated Mortar Bar Test (AMBT)

AMBT expansion results in Figure 2a of mortars with no SCMs suggest that limestone in the binder up to 17% has no influence on ASR. Expansion data at 0, 8, 12 and 17% ground limestone addition show identical behaviour suggesting that the dilution effect is not a factor in cements with elevated limestone content. A similar behaviour can also be observed with the SCM mixes. Figure 2b and 2c which contain 25% fly ash and 65% slag respectively show almost no expansion regardless of limestone content which means that the SCMs are effectively mitigating ASR. The addition of limestone is observed to have no influence on the mitigating action of the SCMs.

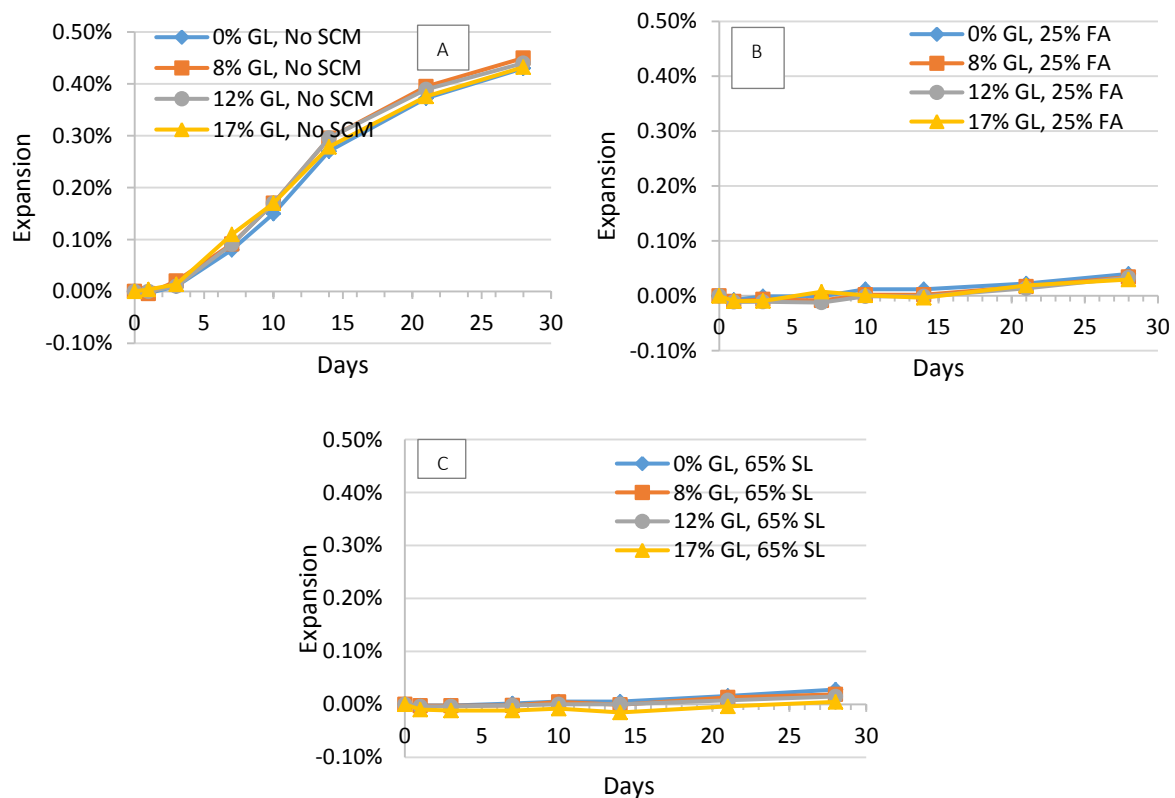


Figure 2: AMBT expansion results showing effect of increasing ground limestone (GL) content in cement on ASR expansion and mitigation: a) No SCM, b) 25% FA and c) 65% SL

Figure 3 shows the effect of interground limestone in cements on ASR expansion. A minimum dosage of 15% for FA and 35% for SL was found sufficient to mitigate expansion. Increasing the dosage to 25% for FA and 65% for SL further lowers the expansion as expected. Moreover, at a fixed SCM type and dosage, regardless of interground limestone content, the expansion behaviour closely mimic each other. Increased amount of limestone appear to have minimal influence on expansion. These results agree with that of the effect of ground limestone presented in Figure 2.

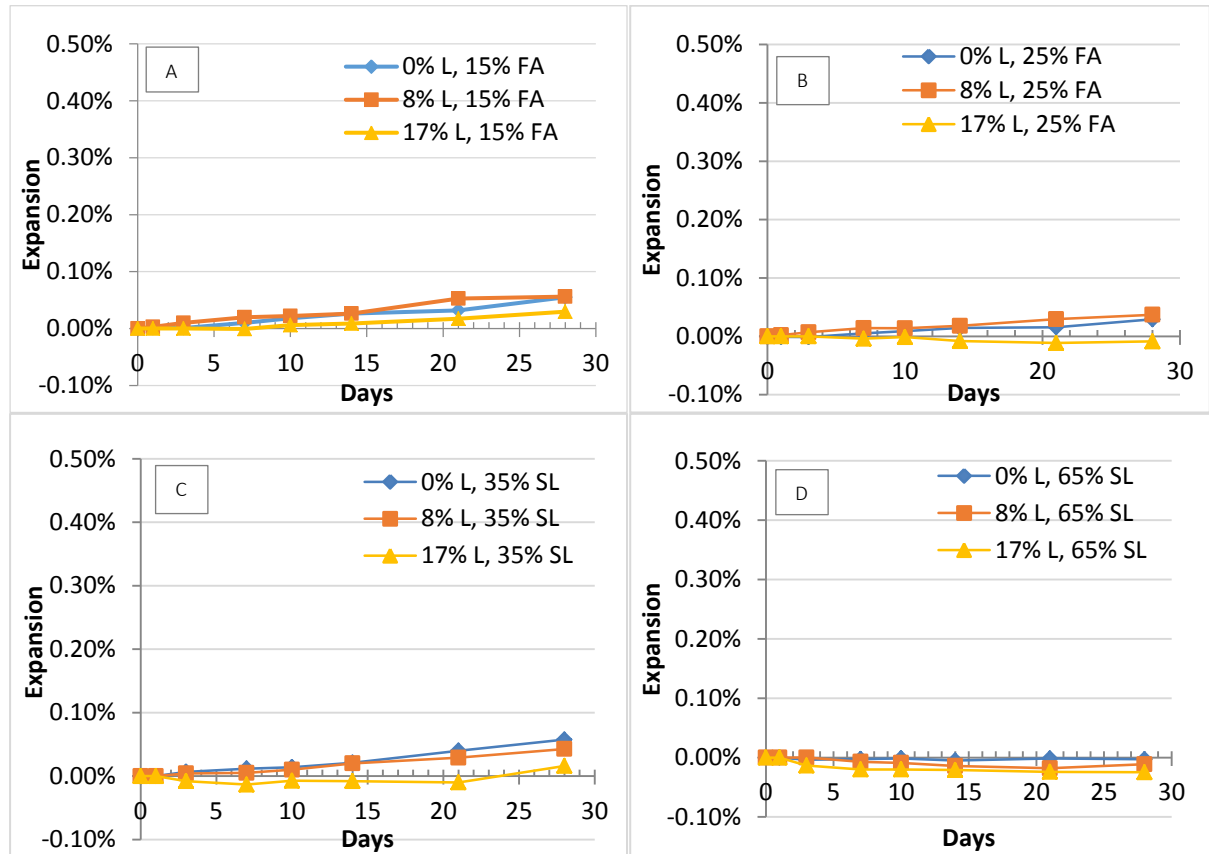


Figure 3: AMBT expansion results showing the effect of increasing interground limestone: a) 15% FA, b) 25% FA, c) 35% SL and d) 65% SL

The expansion data presented in this work, both for ground limestone and interground limestone, agrees with the work of Thomas et al. [5] which showed that the expansion levels for Portland cement (PC) and Portland-limestone cement mixtures (PLC, 12% limestone addition) are almost identical for mixtures with the same SCM and replacement level and that the efficacy of cement replacement with Class F fly ash or slag cement does not appear to be influenced by the presence of 12% limestone in the cement.

3.2 Portlandite Measurement

TG results in Figure 4 show that while portlandite increases as a function of time, it decreases as limestone content increases. As more ground limestone is added, lower cement is available which means lower amount of portlandite generated. However, as AMBT did not

detect any difference in ASR expansion as a function of limestone content, this suggests that the effect of cement dilution is beyond the capacity of the test method.

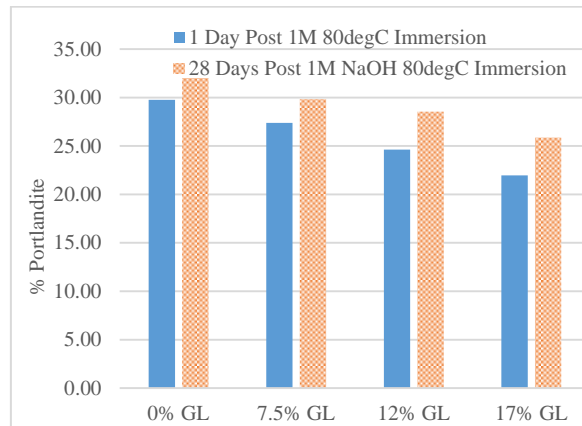


Figure 4: Portlandite content of pastes with varying amount of limestone obtained using TG

4. CONCLUSIONS

This paper compares the effect of ground limestone and interground limestone on ASR expansion. Both binder systems showed that limestone content up to 17% has no influence on the ability of SCMs to mitigate ASR. While the effectivity of SCMs is established, the negligible difference in expansion may also be partly attributed to the “masking effect” of the SCMs. That is, the mitigating properties of the SCMs are overpowering the dilution effect of the limestone. Interestingly however, for systems without SCMs, the limestone also showed no effect on ASR expansion. As this goes against the known effect of cement dilution, this may suggest that while AMBT is a relatively good method to assess efficacy of SCMs in mitigation, it is not sensitive enough to detect the effect of dilution due to excessive supply of alkalis. More work is however required to verify the hypothesis.

ACKNOWLEDGEMENT

The work carried out in this study was funded by the Australian Research Council (ARC) Research Hub for Nanoscience Based Construction Materials Manufacturing (NANOCOMM) and Cement Concrete and Aggregates Australia (CCAA).

REFERENCES

- [1] Scrivener, K.L., V.M. John, and E.M. Gartner, *Eco-Efficient Cements: Potential, economically viable solutions for a low CO₂ cement-based materials industry*. 2016, United Nations Environment Program.
- [2] Tennis, P.D., M.D.A. Thomas, and W.J. Weiss, *State-of-the-Art Report on Use of Limestone in Cements of up to 15%*. 2011, Portland Cement Association.
- [3] Mohammadi, I. and W. South, *General purpose cement with increased limestone content in Australia*. *ACI Materials Journal*, 2016. **113**: p. 335-347.
- [4] Mohammadi, J., W. South, and D. Chalmers. *Towards a More Sustainable Australian Cement and Concrete Industry in 27th biennial national conference of the concrete institute of*

Australia in conjunction with the 69th RILEM week conference. 2015. Melbourne, Australia: Concrete Institute of Australia.

- [5] Thomas, M.D.A., et al., *Equivalent Durability Performance of Portland Limestone Cement*. Concrete International, 2013: p. 39-35.
- [6] Hooton, R.D., M. Nokken, and M.D.A. Thomas, *Portland-Limestone Cement: State of the Art Report and Gap Analysis For CSA A 3000*. University of Toronto, 2007.
- [7] Rajbhandari, N., *Determining the Effect of Intergrinding Limestone with Portland Cement on the Durability of Concrete with and without SCM in Civil Engineering*. 2010, The University of New Brunswick.
- [8] Thomas, M., et al., *Test methods for evaluating preventive measures for controlling expansion due to alkali-silica reaction in concrete*. Cement and Concrete Research 2006. **36**: p. 1842–1856.
- [9] Standards Australia, *Alkali Aggregate Reaction—Guidelines on Minimising the Risk of Damage to Concrete Structures in Australia*. 2015, SAI Global Limited: Sydney, Australia.

SYNTHESIS AND CHARACTERIZATION OF ALKALI-SILICA REACTION PRODUCTS

Z. Shi (1), B. Lothenbach (1) and A. Leemann (1)

(1) Laboratory for Concrete & Construction Chemistry, Swiss Federal Laboratories for Materials Science and Technology (Empa), Dübendorf 8600, Switzerland

Abstract

Despite of numerous investigations on alkali-silica reaction (ASR), its mechanism is still not explicitly understood due to the difficulties to monitor the reaction and to characterize the tiny amount of ASR products in concrete. In this study, ASR products are synthesized using samples with initial Ca/Si ratio of 0.3 and Na/Si ratios of 0, 0.25, 0.5, 0.75 and 1 and equilibrated for 90 days in the presence of a surplus of water at 80 °C. The obtained reaction products are dried and subsequently characterized by X-ray powder diffraction (XRD) and thermogravimetric analysis (TGA). The pH and chemical composition of the solution for each sample are also measured by pH meter and ion chromatography (IC). The results show that calcium-silicate-hydrate (C-S-H) is formed at low and very high $\text{Na}_{\text{initial}}/\text{Si}$ ratios (i.e., 0, 0.25 and 1) at a Ca/Si ratio of 0.3. With the same Ca/Si ratio, crystalline ASR products, namely Na-shlykovite which has similar XRD pattern as K-shlykovite, are formed at the intermediate Na/Si ratios of 0.5 and 0.75. The calculated saturation indices with respect to C-S-H and amorphous silica are generally consistent with the phases precipitated as seen from XRD. Mass balance calculations indicated a Ca/Si from 0.3 to 0.5 and a Na/Si from 0.2 to 0.3 in the solid phase for the samples where Na-Shlykoveite was the main solid. The good agreement of these molar ratio with those observed in field samples of ASR products tentatively indicates that the obtained shlykovite-like phase could be in fact a synthetic proxy for ASR products.

Keywords: alkali-silica reaction, shlykovite, C-S-H, saturation index,

1. INTRODUCTION

Alkali-silica reaction (ASR) causes expansion and cracking of concrete as a result of reaction between the reactive SiO_2 from the aggregates with alkalis and hydroxide ions from the pore solution in presence of calcium ions. The ASR products within aggregates are composed predominantly of silicon, alkalis and calcium with atomic ratios of $(\text{Na}+\text{K})/\text{Si} \sim 0.25$ and $\text{Ca}/\text{Si} \sim 0.25$ [1–3], while the morphology of the ASR products vary depending on the locations where they are formed. The ASR products formed in the interior

of an aggregate particle are predominantly crystalline with plate like morphology, whereas reaction products along particle edges and in cement paste cracks are mostly amorphous [4]. Formation of ASR products has been reported to be influenced by many factors such as the reactivity of the aggregates, alkali concentration, type of alkalis, presence of calcium and aluminum and lithium ions [5]. Although ASR was reported first time in 1940's and is investigated since many decades, the precise mechanisms of the reaction are still not well understood due to difficulties to monitor the reaction in situ and to characterize the reaction product within concrete. Due to this lack of the in-depth knowledge, predictions of the occurrence and kinetics of the ASR and the resulting expansion within concrete are difficult. In this study, the effect of the Na/Si ratio on synthetic ASR product is studied. The saturation indices with respect to C-S-H and amorphous silica are also calculated to understand under which conditions rather ASR products than C-S-H is formed.

2. EXPERIMENTAL

2.1 Materials and sample preparations

Samples with a constant molar Ca/Si of 0.3 and varying Na/Si ratios of 0, 0.25, 0.5, 0.75 and 1 were synthesized by mixing appropriate quantities of SiO₂ (hydrophilic silica, surface area 200 m²/g, from EVONIK industries) with CaO (obtained by burning calcium carbonate for 12 h at 1000 °C) and analytical NaOH pellet as shown in Table 1. Higher water/solid ratios were applied for samples with lower Ca/Si ratios of 0 and 0.25 in order to well disperse the solids in the slurry. All samples were prepared in Teflon bottles in a N₂ filled glove box to minimize CO₂ contamination. Samples were reacted in an incubator at 80 °C for 90 days prior to filtration. Afterwards, roughly 5 mL solution was obtained by filtration of the samples using paper filters with mesh size of 20 µm. The obtained solution was immediately filtered with 0.45 µm syringe filter for pH measurements and analysis of the solution compositions. The solids were rinsed first with approximately 50 mL of 1:1 water-ethanol solution and then with 50 mL 94% ethanol solution in the N₂ filled glove box. The obtained solids were then vacuumed dried for 7 days, and stored in N₂ filled desiccators with CO₂ absorbent to prevent carbonation.

Table 1: Starting materials and mix proportions for the samples.

Sample	Ca/Si	Na/Si	SiO ₂ (am)	CaO	NaOH	H ₂ O	w/s	NaOH
	-	-	g	g	g	g	-	mM
C _{0.3} N ₀ S	0.3	0	4.0000	1.1200	0.0000	100	19.5	0
C _{0.3} N _{0.25} S	0.3	0.25	4.0000	1.1200	0.6657	100	17.3	166
C _{0.3} N _{0.5} S	0.3	0.5	4.0000	1.1200	1.3315	60	9.3	555
C _{0.3} N _{0.75} S	0.3	0.75	4.0000	1.1200	1.9972	60	8.4	832
C _{0.3} N ₁ S	0.3	1	4.0000	1.1200	2.6629	60	7.7	1110

2.2 Methods

The pH measurements were carried out immediately after filtration using a small fraction of the filtrated solution at room temperature (23 °C) with a Knick pH meter (pH-Meter 766) equipped with a Knick SE100 electrode. Another part of filtrated solution was diluted with MilliQ water in ratios of 1:10, 1:100 and 1:1000 immediately after filtration and used for ionic chromatography (IC) analysis.

Saturation indices with respect to amorphous silica and C-S-H were calculated based on the measured concentrations in the solutions using the thermodynamic modelling GEMS together with the Cemdata18 database using the CSHQ model for C-S-H [6].

X-ray powder diffraction (XRD, PANalytical X'pert Pro) with $\text{CoK}\alpha$ radiation was used to identify the formation of the different phases. Thermogravimetric analysis (TGA/DTA) was done with a Mettler Toledo TGA/SDTA 8513 on 10 to 30 mg samples using a heating rate of 20 °C/min from 30 to 980 °C.

3. RESULTS AND DISCUSSION

3.1 Phase assemblages

The powder X-ray diffraction (XRD) patterns of the samples with different initial Na/Si ratios after 90 days of reaction are shown in Figure. 1. The results show that the major phase formed in samples with relative low ($\text{Na}_{\text{total}}/\text{Si} = 0$ and 0.25) and very high sodium content ($\text{Na}_{\text{total}}/\text{Si} = 1$) are C-S-H. Some amorphous silica remains unreacted in samples with lower Na/Si, with its intensity at $26^\circ 2\theta$ decreases with increasing Na/Si ratio. At high Na/Si of 1, no unreacted silica but traces of natrite (PDF# 98-006-8104) is observed indicating a slight carbonation of the solution. The results obtained from thermogravimetric analysis (TGA) on the studied samples are shown in Figure 2. These data confirm the presence of C-S-H in the samples with Na/Si ratios of 0, 0.25 and 1 as visible by the gradual loss of weight observed from 30°C up to 400 °C.

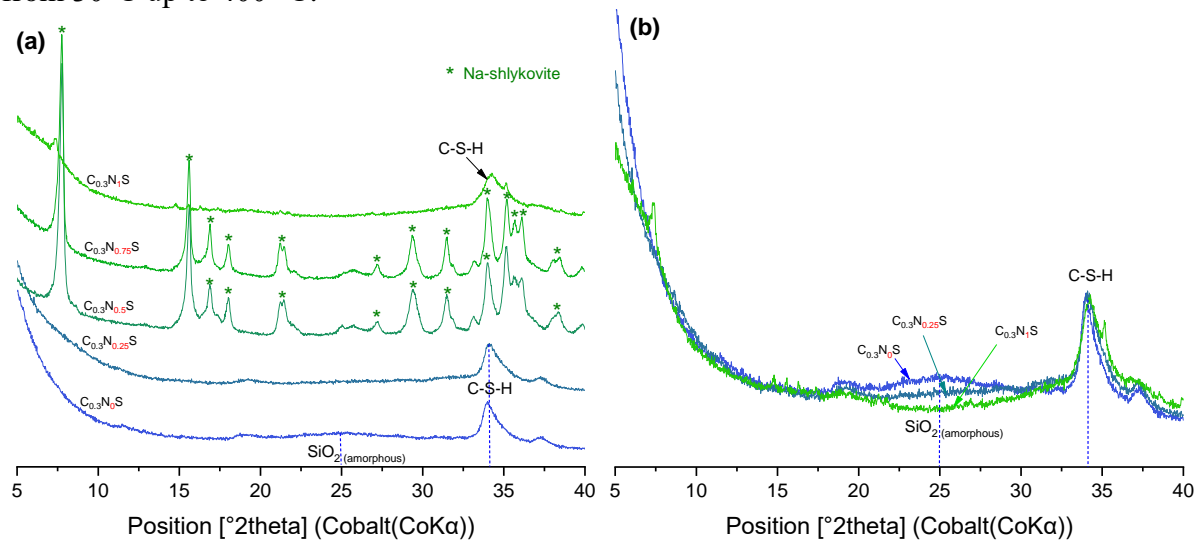


Figure 1: XRD patterns for the samples with different Na/Si ratios showing (a) effect of Na/Si ratio on phase precipitations; (b) effect of Na/Si on unreacted amorphous silica, replotted with the same data as in Figure 1(a).

The formation of a phase with high crystallinity is observed in samples with intermediate Na/Si ratios, i.e., 0.5 and 0.75. Comparison of the XRD patterns of this phase with that of K-shlykovite ($\text{KCa}[\text{Si}_4\text{O}_9(\text{OH})]\cdot 3\text{H}_2\text{O}$) observed in nature [7], shows a high similarity of the basal spacing (13 Å) and several other reflections. This observations suggests that this phase (namely Na-shlykovite reported first time in this study) may have a similar structure to K-shlykovite, which has a layered silicate structure with its SiO_4^{4-} tetrahedron charge balanced by K^+ and Ca^{2+} in the main layer and by OH^- attached to the interlayer [8].

The TGA shows multi-step weight loss for the samples with formation of Na-shlykovite at intermediate Na/Si ratios of 0.5 and 0.75. The weight losses observed up to 200 °C indicate the presence of free water and loosely bound water as well visible in DTG curves of these samples. The further weight loss observed between 250 and 400°C indicates towards water loss from hydroxyl groups present in the main layer of the shlykovite structure. AFm phases, common in hydrated cement, have a similar a layered structure and show a comparable water loss pattern: water loss of surface and interlayer water in two different weight loss areas up to 250°C and a further weight loss up to 400°C due to the dewatering of the main layer [9]. These results indicating a layered structure are in accordance with the XRD measurements, as shlykovite has an ordered layer structure.

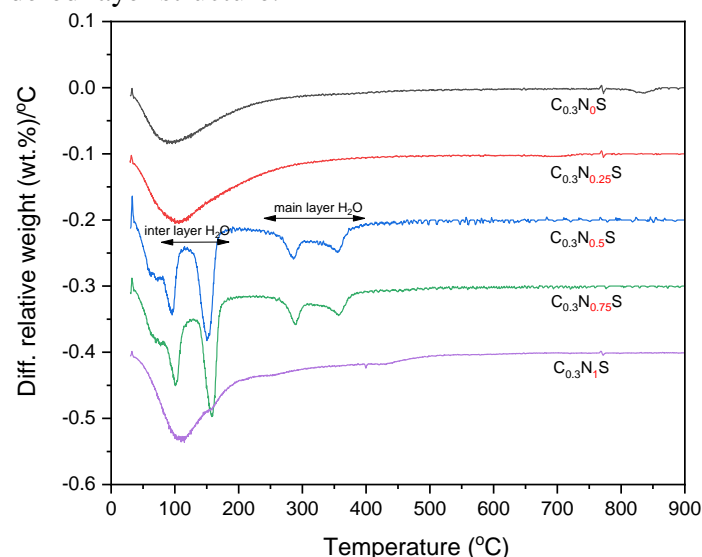


Figure 2: DTG curves of the samples with different Na/Si ratios.

3.2 Solution chemistry

The measured concentrations of Si, Ca and Na of the solutions in the supernatants together with calculated OH^- ion concentrations from the measured pH values are shown in Table 2. It is obvious that the pH of the equilibrium solution increases with increase of Na/Si ratio (or the addition of Na_2O), at the same time the Si concentration is also substantially increased with increasing pH. In contrast, the Ca concentrations are significantly reduced with increasing Na/Si ratio and pH values, in particular for samples with Na/Si ratio 0.5 and above. The results indicate that nearly all Ca in these samples has participated in the reactions to form shlykovite or C-S-H phase.

The calculated saturation indices with respect to amorphous silica and C-S-H based on the measured concentrations is also summarized in Table 2. For the sample without Na, the result

indicates that amorphous silica is nearly saturated. The saturation indices with respect to amorphous silica become more negative with increase of Na/Si ratio, which is consistent with the observation from XRD showing the decreased intensity of amorphous silica with increasing Na/Si ratio. Surprisingly the saturation indices with respect to C-S-H are all negative, even for those samples where the formation of C-S-H had been clearly seen by XRD and TGA data. This is probably related to the C-S-H model used for the thermodynamic modelling, which was not calibrated against data at higher temperatures, indicating the need for more advanced C-S-H models to be able to better take into account the effect of temperature. The samples with Na-shlykovite were all clearly undersaturated with respect to silica (consistent with its absence) and to a similar degree undersaturated with respect to C-S-H indicating the possible presence of a minor amount of C-S-H also in these samples.

The high measured Na and Si concentrations indicate also that a part of the Na and Si initially present remained in solution, such that a higher Ca/Si and lower Na/Si can be expected in the solid formed than in starting samples. In fact, mass balance calculations using the starting composition and the amount of each element in solution indicated for the C-S-H + SiO₂ containing samples a solid Ca/Si from 0.3 to 0.7 and a Na/Si from 0 to 0.3. The two shlykovite samples had a Ca/Si from 0.3 to 0.5 and a Na/Si from 0.2 to 0.3, in fact a composition similar to the composition of ASR products observed in field samples ((Na+K)/Si~0.25 and Ca/Si~0.25 [1–3]). This tentatively indicates that the obtained shlykovite-like phase could be in fact a synthetic proxy for ASR products observed in the field.

Table 2: Measured dissolved concentrations in the solutions of the samples in equilibrium and calculated saturation indices with summary of phases observed from XRD.

Sample	Si	Na	Ca	OH-	pH at 23 °C	Saturation indices		Phase Precipitated
	mM	mM	mM	mM		CSH	SiO ₂ (am)	
C-S-H	3.8	0.02	1.003	0.02	9.2	-1.6	-0.1	CSH, SiO ₂ (am)
C _{0.3} N _{0.25} S	99.2	82.0	0.321	1.48	11.2	-0.5	-0.7	CSH, SiO ₂ (am)
C_{0.3}N_{0.5}S	442.3	382.3	0.075	6.07	11.7	-1.0	-1.5	Na-shlykovite
C_{0.3}N_{0.75}S	427.3	632.1	0.013	90.57	12.9	-1.1	-2.7	Na-shlykovite
C _{0.3} NS	659.0	987.4	0.022	138.8	13.1	-0.8	-2.9	CSH

Further detailed analysis of the structure and composition of these samples and similar samples containing K are ongoing, with the aim to develop thermodynamic data for such proxies of ASR products.

4. CONCLUSIONS

In this study, the effect of Na/Si ratio on the formation of ASR products is investigated in synthetic ASR products at a constant Ca/Si ratio of 0.3. Based on the results the following conclusions can be drawn:

- Calcium-silicate-hydrate is formed at both low and very high $\text{Na}_{\text{initial}}/\text{Si}$ ratios (i.e., 0, 0.25 and 1) at a Ca/Si ratio of 0.3. The reaction extent of amorphous silica is enhanced with increase of Na/Si ratio and pH values between 11.7 and 13.1.
- The calculated saturation indices based on the measured dissolved concentration in the solutions with respect to C-S-H and amorphous silica is generally consistent with the phases precipitated as seen from XRD.
- Na-shlykovite is only observed at intermediate Na/Si ratios of 0.5 and 0.75 at the same Ca/Si ratio of 0.3 at pH values 11.7 and 12.9.
- Mass balance calculations indicated a Ca/Si from 0.3 to 0.5 and a Na/Si from 0.2 to 0.3 consistent with molar ratio observed in field samples of ASR products.
- This tentatively indicates that the obtained shlykovite-like phase could be in fact the synthetic proxy for ASR products observed in the field.

ACKNOWLEDGEMENTS

The authors would like to thank the SNF Singergia: Alkali-silica reaction in concrete (ASR), grant Number CRSII5_17108 and the European Union's Horizon 2020 research and innovation programme under the Marie Skłodowska-Curie grant agreement number 754364.

REFERENCES

- [1] T. Katayama, Petrographic study of the alkali-aggregate reactions in concrete, Grad. Sch. Sci. Univ. Tokyo, Dep. Earth Planet. Sci. (2012).
- [2] A. Leemann, P. Lura, E-modulus of the alkali-silica-reaction product determined by micro-indentation, *Constr. Build. Mater.* 44 (2013) 221–227.
- [3] A. Leemann, T. Katayama, I. Fernandes, M.A.T.M. Broekmans, Types of alkali-aggregate reactions and the products formed, *Proc. Inst. Civ. Eng. Mater.* 169 (2016) 128–135.
- [4] A. Leemann, Raman microscopy of alkali-silica reaction (ASR) products formed in concrete, *Cem. Concr. Res.* 102 (2017) 41–47.
- [5] J. Lindgård, Ö. Andiç-Çakır, I. Fernandes, T.F. Rønning, M.D.A. Thomas, Alkali-silica reactions (ASR): literature review on parameters influencing laboratory performance testing, *Cem. Concr. Res.* 42 (2012) 223–243.
- [6] B. Lothenbach, D. Kulik, T. Matschei, M. Balonis, L.G. Baquerizo, B.Z. Dilnesa, G.D. Miron, D. Myers, Cemdata18: A thermodynamic database for hydrated Portland cements and alkali-activated materials, *Cem. Concr. Res.* (2018) in press.
- [7] I. V Pekov, N. V Zubkova, Y.E. Filinchuk, N. V Chukanov, A.E. Zadov, D.Y. Pushcharovsky, E.R. Gobechiya, Shlykovite $\text{KCa}[\text{Si}_4\text{O}_9(\text{OH})]\cdot 3\text{H}_2\text{O}$ and cryptophyllite $\text{K}_2\text{Ca}[\text{Si}_4\text{O}_{10}]\cdot 5\text{H}_2\text{O}$, new mineral species from the Khibiny alkaline pluton, Kola peninsula, Russia, *Geol. Ore Depos.* 52 (2010) 767–777.
- [8] N. V Zubkova, Y.E. Filinchuk, I. V Pekov, D.Y. Pushcharovsky, E.R. Gobechiya, Crystal structures of shlykovite and cryptophyllite: comparative crystal chemistry of phyllosilicate minerals of the mountainite family, *Eur. J. Mineral.* 22 (2010) 547–555.
- [9] Z. Shi, M.R. Geiker, K. De Weerd, T.A. Østnor, B. Lothenbach, F. Winnefeld, J. Skibsted, Role of calcium on chloride binding in hydrated Portland cement–metakaolin–limestone blends, *Cem. Concr. Res.* 95 (2017) 205–216. doi:10.1016/j.cemconres.2017.02.003.

ANALYTICAL MODELLING TO DESCRIBE ALKALI-AGREGATE REACTION (AAR) INDUCED EXPANSION

N. Goshayeshi (1), L. F. M. Sanchez (1), A. C. D. Santos (1), R. Gorga (1)

(1) Department of Civil Engineering, University of Ottawa, Canada

Abstract

Alkali aggregate reaction (AAR) is one of the most harmful distress mechanisms affecting the durability of aging concrete structures worldwide. Currently, there is a need to forecast the future behaviour of AAR-affected concrete and thus analytical and numerical models have been developed over the years. Larive developed an analytical model able to describe the behaviour of concrete specimens in the laboratory. This model has been widely accepted and used by AAR community, even to predict the behaviour of concrete structures in the field. Larive's model is based upon three main parameters, and although they are normally set according to the given concrete mixture/structure under analysis, there is currently a lack of understanding on the variation of those parameters as a function of the initial potential reactivity of the material. This work aims to calibrate Larive's equation according to the aggregates type and reactivity so that predictions may be performed based on the reactive potential of the mix. First, a comprehensive laboratory testing campaign using a variety of concrete strengths and aggregate types is conducted. Second, Larive's model is matched with laboratory data and a discussion on the main parameters of the equation is performed. Finally, the model is used to appraise the expansive behaviour of blocks containing the same mix-design and reactive aggregates exposed outdoors in Ottawa, Canada.

Keywords: Alkali-aggregate reaction (AAR), Analytical model, Forecasting AAR-induced expansion, Aggregate type and reactivity.

1. INTRODUCTION

Alkali aggregate reaction (AAR) is a chemical reaction between some unstable silica mineral forms found within fine and coarse aggregates used to make concrete and the alkali hydroxides (Na, K – OH) from the concrete pore solution [1]. This reaction generates a gel that swells upon water uptake from the surroundings, leading to volumetric expansion and damage. AAR is one

of the most harmful distress mechanisms affecting the performance (i.e. durability and serviceability) of aging concrete structures worldwide [2]. AAR can be divided in two distinct mechanisms: alkali-silica reaction (ASR) and alkali-carbonate reaction; ASR being by far the most common mechanism found around the globe.

Various factors may affect AAR-induced expansion and damage such as the alkali loading, the reactivity of the aggregates, environmental conditions such as temperature, humidity, exposure, etc. [3]. Forecasting AAR-induced expansion and damage along with its consequences is extremely challenging. A number of analytical and numerical models have been developed over the years and amongst those, Larive's model [4] is widely accepted by AAR community [4]–[7]. It was developed to describe the behaviour of concrete specimens in the laboratory but has been used even to forecast the behaviour of concrete structures in the field. Larive's model is based upon three main parameters: latency and characteristic time and expansion at infinity, and although they have been set according to the given concrete mixture/structure under analysis, there is currently a lack of understanding on the range of those parameters as a function of the reactive potential of a given concrete mix [8].

2. LITERATURE REVIEW

Larive [4] developed an analytical model to describe the reactive behaviour of AAR affected concrete specimens in the laboratory. Larive has worked with over 600 specimens that were subjected to a wide range of environmental and mechanical conditions. Larive's research program focused on the influence of temperature, relative humidity and stress-state on AAR reaction kinetics and development [9]. In Larive's model, AAR kinetics is assumed to be a function of the latency (τ_l) and characteristic (τ_c) times for a given time and an independent stress-state (Figure 1). This model describes a nonlinear time-dependent AAR swelling behavior (normally an S-shape curve) as a function of the final expansion level (i.e. expansion expected to happen at infinity; i.e. $t=\infty$), as presented hereafter [4]:

$$\varepsilon(t, \theta) = \frac{1 - e^{-\frac{t}{\tau_c(\theta)}}}{1 + e^{-\frac{(t - \tau_l(\theta))}{\tau_c(\theta)}}} \times \varepsilon^\infty \quad (1)$$

Where θ is the absolute temperature, τ_c , τ_l are the characteristic and latency time respectively, and ε^∞ is the maximum expansion at infinity [5]. The S-shape curve proposed by Larive's model may be divided into four categories. First, there is a period of AAR gel formation and accommodation within the aggregate particles where almost no expansion is generated. Second, AAR-gel uptakes water and the swelling process starts with almost no cracking formation (up to the inflexion point). Third, cracks are formed within the aggregate particles and surrounding cement paste which makes the expansion rate to decrease over time. Finally, either all of the alkalis or silica (or both) is consumed (which normally happens due to the presence of leaching in laboratory test procedures) and thus there is a levelling off trend of AAR expansion.

3. SCOPE OF THE WORK

Larive's model was primarily developed to describe the behaviour of reactive concrete mixtures in the laboratory. Although very interesting and widely accepted by AAR community, this model does not account for some of the most important physicochemical parameters that influence the chemical reaction such as aggregates type (fine vs coarse), reactivity (low, moderate, high and very high), alkali loading, temperature and relative humidity. This work aims to incorporate two of the prior mentioned parameters (i.e. aggregate type and reactivity) to Larive's initial equation. Therefore, the main parameters of Larive's model (τ_l and τ_c) will be calibrated according to the aggregate's type and reactivity of mixtures incorporating a wide range of reactive aggregates and presenting distinct mechanical properties, so that one may predict AAR expansive behaviour in the laboratory whether the aggregate used in the mix is known. At the end, the model will be applied to forecast the behaviour of blocks exposed outdoors presenting the same aggregates and mix-design as the ones assessed in the laboratory.

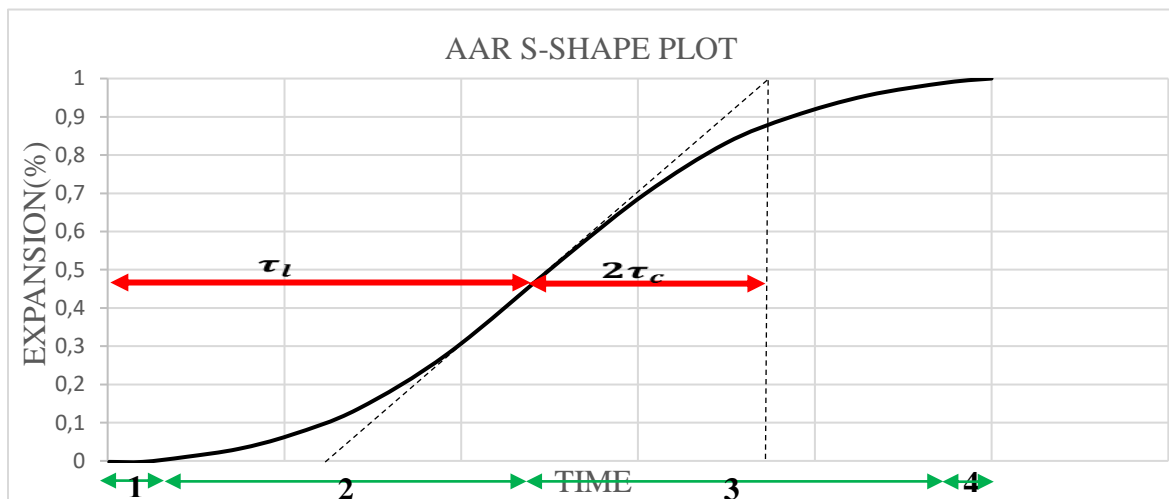


Figure 1: S-shape AAR-induced expansion plot [4].

4. MATERIALS AND METHOD

A number of concrete mixtures incorporating a wide range of reactive aggregates and presenting distinct mechanical properties (i.e. 25, 35, and 45 MPa) were selected for this research as per [10] and illustrated in Table 1. The size of coarse aggregates used ranged from 5 to 20 mm. Non-reactive coarse and fine aggregates were used in combination with the reactive materials for concrete manufacturing. Third-five specimens from each of the concrete mixtures were fabricated and stored at the moist-curing room for 48h. Afterwards, the zero-length reading was taken, and all the samples were then placed in sealed buckets (4 specimens per bucket) and stored at 38°C and 100% R.H. All the specimens were regularly monitored over time until they had their expansion levels stabilized (i.e. three consecutive measurements with no further expansion). They were then classified in terms of reactivity according to [10] and highlighted in Table 2.

Following the experimental tests and results, all the data acquired in the laboratory was used to calibrate Larive's model so that various latency and characteristic times for the different

aggregate types and reactivity levels could be obtained. Finally, the latency and characteristic times gathered from the laboratory results were used to evaluate the behaviour of concrete blocks fabricated using similar aggregates and concrete mixtures and exposed outdoors in Ottawa, Canada [11]. Table 3 shows the two different blocks selected to be used in this research and their respective expansion levels after 10 and 15 years of exposure.

Table 1: Aggregates used in this research. U = USA, C = CANADA, B = Brazil

Aggregate		Reactivity	Location	Rock type	Specific gravity	Absorption	AMBT* 14-day exp (%)
Coarse	K**	R	Kingston (C)	Dolomitic argillaceous limestone	2.69	0.55	0.110
	NM	R	New Mexico (U)	Polymictic Gravel (Mixed Volcanic, quartzite, chert)	2.53	1.59	1.056
	QC	R	Quebec (C)	Siliceous and argillaceous limestone	2.50	1.16	0.302
	Wyo	R	Wyoming	Granite, amphibolite, mixed volcanic	2.64	0.87	0.296
	Conor	R	Halifax (C)	Metagreywacke, shale, siltstone	2.72	0.37	0.365
	Virg	R	Virginia (U)	Metagranite	2.78	0.45	0.090
	Rec	R	Recife (B)	Granite, gneiss, mylonite	2.64	0.59	0.230
	Pots	R	Montreal (C)	Siliceous sandstone (orthoquartzite)	2.57	1.15	0.093
	Dia	NR	Quebec (C)	Diabase (plutonic rock)	3.00	0.51	0.065
	Hp	NR	Newfoundland (C)	High-purity fine-grained limestone	2.68	0.44	0.001
Fine	Tx	R	Corpus Christi (U)	Polymictic sand (granitic, mixed volcanic, quartzite, chert, quartz)	2.60	0.55	0.755
	Wt	R	Texas (U)	Polymictic sand (chert, quartz, feldspar)	2.60	0.4	0.335
	Lav	NR	Quebec (C)	Natural derived from Granite	2.71	0.54	0.068

*AMBT: Accelerated Mortar Bar Test

** Material susceptible to alkali-carbonate reaction (ACR)

Table 2: Classification of the AAR-induced damage degree as per [12].

ASR damage degree	Reference expansion level (%)
Negligible	0.00 - 0.03
Marginal	0.04 ± 0.01
Moderate	0.11 ± 0.01
High	0.20 ± 0.01
Very high	0.30 ± 0.01

Table 3: Aggregates used to fabricate the concrete blocks as per [11].

Type	ID	Reactivity level	Origin	Rock type
coarse	Sp	High	Canada	Siliceous Limestone
coarse	Pots	High	Canada	Siliceous Sandstone

5. RESULTS

Figure 2 shows the calibration of Larive's expansion curves over time to match the results gathered through the concrete prism test (CPT – 38°C and 100% R.H) in the laboratory for all the mixtures studied in this research. As one may notice, the expansive behaviour of the distinct mixes may be classified into three categories: ACR reactive aggregate presenting the fastest expansion kinetics and level; ASR reactive fine aggregates showing a slightly lower reaction kinetics and expansion level when compared to the ACR reactive aggregate and; ASR reactive coarse aggregates which present a much slower reaction kinetics and level when compared to the previous discussed mixtures. Table 4 displays the latency and characteristic times obtained for these three categories.

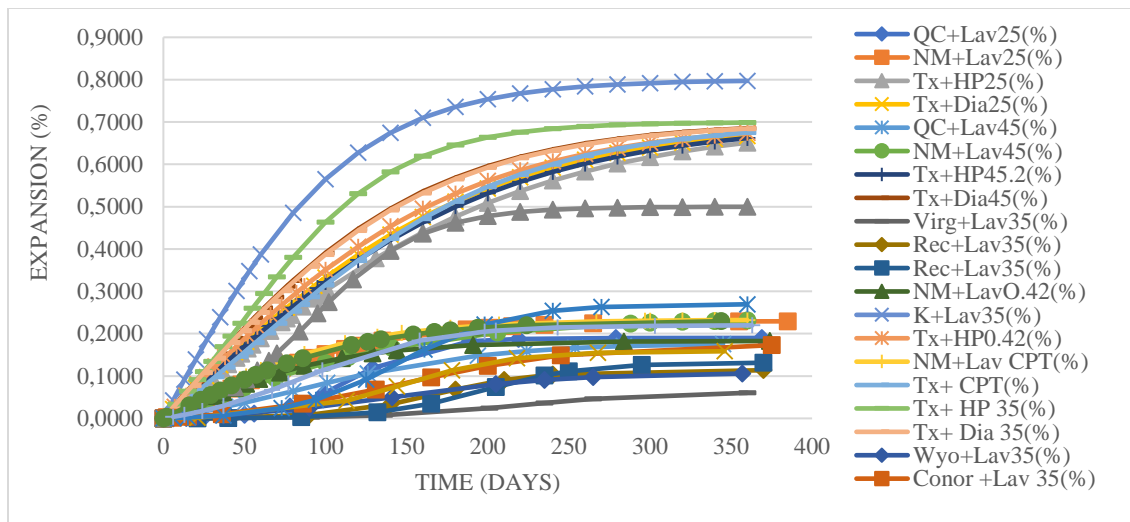


Figure 2: Expansion vs time for various concrete mixtures and aggregate types and natures.

6. DISCUSSION

In this section, the results previously gathered in the calibration of Larive's model will be further discussed and an evaluation of their capacity to appraise blocks exposed to the environment over 15 years will be performed.

In order to assess concrete materials/structural members in service, AAR-accelerated laboratory test procedures need to "represent" the reactive behaviour of a given mix in the field throughout its service life. It is widely known that the latter is unfortunately not necessarily true and thus the correlation "laboratory vs field" is currently a very important topic for AAR community. Otherwise, it has been found that the concrete prism test (CPT), performed at 38°C and 100% R.H., is the test procedure that most resembles field conditions and thus, although not perfect, might be used as benchmark for the reactive potential of a given mix in the field,

especially when mitigation products such as supplementary cementing materials (SCMs) are not used in the concrete mixture. Therefore, in this work it is assumed for the sake of analysis that the 1-year CPT result represents the potential reactivity of a given concrete mixture in the field throughout its service life (i.e. ≈ 50 years). It is worth noting that potential reactivity does not directly mean expansion attained to date but rather the likelihood of the expansion level over time of a given mix whether proper conditions are provided to AAR development.

Table 4: Latency and characteristic times for the different categories of expansion.

AAR mechanism	Damage degree	τ_c	τ_l	Ultimate expansion at infinity (%)
ACR-Reactive coarse	Very High	57	0.00	0.80
ASR-Reactive fine	Very High	93	0.00	0.70
	High	34	146	0.20
ASR-Reactive coarse	High	61	0.00	0.20
	Moderate	39	135	0.11
	Marginal	49	181	0.04

6.1 AAR kinetics and development

From Figure 2 and Table 4 one may notice that the faster AAR kinetics, the lower τ_l , which may be sometimes zero for fast kinetics mechanisms such as ACR along with ASR fine and coarse with very high damage degree. The latter physically means that there is almost no accommodation of the reaction products and thus the swelling process starts right away from the beginning. Moreover, the values of τ_c for fast kinetics mechanisms are significantly higher than the slower reactive mechanisms and mixtures, which means that they are not only faster but also present a higher expansive behaviour (i.e. expansion amplitude) at infinity. The τ_l values ranged from 0 to 181 whereas the τ_c results ranged from 34 to 93.

6.2 Comparison with blocks exposed outdoors

Fournier et al [11] fabricated unreinforced concrete blocks (i.e. 400 by 400 by 700 mm), incorporating a wide range of reactive aggregates and mix-designed as per ASTM 1293 (concrete prism test mix – CPT). These blocks were then stored outdoors in Ottawa (Canada and have been exposed to Canadian climatic conditions and monitored over 15 years. In this work, two reactive aggregates (Sp, very similar lithotype and reactivity to QC and Pots – Table 1) with known behaviour in the laboratory and monitored in the field at 10 and 15 years were selected for further analysis and comparison. Figure 4 illustrates two expansion curves plotted for respectively Pots (Figure 4a) and Sp (Figure 4b) aggregates.

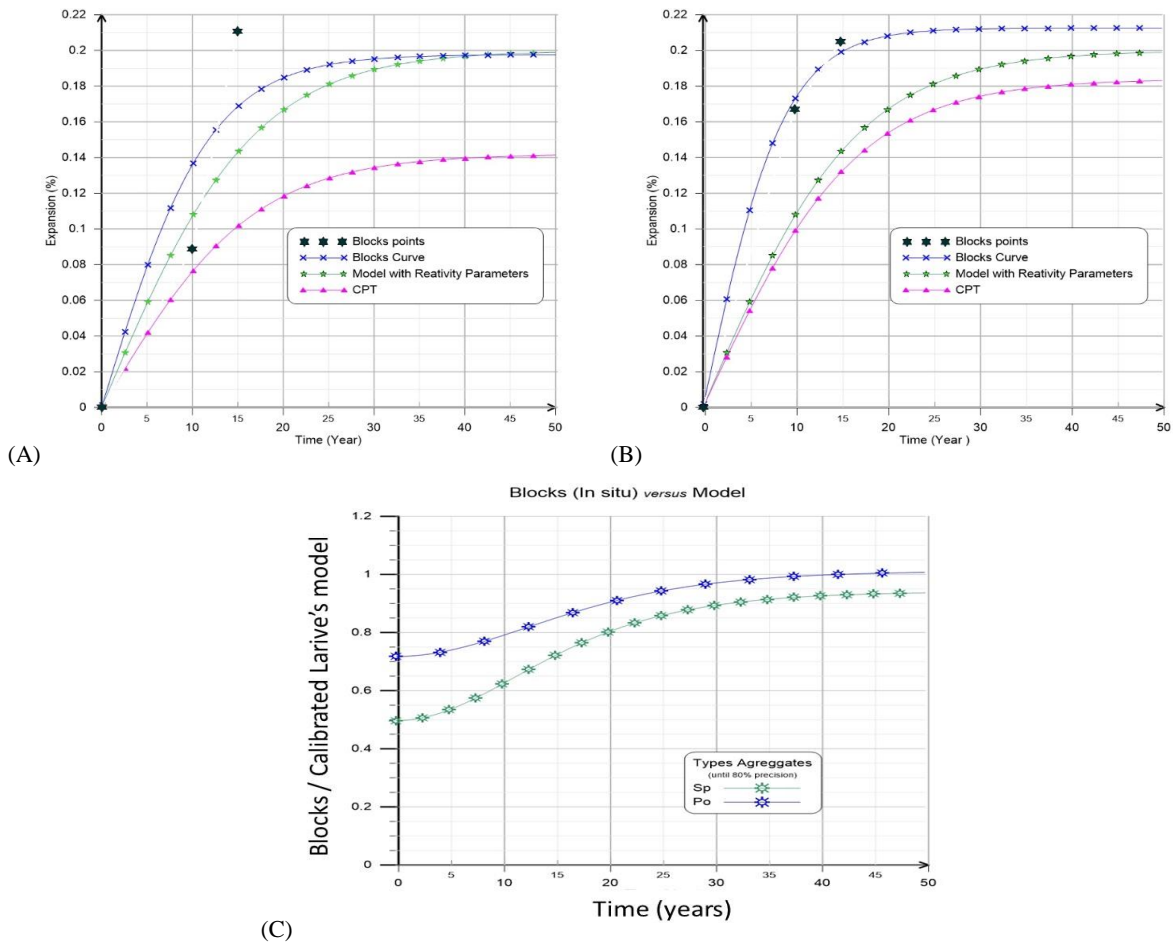


Figure 4: Comparison amongst blocks exposed outdoors (blue curve), CPT performed in the laboratory (pink curve) and calibrated Larive's model (green curve) for a) Pots and, b) Sp.
 Figure 4c illustrates the blocks to Larive's equation expansion ratio over time.

First, Larive's equation was used to best fit the blocks measurements taken at 10 and 15 years (blue curve). Second, the concrete prism test (CPT) was performed in the laboratory presenting the same aggregates and mix-design as the ones used in the blocks (pink curve). Third, Larive's model was used and the τ_l and τ_c parameters obtained in Table 4 were selected accounting for the aggregates type and reactivity to forecast the behaviour of the blocks made with similar aggregates in the field. The values adopted for τ_l and τ_c were 0 & 61 and 39 & 135 for Sp and Pots, respectively. Comparing the results in the plots, one verifies that the blocks expansive behaviour seems to be much higher than the results obtained in the CPT. The latter is very likely due to imperfections in the CPT test procedure such as leaching, which may take place due to the small size of the samples used in the test (i.e. 75 by 75 by 285 mm) and thus may inhibit the concrete mixture to achieve its reactive potential in the laboratory.

Conversely, forecasting the blocks through the use of Larive's model incorporating the calibrated τ_l and τ_c seems to yield much closer values than the ones measured in the field. Figure 4c shows the blocks-to-Larive's model expansion ratio accounting for the aggregates type and reactivity. It is possible to see that the model forecasts the blocks expansion with a

level of accuracy higher than 90% at 15 years which seems promising. Yet, it is worth noting that all the above is only true whether the initial assumption of Larive's model (i.e. 1-year CPT value obtained in the laboratory represents the reactive potential concrete mixtures throughout their life span in the field) is adopted.

7. CONCLUSION

In this research, the original Larive's model was calibrated using data gathered in the laboratory. The idea of the latter was to introduce a physicochemical meaning to Larive's model whether the aggregate's type and reactivity is known. The results obtained highlighted the capacity of the model to forecast both the behaviour of specimens in the laboratory and in the field. Yet, further assessment is still needed to evaluate the reliability of the proposed model with a wider range of exposed members under distinct climatic conditions. Moreover, there is an interest of adding further physicochemical parameters to the analytical model such as the alkali loading, temperature and relative humidity so that the analysis might be more comprehensive.

REFERENCES

- [1] L. F. M. Sanchez, B. Fournier, M. Jolin, and J. Bastien, "Evaluation of the Stiffness Damage Test (SDT) as a tool for assessing damage in concrete due to alkali-silica reaction (ASR): Input parameters and variability of the test responses," *Constr. Build. Mater.*, vol. 77, pp. 20–32, 2015.
- [2] F. Pesavento, D. Gawin, M. Wyrzykowski, B. A. Schrefler, and L. Simoni, "Modeling alkali-silica reaction in non-isothermal, partially saturated cement based materials," *Comput. Methods Appl. Mech. Eng.*, vol. 225–228, pp. 95–115, 2012.
- [3] L. F. M. Sanchez, B. Fournier, M. Jolin, and J. Duchesne, "Reliable quantification of AAR damage through assessment of the Damage Rating Index (DRI)," *Cem. Concr. Res.*, vol. 67, pp. 74–92, 2015.
- [4] C. Larive, "Apports combinés de l'experimentation et de la modélisation à la compréhension de l'alkali-réaction et de ses effets mécaniques," 1998.
- [5] V. Saouma and L. Perotti, "Constitutive model for alkali-aggregate reactions," *ACI Mater. J.*, vol. 103, no. 3, pp. 194–202, 2006.
- [6] M. C. R. Farage, J. L. D. Alves, and E. M. R. Fairbairn, "Macroscopic model of concrete subjected to alkali-aggregate reaction," *Cem. Concr. Res.*, vol. 34, no. 3, pp. 495–505, 2004.
- [7] R. Esposito and M. A. N. Hendriks, "Literature review of modelling approaches for ASR in concrete : a new perspective," *Eur. J. Environ. Civ. Eng.*, vol. 8189, no. December, pp. 1–21, 2017.
- [8] C. Larive, "Combined contribution of experiments and modelling to the understanding of alkali-aggregate reaction and its mechanical consequences (PhD thesis; in: French)," 1998.
- [9] A. Winnicki and S. Pietruszczak, "On Mechanical Degradation of Reinforced Concrete Affected by Alkali-Silica Reaction," *J. Eng. Mech.*, vol. 134, no. 8, pp. 611–627, 2008.
- [10] L. F. M. Sanchez, B. Fournier, M. Jolin, D. Mitchell, and J. Bastien, "Overall assessment of Alkali-Aggregate Reaction (AAR) in concretes presenting different strengths and incorporating a wide range of reactive aggregate types and natures," *Cem. Concr. Res.*, vol. 93, pp. 17–31, 2017.
- [11] R. Fournier, Benoit and Nkinamubanzi, Pierre-Claver and Chevrier, "Comparative Field and Laboratory Investigations on the Use of Supplementary Cementing Materials to Control Alkali-Silica Reaction in Concrete," *Proc. 12th Int. Conf. Alkali-Aggregate React.*, vol. 1, pp. 528–537, 2004.
- [12] L. Sanchez, "Contribution to the assessment of damage in aging concrete infrastructures affected by alkali-aggregate reaction," p. 341, 2014.

MICROSTRUCTURAL ANALYSIS OF ASR IN CONCRETE – ACCELERATED TESTING VERSUS NATURAL EXPOSURE

**Andreas Leemann (1), Ingmar Borchers (2), Mahdiah Shakoorioskooie (1)(3)(4),
Michele Griffa (1), Christoph Müller (2), Pietro Lura (1)(3)**

(1) Empa, Laboratory for Concrete & Construction Chemistry, Switzerland

(2) VDZ gGmbH, D 40476 Düsseldorf, Germany

(3) Institute for Building Materials (IfB), ETH Zurich, Switzerland

(4) Empa, Center for X-ray Analytics, Switzerland

Abstract

Accelerated tests are used to assess the expansion potential of concrete due to ASR. A key question in regard to such tests is the applicability of the results to concrete structures. Expansion of concrete prisms stored in accelerating conditions has been compared to the one determined for blocks produced with the same concrete and exposed to natural conditions in several studies. This allows drawing conclusions about the meaningfulness of the accelerated test. However, such comparisons usually only include length measurements. In this study, the microstructure of a specific concrete mixture produced within the framework of the PARTNER project is tested in accelerated conditions and exposed to field conditions for several years. ASR products are characterized with scanning electron microscopy and Raman microscopy. Additionally, crack patterns are analysed in 3D with X-ray computer tomography.

Keywords: concrete, alkali-silica reaction, acceleration, natural exposure, microstructure

1. INTRODUCTION

Alkali-silica reaction (ASR) is a worldwide issue for the durability of concrete structures. In order to prevent ASR in new structures, the potential reactivity of concrete mix designs has to be tested. Acceleration is achieved by using elevated temperature and relative humidity (compared with room conditions) [1-3]. Based on the testing results, the investigated mix design is approved or rejected for the use in a concrete structure. The critical point in this approach is the transferability of the results obtained to the field. The specific test conditions differ considerably to the ones in natural exposure. Therefore, several sites have been

established where concrete blocks with various mix designs are exposed to field conditions [6,7,8]. However, comparisons are usually done only in regard to length changes, neglecting the implications of ASR on the microstructure.

In this study, one particular concrete mixture produced within the framework of the PARTNER project [1,11] is exposed to both an accelerated test and natural conditions for 13 years. In addition to the length change, the composition of the reaction products and the crack pattern resulting from concrete expansion have been analysed using scanning electron microscopy (SEM) with energy-dispersive X-ray spectroscopy (EDS), Raman microscopy and X-ray tomography.

2. MATERIALS AND METHODS

2.1 Materials

Concrete (B1 (C+F)) was produced in 2004 within the framework of the PARTNER project [1], both for the accelerated test and the outdoor exposure. The cement used for the concrete production was of type CEM I 42.5 R, produced by Norcem, with a total alkali content of 1.26 mass-% Na_2O -equivalent. A cement content of 440 kg/m^3 and a water-to-cement-ratio (w/c) of 0.50 were used. The aggregate was a siliceous limestone from Belgium that has caused damage in several concrete structures such as bridges and dams or weirs. A cube ($300 \times 300 \times 300 \text{ mm}^3$) was produced for the storage in outdoor exposure and three prisms ($75 \times 75 \times 280 \text{ mm}^3$) for the accelerated testing.

In 2017, samples of the laboratory-testing sample and the field exposed sample were cut and locations of interest were identified. Areas close to the surface of the samples were discarded, as they were affected by carbonation. The samples for Raman microscopy were ground with silicon carbide coated papers. Following cleaning with pressurized air, the samples were stored in airtight plastic bags until the analysis. The samples for SEM were dried for three days at 50 °C, impregnated, polished and carbon coated.

2.2 Methods

The particular cube analysed in this study was exposed unsheltered in Valencia/Spain for 13 years.

The accelerated test used corresponds to the RILEM AAR-4.1 [2] and AFNOR P18-454 [12] standards, using a temperature of 60°C and a relative humidity of 100%. Every four weeks a length measurement was conducted, for a total duration of 20 weeks. After the test, the concrete was stored at a temperature of 20 °C and a relative humidity of 60 % for 13 years.

The Raman spectra were acquired using a Raman Bruker Senterra microscope equipped with a Peltier-cooled CCD detector and operated with the software Opus 6.5. The laser wavelength was 532 nm.

The microstructure of the concrete was analysed with a scanning electron microscope (SEM) FEI Quanta 650 using an acceleration voltage of 12 kV and a pressure of $3.0\text{--}5.0 \times 10^{-6}$ Torr. Chemical analysis was performed by energy-dispersive X-ray spectroscopy (EDS) with a Thermo Noran Ultra Dry 60 mm^2 detector and Pathfinder X-Ray Microanalysis Software.

To perform X-ray tomography with high spatial resolution (μm scale) on both the laboratory-testing sample and the field-exposed sample, smaller sub-samples from each type,

with cross-section of $10 \times 10 \text{ mm}^2$ and original height, were carefully cut out under stabilized conditions (by first embedding each sample in epoxy, used to avoid additional crack formation during cutting). X-ray tomography was carried out using an EasyTom XL tomograph produced by RX Solutions, France. The tomographic acquisition was performed at 105 keV maximum photon energy. Tomographic reconstruction was performed with a cone beam filtered back-projection algorithm implemented in the XAct software by RX Solutions. The reconstructed tomograms (3D images) have approximate spatial resolution of $20 \text{ }\mu\text{m}$. The Avizo software (Thermo Fisher ScientificTM) was used to perform image pre-processing (filtering) and crack segmentation.

3. RESULTS AND DISCUSSION.

3.1 Concrete expansion

The lab concrete expanded the fastest during the first four weeks with a continuously decreasing expansion rate afterwards (Figure 1). It reached a final expansion of 0.15% after a test duration of 20 weeks.

The exposed block continuously expanded with approximately constant rate. It reached an expansion of 0.36% after 11 years.

The decreasing expansion in the lab test confirms that leaching is a limiting factor in this type of test [9].

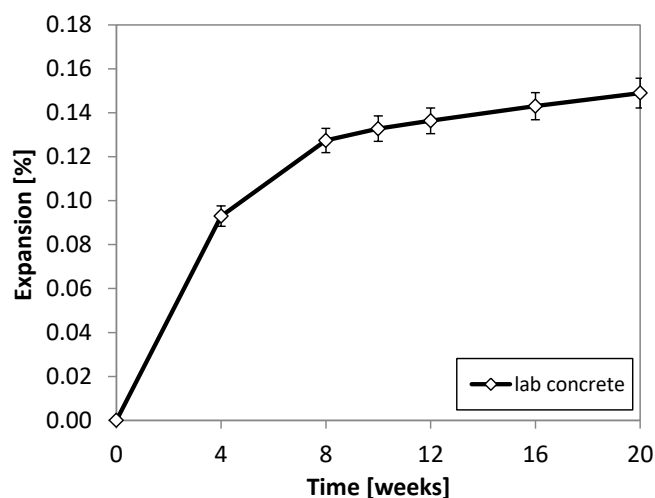


Figure 1 Expansion of concrete prisms in the accelerated test at 60°C according to RILEM AAR-4.1.

3.1 SEM

The majority of the cracks present in the aggregates of the field concrete are entirely filled with ASR products (Figure 2A). In the interior of the aggregates, the ASR products are structured and at the edge of the aggregates they are structureless. This corresponds to a crystalline material in the first case and an amorphous one in the second, as shown in [9]. The ASR product extruding into the cement paste is structureless, occasionally forming layers parallel to the crack boundaries. The chemical composition of the crystalline and amorphous products within the aggregate is essentially identical with silicon as the main components and about equal parts of calcium to alkalis (Figure 3A). The calcium concentration starts to

increase and the alkali content decreases in the area of the interfacial transition zone to the cement paste.

The ASR products in the aggregates of the lab concrete form linings along the crack walls. Only at magnification $> 1000\times$ it becomes apparent that the product is finely structured (Figure 2B). Towards the edge of the aggregates this type of product may fill the crack entirely and it gives way to a homogenous product, as already observed in the field concrete. The chemical composition of the finely-structured product is similar to the one of the field concrete, however with slightly higher calcium content and lower molar Na/K-ratio (Figure 3B). The amount of ASR product extruding into the cement paste is larger compared to the field concrete.

Although there are clear differences in the morphology of the ASR products formed in the differently-exposed concrete samples, the composition of both is in the typical range present in field structures and lab samples tested with the concrete performance test [3,9].

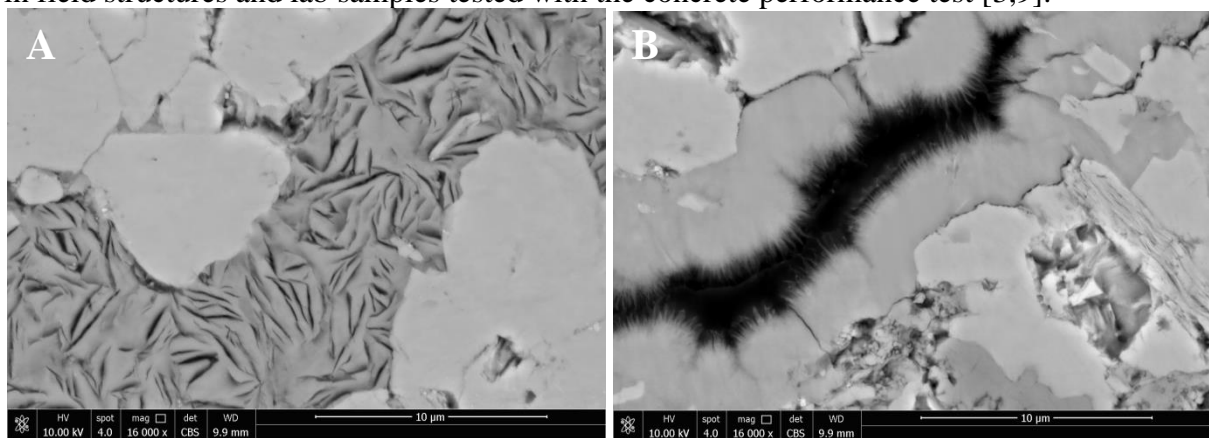


Figure 2: Crack entirely filled with structured ASR products in an aggregate of the field concrete (A) and crack partly filled with finely structured ASR product in an aggregate of the lab concrete (B). The width of the back-scattering electron images corresponds to 26 μm .

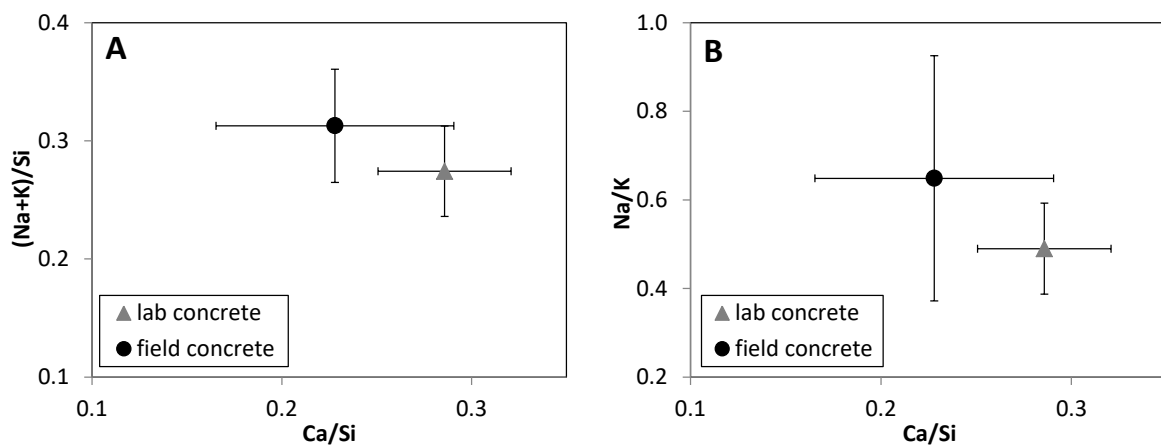


Figure 3: Molar (Na+K)/Si-ratio (A) and Na/K-ratio (B) as a function the molar Ca/Si-ratio of the structured products in the field (unsheltered exposure case) and in the lab concrete.

3.2 Raman microscopy

The Raman spectrum of the crystalline product is dominated by peaks at 602 cm^{-1} and at 1109 cm^{-1} (Figure 4). The first peak corresponds to Si-O-Si bending vibrations and the second to stretching vibration of SiO_2 -tetraedra with three bridging oxygens [9,10].

The spectrum of the finely-structured ASR product in the lab concrete is very similar, with slightly different positions of the peak maxima at 596 and 1086 cm^{-1} (Figure 4).

The spectrum of the crystalline product in the field concrete is a perfect match of the spectra recorded on crystalline ASR products from other two concrete structures [9] and can be clearly identified as a layer silicate. The similarity to the spectrum determined from the finely-structured ASR product of the lab concrete indicates that the latter has a very similar structure, also dominated by sheets of SiO_2 -tetraedra.

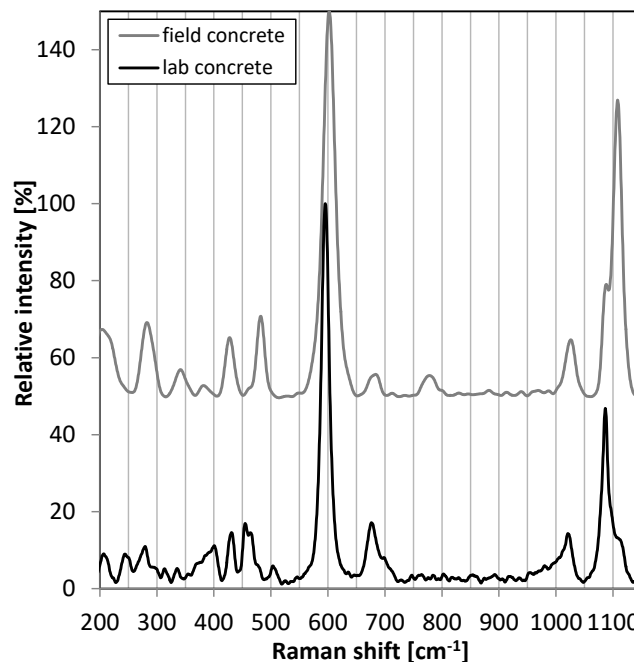


Figure 4: Raman spectra of the structured ASR products in the field and the lab concrete.

3.3 X-ray tomography

The black top-hats transform was used, along with a binary mask excluding the air voids and the sample exterior, to segment the cracks within the concrete structure (Figure 5A). The aggregates were segmented using a simple voxel value thresholding method, thanks to their uniform voxel value. The 3D renderings, comparing the crack patterns in the lab-tested samples with those in the field-exposed samples, are shown in Figure 5C and 5D, respectively. A larger amount of crack volume in the field-exposed sample compared with the lab-tested one is already perceivable visually. However, an additional crack analysis was performed to quantify the crack density within the scanned volume of the samples. The crack density (or crack volume fraction) was calculated as the total crack volume divided by the total volume of the scanned concrete. The crack density of the field-exposed sample (2.0%) is about 1.5 times more than that of the lab-tested sample (1.3%). It has to be considered that these values are based on cracks with a width above $20\text{ }\mu\text{m}$. Narrower cracks are not resolved.

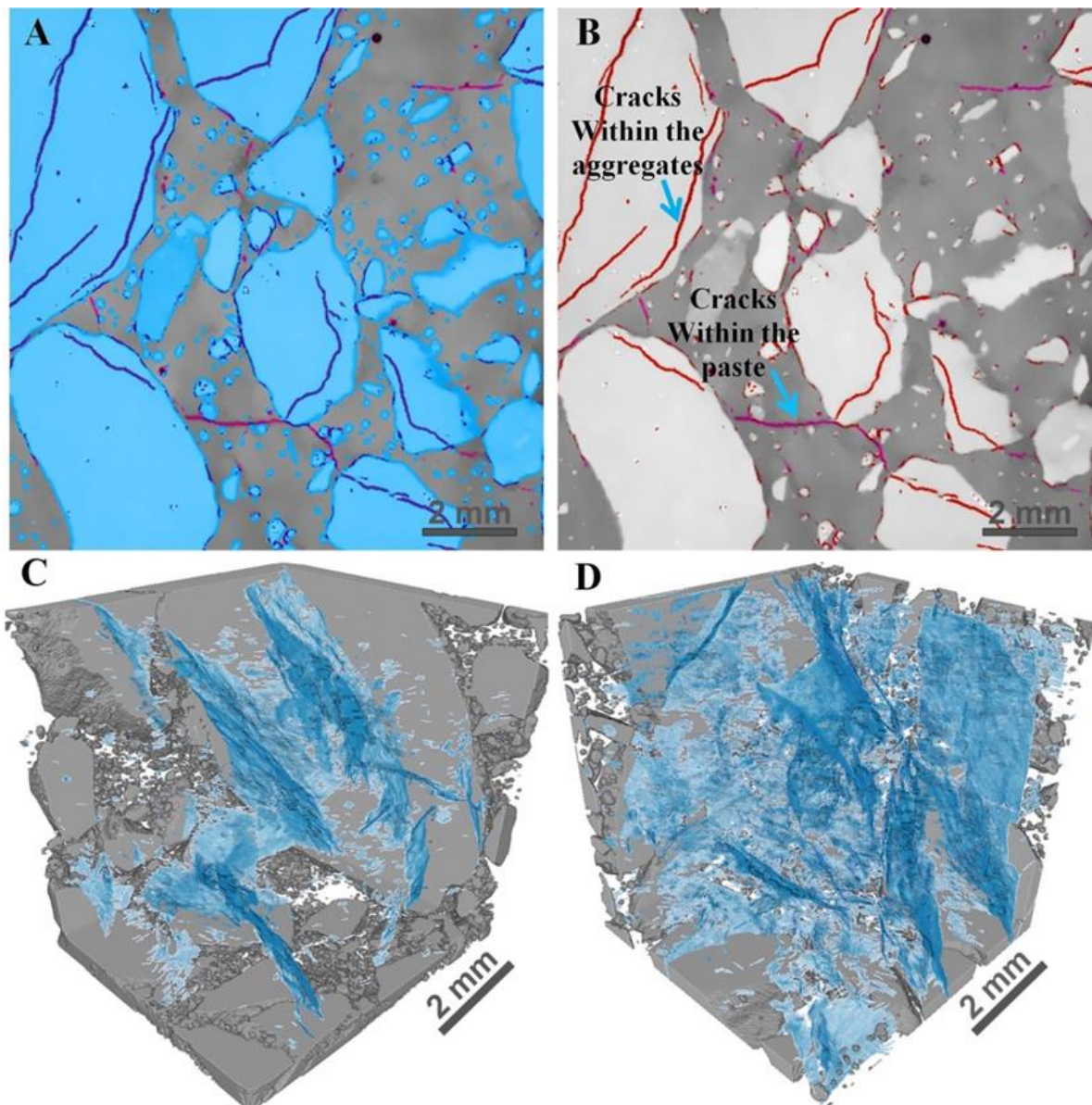


Figure 5: A close-up (A) from a selected 2D digital cross-section (“slice”) from the tomographically reconstructed volume of the field exposed concrete sample, illustrating the segmentation of the cracks (dark purple and pink) and of the aggregates (light blue); (B) same slice as in (A) but highlighting only the cracks with distinction by color between those within the aggregates (labelled in red) and the ones within the mortar matrix (labelled in pink); 3D rendering of all the cracks within the scanned volume of the lab-tested sample (C) and the field exposed sample (D). Part of the segmented aggregates is also visualized in the background of the cracks in both (C) and (D).

4. CONCLUSION

The transferability of results obtained in the laboratory-accelerated ASR test to concrete structures is an important issue in ASR prevention. The microstructural characteristics of a specific concrete mixture tested with a laboratory concrete performance test and exposed to natural conditions for several years are compared using SEM with EDX, Raman microscopy and X-ray tomography. The results allow drawing the following conclusions:

- Although the morphologies of the products formed in the field and the lab concrete differ, their chemical composition is very similar.
- The Raman spectra indicate that the ASR products formed in lab and field conditions are both dominated by sheets of SiO_2 -tetraedra and can therefore be identified as layer silicates.
- In terms of crack volumetric density, the lab-tested concrete sample exhibits smaller values than the field-exposed one.
- The microstructural characteristics of the field and the lab concrete are not identical, but very similar, indicating similar expansion mechanisms in both.

These results have to be extended by studying a larger set of concrete mixtures using a similar approach.

ACKNOWLEDGMENTS

The authors would like to thank A. M. López-Buendía (Aidico), P. Martí Martí (Aidico), E. Menéndez (Eduardo Torroja Institute), A. Santos Silva (LNEC) and J. Custódio (LNEC) for providing the sample exposed to outdoor conditions.

REFERENCES

- [1] Thomas, M., Fournier, B., Folliard, K., Ideker, J. and Shehata, M., 'Test methods for evaluating preventive measures for controlling expansion due to alkali-silica reaction in concrete', *Cem. Concr. Res.* **36** (2006) 1842-1856.
- [2] Lindgård, J., Andiç-Çakır, Ö., Fernandes, I., Rønning, T. F. and Thomas, M. D., 'Alkali-silica reactions (ASR): literature review on parameters influencing laboratory performance testing', *Cem. Concr. Res.* **42** (2012) 223-243.
- [3] Leemann, A. and Merz, C., 'An attempt to validate the ultra-accelerated microbar and the concrete performance test with the degree of AAR-induced damage observed in concrete structures', *Cem. Concr. Res.* **49** (2013) 29-37.
- [4] Fournier, B., Ideker, J. H., Folliard, K. J., Thomas, M. D., Nkinamubanzi, P. C. and Chevrier, R., 'Effect of environmental conditions on expansion in concrete due to alkali-silica reaction (ASR)', *Mater. Charact.* **60** (2009) 669-679.
- [5] Ideker, J.H., Drimalas, T., Bentivegna, A.F., Folliard, K.J., Fournier, B., Thomas M.D.A., Hooton R.D. and Rogers, C.A. 'The importance of outdoor exposure site testing', in Proceedings of the 14th International Conference on Alkali Aggregate Reactions (ICAAR), Austin, Texas (2012)
- [6] Borchers, I.; Müller, C. 'Seven years of field site tests to assess the reliability of different laboratory test methods for evaluating the alkali-reactivity potential of aggregates', in Proceedings of the 14th International Conference on Alkali Aggregate Reactions (ICAAR), Austin, Texas (2012)
- [7] Lindgård, J., Nixon, Ph. J., Borchers, I., Schouenborg, B., Wigum, B. J., Haugen, M. and Åkesson, U., 'The EU "PARTNER" project - European standard tests to prevent alkali reactions in aggregates: Final results and recommendations', *Cem. Concr. Res.* **40** (2010) 611-635.

- [8] Nixon, P.J. and Sims, I., 'RILEM Recommendations for the Prevention of Damage by Alkali-Aggregate Reactions in New Concrete Structures', State-of-the-Art Report of the RILEM Technical Committee 219-ACS (Springer Verlag 2016)
- [9] AFNOR P 18-454, Béton – Réactivité d'une formule de béton vis-à-vis de l'alcali réaction – Essai de performance, Association Française de Normalisation, Paris, 2004
- [10] Lindgård, J., Thomas, M. D., Sellevold, E. J., Pedersen, B., Andiç-Çakır, Ö., Justnes, H. and Rønning, T. F., 'Alkali-silica reaction (ASR)—performance testing: influence of specimen pre-treatment, exposure conditions and prism size on alkali leaching and prism expansion', *Cem. Concr. Res.* **53** (2013) 68-90.
- [11] Leemann, A., 'Raman microscopy of alkali-silica reaction (ASR) products formed in concrete', *Cem. Concr. Res.* **102** (2017) 41-47.
- [12] Balachandran, C., Muñoz, J. F. and Arnold, T., 'Characterization of alkali silica reaction gels using Raman spectroscopy', *Cem. Concr. Res.* **92** (2017).66-74.

NUMERICAL SIMULATION OF THE EXPANSION BEHAVIOR OF FIELD-EXPOSED CONCRETE BLOCKS BASED ON A MODIFIED CONCRETE PRISM TEST

Y. Kawabata (1), K. Yamada (2), S. Ogawa (3) and Y. Sagawa (4)

(1) Port and Airport Research Institute, JAPAN

(2) National Institute for Environmental Studies, JAPAN

(3) Kyushu University, JAPAN

Abstract

The performance testing of concrete is required to assess the alkali-silica reactivity and the potential for swelling for a wide variety of concretes. The performance should be assessed quantitatively in terms of the age and degree of expansion; simply identifying the expansion as harmful or innocuous is insufficient. It is imperative to consider the potential of expansion due to alkali-silica reactions (ASR), the service life of the structure, and the environmental conditions when assessing the real performance of the concrete in the structure. Therefore, it is necessary to develop numerical models to predict the expansion of concrete to re-assess concrete structures. As such, advanced models have been developed to understand the expansive behavior of concrete structures using numerical tools.

Laboratory tests are also important to provide useful data for these numerical models, since these models often require the calibration of some unknown parameters according to the material being tested. To address this, the authors have developed a test method for concrete expansion, the alkali-wrapped concrete prism test (AW-CPT). The predicted expansion of field-exposed concrete blocks subjected to the AW-CPT was found to agree well with experimental results, as reported in a previous study.

In this study, the AW-CPT results were verified by comparing field-exposure tests at different sites. Firstly, the expansion behaviors of concrete blocks exposed to different sites were compared by considering environmental conditions. Then, the AW-CPT results were compared with the results obtained from the numerical simulation.

Keywords: ASR, alkali wrapping, concrete prism test, simulation, environmental condition.

1. INTRODUCTION

Alkali-silica reactions (ASR) are a significant issue for concrete structures since they induce cracks and reduce mechanical properties. When structures are affected by ASR, they may have serious problems in terms of serviceability and/or safety. It is thus important to assess the risk of ASR for newly-constructed structures and to adopt appropriate preventive measures against ASR. With this in mind, the testing of the performance of concrete in the laboratory and the prediction of ASR expansion in concrete are becoming important subjects to mitigate ASR.

It is widely known that ASR depends strongly on environmental conditions as well as the reactivity of the aggregate and the mix proportions of concrete [1]. Particularly, the temperature, relative humidity (R.H.), and rainfall are considered to have a critical impact on the expansion due to ASR [2]. Therefore, even when an adequate field performance of concrete is confirmed in colder areas, the same concrete may show swelling in warm areas. In order to extrapolate laboratory test results to field performance, it is imperative to simulate ASR expansion.

Some advanced models have been developed in order to understand the expansive behavior of concrete structures. These models, however, require calibration of some unknown parameters according to the material being tested. The conventional concrete prism test (CPT) is widely used to calibrate the unknown parameters of the numerical model. However, the concrete expansion being tested is typically smaller than that observed for concrete blocks in the field, mainly due to alkali leaching and drying [3]. Therefore, in-laboratory testing methods should be improved to avoid these negative effects.

Recently, a new performance testing protocol, the Alkali-Wrapped Concrete Prism Test (AW-CPT), was proposed to avoid alkali leaching and drying [4]. In this test, concrete specimens were wrapped with wet cloth containing alkaline solution. The alkali hydroxide solution concentration of the cloth mimicked the concrete pore solution concentration. The results clearly showed that alkali leaching and drying were significantly reduced using the AW-CPT. Also, the threshold total alkali contents determined by the AW-CPT at 60 °C were almost consistent with that determined in a field-exposure test. Previous work on the prediction of expansion using AW-CPT was found to agree with the experimental results [2, 5]. According to these results, the AW-CPT may be a promising method to predict concrete expansion.

In this paper, first, experimental results of concrete block expansion in different environmental conditions are reported to understand the influence of environmental conditions on ASR expansion. Then, by using AW-CPT and numerical models, the expansion behavior of concrete blocks is presented. These results should strengthen our previous conclusion that AW-CPT can predict ASR expansion of field-exposed concrete blocks subjected to various environmental conditions. Finally, the impact of the environmental conditions, especially the moisture supply due to the ambient R.H. and precipitation, is discussed with supplemental simulation results.

2. IMPACT OF ENVIRONMENTAL CONDITIONS ON ASR EXPANSION

Concrete blocks ($0.4 \times 0.4 \times 0.6$ m), manufactured using the same aggregates at the same proportions, were exposed to field conditions in Fukuoka, Okinawa, and Monbetsu. The total alkali content in the concrete was determined to be 3.0 kg/m^3 and the proportion of the reactive aggregate was 10 wt%. The concrete blocks were made on the 2nd of February, 2016 in Fukuoka. The blocks were then wrapped with wet cloths and transported to each exposure site. The exposure tests were started on the 15th of March, 2011 in Fukuoka, on the 20th of April,

2016, in Okinawa, and on the 9th of June, 2016, in Monbetsu. Figure 1 shows an overview of the exposure sites. Measurements of the length change were performed on the 4 lateral sides where studs were installed in the block. In this paper, although the average value was used as a measure of the expansion, the expansion was different on each side; the expansion may be influenced by the direction of solar insolation and rainfall.

Historical meteorological information of these areas, recorded by the Japan Meteorological Agency [6], are presented in Figure 2. Okinawa is the warmest, followed by Fukuoka and Monbetsu. Table 1 summarizes the environmental conditions of the exposure sites in 2016-2017. The annual mean R.H. is higher at colder sites but the annual mean R.H. ranges from 0.71 to 0.77. The annual precipitation is quite different at the exposure sites. Okinawa is a tropical area, with over 2,000 mm of annual precipitation. The amount of precipitation in Okinawa is more than twice that in Fukuoka and Monbetsu.

The expansion of the field-exposed blocks is illustrated in Figure 3. The onset of concrete expansion occurred earliest in Okinawa, followed by Fukuoka and Monbetsu. The order of the onset of expansion was consistent with temperature. At 750 days, the expansion of the block in Fukuoka reached the same magnitude as that in Okinawa. It is interesting to note that the block in Monbetsu only started to expand after 250 days; the expansion gradually increased with time despite lower temperatures and the relatively lower total alkali content of concrete (3.0 kg/m^3). The rate of expansion was 0.10%/year in Okinawa, 0.11%/year in Fukuoka, and 0.05%/year in Monbetsu. The previous study reported that after expansion begins, the rate of expansion is higher at higher temperatures when tested with the AW-CPT [4]. The underlying mechanism is the extrusion of ASR gel from concrete specimens; a portion of the ASR gel may not contribute to ASR expansion. In the field, the temperature and moisture supply due to R.H. and precipitation all have a great impact on the ASR expansion. The effect of each factor on the ASR expansion will be identified using numerical simulations.



Figure 1 Exposure sites (Upper left: Okinawa, Upper right: Monbetsu, Bottom: Fukuoka)

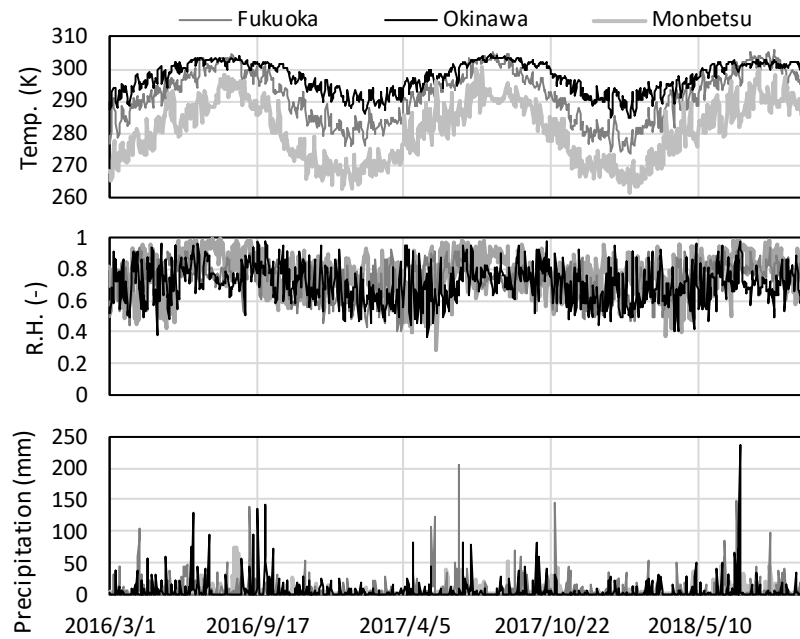


Figure 2 Environmental conditions of the exposure sites

Table 1 Summary of environmental conditions of exposure sites (2016-2017)

	Fukuoka	Okinawa	Monbetsu
Date of concrete casting	15/02/2016		
Date of exposure	15/03/2016	20/04/2016	09/06/2016
Annual mean temperature (K)	291.8	297.3	280.7
Annual mean R.H.	0.71	0.74	0.77
Annual precipitation (mm)	1015.7	2107.5	940.5

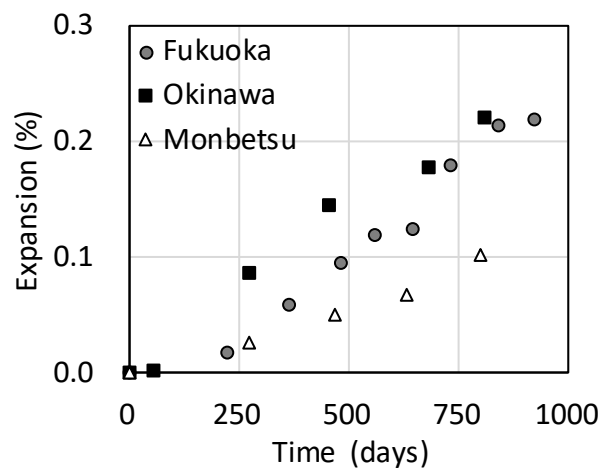


Figure 3 Expansion of field-exposed blocks

3. AW-CPT AND NUMERICAL SIMULATION

3.1 AW-CPT (Alkali-Wrapped Concrete Prism Test)

Concrete prisms (75×75×250 mm) were casted using the same mix proportions and the same aggregate proportions. After demolding, the concrete prisms were submerged in water for 30 minutes. Then, the concrete specimens were wrapped in a polypropylene non-woven cloth containing 50 g of NaOH solution. The concentration of the NaOH solution was 0.73 mol/l, mimicking the alkalinity of the pore solution [7]. The wrapped specimen was covered with plastic film in order to avoid drying. Afterwards, the wrapped specimens were placed in a storage container over water, and the container was placed in a chamber over water at 20 and 40 °C. The length and weight changes were measured periodically. The details of the AW-CPT are described in [4].

The laboratory test results are presented in Figure 4. The curves in the figure are the result of a mathematical model fit (Brunetaud's equation) as follows [8]:

$$\varepsilon_t = \varepsilon_\infty \frac{1 - \exp\left(-\frac{t}{\tau_C}\right)}{1 + \exp\left\{-\frac{(t - \tau_L)}{\tau_C}\right\}} \left(1 - \frac{\phi}{t + \delta}\right), \quad (1)$$

where t is time (day), ε_t is the expansion at time t (%), ε_∞ is the asymptotic final expansion (%), τ_C is the characteristic time (day), τ_L is the latency time (day), and ϕ and δ are experimental constants (days).

The rate of expansion was 0.11%/year at 20 °C, similar to that observed for exposed blocks in Okinawa and Fukuoka. The annual mean temperatures in Okinawa and Fukuoka are 18.8 °C and 24.3 °C, respectively. It should be noted that the rate of expansion at 40 °C changed with time whilst that at 20 °C was almost constant. This might be due to the effect of temperature on the viscoelasticity of ASR gel, which is strongly related to the extrusion of ASR gel.

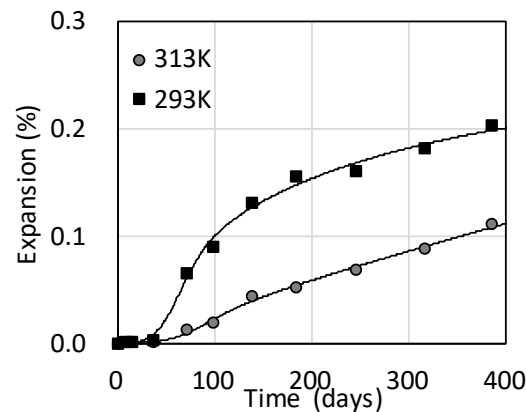


Figure 4 Expansion of concrete prisms tested using the AW-CPT

3.2 Numerical simulations

The numerical models adopted in this paper are briefly described below. The basic procedures of the simulation are described in a previous paper [1].

Equation (1) was used to simulate the ASR expansion. Each parameter was identified from Figure 4. Then, the temperature dependency of each parameter was expressed according to the following equation derived from the Arrhenius law:

$$\frac{X_{(T_1)}}{X_{(T_2)}} = \exp \left[\frac{U_X}{R} \left(\frac{1}{T_1} - \frac{1}{T_2} \right) \right] \quad (2)$$

where X and U_X denote each parameter and its activation energy, respectively, R is 8.314 J/(K mol), T_1 is the temperature (K) of the desired environment, and T_2 is the temperature (K) of the laboratory (313 K in this study).

Three parameters, ε_{∞} , τ_c , and τ_L in Equation (1), are assumed to be moisture-dependent. The moisture dependency can be expressed according to the following equations [9]:

$$\varepsilon_{\infty(s)} = \varepsilon_{\infty(100\%)} \left(\frac{\langle s - s_{\infty_ \varepsilon_{\infty}} \rangle^+}{1 - s_{\infty_ \varepsilon_{\infty}}} \right)^{m_{\varepsilon_{\infty}}} \quad (3)$$

$$\tau_{c, l(s)} = \tau_{c, l(100\%)} \left(\frac{\langle s - s_{\infty_ \tau_{c, l}} \rangle^+}{1 - s_{\infty_ \tau_{c, l}}} \right)^{m_{\tau_{c, l}}} \quad (4)$$

where $s_{\infty_ x}$ is the threshold saturation degree of parameter x below which no expansion occurs and m_x is the nonlinearity parameter of x ($s_{\infty_ x} = 0.8$ and $m_x = 1.0$ in this study).

The moisture transfer in concrete may be calculated by solving the differential equation. For the diffusion coefficient, the nonlinear diffusion model proposed by Bazant and Najjar was used [10]. The main change from study [2] was the model for moisture transfer during precipitation. In [2], R.H. was assumed to be 100% during the day and in the two subsequent days when precipitation was observed. In this study, during rainfall, the capillary suction is simulated in parallel with the diffusion model. In order to express the capillary suction, the moisture transfer coefficient k_w at the concrete surface was simply increased to 100 as proposed by Wattanapornprom and Ishida [11]. Each parameter for the moisture transfer was identified to fit the experimental result [12].

In the calculation, no moisture transfer was assumed before exposure since the blocks were wrapped with wet cloths. The initial degree of saturation was 0.9. After exposure, actual temperatures and R.H. collected by the Japan Meteorological Agency (Figure 2) were used. It was assumed that, if precipitation occurred, the R.H. was 1.0 during that day. Also, thermal expansion/shrinkage and drying shrinkage was implemented [2]. For the thermal calculation, it was assumed that the temperature of the concrete blocks was instantaneously equal to the ambient temperature.

Figure 5 shows the simulated expansion of concrete blocks based on the AW-CPT results. The simulated results for Okinawa and Monbetsu were consistent with the experimental results. The simulated results also indicate the impact of the environmental conditions on ASR expansion, since the earlier onset of expansion at higher temperatures was simulated. For Fukuoka, the simulation showed an earlier onset of expansion and a smaller expansion after 700 days. The reasons remain unclear, but the expansion of concrete blocks was influenced by the direction of solar insolation, wind, and so on. The consistency of the simulated and experimental results for Okinawa and Monbetsu show that the AW-CPT has an ability to predict the behavior of concrete blocks exposed to real environmental conditions.

In order to investigate the influence of environmental conditions on the ASR expansion, trial simulations were performed with two additional cases. One is a simulation assuming that R.H. was always 100%, meaning that ASR was always active due to the wet conditions. The other is a simulation in which only the R.H. without precipitation was considered. The simulated results, compared to the results from Figure 5, are illustrated in Figure 6. As described above, the Fukuoka case showed a smaller expansion after 700 days. When 100% R.H. was assumed, the

expansion was fairly well simulated after 700 days. On the contrary, the original and 100% R.H. simulation showed a larger expansion at an early age (before 250 days) compared to the experimental results. Therefore, the boundary conditions or moisture transfer properties might be different from the actual conditions. It should be noted, however, that the original simulation was consistent with the experiments in Okinawa and Monbetsu. Therefore, further investigation will be necessary to evaluate the difference between Fukuoka and the other two sites.

When only R.H. was considered, there were only small expansions. This is because the modification of R.H. leads only to a reduction in the mean saturation of the concrete, resulting in drying and no ASR expansion. This tendency was already reported in our previous study [2]. The results show that the degree of saturation of the original simulation was 0.95 at 900 days whilst the case with only R.H. in consideration was 0.72. Our previous study also claimed that smaller blocks were more sensitive to the changing environment, while larger blocks maintained almost the same degree of saturation [2]. This indicates that special caution should be taken when extrapolating the results of smaller concrete blocks to larger concrete structures.

From the results, it can be concluded that the predictions using the AW-CPT were consistent with the experimental exposure test results when appropriate environmental inputs are provided. Therefore, the AW-CPT will be a beneficial testing method for expansion simulations.

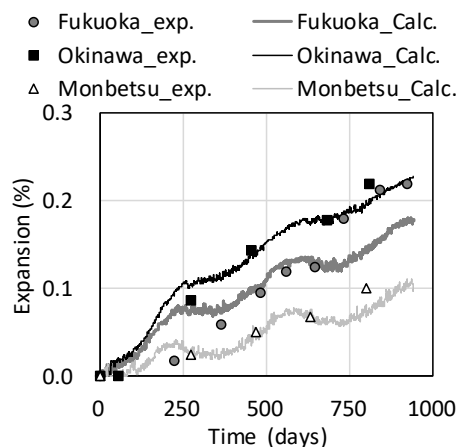


Figure 5 Simulated expansion of concrete blocks based on the AW-CPT results

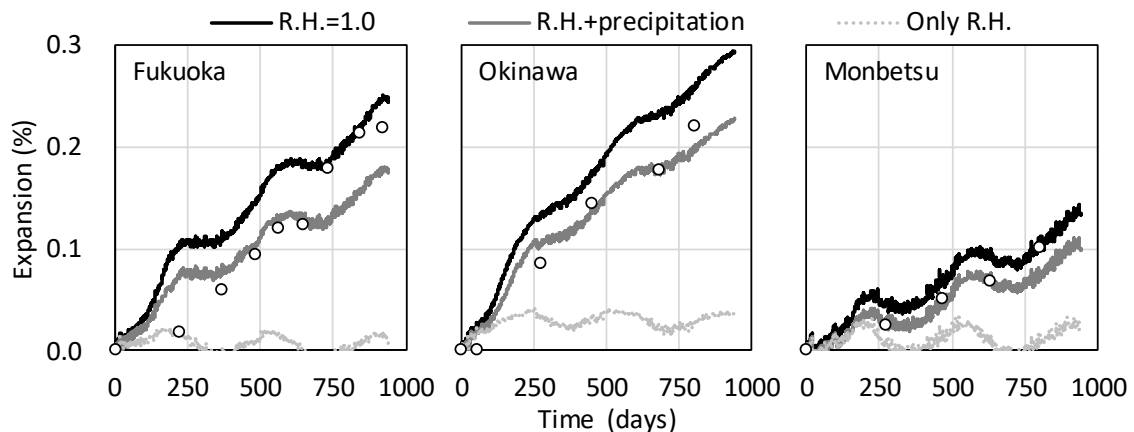


Figure 6 Simulated expansion of concrete blocks with different moisture conditions

5. CONCLUSIONS

This paper presents the impact of the environmental conditions on the ASR expansion of field-exposed concrete blocks through experiments and numerical simulations. The following conclusions may be drawn from this study:

- A clear difference in the ASR expansive behavior at the different exposure sites in Japan was confirmed through exposure tests and simulation.
- A comparison between the experiments and numerical simulations presented in this study showed that the modeling of the environmental conditions has a great impact on the ASR expansive behaviors.
- Numerical simulations based on the AW-CPT were consistent with the expansion of the concrete blocks, indicating that the AW-CPT is a useful method to predict the ASR expansion of concrete subjected to actual environmental actions.

ACKNOWLEDGEMENTS

Part of this work was financially supported by the Japan Society for the Promotion of Science (JSPS, No. 16H04393, No. 17H03292).

REFERENCES

- [1] Fournier, B., et al., 'Effect of environmental conditions on expansion in concrete due to alkali-silica reaction (ASR)', *Mat. Charact.* **60** (2009) 669-679.
- [2] Kawabata, Y., Yamada, K. and Ogawa, S., 'Modeling of environmental conditions and their impact on the expansion of concrete affected by alkali-silica reaction', *Swelling Concrete in Dams and Hydraulic Structures*, Sellier, Grimal, Multon and Bourdarot (Eds.), Wiley (2017) 163-175.
- [3] Lindgård, J. et al., 'Alkali-silica reaction (ASR) – performance testing Influence of specimen pre-treatment, exposure conditions and prism size on alkali leaching and prism expansion', *Cem. Concr. Res.* **53** (2013) 68-90.
- [4] Kawabata, Y. et al., 'Alkali-Wrapped Concrete Prism Test (AW-CPT) – New testing protocol toward a performance test against alkali-silica reaction–', *J. Adv. Con. Tech.* **16** (2018) 441-460.
- [5] Kawabata, Y. et al., 'Correlation between laboratory expansion and field expansion of concrete: Prediction based on modified concrete expansion test', *Proceedings of 15th ICAAR*, 2016, 034.
- [6] <https://www.data.jma.go.jp/obd/stats/etrn/index.php> (accessed 1st October 2018)
- [7] Kawabata, Y. and Yamada, K., 'Evaluation of alkalinity of pore solution based on the phase composition of cement hydrates with supplementary cementitious materials and its relation to suppressing ASR expansion', *J. Adv. Con. Tech.* **13** (2015) 538-553.
- [8] Brunetaud, X., et al., 'Delayed ettringite formation: Suggestion of a global mechanism in order to link previous hypotheses', *7th Int. Conf. on Recent Advances in Concrete Technology*, 2004, 63-76.
- [9] Poyet, S., 'Etude de la dégradation des ouvrages en béton atteints par la réaction alcali-silice: approche expérimentale et modélisation numérique multi-échelles des dégradations dans un environnement hydro-chemo-mécanique variable', Université de Marne la Vallée (2003)(in French)
- [10] Bazant, Z. P. and Najjar, L. J., 'Nonlinear water diffusion in nonsaturated concrete', *Mat. Struct.* **5** (1972) 3-20.
- [11] Wattanapornprom, R. and Ishida, T., 'Modeling of chloride penetration into concrete under airborne chloride environmental conditions combined with washout effects', *J. Adv. Con. Tech.* **15** (2017) 126-142.
- [12] Martin, R.-P., et al., 'Importance of considering the coupling between transfer properties, alkali leaching and expansion in the modelling of concrete beam affected by internal swelling reactions', *Const. Build. Mat.* **49** (2013) 23-30.

**International Conference on Sustainable
Materials, Systems and Structures
(SMSS 2019)**
Durability, Monitoring and Repair of Structures

Reinforcement corrosion

STUDY ON NON-UNIFORM CORROSION OF STEEL BARS IN CONCRETE

Yuxi Zhao(1), Xiaowen Zhang(1), Wang Kun(1), Chen Ju(1) and Hailong Wang(1)

(1) Institute of Structural Engineering, Zhejiang University, Hangzhou 310058, China

Abstract

Non-uniformly distributed corrosion products will have different effects on predicting the time to corrosion-induced cracking. Corrosion layers at the steel/concrete interfaces of reinforced concrete specimens subjected to chloride ion ingress were observed and measured by SEM; corrosion area of steel bars on the longitudinal direction were observed by 3D scanning in this paper. A Gaussian function was used to model the distribution of the non-uniform corrosion on both horizontal and vertical section. The physical meaning of the parameters in the Gaussian model and the relationships among these parameters are discussed.

Keywords: Steel reinforced concrete; SEM; Corrosion; 3D scanning

1. INTRODUCTION

The corrosion of steel has been identified as the major cause of deterioration in reinforced concrete structures [1, 2]. The corrosion of steel produces pressure on the surrounding concrete because the volume of corrosion product is 2 - 6 times the volume of the original steel [3 - 5]. Accurately predict the time taken to reach the limiting state of the cracking is very important for the durability of reinforced concrete structures. Therefore, the development of a concrete cracking model is very important.

Analytical models [1,6] usually assume a uniform expansion of corrosion products around the rebar circumference while the scenarios of uniform or non-uniform corrosion of reinforcement obviously have different effects on predicting the time to corrosion-induced cracking [7–11] and the non-uniform corrosion around the rebar perimeter is the real situation, the authors demonstrated that a Gaussian model can describe the non-uniform corrosion around the steel bar. Also, very limited research work has previously been undertaken to examine the non-uniform corrosion in the longitudinal direction. Focusing on the non-uniformity of the

section of the steel bar cannot completely analyze the development law of the corrosion situation. Therefore, it is also very important to study the longitudinal non-uniformity of the steel bar in the concrete.

This paper will briefly introduce the model of the corrosion layers at the steel/concrete interfaces and the corrosion area of steel bars on the longitudinal direction. According to the relationship between the horizontal and vertical steel corrosion areas, these models can be combined and further extended to establish a 3D non-uniform corrosion model in the cylindrical coordinate system, which has a practical application value for subsequent theoretical analysis and numerical simulation.

2. NON-UNIFORM CORROSION DISTRIBUTION AROUND THE PARAMETER OF STEEL BAR

2.1 Experimental program

2.1.1 Specimens and their exposure history

The two specimens used in this experiment were provided by Port and Airport Research Institute in Yokosuka, Japan. The size and dimensions of the specimens has been shown in Fig. 1, and the nature of the mixture and the tested concrete properties are reported in Table 1. The specimen exposed in the natural environment is labelled N, while the other specimen in an artificial environment is labelled M.

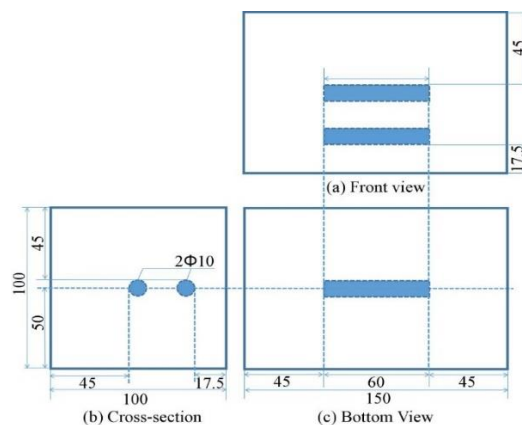


Figure 1. Dimensions, rebar arrangement and cross-section of test piece (in mm).

From October 2003 to March 2009, the specimen N was in the exposure area at the Port and Airport Research Institute to experience the real situation of the tidal zone of the Yokohama coastline. While the specimen M was in the accelerating chamber to experience wetting and drying cycles from October 2003 to March 2007 and then removed to store at room temperature. Next, both the specimens were sent to Zhejiang University in March 2009 and stored in the laboratory until unwrapped and investigated in May 2016.

Table 1: Concrete proportions of the two specimens.

Quantities (kg/m ³)				Max size of aggregate (mm)	Air (%)	Slump (mm)	W/C
Water	Cement	Sand	Coarse aggregate				
165	243	912	970	20	4	12	0.68

2.1.2 Sample preparation

A SYJ200 abrasive cutter was used to cut slices into 25 mm×25 mm×8 mm samples. The boundaries of the rebar, corrosion layer and concrete of each sample were observed by a scanning electron microscope (QUANTA FEG650) in backscattering mode. Approximately 70 points around the perimeter of the steel bar were recorded in each sample, the thickness of corrosion layer in each measuring point was tested and recognized as T_{cl} .

2.2 Model of the cross-section corrosion

The authors found that the Gaussian model can well describe the variation of the thickness of the corrosion layer (T_{cl}) around the steel bar

$$T_{cl} = \frac{a_1}{a_2 \sqrt{2\pi}} e^{-\left(\frac{\theta-\pi}{\sqrt{2}a_2}\right)^2} + a_3 \quad (1)$$

where T_{cl} is the thickness of the corrosion layer at coordinate θ ; the parameters a_1 , a_2 and a_3 are the fitting parameters, which describe various characteristics of the corrosion layer. a_1 is the non-uniform coefficient of the corrosion layer, a_2 is the spread coefficient of corrosion layer, and a_3 is the uniform coefficient of the corrosion layer.

According to the T_{cl} data measured by SEM, use the Origin software to fit the data by the Gaussian model, fix the axes of the Gaussian model at the position of corrosion peaks, the parameters of the model are calculated.

The scanning diagram and Gaussian fitting results of the slices are observed, as shown below in Fig 2.

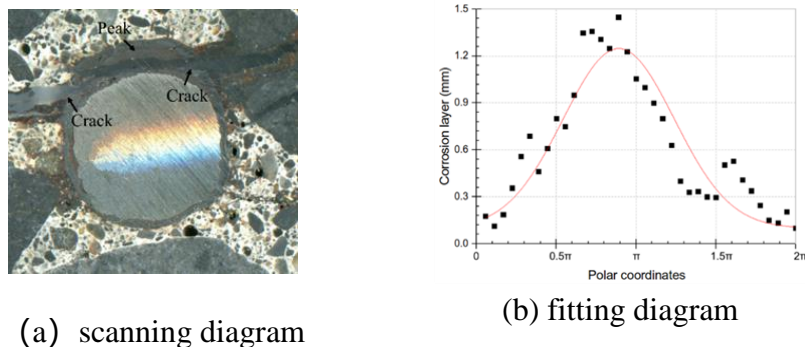


Figure 2 Comparison of steel corrosion condition of slices.

A typical case of the non-uniform corrosion layer, which could be described by the Gaussian model, are illustrated in Fig. 3. a_3 , defined as the uniform coefficient, is independent of the value of θ and can describe the thickness of the corrosion layer. If the corrosion products develop across the entire circumference of the steel bar, a_3 (in mm) represents the minimum thickness of the corrosion layer T_{cl-min} . Also, it is clear that a_2 is lineally proportional to the full width at half maximum W_{hm} , which is also shown in Fig.3. The larger a_2 , corresponding to the greater W_{hm} , physically means that corrosion products spread more extensively, leading to a flatter shape of the corrosion layer.

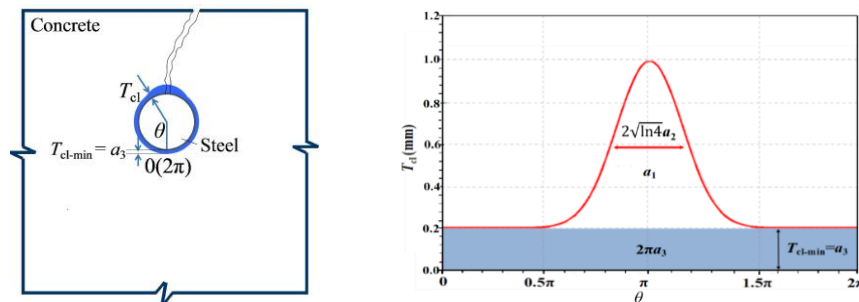


Figure 3 A typical cases of a non-uniform corrosion layer.

3. NON-UNIFORM CORROSION DISTRIBUTION ALONG THE LONGITUDINAL DIRECTION OF STEEL BAR

3.1 Experimental Program

3.1.1 Concrete beams

The basic information of the concrete beam used in this experiment is shown in Fig.4. The details of the mix proportions have been shown in Table 2.

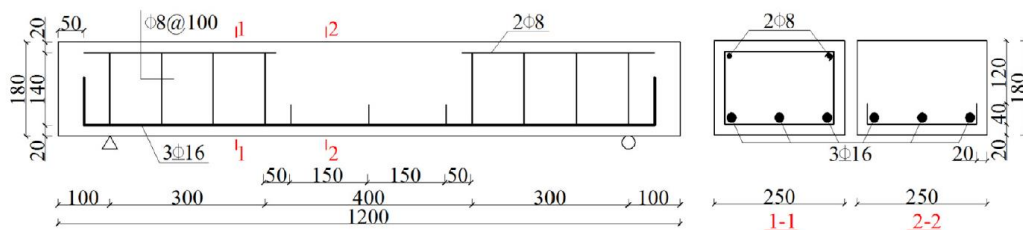


Figure 4. Dimensions and reinforcement information of the beams.

Table 2: Compositions of the concrete used in the beams (kg/m³).

Cement	Fly ash	Slag	Water	Fine aggregate	Coarse aggregate	Water reducing agent
282	41	53	184	752	985	7.5

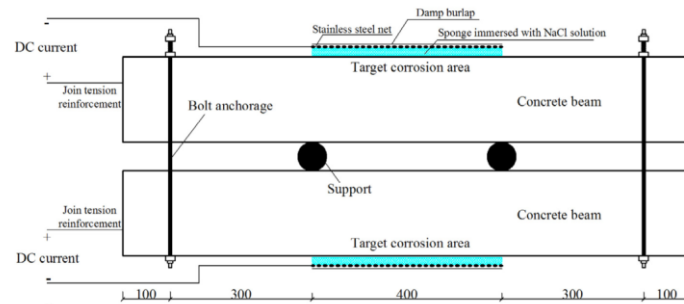


Figure 5 Electro-migration tests on the beams.

3.1.2 Sustained loading and accelerated steel corrosion

All the beams were subjected to electro-migration, which means that the chlorides were electro migrated into the concrete cover by means of an electrochemical method, the same as that of Dong [23]. After the electro-migration method, the beams were loaded in a four-point bending configuration, as shown in Fig.5.

Each cycle consisted of a 4-day wetting period and a 10-day drying period. During the wetting period, the target corrosion area was wrapped in the sponge materials immersed in 5% NaCl solution and constant current was applied between the tension-reinforcing steel bars (acting as anodes) in the beams and the stainless-steel nets (acting as cathodes). The applied current was $100 \mu\text{A}/\text{cm}^2$. The wetting and drying cycles coupled with DC power lasted for 31 cycles until the maximum crack width on the surface of the protective layer reached 1 mm.

3.1.3 Sample observation

The treated steel bars were scanned using a LPX-600 3D laser scanner manufactured by Roland to study the longitudinal distribution of the steel corrosion.

The scanning results were denoised and reconstructed using the 3D reconstruction software Geomagic Studio. The cross-sectional area of the steel after corrosion is extracted by Pro/Engineer software. In the Pro/Engineer software, the direction of the steel bar axis is determined as the axial direction of the cross-sectional area, and 1 mm is used as the spacing between the different cross-sections to ensure that the extracted cross-sectional area can fully reflect the longitudinal corrosion of the steel bar.

3.2 Model of the longitudinal corrosion

Based on the scan results, the longitudinal distribution of the cross-sectional area of the C1, M and C2 steel bars after corrosion are recorded. The black dotted line indicates the position of the stirrup.

It can be found clearly in Fig.6 that the corrosion near the stirrups are significantly weaker than other areas. According to the electrochemical corrosion mechanism, when two metals with different potentials are overlapped, it is possible to cause a galvanic effect. Since the inner side of the stirrups are overlapped with the longitudinal steel bar, a galvanic cell with the stirrup as

the anode and the longitudinal steel bar as the cathode will be formed, so that the corrosion of the stirrups will become more severe, and the longitudinal steel bar is then protected.

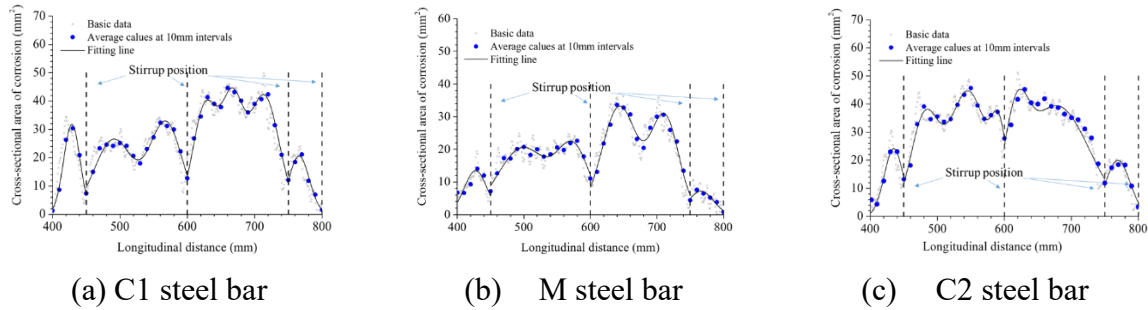


Figure 6 Fitting results of the longitudinal corrosion of steel bars

Similar with Section 2, according to the measured data, the longitudinal distance is used as the independent variable, and the cross-sectional area of the steel is used as the dependent variable for parameter. When there are multiple corrosion peaks in the longitudinal corrosion, the fitting equation can be expressed as

$$A_{\Delta} = \sum_{i=1}^n \frac{b_{i1}}{b_{i2} \sqrt{2\pi}} e^{-\left(\frac{z-z_i}{\sqrt{2}b_{i2}}\right)^2} + b_3 \quad (2)$$

where A_{Δ} is the corroded area of the steel bar (in mm^2) at the abscissa z (in mm) which can be obtained by subtracting the average cross-sectional area of the corroded steel bar from the average cross-sectional area of the uncorroded steel bar; the parameters b_1 , b_2 and b_3 are the fitting parameters, which describe various characteristics of the longitudinal corrosion similar to the calculations in Section 2. b_1 is the non-uniform coefficient of longitudinal corrosion, b_2 is the spread coefficient of longitudinal corrosion, and b_3 is the uniform coefficient of longitudinal corrosion. z_i is the abscissa value of the position where the corrosion peak is located. The meaning of each parameter is identified in Fig.7.

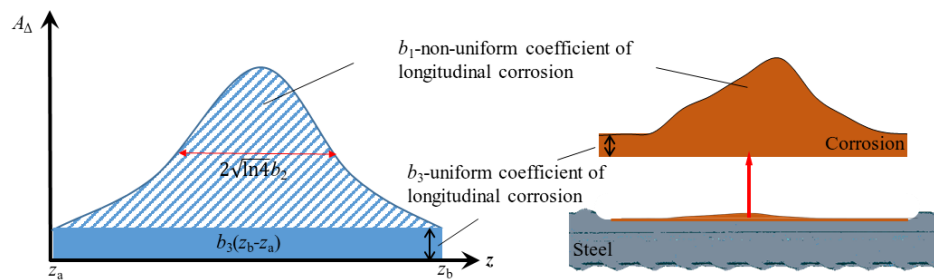


Figure 7 Parameter meaning diagram

4. 3D CORROSION DISTRIBUTION MODEL

The area of the non-uniform corrosion can be expressed as

$$A_{cl} = a_1 R \quad (3)$$

where A_{cl} is the area of the corrosion layer (in mm^2); R is the radius of steel bar (in mm).

Based on the relationship between the corroded area on the cross section of the steel bar and the area of the corresponding corrosion layer, the correlation between the two can be established as

$$A_{cl} = a_1 R = n A_\Delta \quad (4)$$

where n is the corrosion volume expansion ratio, generally between 2-6.

take the axial direction of the steel bar as the z -axis. To simplify the analysis, it is considered that the non-uniform corrosion distribution of the cross-section of the steel bar conforms to the single-peak Gaussian distribution model and also regardless of the effects of uniform corrosion in the longitudinal and transverse directions.

Substituting Eq. (4) into Eq. (2), a_1 can be obtained as

$$a_1 = \frac{n}{R} \sum_{i=1}^n \frac{b_{i1}}{b_{i2} \sqrt{2\pi}} e^{-\left(\frac{z-z_i}{\sqrt{2}b_{i2}}\right)^2} \quad (5)$$

Substituting Eq. (5) into Eq. (2), the variation of the thickness of the corrosion layer in the cylindrical coordinate system can be obtained as

$$\begin{aligned} T_{cl}(\theta, z) &= \frac{n}{R} \sum_{i=1}^n \frac{b_{i1}}{b_{i2} \sqrt{2\pi}} e^{-\left(\frac{z-z_i}{\sqrt{2}b_{i2}}\right)^2} \cdot \frac{1}{a_2 \sqrt{2\pi}} e^{-\left(\frac{\theta-\pi}{\sqrt{2}a_2}\right)^2} \\ &= \frac{n}{R} \sum_{i=1}^n \frac{b_{i1}}{2\pi \cdot b_{i2} \lambda_2} e^{-\left(\left(\frac{z-z_i}{\sqrt{2}b_{i2}}\right)^2 + \left(\frac{\theta-\pi}{\sqrt{2}a_2}\right)^2\right)} \end{aligned} \quad (6)$$

So that two Gaussian models which are used to indicate the cross sectional and longitudinal corrosion distribution of steel bars can be combined to establish a 3D non-uniform corrosion model. It can be seen that the overall steel corrosion situation can be expressed by one equation Eq. (6), which has a practical application value for subsequent theoretical analysis and numerical simulation. The parameters of this model are worthy of further exploration and will be refined in subsequent studies in conjunction with the discussion in the previous Sections.

5. CONCLUSION

This paper introduces the model of the corrosion layers at the steel/concrete interfaces and the corrosion area of steel bars on the longitudinal direction, and these models are combined and further extended to establish a 3D non-uniform corrosion model in the cylindrical coordinate system. The following conclusions were drawn from this study:

- The physical meaning of the parameters in the Gaussian model on both cross section and longitude are discussed.

- Due to the protective effect of the stirrups on the longitudinal steel bar, the longitudinal corrosion near the stirrups is much lower than other positions.
- Combined with the existing non-uniform corrosion model on the cross section, the Gaussian non-uniform corrosion distribution model is further extended, and the 3D non-uniform corrosion model in the cylindrical coordinate system is proposed. The 3D non-uniform corrosion model can be used to characterize the comprehensive non-uniform corrosion of the steel.

ACKNOWLEDGMENTS

Financial support from the National Key R&D Program of China through Grant No. 2017YFC0806101-02 is gratefully acknowledged.

REFERENCES

- [1] Z.P. Bazant, Physical model for steel corrosion in sea structures - applications, J. Struct. Div. 105 (1979) 1137 - 1153.
- [2] P.B. Bamforth, Enhancing reinforced concrete durability: guidance on selecting measures for minimizing the risk of corrosion of reinforcement in concrete, Concrete Society Technical, Report No. 61 (2004).
- [3] R.M. Cornell, U. Schwertmann, The Iron Oxides, VHC Verlagsgesellschaft, Weinheim, Germany, 1996.
- [4] T.D. Marcotte, C.M. Hansson, Corrosion products that form on steel within cement paste, Mater. Struct. 40 (2007) 325 - 340.
- [5] A. Bentur, S. Diamond, N.S. Berke, Steel Corrosion in Concrete, E & FN Spon, London, 1997.
- [6] Y.P. Liu, R.E. Weyers, Modeling the time-to-corrosion cracking in chloride contaminated reinforced concrete structures, ACI Mater. J. 95 (1998) 675 - 681.
- [7] Y.X. Zhao, A.R. Karimi, H.S. Wong, B.Y. Hu, N.R. Buenfeld, W.L. Jin, Comparison of uniform and non-uniform corrosion induced damage in reinforced concrete based on a Gaussian description of the corrosion layer. Corros. Sci. 53(9) (2011) 2803 - 2814.
- [8] Y.S. Yuan, Y.S. Ji, Y.J. Mu, Propagation and model of distribution for corrosion of steel bars in concrete, China Civil Eng. J. 40 (2007) 5 - 11.
- [9] B.S. Jang, B.H. Oh, Effects of non-uniform corrosion on the cracking and service life of reinforced concrete structures, Cem. Concr. Res. 40 (2010) 1441–1450.
- [10] Y.T. Liu, Corrosion damage and the durability of corner steel bars of different structures. Shanghai university, Shanghai, P.R. China, 2005. (In Chinese).
- [11] Y.X. Zhao, B.Y. Hu, J. Yu. W.L. Jin, Non-uniform distribution of rust layer around steel bar in concrete. Corros. Sci. 53(12)(2013) 4300 - 4308.

EVOLVING PERFORMANCE BASED ENVIRONMENTAL CLASSIFICATIONS FOR CHLORIDE EXPOSURE

(1) B. S. Dhanya, (2) Manu Santhanam, (3) Santhosh George Cheriyan

(1) Assistant Professor in Civil Engineering, RIT, Govt. Engg. College, Kottayam, India

(2) Professor in Civil Engineering, IIT Madras, India

(3) Planning In charge, L&T Construction, Transportation Infrastructure IC L&T, India

Abstract

Corrosion of reinforcement in reinforced concrete structures is a matter of pervasive concern to the engineers, owing to its huge economic implications. Of the two major causes of corrosion, chloride induced corrosion is more dangerous because of its pitting nature. This is the major cause of deterioration of reinforced concrete structures in countries having a long coastline. The present paper discusses the performance of four commonly used accelerated test methods such as Wenner 4-probe resistivity, rapid chloride permeability test, rapid migration test and chloride conductivity test to assess chloride ingress into concretes which are having different supplementary cementitious materials such as slag, Class F fly ash and Class C fly ash. The correlations between different test results were explored. Using the results, a new classification criterion is proposed for concrete quality (considering chloride penetration resistance). The criterion combines both surface resistivity and one of the other durability parameters based on conduction/migration such as charge passed, non-steady state migration coefficient or chloride conductivity.

Keywords: chloride ingress, supplementary cementitious materials, combined classification criteria

1. INTRODUCTION

Durability of concrete is its resistance against any form of deterioration. The major aggressive species that can lead to the deterioration of concrete include chlorides, carbon dioxide, sulphates, moisture etc. These destructive agents can enter into the concrete through the cover and can lead to either deterioration of concrete or corrosion of embedded reinforcing bars. The transport of the aggressive species into concrete occurs by different transport or

transfer mechanisms, including diffusion (movement due to concentration gradient), permeation (movement due to pressure difference), sorption (intake due to capillary action), absorption (bulk intake), adsorption (process of attachment of molecules on the surface as well as in the pore walls), migration (ionic movement due to the difference in the electrical potential), wick action (capillary transport to an exposed surface, where liquid evaporates and any dissolved ions are precipitated) etc.

To assess chloride penetration into concrete, there exist different categories of test methods such as Diffusion tests (Bulk diffusion test, Salt ponding test, Steady state diffusion tests), Migration tests (Steady state migration test, Rapid chloride permeability test, Rapid migration test, Multi regime method, Permit ion migration test, Whiting method), Resistivity or conductivity tests (Direct resistivity test, Wenner 4 Probe resistivity test, Two point method, Disc method, Chloride conductivity test) and Pressure penetration techniques. Diffusion tests consume relatively more time and can be categorized as long -term tests whereas the others can be grouped into accelerated tests. The major drawback pointed out for the accelerated test methods is the prevalence of more than one transport mechanism [1].

The present paper discusses the performance of four commonly used accelerated test methods to assess chloride ingress into the concrete. The tests include Rapid Chloride Permeability Test (ASTM C 1202 [2]), Rapid Migration Test (NT BUILD 492 [3]), Chloride Conductivity Test (Durability Index Testing Manual, South Africa [4]) and Wenner 4-Probe Resistivity Test [5]. These tests were performed on 24 concretes having a mean strength ranging between 20 to 50 MPa, having different replacement levels of Supplementary Cementitious Materials (SCMs) such as slag, Class F fly ash and Class C fly ash. The correlations obtained between the durability parameters were studied, and an attempt to evolve performance classifications for different exposure conditions was made.

2. EXPERIMENTAL PROGRAMME

Totally 24 types of concrete were designed using the following four independent variables: (1) water-binder ratio, (2) total binder content, (3) supplementary cementitious materials content, and (4) curing period. The four water-binder ratios considered were 0.50, 0.55, 0.60, and 0.65. The three different total binder contents used were 280, 310, and 340 kg/m³. In addition to Ordinary Portland Cement (53 grade, conforming to IS 269), three SCMs (i.e., slag, Class C fly ash, Class F fly ash) were used at 0, 15 and 30 % replacement. Two slags from two different sources were used. The Class C fly ash was procured from the thermal power plant in Neyveli, Tamil Nadu, India. The Class F fly ash was obtained from thermal power plant in Ennore, Tamil Nadu, India. The curing periods were 28 and 90 days.

All the concretes were prepared with a fine aggregate (river sand) to coarse aggregate ratio of 40:60. The coarse aggregates used were a combination of 20 mm down and 10 mm down crushed granite, in a proportion of 60:40. A Sulphonated Naphthalene Formaldehyde (SNF) based admixture was used to obtain slump values between 80 - 150 mm.

The mixes are grouped into 4 sets depending on their binder content and water binder ratio. Group one had a total binder content of 280 kg/m³ and w/b of 0.65. Slag A, Slag B and Class F fly ash were replaced at 30% in this category. In the second and third group, which had total binder content and water binder ratio combinations of 340 kg/m³, 0.55 and 310 kg/m³, 0.60 respectively, all the four SCMs were replaced at 15%. The fourth group of mixes had a total binder content of 310 kg/m³ and water binder ratio 0.50. For slag B and Class F fly ash, three

replacement levels such as 15, 30, and 50% were done. Class C fly ash was used at 15 and 30 % replacements in another two mixes. In one mix, slag A was used at 15% replacement. In all the groups, there were mixes which had only OPC as the binder.

2.1 EXPERIMENTAL METHODS

Four different accelerated test methods were used to assess the resistance of concrete against chloride ion penetrability. The details of the test methods used are as follows. Figure 1 shows the set up for the experiments, along with the classification criteria applicable for the result.

Resistivity is dependent on the quantity and conductivity of the pore solution and the size, interconnectivity and tortuosity of pores [6]. Many researchers [1,7] favour surface resistivity as a good method for assessing concrete durability. Service life prediction models are also proposed based on this non-destructive method [8]. In terms of resistivity, many classification criteria for concrete quality have been proposed by different researchers. Some researchers relate resistivity and concrete quality [9] whereas some others have tried to link resistivity and corrosion risk [7,10]. The classification system relating resistivity and corrosion rate shown in Figure 1 has been given in ACI Committee report 222R [11] on Protection of Metals in Concrete against Corrosion. For the present study, the resistivity measurements were made on 150 mm cubes. The cubes were fully saturated in order to minimize the variations due to moisture content in the sample.

Rapid chloride permeability test (RCPT) is a most widely used durability test method to assess the chloride ion penetrability of concrete. The test was developed by Whiting in 1981 [12]. RCPT is standardized by both ASTM and AASHTO as ASTM C 1202 [2] and AASHTO T277-07 [13] respectively. For the present study, the RCPT was conducted on three specimens, each of thickness 50 mm and diameter 100 mm, which were prepared from a cylinder of diameter 100 mm and height 200 mm. After cutting, the peripheral curved surface of the specimens was coated with epoxy. Then, the specimens were vacuum saturated with saturated $\text{Ca}(\text{OH})_2$ solution.

The rapid migration test (RMT) was developed by Tang and Nilsson in 1992 at the Chalmers Technical University, Sweden [14]. Thus, this test is also known as the CTH test. This test method is standardized by NORD as NT BUILD 492 [3] and AASHTO as AASHTO TP 64:2003 [15]. The specimens and the preparation methodology is similar to that adopted for the RCPT study as described before. The classification criteria suggested by the developers of the test Tang and Nilsson (as per [9]) are adopted in the study.

The chloride conductivity test method was proposed by Streicher and Alexander of the University of Cape Town in South Africa in 1995 [16]. This test is developed based on the electrochemical theory and is very rapid as it involves only single current measurement. Chloride conductivity test is standardised in the Durability Index Testing Procedure Manual, South Africa [4] and is a widely used test method in that country. The classification criteria developed by Alexander et al. [17] with respect to chloride conductivity is provided in Figure 1.

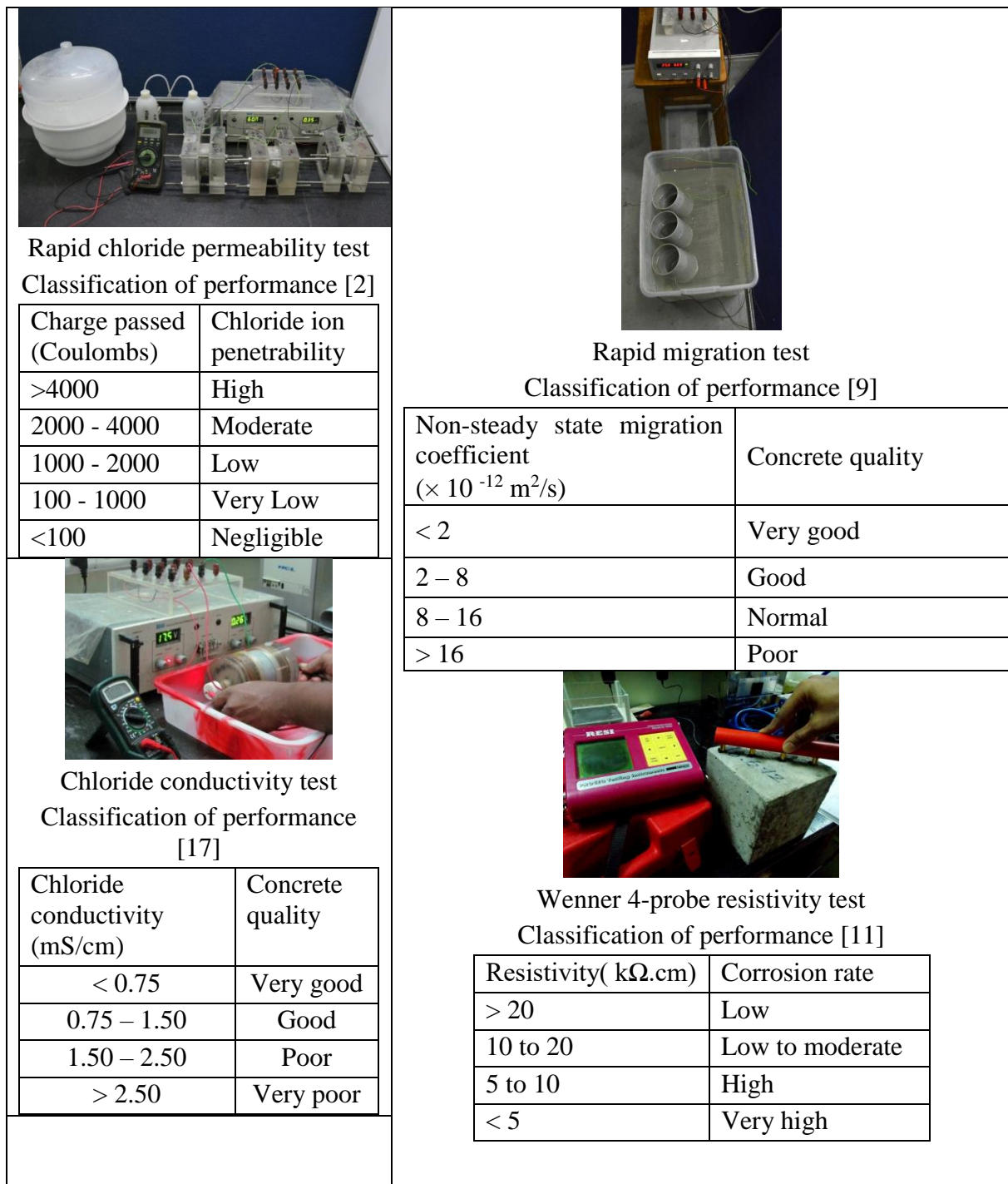


Figure 1: Experimental set ups

3. RESULTS AND DISCUSSION

3.1 Correlation between different durability parameters in the current study

Good inverse correlation (Coefficient of regression R^2 more than 0.9, 0.75 and 0.76 respectively) was seen to exist between surface resistivity and other parameters such as charge passed, non-steady state migration coefficient and chloride conductivity. These parameters are measures of the conductivity of concrete, which is the inverse of resistivity. This conclusion is in line with that made by Ramezani-pour et al. [18] who had evaluated the correlation between surface resistivity, water penetration, rapid chloride penetration, and compressive strength. The authors were able to get good correlation between surface resistivity and water penetration depth. There was no correlation between surface resistivity and compressive strength. The authors suggested the use of surface resistivity as a good, quick, non-destructive test to assess concrete quality.

3.2 Classification systems based on more than one durability parameter

The existing classification systems for concrete quality based on the current four durability parameters were analysed critically. It is observed that none of the mixes got a surface resistivity value less than 5 k Ω .cm (very high corrosion rate according to ACI 222R [11]). The mixes tested in this project include very lean mixes, which have total binder content of as low as 280 kg/m³ and w/b as high as 0.65. Even for these mixes, the surface resistivity values obtained were close to 8 k Ω .cm, when tested in a fully saturated condition. At an age of 28 days, this low level of resistivity (i.e., 5 k Ω cm) is not expected to be shown by low to moderate strength concrete mixes.

The values for charge passed were not below 100 Coulombs for any mix tested. This level of durability can be achieved only by using SCMs like silica fume in high grade concrete (say, characteristic compressive strength, $f_{ck} > 60$ MPa). Thus, the classification for concrete below 100 Coulombs (negligible chloride ion penetrability as per ASTM C1202 [2]) seems to be irrelevant in the case of normal concrete. In a similar way, the non-steady state migration coefficient value of less than 2×10^{-12} m²/s ('very good' concrete quality as per [9]) also appears to be an inappropriate limiting value in the case of normal concrete.

In the case of chloride conductivity test results, very few results went beyond 1.5 mS/cm limiting value. None of the concretes had conductivity value beyond 2.5 mS/cm. Further, too much clustering of data points is found between conductivity values 0.75 and 1.5. Most of the concretes having resistivity value between 10 and 20 k Ω .cm had a conductivity value between 1 and 1.5 mS/cm. Thus, it seems to be appropriate to introduce a new limiting value as 1 mS/cm.

Thus, a new classification criterion is proposed for concrete quality, considering chloride penetration resistance. The criterion combines both surface resistivity and one of the other durability parameters based on conduction/migration such as total charge passed, non-steady state migration coefficient or chloride conductivity. The ranges of these parameters for different categories of concrete are presented in Table 1. From Table 1, a concrete is classified as 'excellent' when the surface resistivity is above 20 k Ω .cm and the charge passed is less than 1000 Coulombs. Similarly, concrete mixes with surface resistivity values greater than 20 k Ω .cm and the non-steady state migration coefficient less than 8×10^{-12} m²/s are also classified as 'excellent'. In a similar way, concrete mixes having a surface resistivity values greater than

20 k Ω .cm and chloride conductivity values less than 0.75 mS/cm are classified in the ‘excellent’ category.

These categories and their limiting values are represented in the form of scatter plots between surface resistivity and other parameters such as charge passed, non-steady state migration coefficient and chloride conductivity in Figures 2 to 4.

Table 1: Classification criteria based on more than one durability parameter

Category	Surface Resistivity (k Ω .cm)	Charge passed (Coulombs)	Non-steady state migration coefficient $\times 10^{-12}$ m ² /s)	Chloride conductivity (mS/cm)
		AND	OR	OR
Excellent	>20	<1000	<8	<0.75
Very Good	>20	1000 – 2000	8 – 16	0.75 – 1.00
Good	10 – 20	1000 – 2000	8 – 16	0.75 – 1.00
Moderate	10 – 20	2000 – 4000	16 – 24	1.00 – 1.50
Poor	< 10	> 4000	>24	> 1.50

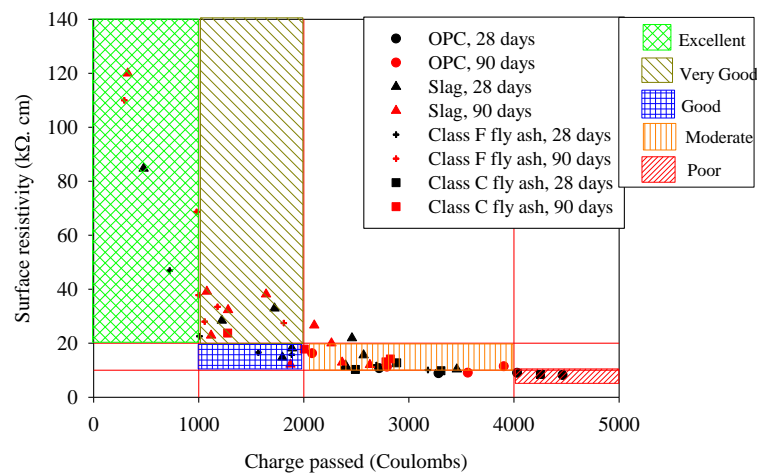


Figure 2: Classification criteria based on surface resistivity and charge passed

In the classification presented above, all the categories can be defined based on more than one parameter. This type of classification can lead to more stringency in material selection as more than one durability parameter needs to be satisfied in order to qualify for a particular service environment.

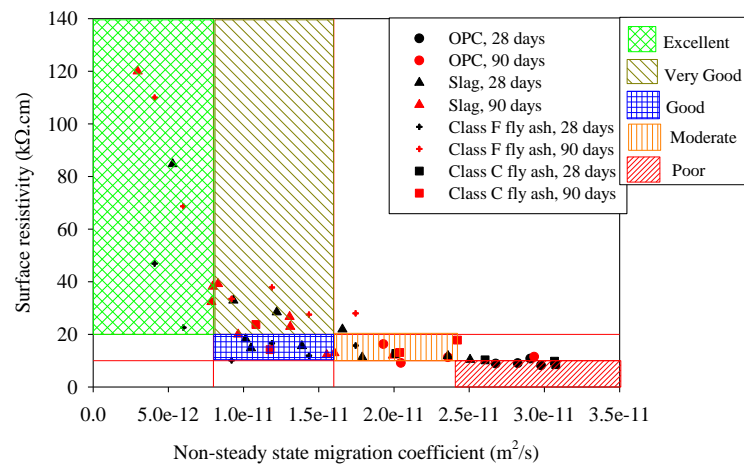


Figure 3: Classification criteria based on surface resistivity and non - steady state migration coefficient

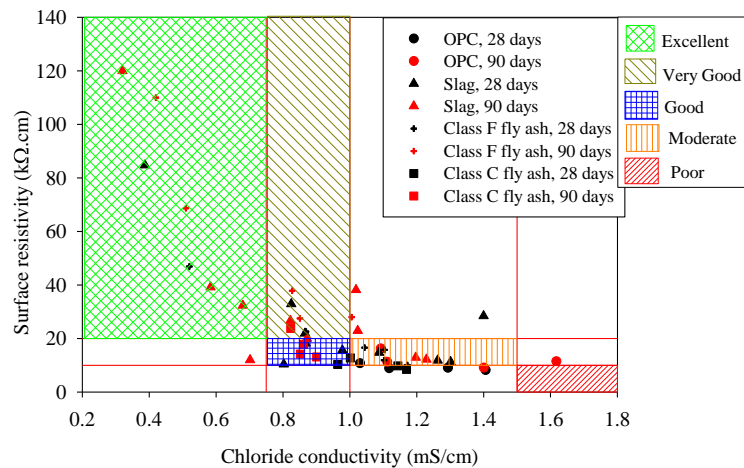


Figure 4: Classification criteria based on surface resistivity and chloride conductivity

4.0 CONCLUSIONS

- Good inverse correlation exists between surface resistivity and other parameters such as charge passed, non-steady state migration coefficient and chloride conductivity.
- A new classification criterion is proposed for concrete quality (considering chloride penetration resistance), which combines both surface resistivity and one of the other durability parameters based on conduction/migration such as charge passed, non-steady state migration coefficient or chloride conductivity. All the categories can be defined based on more than one parameter. This type of classification can lead to more stringency in material selection as more than one durability parameter needs to be satisfied in order to qualify for a particular service environment.

REFERENCES

- [1]. Andrade, C. (1993) Calculation of chloride diffusion coefficients in concrete from ionic measurements, *Cement and Concrete Research*, 23, 724-742.
- [2]. ASTM C1202 (2010) Standard test method for electrical indication of concrete's ability to resist chloride penetration, Annual book of ASTM standards, West Conshohocken, PA, USA.
- [3]. NT BUILD 492 (1999) Concrete, Mortar and Cement-based repair materials: Chloride migration coefficient from non-steady-state migration experiments, Nordic Council of ministers, Finland.
- [4]. Durability Index Testing Procedure Manual (2009), Concrete durability index testing, South Africa.
- [5]. ASTM G 57 (2012) Standard test method for field measurement of soil resistivity using the Wenner Four-Electrode method, Annual book of ASTM standards, West Conshohocken, PA, USA.
- [6]. Andrade, C., Polder, R. and Basheer, M., Non-destructive methods to measure ion migration pp. 91 - 112 *In: Torrent, R., and Luco, L. F., Non-Destructive Evaluation of the Penetrability and Thickness of the Concrete Cover - State-of-the-Art Report of RILEM Technical Committee 189-NEC*, RILEM publications, 2007.
- [7]. Andrade, C. and Alonso, C. (1996) Corrosion rate monitoring in the laboratory and on-site, *Construction and Building Materials*, 10 (5), 315-328.
- [8]. Andrade, C., Prieto, M., Tanner, P., Tavares, F., and d'Andrea, R. (2013) Testing and modelling chloride penetration into concrete, *Construction and Building Materials*, 39, 9- 18.
- [9]. Bjegović, D., Serdar, M., Oslaković, I. S., Jacobs, F., Beushausen, H., Andrade, C., Monteiro, A. V., Paulini, P., Nanukuttan, S., Test methods for concrete durability indicators, *In: Beushausen, H. (eds.), Performance-based specification and control of concrete durability, State of the art report prepared by RILEM technical committee TC 230 – PSC*, 2015.
- [10]. Andrade, C., Alonso, C., Gulikers, J., Polder, R., Cigna, R., Vennesland, O., Salta, M., Raharinaivo, A., and Elsener, B (2004) Test methods for on-site corrosion rate measurement of steel reinforcement in concrete by means of the polarization resistance method, *Materials and Structures*, 37, 623-643.
- [11]. ACI 222R (2001), Protection of metals in concrete against corrosion, Reported by ACI Committee 222, American Concrete Institute, Farmington Hills, USA.
- [12]. Whiting, D (1981) Rapid determination of the chloride permeability of concrete, Report No. FHWA/RD-81/119, Federal Highway Administration, Washington DC.
- [13]. AASHTO T 277 - 07 (2008) Rapid determination of the chloride permeability of concrete, American Association of States Highway and Transportation Officials, Washington, DC, USA.
- [14]. High performance concrete structural designers' guide (2005) FHWA Publication No. FHWA-RCBAL-05-007, Federal Highway Administration, U.S. Department of Transportation.
- [15]. AASHTO TP 64:2003 (2007) Standard Method of Test for Predicting Chloride Penetration of Hydraulic Cement Concrete by the Rapid Migration Procedure, American Association of States Highway and Transportation Officials, Washington, D. C., U.S.A.
- [16]. Streicher, P. E., and Alexander, M. G. (1995), A chloride conduction test for concrete. *Cement and Concrete Research*, 25 (6), 1284-1294.
- [17]. Alexander, M.G., Ballim, Y. and Mackechnie, J.R. (1999) Guide to the use of durability indexes for achieving durability in concrete structures. Achieving durable and economic concrete construction in the South African context, Research Monograph, 2, 5-11.
- [18]. Ali Akbar Ramezaniapour, A.P., Mahdikhani, M. and Moodi, F. (2011) Practical evaluation of relationship between concrete resistivity, water penetration, rapid chloride penetration and compressive strength, *Construction and Building Materials*, 25, 2472-2479.

INFLUENCE OF THE BARS POSITION IN THE REINFORCED CONCRETE FOR THE PREDICTION OF THE CHLORIDE CONCENTRATION IN THE LAYER STEEL-CONCRETE

F. Tavares (1) and C. Andrade (2)

(1) University of Cordoba-Spain

(2) CIMNE-Spain

Abstract

Corrosion of reinforcing steel in concrete due to chloride ingress is one of the main causes of the deterioration of reinforced concrete structures. The corrosion process is accompanied by an increase in volume, which induces tensile stresses in the surrounding concrete, which may result in cracking and spalling of the concrete cover if the concrete tensile strength is exceeded. The mathematical formulation idealized the corrosion sequence as a two-stage process: an initiation stage, during which chloride ions penetrate to the reinforcing steel layer and depassivate it, and a propagation stage, in which active corrosion takes place until cracking of the concrete cover. Until now the process of chloride penetration has been modelled assuming semi-infinite boundary due to the thickness of the concrete is usually comparatively large, however this is not the case at the rebar position as the chlorides find the bar surface a do not progress more being accumulated in the steel/concrete interface. The study in this paper shows a deterministic analysis of the chloride diffusion process by the finite element method (FEM) which numerically solves Fick's second Law taking into account the position of the reinforcing bar. The results show that the chloride threshold are reached before than if semi-infinite conditions are considered and that the stresses produced are different than if generalized corrosion is simulated, aiming into the calculation of shorter service life. The finite boundary should be the condition used for the calculation of time to corrosion if second Fick's law is applied.

Keywords: reinforcement corrosion, chlorides boundary conditions, service life

1. INTRODUCTION

Chlorides develop corrosion when they arrive to the reinforcement in an amount above of the threshold value. The oxides generated occupy a larger volume than the parent steel and

induce the cracking of the concrete cover. The most accepted model to calculate the time to corrosion initiation is the solution of Fick's second law, equation (1) [1]:

$$-J(x) = \frac{\partial C(x)}{\partial t} = D_{ap} \frac{\partial^2 C}{\partial x^2} \quad (1)$$

Assuming semi-infinite boundary conditions, the typical solution is the so named the “error function” equation [2] is formulated where x is the penetrated distance:

$$C_{th} = C_s \left(1 - \operatorname{erf} \frac{x}{2\sqrt{D_{ap}t}}\right) \quad (2)$$

However, at the rebar position the boundary conditions are not semi-infinite and an accumulation of chlorides is produced as published by Sagües [2] which leads to produce an earlier depassivation than predicted by the classical equation (2). This circumstance has not been taken into account in recent models proposed by fin Model Code 2010 [3]. In present paper is analyzed through a Finite Element Method how is the process in the rebar surface and which are the consequences in the service life calculation of not considering the finite boundaries and consequent chloride accumulation.

2. EXPERIMENTAL

The bar position (figure 1-left) can be modelled by FEM employing the Galerkin weighted residual method, as a barrier interrupting the transport of the ions chloride. Such barrier can be expressed mathematically by the Neumann boundary condition, equation (3):

$$\frac{\partial c}{\partial n_i} = 0 \quad (3)$$

Where n_i is the normal vector on the interface rebar/concrete. For the mesh it is used a linear triangular element with straight sides and a node at each corner. There is one degree of freedom associated to each node, field variable chloride concentration.

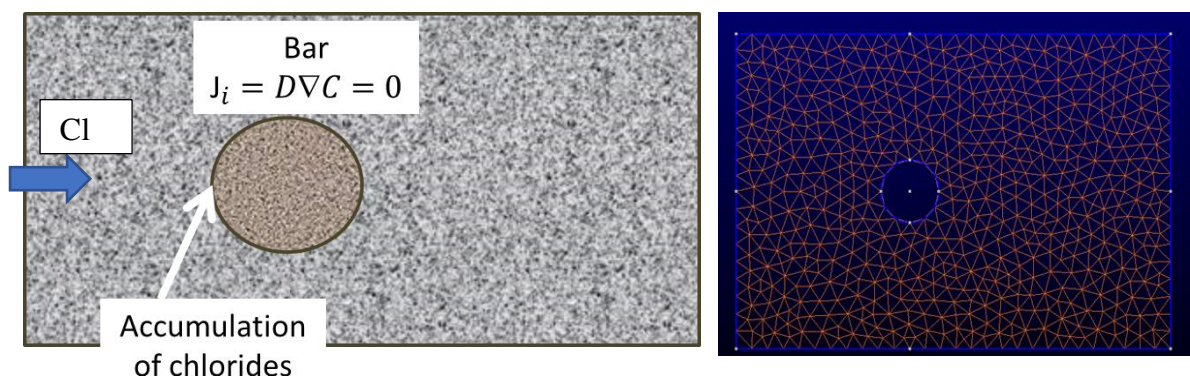


Figure 1: Left: Rebar is acting as a barrier against the chloride diffusion where J_c is the chloride flux. Right: mesh used

Several theoretical examples were numerically tested considering the variation of:

- The cover depth
- The value of the diffusion coefficient
- Service life duration
- The bar diameter

In all examples the surface concentration has been maintained constant and equal to 1%. And a threshold value for corrosion initiation of 0.4%.

3. RESULTS

3.1. Cover depth

Figure 2 shows the chloride concentration after 25 years at the rebar level of 1 cm for a $D = 10^{-9} \text{ cm}^2/\text{s}$. With a critical concentration of chlorides of 0.4%, the time to depassivate the reinforcing bar with the classical error function solution (equation(2)) is 8220 days (around 22 years a half) while if the bar position is considered, the time would be of 1080 days (around 3 years). Thus, the overestimation of the service life would be of almost 20 years.

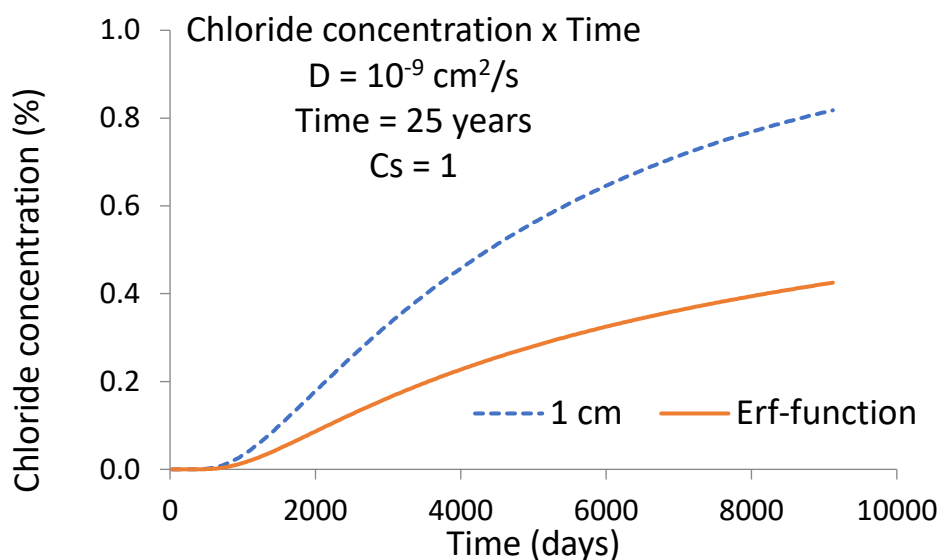


Figure 2: Chloride concentration (%) vs time for a concrete cover of 1cm.

Figure 3 shows the chloride profiles for different rebar positions with the same $D = 10^{-9} \text{ cm}^2/\text{s}$ and $t = 25$ years as in figure 2. The overestimation of the time to corrosion initiation decreases with the cover depth in such a manner that for cover depths above 3 cm the differences are not significant because the D value of $10^{-9} \text{ cm}^2/\text{s}$ is very low.

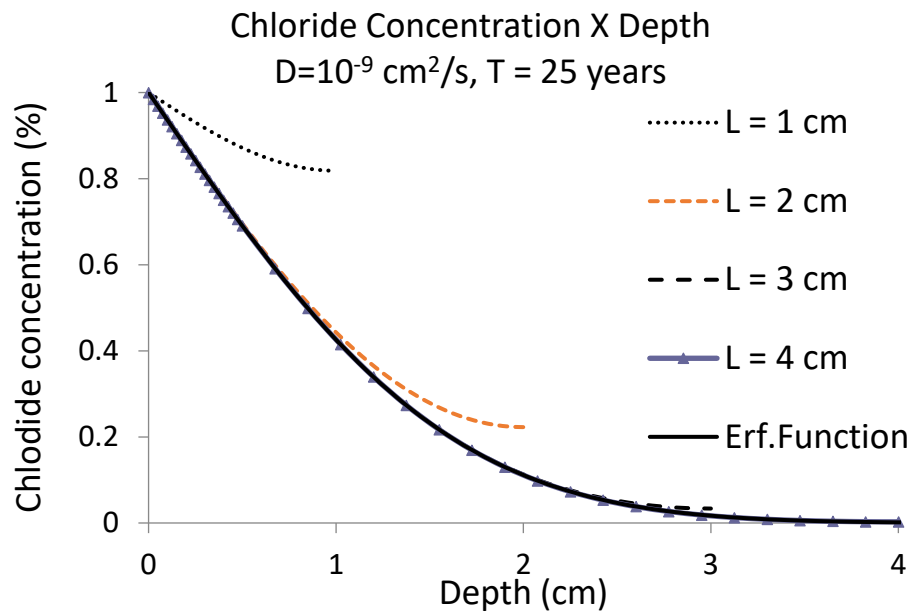


Figure 3: Chloride concentration vs cover depth for chloride diffusion coefficient $D = 10^{-9} \text{ cm}^2/\text{s}$ during 25 years.

3.2. Diffusion coefficient influence

In figure 4 is represented the chloride concentration versus the depth for a diffusion coefficient of $D= 10^{-8} \text{ cm}^2/\text{s}$. Now the influence of the cover depth is much more important and cover depths of 3 cm give very different critical chloride concentrations than when non considering the presence of the rebar (the classical error function solution).

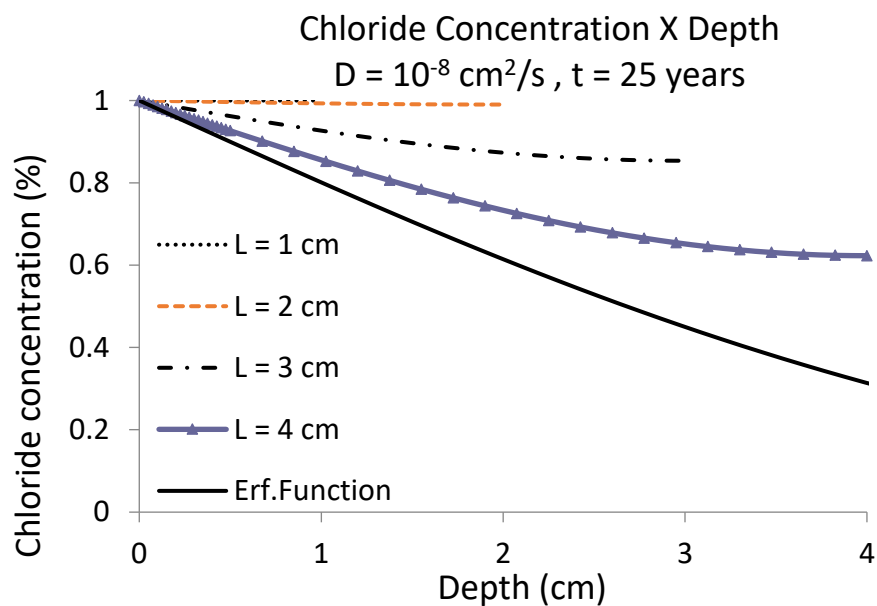


Figure 4: Chloride concentration vs cover depth for chloride diffusion coefficient $D = 10^{-8} \text{ cm}^2/\text{s}$ during 25 years.

Figure 5 depicts the chloride profiles with $D = 10^{-9} \text{ cm}^2/\text{s}$ for 50 years' service life instead of 25 years. At this age the cover depth of 3 cm presents a difference with the classical error function while at 25 years it presented the same value. This enables to deduce that the overestimation of the classical error function is higher as the service life is longer.

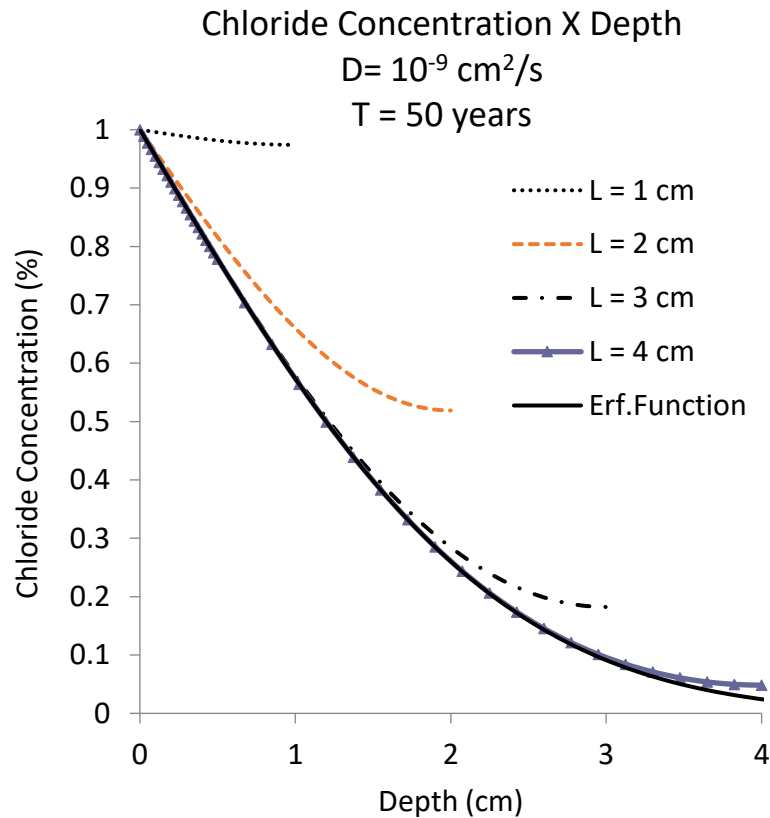


Figure 5: Chloride concentration x depth considering chloride diffusion coefficient $D = 10^{-9} \text{ cm}^2/\text{s}$ during 50 years.

3.3. Rebar diameter influence

The effect of the bar diameter is given in figure 6 for bars of 2 cm and 4 cm in Diameter. The concrete cover selected for the example was of 3 cm and a $D = 10^{-8} \text{ cm}^2/\text{s}$. The results indicate a difference of around 0.1% in chloride concentration at the rebar level of 25 and 50 years of exposure.

Figure 7 shows the same but for other bar diameters and a smaller $D = 10^{-9} \text{ cm}^2/\text{s}$. The differences at 25 and 50 years can be quite important for thick bars.

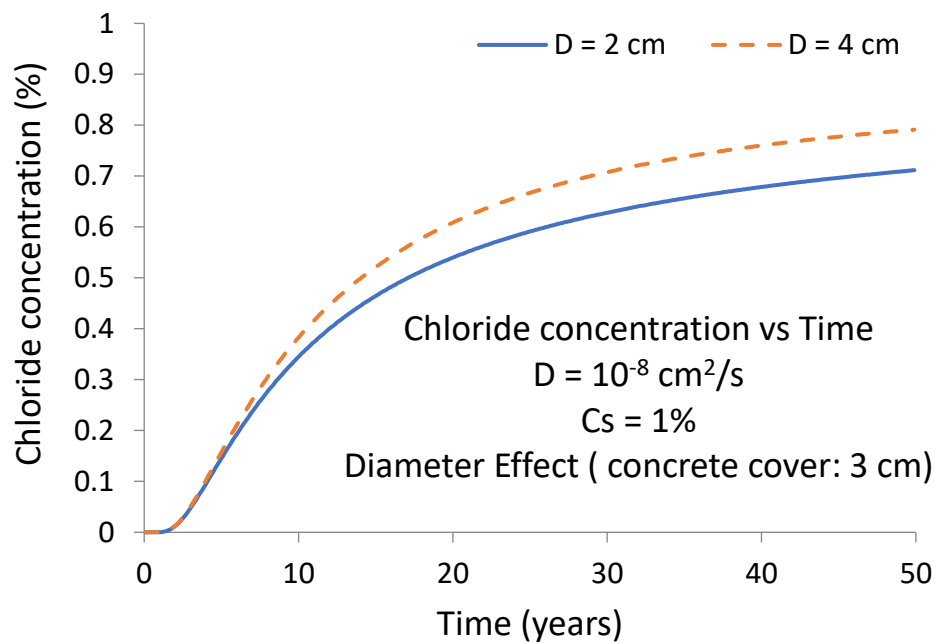


Figure 6: Chloride concentration versus time for two diameters at a same concrete cover.

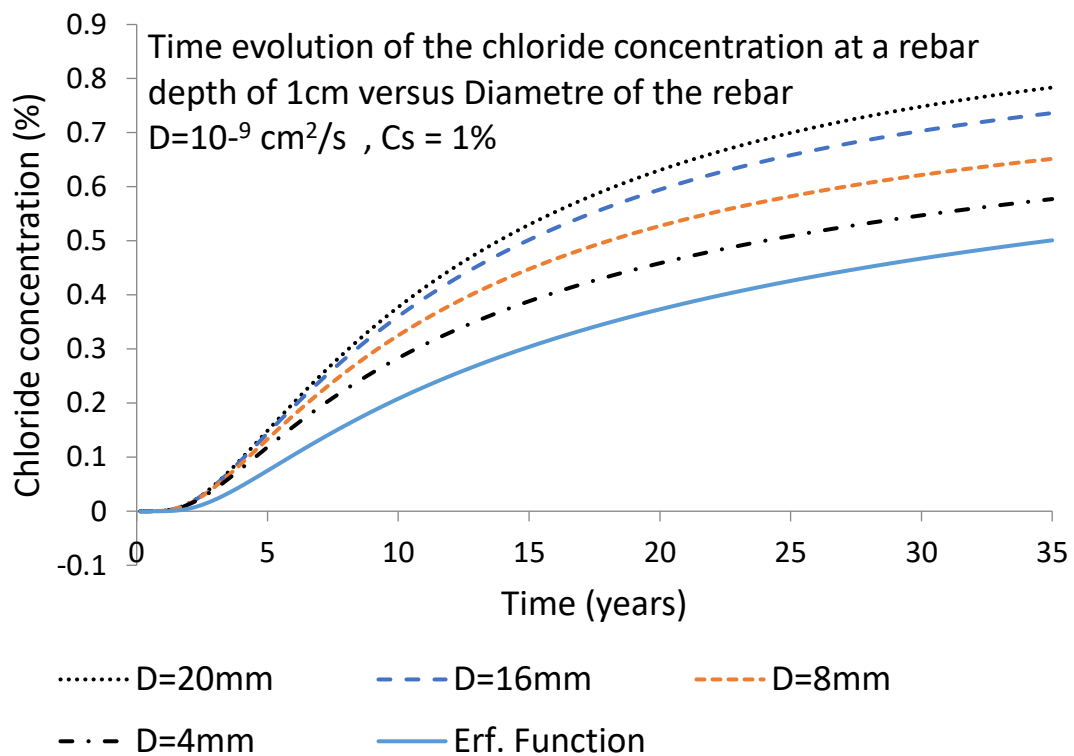


Figure 7: Chloride profile variation for different rebar diameter with a same concrete cover.

Table 1 gives the time overestimated of the time to corrosion initiation of the classical Erf-Function equation in comparison with the results taking into account the rebar position. The concrete cover for those simulation is 1 cm.

Table 1: Service life time variation for different rebar diameter with a same concrete cover.

Rebar Diametre	Time to depassivation $C_{critical}=0.4\%$	Overestimation	Overestimation
Erf. Function	22.4 years	0%	100%
4 mm	15.68 years	42.86%	30.00%
8 mm	12.88 years	73.91%	42.50%
16 mm	11.2 years	100.00%	50.00%
20 mm	10.64 years	110.53%	52.50%

Finally in figure 8 the chloride concentration distribution for two different diameters (left diameter of 40 mm and right diameter of 20 mm) is shown. The critical concentration will arrive first at the thicker rebars because higher diameter represents a larger barrier for the chloride ions flux.

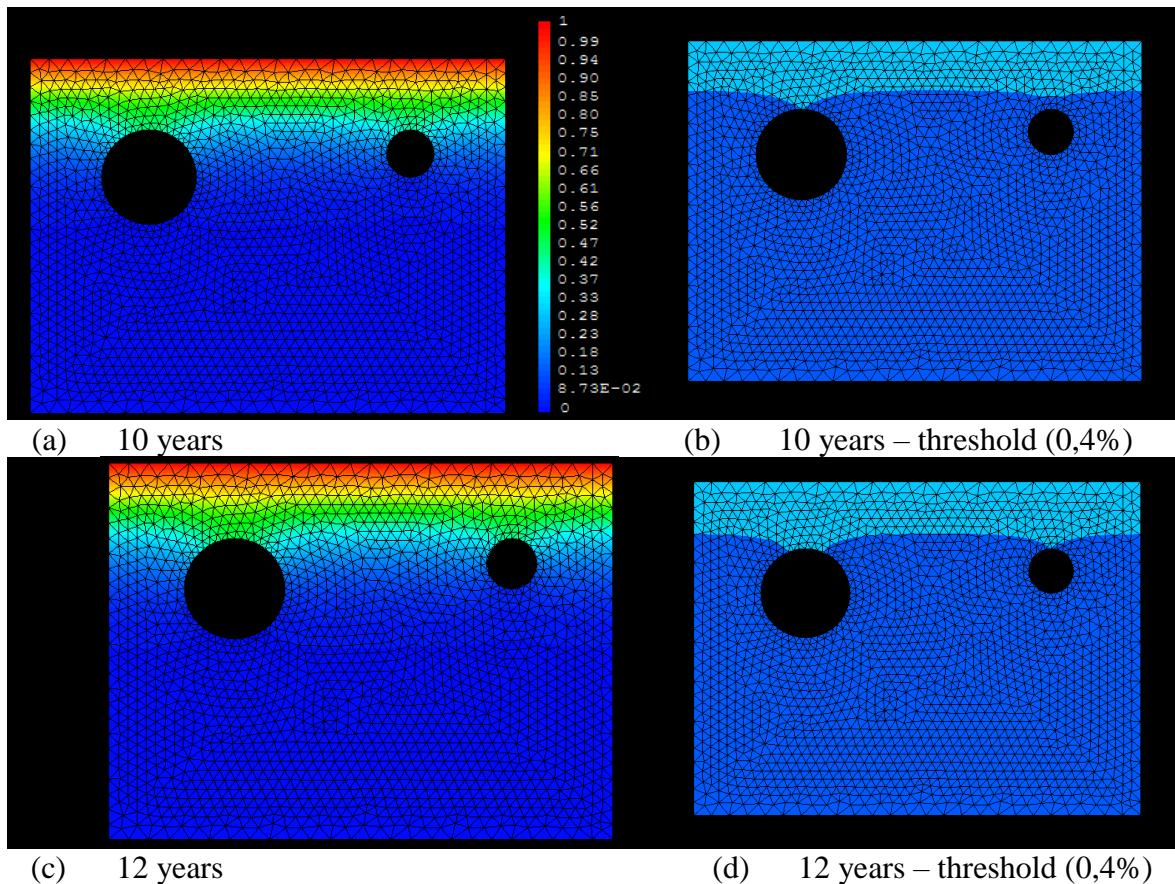


Figure 8: Diameter effect at the same concrete cover of 3 cm.

4. CONCLUSION

Present models based in Fick's second law of diffusion with a solution based in semi-infinite boundary conditions has many limitations due to the real process does not strictly follow that equation. Numerical calculations based on FEM are more mathematically capable of modelling the several time evolutions of the input parameters. Thus, the analytical solutions considered in many of the studies do not respect the differential base equation.

The bar represents a barrier for the chloride penetration and then, the ions accumulate at the bar surface aiming to an increase of the chloride concentration with respect to the solution based in the classical error function equation. Through the use of the finite element approach the consequences in the predictions of considering finite boundary conditions for the bar position have been deduced.

The chloride threshold concentration will be reached as faster:

- as thinner the cover is,
- as higher the diffusion coefficient is
- as longer the service life is and
- as thicker the bar is.

ACKNOWLEDGEMENT

The authors are grateful to the Institute of Construction Sciences of the High Research Council (CSIC) of Spain where the study was made. They are also grateful to the Ministry of Education and Science for providing the funds.

5. REFERENCES

- [1] Tuutti, K., "Corrosion of steel in concrete", Swedish Cement and Concrete Institute (CBI) n° 4-82. Stockholm (1982).
- [2] Kranc, S. C., Sagues, A. A., & Presuel-Moreno, F. J. (2002). Decreased corrosion initiation time of steel in concrete due to reinforcing bar obstruction of diffusional flow. *ACI Materials Journal*, 99(1).
- [3] Model Code 2010. fib (2012).

DAMAGE PARAMETERS OF REBARS IN MARINE ENVIRONMENT AND FATIGUE LIFE

Charis Alk. Apostolopoulos (1), Konstantinos F. Koulouris (2) and Maria A. Basdeki (2)

(1) Associate Professor, Department of Mechanical Engineering & Aeronautics, University of Patras, Greece

(2) Civil Engineer, PhD candidate, Department of Mechanical Engineering & Aeronautics, University of Patras, Greece

Abstract

A major task in civil engineering is the estimation of service lifetime of all structures and especially of these of high importance. Infrastructures, like highway bridges in marine environment, during their lifetime are subjected to heavy traffic loadings and in aggressive corrosive environment, and the consequence is the gradual structural deterioration. Due to the abovementioned, the durability of RC structures is affected and a significant reduction of the remaining service life is induced.

As it is widely known, corrosion constitutes a major deterioration factor for infrastructures which are located on coastal areas. This paper presents the results of the corrosion fatigue behaviour of reinforcing steel bars. Fifty two steel bars were divided into 2 groups of different exposed length (long – short) in marine environment and into 6 different exposure time of 25h, 50h, 75h, 150h, 200h and 230h simulating XS exposure (wetting-drying cycles). The steel bars were cleaned, weighed and their surface damage was examined and fatigue tests were performed. The results demonstrated that the corrosion damage (in terms of mass loss) of both specimens' groups is closely related to the exposed, each time, length to the corrosion environment (differential aeration corrosion). As a consequence, the lifetime of reinforcing steel bars with short exposed length depicts unexpectedly a dramatic reduction in comparison with those with long exposed length. Extrapolating the results of the present study on reinforcement of linear RC elements in marine environment, issues are raised concerning the assessment of high importance structures in relevant aggressive environment.

Keywords: differential aeration corrosion, fatigue life, reinforcing steel, marine environment

1. INTRODUCTION

Corrosion of reinforcement steel is one of the main degradation problems in reinforced concrete structures. In particular, in coastal regions, where the prevailing high (mean) temperature is combined with high concentration of chlorides, the corrosion phenomena are intense [1]. The most significant negative consequences of rebars' corrosion, as these are described analytically in existing literature [2-4], are the reduced cross-sectional area (mass loss), the development of pits and notches which are responsible for the development of stress concentration points, the degradation of mechanical properties, as strength capacity and ductility, and cracking and spalling of concrete cover, which leads to the bond loss between steel and concrete. Therefore, corrosion affects the bearing capacity of RC elements.

All structures, such as highway bridges, are subjected to cyclic loading during their lifetime and the repeated stress results in fatigue damage of materials. Previous studies showed that fatigue without corrosion has a small impact on RC structures, notwithstanding experimental observations showed that severe corrosion impairs the fatigue accumulation and significantly reduce the useful life of a structure, especially at strain amplitudes of around 1% in LCF conditions. Prompted by these data, during the past decades, many researchers focused on relative topics such as the destructive consequences of both corrosion and fatigue. Apostolopoulos et al [4] used the low cycle fatigue test of steel to assess the effect of accumulating corrosion damage. Experimental data of low-cycle fatigue tests performed on corroded reinforced columns [5-8] report the importance of corrosion damage on the reduction of serviceability, which, to date, is the main criterion for the design of the structure. In the present research, an experimental investigation had been conducted, so as to account for the effect of different exposed to corrosion length on reinforcing steel bars, which subsequently affects the structural performance and service time of RC structures.

2. EXPERIMENTAL PROCEDURE

2.1 Material and Specimens

The experiments of this study were conducted on ribbed steel reinforcing bars of 16mm nominal diameter and of B500c class. The chemical composition of steel B500c is given in Table I. Totally, fifty two specimens were cut, each with a total length of 300 mm.

Previous studies [9-11] had demonstrated that corrosion damage depends on the exposed to corrosion length. According to the abovementioned results, differential aeration corrosion may contribute to the electrochemical process of corrosion, Differential aeration corrosion is a type of corrosion that occurs when oxygen concentrations vary across a metal's surface, creating an anode and a cathode on it, thus oxidation occurs. In differential aeration corrosion, the area with the higher oxygen concentration becomes the cathode and that with the lower oxygen concentration becomes the anode. Consequently, the portion of the metal that has the lower oxygen concentration is the portion subject to corrosion. The anodic dissolution rate depends solely upon the potential difference across the electrolyte-metal interface.

In order to probe the corrosion consequences in different exposed lengths, the rebars were subdivided into two groups, these being 2 cm and 12 cm free to be corroded and the rest of rebar's length was protected with a wax layer, as it is shown in Figure 1.

Table 1: Chemical composition of reinforcing steel (% by wt.)

Element	C	Mn	Si	Cr
% by wt.	0.21	1.04	0.2	0.17



Figure 1: Preparation of the “long” specimens (exposed length 12cm – left) and “short” specimens (exposed length 2cm – right)

2.2 Accelerated corrosion

Since corrosion phenomenon is a slow natural process, it would be required a long testing period. In order to have faster results, each group of rebars was subjected to artificial accelerated corrosion. The tests were carried out in polymer (plastic) cells containing 5% NaCl. Four "bare" reinforcing bars and one stainless steel bar were immersed in each cell. In this method, a D.C. power supply is used to accelerate the corrosion process. The reinforcing bars were connected to the positive terminal of the power supply, acting as anode of electrochemical circuit, and stainless steel bar was connected to the negative terminal, respectively, acting as the cathode (Figure 2) Generally, coastal areas are classified into three different zones, according to their susceptibility to corrosion.

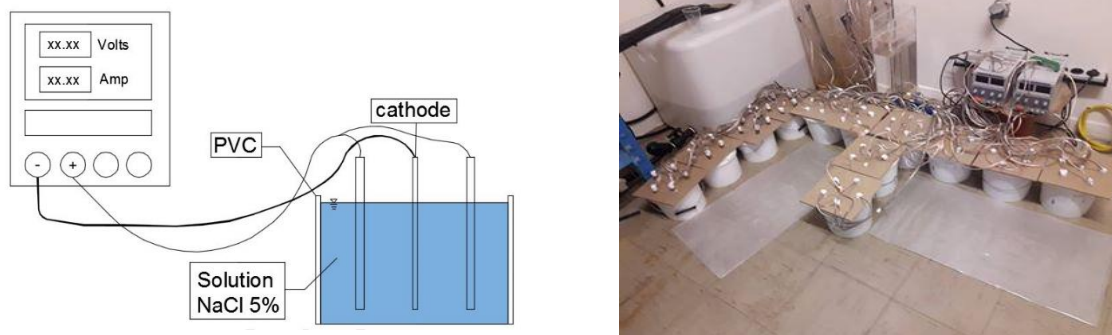


Figure 2: Procedure of accelerated electro-corrosion. (Left) Schematic representation, (Right) Experimental setup

Precisely, the cases of submersion, splash and tidal circumstances and atmospheric corrosion, are the three exposure zones. Splash and tidal environments are the most aggressive among the three cases, given the high chloride concentration and the wetting- drying cycles [12,13]. Hence, a cyclic exposure was performed, with 8 hours wet, by impressing current density of 1 mA/cm^2 on the specimens, and 16 hours in dry mode. In order to obtain different corrosion levels, specimens were subjected to six different exposure times, these being 25, 50,

75, 150, 200 and 230h, respectively. After the accelerated corrosion exposure, the specimens were washed, and mass loss evaluation was made in accordance with ASTM G1-03 [9], so as to obtain the degree of corrosion. The percentage mass loss was calculated as shown in Eq. 1 :

$$M_t = \frac{M_i - M_f}{M_i} \times 100 \quad (1)$$

2.3 Mechanical Tests

Due to the limited corrosion damage of specimens with the long exposed to corrosion length, only the specimens with the short exposed to corrosion length were subjected to mechanical tests.

Monotonic tests were carried out on non-corroded and 230h "short" corroded specimens according to the ISO 15630-1 Standard [14], which can be used as an initial assessment of the corrosion damage. Each specimen had a total length of 600 mm. For the tests, a servohydraulic MTS 250 kN machine was used. The employed displacement rate was set to 2 mm/min. The mean values of yield stress (R_p), ultimate stress (R_m), and plastic strain at maximum force (A_g) were determined, after three tests for each category.

Moreover, cycle fatigue tests were also conducted on non-corroded and 230h "short" corroded reinforcing bars, in accordance with the ISO 15630-1 Standard [15], respectively with the tensile tests. As the common distance between the transverse reinforcement is 6D in real RC elements, the tested free length was selected to be 96 mm, Figure 3. Constant strain amplitudes, $\pm 0.75\%$, $\pm 1.00\%$ and $\pm 1.25\%$ of the free length, were selected in order to limit the buckling phenomena. All tests were carried out at a frequency of 2 Hz and a stress ratio $R = -1$. For both categories (non-corroded and 230h "short" corroded specimens), three repetitions were conducted for each strain amplitude. Additionally, for the reproducibility of the testing results, five "short" specimens were also subjected to exposure time of 230h, so as to complete three specimens per strain amplitude.

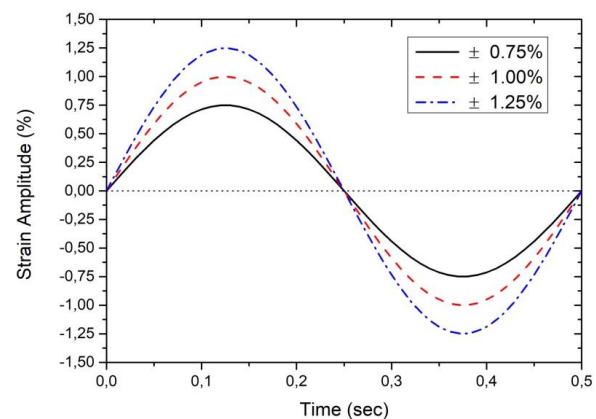


Figure 3: (Left) Experimental fatigue test (free length 96 mm). (Right) Strain waveforms received as input

3. RESULTS AND DISCUSSION

As expected, corrosion damage increases with increasing exposure time to electro-corrosion. The exposure caused the production of an oxide layer which covered each specimen on its exposed to corrosion part (not on the protected with the wax layer part). The

oxide layer is associated to an appreciable loss of the specimens' mass. The average mass loss degradation, as this was evaluated uniformly for both specimens' groups, is shown in Figure 4.

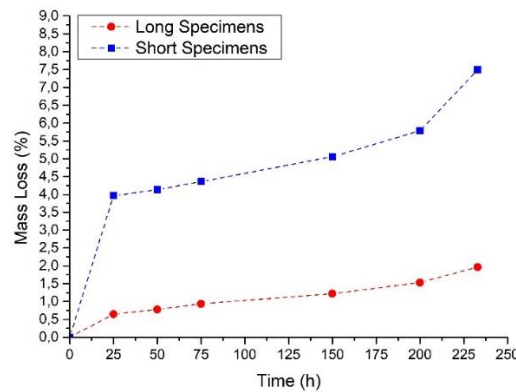


Figure 4: Mass loss of "long" specimens (exposed length 12cm) and "short" specimens (exposed length 2cm).

It is obvious that the specimens with exposed length equal to 2 cm showed greater mass loss in comparison with these with exposed length of 12 cm. Moreover, it is noteworthy that when the exposed to corrosion length is short, the mass loss is rapid since the first exposure hours, as the corrosion phenomenon is limited to a smaller area. The mass loss of the specimens with the long exposed to corrosion length demonstrated percentage mass loss less than 2% for the entire testing time, whereas the specimens with the short exposed to corrosion length showed 7.5% mass loss (about 4 times greater) by the end of the exposure time.

Prior to mechanical tests, the corroded surface of specimens was investigated by visual microscopic inspection, according to the ASTM G46 - 94 Standard [16], in order to estimate the size of pits. An area of 1cm² was selected in the corroded part of each specimen with 75h, 150h and 200h exposure time, respectively. The average values of pit density, pit area and pit depth were evaluated for both specimens' groups, as shown in Table 2. According to this, a dense cover of pits on the specimens' surface was observed, however, their size was deemed to be insufficient. Hence, general corrosion was considered for both groups ("long" and "short") specimens. Due to the experimental procedure, where the tested reinforcing bars were bare and not embedded in concrete, as in real structures, the general corrosion is justifiable.

Table 2: Pitting evaluation by visual microscopic inspection.

corrosion time (h)	Long exposed length (12 cm)				Short exposed length (2 cm)			
	Mass loss (%)	pit density (pits/cm ²)	pit area (mm ²)	pit depth (μm)	Mass loss (%)	pit density (pits/cm ²)	pit area (mm ²)	pit depth (μm)
75	0.94	348	0.06	40	4.36	265	0.12	53
150	1.22	390	0.08	53	5.06	<u>210</u>	0.14	66
200	1.53	358	0.08	50	5.79	<u>234</u>	0.12	70

Due to the limited corrosion damage of specimens with the long exposed to corrosion length, only the specimens' group with the short exposed to corrosion length was subjected to mechanical tests. In particular, monotonic tests were conducted to non-corroded specimens

and 230h-corroded "short" specimens, with recorded mass loss of 7.5%. The σ - ϵ curves for each case is shown in Figure 5.

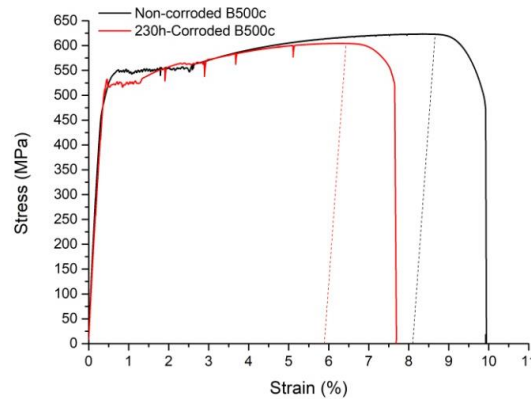


Figure 5: Tensile graphs for non-corroded and 230h-corroded "short" rebars B500c

Corrosion results in the degradation of the mechanical properties significantly. As it is shown in Figure 5, mean values' reduction of yielding stress R_p (from 550 MPa to 523 MPa) and of ultimate stress R_m (from 623 MPa to 604 MPa) is noted. However, the main factor, which is affected by the corrosion phenomenon, is the ductility capacity. In particular, the mean value of percentage plastic strain, at maximum force, A_g was fallen from 8.10% to 6.89%. Ductility is strongly associated with the absorbed energy. This observation, referring to the monotonic curve, can become an initial indication in the interpretation of the following fatigue life results.

The results of the experimental setup of LCF are given in Table 3, where the average number of cycles to failure N_f for different applied strain amplitudes are presented. Below, two indicative fatigue graphs are shown (Figure 6), for strain amplitude equal to $\pm 1.25\%$, for non-corroded and 230h corroded specimens, respectively. Shortly after the start of the exposure time, corrosion occurs and intensifies with time. As the corrosion aggressiveness increased, so the number of cycles to failure decreased (corroded steel rebars failed earlier), for all selected strain amplitudes, which is a clear indication of softening of the material. More specific, for a low range of strain amplitude, this of $\pm 0.75\%$, number of cycles decreased by 16.7%. Between corroded and non-corroded bars, for strain amplitude equal to $\pm 1.00\%$ and $\pm 1.25\%$, the reduction of fatigue life is 38.1% and 41.1%, respectively.

Reasons for "health monitoring", during the assessment of material degradation, push engineers to express the corrosion damage in terms of mass loss. However, the parameter of exposed to corrosion length is not involved in this generally followed practice. It is noteworthy that, according to the experimental results, "short" specimens, under the same exposure time, recorded greater mass loss than that of "long" ones, leading to reduced fatigue life.

As it is known, stress concentration at the root of transverse rib arises due to geometry of reinforcing steel bar, leading to fatigue crack initiation from the rib root. In corroded specimens, ribs diminish and thus the specimens are exempted from such critical points of stress concentration. Based on the abovementioned, one would expect greater average number of cycles to failure N_f of the corroded specimens, in contrary to reference specimens, where ribs results to an increase in stresses and therefore the starting point for an incipient crack. It

is also apparent that the longer corrosion persists in lower strain amplitudes, and the more severe it is, the lower is the fatigue life. The results depicted that rebar subjected to aggressive environment, recording high mass loss, are able to endure far fewer cycles to failure N_f and subsequently showed degradation of their mechanical performance than rebars with lower recorded mass loss. Hence, the effect of corrosion on fatigue behaviour is still dominant.

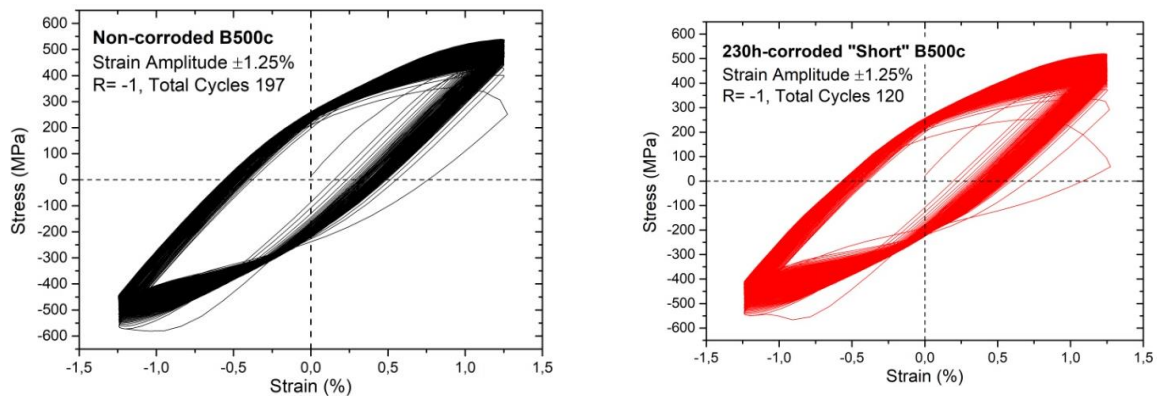


Figure 6: Fatigue graphs for non-corroded and 230h-corroded "short" rebars B500C

Table 3: Number of cycles to failure N_f of non-corroded specimens and 230h-corroded specimens (with mean mass loss 7.5%)

Strain amplitude	Number of cycles (N_f)	
	Non-corroded specimens	230h-corroded specimens
$\pm 0.75\%$	1750	1458
$\pm 1.00\%$	512	317
$\pm 1.25\%$	197	116

4. CONCLUSIONS

A study was carried out on the corrosion (low cycle fatigue – strain controlled) fatigue behaviour of rebar. Based on the experimental results, the main outcomes can be drawn as follows:

- Corrosion presents dominant influence on the mass loss of rebars, depending also on the length of exposed corroded rebar. More specific, for same exposure time, rebars with shorter exposed length show greater mass loss percentage than rebars with long exposed length.
- The corrosion damage of reinforcement mainly affects rebars' ductility and reduces their capacity to absorb energy.
- Corrosion shortens the number of cycles to failure. As a consequence, the fatigue life of rebar exposed simultaneously to corrosion and fatigue is, even if the mass loss is low, always shorter than that of rebar exposed to fatigue only. Hence, during monitoring, both parameters should be taken into account.

- During the assessment of RC structures in marine environment, the corrosion damage of reinforcing steel bars is expressed in terms of mass loss. The results of the present manuscript suggest the crucial parameter of exposed to corrosion length to be involved in predictive degradation models.

REFERENCES

- [1] Apostolopoulos, C.A., Demis S., Papadakis, V.G., 'Chloride-induced corrosion of steel reinforcement – mechanical performance and pit depth analysis', *Constr. Build. Mater.* **38** (2013) 139–46.
- [2] Papadopoulos, M.D., Apostolopoulos, C.A., Zervaki, A.D., Haidemenopoulos, G.N., 'Corrosion of exposed rebars, associated mechanical degradation and correlation with accelerated corrosion tests', *Jour. Constr. Build. Mater.* **25** (2011) 3367-3374.
- [3] Apostolopoulos C., 'The influence of Corrosion and Cross- Section Diameter on the Mechanical Properties of B500c Steel', *Journal of Materials Engineering and Performance* **18** (2) (2009) 190-195.
- [4] Apostolopoulos C., Konstantopoulos G., Koulouris K., 'Seismic resistance prediction of corroded S400 (BSt420) reinforcing bars', *International Journal of Structural Integrity* **9** (1) (2018) 119-138.
- [5] Afsar E., Kashani M.M., 'Exploring the impact of chloride-induced corrosion on seismic damage limit states and residual capacity of RC structures', *Structure and Infrastructure Engineering* **14** (6) (2017) 714-729.
- [6] Ma, Y., Che, Y., & Gong, J., 'Behaviour of corrosion damaged circular reinforced concrete columns under cyclic loading', *Construction and Building Materials* **29** (2012) 548-556.
- [7] Li, X., Liang, Y.-S., Zhao, Z.-H., & Ly, H.-L., 'Low-cycle fatigue behavior of corroded and CFRP-wrapped reinforced concrete columns', *Construction and Building Materials*, **101** (2015) 902-917.
- [8] Apostolopoulos C., Papadopoulos M., 'Tensile and low cycle fatigue behaviour of corroded reinforcing steel bars S400', *Constr Build Mater.* **21** (4) (2007) 855–64.
- [9] Drakakaki, Arg., Apostolopoulos, C., 'The size effect of rebars, on the structural integrity of reinforced concrete structures, which are exposed to corrosive environments', *MATEC Web Conf.* **188** (2018).
- [10] Apostolopoulos, C., Drakakaki, Arg., 'Correlation between the electrochemical corrosion parameters and the corrosion damage, on B500c dual-phase steel', *Innovations in Corrosion and Materials Science* **8** (1) (2018) 42-52.
- [11] Angst, U.M., Elsener, B., 'The size effect in corrosion greatly influences the predicted life span of concrete infrastructures', *Applied Sciences and Engineering* **3** (8) (2017).
- [12] Guo, A.X., Li, H.T., Ba, X., Guan, X.C., Li, H., 'Experimental investigation on the cyclic performance of reinforced concrete piers with chloride-induced corrosion in marine environment, *Engineering Structures*' **105** (2015) 1–11.
- [13] Glass, G.,K., Hassanein, A.M., Buenfeld, N.R., 'CP criteria for reinforced concrete in marine exposure zones', *J. Mater. Civ. Eng.* **12** (2) (2000) 164-171.
- [14] ASTM G1-03, Standard practice for preparing, cleaning and evaluating corrosion test specimens, **90** (2011).
- [15] ISO 15630-1:2010, Steel for the reinforcement and prestressing of concrete – Test methods – Part 1: Reinforcing bars, wire rod and wire.
- [16] ASTM G46-94, Standard Guide for Examination and Evaluation of Pitting Corrosion.

THE RELIABILITY OF CORROSION DETECTION WITH REGARD TO CHOSEN GRID SIZE

Sylvia Keßler

(1) Centre for Building Materials, Technical University of Munich, Germany

Abstract

The global dimension of corrosion-related durability challenges for infrastructure requires more effort in research for reliable corrosion inspection and condition assessment. For maintaining infrastructure durability especially in the field of reinforced concrete structures this information about the current condition is essential for scheduling future inspection or if necessary repair measures. Main reason of corrosion initiation in infrastructures is the application of de-icing salt during wintertime or chlorides from marine environment. If initiated, corrosion can lead to structural damage like cracking and spalling of the concrete cover.

The half-cell potential measurement method is the only available non-destructive measurement method to detect on-going corrosion. The information gained during half-cell potential measurement can be translated into structural reliability using common probabilistic models for predicting the service life of existing structures. In the case of chloride induced corrosion these models predict probabilistically the time to corrosion initiation respectively the corrosion probability at the time of inspection. Major impact on the accuracy of the updated service life besides the probabilistic model itself has the reliability and the evaluation of the half-cell potential measurement. However, one of the main influencing factors on the reliability of the half-cell potential method has the chosen grid size. Therefore, this paper presents a case study for updating the service life with the focus on how the chosen grid size influences the reliability of corrosion detection.

Keywords: half-cell potential measurement, reinforcement corrosion, concrete structures, corrosion probability

1. INTRODUCTION

1.1 Background

Reinforcement corrosion of concrete structures is major reason for premature repair measures. Especially the exposure of chloride ions from sources such as de-icing salts or marine

environment leads to corrosion initiation. Chloride ions penetrate through the porous concrete and as soon as a critical chloride concentration reaches the reinforcement level chloride-induced corrosion becomes likely. The deterioration process continues with a local loss of cross section followed by cracking and spalling of the concrete cover. However, civil engineering structures should fulfil long-term serviceability and long-term load-bearing capacity since these structures are very costly to build. But considering the increasing age of our infrastructure unexpected maintenance costs become more likely which could lead to severe economic consequences. Consequently, we need reliable information concerning the remaining service life to schedule in advance the needed repair measures and to predict the needed financial reserves. Therefore, corrosion condition assessment of reinforced concrete structures forms a vital aspect of achieving reliable condition data.

1.2 Corrosion detection in reinforced concrete structures

Reinforcement corrosion is a very instantaneous electrochemical process which can vary in intensity and from point to point [1-3]. Thus, the degree of corrosion deterioration can show huge spatial variability within one structure. The used corrosion inspection method shall reflect this issue by enabling a scanning data acquisition. The non-destructive half-cell potential measurement is such as method [4-8] which detects corrosion initiation before structural damage such as cracking and spalling occur.

Due to the initiation of reinforcement corrosion the anodic and cathodic areas on the reinforcement form a galvanic element. The resulting corrosion current which flows in between anode and cathode causes a potential field in the concrete. An external reference electrode on the concrete surface is able to measure the potential field when the electrode is as well connected through a high resistance voltmeter with the reinforcement. The anodes where the ion dissolution takes place and the cathodes are different electrodes with differences in their free corrosion potential and polarization behaviour. This electrochemical characteristic allows identifying anodic areas at these spots where more negative potential are measured in combination with a pronounced potential gradient. By scanning the whole surface the half-cell potential measurement provides spatial information of the corrosion condition.

Nevertheless, the half-potential readings does not only depend on the corrosion condition of the reinforcement other factors such as concrete resistivity, chosen grid size and so on [9,10] affect the reliability of the test method. Within the influencing factors the grid size is the only factor which the engineer can determine. With smaller grid size the reliability of the corrosion detection increases [10] but due to longer measurement time the costs increase as well. Common guidelines recommend the grid size in between $15 \times 15 \text{ cm}^2$ [4,5] up to $25 \times 25 \text{ cm}^2$ [5,6]. If higher detectability is needed a grid size of $10 \times 10 \text{ cm}^2$ is feasible. These recommendations are based on expert experience. Keßler et al. [10] quantified for the first time corrosion detectability with respect to the grid size. In addition to that, this paper presents a case study on the reliability of corrosion detection with regard to the chosen grid size. Half-cell potential measurement data from one component with different grid sizes is used for updating the corrosion probability.

2. CASE STUDY

2.1 Structure

The structure under investigation is a tunnel built in 1998 which is located in the south of Bavaria. The used concrete composition is a B35 made with Portland cement. It is assumed a water-to-binder ratio of about 0.5. During winter time the structure is exposed to chloride contaminated splash and spray water coming from de-icing agents. All year long drying and wetting cycles can be expected due to splash and spray water from the cars and trucks. Consequently, chloride-induced reinforcement corrosion is the decisive deterioration mechanisms. The measured concrete cover with a mean value of 65 mm ($\sigma = 8$ mm) is high but the chloride contamination is high as well. Based on chloride profiles taken from the structure the surface chloride concentration is about 2.93 m%./binder ($\sigma = 0.82$ m%./binder) and the apparent diffusion coefficient is about $1.46 \cdot 10^{-12}$ m²/s ($\sigma = 0.52 \cdot 10^{-12}$ m²/s). There is no dependency of the chloride contamination with regard to length of the tunnel or the height. With these data the a-priori depassivation probability is estimated.

2.2 A-priori depassivation probability

The a-priori depassivation probability is calculated according to the corrosion initiation model presented in the *fib* Model Code for Service Life Design [11]. Table 1 summarizes the model input parameters.

Table 1: Model input parameters for the service life prediction

Parameter	Unit	Distribution	μ	σ
D_{app}	10^{-12} m ² /s	Normal	1.46	0.52
α_{RCM}	-	Beta	0.30	0.12
t_0	a	Constant	15	
t	ar	Constant	100	
T_{ref}	K	Constant	293	
T_{real}	K	Normal	283	7
b_e	K	Normal	4800	700
$C_{S,\Delta x}$	m.-%/b	LogNormal	2.93	0.82
Δx	mm	Beta (0; 50)	10	5
C_{crit}	m.-%/b	Beta (0.2; 2.0)	0.6	0.15
C_0	m.-%/b	Constant	0	
c	mm	Normal	65	8

The resulting depassivation probability of the tunnel structure is shown in Figure 1.

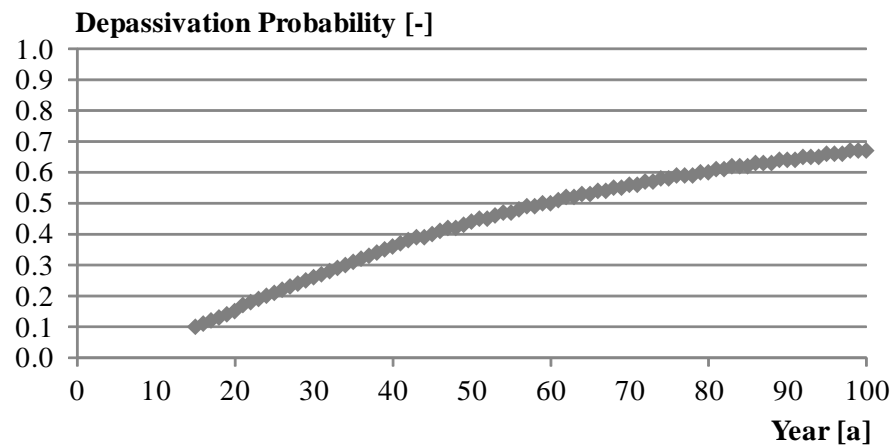


Figure 1: A-priori depassivation probability of the tunnel structure

After 15 years in service the whole structure shows a depassivation probability of about 10 %. Within the next 20 years the depassivation probability increases up to 30 %. There is a high probability that corrosion is already initiated or will be initiated soon. Therefore, the half-cell potential measurement has been performed to control the real corrosion condition state.

2.3 Inspection results

The corrosion condition assessment has been performed in 2014 according to the half-cell potential measurement Guideline B3 [5] when the structure was 15 years old. The used grid size is with $10 \times 10 \text{ cm}^2$ relatively small. The case study focuses on one segment with a size of 10 m length and 3 m height for the sake of clarity. Figure 2 shows the half-cell potential measurement data. The part where no data is available was the location of a lamp.

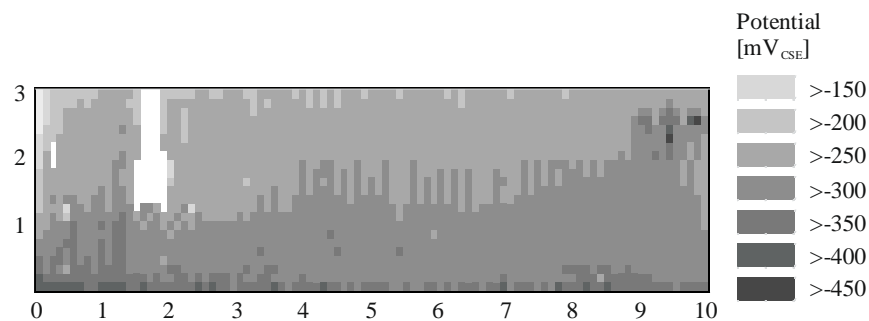


Figure 2: Inspection results of the half-cell potentials vs. Cu/CuSO₄

Since the tunnel segment is a vertical component the dependency of the concrete resistivity on the half-cell potential data is noticeable. With increasing height of the segment increases as well the half-cell potential data due to higher concrete resistivity. Some very low potential readings are at the bottom especially on the left corner. One potential gradient with low potentials is on the upper part (height app. 2.3 m) on the right side (length app. 9.8 m).

Now the half-cell potential data are subdivided into potential fields with different grid sizes by filtering. For the sake of comparison the half-cell potential data are translated into depassivation probability.

2.4 A-posteriori depassivation probability in dependence of the grid size

The original grid size of the half-cell potential measurement of $10 \times 10 \text{ cm}^2$ enables easily the generation of potential field grid sizes of $20 \times 20 \text{ cm}^2$ and $30 \times 30 \text{ cm}^2$. In dependence of the measurement starting point the filtering results in two grid sizes of $20 \times 20 \text{ cm}^2$ and in three grid sizes of $30 \times 30 \text{ cm}^2$. Figure 3 shows the depassivation probability in dependence of the grid size. The calculation of the depassivation probability out of the half-cell potential measurement is explained in [3]. The big advantage of this procedure is that the spatial information of the corrosion condition is maintained.

Comparing the pure half-cell potential readings, Figure 2, with the updated corrosion probability with same grid size the interpretation of the half-cell potential measurement becomes much more sophisticated. Spots with high corrosion probability are much easier detectable.

As larger the grid size as coarser is the resulting corrosion probability plot. Smaller spots with high corrosion probability in the $10 \times 10 \text{ cm}^2$ plot does not appear or appear only partly in the larger grid sizes. With a grid size of $20 \times 20 \text{ cm}^2$ the larger spots with higher corrosion probability (left corner bottom and right corner in the height) are detected. But with even higher grid size of $30 \times 30 \text{ cm}^2$ theses spots are not always detectable.

Based on these results a grid size of $20 \times 20 \text{ cm}^2$ or even smaller is recommendable. This result is in line with the recommendation given in [4,5,10] to match detection reliability and economic constrains. In case of high requirements on the corrosion detectability a grid size of $10 \times 10 \text{ cm}^2$ should be chosen.

Table 2 shows the mean values of the corrosion probability with regard to the grid size.

Table 2: Mean value of the depassivation probability in dependence of the grid size

Grid size [cm^2]	10x10	20x20_01	20x20_02	30x30_01	30x30_02	30x30_03
Corrosion probability [%]	11.4	10.8	12.0	12.4	11.3	10.3

The mean value of the corrosion probability in dependence of the grid size varies in between 10.3 % up to 12.4 %. This variation is really small. These values cope very well with the a-priori depassivation probability, Figure 1, of 10 %. Thus, the *fib* Model Code for Service Life Design [11] is an effective tool to estimate the corrosion condition of concrete structures.

At the end of the inspection a probing of the right spot (length app. 9.8 m) confirmed corrosion initiation with a loss of cross section of about 10 %.

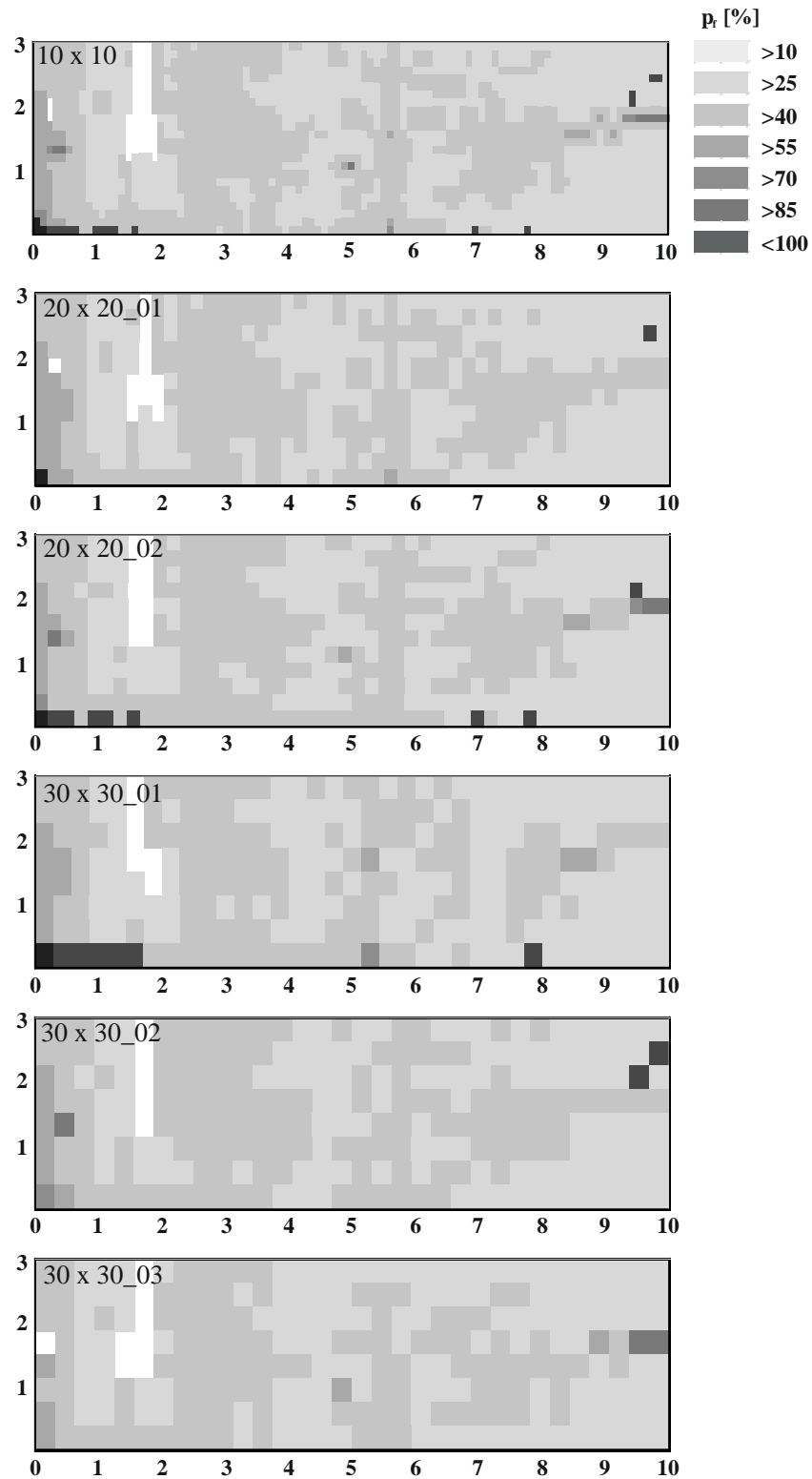


Figure 3: Depassivation probability in dependence of the grid size

3. CONCLUSIONS

The presented case study showed the reliability of corrosion detection with regard to the chosen grid size when half-cell potential measurements are performed. The comparison is based on the corrosion probability by updating the half-cell potential measurement data. The transformation of the half-cell potentials readings into corrosion probability enables a clear interpretation on the corrosion condition state.

It can be concluded that at least a grid size of 20 x 20 cm² or even smaller is recommendable as already stated in [4,5]. In case of high requirements on the corrosion detectability a grid size of 10 x 10 cm² should be chosen especially if the location of each corrosion spot needs to be known.

Knowing the current corrosion condition supports the scheduling of future inspection or if needed repair measures.

REFERENCES

- [1] Keßler, S., Fischer, J., Straub D., Gehlen C.: Updating of service-life prediction of reinforced concrete structures with potential mapping, In: *Cement & Concrete Composites* 47 (2014) 47–52.
- [2] S. Keßler, M. Huber, D. Straub, C. Gehlen, “Spatial variability of potential fields in reinforced concrete structures,” *ICASP* (2011), Zurich.
- [3] Kessler, S.; Gehlen, C.: Probability of Detection of Potential Mapping and its Impact on Service Life Prediction. In *Proceeding 12th International Conference on Applications of Statistics and Probability in Civil Engineering, ICASP12 Vancouver, Canada, July 12-15, 2015* <http://hdl.handle.net/2429/53300>.
- [4] Elsener B., Andrade C., Gulikers J., Raupach M. (2003). Half-Cell Potential Measurements - Potential Map-ping on Reinforced Concrete Structures. *RILEM TC 154-EMC. Materials and Structures* 36(261), 461-470.
- [5] DGZFP Merkblatt B3 (2014). Elektrochemische Potentialmessungen zur Detektion von Bewehrungsstahlkorrosion (In English available).
- [6] SIA Merkblatt 2006 (2013). Planung, Durchführung und Interpretation der Potentialfeldmessung an Stahlbetonbauten. Schweizerischer Ingenieur- und Architekten-Verein (in German)
- [7] ASTM C876 -09 (2009). Standard Test Method for Corrosion Potentials of Uncoated Reinforcing Steel in Concrete.
- [8] Reichling K., Raupach M., Broomfield J., Gulikers J., L’Hostis V., Kessler S., Osterminski K., Pepenar I., Schneck U., Sergi G., and Tache G. 2013 Full surface inspection methods regarding reinforcement corrosion of concrete structures, In *Materials and Corrosion*, 64, No. 2.
- [9] Keßler, S.; Gehlen, C.: Studie zur Potentialfeldmessung an 40 Jahre alten Stahlbetonbauteilen vom Olympiastadion München - Einfluss des Elektrolytwiderstands und des Messrasters; In: *Beton- und Stahlbetonbau* 108 (2013), Heft 9.
- [10] Kessler, S.; Gehlen, C.: Reliability evaluation of half-cell potential measurement using POD, *Journal of Infrastructure Systems*, 23, 2, (2017).
- [11] fib bulletin 34, “Model code for service life design,” (2006).

CHLORIDE INGRESS IN CONCRETE EXPOSED TO A SWEDISH ROAD ENVIRONMENT FOR OVER 20 YEARS

Luping Tang (1), Dimitrios Boubitsas (2) and Peter Utgenannt (2)

(1) Division of Building Technology, Chalmers University of Technology, Sweden

(2) RISE CBI Swedish Cement and Concrete Research Institute, Sweden

Abstract

In the middle of 1990's many reinforced concrete specimens with various qualities were exposed at the field site by a Swedish highway. The main variations include water-binder ratio (0.3, 0.35, 0.4 and 0.5), binder type (eight types of binder including five types of commercial cement and three types of blended cement with different additions of limestone, silica fume and ground granulated blast-furnace slag), and air content (5% entrained air and non-entraining). Measurements of chloride ingress profiles have been made after exposure for 1, 5, 10 and 20 years. The results show that, under Swedish de-icing salt environment chloride ingress in concrete with w/b 0.5 can reach the threshold level 0.4% by mass of binder (as the maximum allowed in EN 206-1) at the depth of 30-40 mm after exposure for 20 years, whilst in concrete with $w/b \leq 0.4$ the ingress depth at which the threshold level is reached will be less than 30 mm after the same exposure duration. Concerning chloride ingress in concrete, Swedish de-icing salt road environment is not as severe as Swedish marine splash environment.

Keywords: cement, concrete, chloride, durability, field exposure

1. INTRODUCTION

Chloride induced reinforcement corrosion is one of the most common reasons for the damage of concrete bridges. Sea water and de-icing salt are two external sources of chlorides which can ingress into concrete and initiate corrosion of reinforcement steel. To obtain the "first-hand" information about the long-term behaviour of concrete concerning chloride ingress and reinforcement corrosion under the de-icing highway environment, reinforced concrete specimens with different qualities have been exposed at the field site by Swedish highway 40 since 1996. Measurements of chloride ingress profiles in some selected types of concrete (Anl and Anl+5%SF, w/b 0.4) have been made after exposure for 1 and 5 years, and

in all types of concrete after exposure for 10 and 20 years. This paper presents the results from these measurements.

2. CONCRETE MATERIALS AND EXPOSURE CONDITIONS

2.1 Concrete materials

Eight types of binder (Table 1), including five types of commercial cement and three types of blended cement with different additions of limestone, silica fume and ground granulated blast-furnace (ggbf) slag, were used in concrete mixes with water-binder ratios of 0.3, 0.35, 0.4 and 0.5. Some of the mixes contained about 5% entrained air. Natural sands of size 0-8 mm and gravels (granitic type) of size 8-16 mm were used as aggregate. The detailed mix proportions were published elsewhere [1]. Concrete blocks with size 400×300×300 mm were manufactured in the laboratory and placed at the field site after moist curing in the laboratory for 35 to 70 days.

Table 1: Types of binder used in the concrete

Code	Binder type
Anl	Swedish sulphate resistant cement (SRPC) (CEM I MH/SR/LA), corresponding to 42.5N
Slite	Swedish Portland cement, produced in Slite (CEM I), corresponding to 52.5N
KalkC	Swedish Portland cement with 10-15% limestone filler (CEM II/A-LL), corresponding to 52.5N
FinStd	Finnish standard Portland cement with 15-18% ground granulated blast-furnace slag (CEM II/A-S), corresponding to 42.5N
FinRpd	Finnish rapid Portland cement (CEM II/A-LL), corresponding to 42.5R
Anl+5%SF	Anl replaced by 5% SF (Silica fume produced by Elkem. Norway)
Anl+10%SF	Anl replaced by 10% SF
FinRpd+44%SL	FinRpd replaced by 44% SL (ggbf slag)

2.2 Exposure conditions

The field exposure site at highway 40 was established in the autumn of 1996. It consists of a gravel area of 200 meter in length and a couple of metres in wideness along the highway, with specimens mounted in steel frames at road level, as shown in Figure 1. A guard rail was installed to separate the exposure site from the traffic. It was placed in such a way as to ensure the traffic safety and to have the specimens fully exposed to the splash water from the traffic. The climate around the specimens is moist, and the specimens are exposed during the winter to low temperatures and de-icing salts, producing a climate corresponding to exposure class XD 3/XF 4 in EN 206-1.

Highway 40 leads from Gothenburg to the east, through Borås and towards Jönköping. Over the year, the daily average number of vehicles passing the field exposure site is around 12000, of which 1250 are heavy vehicles (data from measurements carried out by the Swedish National Road Administration in 2000). For safety reasons, de-icing salts are used during the

winter in many parts of Sweden to keep road surfaces free from snow and ice. The de-icing agent used is sodium chloride, which is spread either in the form of a solution (about 24% NaCl) as a preventive measure, or as crystals when spread on snow. In this region, de-icing salts are normally used between October and April. The average amount of salt spread on the highway pavement each winter was 1.9-2.4 kg/m² between 1996/1997 and 1999/2000, but reduced to 1.1-1.3 kg/m² since the winter 2000/2001 due to the introduction of the new method of applying salt. The registered annual average temperature was about 7 °C. If the freezing period is excluded, the average temperature will be about 10 °C.

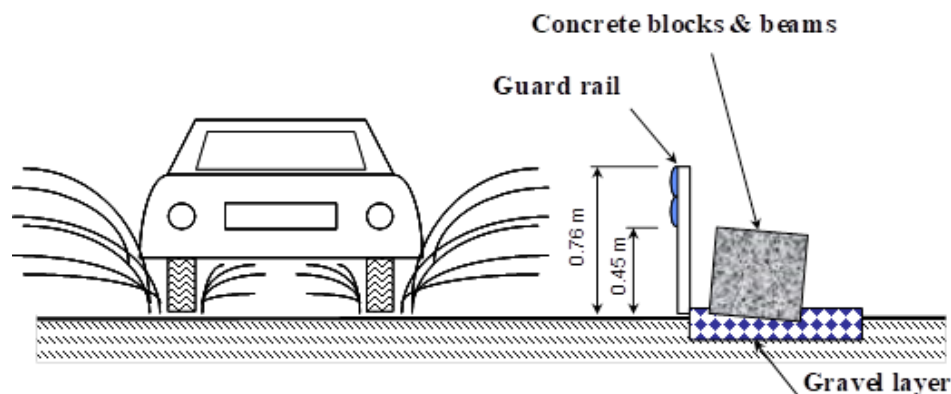


Figure 1: Illustration of concrete blocks placed at the field site.

3. MEASUREMENT OF CHLORIDE PROFILES

After specified exposure durations (1, 5, 10 and 20 years), cores of 100 mm in diameter were taken from the vertically exposed surface of the concrete block. When the cores became surface dry after coring, they were individually sealed in double thick plastic bags to prevent from further evaporation of moisture. Powder samples were taken from each core by means of dry-grinding on a lathe with a diamond tool, successively from the exposed surface to a certain depth. The depth of each sample was measured from the lathe with an accuracy of 0.5 mm. After the grinding, the powder samples were immediately dried at 105 °C and then stored in a desiccator for later chloride and calcium analysis.

The acid soluble chloride content in each sample was determined principally in accordance with AASHTO T260 using potentiometric titration on an automatic titrator with silver nitrate solution and chloride selective electrode. A sample size of about 1 gram was used to facilitate the parallel calcium analysis.

To determine the binder content in each sample, the soluble calcium content was determined parallel to the determination of chloride content, using the technique reported by Tang [2], that is, after the titration for chloride, the solution was alkalized to pH 12-13 and potentiometrically titrated with EDTA solution and calcium selective electrode.

4. RESULTS AND DISCUSSIONS

4.1 Effect of cement type

Figure 2 shows the chloride ingress profiles in concrete with five types of commercial cement. It can be observed that the chloride content at a specific depth differ very irregularly

between these types of cement. It is difficult to rank the resistance of cement to chloride ingress, although it looks clear that Finnish rapid cement revealed the lowest chloride ingress when $w/b \leq 0.4$. However, a general tendency is that the chloride ingress is deeper in concrete with higher water-binder ratio, as expected.

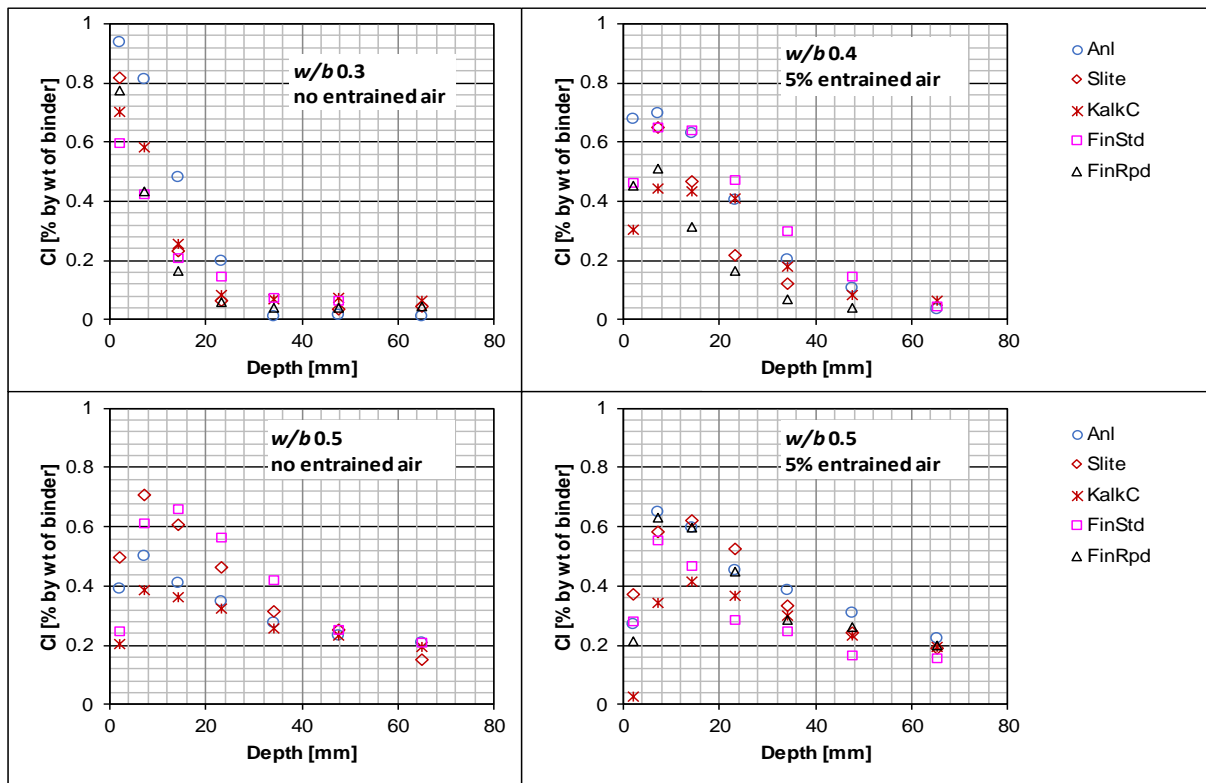


Figure 2: Chloride ingress profiles in concrete with different commercial cement after exposure for 20 years in a de-icing road environment.

4.2 Effect of mineral additions

Figure 3 shows the chloride ingress profiles in concrete with the replacement of silica fume and ggbf slag. It seems no markedly effect on chloride ingress when Swedish SRPC was replaced with 5% silica fume, but the effect became clear when replaced with 10% silica fume.

For Finnish rapid cement replaced with 44% slag, the effect on chloride ingress was not markedly in concrete with $w/b 0.3$, but clearer in concrete with $w/b 0.4-0.5$.

4.3 Effect of exposure durations

Figure 4 shows chloride ingress profiles in two types of concrete after exposure for different durations. For the concrete with Swedish SRPC, the chloride profiles after exposure for 1-10 years were similar, and markedly less than that after exposure for 20 years. For the concrete with Swedish SRPC with a replacement of 5% silica fume, the chloride ingress in the depth of 0-20 mm was unexpected. The ingress after exposure for 1-5 years was higher than that after exposure for 10-20 years, probably due to higher amount of salt spread under the first four winters (1996-2000). Figure 5 shows the chloride ingress profiles of concrete with eight types of binder with $w/b 0.3-0.4$ after exposure for 10 and 20 years. It can be observed

that the profiles after exposure for 20 years are in general somewhat deeper than those after exposure for 10 years. However, the difference is small, indicating that for these types of concrete with w/b 0.3 the ingress in the actual highway environment is very slow after 10 years exposure.

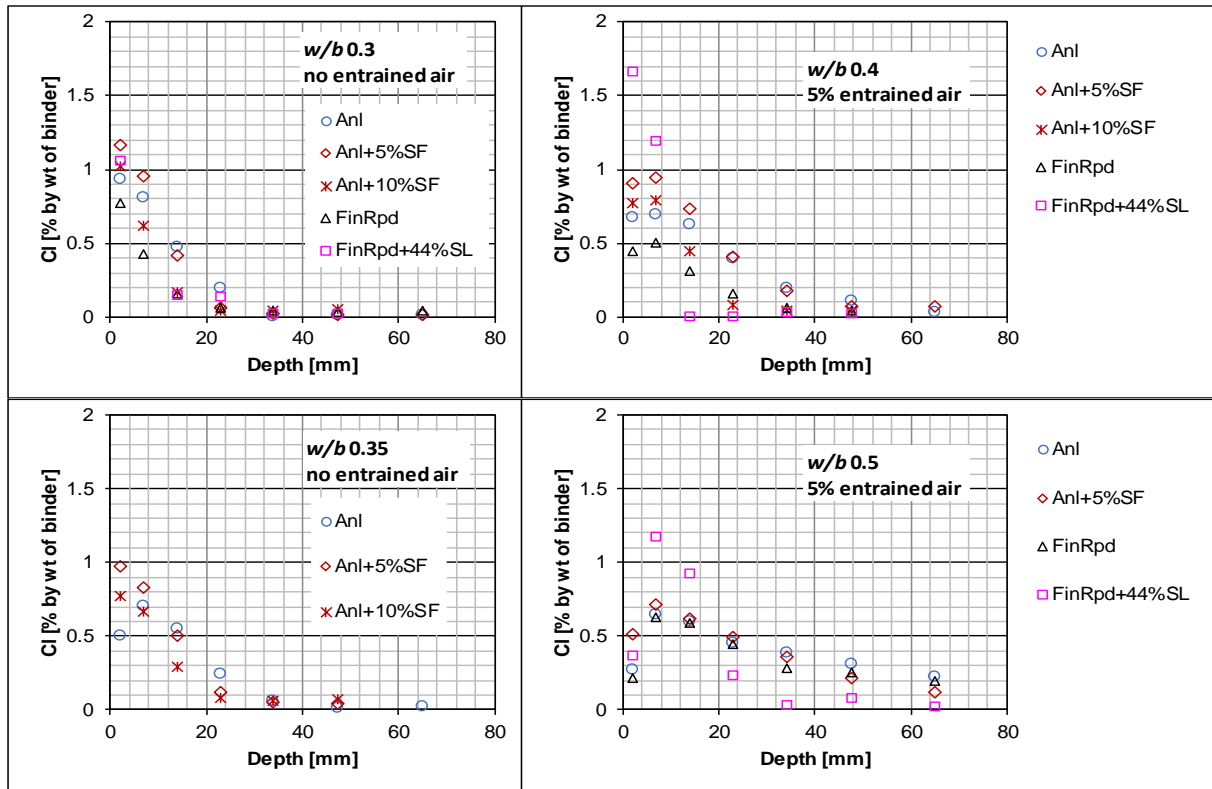


Figure 3: Chloride ingress profiles in concrete with replacement of silica fume and ggbf slag after exposure for 20 years in a de-icing road environment.

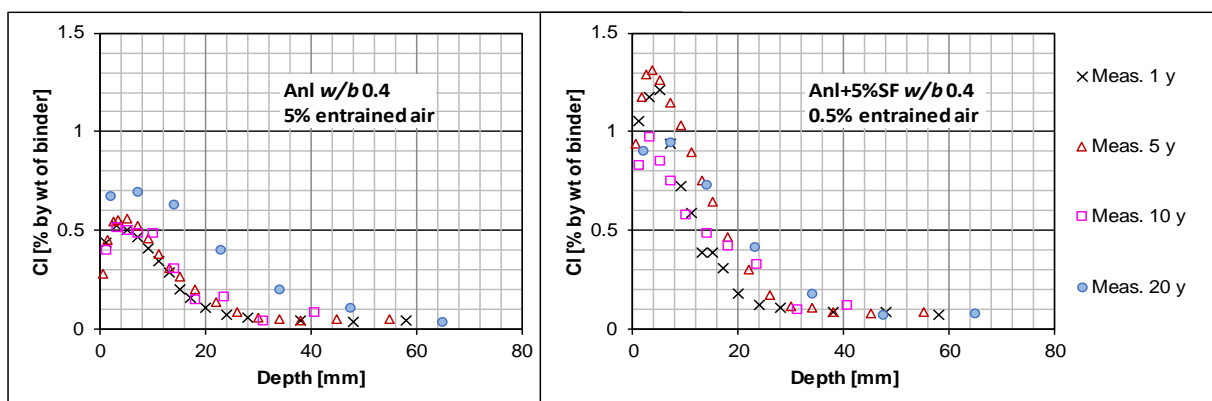


Figure 4: Chloride ingress profiles in two types of concrete after exposure for different years in a de-icing road environment.

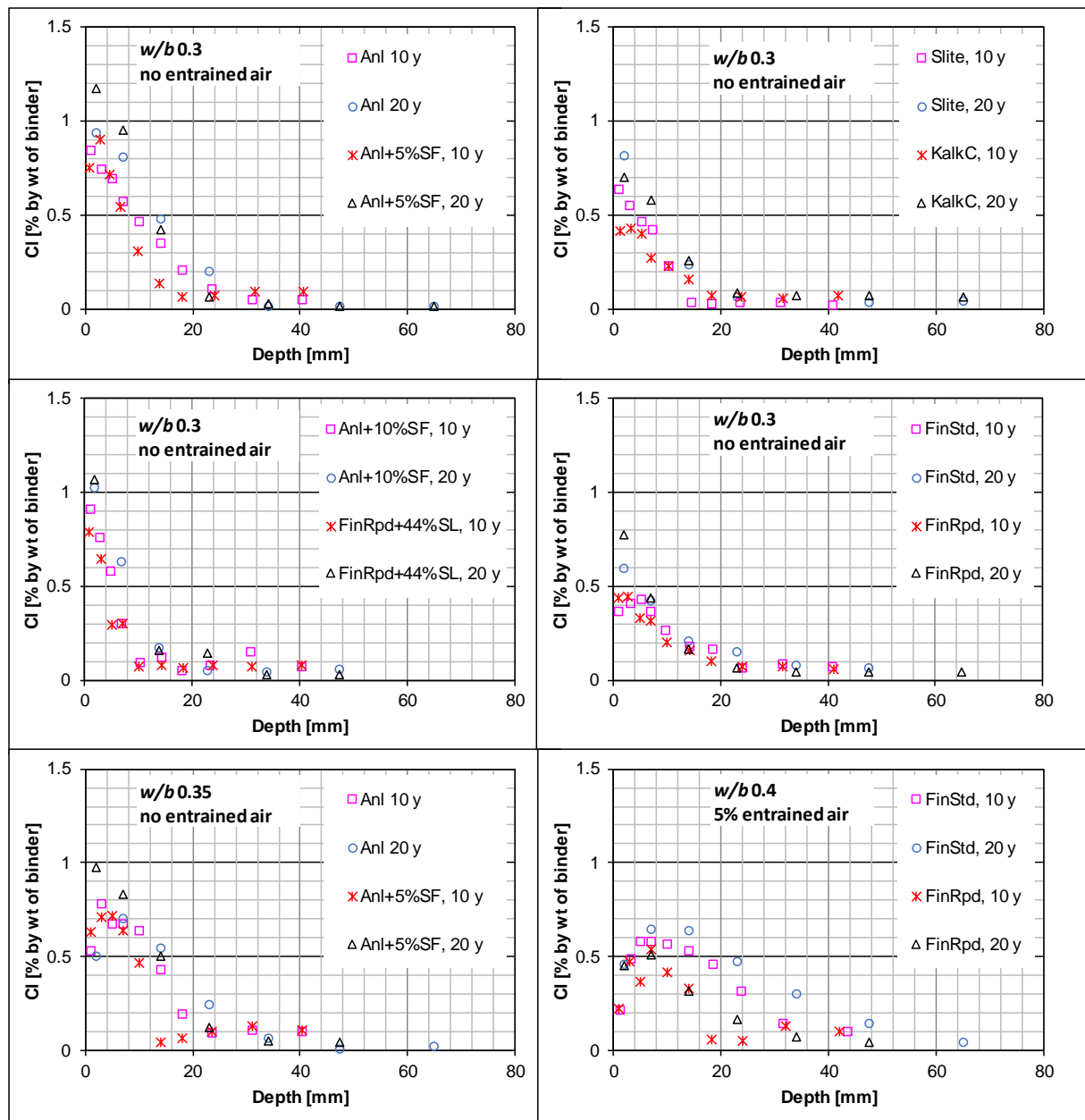


Figure 5: Chloride ingress profiles in different types of concrete after exposure for 10 and 20 years in a de-icing road environment.

4.4 Effect of exposure environments

In our previous work [3] many chloride ingress profiles in concrete with Swedish SRPC were collected from a marine exposure site along Swedish west coast after exposure for 20 years. Figure 6 shows the comparisons of chloride ingress in two similar types of concrete (with the same types of binder, similar other raw materials and mix proportions, manufactured in the same laboratory), but exposed to these two different environments. Clearly, the exposure in the marine environment led to significantly higher chloride ingress.

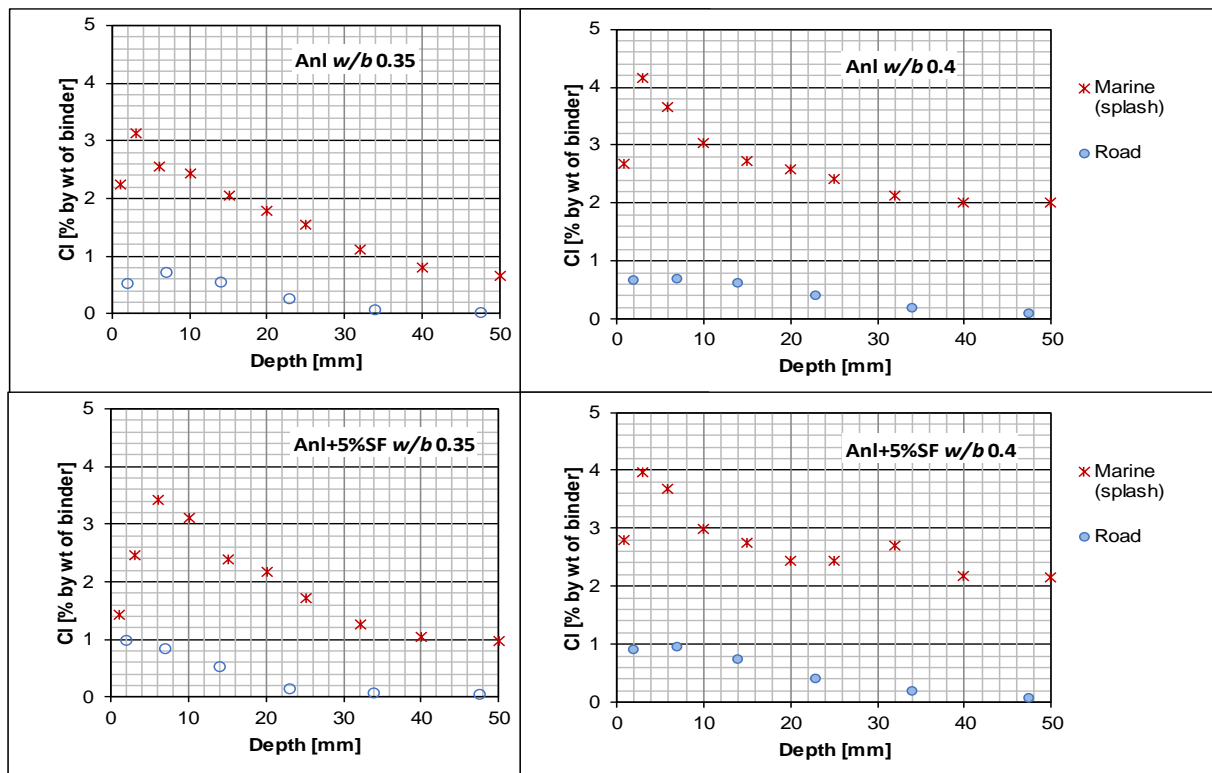


Figure 6: Chloride ingress profiles in two types of concrete after exposure for 20 years in a marine splash zone and a de-icing road environment.

4.5 Discussions

From the above results it can be found that for different types of binder with the same water-binder ratio the chloride ingress profiles markedly vary (see Figure 2), as also observed in the previous studies [1][5]. Possible reasons may include inhomogeneities in spread of de-icing slats on the road surfaces, splash of the salt water or mud by vehicles, and snow lumps shovelled from the traffic lanes to the sides that covered the concrete specimens and protected them from further contact with the splashed salts.

Although there is a great scatter in chloride threshold value for corrosion initiation [6], the maximum chloride content 0.4% by weight of binder was specified in European standard EN 206-1 for concrete containing steel reinforcement. Taking this value as chloride threshold level, we can find that the chloride ingress in concrete with $w/b \leq 0.4$ under the de-icing road environment is less than 30 mm in depth after exposure for 20 years, whilst under the marine splash environment the chloride ingress clearly reached 50 mm. Therefore, the results from both long-term field exposure sites demonstrate that Swedish marine splash environment is severer than its de-icing road environment.

For the concrete with w/b 0.5, the chloride content can reach the threshold value at the depth of 30-40 mm after exposure for 20 years, as shown in figure 2. This is in reasonably good agreement with the chloride ingress profiles measured from three Swedish road bridges made of Swedish SRPC (Anl) after having been in service for 25-30 years [4].

For the most of chloride ingress profiles in concrete with $w/b > 0.3$, there appears a peak in the near surface zone, owing to the drying-wetting cycles in the road environment [7]. This

peak phenomenon makes the prediction difficult when using models based on Fick's law. Some further modifications should be made when using such models for prediction of chloride ingress profiles under the de-icing road environment.

5. CONCLUSIONS

Based on the results measured from the concrete blocks exposed to the Swedish de-icing salt road environment the following conclusions can be drawn.

- Among five types of commercial cement, Finnish rapid cement revealed the lowest chloride ingress in concrete with $w/b \leq 0.4$, but the uncertainty is high.
- Among the three types of blended cement, both Swedish SRPC replaced by 10% silica fume and Finnish rapid cement replaced with 44% slag reveal better resistance to chloride ingress.
- Under Swedish de-icing salt environment chloride ingress in concrete with w/b 0.5 can reach the threshold level 0.4% by mass of binder at the depth of 30-40 mm after exposure for 20 years, whilst in concrete with $w/b \leq 0.4$ the ingress depth at which the threshold level is reached will be less than 30 mm after the same exposure duration.
- Concerning chloride ingress in concrete, Swedish de-icing salt road environment is not as severe as Swedish marine splash environment.

ACKNOWLEDGEMENTS

Financial supports by Swedish National Traffic Administration and Cementa AB to this work are greatly appreciated.

REFERENCES

- [1] Tang, L. and Utgenannt, P., 'Chloride ingress and reinforcement corrosion in concrete under de-icing highway environment – A study after 10 years' field exposure', SP Report 2007:76, SP Swedish National Testing and Research Institute, Borås, Sweden, 2007.
- [2] Tang, L., 'Estimation of cement/binder profile parallel to the determination of chloride profile in concrete – Nordtest project No. 1581-02', SP Report 2003:7, SP Swedish National Testing and Research Institute, Borås, Sweden.
- [3] Boubitsas, D., Tang, L. and Utgenannt, P., 'Chloride ingress in concrete exposed to marine environment - Field data up to 20 years exposure', SBUF Report 12684, CBI Swedish Cement and Concrete Research Institute, Borås, Sweden, 2014.
- [4] Lindvall, A., 'Environmental actions and response - reinforced concrete structures exposed in road and marine environments', Licentiate thesis, Dept. of Building Materials, Chalmers University of Technology, Publication No. P-01:3, Gothenburg, Sweden, 2001.
- [5] Lindvall, A., 'Chloride ingress in a Swedish road environment – Five years exposure for three concrete compositions', Publication P02:4, Building Materials, Chalmers University of Technology, 2002.
- [6] Angst, U., Elsener, B., Larsen, C.K. and Vennesland, Ø., 'Critical chloride content in reinforced concrete - A review'. *Cem. Concr. Res.*, 39 (2009) 1122-1138
- [7] Hong, K. and Hooton, R.D., 'Effects of cyclic chloride exposure on penetration of concrete cover', *Cem. Concr. Res.*, 29 (1999) 1379-1386.

NEW MECHANISM OF STRESS CORROSION CRACKING: FRACTO-SURFACE MOBILITY MECHANISM

J. Sanchez (1), E. Torres (1), N. Rebolledo (1), A. Ridruejo (2)

(1) Institute Eduardo Torroja of Construction Sciences (IETcc-CSIC), Spain

(2) ETSI Caminos, Canales y Puertos, Politechnical University of Madrid (UPM), Spain

Abstract

The mechanism of stress corrosion cracking on steels has yet to be fully understood. It is a surface process that implies a corrosion and stress synergy, but the most practical consequence is that stress corrosion cracking can modify the mechanical characteristics of the metal causing brittle failure.

The mechanism proposed in this article merges the surface mobility mechanism proposed by Galvele and the fracture mechanics principles. Also, a model of stress corrosion cracking is proposed where the source of vacancies is by anodic dissolution, and the vacancies are driven by a stress gradient to the crack tip under non-stationary conditions. The mechanism is denominated the fracto-surface mobility mechanism (FSMM).

Keywords: stress corrosion, steel, hydrogen embrittlement, surface mobility, fracture mechanics

1. INTRODUCTION

Up to present the mechanism of SCC has not been explained satisfactorily. Numerous mechanisms have been proposed to explain the brittle failure of metals under stress, but only some of them, five specially, are considered to be relevant: i) Mechanism of Anodic Dissolution; developed by Parkins [1], ii) Film-induced Cleavage Model; whose theoretical aspects have been developed by Newman [2], iii) Surface Mobility SCC Mechanism; developed by Galvele [3], iv) Environmentally Enhanced Plasticity; developed by Magnin et al. [4], and v) Hydrogen Embrittlement [5].

The Surface Mobility Mechanism (SMM) proposes a new perspective in which the crack advances, not due to anodic dissolution but to diffusion of atomic vacancies created in the lips of the crack towards its tip. SMM is the only mechanism that proposes equations enabling the prediction of crack propagation rate and that incorporates the effect of the hydrogen produced

during the process, achieving to formulate an extension of the theory on SCC to hydrogen embrittlement.

Coherent with the lack of agreement in the type of mechanism that operates, an agreed testing method does not exist for the study of the susceptibility to SCC or to hydrogen embrittlement [6]. In the case of high strength steel wires for prestressed concrete, there are a standard tests where the aggressiveness is enhanced to accelerate the process. These tests enables to detect the susceptibility to hydrogen embrittlement of steel and serves as quality control test to detect faults [7]. Other authors suggest a test closer to concrete performance, which is based on the application of the theory of anodic dissolution [7-11] to specimens in alkaline solutions containing chlorides or of sodium bicarbonate [12] or in the use of pre-cracked specimens induced by fatigue [9, 13, 14] in whose studies the fracture toughness is calculated by fracture mechanics. None of these tests for prestressing wires can be generalized and give conclusive results. For the case of high strength wires, the existing test [7] has seemed not appropriate for other electrolytes and far from the chemical composition of the concrete pore solution. It has been then, necessary to try to develop a more suitable testing method for prestressing wires. The main conditions are: the test should be simple, able to be used for control of production and for making predictions of long term performance which should allow verifying the mechanism of progression of the SCC cracks.

2. EXPERIMENTAL METHODOLOGY

The materials and equipment used were described in previous papers [6, 15, 16]. A steel of eutectic composition has been tested in two conditions: cold drawn steel (1510 MPa yield strength) and the modified parent pearlitic steel (1300 MPa yield strength).

In present work, a more realistic testing methodology is made to propose the integration of the SMM to the fracture mechanics principles. The result is called the Fracto Surface-Mobility Mechanism, FSMM. Regarding the testing methodology it is used for the study of the mechanisms of SCC in prestressing wires and has been crucial to develop the proposed model. This methodology enabled to calculate the fracture toughness of the wire and to predict the crack propagation rate [6]. The fracture toughness is calculated by Fracture Mechanics (FM). Due the observations made in the tests, the theory of the SMM was modified to fit into the results obtained.

The methodology was described by Sanchez et al [17, 18]. The aim of the methodology is to achieve a more realistic and controlled test conditions than those that generate the surface defect by a fatigue because in present case fatigue is not operating in the process. In the proposed test the crack is generated by electrochemical dissolution by nucleating a pit in a hole made in an epoxy applied to cover the surface. Then the wire is stressed and tested to induce the crack that nucleates in the bottom of the notch. The testing method consists then of several stages. Two types of steel were used. The methodology is based in the control of the following electrochemical and mechanical parameters:

- 1) Mechano-electrochemical generation of a crack in the wire: The zone of the steel exposed to the electrolyte is first covered by epoxy resin. In order to localize the attack, a notch is then produced in the middle of the epoxy covered zone. The specimen is thus strained to 80% of its yield strength. It is next immersed in a solution of sodium bicarbonate at constant temperature. A fixed potential is applied, during around 100h, and the current is registered by a data logger simultaneously. The specimens are then removed from the solution and dried.

2) Slow Strain Rate Test (SSRT): SSRT is performed in air at a rate of $3 \cdot 10^{-7} \text{s}^{-1}$ in order to determine the fracture toughness.

3) Scanning Electron Microscopy (SEM) analysis: SEM is used to identify brittle zones, cleavage and the different zones of the fractured surface. The crack dimensions are measured and the reduction of area is accounted.

3. RESULTS AND DISSCUSION

The mechanism is proposed according to the results obtained in previous papers [6, 15, 19, 20] where it is shown electrochemical, mechanical and geometrical parameters.

It is important to start by mentioning that the SMM [3] is based in a set of assumptions which could not be verified in the observation of the fractures obtained and shown in previous figures. We propose to change some hypothesis of the SMM to be coherent with the experimental observations: i) the source of vacancies are not lying on the crack surfaces but in the notch at the metal surface where the oxides are observed, ii) consequently, the path length of the vacancies is the crack depth and not the atomic distance, iii) the diffusion cannot be in steady state conditions but the process is clearly non stationary, and iv) the stress influences the vacancy rate towards the crack tip and a new formulation of the influence of the mechanical conditions in the crack progression is necessary. We proposed that the vacancy generation is due to the anodic dissolution in the surface defect. Then, according to Faraday's Law it is possible to estimate the vacancy flux (J_V) from the cell current intensity:

$$J_V = CI \quad (1)$$

where, C is a constant which depends on geometry conditions and I is the anodic intensity.

It is proposed the hypothesis that the diffusion barrier depends on the stress. The atoms diffuse to lower energy states (less strained areas) while the vacancies diffuse to high energy areas and relax the material. According to this hypothesis, the stress gradient change the surface diffusion coefficient and it is possible to apply the Stress Intensity Factor (K) to define this stress gradient. Following Irwin theory [21] it is possible to estimate the mechanical energy created by a stress concentration. We propose to change the diffusion coefficient of Galvele's expression by adding the square of the Stress Intensity Factor to the activation energy parameter, as is shown in the following equation:

$$D_S = D^0 \exp \left[\frac{-Q^{act}}{RT} + \beta K_I^2 \right] = D_{S,\sigma=0} \exp[\beta K_I^2] \quad (2)$$

where: $D_{S,\sigma=0}$ is the surface diffusion coefficient without stress, β is a constant, K_I is the mode-I stress intensity factor.

Equation 2 includes the three main factors of SCC process: the material, the environment and the stress conditions. This way it is possible to merge the Fracture Mechanics and the Surface Mobility Mechanism to aim into a Fracto-Surface Mobility Mechanism.

Until now we have not taking into account the role of the hydrogen evolution. According to present theoretical frame, the corrosion anodic current generates the vacancies at the notch and they diffuse to the crack tip by the stress gradient. Our proposal is that it is necessary to change the activation energy reducing it according to the hydrogen interaction-vacancy (Q_H):

$$D_{S,\sigma=0} = 0.014 \cdot 10^{-4} \exp \left[\frac{-13Tm + Q_H}{RT} \right] \quad (3)$$

Where T_m is the melting point.

This means that the hydrogen role is to drive the vacancies to the crack tip and it also can penetrate the metal at the crack tip. Therefore, hydrogen seems to have a double effect: i) it enhances the surface diffusion, and ii) it penetrates in the metal at the crack tip leading into the noticed hydrogen embrittlement which reduces the mechanical properties [16, 22-26].

We have estimated the β parameter of equation 2 by iteration method considering the experimental results. The values of β parameter get the same for both materials: $\beta_{parent\ steel} = 7.2 \cdot 10^{-4} \text{ MPa}^{-2}\text{m}^{-1}$ and $\beta_{cold\ drawn} = 8.1 \cdot 10^{-4} \text{ MPa}^{-2}\text{m}^{-1}$. These results are coherent with the theoretical model because the β parameter depends only from the elastic properties and both materials have the same elastic behaviour and the same chemical composition. For enabling predictions it is necessary to also consider the crack propagation rate. From the theoretical model proposed it is also possible to estimate several parameters from the experimental conditions: i) a crack growth rate is not constant, ii) the possibility that the crack arrests, and iii) the occurrence of a failure of material during the test. For SCC growth to be sustained, it is a necessary, but not sufficient, condition that the current in the potentiostatic test remains anodic. Notable results are the crack stops. The crack propagation rate also increases with the remote load, but the crack arrests when the yielding is reached at the crack tip. Finally, the growing of the crack is affected by the crack geometry [15, 17]. Both conditions are related with the stress gradient on the crack walls. In other cases the steel reaches the failure during a SCC test and then it enabled to analyze the fracture toughness in the particular environment-electrochemical conditions. This is an important material characteristic that also influences the crack rate and it has to be emphasized the interesting observation that the toughness did not remained constant as was previously stated [6, 16, 17]. This result calls for the need to review the damage tolerance of prestressed structures in contaminated atmospheres and under hydrogen evolution. Figure 1 shows the reduction of ultimate strength (P_r/P_0) for different defects of depth a in a bar of diameter D .

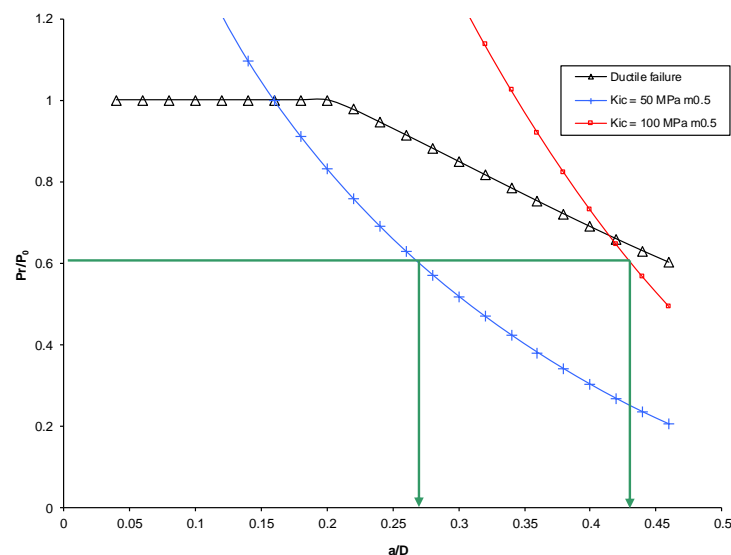


Figure 1: Damage torerance diagram.

4. CONCLUSIONS

In present paper, we try to contribute to surface mobility theory by presenting several modifications which complement it and serve to justify several experimental observations in high strength steel wires used for prestressing concrete. According to the extended SMM, that we call “fracto-SMM”, FSMM, in order to visualize the integration with fracture mechanics, it is possible to estimate the crack propagation rate or mechanical behaviour from the electrochemical, geometrical and material conditions according table 2. The main contribution consists in the integration of fracture mechanics into the Surface Mobility theory. Other integrating concepts to SMM are the vacancies are generated by anodic dissolution and they are driven by a stress gradient to the crack tip in non stationary conditions. By these integrations, the Stress Corrosion Cracking phenomenon is explained from the material, environment and mechanical point of view.

The hydrogen changes the activation energy of vacancies diffusion which means that the hydrogen role is to enhance the surface diffusion, and to penetrate in the metal at the crack tip leading into the hydrogen embrittlement which reduces the mechanical properties. We point that this methodology should be applied to safety and durability studies of prestressed structures in contaminated atmospheres.

ACKNOWLEDGEMENTS

The authors wish to thank Spanish Ministry for the Grant No. BIA2010-18863 “Surface Mobility of High Strength Steels in Solution: From Theory to Experiments”.

REFERENCES

- [1] Parkins, R.N., Predictive approaches to stress-corrosion cracking failure. *Corrosion Science*, 1980. 20(2): p. 147-&.
- [2] Sieradzki, K. and R.C. Newman, Stress-corrosion cracking. *Journal of Physics and Chemistry of Solids*, 1987. 48(11): p. 1101-1113.
- [3] Galvele, J.R., A stress-corrosion cracking mechanism based on surface mobility. *Corrosion Science*, 1987. 27(1): p. 1-33.
- [4] Magnin, T., A. Chambreuil, and B. Bayle, The corrosion-enhanced plasticity model for stress corrosion cracking in ductile fcc alloys. *Acta Materialia*, 1996. 44(4): p. 1457-1470.
- [5] Birnbaum, H.K. and P. Sofronis, Hydrogen-enhanced localized plasticity - a mechanism for hydrogen-related fracture. *Materials Science and Engineering a-Structural Materials Properties Microstructure and Processing*, 1994. 176(1-2): p. 191-202.
- [6] Sanchez, J., et al., Stress corrosion cracking mechanism of prestressing steels in bicarbonate solutions. *Corrosion Science*, 2007. 49(11): p. 4069-4080.
- [7] Elices, M., et al., Hydrogen embrittlement of steels for prestressing concrete: The FIP and DIBt tests. *Corrosion*, 2008. 64(2): p. 164-174.
- [8] Caballero, L., M. Elices, and R.N. Parkins, Environment-sensitive fracture of austempered ductile iron. *Corrosion*, 2005. 61(1): p. 51-57.
- [9] Parkins, R.N., et al., Environment sensitive cracking of pre-stressing steels. *Corrosion Science*, 1982. 22(5): p. 379-405.
- [10] Parkins, R.N. and S. Zhou, The stress corrosion cracking of C-Mn steel in $\text{CO}_2\text{-HCO}_3\text{-CO}_3^{2-}$ solutions .1. Stress corrosion data. *Corrosion Science*, 1997. 39(1): p. 159-173.
- [11] Parkins, R.N. and S. Zhou, The stress corrosion cracking of C-Mn Steel in $\text{CO}_2\text{-HCO}_3\text{-CO}_3^{2-}$ solutions .2. Electrochemical and other data. *Corrosion Science*, 1997. 39(1): p. 175-191.

- [12] Andrade, C., et al., Preliminary testing of Na₂PO₃F as a curative corrosion-inhibitor for steel reinforcements in concrete. *Cement and Concrete Research*, 1992. 22(5): p. 869-881.
- [13] Toribio, J., A.M. Lancha, and M. Elices, Hydrogen embrittlement of pearlitic steels - phenomenological study on notched and precracked specimens. *Corrosion*, 1991. 47(10): p. 781-791.
- [14] Valiente, A. and M. Elices, Premature failure of prestressed steel bars. *Engineering Failure Analysis*, 1998. 5(3): p. 219-227.
- [15] Sanchez, J., C. Andrade, and J. Fullea, Reasons for Crack Arrest in Stress Corrosion Cracking Tests-Crack Propagation Rate in High-Strength Steels. *Corrosion*, 2009. 65(6): p. 368-375.
- [16] Sanchez, J., J. Fullea, and C. Andrade, Fracture toughness variation induced by stress corrosion cracking of prestressing steels. *Materials and Corrosion-Werkstoffe Und Korrosion*, 2008. 59(2): p. 139-143.
- [17] Sanchez, J., *Stress Corrosion Cracking of High Strength Steels*. 2007, Complutense of Madrid: Madrid.
- [18] Sanchez, J., J. Fullea, and C. Andrade, Stress corrosion cracking mechanism of prestressing steels in bicarbonate solutions. *Advances in Construction Materials 2007*, 2007: p. 397-404.
- [19] Sanchez, J., J. Fullea, and C. Andrade, Fracto-surface mobility mechanism in high-strength steel wires. *Engineering Fracture Mechanics*, 2017. 186(Supplement C): p. 410-422.
- [20] Sanchez, J., J. Fullea, and C. Andrade. Stress corrosion cracking and fracture toughness of High Strength Steels. in *Proceedings of the 8th International Conference on Fracture Mechanics of Concrete and Concrete Structures, FraMCoS 2013*. 2013.
- [21] Krafft, J.M., A.M. Sullivan, and G.R. Irwin, Relationship between the fracture ductility transition and strain hardening characteristics of a low carbon steel. *Journal of Applied Physics*, 1957. 28(3): p. 379-380.
- [22] Sanchez, J., et al., Hydrogen in alpha-iron: Stress and diffusion. *Physical Review B (Condensed Matter and Materials Physics)*, 2008. 78(1): p. 014113.
- [23] Sanchez, J., et al., Hydrogen Embrittlement of High Strength Steels. *Diffusion in Materials - Dimat2008*, 2009. 289-292: p. 203-209.
- [24] Ramasubramaniam, A., et al., Effect of atomic scale plasticity on hydrogen diffusion in iron: Quantum mechanically informed and on-the-fly kinetic Monte Carlo simulations. *Journal of Materials Research*, 2008. 23(10): p. 2757-2773.
- [25] Serebrinsky, S., E.A. Carter, and M. Ortiz, A quantum-mechanically informed continuum model of hydrogen embrittlement. *Journal of the Mechanics and Physics of Solids*, 2004. 52(10): p. 2403-2430.
- [26] Jiang, D.E. and E.A. Carter, Diffusion of interstitial hydrogen into and through bcc Fe from first principles. *Physical Review B*, 2004. 70(Copyright (C) 2009 The American Physical Society): p. 064102.

DIFFUSION COEFFICIENT OF H IN FE: FIRST PRINCIPLES CALCULATION

P. de Andres (1), J. Sanchez (2), A. Ridruejo (3)

(1) Instituto de Ciencias de Materiales de Madrid (ICMM-CSIC), Spain

(2) Institute Eduardo Torroja of Construction Sciences (IETcc-CSIC), Spain

(3) ETSI Caminos, Canales y Puertos, Politechnical University of Madrid (UPM), Spain

Abstract

First principles density functional theory was used to calculate the phonon spectrum of a bcc iron lattice with interstitial hydrogen to find the vibrational contribution to the Helmholtz free energy, F . Clear differences between high (Fe:H=1:1) and low (Fe:H=16:1) concentration conditions were observed, particularly in connection with the proportion of H occupancy of octahedral and tetrahedral sites in the lattice. The variation in the diffusion coefficient with temperature was estimated by applying a simple mixing rule to these populations and factoring in the temperature-dependence of F . This prediction proved to be in good agreement with experimental results reported by McLellan (Acta Metal. 31, 961).

Keywords: hydrogen embrittlement, Ab-initio calculations, phonons

1. INTRODUCTION

Steel is the quintessential structural material. Therefore, a full understanding of the mechanisms that may compromise its structural integrity is of paramount importance. Associated to other phenomena, such as stress corrosion cracking (SCC) [1-3], hydrogen embrittlement (HE), is one of the primary causes of failure. Despite having been discovered almost one century ago, its acting mechanisms still elude our comprehension. Much theoretical progress has been done in the field [4-15], and a certain consensus has been reached: whilst hydrogen is not bonded to iron atoms in ferritic steel [16], its presence distorts the iron lattice and effectively weakens the iron-iron bond [9], i.e., reducing the fracture energy of the steel [4, 6, 19, 20]. Diffusion is an interstitial phenomenon [17, 18], being tetrahedral and octahedral sites the preferential routes. Although the interaction of hydrogen with lattice defects plays a relevant role. In fact, vacancies, dislocations, inclusions or grain boundaries are preferential sites for hydrogen and possess an associated binding energy. For this reason, they are considered

hydrogen traps, and they are expected to slow down hydrogen diffusion [21, 22]. Lattice vibrations, or phonons in the language of solid state physics, also modify the diffusion properties and the relative occupation of tetrahedral and octahedral sites as a function of temperature. This paper addresses by means of DFT calculations the dispersion relations and presents a simple mixing rule accounting for these effects.

2. METHODOLOGY

The theoretical calculations performed were based on density functional theory, pseudopotential theory and Bloch's theorem [27]. They were conducted using a plane-wave basis set to represent the Kohn-Sham wave equations [28]. In this approach, the accuracy of the calculations is governed essentially by two parameters: the maximum cut-off energy and the number of points used in reciprocal space to represent the wave equations ('k points'). The exchange-correlation energy problem was addressed with an exchange-correlation functional calculated using gradient approximation [29] and ultrasoft pseudopotentials [30]. CASTEP computer code [31] was applied to solve the self-consistency of the problem, together with a highly efficient iterative method based on ideas put forward by Carr and Parrinello [32].

Ab initio calculations were performed on two types of cells to simulate high and low hydrogen concentration: cubic (Fe_2H) and $2\times 2\times 2$ (Fe_{16}H). The phonons were calculated for both cells with H occupying the high symmetry octahedral and tetrahedral sites (Figure 1).

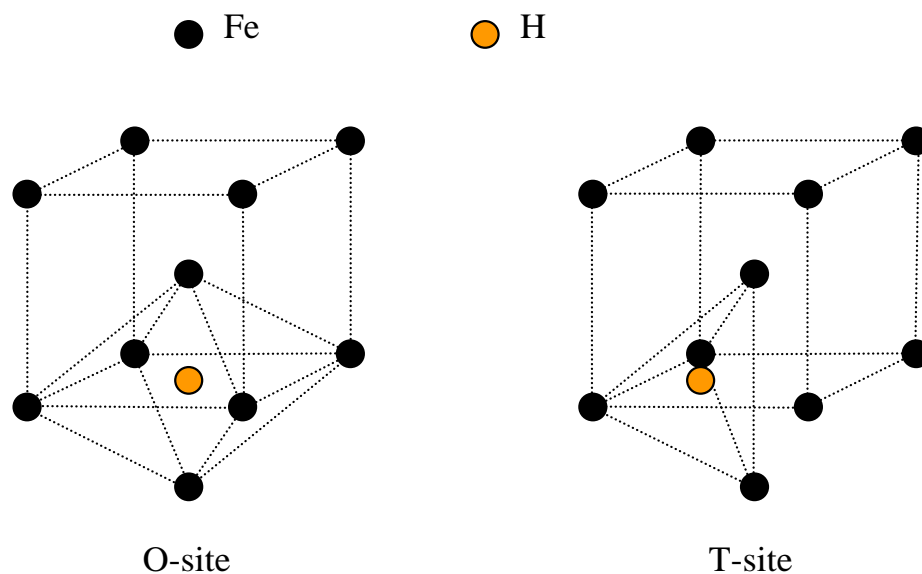


Figure 1: High symmetry octa- and tetrahedral sites in the iron lattice

The model was verified by simulating pure iron, for which the vibration frequencies are well known. Figure 2 shows the results of the theoretical calculations (blue dots) and the experimental findings (red triangles).

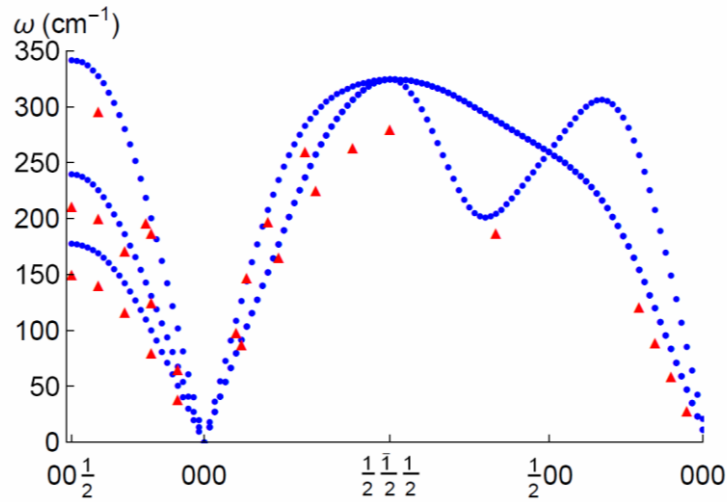


Figure 2: Phonon calculation for ferromagnetic bcc iron (blue dots = theoretical calculations; red triangles = experimental findings)

Vibration frequencies can be used to find the Helmholtz free energy (F) and with it other thermodynamic variables such as entropy (S):

$$F = -k_B T \ln(Z) = -k_B T \sum_k \ln z(T, w_k) \quad (1)$$

$$Z(N, V, T) = \prod_k \frac{e^{-\frac{\hbar w_k}{2k_B T}}}{1 - e^{-\frac{\hbar w_k}{k_B T}}} = \prod_k z(T, w_k) \quad (2)$$

$$S = -\left(\frac{\partial F}{\partial T}\right)_{V,N} = k_B T \left(\frac{\partial Z}{\partial T}\right)_{V,N} + k_B \ln(Z) \quad (3)$$

Where k_B is the Boltzman constant, T is the absolute temperature and V is the volume.

3. RESULTS AND DISSCUSION

The high and low density calculations for the two high symmetry sites are discussed below. Pursuant to the methodology described, the diffusion barrier was calculated from the following equation:

$$U_T = F + TS = k_B T^2 \left(\frac{\partial Z}{\partial T}\right)_{V,N} \quad (4)$$

The variation in the diffusion barrier for high hydrogen density and for low hydrogen density in the Fe lattice is calculated. The diffusion barrier, corrected for entropy, can be used to estimate the diffusion coefficient for all the scenarios analysed from the following equation:

$$D = D_0 \exp[U_T/k_B T] \quad (5)$$

The D_0 coefficient proposed by Jiang and Carter [33] was used here.

The diffusion coefficient is plotted against temperature in Figure 3 in an Arrhenius-like plot for octahedral-octahedral and tetrahedral-tetrahedral jump diffusion.

Further to the barriers calculated, the quickest diffusion route was tetrahedral-tetrahedral jump diffusion, which exhibited perceptibly higher values than the route stabilising the octahedral site.

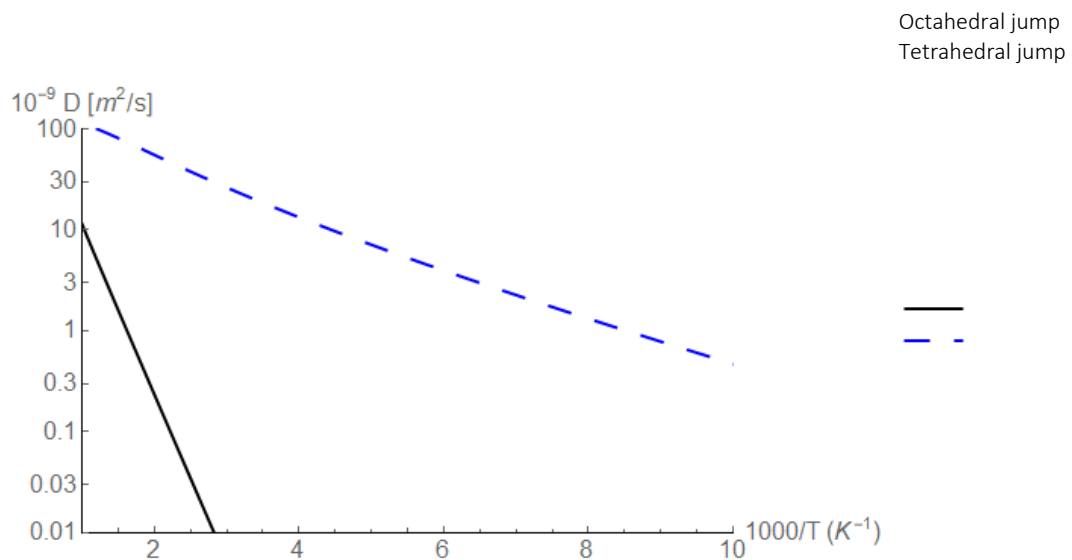


Figure 3: Diffusion coefficient vs temperature for octahedral-octahedral and tetrahedral-tetrahedral jump diffusion

Stabilisation favoured or enabled different diffusion routes for tetrahedral and octahedral sites. Where hydrogen occupied a tetrahedral site, tetrahedral-tetrahedral jump diffusion was stabilised, whereas when it occupied an octahedral site, octahedral-octahedral jump diffusion, which had a much lower diffusion coefficient, was stabilised.

In earlier studies [17] the *ab initio* molecular dynamic approach was deployed to calculate the variations with temperature in H residence time in the octahedral site for high and low density H (Figure 4).

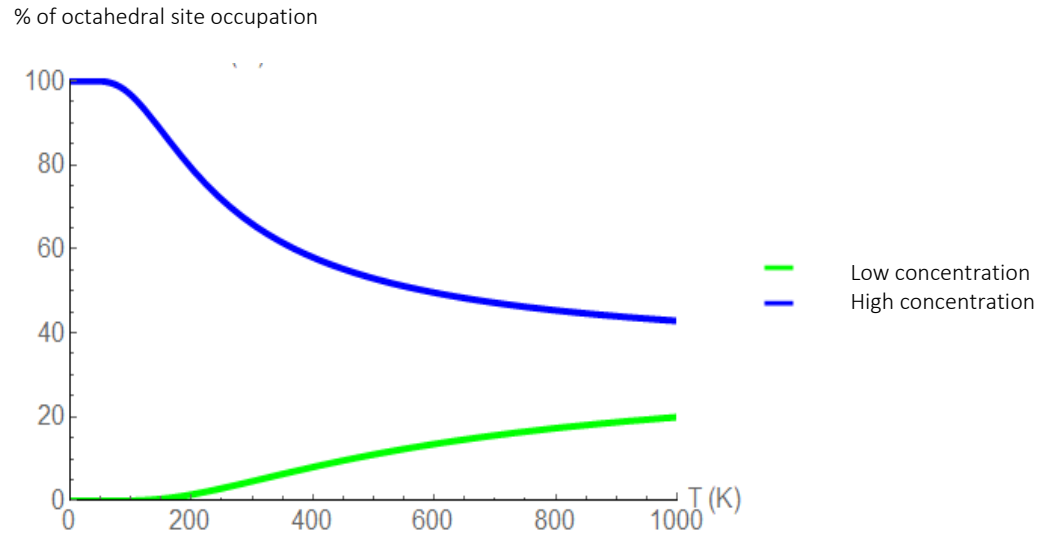


Figure 4: Percentage occupancy of octahedral sites vs temperature for high and low density H

The percentage of time H remains in each site for the H density state in the Fe lattice can be used to predict whether jump diffusion will be octa- or tetrahedral. The (temperature-dependent) diffusion coefficient can be predicted by applying a mixing rule to this problem [34] as the linear combination of the octahedra-octahedral and tetrahedral-tetrahedral diffusion routes, with the percentage determined by the percentage the respective sites were occupied:

$$D(T) = n_O(T)D_O(T) + n_T(T)D_T(T) \quad (6)$$

where n_i is occupancy and D_i the diffusion coefficient for each site i for octahedral (O) or tetrahedral (T) sites.

In other words, the diffusion coefficient for H in a pure Fe lattice can be estimated by combining site occupancy in the high and low hydrogen density scenarios.

Experimentally, Kiuchi and McLellan [34] proposed the following equations for H diffusion in iron:

$$D = 7.23 \cdot 10^{-8} \exp(-Q/RT) [m^2/s] \quad (7)$$

where $Q=5.69$ kJ/mol for temperatures ranging from 50 °C to 550 °C, and

$$D = (1-2.52) \cdot 10^{-8} \exp(-Q/RT) [m^2/s] \quad (8)$$

where $Q=6.70$ kJ/mol to 7.12 kJ/mol for temperatures under 50 °C.

Figure 5 plots diffusion coefficient against temperature in an Arrhenius-like plot for the predictions calculated here.

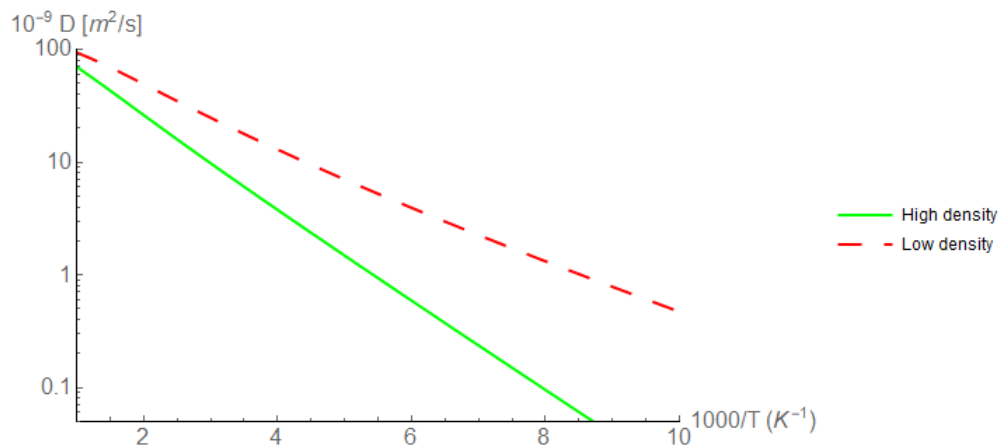


Figure 5: Diffusion coefficient vs temperature estimated by various methods

This analysis revealed that pre-factor D_0 had a heavy impact on the results. That factor was the same for the theoretical calculations performed here and proposed by Jiang and Carter but differed from the Kiuchi and McLellan analysis. The Jiang and Carter results exhibited good agreement with the present low H density findings. Although the experimental curve was lower than both under those conditions, it concurred at high temperatures with the high H density scenario analysed in this study. The divergence from the experimental curve at lower temperatures may be explained by defects in the iron lattice such as vacancies or grain boundaries, inevitably present in tests.

4. CONCLUSIONS

The Helmholtz free energy found with phonon calculations for the H-Fe system was used to estimate H diffusion barriers under different conditions.

Those calculations were then applied to determine the H diffusion coefficient in the pure Fe lattice. The theoretical calculations concurred with experimental findings at high temperatures, where diffusion stabilises in octahedral sites. Possible discrepancies at low temperatures may be attributed to the effect of lattice defects such as vacancies or grain boundaries on the diffusion coefficient.

ACKNOWLEDGEMENTS

This study was funded by the Spanish Ministry of the Economy (MAT2017-85089-C2-1-R), the EU's ERC Synergy Program (ERC-2013-SYG-610256 NANOCOSMOS). The cluster calculations performed by CTI-CSIC are gratefully acknowledged.

REFERENCES

- [1] Sanchez, J., et al., Stress corrosion cracking mechanism of prestressing steels in bicarbonate solutions. *Corrosion Science*, 2007. 49(11): p. 4069-4080.
- [2] Elices, M., et al., Hydrogen embrittlement of steels for prestressing concrete: The FIP and DIBt tests. *Corrosion*, 2008. 64(2): p. 164-174.
- [3] Elices, M., et al., Failure analysis of prestressed anchor bars. *Engineering Failure Analysis*, 2012. 24(0): p. 57-66.

- [4] Song, J. and W.A. Curtin, Mechanisms of hydrogen-enhanced localized plasticity: An atomistic study using α -Fe as a model system. *Acta Materialia*, 2014. 68(0): p. 61-69.
- [5] Gangloff, R.P., et al., Measurement and Modeling of Hydrogen Environment-Assisted Cracking in Monel K-500. *Metallurgical and Materials Transactions A*, 2014.
- [6] Song, J. and W.A. Curtin, Atomic mechanism and prediction of hydrogen embrittlement in iron. *Nat Mater*, 2013. 12(2): p. 145-151.
- [7] Castedo, A., et al., Hydrogen induced changes in structural properties of iron: Ab initio calculations, in *RILEM Bookseries*. 2012. p. 79-84.
- [8] Sanchez, J., J. Fullea, and C. Andrade, High Strength Steels Fracture Toughness Variation by the Media. *Modelling of Corroding Concrete Structures*, 2011. 5: p. 137-146.
- [9] Castedo, A., et al., Ab initio study of the cubic-to-hexagonal phase transition promoted by interstitial hydrogen in iron. *Physical Review B*, 2011. 84(9): p. 094101.
- [10] Serebrinsky, S., E.A. Carter, and M. Ortiz, A quantum-mechanically informed continuum model of hydrogen embrittlement. *Journal of the Mechanics and Physics of Solids*, 2004. 52(10): p. 2403-2430.
- [11] Birnbaum, H.K., I.M. Robertson, and P. Sofronis, Hydrogen effects on plasticity, in *Multiscale Phenomena in Plasticity: From Experiments to Phenomenology, Modelling and Materials*, J. Lepinoux, et al., Editors. 2000. p. 367-381.
- [12] Oriani, R.A. and P.H. Josephic, Equilibrium and kinetic studies of hydrogen-assisted cracking of steel. *Acta Metallurgica*, 1977. 25(9): p. 979-988.
- [13] Oriani, R.A., Mechanistic theory of hydrogen embrittlement of steels. *Berichte Der Bunsen-Gesellschaft Fur Physikalische Chemie*, 1972. 76(8): p. 848-857.
- [14] Williams, D.P. and H.G. Nelson, Evaluation of hydrogen embrittlement mechanisms. *Metallurgical Transactions*, 1971. 2(7): p. 1987-&.
- [15] Westlake, D.G., A generalized model for hydrogen embrittlement. *Asm Transactions Quarterly*, 1969. 62(4): p. 1000-&.
- [16] Sanchez, J., et al., Hydrogen in α -iron: Stress and diffusion. *Physical Review B - Condensed Matter and Materials Physics*, 2008. 78(1).
- [17] Sanchez, J., et al., Ab initio molecular dynamics simulation of hydrogen diffusion in α -iron. *Physical Review B - Condensed Matter and Materials Physics*, 2010. 81(13).
- [18] Sanchez, J., et al., Hydrogen Embrittlement of High Strength Steels. *Diffusion in Materials - Dimat2008*, 2009. 289-292: p. 203-209.
- [19] Jiang, D.E. and E.A. Carter, First principles assessment of ideal fracture energies of materials with mobile impurities: implications for hydrogen embrittlement of metals. *Acta Materialia*, 2004. 52(16): p. 4801-4807.
- [20] Song, J. and W.A. Curtin, A nanoscale mechanism of hydrogen embrittlement in metals. *Acta Materialia*, 2011. 59(4): p. 1557-1569.
- [21] Li, D.M., R.P. Gangloff, and J.R. Scully, Hydrogen trap states in ultrahigh-strength AERMET 100 steel. *Metallurgical and Materials Transactions a-Physical Metallurgy and Materials Science*, 2004. 35A(3): p. 849-864.
- [22] Thomas, R.L.S., et al., Trap-governed hydrogen diffusivity and uptake capacity in ultrahigh-strength AERMET 100 steel. *Metallurgical and Materials Transactions a-Physical Metallurgy and Materials Science*, 2002. 33(7): p. 1991-2004.
- [23] Toribio, J. and E. Ovejero, Failure analysis of cold drawn prestressing steel wires subjected to stress corrosion cracking. *Engineering Failure Analysis*, 2005. 12(5): p. 654-661.
- [24] Sancho, J.M., et al., An embedded cohesive crack model for finite element analysis of mixed mode fracture of concrete. *Fatigue & Fracture of Engineering Materials & Structures*, 2006. 29(12): p. 1056-1065.

- [25] Sanz, B., J. Planas, and J.M. Sancho, An experimental and numerical study of the pattern of cracking of concrete due to steel reinforcement corrosion. *Engineering Fracture Mechanics*, 2013. 114: p. 26-41.
- [26] Fathy, A.M., et al., Determination of the bilinear stress-crack opening curve for normal- and high-strength concrete. *Fatigue & Fracture of Engineering Materials & Structures*, 2008. 31(7): p. 539-548.
- [27] R. Martin, "Electronic Structure", Cambridge University Press, 2004.
- [28] W. Kohn and L.J. Sham, *Phys. Rev.* 140, A1133, 1965.
- [29] J. P. Perdew, K. Burke, and M. Ernzerhof, *Phys. Rev. Lett.* 77, 3865 (1996).
- [30] D. Vanderbilt, *Phys. Rev. B* 41, 7892, 1990.
- [31] S. Clark, M. D. Segall, C. Pickard, P. Hasnip, M. J. Probert, K. Refson, and M. C. Payne, *Z. fuer Kristallographie* 220, 567 (2005).
- [32] R. Carr y M. Parrinello, *Phys. Rev. Lett.* 55,2471, 1985.
- [33] D. E. Jiang and E. A. Carter, *Phys. Rev. B* 70, 064102 (2004)
- [34] K. Kiuchi and R. B. McLellan, *Acta Metall.* 31, 961 (1983).

CRACK PROPAGATION RATE BY HYDROGEN EMBRITTLEMENT IN HIGH STRENGTH STEELS: TRAP-CONTROLLED DIFFUSION

A. Ridruejo (1), J. Sanchez (2), E. Torres (2), N. Rebolledo (2)

(1) ETSI Caminos, Canales y Puertos, Politechnical University of Madrid (UPM), Spain

(2) Institute Eduardo Torroja of Construction Sciences (IETcc-CSIC), Spain

Abstract

Hydrogen embrittlement is often attendant upon structural steel failure. Earlier atomic-level studies of the effect of hydrogen in periodic iron lattices concluded that hydrogen establishes no significant chemical bonds with iron. Rather, it introduces internal stress that weakens the iron-iron bonds and lowers fracture toughness. Hydrogen-induced crack growth was simulated here. Hydrogen transport, stress gradients and the variations in fracture toughness were analysed jointly in a multiphysics finite element model. Fracture behaviour has been simulated in the literature using both linear and polynomial cohesive process models. The findings show that the choice of the cohesive model affects the results for crack growth rate and hydrogen concentration profiles. This study explored the effect of hydrogen entrapment on hydrogen transport, concentration contours and crack growth rate.

Keywords: hydrogen embrittlement, fracture toughness, trap

1. INTRODUCTION

Hydrogen embrittlement (HE), one of the primary causes of failure in metal components exposed to aggressive environments, is deemed to be associated with other types decay, such as stress corrosion [1-3]. From a theoretical standpoint, the resistance of different metals or alloys to HE can be reproduced more or less accurately using a number of approaches [4-15]. Whilst H does not bond to Fe atoms in ferritic steel [16], it stresses/distorts the bcc Fe lattice, conditioning interstitial element diffusion [17, 18] while weakening the Fe-Fe bond [9], i.e., reducing the fracture energy of the steel [4, 6, 19, 20].

A good deal has been published on the variations in H diffusion in steel depending on the medium and the traps present and their desorption [21, 22], as well as on mechanical performance and reduction of fracture toughness [2, 8, 23]. In the context of fracture mechanics, in turn, the problem of crack growth has been broached from a number of perspectives, one of

the most common being the cohesive crack model to study the growth of discrete cracks [24-26]. Some authors have applied this method to HE in steel [10].

The present study factored the effect of hydrogen traps into the hydrogen embrittlement model to estimate crack growth rate.

2. METHODOLOGY

The parameters addressed in the methodology adopted to simulate hydrogen embrittlement-induced crack growth, described below, included the generation of hydrogen on the crack surface and hydrogen transport toward the fracture process zone, where a stress gradient is present. A cohesive zone model in which the presence of hydrogen was penalised was deployed.

This study was confined to the hydrogen present in the iron lattice and traps. In addition to the hydrogen concentration gradient (C), the stress gradient based on hydrostatic pressure (p) was taken into consideration in the diffusion equation [10]:

$$\frac{\partial C}{\partial t} - D \nabla^2 C + \frac{DV_H}{RT} \nabla C \nabla p = - \frac{DV_H}{RT} C \nabla^2 p \quad (1)$$

where V_H is the partial molar volume of hydrogen, R the universal gas constant and T absolute temperature.

The boundary conditions applied in this model were based on hydrogen adsorption when in equilibrium with the medium, in turn dependent upon mechanical stress [10]. Those conditions were applied to the crack surface:

$$C = C_{eq}(p) = C_{eq}(0) e^{pV_H/RT} \quad (2)$$

where $C_{eq}(p)$ is the equilibrium concentration on the crack surface at hydrostatic pressure p and $C_{eq}(0)$ the equilibrium concentration at nil hydrostatic pressure [10].

The Langmuir relation was used to equate hydrogen adsorption to the equilibrium concentration of hydrogen on the steel surface at constant temperature:

$$\theta = \frac{C}{C + e^{\frac{-\Delta g_b^0}{RT}}} \quad (3)$$

where Δg_b^0 is the difference between energy for hydrogen on the crack surface and energy for hydrogen in the iron lattice.

Failure behaviour was simulated with a sixth order cohesive model, (Coh_{nolin}) similar to the one proposed by Elices et al. [27]. It was approximated with a sixth order polynomial, fitting the end part with exponential function to favour finite element program convergence:

$$Coh_{nolin}(u) = \begin{cases} f_t - B_{nolin} u^6 & , u < 0.95 u_f \\ (f_t - B_{nolin} (0.95 u_f)^6) e^{((0.95 u_f - u) 20 \times 10^5)} & , 0.95 u_f < u \end{cases} \quad (4)$$

where u is the crack opening and u_f the critical opening above which the material is deemed to be ‘decohesive’ and $B_{nolin}=f_t/u_f^6$.

Another parameter defining the cohesive model is f_t , the initial stress when $u=0$. Some authors suggest that this value is approximately four times yield stress, σ_{y0} [10].

$$f_t = 4\sigma_{y0} \quad (5)$$

Experimentally, steel fracture toughness has been observed to decline in the presence of hydrogen [29]. Based on *ab initio* calculations, Jiang and Carter [19] proposed the following equation to relate the decline in fracture energy (Q) to the hydrogen layer (θ):

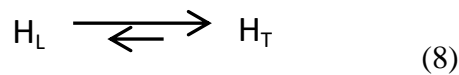
$$Q = 1 - 1,0467\theta + 0,1687\theta^2 \quad (6)$$

Consequently, where hydrogen embrittlement is involved, in finite element calculations the fracture energy (G_f^{HE}) must be updated in keeping with variations in the hydrogen concentration in the lattice (C_L).

The Q factor can be applied directly to the fracture energy, which lowers the initial stress on the f_t softening curve. That approach penalises not the critical opening, u_f , but only maximum stress, f_t . In the following equation, proposed to attain that effect, a change in variables modified the cohesive model, lowering both f_t and u_f depending on hydrogen concentration, C .

$$G_f^{HE} = G_f Q(C) = (Q(C))^{0.6} \int_0^{u_f} f\left(\frac{u}{(Q(C))^{0.4}}\right) du \quad (7)$$

In contrast to earlier studies, the effect of traps was introduced, distinguishing between hydrogen in the iron lattice (H_L) and trapped hydrogen (H_T). The capacity to store trapped hydrogen was assumed to be constant and uniform across the material. The barrier preventing hydrogen from exiting the traps was deemed to be very large compared to H movement in the lattice. As a result equilibrium was shifted toward H entrapment until the traps were ‘filled’. In this study H_T concentration was deemed to be 1 ppm.



3. RESULTS AND DISSCUSION

The first finding shown is the mechanical stress-induced variation in concentration, considering the linear elastic behaviour of the material. The simulation was based on a $1 \times 1 \text{ mm}^2$ plate with two symmetrical circular notches with radii of 0.2 mm positioned centrally on both sides (Figure 1). Calculations were performed for a tensile load of 400 MPa uniformly applied to both the top and bottom edges. H injection initiated at the notch was interrupted after 100 s

and hydrogen transport was defined as in Equation 1. Further to *ab initio* calculations [17], the diffusion coefficient found experimentally by several authors [10, 21] and used here, $10^{-10} \text{ m}^2/\text{s}$, was indicative of a fairly high hydrogen concentration.

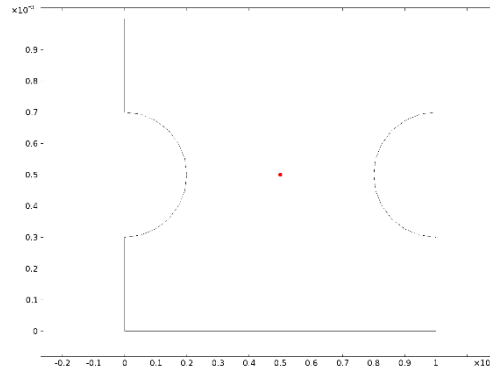


Figure 1: Plate geometry and point where concentration was measured

Figure 2a shows the variation in hydrogen concentration both in the lattice and in the traps at the geometric centre of the plate. The H traps began to fill up first, after which hydrogen diffused inside the lattice. Equilibrium was reached at this centre point after approximately 1100 s. Figure 2b shows the variation in the total concentration of the two species across the entire domain of the model. In other words, concentration for H_L and H_T was integrated over the entire geometry. It is represented in relative terms to better visualise the pattern. After 100 s when the H flow was interrupted, the percentage of H_T began to rise until equilibrium was reached, i.e., when all the traps were full.

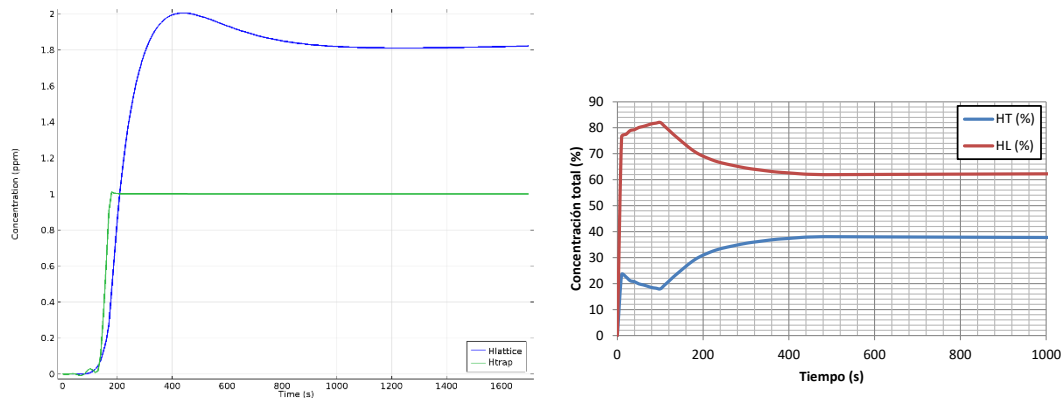


Figure 2: a) Hydrogen concentration vs time at the geometric centre of the plate. b) Total concentration of hydrogen (in traps and diffusing across the lattice) vs time

The H_L concentration profile at time $t = 1700 \text{ s}$ is shown in Figure 3. A substantial difference was observed between the concentration in the areas closest to the notch (2.3 ppm) and those on the edges (1.4 ppm). The concentration field mirrored the stress field.

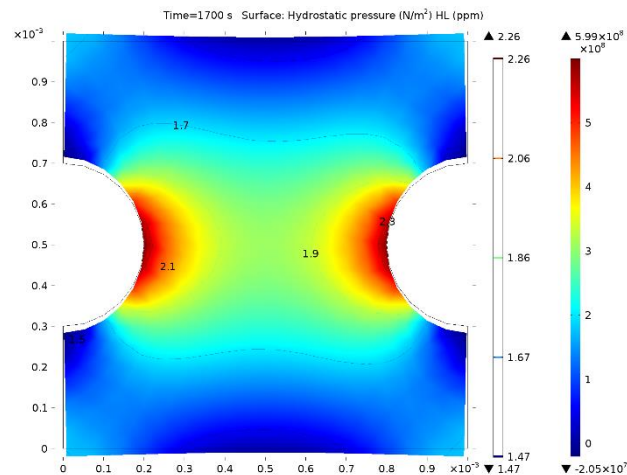


Figure 3: Isolines for HL concentration and surface field for hydrostatic pressure

A 20x20 mm² steel plate with a $2a=0.8$ mm initial crack was defined for the simulations. Tensile stress was applied to both top and bottom across the entire length (Figure 4).

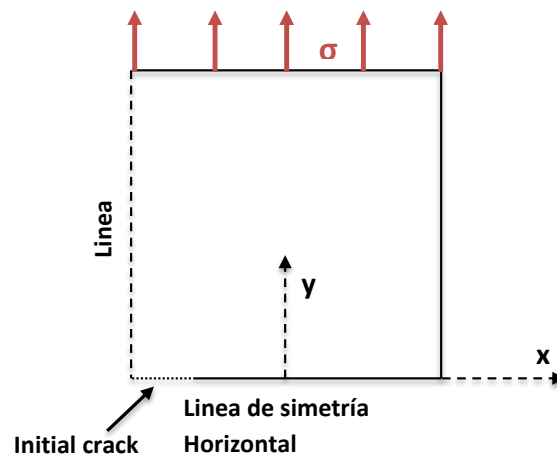


Figure 4: Geometry, boundary conditions and symmetry of the 20x20 mm² steel plate with a crack

Given that two planes of symmetry perpendicular to the vertical and horizontal axes crossed the specimen in the centre, calculations were simplified to include just $\frac{1}{4}$ of the specimen. The crack was assumed to grow along the x axis. The cohesive model for a non-linear spring-like boundary condition was applied to that axis, introducing the shift value, $2u$, as the crack opening in the model.

A remote stress of 1400 MPa was applied. The initial hydrogen concentration was nil and hydrogen was assumed to enter the plate at the crack surface. Here a constant concentration of 2 ppm was adopted.

Table 1 lists the steel mechanical properties and Table 2 the hydrogen transport parameters in the material.

Table 1: Steel mechanical properties

E (GPa)	ν	ρ (kg/m ³)	K_{IC} (MPa \sqrt{m})
207	0.3	7850	75

Table 2: Hydrogen transport parameters in steel

D_{eff} (m ² /s)	V_H (m ³ /mol)	Δg_b^0 (kJ/mol)
10^{-10}	$2 \cdot 10^{-6}$	30

Figure 5a shows the concentration of diffusible H at the crack tip. As in earlier simulations in which the entrapped H was disregarded, a peak H_L concentration was observed that defined the position of the crack. The H_T concentration at the crack tip up to the 1 ppm maximum is shown in Figure 5b.

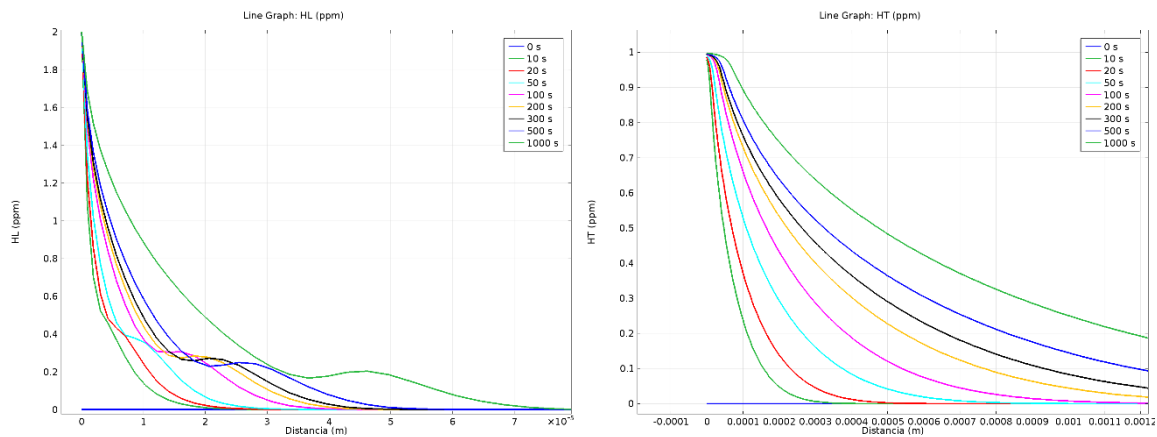


Figure 5: a) H_L hydrogen concentration at the crack tip. b) H_T hydrogen concentration at the crack tip

The position of the crack tip is plotted versus time in Figure 6. As in preceding calculations, the crack grew discontinuously with jumps measuring approximately 2 μ m.

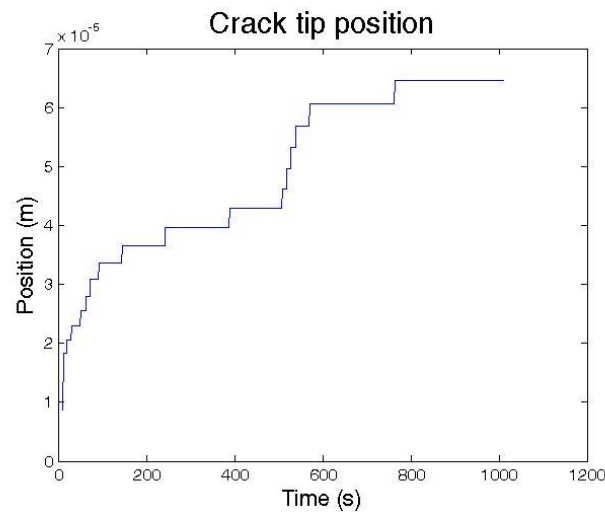


Figure 6: Crack tip position vs time

4. CONCLUSIONS

Hydrogen embrittlement-induced crack growth rate depends on the cohesive model used and interstitial H, which lowers fracture energy. Taking the H traps into consideration alters the concentration profile of the interstitial H and with it crack growth rate.

As in earlier calculations, crack growth is observed to be discontinuous with jumps of approximately 2 μm , which is consistent with experimental findings.

REFERENCES

- [1] Sanchez, J. et al., Stress corrosion cracking mechanism of prestressing steels in bicarbonate solutions. *Corrosion Science*, 2007. 49(11): p. 4069-4080.
- [2] Elices, M. et al., Hydrogen embrittlement of steels for prestressing concrete: The FIP and DIBt tests. *Corrosion*, 2008. 64(2): p. 164-174.
- [3] Elices, M. et al., Failure analysis of prestressed anchor bars. *Engineering Failure Analysis*, 2012. 24(0): p. 57-66.
- [4] Song, J. and W.A. Curtin, Mechanisms of hydrogen-enhanced localized plasticity: An atomistic study using α -Fe as a model system. *Acta Materialia*, 2014. 68(0): p. 61-69.
- [5] Gangloff, R.P., et al., Measurement and Modeling of Hydrogen Environment-Assisted Cracking in Monel K-500. *Metallurgical and Materials Transactions A*, 2014.
- [6] Song, J. and W.A. Curtin, Atomic mechanism and prediction of hydrogen embrittlement in iron. *Nat Mater*, 2013. 12(2): p. 145-151.
- [7] Castedo, A. et al., Hydrogen induced changes in structural properties of iron: Ab initio calculations, in *RILEM Bookseries*. 2012. p. 79-84.
- [8] Sanchez, J., J. Fullea, and C. Andrade, High Strength Steels Fracture Toughness Variation by the Media. *Modelling of Corroding Concrete Structures*, 2011. 5: p. 137-146.
- [9] Castedo, A. et al., Ab initio study of the cubic-to-hexagonal phase transition promoted by interstitial hydrogen in iron. *Physical Review B*, 2011. 84(9): p. 094101.

- [10] Serebrinsky, S., E.A. Carter, and M. Ortiz, A quantum-mechanically informed continuum model of hydrogen embrittlement. *Journal of the Mechanics and Physics of Solids*, 2004. 52(10): p. 2403-2430.
- [11] Birnbaum, H.K., I.M. Robertson, and P. Sofronis, Hydrogen effects on plasticity, in *Multiscale Phenomena in Plasticity: From Experiments to Phenomenology, Modelling and Materials*, J. Lepinoux, et al., Editors. 2000. p. 367-381.
- [12] Oriani, R.A. and P.H. Josephic, Equilibrium and kinetic studies of hydrogen-assisted cracking of steel. *Acta Metallurgica*, 1977. 25(9): p. 979-988.
- [13] Oriani, R.A., Mechanistic theory of hydrogen embrittlement of steels. *Berichte Der Bunsen-Gesellschaft Fur Physikalische Chemie*, 1972. 76(8): p. 848-857.
- [14] Williams, D.P. and H.G. Nelson, Evaluation of hydrogen embrittlement mechanisms. *Metallurgical Transactions*, 1971. 2(7): p. 1987-&.
- [15] Westlake, D.G., A generalized model for hydrogen embrittlement. *Asm Transactions Quarterly*, 1969. 62(4): p. 1000-&.
- [16] Sanchez, J. et al., Hydrogen in α -iron: Stress and diffusion. *Physical Review B - Condensed Matter and Materials Physics*, 2008. 78(1).
- [17] Sanchez, J. et al., Ab initio molecular dynamics simulation of hydrogen diffusion in α -iron. *Physical Review B - Condensed Matter and Materials Physics*, 2010. 81(13).
- [18] Sanchez, J. et al., Hydrogen Embrittlement of High Strength Steels. *Diffusion in Materials - Dimat2008*, 2009. 289-292: p. 203-209.
- [19] Jiang, D.E. and E.A. Carter, First principles assessment of ideal fracture energies of materials with mobile impurities: implications for hydrogen embrittlement of metals. *Acta Materialia*, 2004. 52(16): p. 4801-4807.
- [20] Song, J. and W.A. Curtin, A nanoscale mechanism of hydrogen embrittlement in metals. *Acta Materialia*, 2011. 59(4): p. 1557-1569.
- [21] Li, D.M., R.P. Gangloff, and J.R. Scully, Hydrogen trap states in ultrahigh-strength AERMET 100 steel. *Metallurgical and Materials Transactions a-Physical Metallurgy and Materials Science*, 2004. 35A(3): p. 849-864.
- [22] Thomas, R.L.S. et al., Trap-governed hydrogen diffusivity and uptake capacity in ultrahigh-strength AERMET 100 steel. *Metallurgical and Materials Transactions a-Physical Metallurgy and Materials Science*, 2002. 33(7): p. 1991-2004.
- [23] Toribio, J. and E. Ovejero, Failure analysis of cold drawn prestressing steel wires subjected to stress corrosion cracking. *Engineering Failure Analysis*, 2005. 12(5): p. 654-661.
- [24] Sancho, J.M. et al., An embedded cohesive crack model for finite element analysis of mixed mode fracture of concrete. *Fatigue & Fracture of Engineering Materials & Structures*, 2006. 29(12): p. 1056-1065.
- [25] Sanz, B., J. Planas, and J.M. Sancho, An experimental and numerical study of the pattern of cracking of concrete due to steel reinforcement corrosion. *Engineering Fracture Mechanics*, 2013. 114: p. 26-41.
- [26] Fathy, A.M. et al., Determination of the bilinear stress-crack opening curve for normal- and high-strength concrete. *Fatigue & Fracture of Engineering Materials & Structures*, 2008. 31(7): p. 539-548.
- [27] Elices, M. et al., The cohesive zone model: advantages, limitations and challenges. *Engineering Fracture Mechanics*, 2002. 69(2): p. 137-163.
- [28] Irwin, G.R., Analysis of stresses and strains near the end of a crack traversing a plate. *Journal of Applied Mechanics*, 1957. 24: p. 361-364.
- [29] Enos, D.G. and J.R. Scully, A critical-strain criterion for hydrogen embrittlement of cold-drawn, ultrafine pearlitic steel. *Metallurgical and Materials Transactions a-Physical Metallurgy and Materials Science*, 2002. 33(4): p. 1151-1166.

**International Conference on Sustainable
Materials, Systems and Structures
(SMSS 2019)**
Durability, Monitoring and Repair of Structures

Carbonation of concrete with SCMs

X-RAY DIFFRACTION STUDY OF CARBONATION RATE OF C-S-H(I) WITH DIFFERENT CA/SI RATIO

Bei Wu (1), Guang Ye (2)(3)

(1) (2) Microlab, Delft University of Technology, 2628 CN, Delft, The Netherlands

(3) Magnel Laboratory for Concrete Research, Ghent University, 9052 Ghent, Belgium

Abstract

As the major calcium-bearing phases in the hydration products of blended cement, the C-S-H has a relatively lower average Ca/Si ratio (C/S) than that found in the portland cement paste. Moreover, the Ca/Si ratio of C-S-H vary from supplementary cementitious materials (SCMs) or portion of SCMs to another. Therefore, it's important to study the carbonation mechanism of C-S-H with different C/S when talking about the durability problem of blended cement concrete under the carbonation environment.

In this paper, synthesized C-S-H(I) phases (Ca/Si ratio: 0.66 to 2.0) were exposed to the accelerated carbonation to study the carbonation of C-S-H. C-S-H(I) phases were identified by X-ray diffraction, as well as the carbonation rate and products. The results show that relatively pure C-S-H(I) phases with different Ca/Si ratio (lower than 1.40) were synthesized successfully. C-S-H(I) with the lower Ca/Si ratio is decomposed in the faster way than that with a higher Ca/Si ratio.

Keywords: C-S-H(I), Ca/Si ratio, carbonation rate

1. INTRODUCTION

Carbonation of portlandite (CH) and C-S-H are the main carbonation reactions happened inside the concrete. The consequence is the reduction of alkalinity, which increases the corrosion risk of the reinforcement. Carbonation of CH leads to a reduction of the porosity, which is ascribed to the positive difference of molar volume between CH and CaCO_3 [1, 2]. However, CH in blended cement concrete is consumed in pozzolanic reactions. The major carbonation reaction will be the carbonation of C-S-H, which is a complex decalcification-polymerization process of the SiO chain and formation of silica gel [3, 4]. Molar volume change of this reaction is depended on the properties of C-S-H (like Ca/Si ratio (C/S), water

content) and the water remained in silica gel. The effect of the C-S-H carbonation on the porosity development is still controversial.

Moreover, C-S-H produced from pozzolanic reactions has a C/S lower than that in the Portland cement concrete. Both structure can be inferred by omission of bridging tetrahedra (BT) and incorporation of additional calcium from the refined structure of 11Å tobermorite ($\text{Ca}_{4.5}\text{Si}_6\text{O}_{16}(\text{OH})\cdot 5\text{H}_2\text{O}$) [5], which consists of three parts: CaO_2 sheet, 'dreierkette' form SiO chain and interlayer. If all the BT are removed, the C/S will increase to 1.25 [6, 7]. Incorporation of extra Ca^{2+} in the interlayer can bring further increase of C/S. When all the bridge sites are removed and taken up by extra Ca^{2+} , the C/S will increase to 1.50. Structure of C-S-H with C/S more than 1.50 can be described by the C-S-H/CH (portlandite) 'solid solution' (T/CH model). From the above discussion, three types of Ca exist in the C-S-H structure (classification by the position of Ca): Ca in the CaO_2 sheet layer, Ca in the interlayer and Ca from the CH in the 'solid solution'. The proportions of them vary among C-S-H with different Ca/Si ratio. Apparently, to remove the Ca from the three chemical sites needs different energy, which means the decalcification rate are different among C-S-H phases with different Ca/Si ratio. Moreover, the removal of Ca in the latter two site causes less changes of the structure than that in the CaO_2 sheet layer. This is why the decalcification of C-S-H may cause the shrinkage of cement paste, especially for the C-S-H with Ca/Si lower than 1.2 [8].

The aim of this work is to synthesize the single C-S-H phase with different C/S and study their carbonation rate and products. Base on this, to explain the phase transformation and microstructure development of blended cement paste during the carbonation, discovered in the previous research[9].

2. EXPERIMENTS AND TEST METHODS

2.1. Raw Materials

The raw materials used in the synthesis are CaO and fumed silica. CaO is freshly prepared by the calcination of CaCO_3 under 1000 °C for at least 4 hours before synthesis. Fumed silica is from Sigma-Aldrich, with the surface area of 175-225 m²/g.

2.2. Synthesis of C-S-H with different C/S

C-S-H gels were prepared by using stoichiometric amounts of CaO and fumed silica, to give approximate C/S ranging between 0.66 and 2.0. The mix design of different C-S-H is listed in Tab. 1. Solid agents were mixed together with CO₂-free water, with the water/solid ratio of 50:1. The solution was stirred by magnetic stirrer at 20 °C, under the N₂ protection to minimize carbonation. After 2- or 4-weeks' reaction, slurry samples were extracted and flited through a Balston No. 45 paper. Then they were quickly moved into the vacuum drying chamber and dried under 35 °C for 24 h. After drying, the samples were stored in the desiccator with the relative humidity of 30%, regulated by the standard saturated $\text{CaCl}_2\cdot 6\text{H}_2\text{O}$ solution. The set-up of the synthesis device is illustrated in Figure 1.

2.3. Accelerated carbonation of C-S-H

Well-dried C-S-H samples synthesized for 4 weeks were used for the accelerated carbonation. CO₂ concentration in the carbonation chamber is maintained at 3% ± 0.2 automatically by the solenoid valve connected with a CO₂ sensor. The temperature is

regulated at 20 °C and the relative humidity is controlled at around 75% by using the saturated NaCl solution. The carbonation time varies from 0.5 h to 7 days.

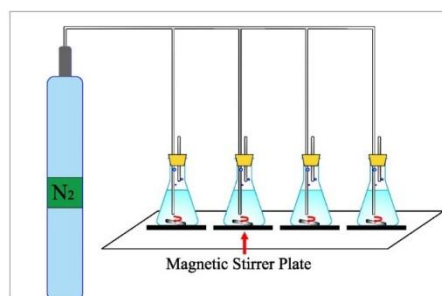


Figure 1 Schematic diagram of the synthesis set-up

Table 1 Mass fraction of raw materials for preparing different C-S-H

Sample NO.	Ca/Si ratio	CaO (g)	SiO ₂ (g)	H ₂ O (g)
1	0.66	3.0	4.9	400
2	0.86	3.6	4.4	400
3	1.18	4.2	3.8	400
4	1.40	4.5	3.5	400
5	1.70	4.9	3.1	400
6	2.00	5.2	2.8	400

2.4. Test methods

X-ray diffraction (XRD) was used for the identification of different types of C-S-H and the carbonation products. XRD was performed by a Philips PW 1830 diffractometer using CuK α radiation ($\lambda = 0.154056$ nm, 60 mA, 40 KV). Two types of scanning were performed on different samples. The first one is the normal scanning with a scan step size of 0.03°, 3 s per step, which was used for analyzing the synthetic products and carbonated products. The second one is the slow scanning with a scan step size of 0.02°, 8 s per step, which was performed on samples used for studying the carbonation rate. Both types of scanning are covering the range from 5° to 70°.

Before the test, well-dried synthetic products and carbonated samples were ground into powders with an average particle size less than 75 μ m. Then the powders were packed in the sample holders for the measurement. Especially, approximate 12 - 13% of corundum (Al₂O₃) was added to the carbonated sample as an internal standard before carbonation.

Samples used for studying carbonation rate, were blended with the internal standard as well and kept inside the sample holder during the carbonation. After each carbonation stage, the sample was taken out with the holder and tested by the XRD slow scanning.

3. RESULTS AND DISCUSSION

3.1. Synthetic products identification

3.1.1. XRD qualitative information

The XRD test results of synthetic products are described in Figure 2. The identical peaks with the d-spacing value of 3.04, 2.79, 1.82, 1.66 Å indicate that the C-S-H phase synthesized

from CaO and fumed silica in the solution is similar to C-S-H (I), which is one of the C-S-H phases found in the Portland cement concrete[10]. Due to the high reactivity of fumed silica, the C-S-H phases can be formed after 2 weeks' reaction, see Figure 2 (a). When the designed C/S is less than 1.40, the XRD pattern only shows the diffraction related to C-S-H phase. However, the peaks of portlandite appears when the designed C/S is higher than 1.40, see Figure 2 (b). This is consistent with other researchers' results[11-13].

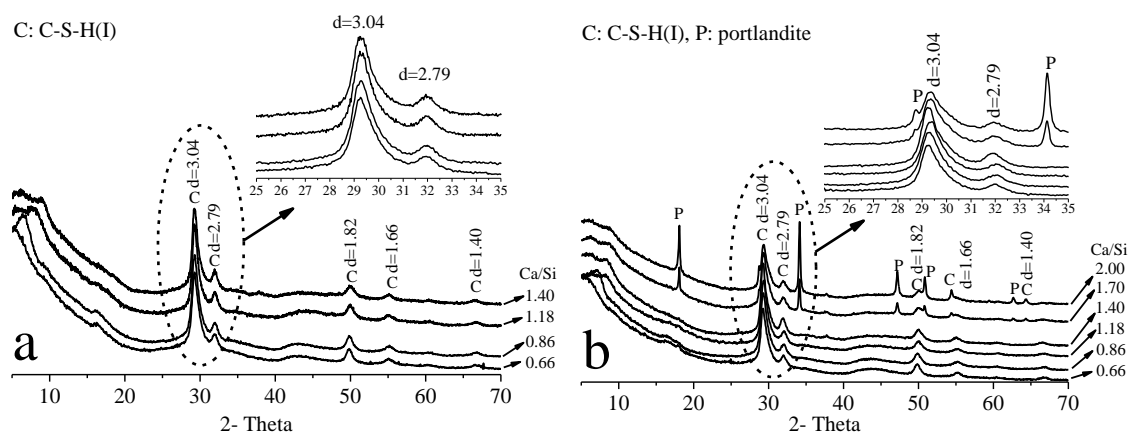


Figure 2 XRD test results of C-S-H with C/S of 0.66-2.0. C-S-H d-spacings are noted above the respective peaks as per Ångstrom (Å). a-synthesis for 2 weeks; b-synthesis for 4 weeks

No traces of any reflection indicating CaCO_3 polymorphs were visible in the diffraction patterns. Some surface carbonation is inevitable during the analysis, but the quantity produced lies below the detection limit of the test method. Nevertheless, the Ca-rich sample may be carbonated extensively in contact with air, as has been proven by FTIR spectroscopy[14].

3.1.2. Position of the 001 reflection

The peak at around 7.4° (2θ , Cu $K\alpha$) is the 001 reflection of C-S-H layer structure, which has the most conspicuous variations, both in position and in intensity. It shifts towards low d spacing (high diffraction angles) with increasing C/S ratio, which can be considered as a characteristic to distinguish C-S-H with different C/S. Positions of 001 reflection were extracted from the XRD patterns of C-S-H with different C/S, synthesized for 2 or 4 weeks. They were plotted versus C/S and compared with the data observed by other researchers [11, 15-20] in Figure 3.

Apparently, the position of 001 reflection in the synthesized C-S-H shifts to lower d spacing when the C/S increases from 0.66 up to 1.18. However, with further increasing of the C/S, the 001 reflection will not have obvious changes in the position anymore. Variations in the position of 001 reflection proved that C-S-H with different C/S was synthesized successfully. Moreover, the target C/S is close to the designed value when comparing with other data in Figure 3. The results also provided further supports for the abrupt change in the structure between C-S-H with C/S of 1.18 and that with C/S of 1.4, confirmed by the previous published ^{29}Si NMR data [14]. C-S-H phases with bulk C/S in the range 0.66 - 1.18 (or theoretical value of 1.25) can reasonably be explained by the defect - tobermorite structural model by omission of bridging Si-tetrahedra accompanied by occupancy of the Ca-interlayer.[15]. With further incorporation of Ca in the interlayer or formation of

nanocrystalline portlandite, the bulk C/S will increase further in the C-S-H. However, the position of 001 reflection will be stable.

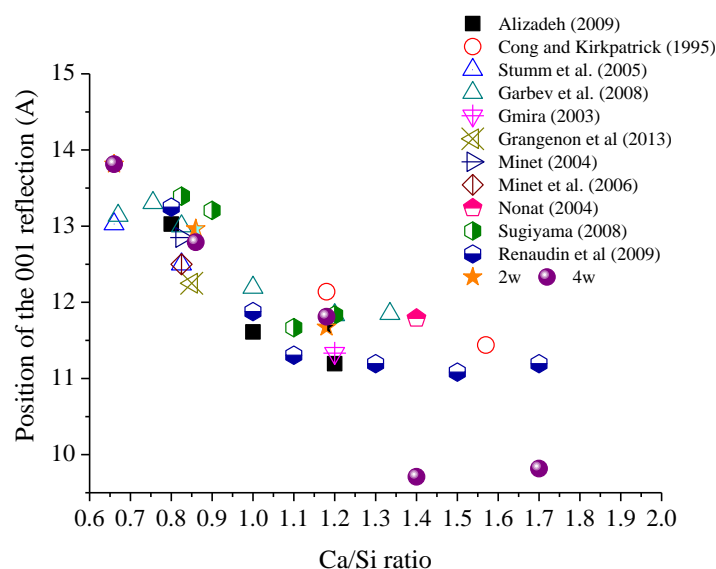


Figure 3 Variation in the position of 001 reflection in C-S-H versus Ca/Si ratio. Published XRD patterns having too weak 001 reflection or showing the presence of portlandite were excluded.

3.2. Carbonation of C-S-H with different C/S

3.2.1. Qualitative information of carbonation products

Carbonation products of the C-S-H with the C/S of 0.66 to 1.40 were tested by the normal scanning to identify the carbonates. The carbonation time varied from 1 day to 7 days. The test results are described in Figure 4.

Calcium carbonate (CaCO_3) has three polymorphs: Calcite, Aragonite and Vaterite ($\mu\text{-CaCO}_3$). The latter two are the metastable phase of calcium carbonate. Apparently, the characteristic peaks of all the three polymorphs are found in the XRD spectrum of carbonated C-S-H. And the peak intensity is increasing as the carbonation time goes on. The major carbonates in the carbonated product of C-S-H are aragonite and vaterite when the C/S is 0.66 or 0.86. Further increasing the C/S to 1.18 or 1.4, both the number and intensity of peaks indicating calcite increase dramatically. Calcite becomes the major carbonate in the carbonated product of C-S-H with high C/S (1.18 or 1.4). The other carbonation product of C-S-H is silica gel, confirmed by the previous ^{29}Si NMR test results [14]

3.2.2. Qualitative information of carbonation rate

In order to track the minor changes of peaks related to carbonates, samples carbonated for hours were tested by XRD slow scanning. These samples were mixed with corundum as well and carbonated together with the sample holder. The carbonation time varied from 0.5 h to 24 h. The test results are described in Figure 5.

In the spectrum, the major peaks are the characteristic peaks of corundum and C-S-H. And there are nearly no changes of these peaks in the spectra of C-S-H with the Ca/Si of 1.18 and

1.40, during the carbonation. However, in the spectrum of C-S-H with the Ca/Si of 0.66 or 0.86, three peaks ($2\theta = 24.9$, 27.0 and 32.8) appear after 1 hour's carbonation, which are the characteristic peaks of vaterite and aragonite.

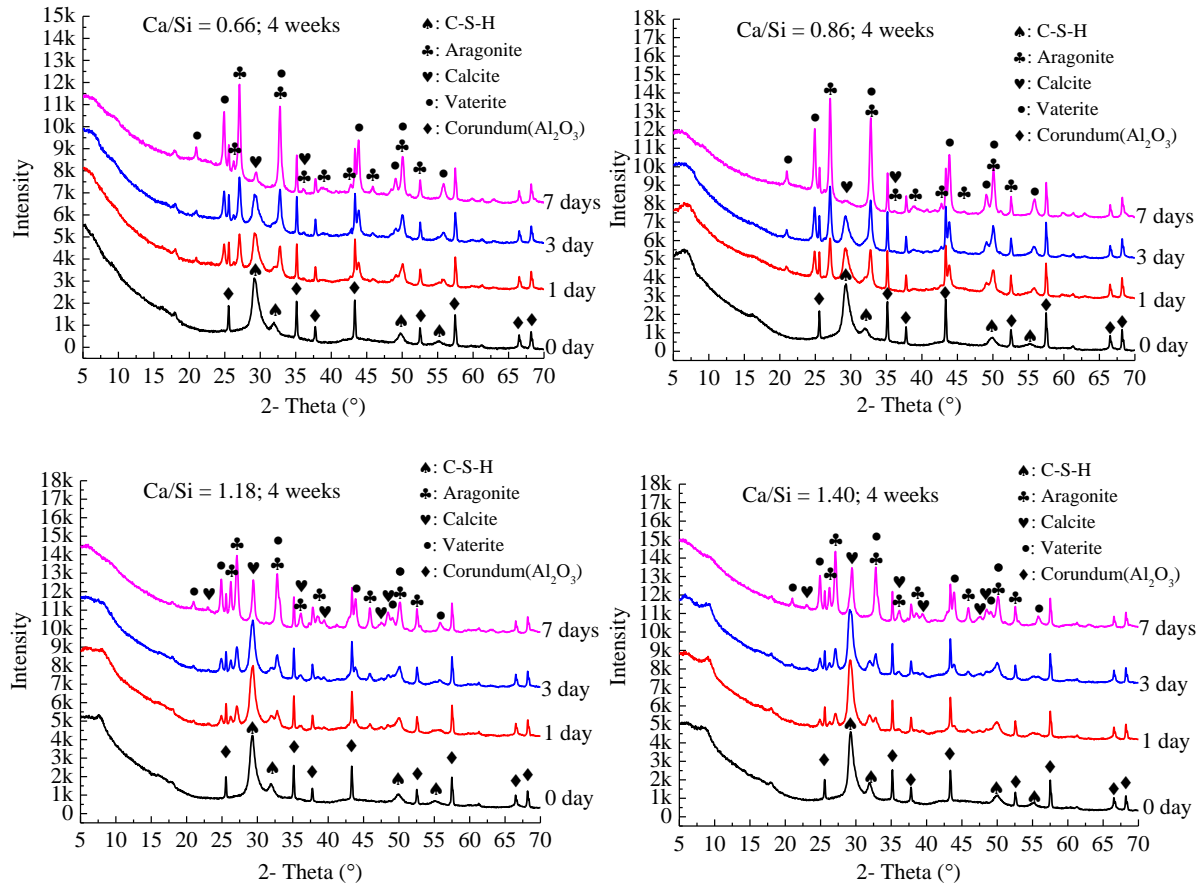
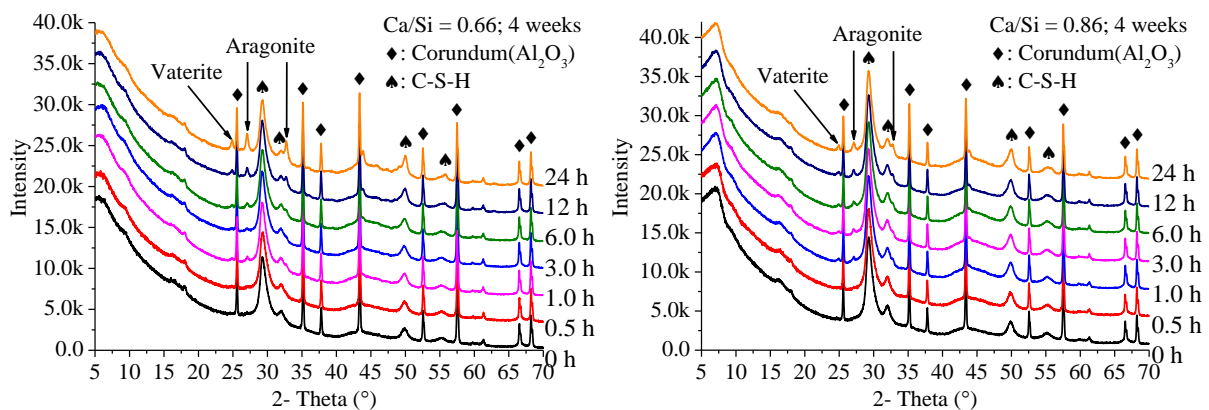


Figure 4 XRD normal scanning of different types of C-S-H, carbonated for different days



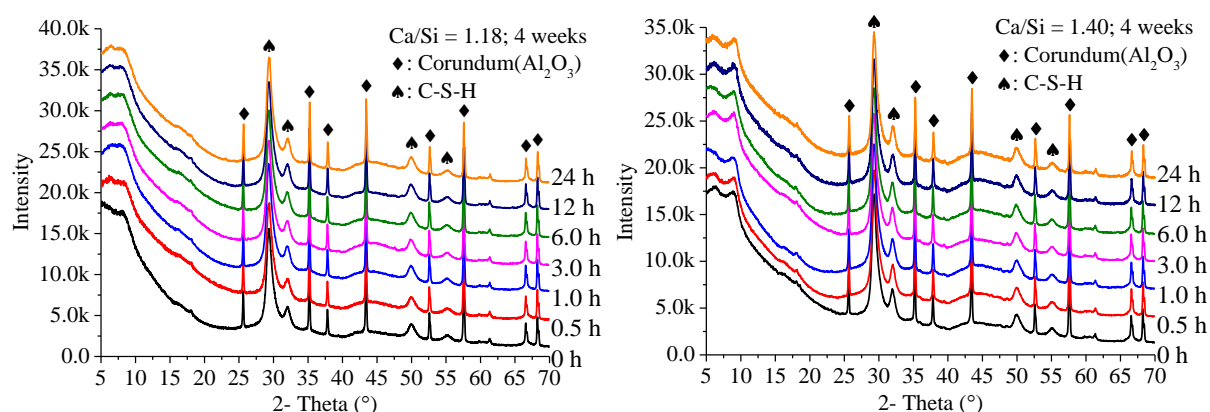


Figure 5 XRD slow scanning of different types of C-S-H, carbonated for different hours

Normally, the identical peaks of the crystal can be found in the XRD spectra only when the weight percentage of this phase is more than 5%. Therefore, the carbonation is developed much faster in the C-S-H with lower Ca/Si ratio (0.66 or 0.86), which is consistent with the FTIR test results [14].

4. CONCLUSIONS

In the paper, the C-S-H with different C/S is synthesized from CaO and fumed silica in the solution protected by the N₂ flow. Carbonation mechanism of C-S-H including final products and rate are studied by different types of XRD scanning. Carbonation resistance among different types of C-S-H are discussed. The main conclusions are as follow:

- Relatively pure phase of C-S-H(I) with different target C/S were synthesized successfully in this research. When the designed Ca/Si ratio is over 1.40, the portlandite will appear in the synthetic products.
- Vaterite and aragonite are the major polymorphs of calcium carbonate in the carbonated C-S-H with low C/S (0.66 or 0.86). Calcite will appear in the carbonates when the C/S increases to 1.18 or 1.40.
- The C-S-H with high C/S has relatively better resistance to the carbonation.

Acknowledgements

The authors are grateful for the technicians (John van den Berg, Gerrit Nagtegaal and Arjan Thijssen) and experimental supports from Microlab, Delft University of Technology. The authors also appreciate the financial support from China Scholarship Council (CSC).

Reference

- [1] Ngala VT, Page CL. Effects of carbonation on pore structure and diffusional properties of hydrated cement pastes. *Cement Concrete Res.* 1997;27(7):995-1007.
- [2] Delmi MMY, Al't-Mokhtar A, Amiri O. Modelling the coupled evolution of hydration and porosity of cement-based materials. *Constr Build Mater.* 2006;20(7):504-14.
- [3] Black L, Breen C, Yarwood J, Garbev K, Stemmermann P, Gasharova B. Structural features of C-S-H (I) and its carbonation in air—a Raman spectroscopic study. Part II: carbonated phases. *J Am Ceram Soc.* 2007;90(3):908-17.

- [4] Morandea A, Thiery M, Dangla P. Investigation of the carbonation mechanism of CH and CSH in terms of kinetics, microstructure changes and moisture properties. *Cement Concrete Res.* 2014;56:153-70.
- [5] Merlino S, Bonaccorsi E, Armbruster T. The real structure of tobermorite 11Å normal and anomalous forms, OD character and polytypic modifications. *Eur J Mineral.* 2001;13(3):577-90.
- [6] Richardson I. Tobermorite/jennite-and tobermorite/calcium hydroxide-based models for the structure of CSH: applicability to hardened pastes of tricalcium silicate, β -dicalcium silicate, Portland cement, and blends of Portland cement with blast-furnace slag, metakaolin, or silica fume. *Cement Concrete Res.* 2004;34(9):1733-77.
- [7] Taylor H, Howison J. Relationships between calcium silicates and clay minerals. *Clay Minerals Bull.* 1956;3(16):98-111.
- [8] Chen JJ, Thomas JJ, Jennings HM. Decalcification shrinkage of cement paste. *Cement Concrete Res.* 2006;36(5):801-9.
- [9] Wu B, Ye G. Development of porosity of cement paste blended with supplementary cementitious materials after carbonation. *Constr Build Mater.* 2017;145:52-61.
- [10] Chen JJ, Thomas JJ, Taylor HF, Jennings HM. Solubility and structure of calcium silicate hydrate. *Cement Concrete Res.* 2004;34(9):1499-519.
- [11] Renaudin G, Russias J, Leroux F, Frizon F, Cau-dit-Coumes C. Structural characterization of C–S–H and C–A–S–H samples—Part I: Long-range order investigated by Rietveld analyses. *Journal of Solid State Chemistry.* 2009;182(12):3312-9.
- [12] Garbev K, Beuchle G, Bornefeld M, Black L, Stemmermann P. Cell Dimensions and Composition of Nanocrystalline Calcium Silicate Hydrate Solid Solutions. Part 1: Synchrotron-Based X-Ray Diffraction. *J Am Ceram Soc.* 2008;91(9):3005-14.
- [13] Garbev K, Bornefeld M, Beuchle G, Stemmermann P. Cell Dimensions and Composition of Nanocrystalline Calcium Silicate Hydrate Solid Solutions. Part 2: X-Ray and Thermogravimetry Study. *J Am Ceram Soc.* 2008;91(9):3015-23.
- [14] Wu B, Ye G. Carbonation mechanism of different kind of CSH: Rate and products. *Int RILEM Conference on Materials, Systems and Structures in Civil Engineering 2016-Segment on Concrete with Supplementary Cementitious Materials: RILEM; 2016.* p. 163-272.
- [15] Garbev K, Beuchle G, Bornefeld M, Black L, Stemmermann P. Cell dimensions and composition of nanocrystalline calcium silicate hydrate solid solutions. Part 1: synchrotron - based X - ray diffraction. *J Am Ceram Soc.* 2008;91(9):3005-14.
- [16] Matsuyama H, Young J. Effects of pH on precipitation of quasi-crystalline calcium silicate hydrate in aqueous solution. *Adv Cem Res.* 2000;12(1):29-33.
- [17] Richardson IG. Model structures for C-(A)-SH (I). *Acta Crystallographica Section B: Structural Science, Crystal Engineering and Materials.* 2014;70(6):903-23.
- [18] Walker CS, Savage D, Tyrer M, Ragnarsdottir KV. Non-ideal solid solution aqueous solution modeling of synthetic calcium silicate hydrate. *Cement Concrete Res.* 2007;37(4):502-11.
- [19] Grangeon S, Claret F, Roosz C, Sato T, Gaboreau S, Linard Y. Structure of nanocrystalline calcium silicate hydrates: insights from X - ray diffraction, synchrotron X - ray absorption and nuclear magnetic resonance. *Journal of applied crystallography.* 2016;49(3):771-83.
- [20] Grangeon S, Claret F, Linard Y, Chiaberge C. X-ray diffraction: a powerful tool to probe and understand the structure of nanocrystalline calcium silicate hydrates. *Acta Crystallographica Section B, Structural Science, Crystal Engineering and Materials.* 2013;69(Pt 5):465-73.

DIFFERENCE IN CARBONATION BEHAVIOR AT 0.04%, 1% AND 10% CO₂ FOR HIGH-VOLUME FLY ASH MORTAR: EFFECT ON INTERNAL HUMIDITY AND RESISTIVITY

Philip Van den Heede (1) and Nele De Belie (1)

(1) Magne Laboratory for Concrete Research, Ghent University, Belgium

Abstract

Today, there is more and more agreement on the fact that accelerated carbonation experiments involving CO₂ levels that exceed the atmospheric CO₂ concentration of $\pm 0.04\%$ too much, seriously alter the carbonation process. It is expected to result in important chemical, microstructural and mineralogical changes as well as excess water production in the pore system, all having an effect on the transport properties of cementitious binders. This behaviour is not well understood yet, especially for binder systems with high cement replacement levels such as High-Volume Fly Ash (HVFA) mortar. In this research, HVFA mortar was carbonated at 0.04%, 1% and 10% CO₂, while maintaining the ambient temperature and relative humidity (RH) at 20°C and 60%, respectively. During these carbonation experiments, changes in internal humidity due to carbonation related water production were monitored with embedded humidity sensors and multi-ring electrodes for resistivity assessment as a function of depth. All test results seem to point out a key role for excess water production during carbonation in the significant underestimation of the field carbonation coefficient when estimated from accelerated carbonation tests at 10% CO₂.

Keywords: Natural vs. Accelerated Carbonation, High-Volume Fly Ash (HVFA), Humidity sensors, Multi-ring electrodes (MREs)

1. INTRODUCTION

Replacing large portions of ordinary Portland cement in concrete with a supplementary cementitious material, such as pozzolanic fly ash from coal fired electricity production, is seen as a valid way to significantly reduce cement related CO₂ emissions and increase the sustainability of this widely used construction material [1]. However, in environments where carbonation-induced steel corrosion is at risk, one should be careful since High-Volume Fly Ash (HVFA) concrete has a much lower buffering capacity for CO₂ [2]. As a consequence, the carbonation front tends to progress much faster towards the location of any embedded

reinforcing steel [3]. For such concrete applications it is thus imperative to be able to accurately predict the carbonation rate. Today, this is commonly done via accelerated testing, meaning that usually concrete samples are being exposed to elevated CO₂ levels in climatized chambers conditioned at a given temperature and relative humidity. Depending on the literature source and country of assessment, the applied CO₂ concentration for this purpose can easily range between 1-100% [4]. According to some authors, there is serious concern that using a CO₂ level of above 3% drastically changes the carbonation process, in such a way that it is no longer feasible to accurately estimate reliable field carbonation rates from the output of the accelerated experiment using straightforward and easy-to-use conversion formulae [5]. Changes in CH to C–S–H carbonation ratio, the carbonation related mineralogical phases formed and resulting changes in microstructure (both in terms of overall porosity and pore size distribution) are among the reported effects in literature, which have been covered previously in Van den Heede et al. [6]. Another possible non-negligible effect relates to water, a key reaction product of the carbonation reaction. Excess water production at too high CO₂ levels may induce a pore blocking effect hindering further carbonation at its initial rate [7]. Moreover, da Silva et al. also mention that CO₂ solubility is low when high CO₂ concentrations are used. The penetrating CO₂ first needs to transform into acid in the presence of water before the actual carbonation reaction can take place and the amount of CO₂ capable of dissolving in water is limited [8]. This paper specifically addresses the effects of carbonation related water production by performing comparative carbonation experiments during which HVFA mortars were exposed to 0.04% (the atmospheric CO₂ concentration), 1% and 10% CO₂. The internal humidity was monitored both directly with embedded humidity sensors, as well as indirectly with embedded Multi-Ring Electrodes (MREs) for resistivity profiling during carbonation.

2. MATERIALS AND METHODS

2.1 HVFA mortar mix proportions

All tests were performed on HVFA mortar with a low carbonation resistance with the same mix proportions as used in Van den Heede et al. [9]. The proportioning of the sand and binder for one batch of mortar was the same as for the standard mortar specified in NBN EN 196-1, and amounted to 1350 g and 450 g, respectively. The binder portion consisted for 50% of CEM I 52.5 N and for 50% of class F fly ash. The applied water-to-binder (W/B) ratio equalled 0.55, which is higher than the 0.50 value which is normally prescribed for a standard mortar. A high cement replacement level was used to make sure there was less carbonatable material, i.e. portlandite, available. This ensures a lower buffer capacity for the penetrating CO₂ and thus a faster inward movement of the carbonation front [2]. Increasing the W/B ratio facilitated a higher porosity, and thus also a faster ingress of CO₂.

2.2 Sample conditioning prior and during natural and accelerated carbonation

For colorimetric carbonation assessment, a series of forty-five mortar cubes (side: 100 mm) was made. After 24 hours in a wet curing chamber at 20°C and 95% RH the cubes were demoulded, whereupon the cubes were stored again in the wet curing chamber until they reached 7 days of age. Then, they were dried in an oven at 40°C for 4 days to ensure a uniform moisture distribution in the cubes. Subsequently, the cubes were carefully coated with epoxy on all sides except for one exposure side. In this condition, they remained in a climate room at 20°C and 60% RH for 3 days. This preconditioning procedure was the same as in [9]. The next

days, the cubes were equally divided among that same climate chamber, the carbonation chamber at 1% CO₂, 20°C, 60% RH, and the carbonation chamber at 10% CO₂, 20°C, 60% RH. At regular time intervals, three cubes were taken out of each chamber for colorimetric carbonation depth assessment using phenolphthalein.

Besides the above mentioned series of mortar cubes, six 100×30×100 mm³ mortar prisms and three mortar cubes with a 100 mm side, were manufactured as well. They all underwent the same sample preconditioning prior to carbonation testing. The six partially coated 100×30×100 mm³ mortar prisms were divided among the carbonation chambers conditioned at 1% and 10% CO₂. Each of them contained a hole with a diameter of 4 mm at a distance of 15 mm of the exposure surface for embedment of a humidity sensor to monitor changes in internal humidity during carbonation. Finally, three partially coated cubes with a 100 mm side remain. During manufacturing, a multi-ring electrode (MRE) for resistivity monitoring was embedded in each of them. One cube was assigned to each of the three studied CO₂ levels at 20°C and 60% RH, i.e. the atmospheric CO₂ concentration of around 0.04% CO₂, 1% CO₂ and 10% CO₂.

2.3 Colorimetric carbonation assessment

Colorimetric carbonation assessment consisted of splitting three mortar cubes per testing age (every 3 or 6 weeks) and spraying the fractured surfaces with 1% aqueous phenolphthalein solution, which colours uncarbonated sample area purple, while carbonated sample area remains colourless. Per fractured sample surface, the colour change boundary depth was measured every 10 mm, with omission of the two measuring points 10 mm inward from the coated sides, perpendicular to the exposure side. This gives 7 measurements per fractured surface and thus 14 measurements per tested mortar cube in total. The as such determined carbonation depths were plotted as function of the square root of the exposure time to quantify the carbonation coefficient (= the slope of the trend line obtained as such) for each studied CO₂ concentration in mm/√weeks. In accordance with Van den Heede et al. [9], the carbonation coefficient for 10% CO₂ (A_{10%}) was also converted to values that should be representative for 1% CO₂ (A_{1%}) and 0.04% CO₂ (A_{0.04%}) using the conversion approach proposed by Sisomphon and Franke [5]. Under that premise, the ratios of the carbonation coefficients at varying CO₂ concentrations (A_{10%} vs. A_{1%} or A_{0.04%}) can be assumed equal to the ratio of square roots of these CO₂ concentrations (10% vs. 1% or 0.04%). Similarly, the measured carbonation coefficient for 1% CO₂ was converted to an estimated one for 0.04% CO₂.

2.4 Monitoring of internal humidity with embedded relative humidity sensors

A copper rod with a diameter of 4 mm was going through the moulds for the 100×30×100 mm³ mortar prisms at a depth of 15 mm from the bottom cast surface which would later serve as exposure surface during the accelerated carbonation experiments. When starting exposure to 1% and 10% CO₂, Rotronic humidity sensors were positioned in the sample holes created by the copper rods upon casting. Once embedded, the holes at one end were carefully sealed with tape. The critical other ends of the holes where the sensor cables were sticking out, were treated with a combination of tape on both the cables and sample surface and TEC7 sealant at the joints. These measures were all necessary to prevent local carbonation via the holes for the humidity sensors. Figure 1a gives a front and side cross-section of a 100×30×100 mm³ mortar prism with an embedded Rotronic humidity sensor.

2.5 Resistivity profiling with multi-ring electrodes (MREs)

The MREs used for these experiments were provided by SENSORTEC GMBH. They were embedded in the mortar cubes with a 100 side as shown in Figure 1b. It should be noted that MREs are normally positioned in a way that the cable end of the sensor is sticking out from the exposure surface with the sequence of stainless steel and PE insulation rings positioned in the opposite direction relative to the exposure surface. However, to absolutely make sure CO₂ could not penetrate more easily via the sensor mantle interface at the cable end, the MRE was positioned in the other direction with a 5 mm thick PVC spacer in between the exposure surface and the sensor end. In addition, the outer surface of the PVC spacer was covered with TEC7 surface sealant to avoid CO₂ ingress via its interface as well. Upon start of exposure of each cube to either 0.04%, 1% or 10% CO₂, resistivity profiles were recorded manually at regular time intervals using a switch box controlling the stainless steel ring pairs of the MRE and an LCR instrument (L: Inductance; C: Capacitance; R: Resistance). The as such measured resistance R (Ω) as a function of the depth was then converted to resistivity (Ωm) by multiplying the resistance values with the cell constant $k = 0.10$ m.

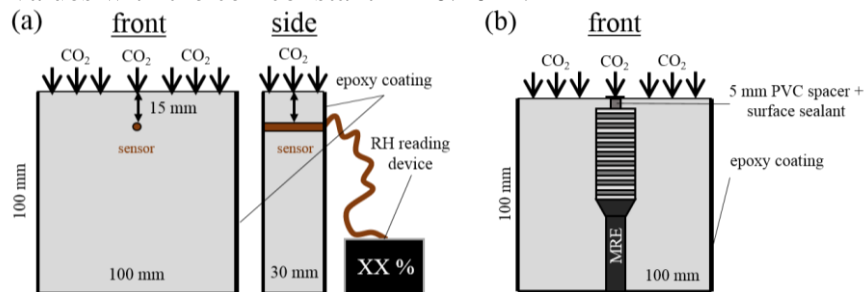


Figure 1: (a) 100×30×100 mm³ mortar prism with an embedded Rotronic humidity sensor, (b) mortar cube with a 100 mm side containing an MRE.

3. RESULTS AND DISCUSSION

3.1 Colorimetric carbonated assessment

Plotting the carbonation depth as a function of the square root of the exposure time resulted in carbonation coefficients of 13.94 mm/ $\sqrt{\text{weeks}}$, 7.54 mm/ $\sqrt{\text{weeks}}$ and 2.12 mm/ $\sqrt{\text{weeks}}$ for the considered CO₂ concentration of 10%, 1% and 0.04%, respectively (Figure 2a).

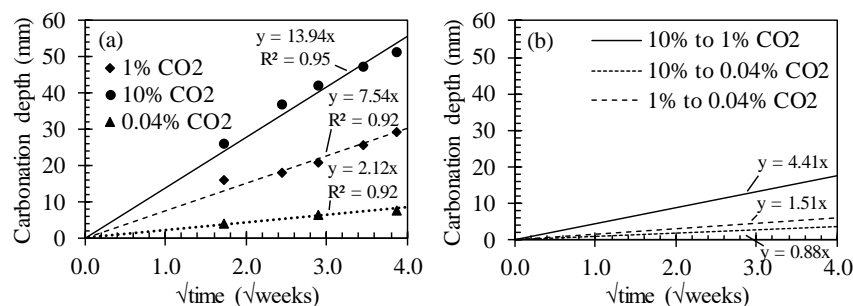


Figure 2: Measured (a) and estimated (b) carbonation coefficients after conversion cf. [9].

When converting the experimental carbonation coefficient obtained at 10% CO₂ to one that should correspond with 1% CO₂, this gives a value of 4.41 mm/ $\sqrt{\text{weeks}}$ (Figure 2b). This highly

underestimates the one that was actually measured at 1% CO₂ (Figure 1a: 7.54 mm/ $\sqrt{\text{weeks}}$). On the other hand, converting the carbonation coefficient at 1% CO₂ to one for the atmospheric CO₂ concentration (0.04% CO₂) results in a significantly lower underestimation (Figure 1b: 1.51 mm/ $\sqrt{\text{weeks}}$), more within range with the actually measured one (Figure 1a: 2.12 mm/ $\sqrt{\text{weeks}}$). This is not the case when considering conversion of $A_{10\%}$ to a value presumably corresponding with the atmospheric CO₂ concentration (Figure 1b: 0.88 mm/ $\sqrt{\text{weeks}}$).

3.2 Monitoring of internal humidity with embedded relative humidity sensors

The evolution of the internal humidity as a function of exposure time to accelerated carbonation significantly differs with the applied CO₂ concentration (Figure 3).

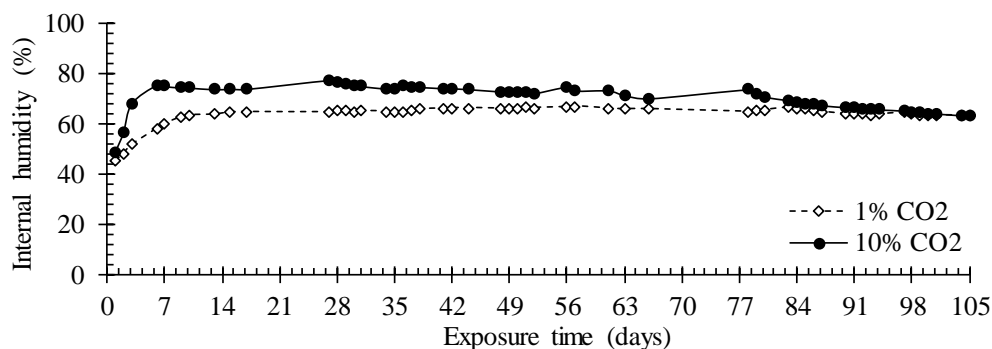


Figure 3: Evolution of the internal humidity during carbonation at 1% and 10% CO₂.

Although initially more or less in the same range after 4 days of oven drying at 40°C and 3 days of conditioning at 20°C and 60% RH, the internal humidity seems to rise faster for the highest CO₂ concentration. An equilibrium value of around 74-75% is reached for this carbonation environment after 7 days of exposure. The equilibrium value for the internal humidity during exposure to 1% CO₂ is significantly lower, i.e. 63-65%. This value is obtained after 10 days of exposure and remains stable for the whole monitoring period of 105 days. This seems less the case for the samples with embedded humidity sensors exposed to 10% CO₂. A slight decrease as a function of exposure time to around 71-72% was observed after 79 days of monitoring. Given the same sample preconditioning and the fact that temperature and relative humidity in both carbonation chambers were the same (20°C and 60% RH), the observed differences in internal humidity can only be attributed to the difference in imposed CO₂ concentration. Carbonation at both considered CO₂ concentrations will result in production of water. However, at the higher CO₂ concentration, the production of water is more abundant and its evacuation via the exposure surface of the samples might occur more slowly and possibly cause an increase in internal humidity which only gradually decreases again. In case of exposure to only 1% CO₂, gradual evacuation of the carbonation-induced water reactant from the samples is possibly still sufficiently feasible leading to a less substantial increase in internal humidity. Nonetheless, this theory still needs to be confirmed further on. Additional comparative carbonation experiments are planned on samples with multiple embedded humidity sensors at a varying depth from the exposure surface. This way, it could be verified further on whether the internal humidity could be linked to the progressing carbonation front. With sensors now at only one depth (15 mm) from the exposure surface, this is not yet possible.

3.3 Resistivity profiling with multi-ring electrodes (MREs)

Although starting off at very similar resistivity profiles at day 0, the profiles clearly further develop in a very different manner depending on the exposure conditions (Figure 4).

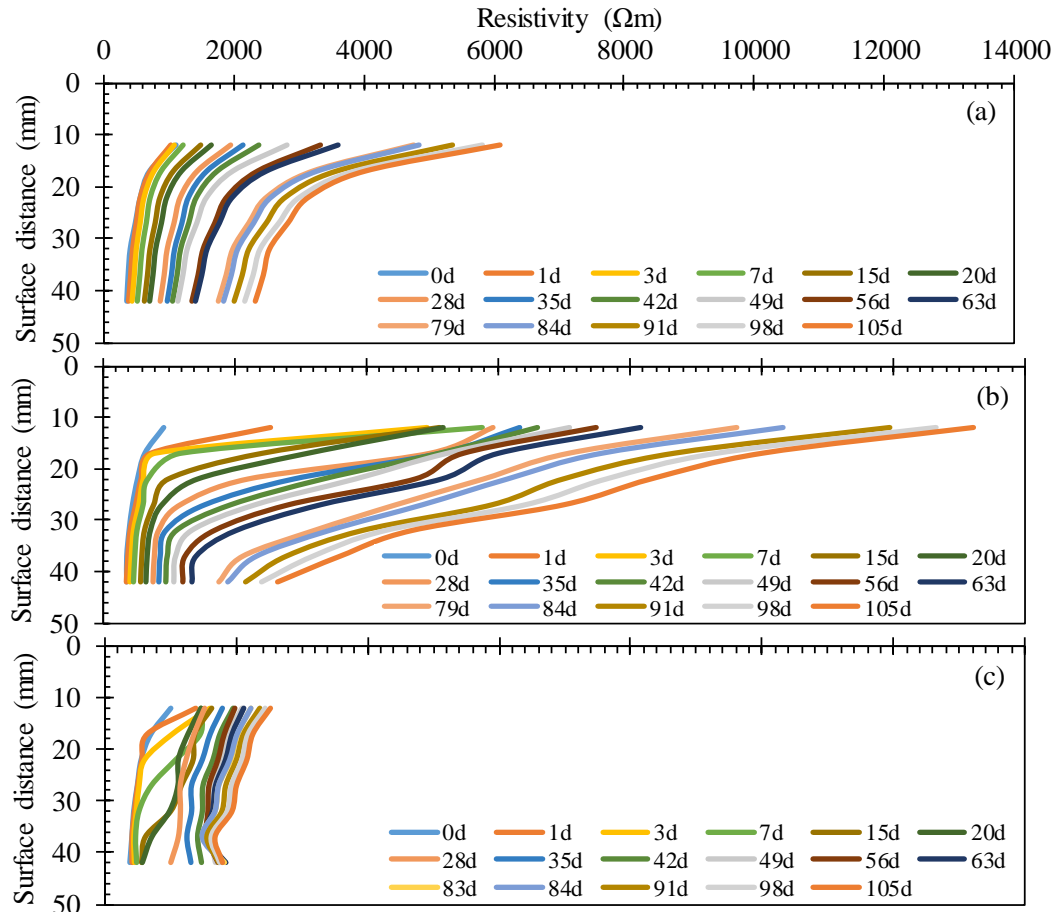


Figure 4: Resistivity profiles during carbonation at (a) 0.04%, (b) 1% and (c) 10% CO₂.

Figure 4a shows the evolution of the resistivity profile during natural carbonation at 0.04% CO₂. It must be said though that carbonation induced-changes in resistivity are probably not really noticeable yet to their fullest extent in this figure, since the colorimetric carbonation assessment in the previous section revealed that the carbonation front after 105 days of exposure only reached a depth of 8 ± 1 mm while the first MRE measuring location was situated at a depth of around 12 mm. In other words, Figure 4a rather represents resistivity profiles for HVFA mortar in uncarbonated instead of naturally carbonated condition. As such, these profiles serve mainly as uncarbonated reference while analysing the resistivity profiles during carbonation at 1% and 10% CO₂ (Figures 4b and 4c). In these figures, the evolution of the resistivity profiles should certainly account for the effects of carbonation since the colorimetrically assessed carbonation depths after 105 days of exposure to 1% and 10% CO₂ amounted to 29 ± 1 mm and 51 ± 5 mm, respectively.

Now, exposure to 1% CO₂, at 20°C and 60% RH causes substantial increases in resistivity in the vicinity of the exposure surface. Already after 1 day of exposure, the resistivity profile clearly deviates in that area from the one obtained at day 0, even though the carbonation front

did not reach the first metal ring couple of the MRE yet. For that layer at a depth of around 12 mm, the resistivity value had jumped from around 1000 Ωm to over 2500 Ωm . By the time of day 105 of the monitoring period, the resistivity value for the outermost layer of the MRE had reached even more than 13000 Ωm . Moreover, similar strong increases in resistivity were also recorded in the subsequent metal ring couples of the MRE. In the end, this effect was observed up to a 42 mm distance from the exposure surface. This was way beyond the colorimetrically assessed carbonation front after 105 days (29 ± 1 mm).

Increasing the CO_2 concentration from 1% to 10% CO_2 for accelerated carbonation experiments does not lead to even higher increases in resistivity. On the contrary, the maximum values obtained during the 105 days of exposure barely exceed 2000 Ωm . In the region close to the exposure surface there is pronounced increase in resistivity from day 1 onwards which soon also develops for the deeper MRE measuring locations. By day 28, all metal ring couples of the MRE had recorded the resistivity increases up to a distance of 42 mm from the exposure surface, giving the overall profile a significantly smaller curvature than the corresponding one obtained at 1% CO_2 . Again, these resistivity effects extend far beyond the location the carbonation front as determined rudimentary with phenolphthalein, which is only expected to be around 30 mm after 28 days. Starting from that day, the resistivity profile then keeps on developing in a more or less parallel manner, except for the deepest MRE measuring location at a depth of 42 mm. There, a slightly faster increase in resistivity was recorded. This resulted in a small dip in the profile at a depth of 37 mm. It should be noted that perhaps with more accurate carbonation assessment methods (e.g. petrographic thin section analysis which also accounts for partially carbonated regions) a more obvious link between carbonation depth and the observed changes in resistivity could be detected. This would be certainly worth verifying further on.

It is difficult to pinpoint the exact cause for the above described pronounced differences in resistivity profile development during carbonation at 1% and 10% CO_2 . For a given mixture and similar temperature and relative humidity conditions, resistivity can change due to variations in internal humidity, porosity and pore size distribution as well as ionic concentration of the pore solution [10]. Carbonation can be associated with all three phenomena. H_2O is reaction product of the carbonation. When generated in large amounts, it could alter the internal humidity of the HVFA mortar under investigation. In terms of porosity and pore size distribution, carbonation can either induce porosity reduction/increase and pore structure refinement/coarsening, depending on whether either CH or C–S–H carbonation gets the upper hand in the carbonation process. The ionic concentration of the pore solution determines its electrical conductivity of the current passing through, hence its resistivity. Given the influencing factors on resistivity mentioned by Harnisch [10], the fact that the resistivity values recorded during exposure at 10% CO_2 remained at all-time lower than those obtained in the 1% CO_2 environment implies probably a combined effect of a higher internal humidity, a higher overall porosity and coarser pore structure, and a higher ionic strength of the pore solution. Knowing from the colorimetric carbonation assessment, that carbonation coefficients/rates for a 1% CO_2 environment estimated from carbonation experiments conducted a 10% CO_2 tend to significantly underestimate carbonation coefficients/rates actually measured at 1% CO_2 , a higher internal humidity that significantly blocks the pores, hampers further CO_2 ingress and its dissolution in the pore solution could explain this behaviour. Nonetheless, further confirmation for the current interpretation of the resistivity data at hand is necessary as MRE measurements cannot isolate the different phenomena in play. Direct monitoring of the internal humidity during carbonation using for instance Nuclear Magnetic Resonance (NMR) could

probably provide further clarification. In addition, with mercury intrusion porosimetry (MIP) and thermogravimetric analysis (TGA) it could be checked whether a C–S–H carbonation-induced pore coarsening also contributed significantly to the now observed resistivity profiles.

4. CONCLUSIONS

During carbonation at 1% and 10% CO₂, both at 20°C and 60% RH, the internal humidity at a depth of 15 mm from the exposure surface is significantly higher at 10% CO₂. After 79 days this internal humidity converges again to the level recorded for 1% CO₂ (63-65%). MRE resistivity profiles during carbonation at 1% and 10% CO₂ differ substantially. During exposure to 1% CO₂, resistivity as a function of depth strongly increases to values in the range of 13000 Ωm near the surface. At 10% CO₂ the whole profile does not reach such high values. Eventually, the whole resistivity profile stabilizes at around 2000 Ωm. Excess water production during carbonation at 10% CO₂ could support both observations. However, further experimental verification on this excess water production and on C–S–H carbonation-induced pore coarsening alongside it, is still required.

ACKNOWLEDGEMENTS

Philip Van den Heede is postdoctoral fellow of Research Foundation—Flanders (FWO) (project No. 3E013917) and acknowledges its support.

REFERENCES

- [1] Malhorta, V.M., Mehta, P.K., 'High Performance, high-volume fly ash concrete: Materials, mixture proportioning, properties, construction practice, and case histories', 2nd Edn (Supplementary Cementing Materials for Sustainable Development Inc., Ottawa, 2005).
- [2] Lammertijn, S., De Belie, N. 'Porosity, Gas Permeability, Carbonation and Their Interaction in High-volume Fly Ash Concrete', *Mag. Concr. Res.* **60** (2008) 535-545.
- [3] Kinoshita, H., Circhirillo, C., San Martin, I., Utton, C.A., Borges, P.H.R., Lynsdale, C.J., Milestone, N.B., 'Carbonation of composite cements with high mineral admixture content used for radioactive waste encapsulation', *Miner. Eng.* **59** (2014) 107-114.
- [4] Ashraf, W., 'Carbonation of cement-based materials: Challenges and opportunities', *Constr. Build. Mater.* **120** (2016) 558-570.
- [5] Sisomphon, K., Franke, L. 'Carbonation rates of concretes containing high volume of pozzolanic materials', *Cem. Concr. Res.* **37** (2007) 1647-1653.
- [6] Van den Heede, P., De Schepper, M., De Belie, N., 'Accelerated and natural carbonation of concrete with high volumes of fly ash: chemical, mineralogical and microstructural effects', *R. Soc. Open Sci.* (2018), revised manuscript under review since 2018-12-06.
- [7] Saetta, A.V., Vitaliani, R.V., 'Experimental Investigation and numerical modeling of carbonation process in reinforced concrete structures, Part I: Theoretical formulation', *Cem. Concr. Res.* **34** (2004), 571-579.
- [8] da Silva, F.G., Helene, P., Castro-Borges, P., Liborio, J.B.L., 'Sources of variations when comparing concrete carbonation results', *J. Mater. Civ. Eng.* **21** (2009) 333-342.
- [9] Van den Heede, P., Snoeck, D., Van Mullem, T., De Belie, N., 'Carbonation resistance of High-Volume Fly Ash (HVFA) mortar: Effect of applied CO₂ concentration', in Proceedings of SynerCrete'18 International Conference on Interdisciplinary Approaches for Cement-based Materials and Structural Concrete, Funchal, Madeira Island, Portugal, October 24-26, 2018.
- [10] Harnisch, J., 'Investigations on subsequently embedded multi-ring-electrodes in concrete', Diplomarbeit, in German (IBAC, RWTH AACHEN, Aachen, 2003).

THERMODYNAMIC MODELLING OF THE CARBONATION PROCESS IN ALKALI-ACTIVATED CEMENTS

Xinyuan Ke (1), Susan A. Bernal (2) and John L. Provis (3)

(1) Department of Architecture and Civil Engineering, The University of Bath, United Kingdom

(2) School of Civil Engineering, University of Leeds, United Kingdom

(3) Department of Materials Science and Engineering, The University of Sheffield, United Kingdom

Abstract

The carbonation of cementitious materials induced by their interaction with atmospheric CO₂, is one of the main degradation mechanisms threatening their durability. Despite the extensive experimental work that has been carried out attempting to determine carbonation resistance of alkali-activated cements, it remains to some degree unknown what factors influence carbonation of these materials, and how carbonation resistance under service conditions can be estimated. Hence, there is an urgent need to develop modelling tools that can be used to predict the potential carbonation behaviour of these materials, based on the bulk binder composition. In this study, a thermodynamic model to predict the phase evolution of alkali-activated slags exposed to an accelerated carbonation environment (1% v/v CO₂) is proposed. This model predicts semi-quantitatively the phase assemblages, as a function of CO₂ exposure, considering the bulk chemistry of the slag and activators used for producing the cementitious binders. Experimental data retrieved from the literature were used to support the development of the proposed model. The challenges identified during the development of this model are also discussed, including recommendations for its future modification.

Keywords: Carbonation, Thermodynamic modelling, Alkali-activated slag, Durability

1. INTRODUCTION

The carbonation of cementitious materials induced by atmospheric CO₂ is one of the main degradation mechanisms that affect the durability of cement and concrete. In Portland cement based materials, portlandite (Ca(OH)₂) performs as a buffer phase to delay the decalcification of the main reaction product, calcium silicate hydrate [1]. However, portlandite is not typically formed as a reaction product in alkali-activated cement systems (especially alkali-

activated slag cements), therefore, different carbonation mechanisms have been observed in these cements [2].

The state-of-the-art investigations of carbonation in alkali-activated cement are based on experimental observations. Under natural conditions (0.04 % CO₂) the carbonation process normally takes place very slowly. Therefore, in practice, most studies on the carbonation of cementitious materials are conducted under accelerated conditions. Bernal et al. compared the carbonation products formed in alkali-activated slags under natural and different acceleration conditions, and identified that 1 % CO₂ at a relative humidity of 65% appears to be the most suitable accelerated test condition for alkali-activated slag [2, 3], as under these carbonation conditions, the phase assemblage of carbonated specimens resembles that identified in materials exposed for several years to natural CO₂. However, even under this accelerated condition, the test duration for a newly proposed mix design will last several weeks. Considering the large variability in the chemistry of raw materials and activators used to produce alkali-activated cements, there is an urgent need to develop modelling tools, considering mix design parameters, for predicting their carbonation behaviour.

Recent developments in the available thermodynamic databases for cement-related phases [4] have enabled and improved the prediction of phase assemblages in cements based on the bulk chemistry of the binder. Myers et al. [5] proposed a new solid-solution model for sodium and aluminium substituted calcium silicate hydrate (C-(N)-A-S-H) type gels, commonly formed in alkali-activated cement, taking consideration of the charge balancing alkalis (mainly Na⁺) within the gel structure. The application of this model for predicting phase assemblages in alkali-activated slag cement [5] showed good agreement with experimental observations. However, the feasibility of using thermodynamic models to simulate carbonation process of alkali-activated slag cements has not previously been explored.

In recent work by Shi et al. [6], a thermodynamic model was proposed for the carbonation process in the ternary Portland cement-metakaolin-limestone system. The modelling methods established in that study reflected the two-step decalcification processes that takes place in the main reaction product (C-S-H type gel): loss of Ca from the interlayer, then loss of Ca from the principal layer. The total mass of CO₂ bound within the solid cements, as predicted by the model, showed good agreement with data from thermogravimetric analysis. A similar step-wise reaction path modelling approach might also be applied to alkali-activated slag cements. However, it is critical to note the significant differences between the chemistry of these two types of cementitious binder systems.

In this study, a thermodynamic model is developed to describe the carbonation process in an alkali-activated slag cement. Experimental data retrieved from the literature were used to support and validate the proposed model. A critical evaluation of the challenges identified during the development of this initial model is also included.

2. METHODS

The method of Gibbs energy minimisation was used to predict the stable phases that may be expected to form in the alkali-activated slag systems during its reaction with CO₂. An extended Debye-Hückel equation was used for calculating the activity coefficients of the aqueous species. The thermodynamic model for alkali-activated slag cements developed by Myers et al. [7] was used as the general framework for predicting the phase assemblage of non-carbonated samples, and open source software GEM-Selektor v.3 (GEMS3) was used to

perform the modelling. The recent published Cemdata18 [4] was used as the main chemical thermodynamic database. The solid solution models for alkali-substituted calcium aluminate silicate hydrate gels (CNASH_{ss}) and for hydroxylated hydrotalcite (MgAl-OH-LDH_{ss}) were used, as described in detail in [5, 7]. In addition to the phases included in this database, another three mineral phase were included: talc, scolecite, and mordenite. The thermodynamic properties of these three phases are shown in Table 1.

Table 1 Thermodynamic properties of mineral phases included for modelling (in addition to the Cemdata18 database [4].)

	ΔG_f° ¹ (kJmol ⁻¹)	ΔH_f° ² (kJmol ⁻¹)	S° ³ (Jmol ⁻¹ K ⁻¹)	Ref
Talc Mg ₃ Si ₄ O ₁₀ (OH) ₂	-5523.670	-5903.290	261.506	[8]
Scolecite* CaAl ₂ Si ₃ O ₁₀ ·3H ₂ O	-5598.150	-6048.810	367.400	[9]
Mordenite-(Ca) Ca _{0.5} AlSi ₅ O ₁₂ ·4H ₂ O	-6401.650	-6937.380	509.200	[10, 11]

¹ Standard molar Gibbs energy of formation

² Molar enthalpy of formation

³ Absolute molar entropy

*Together with sodium natrolite (Na₂Al₂Si₃O₁₀·2H₂O), was introduced as Natrolite-(Ca, Na) ideal solid solution.

The chemical composition of a conventional ground granulated blast furnace slag was used to represent the precursor used in synthesis of the alkali-activated cement, with 42.3 wt.% CaO, 32.2 wt.% SiO₂, 13.3 wt.% Al₂O₃, 5.2 wt.% MgO [7]. The sulfur content measured from XRF analysis (0.8 % when represented as SO₃) was added as equivalent H₂S (0.34 wt.%). An activator dose of 7 wt.% Na₂SiO₃ by total mass of slag, and a water to binder (total mass of slag and the solid activator) ratio of 0.40, were used. A degree of reaction of 75% has been applied to this model, approximating 28 day cured samples [12]. The initial gas phase input was only N₂, representing the reduced redox environment in the alkali-activated slag cement.

A stepwise CO₂ addition was used to mimic the accelerated carbonation conditions [6]; at each step, 1 g of pure CO₂ gas (density 1.98 kg/m³) was added together with 62 g of air (density 1.22 kg/m³), equivalent to 1% v/v of CO₂. The oxygen present in the air was intended to test for the simultaneous oxidation and carbonation processes in these cements during exposure.

3. RESULTS AND ANALYSIS

The phase assemblages and the change of pH in the aqueous phase during step-wise carbonation of an alkali-activated slag cement are shown in Figure 1. Alkali-substituted calcium aluminosilicate hydrate type gel (C-(N)-A-S-H), strätlingite, Mg-Al layered double hydroxide (LDH) and natrolite (representing alkali aluminosilicate gel) were predicted as initial reaction products, in accordance with observations from experimental characterisation of alkali-activated slag cements [13, 14]. With increased addition of CO₂ and air to the system, the mass of C-(N)-A-S-H gel, strätlingite and Mg-Al LDH decreased, while calcite and natrolite-(Na,Ca) increased. Monosulfate, monocarbonate, ettringite and thaumasite were

predicted as transitional phases (hosting both carbonate, and the sulfate generated through sulfide oxidation by air) before the full exhaustion of C-(N)-A-S-H gel upon carbonation. Talc and dolomite were predicted as the final Mg-bearing carbonation products in the absence of any kinetic controls on the formation of these or any other potentially relevant mineral phases, while gypsum was predicted as the final sulfur-bearing phase.

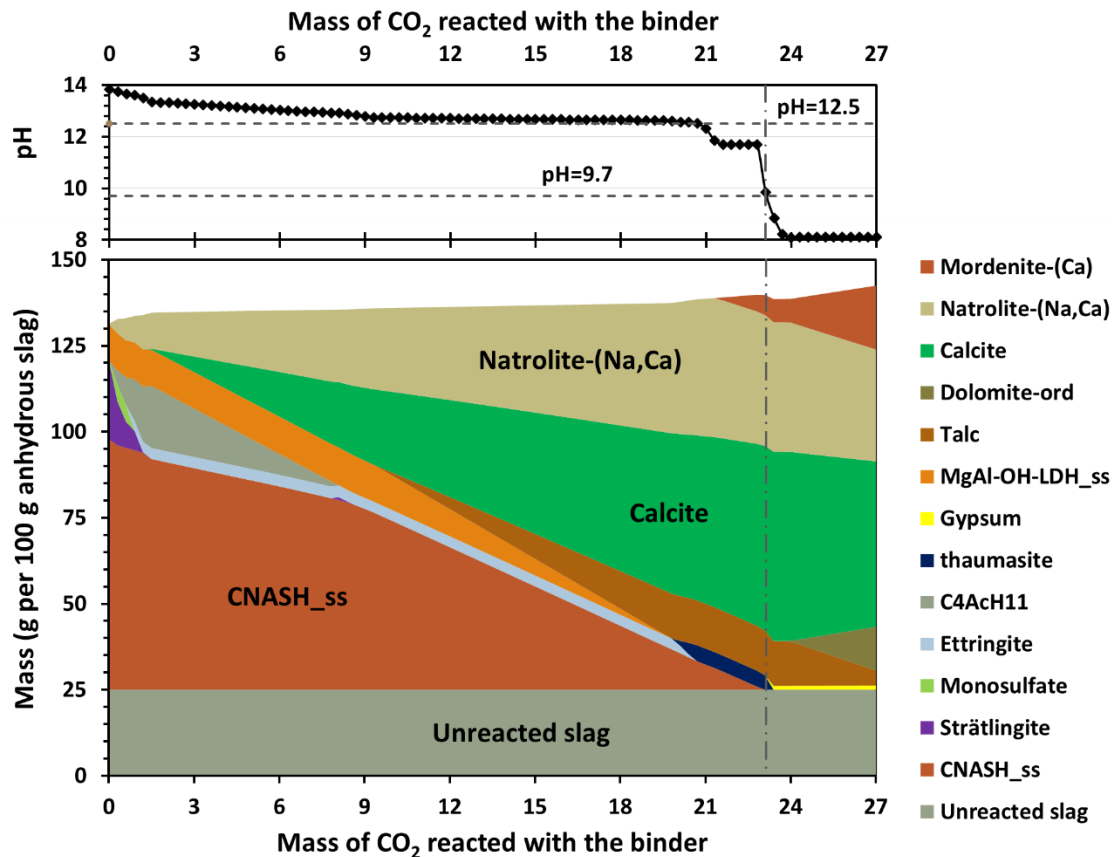


Figure 1. Phase assemblage of alkali-activated slag paste predicted under step-wise accelerated carbonation, and the corresponding pH in the aqueous phase (pore solution). The horizontal dashed lines represent pH values of 12.5 and 9.7 respectively, and the vertical dash-dot line indicates the predicted phase assemblage when the pH in the pore solution dropped to 9.7 (the colour change boundary of the phenolphthalein indicator).

Table 2 shows a summary of the mineral phases observed experimentally in accelerated carbonated alkali-activated slag samples. The thermodynamically predicted phases qualitatively match the experimental observations.

The calculation method used in this study, Gibbs energy minimisation, is not suitable for predicting metastable phases, such as the CaCO_3 polymorphs aragonite and vaterite; distinguishing these phases from calcite is beyond the capacity of this proposed model. The same situation might also apply to the hybrid carbonate salts, such as gaylussite, which was identified in sodium carbonate activated slag as transition phase [20]. However, missing of hydrous sodium carbonates from the modelling results might suggest that the identification of

theses phase from XRD might due to recrystallization of ions in pore solution during sample preparation process, as the system will need sufficient amount of cations (mostly Na^+) to charge balance the amorphous aluminosilicate gel.

Table 2. Summary of mineral phases observed in the literature for carbonated alkali-activated slag paste/mortar/concrete

Mineral phase	Ref.	Mineral phase	Ref.
Calcite	[3, 13, 15-17]	Huntite	[16]
Aragonite	[3, 13, 15, 16]	Dolomite	[16]
Vaterite	[3, 13, 15-17]	Hydrous sodium carbonates	[3, 16, 18]
Monocarbonate	[17]	Gaylussite	[3, 16, 18]
Carbonated hydrotalcite	[13, 17]	(Na,Ca)-aluminosilicate	[18, 19]

3.1 Carbonation of the main binding gel

The simulated mass loss of C-(N)-A-S-H type gel during carbonation showed two stages (Figure 1), possibly related to two different decalcification processes. Figure 2 shows the mass change of C-(N)-A-S-H gels with different interlayer charge balancing cations at different stages of carbonation.

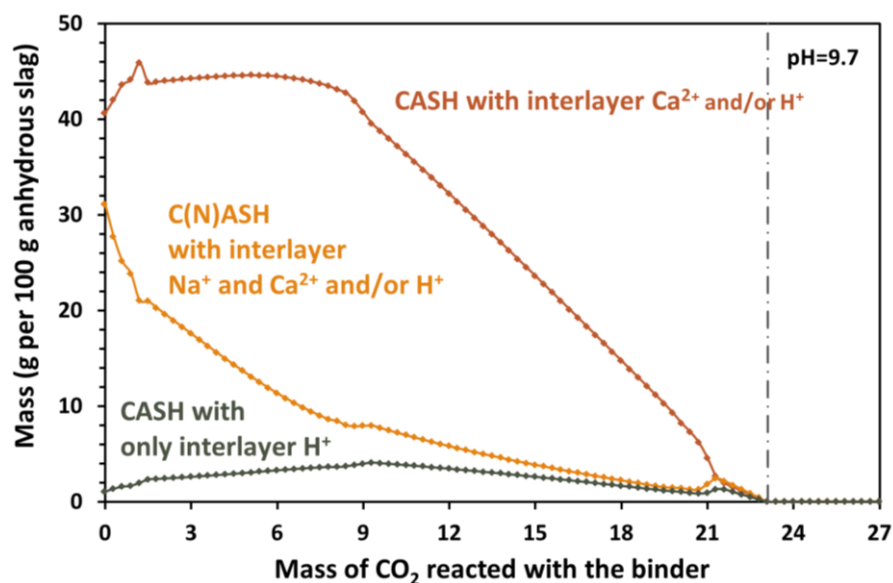


Figure 2. Content of C-(N)-A-S-H with interlayer Na^+ , Ca^{2+} and/or H^+ (5CNA, INFCNA, INFCN endmembers in the CNASH_{ss} model), CASH with interlayer Ca^{2+} and/or H^+ (T5C, 5CA, T2C endmembers), and CASH with only interlayer H^+ (TobH, INFCA endmembers). The specific details of these eight end members can be found in [4, 5].

The modelling results suggest a three-stage decalcification process, (i) the loss of interlayer charge balancing Na^+ , (ii) loss of interlayer Ca^{2+} , and then (iii) loss of structural Ca^{2+} . Although there is a lack of experimental data from literature on the decalcification process of C-(N)-A-S-H gel, these predictions show good consistency with the experimental characterisation of C-A-S-H gel, where a two-step decalcification process (first loss of

interlayer Ca^{2+} , and then loss of structural Ca^{2+}) was observed. The interlayer charge balancing Na^+ was added to the CNASH_ss model to reflect the increased alkali content in alkali-activated cements [5], and it is reasonable to assume that the ionic bonding of interlayer Na^+ would become the least stable charge balancing site when the aqueous pH started to drop.

3.2 Carbonation of secondary reaction products

Figure 1 shows that strätlingite is predicted to be consumed at a very early stage of the simulated carbonation process, while hydrotalcite stayed stable during initial carbonation, and started to decompose when the aqueous pH decreased to 12.5. Monocarbonate (Mc) is commonly identified in sodium carbonate activated slag paste, where the formation of strätlingite does not take place [20]. Carbonate-containing hydrotalcite (HT) is commonly identified in carbonated AAS [13, 17], however dolomite has also been identified in three-year naturally carbonated samples [16]. The basal reflection peaks (2θ) of carbonated HT (11.52°) and Mc (11.70°) are very close to each other, which might be the reason why monocarbonate is less commonly reported as a reaction product in alkali-activated systems. It is also worth noting that talc was included to the calculations as an analogue for a poorly-hydrated magnesium silicate hydrate gel with low Mg/Si ratio [21], as a potential sink for the Mg released by decomposition of Mg-containing LDH phases. The loss of water from carbonated alkali-activated slag cements is significant, as identified from experimental thermogravimetric analysis [3, 15, 17], therefore the formation of hydrated magnesium silicate hydrate gel would be less favoured. Under hydrothermal carbonation conditions (200-300 °C), talc can react with calcite and CO_2 to form dolomite [22], but it is not clear whether the same reaction process can take place at ambient temperature.

3.3 Oxidation of sulfide

The sulfur content in blast furnace slag is primarily in the form of sulfide (S^{2-}) [23], and so sulfate-bearing phases such as monosulfate and ettringite are not reported in non-carbonated alkali-activated slag cements [3, 15, 17]. However, under carbonation conditions, they will be exposed to approximately 20% v/v of O_2 in the gas atmosphere, and therefore it is important to consider sulfate generation by oxidation of sulfide in the pore solution. As a result, monosulfate and ettringite were predicted as transitional carbonation products in Figure 1. Thaumasite, a phase that is sometimes found in Portland cement as a result of specific forms of sulfate attack [24], has been predicted here as another transitional sulfate-bearing phase, which decomposes to gypsum upon further carbonation. Gypsum was also predicted as the final sulfate-bearing phase in blended Portland cements when the pore solution pH dropped below 9.7 [6].

3.4 Formation of aluminosilicate phases

During the simulations, prior to addition of CO_2 into the system, only a small fraction of natrolite-Na was predicted, representing the disordered aluminosilicate gel typically identified in decalcified alkali-activated slag cements [7]. Under carbonation conditions, additional amorphous aluminosilicate gel will form as the result of decalcification of the main reaction product [3, 15, 17]. The ^{29}Si MAS NMR spectra of carbonated samples often show a broad resonance between -90 and -100 ppm [3, 17], likely related to $\text{Q}^4(2\text{Al})$ or $\text{Q}^4(3\text{Al})$ silica environments, yielding a bulk Si/Al ratio of around 1 to 2 [25]. Among all the zeolite-type phases in the Cemdata18 database [4], natrolite-Na was predicted as the preferred phase. Also,

this amorphous aluminosilicate gel will also have the flexibility to take up a small fraction of Ca^{2+} as extra framework cations. Therefore, the solubility data for the Ca-rich end member (scolecite) of the natrolite solid solution (which is treated here as ideal) have been added into the database. During carbonation, the mass of natrolite-(Na,Ca) increased significantly as the mass of added CO_2 increased, representing the increased fraction of framework tetrahedral aluminosilicate gels in the system.

4. CONCLUSIONS

In this study, a thermodynamic model for predicting the phase evolution of alkali-activated slag cements exposed to accelerated carbonation conditions (1% v/v CO_2) is proposed. This model provides semi-quantified phase assemblage predictions of carbonated specimens, considering the bulk chemistry of the slag precursor and the activator used.

The lack of systematic quantitative experimental data is the main challenge for the further improvement of this model. The carbonation process of secondary phases forming in alkali-activated systems remains largely unknown. Particularly, the fate of Al and Mg during the carbonation process is not well understood, hence there is an urgent need to elucidate the mechanisms of carbonation in these phases.

Speciation of sulfur (sulfide vs sulfate) at different carbonation depths will provide useful information for comparing the diffusion rates of O_2 and CO_2 within the binder matrix. This is especially important for designing reinforced concretes.

ACKNOWLEDGEMENTS

This work was funded by EPSRC through grant EP/P013171/1. Participation of X. Ke in this study was sponsored by the Prize Fellowship at The University of Bath. Participation of S.A. Bernal in this study was sponsored by EPSRC through ECF EP/R001642/1.

REFERENCES

- [1] Taylor, H.F.W., Cement Chemistry. 1997: Thomas Telford.
- [2] Bernal, S.A., et al., Factors controlling carbonation resistance of alkali-activated materials. *ACI Special Publication*, vol. 320, p. 2016.
- [3] Bernal, S.A., et al., Gel nanostructure in alkali-activated binders based on slag and fly ash, and effects of accelerated carbonation. *Cem. Concr. Res.*, vol. 53, p. 127-144, 2013.
- [4] Lothenbach, B., et al., Cemdata18: A chemical thermodynamic database for hydrated Portland cements and alkali-activated materials. *Cem. Concr. Res.*, vol. 115, p. 472-506, 2018.
- [5] Myers, R.J., S.A. Bernal, and J.L. Provis, A thermodynamic model for C-(N-)A-S-H gel: CNASH_ss. Derivation and validation. *Cem. Concr. Res.*, vol. 66, p. 27-47, 2014.
- [6] Shi, Z., et al., Experimental studies and thermodynamic modeling of the carbonation of Portland cement, metakaolin and limestone mortars. *Cem. Concr. Res.*, vol. 88, p. 60-72, 2016.
- [7] Myers, R.J., et al., Thermodynamic modelling of alkali-activated slag cements. *Appl. Geochem.*, vol. 61, p. 233-247, 2015.
- [8] Helgeson, H.C., Summary and critique of the thermodynamic properties of rock-forming minerals, H.C. Helgeson, Editor 1978, Kline Geology Laboratory, Yale University: New Haven .
- [9] Johnson, G.K., et al., Thermodynamic studies of zeolites: natrolite, mesolite and scolecite. *American Mineralogist*, vol. 68, p. 1134-1145, 1983.
- [10] Johnson, G.K., et al., Thermodynamic studies of mordenite, dehydrated mordenite, and gibbsite. *American Mineralogist*, vol. 77, p. 85-93, 1992.

- [11] Blanc, P., et al., ThermoChimie database developments in the framework of cement/clay interactions. *Appl. Geochem.*, vol. 55, p. 95-107, 2015.
- [12] Myers, R.J., et al., The role of Al in cross-linking of alkali-activated slag cements. *J. Am. Ceram. Soc.*, vol. 98, p. 996-1004, 2014.
- [13] Bernal, S.A., et al., MgO content of slag controls phase evolution and structural changes induced by accelerated carbonation in alkali-activated binders. *Cem. Concr. Res.*, vol. 57, p. 33-43, 2014.
- [14] Winnefeld, F., et al., Influence of slag composition on the hydration of alkali-activated slags. *J. Sust. Cem. Based Mater.*, vol. 4, p. 85-100, 2015.
- [15] Puertas, F., M. Palacios, and T. Vázquez, Carbonation process of alkali-activated slag mortars. *J Mater Sci*, vol. 41, p. 3071-3082, 2006.
- [16] Bernal, S.A., et al., Accelerated carbonation testing of alkali-activated binders significantly underestimates service life: The role of pore solution chemistry. *Cem. Concr. Res.*, vol. 42, p. 1317-1326, 2012.
- [17] Ke, X., et al., Slag-based cements that resist damage induced by carbon dioxide. *ACS Sustainable Chem. Eng.*, vol. 6, p. 5067-5075, 2018.
- [18] Bernal, S.A., et al., Natural carbonation of aged alkali-activated slag concretes. *Mater Struct*, vol. 47, p. 693-707, 2014.
- [19] Bernal, S.A., et al., Evolution of binder structure in sodium silicate-activated slag-metakaolin blends. *Cem. Concr. Compos.*, vol. 33, p. 46-54, 2011.
- [20] Ke, X., S.A. Bernal, and J.L. Provis, Controlling the reaction kinetics of sodium carbonate-activated slag cements using calcined layered double hydroxides. *Cem. Concr. Res.*, vol. 81, p. 24-37, 2016.
- [21] Vespa, M., et al., Characterisation of magnesium silicate hydrate phases (M-S-H): A combined approach using synchrotron-based absorption-spectroscopy and ab initio calculations. *Cem. Concr. Res.*, vol. 109, p. 175-183, 2018.
- [22] Power, I.M., S.A. Wilson, and G.M. Dipple, Serpentine carbonation for CO₂ sequestration. *Elements* vol 9, p. 115-121, 2013.
- [23] Roy, A., Sulfur speciation in granulated blast furnace slag: An X-ray absorption spectroscopic investigation. *Cem. Concr. Res.*, vol. 39, p. 659-663, 2009.
- [24] Rahman, M.M. and M.T. Bassuoni, Thaumasite sulfate attack on concrete: Mechanisms, influential factors and mitigation. *Constr. Build. Mater.*, vol. 73, p. 652-662, 2014.
- [25] Engelhardt, G. and D. Michel, High-Resolution Solid-State NMR of Silicates and Zeolites. 1987, Chichester: John Wiley & Sons.

TRADITIONAL COATINGS AS PROTECTION OF PORTLAND CEMENT CONCRETE AGAINST CARBONATION

Rui Cunha Reis (1), Aires Camões (1) and Manuel J. P. Ribeiro (2)

(1) CTAC, University of Minho, Azurém, Guimarães, Portugal

(2) UIDM, ESTG, Polytechnic Institute of Viana do Castelo, Portugal

Abstract

Reinforced concrete is usually subjected to carbonation attack. Although it is a slow development pathology, the consequences can be high, precisely in the places with greater human, residential or industrial occupation. To make matters worse, carbon dioxide concentration in the atmosphere has been increasing due to the impact of climate changes and also to the growth of number of large cities. One of the ways to increase the resistance to carbonation attack may be through the application of concrete coatings. In fact, many current constructions have a protective skin on the concrete, often ignored in the durability design project. For these reasons, this research has looked into the efficiency of the coatings when applied on concrete. Priority was given to traditional unpainted coatings, with cementitious base, hydrated lime or both. A coating based on fly ash and a thin coating of cement were also tested. All of them were applied in an ordinary Portland cement concrete. Accelerated carbonation tests were performed and the results were excellent. It was observed that the performance of the coated concretes was, on average, about 65% better when compared to the uncoated concrete.

Keywords: Carbonation, coating, skin, durability

1. INTRODUCTION

Corrosion by carbonation of reinforced concrete is one of the most severe and frequent forms of structures damage [1]. This type of pathology is more typical in more densely populated or industrial locations because the concentration of carbon dioxide is higher [2]. Although the concentration of carbon dioxide is “low” in absolute values, it is enough to promote carbonation. In addition, the *Keeling curve*, with historical data, shows that the concentration increases without signs of slowdown [3, 4]. However, the damage intensity is also related to the quality of the concrete [5], as well as the presence and type of protection, which is the focus of this research.

One of the most common ways to protect concrete against carbonation is the application of coatings [6]. It is still a complex area, which will require more research. For instance, one persisting issues, is that when coatings function as a diffusion barrier for carbon dioxide, its low permeability can retain the moisture of the concrete. Also, it is necessary to ensure the adhesion of the concrete coatings, over time [7, 8]. With regard to the constitution, coatings may be based on alkyds, acrylics, vinyl, vinyl acrylics, polyurethanes, butadiene styrene or even reactive crystalline materials [6-8]. Coatings may also be permeable and still work against carbonation, such as gypsum [9]. But, on a regular basis, the constructions and consequently the structures, are protected by traditional coatings although often ignored in the durability design project. Thus, the composition of the concrete is overestimated, with economic and environmental costs.

Traditional coatings can be defined as *strong* or *weak*, depending on its cement content. *Strong coatings*, with high cement content, have better workability, better adhesion and lower porosity [10]. They also provide chemical protection against carbonation, due to the presence of large amount of calcium hydroxide, which is a product of the cement reaction and will be greater as the *stronger* is the coating. In the presence of alkaline compounds, the aqueous solution in the pores of the concrete, forms a protective, compact, high adhesion, almost impenetrable and invisible protective film, called *passive layer*. With the protection of this *passive layer*, the corrosion rate is extremely low, about 1 $\mu\text{m}/\text{year}$, considering that the concrete is protected as long as it is of good quality and that its physical-chemical characteristics do not change [11-14]. In turn, the *weak coatings*, with low cement content, are less susceptible to cracking, preventing the ingress of external agents. A further advantage of *weak coatings* is its rapid carbonation: as the calcium carbonate is denser than its reactants [15, 16], it may eventually form a physical barrier to aggressive agents.

These traditional coatings are usually made up of several layers. Thus, the porosity, shrinkage and cracking can be further reduced, especially when using *strong coatings*. Usually, three or more layers: *coarse mortar*, *base layer* (with one or more layers) and *finish*. The function of *coarse mortar* is to improve adhesion, so it must be a discontinuous, rough and high binding binder layer. *Base layer*, is homogeneous, allows to guarantee the flatness, the verticality, contributed to the surface regularity, as well as provide impermeability and ensure a good adhesion to the next layer. *Finish*, has decorative functions, waterproofing and resistance to shocks. However, in order to obtain these advantages, enforcement must ensure compliance with two fundamental rules. First, the rule of *regressivity of the binder*: the binder content has to decrease from the inner to outer layers. The goal is that in case of a crack, it does not go through the entire coating. Second, the *drying time*: the drying intervals must be extended, so that the shrinkage of each layer will be partially achieved before the application of the next layer [10].

Thus, as can be seen, traditional coating presents characteristics that may be functional in face to carbonation attack: good adhesion to concrete, made up of several layers, the regressive content of binder and probably, proper water vapour diffusion. In this context, an experimental program was developed with the main objective of evaluating the efficiency of several traditional coatings applied on ordinary Portland cement concrete (OPCC). The composition of the coatings used was based on reference publication [10], considering the *coarse mortar* and *base layer* without the *finish*. Coatings with different levels of cement, intending as a chemical and physical barrier, were considered. Coatings with hydrated lime and fly ash were also

considered, intended to provide a physical barrier. Finally, a thin coating was investigated, with a higher content of cement, which is intended to act as a physical and chemical barrier.

2. EXPERIMENTAL PROGRAM

2.1 Materials

The selected concrete was an ordinary Portland cement concrete (OPCC), with 330 kg/m³ of cement content and a water cement ratio (W/C) of 0.65. Table 1 shows the composition. The goal for this high W/C ratio was to ensure a significant carbonation depth of the concrete during trial period. The cement used was a *CEM I 42.5 R*, produced by *SECIL* at *Maceira-Liz* plant, corresponding to standard EN 197-1 [17]. The clinker content is more than 95%, with rapid development of strengths, for general application in civil engineering works or with special requirements (Table 2). Three types of aggregates were used: rolled sand from *Entre-os-Rios* (Douro River), called "*Sand 0-4*"; two granite gravel, from the granitic quarry "*Sorte do Mato do Monte das Lagedas*" (District of Guimarães), called "*Coarse 4-8*" and "*Coarse 6-12*".

Table 1: Concrete composition by weight

Mix	CEM I 42.5 R [kg/m ³]	Sand 0-4 [kg/m ³]	Coarse 4-8 [kg/m ³]	Coarse 6-12 [kg/m ³]	A/C [-]
I	330.0	752.1	583	332.9	0.65

Table 2: Materials characteristics

	<i>C- I 42.5 R</i>	<i>FA-Pego</i>	<i>HL-Lusical</i>
<i>Chemical properties [%]</i>	[18]	<i>XRF</i>	<i>STA/ [19]</i>
SiO ₂	17.85	55.10	< 0.35 [19]
Al ₂ O ₃	4.75	26.60	< 0.20 [19]
Fe ₂ O ₃	3.71	5.70	< 0.20 [19]
CaO	65.07	2.58	> 80 [19]
MgO	1.85	1.30	< 5 [19]
SO ₃	3.44		< 2.0 [19]
K ₂ O	0.91	1.41	
Na ₂ O	0.28	0.26	
TiO ₂		1.33	
P ₂ O ₅		0.73	
Cl ⁻	0.06		
CO ₂			1.8
H ₂ O free (<i>STA</i>)			1.92
Ca(OH) ₂ (<i>STA</i>)			89.78
CaCO ₃ (<i>STA</i>)			3.56
Loss on ignition	2.15	2.73	
Insoluble residue	0.99		
<i>Physical properties</i>			
D10 (laser an.) [%]	1.33	1.53	1.36
D50 (laser an.) [%]	9.30	8.55	3.80
D90 (laser an.) [%]	24.16	20.19	7.73
Sp. gravity [kg/m ³]	3130	2420	2317

For the coatings, the same type of cement was used as in concrete. Fly ash (FA), was obtained from the *Pego* thermoelectric power plant (Portugal), made up of very fine spherical particles and consisting mainly by aluminium silicates. FA particles have a vitreous phase (reactive) of 62.5% and a pozzolanic activity index of 525.2 mg Ca(OH)₂/g [20]. The hydrated lime is type *H100*, produced by *Lusical*, consisting essentially of calcium hydroxide (88.69%). More information can be found in previous work [21, 22].

Nine coatings were used. Mortars with cement binders, hydrated lime and fly ash (Table 3). At most, 3 layers were considered: *coarse mortar*, *first base layer* and *second base layer*. *Coarse mortar*, refers to an irregular layer, composed of a bonding agent with cement content. The purpose of this layer is to promote strong adherence to the following layers. Therefore, it was added to the *coarse mortar* constitution, a commercial adhesion promoter, designated *Sika Latex*. The *first layer* and *second base layer*, are traditional coating layers, which ensures water tightness and also allow to apply a *finish*. The *finish* was not considered in this investigation.

Thus, "*coating 1*" refers to the concrete specimen without any coating (reference). "*Coating 2*" refers only to "*coarse mortar*" with *Sika latex* added. The "*coatings 3 to 5*" refers to traditional cementitious coatings. In "*coatings 6 to 8*", hydrated lime was used. In "*coating 9*", fly ash was used as a binder. Finally, in the "*coating 10*", a thin layer of strong mortar, with cement and without *course mortar*. The rest, 10 mm for each layer.

Layer thicknesses also vary. "*Coarse mortar*", as is a discontinuous layer, between 0 and about 5 mm. "*Coating 10*", as it is a thin cover, 3 mm. The rest, 10 mm for each layer. Thus, the maximum coating thickness is 20 mm, without including the "*coarser mortar*".

Table 3: Coating composition by volume

Coating	Designation	Layers	Thickness [mm]	Coarse mortar		1st base coat					2nd base coat			
				CE M [Vol]	San d [Vol]	CE M [Vol]	F A [Vol]	H L [Vol]	S and [Vol]	W /B [-]	CE M [Vol]	H L [Vol]	S and [Vol]	W /B [-]
1	REF	0	0	--	--	--	-	-	-	--	--	-	-	--
2	Coarse mortar 0/5 mm	1	0/5	1	1	1	-	-	1	0.43	--	-	-	--
3	C+S 1:3-10 mm	2	10	1	1	1	-	-	3	0.80	--	-	-	--
4	C+S 1:3-20 mm	2	20	1	1	1	-	-	3	0.80	--	-	-	--
5	(C+S)+(C+S) (1:3)+(1:4)-20 mm	3	10+ 10	1	1	1	-	-	3	0.80	1	-	4	0.95
6	HL+S 1:3-10 mm	2	10	1	1	-	-	3	-	0.20	--	-	-	--
7	C+HL+S 1:0.5:4.5-10 mm	2	10	1	1	1	-	0.5	3	0.70	--	-	-	--
8	(C+S)+(C+HL+S) (1:3)+(1:0.5:4.5)-20 mm	3	10+ 10	1	1	1	-	-	3	0.80	1	0.5	4	0.70
9	C+FA+S 1:0.5:4.5-10 mm	2	10	1	1	1	0.5	-	4	0.80	--	-	-	--
10	C+S 1:2	1	3	--	--	1	-	-	2	0.90	--	-	-	--

4.2 Methodology

The methodology involved several steps (Figure 1). First, the concrete specimens were prepared. This will serve as a reference ("*coating 1*") and also as a support for the coatings ("*coating 2 to 10*"). These specimens consisted of small beams, made with 850x100x100 mm³ moulds, divided into 3 parts. These specimens remained in moist curing, submerged in water, until 90 days of maturity. After, were submitted to a preconditioning, in an oven at 40 °C, for 7 days. Afterwards, the coatings were placed on the beams on the two lateral sides, taking care to apply the layers 3 days apart from each other. Then, the tops of beams were sealed with paraffin. The specimens were placed in a climatic chamber with a carbon dioxide concentration of $4 \pm 0.5\%$, temperature of 20 ± 2 °C and relative humidity of $55 \pm 5\%$. They remained in the chamber for 60 days, enough for the accelerated carbonation test of the coated concrete. Finally, the carbonation depth was measured only on concrete specimens, using thymolphthalein as the acid-base indicator [23].

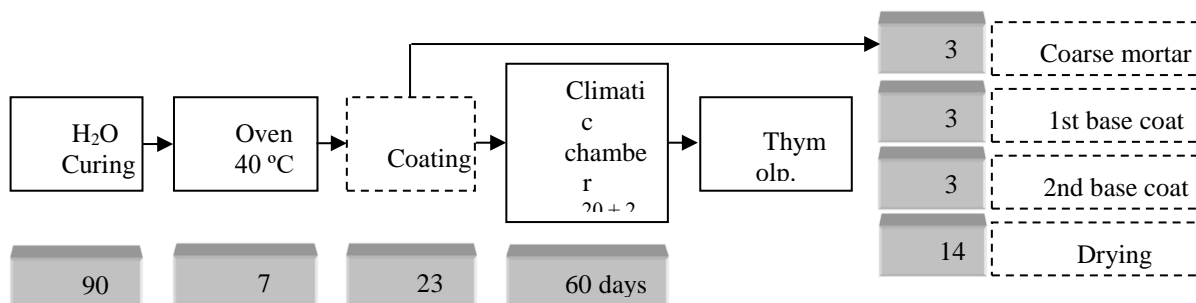


Figure 1: Experimental work schedule

To determine the performance, was used equation 1. It relates the depth of carbonation of each coating ($C_{depth\ coating}$) as a function of the carbonation depth of the concrete without any coating ($C_{depth\ REF}$).

$$Performance\ (\%) = - (C_{depth\ coating} - C_{depth\ REF}) / C_{depth\ REF} \quad (1)$$

3. RESULTS

The carbonation depth results, obtained by thymolphthalein indicator, is on Figure 2. On the left hand, the absolute values. On the right hand, the relative values, or performance. As expected, unprotected concrete is susceptible to attack by carbonation. For this reason, the worst result is for uncoated concrete, the reference, "*coating 1*". All coatings protect concrete, with an average performance of about 65%. These results suggest that the use of coatings may be so important in the concrete durability design project.

The *coarse mortar* coating, "*coating 2*", achieve 56% reduction. Although this coating is discontinuous, as it has a high cement content, it therefore provides a high alkalinity. In this way, it probably provided chemical protection against carbonation. It is found that *coarse mortar* was also applied in the "*coatings 3 to 9*", giving a total performance of the coatings similar or superior to "*coating 2*" (except "*coating 9*"). This may mean that the *coarse mortar per se* has not always been dominant. However, it should also be noted that this coating contains

an adhesion promoter (*Sika Latex*) and may, therefore, play a relevant role in the protection of concrete. This point should be investigated in more deeply in further works.

Coating with cement and fly ash, “*coating 9*”, results in a 41% performance. This result is excellent, considering that fly ash consumes calcium hydroxide, leading to lower alkalinity of the protection. Then, the coating is likely to be susceptible to carbonation, forming mainly a physical barrier against the external agents. In a different but also efficient way, the coating consisting of thin layer of cement and without *coarse mortar*, “*coating 10*”, achieves a result 48% better than the reference. As the cement content is high, this protection is not expected to react with atmospheric carbon dioxide. It is understood that to carry out good performance, one may be sufficient, whether it has high alkalinity or not.

These results, according to coatings thickness, shows that the greater, the less depth of carbonation. “*Coating 2*” has a very small w/b, but cannot stand out from “*coating 3*”. “*Coating 4*”, as it is thicker, is slightly better than “*coating 3*”. With 3 mm, “*Coating 9*”, has worse results compared to almost all coatings with 10 mm (“*coating 3, 6, and 9*”). But, it is remarkable that more important than the thickness, is the number of layers.

The best results are obtained from two-base coatings referenced with the letter “*D*”. This excellent behaviour may be due to the combination of a larger thickness with a larger number of interfaces, achieving a synergy of chemical protection and physical protection. The “*coating 8*”, is the outstanding result of this research, with a performance greater than 100%. In fact, this solution did not show any visible carbonation depth. Moreover, it is found that the 1st base layer is also not fully carbonated. The results suggest that after carbonation, the hydrated lime of the second base layer, can act as a physical barrier, while the first base layer acts as a chemical protection.

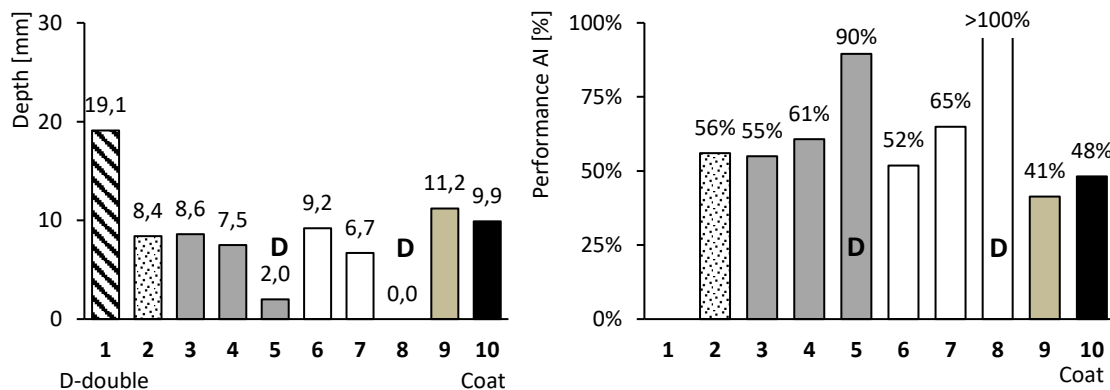


Figure 1: Carbonation results: absolute values (left); relative values (right)

These results according to coatings thickness, shows that the greater, the less depth of carbonation. “*Coating 2*” has a very small W/B, but cannot stand out from “*coating 3*”. “*Coating 4*”, as it is thicker, is slightly better than “*coating 3*”. “*Coating 9*”, with 3 mm, has worse results compared to almost all coatings with 10 mm (“*Coating 3, 6, and 9*”). But, it is remarkable that more important than the thickness, is the number of layers.

4. CONCLUSIONS

- Unprotected concrete is susceptible to attack by carbonation and the use of coatings can increase the useful life of reinforced concrete structures. The average performance of the coatings in this investigation is about 65%. This means that, on average, the coated concrete has 65% less carbonation depth than the concrete without any type of protection.
- Multi-layer coatings give the best results with performances of more than 90%. Thicker coatings combined with a greater number of interfaces guarantee greater protection.
- The introduction of hydrated lime in the coatings can be useful in creating a physical barrier.
- Thin coatings with high cement content can provide physical and chemical protection, with performance of 48%.
- In future studies, it is important to investigate the role of *coarse mortar* and adhesion promoters.
- The service life of coatings should be investigated with regard to protection against carbonation. If the protection is effective over time, the concrete specification could be improved and optimized.

REFERENCES

- [1] Thiery, M., 2005. Model of atmospheric carbonation of cementitious materials: taken into account kinetic effects and microstructural and water changes (in French). PhD thesis. Ecole des Ponts Paris Tech.
- [2] Papadakis, V.G., 2000. Effect of supplementary cementing materials on concrete resistance against carbonation and chloride ingress. *Cement and Concrete Research*, 30(2), pp.291-299.
- [3] Barnola, J.M., Raynaud, D., Lorius, C. and N.I., B., 2003. Historical CO₂ record from the Vostok ice core. In *Trends: A compendium of data on global change*. [online] Oak Ridge, Tenn., U.S.A: Carbon Dioxide Information Analysis Center - U.S. Department of Energy. Available at: > <http://cdiac.ornl.gov/trends/co2/vostok.html>>.
- [4] NOAA, 2016. Global greenhouse gas reference network: Trends in atmospheric carbon dioxide. [online] Mauna Loa: NOAA (National Oceanic and Atmospheric Administration). Available at: > <https://www.esrl.noaa.gov/gmd/ccgg/trends/global.html>> [Accessed 30-04-2017].
- [5] Baroghel-Bouny, V., 2004. Concrete design for a given lifetime of structures: control of durability against reinforcement corrosion and alkali-reaction (in French). Paris: AFGC.
- [6] Simas, M., 2007. Concrete protection systems against carbonation (in Portuguese). MSc. New University of Lisbon.
- [7] McGrath, P.F., 2016. A simple chamber for accelerated carbonation testing of concrete. McGrath Engineering Ltd.
- [8] Serrano, I.D. and Moreno, E.I., 2006. Barrier films: an option against carbonation of reinforced concrete (in Castilian). *Ingeniería, Revista Académica de la FI-UADY*, 10-2(2006), pp.37-45.
- [9] Janotka, I., Bačuvčík, M. and Paulík, P., 2018. Low carbonation of concrete found on 100-year-old bridges. *Case Studies in Construction Materials*, 8(2018), pp.97-115.

- [10] Veiga, M.R. and Faria, P., Coating of mineral and mixed binders, based on cement, lime and synthetic resin (in Portuguese). In: LNEC ed. 2004. Specialization in wall coverings. Lisbon: LNEC (Laboratório Nacional de Engenharia Civil). Ch.II. pp. 40-120.
- [11] Monteiro, I., 2010. Model of evolution of carbonation in reinforced concrete elements (in Portuguese). MSc thesis. Technical University of Lisbon. Higher Technical Institute
- [12] Tuutti, K., 1982. Corrosion of steel in concrete. PhD thesis. Lund University.
- [13] Rincón, O., Aleida, C., Carmen, A., Paulo, H. and Isabel, D., eds. 1997. Manual for inspection, evaluation and diagnosis of corrosion in reinforced concrete structures (in Spanish). Habana, CYTED (Programa Iberoamericano de Ciência y Tecnología para el Desarrollo).
- [14] Benítez, A., Manzelli, A., Macchi, C., Charreau, G., Risetto, J., Luco, L.F., Guitelman, N. and Morris, W., Ações sobre as estruturas de concreto. In: P. Helene ed. 2008. Manual de reparo, proteção e reforço de estruturas de concreto. São Paulo: Degussa Construction Chemical Brasil. Ch.01.
- [15] Lee, H.J., Kim, D.G., Lee, J.H. and Cho, M.S., 2012. A study for carbonation degree on Concrete using a phenolphthalein indicator and fourier-transform infrared spectroscopy. International Journal of Civil and Environmental Engineering, 34(62), pp.184-190.
- [16] Villain, G., Thiery, M. and Platret, G., 2007. Measurement methods of carbonation profiles in concrete: thermogravimetry, chemical analysis and gammadensimetry. Cement and Concrete Research, 37(8), pp.1182-1192.
- [17] IPQ, 2001. EN 197-1:2001. Cement. Part 1: composition, specifications and conformity criteria for common cements (in Portuguese). Caparica, IPQ (Instituto Português da Qualidade).
- [18] SECIL, 2014. Bulletin N. ACM-008/2014 - portland cement - EN 197-1 CEM I 42.5 R: results of Self-control (in Portuguese). Maceira-Liz: SECIL.
- [19] Lusical, 2012. Product specification sheet: hydrated lime H100 (in Portuguese). Lusical-Companhia lusitana de cal SA.
- [20] ABNT, 2010. ABNT NBR 15895:2010. ABNT NBR 15895:2010. Pozzolanic materials - Determination of calcium hydroxide fixed - Modified Chapelles's method (in Portuguese). Rio de Janeiro, ABNT (Associação Brasileira de Normas Técnicas).
- [21] Reis, R., Malheiro, R., Camões, A. and Ribeiro, M., 2014. Carbonation resistance of high volume fly ash concrete. Key Engineering Materials, 634(2015), pp.288-299.
- [22] Reis, R., Ribeiro, M., Abrantes, J.C.C., Camões, A., Teixeira, E. and Malheiro, R., 2016. Methodology for analysis of the reactivity of coal fly ash using selective dissolution by hydrofluoric acid. Key Engineering Materials, 711, pp.1126-1133.
- [23] CEN, 2010. FprCEN/TS 12390-12:2010. Testing hardened concrete-Part 12: Determination of the potential carbonation resistance of concrete: Accelerated carbonation method. Brussels, CEN (European Committee for Standardization).

INVESTIGATIONS OF CORROSION DUE TO CALCIUM LEACHING

S. v. Greve-Dierfeld (1), Yves Schiegg (1) and Fritz Hunkeler (1)

(1) TFB, Technology and Research for Concrete Structures, Wildeg, Switzerland

Abstract

This paper presents on investigations performed in order to assess the corrosion risk due to calcium (Ca-)leaching in saturated ammonium nitrate solution. The results show, that the time for corrosion initiation increases with the CaO content at the same w/b ratio. Leaching investigations and electrochemical measurements give only little differences in initiation times in this testing protocol for OPC, and OPC blended with fly ash (Fa) and lime stone (LS). But for OPC blended with high amounts of (blast furnace) slag, depassivation testing gives app. two times longer initiation phase than determined from electrochemical measurements and rebar investigation. pH from powder suspension at visible corrosion initiation (pH-crit) for LS, FA and slag blended cement mortars were in the range of $8.0 \leq \text{pH} \leq 8.5$ and for plain OPC at $8.8 \leq \text{pH} \leq 9.2$ and did not change significantly during corrosion process, except for OPC.

Keywords: Ca-leaching, supplementary cementitious materials (SCM), corrosion, critical pH

1. INTRODUCTION

If cement-based materials are in long lasting contact with liquids with lower ion concentration such as rain, drinking or ground water, the chemical potential gradient induces the diffusion of ions, here in particular calcium ions, from the pore solution towards the solvent with lower Ca-ion concentration. This changes the chemical equilibrium of the pore solution and forces primarily the dissolution of portlandite and at a low Ca-ion concentration ($< 15\text{-}21 \text{ mmol/l}$) the decalcification of C-S-H to finally ($< 1\text{-}2 \text{ mmol/l}$) transform to silica gel. This increases porosity which enhances the ingress of corrosion promoting substances. It reduces the pore solution pH in such a way, that reinforcement is no longer protected from corrosion [1].

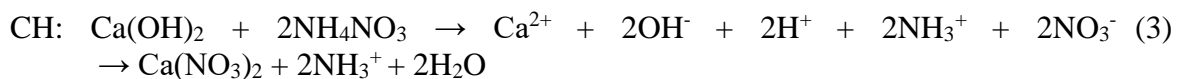
2. MECHANISM AND KINETIK OF LEACHING AND CORROSION

Under natural conditions, CO_2 dissolves in soft water forming carbonic acid that dissociates to hydronium and, in dependency of pH, to bicarbonate or carbonate ions (CO_3^{2-}).

At high pH CO_3^{2-} reacts with Ca^{2+} to form calcium carbonate (CaCO_3) that precipitates. When pH drops, H_2CO_3 dissolves CaCO_3 by releasing Ca^{2+} . In turn, the released Ca^{2+} raise the pH and Ca^{2+} again reacts with CO_3^{2-} , Eq. (1-2) e.g. [2].

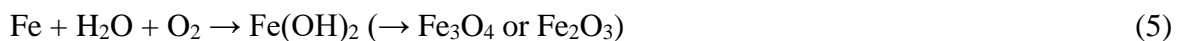


Leaching in saturated ammonium nitrate accelerates the process by a factor of 20 to 300 [4], as ammonium ions NO_3^- react with the calcium ions of all calcium bearing phases to highly soluble calcium nitrate $\text{Ca}(\text{NO}_3)_2$ in an exchange reaction, e.g. Eq. (3-4), that diffuses outwards. The ammonia in solvent converts to ammoniac and escapes from the eluent.



Leaching is usually modelled based on Fick's second law, considering e.g. concentration changes (depletion/enrichment), dissolution and reaction rates or chemical potentials [3, 4]. For ammonium nitrate solution, the model based on Fick's first law is applied, because reaction kinetic is fast and the escape of ammoniac maintains the reaction rate. Herein, the effective diffusion coefficient of Ca-ions is assumed constant and the depth dependent availability of Ca-ions decreases.

If the pH of pore solution undergoes a certain limit of app. $< 11 - 11.5$ [5], the protection of the thermodynamic instable carbon steel by the oxide layer disappears and the reinforcement may corrode. The overall reaction is given in Eq. (5), the half-cell reactions are given in Eq. (6-7), which are running simultaneously at adjacent locations, close to each other (micro-cell), or separated (macro-cell). To calculate corrosion rate from macro cell measurement Ohm's and Faraday's law is applied.



3. EXPERIMENTS

3.1 Mortar composition and preparation

For the investigations three types of binders were selected, cp. Table 1. Standard mixes according to SN EN 197-1 with w/b 0.65 were prepared, cp. Table 2. All samples were demoulded after 1 day and stored in saturated $\text{Ca}(\text{OH})_2$ -solution for 13 day.

3.2 Sample exposure and investigations

Cylindrical samples height 100 mm and diameter 30 mm with and without 10 mm diameter (ordinary black) carbon steel reinforcement were prepared for each mix. Figure 1 (a) shows the preparation of samples with reinforcement. Figure 1 (b and c) shows the sample storage. In each container, three reinforced sample and one unreinforced sample of one type of cement were stored. Each container was filled with 3.7 L 6 M NH_4NO_3 solution permanently stirred

with a pump. In one container (fig. 1 (b)), the rebar (carbon steel) acting as working electrode was electrically connected with an L-shaped stainless steel plate (1.4404; $\Delta E \sim 100$ mV) acting as counter electrode (carbon steel: stainless steel = 22:156 cm² = 1:7) through a one- Ω shunt resistance. One Ω was selected in order to minimize disturbance of current flow. The macro cell corrosion current, i.e. the current flowing between the stainless steel and the embedded bar was monitored by measuring the voltage drop across the resistance. In the other container (c), each rebar-sample was temporarily connected with an Ag/AgCl reference electrode (SSE) in order to measure the open circuit potential (OCP) with a high Ω -volt meter.

Table 1: Chemical composition proportions in [%]

No	Binder	CaO	SiO ₂	Al ₂ O ₃	Fe ₂ O ₃	MgO	K ₂ O	Na ₂ O	Na ₂ O Äquiv.	SO ₃
C1	CEM I	63	20.7	4.7	3	2.2	0.9	0.2	-	3.4
C2	FA	4	54.3	26.9	5.5	3.3	3.2	0.6	-	0.5
	CEM II/A-LL	62	19.9	5.8	2.9	3.5	1.3	0.4	-	2.9
C3	CEM III/B	48	30.5	8.1	1.1	6.3	0.7	0.37	0.83	2.8

Table 2: Mortar mix composition (binder EN 206 + additive), compressive strength

Mix	Aggre- gate [g]	Binder	Binder content [g]	Additive content [g]	Water content [g]	w/b [-]	CaO [%]	w/CaO [-]	f _{c,14d} [MPa]	f _{c,28d} [MPa]
C1*)	1350	CEM I	450	0	292.5	0.65	63	1.03	26.7	31.7
C2	1350	CEM II/A-LL + FA	241	FA: 209	292.5	0.65	35	1.86	13.2	17.2
C3	1350	CEM III/B	450	0	292.5	0.65	48	1.35	27.3	36.8

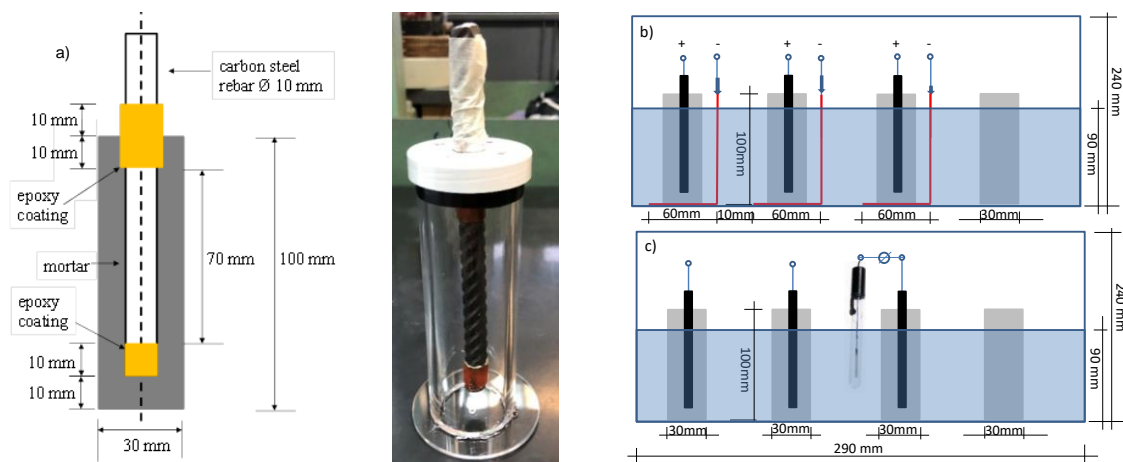


Figure 1: (a) Rebar-sample geometry; (b-c) Storage and electrochemical measurement

At corrosion initiation either assumed by an increase in macro cell current, or a potential drop of more than 100 mV the sample was removed. The sample was broken and the reinforcement was investigated with light microscope. The mortar adjacent to the rebar was powdered, and solved in deionized water (solvent powder ratio 2:1) stirred for 2 minutes, and the pH was measured immediately with a pH laboratory electrode.

In addition to that, in each container, one sample without reinforcement was stored in order to measure the leaching depth of cut off slices of app. 20 mm sprayed with phenolphthalein solution. The depth were measured by photo analyses (ImageJ), as this protocol reduces the scatter compared hand measurement. At several times 100 ml of solvent were removed, replaced and the Ca concentration was analysed by ICP-OES.

The solvent pH was monitored during the first two weeks against a laboratory pH electrode (Fig. 2). After one day the pH maintains at app. pH 8, which is lower than the pH value given for equilibrium constant of the reaction $\text{NH}_4^+ \rightarrow \text{NH}_{3\text{aq}} + \text{H}^+$ of pH 9.25 [6].

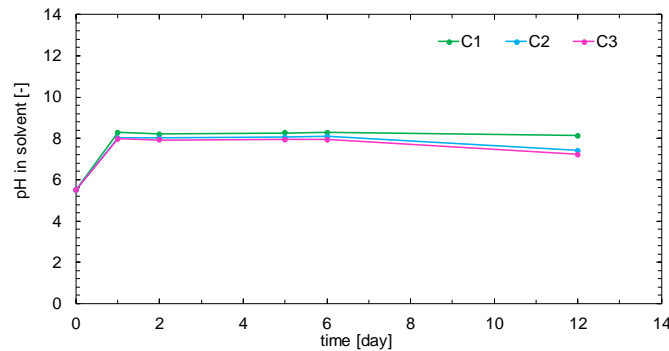


Figure 2: Solvent pH

4. RESULTS

4.1 Ca-release

Fig. 3 shows the cumulative release of Ca-ions per sample (symbols) measured in solvent compared with the total amount of Ca in mortar until rebar is reached (dotted line). No precipitation (CaCO_3) has been detected in the container.

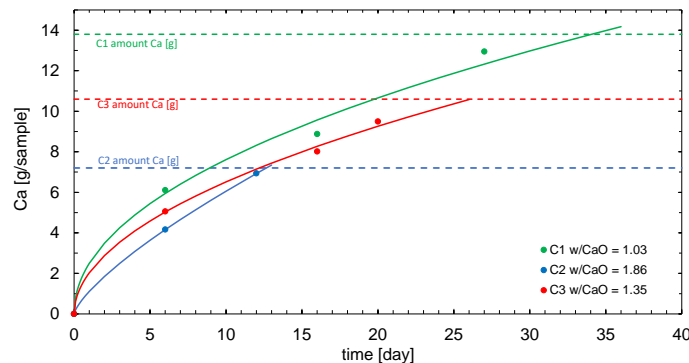


Figure 3: Released Ca in solvent versus total amount of Ca mortar until rebar is reached

4.2 PH indicator

Fig. 4 (a) shows pictures after spraying pH indicator (phenolphthalein). According to thermodynamic simulations from [7] pink colour should be seen if $\text{pH} \geq 9.7$, where only $\text{Ca}(\text{OH})_2$ dissolution and release takes place while no colour should occur at $\text{pH} \leq 8.3$ indicating partial C-S-H decalcification and reprecipitation.

For the CEM III/B samples, not only the colour of pH indicator is visible but also a white outer ring, which may be a result of the oxidation (greening) [8]. Fig. 3 (b) shows the leaching

depth measured at colour change and the therefrom calculated leaching rates. The Ca-leaching process (curve) is modelled taking into account depth dependent Ca from initial CaO. Leaching kinetic is the highest for C2 (CEM II/A-LL+FA), also due to the low compressive strength (raw density) and with this higher porosity.

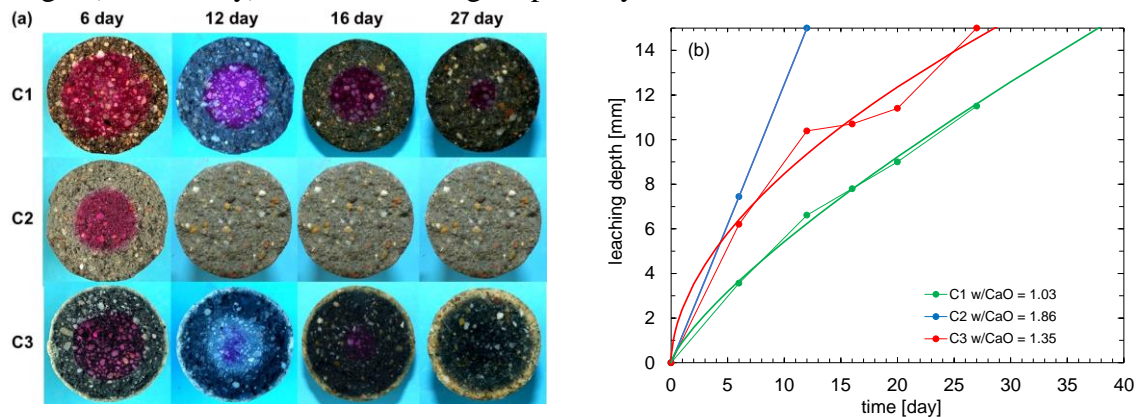


Figure 4: Leaching depth determined with pH-indicator

4.3 Electrochemical investigations (OCP, macro cell current)

Fig. 5 (a) shows the open circuit potential and fig. 5 (b) the macro cell current density respectively. The current density is calculated taking the entire exposed rebar surface (22 cm^2) into account, although corrosion initiation may start with small areas of passive layer disruption.

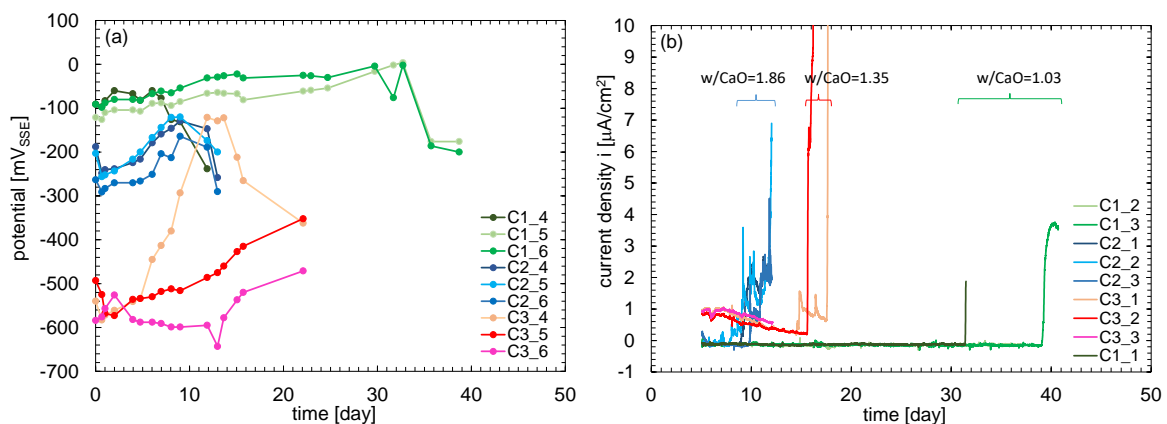


Figure 5: (a) Open circuit potential and (b) Short circuit current density

Initial potential of C1 and C2 samples are on an expected level for passive steel, and a current density $\pm 0.2 \mu\text{A}/\text{cm}^2$ was assigned to passive behaviour. Open circuit potential of C3 samples (slag cement) initially exhibit unexpected low potential, and the corrosion current density was initially in the range of $1 \mu\text{A}/\text{cm}^2$. Therefore, one sample was removed from current measurement (pink line), but did not show any signs of corrosion. The initially low potential may be explained with the initial high contents of sulphides S^{2-} supplied by the slags that reduce the redox potential of the pore solution. The initially increased corrosion may be explained with oxidization of sulfide. In the initial absence of oxygen, S^{2-} can react with e.g. metal ions Fe^{2+} to form iron(II) sulfide (greening). When oxygen is available, the sulfides

react to e.g. iron oxide Fe_2O_3 and sulfate SO_4^{2-} [8]. The electrons that are released during oxidation flow through the rebar to the counter electrode simulating a corrosion current. Hence, with time and oxidization the free corrosion potential increases and the macro cell current decreases.

One Portland cement sample indicated an early corrosion initiation, which was due to crevice corrosion under the epoxy coating (cp. fig. 6 C1_4).

The time to potential and current drop increases with decreasing w/CaO (increasing CaO). But the low strength and with this high porosity affects the initiation time of C2. The corrosion initiation time indicated by potential and current drop is similar.

4.4 Light microscopy

Fig. 6 shows light microscopy pictures. C1_1, C2_1 and C3_1 show signs of corrosion after corrosion current drop. C1_4 shows crevice corrosion, C2_4 was investigated nine day after potential drop and shows significant corrosion (corrosion propagation). C3_3 shows no signs of corrosion and greening of cement.

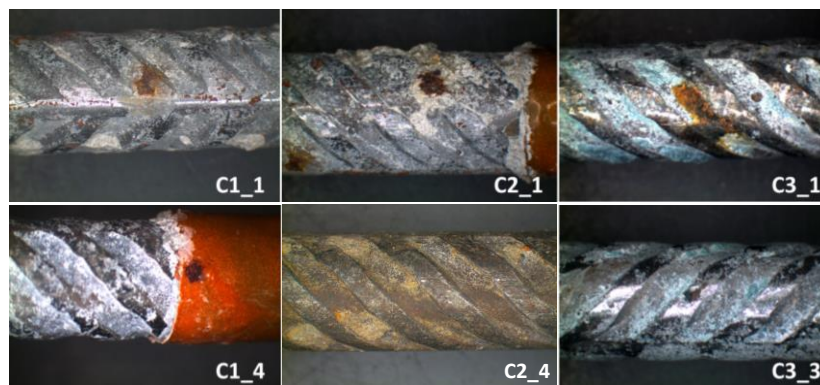


Figure 6: Light microscopy images (C1: OPC, C2: OPC+LS+FA, C3: OPC+slag)

4.5 pH measurement

Fig. 7 summarizes the measured pH in powder suspension at actual sample removal time (numbers). pH determined from powder suspension of OPC reference sample is pH 12.5 corresponding to pH of saturated $\text{Ca}(\text{OH})_2$ solution. Hence, initial pH in powder suspension is systematically lower than calculated from pore solution OH^- concentration [9]. Blends with LS, FA and slag show lower values. At corrosion initiation pH is for OPC sample $8.8 \leq \text{pH} \leq 9.2$, for LS, FA and slag blends $8.0 \leq \text{pH} \leq 8.5$ and for OPC higher than given in [7]. pH after further corrosion progress (7 to 10 day corrosion) is on a similar level like immediately after initiation (except for OPC).

4.6 Corrosion rate

Fig. 8 shows the corrosion rates of the samples C1_3, C2_4 and C3_4. The corrosion rates in this case (A_c/A_a : 7 times, A_c : stainless steel 1.4404, leaching in saturated ammonium nitrate solution) are on a level of 0.02 to 0.28 mm/year. Corrosion rates are up to 10 times higher than those for carbonation induced macro cell corrosion under moist conditions [10], probably due to a low electrolytic resistivity (high conductive solution), generally increased porosity due to leaching instead of a reduced porosity (for OPC cements) due to carbonation. Macro cell corrosion rates are in the range of those determined for chloride induced corrosion [11]. It

has to be considered, that macro cell current is dependent on A_c/A_a . From fig. 6 (C2_4) it seems necessary to assume that micro cell corrosion rate increases the overall corrosion rate. But the authors are not aware of any investigations on micro cell corrosion due to Ca-leaching. The sample with slag cement shows the highest corrosion rates followed by the sample with blends of LS + FA and low compressive strength. The lowest values are determined at the OPC sample.

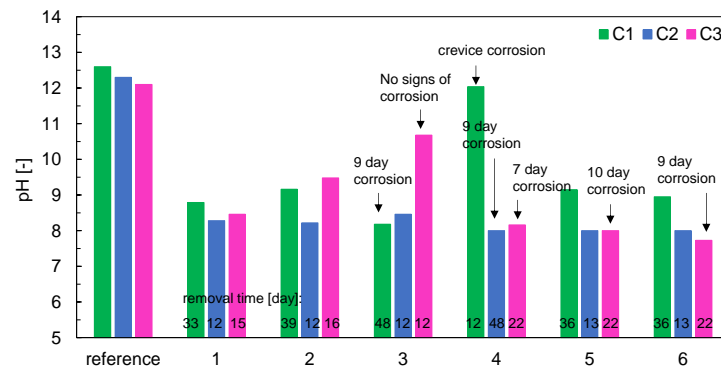


Figure 7: pH of powder suspension extracted from powder adjacent to rebar

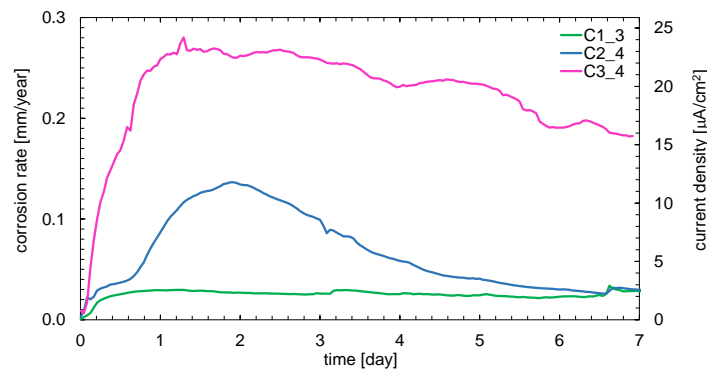


Figure 8: Corrosion rate of samples C1_3, C2_4 and C3_4

5. DISCUSSION AND CONCLUSIONS

Leaching in saturated ammonium nitrate allows for the investigation of corrosion initiation due to (Ca-)leaching in a reasonable short time, the strongly increased porosity and due to its high conductivity. Table 3 shows the times to corrosion initiation assumed by pH indicator phenolphthalein, released Ca, indicated by potential drop and indicated by current drop. Samples with crevice corrosion or no corrosion signs are excluded in table 3.

Table 3: Assessment of corrosion initiation time by different methods

Type of investigation performed in order to assess time to corrosion initiation		Time to corrosion initiation [day]		
		C1	C2	C3
Depassivation	phenolphthalein pH indicator	38	≥ 12	27
	Ca-release ICP-OES	33	13	25
Corrosion	open circuit potential	36	13	16
	macro cell current	31-39	8-10	15-16

The time to corrosion initiation assessed by Ca-release is partly shorter than with pH indicator. pH indicator measures H_3O^+ concentration coming from KOH, NaOH and CaOH while Ca in solvent results from CaOH and C-S-H and presumably from CaCO_3 in limestone. But it must be considered, that there are simplifications in the calculated total amount of Ca (porosity, densities, buffering capacity, release from bottom and top faces). Open circuit potential and macro cell corrosion shows similar corrosion initiation time. Leaching investigations and electrochemical measurements give initiation times in a similar range for OPC, Fa and LS blends in this eluent. But for slag blended cement, depassivation testing indicates a two times longer initiation phase than determined from electrochemical measurements and rebar investigation (visual signs of corrosion). pH from powder suspension at visible corrosion initiation for Fa and Slag cement mortars where in the range of $8.0 \leq \text{pH} \leq 8.5$ and for OPC at $8.8 \leq \text{pH} \leq 9.2$ and did not change significantly during corrosion process. The corrosion rates due to leaching in this testing protocol are in the range of rates determined for chloride induced corrosion. The visual investigations let assume that micro cell corrosion increase corrosion loss. In further experiments the effect of (Ca-)leaching on corrosion of reinforcement will be investigated in natural eluents and exposures (e.g. carbonic acid, condensation water) as broader leaching gradients are expected [2]. The preconditioning will be improved (increased curing time, drying before exposure for slag).

REFERENCES

- [1] Carde, C., Francois, R. and Torrenti, J. 'Leaching of both calcium hydroxide and C-S-H from cement paste: modelling the mechanical behaviour', *Cement and Concrete Research* **26** (8) (1996) 1257-1268.
- [2] Leemann, A., Lothenbach, B., Siegrist and H., Hoffmann, C. 'Influence of water hardness on concrete surface deterioration caused by nitrifying biofilms in wastewater treatment plants', *International Biodeterioration & Biodegradation* **64** (2010) 489-498.
- [3] Perlot, C., Carcasses, M. and Verdier, J. 'Diffusivity evolution under decalcification: influence of aggregate natures and cement type', *Materials and Structures* **46** (2013) 787-801.
- [4] RILEM STAR 211-PAE Performance of cement based materials in aggressive aqueous environments (2013) ISBN 978-94-007-5413-3.
- [5] Parrott, L. 'Damage caused by carbonation of concrete', *MatStru.* **23** (1990) 230-234.
- [6] Wan, K., Li, L. and Sun, W. 'Solid-liquid equilibrium curve of calcium in 6 mol/L ammonium nitrate solution', *Cement and Concrete Research* **53** (2013) 44-50.
- [7] Shi, Z., Lothenbach, B., Geiker, M., Kaufmann, J., Leemann, A., Ferreira, S., Skibsted, J., 'Experimental studies and thermodynamic modelling of the carbonation of Portland cement, metakaolin and limestone mortars', *Cement and Concrete Research* **88** (2016) 60-72.
- [8] Criado, M., Bernal, S., Garcia-Trinanes, P., Provis, J., 'Influence of slag composition on the stability of steel in alkali activated cementitious materials', *Jour. Mat. Sci.* **53** (2018) 5016-5035.
- [9] Vollpracht, A., Lothenbach, B., Snellings, R., Haufe, J. 'The pore solution of blended cements: a review', *Materials and Structures* **49** (2016) 3341-3367.
- [10] Stefanoni, M., Angst, U., Elsener, B., 'Corrosion rate of carbon steel in carbonated concrete—A critical review', *Cement and Concrete Research* **103** (2018) 35-48.
- [11] Warkus, J., Raupach, R. 'Modelling of reinforcement corrosion – geometrical effects on macrocell corrosion', *Materials and Corrosion* **61** (2010) 494-504.

REACTION PRODUCTS FORMED IN EARLY AGE CEMENT PASTES WITH GRANULATED BLAST FURNACE SLAG EXPOSED TO ACCELERATED CO₂ INGRESS

H. Vanoutrive (1), Ö. Cizer (2), P. Minne (1), I. Van de Voorde (3), E. Gruyaert (1)

(1) KU Leuven, Department of Civil Engineering, Construction TC, Structural Mechanics and Building Materials, Ghent, Belgium

(2) KU Leuven, Department of Civil Engineering, Building Materials and Building Technology Section, Leuven, Belgium

(3) KU Leuven, Department of Microbial and Molecular Systems, Bioengineering Technology TC, Ghent, Belgium

Abstract

Durability and sustainability have gained an increasing importance over the last years. The production of ordinary Portland cement (OPC) has a significant impact on the CO₂ emission and more eco-friendly alternatives, or supplementary cementitious materials (SCMs), as a partial replacement of the clinker in OPC are desirable and already common in use. Despite the growing gain of the production and consumption of cement with SCMs over pure OPC, more research is needed to completely understand the evolution of the microstructure of young cement pastes exposed to environmental attack, such as CO₂ ingress, to estimate more accurately the impact of the early removal of formwork or short curing periods on the durability of concrete structures. To investigate the extent of carbonation, hydration and carbonation products of cement pastes with two replacement levels of ground granulated blast furnace slag (GBFS) and exposed after 3, 7 and 28 days of sealed curing to accelerated CO₂ ingress were investigated by Attenuated Total Reflection Fourier Transform InfraRed spectroscopy (ATR-FTIR). When GBFS is used, irrespective of the replacement level, the carbonation of the calcium silicate hydrates (C-S-H) after 3 days sealed curing evolves similarly. For longer curing periods, the decalcification of C-S-H is slowed down by decreasing the replacement level by GBFS.

Keywords: ground granulated blast furnace slag, accelerated carbonation, curing, ATR-FTIR, C-S-H

1. INTRODUCTION

In West European climates, carbonation of concrete is one of the two major deterioration mechanisms occurring in reinforced concrete structures exposed to wetting and drying cycles and carbon dioxide present in the air. Carbonation induces serious consequences on the physical and chemical properties of the concrete. Due to a gradual decrease of pH and consequently a

depassivation of the reinforcing steel, propagation of corrosion of the embedded rebar can ultimately occur.

Two major parameters influencing the resistance of concrete against CO₂ ingress can be distinguished: (i) pore structure of the cement matrix before and during carbonation (ii) ability of the binder to bind carbon dioxide (CO₂ buffer capacity) [1]. It is generally known that carbonation of calcium hydroxide (portlandite) densifies the pore structure due to an increase in volume of CaCO₃ compared to portlandite. This reaction mechanism, which is the most pronounced in pure OPC pastes, improves the resistance against CO₂ ingress. Additionally, the binding capacity of this type of cement is also larger compared to the other binders due to the higher initial CaO content. If binders with an OPC replacement by ground granulated blast furnace slag (GBFS) are considered, the densification of the cement matrix is less pronounced because with increasing GBFS replacement, less reactive CaO is available to form calcium hydroxide during hydration. Instead more calcium silicate hydrates (C-S-H) are formed with a lower Ca/Si ratio [2]. It is stated that decalcification of this phase leads to a coarsening of the pore structure and therefore lower resistance against CO₂ ingress [3]. It can be assumed that investigation of the C-S-H structure at specific hydration and carbonation stages gives an indication of the extent of carbonation and the pore structure.

FTIR is shown to be a suitable method to examine the main hydration products such as portlandite and C-S-H, but also the formation of the different carbonate polymorphs by monitoring the changes in characteristic infrared vibration modes [4]–[8]. This method is also quick and requires only very small amounts of powder. Only a qualitative and semi-quantitative assessment of the hydration and carbonation products is possible.

For the main hydration products analysed in transmission mode, the presence of Ca(OH)₂ is characterized by a strong O-H stretching band at ~3640 cm⁻¹ and the H-O-H bending vibration at ~1617 cm⁻¹ [9]–[12]. The characteristic peak for C-S-H is mostly pronounced at wavenumber ~971 cm⁻¹ in case the sample is not carbonated. This wavenumber increases with increasing polymerisation of the silicate chain to silica gel.

When concrete undergoes carbonation, CaCO₃ is formed. Three common crystalline polymorphs can be distinguished, namely calcite, aragonite and vaterite depending on the composition and curing conditions. The main internal vibration modes of CO₃²⁻ of these polymorphs are given in Table 1. Also, amorphous CaCO₃ can form during early age carbonation in environments with high relative humidity. This unstable phase is detected with a broad ν_3 absorption peak centred at wavenumber ~1423 cm⁻¹ due to a lack of symmetry in the environment around the CO₃²⁻ ions [12]. This band sharpens upon the formation of more crystalline polymorphs of CaCO₃ [4]. The absorption band at ~1074 cm⁻¹, which is attributed to the symmetric C-O stretch (ν_1) in non-centrosymmetric structures, is also a characteristic feature of amorphous CaCO₃. Finally, also less strong combination bands are visible such as $\nu_4+\nu_1$, $\nu_4+\nu_3$, $2\nu_3$ and $2\nu_2+\nu_4$ [6][12]. Depending on the FT-IR measuring method, such as transmission through a KBr pellet or reflectance on a diamond surface, slight shifts of the wavenumbers are noticed.

Results of this research provide better insight in the evolution of the reaction products (portlandite, C-S-H and calcium carbonates) in cement pastes with GBFS at early age exposed to CO₂ with a limited reaction degree of the SCM.

Table 1: Characteristic internal vibration modes of CaCO₃ polymorphs.

	v ₁ symmetric stretching	v ₂ out of plane bending	v ₃ asymmetric stretching	v ₄ in plane bending	Source
Calcite		870-875	1422-1430	710-715	[4], [9], [13]
Aragonite	1080-1085	850-855	1470-1485 1440-1460	700 710-715	[4], [13], [11]
Vaterite	1070-1090	870-875	1420 1444 1490	740-750	[4], [9], [13]
Amorphous	1065-1075	864	1420-1425 1490	690 725	[4]

2. MATERIALS AND METHODS

2.1 Materials

Three series of cement pastes were prepared, sealed cured for 3, 7 and 28 days and subsequently exposed to 2.0 ± 0.1 % CO₂ at $20.0 \pm 2.0^\circ\text{C}$ and 60.0 ± 5.0 % relative humidity. The binder compositions consist of pure OPC (CEM I 52.5 R HES, named as 100PC) and OPC partially replaced by ground granulated blast furnace slag (OPC:GBFS = 60:40 by mass, named as 60PC40S and OPC:GBFS = 30:70 by mass, named as 30PC70S). Chemical and physical properties of the binders are given in Table 2 and Table 3.

Table 2: Chemical composition of CEM I 52.5 R HES and GBFS

%	CaO	SiO ₂	Al ₂ O ₃	Fe ₂ O ₃	MgO	K ₂ O	Na ₂ O	SO ₃	Mn ₂ O ₃	Cl ⁻	S ²⁻
OPC	64.1	20.7	4.3	2.7	2.0	0.7	0.3	3.3	0.04	0.11	-
GBFS	39.1	34.1	12.6	0.6	8.1	0.5	0.2	0.1	0.3	0.02	0.87

Table 3: Physical properties of CEM I 52.5 R HES and GBFS

Binder	Density [kg/m ³]	Blaine value [cm ² /g]	LOI [%]
OPC	3180	5050	0.70
GBFS	2890	4045	0.41

The cement pastes were prepared with demineralized water and a water to binder ratio of 0.45. Prior to the main mixing process, the binders were mixed for 30 seconds in a Hobart mixer at 120 rpm without water to ensure a homogenous mixture. No grinding of the powders was applied so the fineness of the powders remained unchanged. After this pre-mixing, the binder mix and the demineralized water were mixed for 2 minutes and cast in PVC tubes with 40 mm diameter and 250 mm length. No demoulding agent was used to avoid deviant paste structures at the cast surface. To avoid segregation, the cylinders were rotated at 13 rpm for 8 to 24 hours depending on the expected hardening time. After the sealed curing period at $20.0 \pm 2.0^\circ\text{C}$ in a climate chamber, the cylinders were subjected to accelerated CO₂ ingress.

2.2 Methods

After 0, 7, 14, 28, 56 and 90 days of accelerated CO₂ ingress, a transverse section is made by splitting the cylinder in half. At each side of this transverse section, a second transverse section of ~20 mm thickness was broken off. A phenolphthalein solution consisting of 1g phenolphthalein in 70 ml ethanol and diluted to 100 ml with demineralized water was sprayed on one slice to examine the carbonation depth and consequently to estimate the carbonation rate. The carbonation rate is the gradient of the linear regression between the carbonation depth in function of the square root of time. The other slice was used to extract carbonated and uncarbonated parts for the infrared analysis. Reaction products formed during the hydration and carbonation processes were examined by ATR-FTIR using a Thermo Electron Nicolet 6700 spectrometer equipped with a Thermo Electron Smart Orbid ATR sampling accessory with a diamond crystal. The reference measurement before accelerated carbonation and the measurements at 28 and 90 days in the carbonation chamber were executed on two independent samples. For the other ages, only one sample was tested. The final spectrum at each age consists of three measurements for each carbonated and uncarbonated powder sample. The powders were obtained by manually grinding of pieces extracted with a pincer or in the case of very small carbonated or uncarbonated surfaces with a mechanical mill (Dremel model 4000 + Tile cutting bit (562) with bit diameter of 3.2mm). To stop hydration and remove free water in the powders, solvent replacement by isopropanol was applied [14].

3. RESULTS

3.1 Change of hydration products during accelerated carbonation

Figure 1 shows a typical ATR-FTIR spectrum of a cement paste and highlights the most interesting and detectable wavenumbers with regard to hydration and carbonation. According to [2], [9], [11], [15], the characteristic wavenumber for the C-S-H phase in uncarbonated cement paste is 971 cm⁻¹ in transmission mode. Using the reflectance mode, this characteristic wavenumber is slightly shifted and results in an average value of 948.7 cm⁻¹ with a standard deviation of 1.5 cm⁻¹ according to the measurements on uncarbonated powder. When carbonation takes place, the calcium bearing phases will react and form different CaCO₃ polymorphs. In case of decalcification of the C-S-H phases, this will physically lead to a coarsening of the pore structure and to the polymerisation of the silicate chains resulting in a higher wavenumber. Figure 2 shows the evolution of the measured maximal characteristic wavenumber for each sample during accelerated CO₂ ingress for the three series of cement paste subjected to different curing periods. It can be seen that the decalcification of C-S-H in pure OPC pastes after 28 days of accelerated testing is minimal. The wavenumber of the characteristic peak remains the same during carbonation irrespective of the length of the sealed curing period. After 56 days of exposure to 2.0 % CO₂, decalcification of C-S-H becomes slightly visible in the pure OPC paste, most pronounced in the samples with the shortest curing period by a shift from wavenumber 947 cm⁻¹ to 955 cm⁻¹. Regarding the characteristic wavenumbers for portlandite, after 56 days of testing, distinct peaks are still noticeable in Figure 1 whereby it can be stated that carbonation of portlandite and C-S-H occurs at the same time [16][17], but preferably of portlandite.

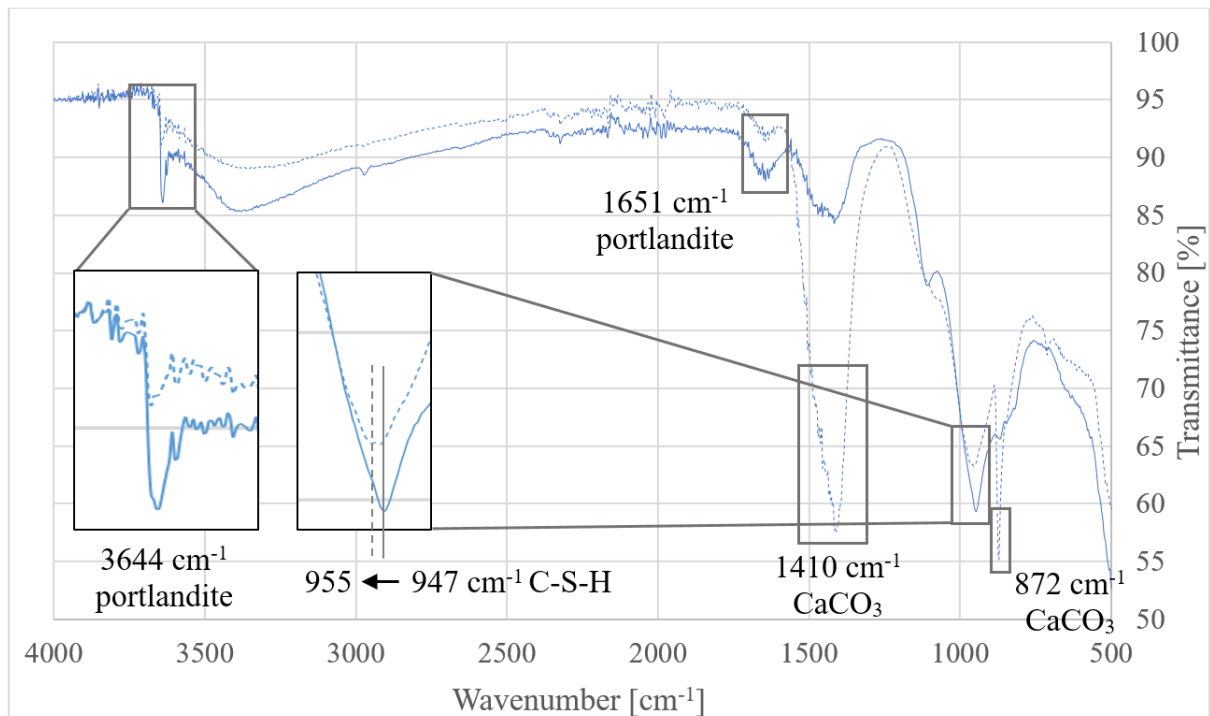


Figure 1: ATR-FTIR spectrum of uncarbonated (full line) and carbonated (dotted line) 100PC paste after 3 days sealed curing and subjected to 56 days of accelerated CO_2 ingress.

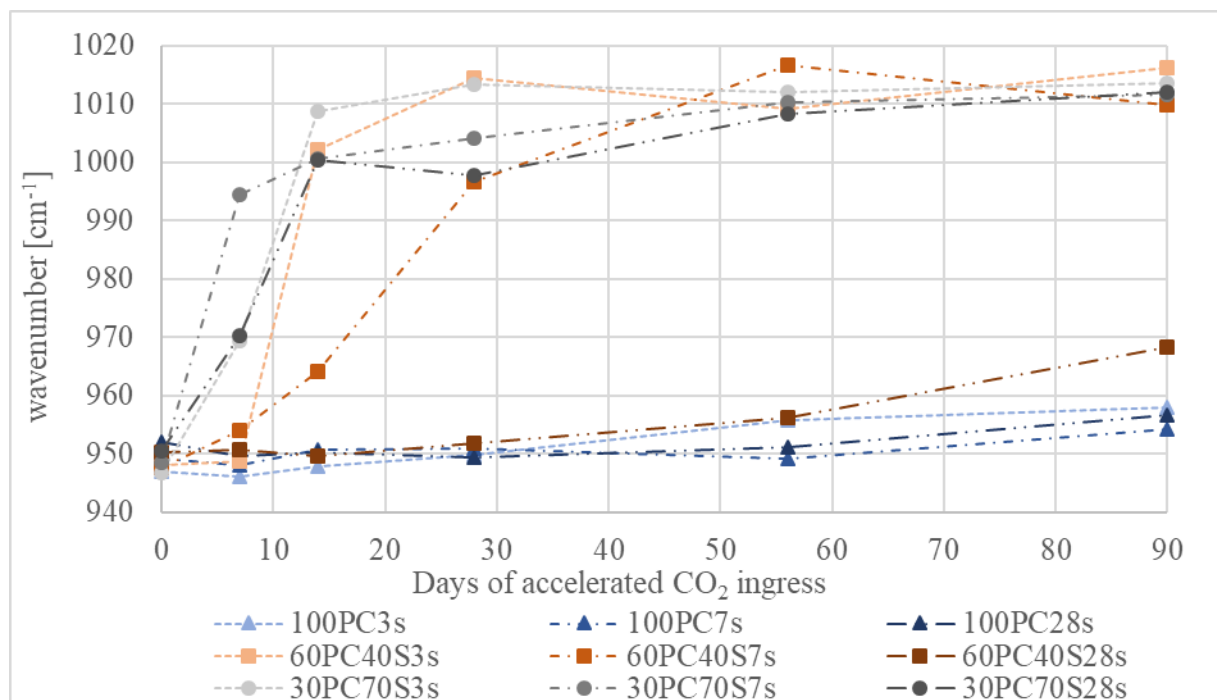


Figure 2: Shift of the characteristic wavenumber of C-S-H due to carbonation of 100PC, 60PC40S and 30PC70S with different sealing periods (3, 7 and 28 days) after 0, 7, 14, 28, 56 and 90 days of accelerated CO_2 ingress

For the cement pastes with a replacement of 40% by mass of OPC by GBFS, the 28 days sealed curing period provided enough time for the formation of a portlandite buffer although the intensity of this characteristic peak ($\sim 3641 \text{ cm}^{-1}$) is less than the neat system. For both systems, the decalcification of C-S-H is similar and also the carbonation rate is comparable as shown in Table 4. It is important to note that the carbonation depth measured for 100PC and 60PC40S samples cured for 28 days is not very accurate because of preferential splitting in cracks, induced due to shrinkage of the cement paste. An irregular carbonation front is obtained in this case (

Figure 3). A uniform radial ingress is observed in the cement pastes with 70% GBFS replacement although more and bigger surface cracks are visually detected.

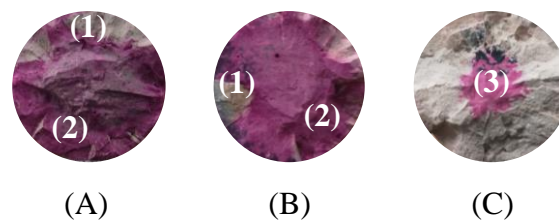


Figure 3: Carbonation depth measurement for 100PC (A), 60PC40S (B) and 30PC70S (C) sealed for 28 days and subjected to 28 days of accelerated CO_2 ingress. (1) Large carbonation depth due to superficial carbonation at the crack planes (2) Very limited carbonation in the sound (non-cracked) zones (3) uniform radial ingress

Table 4: Carbonation rate and regression coefficient of 100PC, 60PC40S and 30PC70S

[mm/year ^{0.5}]	100PC		60PC40S		30PC70S	
Curing period	k_{ACC}	R^2	k_{ACC}	R^2	k_{ACC}	R^2
3 days	5.47*	0.54	26.04	0.91	64.31	0.99
7 days	4.88*	0.87	20.17	0.91	52.47	0.98
28 days	7.56*	0.69	9.19*	0.93	47.01	0.99
* The carbonation rate is based on an irregular carbonation front						

When subjecting the cement pastes with GBFS and with shorter curing periods to accelerated CO_2 ingress, the decalcification of C-S-H is accelerated. In Figure 2 it is shown that the shift of the C-S-H characteristic peak for the 60PC40S3s and 30PC70S3s system is almost similar, so in the case of very short curing times of only three days, the replacement level is less critical for the polymerisation of C-S-H than the curing period. In addition, looking at the 30PC70S pastes with different curing periods, due to almost no formation of portlandite during hydration, the curing length is less influential for the carbonation rate and the decalcification rate of C-S-H (Figure 2 and Table 4).

The characteristic wavenumber for C-S-H in cement pastes with GBFS subjected to 2% CO_2 after short curing periods of 3 and 7 days converges after 90 days of accelerated testing to approximately $1010 - 1015 \text{ cm}^{-1}$. This confirms the decrease in Ca/Si ratio with increasing formation of carbonate species [5] directing to pure silicate gel (SiO_4^{2-} with characteristic wavenumber $\sim 1121 \text{ cm}^{-1}$ [15]). It is also possible that 60PC40S28s will converge to this wavenumber after longer exposure to accelerated CO_2 ingress but this requires further investigation.

3.2 Formation of carbonates during accelerated carbonation

To estimate the extent of carbonation, the integrated area of wavenumber $1400 - 1500 \text{ cm}^{-1}$ provides a good indication of the amount of carbonation [6] and also the buffer capacity of the cement paste. This characteristic vibration band is typical for the asymmetric stretching of CO_3^{2-} in the amorphous and the three crystalline CaCO_3 polymorphs [12]. For the different series of cement types, the integrated area of wavenumber $1300 - 1550 \text{ cm}^{-1}$ and standard deviations are shown in Figure 4. It can be seen that for the 3 and 7 days sealed curing period, the amount of carbonation of pure OPC is less than for the pastes with a replacement by GBFS. For the 28 days sealed curing period, the amount of carbonation is in general lower compared with the shorter curing periods. Also, the behaviour of 100PC and 60PC40S for this curing period is comparable which shows similarities with the polymerisation behaviour of the silicate chains and the carbonation rates for these pastes.

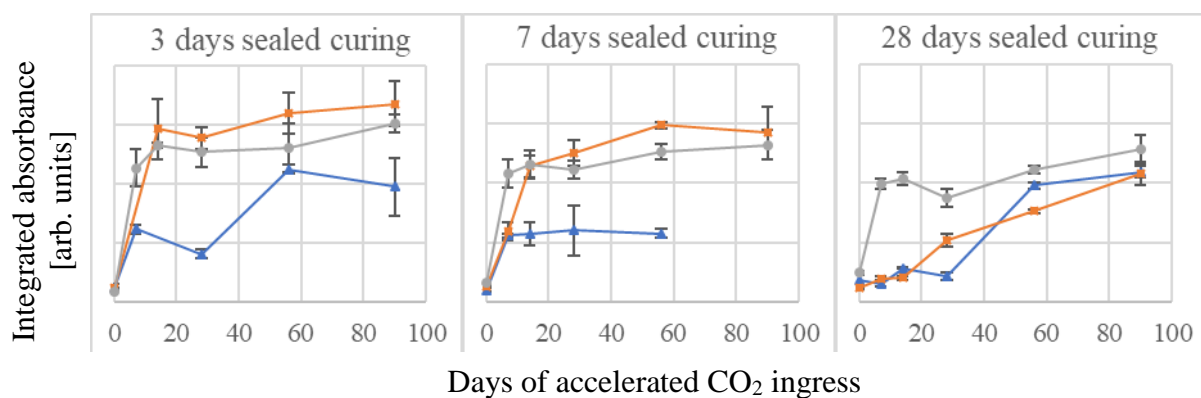


Figure 4: Integrated area of wavenumber $1300 - 1550 \text{ cm}^{-1}$ for 100PC (blue triangles), 60PC40S (orange squares), 30PC70S (grey dots) for 3, 7 and 28 days sealed curing period.

4. CONCLUSIONS

- The decalcification of C-S-H in OPC after 90 days of accelerated CO_2 ingress is minimal.
- Irrespective of the replacement levels of GBFS considered in this research, the carbonation of C-S-H after 3 days sealed curing evolves to the same extent.
- For longer curing periods, the decalcification of C-S-H is slowed down by decreasing the replacement level by GBFS.
- The integrated area of wavenumber $1400 - 1500 \text{ cm}^{-1}$ is in relationship with the results of the polymerization of silicate chains.

ACKNOWLEDGEMENTS

The research leading to the results reported in this paper was made possible by internal funding of KU Leuven. The authors also acknowledge CBR (HeidelbergCEMENT group) for the cement samples and the performed chemical and physical analysis on the cement.

REFERENCES

- [1] A. Leemann, P. Nygaard, J. Kaufmann, and R. Loser, "Relation between carbonation resistance, mix design and exposure of mortar and concrete," *Cem. Concr. Compos.*, vol. 62, pp. 33–43,

- 2015.
- [2] B. Lothenbach, K. Scrivener, and R. D. Hooton, "Supplementary cementitious materials," *Cem. Concr. Res.*, vol. 41, no. 12, pp. 1244–1256, 2011.
 - [3] E. Gruyaert, P. Van Den Heede, and N. De Belie, "Carbonation of slag concrete: Effect of the cement replacement level and curing on the carbonation coefficient - Effect of carbonation on the pore structure," *Cem. Concr. Compos.*, vol. 35, no. 1, pp. 39–48, 2013.
 - [4] F. A. Andersen and L. Brečević, "Infrared Spectra of Amorphous and Crystalline Calcium Carbonate.," *Acta Chemica Scandinavica*, vol. 45, pp. 1018–1024, 1991.
 - [5] J. A. Herterich, "Microstructure and Phase Assemblage of Low-Clinker Cements during Early Stages of Carbonation," The University of Leeds, 2017.
 - [6] R. Ylmén and U. Jäglid, "Carbonation of Portland cement studied by Diffuse Reflection Fourier Transform Infrared Spectroscopy," *Int. J. Concr. Struct. Mater.*, vol. 7, no. 2, pp. 119–125, 2013.
 - [7] Y. Lo and H. M. Lee, "Curing effects on carbonation of concrete using a phenolphthalein indicator and Fourier-transform infrared spectroscopy," *Build. Environ.*, vol. 37, pp. 507–514, 2002.
 - [8] R. Ylmén, U. Jäglid, B. M. Steenari, and I. Panas, "Early hydration and setting of Portland cement monitored by IR, SEM and Vicat techniques," *Cem. Concr. Res.*, vol. 39, no. 5, pp. 433–439, 2009.
 - [9] N. Li, N. Farzadnia, and C. Shi, "Microstructural changes in alkali-activated slag mortars induced by accelerated carbonation," *Cem. Concr. Res.*, vol. 100, no. July, pp. 214–226, 2017.
 - [10] T. L. Hughes, C. M. Methven, T. G. J. Jones, S. E. Pelham, P. Fletcher, and C. Hall, "Determining cement composition by Fourier transform infrared spectroscopy," *Adv. Cem. Based Mater.*, vol. 2, no. 3, pp. 91–104, 1995.
 - [11] G. Villain, M. Thiery, and G. Platret, "Measurement methods of carbonation profiles in concrete: Thermogravimetry, chemical analysis and gammadensimetry," *Cem. Concr. Res.*, vol. 37, no. 8, pp. 1182–1192, 2007.
 - [12] Ö. Cizer, C. Rodriguez-Navarro, E. Ruiz-Agudo, J. Elsen, D. Van Gemert, and K. Van Balen, "Phase and morphology evolution of calcium carbonate precipitated by carbonation of hydrated lime," *J. Mater. Sci.*, vol. 47, no. 16, pp. 6151–6165, 2012.
 - [13] M. Sato and S. Matsuda, "Structure of vaterite and infrared spectra," *Zeitschrift fur Krist. - New Cryst. Struct.*, vol. 129, no. 5–6, pp. 405–410, 1969.
 - [14] R. Snellings *et al.*, "Report of TC 238-SCM: hydration stoppage methods for phase assemblage studies of blended cements—results of a round robin test," *Mater. Struct. Constr.*, vol. 51, no. 4, 2018.
 - [15] E. T. Stepkowska, J. M. Blanes, C. Real, and J. L. Perez-Rodriguez, "Hydration products in two aged cement pastes," *J. Therm. Anal. Calorim.*, vol. 82, no. 3, pp. 731–739, 2005.
 - [16] A. Morandau, M. Thiéry, and P. Dangla, "Investigation of the carbonation mechanism of CH and C-S-H in terms of kinetics, microstructure changes and moisture properties," *Cem. Concr. Res.*, vol. 56, pp. 153–170, 2014.
 - [17] M. Castellote, L. Fernandez, C. Andrade, and C. Alonso, "Chemical changes and phase analysis of OPC pastes carbonated at different CO₂ concentrations," *Mater. Struct. Constr.*, vol. 42, no. 4, pp. 515–525, 2009.

NATURAL AND ACCELERATED CARBONATION RATES OF ALKALI-ACTIVATED SLAG/FLY ASH BLENDED CONCRETES

Susan A. Bernal (1), Jannie S.J. van Deventer (2,3) and John L. Provis (4)

(1) School of Civil Engineering, University of Leeds, Woodhouse Lane, LS2 9JT, Leeds, United Kingdom

(2) Department of Chemical & Biomolecular Engineering, The University of Melbourne, Victoria 3010, Australia

(3) Zeobond Pty Ltd, P.O. Box 23450, Docklands, Victoria 8012, Australia

(4) Department of Materials Science and Engineering, The University of Sheffield, S1 3JD, Sheffield, United Kingdom

Abstract

Carbon dioxide present in the air is one of the main threats to our cement-based built environment. Its diffusion through mortars and concretes, and its dissolution in the pore water present in these materials, initiate acid-base reactions known as carbonation, leading to degradation or corrosion processes that can compromise the integrity of structures. In this study the carbonation rates of alkali-activated concretes produced with blast furnace slag/fly ash blends were determined. All concretes were designed to achieve a compressive strength of 60 ± 5 MPa after 28 days of curing. The results are compared with those obtained for concretes solely based on alkali-activated blast furnace slag. Natural (0.04% CO₂) and accelerated (1% CO₂) carbonation was induced in the specimens under a controlled relative humidity of 65% at 23°C. The partial substitution of slag for fly ash increased the carbonation rates of alkali-activated concretes when tested under accelerated carbonation conditions; however, under natural carbonation the partial replacement of slag seemed to have a negligible effect on the carbonation rate of these materials, at least during the period evaluated in this study (90 days).

Keywords: Alkali-activated concretes; slag/ fly ash blends; carbonation, durability, long-term performance

1. INTRODUCTION

The increased concentration of CO₂ in the atmosphere poses a major threat to our cement-based built environment. Once CO₂ enters concrete, it can initiate a series of acid-base reactions known as carbonation, that can lead to reduction in the alkalinity of the system and hence destabilise the passive layer of steel rebars, along with changes in the microstructure of the cementitious matrix itself, and potentially modify the mechanical performance of the affected

structure [1]. Carbonation of cementitious materials is a phenomenon that has been studied for several decades, however due to the low concentrations of CO₂ present in air, carbonation processes are typically very slow. Laboratory studies inducing carbonation under accelerated conditions (using CO₂ concentrations from 1% - 100%) are typically adopted for prediction of long-term performance [2]. However, inconsistencies between natural and accelerated carbonation rates are typically identified when changes in either the characteristics of the concretes or the accelerated testing conditions occur [3]. This is particularly the case for alkali-activated concretes, where it has been demonstrated that small variations in accelerated carbonation testing conditions (e.g. CO₂ concentration and relative humidity) induce significant changes in the carbonation rates [4, 5].

Alkali-activated cements are attracting significant attention due to their environmental credential, but also as a suitable alternative for the management and/or valorisation of wastes from different industries [6]. Most alkali-activated concretes are based on blast furnace slag to achieve higher early strength at lower activator doses [7], however, shortage of this by-product in some countries has led to exploring the production of alkali-activated blended systems with the partial substitution of slag by metakaolin [8, 9] or fly ashes [10, 11]. The incorporation of fly ash into alkali-activated slag systems has been mainly studied in pastes and mortars [12], where it has been reported that fly ash brings advantages in terms of rheology and workability, aiding reductions in water content, as well as cost in areas where slag can be much more expensive than fly ash. There are a very limited number of studies dedicated to the assessment of durability of alkali-activated slag/fly ash blended materials, particularly their carbonation resistance [13].

Pasupathy et al. [14] identified that slight changes in the slag/fly ash ratio and activator induced significant differences in the carbonation extent of alkali-activated concretes exposed to nature conditions for 8 years, so that some alkali-activated concretes presented similar carbonation performance to Portland cement concretes. Li et al. [15] reported that the partial substitution of slag by fly ash induces higher susceptibility to carbonation in alkali-activated concretes evaluated under accelerated carbonation conditions, mainly due to the differences in pore structure taking place as fly ash contents increased. This is in good agreement with the observations of Nedeljković et al. [16], who evaluated natural carbonation after 1 year of exposure of alkali-activated slag/fly ash blended pastes formulated with comparable doses of activator and water content.

In this study, concretes designed to achieve comparable compressive strengths after 28 days of curing, optimising mix design, were evaluated. In order to minimise the number of factors potentially modifying the carbonation performance of these materials, all concretes were stored in controlled environmental chambers at constant relative humidity and temperature, solely varying the concentration of CO₂. Carbonation extent and changes in weight of the specimens over the time of exposure were determined.

2. EXPERIMENTAL PROGRAMME

2.1. Materials

A Class F fly ash (FA) from Bayswater Power Station, New South Wales, Australia, and a commercial granulated blast furnace slag (GBFS) were used as solid precursors for the preparation of the concretes assessed; their chemical compositions are shown in Table 1.

The activating solution was produced by blending commercial sodium metasilicate, with a chemical composition of 50.5 wt% Na₂O and 46.0 wt% SiO₂ (balance H₂O), and tap water. Crushed gravel and sand were used as coarse and fine aggregates in the manufacture of concretes. The coarse aggregate was of 20 mm maximum size, with a specific gravity of 2830 kg/m³ and absorption of 1.10%. The specific gravity and absorption of the sand are 2550 kg/m³ and 0.90% respectively.

Table 1. Composition of fly ash, GGBFS and OPC, from X-ray fluorescence analysis. LOI is loss on ignition at 1000°C

Precursor	Component (mass % as oxide)								
	SiO ₂	Al ₂ O ₃	Fe ₂ O ₃	CaO	MgO	SO ₃	Na ₂ O	K ₂ O	LOI
Fly ash	63.88	25.28	5.30	< 0.1	1.03	0.23	0.16	1.33	2.68
Slag	34.20	13.84	0.40	43.06	5.40	0.84	0.06	0.36	1.83

2.2. Concretes mix design

Three sets of concrete samples were produced with slag to fly ash ratios as shown in Table 2. All concretes were produced with an activator dose of 8 wt.% of the total amount of the precursor (GBFS + FA) to be activated. All concretes were designed with a similar content of aggregates, however, the water to binder ratios (w/b) was modified depending on the FA content, targeting strengths of 60 ± 5 MPa after 28 days of curing.

Table 2. Mix designs of concretes assessed (amounts in kg/m³ of fresh concrete)

Sample ID	Slag	Fly ash	Water	Coarse aggregate	Fine aggregate	Activator	Water/Binder
S100	400	-	160	1150	640	32	0.40
S75	300	100	154	1150	640	32	0.38
S50	200	200	188	1150	640	32	0.36

Concrete samples were mixed in an electric pan mixer following the Australian Standard for concrete mixing, AS1012 [17]. Specimens were cast in 100 mm diameter × 200 mm height cylinder moulds, and vibrated for approximately two minutes. The concretes were then cured in a water bath at ambient temperature (20-23°C) until testing.

2.3. Compressive strength and water absorption properties

Compressive strengths of concretes were determined after 1, 3, 7, 14, 28, 56 and 90 days of curing, following the standard procedure ASTM C39 [18] using an ELE ADR Auto 1500 compression testing machine. Specimens were loaded at a rate of 1.0 kN/sec until failure. Volume of permeable voids (VPV) was determined for concretes after 7, 28, 56, 90 days of curing, according to the standard test ASTM C 642-06 [19] drying the specimens at 100°C until reaching constant weight, strictly following the standard recommendations. The results reported correspond to measurements of four slices taken from two cylinders, for a total of 8 measurements.

2.4. Resistance to natural and accelerated carbonation

After 28 days of curing, samples were removed from the water bath and stored at laboratory conditions for 24 h prior to testing. To induce accelerated carbonation, cylindrical concrete specimens were stored in a chamber with a CO_2 concentration of $1.0 \pm 0.2\%$, temperature of $23 \pm 2^\circ\text{C}$, and relative humidity (RH) of $65 \pm 5\%$. This carbonation condition was selected as it has been found to best replicate the phase assemblage identified in naturally carbonated pastes [20]. For the natural carbonation study, concrete specimens were stored in a second chamber conditioned with similar RH and temperature to that of the accelerated carbonation test, but without circulating CO_2 . This experimental protocol was selected with the aim of assessing the effect of CO_2 concentration on carbonation resistance of these alkali-activated concretes, minimising the number of factors that might influence how carbonation progresses. The accelerated and naturally carbonated specimens were exposed to the controlled environments for up to 90 days. Changes in pH in the sample, which are typically associated with carbonation, were determined periodically by treating the surface of freshly cleaved samples with a 1 % solution of phenolphthalein in alcohol. Changes in weight of the specimens were also recorded.

3. RESULTS AND DISCUSSION

3.1 Correlation between compressive strength and permeability

Detailed characterisation of some of the concretes assessed here has been reported previously [21, 22] where it was identified that modifying the water content in alkali-activated slag/fly ash concretes is a suitable strategy for the production of alkali-activated slag concretes with comparable mechanical strengths (Figure 1A), with up to 50 wt.% fly ash replacement. Significant changes in the VPV values are identified in all concretes at different times of curing and slag contents (Figure 1B) particularly after 28 days of curing, despite all concrete presenting a comparable compressive strength.

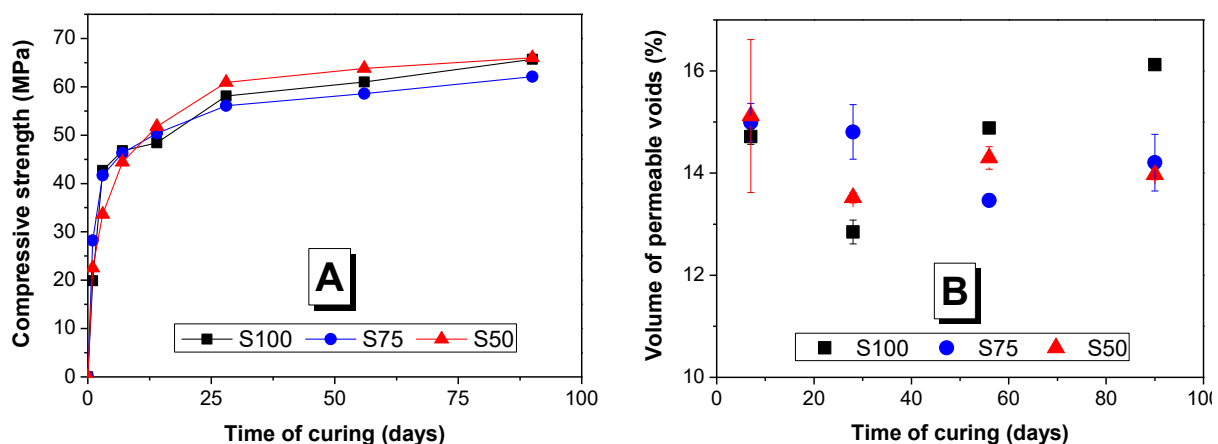


Figure 1 (A) Compressive strength and (VPV) evolution of alkali-activated slag/ fly ash blended concretes

Based on the VPV results (Figure 1B), all concretes can be classified as showing an expected moderate durability. It has been reported that the substitution of slag by fly ash in alkali-activated materials leads to an increased permeability of these systems [23]; however, neither

a correlation between VPV values for a given mix at different curing durations, nor a correlation between compressive strength and VPV, is identified in this study. The differences in the chemistry and structure of the main binding phases forming in slag/fly ash blended systems, compared with binders solely based on slag, will induce changes in the pore network of these materials [24], particularly upon drying. The reaction products forming in alkali-activated materials containing fly ash are particularly susceptible to desiccate as the water is more loosely bounded to the gel structure [22]. The variability in VPV results question how representative are these values regarding the permeability of these systems, and indicates that VPV might not be a suitable testing method for alkali-activated materials, due to the severe microcracking induced by sample pre-conditioning (drying) prior to testing.

3.2 Correlation between natural and accelerated carbonation

Weight changes recorded for concretes stored in the controlled environmental chambers are shown in Figure 2A. In samples exposed to natural carbonation, fluctuations of weight are observed throughout the exposure time, which are most likely due to the drying of the specimens at the low RH at which they have been stored. Conversely, in samples exposed to 1% CO₂, a higher weight loss is identified at extended exposure times, which might be associated with the combined effect of weight loss due to drying of the specimens, and changes in the density of the concrete carbonated layer. The weight loss increased at higher contents of fly ash in all the concretes, although the differences between concretes containing 25 or 50 wt.% fly ash are small.

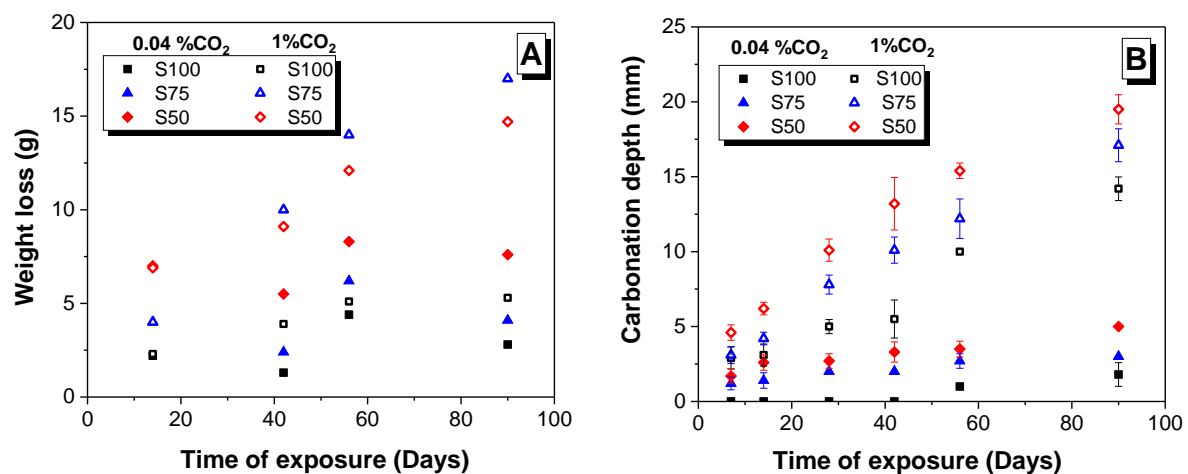


Figure 2 (A) Weight loss upon carbonation and (B) carbonation depth of alkali-activated slag/fly ash blended concretes. Error bars correspond to one standard deviation of ten measurements

Carbonation depths are shown in Figure 2B. Under natural carbonation conditions, concretes solely based on alkali-activated slag did not show any carbonation up to 42 days of exposure, and negligible values were then identified up to 90 days of carbonation. Alkali-activated slag/fly ash blended concretes exhibited a small carbonation depth (< 5mm) during the testing time. The carbonation depths are slightly higher as the content of fly ash increases, at early times of exposure (< 42 days of exposure). However, negligible changes in the carbonation depths are

identified in all the concretes assessed, independent of the fly ash content, at extended carbonation durations. Provis [25] reported that an initial ‘skin’ of carbonation material has been identified in several alkali-activated concretes as a non-zero carbonation depth at the beginning of exposure to natural carbonation conditions. The concretes evaluated here were close to fully saturated prior to carbonation testing, due to the curing conditions used in this study (see section 2.2); however, the carbonation readings after 7 days of storage in the chamber are most likely related to the superficial carbonation skin identified in other alkali-activated concretes.

Upon accelerated carbonation at early times of 1% CO₂ exposure (<7 days) the carbonation depths of all concretes are comparable; however, at extended exposure times significant differences in the carbonation depth among the tested concretes are observed. Concretes formulated with higher contents of fly ash show significantly higher carbonation depths compared to those specimens without fly ash, and these values increase with extended carbonation durations.

A direct correlation between weight changes in the samples and carbonation depth identified at different exposure times is solely observable in alkali-activated slag/fly ash concretes when tested under accelerated carbonation conditions (1% CO₂), where higher carbonation depths induce an increase in the weight loss. Conversely, in the sample solely based on slag, although carbonation depths continue to increase over time of exposure to 1% CO₂, the weight loss does not seem to vary significantly. This indicates that for alkali-activated slag concretes changes in phase assemblage upon carbonation, particularly under accelerated conditions, will not lead to significant changes in the density of the material, in contrast to concretes containing fly ash.

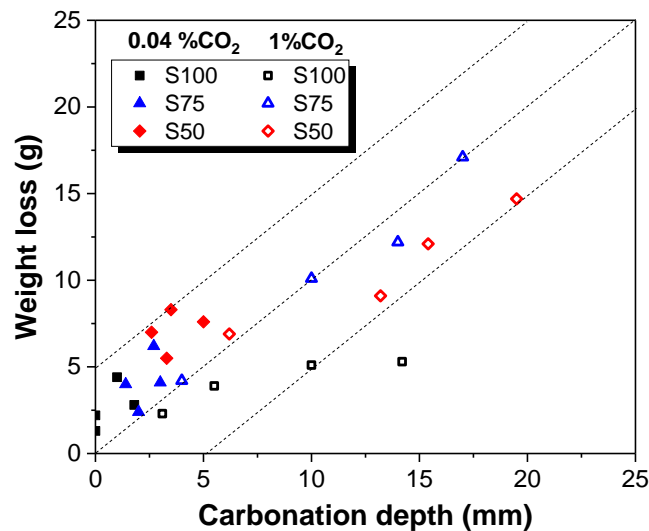


Figure 3 Correlation between weight loss and carbonation depth of alkali-activated slag/fly ash blended concretes, as a function of the carbonation exposure conditions

4. GENERAL REMARKS

- The partial replacement of slag by fly ash in alkali-activated concretes does not lead to reduction in the compressive strength development, if concrete mix designs are optimised

- The VPV testing procedure does not provide a clear indication of permeability of alkali-activated concretes, independent of the concrete mix design
- Under natural carbonation exposure conditions, all concretes exhibited negligible carbonation depths for the duration of the exposure; however, under accelerated carbonation conditions, significant carbonation depths were recorded, particularly in concretes based on alkali-activated slag/fly ash blends.
- Despite the differences in values between natural and accelerated carbonation depths, both tests are depicting similar trends in terms of carbonation susceptibility of alkali-activated concretes, as in both carbonation conditions assessed, concretes with higher contents of fly ash are more susceptible to carbonation.

ACKNOWLEDGEMENTS

This work was partially funded by the Australian Research Council, through a Linkage Project co-sponsored by Zeobond Pty Ltd. Participation of S.A. Bernal in this study was sponsored by EPSRC through ECF EP/R001642/1. A. Kilcullen and D. Brice are greatly acknowledged for assistance producing specimens, and collecting some of the data reported.

REFERENCES

- [1] Poonguzhali A., Shaikh H., Dayal R.K., Khatak H.S., 'A review on degradation mechanism and life estimation of civil structures', *Corr Rev* **26** (4) (2008) 215-294.
- [2] Bernal S.A., 'The resistance of alkali-activated cement-based binders to carbonation', in: Pacheco-Torgal F., Labrincha J., Leonelli C., Palomo A., Chindaprasit P. (Eds.), *Handbook of Alkali-Activated Cements, Mortars and Concretes*, Woodhead Publishing, Cambridge, UK (2014) 319-329.
- [3] Sanjuán M.A., Andrade C., Cheyrezy M., 'Concrete carbonation test in natural and accelerated conditions', *Adv Cem Res* **15**(4) (2003) 171 - 180.
- [4] Bernal S.A., Provis J.L., Mejía de Gutiérrez R., van Deventer J.S.J., 'Accelerated carbonation testing of alkali-activated slag/metakaolin blended concretes: effect of exposure conditions', *Mater Struc* **48** (2015) 653-669.
- [5] Bernal S.A., Provis J.L., Walkley B., San Nicolas R., Gehman J., Brice D.G., Kilcullen A., Duxson P., van Deventer J.S.J., 'Gel nanostructure in alkali-activated binders based on slag and fly ash, and effects of accelerated carbonation', *Cem Concr Res* **53** (2013) 127-144.
- [6] Bernal S.A., Rodríguez E.D., Kirchheim A.P., Provis J.L., 'Management and valorisation of wastes through use in producing alkali-activated cement materials', *J Chem Tech Biotech* **91**(9) (2016) 2365-2388.
- [7] Duxson P., Provis J.L., 'Designing precursors for geopolymer cements', *J Amer Ceram Soc* **91**(12) (2008) 3864-3869.
- [8] Bernal S.A., Mejía de Gutierrez R., Rose V., Provis J.L., 'Effect of silicate modulus and metakaolin incorporation on the carbonation of alkali silicate-activated slags', *Cem Concr Res* **40**(6) (2010) 898-907.
- [9] Bernal S.A., Mejía de Gutiérrez R., Provis J.L., 'Engineering and durability properties of concretes based on alkali-activated granulated blast furnace slag/metakaolin blends', *Constr Build Mater* **33** (2012) 99-108.
- [10] Puertas F., Fernández-Jiménez A., 'Mineralogical and microstructural characterisation of alkali-activated fly ash/slag pastes', *Cem Concr Comp* **25**(3) (2003) 287-292.
- [11] Puertas F., Martínez-Ramírez S., Alonso S., Vázquez E., 'Alkali-activated fly ash/slag cement. Strength behaviour and hydration products', *Cem Concr Res* **30** (2000) 1625-1632.

- [12] Provis J.L., Bernal S.A., 'Binder Chemistry – Blended Systems and Intermediate Ca Content', in: Provis J.L., van Deventer J.S.J. (Eds.), *Alkali Activated Materials*, Springer Netherlands (2014) 125-144.
- [13] Arbi K., Nedeljković M., Zuo Y., Ye G., 'A Review on the durability of alkali-activated fly ash/slag systems: advances, issues, and perspectives', *Ind Eng Chem Res* **55**(19) (2016) 5439-5453.
- [14] Pasupathy K., Berndt M., Castel A., Sanjayan J., Pathmanathan R., 'Carbonation of a blended slag-fly ash geopolymer concrete in field conditions after 8 years', *Constr Build Mater* **125** (2016) 661-669.
- [15] Li Z., Li S., 'Carbonation resistance of fly ash and blast furnace slag based geopolymer concrete', *Constr Build Mater* **163** (2018) 668-680.
- [16] Nedeljković M., Šavija B., Zuo Y., Luković M., Ye G., 'Effect of natural carbonation on the pore structure and elastic modulus of the alkali-activated fly ash and slag pastes', *Constr Build Mater* **161** (2018) 687-704.
- [17] Standards Australia, AS 1012: Methods of testing concrete, 1994.
- [18] ASTM International, Standard Test Method for Compressive Strength of Cylindrical Concrete Specimens (ASTM C39/C39M - 10), West Conshohocken, 2010.
- [19] ASTM international, Standard test method for density, absorption, and voids in hardened concrete (ASTM C642-06), 2006.
- [20] Bernal S.A., Provis J.L., Brice D.G., Kilcullen A., Duxson P., van Deventer J.S.J., 'Accelerated carbonation testing of alkali-activated binders significantly underestimate the real service life: The role of the pore solution', *Cem Concr Res* **42**(10) (2012) 1317-1326.
- [21] Ismail I., Bernal S.A., Provis J.L., San Nicolas R., Brice D.G., Kilcullen A.R., Hamdan S., van Deventer J.S.J., 'Influence of fly ash on the water and chloride permeability of alkali-activated slag mortars and concretes', *Constr Build Mater* **48** (2013) 1187-1201.
- [22] van Deventer J.S.J., San Nicolas R., Ismail I., Bernal S.A., Brice D.G., Provis J.L., 'Microstructure and durability of alkali-activated materials as key parameters for standardization', *J Sustain Cem Mater* **4**(2) (2015) 116-128.
- [23] Provis J.L., Myers R.J., White C.E., Rose V., van Deventer J.S.J., 'X-ray microtomography shows pore structure and tortuosity in alkali-activated binders', *Cem Concr Res* **42**(6) (2012) 855-864.
- [24] Ismail I., Bernal S.A., Provis J.L., San Nicolas R., Hamdan S., van Deventer J.S.J., 'Modification of phase evolution in alkali-activated blast furnace slag by the incorporation of fly ash', *Cem Concr Comp* **45** (2014) 125-135.
- [25] Provis J.L. Alkali-activated cement and concretes - Durability testing to underpin standardisation, in: Basheer P.A.M. (Ed.) ICDCS2018: 6th International Conference on Durability of Concrete Structures, Whittles Publishing, Leeds, United Kingdom (2018) 16-25.

ACCELERATED CARBONATION OF RECYCLED AGGREGATE CONCRETE

Andreas Leemann (1), Roman Loser (1)

(1) EMPA, Laboratory for Concrete & Construction Chemistry, CH 8600, Dübendorf, Switzerland

Abstract

The use of cement with reduced clinker content or the reuse of concrete waste provided by the demolition of buildings in recycled aggregate concrete (RC) leads to a reduction of the environmental impact of concrete production. In Switzerland, there is a combination of these two approaches applied for house building. However, due to a lack of data the carbonation resistance of RC and with it the durability of buildings constructed with it are scrutinised. In this study, the carbonation resistance of RC with the typical composition used in the Swiss building industry is investigated to clarify the influence of recycled aggregate and type of cement used. RC with two different replacement levels of natural aggregates is produced using three different blended cements.

Keywords: recycled aggregate concrete, blended cement, carbonation

1. INTRODUCTION

Different strategies are used to reduce the environmental impact of concrete production. One possibility is the reuse of concrete waste provided by the demolition of buildings in recycled aggregate concrete (RC). Another is the use of cement with reduced clinker content. In the Switzerland, these two approaches are combined in concrete used for house building. Blended cements typically contain up to 20 or 35 mass-% of mineral additions corresponding to CEM II/A and CEM II/B according to [1]. The level of substitution of natural aggregates (NA) by RA is typically between 25 and 50 %.

The production of RC is an established technique in Switzerland. This was made possible by owners requesting RC for specific projects, by innovative contractors and by simultaneously conducted research projects [2,3]. Based on the results of various research projects lead to the publication of a guideline [4] providing information to civil engineers. In research, the emphasis so far has clearly been on the mechanical and time-dependent visco-elastic properties of the concrete [5-6]. However, carbonation may be an issue. Lack of data has given rise to doubts about the durability of RC.

In this study, concrete with the typical composition used in the Swiss market is investigated in regard to its carbonation resistance to clarify the influence of the recycled aggregate percentage and the type of cement used. Three different blended cements are used to produce RC with two different replacement levels of NA. The RA is provided by two different industrial sources. Bulk density and water absorption of the aggregates and compressive strength and accelerated carbonation of the concrete are determined.

2. MATERIALS AND METHODS

2.1 Materials

The cements used for concrete production (Table 1) were CEM II/A-LL (containing approximately 15 mass-% of limestone powder), CEM II/B-M (T-LL) (containing approximately 15 mass-% of limestone powder and 15 mass-% of burnt oil shale) and CEM III/B (containing a minimum of 66 mass-% of slag) according to [1]. As it is typical for large parts of Switzerland, well rounded river sand and gravel were used as NA (0-4 mm: 35 mass-%, 4-8 mm: 16 mass-%, 8-16 mm: 17 mass-%, 16-32 mm: 32 mass-%). The water absorption of the NA with the given grain size distribution was 0.5 volume-% [7]. Two different RA from two industrial plants were used. Both RA consist of crushed concrete.

RA-1 was delivered in the same four grain size fraction as stated for the NA above. RA-2 was delivered in grain size of 0-16 mm. The sieve curve shows an amount of 38.5 mass-% of 0-4 mm, 21.9 mass-% of 4-8 mm and 39.6 mass-% of 8-16 mm. Particle density and water absorption of the two RA are given in Table 2.

Four concrete mixtures were produced with NA as reference (REF 01-04). The substitution of NA with RA was either 25 or 50 mass-%.

Concrete mixtures corresponding to the compressive strength classes of C20/25 (type A), C25/30 (type B) and C30/37 (type C), respectively, were produced [8]. Because of the higher loose bulk density of the RA compared to the NA the cement content was increased by 10-15 kg/m³ in the RC mixtures resulting in a higher cement paste volume. This made it possible to fill the voids between the aggregates and produce a concrete with good workability.

The w/c is given as two numbers representing the total water in the concrete (w_{total}/c) and the total water minus water absorption of the aggregates as shown in Table 2 (w_{EN}/c). The water absorption of the sand 0/4 mm of RA-1 (not analysed) was assumed to be identical to the one of the grain size fraction 4/8 mm.

Three cubes (150 X 150 X 150 mm³) were produced for compressive strength and one prism (120 X 120 X 360 mm³) for the determination of the carbonation depth.

Table 1: Chemical composition of the cements (LOI = loss on ignition, TC = total carbon).

	SiO ₂	Al ₂ O ₃	Fe ₂ O ₃	Cr ₂ O ₃	MnO	TiO ₂	P ₂ O ₅	CaO	MgO	K ₂ O	Na ₂ O	SO ₃	LOI	TC
CEM II/A	17.8	4.0	2.6	0.0	0.0	0.3	0.1	60.8	1.8	0.9	0.2	2.9	8.3	2.0
CEM II/B	19.8	4.9	3.1	0.0	0.0	0.3	0.2	56.9	1.8	1.1	0.2	3.2	8.3	2.0
CEM III/B	29.3	7.7	1.3	0.0	0.3	0.6	0.2	48.5	4.5	0.7	0.3	4.6	1.8	0.5

Table 2: Particle density and water absorption of the recycled aggregates (sand 0/4 mm of RA-1 not analysed).

aggregate		RA-1			RA-2
grain size	[mm]	4/8	8/16	16/32	4/16
apparent particle density	[kg/m ³]	2679	2691	2679	2718
oven-dried particle density		2397	2369	2427	2517
saturated surface-dry particle density	[kg/m ³]	2503	2552	2521	2591
water absorption	[volume-%]	4.38	3.35	3.86	2.94

2.2 Methods

The compressive strength of the concrete cubes was measured according to EN 12390-3 [9]. The carbonation coefficient K_{ACC} was determined according to SN 505 262/1 [10] and as described in [11-13] using a CO₂ concentration of 4 % and a RH of 57 %. The samples were demoulded after 24 hours, placed in water for two days and stored in climate chamber at 20 °C and 57 % RH. At the age of 28 days, they are placed in the carbonation chamber for a duration of 63 days. The carbonation coefficient K_N of the concrete exposed outdoors was determined after an exposure of one year. The carbonation coefficient K was determined by calculating the regression of the carbonation depth as a function of the square root of time (equation 1):

$$K = \frac{(d_K - A)}{\sqrt{t}} \quad (1)$$

where K is the carbonation coefficient in mm/ \sqrt{y} , d_K the carbonation depth in mm, A the initial carbonation depth in mm after curing and t the time in years.

Table 3: Concrete mix design.

mix	cement	cement content [kg/m ³]	w_{total}/c^1	w_{EN}/c^2	SP [kg/m ³]	concrete type	RA [mass-%]
REF-01	CEM II/A	330	0.45	0.43	1.6	C	-
REF-02	CEM II/A	310	0.50	0.48	0.6	C	-
REF-03	CEM II/A	290	0.60	0.57	-	B	-
REF-04	CEM II/A	280	0.65	0.62	-	A	-
RC-01	CEM II/A	300	0.66	0.51	-	B	50 (RA-1)
RC-02	CEM II/A	300	0.66	0.51	-	B	50 (RA-1)
RC-03	CEM II/B	300	0.66	0.51	-	B	50 (RA-1)
RC-04	CEM II/A	325	0.53	0.44	0.7	C	25 (RA-1)
RC-05	CEM II/A	325	0.53	0.44	0.7	C	25 (RA-1)
RC-06	CEM II/A	325	0.57	0.43	1.3	C	50 (RA-1)
RC-07	CEM II/A	325	0.57	0.43	1.3	C	50 (RA-1)
RC-08	CEM II/A	300	0.64	0.52	1.2	B	50 (RA-2)
RC-09	CEM II/A	300	0.64	0.52	1.2	B	50 (RA-2)
RC-10	CEM II/A	325	0.54	0.42	3.4	C	50 (RA-2)
RC-11	CEM II/A	325	0.54	0.42	3.9	C	50 (RA-2)
RC-12	CEM II/B	325	0.54	0.42	4.2	C	50 (RA-2)
RC-13	CEM III/B	325	0.51	0.42	1.6	C	25 (RA-1)
RC-14	CEM III/B	325	0.51	0.42	2.0	C	25 (RA-1)
RC-15	CEM III/B	325	0.55	0.41	2.0	C	50 (RA-1)
RC-16	CEM III/B	325	0.55	0.40	2.0	C	50 (RA-1)
RC-17	CEM III/B	410	0.48	0.38	6.2	C	50 (RA-1)

¹ w_{total} = total water

² w_{EN} = total water subtracting the water absorption of the aggregates as stated in Table 2 according to [2]

SP = superplasticizer

3. RESULTS AND DISCUSSION

3.1 Summary

The summarized results are shown in Table 4.

3.2 Compressive strength

The compressive strength of the RC is significantly higher on average than the one of the REF at a given w/c , if the total water content is considered (Figure 1). Assuming completely water saturated aggregates, the ratio is the same for both types of concrete at $w/c \geq 0.43$ (Figure 2). At $w/c \leq 0.42$, the ratio between compressive strength and w/c changes, with considerably higher values for the RC, mainly the one produced with RA-2.

The higher strength of RC (Figure 1) is a result of the higher water absorption of RA, decreasing the effective w/c of the cement paste. The w_{EN}/c is a better parameter to assess compressive strength of RC than the w_{total}/c (Figure 2). The exaggerated non-linear strength increase at low w/c is possibly caused by the fact that the relative amount of the total water absorbed by RA increases with decreasing w/c and due to the higher amount of fines in RA-2.

Table 4: Summary of the results (air = air void content; ρ = bulk density of the concrete; SF = slump flow; $f_{c,28}$ = compressive strength at 28 days; K_{ACC} = carbonation coefficient in accelerated conditions;).

mix	air	ρ	SF	$f_{c,28d}$	K_{ACC}
	[%]	[kg/m ³]	[cm]	[MPa]	[mm/y ^{0.5}]
REF-01	2.6	2384	35	43.6	2.3
REF-02	3.0	2363	36	36.6	2.8
REF-03	1.3	2394	48	30.6	4.2
REF-04	1.0	2407	51	27.8	5.2
RCA-01	1.7	2341	40	32.4	3.7
RCA-02	1.9	2344	41	33.5	3.8
RCA-03	2.0	2319	40	37.1	4.4
RCA-04	2.7	2368	38	37.0	2.6
RCA-05	1.6	2410	39	40.6	2.8
RCA-06	1.8	2366	39	43.3	2.9
RCA-07	1.5	2370	39	42.2	2.8
RCA-08	2.4	2286	47	31.1	3.8
RCA-09	2.8	2308	36	31.5	4.2
RCA-10	1.7	2366	30	47.7	2.4
RCA-11	1.6	2375	35	51.1	2.3
RCA-12	2.0	2367	33	55.7	2.6
RCA-13	1.4	2379	46	50.0	4.4
RCA-14	1.4	2379	35	45.4	5.0
RCA-15	1.2	2364	35	47.9	4.6
RCA-16	1.5	2366	39	48.0	4.4
RCA-17	1.4	2373	56	66.5	3.0

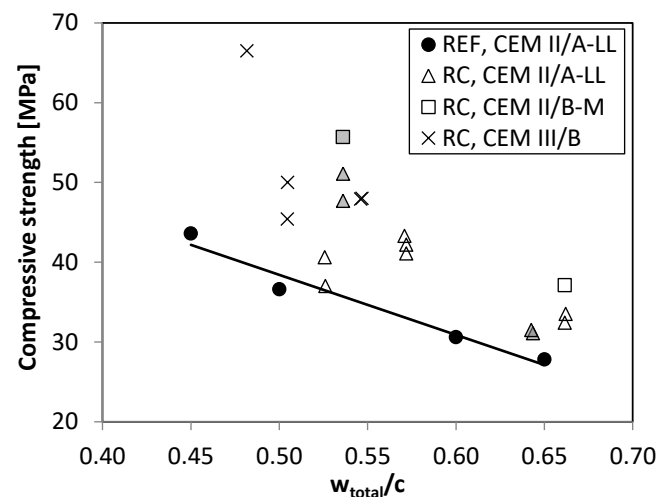


Figure 1: Compressive strength at 28 days as function of the w_{total}/c . The line represents the linear regression for REF. The filled signs mark the concrete produced with RA-2.

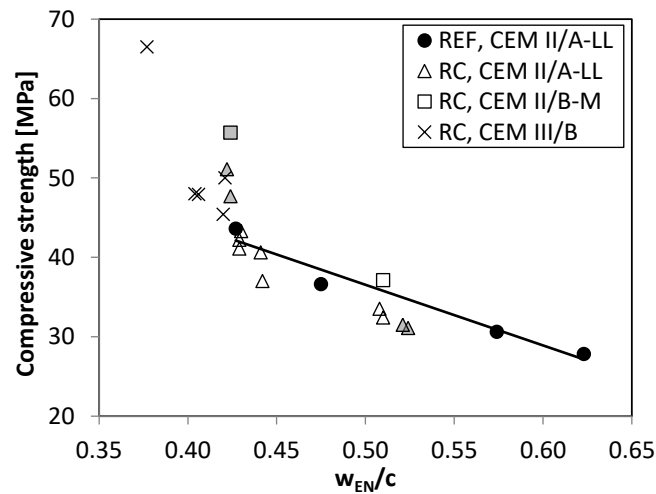


Figure 2: Compressive strength at 28 days as function of w_{EN}/c . The line represents the linear regression for REF. The filled signs mark the concrete produced with RA-2.

3.2 Carbonation resistance

RC produced with CEM II/A-LL shows about the same relation between compressive strength and carbonation coefficient K_{ACC} as REF (Figure 3). The two RC produced with CEM II/B-M have a slightly increased carbonation coefficient K_{ACC} compared to the concrete produced with CEM II/A-LL, while the values are significantly increased in the case of RC produced with CEM III/B.

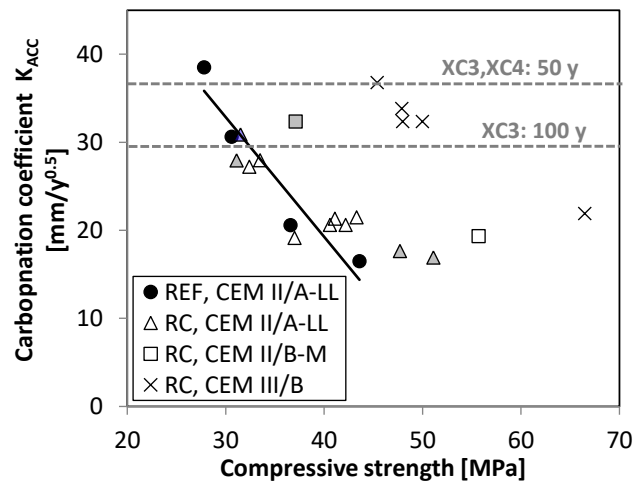


Figure 3: Carbonation coefficient K_{ACC} as a function of compressive strength at 28 days. Limit values of carbonation coefficient K_{ACC} depending on exposure class and planned service life according to [2].

The increase of the carbonation coefficient K in the concrete produced with CEM II/B-M and CEM III/B is directly linked to the lower clinker content compared to CEM II/A-LL and the decreased CO_2 buffer capacity [12,13]. As such, compressive strength can only be used as a control factor for carbonation resistance within a group of concrete produced with the same

cement type. The low w/c needed for concrete produced with CEM III/B to have a carbonation coefficient K_{ACC} below the limit value leads to a much higher compressive strength than required for the strength class C30/37.

4. CONCLUSIONS

RC was produced using two different RA at varying amounts. Its carbonation resistance was determined in accelerated and natural conditions. Concrete produced with natural aggregates was used as reference (REF).

- Water absorption of RA has a significant impact on compressive strength. Therefore $w_{EN/c}$ should be used to compare concrete produced with aggregates of varying water absorption.
- The carbonation coefficient K_{ACC} of RC produced with CEM II/A-LL is slightly increased compared to REF produced with the same cement type.
- Using cement with reduced clinker content leads to a slight (CEM II/B-M) and a significant (CEM III/B) increase of carbonation coefficient K_{ACC} at a specific compressive strength.
- The low w/c required in the case of concrete produced with CEM III/B to fulfil the required limit values for carbonation resistance result in too high compressive strength for housebuilding and requires a very high cement content thereby increasing costs.

ACKNOWLEDGEMENTS

The authors would like to thank cemsuisse for financing the study and Pietro Lura for reviewing the manuscript.

REFERENCES

- [1] EN 197-1, 'Cement. Composition, specifications and conformity criteria for common cements', CEN, Brussels (2011).
- [2] Hoffmann, C., Schubert, S., Leemann, A., & Motavalli, M.. 'Recycled concrete and mixed rubble as aggregates: Influence of variations in composition on the concrete properties and their use as structural material', *Constr. Build. Mater.*, **35** (2012) 701-709.
- [3] Schubert, S., Hoffmann, C., Leemann, A., Moser, K., & Motavalli, M.. 'Recycled aggregate concrete: experimental shear resistance of slabs without shear reinforcement', *Eng. Struct.* **41** (2012) 490-497.
- [4] SIA 2030, 'Recycling Concrete', SIA, Zürich (2010) (in French and German).
- [5] McNeil, K., & Kang, T. H. K.. 'Recycled concrete aggregates: A review', *Int. J. Concr. Struct. Mater.*, **7**(1) (2013) 61-69.
- [6] Bravo, M., de Brito, J., Pontes, J., & Evangelista, L., 'Mechanical performance of concrete made with aggregates from construction and demolition waste recycling plants', *J. Clean. Prod.*, **99**, (2015) 59-74.
- [7] EN 1097-6, 'Tests for mechanical and physical properties of aggregates. Determination of particle density and water absorption', CEN, Brussels (2013).
- [8] SN EN 206, 'Concrete. Specification, performance, production and conformity', National Appendix. SIA, Zürich (2013) (in French and German).
- [9] EN 12390-3, 'Testing hardened concrete – Part 3: Compressive strength of test specimens', CEN, Brussels (2002)

- [10] SN 505 262/1 'Betonbau - Ergänzende Festlegungen, Anhang I, Karbonatisierungswiderstand', SIA, Zürich (2013) (in French and German).
- [11] Leemann, A., Nygaard, P., Kaufmann, J., Loser, R., 'Relation between carbonation resistance, mix design and exposure of mortar and concrete, *Cem. Concr. Compos.* 62 (2015) 33-43.
- [12] Leemann, A., Moro, F., 'Carbonation of concrete: the role of CO₂ concentration, relative humidity and CO₂ buffer capacity', *Mater. Struct.* **50** (2017) 30.
- [13] Leemann, A., Loser, R., Münch, B., & Lura, P., 'Steady-state O₂ and CO₂ diffusion in carbonated mortars produced with blended cements', *Mater. Struct.* **50(6)** (2017) 247.

ON THE DETERMINATION OF CARBONATION IN CEMENTITIOUS MATERIALS

Charlotte Thiel (1) and Christoph Gehlen (1)

(1) Centre for Building Materials, Technical University of Munich, Germany

Abstract

For material testing, qualification and subsequent assessment fast, simple, reliable and economic methods are needed. This paper provides an overview of different techniques to determine the depth of carbonation in cementitious materials. The easiest and cheapest way is to remove a core or a fragment of concrete cover and spray a colour indicator on the fresh fractured surface (by splitting). Here, 1 % phenolphthalein in 70 % ethanol is most widely used. However, this only indicates in which area the concrete has a pH value below 8.2 - 10, but not the actual carbonation front which is on average about 20 % higher. Since phenolphthalein is carcinogenic, alternative colour indicators were investigated in the laboratory. 0.5 % Curcumin showed similar colour change to phenolphthalein. In addition, 0.1 % thymolphthalein proved to be an alternative. Scattering within one measurement was lower than for phenolphthalein and the results were closer to the carbonation depths determined by different analytical methods (TGA and LA-ICP-MS). Furthermore, the transition pH-value of thymolphthalein is in the area of 9.3 - 10.5 which is closer to the actual carbonation front, allowing a more accurate assessment of the risk of reinforcement corrosion.

Keywords: colour indicators, carbonation, test methods

1. INTRODUCTION

The increasing CO₂ concentration of the ambient air [1] and the increasing use of clinker-reduced concretes [2] as well as new raw materials (i.e. alkali-activated binders) make the carbonation of cementitious building materials a topical issue. The mechanisms involved are still subject of current research [3 - 5]. CO₂ diffuses inside the porous system and dissolves in pore solution. The calcium-containing phases of the cement paste react with carbonic acid under the formation of CaCO₃, H₂O and calcium-free or calcium-poor phases [6].

The positive consequences of carbonation of Ordinary Portland cement (OPC) based materials are a decrease in total porosity [4, 7, 8] and the associated increase in compressive strength as well as an increase in resistance to penetrating liquids and gases [9, 10]. However, the carbonation of cementitious materials containing certain additives (i.e. fly ash, ground

granulated blast-furnace slag) often leads to a coarsening of the pore structure [5, 7, 11] and thus to a reduced resistance against penetrating substances. Furthermore, carbonation lowers the pH value of the pore solution and therefore leads to a risk of reinforcement corrosion.

2. METHODS FOR MEASURING CARBONATION DEPTHS

Table 1 gives an overview of common methods for determining the carbonation depth. Methods for measuring the pH in concrete are reviewed in [12]. In addition, there are many approaches for deriving the carbonation progress from changes in the physical properties of the concrete near-surface zone. For example, Thiery et al. [13] have successfully used gammadensitometry to draw conclusions about the carbonation progress based on the density change. Also μ -CT has been used to determine the carbonation depth due to changes in the pore system [14]. In [15, 16] neutron diffraction was used to study the evolution of portlandite and calcite in hardened cement pastes during carbonation non-destructively. It is also possible to determine the hardness in different depths using μ -indentation or even nano-indentation and correlate it to carbonation depth [17]. However, it must be noted that these indirect methods are strongly affected by other parameters (salt absorption, hydration, etc.).

Table 1: Common methods for determining the carbonation depth

Test method	Benefits	Drawbacks	References
Colour indicator	Fast, economic and easy	Indirect, destructive, Phenolphthalein underestimates carbonation depth	[11-14, 18-25]
Embedded pH-sensors	Real-time monitoring of structures is possible	Validation of sensors is missing	[11] and references therein
FT-IR:	fast	Scale effect*, **	[7, 17, 22]
pH profile method (Pore solution analysis)	Fast and easy, Information on all chemical substances involved	Extensive sample preparation, Scale effect*	[22, 26]
Polarization Microscopy	High resolution, carbonated C-S-H can be revealed	Scale effect and extensive sample preparation, *	[11, 22, 24, 27]
Raman spectroscopy	Polymerization of C-S-H can be observed, not interfered by water	Sensitive to impurities, scale effect*	[28]
SEM/EDX, SEM -EDS	High-resolution images (nano-scale)	Very sensitive and time consuming sample-preparation, *	[5, 29]
²⁹ Si-NMR-spectro-scopy	Different bindings of Si tetrahedrons can be determined	No information on CH carbonation, *	[3, 4, 30,31]
Thermo-analytical methods (TGA)	Direct observation of formed phases	*, **	[3-5, 7-8, 13, 15, 27]
XRD	CaCO ₃ modifications can be observed	*, some phases are amorphous to X-rays (i.e. amorphous CaCO ₃)	[3-5, 7, 32]

* Scale effect: Only a very small amount of cementitious material is examined. Extrapolating the results to concrete is often linked with high scatter.

** Precision and applicability vary greatly with inhomogeneity of the sample and composition of aggregates (i.e. Calcitic aggregates or calcite from limestone fillers cannot be distinguished from CaCO₃ formed during carbonation)

In terms of costs, time, equipment and operator training, the colour indicator method remains superior to other test methods. However, it is destructive and likely to imprecise readings [22, 23].

3. MATERIALS AND METHODS

3.1 Materials

Prisms (10 x 10 x 50 cm³) from 20 different concrete mixes (table 2) were cast and demoulded after one day. Different aggregates (calcitic and quarzitic) with a maximum grain

size of 16 mm were used. After demoulding, the samples were stored at $20 \pm 1^\circ\text{C}$ under water for 6 days. Afterwards, the samples were pre-conditioned at $20 \pm 1^\circ\text{C}$ and $65 \pm 2\%$ RH for 21 days. At the age of 28 days, the carbonation depth was determined with different methods by cutting a 5 cm thick piece from each prism. The remaining samples were then exposed to accelerated carbonation ($20 \pm 1^\circ\text{C}$, $65 \pm 1\%$ RH and $2.0 \pm 0.1\%$ vol. CO_2). After an exposure period of another 28 days, further 5 cm thick slices were split from the surface and the carbonation depth was measured.

Table 2: Concrete compositions

	Cement type (kg/m ³)	Additive (kg/m ³)	w/b-ratio
1	OPC: CEM I 42.5 R (320)		0.60
2	Slag cement: CEM III/B 42.5 N (320)		0.60
3	OPC: CEM I 42.5 R (334)	Limestone(71)	0.43
4	OPC: CEM I 42.5 R (310)	Limestone (40)	0.52
5	OPC: CEM I 42.5 R (300)	Limestone (20), Fly ash (85)	0.53
6	OPC: CEM I 42.5 R (280)	Fly ash (70)	0.59
7	Slag Cement: CEM III/A 32.5 N (360)		0.50
8	Slag Cement: CEM III/A 32.5 N (315)		0.58
9	Slag Cement: CEM III/A 32.5 N (330)	Fly ash (80)	0.50
10	Slag Cement: CEM III/A 32.5 N (290)	Fly ash (60)	0.58
11	Slag cement: CEM III/B 32.5 N (330)	Fly ash (60)	0.50
12	Slag cement: CEM III/B 32.5 N (290)	Fly ash (60)	0.58
13	Slag cement: CEM II/B-S 42.5 N (360)		0.50
14	Slag cement: CEM II/B-S 42.5 N (315)		0.58
15	Slag cement: CEM II/B-S 42.5 N (330)	Fly ash (60)	0.50
16	Slag cement: CEM II/B-S 42.5 N (290)	Fly ash (60)	0.58
17	OPC: CEM I 42.5 R (370)		0.49
18	OPC: CEM I 42.5 R (300)		0.70
19	OPC: CEM I 42.5 R (350)		0.60
20	Slag cement: CEM III/B 42.5 N (350)		0.60

3.2 Methods

Overview

The focus of this study was to compare 1 % phenolphthalein with 0.1 % thymolphthalein. In addition, further colour indicators were analysed on selected samples. Manually readings according to [18] and automatic readings using the free software *PlotDigitalizer* were compared. Furthermore, the carbonation depth was determined with a well-established method (TGA) and a relatively new method laser ablation inductively coupled plasma mass spectrometry (LA-ICP-MS) on selected samples.

Colour indicators

For the measurements, a 5 cm thick piece of a beam was split in a press, freed from loose parts and immediately sprayed with a colour indicator, Fig. 1. Colour indicators are in principle dyes that react as self-corresponding acid-base pairs, so that their color change depends on the pH value of the solution. Due to their practical relevance, the indicators in table 3 were used.



Figure 1: Cutting and Cleaning of concrete prisms

Table 3: Colour indicators

Name	pH-value range of colour change	Health risk
1 % Phenolphthalein in 70 % Ethanol	8.2 – 10 (transparent to fuchsia)	Genetically harmful and cancerogen
0.1 % Thymolphthalein in 90% Ethanol	9.3 – 10.5 (transparent to blue)	None
Rainbow Indicator*	9 – 11** (green to purple)	None
0.5 % Curcumin in Ethanol	7.4 – 8.6 (yellow to orange)	None (even used as food additive)

* Ready mixed indicator from Germann Instruments

Curcumin is a natural dye obtained from the ginger plant turmeric. The colour change is close to phenolphthalein. Chinchón-Paye et al [20] found the indicator to be as reliable as phenolphthalein with the advantage that it is safe to use.

The Rainbow Indicator is a mixture of different chemicals that produces a variety of different colors depending on the pH value, Fig. 2. Here, only the colour change from green to purple (pH 9 to pH 11) was evaluated.

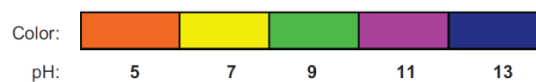


Figure 2: Colour range at different pH for the Rainbow Indicator [21]

Due to the importance of the reading time discussed in section 2, a uniform reading time between 3 and 4 h after spraying was chosen for all measurements. In addition, a part of the samples was also determined after 10 min and 24 h.

TGA

The carbonation depth was also determined by TGA on selected samples. Therefore, sample material was obtained using a precision saw in steps as small as 2 mm. The areas were chosen according to the results of the colour indicator spray test. The samples were ground in a ball mill under CO₂-free atmosphere and dried at 40°C. The sample was then heated at 10°C/min in argon atmosphere from 20°C to 1100°C. For the measurements the *STA 449 F3 Jupiter* from *NETZSCH* was used.

LA-ICP-MS

In order to evaluate the potential of new, high precision techniques, LA-ICP-MS was used on selected samples in order to determine the depth of carbonation. Here, the solid surface evaporates due to a directional laser pulse. The particles are ionized and can be counted after separation by the mass/charge ratio. A 1 cm thick and 4.5 cm wide disc was sawn out of the middle of the concrete prism. The sample was then polished and investigated with the *Nd:YAG* laser with a wavelength of 213 nm and a pulse duration in the range of 3 to 5 nanoseconds (*NWR213*), and a *NexION 300D* mass spectrometer from *Perkin Elmer*.

4. RESULTS AND DISCUSSION

4.1 Colour indicators and TGA

Fig. 3 shows an example of a sample surface 3-4 hours after spraying with different indicators. The colour change of phenolphthalein and curcumin was very well visible from the reading accuracy even with dark concrete compositions. The colour changes of thymolphthalein and the Rainbow Indicator were not quite so well recognizable.



Figure 3: Colour change on a concrete sample determined with different indicators (from left to right: 0.1 % thymolphthalein, 0.5% curcumin, Rainbow Indicator, 1% phenolphthalein)

The colour front increased on average about 8 % from 10 minutes readings to 3-4 hours (maximum 16%). No significant change occurred from 3-4 hours to 24 hours. However, after 24 hours, the colour of 0.1 thymolphthalein completely faded. Fig. 4 shows a good correlation ($R^2 > 0.98$) for all indicators, with the alkali border (\approx depth of carbonation) being indicated as expected: curcumin < phenolphthalein < thymolphthalein < Rainbow Indicator. The presented reading time were 3-4 hours. Fig. 4 d) shows the gradual carbonation front determined with TGA. From this, 0.1% thymolphthalein and the Rainbow indicator are the closest to the area where no further $\text{Ca}(\text{OH})_2$ decrease is measured.

Fig 4 a) also shows the results from Jung et al [25]. Here, the trend towards higher carbonation depths is more pronounced (29 % resp. 19 %) and the scatter is higher. Jung et al. investigated real bridges in Korea where the higher scatter can be explained by environmental effects (i.e. different moisture conditions of the bridges).

According to [18] the reading is to be done manually with a ruler. On the one hand this has the advantage that anomalies can be recorded consciously, on the other hand the accuracy can be increased by automatic reading, since no rastering is necessary.

To compare manual and automatic readings, the coefficient of variation (CoV) was determined for all results higher than 2 mm. This limit was chosen because the standard deviation below 2 mm was very high due to difficulties in manual readings. While the average CoV for the phenolphthalein experiments was 24 % for manual reading, it was reduced to 16 % by automatic reading using *PlotDigitalizer*.

4.2 LA-ICP-MS

Depending on the signal of the substance, a different colour is reproduced (high amount = red, low amount = blue, fig. 5 top). The scaling of the colours is done by assigning dark red to the maximum value of the respective measurement. The remaining colours are adjusted as a percentage with their proportion in relation to the maximum. This procedure can theoretically lead to the loss of substances with a generally small but practically relevant proportion if a disturbing artefact with high concentrations of the specific element is present. Fig. 5 shows two examples of the frequency distribution of Ca and C over the depth of concrete 2 (left), which was produced with calcitic aggregates and slag cement and concrete 19 (right). Concrete 19 contained OPC and quartzitic aggregates.

The Ca colour spectrum allows the aggregates to be easily separated from the cement matrix. The content of C between 10 and 12 mm decreases noticeably (from green to blue) in the cement matrix, so that the carbonation front can be observed. Phenolphthalein showed a colour change of 11 mm here. With quartzitic aggregates (Fig. 5 right), the differentiation was much more pronounced as the aggregate is free of carbon. Here, carbonation led to a change from dark red

to dark green while aggregates were blue. The change in C colour spectrum from red to green was in between 3.5 to 4.5 mm which was exactly the colour change determined with different colour indicators (phenolphthalein and curcumin 3.5, thymolphthalein 4.2 and Rainbow Indicator 4.3 mm).

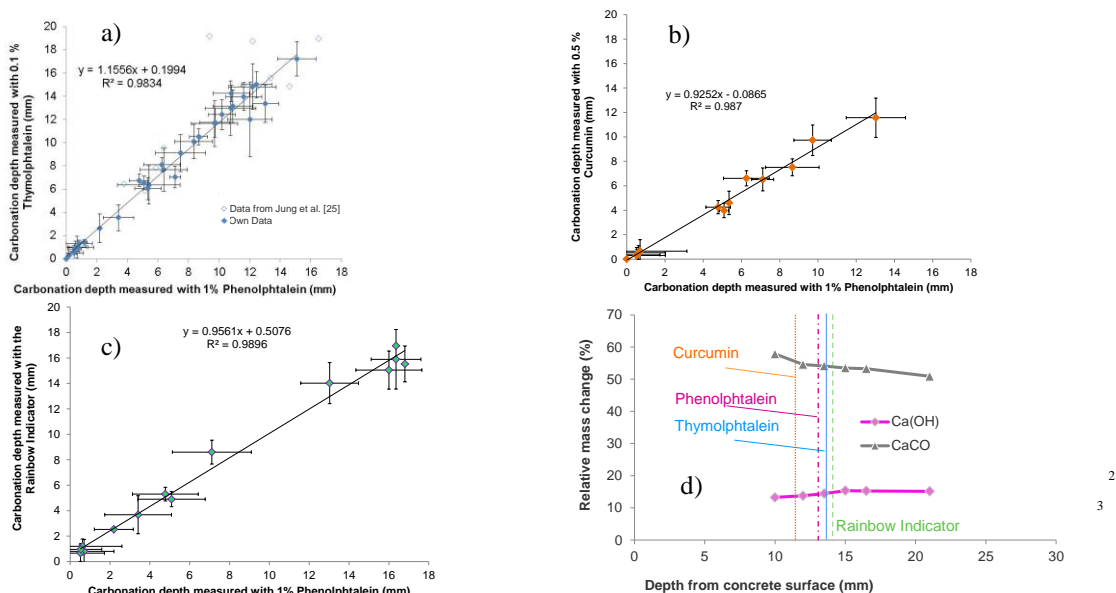


Figure 4: Correlation of carbonation depth measured with different methods: a) phenolphthalein vs. thymolphthalein, b) phenolphthalein vs. curcumin, c) phenolphthalein vs. Rainbow indicator, d) Comparison of TGA results measured at 9-11 mm, 11.5-12.5 mm, 13-14 mm, 14.5-15.5 mm, 16-17mm and 20-22 mm with different colour indicators

5. CONCLUSIONS

Choosing adequate methods depend on the desired results. In most cases, the use of several methods can compensate for the disadvantages of one. For example, TGA can be used to determine the amount of CaCO_3 formed, while the type of modification (calcite, vaterite or aragonite) can be determined with XRD. In addition, ^{29}Si -NMR is suitable to observe carbonation of the C-S-H-phases. Though it is very simple in regard to handling, inhomogeneities of the split surfaces (pores, cracks, aggregates) and the subjective choice of colour-border as well as too early readings affect the results of the colour indicator method.

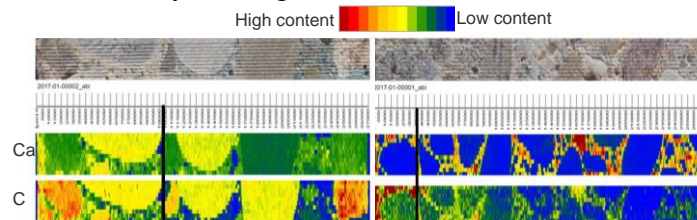


Fig. 5: La-ICP-MS measurements: Top to bottom: Colour scale, investigated concrete sample, Depth from surface (μm), Relative Ca content, Relative C content

From our measurements following conclusions can be drawn:

- Automatic readings helped to increase the accuracy for all colour indicators.
- Phenolphthalein underestimates the carbonation front by about 20 %.

- Carcinogenic phenolphthalein can be well substituted with 0.1 % thymolphthalein and 0.5 % curcumin without health risk.
- 0.1% thymolphthalein and the Rainbow Indicator are closer to the threshold value for rebar corrosion than 0.5 % curcumin and 1% phenolphthalein.
- LA-ICP-MS proofed to be a good method to determine the carbonation depth even in cementitious materials containing carbonates from other sources (i.e. limestone fillers or calcitic aggregates). Although our device is only suitable for laboratory samples, LIBS also showed promising alternatives for field use [34].

ACKNOWLEDGEMENTS

Marco Decker's, M. Sc. support for the LA-ICP-MS measurements as well as our discussions are greatly acknowledged. We thank A. Pollerspöck, L. Maier and K. Linz for their support in the practical work. Our sincere thanks go to TPA GmbH for providing most of the concrete specimens used.

REFERENCES

- [1] <https://www.climate.gov/news-features/understanding-climate/climate-change-atmospheric-carbon-dioxide> (02.09.2018).
- [2] Verein Deutscher Zementwerke e. V. 'Zahlen und Daten', Ed. (2018).
- [3] Auroy, M., Poyet, S., Le Bescop, P., Torrenti, J.-M., Charpentier T., Moskura, M. and Bourbon, X., 'Comparison between natural and accelerated carbonation (3% CO₂): Impact on mineralogy, microstructure, water retention and cracking,' *Cem Con Res* (109) (2018) 64-80.
- [4] Thiel C., 'Einfluss von CO₂-Druck und Betonfeuchtegehalt auf das Porengefüge des Betons während der Carbonatisierung' doctoral thesis, Technical University of Munich (in preparation)
- [5] Shah, V., Scrivener, K., Bhattacharjee, B. and Bishnoi, S., 'Changes in microstructure characteristics of cement paste on carbonation' *Cem Con Res* (109) (2018) 184–197.
- [6] Glasser, F. and Matschei, T., 'Interactions between portland cement and carbon dioxide' ICCI, Montreal (2007).
- [7] Bier, T., 'Karbonatisierung und Realkalisierung von Zementstein und Beton' doctoral thesis, Karlsruhe (1988).
- [8] Morandeau, A., Thiery, M., Faure, P., Platret, G., Bouteloup, J.-F., Dangla, P. and Baroghel-Bouny, V., 'Effect of carbonation on the microstructure and the moisture properties of cement-based materials', XII DBMC, Porto, Portugal, (2011).
- [9] Houst, Y.F and Wittmann, F.H., 'Influence of porosity and water content on the diffusivity of CO₂ and O₂ through hydrated cement paste, *Cem Con Res* **24** (6) (1994) 1165–1176.
- [10] Johannesson, B. and Utgenannt, P., 'Microstructural changes caused by carbonation of cement mortar' *Cem Con Res* **31** (6) (2001) 925–931.
- [11] Gruyaert, E., Van den Heede, P. and de Belie, N., 'Carbonation of slag concrete: effect of the cement replacement level and curing on the carbonation coefficient–effect of carbonation on the pore structure, *Cem Con Comp* **35** (1) (2013) 39–48.
- [12] Behnood, A., v. Tittelboom, K. and de Belie, N., 'Methods for measuring pH in concrete: A review' *Con Build Mat* (105) (2016) 176-188
- [13] Thiery, M., Villain, G., Dangla, P. And Platret, G., 'Investigation of the carbonation front shape on cementitious materials: Effects of the chemical kinetics' *Cem Con Res* (37) (2007) 1047–1058
- [14] Han, J., Sun, W. and Pan, G. 'X-ray microtomography of the carbonation front shape evolution of cement mortar and modeling of accelerated carbonation' *Reac J of Wuhan University of Technology-Mater Sci Ed* (2013) 303-308.

- [15] Castellote, M., Andrade, C., Turrillas, X., Campo, J. and Cuello, G.J., 'Accelerated carbonation of cement pastes in situ monitored by neutron diffraction' *Cem Con Res* (38) (2008) 1365-1373.
- [16] Galan, I., Sanchez, J., Andrade, C. and Evans, A., 'Carbonation profiles in cement paste analyzed by neutron diffraction' *J Phys Conf Ser* **340** (1) 1-6
- [17] Copuroglu, U., Schlangen, E. and Zhu, W., 'Effect of carbonation on the micro-mechanical properties and frost salt scaling of cement pastes: Experimental and modelling aspects' 2nd Int Symp on Advances in Concrete through Science and Engineering (2006), Quebec City, Canada
- [18] RILEM Committee TC56, 'Measurement of hardened concrete carbonation depth-CPC 18, *Mat Struc* **21** (126) (1988) 453-455.
- [19] <https://echa.europa.eu/substance-information/-/substanceinfo/100.000.914> (21.12.2018).
- [20] Chinchón-Payá, S., Andrade, C. and Chinchón, J.S., 'Indicator of carbonation front in concrete as substitute to phenolphthalein' *Cem Con Res* (82) (2016) 87-91.
- [21] Campbell, D.H., Sturm, R.D. and Kosmatka, S.H., 'Detecting Carbonation' *Concrete Technology Today* **12** (1) (1991) 1-5
- [22] Herrera, R., Kinrade, S.D. and Catalan, L. J. J., 'A comparison of methods for determining carbonation depth in fly-ash blended cement mortars' *Mat J* **112** (2) (2015) 287-294.
- [23] Lo, Y. and Lee, H.M., 'Curing effects on carbonation of concrete using a phenolphthalein indicator and Fourier-transform infrared spectroscopy' *Build Env* **37** (5) (2002) 507-514.
- [24] Schießl, P. 'Zur Frage der zulässigen Rissbreite und der erforderlichen Betondeckung im Stahlbetonbau unter besonderer Berücksichtigung der Karbonatisierung des Betons' Heft 255, Deutscher Ausschuss für Stahlbeton e.V., Beuth Verlag, Berlin, Deutschland, 1976.
- [25] Jung, W.-Y., Yoon, Y.-S. and Sohn, Y.-M., 'Predicting the remaining service life of land concrete by steel corrosion' *Cem Con Res* **33** (5) (2003) 663-677.
- [26] McPolin, D.O., Basheer, P.A., Long, A.E., Grattan, K.T. and Sun, T. 'New Test Method to Obtain pH Profiles due to Carbonation of Concretes Containing Supplementary Cementitious Materials' *J Mater Civ Eng* (19) (2007) 936-946.
- [27] Revert, A. B., De Weerd, K., Hornbostel, K. and Geiker, M.R. 'Investigation of the effect of partial replacement of Portland cement by fly ash on carbonation using TGA and SEM-EDS', Int. RILEM Conf. on Materials, Systems and Structures in Civil Eng., Lyngby, Denmark (2016) 413-422.
- [28] Bensted, J. 'Raman spectral studies of carbonation phenomena' *Cem. Concr. Res.* (7) (1977) 161-164.
- [29] Rossen, J. E. and Scrivener, K., 'Optimization of SEM-EDS to determine the C-A-S-H composition in matured cement paste samples' *Mat Char* (123) (2016) DOI: 10.1016/j.matchar.2016.11.04.
- [30] Castellote, M. Fernandez, L., Andrade, C. and Alonso, C., 'Chemical changes and phase analysis of OPC pastes carbonated at different CO₂ concentrations' *Mat Struct* (42) (2009) 515-525.
- [31] Sevelsted, T. F. and Skibsted, J. , 'Carbonation of C-S-H and C-A-S-H samples studied by ¹³C, ²⁷Al and ²⁹Si MAS NMR spectroscopy', *Cem Con Res* (71) (2015) 56-65.
- [32] Saumann, Z. 'Carbonization of porous concrete and its main binding components' *Cem Con Res* **1** (6) (1971) 645-662.
- [33] <http://www.bcp.fu-berlin.de/chemie/chemie/sicherheit/sicherheit/ersatzstoffe/index.html> (06.09.2018).
- [34] Eto, S., Matsuo, T., Matsumura, T., Fujii, T. and Tanaka, M.Y., 'Quantitative estimation of carbonation and chloride penetration in reinforced concrete by laser-induced breakdown spectroscopy' *Spectrochimica Acta Part B: Atomic Spectroscopy* **101** (1) (2014) 245-253.

CONSTRUCTION AND DEMOLITION WASTE AS AN ADDITION IN NEW CEMENTS. EFFECT ON CARBONATION

C. Medina (1+), I.F. Sáez del Bosque (1), E. Asensio (2), M. Frías (2+) and M. I. Sánchez de Rojas (2+)

(1) Polytechnical School, Cáceres. University of Extremadura. University Institute of Research on Sustainable Regional Development (INTERRA)

(2) Department of Materials Recycling, Eduardo Torroja Institute for Construction Science, (National Research Council) Madrid, Spain

+ SOSMAT (UEX-CSIC) Associated Research Unit

Abstract

In recent decades the cement industry has sought new additions to reduce the clinker content and CO₂ emissions in cement manufacture. That pursuit has roused growing interest in the international scientific community around how the durability of these new cements may be affected by the use of industrial waste from steel mills, construction and demolition or others as supplementary cementitious materials. Particular attention has focused on carbonation, which induces concrete reinforcement corrosion.

That type of decay merits attention, for approximately two-thirds of the existing concrete structures are exposed to environments where carbonation is a real risk. This study analysed the viability of designing new eco-efficient cements with 25 wt% construction and demolition waste from a dual perspective: their mechanical performance and their durability when exposed to natural carbonation. The research consisted in testing the compressive and flexural strength in 28 day 4x4x16 cm³ mortar specimens and the same parameters after 3 months and 6 months of natural carbonation, as described in Spanish standard UNE 83993-1.

The findings showed that irrespective of the type of waste, the specimens complied with the mechanical requirements laid down in European standard EN 197-1. Carbonation was observed to penetrate the additioned specimens more deeply than the control, as reported for cement bearing standardised additions such as blast furnace slag and fly ash.

Keywords: construction and demolition waste, carbonation depth, mechanical strength, supplementary cementitious materials

1. INTRODUCTION

The ‘take-make-use-dispose’ linear model presently in place in developed economies is neither sustainable over time nor aligned with today’s socioeconomic context. The European Union has consequently passed legislation to further a circular model based on prevention, reduction, reuse and recycling to minimise environmental impact, lengthen materials’ life cycle and use waste as a secondary raw material, thereby contributing to sustainable development [1].

Traditional cement manufacture has been deemed to be scantily respectful of the environment due to the large volumes of natural resources and energy consumed in the process, not to mention the CO₂ emissions generated, which presently account for 7 % of the worldwide anthropogenic total [2].

That has driven the industry to undertake huge efforts in recent decades to design new cements with alternative inputs, known as supplementary cementitious materials (SCMs). Much research has been conducted the world over to analyse the viability of valorising industrial waste, primarily from the construction, fired clay (or ceramic), agroforestry, steelmaking and ornamental stone industries as raw materials for construction.

The first group, construction and demolition waste, is a source of huge quantities of debris. According to the European Commission’s Environment, Maritime Affairs and Fisheries policy area, despite the crisis affecting the industry in recent years, the Union generates a mean of 820 x 10⁶ tonnes of such waste yearly [3], adding to the 500 x 10⁶ tonnes produced in the United States and the 1.13 x 10⁹ tonnes in China [4].

Recent research has analysed the viability of valorising construction and demolition waste (C&DW) as a raw material in the design and manufacture new eco-efficient binders. Two major applications have been defined: as fine or coarse aggregates in sustainable concrete [5], mortar or other civil construction applications and as a partial cement replacement in new cements [6, 7].

In the latter vein, the authors of this article showed in earlier studies that C&DW is apt for use as an active addition. On the grounds of its composition (SiO₂ (reactive SiO₂ > 25 %) + Al₂O₃ + Fe₂O₃ > 70 %), it can be deemed a natural burnt pozzolan [8] with activity comparable to that of other widely used industrial by-products such as silica fume, metakaolin, rice husk ash and coal fly ash.

The research conducted worldwide to date on the valorisation of such waste in cement is sparse and focuses primarily on mechanical strength or sulfate resistance. No studies have yet been published on its resistance to carbonation.

Information in that regard is imperative to predicting the service life of new cement-bearing concrete structures exposed to environments where reinforcement corrosion is associated with carbonation (XC exposure classes).

This study assesses the flexural and compressive strength and carbonation penetrability of new cements in which 25 % of the OPC was replaced by ceramic or concrete C&DW-based supplementary cementitious materials (SCMs).

2. MATERIALS AND METHODOLOGY

2.1 Materials

Two types of construction and demolition waste were used: fired clay (ceramic) waste, here denominated CrW, consisting in partition and enclosure wall waste, and mixed waste or C_HW,

comprising ≥ 80 % concrete and ≤ 20 % ceramic materials. Both were pre-conditioned to a particle size of under $63 \mu\text{m}$.

In addition to the main constituent, SiO_2 (>48.49 %), both contained other acidic oxides such as Al_2O_3 (>10.26 %) and Fe_2O_3 (>2.45 %), present as well in other pozzolanic materials [8]. Both materials also had a reactive silica content of over 25 %, the threshold value laid down in European standard EN 197-1 [9] for a material to be deemed pozzolanic. The mineralogical phases present included, most prominently, illite, quartz, orthoclase, anorthite, calcite, dolomite and hematite [8].

When assessed for pozzolanicity with an accelerated method [10], this waste fixed ~ 75 % of the lime present in solution within 28 d, exhibiting activity slightly higher than found in fly ash (~ 40 %) [8].

The ordinary grey CEM I 42.5 R-type cement (OPC) used and supplied by the Lafarge-Holcim plant located at Toledo, Spain, was EN 197-1 [9] -compliant in every respect.

The 25 % CrW or $\text{C}_\text{H}\text{W}$ and 75 % OPC materials were blended in a shaker-mixer to ensure uniformity and respectively labelled OPC-CrW and OPC- $\text{C}_\text{H}\text{W}$.

2.2 Methodology

The procedure described in European standard EN 196-3 [11] was followed to determine the initial setting times for the new materials with a Vicat needle.

Normal consistency cement paste was tested with a Le Chatelier analyser, likewise as specified in the aforementioned European standard [11], to establish its soundness.

The effect of the inclusion of the C&DW on the compressive and three-point flexural strengths of the new eco-efficient materials was assessed pursuant to European standard EN 196-1 [12]. The $4 \times 4 \times 16 \text{ cm}^3$ mortar specimens tested for compressive and flexural strength were prepared with a sand/cement ratio of 3/1 and a water/cement ratio of 1/2. Twenty-four hours after preparation they were removed from the moulds and cured at a temperature of 20 ± 1 °C and a relative humidity of 100 % until tested.

CO_2 permeability was determined using the natural carbonation method described in European standard CEN/TS 12390-10 [13] and Spanish standard UNE 83993 [14], in which the actual environmental conditions to which the material is exposed are reproduced.

After curing for 28 d, the $4 \times 4 \times 16 \text{ cm}^3$ specimens used for this set of tests were stored in laboratory conditions (20 ± 2 °C and 65 % to 75 % RH) for 7 d and subsequently exposed to the outdoor environment for 90 d or 180 d, albeit under cover from the rain. The mean CO_2 concentration during the test periods was 400 ppm. The exposure conditions are depicted in Figure 1.

The specimens were tested for mechanical strength at the specified age, after which the mean and maximum carbonation depths were determined on the failed materials with the colorimetric method set out in Spanish standard UNE 112-011 [15]. Further to that method, the inner surface of the specimens was cleaned and sprayed with 1 g phenolphthalein dissolved in 70 % ethanol, an indicator that turns the non-carbonated concrete surface pinkish red while leaving the original colour of the carbonated surface unchanged.



Figure 1. Specimens exposed to outdoor environment

3. RESULTS

3.1 Physical properties

As the comparison of the initial setting times and expansion values for the new cements to the requirements laid down in European cement standard EN 197-1 (Table 1) clearly shows, the inclusion of the additions did not compromise binder compliance.

Table 1. Cement compliance with standard-required initial setting time and soundness

Cement	Initial setting time (min)	Expansion (mm)
OPC	165	1
OPC-CrW	160	1
OPC-C _H W	155	1
EN 197-1 requirement [9]	≥ 60	≤ 10

OPC replacement with the C&DW-based SCMs was observed to shorten the initial setting time by 3.03 % in OPC-CrW and 6.06 % in C_HW relative to OPC. That slight acceleration in hydration might be associated with the initial filler effect attributable to the fine particle size of the SCMs.

The inclusion of C&DW in the cements induced no change in post-setting cement soundness (=expansion), for the value was the same as observed for the conventional OPC.

3.2 Mechanical properties

As the 7 d and 28 d compressive strength values plotted in Figure 2 show, the latter were consistently greater than or equal to 42.5 MPa (42.5 N and 42.5 R), denoting compliance with the mechanical specifications set out in EN 197-1 for 42.5 MPa strength class cements.

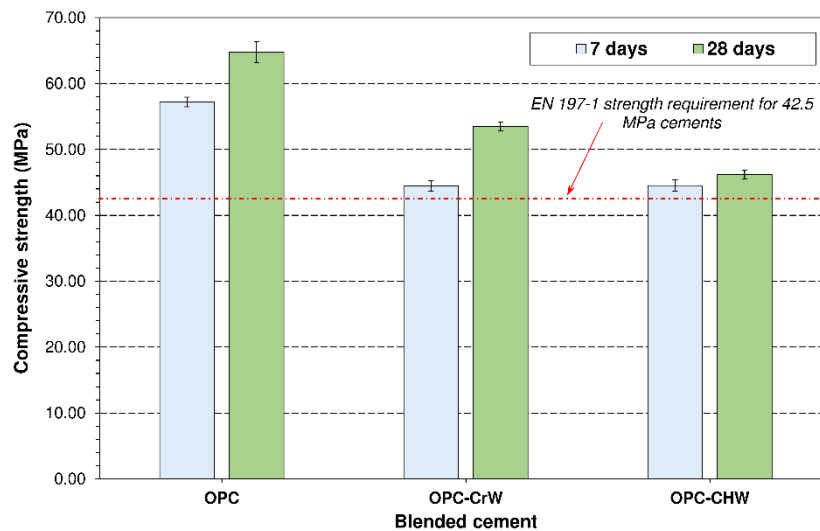


Figure 2. Compressive strength of the cements studied (average value = bars \pm standard deviation)

The figure also shows that strength declined by 17.44 % in OPC-CrW and 28.71 % in C_{HW} relative to the reference OPC. That difference in performance between the two was related to their respective pozzolanicity: Asensio et al. [8] observed CrW to fix more lime than C_{HW} .

3.3 Carbonation

Irrespective of the type of cement, compressive strength rose with exposure time (Figure 3), more steeply in OPC-CrW and OPC- C_{HW} due to the greater intensity of carbonation taking place in the new blended cements (Table 2). That effect was due to the decalcification attendant upon carbonation, primarily of the portlandite in the outer layers. The chemical reaction involved induced the precipitation of small rhomboid calcite crystals which reduced the number of macropores, the fraction with the most adverse effects on mechanical performance [17], and with it total porosity. The ultimate outcome was a more refined pore structure, as reported earlier by Leemann et al. [18].

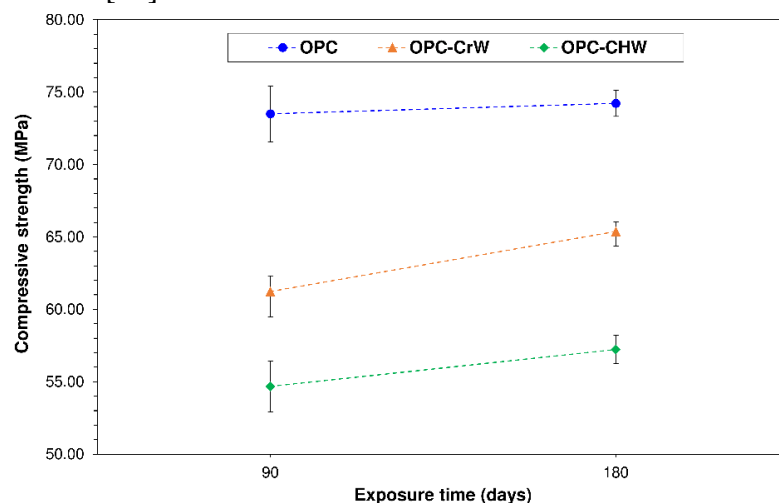


Figure 3. Compressive strength after exposure to CO_2

According to the mean and maximum carbonation depth data in Table 2, the presence of C&DW in the mortars tested induced a rise in CO₂ permeability, with increases over the OPC value in the 180 d means of +0.12 mm for OPC-CrW and +0.17 mm for C_HW. The same trend was observed for the maximum CO₂ penetration depth.

Table 2. Mean and maximum carbonation depth

Cement type	Mean depth (mm)		Maximum depth (mm)	
	90 d	180 d	90 d	180 d
OPC	0.10	0.10	0.26	0.30
OPC-CrW	0.13	0.22	0.34	0.36
OPC-C _H W	0.12	0.27	0.44	0.48

The pozzolanic reaction mediated by the addition and the dilution concomitant with cement replacement reduced the amount of portlandite available to react with the CO₂. That in turn raised the likelihood of its penetration, explaining the slight rises observed [19, 20]. Moreover, in concretes made with cements bearing replacements, deeper carbonation is attributable not only to the dilution associated with the smaller amount of clinker. These new cements generally require a longer curing time than CEM I-type OPC, resulting in the absence of the addition-mediated pozzolanicity that fills pores with its reaction products (depending on the addition) [21].

That pattern was consistent with the results reported by earlier authors [22] who, replacing 25 % of the cement used to manufacture concrete with fly ash (FA) or ground granulated blast furnace slag (GGBFS), found the carbonation front to be +6.7 mm deeper in FA and +10.9 mm in GGBFS than in the reference material.

The carbonation fronts (uncoloured areas) in the mortars made with OPC, OPC-CrW and OPC-C_HW cements depicted in Figure 4 clearly show that CO₂ diffusion was greater in the mortars containing 25 % C&DW-bearing cement, irrespective of the type of waste involved.

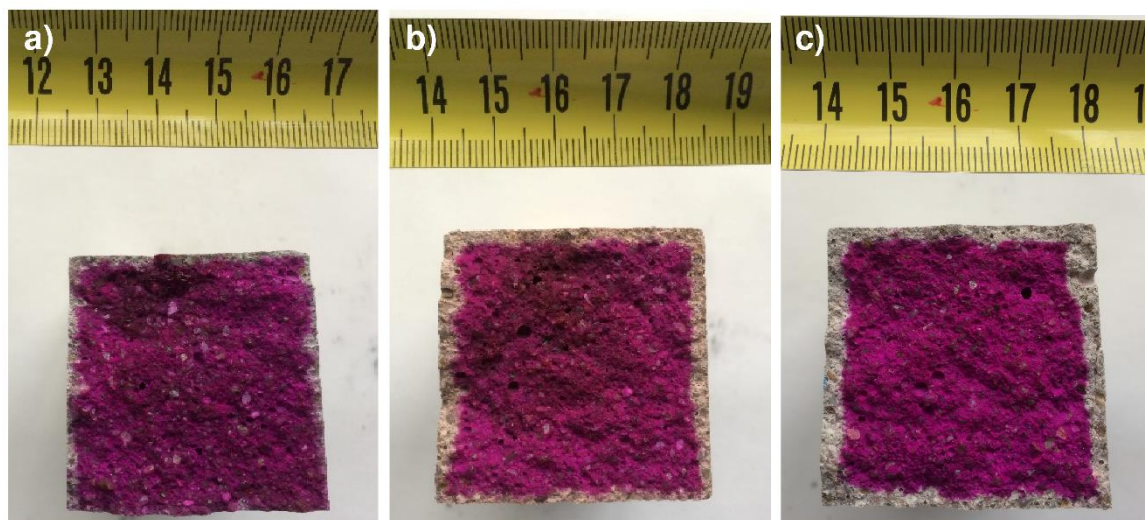


Figure 4. Carbonation front: a) OPC; b) OPC-CrW; c) OPC-C_HW

4. CONCLUSIONS

The following conclusions can be drawn from this study.

- As the replacement of OPC with 25 % construction and demolition waste-based SCMs does not adversely affect cement soundness or initial setting time, the new materials are EN 197-1-compliant.
- The new cements exhibit 28 d compressive strengths higher than the 42.5 MPa required by EN 197-1 for 42.5 R class cements.
- The inclusion of the additions induces greater mean and maximum carbonation depths.
- Further study of later age carbonation would be required to predict the rate of advancement and estimate the service life of reinforced concretes made with new eco-efficient cements.

ACKNOWLEDGEMENTS

This study was funded under European Regional Development Fund (ERDF) Interreg-POCTEP research grant 0008_ECO2CIR_4_E, Spanish Ministry of Science and Innovation under project BIA2016-76643-C3-1-R and grant GR 18122 awarded to the MATERIA Research Group by the Regional Government of Extremadura and the European Regional Development Fund, ERDF.

REFERENCES

- [1] J. Korhonen, A. Honkasalo, J. Seppälä, Circular Economy: The Concept and its Limitations, *Ecological Economics*, 143 (2018) 37-46.
- [2] C.-Y. Zhang, R. Han, B. Yu, Y.-M. Wei, Accounting process-related CO₂ emissions from global cement production under Shared Socioeconomic Pathways, *Journal of Cleaner Production*, 184 (2018) 451-465.
- [3] J.-L. Gálvez-Martos, D. Styles, H. Schoenberger, B. Zeschmar-Lahl, Construction and demolition waste best management practice in Europe, *Resources, Conservation and Recycling*, 136 (2018) 166-178.
- [4] A. Akhtar, A.K. Sarmah, Construction and demolition waste generation and properties of recycled aggregate concrete: A global perspective, *Journal of Cleaner Production*, 186 (2018) 262-281.
- [5] V.W.Y. Tam, M. Soomro, A.C.J. Evangelista, A review of recycled aggregate in concrete applications (2000–2017), *Construction and Building Materials*, 172 (2018) 272-292.
- [6] E. Asensio, C. Medina, M. Frías, M.I. Sánchez de Rojas, Use of clay-based construction and demolition waste as additions in the design of new low and very low heat of hydration cements, *Materials and Structures*, 51 (2018) 101.
- [7] E. Asensio de Lucas, C. Medina, M. Frías, M.I. Sánchez de Rojas, Clay-based construction and demolition waste as a pozzolanic addition in blended cements. Effect on sulfate resistance, *Construction and Building Materials*, 127 (2016) 950-958.
- [8] E. Asensio, C. Medina, M. Frías, S. Rojas María Isabel, Characterization of Ceramic-Based Construction and Demolition Waste: Use as Pozzolan in Cements, *Journal of the American Ceramic Society*, 99 (2016) 4121-4127.
- [9] European Committee for Standardization, EN 197-1. Cement. Composition, specifications and conformity criteria for common cements.

- [10] M.I. Sánchez de Rojas, F. Marin, J. Rivera, M. Frias, Morphology and properties in blended cements with ceramic wastes as a pozzolanic material, *Journal of the American Ceramic Society*, 89 (2006) 3701-3705.
- [11] European Committee for Standardization, EN 196-3. Methods of testing cement - Part 3: Determination of setting times and soundness.
- [12] European Committee for Standardization, EN 196-1. Methods of testing cement - Part 1: Determination of strength.
- [13] European Committee for Standardization, CEN/TS 12390-10: Testing hardened concrete. Determination of the relative carbonation resistance of concrete.
- [14] Spanish Committee for Standardization, UNE 83993-1:2009. Durability of concrete. Test method. Measurement of carbonation penetration rate in hardened concrete. Part 1: Natural method.
- [15] Spanish Committee for Standardization, UNE 112011. Corrosion of concrete reinforcement steel. Determination of the carbonation depth for in-service concrete.
- [16] H.F.W. Taylor, *Cement Chemistry*, Second Edition ed., Thomas Telford Publishing, London, 1997.
- [17] P. Kumar Metha, P.J.M. Monteiro, *CONCRETE: Microstructure, Properties and Materials*, Third Edition ed., McGraw-Hill, United States of America, 2006.
- [18] A. Leemann, H. Pahlke, R. Loser, F. Winnefeld, Carbonation resistance of mortar produced with alternative cements, *Materials and Structures*, 51 (2018) 114.
- [19] N. Singh, S.P. Singh, Carbonation and electrical resistance of self compacting concrete made with recycled concrete aggregates and metakaolin, *Construction and Building Materials*, 121 (2016) 400-409.
- [20] V. Shah, S. Bishnoi, Carbonation resistance of cements containing supplementary cementitious materials and its relation to various parameters of concrete, *Construction and Building Materials*, 178 (2018) 219-232.
- [21] S.O. Ekololu, Model for practical prediction of natural carbonation in reinforced concrete: Part 1-formulation, *Cement & Concrete Composites*, 86 (2018) 40-56.
- [22] A.B. Ribeiro, T. Santos, A. Gonçalves, Performance of concrete exposed to natural carbonation: Use of the k-value concept, *Construction and Building Materials*, 175 (2018) 360-370.

INFLUENCE OF EXPOSURE ENVIRONMENTS ON THE CARBONATION RESISTANCE OF CONCRETE STRUCTURES

A.AL-Ameeri (1,2) M. I. Rafiq (1) and O.Tsioulou (1)

(1) School of Environment and Technology, University of Brighton, Brighton, UK.

(2) Engineering College, University of Babylon, Babylon, Iraq.

Abstract

There is agreement that the greenhouse gases, in term of CO₂ emissions, are the main contributor to global warming. Increasing atmospheric CO₂ emissions are likely to increase the average of maximum temperature and reduce the relative humidity, RH. These changes in CO₂ concentration, temperature and RH have considerable impacts on the durability of concrete structures, in particular, the carbonation rate, chloride penetration, and corrosion rate.

This study aims to investigate the potential impact of temperature, relative humidity and permeation properties on the carbonation resistance or depth of carbonation (DoC). The study programme involves casting samples with different water-cement ratio (w/c), 0.4, 0.5 and 0.6. These samples exposed to different temperatures of 25, 35 and 45°C and three levels of humidity 65, 75 and 85 %. Carbonation depth was determined using an accelerated environment test programme based experimentally on the BS EN13295:2004 by phenolphthalein indicator. The results have indicated that (i): The depth of carbonation (DoC) increased with the increase in water-cement ratio under different exposure environments. (ii): There is a considerable influence of relative humidity and relative increase in temperature on the carbonation depth in concrete structures. Finally, the permeation properties for all mixes used of concrete, porosity and gas permeability has a significant impact of DoC.

Keywords: Carbonation, Phenolphthalein indicator, temperature, and Relative humidity.

1. INTRODUCTION

Carbonation is the chemical reaction between carbonic acid (H₂CO₃), resulting from a combination of atmospheric carbon dioxide (CO₂) with water, and calcium ion (Ca²⁺) from dissolution of hydrated cement products such as calcium hydroxide Ca(OH)₂, calcium silicate hydrates (C-S-H) and calcium aluminates hydrates (C-A-H). The calcium carbonate (CaCO₃) is formed from this reaction [1, 2]. The carbonation resistance of concrete structures is controlled by their capacity to delay ion and fluid transport inside concrete. The transport properties of fluid into concrete are represented through permeability and cracks. The permeability is influenced by variation of the material composition of concrete, such as quantity

of cement, water cement ratio w/c, curing period, type of cement and type and dosage of chemical admixtures [1, 3]. The carbonation is a function of the pore system of the hardened cement paste due to the diffusion of CO₂ in concrete structures [1]. The second significant factor affecting transport properties is cracks. The cracks in concrete structures are predictable in reinforced concrete members due to the weakness of tension capacity in concrete. Carbonation rates in the vicinity of the cracks are considerably higher due to the relatively faster penetration of CO₂ into the crack followed by orthogonal outward diffusion into the un-cracked concrete surrounding the crack [4]. On the other hand, the exposure environments, carbon dioxide, temperature, and relative humidity, have a considerable impact on the carbonation rate of concrete structures [5]. Chi et al. [6] observed a linear correlation between the increase in the CO₂ concentration and the increase in the rate of carbonation. Roy et al. [7] concluded that there is a significant increase in carbonation rate when relative humidity, RH, ranges between 52-75%. However, there is a reduction in it as the relative humidity increases up to 84%. There is again an increase in carbonation depth; which begins at 84% RH upwardly until 92%. The maximum rate of carbonation in different mixes used in his study was found for a relative humidity level of 92%. It seems that the causes of this abnormal behaviour at the higher humidity level were unknown at that time. Russell et al. [8] demonstrated that the peak of the carbonation rate is reached at a relative humidity range of 55-65%. There are high variations in carbonation rate in the previous two studies [8, 9] for the same w/c ratio 0.55 and 0.7. Roy et al. [7] found the carbonation rates are 10.89 and 15.5(mm/y^{0.5}) respectively, while Russell et al. [9] got the carbonation rates are 32.3 and 79 (mm/y^{0.5}).

Finally, Drouet et al. [9] tested two hardened cement pastes using 100% CO₂ at different temperature and relative humidity (RH) levels and concluded that the impact of temperature on carbonation rate is dependent on the types of cement. It was also concluded that the decrease in RH causes an increase in carbonation rate. The changes in the mineralogy of cement products due to carbonation is not the same in high concentration CO₂ environment (10 - 100%). The results in a microstructure are not like those corresponding to natural carbonation at 0.03% of CO₂ [10].

Even though there is a chemical explanation about the temperature dependence of the diffusion coefficient based on an Arrhenius Equation [5,11,12], investigations on the effect of temperature on DoC scarce in the literature.

Consequently, the exposure environments, permeability, and cracks in concrete have influenced the diffusivity of aggressive species (CO₂) affecting durability. Therefore, it is important to study and consider how the exposure environments, the permeability and the presence of cracks may affect the rate of carbonation in concrete structures. Finally, the present paper examines the effect of external factors, temperature and RH, and internal parameters, porosity and cracks width on the depth of carbonation (DoC) what extent can this concrete resist the carbon dioxide attack.

2. EXPERIMENTAL WORK

2.1 Materials

Portland Limestone cement (CEM II/A-LL 32,5R) with a specific gravity of 3.05 was used in this study. Chemical and physical properties of the cement satisfy the BS EN 197-part 1: 2011. Natural sand was used as fine aggregates, and coarse aggregate was crushed gravel with a size range of 5-14 mm. The grain size analysis, chloride and sulphate content satisfy BS

882:1983. Deformed or ribbed steel (8mm) are used to reinforce the concrete prisms (to achieve the crack in samples).

2.2 Concrete Mixes Design

In order to achieve various properties of concrete, different water to cement ratios were used. Building Research Establishment method was employed to design the mixes used in this study. The mix proportions (water, cement, sand and gravel) were (205:513:653:980) kg/m³, (205:410:711:1023) kg/m³ and (205:350:711:1041) kg/m³ of concrete for mixes M 0.4 , M 0.5 and M 0.6 respectively. The mixing method is important to obtain the required workability and homogeneity of the concrete mix by mechanical mixing. The flexural method was used to induce the cracks, reinforced concrete prisms were used by fixing reinforcement in moulds with concrete cover 2 cm. Samples were cast in two layers. Each layer was vibrated using an electrical vibrating device to achieve the homogenous concrete and avoid the segregation of concrete. The specimens were demoulded and cured in a sink filled up with tap water until the time of testing or exposure to CO₂ environment condition at the age of 28 days.

2.3 Methodology

The main objective of the study is to investigate the effect of exposure environments, the permeability and crack width on the carbonation in concrete structures. Cracked concrete prisms were designed and exposed to these parameters of carbonation environment, temperature, and relative humidity. The flexural method was employed to induce the cracks in concrete samples. Four different crack width ranges, (0, 0.05-0.15mm, 0.15-0.25mm and 0.25-0.35mm) were applied to 100*100*500 mm concrete prisms. The crack width was measured by microscope meter with accuracy 0.01 mm. In this study, the one face of the specimens were exposed to accelerated environment conditions in a CO₂ incubator under the different scenarios.

Three relative humidity level (65, 75 and 85) and three temperature degree (25, 35 and 45) have been separately used with 5% CO₂ for all series.

All samples were exposed to accelerated environment conditions in a CO₂ incubator with 5% concentration for 8 weeks. This concentration has the same mineral –change in the microstructure of cement due to carbonation to the natural condition [7]. After exposure, the samples were split by compression machine into two parts. The parts were sprayed by phenolphthalein solution with one gram of phenolphthalein powder and dissolved into a solution of 70 ml and 30 ml of ethanol and deionized water respectively (CEN/TS 12390-10:2007) to measure (DoC).

2.4 Concrete Samples Tests

For all specimens, compressive strength, porosity, gas permeability, and carbonation depth were measured. The porosity, gas permeability, and compressive strength test were performed in accordance with ASTM C642:2013, RILEM TC-116-PCD-1999 and BS EN 12390, part 3:2000 respectively by using 100 mm cube specimens. The test procedure is given in CEN/TS 12390-10:2007 was used to determine the DoC by phenolphthalein indicator using 100 × 100 × 500 mm prisms.

3. RESULTS AND DISCUSSION OF TESTS

In this section, the results of the experimental works are presented and discussed. These results and their discussions are mainly focused on three aspects; the impact of temperature and relative humidity with different w/c ratio and crack width on DoC.

3.1 Effect of w/c ratio and crack width on Gas permeability

Gas permeability test was used to evaluate the microstructure and permeation properties of concrete (e.g., permeability, sorptivity, and diffusivity) [13, 14]. The values of gas permeability coefficient or Darcy's factor, K for the various types of concrete are shown in Table 1. The K' increased with the increase w/c ratio and crack width, as presented in Table 3. The results are indicated that the K value increases by increasing the w/c ratio for sound and cracked concrete. This increase of K values for concrete results from the increase in the volume of connected voids in the microstructure of concrete or the porosity of concrete due to w/c ratio [15]. On the other hand, cracked samples can increase permeation properties that lead to increase gas permeability coefficient as well.

Table 1: Effect of crack width and types of mixes on gas permeability

Crack width mm	Gas permeability coefficient, K, $\cdot 10^{-17}$, m ²		
	M 0.4	M 0.5	M 0.6
Un-cracked	6.1	7.1	10.6
0.05- 0.15	10.3	12.7	14.8
0.15 - 0.25	12.4	14.2	16.4
0.25- 0.35	12.6	14.7	16.7

3.2 Effect of relative humidity on Carbonation Depth in Concrete

The depth of carbonation (DoC) is a measure of diffusivity of carbon dioxide in concrete and reduction of alkalinity of pore water solution in concrete. The phenolphthalein solution was used to indicate DoC (CEN/TS 12390-10:2007). It is sprayed on concrete. In non-carbonated parts of concrete, the colour of these parts ranges from purple to red, due to concrete is still highly alkaline pH is greater than 9. While, the carbonated parts of concrete, the alkalinity is reduced, no colouration happened due to converting the Ca (OH)₂ to calcium carbonate by reacting with carbonate ion (CO₃²⁻). These samples have been exposed to three targets of relative humidity, 65 %, 75% and 85% with accelerated CO₂ environment 5% and temperature 25°C. The DoCs of all cases with different cracks width over the 8-week period are illustrated in Figure 1 (a, b and c) and presented samples are shown in Figure 2(a, b and c). The overall trend in these figures is that of decreasing DoC with increasing RH. However, the DoC does not appear to change at a constant rate over the range of RH investigated. For almost all of the samples with different cracks width and w/c, the maximum carbonation depth occurred at 65% target RH. On the other hand, there are two cases unlike the general trend due to other factors might have influenced the DoC at this RH values such as crack width. Also, the results indicated the (DoC) in concrete increases with increasing w/c ratio with different RH and crack width, the percentage increases in (DoC) for samples (sound and cracked) with respect to the control concrete samples (M 0.4 mixes) are presented in Table 2.

Also, the increase of w/c ratio leads also to increase the porosity in concrete and decrease compressive strength of concrete. According to Roy et al. [8], the rate of carbonation is

inversely proportional to the strength. The porosity and compressive strength of concrete have a significant impact on carbonation depth.

The results show the RH affects the DoC, the effect is not the same for all the mixes investigated. The effect of w/c ratio on DoC is the highest at 65% RH and is the least at 85% RH. This can be attributed to the fact that the pores are free of moisture at low RH, i.e. the impact of open porosity is gotten at the low RH. Overall the tendency of declining DoC with increasing RH within this range is like that which could be expected. However, what the results show is that there is a wide range of variability depending on the mix proportions and the quality of the concrete [8,9].

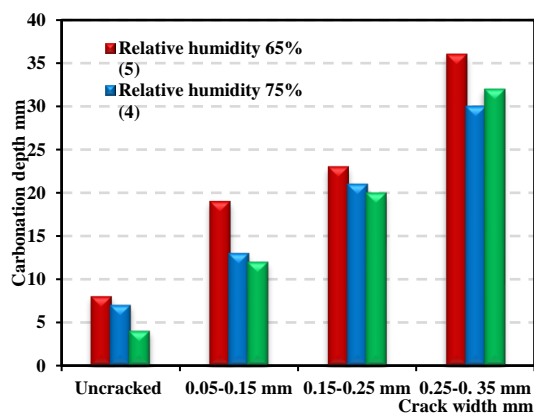


Figure 1-a: M 0.4 (w/c=0.4)

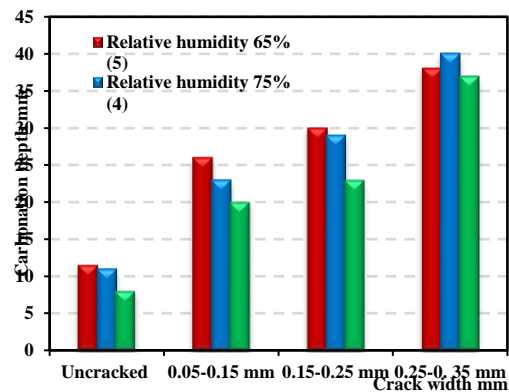


Figure 1-b: M 0.5 (w/c=0.5)

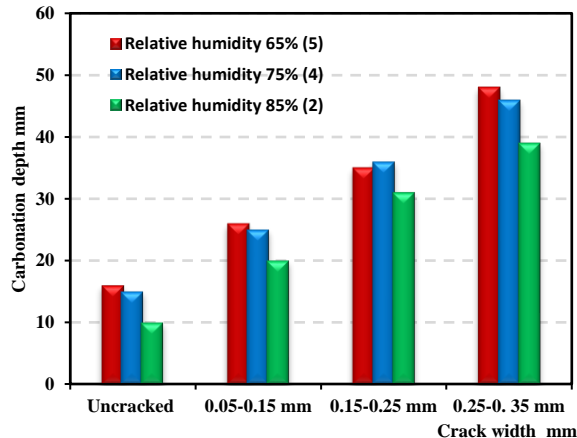


Figure 1-c: M 0.6 (w/c=0.6)

Figure 1: Effect of type of relative humidity on carbonation depth for different crack width in the concrete sample exposed to $T=25^{\circ}\text{C}$ and $\text{CO}_2=5\%$ for 8 weeks period.

(): Number of series that used in the study

The increase of (DoC) for concrete mixes with increasing the w/c ratio and crack width. That is a result the rise the porosity of concrete and volume of permeable voids which helps CO_2 to penetrate and react with water to form carbonate acid. The latter reacts with $\text{Ca}(\text{OH})_2$ (aq) to occur the carbonation [4,15] as shown in Figure 3. Furthermore, the fundamental influence controlling carbonation rate is the diffusivity of the hardened cement paste, which is a function of the pore system of the hardened cement paste during the period when the diffusion of CO_2 takes place [1].



Figure 2-a: M 0.6 , 65% RH



Figure 2-b: M 0.6 , 75% RH



Figure 2-c: M 0.6 , 85% RH

Figure 2: Effect of RH on DoC for M 0.6 – Uncracked, CO₂ 5% and T =25°C for 8 weeks

Table 2: Increase percentage in DoC with increase w/c ratio

Crack width mm	DoC of (M 0.5/ M 0.4) %			DoC of (M 0.6/ M 0.4) %		
	65% RH	75% RH	85% RH	65% RH	75% RH	85% RH
0	44	57	100	100	114	150
0.05- 0.15	37	77	67	37	92	67
0.15 - 0.25	30	38	15	52	71	55
0.25- 0.35	6	33	16	33	53	22

3.3 Effect of Temperature on Carbonation Depth in Concrete

The effect of the temperature on the DoC for M0.4, M0.5 and M0.6 for CO₂ 5% and RH 65% for 8 weeks, are presented in Figure 4. The samples were exposed to three different temperatures, 25°C, 35°C, and 45°C. Samples exposed to these conditions showed that the (DoC) increases with the temperature. Also, it was noted that when the samples were exposed to accelerated CO₂ condition at 45°C, the higher the w/c ratio in the samples' mix design, the less resistance of carbonation was found as shown in Figure 5 (a, b and c). Exposing at elevated temperatures altered the mineral composition of cement products due to carbonation and increased its depth in samples, but performance some of the cracked samples were not consistent with the un-cracked samples results. The results also show that the DoC in concrete increases with increasing w/c ratio with different temperatures and crack width, the percentage increases in DoC for samples (sound and cracked) with respect to the control concrete samples (M 0.4 mixes) are presented in Table 3.



Figure 4-a: M 0.6 , 25 °C T



Figure 4-b: M 0.6 , 35 °C T



Figure 4-c: M 0.6 , 45 °C T

Figure 4: Effect of temperature on DoC for M 0.6 - Uncracked, CO₂ 5% and RH 65% for 8 weeks

The effect of accelerating CO₂ condition with increase temperature encourages the diffusion of carbonate ion into concrete, due to amplified molecular activity and an increase in the reaction rate between carbonate ion CO₃⁻² and Ca²⁺ resulting from dissolve of H₂CO₃ and Ca (OH)₂ respectively in the pore water of concrete and forms CaCO₃ [11,12].

The main reason for the increase of DoC for concrete mixes with increasing the w/c ratio and crack width is the same reason as mentioned in the previous section. On the other hand, the increase of crack width was an important factor of CO₂ penetration, is deeper and reacting with Ca(OH)₂ to form carbonation compound, CaCO₃.

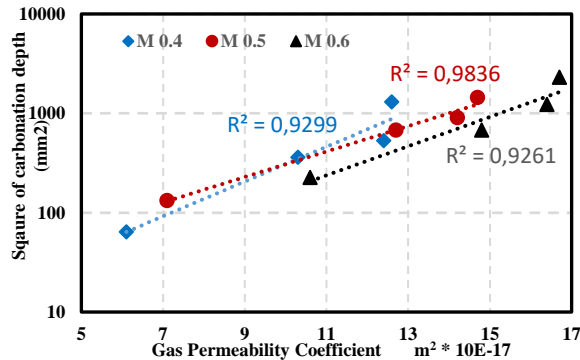


Figure 3: DoC in 5% CO₂, 65% RH and 25 °C as a function of concrete gas permeability

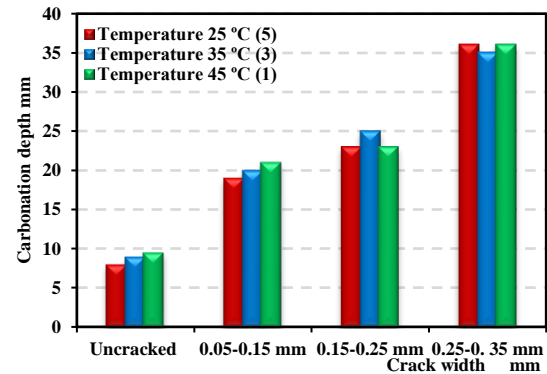


Figure 5- a:M 0.4

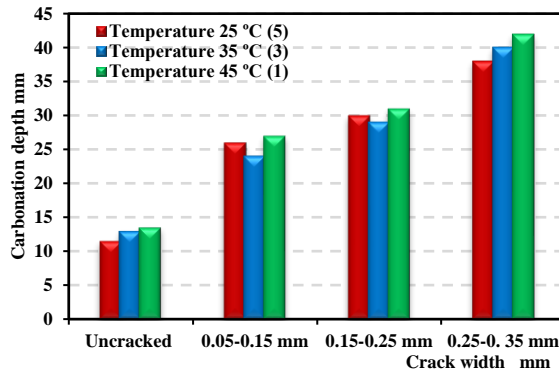


Figure 5-b:M 0.5

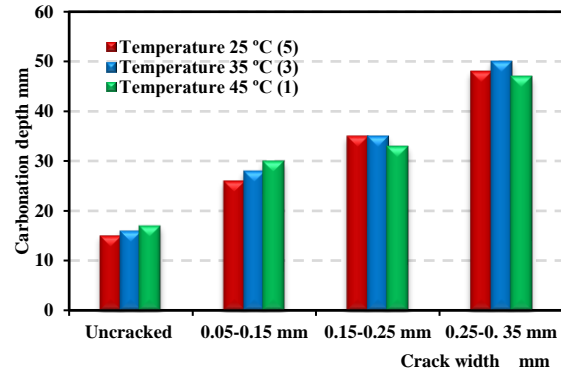


Figure 5-c: M 0.6

Figure 5: Effect of type of temperature on carbonation depth for different crack width in the concrete sample exposed to RH =65% and CO₂=5% for 8 weeks period

Table 3: Increase percentage in DoC with increase w/c ratio with temperature (T)

Crack width mm	DoC of (M 0.5/ M 0.4) %			DoC of (M 0.6/ M 0.4) %		
	T = 25 °C	T = 35 °C	T = 45 °C	T = 25 °C	T = 35 °C	T = 45 °C
0	44	44	42	88	78	79
0.05- 0.15	37	20	29	37	40	43
0.15 - 0.25	30	16	35	52	40	43
0.25- 0.35	6	14	17	33	43	31

4. CONCLUSION

This study has considered the influence of exposure environment and properties of concrete on the DoC in concrete structures. The effect of three level of RH, temperatures and w/c ratio

on DoC have been investigated by accelerated CO₂ environment condition. The following conclusions can be drawn from the results:

- For samples exposed to an accelerated CO₂ environment, increase in RH led to a reduction in the DoC.
- The increment in the temperature increased the DoC due to relatively fast penetration of CO₂ into the concrete and an increase in the reaction rate with cement products, which led to the formation of the carbonation compound CaCO₃.
- The DoCs in concrete samples are influenced by material behaviours such as the permeation properties (permeability and gas permeability) and compressive strength due to the impact of diffusivity of CO₂.
- The crack width significantly increased the DoC for mixes with different RH and temperature.

REFERENCES

- [1] Neville, A.M., 'Properties of concrete', Five and Truly Final Edn, (Pearson Education Limited, London,2011).
- [2] Tarun R. and Rakesh, K., 'Global warming and cement-based materials', (UWM Center for By-Products Utilization, Milwaukee, Wisconsin USA,2010).
- [3] AL-Khaiat, H., Haque, M. N., and Fattuhi, N., 'Concrete Carbonation in Arid Climate'. 29th Conference on our world in concrete & structure. Singapore, 2004.
- [4] AL-Ameeri, A., Rafiq, M., Tsioulou, O. 'Influence of cracks on the carbonation resistance of concrete structures', Proceedings of a Sixth International Conference on the Durability of Concrete Structures, Leeds, July 2018(University of Leeds) 358-367.
- [5] Dyer, A., 'Concrete durability', (Taylor& Francis Group, LLC, New York,2014).
- [6] Chi, J. M., Huang, R.and Yang, C. C., 'Effect of Carbonation on Mechanical Properties and Durability of Concrete Using Accelerating Testing Method', *Journal of Marine Science and Technology*, 10(1) (2002)14-20.
- [7] Roy, S, Poh, K and Northwood, D., 'Durability of concrete accelerated carbonation and weathering studies', *Building and Environment*, 34 (5) (1999) 486-595.
- [8] Russell, D., Basheer, M., Rankin, G., and Long, A., Effect of relative humidity and air permeability on the prediction of the rate of carbonation of concrete. Proceedings of the Institution of Civil Engineers - Structures and Buildings, 146 (3) (2001) 319-326.
- [9] Drouet, E., Poyet, S., Le Bescop, P., Torrenti, J.M. and Bourbon, X., 'Carbonation of hardened cement pastes: Influence of temperature'. *Cement and Concrete Research*, 115(2019) 445-459.
- [10] Castellote, M., Lorenzo Fernandez, L., Andrade, C., Alonso, C., 'Chemical changes and phase analysis of OPC pastes carbonated at different CO₂ concentrations'. *Materials and Structures*, Vol. 42(2009) 515–525.
- [11] Yoon, I., Copuroglu, O.and Park K., ' Effect of global climatic change on carbonation progress of concrete', *Atmospheric Environment*, 41(34) (2007)7274–7285.
- [12] Talukdar, S., Banthia, N., and Grace J., 'Carbonation in concrete infrastructure in the context of global climate change: Part 1 – Experimental results and model development', *Cement and Concrete Composites*, 34(8)(2012)924– 930.
- [13] Yang, K., Basheer, P.A.M., Magee, B., Bai, Y. and Long, A.E., Repeatability and reliability of new air and water permeability tests for assessing the durability of high-performance concrete. *Journal of Materials in Civil Engineering*, 27(12), (2015) 04015057.
- [14] Hilsdorf, H. and Kropp, J., Performance criteria for concrete durability. 2014, CRC Press.
- [15] RILEM TC 116-PCD-1999'measurement of the gas permeability of concrete - Cembureau Method', *Materials and Structures/Matériaux et Constructions*, Vol. 32, (April 1999) 174-179.

THE INFLUENCE OF CRACKS AND CARBONATION LEVEL ON THE SALT SCALING RESISTANCE OF NATURAL AND RECYCLED AGGREGATE CONCRETE

Vedran N. Carević (1), Ivan S. Ignjatović (1)

(1) Faculty of Civil Engineering, University of Belgrade, Serbia

Abstract

The use of recycled concrete aggregate (RCA) for the production of new concrete can be a promising solution for enormous use of raw materials, great energy consumption and large waste production. However, durability of recycle aggregate concrete (RAC) remains as an important issue regarding its sustainability. With relatively low tensile strength of concrete, the cracking of structural elements is almost inevitable due to the effect of load, so the influence of cracks on concrete durability also must be taken into consideration. Furthermore, the real environmental impact on concrete elements is not only one but a combination of different deterioration mechanisms. The influence of loading induced cracks (0.08 mm and 0.20 mm width) on natural or recycled aggregate concrete (NAC or RAC) resistance to salt scaling and the impact of previous carbonation on the salt scaling resistance of both concrete types was presented in this paper. Experimental results show that the presence of cracks on the concrete surface can increase the salt scaling resistance. Both the crack width and a number of cracks proved to be an important factor influencing concrete resistance to salt scaling. Also, it is shown that previous carbonation of RAC decreases the salt scaling resistance of concrete for more than 2.5 times.

Keywords: recycle aggregate concrete, cracks, salt scaling, carbonation

1. INTRODUCTION

Reuse of recycled concrete aggregate (RCA) for the production of new concrete can be a promising solution for the problem of enormous use of natural stone as aggregate. However, durability of recycle aggregate concrete (RAC) remains questionable. This is an important topic because durability is an increasing concern in the concrete industry. The existing models of deterioration mechanisms have been established on the basis of tests made on concrete with natural aggregate (Natural Aggregate Concrete – NAC). Due to the intensive development of

RAC, it is crucial to show that this type of concrete represents a viable alternative to NAC, which would lead to its greater use in practice.

Salt scaling is a result of freeze and thaw cycles with salt solution on the concrete surface. Damage caused in this way is progressive and consists of small flakes of binder (cement and supplementary cementitious material if used) with very few small aggregate parts removed. Since salt scaling damages concrete surface, mechanical properties of concrete will not be affected. However, this reduces the concrete cover which is the only barrier to prevent penetration of moisture and other harmful substances causing corrosion of reinforcement.

Factors that affect the resistance of the salt scaling of concrete are pore structure, concrete strength, water to cement ratio (w/c), degree of saturation, type of the used aggregate, quality of concrete finishing and type of mineral admixtures [1]. However, the amount of scaled material depends on the salt concentration in the solution, as well as the height of the solution on concrete surface [1].

Numerous tests have been dealing with this phenomenon on concrete samples without cracks. However, cracks damage the structure of concrete cover and represent the channels for transport of harmful agents, leading to other types of concrete deterioration and as a final result leading to the corrosion of reinforcement [2]–[4]. Accordingly, the cracks must be taken into account as a parameter in defining the service life of structures.

2. EXPERIMENTAL PROCEDURES

2.1 Materials and mix design

The objective of the study presented in this paper was to determine the influence of cracks on the chloride induced corrosion and resistance to salt scaling of RAC, as well as the impact of carbonation to their resistance to salt scaling. RAC was made with 100% of natural coarse aggregate replaced with recycled aggregate, while the reference concrete was made with natural aggregate (NAC), Table 1.

Table 1: Concrete mixture proportions and properties of fresh and hardened concrete

Mix ingredients (kg/m ³)	NAC	RAC
Coarse aggregate, 8–16 mm	459.2	460.3
Medium aggregate, 4–8 mm	551.0	552.6
Fine aggregate, 0–4 mm	829.9	817.0
Cement CEM II S-L 42.5R	284.6	285.0
Total water	175.0	175.0
w/c	0.615	0.614
Fresh concrete density [kg/m ³]	2342	2281
Hardened concrete density [kg/m ³]	2320	2241
Entrained air [%]	3.20	3.15
Slump [cm]	15.3	14.8
f _{c,14} [MPa]	23.13	34.03
f _{c,28} [MPa]	35.04	41.55

RCA was obtained from a demolished 40-year old highway bridge in the vicinity of Belgrade, Serbia. After crushing, the RCA was sieved into fractions II (4-8 mm) and III (8-16 mm). The RCA had a bulk density of 2370 kg/m^3 and water absorption of 3.9% after 24 hours. Based on these parameters it can be classified as class B1 [5].

The commercially available blended Portland cement CEM II/A-M (S-L) 42.5R was used for the production of all types of concrete. This type of cement had additions (grinded slag and limestone) up to 20 % of the total mass. The specific gravity was 3040 kg/m^3 .

2.2 Casting, curing and testing of specimens

Salt scaling resistance was tested on reinforced concrete prisms with dimension $10 \times 10 \times 50 \text{ cm}$. After finishing, the specimens were covered with wet fabric and stored in casting room at $20 \pm 2^\circ\text{C}$. They were demoulded after 24 h. After that, concrete cubes ($a=15 \text{ cm}$) were kept in a water tank until compressive strength testing and concrete prisms were covered with the wet fabric for additional 7 days after which they are stored in a casting room at $20 \pm 2^\circ\text{C}$. At the age of 28 days, three point bending test was used to induce cracks on the samples, Figure 1. After the crack opening displacement reaches a desired width, applying of force using a torque wrench was stopped.



Figure 1: Experiment setup for salt scaling

Freeze/thaw tests with de-icing salt solution were performed during 25 cycles. The cycle consisted of placing the specimens in a “freezing” environment where the temperature of air is reduced to $-20 \pm 2.0^\circ\text{C}$ for 16-18 h; then the specimens were moved to the laboratory and cured in air conditions at $23 \pm 3^\circ\text{C}$ for 6-8 h. This method consists of confining a pool of 3 wt% NaCl solution with a depth of 3 mm on the concrete surface. After every 5 cycles the amount of scaled material from the concrete surface was measured.

Two types of samples were prepared: one with two different crack widths (0.08 and 0.2 mm) and the other without cracks - reference samples. Also, the influence of carbonation on the salt scaling resistance of concrete was examined. To examine the influence of carbonation on the salt scaling resistance, samples at age of 28 days with and without cracks were exposed to 2% of carbon-dioxide (CO_2) for 28 days at a relative humidity of 65% and a temperature of 20°C , before they exposed to freeze/thaw test. Notation and concrete sample labels are shown in Figure 2 and Table 2.

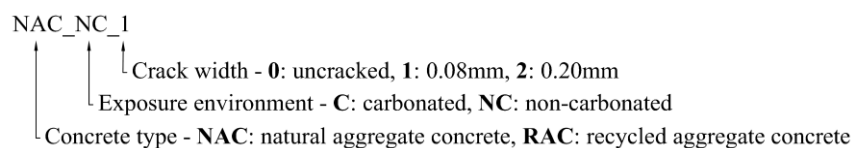


Figure 2: Specimen notation used in the presentation of experimental results

Table 2: Labels of the concrete samples in this study and their crack width

Sample ID	Type of sample	Number of cracks	Crack pattern [crack width]
NAC_NC_0	cube	-	-
NAC_C_0	prism	-	-
NAC_NC_1	prism	2	0.08 / 0.05
NAC_C_1	prism	2	0.08 / 0.08
NAC_NC_2	prism	2	0.20 / 0.05
NAC_C_2	prism	2	0.20 / 0.10
RAC_NC_0	cube	-	-
RAC_C_0	prism	-	-
RAC_NC_1	prism	2	0.08 / 0.03
RAC_C_1	prism	2	0.08 / 0.08
RAC_NC_2	prism	3	0.20 / 0.15 / 0.05
RAC_C_2	prism	2	0.20 / 0.15

3. RESULTS AND DISCUSSION

3.1 The influence of cracks on concrete resistance to salt scaling

Cumulative mass of scaled material of samples with and without cracks is presented in Figure 3. The crack width of both 0.08 mm and 0.2 mm reduced the amount of scaled material for 1.57 times compared to uncracked samples. Increasing the crack width does not lead to increasing the resistance of concrete or further reduction of the amount of scaled material, although some differences were noticed after smaller number of cycles applied, Figure 3.

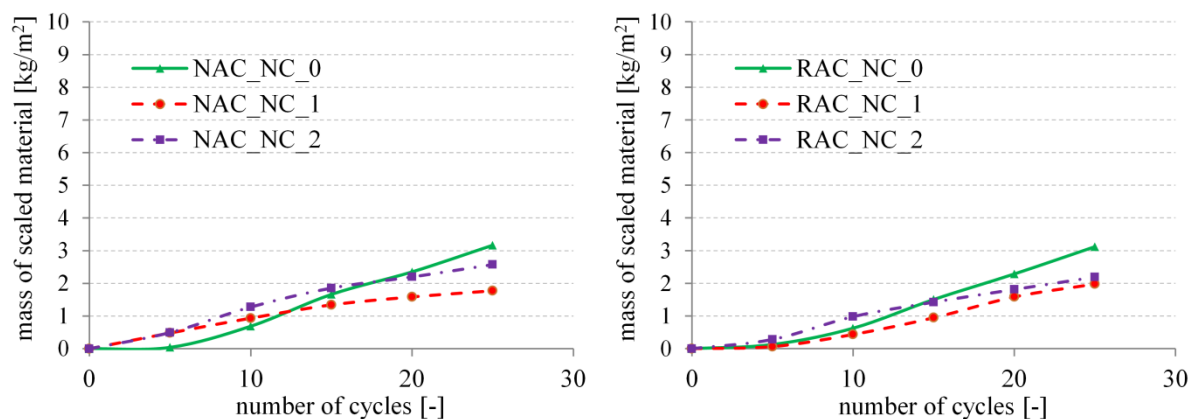


Figure 3: Influence of crack widths on mass of scaled material for NAC (left) and RAC (right)

These results can be explained by the glue spall mechanism of the salt scaling [6]. When water freezes on the concrete surface it forms a composite of two materials (ice and concrete). As the composite temperature is reduced below the melting point of the solution, the ice layer tends to contract 5 times as much as the underlying concrete, which will lead to the formation of tensile stress in the ice [7]. Cracks in ice will also propagate through the cement matrix. The pressure of crystals in the open pores in the concrete crack will form a small damage that will propagate into a plain parallel to the concrete surface. This will result in the removal of a scallop [6]. If there are discontinuities in concrete surface ("expansion joint") there will be a

relaxation of the tensile stress in the ice, so the amount of scaled material will be smaller. Relaxation of that stress will depend on the number and spacing between "expansion joints". Accordingly, the appearance of cracks will cause a reduction of tensile stress in the ice and reduce the amount of scaled material.

Figure 4-left shows the comparison of concrete samples with natural and coarse recycled aggregate, which have the same amount of entrained air of fresh concrete mixture. The samples showed the same amount of scaled material during all cycles, although concrete with recycled coarse aggregate had a 36% higher strength. The reason may be that these concretes have a greater amount of ITZ compared to concrete with natural aggregates, and therefore a greater porosity and water absorption. ITZ represents a critical phase in the resistance of concrete to deterioration mechanisms, so its increase leads to a decrease in the resistance to salt scaling. In case of samples with cracks, RAC had slightly better resistance (Figure 4-right).

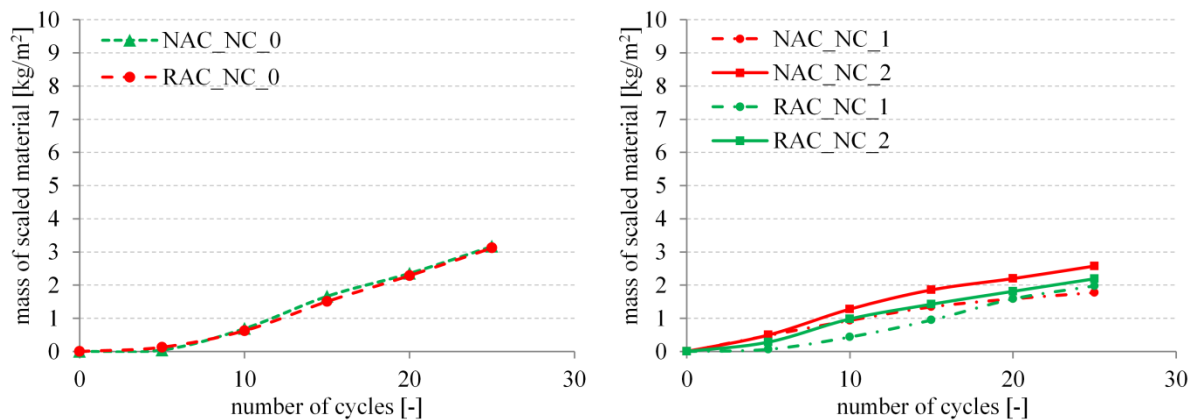


Figure 4: Comparison of NAC and RAC with the same quantity of entrained air in fresh concrete mixture – samples without cracks (left) and with cracks (right)

Concrete samples with a crack width of 0.08 mm (NAC_NC_1 and RAC_NC_1) showed an almost identical amount of scaled material regardless of aggregate type, while sample with a crack width of 0.2 mm with natural aggregate concrete (NAC_NC_2) had a 18% greater amount of scaled material compared to concrete with recycled aggregate (RAC_NC_2). The difference in resistance between these two samples was in the number of cracks which were formed on the surface (Figure 5).



Figure 5: Position and cracks of samples NAC_NC_2 and RAC_NC_2

Sample of RAC_NC_2 had three cracks (0.20, 0.15 and 0.05 mm), while the sample of NAC_NC_2 had only 2 cracks (0.20 and 0.05 mm). Therefore, RAC_NC_2 sample had a greater number of "expansion joints" in the process of ice shrinking, which reduced the amount of scaled material. Accordingly, it can be concluded, in this case, that the strength of RAC is not a crucial factor when comparing the salt scaling resistance of these concretes with NAC. More important factor is the number of cracks formed on the exposed surface and their widths.

3.2 Influence of carbonation on concrete resistance to salt scaling

The reaction of CO_2 from the environment with $\text{Ca}(\text{OH})_2$ from concrete leads to the formation of crystals of calcium carbonate (CaCO_3) with a higher volume than the starting solid compounds of reaction. Accordingly, the carbonation of hardened cement paste in concrete makes concrete structure denser, reducing porosity and water absorption and thus improves the resistance of paste to salt scaling. Cumulative amounts of scaled material for carbonated and non-carbonated uncracked samples are shown in Figure 6. Carbonation reduced the amount of scaled material of NAC after 25 cycles for 1.24 times. In the case of small number of cycles (up to 10 cycles), carbonated sample had more amount of scaled material compared with non-carbonated. This was negligible after 20 cycles. On the other hand, tests showed that carbonation of RAC increased the amount of scaled material for 2.76 times compared to non-carbonated samples. This difference was noticeable from the start of the testing. The cause may be the fact that the carbonation makes the old ITZ and hardened cement paste brittle, which affects their resistance to salt scaling [8]. The use of coarse recycled aggregates can decrease salt scaling resistance if the concrete surface was carbonated before the testing.

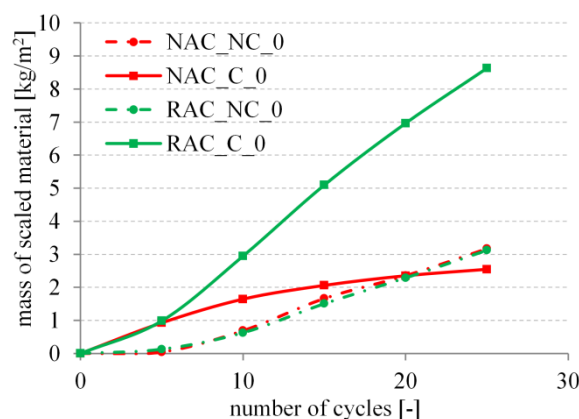


Figure 6: Influence of carbonation on scaled material of NAC and RAC

This trend also appeared in cracked samples. Figure 7 shows a comparison between carbonated and non-carbonated samples with and without cracks. Carbonated RAC samples showed a greater amount of scaled material in relation to non-carbonated samples, regardless of the crack widths.

Occurrence of smaller crack widths of 0.08 mm (RAC_C_1) reduced the amount of scaled material for 1.51 times in comparison to the uncrack samples (RAC_C_0). Samples with cracks of a greater width of 0.2 mm (RAC_C_2) showed less resistance compared with samples with a crack width of 0.08 mm and the uncrack samples, after 25 cycles of freezing

and thawing with de-icing salt. Wider cracks (0.2 mm) allow greater penetration of water and act as an additional exposed surface thereby increasing the amount of scaled material. The carbonation along crack may also influence the performance. However, the difference in mass of scaled material between sample with crack of 0.2 mm and uncrack sample was at the level of measurement error. It is necessary to conduct additional studies to determine the true difference between these two types of samples.

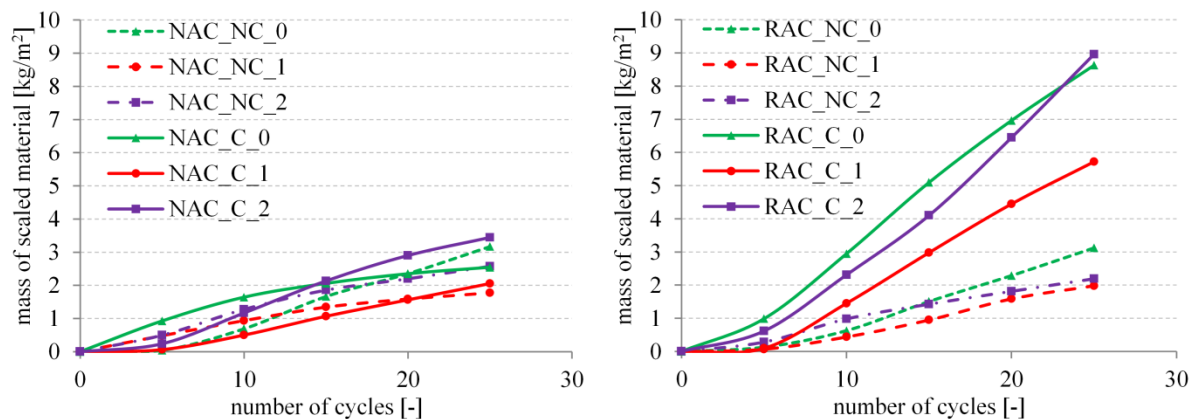


Figure 7: Influence of carbonation on scaled material of NAC and RAC with different crack widths

In case of NAC situation is not so simple. Tests had shown that appearance of small crack (NAC_C_1) in carbonated samples leads to a decrease in the amount of scaled material, while in the case of wider cracks (NAC_C_2) there is an increase in the amount of scaled material compared with uncracked samples. It is necessary to conduct additional testing in order to make clearer conclusions.

4. CONCLUSIONS

- Presence of 0.08 mm crack width on the concrete surface can increase the salt scaling resistance of RAC. Larger cracks, of 0.20 mm width, did not lead to increased resistance of concrete or further reduction of scaled material compared to smaller cracks of 0.08 mm width. Those cracks allow greater penetration of water and act like an additional exposed surface thereby increasing the amount of scaled material compared to smaller widths. In further investigation it is necessary to determine the critical crack width, which affects the improvement of salt scaling resistance of RAC concrete.
- RAC compressive strength was not a crucial factor when comparing the resistance to salt scaling of these concretes with natural aggregate concrete.
- Number of cracks is an important factor influencing concrete resistance to salt scaling. Increasing the number of cracks (from two to three) on concrete sample leads to the relaxation of tensile stress in ice, so the amount of scaled material will be smaller.
- Carbonation of RAC decreases the salt scaling resistance of concrete. The reason may lie in the fact that carbonation makes the old ITZ zone and the hardened cement paste brittle which decreases the salt scaling resistance.

ACKNOWLEDGEMENTS

The work reported in this paper is a part of the investigation within two research projects: TR36017, 'Utilization of byproducts and recycled waste materials in concrete composites in the scope of sustainable construction development in Serbia: investigation and environmental assessment of possible applications', supported by the Ministry of Education, Science and Technological Development, Republic of Serbia.

REFERENCES

- [1] B. T. R. Naik, R. N. Kraus, B. W. Ramme, and Y. Chun, "Utilization laboratory and field evaluation of concrete containing up to 70 % class C and class F fly ash," in *Symposium on Concrete Durability: Deicing Chemicals and Freezing-Thawing*, 2003, no. March, p. 41.
- [2] B. J. Pease, "Influence of concrete cracking on ingress and reinforcement corrosion," Technical University of Denmark, 2010.
- [3] A. Blagojevic, "The Influence of Cracks on the Durability and Service Life of Reinforced Concrete Structures in relation to Chloride - Induced Corrosio A Look from a Different Perspective," Delft University of Technology, 2016.
- [4] M. Otieno, H. Beushausen, and M. Alexander, "Chloride-induced corrosion of steel in cracked concrete - Part I: Experimental studies under accelerated and natural marine environments," *Cem. Concr. Res.*, vol. 79, pp. 373–385, 2016.
- [5] R. V. Silva, J. De Brito, and R. K. Dhir, "Properties and composition of recycled aggregates from construction and demolition waste suitable for concrete production," *Constr. Build. Mater.*, vol. 65, pp. 201–217, 2014.
- [6] J. J. Valenza II and G. W. Scherer, "Mechanism for salt scaling of a cementitious surface," *J. Am. Ceram. Soc.*, vol. 89, no. 4, pp. 1161–1179, 2006.
- [7] G. W. Scherer, "Stress from crystallization of salt," *Cem. Concr. Res.*, vol. 34, pp. 1613–1624, 2004.
- [8] J. Xiao and L. Li, "Review on Recycled Aggregate Concrete in the Past 15 Years in China," in *Third International Conference on Sustainable Construction Materials and Technologies*, 2013.

ACCELERATED CARBONATION OF RECYCLED CONCRETE AGGREGATES: THE FASTCARB PROJECT

Jean Michel Torrenti (1)

(1) Ifsttar, France, on behalf of the FastCarb project

Abstract

The FastCarb project is the result of the conjunction of two facts. On one hand, the production of cement is an important source of CO₂ in the world (5-7% of the total emissions). Around two thirds of these emissions are due to de-carbonation of limestone during the Portland cement manufacturing process.

On the other hand, a large quantity of recycled concrete coming from the deconstruction is available while natural resources have to be preserved. Even if recycled concrete aggregates (RCA) can already be used in concrete by adjusting mix designs, their larger porosity has an impact on the performances.

However recycled aggregates incorporate portlandite and hydrated silicates that can be carbonated in a faster way. The aim of the FastCarb project is to store CO₂ in RCA, improving the quality of these aggregates by the clogging of the porosity and finally decreasing the CO₂ impact of concrete in structures. It has two main objectives: to optimize in laboratory conditions of the accelerated carbonation process which can be transposed at industrial scale at a suitable cost and to show that the process could be used in industrial conditions.

Keywords: concrete, carbonation, recycled aggregate, CO₂, circular economy, environmental impact

1. INTRODUCTION

The FastCarb project (Accelerated carbonation of recycled concrete aggregate – www.fastcarb.fr) is the outcome of the coming together of two observations. First, the production of cement is a major source of global CO₂ emissions, accounting for 5-7% of the total. Approximately two-thirds of these emissions are due to the decarbonation of limestone during the manufacture of Portland cement. The reversal of this process occurs naturally and is referred to as the carbonation of concrete. However, natural carbonation is a very slow process.

Second, a large amount of the recycled concrete that comes from the deconstruction of buildings and structures is available, while natural resources must be conserved. Even if recycled concrete aggregate (RCA) can be used as such in concrete by adjusting the mixtures, it has higher porosity. This impacts the performance of recycled aggregate concrete, resulting in higher porosity, greater water absorption and slightly impaired mechanical performance. As a result, in order to use high recycling rates without losing the engineering properties required of concrete, it is necessary to increase the mixture's binder content.

Nevertheless, recycled aggregate contains portlandite and hydrated silicates which may be carbonated more rapidly than the concrete in structures. The goal of the FastCarb project is thus to store CO₂ in the RCA, while improving the quality of this aggregate by plugging the porosity and ultimately reducing the impact of the CO₂ in the concrete contained in structures.

2. CONTEXT AND ISSUES

2.1 Using recycled concrete in concrete

In France, the building and civil engineering sector generates almost 200 million tonnes of inert materials every year, 17 million tonnes of which are from concrete [1]. It is estimated that only half of this concrete waste is currently recycled in the form of recycled concrete aggregate (RCA). Moreover, the volume of waste generated by the deconstruction of end-of-life buildings and structures is increasing, and will become very large in the next few years. Based on the normal construction cycle, a proportion of the buildings that are more than 50 years old will soon reach the end of their service life and be demolished. When this occurs, there will be a huge quantity of concrete to be recycled.

Currently, recycled concrete aggregate (RCA) is mainly treated in one of two ways: it either goes to landfill, or it is recycled as low cost fill for road earthworks. The road construction sector will be unable to cope with the arrival of larger amounts of RCA in the near future and the environmental cost of processing it will therefore significantly increase. In addition, if RCA were to be used as an aggregate in concrete, the road construction sector would be able to make greater use of inert materials such as steel industry slag or bottom ash from the incineration of non-hazardous waste.

At the same time, the natural aggregate which is used to manufacture concrete or pavement wearing courses is a non-renewable resource, which although technically unlimited, is becoming increasingly difficult to obtain for societal and environmental reasons. Consequently manufacturing concrete while reducing aggregate consumption is an important challenge.

The current standards permit the use of RCA on the basis of its characteristics (and the percentage of materials other than concrete or aggregate which contaminate it) and on the basis of the exposure classes of the structures that are built, which depend on their environment. The proportion of RCA is highly restricted: it can only be used as a substitute for up to 30% of the natural aggregate, and, for example, the re-use of fine RCA to manufacture reinforced concrete is prohibited.

The main reason for these restrictions is the very high porosity of RCA which means it absorbs a great deal of water and has mechanical properties, in terms of impact resistance and brittleness, that are inferior to those of natural aggregate. These characteristics either result in concretes with poor mechanical performance and durability, or, if a good level of performance is sought, the need to limit the amount of recycled aggregate used must be limited to

approximately 10% of the total amount of aggregate, unless the amount of cement in the new concrete is increased.

The work of the National Recybéton project has provided a number of results which allow us to improve the mix design of concretes with high rates of RCA and enhance their properties in the fresh and hardened state in order, ultimately, to enable standardisation to allow for greater use of RCA in concretes.

2.2 The potential for re-carbonating recycled concrete

The performance of RCA can be further enhanced by the application of treatment techniques, in particular with a view to reusing fine RCA in concrete. Of the many possibilities that have been explored, it is carbonation which we propose to study in this project. The re-carbonation of recycled concrete aggregate is a currently emerging topic for research. The literature on this topic highlights the potential of RCA which represents a possible carbon sink. In addition, the carbonation involved in such capture would improve RCA's constructional properties, and therefore facilitate its re-use in construction [16].

Deconstruction concrete acts as a CO₂ sink as a result of the cement matrix which surrounds the natural aggregate. The manufacture of 1 tonne of this cement generates approximately 800 kg of CO₂ (in the case of type CEM I cement). Sixty percent of this CO₂ – i.e. almost 500kg/T of cement – is due to the decarbonation of limestone and may theoretically be stored once again by the reverse operation. This reversal may occur naturally, but in this case its kinetic is very slow. The FastCarb project will test accelerated carbonation techniques. IFSTTAR's preliminary tests have shown that, in a very short amount of time, it is possible to store 50kg of CO₂/T of RCA [2]. Recent findings in the literature show that this level of uptake can be achieved above all for fine fractions [3].

France currently produces about 13 million tonnes of clinker (www.infociments.fr). As we have already seen, the production of a tonne of clinker leads to the emission of some 800kg of CO₂. France's annual production therefore generates 10.4 million tonnes of CO₂. If we assume that 20 million tonnes of RCA is available for re-carbonation, applying the storage hypothesis of 50 kg of CO₂/T of RCA, we have the potential to store 1 million tonnes of CO₂, i.e. 10% of cement-related emissions.

France's annual production of concrete is currently around 100 million tonnes. According to the French National Ready-Mix Concrete Association (www.snbpe.org), in 2015, 35 million m³, i.e. about 77 million tonnes, of this consists of ready-mix concrete and according to the French Concrete Industry Federation (www.fib.org) 19 million tonnes consists of precast concrete products. Even if it is above all the rate of deconstruction and the organisation of the recycling sector which will determine the future potential for RCA that may be re-carbonated, it will rise over time and with it the amount of CO₂ that can be stored in RCA. With the same hypotheses as above, if we take the figure of 100 million tonnes of RCA we reach a figure of 5 million tonnes of stored CO₂, i.e. 42% of the emissions currently due to cement.

It will not, of course, be either economically or environmentally viable to re-carbonate all the RCA (transport is a factor to be borne in mind when making assessments). Nevertheless, the foregoing figures show that the process provides a way of storing a non-negligible proportion of concrete-related CO₂ emissions.

In a context in which for buildings we now consider not only their energy consumption in service but also their environmental footprint, as with the French E+C- label, and, in view of

the possibility that climate-related considerations will lead to an increase in the cost of a tonne of CO₂, the goal is to reduce the carbon impact of building in concrete even further, even though studies show that concrete construction systems already compare well with other materials.

One consequence of improving the insulation of buildings is that construction materials assume greater and greater importance in the energy and carbon balance. Reducing the carbon footprint of construction materials will therefore become an important technical and economic goal for the years to come.

The aim of the FastCarb project is therefore to show that it is possible to store a large amount of CO₂ in recycled concrete aggregate, which will improve its quality and reduce the environmental impact of concretes that are manufactured with this treated aggregate, achieving these ends under industrially feasible conditions. At the same time, we will improve our carbonation models and our ability to quantify the natural carbonation of concretes.

Twenty-two stakeholders are currently involved in this partnership project, drawn from university laboratories, public and private sector research centres, cement, aggregate and concrete manufacturers and firms from the recycling and construction sectors. It got under way in 2018 with support from the Ministry in charge of ecology and is scheduled to last for 3 years.

3. CURRENT STATE OF KNOWLEDGE

3.1 Carbonation as a means of improving the aggregate in recycled concrete

Carbonation is the process by which CO₂ reacts with the hydrates in the hydrated cement paste (portlandite and C-S-H). In simplified form the reactions are as follows:



It should be noted that depending on the conditions under which the reactions take place, the CaCO₃ may be present as several polymorphs, for example calcite, vaterite and aragonite. This is problematic when we are concerned about the representativeness of an accelerated carbonation test, for example in the framework of a performance-based approach to a concrete's durability [4]. Our project is not concerned with being representative, but with storing a maximum amount of CO₂.

The consequences of these reactions are as follows:

- consumption of OH⁻ ions. This reduces the pH of the interstitial solution from about 13 to 9. This may lead to the corrosion of reinforcement, and for this reason the attempt is made to minimise it in reinforced concrete structures. In the case of our project, as the treated GBR is once again mixed with cement which will increase the pH, carbonation is not perceived as a problem but as a carbon sink.
- an increase in mass and a reduction in total porosity. In the case of cement pastes manufactured with CEMI cement with water/cement ratios of 0.45 and 0.6, Morandau et al. measured variations in porosity of between 6 and 8% for the paste with a water/cement ratio of 0.45 and of approximately 10% for that with a water/cement ratio of 0.6 [5]. These researchers demonstrated that this variation was due to the formation of calcite, the decalcification of portlandite and C-S-H leading in contrast to higher porosity. These findings have been confirmed by a large number of

authors, for example Auroy et al., who have shown the impact of carbonation on microstructure with impacts on desorption isotherms and transport properties [6]. Carbonated RCA also absorbs less water [7, 8]. The mechanical properties of carbonated RCA are also better [8, 9, 10].

The increase in mass due to the trapping of CO₂. Estimates of this increase in mass depend, obviously, on the experimental technique used to carbonate the concrete and the duration of treatment (see 3.2). There is, however, general agreement in the literature that natural carbonation is able to recover between 25 and 30% of the CO₂ emitted during the manufacture of the cement in the concretes in question [11]. The authors of the impact study of the natural carbonation have even arrived at the figure of 40% [12].

3.2 Main factors affecting the accelerated carbonation of RCA

The problem with natural carbonation (which is beneficial for structures) is that it takes place very slowly. In order to optimise the duration of an industrial treatment, this process must be accelerated. A number of techniques are available to achieve this. They generally involve a partial pressure of CO₂ which is very much higher than in nature, possibly combined with an increase in pressure and/or heating. Applying the treatment to RCA is also beneficial because of the large exchange surface. Based on data in the literature we can already propose the following parameters:

- The water content. As with natural carbonation, there is an optimum water content in the cement paste for maximising carbonation. This is at a relative humidity of about 50 to 70% [2, 3, 13, 14]. This parameter is absolutely crucial as an excessively low water content may reduce the rate of carbonation very considerably.
- The CO₂ content of the gas that is in contact with the RCA. This content affects the ability to fix CO₂ within the RCA. Fang et al. have shown that above 20%, the CO₂ concentration has little impact on the amount which is stored in the RCA, as increasing this concentration leads to the formation of more carbonated materials but does not help to dissolve hydrates, which limits the maximum rate of carbonation [3].
- The temperature. This also plays a decisive role in the carbonation process, in particular on transport properties and the solubility of the cement hydrates which react with the CO₂. Drouet has thus shown that in the case of a CEMI cement paste, the rate of carbonation increases with temperature [15].
- The size of the RCA particles. The smaller the aggregate particles, the more CO₂ they can store [3, 14]. Two effects explain this: the fine fraction contains more cement paste - which is why it is used at the present time to remake concrete – and it has a larger exchange surface. The fine fraction is of particular interest for the FastCarb project from the standpoint of both environmental impact and recycling issues.
- The industrial process. The carbonation process may play a role by modifying some of the experimental parameters [3]: increasing pressure may increase the rate of carbonation and CO₂ capture by accelerating the penetration of the gas and, like pressure, a greater rate of flow increases CO₂ capture.

In addition, comparisons between the pressurised carbonation test and the flow-through carbonation test show that the pressurised procedure results in greater CO₂ capture. The tests in question are nevertheless “batch” tests and it is still necessary to test them in a rotating drum. Finally, the use of supercritical CO₂ gives spectacular results but would be economically unviable [2].

4. RESEARCH PROGRAMME

4.1 Research methodology

In order to reduce the carbon footprint of concrete by accelerated carbonation, the FastCarb project will apply two approaches, one directed upstream and the other directed downstream:

- the goal of the upstream approach will be to validate theoretically and experimentally the technical proof of the concept of accelerated carbonation of RCA that has already been obtained in the laboratory. This part of the project will also allow us to accurately determine the parameters that affect the process (the water content of the aggregate, the treatment temperature, the gas pressure...) and model the processes at work.
- the goal of the downstream approach will be to design an accelerated carbonation process and implement it at the pre-industrial scale, to verify that the concretes manufactured with the treated aggregate have the required properties and to characterise the environmental and economic viability of the considered industrial recycling process. This last point will also provide some findings which depend on economic conditions (such as the cost of a tonne of CO₂) concerning the optimum between CO₂ capture, the cost of the treatment and the improvement in the properties of the aggregate.

4.2 Organisation of the research

The research structure consists of working groups which reflect the points mentioned above. GT1 deals with the upstream “laboratory” and GT2 with the downstream “industrial” approach. A third working group (GT3) has also been set up to exploit the results of the project.

GT1 consists of 3 sub-groups:

- GT1.1 deals with the experimental approach in the laboratory. It will supply the experimental data that are necessary to analyse the processes that occur during the acceleration carbonation of RCA and to understand the influence of the major parameters (such as water content) in order to be able to optimise the process.
- GT1.2 will model the accelerated carbonation process. A comparison will be conducted between different carbonation models that are appropriate for accelerated carbonation. We will also take advantage of the fact that several research teams which are specialised in carbonation are involved in the project in order to provide input that will assist the inclusion of natural carbonation in the environmental section of the future “Product Category Rules for Concrete” standard. The reason for this is that natural carbonation may have a non-negligible impact on the greenhouse gas balance [12].
- GT1.3 will deal with a specific treatment – bio-carbonation – which is a possibility that is much further in the future than those covered in GT2.

GT2 also consists of 3 sub-groups:

- GT2.1 has as its goal the application of the accelerated carbonation process on an industrial scale. In coordination with the experiments conducted in the framework of GT1.1, manufacture will be performed under industrial conditions in order to test the

feasibility of the methods. Such manufacturing could combine the use of the available materials (for example air which contains a certain percentage of CO₂ that has been recovered from the exhaust gases of a cement factory kiln) and possible techniques (total or partial pressure). After this treatment, the aggregate in question will be characterised and the results compared to those obtained in the laboratory, primarily in order to verify the applicability of the models developed by GT1.2. Last, conclusions will be drawn from these experiments for aggregate standardisation.

- GT2.2 deals with a transfer to concrete and applications to precast elements and structures that are cast in situ. Concretes will be manufactured with aggregates that have been made in the framework of the project, and this will include the pouring of precast elements or parts of structures in situ. This will allow us to measure the impact of the treatment on the density of the aggregate grains and their mechanical performance in the concrete in which they are recycled in order to identify any impact on the optimisation of mix design. The aim is also to characterise not only the mechanical performance of concretes that include RCA but also their durability. With regard to the latter, in particular it will be verified that the treatment of the aggregate does not increase the risk of reinforcement corrosion in reinforced concrete.
- The role of GT2.3 is to perform economic and environmental evaluations of the process. It will carry out an economic evaluation which will include any possible conflicts of use. This will be a forward-looking study that will take account of possible changes in the cost of a tonne of CO₂. An environmental evaluation of the process (Life Cycle Analysis – LCA) will be conducted based on this economic analysis.

5. CONCLUSIONS

The results that are currently available in the bibliography and the preliminary tests that have been conducted as part of the FastCarb project show that RCA can be used to store a significant proportion of the CO₂ emissions that result from the production of cement. The FastCarb project, which began in 2018 and which will last 3 years, will investigate in the laboratory the principal parameters of an accelerated carbonation process and model it. This “upstream” phase of the project should provide a basis for the industrial processes which will be developed in order to manufacture large amounts of carbonated RCA. This aggregate will then be used to characterise the concretes in which they will be included for applications in precast concrete and poured in-situ concrete. The results will be published as the project moves forward.

ACKNOWLEDGEMENTS

The investigations and results reported herein are supported by the French Ministry in charge of construction under the FastCarb research program.

REFERENCES

- Mongear L., Dross A., La ressource en matériaux inertes recyclables dans le béton en France, *rapport du PN RECYBETON*, 2016
- Cazacliu B., Gobert J.B., Condoret J.S., Huchet F., Camy S., Torrenti J.M., Feasibility study of fast carbonation of recycled concrete aggregates, *fib symposium*, Cape Town, 2016

- Fang X., Xuan D., Poon C.S., Empirical modelling of CO₂ uptake by recycled concrete aggregates under accelerated carbonation conditions, *Materials and Structures* (2017) 50:200
- Auroy M., Poyet S., Le Bescop P., Torrenti J.M., Charpentier T., Moskura M., Bourbon X., Comparison between natural and accelerated carbonation (3% CO₂): impact on mineralogy, microstructure, water retention and cracking, *Cement and Concrete Research*, Volume 109, July 2018, Pages 64–80
- Morandea A., Thiery M., Dangla P., Investigation of the carbonation mechanism of CH and C-S-H in terms of kinetics, microstructure changes and moisture properties, *Cement and Concrete Research*, Volume 56, February 2014, Pages 153-170
- Auroy M., Poyet S., Le Bescop P., Torrenti J.M., Charpentier T., Moskura M., Bourbon X., Impact of carbonation on unsaturated water transport properties of cement based materials, *Cement and Concrete Research*, 74 (2015) 44–58
- Zhao Z., Courard L., Rémond S., Damidot D., Fiandaca T., Tentatives de prétraitement des granulats recyclés pour l'amélioration des bétons préfabriqués, *16e édition des Journées scientifiques du Regroupement francophone pour la recherche et la formation sur le béton (RF)2B*, Lausanne, 2015
- Zhang, J., Shi, C.J., Li, Y., Pan, X., Poon, C.S., Xie, Z., Performance Enhancement of Recycled Concrete Aggregates through Carbonation, *J. Mater. Civ. Eng.* 27-11 : 1-7, 2015.
- Parmentier V., Michel F., Courard L., Fixation du CO₂ dans des blocs de béton à base de granulats recyclés, *Quatorzième édition des Journées scientifiques du Regroupement francophone pour la recherche et la formation sur le béton (RF)2B*, Sherbrooke, 2013
- Xuan, D., Zhan, B., Poon, C.S., Assessment of mechanical properties of concrete incorporating carbonated recycled concrete aggregates, *Cement and Concrete Composites*, 65 : 67-74, 2016
- Thiery M., Roussel N., Habert G., Belin P., Dangla P., Comment intégrer quantitativement la carbonatation naturelle dans le bilan carbone des matériaux cimentaires, *colloque GC'09*, 2009.
- Xi F., Davis S.J., Ciais P., Crawford-Brown D., D. Guan, C. Pade, T. Shi, M. Syddall, J. Lv, L. Ji, L. Bing, J. Wang, W. Wei, K.-H. Yang, B. Lagerblad, I. Galan, C. Andrade, Y. Zhang & Z. Liu, Substantial global carbon uptake by cement carbonation, *Nature Geosciences*, 9, pages 880–883 (2016)
- Galan I., Andrade C., Castellote M., Natural and accelerated CO₂ binding kinetics in cement paste at different relative humidities, *Cement and Concrete Research*, 49 (2013)
- Zhan, B., Poon, C.S., Liu, Q., Kou, S.C., Shi, C., Experimental study on CO₂ curing for enhancement of recycled aggregate properties, *Construction and Building Materials*, 67 : 3-7, 2014.
- E. Drouet, S. Poyet, P. Le Bescop, J.M. Torrenti, X. Bourbon, Carbonation of hardened cement pastes: influence of temperature, to be published in *Cement and Concrete Research*, 2018.
- Jang J.G., Kim G.M., Kim H.J., Lee H.K., Review on recent advances in CO₂ utilization and sequestration technologies in cement-based materials, *Construction and Building Materials* 127 (2016) 762–773

DEVELOPMENT OF DURABLE AND STRUCTURAL LIGHTWEIGHT CONCRETE

Maria Ch. Stratoura (1,2), Theofilos-Marios Th. Zavras (3), Efstratios G. Badogiannis (2), Kosmas K. Sideris (4) and Vagelis G. Papadakis (1)

- (1) Department of Environmental and Natural Resources Management, University of Patras, Patras, Greece
- (2) School of Civil Engineering, National Technical University of Athens, Athens, Greece
- (3) School of Chemical Engineering, National Technical University of Athens, Athens, Greece
- (4) Department of Civil Engineering, Democritus University of Thrace, Xanthi, Greece

Abstract

In this work, various structural lightweight concrete (LWC) mixtures were developed by using natural lightweight aggregates, such as pumice, perlite and rice husk ash. The durability performance of these lightweight mixtures was evaluated and compared to that of concrete with normal-weight aggregates, in terms of fresh and hardened concrete's properties. Slump, air content and compressive strength were also evaluated, along with durability characteristics, such as sorptivity due to capillary absorption, porosity and chloride penetration coefficient. The comparative analysis of the test results led to the conclusion that all produced lightweight concrete mixtures provide satisfactory structural strength and equivalent or even enhanced durability characteristics.

Keywords: lightweight concrete, pumice, perlite, rice husk ash, durability

1. INTRODUCTION

During the last decades a rising need for more environmentally friendly and sustainable building materials has occurred. These materials need to fulfill specific criteria, such as their compatibility with cement, their increased mechanical durability and their friendliness towards the environment [1]. The link between durable design and sustainability is also emphasized, on the newly imposed EN Standards for the sustainable assessment of buildings [2], where a combination of the assessments of environmental and economic performance taking into account the technical and functional requirements of a building is approached and on the next generation structural codes. Although new technologies are constantly being developed and updated to complement current practices in creating sustainable and durable structures, the common objective is that buildings are designed to reduce the overall impact of the built

environment on human health and the natural environment [3]. One of the most urgent challenges that construction industry has to face is the deterioration of reinforced concrete structures. Thus, the scientific community must promote industrial ecology and establish the principles of sustainable management in concrete production, in order to achieve a “green” concrete and a new rigorous approach towards construction of robust durable structures (for a given service life) with the minimum environmental burden [4]. The technological development and use of lightweight concrete (LWC) is estimated to contribute into sustainable development that will respond to the ever-increasing technical requirements of new constructions.

Different types of lightweight aggregates are used for the production of LWC. Pumice is the most widely used natural lightweight aggregate [5]. It is a volcanic rock formed from silica rich lavas that contain more dissolved gases than other types of lava due to their viscosity. As the lava rapidly cools and hardens into a glassy structure, the dissolved gases form pores that result in low density volcanic rock. According to Granata [6] the addition of ground pumice increases the mechanical properties of concrete after 28 days of curing.

Perlite is a volcanic glass which contains 2-6% chemically combined water. Although after heating in 900-1200°C, the water is lost, it expands to a cellular material, of a very low bulk density. In construction, expanded perlite can be used as a part of cement or aggregate in traditional cementitious materials or as a source material for geopolymers. Expanded perlite in construction provides good thermal and sound insulation, good fire resistance and low density [7, 8]. Many researchers investigated the quantitative contribution of ground perlite to the pozzolanic effect. Their studies showed that natural perlite powder has a significant pozzolanic reactivity and it could be an active concrete mineral admixture [9].

Rice Husk Ash (RHA) is an agro-industrial residue deriving from the controlled burning of rice husk. As a material, RHA has a very low bulk density and it is rich in silica and in many cases – depending on the nature of husks and burning/cooling condition – the total silica of RHA exceeds 90% [10]. The potential uses of this by-product could be also as a pozzolanic additive in cement/concrete-production. Many researchers have investigated the pozzolanic properties of RHA concrete and they have obtained very promising results. Kartini, [11] supports through his study that RHA is a pozzolanic material and has beneficial effects on the durability of the concrete.

The study presented here focuses on the use of untreated pumice (Pu), perlite (Pe), rice husk ash (RHA) and waterproof expanded perlite (ePe) in concrete and provides an integrated approach of two mechanisms which are crucial for the durability of reinforced concrete: water absorption and chloride migration. Therefore, open porosity, sorptivity and chloride migration resistance are evaluated. The results regarding the fresh properties and mechanical characteristics of lightweight concrete mixtures are also discussed in order to identify the potential added value of lightweight aggregates to the concrete.

2. MATERIALS AND METHODS

For the purposes of this project, seven different lightweight concrete mixtures were examined with different lightweight aggregates and one reference normal concrete mixture, with limestone aggregates (REF). Typical Portland cement (CEM I 42.5N) was used in all the mixtures. In order to maintain the workability of the concrete, a Sika® Viscocrete superplasticizer was added when required to retain the slump of the fresh concrete at desired levels. For the production of lightweight concrete mixtures, four lightweight aggregates were

used: pumice (Pu), perlite (Pe), expand perlite (ePe) and rice husk ash (R). For the production of normal concrete mixtures, three locally available grades of calcareous limestone aggregates (Ca) were used (sand, small gravel and medium gravel). Table 1 presents the chemical composition of the materials used in this study.

Table 1: Chemical analysis (% w/w) of constituent materials

	SiO ₂	Al ₂ O ₃	Fe ₂ O ₃	CaO	MgO	SO ₃	K ₂ O	Na ₂ O	TiO ₂	P ₂ O ₅	ZnO	L.O.I.
Cement	20.00	4.90	3.50	62.00	3.10	2.70	0.50	0.20	-	-	-	2.80
Pumice	68.58	11.89	1.16	4.11	0.44	-	4.02	2.77	0.12	0.03	-	7.41
Perlite	74.00	13.00	1.00	1.40	0.25	-	3.50	4.50	-	-	-	2.60
RHA	96.03	0.08	0.48	1.29	0.51	-	0.89	0.70	-	-	0.02	6.00

The physical properties (apparent density- ρ_a , water absorption) of the used aggregates are listed in Table 2. In order to improve waterproof properties of expanded perlite, “Aquashield Porus” from Nanovis Inc was used. Expanded perlite was immersed in Aquashield Porus for 24h, then subjected to heat treatment at 400° C for 4h. Finally, the rice husk ash was also thermally treated at 700°C for 2h.

Table 2: Physical properties of aggregates

Symbol	Pu (0-4)	Pu (2-10)	Pu (0-16)	Pe (0-2)	Pe (0-4)	ePe (0-2)	R (0-2)	Ca (0-4)	Ca (4-8)	Ca (8-16)
ρ_a (t/m³)	1.61	1.39	1.13	2.20	2.15	0.96	1.79	2.67	2.67	2.61
Water absorption (%)	19.25	16.98	16.98	4.04	3.37	21.00	13.65	2.14	0.90	0.90

A batch volume of 15 liters, was produced for each composition. Table 3 summarizes the mix proportions for all produces mixes. The water to cement ration (w/c) for all mixtures was kept constant (0.40), considering the absorption water of the aggregates (Table 2). Seven cubic specimens of 100x100x100 (mm) and two cylindrical specimens of 200 mm height and 100 mm diameter were casted for each mixture in order to perform mechanical and durability tests. After 1 day of moist curing, the specimens were water cured at $23 \pm 1^\circ\text{C}$ for 28 days. They were tested under uniaxial compression, in different maturity groups after 2,7 and 28 days. For each age, three specimens were tested and the mean value of these measurements is reported.

The potential pozzolanic activity of the lightweight aggregates was evaluated according to the BS 3892, [12]. More specific, strength activity index (SAI) was evaluated in mortars, when CEM I 52,5R cement was replaced at 30% by pumice, perlite and RHA. The additions were initially ground, achieving similar grain size characteristics (see Fig 1). For each aggregate type, three prismatic samples 40x40x160 (mm) were casted, preserved in a wet chamber with a stable temperature of $23 \pm 1^\circ\text{C}$ and tested in compression after curing (28 days). According to the standard, SAI results greater than 80% are indicative of a positive pozzolanic activity.

Table 3: Mixtures proportions (kg/m³)

Materials	Mixture							
	REF	PeCaPu	ePeCaPu	PePu	RCaPu	Pu	ePePu	RPu
Cement	400	400	400	400	400	400	400	400
Ca (0 - 4)	948	-	-	-	-	-	-	-
Ca (4 - 8)	569	57	-	-	89	-	-	-
Ca (8 - 16)	379	-	107	-	-	-	-	-
Pe (0 - 2)	-	114	-	158	-	-	-	-
Pe (0 - 4)	-	512	479	243	-	-	215	-
Pu (0 - 4)	-	-	-	190	412	537	168	287
Pu (0 - 16)	-	455	320	464	446	381	410	421
Pu (2 - 10)	-	-	-	-	-	59	-	105
ePe (0-2)	-	-	160	-	-	-	140	-
R (0-2)	-	-	-	-	167	-	-	144
Effective water	160	160	160	160	160	160	160	160
SP	0.021	0.038	0.040	0.022	0.014	0.040	0.042	0.084

The durability of the LCW mixtures was evaluated on the basis of the water absorption (open porosity and capillary absorption) and of the chloride's penetration resistance, on specimens cured for 28 days. The open porosity (p) was evaluated by weighting a fully saturated 100 mm cylindrical specimen immersed in water and in air, according to the American standard ASTM C 642. The specimen was weighed again after being oven dried at 105°C until constant mass. The drying period of the specimens ranged between 4 and 7 days. The open porosity, p (%), was calculated by the combination of the three masses [13]. A precise procedure for the measurement of sorptivity (S) has been described by Hall and Tse [14].

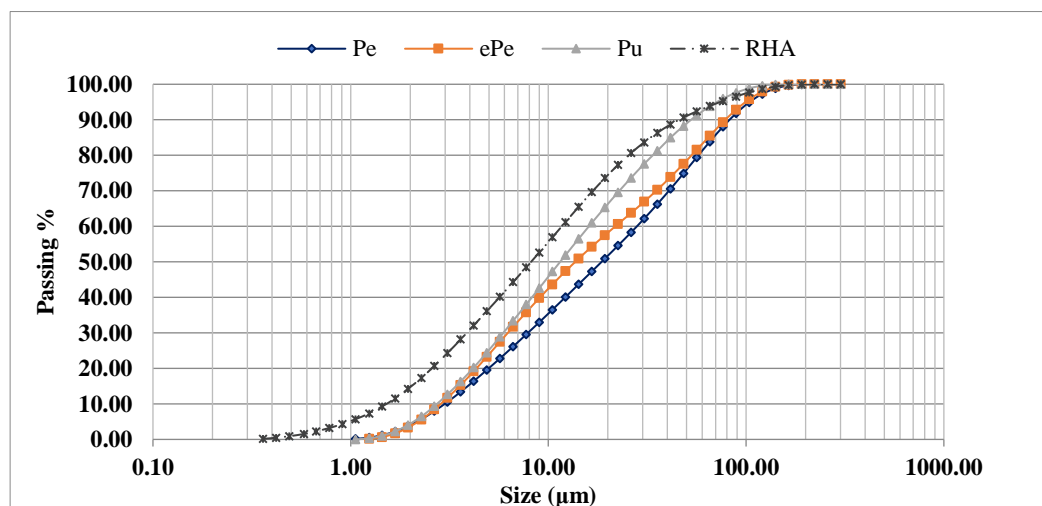


Figure 1: Particle size distribution of ground aggregates samples subjected to pozzolanicity test

The sorptivity test was applied to a concrete cylinder of 100 mm diameter and 50 mm height. The weight changed due to the water uptake (capillary absorption). After mass stabilization, the specimens were coated with the free water films on their lateral surfaces only, in order to ensure uniaxial water absorption. The specimen was rested on rods to allow free access of water to the

surface and the tap water level was kept no more than 3 mm above the base of the specimen. The specimens from each mixture were tested at the age of 28 days, the values were reported and the sorptivity, S ($\text{mm}/\text{min}^{0.5}$), was calculated [15].

The chloride migration was estimated by calculating the (apparent) chloride penetration coefficient, D_{nssm} ($\times 10^{-12} \text{ m}^2/\text{s}$), using a well-established non-steady-state penetration experiment [16]. One 50 mm thick segment, extracted from the middle zone of a cylindrical specimen, was maintained for 24h under a potential difference, between a cathode solution of 10% sodium chloride (NaCl) by mass and an anode solution of sodium hydroxide (NaOH), 0.3 N. It should be noted that the specimens were not dried and preconditioned in a vacuum container as suggested by the test method, due to equipment limitations. However, given that all specimens of the present study have received the same pre-treatment, i.e. full saturation until the age of testing, the relative effect of chloride penetration is expected to be comparable.

After the test completion, the determination of the chloride migration depth was performed by a colorimetric method [17]. Specifically, the tested specimen was axially split into two pieces and one of the two fractured surfaces was sprayed with a 0.1 M silver nitrate (AgNO_3) solution. The average depth of chloride penetration was determined from the colour change in the area where the presence of chlorides chemically leads to the formation of silver chloride (AgCl). The coefficient D_{nssm} was further calculated in accordance with NordTest Build 492 method [16].

3. RESULTS AND DISCUSSION

According to the results of pozzolanic activity test (Table 4), the compositions with Pe, ePe and Pu do not meet the criteria of BS 3892 [12] and thus, they exhibit restricted pozzolanic reactivity. On the contrary, the composition with RHA meets standard's requirements, performing strong pozzolanic reactivity. From the results of this test, it is noticed that in materials with the same mineralogical origin (Pe, ePe) their pozzolanic reactivity differs, a fact that is probably attributed to the used waterproofing addition. However, considering the reported values, it could be assumed that the used lightweight aggregates, are marginally exhibit pozzolanic activity.

Table 4: Results of the pozzolanicity test BS 3892 [12]

Mortar	REF	Pe	ePe	Pu	RHA
Compressive strength in 28days (MPa):	62.10	46.80	53.70	46.70	58.00
SAI (%) in 28 days	-	75.36	56.47	75.20	93.40

The properties of fresh and hardened concrete for all concrete mixes are presented in Table 5. The values obtained by the density of lightweight mixtures, range from $1.48 \text{ t}/\text{m}^3$ to $1.68 \text{ t}/\text{m}^3$. Concrete mixtures having density lower than $1920 \text{ kg}/\text{m}^3$ were produced and therefore all the concrete mixtures are classified as lightweight aggregate concretes [18].

In regards to the compressive strength results, the values for control and light-weight concrete mixtures after 2, 7 and 28 days of curing are illustrated in Table 5. The addition of light weight aggregates reduces the compressive strength compared to that of conventional concrete [19].

Table 5: Test results for all concrete mixes in fresh and hardened state

Mixture	Slump (mm)	Air Content (%)	Density (kg/m ³)	Compressive Strength (MPa)		
				2d	7d	28d
REF	100	1.5	2430	51.61	60.30	64.42
PeCaPu	23	4.8	1680	26.65	31.42	32.56
ePeCaPu	-	4.8	1600	24.09	29.25	34.89
PePu	40	5.1	1590	22.81	26.23	29.30
RCaPu	-	3.0	1580	16.17	20.81	25.03
Pu	60	6.3	1520	19.61	24.15	25.50
RPu	20	5.0	1500	18.08	21.59	25.51
ePePu	-	6.9	1480	19.28	25.05	25.82

The experimental results related to the durability parameters are presented in the following diagrams (Fig. 2-4), where the concrete mixtures are illustrated from left to right, with descending density. The experimental results for the open porosity, *OP* (%) (Fig. 2) show the lightweight aggregates, as they are generally more porous, they performed an increased water absorption when compared with normal aggregates.

With regards to sorptivity *S* (mm/min^{0.5}) test, the results are presented in Fig. 3. The coefficient of correlation (*R*²) values are found to be near to 1 for all specimens, satisfying the high degree of linearity that the standard prescribes. The values obtained by the sorptivity coefficient, range from 0.0691 mm/min^{0.5} to 0.1032 mm/min^{0.5}.

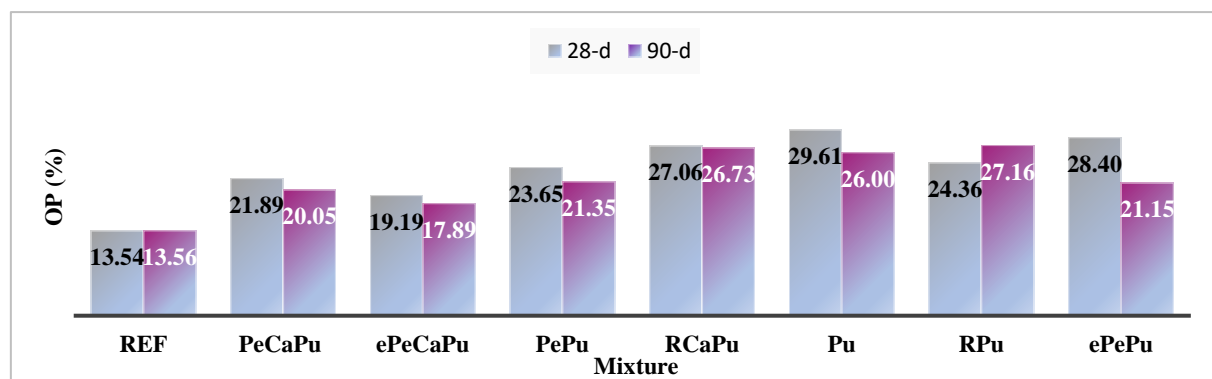


Figure 2: Open porosity, *p* (%) of concrete, at 28th and 90th days

Test results in terms of chloride migration, are shown in Fig.4. As it can be seen the resistance to chlorides in lightweight concrete mixtures is extremely high and very high in some cases and low of conventional concrete, according to the classification given by Nilsson et al [20]. The values obtained by the chloride penetration coefficient for lightweight concrete are in the range of $1.76 \times 10^{-12} \text{ m}^2/\text{s}$ to $3.27 \times 10^{-12} \text{ m}^2/\text{s}$, when a value of $15.73 \times 10^{-12} \text{ m}^2/\text{s}$ is measured for conventional concrete at 90 days. The specimen incorporating 15% RHA and pumice (RPu) had a better performance at 90d (enhancement 90.70%).

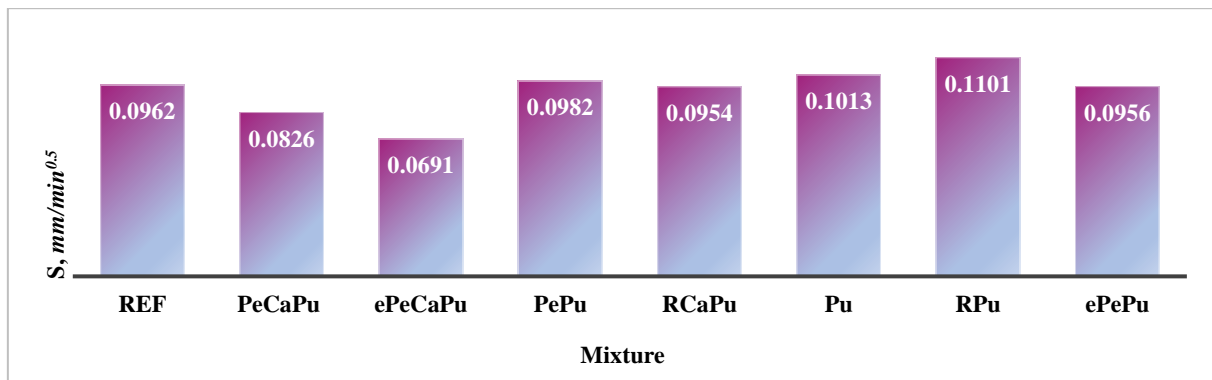


Figure 3: Sorptivity, S (mm/min^{0.5}) of concrete, at 28th days

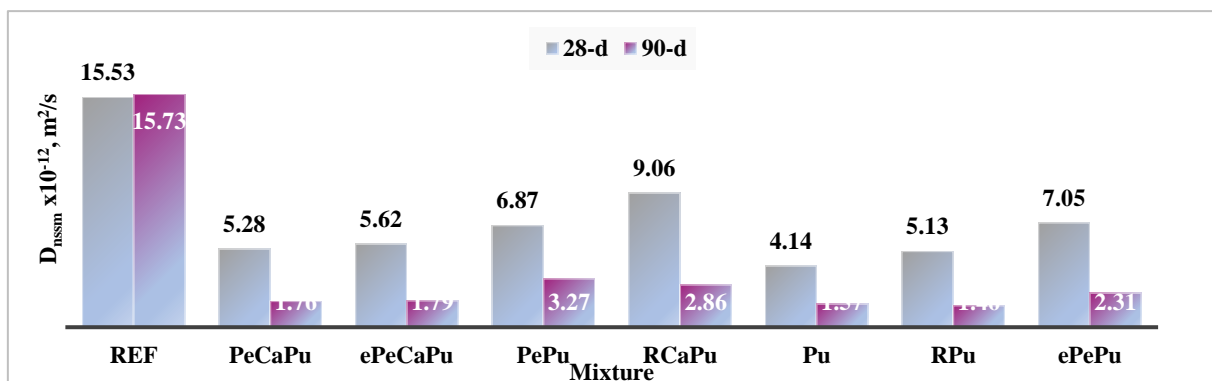


Figure 4: Chloride migration coefficient $D_{nssm} (x10^{-12})$ of the mixtures, at 28th and 90th days

4. CONCLUSION

This paper presents the results of durability tests performed on lightweight concrete incorporating pumice, perlite, expand perlite and rice husk ash in different percentage. The main conclusions of the investigation are:

- Concrete mixtures with pumice and perlite develop satisfactory compressive strength and can be used in structural applications. Particularly the addition of natural perlite aggregates to concrete mixtures does not detract its strength at all.
- The open porosity values of lightweight concrete are generally estimated to be increased. The use of perlite aggregates positively affects the porosity of lightweight concrete mixtures.
- The combination of pumice and waterproof expanded perlite leads to a reduction in the capillary absorption coefficient, compared to conventional concrete.
- The addition of lightweight aggregates, especially the combination of rice husk ash and pumice, positively affected the concrete's resistance to chloride migration coefficient, which is recorded up to ten times lower than conventional concrete's resistance.

ACKNOWLEDGEMENTS

The authors gratefully acknowledge TITAN Cement Company S.A., IMERYS Minerals Ltd and NANOVIS Inc., for the materials supplying.

REFERENCES

- [1] Tapali, J.G., Demis, S., and Papadakis, V.G., 'Sustainable concrete mix design for a target strength and service life', *Computers and Concrete*, **12** (6) (2013) 755-774.
- [2] EN 15643-2, 'Sustainability of construction works – assessment of buildings' (Brussels, Belgium, European Committee for Standardization, 2011).
- [3] Akadiri, P., Chinyio, A.E. and Olomolaiye, O.P., 'Design of A Sustainable Building: A Conceptual Framework for Implementing Sustainability in the Building Sector', *Buildings*, **2** (2012) 126-152.
- [4] Antiohos, S.K., Tapali, J.G., Zervaki, M., Sousa-Coutinho, J., Tsimas, S. and Papadakis, V.G., (2013). 'Low embodied energy cement containing untreated RHA: A strength'. *Construction and Building Materials*, **49** (2013) 455-463.
- [5] Stratoura, M., Iaz, D.R. and Badogiannis, E., 'Chloride Penetration in Lightweight Aggregates Mortars Incorporating Supplementary Cementing Materials', *Advance in Civil Engineering*, 2018.
- [6] Granata, M.F., 'Pumice powder as filler of self-compacting concrete', *Construction and Building Materials*, **96** (2015) 581-590.
- [7] Erdogan, S.T. and Saglik, A.U., 'Early-age activation of cement pastes and mortars containing ground perlite as pozzolan'. *Cement & Concrete Composites*, **38** (2013) 29-39.
- [8] Rashad, A.M., 'A synopsis about perlite as building material – A best practice guide for Civil Engineer'. *Construction and Building Materials*, **121** (2016) 338-353.
- [9] Erdem, T.K., Meral, C., Tokyay, M. and Erdogan, T.Y., 'Use of perlite as a pozzolanic addition in producing blended cements', *Cement & Concrete Composites*, **29** (1) (2007) 13-21.
- [10] Antiohos, S.K., Papadakis, V.G. and Tsimas, S., (2014). 'Rice husk ash (RHA) effectiveness in cement and concrete as a function of reactive silica and fineness'. *Cement and Concrete Research*, (61-62) (2014) 20-27.
- [11] Kartini, K., 'Rice husk ash - pozzolanic material for sustainability', *International Journal of Applied Science and Technology*, **1** (6) (2011).
- [12] BS 3892, 'Specification for pulverized-fuel ash for use in cementitious grouts', Part 3 (BSI, London, 1997).
- [13] ASTM C 642, 'Standard Test Method for Density, Absorption, and Voids in Hardened Concrete' (ASTM International, United States, 1997).
- [14] Hall, C. and Kam-Ming Tse, T., 'Water movement in porous building materials -VII.The sorptivity of mortars', *Building Environment*, **21** (1986) 113-118.
- [15] RILEM TC 116-PCD, 'RILEM Technical Recommendation: Determination of the capillary absorption of water of hardened concrete', In *Materials and Structures*, **32** (1999) 178-179.
- [16] NT Build 492, 'Concrete, mortar and cement-based materials: Chloride migration coefficient from non-steady state migration experiment' (Nordtest, Finland, 1999).
- [17] Kim, H.S., Lee, S.H. and Moon, H.Y., 'Strength properties and durability aspects of high strength concrete using Korean metakaolin', *Construction and Building Materials*, **21** (6) (2007) 1229-1237.
- [18] ACI 211.2-98, 'Standard Practice for Selecting Proportions for Structural Lightweight Concrete', (ACI Committee, United States, 2004).
- [19] Stratoura, M., Badogiannis, E. and Papadakis, V.G., 'Study on the durability parameters of lightweight concrete'. 18th Greek Concrete Conference, Athens, Greece, March, 2018.
- [20] Nilsson, L., Ngo, M.H. and Gjrv, O.E., 'High-performance repair materials for concrete structures in the port of Gothenburg', Proceedings of the Second International Conference on Concrete Under Severe Conditions - Environment and Loading, London and New York, 1998, 1193-1198.

C/S RATIO INFLUENCE ON THE CARBONATION OF CEMENTITIOUS MATERIAL USING DESIGNED MODEL SYSTEMS

Kangni-Foli, E (1,2,4), Poyet, S. (2) Le Bescop, P. (2), L'Hôpital, E. (1), Dautères, A. (1), Charpentier, T. (3), d'Espinose de Lacaillerie, J.-B. (4),

(1) IRSN, Institute of Radiation Protection and Nuclear Safety, PSE-ENV/SEDRE/ LETIS, BP 17, F-92262 Fontenay Aux Roses, France

(2) CEA, DEN, DPC, SECR, Laboratoire d'Etude du Comportement des Bétons et des Argiles, F-91191 Gif-sur-Yvette, France

(3) NIMBE, CEA, CNRS, Université Paris-Saclay, CEA Saclay, F-91191 Gif-sur-Yvette Cedex, France

(4) Soft Matter Science and Engineering, ESPCI Paris, Université PSL, 10 rue Vauquelin, 75005 Paris, France

Abstract

This article presents some preliminary results on the consequences of carbonation on the chemistry, and microstructure of hardened C-S-H pastes. Two pastes were made of pure C-S-H and of C-S-H in presence of portlandite (CH). We formulated pastes of controlled mineralogy aiming at discriminating each phase (namely C-S-H and portlandite) contribution to carbonation. Materials were obtained by mixing stoichiometric quantities of C_3S and colloidal silica to obtain CaO/SiO_2 (C/S) ratios of 1.4 and 3.0. After accelerated carbonation, their crystal-chemical and microstructural changes upon carbonation were characterized. The first results confirmed a lower carbonation rate and a lesser extent of carbonation within the paste including C-S-H and portlandite, due to the higher calcium content and the passivation effect induced by the calcium carbonate precipitation.

Keywords: C-S-H, CH, accelerated carbonation, microstructure

1. INTRODUCTION

Low-pH cementitious materials are considered as constitutive materials for the French geological disposal facility (Cigeo project). The recourse to those materials is justified by the will to minimize the impact of the alkaline plume on the surroundings clayey rocks and to decrease the temperature during the concrete hardening. They are characterized by a reduced

pH of the poral solution due to the replacement of part of the cement by a massive addition of siliceous bearing supplementary cementing materials such as fly ash, slag or silica fume, the latter being the most effective pH lowering addition. Additionally, these substitutions lower the level of embodied CO₂ of the cement, resulting in a more sustainable material.

Several studies focused on low-pH cements durability have been carried out but some information essential to their evolutions upon carbonation are still missing. Auroy *et al.* [1] enlightened increased transport properties and higher cracking rate on low-pH cement paste upon atmospheric carbonation compared to OPC. Serdar *et al.* [2] showed an increase of the steel carbonation-induced corrosion rate.

The lower Ca content for low-pH material induces materials that are portlandite free. Consequently to better understand the impact of C-S-H carbonation on the properties of low-pH cement pastes, model pastes made of pure C-S-H with C/S ratio of 1.4 were designed and compared to paste of C/S ratio of 3 made of C-S-H and portlandite.

2. MATERIALS AND METHODS

Hardened pastes were prepared by hydrating C₃S or C₃S with colloidal silica mixed in stoichiometric ratio to reach targeted molar C/S ratios of 1.4 and 3.0. Kangni-Foli et al. [3]. The paste workability was adjusted using a commercial polycarboxylate superplasticizer and increasing the water-to-binder ratio (w/b in %wt) of the C/S = 1.4 paste because of the high water demand of the colloidal silica (

Table 1). A volume of 1.40 L of each paste was prepared using a planetary mixer and then poured in cylindrical molds (Ø30 mm × H110 mm). After casting, the pastes were kept one month in their molds before unmolding and then two more months in curing solution. Curing solution was obtained by adding crushed sample into water for C/S = 1.4 samples, while saturated solution of calcium hydroxide was fabricated for C/S = 3.0 samples. The aim was to obtain curing solution, which mimic poral solution, in order to reduce the alteration of the materials chemistry.

2.1 Carbonation process

Accelerated carbonation was implemented using a climatic chamber in which the conditions were set to 3% CO₂, 55% RH and 25 °C. Parts of the samples were covered with aluminium foil in order to allow unidirectional carbonation through one of the cylinder's end face. Before carbonation and after curing the pastes were dried in free CO₂ desiccator in presence of salt solution Mg(NO₃)₂, in order to approach the hydric state (55%) of carbonation conditions. The equilibrated state for each paste was determine by mas balance

2.2 Chemical and mineralogical properties

The carbonated sample was cut in two parts; one half was stained with phenolphthalein to measure the carbonated depth and the other one was used to characterize the change in mineralogy (see below).

Thermogravimetric analyses (TGA) data were acquired on a Netzsch STA 409 PC Luxx apparatus. Analyses were ran under constant N₂ flowing (80 ml/min) and a heating rate of 10 °C/min. The weight losses from samples of 120 mg of pastes crushed into powder were recorded from 25 °C to 1150 °C. Quantification were based on weight losses due to portlandite and calcium carbonate decompositions.

Pastes' mineralogical properties were unveiled by powder X-ray diffraction (XRD). Data were collected on a XPD PANalytical X'Pert diffractometer with a Bragg-Brentano geometry,

Θ - Θ configuration, and using Cu $K\alpha$ radiation as a light source operated at 45 kV, 40 mA on samples' surface. The use of an X'Celerator detector made possible to scan a 2Θ angular domain ranging from 5° to 55° with an angular step of 0.017° in less than 20 min. Rietveld refinement were computed on PANanalytical HighScore Plus software. Except C-S-H for which a suitable model structure is not accessible, all the phases detected were accounted for in the refinement process.

2.3 Microstructural evolutions

3D visualization of the chemical and microstructural evolutions within the material was obtained by micro X-ray Computed Tomography (X-ray μ CT). Tomographic projections were acquired on a Bruker SkyScan 1173 equipped with a flat panel sensor of 2240×2240 pixel as X-ray detector. Analyses parameters were set as follow: voltages ranged from 115-130 kV, intensities between 61-69 μ A, 360° scans with a rotational step of 0.3° , exposure time of 1100 ms, and frame averaging varying from 8 to 10.

The pastes' distribution of mean pore entry sizes was scrutinized using mercury intrusion porosimetry (MIP) on a Micrometrics Autopore IV device. Samples were crushed, immersed in liquid nitrogen then kept under vacuum during seven days in order to dry. Analyses were operated at $20^\circ\text{C} \pm 0.1^\circ\text{C}$ using a maximal injection pressure of 414 MPa. Four samples of each C/S ratio were tested.

3. RESULTS

3.1 Non carbonated materials properties

Table 1 gathers the main properties of the two pastes. Paste of C/S = 3.0 included C-S-H and portlandite but the paste of C/S = 1.4 was only composed of C-S-H. Estimation of C-S-H content was achieved using the model proposed by Olson and Jennings [4], based on water desorption isotherms data and samples' water content when equilibrated at RH = 20%. The CH and C-S-H contents correlated quite well with those expected for fully hydrated C_3S pastes (7.0 and 5.4 mol/L for CH and C-S-H respectively).

Table 1: Properties of the pastes

C/S	Porosity (105°C)	Saturated density (g.cm ⁻³)	Water/binder (% wt)	Portlandite (mol/L)	C-S-H (mol/L)
3.0	40.4%	1.89	0.50	7.0	5.4
1.4	55.4%	1.76	0.63	0.0	7.0

The hardened pastes demonstrated different densities due to different compositions and water to binder ratios. Pastes porosities obtained by MIP are displayed in Figure 1. Paste of C/S = 3.0 exhibited a binomial pore distribution: a C-S-H's porosity at lower pore entry diameter (centered at 35 nm) and a capillary porosity at higher pore entry diameter (centered around 200 nm). By comparison, the paste of C/S= 1.4 revealed essentially only the C-S-H porosity with lower critical pore entry diameter centered around 25 nm. The volume of capillary porosity was significantly lowered for the lowest C/S ratio whereas the volume associated to the C-S-H porosity was increased, suggesting thus a higher C-S-H content.

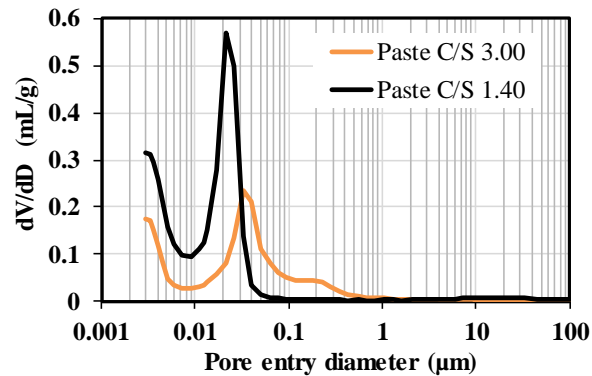


Figure 1 Mercury intrusion porosimetry of C/S = 3.0 and 1.4 paste before carbonation

3.2 Carbonation

From the previous results, it is clear that the two pastes had dissimilar microstructure and chemical composition, and, thus that different behaviour upon carbonation could be expected.

3.2.1 Chemical and mineralogical evolutions

Following two carbonation terms, 28 and 71 days for C/S = 1.4 pastes, 38 and 81 days for C/S = 3.0 pastes the carbonation depths were measured (Figure 2). Lower carbonation depths were observed in paste with C/S = 3.0 compared to the paste of C/S = 1.4. Moreover, all the methods implemented gave consistent value of carbonation depth.

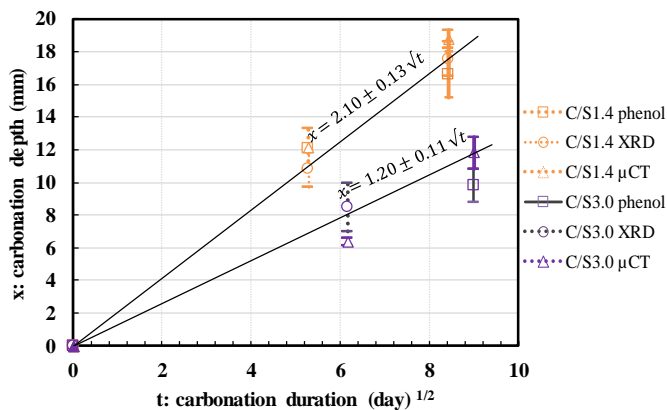


Figure 2 Two carbonation terms for each paste. The carbonation depth are estimated with phenolphthalein (phenol), X-Ray Diffraction (XRD), and micro X-ray Computed Tomography (μ CT). Assuming a diffusion limited regime, the rate of carbonation are characterized

The distribution of calcium amongst all phases (CaCO_3 , Ca(OH)_2 , C-S-H) for the first carbonation term and at different depths is shown on Figure 3 (C/S = 3.0) and on Figure 4 (C/S = 1.4). The distribution of calcium is based on TGA results. First, the Ca's distribution amongst portlandite and C-S-H was determined. After carbonation, the amount of non-carbonated C-S-H calcium is obtained by deducing non-portlandite calcium transformed into

calcium carbonate from the sound C-S-H calcium content. In the carbonated zone of the C/S = 1.40 paste, the C-S-H were completely dissolved and the corresponding calcium was mobilized into calcium carbonate phase. The C/S = 3.0 paste exhibited a different behaviour: C-S-H and Ca(OH)_2 were carbonated simultaneously and the carbonation remained incomplete.

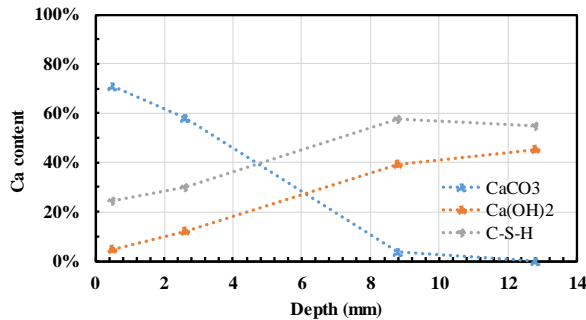


Figure 3 C/S = 3.0 38 days

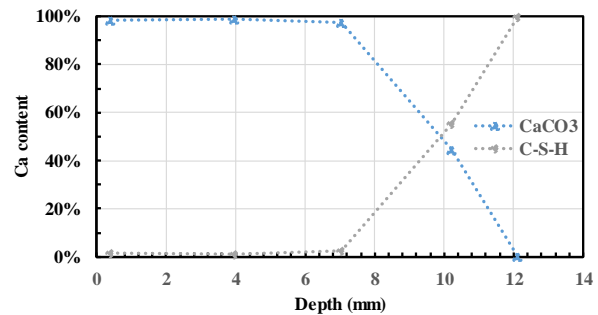


Figure 4 C/S = 1.4 28 days

Figure 5 shows the Ca phases' profile in the C/S = 3.0 paste carbonated during 38 days. The paste contained mainly aragonite in the first millimeter depth. Then calcite was the main phase observed until reaching the carbonation front. Figure 6 displays Ca phases' distribution with respect to the depth of C/S = 1.40 paste carbonated during 28 days. Vaterite was the main phase within the carbonated area, however aragonite was also found. The main carbonate polymorphs found in paste with C/S= 3.0 and 1.4 are characteristic of portlandite and C-S-H carbonation respectively

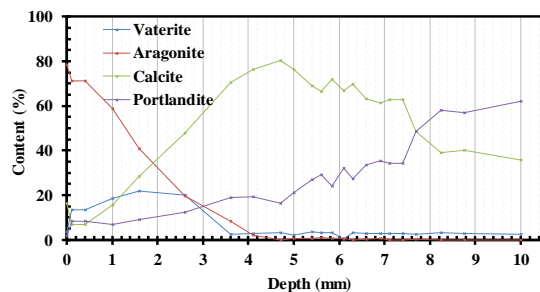


Figure 5: C/S= 3.0 38 days Ca phases content by Rietveld analysis

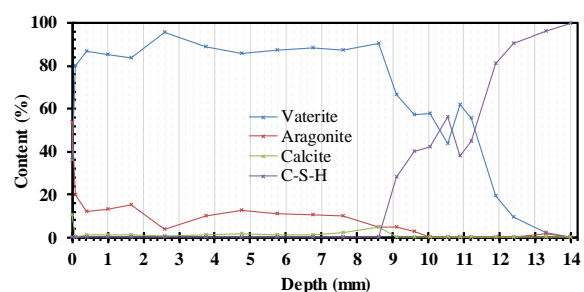


Figure 6: C/S= 1.4 28 days Ca phases content by Rietveld analysis

3.2.2 Microstructural changes

Figure 7 and Figure 8 display slices within the pastes' specimens after the first carbonation term obtained by X-ray tomography. As already observed Wan *et al.* [5] the carbonated parts were cracked. The extent of cracking appeared to be different for each paste. Extent of cracks shown by the pastes varies with the C/S ratio, higher C/S ratio demonstrated lower amount of cracks and reduced crack network throughout the paste.

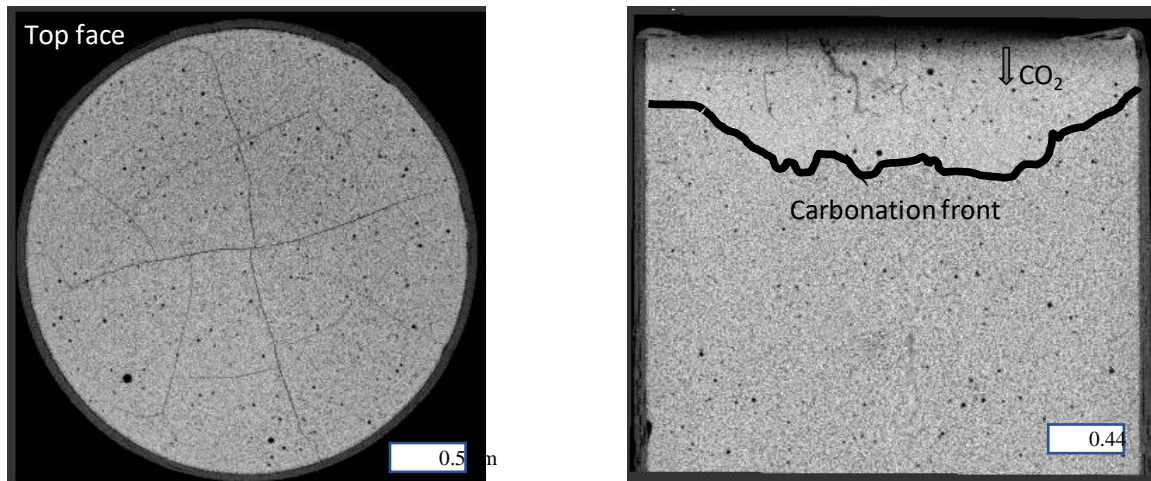


Figure 7: X-ray μ CT of $C/S = 3.0$ paste after 38 days of accelerated carbonation (voxel size $17 \mu\text{m}$)

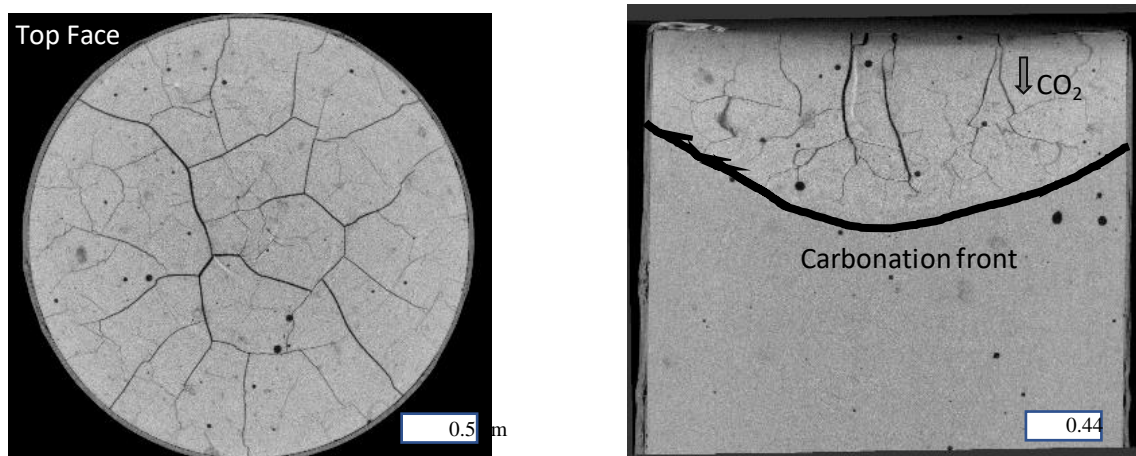


Figure 8: X-Ray μ CT of $C/S = 1.40$ paste after 28 days of accelerated carbonation (voxel size $17 \mu\text{m}$)

4. DISCUSSION

Lower C/S paste demonstrated higher carbonation rate. This could be partly explained by the lower calcium content, which implies a decreased buffering capability upon carbonation Leeman *et al.* [6]. Moreover, the carbonation of the $C/S = 1.4$ paste also led to severe cracking which also contributed to accelerate carbonation by increasing the speed of CO_2 diffusion through the carbonated zone. The relative contributions of these two phenomena (Ca-buffer and cracking) remain to be evaluated.

The paste of $C/S = 3.0$ exhibited a higher CaCO_3 content (% of available Ca) than that of the $C/S = 1.4$ paste. That is to be linked to the fact that the concentration of calcium carbonates precipitated (in mol/L of paste) is greater in the $C/S = 3.0$ paste and that it tends to form a “passivation” layer that limits the dissolution of Ca-bearing phases, explaining also why the carbonation of CH and C-S-H remained incomplete, Thiéry *et al.* [7].

The cracks observed using X-Ray μ CT were believed to be induced by the decalcification of the C-S-H and the subsequent polymerisation of the silicate which produces silicate gel, Swenson *et al.* [8]. Such polymerisation was proven to induce shrinkage and in the end cracking, Chen *et al.* [9].

5. CONCLUSION

In the framework of the research and development related to the French deep geological disposal, the likely recourse to low pH cementitious materials, and the necessary need to evaluate the durability of these materials upon carbonation, we presented some preliminary results on the impact of carbonation on their C-S-H constituent depending on the hardened pastes C/S ratio. We investigated chemical and microstructural evolutions on pastes with target C/S ratios of 3.0 and 1.4. We observed a higher carbonation rate within the paste of lower calcium content as well as a higher extent of cracking. This behavior is possibly related to a lower buffering effect at low Ca content. Paste of higher calcium content (C/S = 3.0) has shown lower extent of carbonation (% of available Ca) along with reduced crack, as a passivation is induced by the carbonation of portlandite slowing thus the carbonation rate within the paste. More insight will be given in the future specially in terms of the diffusive properties of the paste and their contribution to the material's degradation.

ACKNOWLEDGEMENTS

We thank CEA and IRSN for the financial support.

REFERENCES

- [1] Auroy, M., Poyet, S., Le Bescop, P., Torrenti, J.-M., Charpentier, T., Moskura, M., Bourbon, X., 'Impact of carbonation on unsaturated water transport properties of cement-based materials', *Cem. Concr. Res.* **74**, (2015) 44-58.
- [2] Serdar, M., Poyet, S., L'Hostis, V., Bjegović, D., 'Carbonation of low-alkalinity mortars: influence on corrosion of steel and on mortar microstructure', *Cem. Concr. Res.* **101**, (2017) 33-45.
- [3] Kangni-Foli, E., Poyet, S., Le Bescop, P., Dauzères, A., L'Hôpital, E., Charpentier, T., d'Espinose de Lacaillerie, J.-B., 'Designing a model system for Low-pH cement', Proceedings of Symposium NUWCEM, Avignon, France, Oct. 2018.
- [4] Olson, R.A., Jennings H.M., 'Estimation of C-S-H content in a blended cement paste using water adsorption', *Cem. Concr. Res.* **31** (2001) 351-356
- [5] Wan, K., Xu, Q., Wang, Y., Pan, G., '3D spatial distribution of the calcium carbonate caused by carbonation of cement paste' *Cem Concr Comp.* **45** (2014) 255-263
- [6] Leemann A., Nygaard P., Kaufmann J., Loser R., 'Relation between carbonation resistance, mix design and exposure of mortar and concrete'. *Cem Concr Comp.* **62** (2015) 33-43
- [7] Swenson, E.G. and Sereda, P.J., 'Mechanism of the Carbonation Shrinkage of Lime and Hydrated Cement'. *Journal of Applied Chemistry*, **18**, (1968) 111-117
- [8] Thiéry, M., Villain, G., Dangla, P., Platret, G., 'Investigation of the carbonation front shape on cementitious materials: effects of the chemical kinetics' *Cem. Concr. Res.* **37** (2007) 1047-1058
- [9] Chen J.J., Thomas, J.J., Jennings, H.M. 'Decalcification shrinkage of cement paste' *Cem Concr Res.* **36** (2006) 801-809

INFLUENCE OF BIOMASS FLY ASH ON HYDRATION AND CARBONATION OF CEMENTITIOUS MATERIALS

Teixeira E.(1), Camões A.(1) and Fernando F.G.(2)

(1) CTAC, Department of Civil Engineering, School of Engineering, University of Minho, Portugal

(2) ISISE – Coimbra, Department of Civil Engineering, University of Coimbra, Portugal

Abstract

Biomass fly ashes (BFA) properties allow their utilization as an alkaline material and good results are obtained when they are incorporated in concrete. Its utilization can minimize problems associated with cement production and with ash management.

An experimental investigation was conducted to study the hydration and carbonation of cementitious materials with biomass fly ash. In this study BFA was incorporated on the weight of binder to produce some cementitious pastes and the hydration and carbonation of those pastes were studied.

The results obtained show that BFA has a similar behaviour on the hydration of pastes than coal fly ash that is the pozzolanic material most used worldwide. Moreover, its utilization gives alkalinity to the paste mixtures that minimizes the carbonation effect. Thus, it seems that the utilization of BFA can have a positive impact on the durability of concrete structures.

Keywords: Biomass fly ash; Carbonation; Cement; Hydration; Pastes; Pulp and paper industry

1. INTRODUCTION

Worldwide, the emissions of greenhouse gas emission are been limited and the utilization of renewable sources for energy production has been increase. The utilization of biomass for energy production by its combustion or by co-firing with coal is expected to increase more and more [1]. This lead to an increase on a new waste that needs to have a management and this residue is the biomass fly ash (BFA).

Several studies [2–4] have tried to reuse this waste as a partial replacement for cement in mortars and concrete for different rates of cement replacement. There is quite a lot of BFA that has similar pozzolanic activity as coal fly ash, such as: wheat straw, sugar cane straw and wood [2–4]. However, there is some studies [1,5,6] showing that wood biomass ash be better

when used at low percentages of cement replacement or that it may be used as an additive, because otherwise can lead to a decrease on strength and durability.

The current standards for fly ash use in concrete do not consider the using of materials like BFA or co-fired ashes. Some authors reported that biomass ashes from wood may be considered a natural pozzolan depending on their composition [1].

In this study, biomass fly ash was incorporated in cementitious paste, as cement replacement material, to study its effect in the hydration mechanism and carbonation resistance. The main goal of this work was to verify if the using of BFA can be a solution for some issues related to the use of fly ash in concrete, namely its reduced resistance against carbonation.

2. MATERIALS AND METHODS

The effect of using BFA on the hydration compounds and on the extent of carbonation in cement pastes, were evaluated using TGA analysis. During the study, a comparison between plain cement pastes and pastes with BFA or/and pastes with coal fly ash was performed. The physical and chemical characteristics of each material are presented in [8].

A group of cementitious pastes was set, replacing by weight cement by coal fly ash (CFA) and BFA (Fig. 1). The content of fly ash in blended paste was 0, 50 and 100%wt by mass of cement, to understand in each sense the fly ashes contribute for the hydration and carbonation of pastes. Pastes were prepared with 0.5 of water/binder ratio. It was used a CEM I 42.5 R, Portland cement. CFA was sampled from a Portuguese thermoelectric power plant that burned coal as fuel. BFA was sampled in a pulp and paper Portuguese industry.

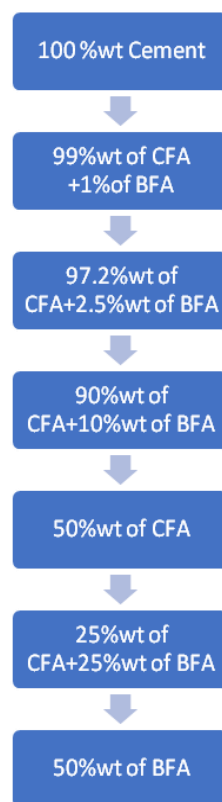


Figure 1 Paste formulations

The pastes were mixed in a standard mechanical mixer as described in [7], for three minutes, and six cubic specimens with 20 mm edge for each formulation were cast for the hydration and carbonation studies. After demoulding, which was made after 24h, all samples were cured in a humidity chamber (with approximately 87% of relative humidity and 21°C of temperature) up to the date of the tests (28 and 90 days). No accelerated carbonation was done, it was just analyzed the hydration and carbonation that occurs during the curing process. The pastes samples were milled until all particles had a diameter below 63µm and stored in a bag closed using a vacuum system, before TGA analysis. It was important to seal the samples before the TGA analysis, to prevent the continuation of samples carbonation that is done by the contact of samples with CO₂ presents in atmosphere. The thermal analysis was carried out using a STA, Netzsch 402 EP with a heating rate of 10°C/min [8].

3. RESULTS AND DISCUSSION

3.1 Thermal Analysis

Figures 2 and 3 present the TG/DTA curves of the tested hydrated pastes at 28 and 90 days of curing. The TG/DTA profiles showed typical reactions occurring in hydrated cement pastes, when submitted to a continuous increase in temperature.

For pastes with 100%wt of cement and 50%wt of cement replacement, it was observed three different peaks. The first peak observed in the graphs of TG/DTA is related to the loss of free water that occurs between 0 and 105°C. The water in the large pores evaporated for temperatures up to 35°C. Above this temperature, the retained water is released by capillarity tension in the capillarity pores [9]. The water that is not chemically combined is not used for the calculation of the level of hydration [9–11]. A weight reduction of samples was observed for temperatures between 150 and 400°C. This is due to the evaporation of the physically combined water from the reaction products (for example C-S-H gel and aluminosilicate gel) [12–14].

In the paste composed by 90%wt of cement replacement by coal fly ash and 10%wt of biomass fly ash, there was noted the highest peak related with the free water released. This is due to the fact that BFA have hygroscopic properties, and with their increase on the paste mixture, the absorption of water also has increased [15].

The Ca(OH)₂ compound is formed during the hydration of dicalcium silicate (C₂S) and tricalcium silicate (C₃S) contained in the cement. Some authors showed that for cement CEM I 42.5, this is formed at 3 days of curing [16]. One of the most noted peaks on the TG/DTA curve (Figs. 2 and 3 – (a), (e), (f) and (g)) corresponds to the mass related with the dehydroxylation of calcium hydroxide, which occurs between the temperatures of 410 and 480°C [17]. Pastes with 50%wt of CFA or with 50%wt of BFA showed a significant reduction in the level of free calcium hydroxide with an increase in the age of hydration, when compared to the cement paste. This can be explained by the pozzolanic reactions and with the calcium hydroxide (CH) produced by the hydration of cement [9]. However, it is important to note that with the increased on the BFA content, the peak related with the calcium hydroxide is higher than for the plain CFA mixture or for a blend with the two types of ashes. This can show that, the ashes used together had a positive effect on the hydration of the cementitious paste, showing a good synergic effect between the two types of ash. Also this is related with the chemical composition of biomass fly ash, that presented a higher content of calcium compounds in its chemical composition, as can be seen in [8].

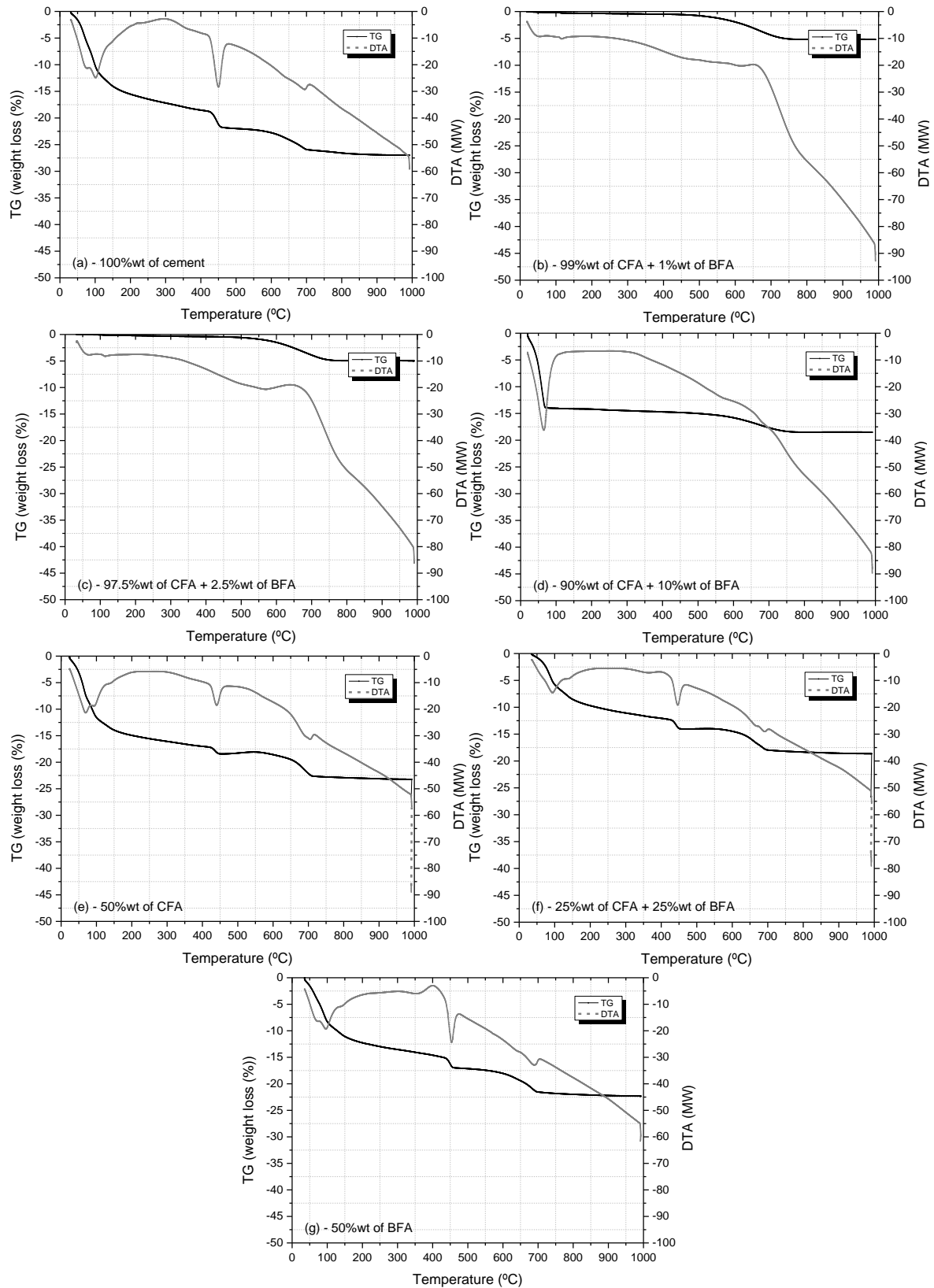


Figure 2 Thermogravimetric analysis of the studied pastes with 28 days of curing.

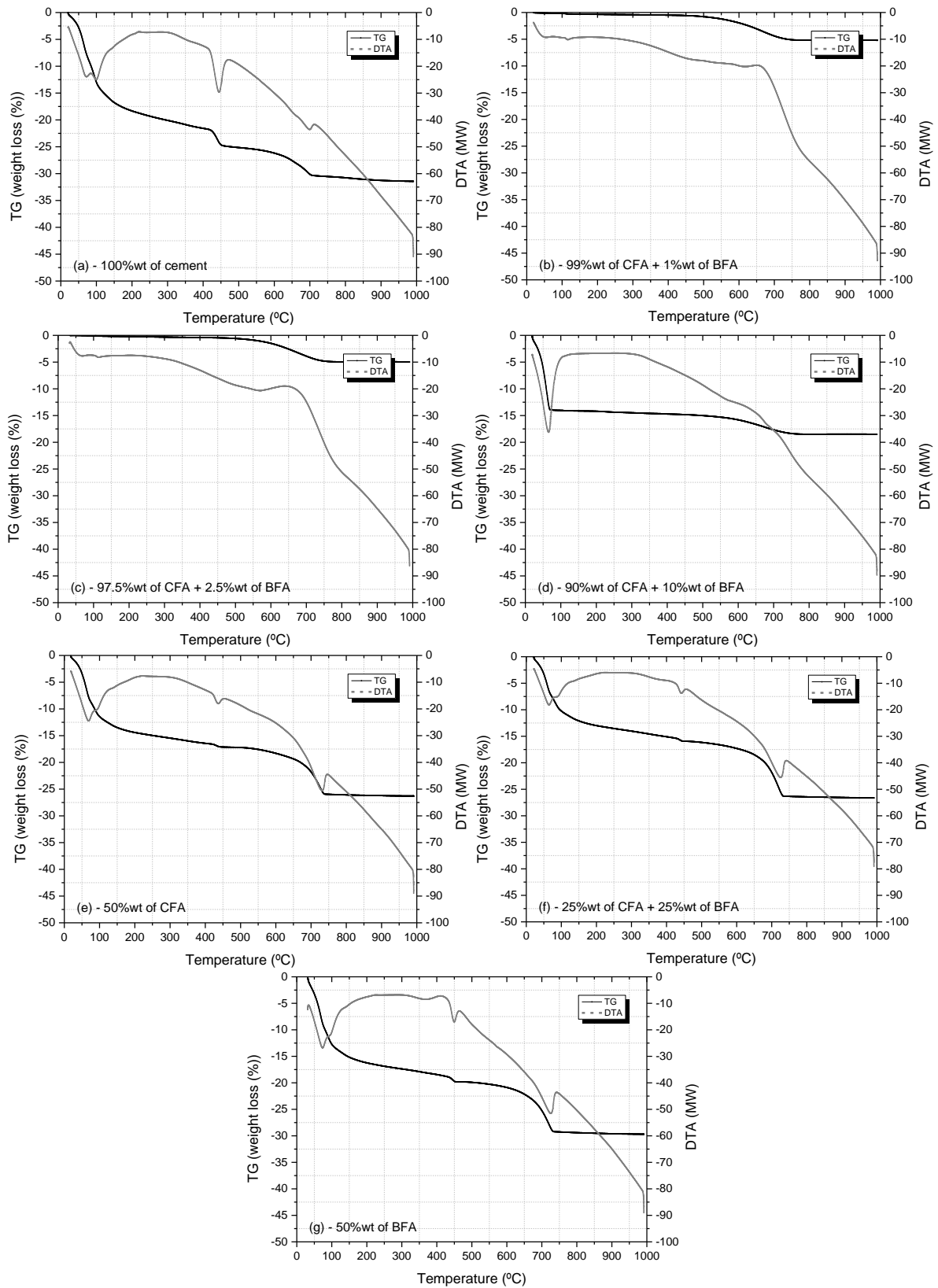


Figure 3 Thermogravimetric analysis of the studied pastes with 90 days of curing.

It is also important to refer that the total consumption of calcium hydroxide for pastes with more period of curing was not observed. Even this compound being consumed by the pozzolanic reaction and by the carbonation mechanisms, similar results were observed in [18–22].

One important observation was that pastes with 100%wt of cement replacement did not presented the peak related with calcium hydroxide once this compound is a result of cement hydration. That means that ashes did not present this calcium compound in their composition and they did not have properties for during hydration formed this compound.

The last peak observed in the thermogravimetric analysis is related with calcium carbonate (650-800°C) (Figs. 2 and 3). This peak was observed for all pastes, with or without cement. Similar results were observed in various studies [12–14,23]. The CaCO_3 analysis is very important because it is related with the carbonation phenomena and can consequently affect the corrosion of concrete reinforcement. As can be seen, the content of calcium carbonate is higher for pastes with fly ash and cement than for pastes containing only cement. The peak related with CaCO_3 released, increased from 28 to 90 days of curing, with an exception of cement paste (100C). This is explained by the fact that the carbonation mechanism is a lengthy process due to the low CO_2 concentration in atmosphere and the physical characteristics of materials, which allow some resistance to the CO_2 penetration [24]. Analysing the TGA results, it can be concluded that the utilization of BFA did not increase the resistance to carbonation, but it was not also verified an increase on the peak, that means that, in terms of calcium carbonated content presented in the pastes with BFA is similar to those with CFA. A complement of the results for the effect of BFA on the carbonation resistance can be observed in a work developed with the same ashes but in mortars [25].

4. CONCLUSIONS

The results show that pastes with BFA promote mixtures with higher alkalinity reserves and probably the BFA increases the hydrated calcium silicates formed in their pozzolanic reaction. A decrease in the CH can be observed in these pastes, when compared to cement paste. However, the content of this compound is much higher than in pastes with CFA, even at 90 days of age.

In terms of calcium carbonate formation, no significant differences were observed between using CFA or BFA, which indicated similar resistance to carbonation, for the cement replacement percentage in study (50%wt). However, a higher consumption of CH during the carbonation mechanism of coal fly ash paste was observed. The use of BFA seems to have a similar behavior to the use of CFA in terms of carbonation.

ACKNOWLEDGEMENTS

The authors wish to thank the Portuguese Foundation for Science and Technology (FCT) and the Eco-Construction and Rehabilitation Doctoral Program for supporting the PhD scholarship (reference PD/BD/52661/2014). This work was also financed by FEDER funds through the Competitivity Factors Operational Programme - COMPETE and by national funds through FCT – Foundation for Science and Technology within the scope of the project POCI-01- 0145-FEDER- 007633 and through the Regional Operational Programme CENTRO2020 within the scope of the project CENTRO-01- 0145-FEDER- 000006.

REFERENCES

- [1] Shearer, C.R. and Kurtis, K.E. 'Use of biomass and co-fired fly ash in concrete', *ACI Mater. J.* 112 (2015) 209–218.
- [2] Wang, S. and Baxter, L. 'Comprehensive study of biomass fly ash in concrete: Strength, microscopy, kinetics and durability', *Fuel Process. Technol.* 88 (2007) 1165–1170.
- [3] Biricik, H., Aköz, F., Berktaş, I. and Tülgar, A.N. 'Study of pozzolanic properties of wheat straw ash', *Cem. Concr. Res.* 29 (1999) 637–643.
- [4] Villar-Cociña, E., Valencia-Morales, E., González-Rodríguez, R. and Hernández-Ruiz, J. 'Kinetics of the pozzolanic reaction between lime and sugar cane straw ash by electrical conductivity measurement: A kinetic-diffusive model', *Cem. Concr. Res.* 33 (2003) 517–524.
- [5] Elinwa, A.U. and Mahmood, Y.A. 'Ash from timber waste as cement replacement material', *Cem. Concr. Compos.* 24 (2002) 219–222.
- [6] Udoeyo, F.F., Inyang, H., Young, D.T. and Oparadu, E.E. 'Potential of Wood Waste Ash as an Additive in Concrete', *J. Mater. Civ. Eng.* 18 (2006) 605–611.
- [7] NP EN 196-1, Norma Portuguesa - Métodos de ensaio de cimentos. Parte 1: Determinação das resistências mecânicas. Portuguese Norm - Methods for testing cement. Part 1: Determination of strength, IPQ, Instituto Português da Qualidade, 2006.
- [8] Teixeira, E.R., Camões, A., Branco, F.G. and Tarelho, L. 'Biomass and coal fly ash as cement replacement on mortar properties', in: *ICCS16 - II Int. Conf. Concr. Sustain.*, Proceedings of an International Conference, Madrid, Spain, 2016, 1–12.
- [9] Anjos, M.A.S., Reis, R., Camões, A., Duarte, F. and Jesus C. 'Evaluation of hydration of cement pastes containing high volume of mineral additions', *Eur. J. Environ. Civ. Eng.* 8189 (2017) 1–17.
- [10] Alarcon-Ruiz, L., Platret, G., Massieu, E. and Ehrlicher, A. 'The use of thermal analysis in assessing the effect of temperature on a cement paste', *Cem. Concr. Res.* 35 (2005) 609–613.
- [11] Baert, G., Hoste, S., De Schutter, G. and De Belie, N. 'Reactivity of fly ash in cement paste studied by means of thermogravimetry and isothermal calorimetry', *J. Therm. Anal. Calorim.* 94 (2008) 485–492.
- [12] Lee, N.K. and Lee, H.K. 'Reactivity and reaction products of alkali-activated, fly ash/slag paste', *Constr. Build. Mater.* 81 (2015) 303–312.
- [13] Bernal, S.A., Rodríguez, E.D., de Gutiérrez, R.M., Gordillo, M. and Provis, J.L. 'Mechanical and thermal characterisation of geopolymers based on silicate-activated metakaolin/slag blends', *J. Mater. Sci.* 46 (2011) 5477–5486.
- [14] Kong, D.L.Y. and Sanjayan, J.G. 'Effect of elevated temperatures on geopolymer paste, mortar and concrete', *Cem. Concr. Res.* 40 (2010) 334–339.
- [15] Ganesan, K., Rajagopal, K. and Thangavel, K. 'Rice husk ash blended cement: Assessment of optimal level of replacement for strength and permeability properties of concrete', *Constr. Build. Mater.* 22 (2008) 1675–1683.
- [16] K. Sisomphon, L. Franke, Evaluation of calcium hydroxide contents in pozzolanic cement pastes by a chemical extraction method, *Constr. Build. Mater.* 25 (2011) 190–194.
- [17] K.L. Scrivener, B. Lothenbach, N. De Belie, E. Gruyaert, J. Skibsted, R. Snellings, A. Vollpracht, TC 238-SCM: hydration and microstructure of concrete with SCMs: State of the art on methods to determine degree of reaction of SCMs, *Mater. Struct. Constr.* 48 (2015) 835–862.
- [18] Tkaczewska, E. and Małolepszy, J. 'Hydration of coal-biomass fly ash cement', *Constr. Build. Mater.* 23 (2009) 2694–2700.
- [19] Sakai, E., Miyahara, S., Ohsawa, S., Lee, S.H. and Daimon, M. 'Hydration of fly ash cement', *Cem. Concr. Res.* 35 (2005) 1135–1140.
- [20] Visser, J.H.M. 'Influence of the carbon dioxide concentration on the resistance to carbonation of concrete', *Constr. Build. Mater.* 67 (2014) 8–13.

- [21] Jiang, L., Lin, B. and Cai, Y. 'A model for predicting carbonation of high-volume fly ash concrete', *Cem. Concr. Res.* 30 (2000) 699–702.
- [22] Chatterji, S., Snyder, K.A. and Marchand, J. 'Depth profiles of carbonates formed during natural carbonation', *Cem. Concr. Res.* 32 (2002) 1923–1930.
- [23] Chindaprasirt, P., Paisitsrisawat, P. and Rattanasak, U. 'Strength and resistance to sulfate and sulfuric acid of ground fluidized bed combustion fly ash-silica fume alkali-activated composite', *Adv. Powder Technol.* 25 (2014) 1087–1093.
- [24] Monteiro, I.F.G. 'Modelação da evolução da carbonatação em elementos de betão armado' ("Modelation of the evaluation on the carbonation of the reinforcement concrete elements"). Master Thesis, Instituto superior técnico. Universidade Técnica de Lisboa, 2010.
- [25] Teixeira, E.R., Mateus, R., Camões A. and Branco F.G. 'Quality and durability properties and life-cycle assessment of high volume biomass fly ash mortar', *Construction and Building Materials.* 197 (2019) 195–207.

COUPLING EFFECT AND DURABILITY IN CEMENT PASTES AND CONCRETES WITH SUPPLEMENTARY CEMENTITIOUS MATERIALS

M. Saillio (1), M. Bertin (2) and V. Baroghel-Bouny (2)

(1) Université Paris-Est, MAST, CPDM, IFSTTAR, F-77447 Marne-la vallée, France

(2) Université Paris-Est, MAST, FM²D, IFSTTAR, F-77447 Marne-la vallée, France

Abstract

The main cause of deterioration of reinforced concrete structures is the corrosion of steel bars, induced by chloride ions (for example in marine environment) and/or by carbonation (atmospheric CO₂). In addition, drying in early age of concrete hydration can also modify the durability of concrete and especially for concrete mixed with supplementary cementitious materials (SCM). Carbonation, chloride and drying of hydrated cementitious materials are usually studied separately in the literature.

In this paper, few coupling effects are investigated. In particular, chloride ingress are studied for concretes and cement pastes partially carbonated. In addition, the effects of coupling between drying and carbonation are also studied. The mixtures contain CEM I alone or substituted by SCM such as Fly Ash, Metakaolin or Ground Granulated Blast furnace Slag.

The results show that chloride ingress is faster when the material is partially carbonated before contact with chloride solution. Finally, results show also that carbonation kinetics of CEM I pastes are not impacted by curing time whereas carbonation kinetics of CEM I with GGBS pastes and concretes are.

Keywords: SCM, durability, coupling effect, hydration, microstructure

1. INTRODUCTION

Corrosion of steel rebars is one of the main causes of reinforced concrete degradation. This corrosion is due to carbonation or chloride ingress [1-4]. If the corrosion due to chloride ions takes place more often in marine environments or in the presence of deicing salts, carbonation occurs systematically, in a more or less high degree, depending of the environmental conditions (relative humidity, temperature...). Numerous studies describe degradation phenomena separately but a few studies state a possible coupling [4-6].

In CO₂ free environment, the hydrated Portland cement consists of hydrated phases (portlandite, C-S-H, AFm, AFt,...) in equilibrium with a pore solution in which the pH is around 13.5. Under natural conditions of temperature and pressure, the atmospheric CO₂ is dissolved into the pore solution and reacts with portlandite. When the portlandite is

completely dissolved, the pH of the pore solution becomes lower than 9. During the carbonation process, the dissolution can affect not only portlandite but also C-S-H, AFm, AFt [3,6].

These modifications of hydrated phases are particularly important when the binder contains supplementary cementitious materials (SCMs) [7,8]. SCMs are mainly pozzolanic materials or slag activated materials, including industry waste such as ground granulated blast furnace slag (GGBS) and fly ash (FA). Metakaolin (MK) is also known for having similar effects. In concretes, these SCMs can contribute to improve strength and durability of these materials (e.g. GGBS for chloride ingress). However, they contain less portlandite than CEM I concrete. This is due to the dilution effect and the pozzolanic reactions which consume a part of portlandite. In addition, kinetics of slag activation and pozzolanic reactions are slower than clinker hydration. Consequently, durability of SCM concretes may be not the same at young age (or after drying) than in long terms.

The aim of this research is to investigate few coupling between carbonation and other phenomena (such as chloride and drying at young age) for various cementitious materials (OPC alone or with SCMs). SCMs are here GGBS, FA or MK. In particular, chloride diffusion tests were performed on partially carbonated cementitious materials in contact solution at young age or in the long terms.

2. EXPERIMENTAL

This paper is the synthesis of several experimental studies. All the cementitious materials used is presented in table 1. Materials are cement pastes and concretes.

Various water-curing times are chosen (from young age to 1 year old) in order to take into account the evolution of the microstructure as a function of the age. After water curing, the materials are cut into slices (11x5cm) and denoted Ref (as Ref materials). After water curing, slices of materials (concrete or cement paste) are dried since carbonation can occur only if cementitious materials are partially dry. They are partially carbonated in chamber (1.5% or 3.0% CO₂, 65% RH and 20°C) and denoted PCM (as Partially Carbonated Materials). In addition, after water curing, some specimens are stored under a roof and are subjected to outdoor relative humidity and temperature variations in Paris region. They are denoted NCM (Naturally Carbonated Materials). The carbonation depth of all exposed specimens has been measured by phenolphthalein test [1].

After water curing (Ref) or after carbonation treatment (PCM and NCM), materials are put in contact with NaCl solutions. The profile method is used in order to reach the apparent chloride diffusion coefficients ($D_{app,Cl}$) as well by migration test [9,10]. The chloride binding isotherms (CBIs) [9-11] is obtained by equilibrium method. Other durability indicators are also measured such as bulk porosity and mercury intrusion porosimetry (MIP).

For the O₂ diffusivity measurement, after the water curing, samples are put in chamber at T=20°C, RH=63% without CO₂ during 7 days for a curing time of 3 days and 28 days for a curing time of 6 months. After this step, samples are put in accelerated carbonation in the same conditions but with [CO₂] =3% or keep in the same conditions. Once the equilibrium is reached, O₂ diffusivity is measured as explained by Boumaaza et al. [12].

Table 1: Cement pastes and concretes mixes.

Name	Type of cement	% of SCM (MK, FA or GGBS) substituted to clinker	W/B	Concrete (C) cement paste (CP)
CEM I	CEM I	0	0.5	C, CP
CEM I MK(10%)	CEM I	10	0.5	C, CP
CEM I MK(25%)	CEM I	25	0.5	C, CP
CEM I FA(30%)	CEM I	30	0.5	C, CP
CEM III GGBS(62%)	CEM III/A	62	0.5	C, CP
CEM III GGBS(82%)	CEM III/C	82	0.5	C, CP
CEM I	CEM I	0	0.57	C, CP
CEM III GGBS (60%)	CEM III/A	60	0.57	C, CP

3. RESULTS AND DISCUSSION

3.1 Carbonation effect on chloride ingress in long cured cementitious materials

Chloride migration tests are performed on Ref or PCM after 365 days of water curing in order to obtain $D_{app,Cl}$, as well by the profile method which is closer to the natural conditions than the migration tests (see Fig. 1 and see also the carbonation depth measured by phenolphthalein test). The results are similar for both tests. When PCM and Ref are compared, the $D_{app,Cl}$ of PCM are higher than those of Ref for CEM I MK(10%), CEM I MK(25%), CEM I FA(30%) and CEM III GGBS(82%). Consequently, chloride ingress is faster in PCM with these cementitious matrixes. In first observation, these results are surprising because the porosity of PCM (see Fig. 2) is lower than Ref one (due to the formation of $CaCO_3$ in porosity). It is possible that carbonation creates microcracks as a result of hindered carbonation shrinkage [1,13]. However, the MIP shows no creation of macroporosity (see Fig. 2) in opposite to other study but for a higher W/B [14]. A loss of chloride binding capacity of the cementitious matrix could be an explanation of these results (see Fig. 3) and in particular for $D_{app,Cl}$ obtained by the profile method. However, it is generally accepted that $D_{app,Cl}$ measured by migration test weakly depends on the binding capacity of the cement matrix [9-11;13-15]. Another explanation is possible: an effect of drying (before carbonation in chamber). In order to verify this hypothesis, migration tests are performed on samples that were beforehand dried at 60°C during 9 months after 365 days of water curing. The $D_{app,Cl}$ values are respectively in this case 14.1 ; 9.9 and 6.0 m^2/s for respectively CEM I ; CEM I MK(10%) and CEM I FA(30%). These results are therefore closer to Ref ones than the PCM ones. The drying effect in the long term is thus limited.

The carbonation treatment prolonged to four months increases $D_{app,Cl}$ of 29% for CEM I (see Fig. 1). Obviously, two months of accelerated carbonation is not sufficient to show a carbonation effect on chloride ingress for CEM I concrete (The carbonation depth of 3.5mm is too low). This increase is observed for almost concrete (include CEM III GGBS(62%)).

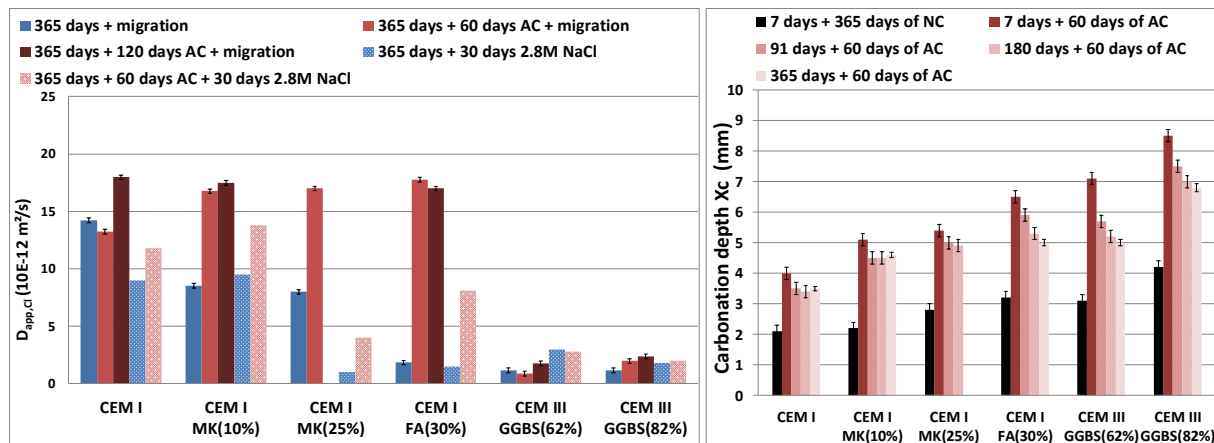


Figure 1: $D_{app,Cl}$ obtained by migration and diffusion test (in left) and carbonation depth on concrete (in right). The results are obtained after water curing (in blue) or after water curing, drying (15 days 60°C) and accelerated carbonation (AC) in chamber (1.5% CO_2 and 65% RH) (in red).

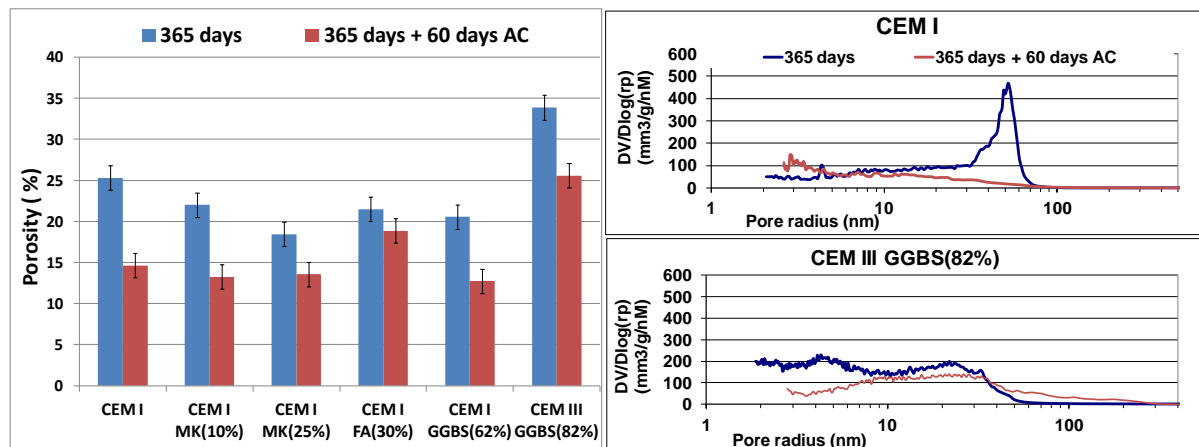


Figure 2: Porosity (in left) and pore size distribution (in right) measured by MIP. They are obtained on crushed cement paste specimens after water curing or after water curing and accelerated carbonation (AC) until constant mass (1.5% CO_2 and 65% RH).

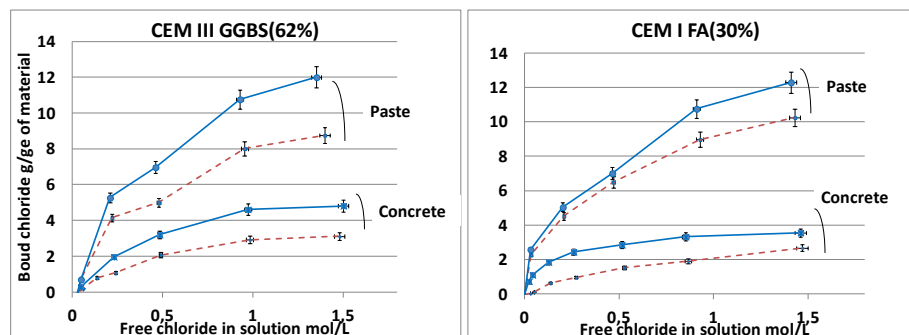


Figure 3: CBIs obtained by the equilibrium method on cement pastes and concretes. They are obtained on crushed materials after 365 days of water curing (blue line) or after water curing and accelerated carbonation (dashed red line) (AC) in chamber (3 days 1.5% CO_2 and 65% RH).

3.2 Carbonation and drying coupling in cementitious materials at young age and their effect on chloride diffusion

The Degree of carbonation (DoC) was calculated by Ochiai [16] and presented in table 2. For both binders, DoC increases with the curing time. This can be explained by the formation of a CaCO_3 protecting film on the crystal of Portlandite [17] which lead to a small part of Portlandite is not accessible to the pore solution. DoC is higher in the CEM I case than the CEM I GGBS(60%) because the calcium is more accessible in the CEM I case. Moreover, the CEM I paste has a better buffer capacity than the CEM I GGBS (60%).

Moreover, carbonation leads to a bigger critical diameter excepted for the CEM I paste cured 3 days (see table 3). Therefore carbonation leads to a coarser pore structure [18]. This is mainly due to the decalcification of C-S-H [19,20] because this increase is more important in the CEM I GGBS(60%) paste case. Furthermore, carbonation leads to decrease the pore volume of gel which can be obtained by the difference between the porosity accessible to water and the porosity obtained by MIP. Indeed, at long term for the CEM I case, the critical diameter increases of one order of magnitude whereas for the CEM I GGBS(60%) pastes case, the critical diameter increases of two orders of magnitude.

Table 2.:Characterization of microstructure of cement pastes.

		CEM I 3d	CEM I 6m	CEM III GGBS (60%) 3d	CEM III GGBS (60%) 6m
Degree of carbonation (%)	Carbonated	71	81	39	55
Porosity (%)	Non-carbonated	46	44	48	45
	Carbonated	34	27	47	39
Porosity Hg (%)	Non-carbonated	34,6	30,0	39,2	31,3
	Carbonated	24,6	18,9	41,0	22,8
Critical diameter (nm)	Non-carbonated	146	38	313	6
	Carbonated	130	174	715	419
Formation factor	Non-carbonated	109	33	193	5
	Carbonated	30	30	13	27

The results of O_2 diffusivity for the non-carbonated and carbonated cement pastes are shown on the Fig. 4. The values obtained for the CEM I are similar to the values obtained by Houst [21]. For the cement pastes two trends are observed. On one hand, for the CEM I paste case, carbonation decreases the D_{O_2} [22]. This is due to the decrease of bulk porosity which is a consequence of the precipitation of CaCO_3 in the porosity. On the other hand, for the CEM I GGBS(60%) paste, carbonation leads to a higher D_{O_2} [23]. This can be explained by the lower tortuosity and a higher connectivity of the material after carbonation as shown by the increase of the formation factor for a curing time of 6 months. For both cement pastes, the trends are the same for the two curing time but longer is the curing time, more important is the difference between the non-carbonated and the carbonated state.

The materials with a binder with GGBS have a D_{O_2} lower than the CEM I materials but after carbonation, it is the opposite case. Therefore, for the studied materials, the use of GGBS leads to a higher sensitivity to the carbonation due to a higher D_{O_2} and a lower buffering power. Moreover, it seems that the O_2 diffusivity should be measured on the carbonated material in order to be used as durability indicator.

For both systems with CEM I, the carbonation depths obtained after 365 days of carbonation are similar which can be explained by the degree profiles of hydration and the

saturation profiles similar for both curing time [24]. By contrast, for both systems with CEM I GGBS(60%), the carbonation depths obtained after 365 days of carbonation decrease with a longer curing time. This can be explained by the increase of the hydration degree leads to an increase of phase amount which can be carbonated but also a higher tortuosity and a lower connectivity of void network (pore + crack). This leads to slow down the transport phenomenon through the material. Therefore, the drying kinetic is slow down which also slow down the carbonation kinetic due to a lower O_2 diffusivity [12]. However, the impact of curing time is lower in the concrete case. This can be explained by a slower transport phenomenon in concrete and by a higher tortuosity of pore network due to the aggregates with good quality of ITZ between the paste and the aggregates.

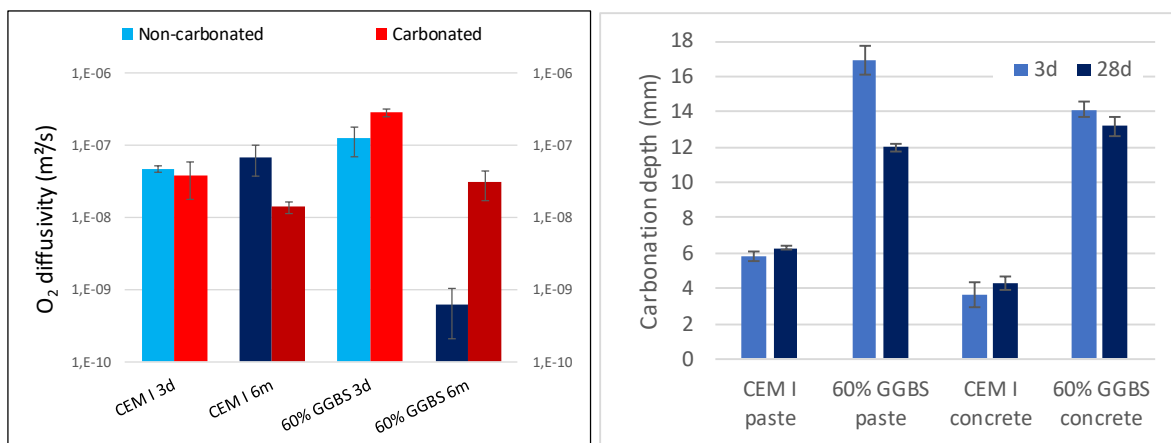


Figure 4: O_2 diffusivity for the cement pastes at $T=20^\circ C$ and $RH=63\%$ (in left) and carbonation depth obtained by Phenolphthalein spraying after 365 days at $T=20^\circ C$, $RH=63\%$ and $[CO_2]=3\%$ (in right).

Chloride migration tests are performed on Ref or PCM for various water curing time in order to obtain $D_{app,Cl}$ (see Fig. 5). At early age, comparing to “7 days” and “7 days + 60 days AC” treatment, $D_{app,Cl}$ is inferior for this last treatment. The cementitious matrix continues to evolve and the drying step (15 days at $60^\circ C$) just after 7 days of water curing does not stop completely the hydration mechanisms or maybe humidity in carbonation chamber can contribute to the hydration process. Consequently, $D_{app,Cl}$ is closer to those of “91 days” treatment than to those of “7 days” treatment”.

Migration tests are also performed on cement materials dried in chamber at lab temperature ($20^\circ C$ and average RH of the chamber measured at 65%, without CO_2) or submitted for 1 year under in-situ conditions. $D_{app,Cl}$ varies depending on the treatment (carbonation, RH , temperature,...) and the cementitious matrix (presence of SCMs). $D_{app,Cl}$ of CEM I concrete show slight variation in regards to its reference value at 365 days water curing. The $D_{app,Cl}$ of GGBS cement matrixes shows also a slightly variation. CEM III GGBS(62%) presents the best results in comparison to the other concretes, whatever the exposure conditions. For other concretes, the $D_{app,Cl}$ varies according to the exposition conditions of the materials. $D_{app,Cl}$ of concretes with FA (and to a lesser degree MK concretes) present large differences (an magnitude of 10). FA cementitious matrix seems particularly sensitive to the exposure conditions (drying and carbonation). The in-situ conditions (changes in temperature, RH and carbonation) have more impact on this concrete than the others at early age. The properties of Ref CEM I FA(30%) are slowly evolving with time (see Fig. 5), consequently, the exposure conditions at 7 days particularly affect the microstructure.

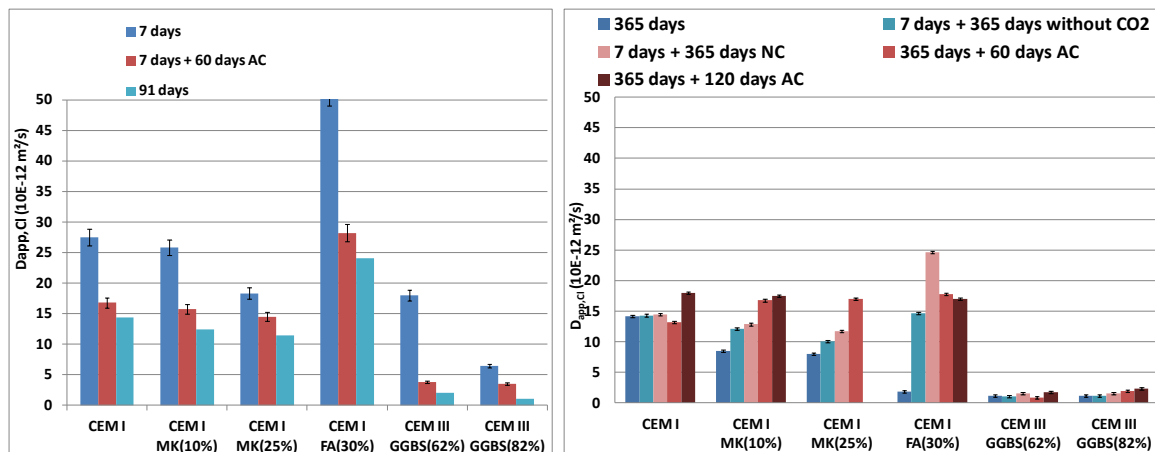


Figure 5: Chloride apparent coefficients ($D_{app,Cl}$) obtained by migration. NC: concretes are exposed during 365 days of in-situ conditions (Natural carbonation and relative humidity and temperature). AC: 15 days of drying (60°C) + accelerated carbonation in chamber (1.5 % CO_2 , 65%).

4. CONCLUSION

This research aimed to investigate the coupling between carbonation and other aggressive environment (drying at young age and chloride) for various concretes and cement pastes.

In the long term, the experimental results demonstrated that chloride ingress is accelerated by carbonation. This increase is explained by a change in the microstructure and the pore solution but also by a lower chloride binding. With regard to chloride ingress, there are differences between the various cementitious matrices. CEM III GGBS(62%) seems to be the most resistant to the effect of carbonation on chloride ingress. However, it was also shown that the experimental conditions and pre-treatment (curing time, drying and relative humidity) also have an influence on the results of chloride ingress in particular at young age. For example, the cementitious materials with fly ash are the most sensitive among all tested cementitious materials to the exposure conditions and especially to drying during its slow hydration process. It is therefore important to perform tests in natural conditions at young age (“in situ” conditions), in addition to accelerated tests in long term.

ACKNOWLEDGEMENTS

Authors are grateful to Bouygues-TP (France) and Nanocem for the founding of this study.

REFERENCES

- [1] Villain G., Thierry M., Platret G., ‘Measurement of carbonation profiles in concrete: Thermogravimetry, chemical analysis and gammadensimetry’, *Cement and Concrete Research* **37** (2007) 1182-1192.
- [2] Bouteiller V., Cremona C., Baroghel-Bouny V., Maloula A., ‘Corrosion initiation of reinforced concretes based on Portland or GGBS cements: chloride contents and electrochemical characterizations versus time’, *Cement and Concrete Research* **42** (2012) 1456-1467.
- [3] Castellote M., Fernandez L., Andrade C., Alonso C., ‘Chemical changes and phase analysis of OPC pastes carbonated at different CO_2 concentrations’, *Cement and Concrete Research* **42** (2009) 515-525.
- [4] Balonis M., Lothenbach B., Le Saout G., Glasser F.P., ‘Impact of chloride on the mineralogy of hydrated Portland cement systems’, *Cement Concrete Research* **40** (2010) 1009-1022.

- [5] Maes M., De Belie N., 'Resistance of concrete and mortar against combined attack of chloride and sodium sulphate', *Cement and Concrete Composites* **53** (2014) 59-72.
- [6] Cowie, J., Glasser, F.P., 'Accelerated friedel salt in calcium aluminate cement paste', *Cement and Concrete Research* **33** (1) (2003) 119-134.
- [7] Borges, P.H.R., Costa, J.O., Milestone, N.B., Lynsdale, C.J., 'Carbonation of CH and C-S-H in composite cement pastes containing high amounts of BFS', *Cement and Concrete Research* **40** (2010) 284-292.
- [8] Bouikni, A., Swamy, R.N., Bali, A., 'Durability of concrete containing 50% and 65% slag', *Construction and Building Materials* **23** (8) (2009) 2836-2845.
- [9] Baroghel-Bouny, V., Kinomura, K., Thiery, M., Moscardelli, S., 'Easy assessment of durability indicators for service life prediction or quality control of concretes with high volumes of supplementary cementitious materials', *Cement and concrete Composites* **33** (8) (2011) 832-847.
- [10] Andrade, C., Prieto, M., Tanner, P., Tavares, F., D'Andrea, R., 'Testing and modelling chloride penetration into concrete', *Construction and Building Materials* **39** (2013) 9-18.
- [11] Saillio M., Baroghel-Bouny V., Barberon F., 'Chloride binding in sound and carbonated cementitious materials', *Construction and Building Materials* **68** (2014) 82-91.
- [12] Boumaaza, M., B. Huet, G. Pham, P. Turcry, A. Aït-Mokhtar, C. Gehlen. 'A new test method to determine the gaseous oxygen diffusion coefficient of cement pastes as a function of hydration duration, microstructure, and relative humidity'. *Materials and Structures* **51** (2018) 51.
- [13] Morandeau A., Thiery M., Dangla P., 'Investigation of the carbonation mechanism of CH and C-S-H in terms of kinetics, microstructure changes and moisture', *Cement and Concrete Research* **56** (2014) 153-170.
- [14] Morandeau A., Thiery M., Dangla P., 'Impact of accelerated carbonation on OPC cement paste blended with fly ash', *Cement and Concrete Research* **67** (2015) 226-236.
- [15] Baroghel-Bouny V., Wang X., Thiery M., Saillio M., Barberon F., 'Prediction of chloride binding isotherms of cementitious materials by analytical model or numerical inverse analysis', *Cement and Concrete Research* **42** (2012) 1207-1224.
- [16] Ochiai, T., 'Carbonation of autoclaved light-weight concretes', *Gypsum and Lime* **242** (1993) 22-31.
- [17] Galan, I., Glasser, F.P., Baza, D., Andrade, C., 'Assessment of the protective effect of carbonation on portlandite crystals', *Cement and Concrete Research* **74** (2015) 68-77.
- [18] Bier, Th A., 'Influence of type of cement and curing on carbonation progress and pore structure of hydrated cement pastes', *MRS Online Proceedings Library Archive* **85** (1986).
- [19] Groves, A., Geoffrey W., Brough, A., Richardson, I.G., Dobson, C.M., 'Progressive Changes in the Structure of Hardened C3S Cement Pastes Due to Carbonation', *Journal of the American Ceramic Society* **74** (1991) 2891-96
- [20] Herterich, J., 'Microstructure and phase assemblage of low-clinker cements during early stages of carbonation', (2017) PhD Thesis manuscript, University of Leeds.
- [21] Houst, Y., Folker, F., Wittmann, H., 'Influence of Porosity and Water Content on the Diffusivity of CO₂ and O₂ through Hydrated Cement Paste', *Cement and Concrete Research* **24** (1994) 1165-76.
- [22] Papadakis, V., Vagelis G., Costas G., Vayenas, M., Fardis, N., 'Experimental investigation and mathematical modeling of the concrete carbonation problem', *Chemical Engineering Science* **46** (1991) 1333-38.
- [23] Turcry, P., Gendron, F., Aït-Mokhtar. A., 'CO₂ diffusion in cementitious materials made with blast furnace slag - influence of an accelerated carbonation'. (2017) In Edition, 883-87. Brussels, Belgium.
- [24] Bertin, M., 'Impact of drying at early age on the carbonation in the long-term for low clinker binders' (*in French*), (2017) PhD Thesis, University of Paris-Est.

**International Conference on Sustainable
Materials, Systems and Structures
(SMSS 2019)**
Durability, Monitoring and Repair of Structures

Influence of high temperatures

NUMERICAL INVESTIGATIONS ON POST-FIRE BOND BEHAVIOR OF REINFORCEMENT IN CONCRETE

Arunita Das (1), Josipa Bosnjak (2), Akanshu Sharma (1)

(1) Institute of Construction Materials, University of Stuttgart, Germany

(2) Materials Testing Institute, University of Stuttgart, Germany

Abstract

A safe and efficient stress transfer between reinforcement and concrete can take place if adequate bond between them is ensured. Failure of bond between reinforcement and concrete could be controlled by pull-out behaviour (pure bond failure) or premature splitting of concrete. Under normal conditions, bond behavior was extensively investigated and the design guidelines are well-established (EC2, fib MC2010). However, this behavior is relatively less-investigated under fire and post fire scenario. The studies performed so far were mainly limited to the investigations on bond pull-out behavior using confined test conditions at elevated temperature (slow heating). These test conditions don't replicate the realistic boundary conditions that involve fast heating due to fire, low covers and unconfined setup. Recently the authors have shown that the real conditions could be well-simulated using beam-end-specimen.

In this work, 3D FE numerical studies have been performed to investigate the influence of fire on residual bond capacity using beam-end specimen. A transient three-dimensional thermo-mechanical model utilizing the temperature dependent microplane model is employed as the constitutive law for concrete. Two heating types are considered to simulate the exposure conditions in a slab and beam, following ISO 834 fire scenario. First the numerical model is validated against the results of the tests performed by the authors. The validated numerical model was then used for parametric studies to investigate the influence of parameters such as concrete-cover, concrete strength, bond length etc. on the effective bond strength. The results clearly show that under realistic conditions of concrete cover, confinement and fire exposure, concrete splitting almost always governs the bond behavior before pull-out due to the irreversible damage caused in concrete owing to high thermal gradients generated during fire and during cooling. These results leads to a strong degradation of the effective bond strength and must be considered in the design recommendations.

Keywords: Beam-end test specimen, Bond strength, microplane, Splitting crack

This work was invited for publication in the open access journal RILEM Technical Letters. You can visit the journal and benefit from the full open access to the published articles at: letters.rilem.net.

EFFECTS OF RECURRING CONDITIONS ON THE MECHANICAL RECOVERY AND THE PROPERTIES OF PORTLAND CEMENT PASTE SUBJECTED TO HIGH TEMPERATURE

Heongwon Suh (1), Taehoon Park (1), Hyeonseok Jee (1), Bumyeon Cho (2) and Sungchul Bae (1)

(1) Department of Architectural Engineering, Hanyang University, Republic of Korea

(2) Korea Institute of Civil Engineering and Building Technology, Republic of Korea

Abstract

When concrete is exposed to fire, decomposition of the cement paste results in critical damage to the sustainability of the building. In this study, the mechanical properties of ordinary cement paste heated to different temperatures (200 °C, 500 °C, 800 °C, and 1000 °C) and the effects of various recurring conditions (in 20 °C 60%RH and in water for different recurring times) on the mechanical recovery were investigated. The results showed remarkable compressive strength enhancements immediately after heating to 200 °C and for samples water recurred after heating to 500 °C. For the samples heated to 200 °C, this was due to the hydration of the anhydrate clinker phase. And for the samples heated to 500 °C and water recurred, this was due to the reaction between water and amorphous CaO (produced by the decomposition of Ca(OH)_2), which forms hydrates. On the other hand, the samples heated to 800 °C and 1000 °C did not show mechanical recovery due to water recurring. Also, ^{29}Si nuclear magnetic resonance analysis showed that the mean chain length of calcium silicate hydrates was directly proportional to the compressive strength.

Keywords: Cement paste; Fire; Recurring; Mechanical recovery; NMR

1. INTRODUCTION

Concrete is considered a refractory material, but when it is exposed to high temperatures, its mechanical properties, such as durability, load capacity, and fire resistance are deteriorated [1-3]. Therefore, in order to recover the damage after fire, recurring methods for fire-damaged concrete have been studied.

Especially, Water-recurring methods have been evaluated actively. Heated concrete is commonly exposed to water because water is widely used for extinguishing fires these days; however, the effect of water on heated concrete and cement paste have not been fully investigated. Even though previous studies involved the analysis of cement paste or concrete after exposure to high temperatures, the recurring duration was relatively long, lasting from

28 days to 105 days [4-6]. Furthermore, these studies only explain the reason of an increase in strength that the increased amount of hydrates and change of porosity [4-6].

In this study, the recurring conditions in water were defined as to have relatively short duration i.e. 3 h and 24 h. In addition, the structural changes of hydrates due to the recurring, especially calcium silicate hydrates (C-S-H), were studied by ^{29}Si solid-state nuclear magnetic resonance (^{29}Si NMR) spectroscopy. The aim of this study was to measure the changes in cement paste under different temperatures (200 °C, 500 °C, 800 °C, and 1000 °C) and the effects of various recurring conditions, by examining the physical properties and changes of hydrates.

2. MATERIALS AND METHOD

2.1 Sample preparation

The samples were made using ordinary Portland cement (OPC), whose chemical composition is shown in Table 1. The water-to-cement ratio was 0.4 and the samples were cured in water for 28 days before being used in all experiments. The small size of the samples ($5 \times 5 \times 10 \text{ mm}^3$) allowed for even distribution of heat when the samples were heated.

Table 1: Composition of OPC measured by X-ray Fluorescence spectroscopy

Chemical compositions	SiO ₂	Al ₂ O ₃	Fe ₂ O ₃	CaO	MgO	K ₂ O	SO ₃	TiO ₂	LOI	Total
(wt. %)	18.43	2.83	2.17	68.17	2.37	1.11	3.03	0.15	1.72	100

2.2 Heating Process of the Specimens

The heating process was composed of three steps (Figure 1): i) heating to target temperatures (200 °C, 500 °C, 800 °C, and 1000 °C), ii) maintaining the sample at the target temperature for 2 h, and iii) cooling to room temperature in the furnace by natural cooling. Some samples were water recurred immediately after the heating, as shown in Figure 1.

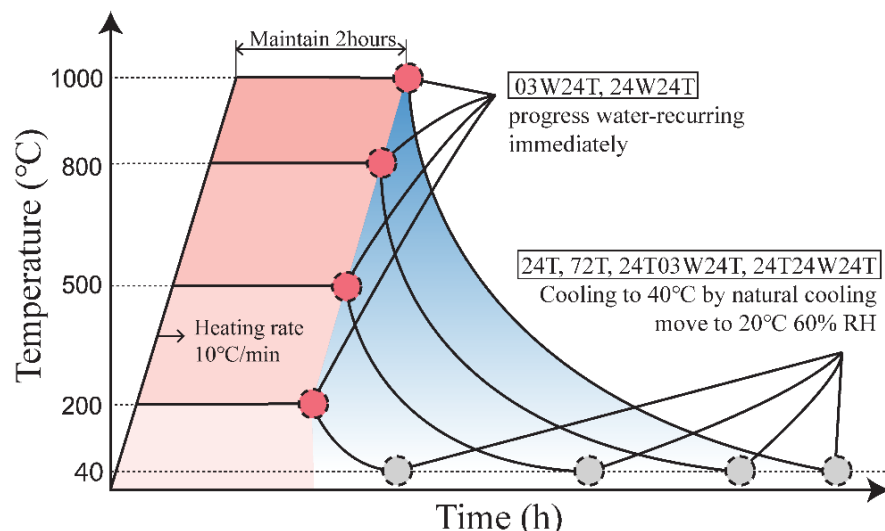


Figure 1: Heating curve for each target temperature and starting point of the recurring process

2.3 Recurring conditions

Two types of recurring conditions, thermo-hygrostat recurring (20 °C and 60%RH) and water recurring were employed. Each temperature experiment consisted of seven different conditions (after, 24T, 72T, 03W24T, 24W24T, 24T03W24T, and 24T24W24T). The details of the recurring conditions and notations are listed in Table 2. In each condition, T and W indicate 20 °C 60%RH recurring and water recurring, respectively.

Table 2: Notation method for samples according to each recurring condition

Temperature	Recurring condition (T: 20°C and 60% RH, W: Water-recurring)				
	T	W	T	Notation	Meaning
200°C 500°C 800°C 1000°C	-	-	-	(Temp)-Before	Before heating
	-	-	-	(Temp)-After	Immediate after heating
	-	03	24	(Temp)-03W24T	(immediately after heating) Water-recurring 3 h, 20°C 60% RH 24 h
	-	24	24	(Temp)-24W24T	(immediately after heating) Water-recurring 24 h, 20°C 60% RH 24 h
	24	03	24	(Temp)-24T03W24T	20°C 60% RH 24 h, Water-recurring 3 h, 20°C 60% RH 24 h
	24	24	24	(Temp)-24T24W24T	20°C 60% RH 24 h, Water-recurring 24 h, 20°C 60% RH 24 h
	-	-	24	(Temp) -24T	20°C 60% RH 24 h
	-	-	72	(Temp) -72T	20°C 60% RH 72 h

2.4 Mechanical Test and Structural Determination

The compressive strength of the samples was measured by a Deben Microtest machine (5K Dual Leadscrew Stage Controller, UK). X-ray diffraction (D2 phaser, Bruker, Germany) was used to determine the formation and decomposition of hydrates (Cu K α , $\lambda = 1.54 \text{ \AA}$, $\lambda = 1.5406 \text{ \AA}$, measuring range: 7-70°, step time: 1.5 s, step size: 0.01°). Solid-state magic-angle spinning ^{29}Si nuclear magnetic resonance measurements were conducted to investigate the relation between the mechanical properties of the cement paste and the chain length of C-S-H. (spinning speed: 10 kHz, pulse width: 3.6 μs , relaxation delay: 30 s, total 2048 scans). The number of oxygen atoms shared by the silicate tetrahedron is noted by n in Q^n , P indicates pairing tetrahedra, and B indicates bridging tetrahedra. The formula for obtaining the mean chain length (MCL) of C-S-H is as follows [7]:

$$\text{MCL} = 2 \left(1 + \frac{Q^2}{Q^1} \right) \quad (1)$$

The value of MCL can be calculated for degree of silicate polymerization of C-S-H, which

is the most important property for the strength development of cement pastes [8, 9].

3. RESULTS AND DISCUSSION

3.1 Variation in compressive strength

Immediately after heating to 200 °C (Figure 2(a)), the compressive strength increased. This was because the anhydrate clinker phase, which remained in the cement, formed hydrates when subjected to high temperatures, resulting in the enhancement of the strength [3]. For 200-24T, the shrinkage due to heating and recovery due to relaxation of the cement-paste matrix resulted in micro-cracks, which led to the decrease in the compressive strength. In addition, for all samples that were water-recurred at 200 °C, the compressive strength decreased. This could be because the micro-cracks generated by heating became larger when the samples were recurred in water due to water infiltration [6].

Immediately after heating to 500 °C, the compressive strength decreased (Figure 2(b)). For thermo-hygrostat recurring, the strength decreased for 500-24T but was recovered for 500-72T. On the other hand, for every water-recurring process at 500 °C, relatively high strength values were obtained when compared to the corresponding thermo-hygrostat samples. This is especially true for samples cured in water immediately after heating (500-03W24T and 500-24W24T), where the enhancement of strength was dramatic.

At 800 °C and 1000 °C, the strength decreased rapidly after heating due to the formation of cracks; no significant recovery was observed. The rapid decrease of strength after heating was because of the decomposition of C-S-H which results in the loss of physical properties of cement paste. In addition, the samples disintegrated under the water-recurring conditions.

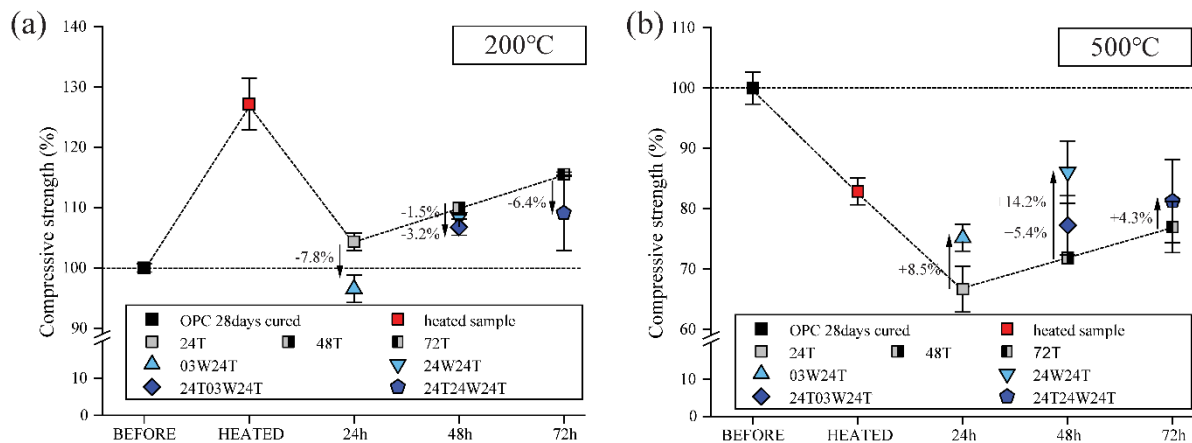


Figure 2: Compressive strength for samples recurred after heating to (a) 200 °C and (b) 500 °C

3.2 Variation in x-ray diffraction

Figure 3 shows the result of XRD for different heating temperatures. As, it can be seen in the results, after heating to 200 °C the peaks attributed to ettringite disappeared due to decomposition by high temperature. The intensity of the peaks attributed to $\text{Ca}(\text{OH})_2$ logically increased because of the hydration of the anhydrate clinker phase, which remained in the cement paste [6].

After heating to 500 °C, the peaks of Ca(OH)_2 disappeared because of the decomposition of Ca(OH)_2 [1]. A product of this decomposition is amorphous CaO , which cannot be detected by XRD [1, 2, 10] and reacts with silicate and water in the cement paste to produce hydrates such as C-S-H [5, 10]. This caused a prominent recovery of the compressive strength for samples that were water cured at 500 °C.

After heating to 800 °C and 1000 °C, CaCO_3 and C-S-H were decomposed gradually, resulting in the formation of $\beta\text{-C}_2\text{S}$ and quartz [2, 5]. The decomposition of C-S-H caused the decrease of strength in samples after heating to 800 °C.

For each heating temperature, obvious differences could not be detected between the XRD results for the different recurring conditions. This is because of the amount of hydrates formed during the recurring times used in this study was insufficient to be distinguished in the XRD analysis.

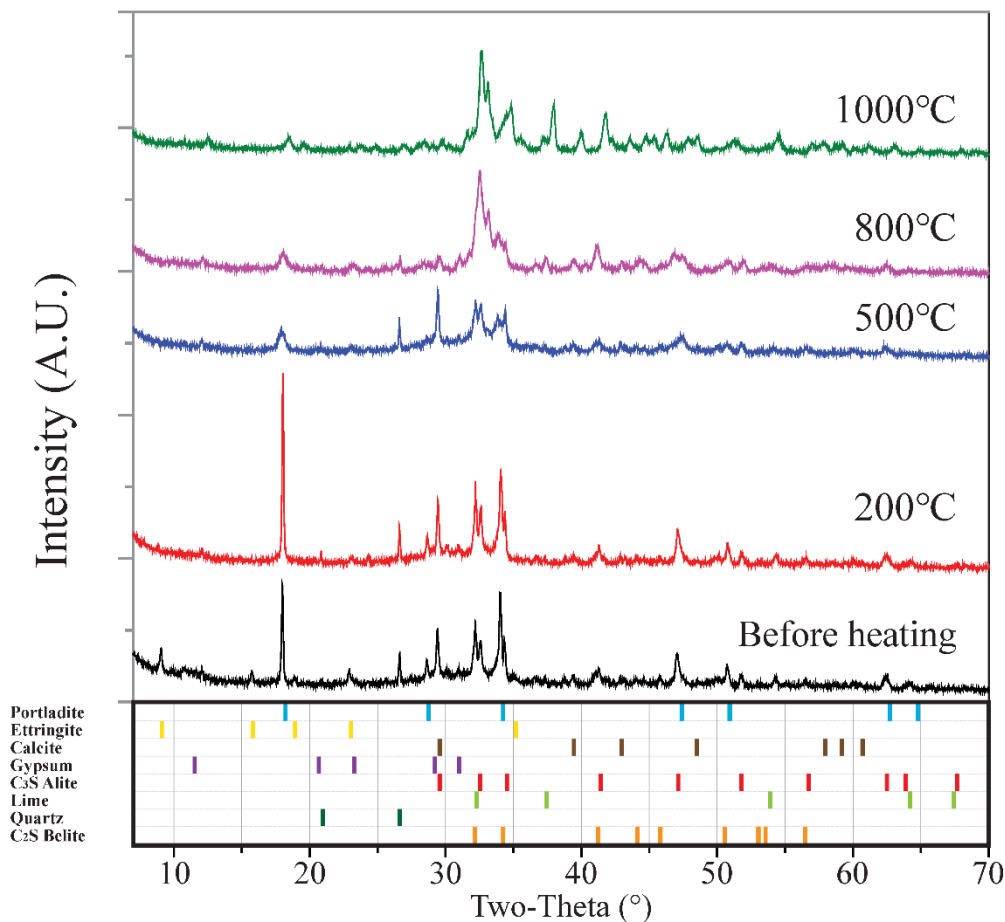


Figure 3: Results of XRD analysis for different heating temperatures
 References: Portlandite (COD 1001769), Ettringite (COD 9011576), Calcite (COD 9009668),
 Gypsum (COD 1010981), C_3S Alite (COD 9016125), Lime (COD 1000044), Quartz (COD
 9000775), C_2S Belite (COD 2103316)

3.3 ^{29}Si solid-state nuclear magnetic resonance spectroscopy

Immediately after heating to 200 °C, the MCL of C-S-H increased due to hydration of the anhydrate clinker phase (Figure 4 (e)). The MCL further increased when samples were recurred in water compared to a thermo-hygrostat. The increase of the MCL for samples recurred in water immediately after heating for 24 h (200-03W24T and 200-24W24T) was higher than that for samples recurred in water after recurring under 20 °C 60%RH conditions for 24 h (200-24T03W24T and 200-24T24W24T). This means that immediate water recurring was more efficient to increase the MCL of C-S-H. On the other hand, the MCL results were different from the compressive strength results, which showed that the strength was lower when the samples were recurred in water immediately after heating. This can be explained by the fact that when the samples were water recurred immediately after heating, the generated micro-cracks became larger by water infiltration. the decrease in strength due to the cracks was larger than the increase in strength due to the higher MCL. Therefore, the chain-length increase rate is different from the compressive-strength increase rate (Figure 5).

For 500-After the MCL decreased (Figure 4 (f)) but increased again to the initial value at 500-24T. This shows that, except for 500-After (where there was not enough time to produce C-S-H), the MCL of C-S-H and compressive strength were proportional, regardless of the recurring conditions unlike the samples heated to 200 °C.

After heating to 800 °C and 1000 °C, the MCL decreased dramatically (Figure 4 (c) (d)). when samples subjected to thermo-hygrostat curing, such as 800-T24 and 800-T72, did not show any increase in MCL. This is because 800 °C was above the decomposition temperature of C-S-H, and the recurring times used in this study were insufficient to produce new C-S-H.

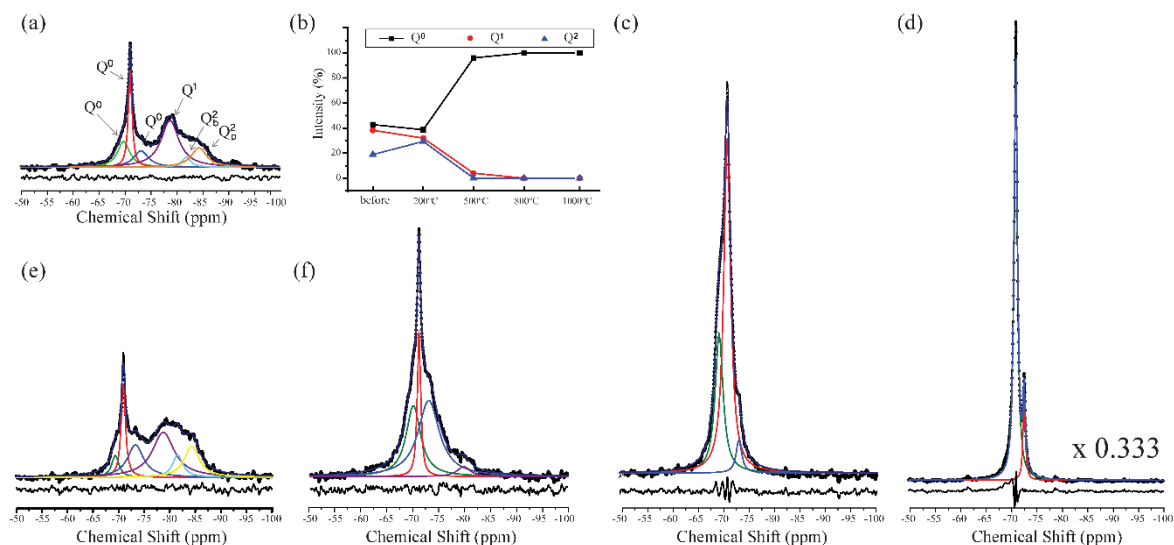


Figure 4: ^{29}Si NMR spectrum of (a) sample before heating (b) relative intensity change of the silicate peak for each heating temperature; ^{29}Si NMR spectrum of samples after heating to (c) 800°C (d) 1000°C (e) 200°C, and (f) 500°C

The growth rate of the MCL for samples heated to 200 °C and 500 °C was, remarkably, directly proportional to the rate of increase in compressive strength (Figure 5), except for three cases: 200-03W24T, 200-24W24T, and 500-After. On the other hand, for samples heated to

800 °C and 1000 °C i.e., higher than the C-S-H decomposition temperature, the rates were not proportional. These results demonstrate that the increase in the MCL of C-S-H is directly related to the compressive strength.

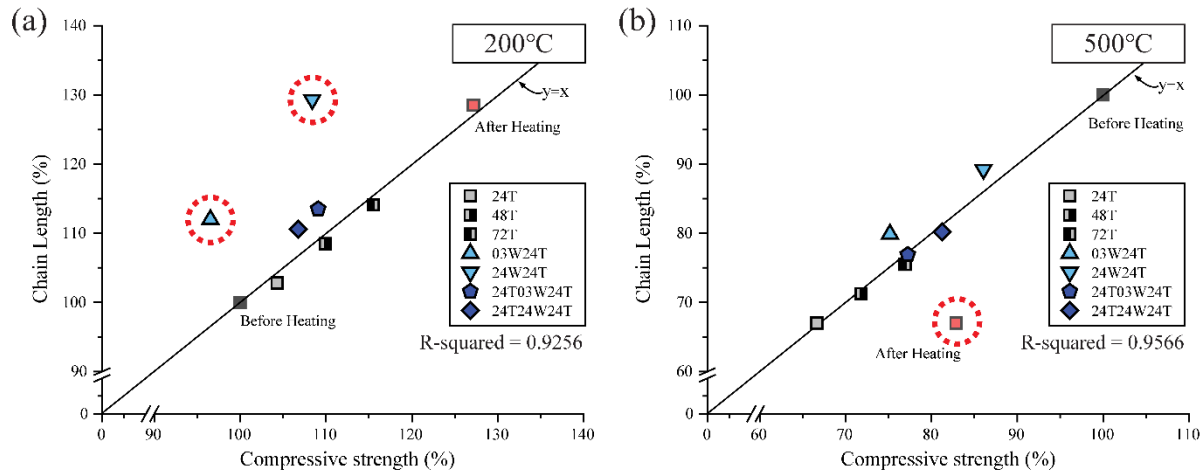


Figure 5: MCL of C-S-H for samples recurred after heating to (a) 200 °C and (b) 500 °C

4. CONCLUSION

In this study, the effect of recurring conditions on a cement paste by water recurring and thermo-hygrostat recurring (20 °C, 60%RH) after heating the samples to 200 °C, 500 °C, 800 °C, and 1000 °C were studied. The obtained results are summarized as follows:

- Most of the samples showed a decrease in strength immediately after heating and strength recovery during the recurring process. Particularly, at 200 °C, there was an exceptional result where the strength increased immediately after heating due to the formation of hydrates and then decreased due to cracking of the matrix during water recurring. We also observed a prominent strength enhancement for samples subjected to water recurring at 500 °C.
- The XRD results showed that at 200 °C, the anhydrate clinker phase was hydrated and resulted in an increase of strength after heating. This contributed to the additional formation of C-S-H, which was detected by ^{29}Si NMR analysis. In addition, the prominent strength recovery for samples after water recurring at 500 °C was due to the hydration of amorphous CaO, produced by the decomposition of $\text{Ca}(\text{OH})_2$. At 800 °C, the decomposition of C-S-H resulted in a dramatic decrease in strength. At 1000 °C, the matrix of the cement paste was completely decomposed and lost its original properties. The XRD results for different samples heated to the same temperature were similar because the recurring times were insufficient for the formation of enough hydrates to be able to be distinguished by XRD.
- The ^{29}Si NMR results showed that for samples recurred in water or under 20 °C 60%RH conditions after heating to 200 °C and 500 °C, the MCL of C-S-H increased. The results confirmed that the increase rate of the compressive strength and the increase of the MCL were directly proportional at 200 °C and 500 °C, except for a few special cases, which

means that the MCL of the C-S-H was directly correlated to the compressive strength of cement paste.

- However, unlike an actual construction structure, the samples in this study were free from contraction and expansion effects and they were deliberately chosen to be small-sized to obtain a uniform temperature distribution. As such, it was not possible to analyze the effects of the MCL increase simultaneously with other factors that influence strength recovery, such as density variation and the formation of other hydrates. Further research is needed based on the above experimental results.

ACKNOWLEDGEMENTS

This research was supported by the Ministry of Land, Infrastructure and Transport, Korea (16TBIP-C111710-01)

REFERENCES

- [1] Lin, W. M., Lin, T. D. and PowersCouche, L. J., 'Microstructures of fire-damaged concrete.' *Aci Mater J* 93(3) (1996) 199-205.
- [2] Zhang, Q. and Ye, G., 'Quantitative analysis of phase transition of heated Portland cement paste.' *J Therm Anal Calorim* 112(2) (2013) 629-636.
- [3] Liu, J. H., Jiang, R. N., Sun, J. H., Shi, P. F. and Yang, Y. F., 'Concrete Damage Evolution and Three-Dimensional Reconstruction by Integrating CT Test and Fractal Theory.' *J Mater Civil Eng* 29(9) (2017).
- [4] Farage, M. C. R., Sercombe, J. and Galle, C., 'Rehydration and microstructure of cement paste after heating at temperatures up to 300 degrees C.' *Cement Concrete Res* 33(7) (2003) 1047-1056.
- [5] Alonso, C. and Fernandez, L., 'Dehydration and rehydration processes of cement paste exposed to high temperature environments.' *J Mater Sci* 39(9) (2004) 3015-3024.
- [6] Wang, G. M., Zhang, C., Zhang, B., Li, Q. and Shui, Z. H., 'Study on the high-temperature behavior and rehydration characteristics of hardened cement paste.' *Fire Mater* 39(8) (2015) 741-750.
- [7] Kunther, W., Ferreiro, S. and Skibsted, J., 'Influence of the Ca/Si ratio on the compressive strength of cementitious calcium-silicate-hydrate binders.' *J Mater Chem A* 5(33) (2017) 17401-17412.
- [8] Rejmak, P., Dolado, J. S., Stott, M. J. and Ayuela, A., 'Si-29 NMR in Cement: A Theoretical Study on Calcium Silicate Hydrates.' *J Phys Chem C* 116(17) (2012) 9755-9761.
- [9] Singh, L. P., Zhu, W., Howind, T. and Sharma, U., 'Quantification and characterization of C-S-H in silica nanoparticles incorporated cementitious system.' *Cement Concrete Comp* 79 (2017) 106-116.
- [10] Zhang, Q., Ye, G. and Koenders, E., 'Investigation of the structure of heated Portland cement paste by using various techniques.' *Constr Build Mater* 38 (2013) 1040-1050.

HIGH-TEMPERATURE BEHAVIOR OF HEAVY-WEIGHT CONCRETES

Flora Faleschini (1,2), Raissa Njinwoua (3), Anne-Lise Beaucour (3), Prosper Pliya (3), Albert Noumowe (3), and Carlo Pellegrino (1)

(1) Department of Civil, Environmental and Architectural Engineering, University of Padua, Italy

(2) Department of Industrial Engineering, University of Padua, Italy

(3) Laboratoire de mécanique et matériaux du génie civil, Université de Cergy-Pontoise, France

Abstract

Heavy-weight concretes may be efficiently used to design shields for radioprotection in strategic structures, such as reactor vessels, nuclear research facilities, hospitals, etc. However, for many applications, they can undergo high-temperature exposition, or even accidental fire.

In this work, the behavior of three types of concrete are analyzed, when exposed to increasing temperatures at two heating rates. The heavy-weight mixes are realized with barite (BAR) and Electric Arc Furnace (EAF) slag; additionally, a normal-weight concrete is tested too, made with natural aggregates (REF). Concretes were exposed at 150 – 300 – 450°C at low rate of heating (1°C/minute), to study their behavior under high temperature; then, they were subject to 600°C with high rate of heating (10°C/minute), to assess potential spalling occurrence. After such exposition, specimens were analyzed in terms of mass loss, density, residual compressive strength and dynamic modulus of elasticity.

Results demonstrate that it is possible to design heavy-weight concrete shields with similar (or even better) performances at high temperature than normal concrete. Particularly, EAF concrete displayed less strength reduction at increasing temperatures, and at the same time, it is characterized by high gamma-ray attenuation coefficient.

Keywords: heavy-weight concrete; high-temperature; residual mechanical properties; spalling; sustainability.

1. INTRODUCTION

Heavy-weight concrete is generally used to design shielding barriers against radiations, due to its high attenuation capacity against gamma radiations. It can find large application in several kind of strategic structures, such as reactor vessels, nuclear facilities, research laboratories,

hospitals and industrial facilities. During their service life, however, these structures might be subject to extreme conditions, such as high-temperature or even fire exposure, and due to their strategic functions, it is mandatory to guarantee their safety especially under such conditions. As an indicative example, the inner face of shielding concretes in nuclear facilities is often exposed to direct heat from the reactor core, and hence both physical and mechanical properties of such concretes might severely deteriorate.

To achieve the goal of producing shields with high attenuation capacity, two strategies might be followed, depending on the type of radiations that are required to be shield. The presence of heavy-weight nuclei acts as a shield for gamma radiations; instead, water and more generally speaking light-weight nuclei, act as neutron-absorbing materials. The effectiveness of heavy-weight concrete in shielding both gamma radiations and neutron radiations, as well as mixed fields of both, relies in the possession of both the above characteristics. Indeed, the presence of heavy-weight aggregates and, at the same time, water content in the range of 120 – 200 kg/m³, ensure achieving the mentioned requirements.

Concerning the types of heavy-weight aggregates that might be used for such scope, the typical natural materials that have been largely used in the practice are barite, ferro-phosphorus, magnetite and hematite [1]-[3]. Recently, also some recycled alternatives have been investigated, with the aim of reducing the high-costs linked to the use of such minerals and preserving natural resources. Among others, Electric Arc Furnace (EAF) slag seems a good candidate to realize heavy-weight concretes with shielding properties, because of its high density and good mechanical strength. A first work by González-Ortega et al. [4] presented some preliminary results on the radiation shielding properties of concretes with EAF slag, obtaining similar shielding properties than concrete with barite aggregates.

EAF slag is a by-product of steelmaking process, and it can be from carbon or stainless steel production [5]. Particularly the first is very abundant in Italy, Spain and Greece, due to the large diffusion of steelmaking production in electric arc furnaces. Such material, when used in concrete, allows achieving enhanced properties in terms of compressive and tensile strength gain (up to 30-40%), increased elastic modulus (between 15 and 30%), and it generally leads to an increase of the overall specific weight of the mix (15-25%) [6]. This is caused by the presence of iron, aluminum, magnesium, manganese and other metals in the composition, other than calcium and silicon oxides [7].

In this paper, an experimental research has been carried out to compare the thermo-mechanical behavior of EAF concrete with two other mixes, one heavy-weight made of barite aggregates and a normal-weight one, realized with silico calcareous aggregates. Such concretes have been first characterized in terms of radiation attenuation capacity against gamma rays, whose details of such evaluation can be found elsewhere [8]. Then, their residual physical and mechanical properties are compared after the exposure at varying temperatures (150 – 300 – 450°C); additionally, also spalling behavior at 600°C was analyzed, when high rate of heating was used.

2. MATERIALS AND METHODS

2.1 Materials

Three concrete mixes were casted, each having the same mix composition but differing due to the type of aggregate used. The specimens were realized using Portland cement type I 52.5R, with a dosage of 400 kg/m³ and water/cement (w/c) ratio of 0.4, which is the recommended

ratio for concretes employed for nuclear purposes [9]. Water comes from the urban supply system of the city of Padova, and it does not contain any substances that might affect the final quality of the concrete. A water reducing admixture was also used in order to achieve a slump value ranging from 150 to 210 mm, therefore corresponding to consistency class S4, according to the standard NF EN 206-1. Its amount differs depending on the concrete mix, depending on the type of aggregates used.

Two types of heavy-weight coarse aggregates were used: EAF slag (4-16 mm size), coming from a steelmaking plant situated in Padova, where only carbon steel is produced; and a barite aggregate (4-14 mm size), consisting of barium sulphate, coming from Italy too. Alluvial silico-calcareous aggregate (4-16 mm size) was used as the normal-weight aggregate, to cast the reference mix. For all the mixes, fine aggregate (0-4 mm size) was an alluvial sand. Their physical properties are listed in Table 1. Overall, the same volume of aggregates was used for all the concretes (690 liters), as it is shown in Table 2, which summarized the details of the mixes.

For each concrete mix, eighteen cylindrical specimens 100x200 mm (diameter x height) were casted for studying their thermo-mechanical properties; further, three cubic specimens were subjected to gamma rays irradiation.

Table 1: Physical properties of the aggregates.

	COARSE NA	BARITE	EAF SLAG	FINE NA
Size (mm)	4-16	4-14	4-16	0-4
Apparent density (kg/m ³)	2701	3817	3854	2703
Water absorption (%)	0.75	1.90	0.84	1.18
Water porosity (%)	2.03	7.25	3.24	3.19
Los Angeles (%)	28	65	15	-
Shape	Roundish	Crushed	Crushed	Roundish

Table 2: Concrete mix details.

Dosage (kg/m ³)	REF-concrete	BAR-concrete	EAF-concrete
Cement	400	400	400
Coarse NA	971	-	-
Barite	-	1371	-
EAF slag	-	-	1270
Fine NA	913	897	966
Water Reducing Admixture	3.2	4.0	3.2

2.2 Shielding properties of the concretes

After the standard 28-days maturation, three cubic specimens per each mix were exposed to a gamma-rays source at the Legnaro National Laboratories (LNL) of the National Institute of Nuclear Physics (INFN) in Legnaro, Padova, Italy. The radioactive source is characterized by an activity of 8.97 TBq (as estimated on July 2016), allowing a dose-rate of 53 Gy/hour at 20 cm from the source; it emits two gamma-rays per decay at average energy of 1.25 MeV. The details of the experimental and numerical characterization of the radiation attenuation properties of these concretes can be found in [8]. Table 3 summarizes the shielding properties

of the analyzed concretes, as expressed in terms of half-value layer (HVL), that is thickness of the absorbing medium required to reduce gamma radiation to one-half of its original intensity. The higher the HVL, the better attenuation capacity is displayed by the shield.

Table 3: Shielding properties of the concretes expressed in terms of HVL.

	Experimental (cm)	Numerical (cm)
REF-concrete	5.341±0.165	5.574
BAR-concrete	4.660±0.140	5.024
EAF-concrete	4.617±0.139	4.931

2.3 Heating and cooling procedure

In order to study the high temperature behavior of the concrete mixes, two heating rates were applied: on one hand, to study the spalling sensitivity, a test at an intermediate heating rate of 10°C/min was used, reaching up to 600°C; on the other hand, to investigate the residual properties of the specimens a slow rate of 1°C/min was performed, at varying temperatures. Specimens were located in an electric furnace with inner dimensions 1100 x 1200 x 1100 mm (L x D x H) and a power of 150 KW; for temperature monitoring, type K thermocouples were used. After reaching the target temperature, it was maintained for a period of 2 hours as a stabilization; then, specimens were cooled at room temperature with a rate of 1°C/min. The low heating rate ensures the homogeneity of temperature and limits the thermal gradient within the specimen. Figure 1 shows some details of the specimens heating procedure.

For the spalling test, a visual detection was carried out, to assess if the aggregates have different spalling sensitivity; additionally, mass loss was evaluated. Concerning the study of concretes residual properties, compressive strength (f_c), dynamic young modulus (E) and mass loss were measured after the different heating-cooling cycle at 1°C/min.



Figure 1: Left: electric arc furnace for specimens heating; right: specimens instrumented with inner thermocouples.

3. RESULTS AND DISCUSSION

3.1 Visual observation after heating

No explosive spalling was observed after the 10 °C/min heating test in all the tested specimens. However, for the EAF and BAR-concretes, some aggregates locally exhibited spalling behavior in one (of three) specimen at this heating rate. The depth of concrete damage, for these cases, was reported being about 5 mm. It is worth recalling that spalling aggregate phenomenon seemed more remarked after heating test at 450°C (heating rate at 1°C/min), than for the thermal stability test at the highest heating rate. These crater-shaped spalling can be attributed to aggregate failures and/or thermal expansion of coarse aggregate close to the specimen surface. Such explanation is confirmed also by the work of Ling and Poon, who showed that spalling occurred on the surface of barite concrete samples after exposure to 600°C at 5°C/min, and they correlated that to the high thermal expansion of barite aggregates [10]. Instead, no spalling occurred in any cases for the reference mix, although major cracks were visible. Figure 2 shows spalling of some aggregates after the thermal stability test at 600 °C.

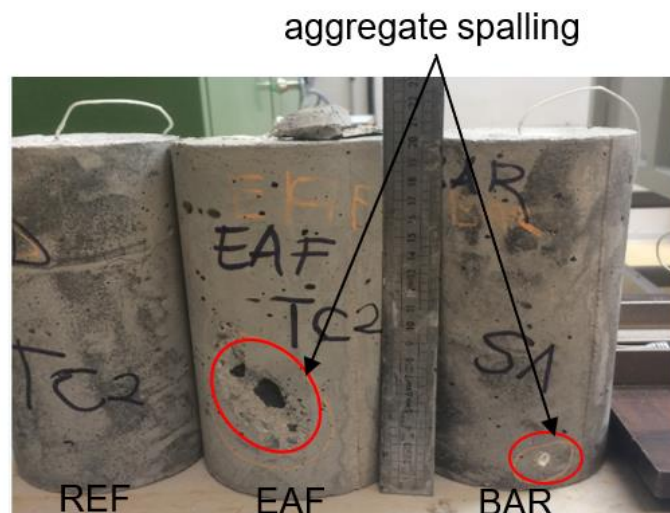


Figure 2: Aggregates spalling phenomenon on EAF and BAR specimens after 10°C/min heating test up to 600°C.

3.2 Residual physical properties: mass loss and density

Figure 3 shows the evolution of the mass loss for EAF, BAR, and REF-concretes, as a function of the temperature. Because of the difference in concrete density, the mass loss was not evaluated in percentage, but by difference of masses, to allow a comparison between the three series of concrete. It is worth to recall that only not spalled specimens were taken into account in the calculations.

As expected, the mass loss increases with temperature. At 150°C, BAR-concrete exhibits a slightly higher mass loss as compared to EAF and REF-concretes, due to the higher water absorption of barite. Instead, in the range between 300 and 450°C, all the mixes show a similar mass loss. Most of the weight loss occurs before 300°C, due to the evaporation of capillary water from macro-pores, evaporation of gel water from gel pores of cement paste and partial dehydration of C-S-H. The weight loss observed at 450°C may be attributed to Portlandite

decomposition, whereas at 600°C to the dehydration of residual Portlandite and the beginning of calcium carbonate decarbonation of the hydrated cement paste and calcareous aggregate.

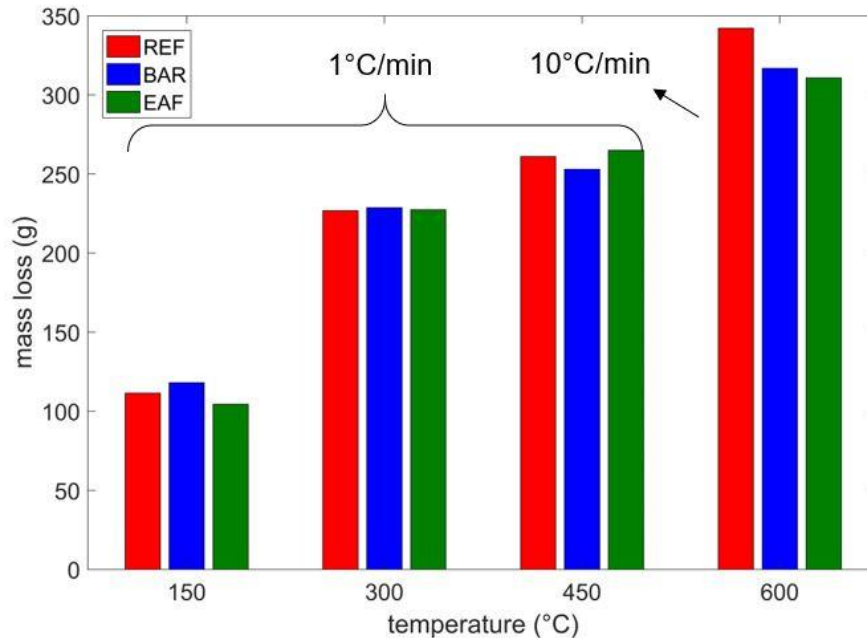


Figure 3: Mass loss of 100x200 mm concrete cylinders at slow heating rate (1°C/min – up to 450°C) and at moderate heating rate (10°C/min – 600°C).

Figure 4 shows the evolution of density with temperature for the different concretes. As expected, the concrete density decreases with temperature: until 300°C, both densities of EAF and BAR mixes are higher than 2600 kg/m³, that is the unit weight volume considered as a threshold for a heavyweight concrete. Comparing these results to the room temperature density of the analyzed concretes, at 20°C EAF mix has an average density of 2805 kg /m³; BAR-concrete instead has a density of 2766 kg / m³, a value quite close to that of the other heavyweight mix. Finally, the REF-concrete, is characterized by a density of 2401 kg/m³.

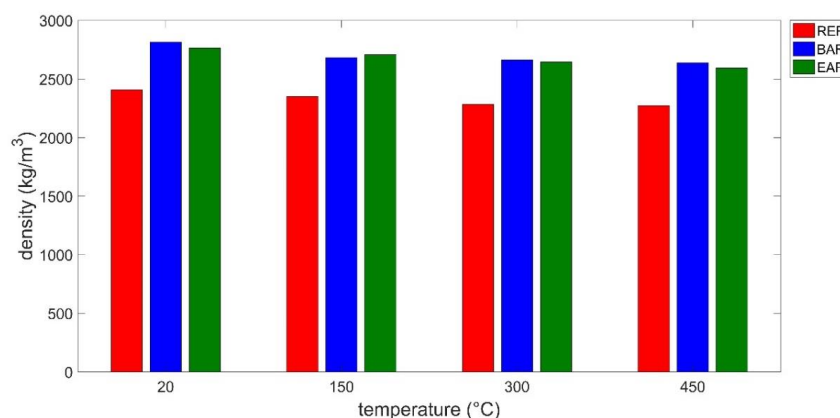


Figure 4: Residual density of the analyzed concretes as a function of the heating temperature.

3.3 Residual mechanical properties: compressive strength and dynamic modulus of elasticity

Mechanical tests were performed before and after heating (these latter, after cooling, as described in Section 2.3), to evaluate the influence of the aggregates on the residual properties achieved by each mix. It is worth mentioning that EAF-concrete displays the best performances at room temperature. Figure 5 shows the compressive strength of EAF, BAR and REF-concretes from room temperature to 600 °C. As expected, exposure to elevated temperature leads to a reduction in compressive strength of all the specimens. Overall, the compressive strength values of EAF concretes were higher than that of REF and BAR concretes, whatever the temperature. Between 150 and 300°C, the relative strength of the REF-concrete is almost constant, while there is a strength decrease for the heavyweight concretes. At 450°C, REF-concrete only keeps 20% (9. MPa) of its initial compressive strength; instead, EAF and BAR-concretes exhibit 60% (39 MPa) and 53% (25 MPa) of their initial strength, respectively. The poor behavior of the reference mix is related to the aggregates type: dolomite aggregate particles are rounded, and their smooth surface texture causes a lower bond strength than angular aggregate particles (like slag and barite).

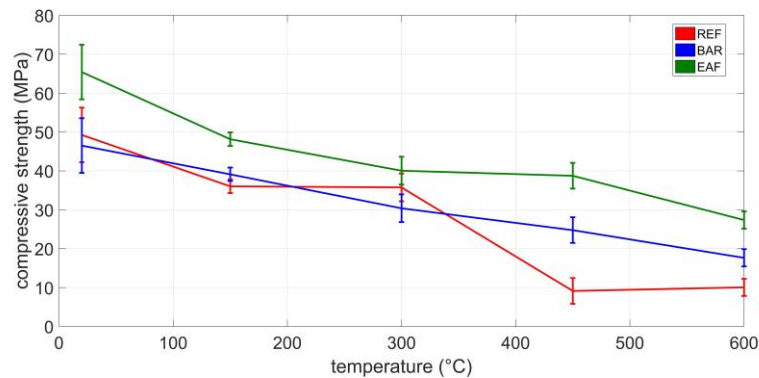


Figure 5: Residual concrete compressive strength as a function of the temperature

Figure 6 shows instead the behavior of the concretes in terms of dynamic modulus of elasticity, having the same trend of the compressive strength evolution, due to the same deteriorating process leading to the formation of a developed network of cracks in the specimens.

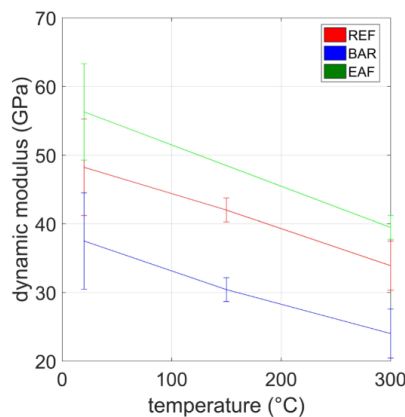


Figure 6: Residual dynamic modulus of elasticity as a function of the temperature

4. CONCLUSIONS

This study aims to compare the behavior of two different heavy-weight concretes and a normal-weight concrete, all subject at high temperature. From the results achieved here it is possible to conclude that EAF slag can be satisfactorily used to produce heavy-weight concrete, and it is characterized by a high radiation attenuation against gamma radiation, similar and even higher than concrete made with barite aggregates. Additionally, when it is exposed to high temperature, its residual properties are higher than that of both heavy- and normal-weight concretes. Particularly, compared to the former, it is worth recalling that barite is characterized by high brittleness, which leads generally to a poorer behavior than EAF concrete. The same occurs in this experimental campaign for the reference concrete, made by dolomitic aggregates, which displays insufficient residual properties at high temperature.

REFERENCES

- [1] L.P. Witte, J.E. Backstrom, "Properties of heavy concrete made with barite aggregates", *ACI Mater. J.*, vol. 51, no. 6, pp. 65–88, 1954.
- [2] Komarovskii A.N., "Shielding materials for nuclear reactors", *Pergamon Press*, London, 1961.
- [3] Bouniol P., "Structures des réacteurs nucléaires. Bétons spéciaux de protection", in 'Les Techniques de l'Ingénieur' (in French), *Génie Nucléaire*, Article BN 3740.
- [4] González-Ortega M.A., Segura I., Cavalaro S.H.P., Toralles-Carbonari B., Aguado A., Andrello A.C., "Radiological protection and mechanical properties of concretes with EAF steel slags", *Construction and Building Materials*, vol. 51, pp. 432–438, 2014.
- [5] Adegoloye G., Beaucour A-L, Ortola S., Noumowé A., "Mineralogical composition of EAF slag and stabilized AOD slag aggregates and dimensional stability of slag aggregates concretes", *Construction and Building Materials*, vol. 115, pp. 171-178, 2016.
- [6] Faleschini F., Hofer L., Zanini M.A., dalla Benetta M., Pellegrino C., "Experimental behavior of beam-column joints made with EAF concrete under cyclic loading", *Engineering Structures*, vol. 139, pp. 81–95, 2017.
- [7] Faleschini F., Brunelli K., Zanini M.A., Dabalà M., Pellegrino C., "Electric Arc Furnace Slag as Coarse Recycled Aggregate for Concrete Production", *Journal of Sustainable Metallurgy*, vol. 2, no. 1, pp. 44-50, 2016
- [8] Pomaro B., Gramegna F., Cherubini R., De Nadal V., Salomoni V., Faleschini F., "Gamma-ray shielding properties of heavyweight concrete with electric arc furnace slag as aggregate: an experimental and numerical study" (in review).
- [9] İlker Bekir Topçu, "Properties of heavyweight concrete produced with barite", *Cement and Concrete Research*, vol. 33, pp. 815–822, 2003.
- [10] Ling T.C. and Poon C.S., "High temperature properties of barite concrete with cathode ray tube funnel glass", *Fire and Materials*, vol. 38, pp. 279-289, 2014.

PREDICTING THE FIRE RATING OF REINFORCED CONCRETE COLUMNS: EFFECT OF LOAD INDUCED THERMAL STRAINS (LITS)

Hitesh Lakhani (1), Joško Ožbolt (1) and Batsuuri Boldbaatar (2)

(1) Institute of Construction Materials, University of Stuttgart, Germany

(2) COMMAS, University of Stuttgart, Germany

Abstract

The behaviour of Reinforced Concrete (RC) structures at elevated temperatures is a complex problem to simulate. This is due to the dependency of various material properties (thermal/mechanical) on temperature; the damage caused due to thermal cracking and steep thermal gradients. At elevated temperature the total concrete strain consists of instantaneous stress related strain, Free-Thermal-Strains (FTS) and Load-Induced-Thermal-Strains (LITS). The least understood strain component and the one which has most uncertainties associated with it, is the LITS. This strain component basically accounts for strains due to chemical changes, moisture loss, transient creep, shrinkage etc.

In the present paper, a 3-D fully-coupled thermo-mechanical model, for predicting the fire rating of RC columns is discussed. The paper also presents a numerical study to compare the suitability of various LITS formulations for studying the behaviour of RC columns under fire. LITS formulations viz. Anderberg & Thelanderson model, Diederich's model, Schneider's model and Terro's model were chosen for the study. It was observed that the predicted behaviour of columns in terms of axial deformations with exposure time and fire rating were very sensitive to the LITS formulation. The predicted fire rating of RC columns, using Schneider's model, were in good agreement with the experimental results.

Keywords: microplane model, thermo-mechanical model, structural fire safety, load induced thermal strain

1. INTRODUCTION

Concrete as a construction material is considered to have good fire resistance mainly because of its incombustible nature, low thermal conductivity and high specific heat capacity. It is also known that with increase in temperature concrete mechanical properties-compressive strength, young's modulus and tensile strength reduces. This is mainly due to structural and chemical

changes in material due to rise in temperature. The effect of temperature on the mechanical properties of concrete had been extensively studied by many researchers over the last six decades and a summary of the same can be found in literature [1-4]. Readers may further refer to Li & Purkiss (2005) [5] and Youssef & Moftah (2007) [6] for the stress-strain constitutive law for concrete at elevated temperature.

Over the year it has also been established/accepted that the loaded and unloaded concrete behaves differently at elevated temperatures [7, 8]. Also, the behaviour of concrete under thermal steady state and transient state conditions have been the topic of interest for many researchers [9,10] which have been reviewed by Torelli et al (2016) [11]. The constitutive model for concrete under high temperature may be expressed by Eq. (1), where ε is total strain at time t ; σ is stress; T is temperature and $\tilde{\sigma}$ is stress history. The total strain includes four parts – mechanical strain (ε_σ) (elastic and plastic component), free thermal strain (ε_{th}), creep strain (ε_{cr}) and transient strain (ε_{tr}), as given by Eq. (2). Because of practical limitations to separate the creep strain and transient strains, in practice they are referred as transient creep strains/load induced thermal strains.

$$\varepsilon = \varepsilon(\sigma(t), T(t), \tilde{\sigma}) \quad (1)$$

$$\varepsilon = \varepsilon_{th}(T) + \varepsilon_\sigma(\sigma, T) + \varepsilon_{cr}(\sigma, T, t) + \varepsilon_{tr}(\sigma, T) \quad (2)$$

The least understood strain component and the one which has most uncertainties associated with it, is the LITS [12]. The importance of considering LITS for predicting the fire rating of structural members has been highlighted time and again by different researchers [13-15]. For the accurate/realistic finite element analysis of RC columns exposed to fire, LITS is a crucial parameter, as it is not only a function of temperature but also the stress level. Also, there are different LITS formulations available in literature, having different level of complexity depending on the various factors accounted. Hence, there is a need to study the suitability/sensitivity of using these formulations for numerically predicting the fire rating of RC columns.

Over the year the behaviour of RC structures have been experimentally investigated. The issue with such investigations is the fact that they are rather demanding, i.e. one has to perform loading and measurement at extremely high temperatures. Furthermore, such experiments can be carried out only on isolated structural members or on relatively small structures. To better understand behaviour of concrete structures, one can resort to numerical analysis. However, one needs models, which can realistically predict behaviour of concrete at high temperature.

In the present paper a three-dimensional (3D) model that is based on the thermo-mechanical coupling between mechanical properties of concrete and temperature is discussed. The isothermal microplane model is used as a constitutive law for concrete with temperature dependent model parameters. The model is used for performing a numerical study to investigate the sensitivity of the predicted behaviour of columns during fire, to various LITS formulations. The finite element analysis is performed in two steps. In the first step internal temperature distribution is calculated for the given thermal boundary conditions. In the second step the required load history is applied with taking into account the influence of temperature on the concrete mechanical properties.

2. THERMO-MECHANICAL MODEL

The thermo-mechanical models are sequentially coupled model where the mechanical properties of concrete are temperature dependent but they do not influence the temperature distribution. These models are adequate to realistically predict an overall response of structural elements exposed to elevated temperatures and mechanical loads.

2.1 Transient heat transfer analysis

As the first step of coupling between mechanical properties of concrete and temperature, for given thermal boundary conditions at time t temperature distribution over a solid structure of volume Ω has to be calculated. In each point of continuum, which is defined by the Cartesian coordinates (x, y, z) , the conservation of energy has to be fulfilled. This can be expressed by the following differential equation (Eq 3.):

$$\lambda \Delta T(x, y, z, t) + W(x, y, z, T) - c\rho \frac{\partial T}{\partial t}(x, y, z, t) = 0 \quad (3)$$

where T = temperature, λ = conductivity, c = heat capacity, ρ = density, W = internal source of heating and Δ = Laplace-Operator. The surface boundary condition that has to be satisfied is given by Eq. (4):

$$\lambda \frac{\partial T}{\partial n} = \alpha(T_M - T) \quad (4)$$

where n = normal to the boundary surface Γ , α = equivalent heat transfer coefficient and T_M = temperature of the media in which surface Γ of the solid Ω is exposed to (for instance temperature of air). The above mentioned differential equations are solved using finite element method.

The variation of thermal properties (specific heat and conductivity) with temperature for concrete was taken from Eurocode2 [16] based on the studies from Lakhani et al (2013) [17]. (Lower bound conductivity and specific heat for dry concrete were used).

2.2 Constitutive laws

In the present model the total strain tensor for concrete has three components viz., mechanical strain, free thermal strain and load induced thermal strain. The mechanical strain component is further composed of elastic, plastic and damage part. In the present model temperature dependent microplain model is used as constitutive law [18,19]. The temperature dependencies of various properties of concrete are shown in Figure 1.

Steel is modelled using classical plasticity model (Von-Mises). Figure 2 shows the variation of Young's modulus and yield strength with temperature, used in the model.

The free thermal strain for concrete and reinforcing steel were taken from Eurocode2.

3. LITS MODELS

The numerical studies were performed to evaluate the suitability of four LITS formulations available in literature and commonly used by different researchers for numerical modelling of concrete at elevated temperature. These formulations include Anderberg & Thelanderson model [20], Schneider's model [1], Diederich's model, and Terro's model [22], which are elaborated in the following sections.

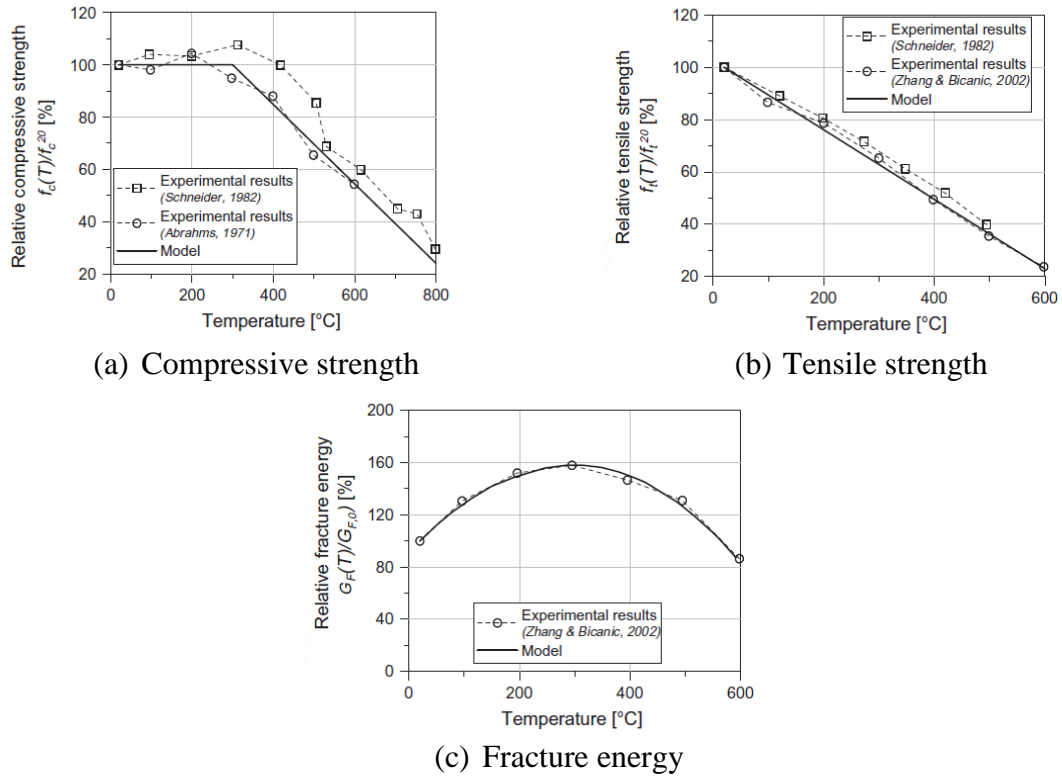


Figure 1: Properties of concrete as function of temperature

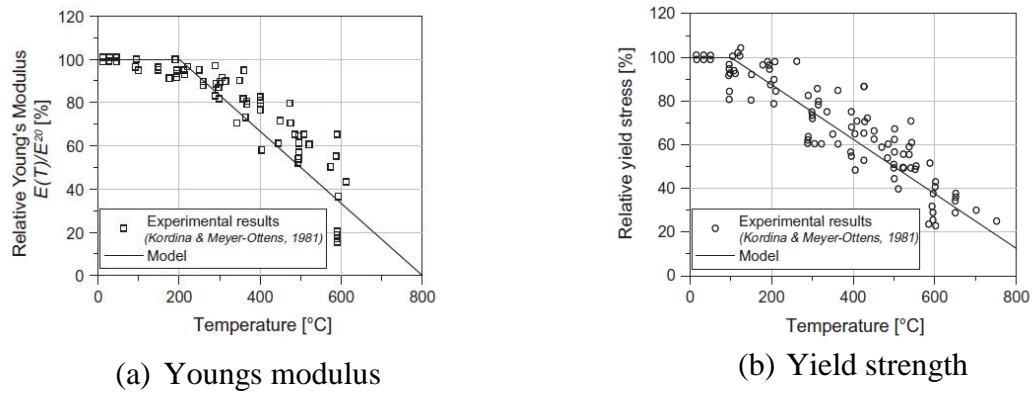


Figure 2: Properties of reinforcing steel as function of temperature

3.1 Anderberg and Thelander model

Based on their experimental study Anderberg and Thelander (1976) proposed the LITS formulation given by Eq. (5) and (6). According to their model LITS is function of applied load level and free thermal strain.

$$\varepsilon_{tr} = k_2 \cdot \frac{\sigma}{f_c} \cdot \varepsilon_{th} \quad T \leq 550^\circ\text{C} \quad (5)$$

$$\frac{\partial \varepsilon_{tr}}{\partial T} = 0.0001 \cdot \frac{\sigma}{f_c} \quad T \geq 550^\circ\text{C} \quad (6)$$

where, f'_c is concrete compressive strength at ambient temperature, σ is applied stress level, k_2 is a dimensionless constant which varies between 1.8 to 2.35 depending on the nature of the aggregate. Based on the regression analysis $k_2 = 2.35$ is proposed for calcareous aggregate

3.2 Schneider's model

The Schneider's model is the most complex of the selected LITS models. The model variables include Youngs modulus (as function of temperature); aggregate type and moisture content. Equation (7) to (11) gives the Schneider's LITS formulation.

$$\varepsilon_{ir} = \frac{\Phi}{g} \frac{\sigma}{E_{cT}} \quad (7)$$

$$g = 1.0 + \frac{\sigma}{f'_c} \times \frac{T - 20}{100} \quad ; \quad \frac{\sigma}{f'_c} \leq 0.3 \quad (8)$$

$$\Phi = g\phi + \frac{\sigma}{f'_c} \times \frac{T - 20}{100} \quad (9)$$

$$\phi = C_1 \tanh(\gamma_w(T - 20)) + C_2 \tanh(\gamma_0(T - T_g)) + C_3 \quad (10)$$

$$\gamma_w = (0.3w + 2.2)10^{-3} \quad (11)$$

where, Φ is the creep function, ϕ is function for transient creep flow, f'_c is concrete compressive strength at ambient temperature, σ is applied stress level, E_{cT} is Youngs modulus of concrete at elevated temperature, γ_w accounts for the moisture content w (%) by weight and γ_0 , T_g , C_1 , C_2 & C_3 are constants for different concrete (Values for these parameters may be found in various sources [1,5,6]).

3.3 Diederich's model

The authors were unable to access/obtain the original publication of the model. Hence, the formulation was taken from other sources [6]. The relatively simple Diederichs model is given by Eq. (11)

$$\varepsilon_{ir} = \frac{\sigma}{f'_c} (3.3 \times 10^{-10}(T - 20)^3 - 1.72 \times 10^{-7}(T - 20)^2 + 0.0412 \times 10^{-3}(T - 20)) \quad (11)$$

where, f'_c is concrete compressive strength at ambient temperature, σ is applied stress level

3.4 Terro's model

Terro (1998) fitted a master curve for a stress level of $0.3 f'_c$ based on the results of Khoury et al (1985), which could be scaled for other load levels using Eq (12)

$$\varepsilon_{ir} = \varepsilon_{0.3} \left(0.032 + 3.226 \frac{\sigma}{f'_c} \right) \frac{V_a}{0.65} \quad (12)$$

where, V_a is the volume fraction of aggregate, f'_c is concrete compressive strength at ambient temperature, σ is applied stress level and $\varepsilon_{0.3}$ (master curve) for siliceous and carbonate aggregate concrete can be computed using Eq (13) and (14) respectively.

$$\varepsilon_{0.3} = -1625.78 \times 10^{-6} + 58.03 \times 10^{-6} T - 0.6364 \times 10^{-6} T^2$$

$$+ 3.6112 \times 10^{-9} T^3 - 9.2796 \times 10^{-12} T^4 + 8.806 \times 10^{-15} T^5 \quad (13)$$

$$\varepsilon_{0.3} = -48.87 \times 10^{-6} + 2.73 \times 10^{-8} T + 6.35 \times 10^{-8} T^2 - 2.19 \times 10^{-10} T^3 + 2.77 \times 10^{-13} T^4 \quad (14)$$

4. NUMERICAL STUDY

The experimental investigation of columns under fire by Lie and Woolleerton (1988) [23] was simulated for the numerical study. The columns had a total length of 3.81m with a fire exposed length of 3.04m. Columns had a cross-section of 305 × 305 mm, with 4 -25 dia (#8) rebars and 9 dia (#3) rebars at 305mm c/c spacing for stirrups. The longitudinal reinforcement had a clear cover of 48mm. Preload was applied on the columns before fire exposure and was maintained constant thereafter. The columns were exposed to standard ASTM E119 fire until failure. The column was fixed at the bottom end and the top end was free to have axial translation only. Figure 3 shows the discretization of concrete and the reinforcement for the RC columns. Table 1 summarises the various combinations of aggregates and load level considered for the numerical study.

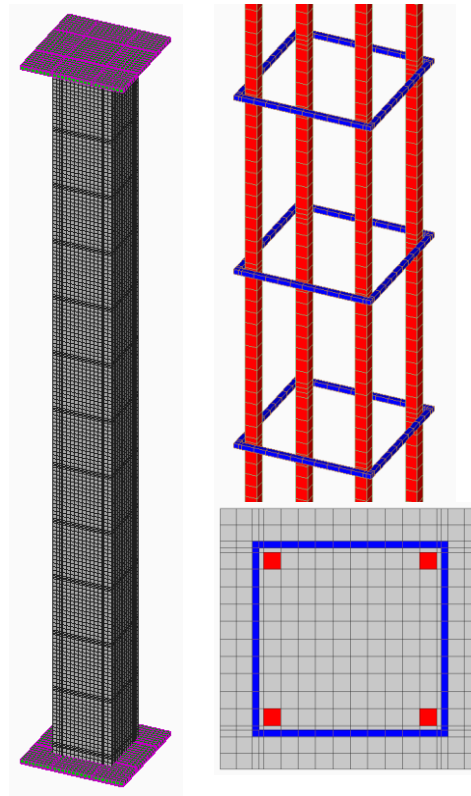


Figure 3: Discretised view of RC column

Table 1: Various cases of RC columns simulated

Column	Aggregate type	f'_c (MPa)	Load level (kN)
Col-5	Siliceous	34.8	1778
Col-6	Siliceous	38.3	1333
Col-7	Carbonate	40.9	800
Col-9	Carbonate	39.9	1778

It can be seen from figure 4 that the predicted axial deformation-time curve for column col-6 is very sensitive to the LITS formulation used. Hence, also predicts different fire rating of the column. Figure 4 also shows that the predicted behaviour of column was closest to the experimentally observed behaviour when Schneider's model is used. Therefore, further analyses were performed using Schneider's model for columns made with different aggregate types and different load levels. The comparison between predicted and experimental deformation-time curves for 4 different cases (2 different aggregates \times 2 different load level) is shown in figure 5. The predicted maximum axial expansion, deformation-time and failure time (Fire rating) are in good agreement with the experimental results.

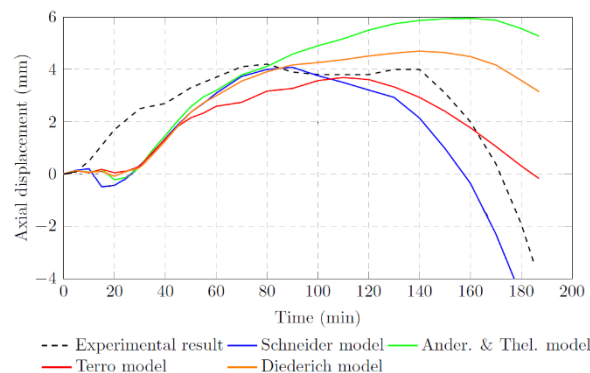
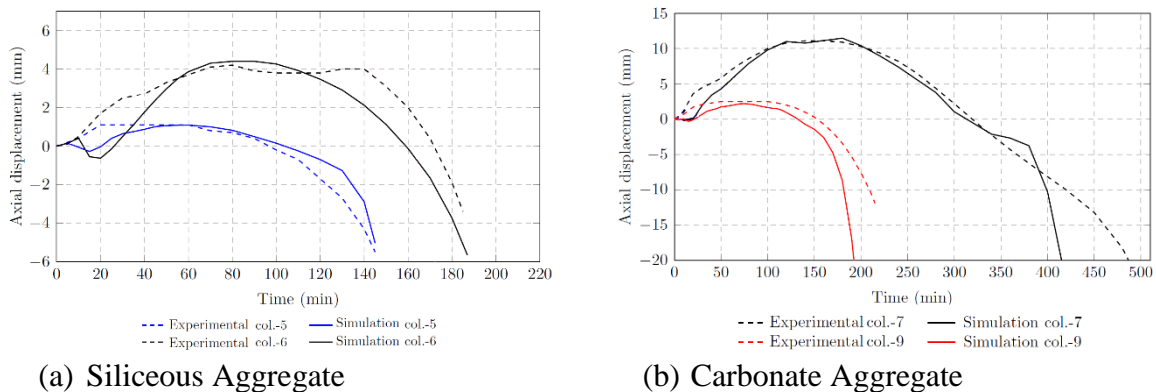


Figure 4: Influence of LITS on the predicted deformation-time behaviour of Col-6



(a) Siliceous Aggregate

(b) Carbonate Aggregate

Figure 5: Comparison of predicted behaviour of columns with experimental results

5. CONCLUSIONS

In the present paper a transient 3D thermo-mechanical model for simulating the behaviour of RC columns during fire has been discussed. The sensitivity of the model to four different LITS formulations viz. Anderberg & Thelanderson model, Diederich's model, Schneider's model and Terro's model was studied. The numerical study has shown that the LITS have a significant influence on the behaviour of RC columns at elevated temperatures. Among the various LITS model studied, Schneider's model provided good predictions for behaviour of RC columns during fire. The discussed thermo-mechanical model was further validated with 4 different cases (2 \times aggregate type + 2 \times load level), which demonstrated the capability of the model to predict the behaviour of RC columns during fire accounting for different aggregate type and load levels.

REFERENCES

- [1] Schneider U., 'Concrete at high temperatures: A general review', *Fire Safety Journal*, 13 (1988) 55-68.
- [2] Bazant Z.P. and Kaplan M.F., 'Concrete at high temperatures' (Longman Group Limited, 1996).
- [3] Phan L.T. and Carino N.J., 'Review of mechanical properties of HSC at elevated temperature', *Journal of materials in civil engineering*, 10(1) (1998).
- [4] Ma Q., Guo R., Zhao Z., Lin Z. and He K., 'Mechanical properties of concrete at high temperature - A review', *Construction and Building Materials*, 93 (2015) 371-383.
- [5] Li L. and Purkiss J.A., 'Stress strain constitutive equations of concrete material at elevated temperatures', *Fire Safety Journal*, 40 (2005) 669 - 686.
- [6] Youssef M.A. and Moftah M., 'General stress-strain relationship for concrete at elevated temperatures', *Engineering Structures*, 29 (2007) 2618-2634.
- [7] Abrams M.S., 'Compressive strength of concrete at temperatures to 1600 °F', Report No. RD016.01T (Portland Cement Association, 1973).
- [8] ACI/TMS216.1-14, 'Code requirements for determining fire resistance of concrete and masonry construction assemblies' (Detroit: American Concrete Society, 2014).
- [9] Schneider U., 'Behaviour of concrete under thermal steady state and non-steady state conditions', *Fire and Materials*, 1 (1976) 103-115.
- [10] Khoury G.A., Grainger B.N. and Sullivan P.J.E., 'Transient thermal strain of concrete: literature review, conditions within specimen and behaviour of individual constituents', *Magazine of Concrete Research*, 37 (1985) 131-144.
- [11] Torelli G., Mandal P., Gillie M. and Tran V.X., 'Concrete strains under transient thermal conditions: A state of the art review', *Engineering Structures*, 127 (2016) 172-188.
- [12] Ellingwood B. and Shaver J.R., 'Analysis of reinforced concrete beams subjected to fire', NBS Building Science Series 76 (National Bureau of Standard, US Department of Commerce; 1979)
- [13] Bratina S., Saje M. and Planinc I., 'The effect of different strain contributions on the response of RC beams in fire', *Engineering Structures*, 29 (2007) 418-430.
- [14] Gernay T. and Franssen J.M., 'A formulation of the Eurocode2 concrete model at elevated temperature that includes an explicit term for transient creep', *Fire Safety Journal*, 51 (2012) 1-9.
- [15] Kodur V.K.R. and Alogla S.M., 'Effect of high temperature transient creep on response of reinforced concrete columns in fire', *Materials and Structures*, 50 (2017).
- [16] Eurocode2, 'Design of concrete structures - Part 1-2: General rules - Structural fire design' (Brussels: European Committee for Standardization, 2004).
- [17] Lakhani H., Kamath P., Bhargava P., Sharma U.K. and Reddy G.R., 'Thermal analysis of reinforced concrete structural elements', *Journal of Structural Fire Engineering*, 4(4) (2013) 227-243.
- [18] Ozbolt J., Li Y.J. and Kozar I., 'Microplain model for concrete with relaxed kinematic constraint', *International Journal of Solids and Structures*, 38 (2001) 2683-2711.
- [19] Ozbolt J., Kozar I., Eligehausen R. and Periskic G., 'Three-dimensional FE analysis of headed stud anchors exposed to fire', *Computers and Concrete*, 2(4) (2005) 249-266.
- [20] Anderberg Y. and Thelandersson S., 'Stress and deformation characteristics of concrete at high temperature, 2: Experimental investigation and material behaviour model', Bulletin 54 (Lund Institute of Technology, Lund, Sweden, 1976).
- [21] Terro M.J., 'Numerical modeling of behaviour of concrete structures in fire', *ACI Structural Journal*, 95(2) (1998) 183 - 193.
- [22] Lie T.T. and Woollerton J.L., 'Fire resistance of reinforced concrete columns: Test results'. Internal Report No. 569 (Institute for Research in Construction, National Research Council Canada; 1988).

EXPLOSIVE SPALLING POTENTIAL OF ULTRA-HIGH PERFORMANCE CONCRETE PREPARED BY A NOVEL APPROACH

X.J. Niu (1), G.F. Peng (1), Y.J. Shang (1), X. W. Chen (2), H. Ding (2)

(1) Faculty of Civil Engineering, Beijing Jiaotong University, China

(2) Beijing Construction Engineering Group, Advanced Construction Materials Co., China

Abstract

An experimental investigation was conducted on combined curing as a novel approach to prepare ultra-high performance concrete (UHPC), which is composed of precuring in water and heating in dry air. The results indicate that the combined curing improves the mechanical properties of UHPC remarkably. More importantly, the combined curing is quite efficient to enhance the resistance of UHPC to explosive spalling under high temperature, which should be a novel approach to prohibit spalling occurrence, different from adding polypropylene fiber. Further hydration can be activated to form dense crystals including sheet-like tobermorite and needle-like xonotlite, while a large amount of internal free water has been consumed. The mechanism for the effect of the combined curing is that a dense microstructure forms while internal free water has been consumed.

Keywords: ultra-high performance concrete, combined curing, mechanical properties, explosive spalling, microstructure

1. INTRODUCTION

Ultra-high performance concrete (UHPC) is a new generation of cement-based material exhibiting superb properties with respect to mechanical strength, durability and toughness [1-3]. Heat curing is considered as an effective method to alter microstructure and improve mechanical properties of UHPC, owing to promotion of hydration process and intensification of pozzolanic activity [4-6]. Meanwhile, duration and initiative time of heat curing can affect the hydration degree, and thus influence the properties of UHPC [7, 8].

In order to improve properties of UHPC, various heat curing regimes, such as hot water curing, steam curing, dry air heating and autoclaving have been explored [6, 9-11]. UHPC with a water/binder ratio of 0.15 cured in hot water at 90 °C for 6 days exhibited approximately 20% higher compressive strength, 10% higher flexural strength and 15% higher fracture energy than

that cured in water at 20 °C [9]. Additionally, steam curing and autoclaving also improve compressive strength of UHPC, especially the latter one [10]. Moreover, rising temperature and increased pressure in the autoclaving process can obviously increase the crystallinity of C-S-H [11]. However, unnecessarily too long a duration or too high vapor pressure may cause the excessive crystallization of C-S-H accompanied by a strength reduction [7].

Apart from the curing regimes mentioned above, which may be called as mono-curing, different combined curing regimes have been gradually employed in preparation of UHPC [12-13]. Liu et al. [12] investigated the influence of a combined curing, composed of 90 °C steam curing for 3 days and 150 °C dry air heating for 1 day, on mechanical properties of UHPC. The results showed that, based on a water/binder ratio of 0.20 and cement content of 150 kg/m³, compressive strength and flexural strength of the UHPC under this combined curing were 97.2% and 70% higher than that only subjected to 90 °C steam curing for 3 days, respectively. Furthermore, the combined curing composed of autoclaving and dry air heating has a prominent advantage in terms of compressive strength of UHPC over that composed of steam curing and dry air heating [13].

Nevertheless, the influence of combined curing on explosive spalling of UHPC subjected to high temperature has been reported rarely. Explosive spalling governed by a vapor pressure mechanism remains to be a great threat to the concrete structures [14]. The vapor pressure is mainly caused by internal free water of concrete [15]. In literature, adding polypropylene (PP) fiber is a usual approach to release the vapor pressure attributed to PP fiber melting under elevated temperature, which can create a connected-channel network in concrete [16].

This paper intends to investigate the influence of a combined curing composed of precuring in water and heating in dry air on mechanical properties and explosive spalling of UHPC under high temperature. Microstructure of hardened cement paste in the UHPC under the combined curing was also determined by means of scanning electron microscope (SEM).

2. EXPERIMENTAL PROGRAM

2.1 Raw materials and mix proportions

Table 1: Mix proportions of UHPC (unit: kg/m³)

Type	Cement	SF	FA	GGBFS	Artificial sand	Basalt coarse aggregate	PP fiber	Steel fiber
Plain UHPC	540	90	180	90	620	930	0	0
S-UHPC	540	90	180	90	620	930	0	39
PS-UHPC	540	90	180	90	620	930	1.35	39

Cement: Portland cement (CEM I 52.5-R according to EN 197-1: 2011). Mineral admixtures: silica fume (SF), fly ash (FA) and ground granulated blast furnace slag (GGBFS). Two types of coarse basalt aggregate, with particle size of 5-10 mm and 10-16 mm respectively, were mixed by mass ratio of 3:7. Artificial sand, with the modulus of fineness of 2.94. Polyacrylate superplasticizer with 50% solid content was used to maintain the slump of mixture around 200 mm.

Crimped recycled steel fiber with a length of 46 mm, diameter of 1.0 mm, density of 7.8

g/cm³ and tensile strength of 2000 MPa was used. Straight PP fiber with a length of 19 mm, diameter of 0.02 mm, density of 0.91 g/cm³ and tensile strength of 400 MPa was also employed. Three types of UHPC with a water/binder ratio of 0.18 were prepared, of which the mix proportions are given in Table 1.

2.2 Curing regimes

Table 2: Curing regimes adopted in this study

Curing regime		Identification	Curing feature
Mono-curing	Normal water	NW	20 °C water curing for 27 days
	Hot water curing	HW2	90 °C hot water curing for 2 days
	Dry air heating	200DA2	200 °C dry air heating for 2 days
Combined curing	Normal water curing and dry air heating	NW6-200DA2	20 °C water precuring for 6 days and 200 °C dry air heating for 2 days
	Hot water curing and dry air heating	HW2-200DA1/2/3	90 °C hot water precuring for 2 days and 200 °C dry air heating for 1/2/3 days respectively
		HW2-250DA3	90 °C hot water precuring for 2 days and 250 °C dry air heating for 3 days

Specimens were demoulded at one day and then cured under different curing regimes, as summarized in Table 2. After curing, the specimens except those cured under NW were stored in air at temperature of 20 ± 2 °C with relative humidity of $50 \pm 5\%$ until the age of 28 days.

2.3 Test methods

Cube specimens of 100 mm were used for compressive strength and tensile splitting strength determination in compliance with the China standard GB/T 50081. Explosive spalling tests were conducted on 100 mm cube specimens in an electric furnace at a heating rate of approximately 10 °C/min, from 20 °C to 800 °C. The mechanical properties and explosive spalling of UHPC under high temperature were tested at the age of 28 d, which was usually chosen by many researches [17, 18]

For SEM observations, a HITACHI S4800 SEM equipped with an energy dispersive spectrometer (EDS) was used, and the samples were prepared by taking small pieces with a thickness of 8 mm from the inner part of the cube specimens. All the samples were immersed in acetone for 4 days to stop the cement hydration and then dried in an oven at 105 °C for 1 day. Before the observation, the samples were coated with gold prior to examination.

3. RESULTS AND DISCUSSION

3.1 Mechanical properties

The results of compressive strength and tensile splitting strength of the plain UHPC under various curing regimes are presented in Fig. 1. Compared with mono-curing, combined curing regimes obviously improved the strength of UHPC, especially the combined curing composed

of precuring in hot water and heating in dry air. The highest compressive strength (177.6 MPa) and tensile splitting strength (7.5 MPa) were obtained from the UHPC subjected to HW2-200DA2, exhibiting the increments of 48.7% and 65.9% relative to that cured under NW, respectively. Moreover, it is shown in Fig. 2 that compressive strength and tensile splitting strength of plain UHPC under the combined curing increased with the duration prolonged from 1 day to 3 days.

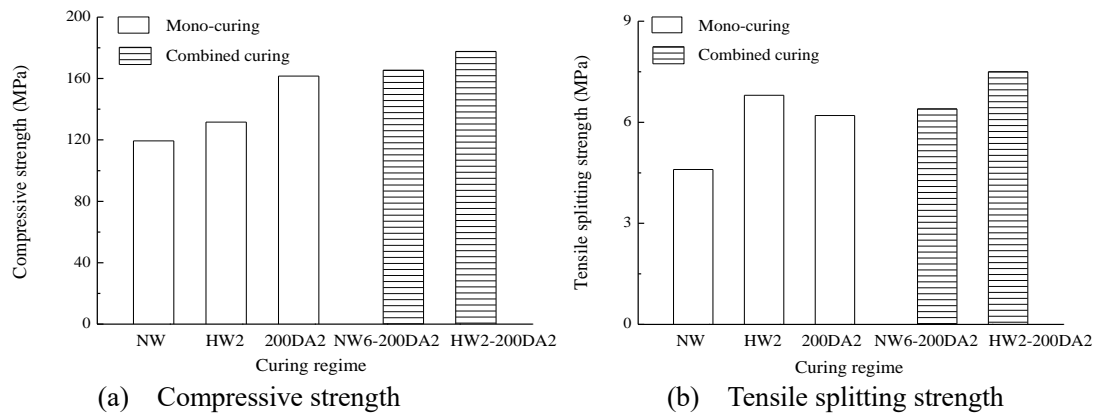


Fig. 1: Compressive strength and tensile splitting strength of plain UHPC under various curing regimes

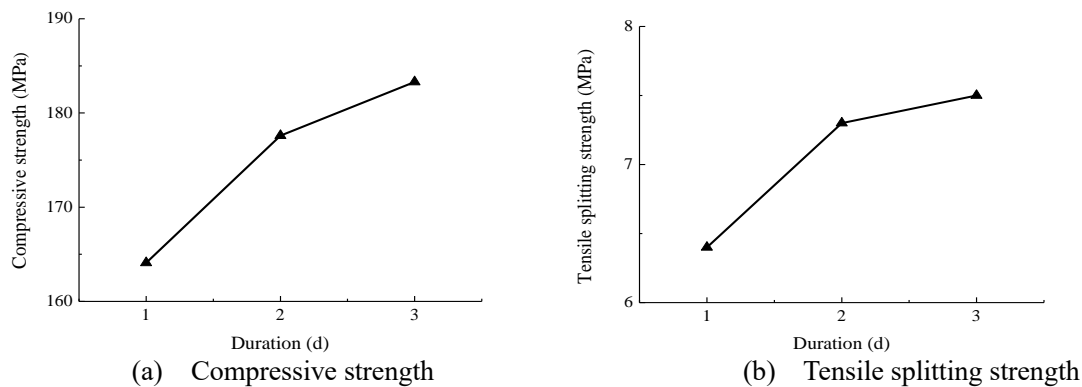


Fig. 2: Compressive strength and tensile splitting strength of plain UHPC under the combined curing with various durations of dry air heating, based on the same precuring (90 °C hot water curing for 2 days) and dry air heating temperature (200 °C)

Based on a given dry air heating duration of 3 days, the compressive strength and tensile splitting strength of the S-UHPC subjected to HW2-250DA3 were 10.3% and 16.1% higher than that cured under HW2-200DA3, respectively, as shown in Fig. 3. The higher the temperature of dry air heating in the combined curing, the higher the strength of UHPC.

Nevertheless, tensile splitting strength of the PS-UHPC subjected to 250 °C heating in Fig. 3(b) was slightly lower than that subjected to 200 °C. It has been recognized in literature [19] that, some connected channels can be formed in concrete, when temperature exceeds the melting temperature of PP fiber. In this research, these connected channels may coarsen with dry air heating temperature rising from 200 °C to 250 °C, thus affecting tensile splitting strength negatively and resulting in a slight loss in it.

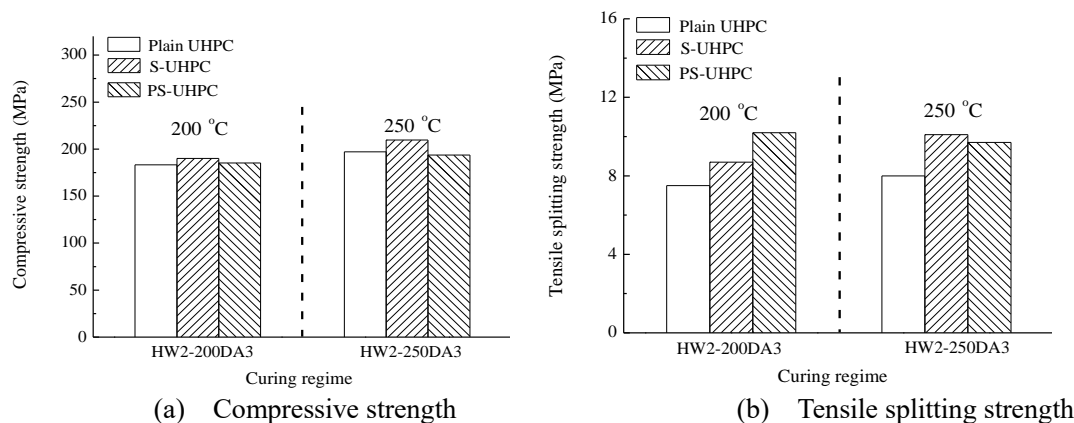


Fig. 3: Compressive strength and tensile splitting strength of UHPC under the combined curing with various temperatures of dry air heating

3.2 Explosive spalling

Table 3: Explosive spalling results of plain UHPC under various curing regimes







Explosive spalling results	Mono-curing			Combined curing	
	NW	HW2	200DA2	NW6-200DA2	HW2-200DA2
Morphology					
Temperature for spalling occurrence	373.8 °C ~ 569.2 °C (195.4 °C) ^a	410.7 °C ~ 665.3 °C (254.6 °C) ^a	578.6 °C ~ 584.9 °C (6.3 °C) ^a	No spalling	No spalling

Note: ^a The data inside the brackets are the ranges of temperature for spalling occurrence.

The results of the plain UHPC under various curing regimes in the trial test of spalling are given in Table 3. All the specimens cured under NW and HW2 with highly moisture content were broken into small fragments during the spalling test. It is clear that the combined curing is quite efficient to enhance the resistance of the plain UHPC to explosive spalling under high temperature, since there was no spalling occurrence on the UHPC cured under NW6-200DA2 and HW2-200DA2.

The results of three types of UHPC subjected to the combined curing with various temperatures of dry air heating in the formal test of spalling are given in Table 4. Slight spalling occurred on the plain UHPC cured under HW2-200DA3 with a thin layer spalled from the top surface of concrete, whereas no spalling occurred on the plain UHPC subjected to HW2-250DA3. It proves that the combined curing has a positive effect on preventing explosive spalling of UHPC under high temperature, and the effect can be enhanced with rising temperature of the dry air heating therein.

Table 4: Explosive spalling results of UHPC under the combined curing with various temperatures of dry air heating

Explosive spalling results	Combined curing					
	HW2-200DA3 (200 °C)			HW2-250DA3 (250 °C)		
	Plain UHPC	S-UHPC	PS-UHPC	Plain UHPC	S-UHPC	PS-UHPC
Morphology						

After curing under HW2-250DA3, neither the S-UHPC nor the PS-UHPC spalled during the spalling test. It is estimated that lots of internal free water should have been consumed during the further hydration activated by the combined curing, leading to the extremely low moisture content of concrete. Therefore, the vapor pressure inside UHPC under high temperature will be not high enough to induce spalling occurrence which is dominated by the vapor pressure mechanism..

3.3 Microstructure of hardened cement paste in UHPC

A loose microstructure with many amorphous C-S-H gels was formed in the sample under 20 °C water curing (NW). The porous and continuous honeycombed C-S-H gels that apparently similar to C-S-H (II) existed, with the Ca/Si ratio of 0.92 determined at Point 1 marked in Fig. 4(a). Besides, a type of fibrous C-S-H gel (Ca/Si = 0.68, determined at Point 2 marked in Fig. 4(b)) which resembles to C-S-H (I) was observed in the sample. It has been reported that C-S-H (I) may be fibrous with a length up to about 2 μm [20].

For the sample cured under HW2-200DA3, a considerable amount of sheet-like C-S-H crystals were found (Fig. 4(c)). The Ca/Si ratio of this C-S-H crystal (i.e. Point 3) was 0.98, which should be the 1.1 nm tobermorite. Tobermorite, as a sort of hydrated calcium silicate with the chemical formula $\text{C}_5\text{S}_6\text{H}_5$, has a crystalline structure that can provide strength and stability [20]. Moreover, many dense fold-like amorphous C-S-H gels were formed in the sample as well, with the Ca/Si ratio of 1.01 determined at Point 4 marked in Fig. 4(d).

In addition, the morphology of C-S-H can be changed with dry air heating temperature rising. Some needle-like C-S-H crystals were formed under HW2-250DA3, which should be xonotlite characterized by the Ca/Si ratio of 1.2, determined at Point 5 marked in Fig. 4(e). Generally, the Ca/Si ratio of xonotlite is 1.0 according to the chemical formula $\text{C}_6\text{S}_6\text{H}$, but it may actually vary in a range of 0.8-1.2 [21]. Meanwhile, denser spherical C-S-H gels were also detected in the sample, as shown in Fig. 4(f). The formation of both xonotlite with higher hardness at the Mohs scale than tobermorite [8] and denser spherical C-S-H gels should be responsible for the 7.5% increase in compressive strength of the plain UHPC subjected to HW2-250DA3, compared to that cured under HW2-200DA3.

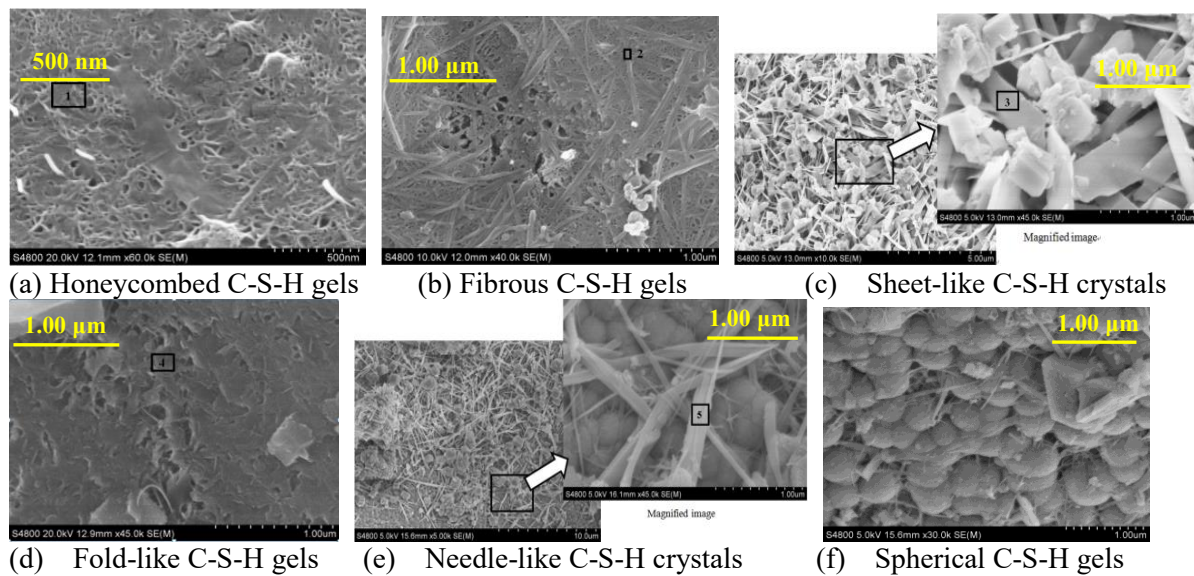


Fig. 4: Morphology of C-S-H in the samples subjected to various curing regimes

3.4 Mechanism for the effect of the combined curing

During the combined curing, some amorphous C-S-H gels are initially formed in UHPC under the water precuring, which may be further transformed under the dry air heating into C-S-H crystals such as tobermorite and xonotlite, as shown in Fig. 4, filling in the pore structure of hardened cement paste. However, excessive crystallization of hydrates may cause deterioration of interfacial transition zone (ITZ) and affect the mechanical properties negatively [11, 20]. The effect of the combined curing on improving the resistance of UHPC to explosive spalling under high temperature is attributed to the internal free water minimizing mechanism. Therefore, the combined curing can be regarded as a novel approach to prevent explosive spalling of UHPC when subjected to high temperature, different from adding polypropylene fiber usually employed.

4. CONCLUSIONS

- The combined curing can improve the mechanical properties of UHPC remarkably.
- The combined curing can greatly enhance the resistance of UHPC to explosive spalling under high temperature, attributed to the internal free water minimizing mechanism, different from adding polypropylene fiber usually employed.
- The C-S-H products formed in UHPC subjected to the combined curing differ greatly from those subjected to water curing only. A considerable amount of sheet-like tobermorite and needle-like xonotlite can be formed in UHPC under the combined curing with 200 °C or 250 °C dry air heating.
- The mechanism for the effect of the combined curing is that a dense microstructure is formed while internal free water has been consumed during the further hydration.

ACKNOWLEDGMENTS

The authors would like to express their gratitude to the financial supports of National Science Foundation of China (Project Nos. 51078030, 51278048 and 51878032).

REFERENCES

- [1] Richard, P. and Cheyrezy, M., 'Reactive powder concretes with high ductility and 200-800 MPa compressive strength', *ACI Mater. J.* **144** (1994) 507-518.
- [2] Schmidt, M., 'Sustainable building with ultra-high-performance concrete (UHPC)-coordinated research program in Germany', Proceedings of the 3rd international symposium on UHPC and nanotechnology for high performance construction materials, Kassel, 2012, 17-26.
- [3] Li, Y.E., Guo, L., Rajlic, B. and Murray, P., 'Hodder avenue underpass: an innovative bridge solution with ultra-high performance fiber-reinforced concrete', Proceedings of the 10th international symposium on high performance concrete – innovation and utilization, Beijing, 2014, 37-42.
- [4] Shi, C.J., Wu, Z.M., Xiao, J.F., Wang, D.H., Huang, Z.Y., and Fang, Z., 'A review on ultra high performance concrete: Part I. Raw materials and mixture design', *Constr. Build. Mater.* **101** (12) (2015) 741-751.
- [5] Yoo, D.Y., and Banthia, N., 'Mechanical properties of ultra-high-performance fiber-reinforced concrete: A review', *Cem. Concr. Compos.* **73** (10) (2016) 267-280.
- [6] Cheyrezy, M., Maret, V. and Frouin, L., 'Microstructural analysis of RPC (Reactive powder concrete)', *Cem. Concr. Res.* **25** (7) (1995) 1491-1500.
- [7] Yazıcı, H., 'The effect of curing conditions on compressive strength of ultra high strength concrete with high volume mineral admixtures', *Build. Environ.* **42** (5) (2007) 2083-2089
- [8] Tam, C.M. and Tam, V.W., 'Microstructural behaviour of reactive powder concrete under different heating regimes', *Mag. Concr. Res.* **64** (3) (2012) 259-267.
- [9] Yang, S.L., Millard, S.G., Soutsos, M.N., Barnett, S.J. and Le, T.T., 'Influence of aggregate and curing regime on the mechanical properties of ultra-high performance fibre reinforced concrete (UHPFRC)', *Constr. Build. Mater.* **23** (6) (2009) 2291-2298.
- [10] Yazıcı, H., Yardımcı, M.Y., Aydın, S. and Karabulut, A.Ş., 'Mechanical properties of reactive powder concrete containing mineral admixtures under different curing regimes', *Constr. Build. Mater.* **23** (3) (2009) 1223-1231.
- [11] Yazıcı, H., Deniz, E. and Baradan, B., 'The effect of autoclave pressure, temperature and duration on mechanical properties of reactive powder concrete', *Constr. Build. Mater.* **42** (2013) 53-63.
- [12] Liu, J.H. and Song, S.M., 'Effects of curing systems on properties of high volume fine mineral powder RPC and appearance of hydrates', *J. Wuhan Univ. Technol.* **25** (4) (2010) 619-623.
- [13] Mostofinejad, D., Nikoo, M.R. and Hosseini, S.A., 'Determination of optimized mix design and curing conditions of reactive powder concrete (RPC)', *Constr. Build. Mater.* **123** (2016) 754-767.
- [14] Ma, Q.M., Guo, R.X., Zhao, Z.M., Lin Z, and He, K., 'Mechanical properties of concrete at high temperature-A review', *Constr. Build. Mater.* **93** (6) (2015) 371-383.
- [15] Peng, G.F. and Huang, Z.S., 'Change in microstructure of hardened cement paste subjected to elevated temperatures', *Constr. Build. Mater.* **22** (4) (2008) 593-599.
- [16] Kalifa, P., Chéné, G. and Gallé, C., 'High-temperature behavior of HPC with polypropylene fibers from spalling to microstructure', *Cem. Concr. Res.* **31** (10) (2001) 1487-1499.
- [17] Xiong, M.X. and Liew, J.Y.R., 'Spalling behavior and residual resistance of fibre reinforced Ultra-High performance concrete after exposure to high temperatures', *Mater. Construct*
- [19] Ju, Y., Wang, L., Liu, H.B. and Tian, K.P., 'An experimental investigation of the thermal spalling of polypropylene-fibered reactive powder concrete exposed to elevated temperatures', *Sci. Bull.* **60** (23) (2015) 2022-2040.
- [20] Taylor, H.F.W., 'Cement chemistry'. Academic Press, London, UK, 1990.
- [21] Shaw, S., Clark, S.M. and Henderson, C.M.B., 'Hydrothermal formation of the calcium silicate hydrates, tobermorite ($\text{Ca}_5\text{Si}_6\text{O}_{16}(\text{OH})_2 \cdot 4\text{H}_2\text{O}$) and xonotlite ($\text{Ca}_6\text{Si}_6\text{O}_{17}(\text{OH})_2$): an in situ synchrotron study', *Chem. Geol.* **167** (1) (2000) 129-140.

MULTIAXIAL BEHAVIOUR OF FIBRE REINFORCED MORTAR FOR MASONRY STRENGTHENING SUBJECTED TO HIGH TEMPERATURES

João A.P.P. Almeida (1), Eduardo N.B. Pereira (1), Hernán Xargay (2), Paula Folino (2) and Joaquim A.O. Barros (1)

(1) ISISE, Department of Civil Engineering, School of Engineering, University of Minho, Portugal

(2) LMNI, INTECIN, FIUBA, Materials and Structures Laboratory, Faculty of Engineering, University of Buenos Aires, Argentina

Abstract

This paper analyses the effects of high temperature exposure up to 700°C on the residual multiaxial behaviour of a fibre reinforced mortar for overlay strengthening of masonry. Temperature has a detrimental effect in cementitious materials that can be simulated by advanced numerical models disposing of proper constitutive laws. Additionally, a multiaxial stress state can be found in localized areas of structural elements. The experimental residual behaviour from the mutual effect of temperature and multiaxial stress is evaluated and discussed. The analysis of the results show a clear loss of density and uniaxial strength after temperature exposure. The residual behaviour from specimens subjected to triaxial tests shows also a progressive change on the residual deviator stress vs confinement pressure response with the increase of temperature.

Keywords: Fibre reinforced mortar; Natural hydraulic lime; PAN fibres; Thermal effect; Multiaxial stress state

1. INTRODUCTION

The research on overlay strengthening systems for masonry has increased over the last years. The overlay systems are versatile and frequently involve the use of shotcreted layers of fibre reinforced mortars (FRM) [1]–[3]. FRM can also include continuous fibre reinforcement, commonly of carbon or glass material type, and in the form of grids (TRM), for ensuring higher strengthening effectiveness [4], [5].

Temperature in general has a strong negative effect on the behaviour of cementitious materials, namely by decreasing its stiffness and strength. Fibre reinforcement may have a

favourable effect in this respect, mainly in terms of avoiding the spalling and increasing the integrity of the material. The effect of different fibres on the residual compressive strength, ultimate load and flexural toughness after the exposure to high temperatures of a self-compacting high performance concrete (SCHPC) was studied by Ding et al. [6]. They concluded that micro polypropylene fibres could mitigate spalling under high temperature exposure, but the mechanical properties of concrete itself are not significantly improved by this type of fibre reinforcement. On the other hand, macro steel fibres assured higher ultimate load than the reference SCHPC before and after high temperature exposure.

When a fibre reinforced composite is exposed to high temperatures, several physical phenomena occur. For simulating these phenomena, thermo-hygro-mechanical constitutive models should be employed, which require specific and extensive experimental characterization to define the parameters of these models. This work was dedicated to the mechanical characterization of FRM specimens subjected to uniaxial and multiaxial stress state, after the exposure to high temperatures. This work was carried out within the context of a research programme dedicated to the development of lime-based FRM overlay reinforcements for masonry, aiming at developing reinforcement systems that both provide stiffness and strength recovery at ambient temperatures, and improved performance under high temperature exposure.

2. MATERIALS AND METHODS

Short randomly dispersed synthetic polyacrylonitrile (PAN) fibres were added to a cementitious matrix composed by a natural hydraulic lime (NHL) binder, limestone aggregates, additives and superplasticizer. The composition of the mixture per m³ included: 676.1 kg of NHL5.0; 67.6 kg of white Portland cement CEM 52.5; 1014.1 kg of sand with 0-2.0 mm diameter; 290.7 l of water; 6.8 kg of superplasticizer Sika 3002HE, and 11.9 kg of PAN fibres.

The high temperature exposure behaviour was evaluated for different temperatures: room temperature; 300°C; 500°C and 700°C. These levels of temperature were chosen considering that at approximately 300°C there is a significant decrease in the mass of the PAN fibres, see Figure 1a, therefore a strong decrease of their effectiveness in terms of contributing for the reinforcement of cement based materials is expected. Additionally, in the cementitious matrix the free water dehydration (HP_{DH}) occurs at slightly higher temperatures. Between 300°C and 500°C the portlandite dehydrates (P_{DH}). Between 600 and 800°C there is a phase change in the cementitious matrix due to the belite decomposition [7] and the carbonates decomposition (C_{DC}) that are part of the aggregates [8], see Figure 1b.

The residual multiaxial mechanical characterization after temperature exposure was carried out at room temperature by triaxial tests with two levels of confinement pressure $0.33f_c$ and $0.66f_c$. Additionally, uniaxial compressive tests were performed following the EN 12390-3 [10]. The specimens, with a diameter of 50 mm and a height of 100 mm were kept in a curing chamber under 25°C and 90% relative humidity conditions. The tests were carried out 90 days after casting of the specimens because mortars with natural hydraulic lime tend to show significant increments on the mechanical properties and matrix alterations until late ages.

FRM specimens were exposed to high temperatures 4 days before the mechanical tests. The procedure was similar to the one suggested by RILEM recommendation 129-MHT [11]. Temperature exposure was initiated with a heating cycle in the furnace at a constant heating rate of 4°C/min up to the maximum temperature. Subsequently, a plateau of 60 minutes was imposed, during which the temperature was kept constant at the maximum value. The cooling

process started by turning off the furnace and keeping the specimens inside until room temperature was reached.

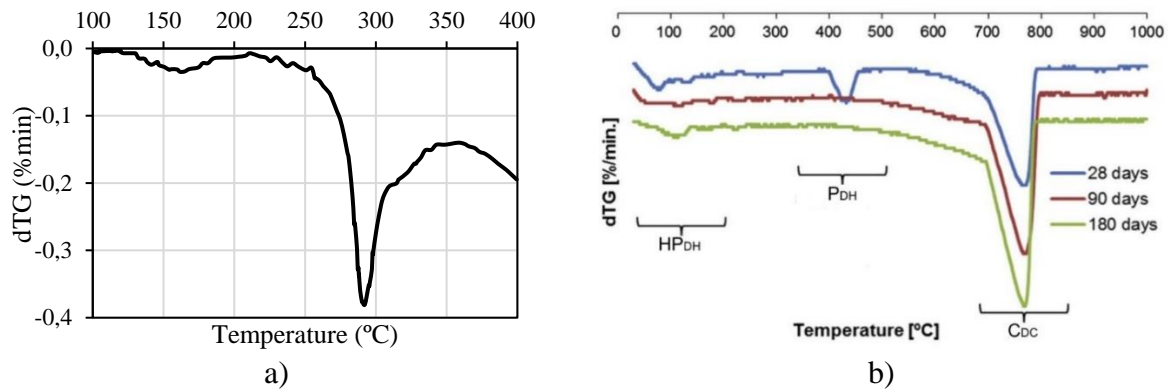


Figure 1: Derivative thermogravimetric analysis: a) PAN fibres [9]; b) NHL mortar (HP_{DH}-free water dehydration, P_{DH} - portlandite dehydration, C_{DC} - carbonates decomposition [8].

The mechanical tests were performed using a 2000 kN closed-loop servo hydraulic GCTS testing machine with 100 mm stroke and an axial stiffness of 3500 kN/mm. Displacement control of the actuator at a rate of 0.02 mm/s was imposed during the tests, see Figure 2. For the triaxial tests a high pressure triaxial cell with 70 MPa confining pressure capacity was used.

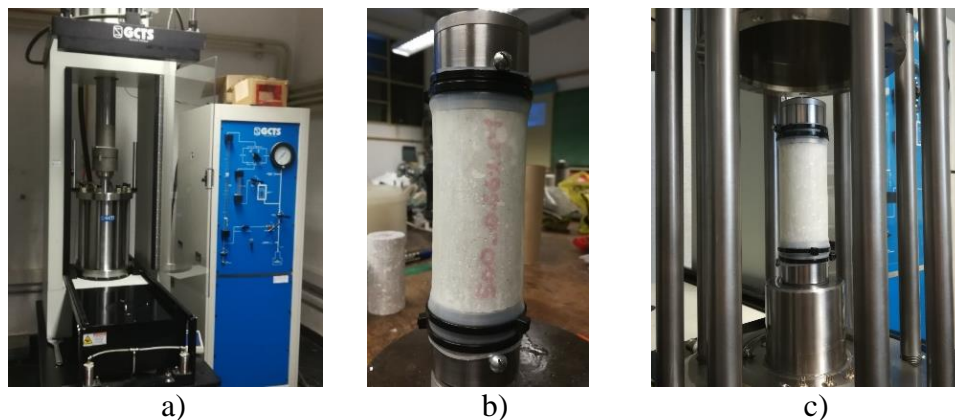


Figure 2: Equipment used to perform the multiaxial tests: a) general view of the GCTS equipment; b) detail of the sleeve to avoid direct contact with the oil; c) detailed view of a specimen prepared for triaxial testing.

3. RESULTS

The visual appearance of the specimens after the exposure to high temperature, and immediately before carrying out the uniaxial and triaxial tests, is shown in



Figure 3. A change in the colour of the specimens is observed with the increase of the temperature exposure. The presence of relatively large cracks is noticed for specimens exposed to 700°C. The specific weight of the specimens was measured before and after the thermal treatment, being 16.80, 15.73, 15.51 and 15.13 kN/m³ for 25, 300, 500 and 700°C, respectively.

The level of confinement stress imposed and the residual value of the deviatoric load obtained for the different levels of maximum temperature exposure are presented in Figure 4. As expected, the results show a clear decrease of the residual stress deviator with the increase of the temperature exposure. On the other hand, with the increase of the confinement stress also the residual value of the deviatoric stress increases.



Figure 3: Visual appearance of the specimens after high temperature exposure.

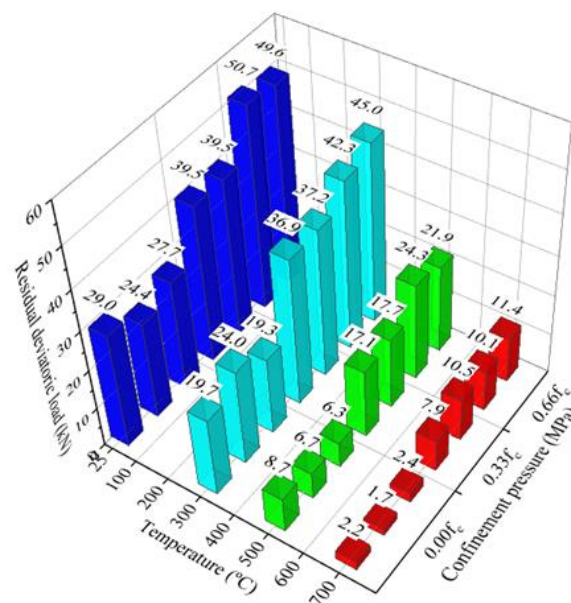


Figure 4: Uniaxial and triaxial test results after different levels of maximum temperature exposure. For each case three specimens have been tested and the average was computed.

4. DISCUSSION OF RESULTS

Images with the detail of the upper surface of the specimens after 300°C and 700°C of temperature exposure are shown in Figure 5. The surface obtained after the exposure to 300°C shows dots in dark colour, which represent PAN fibres that underwent carbonization.

Figure 5b shows the detail of a matrix crack which intersects an aggregate after the exposure to 700°C, likely caused by the onset of the calcination process, as discussed by Grilo et al. [8]. Additionally, it is possible to observe small dots in the matrix area, which were occupied by the fibres before volatilizing due to high temperature exposure. These results partially justify the decrease of the specific weight for the specimens exposed to high temperature. The specimens weight variation of about 8.0% obtained at an exposure temperature of 300°C is mainly due to the free water dehydration, and at a minor extent to the thermal induced volatilization of the fibres. At 700°C the weight variation of about 12.8% was caused by the cumulative effect of the previous alteration mechanisms plus the chemical alteration of the portlandite, belite and calcium carbonate.

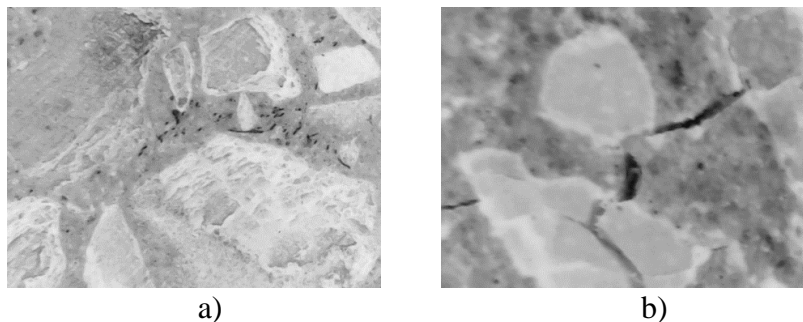


Figure 5: Detail of the top surface of the specimens: a) fibres denoted by dark colour after 300°C of temperature exposure; b) cracking of the matrix and aggregate after 700°C of temperature exposure.

The failure of specimens under uniaxial compressive stress at 25°C occurred after the formation of diagonal macro-cracks, while those specimens exposed to 300 and 500°C of temperature have failed due to the formation of diagonal and vertical macro-cracks. Finally, for specimens exposed to 700°C failure was characterized by the lack of cohesion between particles due to carbonates decomposition, as shown by Grilo et al. [8], see Figure 1b.

The compressive stress vs. strain responses obtained for the uniaxial tests are presented in Figure 6. For the sake of comparison of the responses, the maximum strain is limited to 0.035 mm/mm. As expected, the peak stress reached in each specimen decrease significantly with the increase of the temperature exposure. Additionally, the post peak residual stress also decreased for higher temperature exposure. The experimental responses in terms of residual deviatoric stress vs. axial strain for a confinement pressure of $0.33f_c$ and $0.66f_c$ are presented in Figure 7 and Figure 8. The legend of each specimen includes the temperature at which the specimen was exposed, the level of confinement stress and the specimen's number (Temperature_Confinement pressure_Specimen's number).

The evolution of the normalized value f_{cm}^T/f_{cm}^{25} vs. maximum temperature exposure for the uniaxial and triaxial tests is presented in Figure 9, where f_{cm}^T and f_{cm}^{25} are the average of the residual compressive strength of the specimens after exposure to temperature T and at room

temperature (25 degrees), respectively. Additionally, f_{cm}^T/f_{cm}^{25} curves for calcareous aggregates concrete proposed by EN 1992-1-2 [12] and ACI 216.1-97 [13] are also presented. The curves obtained experimentally and the ones from the standards show clear differences. The EN 1992-1-2 curve presents higher strength retention than the experimental ones for the entire temperature range. In the case of the ACI 216-97, up to 400°C the normalized values are lower than the experimental ones, but above this limit the tendency was the opposite.

The Residual deviatoric stress vs Confinement stress for the different temperature exposure levels is shown in Figure 10. The value of the deviatoric stress was plotted for a strain of 35×10^{-3} . There seems to exist a correlation between the residual deviatoric stress and the confinement stress for different exposure temperatures, and this correlation seems to show an evolution. The regression slope obtained evolved from 1.32 to 1.66, 3.35 and 6.29 when considering rising exposure temperatures of 25°C to 300, 500 and 700°C.

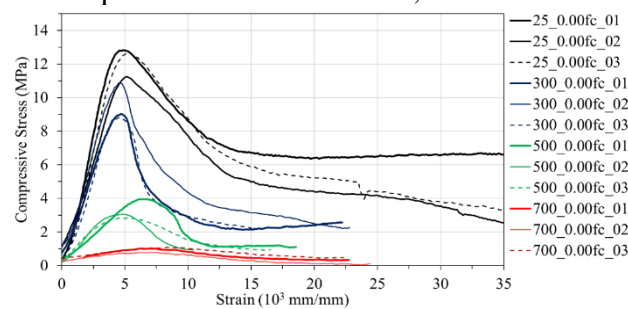


Figure 6: Compressive stress vs. strain responses after the uniaxial tests.

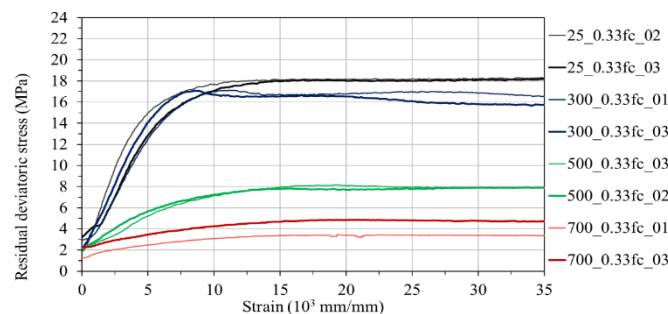


Figure 7: Compressive stress vs. strain responses after the triaxial tests with a confinement pressure of 0.33fc.

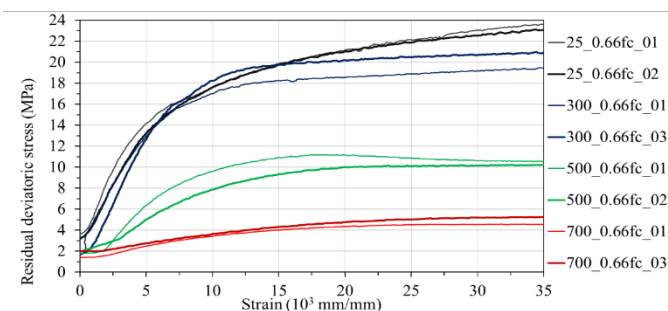


Figure 8: Stress vs. strain responses after triaxial tests with a confinement pressure of 0.66fc.

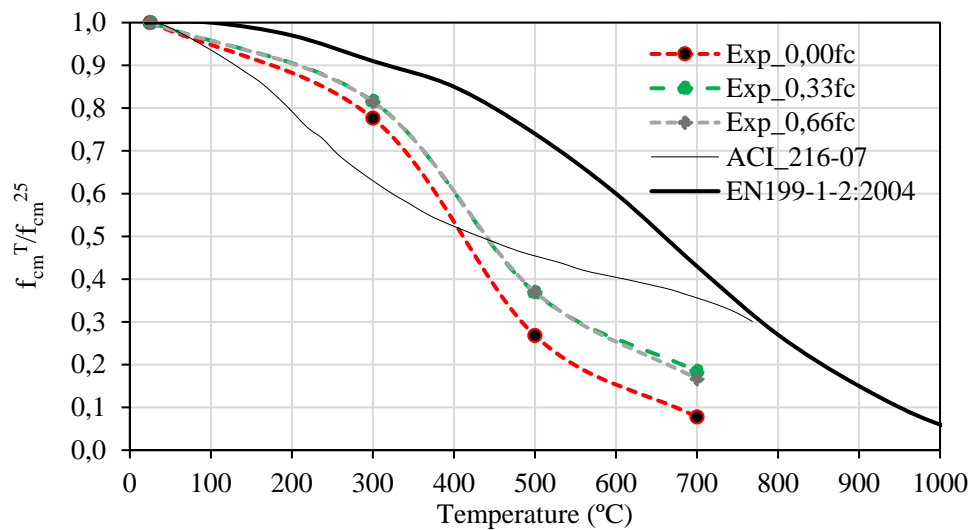


Figure 9: Evolution of the f_{cm}^T/f_{cm}^{25} ratio with maximum exposure temperature.

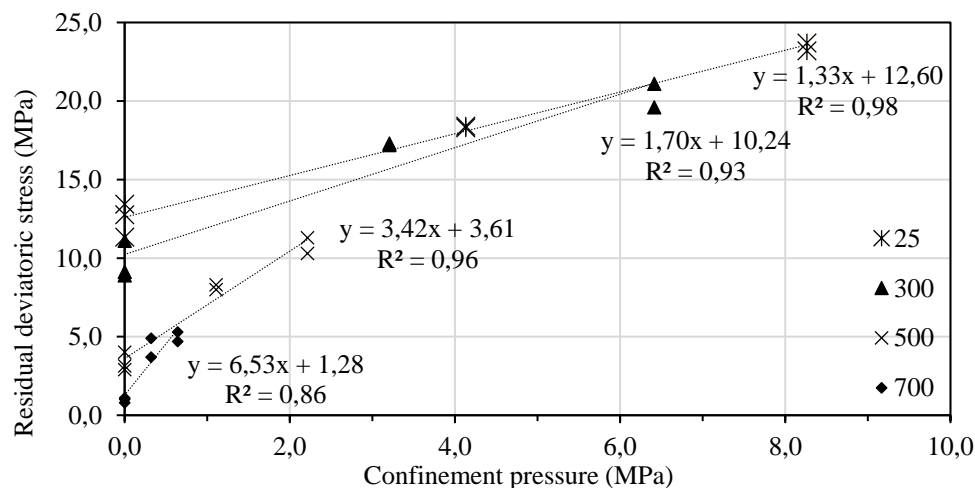


Figure 10: Influence of confinement pressure and temperature exposure on the evolution of the residual stress deviator.

5. CONCLUSIONS

In the context of the development of lime-based FRM for masonry strengthening, this study was dedicated to the assessment of the influence of high temperature exposure and confinement stress level on the residual, post high temperature exposure, compressive strength of fibre reinforced mortar (FRM). Triaxial tests results with cylindrical FRM specimens have revealed the detrimental effect of high temperature on the compressive strength. However this effect was attenuated at increasing levels for increasing confining stresses. The synthetic fibres adopted for the FRM, together with the low strength and high porosity typical in this type of FRM, have led to the avoidance of the occurrence of spalling even when specimens were exposed to the maximum temperature (700°C).

The comparison of the f_{cm}^T/f_{cm}^{25} vs temperature relationship obtained experimentally according to the recommendations of EN1992-1-2 and ACI 216.1-97 has shown that, for

temperatures higher than 400°C, common standards approaches over predict the strength retention observed in the tested FRM. Therefore, the corresponding equations should be adaptable and allow modifications in order to describe the variation of the compressive strength of FRM exposed to high temperatures. The development of improved analytical approaches requires additional research and experimental characterization.

ACKNOWLEDGEMENTS

The first author wish to acknowledge the grant SFRH/BD/115090/2016, provided by FCT. The support provided by SUPERCONCRETE, Marie Skłodowska-Curie Actions, RISE, proposal 645704, is acknowledged.

REFERENCES

- [1] C. Jiang, S. Huang, Y. Zhu, Y. Lin, and D. Chen, “Effect of polypropylene and basalt fiber on the behavior of mortars for repair applications,” *Adv. Mater. Sci. Eng.*, vol. 2016, pp. 14–16, 2016.
- [2] Y. Lin, L. Wotherspoon, A. Scott, and J. M. Ingham, “In-plane strengthening of clay brick unreinforced masonry wallettes using ECC shotcrete,” *Eng. Struct.*, vol. 66, pp. 57–65, 2014.
- [3] A. Dehghani, G. Fischer, and F. Nateghi Alahi, “Strengthening masonry infill panels using engineered cementitious composites,” *Mater. Struct.*, pp. 1–20, 2013.
- [4] D. García and J. Díez, “Stone masonry walls: Strengthening with TRM (I),” in *Structural Analysis of Historic Construction*, 2008, no. I, pp. 851–859.
- [5] G. Marcari, M. Basili, and F. Vestroni, “Experimental investigation of tuff masonry panels reinforced with surface bonded basalt textile-reinforced mortar,” *Compos. Part B Eng.*, vol. 108, pp. 131–142, 2017.
- [6] Y. Ding, C. Azevedo, J. B. Aguiar, and S. Jalali, “Study on residual behaviour and flexural toughness of fibre cocktail reinforced self compacting high performance concrete after exposure to high temperature,” *Constr. Build. Mater.*, vol. 26, no. 1, pp. 21–31, 2012.
- [7] I. Hager, “Behaviour of cement concrete at high temperature,” *Bull. Polish Acad. Sci. Tech. Sci.*, vol. 61, no. 1, pp. 145–154, Mar. 2013.
- [8] J. Grilo, A. Santos Silva, P. Faria, A. Gameiro, R. Veiga, and A. Velosa, “Mechanical and mineralogical properties of natural hydraulic lime-metakaolin mortars in different curing conditions,” *Constr. Build. Mater.*, vol. 51, pp. 287–294, 2014.
- [9] J. Meinel, K. Schönfeld, M. Kirsten, K. Kittler, A. Michaelis, and C. Cherif, “Optimization of the temperature program to scale up the stabilization of polyacrylonitrile fibers,” *Compos. Part A Appl. Sci. Manuf.*, vol. 96, pp. 37–45, 2017.
- [10] Comité Européen de Normalisation, “EN 12390-3:2009 Testing hardened concrete Part 3: Compressive strength of test specimens,” no. August, 2009.
- [11] Rilem Tc 129-Mht, “Compressive strength for service and accident conditions,” *Mater. Struct.*, vol. 28, no. 4, pp. 410–414, May 1995.
- [12] Comité Européen de Normalisation (CEN), “EN 1992-1-2:2004 Design of concrete structures - Part 1-2: General rules - Structural fire design.” Brussels, 2004.
- [13] ACI/TMS Committee 216, “ACI 216.1-97 / TMS 0216.1-97: Standard Method for Determining Fire Resistance of Concrete and Masonry Construction Assemblies,” *Manual of Concrete Practice*. pp. 1–26, 1997.

NUMERICAL MODEL OF AN EXPERIMENTALLY TESTED TIMBER-CONCRETE COMPOSITE SLAB EXPOSED TO FIRE

Cvetanka Chifliganec (1), Meri Cvetkovska (2), Ljupco Lazarov (3), Ana Tormbeva Gavriloska (4)

(1) (2) (3) Ss. Cyril and Methodius University in Skopje, Faculty of Civil Engineering, Macedonia

(4) Ss. Cyril and Methodius University in Skopje, Faculty of Architecture, Macedonia

Abstract

Nowadays, TCC floors are successfully used in: new buildings, refurbishment of existing buildings, bridges etc. In their most common application they have to provide REI30 and REI60 performance. Although experimental testing is the best way, numerical modelling is a cheaper alternative to provide reliable information regarding the fire resistance and performance of a TCC system.

This paper presents a novel numerical model for analysis of timber-concrete composite slab with screwed connections in fire. Validation of this numerical model, conducted with the computer program SAFIR, is made by comparison of the results with one experimentally tested timber-concrete composite slab exposed to fire. The results achieved by the numerical model are in very good agreement with the experimental results.

Keywords: timber-concrete composite (TCC) slab, screwed connection, fire, numerical model

1. INTRODUCTION

Even though an increased number of large-scale and small-scale testings of TCC structures in fire are performed in recent years, numerical modelling is done only for a small number of cases [1].

Modelling the behaviour of timber-concrete composites (TCC) in fire is a very complex process. The behaviour of TCC slabs in fire is mainly governed by the timber and the connection between the concrete slab and the timber beam. Due to the temperature rise, change of stiffness and strength of all materials in the composite occurs. Also, timber is a combustible material and exhibits reduction of the cross section when exposed to fire.

The numerical models should provide a realistic analysis of the TCC structure exposed to fire. They should be based on fundamental physical behaviour in such a way as to lead to a reliable approximation of the expected behaviour of the structure under fire conditions. They can be used for determination of: (1) charring depth, (2) development and distribution of the temperature within structural members (thermal response model), and (3) evaluation of the mechanical behaviour of the structure or of any part of it (structural response model) [2].

In order to determine the behavior in fire and also calculate the slip between the subcomponents of the composite system, a novel method for analysis of TCC slabs in the computer program SAFIR was developed. This paper presents one such numerical model for an experimentally tested TCC slab with screwed connection in fire.

2. NUMERICAL ANALYSIS

2.1 Description of the model

The subject of analysis is the TCC slab with screwed connections in fire tested by Frangi et al. [3] [4] [5]. In [4] only thermal and no structural numerical modelling was done.

Short description of the TCC slab:

- Span 5.21 m and width 2.8 m, exposed to standard ISO fire until failure.
- Slab consists of four glulam beams GL24h with cross-section dimensions of 180 mm x 240 mm, a 20 mm thick timber board and an 80 mm thick concrete slab.
- The screws in the connection have 45° of inclination. The distance between the screws, with 100 mm of its length embedded in the timber and 50 mm in the concrete, is 120 mm. In the cross-section there are two pairs of screws (Figure 3) and the side cover of the screws is 50 mm.
- The mechanical load $F_{\text{fire}}=40$ kN, applied at about a third of the span, is kept constant during the fire test.
- The slab is designed to survive 60 minutes of fire exposure.

The nonlinear 2D numerical analyses were conducted with the computer programme SAFIR specialized for structural fire analysis [6] [7]. The analysis of the structure exposed to fire consist of two steps. The first step involves predicting the temperature distribution inside the structural members, termed as ‘thermal analysis’. The second part of the analysis, termed as ‘structural analysis’, is carried out for the main purpose of determining the response of the structure due to static and thermal loading.

In the thermal analysis [1], the cross-section of the TCC beam was analysed as a T-section with standard fire exposure (ISO 834) on the bottom side (Figure 1 a). SOLID elements were used to model the cross-sections (Figure 1 b). Figure 2 gives the temperature fields in the cross section at different time moments. Figure 3 compares the temperatures around the screw calculated with SAFIR and the temperature calculated with the expression (Equation 1) developed by Frangi et al. [5], based on the results from the fire tests conducted on wood members exposed to ISO fire exposure from one side. The temperature-time curve which describes the evolution of temperature at point A of the screw was applied to the boundary of the cross-section of the steel verticals who represent the connection in the structural analysis in SAFIR.

$$T(x) = 180\left(\frac{\beta t}{x}\right)^{\alpha} ; \alpha(t) = 0.025t + 1.75 ; x = 50 \text{ mm} \quad (1)$$

β - charring rate in mm/min

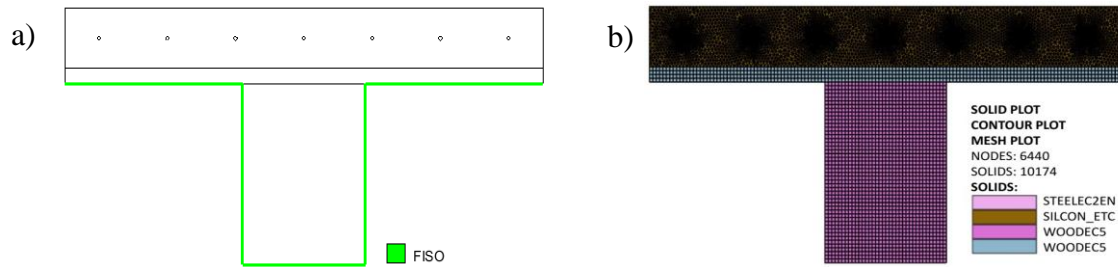


Figure 1: Cross section of the TCC beam a) ISO time-temperature curve applied to describe the environment around the model b) FE mesh plot

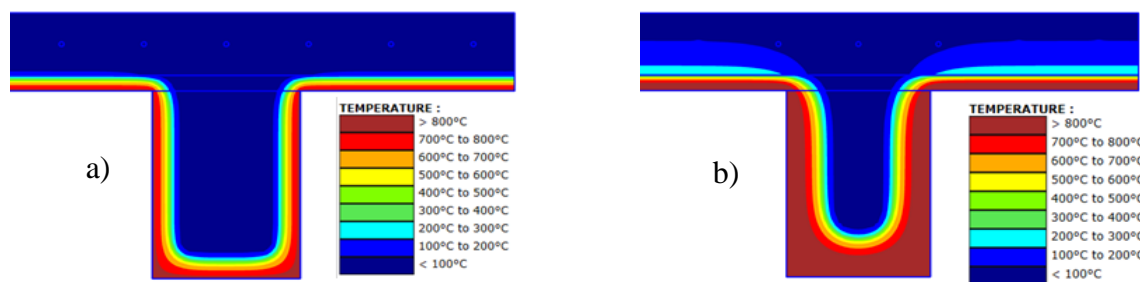


Figure 2: Temperature fields in the cross-section at different time moments a) t=30 min b) t=67 min (failure of the slab in the test)

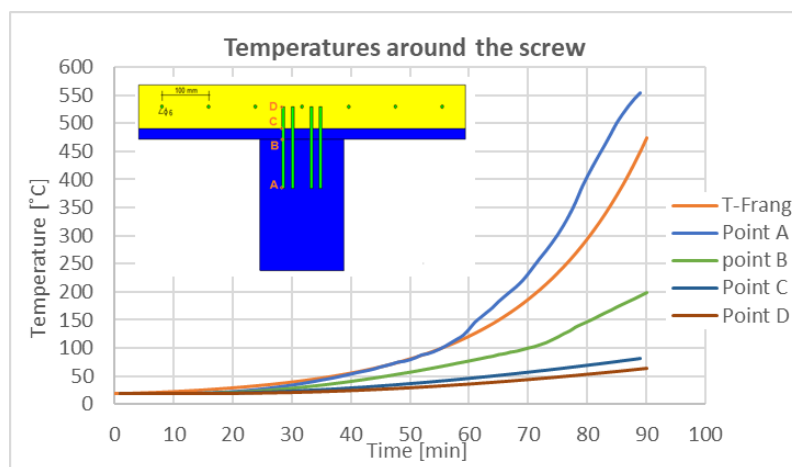


Figure 3: Comparison of temperatures around the screw calculated with SAFIR and with the expression for calculation of temperature profile in a wood member subjected to ISO fire exposure from one side given in Frangi et al. [5]

In the structural analysis, three different models were considered [1]. The structural system of the TCC slab in each considered model is presented in Table 1.


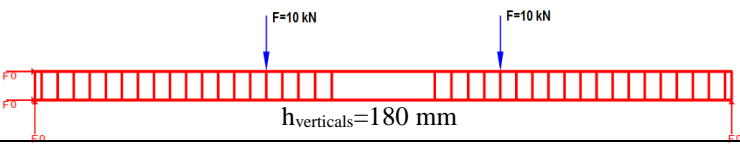
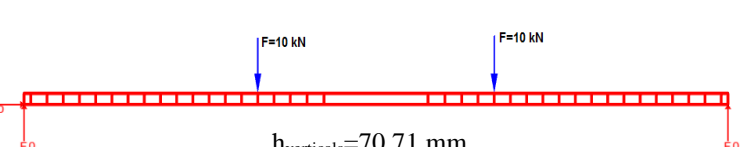
In order to compare the response of the real TCC slab with flexible shear connection to a theoretical case of a TCC slab with rigid connection, Model I was created.

In Model II and Model III the TCC beam was treated as a simply supported Vierendeel truss. The top chords represent the concrete slab, the bottom chords represent the timber beam and the verticals represent the connections. The vertical steel beam elements are placed at the exact

position of the screws through the length of the tested TCC beam. The only difference between Model II and Model III is the height of the steel verticals.

The main task in these numerical models was to properly model the connections. According to Frangi [4], one pair of the 45° inclined screws has: characteristic load-carrying capacity $F_{v, rk}=14.3$ kN. According to ETA-13/0699 [8], these screws have: $F_{v, rk}=18.38$ kN and $K_{ser}=17.21$ kN/mm. In the numerical model, the steel verticals representing the connections are modelled as steel beam elements with the same load carrying capacity as the 45° inclined screws in Frangi [5].

Table 1: Structural system and connection characteristics in each considered model in the structural analysis

Numerical model	Connection characteristics	Structural system
Model I	Rigid connection (no slip between the subcomponents occurs)	
Model II	Flexible connection (slip between the subcomponents occurs)	
Model III	Flexible connection (slip between the subcomponents occurs)	

2.2 Material models

For concrete, steel and wood, the thermal models used in the numerical analysis are based on the corresponding Eurocodes. For concrete the SILCON ETC [9] material model is used. This model is based on the laws of EN 1992-1-2 [10] except that in the ETC model the transient creep strain treated by an explicit term in the strain decomposition. For structural carbon steel (used for the steel verticals), the material model is based on EN 1993-1-2 [11]. For reinforcing carbon steel (used for the reinforcement in the concrete slab), the material model is based on the EN 1992-1-2 [10]. For describing the temperature-dependent mechanical behaviour of wood the uniaxial material model of Annex B of EN 1995-1-2 [2] is used.

The input data describing the mechanical and thermal characteristics of the materials used in the numerical analysis are taken from the tests given in [4].

2.3 Results from the numerical analysis

The numerical model of TCC slab in fire in SAFIR was able to calculate the slip between the subcomponents of the composite (concrete and timber), which was one of the main goals. Comparison of deflection curves and slip curves from the numerical models in SAFIR, the experiment and the simplified calculation method developed by Frangi et al. [5] are presented in Figure 4 and Figure 5, respectively. The main results from the analyses are presented in Table 2.

As expected, Model I gave lower deflection in comparison to the fire test (Figure 4).

The time-deflection curve calculated with Model II matches the results from the fire test up to 50 minutes, but afterwards the deflection is slightly underestimated. In terms of the slip this model overestimates the relative slip between the concrete slab and the timber beam.

Model III gave best results in term of both deflection and slip. The results in this model are highly influenced by the diameter of the steel vertical. Model III with diameter of the steel verticals of 16 mm gave time-deflection curve which is somewhere between the curves from the fire test and the simplified model up to 45 minutes, but afterwards this curve matches the one from the fire test. The slip values in this model are highly overestimated. Model III but with increased diameter to 16.5 mm and 17 mm lead to slightly decreased deflections and significantly decreased slips. In terms of slip, Model III with 17 mm gave results that are in very good agreement with the results from the fire test. Here, the apparent “peak” in the time-slip curve that occurs at $t=30$ minutes (zero slip) is due to the change of rotation of the outer steel verticals during the deformation of the structure.

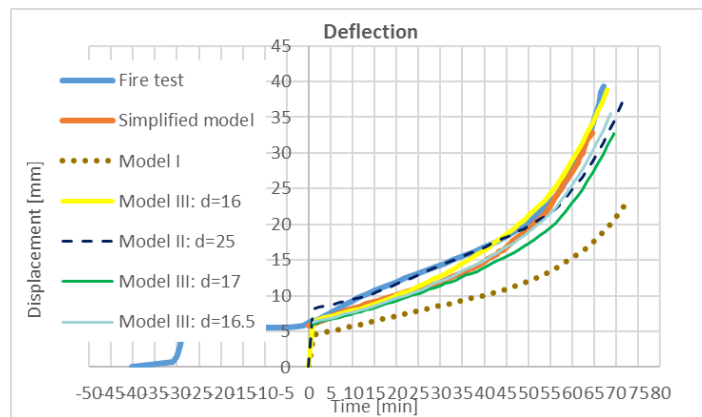


Figure 4: Comparison between the calculated deflection in Safir, the measured deflection in the experiment and the calculated deflection with the simplified method proposed by Frangi et al. [5]

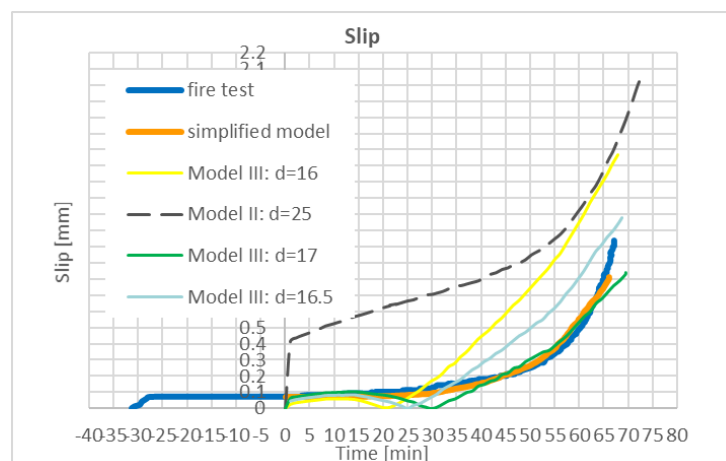


Figure 5: Comparison between the calculated relative slip in SAFIR, the measured slip in the experiment and the calculated slip with the simplified method proposed by Frangi et al. [5]

Table 2: Results from the structural analysis: fire resistance, deflection and slip


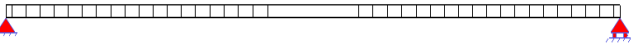
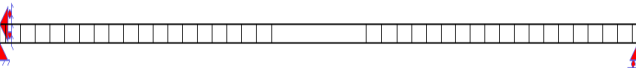
		t_{fr} [min]	$t_{fr, model}$ / $t_{fr, test}$	Deflection at failure Δy [mm]	Δy_{model} / Δy_{test}	Slip at failure Δx [mm]	Δx_{model} / Δx_{test}
Fire test		67		≈ 39.4		≈ 1.04	
Simplified model		65	0.97	≈ 33	0.84	≈ 0.8	0.77
Model I (rigid connection)		71.8	1.06	22.5	0.57	/	
Model II $h_{verticals}=180$ [mm]	$d=25$ [mm]	72	1.07	38.4	0.97	2.02	1.94
Model III $h_{verticals}=70.71$ [mm]	$d=16$ [mm]	68	1.01	38.9	0.99	1.57	1.51
	$d=16.5$ mm	68.8	1.03	35.5	0.90	1.18	1.13
	$d=17$ mm	69.5	1.04	32.7	0.83	0.84	0.81

2.4 Results from the numerical analysis

Several factors in the numerical models had high influence on the results that describe the global response of the TCC structure:

- The mesh size in the thermal analysis: Proper sized finite elements are necessary to avoid skin effect at the surfaces and to correctly calculate the area of all elements in the cross-section (timber beam, concrete slab, reinforcement).
- The diameter of the steel verticals: Different structural systems need different diameter of the steel verticals to simulate the global structural response (deflection and slip) of the slab. Change of 0.5 mm in the diameter of the steel verticals in one structural system makes difference in the results.
- The structural system in the structural analysis (see Table 3).

Table 3. Variations in the structural system of Model III

Description		Structural system
a)	Vierendeel truss without steel verticals at the end	
b)	Vierendeel truss with steel verticals at the end	
c)	Vierendeel truss with steel verticals at the end and horizontal constraint at the left end	

In order to assess how the change of diameter and structural system influence the response of the structure, a parametric analysis was made.

Figure 6 and Figure 7 compare the deflection and slip curves for:

- one particular model - Model III with $d_{\text{verticals}}=16$ mm, but with variation in the structural system as presented in Table 7.
- Model III b), but with $d_{\text{verticals}}=16$ mm and $d_{\text{verticals}}=16.5$ mm.

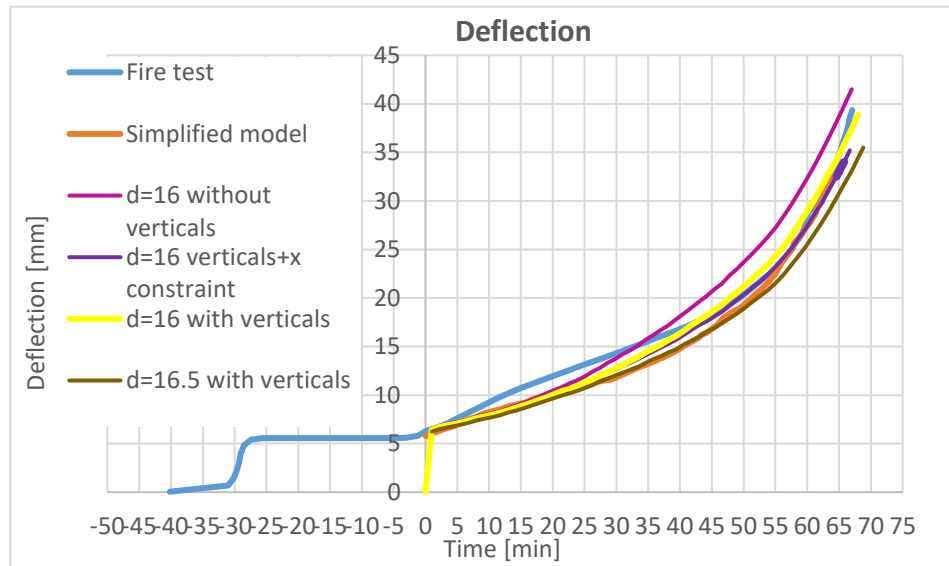


Figure 6: Comparison of time-deflection curves for different structural systems and different diameters of the steel verticals

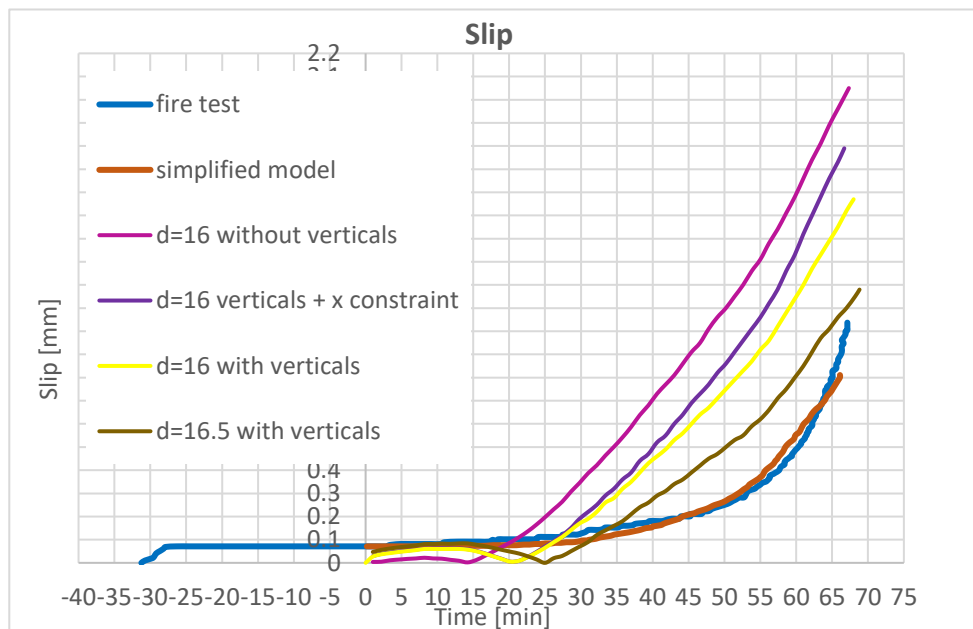


Figure 7: Comparison of time-slip curves for different structural systems and different diameters of the steel verticals

3. CONCLUSION

A novel numerical model for analysis of timber-concrete composite slabs with screwed connection in fire was developed in SAFIR. The numerical model successfully predicted the general behaviour of the structure in fire. The calculated: fire resistance, deflection and slip between the subcomponents of the TCC structure from the numerical model were in very good agreement with the experimental results.

The mesh size in the thermal analysis, the diameter of the steel verticals and the structural system in the structural analysis are factors that have highest influence on the response of the TCC structure's numerical model.

ACKNOWLEDGEMENTS

The COST Action FP1404 "Fire Safe Use of Bio-Based Building Products" (www.costfp1404.com, 2014-2018) is gratefully acknowledged for facilitating and providing financial support for the first author's short term scientific mission at ETH Zurich, resulting in research which is in some parts presented in this paper.

REFERENCES

- [1] Chifliganec C., Short term scientific mission report COST FP1404, May 2018.
- [2] CEN (European Committee for Standardization), EN 1995-1-2: Eurocode 5 – Design of timber structures - Part 1-2, 2004.
- [3] Frangi A., Fontana M., 'Experimental tests on timber-concrete composite slabs at room temperature and under ISO-fire exposure', Rep. No. 249, Institute of Structural Engineering, ETH Zurich, Switzerland, 2000.
- [4] Frangi A., 'Brandverhalten von Holz-Beton-Verbunddecken', PhD thesis no 14328, Institute of Structural Engineering, ETH Zurich, Switzerland, 2001.
- [5] Frangi A., Knobloch M., Fontana M., 'Fire design of timber-concrete composite slabs with screwed connections', *ASCE Journal of Structural Engineering* 136 (2) (2010) 219–228.
- [6] SAFIR University of Liège, Liège, Belgium, 2014
- [7] Franssen J., 'SAFIR: A Thermal/Structural Program for Modeling Structures Under Fire', *AISC Eng. J.* (2005) 143–158.
- [8] EOTA (European Organization for Technical Approval), European Technical Approval ETA-13/0699, June 2013-June 2018.
- [9] Gernay T., Franssen J.-M., 'A formulation of the Eurocode 2 concrete model at elevated temperature that includes an explicit term for transient creep', *Fire Safety Journal* 51 (2012) pp. 1-9.
- [10] CEN (European Committee for Standardization), EN 1992-1-2: Eurocode 2 – Design of concrete structures - Part 1-2, 2005.
- [11] CEN (European Committee for Standardization), EN 1993-1-2: Eurocode 3 - design of steel structures – Part 1–2, 2005.

**International Conference on Sustainable
Materials, Systems and Structures
(SMSS 2019)**
Durability, Monitoring and Repair of Structures

*Condition assessment and
monitoring of structures*

DURABILITY OF REINFORCED CONCRETE STRUCTURES – AN OVERVIEW OF PAST AND CURRENT RESEARCH ACHIEVEMENTS IN CROATIA

Dubravka Bjegović (1), Marijana Serdar (1) and Ana Baričević (1)

(1) Faculty of Civil Engineering, University of Zagreb, Croatia

Abstract

Croatia is relatively small in area, but has a strongly identified Adriatic coastline. A significant part of the developed road infrastructure is located in a distinctly Mediterranean but also in a distinctly continental climate. Both climates, Mediterranean and continental, directly influence the durability of concrete structures. The construction of reinforced concrete structures in Croatia was intensified in the second half of the 20th century, but, due to the lack of relevant legislation and know-how on the durability of RC structures, problems were noticed already after 15 years of service life.

The paper overviews the durability of reinforced concrete structures in Croatia within road infrastructure and along the coast as well as the research into the area of material durability in reinforced concrete structures.

Keywords: durability, sustainability, modelling service life, concrete additions, alternative binders

1. INTRODUCTION

Croatia has a shape of a horseshoe with the land area of 56 594 km² and is the 19th country by area in the European Union, between Latvia and Slovakia. It is an extremely diverse country in relief and climate. As a Pannonian and Adriatic country, and as the Mediterranean line of Central Europe, its location is favourable in terms of transport geography and its position at the crossroads of important European transport corridors resulted in the state strategy of constructing road infrastructure. Thus, the road network of highways and semi-highways covers a total of 1.288,5 km (as of December 31, 2013), Figure 1, which is managed by four concessioners [1].

Industrial and public buildings were already built at the beginning of the last century [2,3], but significant construction of road infrastructure in Croatia was developed in the second half of the 20th century, predominantly the construction of reinforced concrete structures, for which

resources existed. Cement was produced in four plants in Croatia, and also, because of the proximity cement from Slovenia, Serbia and Bosnia and Herzegovina was used. Natural deposits of aggregate were abundant, from aggregate washed up by rivers to crushed rock, mainly limestone. The design and construction followed German standards and recommendations as well as the regulations of the then state which, it should be noted, did not cover the wearing down of structures. It should also be said that the world experts and scientists started to tackle the issue of reinforced concrete durability and published papers on the topic only then.



Figure 1: a) Highway network in Croatia [1]

This paper will give an overview of the problems of reinforced concrete durability in Croatia on road structures and buildings on the coastline. Furthermore, systematic inspections of reinforced concrete structures are described, which were the basis for the strategy of research at the Department of Materials of the Faculty of Civil Engineering in Zagreb, in the field of the durability of materials in reinforced concrete structures.

2. SYSTEMATIC INSPECTIONS OF REINFORCED CONCRETE STRUCTURES

Satisfactory durability is the second most important property of structures following the usual mechanical properties, such as strength and ductility, of the basic materials. In the Republic of Croatia, already in the mid 20th century the problems of durability of concrete structures were noticed, but the first systematic inspection of concrete structures in the Adriatic area of Croatia was conducted by the experts from the Faculty of Civil Engineering of Zagreb under the leadership of professor Zlatko Kostrenčić, in the period from the autumn of 1962 to the summer of 1964. The inspection was funded by the then Republic Fund for Science in Zagreb [4]. Sixty structures on the coast, from Kopar to Šibenik, were inspected. Most structures were built between 1910 and 1930.

Industrial buildings, such as the cement plants in Istria and Dalmatia, were constructed between 1920 and 1930, while a number of smaller buildings were built before 1890. As already mentioned in the introduction, a significant construction of road infrastructure in Croatia was carried out in the second half of the 20th century. In the Adriatic region some reinforced concrete bridges were badly damaged by the marine environment, which was noticed after 15 years of service. The Mediterranean climate is characterized by the strong wind, so called *bura*, which carries salt to the structure, and the salt penetrates into concrete to the reinforcement which then wears down fast, Figure 2. [3,5].

The inspections of reinforced concrete structures, particularly bridges, were mainly carried out according to the methodologies laid out by the international work groups, published in [6-10]. The paper [11] describes the chronology of the construction of both arches on Krk bridge, the specificities of the location of the construction and their impact on the reinforced concrete structure of the bridge. The testings on both the smaller and the larger arch and the solutions for repair and protection are described. The first inspection was conducted in October 1981, and then again in November 1984, April and May 1989, November 1990 and the last one in 2001 within the program of establishing the state of the material of the reinforced concrete structure on the larger arch. Underwater diving inspections and the controls of the state of the concrete in the larger arch's inclined strut, as one of the most endangered structural elements of the arch, were carried out several times. The paper [11] gives the list of the published papers and studies of bridges in Croatia.

3. MASTER'S AND DOCTORAL PAPERS ON THE DURABILITY OF REINFORCED CONCRETE

The study of the durability of concrete started several decades ago and is still the subject of numerous scientific and technical committees [12-14] and national and international conferences. The main conclusion of all intentions in this field is that a holistic approach towards durability design is necessary, consisting of tailoring appropriate material and its properties in the design phase, controlling and assuring that the properties are met in the construction phase, and maintaining and assessing a pro-active instead of a reactive repair during the entire service life [15]. Different groups of professionals are urgently needed in order to tackle the grand challenge of RC infrastructure ageing in industrialized countries and to ensure the design and construction of durable infrastructures in emerging regions [16].

At the end of the last century the strategy with a number of guidelines for the research into the durability of reinforced concrete was designed at the Materials Department and it is as follows: 1) developing testing methods, 2) determining the impact of the composition of concrete on the durability of structures, 3) designing the types of concrete with enhanced properties by adding cement replacement materials and micro reinforcements, 4) developing the models of designing the durability of reinforced concrete with traditional, but also with modified types of reinforcement, 5) developing repair and protection materials and procedures. At the beginning, the research was carried out within the scope of master's and doctoral theses, but the new access to European funds and cooperation with the European research projects it has been extended and the industry has joined the academic community. Figure 2 [17-57] shows the chart with the research results within the scope of master's and doctoral theses conducted at the Materials Department, the Faculty of Civil Engineering, Zagreb University. The overview is given on a time scale for the above mentioned topics.

Over the years, a lot of effort within the research group was put into the numerical description of service life of structures. As a part of the research mathematical dependency between durability properties of concrete and concrete mix design were established and introduced into the model CHLODIF++ for modeling and predicting the service life of reinforced concrete structure exposed to marine environment [46, 48]. During research in this field, innovative expressions correlating chloride loading and wind effects were proposed, Figure 3 a) [48], with the aim of describing more precisely the amount of chlorides as environmental loading. Focus went beyond the corrosion initiation phase towards the

propagation phase, through comprehensive research of mechanical behavior of steel during corrosion. Models correlating the level of corrosion activity with reinforced concrete carrying capacity have been developed, which would allow even more precise calculation and management of ageing structures, Figure 3 b) [47].

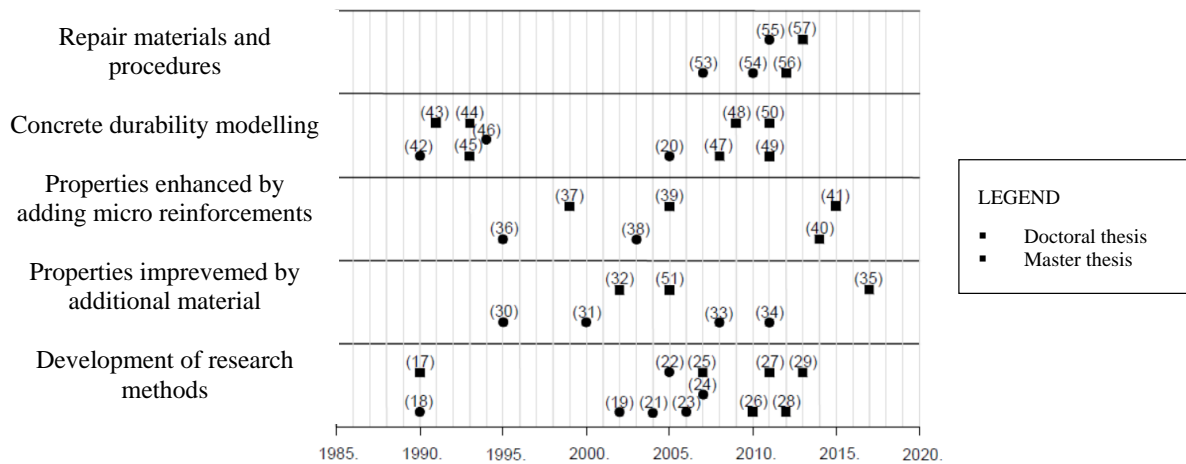


Figure 2: Defended master's and doctoral theses [17-58]

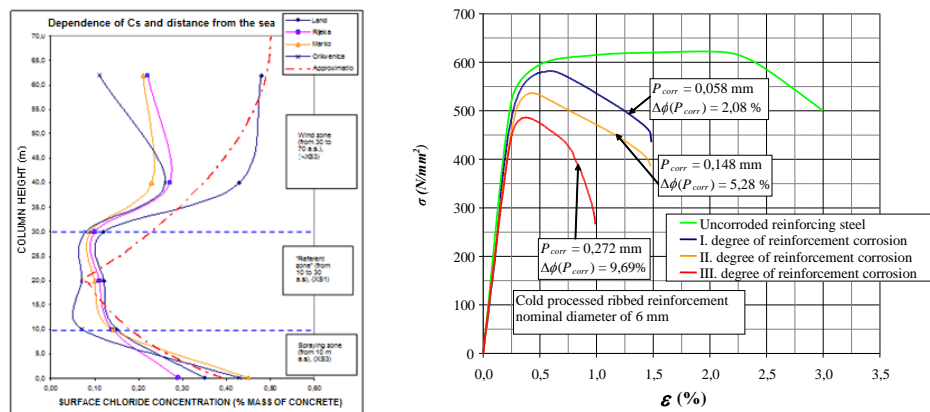


Figure 3 a) Proposed wind zones for determination of chloride loads on concrete construction [48], b) Stress-strain diagrams (σ - ϵ) of reinforcement corroded to different penetration depths [47]

Significant effort was also put into the research of different materials for the enhancement of durability in marine environment. For example, research was performed to establish initiation and propagation diagrams for different types of economically applicable reinforcing steels Figure 4 [50] and correlate their behaviour in laboratory, to real marine environment through establishment of real test site under Krk Bridge. Furthermore, sustainable alternatives to classical additions in concrete were also investigated for their long-term durability, such as recycled steel fibres from end-of-life tires as substitution for industrial fibres.

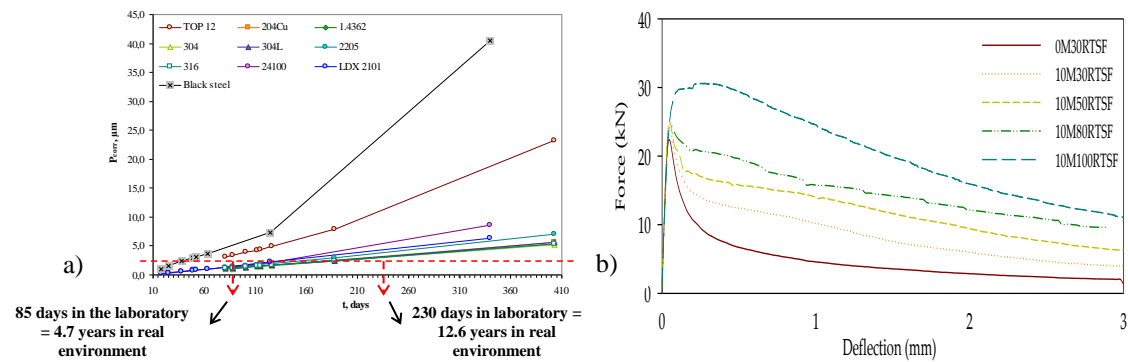


Figure 4 a) Depth of corrosion penetration and expected time to reaching 5 µm of depth [50], b) Force – deflection curves of hybrid fibre reinforced concrete with increased content of unsorted recycled tire steel fibres (RTSF) [40]

The research into the durability of structures as a part of their sustainability, has always been one of the goals of the research team at the Faculty of Civil Engineering. The above has been emphasized recently, when the discussion on the alternative materials use with the reduced ecological impact has become essential, and not a trend. The research team has focused on the durability of concrete with a large proportion of mineral admixtures for the last twenty years, and particularly in the doctoral theses [51,52]. Recently, there has been an additional focus on the change of properties of sustainable materials caused by the environmental effects [59]. The research into the durability and long-term behavior of alternative materials with the aim to prove their sustainability, will be the central interest of the research team in the coming years.

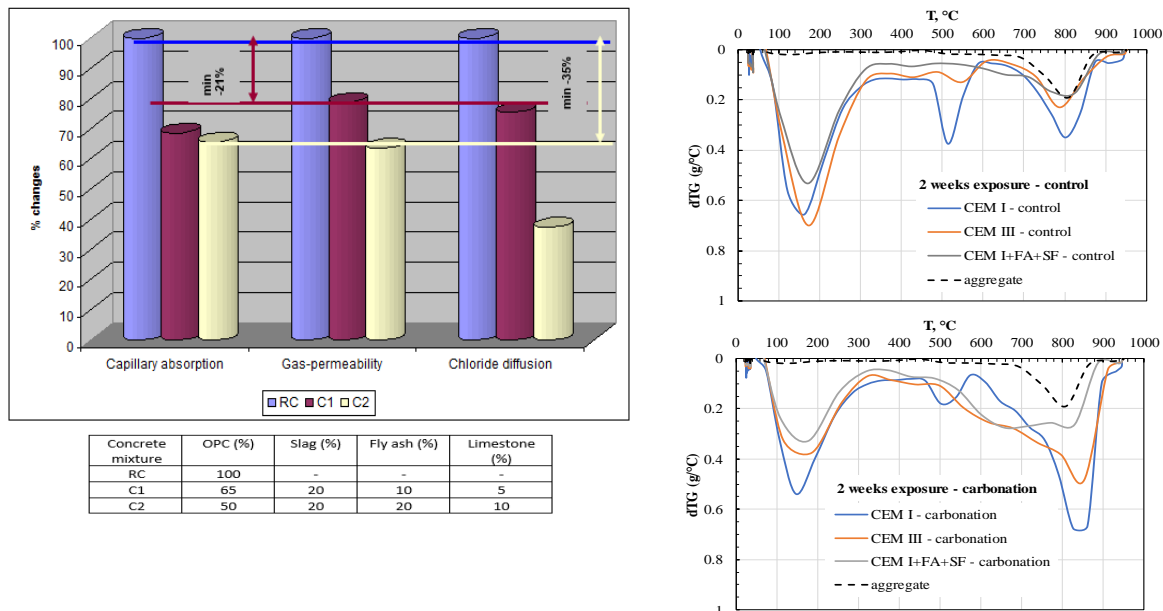


Figure 5 a) The change of concrete penetrability depending on the binder type [52], b) Changes in mineralogical composition of concrete before and after carbonation [58]

4. CONCLUSIONS

The enormous financial effects of the corrosion in infrastructure buildings seem to be insufficiently balanced by educational research activities. In this paper, based on the research carried out in master's and doctoral theses at the Department of Materials, Faculty of Civil Engineering, University of Zagreb, it is shown that concrete should be considered and investigated more than before. Once the research has been completed, several possible implementation mechanisms need to be considered to select the right approach to successful transfer of the technology to the practitioner. Multiple strategies including information dissemination, training workshops, field demonstration pilot projects, hands-on training, equipment loan programs, technical support and continuous educational courses should be considered for research product implementation. Continued coordination of on-going international research and educational programs is also needed. But this action is a long-term process and may require several years of effort.

5. REFERENCES

- [1] https://hr.wikipedia.org/wiki/Autoceste_u_Hrvatskoj
- [2] Bjegović, Dubravka; Stirmer, Nina, Theory and Technology of Concrete, Zagreb University, Faculty of Civil Engineering, 2015, 999 pp.
- [3] Bjegović, D., Stipanović, I., Concrete Structures in Time and Space, lecture, The Days of Concrete 5, February 5-6, 2010, Osijek
- [4] Kostrenčić, Z., Corrosion of Concrete in the Adriatic region of Croatia, 1963, The library of the Materials Department, Faculty of Civil Engineering, Zagreb, inv.no, B-561
- [5] Stipanovic Oslaković, I., Bjegović, D., Radić, J., Case study: LCC analysis for Krk Bridge, Tailor Made Concrete Structures – Walraven & Stoelhorst (eds) 2008 Taylor & Francis Group, London, ISBN 978-0-415-47535-8, 1005-1007.
- [6] Tenžera, D., Puž, G., Radić, J., Inspection of bridges on state roads in Croatia, <https://bib.irb.hr/datoteka/633846>.
- [7] Radić, J., Mandić, A., Augustinović, I., Assessment of Existing Structures, Građevinar Vol. 61 (2009) 9, 901-912.
- [8] Rücker, W., Hille, F., Rohrmann, R., F08a - Guideline for the Assessment of Existing Structures, SAMCO Final Report, Federal Institute of Materials Research and Testing (BAM), Division VII.2 Buildings and Structures, Berlin, Germany, 2006
- [9] Bjegovic, D., Serdar, M., Stipanovic, I., Gulikers, J., Local detailed inspection methods to determine concrete properties on structures. Materials and corrosion, 64(2), 135-140, 2013, <https://doi.org/10.1002/maco.201206648>
- [10] Bjegović, D., Serdar, M., Baričević, A., Jelčić Rukavina, M., Assessing the Condition of Concrete Pier after three Decades of Exposure to Sea Water, Građevinar, Vol. 67 No. 12., 2015.
- [11] Huzjan, B., Ostojić, N., Repair of Krk Bridge, Građevinar Vol. 68 9, 735-743, 2016.
- [12] RILEM, International union of laboratories and experts in construction materials, systems and structures, <http://www.rilem.net/>
- [13] fib, CEB-FIP, The International Federation for Structural Concrete, <http://www.fib-international.org/>
- [14] IABSE, International Association for Bridge and Structural Engineering, <http://www.iabse.org/>
- [15] Bjegovic D., Mikulic D., Stipanović Oslaković I., Serdar M., Performance based durability design of coastal reinforced concrete structures, MWWD & IEMES 2008 Proceedings, 68-69, 2008.
- [16] Ueli M. Angst, Challenges and opportunities in corrosion of steel in concrete, Materials and Structures, 51(1), February 2018.

- [17] Jadrijević, A. The Analysis of Sprayed Concrete and Setting the Parameters for Optimal System, doctoral thesis, mentor Dr. Zlatko Kostrenčić, 1991.
- [18] Blumenschein, N., Impact resistance of industrial floors, master's thesis, mentor Dr. Velimir Ukrainczyk, 2002,
- [19] Marušić, E., Deformation Properties of Superplastificated Concrete, master's thesis, mentor Dr. Dubravka Bjegović, 2004.
- [20] Stipanović, I., Calculation of the service life of reinforced concrete structures exposed to the action of chlorides, master's thesis, mentor Dr. Dubravka Bjegović, 2005.
- [21] Galić, J., Application of non-destructive test methods for determination of polymer modified concrete characteristics, master's thesis, mentor: Dr. Ivana Banjad Pečur, 2005.
- [22] Hranilović, A., Frost with de-icing salts concrete resistance, master's thesis, mentor: Dr. Dunja Mikulić, 2006.
- [23] Ille, M., Modeling of concrete structures durability based on critical degree of saturation, master's thesis, mentor: Dr. Dubravka Bjegović, 2007.
- [24] Banić, D.I., Adhesiveness between concrete and reinforcement in reinforced concrete structures degraded under reinforcement corrosion, master's thesis, mentor: Dr. Dubravka Bjegović, 2007.
- [25] Gabrijel, I. Application of elastic waves for the analysis of setting and hardening in cement composites, doctoral thesis, mentor: Dr. Dunja Mikulić, 2010.
- [26] Sekulić, D., Detection of damages in reinforced structures by elastic waves, doctoral thesis, mentor: Dr. Dubravka Bjegović, 2011
- [27] Marušić, E., Predicting shrinkage deformation of high strength concrete, doctoral thesis, mentor: Dr. Nina Štirmer, 2012
- [28] Milovanović, B., Application of Infrared Thermography for Defect Characterization in Reinforced Concrete, doctoral thesis, mentor: Dr. Ivana Banjad Pečur, 2013
- [29] Jelčić Rukavina, M. Characterisation of self-compacting concretes exposed to high temperatures , doctoral thesis, mentor: Dr. Dubravka Bjegović, 2014
- [30] Šaravanja, K., Rolled Concrete with Reference to the Use of Fly Ashes, master's thesis, mentor Dr. Velimir Ukrainczyk, 1995
- [31] Banjad, I., Optimization of concrete design for tunnel lining, master's thesis, mentor Dr. Velimir Ukrainczyk, 2000
- [32] Banjad-Pečur, I. Optimization of concrete design for tunnel lining, doctoral thesis, mentor Dr. Velimir Ukrainczyk, 2002
- [33] Kovač, D., Recycled aggregate concrete, master's thesis, mentor: Dr. Dubravka Bjegović, 2008
- [34] Würth, D., The Dependence of the Composition and Properties of Self-compacting Concrete, master's thesis, mentor: Dr. Ivana Banjad Pečur, 2011
- [35] Nakić, D. Sludge Application from Wastewater Treatment plants in Concrete Industry, doctoral thesis, Mentor I: assistant professor, Dr. Dražen Vouk, Mentor II: professor, Dr. Nina Štirmer, 2017
- [36] Lončar, A. The experimental investigation of adhesion between polypropylene fibres and concrete matrix, master's thesis, mentor: Dr. Velimir Ukrainczyk, 1995
- [37] Šušteršić, J., High performance fiber reinforced concrete, doctoral thesis, mentor Dr. Velimir Ukrainczyk, 1999
- [38] Skazlić, M., Hybrid high performance fibre-reinforced concrete, master's thesis, mentor Dr. Dubravka Bjegović, 2003
- [39] Skazlić, M., Precast fibre reinforced segments of secondary tunnel lining, doctoral thesis, mentor Dr. Dubravka Bjegović, 2005
- [40] Baričević, A., Contribution to the development of sustainable hybrid fibre reinforced concrete using byproducts from recycling of waste tyres, doctoral thesis, Mentor: Dr. Dubravka Bjegović, 2014.
- [41] Bartolac, M., Properties of Prefabricated Structural Elements with the Reinforcement Partially Replaced with Steel Fibers, doctoral thesis, mentor: Dr. Joško Krolo, co-mentor: Dr. Dubravka Bjegović, 2015

- [42] Sekulić, Z., Rate of Penetration of Chloride Ions into Concrete Exposed to Seawater, master's thesis, mentor Dr. Velimir Ukrainczyk, 1991
- [43] Bjegović, D., Design of concrete structures exposed to chemically aggressive environment, doctoral thesis, mentor Dr. Velimir Ukrainczyk, 1991
- [44] Mikulić, D., Theoretical model of concrete quality insurance, doctoral thesis, mentor Dr. Velimir Ukrainczyk, 1993
- [45] Balabanić, G., Numerical Modeling of Stainless Steel Corrosion Process of Reinforced Concrete Structures in the Sea, doctoral thesis, mentor Dr. Nenad Bićanić, 1993
- [46] Krstić, V., Numerical Model of Durability of Reinforced Concrete Structures, master's thesis, mentor Dr. Jure Radić, co-mentor Dr. Dubravka Bjegović, 1994
- [47] Grandić, D., Calculation procedures for evaluating remaining load bearing capacity and serviceability of corroded reinforced concrete structures, doctoral thesis, mentor: Dr. Dubravka Bjegović, 2008
- [48] Stipanović Oslaković, I. Measuring and prediction of chlorides' transport in concrete, doctoral thesis, mentor: Dr. Dubravka Bjegović, 2009
- [49] Hranilović Trubić, A., Designing of concrete composition resistive to freeze - thaw action , doctoral thesis, mentor: Dr. Dubravka Bjegović, 2011
- [50] Serdar, M., Limit conditions for the application of corrosion resistant steel as reinforcement, doctoral thesis, mentor: Dr. Dubravka Bjegović, 2011
- [51] Rosković, R., Contribution to optimal utilisation of blended cements and sustainable concrete technology, doctoral thesis, mentor Dr. Dubravka Bjegović, 2005
- [52] Rosković, R.; Bjegović, D.; Beslać, J., Contribution of Mixed Cements in production of More Durable and Sustainable Concrete // Proceedings of the International Conference held at the University of Dundee: Achieving Sustainable in Construction / Dhir, Ravindra K ; newlands, Moray D ; White, Andrew (ur.) (ur.).London: Thomas Telford Publishing, 2005, pp. 127-134
- [53] Žugelj, V., Compatibility between industrial floor concrete slab and overlay, master's thesis, mentor Dr. Velimir Ukrainczyk, 1996
- [54] Hranilović, M., Damage Analysis and Rehabilitation procedures of reinforced Concrete Bridges in the Marine Environment, master's thesis, mentor: Dr. Jure Radić, co-mentor Dr. Velimir Ukrainczyk, 2007
- [55] Mavar, K., Influence of repair technology on the mortar adhesion, master's thesis, mentor: Dr. Marijan Skazlić, 2010
- [56] Borovina, B., Repair technology for concrete bridges, master's thesis, mentor: Dr. Zlatko Šavor, co-mentor: Dr. Marijan Skazlić, 2011
- [57] Ille, M., Development of the Surface Protection Model for the Improvement of the Durability of Concrete Structures, doctoral thesis, mentor: Dr. Jure Radić, co-mentor Dr. Marijan Skazlić, 2012
- [58] Serdar, M., Husnjak, D., Matic, D., Šajna, A., Carbonation Induced Changes in Durability Properties of Blended Cement Mortars, Proceedings of the 4th International Conference on Service Life Design for Infrastructures (SLD4), 27-30 August 2018, Delft, The Netherlands

FACTORS AFFECTING DURABILITY OF CONCRETE REPAIRS

Dunja Vla (1), Predrag L. Popovic (2)

(1) Senior Associate, Wiss, Janney, Elstner Associates Inc., USA

(2) Senior Principal and Vice President, Wiss, Janney, Elstner Associates Inc., USA

Abstract

Over the years our company has investigated, designed repairs and conducted construction observations during repairs of numerous concrete structures that had significant levels and a wide range of concrete deterioration due to various factors. Some of those included partial and full depth deterioration of reinforced concrete members due to corrosion of embedded reinforcing bars and pre-tensioned and post-tensioned cables, deterioration due to water infiltration through cracks, construction joints, deterioration due to freeze-thaw damage, fire damage and missing or insufficient thermal protection over hot pipes causing constant exposure of concrete to temperatures over 45°C, cracks in concrete due to settlement, and various other conditions. Some distress was due to premature failure of repairs completed in the past either due to material failure or the poor quality of repairs.

Regardless of the extent, cause and severity of concrete deterioration, type of the concrete structure and its use, exposure to various weather conditions, all repairs should meet high quality and durability criteria. Durability of concrete repairs is directly affected by the surface preparation, materials used for the repairs, compatibility of used materials with substrate, dimensional stability, curing procedures, protection methods, application of coatings and methods of construction.

Keywords: concrete, repairs, durability, factors, deterioration

1. INTRODUCTION

Repair work to address structural and durability concerns of structures is directly affected by design of repairs, construction procedures, and quality assurance. Over the years our company has been involved in the design of concrete repairs caused by a wide range of issues, as well as observations during the repair construction. The repaired structures included exposed building facades, parking garages, bridges, floors and beams inside the buildings, and some special structures like silos, tunnels and mine shafts. We also have had the opportunity to observe the performance of some of these repairs for more than 20 years. A second generation of repairs has been performed on some previously repaired structures.

We have learned from these experiences and have modified the specified repair procedures to improve durability of concrete repairs.

2. FACTORS THAT INFLUENCE DURABILITY OF REPAIRS

2.1 Extent and depth of repair openings

As the reinforcing bar embedded into the concrete corrodes, its corroded steel surface expands and creates large expansive forces which crack the concrete. The delamination and cracking of concrete is concentrated toward the surface of the concrete slab, beam, wall or column because the concrete cover is the smallest in that direction. By sounding the concrete surfaces with chain drag or tapping with a hammer, those delaminated areas on concrete surfaces can be easily detected. When hit with a hammer they create a hollow sound. Those areas are marked as unsound, and concrete at those areas is removed by chipping hammers. The perimeter of those areas should be sawcut at least 1 cm to 2 cm deep and squared off in order to provide more geometrically stable patches. Sawcutting also prevents growth of the repair areas by minimizing the spread of vibration during chipping through the concrete surface that could loosen the sound concrete around the patch. The recommended detail for the partial and full depth concrete repairs is shown in Figure 1.

Depending on the extent of corrosion at reinforcing bars, delamination can be present at the surface of the structural member requiring partial depth repairs, or affecting the full depth section of the member, which should be treated as a full depth repair. Most of the time only an outside portion of the bar perimeter is corroded and the remaining portion of the bar is firmly embedded in sound concrete.

Some of the new patches were not durable and they would start to delaminate after a few years. It was observed over the years that more durable concrete repairs also require removal of sound concrete beyond the unsound area, and around the reinforcing bars. It was found that repairs where the removal of sound concrete was extended 10 cm beyond the unsound concrete were more durable. New patch material, usually concrete, does not have any chlorides in it, while the existing sound concrete underneath the bars is generally saturated with chlorides. Typical concrete patches create an electrochemical environment surrounding the steel immediately adjacent to the patched area. This phenomenon is referred as the halo effect, ring effect, or incipient anode effect. As a result, the well-intended effort spent to repair chloride contaminated structures fixed the immediate problem; however it can result in further damage to adjacent areas within a relatively short time, one to five years.

Durability of repairs is also increased when removal of sound concrete around bars is extended approximately 2 cm below the reinforcing bar. This approach provides a better mechanical anchorage and bond of new repair material to substrate and existing reinforcing bars.

The removal of sound concrete beyond unsound areas and around the bars increases the cost of concrete repair but it is well worth it, and necessary for durable corrosion repair. Use of lighter chipping hammers for detailing around bars should be used in order to minimize the braking of sound concrete beyond reasonable boundaries.

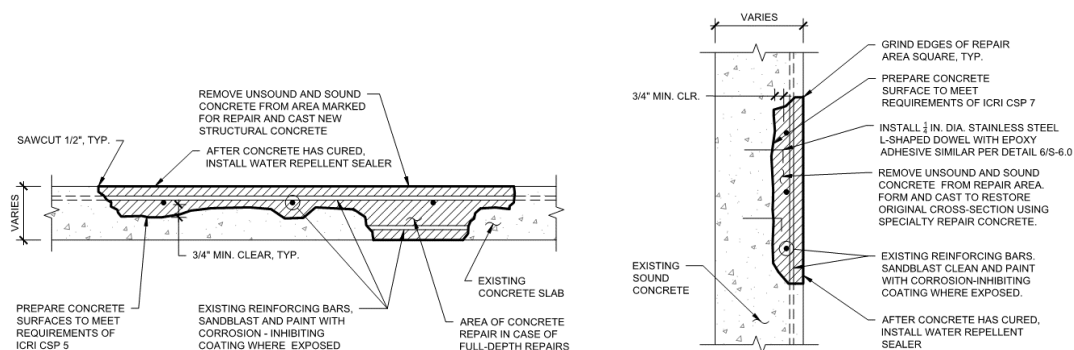


Figure 1: Repair detail for partial and full depth repairs

2.2 Surface preparation of concrete

More often sandblasting of the concrete surfaces is specified as a surface preparation method. At the same time this procedure is used to clean corrosion from the reinforcing bar surfaces. Sandblasting cleans and opens the pores in the concrete surfaces to provide excellent bond. Many tests have been performed to check the actual bond between the substrate concrete and the patch concrete (both in the field and in the laboratory) and have confirmed that this procedure results in more durable concrete repair.

Following the sandblasting, concrete surfaces should be blown with clean compressed air in order to remove debris and contaminants from the sandblasting and chipping procedures. Example of concrete surface preparation is shown in Figure 2.

We have seen concrete repair specifications which require that concrete surfaces be cleaned with high pressure water prior to the installation of the patch material. High water pressure is not defined and is usually understood by the contractor to mean water pressure that can be achieved with a garden hose. High water pressure should be specified as needed to properly clean concrete surfaces.



Figure 2: Surface preparation of concrete and coating of reinforcing bars at partial and full depth patches, and installation of new epoxy coated bars for bonded overlay

2.3 Cleaning and coating of reinforcing bars

After chipping of concrete around reinforcing bars, the bars are typically sandblasted to remove corrosion from the surfaces and coated with a protective coating. The intent is to

provide increased protection for the rebar in addition to the concrete cover. This is especially important in structures where reinforcing bars are close to the surface and the concrete cover cannot be increased during the installation of the new patch. Reinforcing bars should be coated with a corrosion inhibiting paint on all of their sides, as shown in Figure 2. Quite often it is observed that the bottom portions of the reinforcing bars are inadequately cleaned from the corrosion, and they are left unpainted.

If the existing reinforcing bars have lost 15 percent or more of their section due to corrosion, those bars generally should be replaced with new. To increase the durability of repairs, the replacement or supplemental bars should be shop epoxy-coated.

For vertical or overhead repairs, depending on the layout of the existing reinforcing bars, there might be a need to install supplemental dowels in order to provide a mechanical anchorage for the new patch to the substrate. Those dowels are usually stainless steel threaded rods set with an epoxy adhesive in drilled holes, as shown in Figure 3. The spacing and number of additional dowels is determined in the field based on the existing conditions. Care should be taken to provide an adequate concrete cover over newly installed additional reinforcing bars.

Any exposed post-tensioned tendons should be tested for designed tension. If there is a loss of tension, the tendons should be retightened, greased and any damage to their sheathing should be repaired.



Figure 3: Installed stainless steel rods in edge of slab

2.4 Concrete repair materials

Concrete materials used for repairs include ready mix concretes, proprietary concrete mixes and shotcrete. Regardless of the type of repair concrete mix to be used, it should be compatible with the concrete material of the original structure. The most durable repairs were achieved by using ready mix concrete cast in a formed repair opening. Ready mix concrete is created in concrete plants as per specifications, and delivered to the site in mixer trucks.

Proprietary concrete mixes are usually used for the smaller, formed repairs at horizontal and vertical surfaces, and for trowel-applied repairs on vertical and overhead surfaces. In most cases these mixes are used where access to deliver ready mix concrete is difficult. Proprietary bagged concrete mixes should be strictly mixed according to manufacturer's directions in order to achieve specified properties. Although very convenient for use, their cost is relatively high in comparison to ready mix concrete.

Shotcrete is used mostly for large quantities of overhead and vertical repairs in tunnels, parking garages and bridges. To achieve quality repairs, shotcrete should be applied by an experienced certified nozzleman.

Compression strength of concrete used for patching should try to match compression strength of the original concrete. Concrete mixes with higher cement contents are more prone to developing shrinkage cracks which can ultimately affect the durability of repairs.

2.5 Protecting concrete patches

To minimize the future intrusion of moisture and salts into the concrete, including concrete patches, we often specify protective waterproofing membranes, sealers or architectural coatings. They reduce moisture intrusion but some of them if applied early also prevent proper drying of concrete patches and surrounding surfaces. Most of the traffic membrane systems do not allow for any vapor transmission. After the slab is patched, the membrane is applied to the slab surfaces, usually after 28 days. The remaining moisture in the patch is sealed into the concrete and increases the corrosion activity along the edge of the patch. For the overall improved performance of the repaired slab, this trade-off may have to be accepted.

The thickness and number of applied coatings should be strictly followed according to manufacturer's recommendations in order to achieve proper protections of concrete surfaces.

Breathable water repellent sealers applied over the concrete surfaces act as a moisture repellent. They create a hydrophobic layer of concrete that shields against moisture penetration and deicing salts. They are usually invisible protection, not changing appearance of the concrete. Breathable sealers allow for moisture vapors to escape. Sealers usually penetrate the concrete surfaces up to 0.5 cm. They can be applied with sprayers or rollers. The penetration depth of sealers varies based on several factors as type of the sealer, porosity of the concrete, PH of the concrete, location of the application, time of the application.

Galvanic corrosion anodes are also used as a protection for concrete repairs. Their purpose is to mitigate a formation of electrochemical environment surrounding the steel immediately adjacent to the patched area, also known as halo effect. Example of installation of embedded galvanic anodes is shown in Figure 4.



Figure 4: Installation of galvanic corrosion anodes

2.6 Quality assurance

Quality assurance should be conducted on the construction site for each phase of repair work to ensure that each phase of repair process is properly performed. Quality assurance of delivered and used materials must be conducted to ensure that delivered and installed materials, including concrete mixes, match the specified ones for various applications. We have witnessed numerous times that contractors, for various reasons, use materials that differ from the ones that were submitted for approval.

Ready mix concrete should be checked on the site at a minimum for the water-cement ratio, concrete slump, and percentage of air entrainment especially for exterior applications where concrete will be exposed to freezing conditions, temperature of the concrete mix, and the time when the mixer truck had left the plant and duration of delivery time.

The weather forecast should be closely monitored prior to and during the placement of concrete in order to be able to handle challenges that might arise during extremely high or low air temperatures. In the instance of extreme temperatures, when the concrete pour cannot be postponed, the contractor should implement appropriate measures by providing ice, fans, A/C units, enclosures, blankets or heaters in order to prevent premature hardening or freezing of the concrete being placed. Any uncontrolled exposure of the concrete mix can negatively affect the quality of repairs.

After repairs have sufficiently cured they should be sounded. Any unsound repairs should be removed and reinstalled. At structural repairs, more complex structures such as retrofit of column capitals where new collars were installed, non-destructive testing methods should be used to determine the proper bond between existing and new concrete, and to locate the presence of any voids. Those voids are usually later injected with epoxy.

Quality monitoring during surface preparation, priming and installation of waterproofing membrane or architectural coating to provide a protection for concrete surfaces should be conducted during their entire application. The thickness of each coat should be regularly measured during their applications, and curing times in between coats followed as per manufacturer's applications in order to insure the quality of the installed system. Correctly installed protection coating will increase durability of concrete repairs.

2.7 Evaluation of past repairs

Over the years our company had an opportunity to reinspect the past repairs and to observe their performance. Examples described below illustrate examples of evaluation of past repairs.

Extensive concrete repairs were performed on a bridge in Argonne National Laboratory. Figure 5 is showing properly sawcut openings of the concrete deck/curb repairs at the expansion joint, and surface preparation of the concrete prior to painting of the reinforcing bars with corrosion inhibiting coating. The follow up inspection of the bridge was conducted 10 years later. During inspection, new deteriorated concrete due to corrosion of embedded reinforcing bars was observed at the original concrete next to the patch, but the patch was in good condition, as also shown in Figure 5.

On another project, long term effectiveness of use of galvanic corrosion anodes was documented on several buildings in Hawaii exposed to severe marine atmospheric environment. Slab edge balconies repairs were monitored over the period of 10 years. The repairs were completed in 2002 and reinspected in 2012. Approximately 900 m of repairs were inspected. After removal of unsound concrete, longitudinal bars were replaced with new. The transverse bars were cleaned with wire brush. Galvanic anodes were placed at 60 cm on center each way

through in repair areas. During 2012 inspection no evidence of cracking, spalling or delamination within the repaired areas or immediately adjacent to the repairs were found. Only typical shrinkage cracks were observed. The precise distance protected by each galvanic anode is unknown. Some research suggests that anode at 60 cm spacing around the perimeter of a repair without supplemental protection will effectively cathodically protect the radius of a repair to a roughly 30 cm upon placement, decreasing 10 to 15 cm after a year.



Figure 5: View of patches performed at Argonne bridge. Surface preparation of the concrete to the left, and condition of those repairs 10 years after to the right

US Bureau of Reclamation Test M82 was designed to measure how various repair methods affect the corrosion rate and durability of concrete structures. Several different repair methods evaluated included control slab (conventional concrete repair), conventional concrete repair with epoxy coated rebar in the repair, conventional concrete repair with one alkali-activated Galvashield Anode in the repair; and conventional concrete repair with 3 coats of 40% solids silane sealer applied over the entire slab after the repairs were completed. Test results are shown in Figure 6. The test did not include sample with installed waterproofing membrane.

The test has shown that implementation of all repair methods described above will prolong the durability of concrete repairs. Use of galvanic anodes has reduced the total corrosion the most.

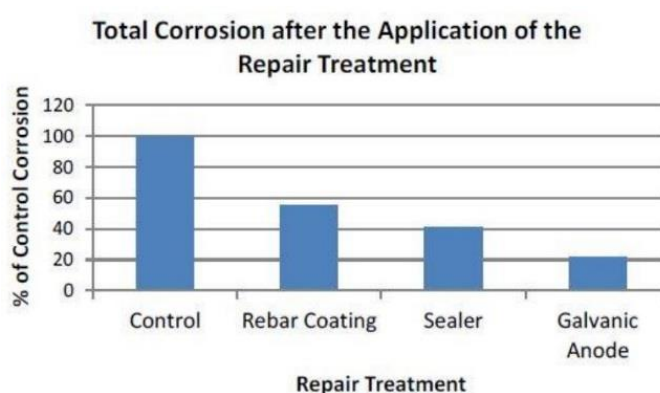


Figure 6: USBR M82 comparison of total corrosion for various repair methods

3. SUMMARY

The principal factors and procedures used to increase the quality of concrete repairs were discussed. To achieve durable concrete repairs, we recommend removal of concrete around exposed reinforcing bars and extending the repair openings into the sound concrete, sandblast cleaning of concrete surfaces and reinforcing bars, painting of exposed bars with corrosion inhibiting paint and/or installation of galvanic corrosion protection anodes. The durability of concrete repairs is also increased by using proper concrete repair materials based on the size, shape and location of the application, installation of a protective coating over completed repairs, as well as conducting effective quality assurance during construction.

REFERENCES

- [1] Douglas F. Burke, 'Naval Facilities Engineering Command, Site Specific Report SSR-NAVFAC-EXWC-CI-1317, April 2013, Performance of Galvanic Anodes in the Repair of Reinforced Concrete Due to Corrosion of Steel'
- [2] Vector Corrosion Technologies, 'Summary of Galvashield® Anode Evaluation'

MISTAKES IN DESIGN AND BUILDING OF CONCRETE STRUCTURES – PRACTICE EXAMPLES

Jure Galić (1), Željko Lebo (2))

(1) Zagreb University of applied sciences, Croatia

(2) Zagreb University of applied sciences, Croatia

Abstract

A large number of reinforced concrete structures in early stage of life show symptoms of deterioration which are consequences of mistakes in design documentation, or based on poor execution. Problems of structure durability and quality insurance by proper recognition of the environmental conditions in which the structure is placed in are often treated with lack of attention and mostly craftsmanship, with insufficient data in design documentation. It is especially visible in problems of design and thickness definition for coating layer, curing conditions and maintenance. In the paper are given some of typical damages caused by wrong presumed environmental conditions, incorrect material selection for structure execution or insufficiently elaborated quality requirements in technical description, bill of quantities etc. By that mean, after analyzing location conditions and possible harmful actions on the observed structure, possible repair techniques are shown due to minimize costs and optimize results required for usage as it is designed. In some cases mistakes by improper environmental conditions assumptions are visible after a certain period of time, when structure is in use, which causes more problems in repairment process, and, in addition, larger expenses and inability of structure usage due to its prior design.

Keywords: design, maintenance, flaws

1. INTRODUCTION

There are numerous factors that influence the final state of executed structures. Flaws that are not visible in present moment cause unsatisfactory condition, and therefore additional measures and costs for maintenance and repair works. Final condition of the structure is connected with mistakes in design and/or construction process which are directly linked to the participants of the construction process. Common mistakes and failures are shown in the form of cracks, colour and texture changes in building materials, or structural damages very soon after the building process is finished.

because there is continuous water leakage inside the structure, and therefore continuous deterioration process of the built-in materials and uselessness of interior space.

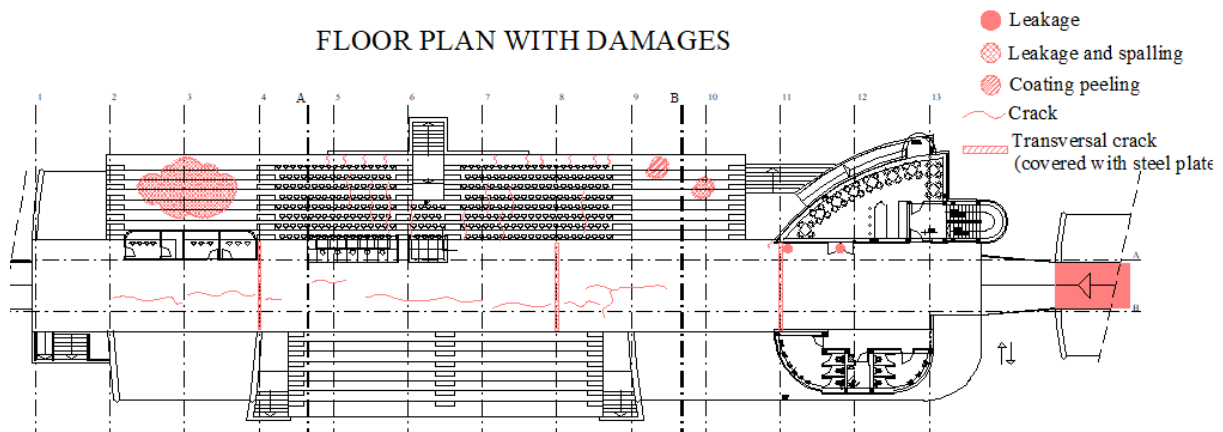


Figure 3: Floor plan with flaws scheme

Although it is common in practice craft that structure length without expansion joints is usually limited to 35 or max. 40 m structure was built in total length of 78,60 m without any which caused structure cracking (self – disjoints) on places with cross section changes e.g. where stress concentration is maximal. Two cracks approximately 1 cm wide, with depth equal to the cross-section depth and all-over transversal span were detected.



Figure 4: Unsatisfactory crack repair (upper and lower side of the structure)

Stages of execution process were not properly considered, respectively to the materials applied. Sufficient water permeability of the concrete should be achieved due to afterward canopy installation. Demanded property should be achieved within concrete properties or with adequate surface coating. Existing surface coating is detached and peeled of the concrete surface (probably caused by improper appliance process). Locally, cracks and spallings of the coating are visible, indicating incompatible applied materials and/or improper building process.

Visual inspection showed that multiple damage types are present, mostly caused by water leakage from upper (outside) surface to the interior (lower side) through the cracks formed in

the self – disjoining process. Also, drainage of the upper structure surface is insufficient because is it is designed for the conditions of Phase II e.g. with canopy set.



Figure 5: Surface coating deterioration (spalling, peeling...)



Figure 6: Typical cracks in upper surface

In almost all interior surfaces signs of leakage and leaching are visible as well as lime sediments. Remanent water from the upper surface is placed inside cracks and with cyclic freezing-thawing process is devastating and degrading impact on surrounding concrete in the moist zone. Leakage and wet spots inside the structure are visible after every heavy rain.



Figure 7: Leakage and lime sediments

For quality and durable solution for all flaws and damages shown in structural elements of tribunes it is necessary to firstly remove present insufficient repair attempts (e.g. steel plates over cracks, additional concrete slabs without function, insufficient surface coating...). After preparation works all cracks must be repaired with epoxy based sludge or mortar, and new impermeable surface coating must be applied on all upper visible surfaces. Also, water insulation must be placed in all perimeter RC walls. Solutions for large transversal cracks and insulation of the foundation deck are processed in individual project and will not be presented in this article. It is important to notice that newly executed structure is more rigid and heavier than original. These facts probably had major impact on damages because ground settling deformations are bigger and structure is cracking throughout respectively. One of the major cause of cracks is probably the fact that there were no expansion joints for length of 78,60 m what is too long for single concrete element.

Reinforced concrete floor structure of the chicken fattening hall is situated in the area of north Croatia. Floor dimensions of the structure are $22,50 \times 168,00$ m and bearing structure is steel frame. Foundation is executed as footings with dimensions 120/200 cm and 50 cm thick all connected with overhead beams. Floor slab of the hall is 15 cm thick and was executed joint free according to the founding structure. One of the floor dilatations is executed continuously in length of 82,00 m without any splitting.

Figure 8: Cross section of the structure

Design documentation states that quartz sand sprinkling on the upper surface coating gives sufficient chemically resistant industrial floor, which is absolutely incorrect. Quartz sand sprinkling gives better mechanical properties (strength, wearing resistance). Comparison of the broken floor pieces at the time of the visual inspection shows significant variations in quartz sand amount what indicates low grade execution. During the usage period of two years in all surfaces concrete surface has changed colour, what indicates chemical reaction between concrete and poultry excrements.

Some parts have significant peeling and spalling, therefore further rapid deterioration is expected.



Figure 9: Surface coating spalling

During the visual inspection larger parts of the concrete floor structure show surface “peeling” signs indicating that concrete surface is chemically attacked and fast degradation is soon expected. Local repairs of the surface were made but with no success.



Figure 10: Surface coating spalling

Also, structural deformations of the concrete floor slab caused by shrinkage process were not taken into the account in the proper way. This caused constant increment of the connection joints between concrete floor slab and surrounding beams. In some parts gap width is up to 40 mm resulting in water and poultry excrements penetration and precipitation and rapid deterioration process of the concrete and reinforcement corrosion.



Figure 11: Joint gap at slab-beam connection

Applied permanently elastic sealing has lost its function, because it is not applicable for gaps bigger than 5 mm. This size gaps should be treated as expansion joints e.g. filled with chemically resistant spongy material or gasket rope and then filled with sealing. All contact surfaces have joint gaps larger than 20 mm indicating that repairment is needed all around in hall.

Considering all mentioned flaws for quality repairment the following is needed:

- Existing surface coating in the whole hall must be removed and new one, chemically resistant coating must be applied. Also working quality regarding to the quartz sand quantity must be provided.
- Existing sealing in all contact surfaces (floor/beam) must be removed, and new sealing must be carried out. Best results are expected for gasket rope filling and afterward filling with permanently elastic sealing with sufficient extensibility and chemical resistance.

4. CONCLUSION

Although building process for all structures is financially demanding, some of the works seemingly simple are executed with lack of care and/or are insufficiently described in technical documentation just with simple sketch and without proper calculation. Mistakes developed in design or execution process are very soon visible and cause significant maintenance expenses, as well as impossibility of structure usage according to the designed purpose, and financial loss for Investor. Most common mistakes in design process are improper assumptions in design and calculation, unsuitable computation model, material selection unsuitable for real conditions and environment of the structure. Most common flaws in building process are carelessness, implementation of poor-quality materials, incorrect implantation, insufficient qualification of workers etc... With a view to reduce mistake possibility to minimum it is necessary to implement project control led by independent qualified personnel. Those persons, that were not included in design process, should have

large knowledge in design process principles as well as large experience in materials technology.

REFERENCES

- [1] TPBK, »Tehnički propis za betonske konstrukcije, NN br. 139/09, 14/10 i 125/10«.
- [2] Galić, J., 2016, “Elaborat o istražnim radovima i projekt sanacije SRP Trate”, INSTITUT IGH d.d., Zagreb, HRVATSKA.
- [3] Galić, J., 2018, “Nalaz i Mišljenje o nedostacima izvedenih građevinskih radova na Farmi za uzgoj peradi”, TRGOVAČKI SUD U ZAGREBU, Zagreb, HRVATSKA.
- [4] Lozančić, S., Klečina, B.M., Penava, D., Baloković, M., ‘Utjecaj projektiranja i izvedbe na trajnost i održavanje objekta’, in ‘Organization and maintenance technology’ Proceedings of an International Conference, Osijek, April, 2018 (Fakultet elektrotehnike i računarstva, Osijek, 2018) 177-183.

INVESTIGATION WORKS AND STRUCTURE CONDITION OF SEWERAGE PIPE UNDER HEINZELOVA STREET IN CITY OF ZAGREB

Jure Galić (1), Ivana Banjad Pečur (2)

(1) Zagreb University of Applied Sciences, Croatia

(2) Faculty of Civil Engineering, University of Zagreb, Croatia

Abstract

Building of the sewerage system for City of Zagreb begun in 1892 and it run parallel with city development, but after WW II it stagnated and rapidly retarded compared to the city rapid development. Nowadays the sewerage system is consisted of two separated subsystems, both connected to the Central water treatment plant for the City of Zagreb (CUPOVZ), which are city areas on the left bank of river Sava with north Zagreb and west Sesvete as one part and city areas on the right bank of river Sava with New Zagreb as the other part. In the documentation design process for reconstruction and development of the sewerage system investigation works and valuation of the existing structure for the sewerage pipe under the Heinzelova Street was carried out. The City of Zagreb plans to extend the tramway network through Heinzelova Street over the sewerage pipe and it is necessary to determine the conditions of the sewerage pipe and its resistant for additional load. Also, as the basic demand is continuity of operation for the pipe all works were carried out in extremely hard environment conditions, as to be shown. The results of both non-destructive and destructive “in situ” and laboratory testing will be presented as they represent good groundwork for the evaluation and selection of the proper retrofitting technology due to the importance and uniqueness of the existing structure.

Keywords: sewerage pipe, “in situ” testing, NDT, deterioration process

1. INTRODUCTION

Existing sewerage under Heinzelova street is placed from the Kvaternik square at north side to the Slavenska avenue at south side. It is consisted of two separate concrete pipes with varying cross section. West pipe is mainly placed bellow the green belt with cross section profile 260/220 cm, and 300/230 cm. Period of construction is placed round year 1920. East pipe is positioned under the nowadays traffic lines of Heinzelova street with cross sections

204/170 cm and 264/250 cm. Period of construction was from 1920 to 1949. Total length of both pipes that were examined is $2.536 + 2.371 = 4.907$ m. Cross section of the east pipe is shown in Figure 1. On the one part of the west pipe, which is placed bellow railroad tracks cross section is rectangular shaped, and the rest of the pipes cross sections are standard shaped as shown in project documentation.

Beside already small clear height, extra difficulties for work execution were due to sludge layer settled at the bottom of the pipe, causing additional clear height shrinkage.

1.1 Cross sections

Both pipes were build without any reinforcement based on the principles of the pressure ring cross section design.

One part of the western pipe that goes under the railroad tracks has different cross section, which is altered from circular to rectangular cross section. All other cross sections are consisted to cross sections presented in technical documentation.

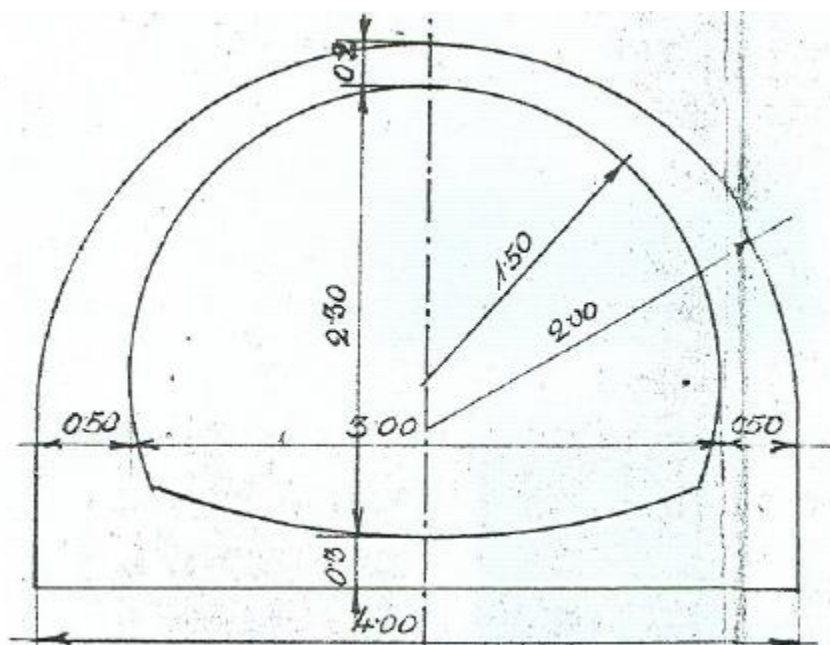


Figure 1: Cross section of the east pipe (264/250 cm), as shown in original drawings (SCAN).

2. INVESTIGATION WORK

All investigation works and visual inspection were executed during night time period because it was not possible to close road tracks and open the access shafts placed on them during the daytime and “rush our” because it is one of the major traffic routes in City of Zagreb. Because of this reasons ventilation of was not possible so the total working time in one shift was significantly reduced.



Figure 2: Preparation for work

Personnel members during the work execution were continuously exposed to the harmful effects of biological agents, unfavourable microclimate conditions and possible gas concentration of H_2S (hydrogen sulphide), CH_4 (methane), CO (carbon monoxide) and CO_2 (carbon dioxide).

Protection equipment used was consisted of rubber overall suits (first layer protection) and cotton one-time overall suits (second layer protection). Disinfection equipment was placed nearby exit shafts. For respiratory protection respirator masks and gas detectors (for H_2S , CH_4 , CO and CO_2) were used.



Figure 3: Work conditions inside the sewerage pipe

Fully viewed results of investigation works together with conclusions based on the visual inspection enable understanding of the deterioration process in these specific conditions and production of rational and successful repair design.

2.1 Visual inspection

Defects like cracks in the vault crown (longitudinal), local concrete spalling as a result of the abrasive action of water and solid particles, and visible aggregate grains due to washing out of the bonding material (cement stone). Because of the aggressive environment spalling is noticed through all length of both pipes. Cracks are mostly placed at the vault crown and at the connection of the arch and the bottom of the pipe due to the execution process.



Figure 4: Deterioration of the concrete cladding

Geometry imperfections were noticed throughout cladding for both pipes. Bigger holes in the concrete body are result of the washing out of the cement stone speeded up with abrasive influence of waste water and hard particles in it. On the entire length signs of water leakage and leaching are visible all over the cross section on the both pipes.

Sludge depth was continuously around 30 cm, and hazardous gas concentration was developed or increased because sludge agitation while walking. Especially hazardous was increase of CO and CO₂ concentration because gas-masks do not provide adequate protection against it so airing out through access shafts was the only solution.



Figure 5: Sludge depth measurement

It is interesting to point out that on the north part of the pipe with smaller cross section (204/170 cm) bigger sludge depth was noticed together with higher gas concentration (CO and flammable gasses). It is not a common fact because smaller profile results with bigger flow speed and consequently smaller sludge depth. It is probably correlated with execution imperfections and obstacles in the cladding base that were covered with sludge and not visible.

3. TESTING RESULTS AND ANALISYS

Although results of detailed visual inspection show that recognised damages and deteriorations are of such level that could potentially reduce structural safety and predicted remaining life period of the structure it is of most importance to carry out in-situ and laboratory testings of structure material due to proper repair technique selection. Testing results and evaluation are shown below.

3.1 Compressive strength

Concrete compressive strength was determined od drilled cores (Φ 100 mm) according to HRN EN 13791 and sampling and samples preparation according to HRN EN 12504-1:2009. Concrete density is uniform and characteristic for concretes that are made and casted “in situ”. Results for concrete density are 2.250 kg/m³ in average. Cores drilled were divided into groups according to geometry type and year of execution of the structure and then analisys was conducted according to the approach A or B of the cited standard for assessment of in-situ compressive strength. Our assumption was that concrete strength is falling down with longer exposure to sulphate agression, due to cement stone melting and larger pores and holes amount respectively. Testing results and calculation results are shown in the table below.

Table 1: Concrete strength of west pipe (Section 300/230 cm) – built 1920.

Sample	Concrete Strength (MPa)	Sample	Concrete Strength (MPa)	Sample	Concrete Strength (MPa)
V1	8,7	1	23,2	V6/D	21,1
V2	25,4	2	15,4	V6/D	4,5
V2	20,9	3	40,1	V1/1	13,6
V3	18,0	3	27,2	V1/3	16,6
V1/2	12,8	4	11,0	V2/3	6,9
V1/2	21,9	4	6,9	V3/3	12,0
V2/2	19,3	5	12,7	V4/3	5,6
V2/2	22,0	5	8,7	V5/3	6,3
V3/2	18,1	6	26,9	V3/4	15,5
V3/2	24,4	V1/4	21,3	V4/4	12,1
V4/D	18,2	V1/4	15,1	V4/V	12,1
V4/D	16,9	V2/4	13,2	V5/4	10,3
V5/D	15,7	V2/4	15,1	V5/4	8,4
V5/D	12,8	V3/4	20,0	V6/4	28,2

Mean in situ strength of n samples $f_{m(n),is}$: 16,82 MPa

The estimated in-situ characteristic strength of the test region is the lower value of (approach A):

$$f_{ck,is} = f_{m(n),is} - k_s \times s = 16,82 - 1,48 \times 7,95 = 5,05 \text{ MPa} \quad (1)$$

or

$$f_{ck,is} = f_{is, \text{lowest}} + 4 = 4,5 + 4 = 9,5 \text{ MPa}$$

($k_2 = 1,48$; s = standard deviation of test results or $2,0 \text{ N/mm}^2$ – whichever is higher value)

Calculated compressive strength is lower than demanded for class C8/10 which is the lowest concrete strength class according to EN 206-1. Concrete strength corresponds to MB100, according to old standards (ex JUS).

Table 2: Concrete strength of east pipe (Section 264/250 cm) – built 1940.

Sample	Concrete Strength (MPa)	Sample	Concrete Strength (MPa)	Sample	Concrete Strength (MPa)
V1/5	16,0	V7/4	14,0	V4/8	22,3
V1/5	20,7	V7/5	18,3	V5/8	14,9
V2/5	25,8	V7/5	20,4	V5/8	10,6
V2/5	28,2	V7/6	42,2	V6/8	17,5
V3/5	22,5	V1/8	25,5	V6/8	12,6
V3/5	31,0	V1/8	34,4	V7/1	21,3
V4/5	24,3	V2/8	14,4	V7/1	19,8
V5/5	21,9	V2/8	21,8	V7/2	14,2
V5/5	23,3	V3/8	26,3	V7/3	11,6
V6/5	20,8	V3/8	28,8	V7/3	23,6
V6/5	30,9	V4/8	27,5	V7/4	15,8

Mean in situ strength of n samples $f_{m(n),is}$: 21,90 MPa

The estimated in-situ characteristic strength of the test region is the lower value of (approach A):

$$f_{ck,is} = f_{m(n),is} - k_s \times s = 21,90 - 1,48 \times 7,00 = 11,54 \text{ MPa} \quad (1)$$

or

$$f_{ck,is} = f_{is, \text{lowest}} + 4 = 10,6 + 4 = 14,6 \text{ MPa}$$

($k_2 = 1,48$; s = standard deviation of test results or $2,0 \text{ N/mm}^2$ – whichever is higher value)

Calculated compressive strength confirms class C8/10 which is the lowest concrete strength class according to EN 206-1. Concrete strength corresponds to MB100, according to old standards (ex JUS).

Table 3: Concrete strength of east pipe (Section 204/170 cm) – built 19490.

Sample	V1/9	V2/9	V3/9	V4/9	V5/9	V6/9
Concrete Strength (MPa)	15,0	18,3	20,9	9,3	15,2	21,2

Mean in situ strength of n samples $f_{m(n),is}$: 16,7 MPa

The estimated in-situ characteristic strength of the test region is the lower value of (approach B):

$$f_{ck,is} = f_{m(n),is} - k \quad (k=7 \text{ for number of samples from 3 to 6}) = 16,7 - 7 = (2) \\ 9,9 \text{ MPa}$$

or

$$f_{ck,is} = f_{is, \text{ lowest}} + 4 = 9,3 + 4 = 13,3 \text{ MPa}$$

Calculated compressive strength confirms class C12/15 which is the lowest concrete strength class according to EN 206-1. Concrete strength corresponds to MB150, according to old standards (ex JUS).

It is important to point out that the compressive strength testing was not applied on the surface layer which is heavily damaged, what additionally contributes to the objectivity of the results. Surface layer was used for chemical analysis of concrete and determination of capillary absorbing and gas permeability.

3.2 Carbonization depth, chloride and sulphate ion content

Carbonization depth was measured by spraying phenolphthalein 1% solution on cores drilled out of the concrete according to HRN EN 14630. Carbonisation depth varies from 0 up to the 50 mm.

Maximum of chloride ions content allowed expressed as function of concrete mass is 0,06% according to HRN EN 206-1 – Table 10. In all tested samples chloride ion content was smaller than critical value. Chloride ions content is under the critical value, although the roads above sewerage pipes are salted for the de-icing purpose. Chloride ions content has lower influence on structure damaging because pipe cladding is built without reinforcement.

Maximum of sulphate ions content allowed (as SO_3) is expressed as function of cement mass is 3,5% according to HRN EN 196-2 and TPBK, Appendix 3. Expressed as a function of concrete mass for assumed cement quantity of 250 kg/m^3 critical value is 0,35%. Sulphate ion content varies from 0,1% up to 0,93% what shows that concrete is continuously exposed to the deterioration process and aggressive sulphur corrosion which additionally weakens concrete structure.

3.3 Rebound hammer

Rebound hammer testing of the structure and determination of concrete compressive strength was conducted according to HRN EN 12504-2:2012. Total number of testing places was 143 for both pipes (west and east). Due to limited space single results will not be presented but only the determination methodology.

Mean value of estimated compressive strength for west pipe (cross section 300/230 totally built in 1920.) is 8,9 MPa which is very similar to the results determined with drilled cores.

Mean value of estimated compressive strength for east pipe (cross section 264/250 - built in 1940.) is 21,34 MPa, but with standard deviation of 1,60 MPa.

Mean value of estimated compressive strength for east pipe (cross section 204/170 - built in 1949.) is 9,8 MPa which is very similar to the results determined with drilled cores.

In general, concrete strength is uniform in all parts of the structure and shows significant correlation with concrete strength determined on drilled cores. Some of the data do show variance from average but it is probably caused by impact on aggregate grains as cement mortar is dissolved by acid environment influence.

3.4 Water and gas permeability

Water (after 25 hours greater than 0,6 and up to 1,2 kg/m²/h^{1/2}) and gas (greater than $>10^{-14}$) permeability point to the damaged and weakened concrete structure. Some samples couldn't be tested at all due to numerous holes and pores. All testing results refer to the very porous and hollowed concrete with non uniform structure. In all tested specimens gas permeability results were greater than 10^{-12} what is border value for poor quality concrete. It is necessary to point out that some of specimens could not be tested because of large amount of holes and pores. This also correlates with compressive strength results because large amount of pores significantly reduces compressive strength.

4. CONCLUSIONS

It is expected further concrete structure deterioration especially due to cement stone melting caused by acid attack. Influence of acid actions on concrete structure is melting of concrete stone, weakening of physical and mechanical characteristics of the concrete cladding. Acid attacks which melt down calcium compounds out of the hardened cement matrix are mostly caused by acids, vegetable and animal fats, dissolved salts and oils which are all present in very high concentrations. Concrete structure deterioration is usually driven very slow as it can be seen on this specific structure.

Inclusively, general condition of the sewerage pipe structure satisfies current purpose and has no indisposed bearing capacity or stability but it is to be expected further structure deterioration. For undisturbed usage in the present mode repair works are necessary to preserve the existing condition as well to lengthen the lifetime expectancy of the existing structure.

REFERENCES

- [1] TPBK, »Tehnički propis za betonske konstrukcije, NN br. 139/09, 14/10 i 125/10«.
- [2] HRN EN 1992-1-1:2008, Eurokod 2: Projektiranje betonskih konstrukcija – Dio 1.1: Opća pravila i pravila za zgrade.
- [3] HRN ISO 15686-2:2002, Zgrade i druge građevine -- Planiranje vijeka uporabe -- 2. dio: Postupci predviđanja vijeka uporabe.
- [4] HRN EN 1766:2001 Proizvodi i sustavi za zaštitu i popravak betonskih konstrukcija - Metode ispitivanja - Referentni betoni za ispitivanje.
- [5] Galić, J., 2016, "Elaborat o istražnim radovima i ocjena postojećeg stanja kolektora ispod Heinzlove ulice", INSTITUT IGH d.d., Zagreb, HRVATSKA.

PRELIMINARY ANALYSIS OF DURABILITY RELATED FIELD INSPECTION OF REINFORCED CONCRETE BRIDGE

Dita Vořechovská (1), Petr Konečný (2), Martina Šomodíková (1), Pavla Rovnaníková (1)

(1) Brno University of Technology, Faculty of Civil Engineering, Brno, Czech Republic

(2) VSB – Technical University of Ostrava, Faculty of Civil Engineering, Ostrava-Poruba, Czech Republic

Abstract

The aim of this work is to summarize and analyze the data from in-situ measurements performed on reinforced concrete bridge 55I-026a built in 1976, which is a part of the road network in the Czech Republic. The explorations were performed in order to evaluate the ability of the concrete to protect steel reinforcement from corrosion. To quantify this, the pH and the amount of water-soluble chlorides were evaluated on concrete samples drilled from the bridge at the age of 38 years. Based on these parameters, the ratio between the concentrations of Cl^- and OH^- , which indicates the ability of concrete to protect reinforcement, was calculated. Consecutively, all the data were statistically summarized and the correlations among them were found.

This study also aims to pick up experiences for the new experimental measurements planned on the actual reinforced concrete bridges in our country.

The analysis of the data from bridges under service is intended to help in the development and enhancement of the methodology for the assessment of durability of reinforced concrete structures.

Keywords: reinforced concrete bridge, corrosion, chloride concentration, pH, in-situ data

1. INTRODUCTION

Steel embedded in a reinforced concrete structural member exposed to the combined effect of carbonation, chlorides ingress and mechanical load is prone to corrosion that threatens its durability and reduces the service life and bearing capacity. Typical constructions are the bridges in the Central European region where the aggressive substance comes from winter de-icing.

The current design of typical structural elements with respect to exposure conditions is executed by the deemed-to-satisfy rules utilizing EN 1992-1 and EN 206. This approach is limited mainly to concrete cover and water/cement ratio with vague assumption of an indicative lifespan, and so without a possibility to control the relevant reliability level and structure design for a specified/required service life.

Currently, the discussion and benchmarking on durability calculations based on these deemed-to-satisfy rules have been undertaken by the European technical committees and fib Commissions. It is intended to replace them with a performance-based design approach (PBD) in future standards [1–3].

An important part of preparation for PBD is analysis of the durability of existing structures under service in order to improve the authenticity of available numerical tools. Some of them are described e.g. in [4–11].

This paper is a part of research aimed at the improvement of the design and prediction methodology for the service life of reinforced concrete structures exposed to de-icing agents in Central Europe. The data from regular inspections of highway bridges in the Czech Republic are analysed herein with respect to the durability aspects and modelling. The chloride concentration profile and pH in various depths of concrete cover are of special interest here. These parameters are important for numerical modelling of corrosion initiation time. However, the relationship among chlorides concentration, pH and time to corrosion initiation is usually neglected even though it has a significant effect [10]. Thus, it is important to evaluate if available data allows for the enhancement of available models with e.g. surface chloride concentration and/or typical diffusion coefficient. The analysis of the bridge No. 55I-026a [12] is primarily discussed below.

2. IN-SITU DATA AND LABORATORY ANALYSIS – BRIEF OVERVIEW

The subject of inspection is the highway bridge No. 55I-026a. It is an overpass of local road No. 36745 in the northern part of the town of Otrokovice. The bridge was built in 1976 and the samples were extracted in the form of drilled cores at the age of 38 years.

For the chemical analysis of concrete, the different locations on the bridge were chosen. They are marked on Figs. 1 and 2 and numbered from 1 to 12. In each location, the samples were taken from three different depths of 0–10, 10–20 and 20–30 mm from the concrete surface. Subsequently, the value of pH and the amount of water-soluble chlorides were measured in water leaches in laboratory [12]. Based on these parameters, the ratio between the concentrations of Cl^- and OH^- that indicates the ability of concrete to protect reinforcement was calculated. In the other words, the higher the ratio is, the higher is the potential risk of corrosion initiation and propagation. As a critical value $c(\text{Cl}^-)/c(\text{OH}^-) = 0.6$ is taken into account [13].

3. SUMMARY OF RESULTS

The values of pH and Cl^- and ratios $c(\text{Cl}^-)/c(\text{OH}^-)$ are graphically depicted in Fig. 3. The water-soluble chlorides Cl^- were measured as mass percentage of concrete. Each parameter was assessed at 12 locations on the bridge and three different depths of concrete. Furthermore, the means and standard deviations were calculated. It is visible from the graphs that there is no significant dependence between the observed parameter and the depth of the concrete. Also,

there is a relatively large scatter for all the measured parameters which is due to variety of locations.

To predict the ability of concrete to protect the reinforcement from corrosion the numerical models are often utilized [4, 7, 8, 9, 11]. Those estimations are usually based on the calculation of so-called initiation time that is estimated either based on critical degree of carbonation or critical concentration of chlorides around the reinforcement. There are several models assuming both the effect of carbonation as well as amount of chlorides. Many existing analytical models are implemented in a probabilistic software FReET-D [4, 5].

For the real structures, the ability of concrete to protect the reinforcement from corrosion is quantified by pH value that indicates the degree of carbonation, mainly from the ratio $c(\text{Cl}^-)/c(\text{OH}^-)$ that connects the effect of both carbonation and chlorides concentration. Note, that the values higher than 0.6 indicate assumption of reinforcement corrosion [13].

To quantify the dependence among the observed parameters, the Spearman correlation was calculated and results are given in Table 1. Almost no correlation of 0.009 is between pH and Cl^- . A very small correlation of 0.55 is between $c(\text{Cl}^-)/c(\text{OH}^-)$ and Cl^- . Correlation of -0.718 for pH and $c(\text{Cl}^-)/c(\text{OH}^-)$ indicates closer connection between these parameters. Thus, it follows from the found correlations that the degree of carbonation and chloride concentration in concrete are independent variables and should not be assumed separately in numerical modelling. In the other words the effect of both should be taken into account.

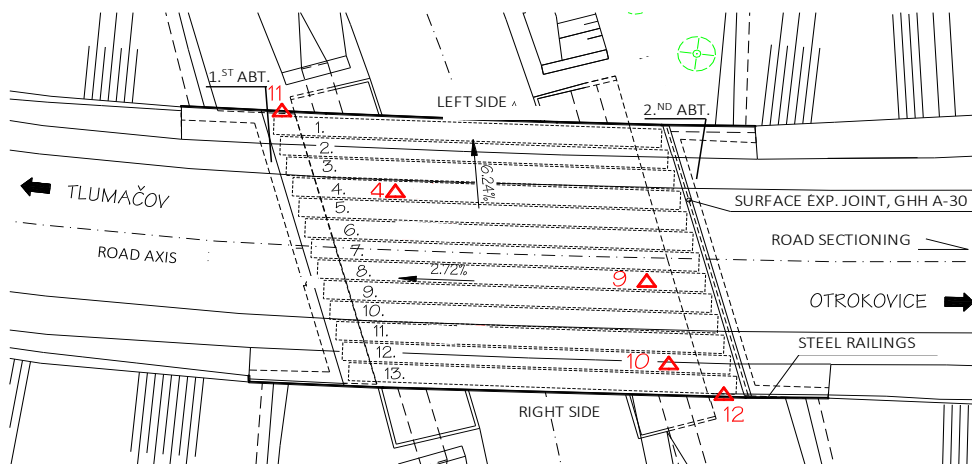


Figure 1: Bridge 55I-026a – Layout and sampling [12].

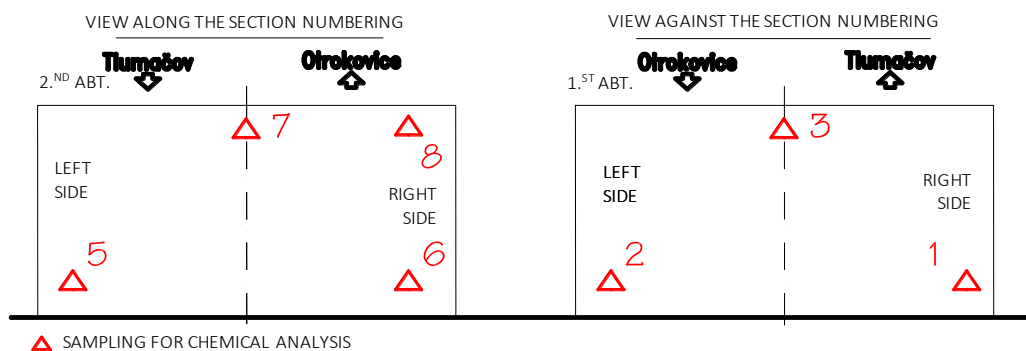


Figure 2: Bridge 55I-026a – Abutments view with indicated locations of sample taking [12].

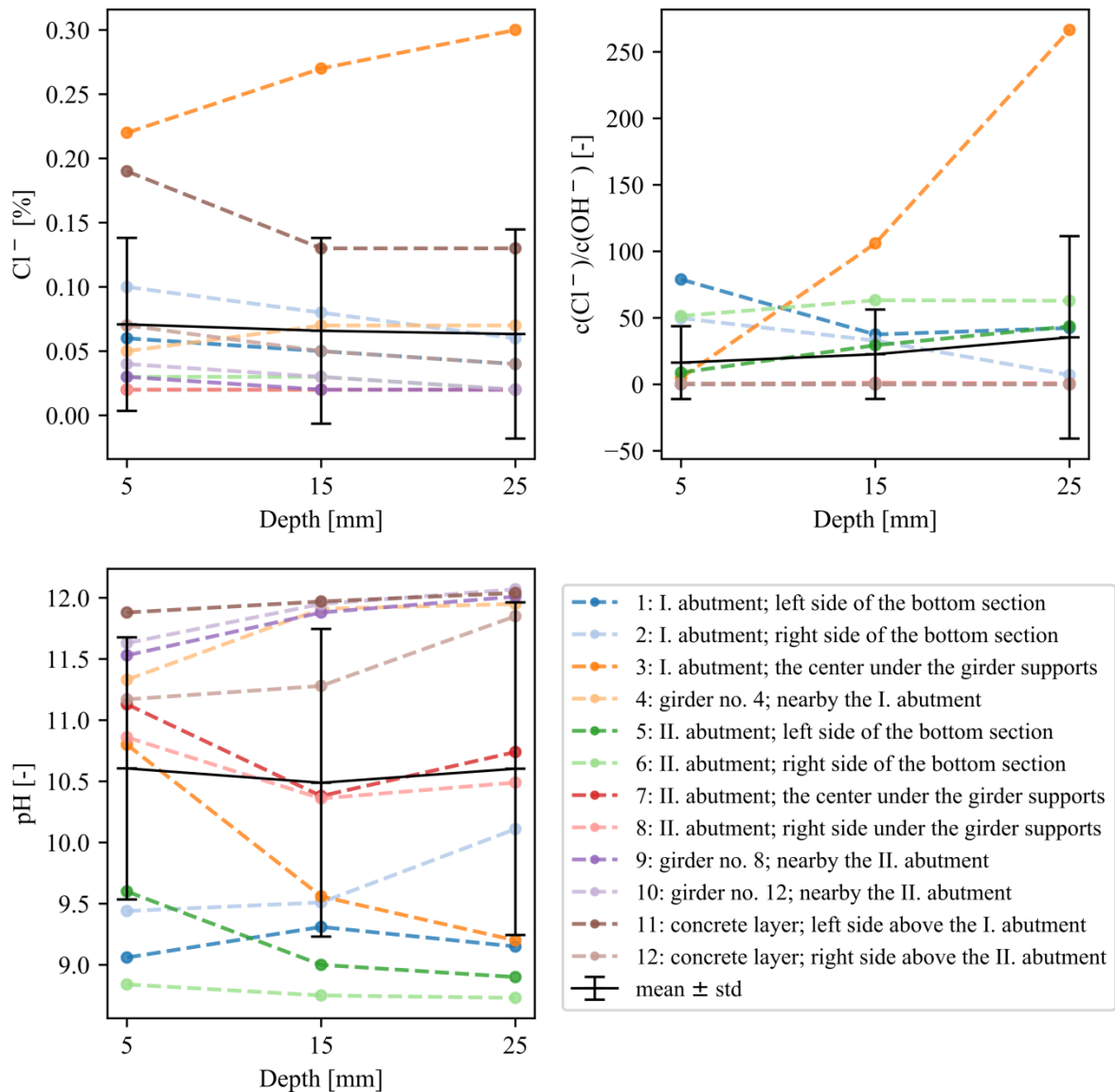


Figure 3: Observed parameters vs. depth of concrete for 12 locations on the bridge.

Table 1: Spearman correlations

	pH	%Cl ⁻	c(Cl ⁻)/c(OH ⁻)
pH	1	0.197	-0.718
%Cl ⁻	0.197	1	0.350
c(Cl ⁻)/c(OH ⁻)	-0.718	0.350	1

The data from the other bridges in the Czech Republic are available as well. Some of them were also processed by the authors of this paper. In Figs. 4–6 see the comparison for five different reinforced concrete bridges under service. The age on the horizontal axis is the age of the bridge

in the time of in-situ observations. The above described bridge (38 years old) is also included in these graphs.

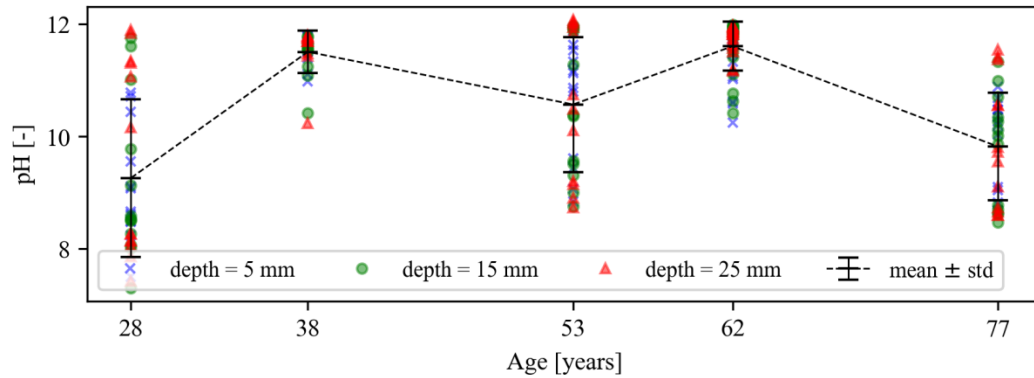


Figure 4: pH vs. age in the time of in-situ measurements for five reinforced concrete bridges.

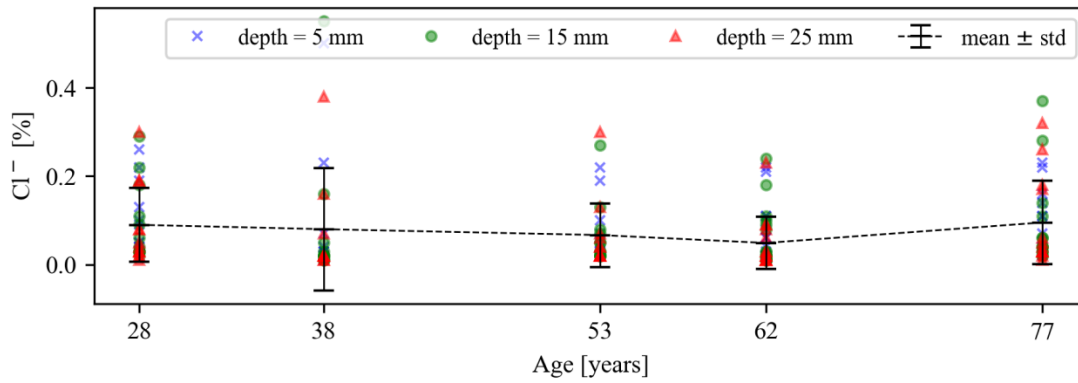


Figure 5: Chloride concentrations vs. age in the time of in-situ measurements for five reinforced concrete bridges.

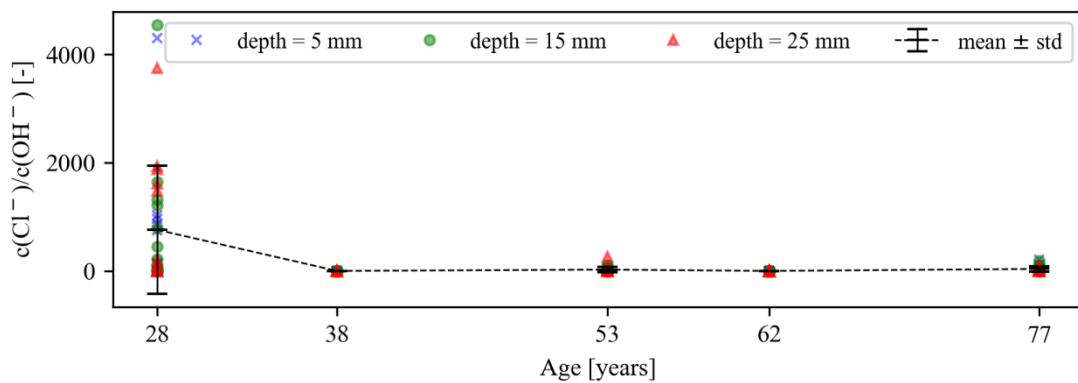


Figure 6: Ratio $c(\text{Cl}^-)/c(\text{OH}^-)$ vs. age in the time of in-situ measurements for five reinforced concrete bridges.

It can be seen from Figs. 4 and 5 that there is no significant relationship between bridge age and pH and Cl^- ratio, respectively. Regarding the results of the $c(\text{Cl}^-)/c(\text{OH}^-)$ ratio, the youngest bridge of the age of 28 years is the most vulnerable to corrosion. The reason is that the $c(\text{Cl}^-)/c(\text{OH}^-)$ ratio is significantly higher in comparison with the other bridges and the values are above the threshold of 0.6 [13]. The difference between the result for the respective bridge and the other bridges deserves further attention.

4. CONCLUSIONS

- The analysis of field inspection of reinforced concrete bridge under service is presented. The explorations were performed in order to evaluate the ability of the concrete to protect steel reinforcement from corrosion. For this purpose, the pH and the amount of water-soluble chlorides were measured and the ratio between the concentrations of Cl^- and OH^- was calculated.
- The detailed analysis of the available data from bridges under service still continues. However, until now it is apparent on the basis of the found correlation that the amount of chlorides evaluated per mass of concrete is not solely proportional to the risk of corrosion initiation and propagation expressed by the ratio $c(\text{Cl}^-)/c(\text{OH}^-)$. Thus, the effect of chloride concentration near to reinforcement on the initiation time should not be assumed separately and as the only parameter in numerical modelling. In other words, the effect of both, carbonation and chloride ingress should be taken into account.
- From the point of view of numerical modelling and predictions of concrete carbonation, chloride ingress and initiation and propagation of corrosion we need more parameters to derive from the measurements on the structure, such as diffusion coefficient, chloride surface concentration, etc.
- As a further step to complement, the available data from bridges under service will be accompanied by the data on concrete samples exposed to the chloride exposure at a real traffic zone. Seasonal variation of chloride loading will be studied via analysis of chloride deposition using analysis of chloride content on deposition plates or analogic device. Also, small concrete cubes are planned to be exposed simultaneously to a similar environment in order to study the correlation between the measured deposition and chloride penetration.

ACKNOWLEDGEMENTS

This contribution has been developed as a part of the research project GACR 18-07949S “Probabilistic Modeling of the Durability of Reinforced Concrete Structures Considering Synergic Effect of Carbonation, Chlorides and Mechanical Action” supported by the Czech Science Foundation.

We are grateful to Mr. Igor Suza from Mostní a silniční, s.r.o. company that enabled the processing of presented data from in-situ measurements carried out by him and his colleagues.

REFERENCES

- [1] Helland, S., 'Performance-Based Service Life Design in the 2021 Version of the European Concrete Standards – Ambitions and Challenges', in *fib Symposium 2016 Performance-Based Approaches for Concrete Structures*, edited by Hans Beushausen, Cape Town, South Africa, 2016.

- [2] fib Model Code 2010, fib Bulletins No. 65 and 66, 2012 and fib Bulletin No. 34, 'Service Life Design', 2006, Lausanne, Switzerland.
- [3] fib T8.3, 'Operational document to support Service Life Design' (Committee headed by Andrade, C.), 2016.
- [4] Novák, D., Vořechovský, M., and Teplý, B., 'FReET – Software for the statistical and reliability analysis of engineering problems and FReET-D: Degradation Module', *Advances in Engineering Software* **72** (2014) 179-192.
- [5] Teplý, B., Matesová, D., Chromá, M. and Rovnaník, P., 'Stochastic degradation models for durability limit state evaluation: SARA – part VI', in *3rd International Conference on Structural Health Monitoring of Intelligent Infrastructure*, Vancouver, British Columbia, Canada, 2007.
- [6] Boddy, A., Bentz, E., Thomas, M.D.A., Hooton, R.D., 'An overview and sensitivity study of a multi-mechanistic chloride transport model', *Cem. & Concr. Res.* **29** (1999) 827-837.
- [7] Stewart, M.G. and Rosowsky, D.V., 'Time-dependent reliability of deteriorating reinforced concrete bridge decks', *Structural Safety* **20** (1) (1998) 91-109.
- [8] Ghosh, P., Konečný, P. and Tikalsky, P.J., 'SBRA model for corrosion initiation of concrete structures', RILEM Bookseries, **5** (2011) 85-100.
- [9] Lehner, P., Konečný, P., Ghosh, P. and Tran, Q., 'Numerical Analysis of Chloride Diffusion Considering Time-Dependent Diffusion Coefficient', *International Journal of Mathematics and Computers in Simulation* **8**(1) (2014), 103-6.
- [10] Vořechovská, D., Podroužek, J., Chromá, M., Rovnaníková, P. and Teplý, B., 'Modeling of Chloride Concentration Effect on Reinforcement Corrosion', *Computer-Aided Civil and Infrastructure Engineering* **24** (6) (2009) 446-58.
- [11] Bentz, E. and Thomas, M.D.A., 'Life-365 Service Life Prediction Model', Program for Predicting the Service Life of Reinforced Concrete Exposed to Chlorides, 2001.
- [12] Diagnostický průzkum mostu ev.č. 55I-026a přes místní komunikaci před městem Otrokovice (Diagnostic exploration of bridge 55I-026a over the local roadway nearby town Otrokovice), Brno, Czech Republic, 2014.
- [13] Raharinaivo, A., Genin, J.M.R., 'Sobre la corrosion de armaduras de hormigón en presencia de cloruros' (On the corrosion of reinforcing steel in concrete in the presence of chlorides), *Materiales de Construcción*, **36** (204) (1986) 5-16.

THE RENEWAL OF MULTI-STORY PREFABRICATED RESIDENTIAL BUILDINGS

Mirjana Đ. Laban (1), Radomir J. Folić (1), Vlastimir S. Radonjanin (1), and Mirjana M. Malešev (1)

(1) Faculty of Technical Sciences, University of Novi Sad, Serbia

Abstract

European cities, due to slow population growth and the majority of towns having less than half a million inhabitants, have the opportunity to deal with the environmental problems and to develop sustainable solutions in future urban planning and construction and in building renewal activities. A special challenge is the renewal of prefabricated residential blocks built in the second half of the twentieth century, particularly the building envelopes.

In the period 1960 – 1990, industrial building technology was the dominant type of residential buildings' construction in Novi Sad (Serbia): over 22,000 flats were built, using prestressed skeletal IMS system, semi-prefabricated NS 71 system or large-panel Montastan system. Construction developed in sparsely populated and inhabited urban areas at that time or within urban blocks reconstruction.

The integrated building envelope renewal model is proposed, based on critical evaluation of eight case studies. The model enables condition assessment, which serves as the basis for renewal requirements definition, priority ranking, renewal methods and techniques evaluation and selection, model verification, as well as selection of the appropriate technical methods for renewal implementation and quality control of construction works.

Keywords: prefabricated buildings, envelopes, renewal model

1. INTRODUCTION

The issue of renewal – revitalization of buildings, or of entire city blocks, is based on the current condition assessment and modelling process which results with selection of optimal solutions for improvement the buildings performances and impact on the environment. One of the most common requests is to improve the quality of the building envelope (waterproofing, thermal and noise protection, surface damages or façade's structure repairs). The improvement of these performances transforms the building envelope, and has multiple implications and long-term impacts on social, urban and nature aspects of the urban environment.

Environmental evaluations of building materials and technologies, and the impact of construction work and buildings on the environment, as well as energy efficiency in buildings, have become topics of interest after 1990 in Serbia.

The research was done in Novi Sad [1], focused on the facade of the industrially built residential blocks in the period 1960 -1990. The research, analysis and critical evaluation of the structures was based on the analysis and examination of the actual condition, building inspections and knowledge accomplished from available technical documents, photos, articles and reviews in the professional or scientific literature and periodicals.

Three building systems were applied in the construction of multi-story residential buildings in Novi Sad urban area: prestressed skeletal system IMS, large-panel system Montastan and semi-prefabricated system NS-71. Typology of buildings was done based on affiliation to the applied construction system, and typology of façade elements was based on available information on buildings (literature, catalogues, building design documentation [2 - 20]).

Location, distribution and number of constructed buildings were determined by field observation and inspection of apartment blocks. The technical condition of façade elements was assessed by in-situ inspection using the method of control charts for attributes [21, 22]. The method of periodization was applied in order to estimate the designed performances of buildings (earthquake resistance, energy efficiency [23], fire safety [24], environmental performances, etc.). Typological classification of buildings based on construction systems, classification and analysis of collected data also enabled the morphologically similar structures grouping within individual systems. Research results were compared to the results of similar studies in some neighbouring countries [25, 26].

Case studies were done following the implementation sustainable renewal strategy, based on the proposed model on: the IMS system (4 examples), the NS-71 system (2 examples) and Montastan system (2 examples). The needs for envelope performances improvement were defined for all analysed typological groups of buildings. In the conclusion part the open-ended questions were listed and the directions for further research were indicated. The renewal model was proposed based on a state-of-the-art review in the research area, with its checking and verification. Research work done enabled the development of original solutions for a strategic approach, process modelling and building envelope renewal model implementation. These solutions simultaneously represent a foundation for further research in this scientific field.

2. PREFABRICATED FACADE ELEMENTS IN NOVI SAD BUILDINGS

The comparative analysis of the research results [27-36] implemented in several European countries (Hungary, Slovenia, Macedonia, Bulgaria, Netherlands, Germany and others) revealed the real situation and the needs for performance improvement of this important house stock in European cities.

In detailed comparison with the research findings in Serbia [1] led to conclusion that demographic trends are very similar (the aging and shrinking of the population) and also very similar construction systems were applied in industrialized building in European cities as in Novi Sad, only in larger quantities. The Serbian housing stock is among the least old in Europe (under 60 years), which justifies the investments in renewal activities.

All three prefabrication building systems developed characteristic design solutions and became recognizable for its appearance.

IMS system provided a wide range of façade design solutions (Fig. 1).

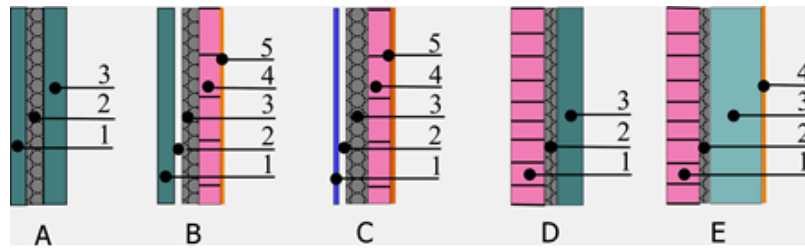


Figure 1. IMS façade, composition [11]: **A** - Prefabricated panel and parapet: 1. Concrete 6 cm; 2. EPS (expanded polystyrene) 6 cm; 3. Concrete 8 cm; **B** - Semi-prefabricated ventilated façade: 1. Prefab concrete casing 6 cm; 2. Air layer 2 cm; 3. EPS 6 cm; 4. Brick 6.5 cm; 5. Compo mortar 1.5 cm; **C** - Lightweight ventilated façade: 1. Asbestos cement sheeting 1 cm; 2. Air layer 2 cm; 3. EPS 6 cm; 4. Brick 6.5 cm; 5. Compo mortar 1.5 cm; **D** - Semi-prefabricated façade with face brick casing: 1. Perforated face bricks 12 cm; 2. EPS 4 cm; 3. Reinforced concrete 8 cm; **E** - Traditionally built façade: 1. Perforated bricks 12 cm; 2. EPS 2 cm; 3. Perforated concrete block 20 cm; 4. Compo mortar 1.5 cm.

Façades in the NS-71 system have two characteristic appearances: precast concrete panels finished in fair-faced concrete with flutes or pebble dashing and compose walls (Fig. 2).

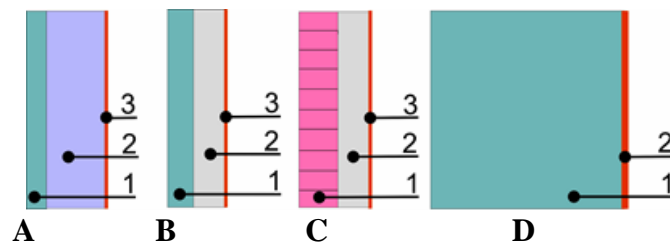


Figure 2. NS 71 façade panel types, composition [2, 3]: **A** – full height wall panel: 1. Concrete 6 cm, Ceramsite concrete 20 cm, 3. Compo mortar 1.5 cm; **B** – façade curtain wall: 1. Natural or pebble dashing concrete 8 cm, 2. Aerated light weight concrete blocks 12.5 cm, 3. Lime mortar 1.5 cm; **C** - Traditionally built façade: 1. Perforated face brick 12 cm, 2. Aerated light weight concrete blocks 10 cm, 3. Compo mortar 1.5 cm; **D** – Façade column: 1. Concrete 60 cm, 2. Thermal mortar 3 cm.

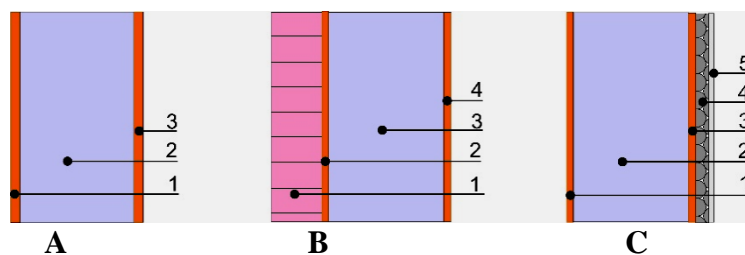


Figure 3: Montastan façade panel types, compositions: **A** - single-layer façade panel: 1. Cement mortar 1.5 cm; 2. Clay block 27 cm; 3. Lime mortar 1.5 cm; **B** – façade panel enclosed by face brick: 1. Face brick 12 cm, 2. Cement mortar 1.5 cm, 3. Clay block 27 cm, 4. Lime mortar 1.5 cm; **C** – Façade panel with internal thermal insulation and gypsum board: 1. Cement mortar 1.5 cm, 2. Clay block 27 cm, 3. Lime mortar 1.5 cm, 4. EPS 2 cm, 5. Gypsum board 1 cm.

Montastan system is recognizable by the characteristic façade panel shaping and hole cropping in prefabricated elements, and façade finishing is usually painted in pastel, bright or dark tones - depending on the designer's choice [10, 17].

Exceptions to the rule are the experimental solutions – precast façade panel enclosed by facing brick or with the addition of layers of insulation and drywall on the inside of the wall [16, 20]. The composition of the façade walls is presented in Fig. 3.

3. ENVELOPE REVITALIZATION – THE INTEGRATED PROCESS OF BUILDING RENEWAL

Based on research done on prefabricated building blocks in Novi Sad and the research results from other European cities, the building envelope assessment criteria were established (Fig. 4).

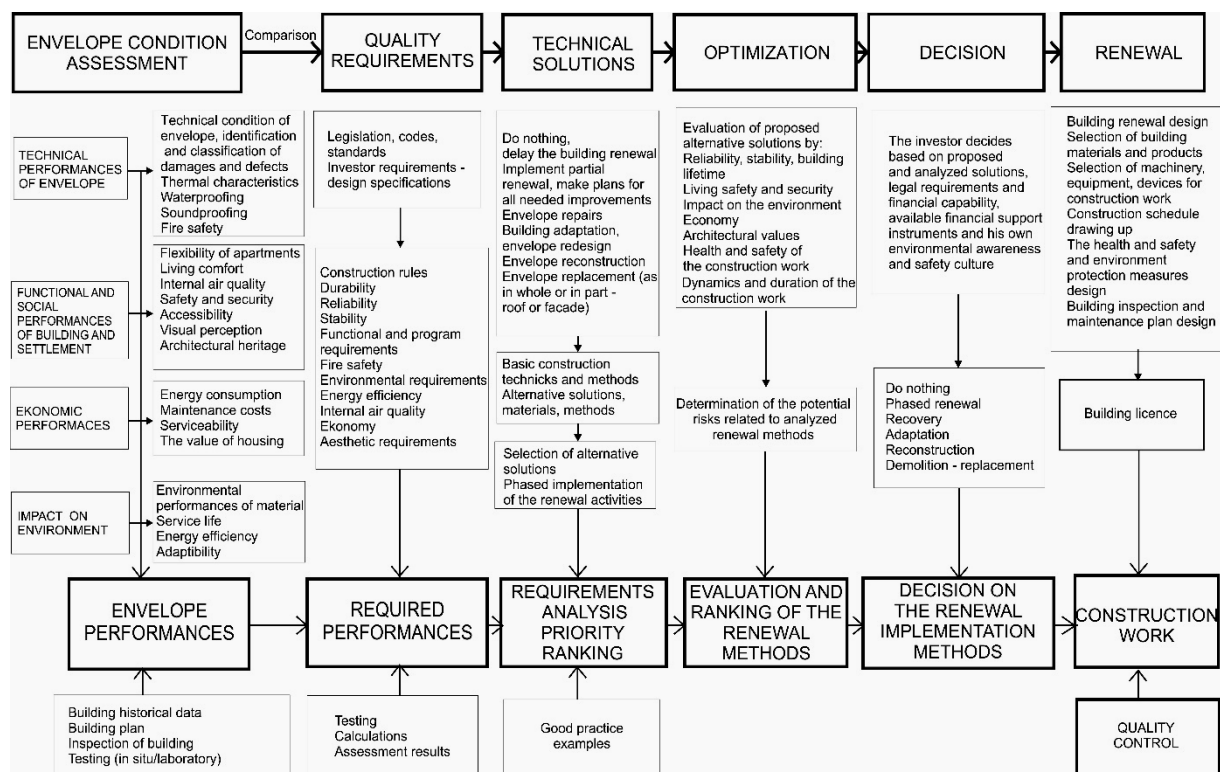


Figure 4. Integrated model of building envelope renewal

Following a comparison of the current envelope condition with the updated quality requirements, it is possible to choose a type of renewal (recovery, adaptation, reconstruction), which will consequently evolve to the envelope revitalization model.

Besides architectural transformation (modification of layout, form, function, program, content) the model includes the environmental aspects (energy efficiency, ecological evaluation of the building materials, construction work environmental impact assessment) as well as safety and security (indoor air quality, fire safety, earthquake resistance and safety and health at work during refurbishment construction works and future building maintenance activities).

An integrated approach to the refurbishment of prefabricated multi-storey residential buildings, based on the proposed model (Fig.4), results in the possibility of simultaneously envelope performances improvements such as:

- Technical performance (stability, capacity, thermal insulation, waterproofing, noise insulation, fire safety, earthquake resistance, maintainability, durability – service life);
- Functional / social performance of buildings and settlements (flexibility, comfort – thermal, acoustical, visual, indoor air quality, security, accessibility);
- Economical performance (reduction of energy consumption and maintenance costs, the value of housing increase);
- Environmental performance / sustainability (low energy consumption, service life, low emission of CO₂ and fossil fuel consumption, adaptability of urban space).
- Building renewal plans and designs should incorporate complete solutions, i.e. it is necessary to take into account all steps of refurbishment that meet the required quality through appropriate, optimal technical solutions. Integrated building envelope renewal model proposal (Fig. 4) includes all the essential activities.

4. CONCLUSIONS

The multidisciplinary methodological approach to research on possibilities for renewal and improvement of the building envelope performance resulted in the formulation of an integrated model proposed for the building envelope renewal. This model is also applicable to all other building construction systems.

The quality requirements include a set of criteria which envelope renewal should meet and which cover current legislation, technical regulations and requirements of investors – design specifications, which can further improve the level of renewal quality, above simply meeting the code requirements.

The resulting synthesis of the comparative analysis of actual and required performances, through case-studies in model verification process, implies some of the most important needs for improvement:

- The reliability and stability of the structures; load bearing capacity and seismic performance checking: in particular the buildings constructed in IMS system before 1964 and upgraded buildings without adequate design documentation;
- Durability of the envelope; in particular prefabricated panels in the IMS system with fair-faced concrete finishing and façade panels in system Montastan;
- Fire safety: particularly high-rise buildings, built in all prefabricated systems;
- Energy efficiency: particularly buildings constructed in Montastan and NS 71 systems, where it is necessary to install 8 to 10 cm of subsequent insulation layer to meet the latest standards (2012) - the additional thermal insulation layer and windows replacement could provide savings of up to 60 % relative to current consumption;
- Accessibility of buildings, built in all prefabricated systems;
- Visual quality of buildings and settlements; it is necessary to remove improper subsequent illegal interventions and renovate the buildings in accordance with the rules of construction and original ideas of design authors;
- Cost-effectiveness of building maintenance and exploitation, in all construction systems.

Based on the results of case studies, it is necessary to not delay the envelope renewal for any group of buildings, but it is possible to plan the work in phases, according to the prioritization of works.

An advantage should be given to the improvements that contribute to the reliability of the construction and safe exploitation of a building (seismic performance, fire safety, indoor air quality), which are necessary to comply with the requirements of energy efficiency, durability and economy. Architectural value of buildings should be preserved or enhanced in any of the alternative solutions, and it is also necessary to achieve a positive impact on the environment.

In order to preserve the added value achieved by the renovation, it is necessary to establish a quality control system: periodic inspections and regular maintenance of buildings. The absence of these activities in the former period of exploitation is one of the main causes of envelope deterioration and devastation of buildings and urban blocks.

ACKNOWLEDGEMENTS

The work reported in this paper is part of the investigation within the Research Project TR 36017: Utilization of by-products and recycled waste materials in concrete composites in the scope of sustainable construction development in Serbia: investigation and environmental assessment of possible applications, supported by the Ministry for Education and Science, Republic of Serbia. This support is gratefully acknowledged.

REFERENCES

- [1] Laban M., Unapređenje performansi omotača montažnih i polumontažnih višespratnih stambenih zgrada u Novom Sadu, doktorska disertacija, mentor prof. em Folić R., Univerzitet u Novom Sadu, Fakultet tehničkih nauka, Novi Sad, 2012, pg. 197
- [2] Cagić, P., Sistem za industrijsku proizvodnju stanova NS 71, DGA – 1479, Sv. 298, 1977, pg. 18
- [3] Cagić, P., Lojanica, M., Stambene zajednice Blok III i Liman III (B-2) u Novom Sadu i sistem za industrijsku proizvodnju stanova NS 71, Časopis Izgradnja, specijalno izdanje Stan i stanovanje, 1974, pg.166-181.
- [4] Čertić D., Horvat A., Kaćanski Đ., Krupnopanelni sistem montažne izgradnje Montastan – prikaz modela za eksperimentalna istraživanja, Četvrti jugoslovenski naučni skup Industrijska izgradnja stanova – INDIS 86, Novi Sad, februar 1986, Zbornik radova knjiga II, str.185–208
- [5] Čertić D., Horvat A., Kaćanski Đ., Černeć T., Krupnopanelni sistem montažne izgradnje stanova Montastan – prikaz rezultata modelskog ispitivanja, Četvrti jugoslovenski naučni skup Industrijska izgradnja stanova – INDIS 86, Novi Sad, februar 1986, Zbornik radova knjiga II, str.209-234
- [6] Čaušević M. Određivanje optimalnog matematičkog modela krupnopanelnog sistema Montastan na osnovu eksperimentalnih mjerenja dinamičkih karakteristika konstrukcije u prirodnoj veličini, Četvrti jugoslovenski naučni skup Industrijska izgradnja stanova – INDIS 86, Novi Sad, februar 1986, Zbornik radova knjiga II, str. 235-250
- [7] Denić N., Vojinović B., Bogunović S., Greške i sanacije montažnih betonskih fasada, Montažne betonske fasade, str. 167-176
- [8] Folić, R., Folić, B.(2002): Veze betonskih elemenata usidrenom i zavarenom armaturom i metalnim spojicama, Građevinski kalendar, Beograd, str. 199-235.
- [9] Folić, R., Spojevi i veze montažnih betonskih zgrada, monografija Montažni građevinski objekti, Ekonomika, Beograd, 1983, str.117-167
- [10] Kaćanski Đ., Krupnopanelni montažni sistem Montastan, Izgradnja br. 4/89, Bgd, 1989, str.10–13

- [11] Kataloški prikaz varijantnih mogućnosti rešavanja fasada u IMS sistemu, Projekat realizovan u Institutu za ispitivanje materijala SR Srbije, u okviru stalnog naučno-istraživačkog rada članica Zajednice IMS, u toku 1981. i 1982. godine
- [12] Krstić, D., Polazne osnove za prikaz stanovanja u Novom Sadu od 1970.-1980.god, DaNS br.6/1986
- [13] Nedić, Lj., Analiza odnosa sekundarnih i primarnih elemenata IMS sistema i mogućnost rešavanja stanova u sistemu, I deo: Fasada kao sekundarni element sistema IMS, Specijalistički rad, Univerzitet u Beogradu - Arhitektonski fakultet, Beograd, 1977, str. 66
- [14] Petrović P., Nedić Lj., Karakteristike fasada, Montažne betonske fasade, Institut IMS, Beograd 1995.g. str.7-19
- [15] Radović, R., Primena opeke u montažnoj izgradnji, Izgradnja, 4 (1989), str. 14-15
- [16] Radović, R., Rind I., Toplotna izolacija u sistemu Montastan, Treći jugoslovenski naučni skup Industrijska izgradnja stanova – INDIS 83, Zbornik radova, Knjiga II, Novi Sad, 1983, 323 – 344
- [17] Reba, B., Montastan – izvorni sistem prefabrikacije, DaNS br.7 (1986) str.16 – 19
- [18] Reba, B., Stupar D., Projektovanje stambenih objekata u sistemu »Montastan«, Izgradnja br.4/89., str.30-32
- [19] Reba B., Horvat A., Kovačević R., Mogućnosti urbanističkog prilagođavanja i arhitektonskog projektovanja stambenih objekata u krupnopanelnom montažnom sistemu Montastan, Četvrti jugoslovenski naučni skup Industrijska izgradnja stanova – INDIS 86, Novi Sad, februar 1986, Zbornik radova knjiga II, str.137 -159
- [20] Sebenji F., Radović R., Mogućnost primene opeke, uz osvrt na nove propise iz toplotne zaštite, kroz elemente sistema Montastan, Četvrti jugoslovenski naučni skup Industrijska izgradnja stanova – INDIS 86, Zbornik radova, Knjiga II, Novi Sad, 1986, str.161 – 183
- [21] Laban M., Folić R., Conceptual analysis of residential buildings' facades applied in industrial building systems in Novi Sad, International symposium about research and application of modern achievements in civil engineering in the field of materials and structures, XXV Congress – Tara October 19-21, 2011, Proceedings (Ed. Radonjanin, V.), pg. 311-318
- [22] Laban M., Folić R., The assesment of composite wall performances after several years, VIII naučno-stručno savetovanje Ocena stanja, održavanje i sanacija građevinskih objekata i naselja, Zlatibor, maj 2013., Zbornik radova (Ed. Folić R.), Savez građevinskih inženjera Srbije, Beograd
- [23] Laban M., Kontrola kvaliteta prefabrikovanih betonskih fasadnih elemenata nakon višegodišnje eksploatacije, Materijali i konstrukcije broj 1-2, 2006., str 3-19
Laban M., (2006.): Kontrola kvaliteta prefabrikovanih betonskih fasadnih elemenata nakon višegodišnje eksploatacije, Materijali i konstrukcije broj 1-2, 2006., str 3-19
- [24] Laban M., Folić R., Energy efficiency of industrially made buildings influenced by thermal properties of facades, Thermal Science, 2012 OnLine-First (00): 147-147, DOI:10.2298/TSCI120417147L <http://www.doiserbia.nb.rs/journal.aspx?issn=0354-9836>
- [25] Laban, M., Milanko, V., (2008) Fire safety assessment in urban environment, Journal of International Scientific Publications: Ecology & Safety, Vol. 2, 2008, ISSN 1313-2563, pg. 105 - 120, www.Science-Journals.Eu
- [26] Folić, R., Laban, M., Milanko, V., (2011) Reliability and sustainability analysis of large panel residential buildings in Sofia, Skopje and Novi Sad, UDC 728.2(497.223)(497.17)(497.113)=111, FACTA UNIVERSITATIS Series: Architecture and Civil Engineering Vol.9, No 1, 2011, pp161-176, DOI 10.2298/FUACE1101161F
- [27] Laban M., (2007.) The sustainable future of large prefabricated housing estates in Hungary, Romania and Serbia, 9th International Symposium Interdisciplinary Regional Research (ISIRR-2007) Novi Sad, June 21st-23rd, 2007, Abstract book, pg. 51
- [28] COST C16 Improving the Quality of Existing Urban Building Envelopes I (Edited by: M.T. Andeweg, S. Brunoro and L.G.W. Verhoef) I State of the Art , Ed. M.T. Andeweg et al., Delft

- University Press, Volume 2, Research in Architectural Engineering Series, Amsterdam, 2007, str. 268
- [29] COST C16 Improving the Quality of Existing Urban Building Envelopes II (Edited by: E. Melgaard, G. Hadjimichael, M. Imeida and L.G.W. Verhoef) II Needs, Ed. E. Melgaard, et al., Delft University Press, Volume 3, Research in Architectural Engineering Series, Amsterdam, 2007, str. 280
 - [30] COST C16 Improving the Quality of Existing Urban Building Envelopes III (Edited by: R. Di Giulio, Z. Bozinovski and L.G.W. Verhoef) III Structures, Ed. R. Di Giulio, et al., Delft University Press, Volume 4, Research in Architectural Engineering Series, Amsterdam, 2007, str. 237
 - [31] COST C16 Improving the Quality of Existing Urban Building Envelopes IV, Facades and Roofs, Edited by: L. Braganca, et al., Delft University Press, Volume 5, Research in Architectural Engineering Series, Amsterdam, 2007, str. 177
 - [32] European Academy of the Urban Environment (Berlin): Analysis Report Thematic Strategy on the Urban Environment, on the basis of reports by EU Working Groups on four Thematic Areas, Sustainable Urban Management, Sustainable Urban Transport, Sustainable Urban Design and Sustainable Urban Construction and Twelve Candidate Countries' Overview Report, European Commission, March 2004., str. 75
 - [33] SUREURO - Sustainable Refurbishment Europe, research project, FP5 City of Tomorrow and Cultural Heritage :
http://cordis.europa.eu/search/index.cfm?fuseaction=proj.document&PJ_RCN=4706084
 - [34] RESTATE - Restructuring Large Housing Estates in European Cities: Good Practices and New Visions for Sustainable Development, research project, FP5 City of Tomorrow and Cultural Heritage:
http://cordis.europa.eu/search/index.cfm?fuseaction=proj.document&PJ_RCN=5907341
 - [35] SURBAN - DATABASE ON SUSTAINABLE URBAN DEVELOPMENT IN EUROPE:
www.eaue.de/winuwd/default.htm
 - [36] Large prefabricated housing estates in Central and Eastern Europe, EAUE – The European Academy of the Urban Environment, Berlin: <http://www.eaue.de/houshome.HTM>

INVESTIGATION AND REPAIR OF STONE BUILDING FACADES

Dunja Vla (1)

(1) Wiss, Janney, Elstner Associates Inc., USA

Abstract

Stone facade blocks and panels have been used for the construction of buildings and other structures for hundreds of years. Based on the investigation of over fifty buildings of various ages and distress, observed defects could be classified into several categories. They include material flaws and durability, lack of proper details to prevent water infiltration into the interior of the building, deterioration of anchors between stone pieces and between stones and a buildings structural systems, improper construction methods, and inadequate design to accommodate movement of the overall structure and/or movement between the stone cladding and connections to the backup walls.

Over the years thicknesses of the stone panels or blocks used for the exterior facades of the buildings have been reduced. In earlier times, the stone blocks had been used as a load-bearing elements for exterior walls. As the building heights have increased over the years, stone blocks have been used mainly as a veneer with thicknesses of 10 cm. In the last fifty years, thicknesses of the stone panels has been reduced to 2.5 cm to 3 cm. Due to a reduction of thicknesses, mechanical properties and durability of these panels became important. Durability and structural stability of thin stone panels has become a major factor in design

Keywords: stone, distress, stability, repairs, durability

1. INTRODUCTION

Buildings clad with stone presented in this paper date from three different eras, 1925, 1953 and 1985, making them 93, 65 and 33 years old. Stone cladding used in each of these eras differs in size and thickness of the stones, as well as in the type and materials used for their connections to the backing walls. All investigated and restored buildings presented in this paper are located in the Chicago area, within 25 miles from each other, and they are exposed to the same climate conditions.

Limestone was used as stone cladding for the building constructed in 1925. Lannon stone and limestone were used for building from 1953 and granite panels were used as cladding for the building from 1985.

Corrodible metal connections were used on the buildings from 1925 and 1953, and stainless steel and epoxy adhesive for the building in 1985. For buildings from 1925 and 1953, moisture intrusion behind the limestone cladding caused the corrosion of concealed corrodible metal straps and shelf angles. Cracking, spalling, and displacement of limestone panels were typical forms of distress observed. Displacement of granite panels was found to be typical distress due to the inability of connections to accommodate movement of the panels, and failed epoxy adhesives.

2. DESCRIPTION OF STONE CLADDING SYSTEMS

2.1 Building from 1925

The building measures 81 m (266 ft) long and is 30 m (97 ft) wide at the east end, 38 m (125 ft) wide at the center, and 23 m (76 ft) wide at the west end. The main portion of the building is 15 stories tall with a roof approximately 54 m (176 ft) above ground level. At the center of the building there is an additional five-story tower. The top of the tower is 84 m (277 ft) above ground level. Limestone blocks used to clad the exterior walls of these buildings vary in size, with an average height and width of 15 cm to 61 cm (6 in. to 24 in.). The typical thickness of limestone blocks is 10 cm (4 in.). Every fourth row of blocks is 20 cm (8 in.), and serves to anchor the stone cladding into the brick masonry behind it. Decorative limestone pieces are present above building entrances, around windows, and at the top of the tower. The limestone facade is anchored to a masonry backup layer and is supported by a series of steel shelf angles and straps. No flashing was installed over shelf angles. Sections of window mullions are connected with steel dowels. The masonry, steel shelf angles, and the building's concrete floors are supported, in turn, by concrete-encased steel beams and columns.

2.2 Building from 1953

The building is two stories tall and was constructed in two phases. The first phase was completed in 1953, and the second phase was completed in 1963. The building plan has a rectangular shape with two wings at its east elevation. The overall dimensions of the building are 40 m by 60 m (133 ft by 196 ft).

The exterior walls, 30 cm (12 in.) thick, are typically composed of 10 cm (4 in.) thick lannon stone with 8 in. brick masonry back up, and limestone bands directly below and above windows, and slate stone tiles between some of the windows. Parapet walls have limestone coping and a 35.5 cm (14 in.) thick limestone band panel located directly below it. Copper flashing was placed below the coping stones.

The limestone blocks above the window lintels are supported by two steel angles. The top angle provides lateral support, and the bottom provides gravity support. Those limestone blocks are hung from the top shelf with two steel anchors set in lead. The bottom portion of stone is notched in order to be supported by a lower shelf angle and for the shelf angle to remain concealed. No flashing was installed over the steel window lintels.

2.3 Building from 1985

The building is a 9-story tall office building. It has an irregular octagon shape in plan view with overall dimensions of 50 m by 48 m (163 ft by 156 ft). The Overall height of the building is 36 m (118 ft).

The exterior face of the building is composed of granite panels from the ground level up to the 3rd floor, with tall windows at the ground level, and precast concrete panels with window openings up to the 8th floor

3. TYPE OF DISTRESS

3.1 1925 Building

Distress observed at the exterior walls, as shown in Figure 1, consists of deteriorated mortar joints between limestone panels; spalled limestone due to corrosion of embedded strap anchors; spalled limestone due to corrosion of embedded shelf angles; cracks observed along the building corners; displaced wall sections with spalled limestone; cracked and displaced window mullions; and cracked and displaced window rosettes, as shown in Figure 2.

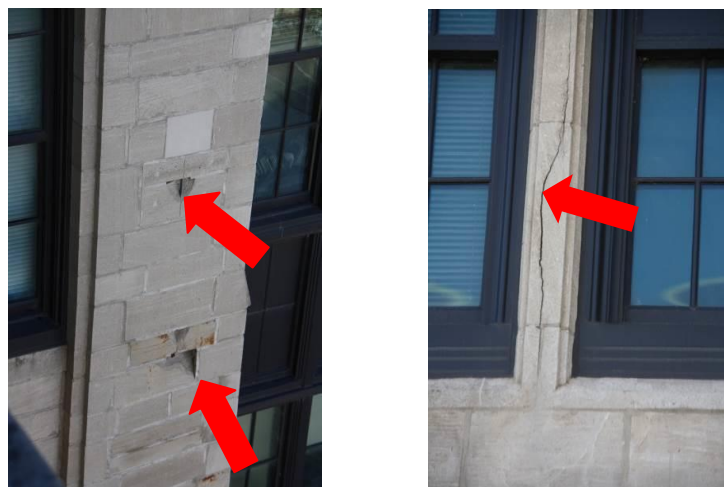


Figure 1 - Spalled, cracked limestone due to corrosion of embedded steel strap anchors and dowels



Figure 2 - Cracked and spalled window mullions and rosettes

3.2 1953 Building

Initial observed distress at the building was minor and consisted mostly of deteriorated mortar joints, several small spalls in limestone blocks, and several slightly displaced limestone panels above the third floor windows and soiled exterior walls.

After removal of displaced limestone panels it was discovered that sections of steel lintels behind the limestone panels above the windows were severely corroded. The expansion of corrosion build-up has created large expansion forces causing pressure on adjacent stone, which caused displacement and cracking of the limestone blocks at their back portion. In addition, it was observed that portions of some of the steel shelf angles were never attached to the concrete beam of the building's structural system, had an insufficient bearing width, and at several locations the attachment anchors were severely corroded. Typical observed distress is show in Figures 3 and 4.



Figure 3 - Severely corroded steel shelf angle and cracked and spalled limestone block due to corrosion



Figure 4 - Overall and close up view of shelf angle detached from structural beam and cracked limestone panel at the back side due to corrosion of shelf angle

3.3 1985 Building

Initial distress observed at the granite panels was mostly related to deteriorated sealant in joints between them. There were several panels at the ground level that were displaced. After close-up inspection and exploratory openings it was determined that connections installed to support granite panels at the ground level were inadequate and completely different from designed, as shown in Figure 5. Instead of using metal clips at the bottom and top of the panels to provide for gravity and lateral support, panels were connected with copper wires glued with epoxy adhesive to the back of the panels. Copper wires were tied to the galvanized angles and attached with anchors to the backing wall.

It was discovered that granite inserts embedded into granite panels along the 3rd floor were debonded from the backing material. In this case, as built conditions were different from designed, as shown in Figure 6.

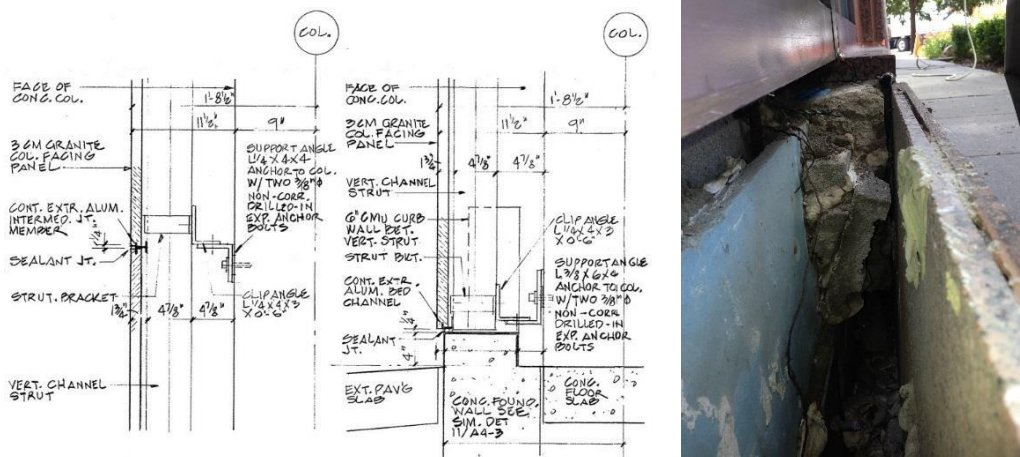
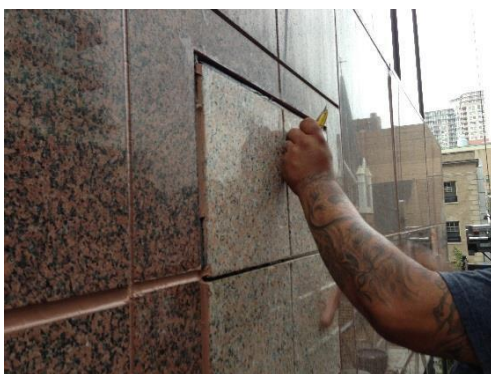


Figure 5 - Details of designed connections and as built connections for granite panels are completely different



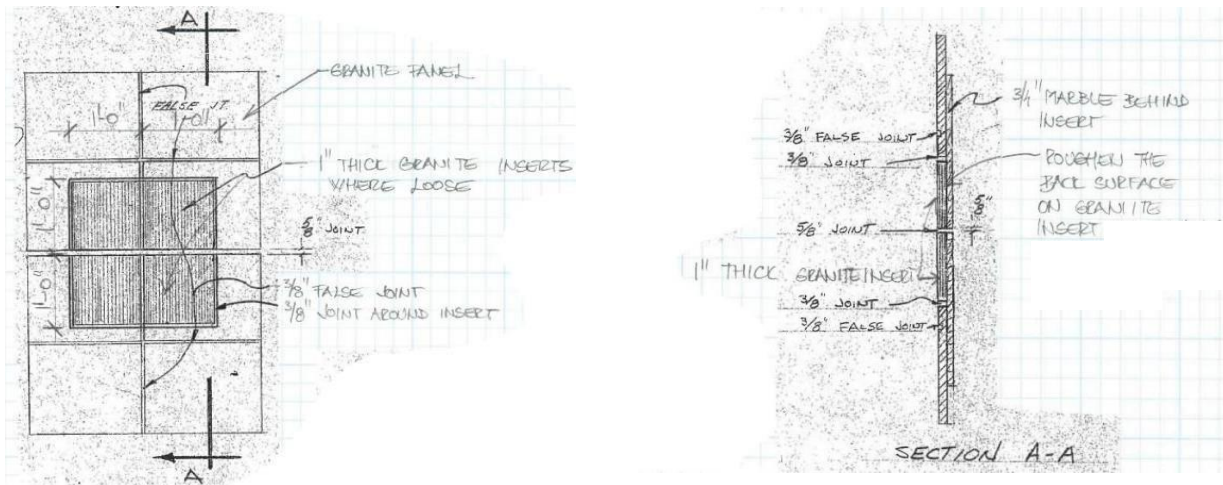


Figure 6 - Granite inserts attached with epoxy adhesive that has failed.
As built conditions are different than designed

4. TYPES OF REPAIRS

Depending on the size of the granite panels and limestone blocks, the extent of their spalling and cracking, their location, and the condition of the steel shelf angles and the adhesives supporting them, the following repair types were implemented to restore their condition and structural integrity:

Repair 1 - Repointing of mortar joints: includes grinding out deteriorated or cracked mortar joints to a depth of 3/4 in. minimum, and installation of new mortar in order to prevent water infiltration into the building. One hundred percent of the exterior wall joints were repointed.

Repair 2 - Patching of spalled limestone: includes removal of sections of deteriorated or damaged limestone and repairing the removed area with a hand-placed mortar patch. Some patches may require stainless steel threaded rods for reinforcement, as shown in Figure 7.

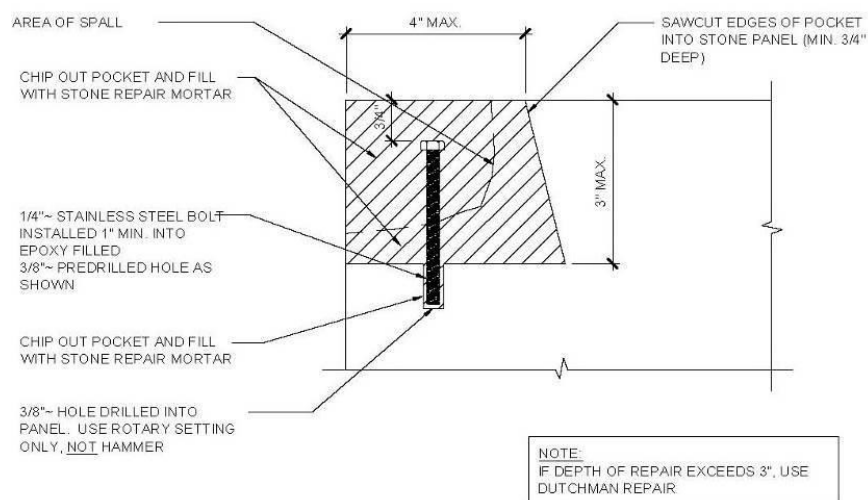


Figure 7. - Limestone patch

Repair 3 - Dutchman repair: includes removal of sections of deteriorated or damaged limestone and repairing the removed area with limestone dutchman held in place with strap anchors and/or stainless steel pins, as shown in Figure 8.

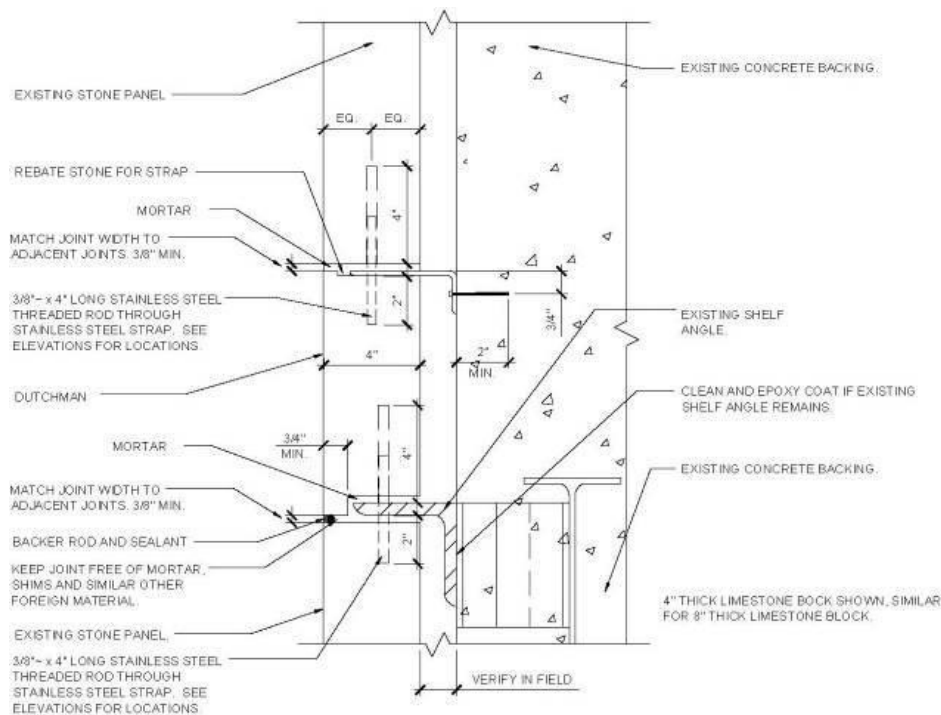


Figure 8 - Dutchman limestone repair

Repair 4 - Replacement of damaged limestone with new: includes removal of deteriorated or damaged limestone blocks and installation of new ones to match in size and texture the original position while providing supplemental stainless steel anchors where necessary.

Repair 5 - Installation of repair anchor to stabilize/secure the movement of displaced stones: includes drilling a hole through mortar joints, masonry, or concrete backing, installing the anchor, and repointing the joint with mortar so that the installation of the anchor is not visible.

Repair 6 - Repair of shelf angle/lintel: includes removal of stones above the shelf angle/lintel as needed to expose the corroded portion of the embedded steel, as shown in Figure 9. The engineer who reviewed the condition of the existing steel and percentage of section loss, based on its condition, will determine if the shelf angle/steel lintel would be repaired or replaced.

If the level of corrosion was acceptable, the corroded steel was sandblasted clean, its surfaces properly prepared, and two coats of epoxy paint applied. Butyl based flashing with a stainless steel drip edge was installed over it. Weep tubes with ropes were installed in vertical joints between stones, and the entire section of the wall was rebuilt with limestone to restore its original profile. New limestone work was installed flush with the existing limestone. If the level of corrosion was severe, the steel lintel/shelf angle was replaced with new material, and flashing with a drip edge was installed over it prior to rebuilding the section with limestone.



Figure 9 - Repair 6, repairing of steel shelf angles / window lintels at building built in

Repair 7 - Replacement of sealant in joints: includes removal of existing sealant, surface preparation and priming of stone surfaces and installation of new sealant in order to prevent water infiltration into the building. One hundred percent of exterior wall joints were resealed.

Repair 8 - Replacement of inadequate connections at granite panels included installation of new stainless steel angles anchored into the backing wall and reattaching granite panels to them.

Repair 9 - Reattaching of granite inserts using epoxy adhesives included removal of existing failed adhesives and backing material and installation of new.

5. SUMMARY

Distress observed in the limestone cladding of the exterior walls was caused by corrosion of embedded steel strap anchors, pins, and steel shelf angles and lintels. Spalled, cracked, and displaced limestone panels had to be repaired. Certain portions of facades had to be rebuilt in areas where corroded, concealed steel supports had significant section loss, insufficient bearing width, or improper anchorage to the structural system of the building. Repairs were necessary in order to remove hazardous conditions which were dangerous for pedestrians, to prevent water infiltration into the building, and to extend the serviceability of the buildings.

Distress observed in the granite cladding was caused by failure of inadequately installed connections for granite panels. Installed copper wires and adhesives were not able to provide the adequate support for granite panels resulting in their displacement. Adhesive and backing material used to attach granite inserts to granite panels was also inadequate and had to be repaired. Adhesive has become hard and brittle over the years causing granite inserts to debond from the backing wall and become loose.

RECONSTRUCTION OF A FAMILY VILLA IN ZAGREB CITY CENTER

Angela Čuljak (1)

(1) UTJECAJNA LINIJA J.D.O.O., ZAGREB

Abstract

This paper presents a reconstruction of a family villa built in Zagreb in 1929. Villa was designed and built by „Brothers Carnelutti“, a family of builders. During they almost seven – decades long activity, two generations of the Carneluttis built more than two hundred buildings, many of which are strong strings in the Zagreb picture, and especially smaller towns in Croatia.

During the reconstruction, a modern family villa was built in the same scale as the original structure, with all the modern features such as the "smart house" systems; with intelligent monitoring and management systems all with the aim to achieve the energy-efficient building.

Keywords: reconstruction of 20th century villa, smart house system, energy-efficient building

1. INTRODUCTION

Villa was designed and built by „Brothers Carnelutti“, a family of builders. During they almost seven –decades long activity, two generations of the Carneluttis built more than two hundred buildings, many of which are staples in any image of Zagreb, and particularly that of smaller towns in Croatia [1]. Condition assessment of the structure showed that a significant reconstruction is needed to satisfy investor's needs. Based on performed condition assessment a reconstruction project was design which encompassed most of the structure elements, except the exterior walls and the inner supporting walls, which were in good condition. In addition to the building built in 1929, a basement section was built in the year 1990. Previous owner had legalized this part of basement, so that the new owners got a home with 1200 m².

As a part of the basement section legalized by the previous owner in order to make the restaurant was very badly executed, the new owners decided to remove this upgraded part of the basement and give that part of the house a different purpose.

However, new owners decided to change the purpose of the basement, from the restaurant to a spa area with a swimming pool, gym room, sauna, steam bath and two technical rooms.

Reconstruction is presented in essential phases, in the pictures, with a brief description of what was being done at each stage. The Investor respected engineering rules in each segment of villa's reconstruction and by doing so has contributed to a successful completion of the

Project. During the reconstruction, a modern family villa was built in the same scale as the original structure, with all the modern features.

2. RECONSTRUCTION PHASES

Firstly, the existing building was demolished in accordance with the plan and the upgraded basement section was removed and excavated to assure the connection of the new rebuilt basement with the old, existing house (Figure 1a). Figure 1b presents details of cleaning and preparation of the old wall and joints with the new wall. The foundations were deepened and reinforced, under the basement part with concrete C25/30, in the segments of 1 m. New design included an elevator, to assure an ease transition through future four floors of the villa. As this was not predicted in the original villa's design, a very demanding digging was performed at the location of future elevator (Figure 1c). Figure 2a it was made so that existing walls and structures were first strengthened and then new walls were built. Part by part, step by step, very carefully. Figure 2b presents a progress on the base plate and elevator foundations.

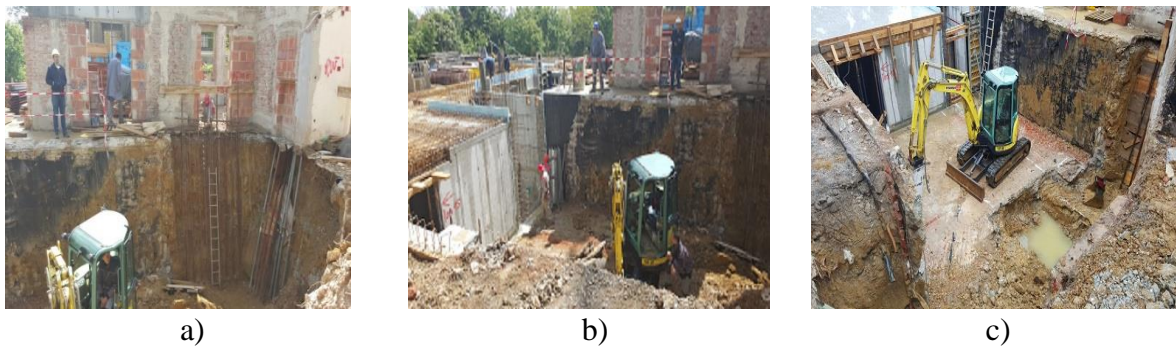


Figure 1: a) cleaning the old walls for preparation for building of the new walls on joints with the old ones b) a newly built basement and a junction with the old wall of the house, c) excavating of the elevators pit

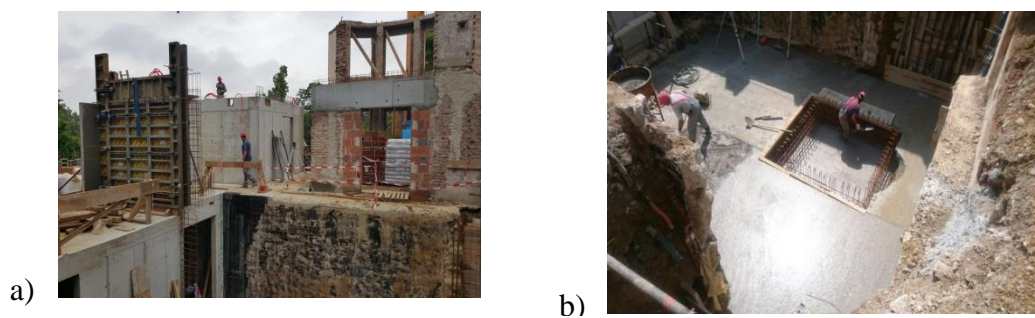


Figure 2: a)work in progress, new walls are being built, b) the floor concrete slab and the foundation of the elevator pit are performing

All reconstruction phases must be done with a great care, where functionality and stability of the structure are in the first place. One should be aware that reconstructions are always full of surprises as it is impossible to detect and predict every phase through the condition assessment and design phase. New basement walls were built, as supporting walls of the

reconstructed building. High quality concrete was used for their construction with addition of waterproofing agent. Also, to prevent the passage of liquids in concrete joints high quality of waterstop have been used.

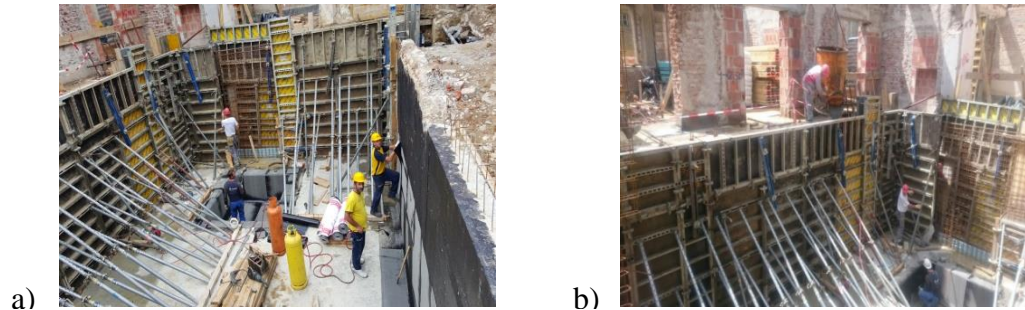


Figure 3: a) formwork and shuttering props are set up in difficult conditions for performing the works b) carefully installation of concrete into the formwork of the walls

Waterproofing and thermal insulation of newly built basement walls was performed, as presented on Figure 4. After completion of the construction works at foundations of the annex, construction is being processed further on the structure of the existing building. Insulation of the existing walls was performed, in the zone of contact with the ground, by injection of the insulating foam (Figure 5).



Figure 4: waterproofing and thermal insulation of the basement area, walls and floor



Figure 5: injection into the zone of contact with the ground (STABILCEM, MAPESTOP, LAMPOCEM, MAPE-ANTIQUE INTONACO NHL)

All the existing walls were strengthened with 6 cm thick gunite concrete(a form of shotcrete in wich a dray cementitious mixture is blown trough a hose to the nozzle, with water injected only at the point of application) C 25/30 is used, and reinforced with mesh Q-424. In this way the bearing capacity of the existing walls was increased. The strengthening works and final appearance of the walls after the reconstruction are presented on Figure 6.

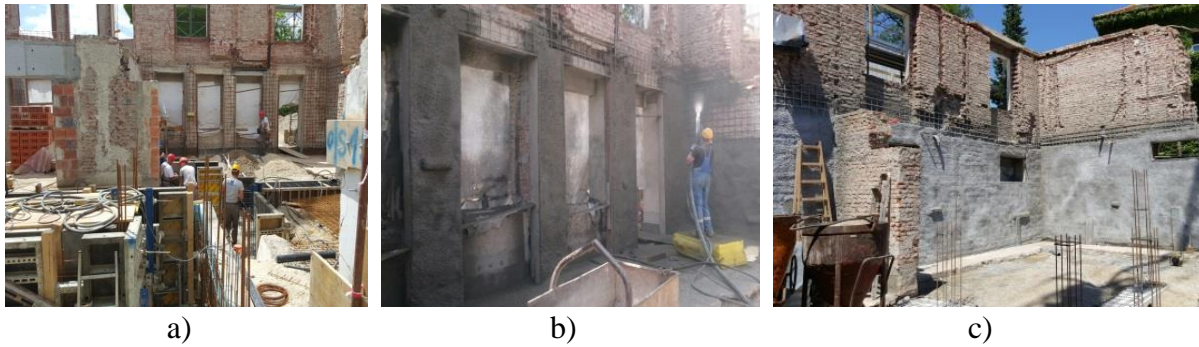


Figure 6: a) installation of the reinforcing mesh on the walls, b) the walls gunite concrete in progress , c) the walls after gunite concrete is done

Stabilization of surrounding ground together with fencing the yard was extremely demanding due to the neighbouring structures. Figure 7 presents preparation works and concreting of the foundations under the yard fence at the neighbour's border.

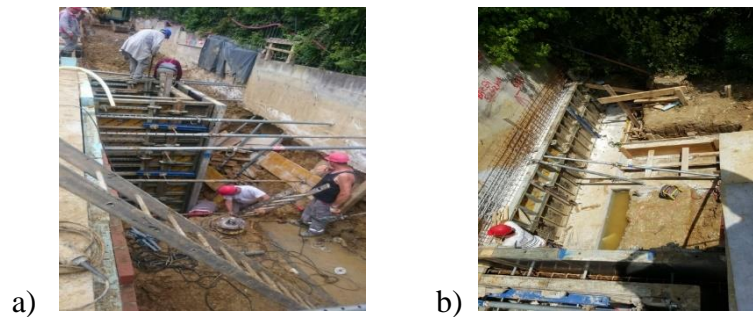


Figure 7: a) providing existing walls of the fall, b) concreting of the foundation of existing walls

The new partition walls are mended and the interior of the building took its final shape (Figure 8).

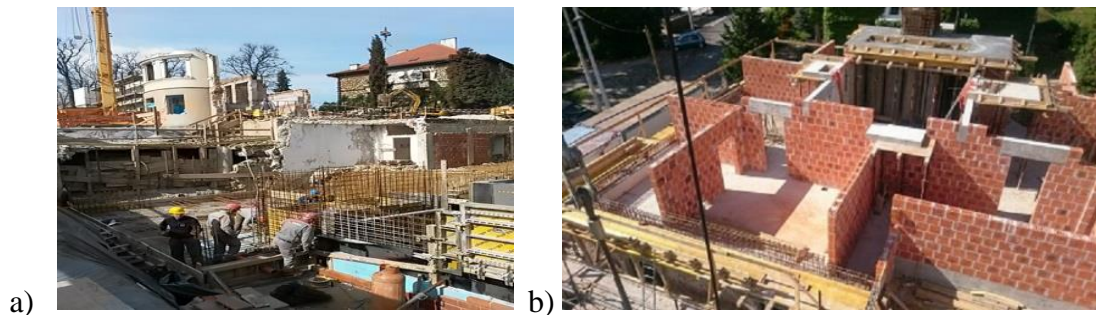


Figure 8: a) works on the construction of the walls of a new basement, b) the new partition walls

The house has basement, sur terre, ground floor and first floor. Most partition walls are of high quality brick, the suspended ceilings are mostly gypsum board and part of the walls where the bedrooms are. The whole house has underfloor heating.

All windows are of high quality triple glass. The house is energy efficient in its fullest sense. “Smart house“ system and KNX technology intelligent management, with its predefined home appliance control actions, saves energy, provides insight into consumption analysis, takes care of the safety, and provides absolute control and manageability over every element of this beautiful home. By implementing GIRA Home Server, it is possible to connect to your home, through visualization on smart devices such as tablets or mobile phones.

The temperature and the lighting for each room or throughout the house, as well as the position of venetian blinds, curtains and windows shades, can be adjusted at any time, from any location, either individually or according to the scenario, depending on your preferences, ie the position of the sun and the weather conditions.

Reconstruction was finished after 24 months and following are works on interior design and decoration. Significant efforts were put to reach high standards of a modern living in 100 years old structure. However, after the completion the appearance and features of the newly refurbished villa had justified all inputted efforts (Figure 9).

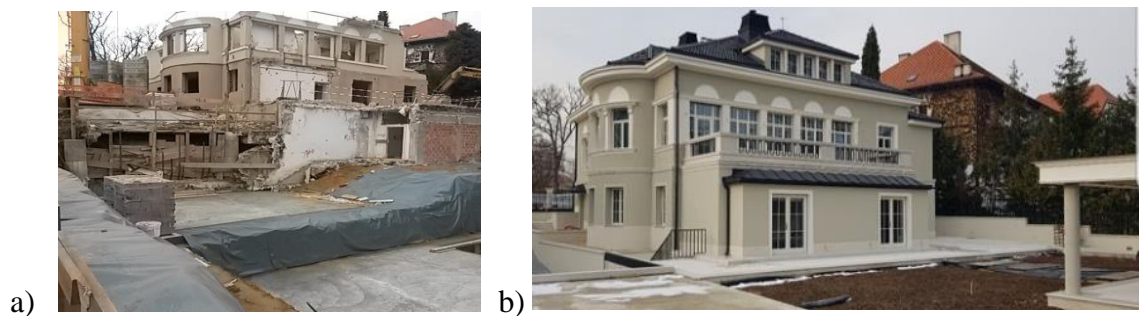


Figure 9: a) the beginning of reconstruction, b) completion of reconstruction

3. CONCLUSIONS

Reconstruction of a beautiful family villa built in the early 20th century in Zagreb presented a great challenge for all involved in the project. To assure its serviceability, stability and prolonged service life, together with complementing all Investors' needs large number of specialists were involved: experts for concrete, reinforcement, carpentry, insulation, installation, finishing works etc. All this has contributed to the successful completion of this demanding project.

AKNOWLEDGEMENTS

As a Project Manager and the main supervisory authority at all stages of the Project, I would like to thank you to my colleagues involved in the Project. Special thanks to the main project designer Mrs. Jadranka Polak, Blos d.o.o., Zagreb. I would also like to thank the main contractor for doing their job professionally and on time, especially I'm grateful to the Investors who were patience and respectful.

REFERENCES

- [1] Darja Radović Mahečić, Rad.Inst. povj.umj.33/2009 ((319-336), Cernelutti Family of Builders.
- [2] Angela Čuljak, „ PRAKTIČNI SAVJETI ZA POČETNIKE U GRAĐEVINARSTVU“ („Practical Tips for Beginners in Construction“), <https://www.prakticnisavjeti-gradjevinarstvo.com/>, Utjecajna linija j.d.o.o., 2018., Zagreb

INFLUENCE OF POUNDING ON SEISMIC PERFORMANCE OF EXISTING BUILDINGS IN THE CITY OF ZAGREB, CROATIA

Jakov Oreb (1), Božen Mušterić (1), Marta Šavor Novak (1) and Josip Atalić (1)

(1) Faculty of Civil Engineering, University of Zagreb, Croatia

Abstract

Many buildings in Zagreb were built before the first seismic codes appeared in the region, thus, the separation gaps between buildings were not constructed in accordance with modern seismic rules and regulations. Therefore, the aim of this study was to investigate potentially detrimental effect of pounding on the existing structures and consequently, improve current building seismic vulnerability database of the city, located in seismically active zone.

Several adjacent buildings were investigated, representing three categories: eccentrically located adjacent buildings, buildings in rows and buildings with different heights.

Three-dimensional numerical models of buildings were constructed on the basis of “as built” structures, calibrated with the results of ambient vibration testing. In everyday practice, adjacent buildings are often analysed as detached units. Therefore, results obtained by time-history analysis of numerical models with separation gaps defined as nonlinear link elements, were compared to the results of analyses performed using traditional methods (response spectrum and equivalent static forces) on adjoining buildings modelled as standalone structures and rigidly connected adjacent structures.

Analyses results show that pounding has different influence on analysed buildings from the three categories: eccentrically located adjacent buildings are the most threatened, followed by buildings with different heights, while buildings in rows are the least vulnerable.

Keywords: seismic performance, existing buildings, separation gaps, structural pounding, numerical models

1. INTRODUCTION

Pounding is the effect which often occurs during an earthquake in urban areas, due to insufficient and/or inadequately constructed separation gaps between buildings. Specific architecture, characteristic of Zagreb and Republic of Croatia, is very unfavourable regarding this issue. Some of those local specific features are construction of city blocks (Donji Grad), buildings in rows (residential buildings in various Zagreb districts) and eccentrically located adjacent buildings (such as Student dormitory Stjepan Radić). Moreover, most of the administrative buildings in Zagreb were built before the first seismic codes appeared in the

region (1964). Those codes introduced the term *seismic gap*. In a later period, “soft” material, such as polystyrene, was usually built in place of adjacent buildings’ separations. However, after the earthquake in El Asnam, Algeria (1980), it was shown that polystyrene has significant compression strength and does not decrease pounding, but instead transfers seismic forces between adjacent buildings [1].

Pounding may significantly modify building’s dynamic behaviour during seismic ground excitations, both in terms of relative displacements and of absolute accelerations; therefore, it must be considered for a proper evaluation of the its seismic performance. Therefore, a number of studies have been reported, especially after the 1985 Mexico City earthquake (Figure 1a). [2] Most of them were performed by using simplified models, starting from Anagnostopoulos 1988 [3], then over 2D and 3D archetypes, in which scientists varied different parameters such as layouts, *gap* elements characteristics, damping, structure-soil interaction, etc. It was shown that pounding was more probable when the soil was softer, and two structures were more different in terms of fundamental period. [4]



Figure 1: a) Examples of pounding effect during an earthquake [2]; b) photographs of separation gaps in analysed examples

Despite this extensive previous research [5], there are still many opened questions; among them, perhaps the most relevant is the lack of comprehensive analyses on pounding effect on real building examples. It was also motivation for this research, taking into account different modelling options of the separation gap that can develop a picture of the state and their impact with regard to the specific architecture of the City of Zagreb. Nowadays, there is no simple method of modelling gaps between adjacent buildings in everyday engineering practice. Therefore, in this study advanced dynamic analysis methods were used in ETABS 2015 software package. [6]

This investigation was conducted in the scope of study on seismic risk mitigation in the City of Zagreb [2], carried out in collaboration with the City Office of Emergency Management. Among many other topics, detailed numerical analyses of characteristic buildings, based on the models calibrated with ambient vibration measurements, are performed within the Study. In the early phases of the Study, some of the analysed existing buildings showed irregular dynamic behaviour around separation gaps and no correlation between experimentally obtained eigenmodes and the ones obtained numerically on standalone structures could be established. Therefore, it was decided that those buildings should be analysed in more detail, with the potential pounding effect. Because of the text length limitations, only two of those buildings will be presented in this paper: 1st pavilion in Student dormitory Stjepan Radić and residential building in Siget district (Figure 1b).

2. DESCRIPTION OF NUMERICAL MODELLING APPROACHES

2.1 Numerical model types

Several types of numerical models were constructed for each analysed building and each type represents the separate case of possible influence of adjacent building. Models are made in accordance with available documentation, visual building examination and conducted experimental field research. Although different analysis methods are used for model analysis, results will be compared in order to preliminarily determine the influence of separation gaps modelling on building response.

The first model type, *SOLO*, is a basic model which represents individual building or case where the building is in no interaction with adjacent buildings. It shows structural response without pounding effect.

The second model type, *TORS*, is individual building model, torsionally restrained in one vertical axis in place of separation gap. Restraints replace adjacent building and allow rotation of observed model around adjacent building as if the adjacent building was absolute rigid and motionless.

The third model type, *RIGD*, is adjacent buildings model rigidly connected with each other. Adjacent buildings behave as joint structure as if there were no separation gaps between them. These models represent a case where adjacent buildings act together during earthquake. There are two ways of modelling such structures. The first one is to model adjacent buildings, so they have a shared edge element (e.g. supporting wall) and the second one is to connect adjacent buildings' edge elements with rigid links.

The fourth model type, *MGAP*, is the most precise numerical model of investigated adjacent buildings in which buildings are connected with separation joints defined as *gap* elements (link elements which have nonlinear behaviour and cannot bear any tensions forces). Other characteristics of the *gap* element are the damping *C*, and stiffness *K* [5]. To conclude, *gap* elements, connecting structure joints, activate when two adjacent buildings approach each other (e.g. when vibrating out of phase) and deactivate when the buildings move away (tension phase). Pounding force is measured when the gap between structures is smaller than previously defined separation gap size, which represents an actual gap between buildings, estimated in field examination (Figure 1b).

2.2 Analysis methods

For simpler numerical models (*SOLO*, *TORS* and *RIGD*), linear response spectrum method was used, while nonlinear time history analysis was conducted for the more complex models with nonlinear link elements (*MGAP*), using ground acceleration time-histories. Although the valid national standard Eurocode 8 [7] demands the use of a minimum of three accelerograms, only one record was applied because the aim of this research was not to design a new building, but to compare different modelling approaches of existing structures. Seismic motion consisting of the two simultaneously acting accelerograms, used in this research, was generated to be compatible with the elastic design spectrum from the valid national standard, by adjusting recorded earthquake record Kalamata, Greece (1986.), taken from the European strong-motion database, available at <http://isesd.hi.is>. The original record already had similar characteristics with target elastic response spectrum, so its frequency content characteristics did not have to change significantly. Original record adjustment, including changing the record's frequency content, record scaling and baseline correction, was conducted in SeismoArtif program [8]. For

the comparison purposes, energy-dissipation capacities were not considered, so in every model analysed by response spectrum method, behaviour factor q was taken as 1,0 (original values from the early Study phases were between 1,5 and 3).

3. ANALYSIS RESULTS

Due to large amount of obtained data, only selected analysis results, such as axial forces in *gap* elements and shear forces in critical structural elements on the ground floor, will be presented in order to determine pounding influence.

3.1 Eccentrically located (floor plan irregular) adjacent building

1st pavilion of Student dormitory Stjepan Radić in Zagreb represents a characteristic eccentrically located building with irregular floor plan (Figure 2). It consists of two wings, bigger and smaller one, which are according to available information separated (the designer involved in the last reconstruction confirmed that the reinforcement does not continue for one wing to another). During a visual field examination, it was observed that the separation gap was concealed by facade, so the actual gap size could not be estimated. Therefore, extra models with different gap sizes were analysed (1 and 10 mm). Eight *gap* elements were placed in the contact corners of balcony and larger wing to represent the actual in situ state. All numerical models were analysed according to chapter 2.1. Figure 2 shows MGAP model and layout of the structural elements on the ground floor.

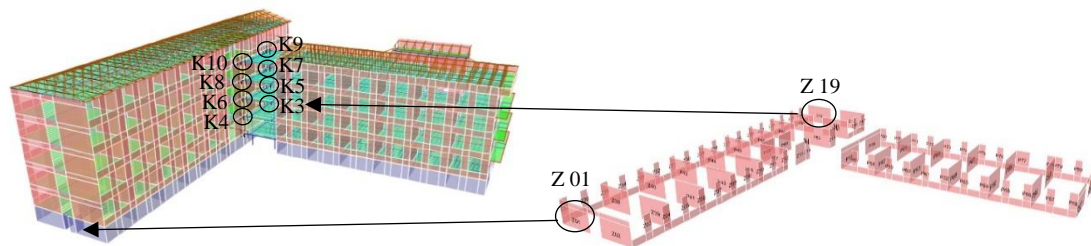


Figure 2: MGAP numerical model and ground floor (GF) structural layout

Table 1 shows forces in each of the 8 *gap* elements in the time step in which the total pounding force is the largest, amounting to 9348 kN for 1 mm gap and 8757 kN for 10 mm gap. Higher pounding forces generally occur on higher floor elements, thus confirming the logical assumption that pounding forces are bigger in higher parts of building due to greater displacements and accelerations than in lower parts. It is interesting to note that higher forces occur in the *gap* elements in the inner edge.

Table 1: Axial compression forces in *gap* elements [kN]

<i>gap</i> element (inner edge)	gap size		<i>gap</i> element (outer edge)	gap size	
	1 mm	10 mm		1 mm	10 mm
K4	-840	0	K3	-659	0
K6	-1587	-1262	K5	-1037	-940
K8	-1967	-1907	K7	-948	-1352
K10	-1875	-2063	K9	-434	-1233
Total				-9348 (1 mm)	-8757 (10 mm)

Table 2 shows shear forces in two critical walls in larger wing. When comparing SOLO and TORS models, there is a shear force increase in Z01 wall by 25% for TORS e.g. when smaller wing becomes a support for the bigger one. It is assumed that there is a real possibility of such case for this and every other similar building, where the eccentricity (floor plan irregularity) problem is expressed. There is also a shear force increase when comparing SOLO and RIGD models. Shear forces in Z01 wall is increased by 29% and in Z19 wall by 46%.

Table 2 Shear forces in critical wall elements [kN]

*comment: not relevant due to the vicinity of restraint

Pounding may influence the response of buildings in rows in, especially when they differ in dynamic characteristics. As an example of buildings in rows, residential building Siget 16 A-F, which comprises three units, in district Siget was chosen. All units are leaned on adjacent ones and space between them is filled, so there is no proper seismic gap between them. Two edge units are identical and the central one is slightly different due to a vehicle passage on ground floor.

Figure 3: Numerical model of three units in a row and *gap* elements marks; unit 3 GF layout

Table 3 shows forces in *gap* elements in two different time steps in which the total pounding force in each separation gap is the largest.

Table 3 Axial compression forces in *gap* elements [kN]

<i>gap</i> element in the left (1) <i>gap</i> *	actual state		<i>gap</i> element in the right (2) <i>gap</i> *	actual state	
	two units**	three units		two units**	three units
K25 (1)	-	-752	K4(2)	-1599	-1458
K26 (1)	-	-605	K5 (2)	-950	-880
K27 (1)	-	-524	K6 (2)	-1254	-1120
other (1)	-	-1237	other (2)	-4052	-2181
Total (1)	-	-3118	Total (2)	-7855	-5639

*number in brackets refers to the separation gap number of specific *gap* element

**two-unit model has only separation gap 2

In models with approximate state of equal stiffness of the adjacent units there are no pounding forces in *gap* elements, so there is no pounding at all, while in actual state models, there are pounding forces in separation gaps. It is important to note that the pounding does not occur simultaneously in both separation gaps in the model with three units, so the total pounding force cannot be obtained by summing up both values, but each gap must be analysed individually. Moreover, it may be noticed that the forces are higher in the second separation gap compared to first one, because of the larger displacements of the central unit in its vicinity.

When comparing two and three-unit models, total pounding force is larger in the case of two units. It is assumed that adjacent buildings in rows prevent each other's displacements and thus greater accelerations and pounding forces.

Table 4 shows that shear forces in critical wall elements for MGAP models with two and three units are nearly equal, because the unit layouts are not so different to cause larger change in shear forces.

Table 4 Shear force in critical elements [kN]; * comment: not relevant due to the vicinity of restraint

Model		Element	
		Z01 wall	Z02 wall
SOLO		+3061 / -3061	+6529 / -6487
TORS		+3937 / -3934	+174 / -149*
RIGD	Two units	+2648 / -2650	+7353 / -7383
	Three units	+2578 / -2581	+7193 / -7227
MGAP	Two units	+3434 / -2774	+6428 / -5848
	Three units	+3412 / -2762	+6498 / -5894

When comparing SOLO, TORS and RIGD models results, there is a significant shear force increase (29%) in Z01 element for TORS. It is assumed that above mentioned case will not occur in analysed building, but more detailed research is recommended for adjacent buildings where this possibility is more likely. The presented results show that there is no significant pounding in case of buildings in rows with equal stiffness because they oscillate in phase. Pounding only occurs when buildings vary in stiffness, but on much smaller level compared to eccentrically located adjacent buildings.

3.3 Buildings with different heights

Pounding is a serious problem for adjacent buildings with different heights. There are several possible cases, but in this research only two adjacent buildings with different heights and same

story levels were analysed. There were no such previous cases in current model database of [2], so initial Siget 16 A-F building model was chosen and modified. Two adjacent units were modelled with different number of stories. Following MGAP models were analysed: a) number of stories: G+4 (lower and higher ground stories + four upper stories) and G+8 (lower and higher ground stories and six upper stories) and b) number of stories: G+6 and G+8 (Figure 4). These models were compared to higher building SOLO model.

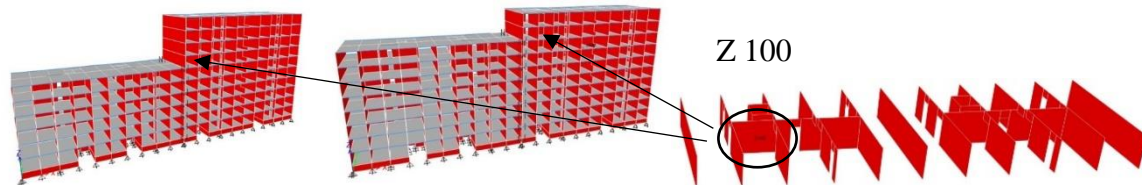


Figure 4: Numerical models with story numbers G+6 and G+8; position of the critical wall

Table 5 shows axial force value in *gap* elements on top two lower building stories, where pounding forces are the largest. Two *gap* elements were defined on each story.

Table 5 Axial compression forces in highest *gap* elements [kN]

Story	G+4 and G+8	Story	G+6 and G+8
3	-6195	5	-4428
	-5373		-3726
4	-4954	6	-3397
	-3682		-2529
Total	-20204	Total	-14080

Bigger pounding force occurs in case of G+4 and G+8 model. It is because difference in vibration period and modal shapes of buildings is greater compared to G+6 and G+8 model.

Table 6 shows that there is a shear force increase in the structural elements of the higher building story which is above the lower building top due to pounding effect, compared to the case when the higher building was analysed as standalone. Consequently, it could result in structural damages or even collapse of upper stories.

Table 6 Shear forces in critical element [kN]

Model	Story	Z100 wall	
		Building with possible pounding influence	Standalone building
G+4 and G+8	4	+3652 / -3159	+3349 / -3373
	5	+3178 / -3769	+2901 / -2704
G+6 and G+8	6	+2481 / -2165	+2329 / -2168
	7	+1891 / -2793	+1599 / -1524

4. CONCLUSION

Pounding between adjacent buildings generates additional forces which can cause structural damage near separation gaps and potentially a collapse. That problem is especially expressed in the case of eccentrically located adjacent buildings and buildings with different heights.

Eccentrically located adjacent buildings will almost certainly collide with each other during an earthquake because they vibrate out of phase. In numerical analyses, it can preliminary be assumed that for analysed standalone model, adequately placed supports may replace adjacent structure. Consequently, the torsional effect is increased which endangers bearing capacity of the most distant structural elements from the assumed supports.

Buildings with different heights are also vulnerable to pounding effect. Critically endangered structural elements are usually located on higher building above the roof level of a lower building. Damage caused during by impact can lead to structural failure and collapse of upper parts of a higher building, usually not designed for the additional pounding forces.

Buildings in rows with equal stiffness are the least threatened by pounding, because they vibrate in phase. This was also confirmed by obtained analysis results which demonstrated that there will be no pounding at all. However, it is difficult to have completely identical stiffness of adjacent buildings in real terms, because of various reconstruction works and space modifications in residential buildings. This problem is particularly evident in older buildings in urban areas such as Zagreb. Therefore, more conservative approach is recommended, and it can be concluded that seismic vulnerability of buildings in rows, especially the edge ones, will nevertheless increase.

An existing database of the Study [2] was upgraded with analysed and presented models, which will be available for further or more detailed research. The results are very valuable for analysing the characteristic Zagreb architecture, because it was shown that pounding can cause a significant increase in structural response (maybe even collapse), what was surely not accounted for during design and reconstruction processes of older buildings, which are a large part of the whole building stock.

REFERENCES

- [1] Bensafi, M., Pironneau G., Sieffert J.G., (1998), Pounding of a building against a rigid wall, 11th European Conference on Earthquake Engineering, Balkema, Rotterdam, ISBN 90 5410 982 3
- [2] Atalić J. et al. 'Study on seismic and post-earthquake safety assessment of buildings in Zagreb, Phases 1 – 5', (2013-2017) Faculty of Civil Engineering, Department of Engineering Mechanics
- [3] Anagnostopoulos SA (1992) "Pounding of buildings in series during earthquakes", *Earthquake Engineering & Structural Dynamics*, 33(8):897-902
- [4] Ghandil, M. and Aldaikh, H. (2016), Damage-based seismic planar pounding analysis of adjacent symmetric buildings considering inelastic structure-soil-structure interaction, *Earthquake Engng Struct. Dyn* 2017; 46: 1141-1159, DOI: 10.1002/eqe.2848
- [5] Lopez-Almansa, L. and Kharazian, A. (2014), Parametric study of the pounding effect between adjacent RC buildings with aligned slabs – Second European conference on earthquake engineering and seismology, Istanbul
- [6] CSI Analysis Reference Manual for SAP2000, ETABS, SAFE and CSiBridge, Computers and Structures, Berkeley, California, SAD, 2011.
- [7] HRN EN 1998-1:2011+/Ispr.2:2015+A1:2014+NA:2011, Eurocode 8: Design of structures for earthquake resistance – Part 1: General rules, seismic actions and rules for buildings (in Croatian), HZN, Zagreb, Hrvatska
- [8] Seismosoft, 'SeismoArtif (2016) – A computer program for generating artificial earthquake accelerograms matched to a specific target response spectrum', <http://www.seismosoft.com>

FUNDAMENTAL STUDY ON DETECTING INTERNAL DEFECT OF TIMBER DUE TO TERMITE AND ITS MECHANICAL IMPROVEMENT WITH RESIN

Akiko Ohtsuka (1), Kei-ichi Imamoto (2) and Chizuru Kiyohara (2)

(1) Faculty of Systems Science & Technology, Akita Prefectural University

(2) Faculty of Engineering, Tokyo University of Science

Abstract

In this study, a basic experiment was carried out with the aim of strengthening a timber member that was internally deteriorated due to termite's damage. Quantitative evaluation of this damage degree was proposed and the effect of reinforcing the inside part with resin and its non-destructive evaluation were verified. It is proved that the internal deterioration can be detected by the ultrasonic method. Meanwhile, improvement of the strength by resin filling increased the velocity of pulse of the ultrasonic. This might indicate that the strength improvement effect by the resin filling could be evaluated by ultrasonic method.

The authors clarified that internal deterioration can be confirmed in the ultrasonic wave propagation test, although the loading strength deteriorated at the deficiency ratio of 30% when a compressive loading test is performed on the simulated and degraded specimen. In this paper, the compressive strength test and the bending strength test of termite's damage specimen are carried out for development to real construction, and the ultrasonic test is examined about the usefulness in the deterioration diagnosis and confirmation of the reinforcing effect.

Keywords: wooden building, termite's damage, reinforcement, ultrasonic wave propagation velocity, resin filling

1. INTRODUCTION

Timber has been used for a long time in Japan, it is a structural material that is still widely used today. Meanwhile, humid environmental of Japan is one of the significant factors to promote the deterioration of timber, which may cause decay and termite's damage. In particular, in valuable wooden buildings that exist for many years, it is important to diagnose the decrease in strength due to deterioration. However, many of the condition assessment of timber structures of Japanese cultural heritage have been done by visual surveys. Evaluation by visual observation results in ambiguity in evaluation criteria. Furthermore, when deterioration does

not appear on the surface like termite's damage, and deterioration progresses only in the inside as shown in Photo 1, it is difficult to judge the deterioration. In Addition, the repair currently underway for cultural property buildings is classified into three categories: repair, maintenance, and basic repair depending on the damage situation¹⁾. At the repair of buildings, sound parts of buildings are retained, and deterioration parts are partially replaced by sound wood by traditional methods such as rooting. Furthermore, in recent years SRF (flexible super strengthening) method and the like which coat high performance fiber are also applied^{2), 3)}. However, with these methods there is a risk that the cultural and design value may be impaired, and there are cases where it is difficult to apply the above method to a member having a unique shape as shown in Photo 2. Meanwhile, the method of resin filling has been studied in recent years, since it is possible to keep the design shape by using the existing parts as much as possible^{5) 6)}. However, there is concern about the stability of reinforcement by resin filling. Furthermore, a method of confirming filling rate and reinforcing effect with a non-destructive manner has not been established yet.



Photo1: Internal degradation



Photo 2: Hikone Castle⁴⁾

2. PURPOSE AND CONTENTS OF RESEARCH

This study aims to propose a non-destructive assessment of the quantitative evaluation of the extent of damage and the effect of reinforcing the interior defect with resin, assuming members degraded internally by termite's damage. Although loading capacity of deteriorated timber specimen decreased significantly compared with the sound one, authors clarified that internal deterioration can be detected by ultrasonic wave propagation test. In this paper, compressive strength test and bending strength test of termite's damaged specimen were carried out, and the ultrasonic test was examined to verify the usefulness in deterioration diagnosis and confirmation of reinforcing effect by filling of resin.

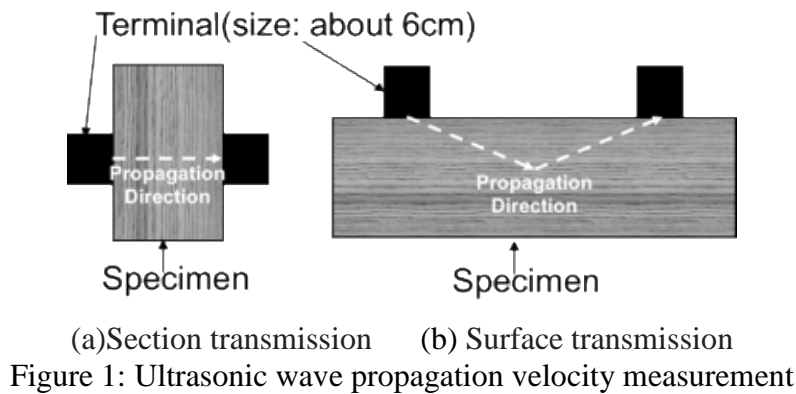
3. ULTRASONIC METHOD AND REINFORCEMENT METHOD WITH RESIN

3.1 Ultrasonic method

Regarding deterioration diagnosis of wood members, in addition to visual inspection and palpation, non/micro destructive test are used. Especially diagnostic equipment such as elastic and ultrasonic wave devices are available as an investigation tool for internal deterioration which is the main object of this research. The device evaluates internal state of wood by measuring the time taken for propagation of wave inside of wood.

If there are defects, voids and density changes, the attenuation of the ultrasonic wave will occur. Using this principle, authors measured the change in passing time due to the speed reduction and the detour of the wave through the deteriorated part of timber. There are several measurement methods for the ultrasonic wave propagation speed. Representative ones are

"Section transmission" and "Surface transmission". The section transmission method might contribute to judging the situation of internal deterioration state by measuring in the perpendicular direction to the member axis and the surface transmission would judge the condition of the surface by measuring in the parallel direction to the axis as shown in Figure 1.



3.2 Select filling materials

Regarding filling materials, literature survey on resin type, method of use and it's frequency was carried out with scientific papers^{5),7) -9)} and Public Interest Foundation Building Preservation Technology Association Database ¹⁰⁾. Table 2 shows the summary of the evaluation by the authors based on the survey results. In Table 2, symbol ⊙ and ○ mean the frequency of use was 30 or more and from 1 to 29 times, respectively. No symbol means no use example.

Epoxy resin was the most common type of resin used, and it was widely used for adhesion, filling and impregnation. Next was an acrylic resin and urethane resin. Focusing on reinforcement by filling and impregnation, epoxy resin and urethane resin were often used. Based on the preliminary tests, the epoxy resin and the polyamine resin were adopted in this study. The mixed two-component curable resin R was selected.

Table 2 - Types of resin and usage examples

Type	Adhesion	Filling	Impregnation
Epoxy	⊙	○	○
Urethane	—	○	⊙
Acrylic	○	—	○
Vinyl acetate	⊙	○	—
Urea	⊙	—	—
Polyester	—	—	○

Example of Use : ⊙over 30, ○1-29, — 0

4. COMPRESSIVE STRENGTH TEST

4.1 Outline of experiment

Authors carried out outdoor termite exposure test on pine wood for about 1 month from June to July. The 8 members with dimensions of $105 \times 105 \times 100$ mm were promoted for termite's damage and 2 members were prepared as references. Regarding the specimen for compression test, since the distribution of defects in the cross section is not uniform, the specimen with $105 \times 105 \times 100$ mm was cut out into similar group of deterioration with the size of $50 \times 50 \times 100$ mm. Photo 3 shows appearance of specimen. a) is a sound specimen, b) is a specimen after the termite's damage, c) is specimen cut from b) and d) is specimen after filling. As a feature of damaged member, eaten part is progressing along with ring from sapwood due to the inclusion of heart part, as shown in Photo 6-b).

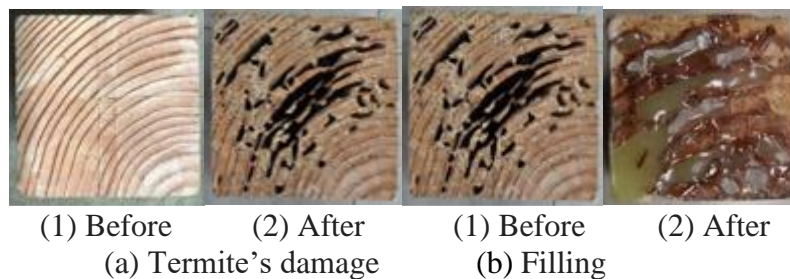


Photo 3: Specimen of termite's damage

4.2 Results of Compressive Strength Test on Termite's Damage

Figure 2 shows the result of compressive strength test. Compressive strength of termite's damaged specimen decreased by 25% compared with reference and improvement of the strength of repaired specimen with resin increased about 18%.

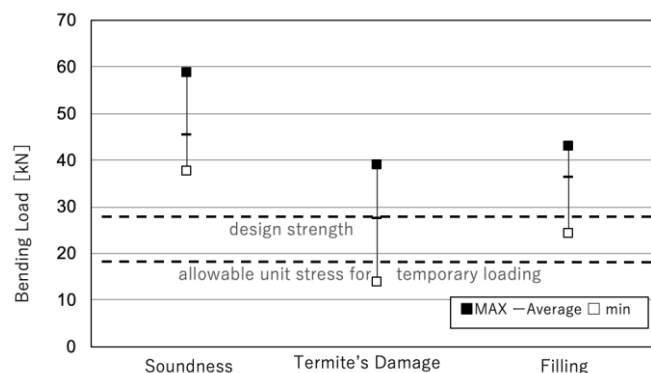


Figure 2 Result of compressive test

4.2 Evaluation of filling property of resin

Figure 3 shows relationship between the ultrasonic propagation velocity ratio and mass ratio based on the reference specimen. The correlation was as high as $R^2 = 0.84$, and it was considered that there is a possibility that the damage on the surface layer and the inside of termite's damage can be evaluated from the viewpoint of the mass ratio from the ultrasonic propagation speed ratio.

Figure 4 shows the relationship between mass ratio and speed ratio of a reinforced specimen by resin filling. The correlation coefficient R^2 was 0.80, indicating that the correlation between the filling situation and the speed ratio was high. It is suggested that the degree of resin filling can be evaluated by ultrasonic method.

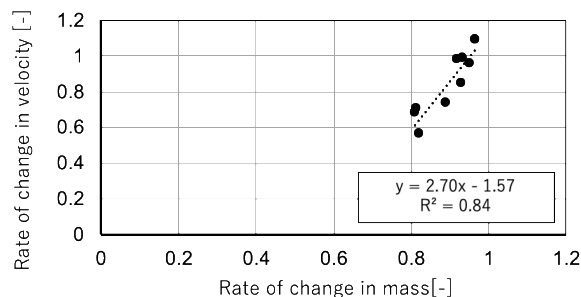


Figure 3: Rate of change in velocity-mass

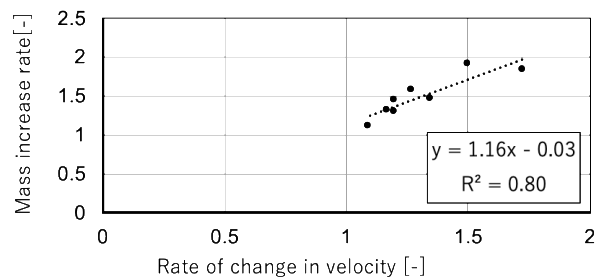


Figure 4: Rate of change in velocity-filling mass

5. BENDING STRENGTH TEST OF TERMITE'S MEMBER

5.1 Outline of Experiments

Due to the possibility of large pulls and foundations as parts to be harmed by termite's damage in wooden buildings, we decided to consider the reinforcement effect on bending. In this experiment, 13 pinewood specimens of $105 \times 105 \times 1000$ mm were prepared, three bodies were used as healthy materials, 10 ants were not harmed for the remaining 10 bodies, about 3 months from April to July, similar to the above outdoors Exposure was done. According to JIS Z 2101 (test method for wood), the bending strength test was carried out by a three-point load bending load test with a fulcrum distance of 800 mm. The outline of the test is shown in Figure 5.

As shown in Photo 4, prior to resin filling of the parts, the curing tape was attached to a part other than the upper surface, and ten upper and lower 10 holes were vertically staggered from one side to the side from the side with a drill.

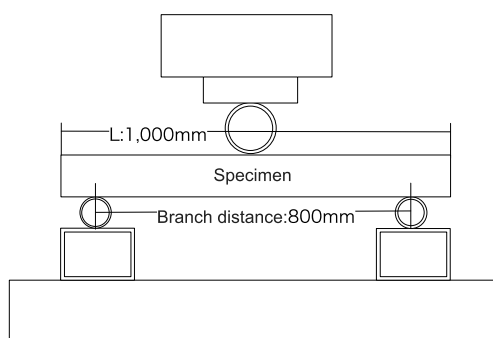


Figure 5: Outline Figure

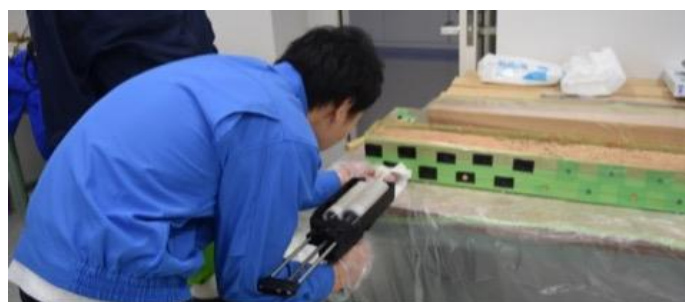


Photo 4: State of the filling

After curing of the resin, curing tape was peeled off and the ultrasonic wave propagation velocity was measured again. Photo 5 shows each test specimen before and after filling. Regarding the degree of filling, mass of the specimen after filling was 1.0 to 1.2 times higher than that of the specimen before termite's and 1.2 to 1.7 times higher than that of after termite's. From this fact, it was considered that the resin was sufficiently filled.



Photo 5: Specimen with termite's damage

5.2 Result of Bending Test

Figure6 shows the results of bending load test. Although the bending load of deteriorated specimen decreased by about 40% compared to that of the reference and about 20% load improvement was recognized by filling with resin. In specimen where the maximum load of the packing member was the minimum, the loaded surface was considered to be only tree surface side¹⁶⁾, and when it was excluded, the strength was increased by about 30%. In either case there was no strength restoring effect leading to the reference. The cause may be cracking due to lateral compression of the filler.

Ultrasonic test surface method was applied to the lower surface of the member affecting bending strength. And the ultrasonic propagation velocity was measured with the terminals distance at 200 mm. Figure7 shows the bending load and ultrasonic wave propagation speed by the surface method. It was difficult to judge that the bending strength can be estimated with only this data. Further research will continue to collect the data.

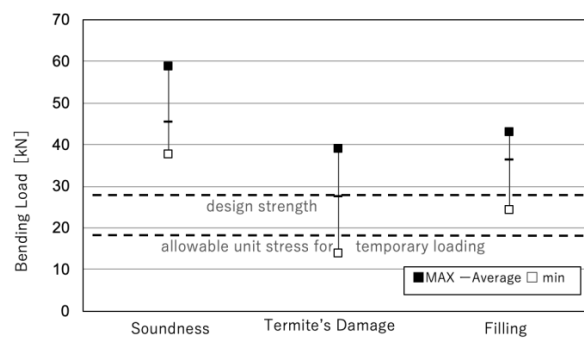


Figure 6: Result of bending test

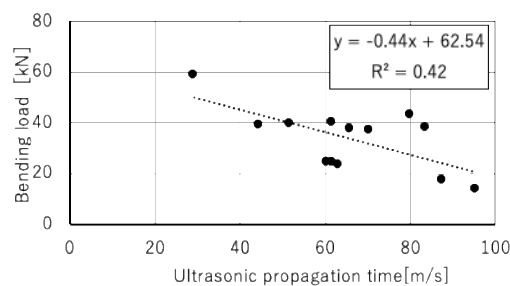


Figure 7: Bending load- ultrasonic propagation time

Figure 8 shows the relationship between bending load and displacement. When comparing the bending stiffness, a sound specimen exhibited highest value (7.7kN/mm^2) followed by a packed specimen (4.9kN/mm^2) and an anesthesia test specimen (2.1kN/mm^2). It was confirmed that recovering of the bending Young's modulus was attained to a certain extent. From the above, although the bending reinforcement by filling had certain effectiveness, its effect was considered to be limited.

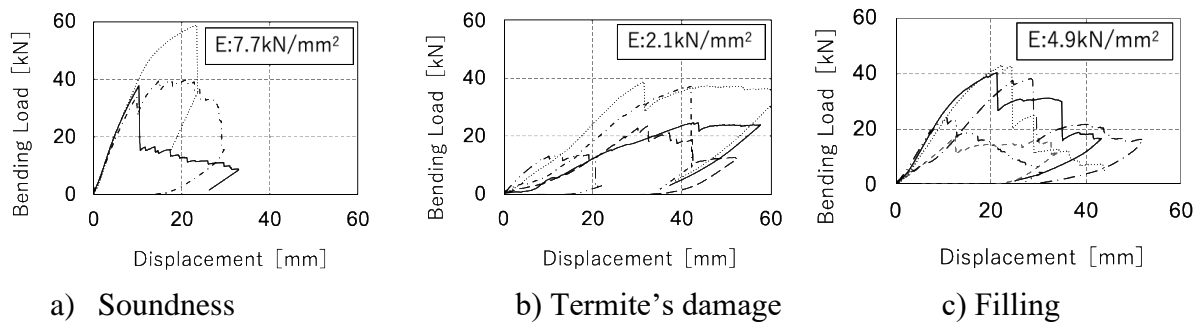


Figure 8: Bending load-displacement

5.3 Degradation Exploration

A comparison between antitoxic test specimens and references by the transmission method of ultrasonic testing is shown in Figure 9. Target specimens that can measure at least seven points on one side are shown and their average values are also shown. It was understood that the propagation speed decreased by 50% as average on the termite's damage specimen compared with the reference. Since the propagation speed decreased with the increase of number of internal voids, there was a possibility that a defect due to termite's damage was confirmed.

5.4 Evaluation of filling property of resin

Figure 10 shows the relationship of the ultrasonic propagation speed by the transmission method before and after resin filling. It can be seen that the speed increased from 150% to 240% with the filling. Moreover, the mass measurement of resin filled specimen was 1.0 to 1.2 times of the specimen before the termite's damage, and 1.2 to 1.7 times for the specimen after termite's damage. In conclusion, it can be said that it is possible to confirm the state of resin filling using the transmission method of ultrasonic testing.

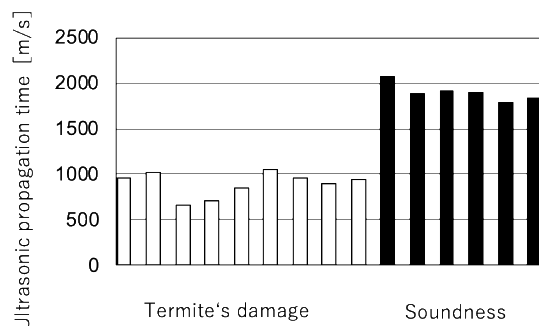


Figure 9: Rate of change in velocity-mass

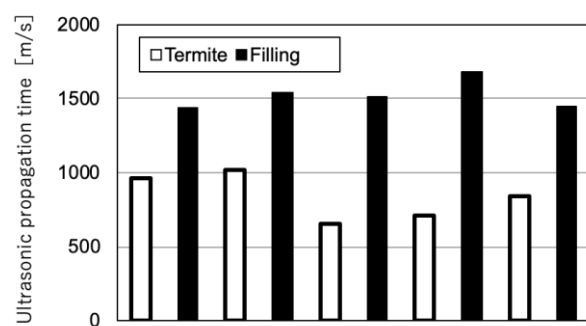


Figure 10 : Rate of change in velocity-filling mass

6. CONCLUSION

In this study, cross-sectional defects caused by internal degradation due to termite was focused. Authors investigated the internal defect and resin filling situation by ultrasonic wave velocity, and the reinforcement effect by resin filling. The findings obtained in this research can be summarized as:

1. A high correlation was found between propagation velocity ratio, mass ratio and filling condition in internally deteriorated timber due to termite in terms of compressive strength. Although this is a limited termite's damage test specimen, it was suggested that the damage of the surface layer and the inside due to termite might be evaluated from the viewpoint of the mass ratio;
2. Reinforcing effect of resin for timber member with termite's damage was evaluated from the viewpoints of compressive strength and bending Young's modulus. It was confirmed that the filling condition could be evaluated by ultrasonic surface method.

In the future, it would be necessary to continue studying to improve not only the bending performance of deteriorated member but also structural performance of the actual member.

REFERENCES

- [1] Counselor of Cultural Heritage (Responsible of buildings), Aiming for progress in conservation and utilization of national treasures and important cultural property buildings, Agency for Cultural Affairs, 2013
- [2] Takenouchi Y. et al. Study on the Deterioration of Synthetic Resins Used in the Restoration of Wooden Buildings. *Science for conservation* (37), 124-136, 1998
- [3] Higuchi S.: A Retrospection: Early Examples of the Application of Synthetic Resins for the Conservation of Japanese Cultural Properties, *Senri Ethnological Reports*, 36, 2003
- [4] [Wooden buildings.com](http://www.woodenbuildings.com/) /access 2018.6.8
- [5] Yoshitake S. et al.: Terminated timber for structural use: mechanical defects and reinforcement, AIJ Kyushu Chapter architectural research meeting, pp 3-10, 2007
- [6] Karube M. et al.: Repair and the effect of decompression filling of epoxy adhesive of GLT beam-to-column drift pin joint: AIJ J. *Journal of technology and design*, 20, pp 93-98, 2004
- [7] Takenouchi Y. et al.: Survey of Synthetic Resins Applied for the Conservation of Japanese Buildings, *Science for conservation* (37), pp 99-123, 1998
- [8] Kataoka Y. et al.: Evaluation of structural material performance of relocated old building, AIJ Tokai Chapter Architectural Research Meeting, 31, pp 205-208, 1993
- [9] Noguchi M. et al.: The compressive strength of the terminated timber, *Journal of structural engineering*, 54B, pp. 171-176, 2008
- [10] The Japanese Association for Conservation of Architectural Monuments Database
<http://www.bunkenkyo.or.jp/archive-site/index.html>

ADVANCES IN DURABILITY MONITORING OF CONCRETE STRUCTURES

Ueli M. Angst (1)

(1) ETH Zurich, Institute for Building Materials, Zurich, Switzerland

Abstract

In order to safely, cost-efficiently, and sustainably maintain our ageing reinforced concrete infrastructures, there is a need for reliable methods to assess and monitor the condition and deterioration of these structures. Major parameters governing the initiation of reinforcing steel corrosion in concrete are the pH and the chloride concentration of the concrete pore solution. So far, the non-destructive in-situ measurement of these parameters was not possible. Here a novel sensor system allowing the determination of these crucial variables is presented.

Once corrosion has initiated, the rate at which the steel sectional loss occurs is crucial for estimating the residual service life, and ultimately to determine the time until an intervention (repair, replacement, etc.) is needed. This contribution presents a recently developed method based on acquiring and processing alternating current signals recorded in the time domain. Thanks to a refined approach of signal processing, this robust approach is capable of delivering in short time a number of parameters relevant for the kinetics of a corroding system.

These recent advances in the field of measuring methods and sensors are discussed in the context of structural health (durability) monitoring, both regarding the initiation and the propagation stage.

Keywords: reinforced concrete; corrosion; monitoring; pH; chlorides; corrosion rate

1. INTRODUCTION

All industrialized countries will in the coming decades be challenged to safely, cost-efficiently, and sustainably maintain their built infrastructure [1, 2]. An increasing number of reinforced and pre-stressed concrete structures will potentially suffer from corrosion. Based on recent modeling efforts, it was estimated that the number of structures needing repair in the coming decades will increase by a factor of 2–5 [3]. However, already today, many countries struggle with maintaining their infrastructures. For instance, it was recently reported that in Germany, over a period of 18 months in the years 2015–2016, the condition of 5968 bridges could be improved thanks to maintenance work, while at the same time the condition of 8747 bridges worsened due to ageing and deterioration [4]. This means that the bridges in Germany, and likely many other industrialized countries as well, cannot be maintained as fast as they degrade. Apart from the implications of this in terms of safety and availability of infrastructures, the need to repair corroding concrete structures also has a huge economic impact [2, 5]. In the European Union alone, the direct costs arising from corrosion of reinforced and prestressed concrete structures is estimated at EUR 25–50 billions *annually*.

Thus, we urgently need to enhance the technologies to more cost-efficiently ensure the safety of our infrastructures. This also has to occur in the context of increasing environmental awareness. The first step in infrastructure maintenance is the assessment of the condition. This is the basis to decide on adequate maintenance strategies and to schedule repair works (“the right method at the right time and at the right locations within a structure”). The better the quality of the condition assessment, the better the basis to derive adequate maintenance strategies. Monitoring the relevant durability parameters on-site has a large potential to improve diagnosing the condition of infrastructures, before measures are taken. This paper presents two examples of recent advances made in the field of measuring methods and sensors for the durability of reinforced concrete structures.

2. MONITORING PH AND CHLORIDE CONCENTRATIONS IN-SITU

The two most important parameters of the concrete pore solution chemistry affecting corrosion of reinforcing steel are the pH and the chloride concentration.

The pH of the pore liquid surrounding the reinforcing steel, that is, at the cover depth, is typically in the highly alkaline range (above pH 12–13), thus ensuring steel passivity [6]. During the service life of a structure, the pH may decrease depending on the exposure condition. If the pH decreases sufficiently, the passive film will not be stable which may lead to active corrosion. Loss of alkalinity may occur due to carbonation, leaching, etc. Traditionally, this is tested by means of using indicator solutions (e.g. phenolphthalein, thymolphthalein) that are sprayed on broken cores retrieved from the structure. This engineering approach, that is widely used in condition assessments, allows to distinguish alkaline concrete (pH > 9–10) from non-alkaline concrete (pH < 9–10). The method, however, provides no information about the actual pH, which means that especially pH changes occurring in the range from 14 down to 10 cannot be detected.

Chlorides may be present in the concrete already at the time of construction, because national standards tolerate some admixed chlorides. The tolerable amount of admixed chlorides is typically in the range 0.2–0.4% acid-soluble chloride by cement weight. This will lead to relatively low (typically considered “negligible”) concentrations of free chlorides. If structures are exposed to chloride-bearing environments, the penetration of chlorides through the concrete

cover will raise the concentration of chlorides at the steel depth over time. It is well known, that this may lead to corrosion initiation [6]. The threshold chloride concentration needed to trigger corrosion, however, scatters widely in the literature [7]. This is typically explained by the variability in test methods used [7], the highly variable properties of the steel-concrete interface [8], or the pH of the pore solution [9-11]. However, as discussed above, the latter can hardly be measured in most experimental setups and particularly on-site.

Thus, recent advances in sensor technology, delivering a sensor for the measurement of both pH and chloride concentrations in concrete, is considered a valuable contribution to the existing array of tools available to study corrosion in concrete [12]. The approach is based on potentiometric sensors, namely silver/silver chloride ion selective electrodes (to measure chlorides) [13-16] and iridium oxide electrodes (to measure the pH) [17, 18]. The main originality of the approach is that through the combined use of different of these electrodes, together with a calculation procedure, the sensor does not need a reference electrode. This is crucial because i) all existing embeddable reference electrodes for concrete are known to have, on the long-term, issues with stability [19], and ii), because potentiometric chloride and pH measurements are highly sensitive towards uncertainties in the potential measurement [20, 21].

Figure 1 shows an example of the application of these sensors in mortar samples when exposed to accelerated carbonation conditions. The data reveals how the pH drops at different times depending on the cover depth. Moreover, and probably most importantly, the novel sensor technology allows quantifying the pH at a given time rather than only distinguishing between non-carbonated and carbonated states. This reveals interesting features, such as the stepwise decrease in pH, first down to approx. 12.5, where the pH is buffered by the Portlandite reserve, following by a steep decrease down to approx. pH 9. It is also interesting to note the time during which the pH stays at approx. 12.5: At a shallow cover depth, this time is relatively short, while it increases with cover depth. This can be explained by the increasingly delayed transport of CO_2 with increasing cover depth, decreasing the rate at which the Portlandite reserve (presumably the same at different cover depths) is consumed [12, 18].

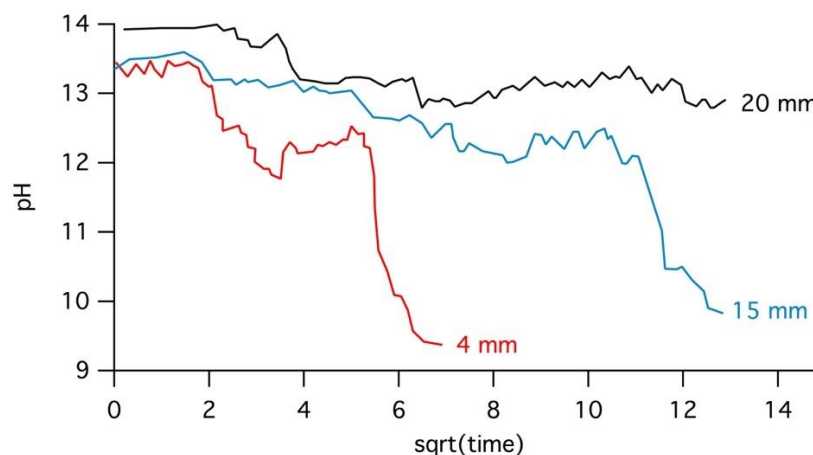


Figure 1: Example of pH measurements in mortar by means of embedded sensors. The different curves show the pH over time at different cover depths, during accelerated carbonation (65%RH, 21°C and 4% CO_2) of mortar samples [12, 18].

Figure 2 shows an example of the simultaneous measurement of pH and chloride concentration during exposure to accelerated carbonation conditions. The sample contained 0.5% admixed chloride, which is of the order of the tolerable amount of chlorides in fresh concrete. The measured data reveals that upon carbonation, the free chloride concentration increased, which can be explained by a release of bound chlorides [22]. The data also shows that although the pH was still alkaline (above 12) after 180 days of exposure, the Cl^-/OH^- ratio was raised clearly above 0.6, which may be considered a critical value for corrosion onset [9].

It is believed that employing these sensors in corrosion studies of reinforcing steel in concrete will contribute to elucidating the mechanism of corrosion initiation in more detail. For instance, the measurement of the pH at the cover depth, resolving differences in the alkaline range, may explain part of the huge scatter in chloride threshold values. Finally, applying these sensors in monitoring of structures would also be highly valuable as it allows measuring the most relevant parameters for corrosion, that is, the pH and the chloride concentration.

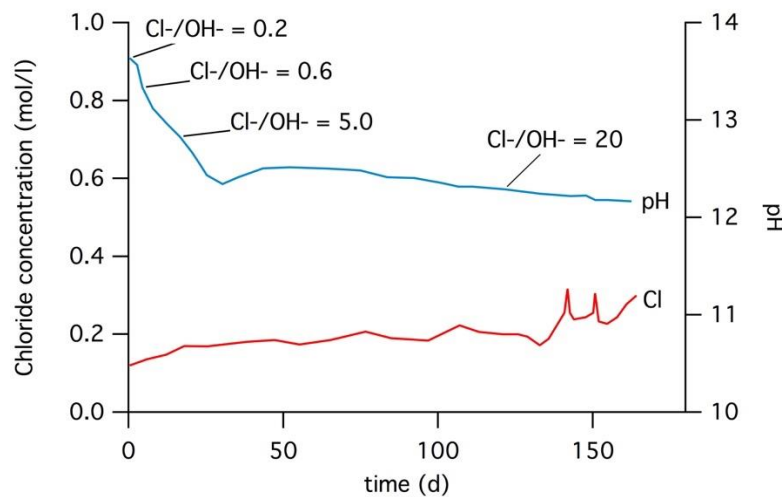


Figure 2: Example of simultaneous pH (blue) and chloride concentration (red) measurements in mortar by means of embedded sensors [23]. The mortar contained 0.5% admixed chloride by mass of cement (Portland cement). While the pH decreased during accelerated carbonation (65%RH, 21°C and 4% CO_2), bound chlorides were released which increased the chloride concentration in the pore solution. The Cl^-/OH^- ratio is indicated at selected times.

2. CORROSION RATE MEASUREMENTS

Measurements of the instantaneous corrosion rate of steel in concrete have long been subject to controversial discussions [24, 25]. For implementation in practice, that is, applying these methods in condition assessments, it is also important to consider that one single measurement typically takes much longer than e.g. potential or concrete resistivity measurements. Recently, a novel approach to measure corrosion rates has been proposed by the present author; the method is in detail described in [26]. The approach is based on stimulating the corroding system with an AC voltage perturbation signal, and recording the current response in the time domain. Subsequently, the data is treated with a computational procedure to remove non-faradaic

currents and to derive the corrosion rate as well as other parameters. The measurement can be performed at frequencies of the order of 100 mHz (or higher), which allows to acquire the relevant information in short time (a few seconds). Figure 3 shows an example of this, when applied to a carbon steel coupon (1 cm^2) embedded in chloride containing mortar (CEM I, $w/c=0.6$, cement:sand=2:1, sand < 4mm, admixed chloride: 4% by mass of cement).

Figure 3b shows the corresponding Lissajous-plot both in terms of recorded signal and after computationally correcting for non-faradaic currents. The green line shows the resulting faradaic component, the dashed black line is the fitted linear curve from which the polarization resistance is derived.

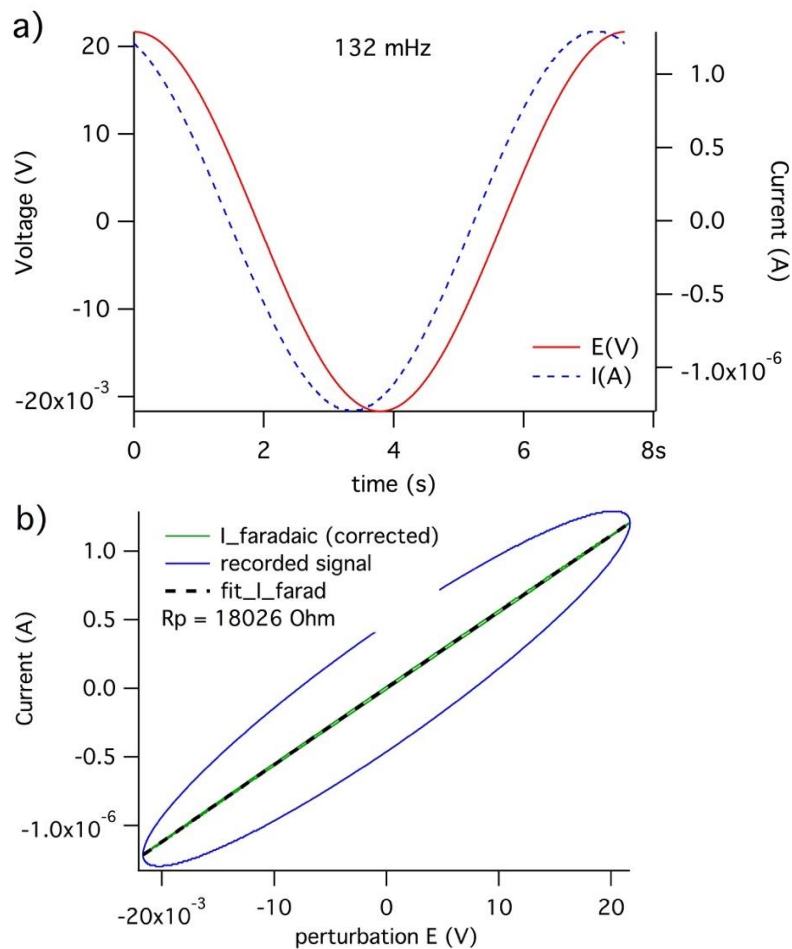


Figure 3: a) example of a perturbing AC voltage signal (amplitude 21 mV) and the recorded current response in the time domain; exhibiting a phase shift of 21° ; b) corresponding Lissajous plot and computationally corrected data (non-faradaic currents removed) with the fitted polarization resistance.

In addition, the procedure suggested in [26] includes Fourier Transformation of the obtained faradaic current signal in the time domain to the frequency domain. Harmonic analysis of the

resulting data is then carried out to again derive the corrosion rate as well as estimates of the anodic and cathodic Tafel slopes. The latter can be used to compute the proportionality constant needed to convert polarization resistance (obtained from the Lissajous analysis described above) to corrosion rate.

Figure 4 compares the results of this with different techniques to measure the instantaneous corrosion rate. All the results were obtained from measurements on the sample described above within the same day. LPR means linear polarization resistance, which is here understood as a potentiodynamic sweep around the open circuit potential. Different sweep rates in the range 0.005 – 1 mV/s were investigated; the plot shows the result obtained at 0.05 mV/s, which is in the range of the recommendations made in [27], the whiskers indicate the scatter arising from varying the sweep rate. EIS means electrochemical impedance spectroscopy and pulse means galvanostatic pulse measurements in combination with analyzing the transient with an equivalent circuit (simplified Randles circuit).

The comparison reveals that EIS and pulse measurements find good agreement with the proposed AC techniques, that is, the Lissajous analysis and the harmonic analysis (HA) of the recorded system response. LPR on the other hand seems to yield lower corrosion rates even at rather high sweep rates. Figure 4 also indicates the time needed for the measurement. While LPR and particularly EIS may take several minutes or even hours (thus not feasible in full surface mapping approaches in condition assessment of structures), the galvanostatic pulse technique and the proposed AC techniques take very short time. The advantage of the AC technique compared to galvanostatic pulse measurements is that based on the data recorded within 8 s (here at 132 mHz) different *independent* (based on different principles) analyses can be performed that give two estimates for the corrosion rate and thus increase redundancy and robustness of the result. In addition, the analyses also deliver estimates for the anodic and cathodic Tafel slope as well as for the capacitance, thus permitting to cross-validate the results.

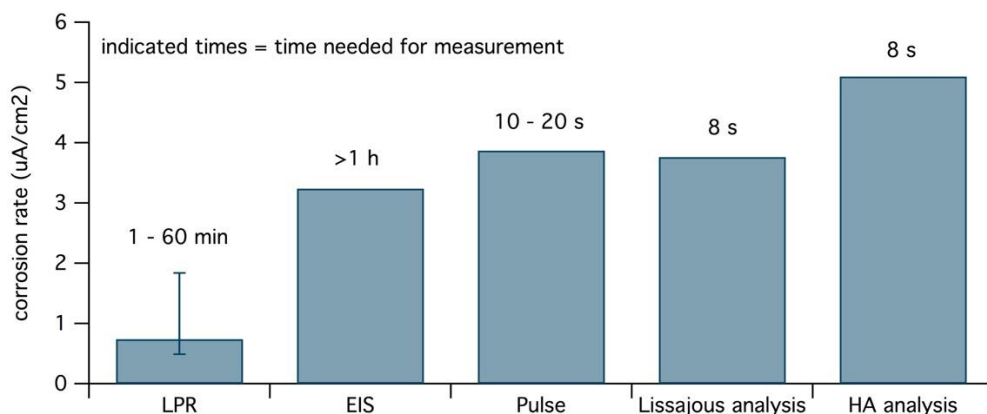


Figure 4: Comparison of different techniques to measure corrosion rates of a carbon steel coupon in chloride-containing mortar. The variability of the LPR method comes from testing different scan rates (highest shown i_{corr} was obtained at 1 mV/s, the lowest at 0.005 mV/s).

Electrochemical impedance spectroscopy, galvanostatic pulse and the here proposed alternating current methods find good agreement. Additionally, these measurements are significantly faster than most of the other techniques.

3. CONCLUSIONS

This paper presents a novel sensor system for pH and chloride in concrete and an innovative method to measure instantaneous corrosion rates. While both approaches may find many applications in research studies, they also offer new opportunities in monitoring the durability of ageing, potentially corroding reinforced concrete structures (pH and chloride sensors) as well as in the condition assessment of corroding structures (corrosion rate measurements).

REFERENCES

- [1] U. M. Angst, R. D. Hooton, J. Marchand, C. L. Page, R. J. Flatt, B. Elsener, C. Gehlen and J. Gulikers (2012) Present and future durability challenges for reinforced concrete structures. *Mater. Corros.* 63(12):1047-1051
- [2] U. M. Angst (2018) Challenges and opportunities in corrosion of steel in concrete. *Mater Struct* 51(4)
- [3] R. Polder, W. H. A. Peelen and W. Courage (2012) Non-traditional assessment and maintenance methods for aging concrete structures -technical and non-technical issues. *Mater. Corros.* 63(12):1147-1153
- [4] L.-M. NAGEL, M. PAULY, V. MUCHA, J. SETZER and F. WILHELM (2016) Wettlauf gegen den Verfall. *Die Welt*, 12. Juli 2016.
- [5] (2016) IMPACT: International measures of prevention, application, and economics of corrosion technologies study (<http://impact.nace.org/>). NACE Int.,
- [6] L. Bertolini, B. Elsener, P. Pedersen, E. Redaelli and R. Polder (2013) *Corrosion of Steel in Concrete: Prevention, Diagnosis, Repair* (2nd Edition). WILEY VCH, Weinheim.
- [7] U. Angst, B. Elsener, C. K. Larsen and Ø. Vennesland (2009) Critical chloride content in reinforced concrete - A review. *Cem. Concr. Res.* 39:1122-1138
- [8] U. M. Angst, M. R. Geiker, A. Michel, C. Gehlen, H. Wong, O. B. Isgor, B. Elsener, C. M. Hansson, R. Francois, K. Hornbostel, R. Polder, M. C. Alonso, M. Sanchez, M. J. Correia, M. Criado, A. Sagues and N. Buenfeld (2017) The steel-concrete interface. *Mater Struct* 50(2)
- [9] D. A. Hausmann (1967) Steel corrosion in concrete. How does it occur? *Mater. Protection* 6:19-23
- [10] V. K. Gouda (1970) Corrosion and corrosion inhibition of reinforcing steel. I. Immersed in alkaline solutions. *Br. Corros. J.* 5:198-203
- [11] V. K. Gouda and W. Y. Halaka (1970) Corrosion and corrosion inhibition of reinforcing steel. II. Embedded in concrete. *Br. Corros. J.* 5:204-208
- [12] Y. Seguí Femenias (2017) Electrochemical durability monitoring in reinforced concrete (DISS. ETH NO. 24669). Dissertation. ETH Zurich, Switzerland
- [13] Y. Femenias, U. Angst, F. Caruso and B. Elsener (2016) Ag/AgCl ion-selective electrodes in neutral and alkaline environments containing interfering ions. *Mater Struct* 49:2637-2651
- [14] U. Angst, B. Elsener, C. K. Larsen and Ø. Vennesland (2010) Potentiometric determination of the chloride ion activity in cement based materials. *J Appl Electrochem* 40(3):561-573
- [15] B. Elsener, L. Zimmermann and H. Böhni (2003) Non destructive determination of the free chloride content in cement based materials. *Mater Corros* 54:440-446
- [16] A. Hidalgo, G. De Vera, M. A. Climent, C. Andrade and C. Alonso (2001) Measurements of chloride activity coefficients in real portland cement paste pore solutions. *J. Am. Ceram. Soc.* 84(12):3008-3012
- [17] Y. Femenias, U. Angst and B. Elsener (2017) Monitoring pH in corrosion engineering by means of thermally-produced iridium oxide electrodes. *Mater Corros* 69:76-88

- [18] Y. S. Femenias, U. Angst and B. Elsener (2017) PH-monitoring in mortar with thermally-oxidized iridium electrodes. *RILEM Techn Lett* 2:59-66
- [19] R. Myrdal (2007) The electrochemistry and characteristics of embeddable reference electrodes for concrete. Woodhead Publishing Limited and Maney Publishing, Cambridge, England.
- [20] U. Angst and Ø. Vennesland (2009) Detecting critical chloride content in concrete using embedded ion selective electrodes - effect of liquid junction and membrane potentials. *Mater Corros* 60(8):638-643
- [21] J. Koryta (1972) Theory and applications of ion-selective electrodes. *Anal Chim Acta* 61(3):329-411
- [22] B. Reddy, G. K. Glass, P. J. Lim and N. R. Buenfeld (2002) On the corrosion risk presented by chloride bound in concrete. 24(1):1-5
- [23] Y. S. Femenias, U. Angst, F. Moro and B. Elsener (2018) Development of a novel methodology to assess the corrosion threshold in concrete based on simultaneous monitoring of pH and free chloride concentration. *Sensors* 18:3101
- [24] P. V. Nygaard and M. R. Geiker (2012) Measuring the corrosion rate of steel in concrete - effect of measurement technique, polarisation time and current. *Mater. Corros.* 63(3):200-214
- [25] U. Angst and M. Büchler (2015) On the applicability of the Stern-Geary relationship to determine instantaneous corrosion rates in macro-cell corrosion. *Mater. Corros.* 66(10):1017-1028
- [26] U. M. Angst and B. Elsener (2014) Measuring corrosion rates: A novel AC method based on processing and analysing signals recorded in the time domain. *Corros. Sci.* 89(0):307-317
- [27] C. Andrade, C. Alonso, J. Gulikers, R. Polder, R. Cigna, Ø. Vennesland, M. Salta, A. Raharinaivo and B. Elsener (2004) Recommendation of RILEM TC 154-EMC: "Test methods for on-site corrosion rate measurement of steel reinforcement in concrete by means of the polarization resistance method". *Mater. Struct.* 37(273):623-643

DEVELOPMENT OF A MULTIFUNCTIONAL CONCRETE WITH CARBON SENSOR

Paulo Cachim (1) and Emanuel Pereira (2)

(1) RISCO & Department of Civil Engineering, University of Aveiro, Portugal

(2) Department of Civil Engineering, University of Aveiro, Portugal

Abstract

Global demand for increasing of behavior of civil engineering structures and infrastructures, combined with the developments on monitoring systems, has lead, in recent years, to the so-called smart infrastructures. Among these, traffic management has received special attention with the development of the Intelligent Transport Systems. Advances in material technology that occurred in last years conducted to the development of smart multifunctioning construction materials that can, autonomously, perform a variety of tasks. With suitable compositions, cement composites can be used, due to their specific conductive properties changes, in monitoring systems because of their intrinsic properties of sensitivity to mechanical stimulus, based in the piezoresistivity principle. This research aims to develop a multifunctional cementitious concrete materials capable of structural monitoring. This is achieved by using a piezoresistive cement composite with carbon black for application on road pavements that aims to assess traffic data in real time. Compressive static and dynamic tests have shown that, through electrical resistivity monitoring of the samples, high sensitive factors were observed with a linear response. These responses are not affected by temperature changes. As a conclusion, this study states that incorporation of sensitive concrete near the pavement surface can be a feasible alternative for traditional traffic monitoring solutions. The main advantages of this solution are its low cost, simplicity, structural properties and sensitivity.

Keywords: multifunctional concrete, carbon black, piezoresistivity

1. INTRODUCTION

Monitoring civil engineering infrastructures has becoming a trend in recent years. This monitoring has been mainly related with maintenance of structural performance through monitoring of stresses and deformations of buildings, bridges, roads or dams, for example. When applied to infrastructures like roads, this monitoring allows a more sustainable and

efficient management and logistics of these infrastructures, , reducing costs and preventing eventual losses with appropriate interventions. Nevertheless, the high implementation cost into large scale structures has been a bottleneck for conventional sensing systems.

Alongside the traditional sensors, such as optic fiber, potentiometers or strain gauges, a new technology has been developed during the last years, based on the piezoresistivity principle and cement-based compositions. Piezoresistivity is the property that defines the dependence of the electrical resistivity of a certain material to its deformation. The resistivity depends on the disposition of the material particles, being bigger as closer they are disposed, because current can flow through the material easier. Therefore, compressing an element can, in principle, increase the electrical conductivity and, consequently, decrease the resistivity.

The use of such cement-based compositions can be used to replace the conventional building materials or to build small sensors to be integrated in a structure [1]. Changes that occur in elements, such as deformation, moisture or temperature, causes a change in its electrical properties. Thus, measuring the variation of the electrical properties will give information regarding the change of the other properties, after proper calibration of the relation between both variables. The first documented attempts of using piezoresistive cement-based materials dated from 1993 with the use of carbon fibers [2] to improve conductivity of cement pastes. Subsequent studies have been made using carbon fibers [3-10], carbon nanotubes [3, 11-13], steel fibers [14-16] and carbon black [9, 17-21]. Carbon black demonstrated some advantages for multifunctional concrete applications when compared with other conductive additions, mostly because of its lower cost and similar results. The purpose of this work is to study the piezoresistive response of cement-based specimens, containing carbon black when subjected to cyclic compressive loads and thus provide a practicable strain sensor material for long-term service monitoring.

2. MATERIALS

The test specimens have dimensions $10 \times 10 \times 10 \text{ cm}^3$ and composition has Portland cement CEM II, fine sand ($< 1 \text{ mm}$), a superplasticizer and carbon black. Properties of carbon black and superplasticizer are shown in Tables 1 and 2, respectively. In addition, a galvanized steel mesh with openings of 5 mm and size $4 \times 3 \text{ cm}^2$ were used as electrodes.

Table 1: Properties of carbon black

Density [g/cm^3]	Apparent density [g/cm^3]	Surface area [m^2/g]
1.7 – 1.9	0.368	78

Table 2: Properties of superplasticizer

Density [kg/dm^3]	pH [$+23 \pm 2^\circ\text{C}$]	Solid content [%]	Chloride content [%]
1.06 ± 0.02	4.3 ± 1.0	26.5 ± 1.3	< 0.1

The relations between the mortar components (by weight or volume) and the mortar composition are presented in Tables 3 and 4.

Table 3. Relations between mortar components.

Water/Cement [weight]	Agg./Cement [apparent volume]	CB/Cement [weight]	SP/Cement [weight]
0.55	2.0	0.065	0.03

Table 4. Mortar composition (kg/m³)

Mixture	Cement	Water	Sand	Carbon black	SP
CB65	545.7	300.1	1265.1	35.5	16.4

The mixture was made by adding the water and the carbon black with half of the superplasticizer, followed by the sonication during 45 minutes. This sonication procedure was essential, because carbon black is extremely fine and difficult to disperse in the water. With this procedure, an appropriate distribution of particles could be attained. Figure 1 shows this process.

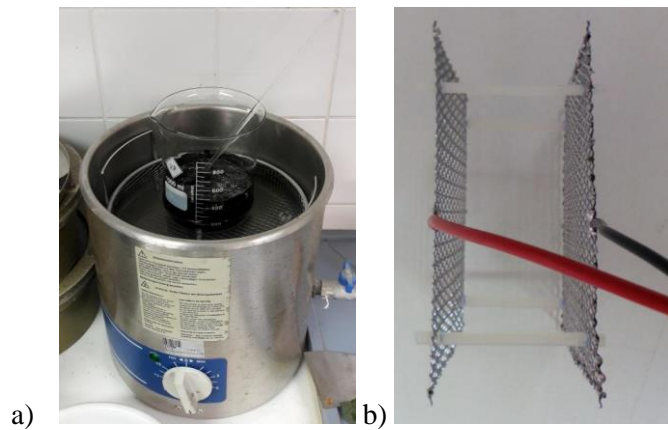


Figure 1: Sonication of mixture (a) and steel mesh electrodes (b)

After sonication, cement was added to the solution and mixed for five minutes until an homogeneous mixture is obtained. Afterwards, the sand and the remainder of superplasticizer was added and mixed for another five minutes. In the molds, the mixture was vibrated for 45 seconds. After that, the steel meshes used as electrodes (see Figure 1) were placed in the test specimen. For 28 days the samples remain in a climatic chamber at 20 °C and relative humidity of 95%. After curing, samples were oven dried at 60 °C for two days, allowing the removal of a significant percent of water from the samples. Figure 2 shows a specimen after demolding.

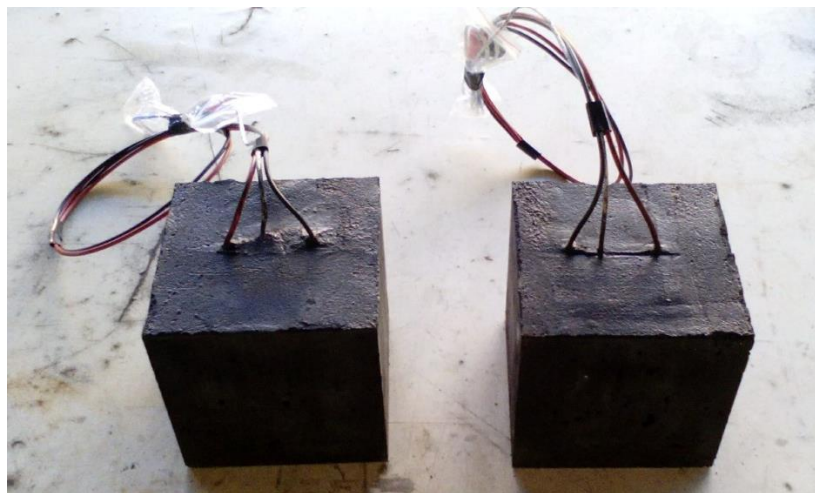


Figure 2: Final view of the test samples with 6.5% of carbon black

3. PIEZORESISTIVITY TEST METHOD

Piezoresistivity tests were performed on a Shimadzu AG-IC hydraulic actuator with a maximum force of 100 kN. Resistivity changes were monitored through a data acquisition system Data Taker DT80. The difference of potential applied during the test was 12 V to the electrodes, electrical current was measured with a 120 Ω resistance.

Because the load frame is metallic, and therefore conductive, it is necessary to insulate the test specimens from the metal plates. To do this, an acrylic plate with 5 mm thickness was placed on the top and bottom of the specimen.

The loading procedure was as follows: a 2 kN force was applied and maintained until the resistivity readings stabilize; afterwards, ten load cycles, with an amplitude of 25 kN, were applied at a speed of 1000 N/s (both loading and unloading). The loading rate was therefore 100.0 kPa/s.

Equations (1) and (2) show how to compute the resistivity ρ of the sensors, as a function of time, by using the first and second statement of Ohm's law, which define the resistance of an element R as

$$R = U / I \quad (1)$$

$$\rho = \frac{A}{L} R \quad (2)$$

Where U is the difference of potential, I is the current intensity, A is the contact area between the electrodes and the material (not the total area of the electrode) and L is the distance between the electrodes and R is the resistance as defined by equation (1). As the deformation of the sensors under compression is very small, the changes in L can be neglected, and it can be concluded from the second statement of the Ohm's law that the fractional change of electrical resistivity (FCR) is equivalent to the fractional change of electrical resistance (equation 3). This is more convenient, since the area A is an ambiguous value.

$$FCR = \frac{\Delta \rho_s}{\rho_s} = \frac{\Delta R_s}{R_s} = \frac{R_s(t) - R_{s,0}}{R_{s,0}} \quad (3)$$

Where $R_s(t)$ is the resistance at a certain instant, t , and $R_{s,0}$ is the initial resistance. The correlation between FCR and strain, defined as sensitivity, was evaluated through Equation (4):

$$\text{sensitivity} = \frac{FCR}{\mu\epsilon} \quad (4)$$

After drying of the test specimens, the lateral surfaces were clean and strain gauges were glued with an epoxydic glue. Two strain gauges were used in each specimen, on opposite sides of the specimen. Strain gauges were glued in the middle of the test specimen between the electrodes. Figure 3 shows a test specimen ready to be tested with strain gauges on both sides and a scheme with placement of electrodes and strain gauges.

Deformation of the specimen during the test was measured by the two strain gauges located on opposite sides of the specimen and an average value was then calculated.

During the piezoresistivity tests, the resistance is measured and the resistivity is calculated afterwards, based on the area and length of the specimen.

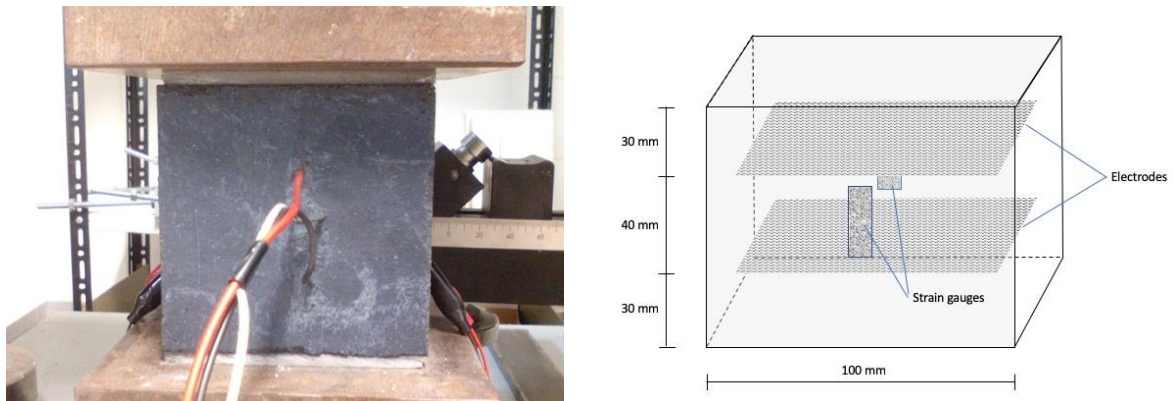


Figure 3. Specimen ready to be tested with strain gauges on both sides and scheme.

4. RESULTS AND DISCUSSION

To assess the strength of the concrete, the cubes were tested in compression, being obtained a compressive strength of 22 MPa.

In Figure 4, the evolution in time of the force and the FCR are plotted. It is apparent that when the force increases, the FCR decreases and vice versa. During the first cycles it can be observed in the experiments that there exists some hysteresis in the load-deformation relation due to the adjustment of the material to the load. This type of behavior is common in concrete materials.

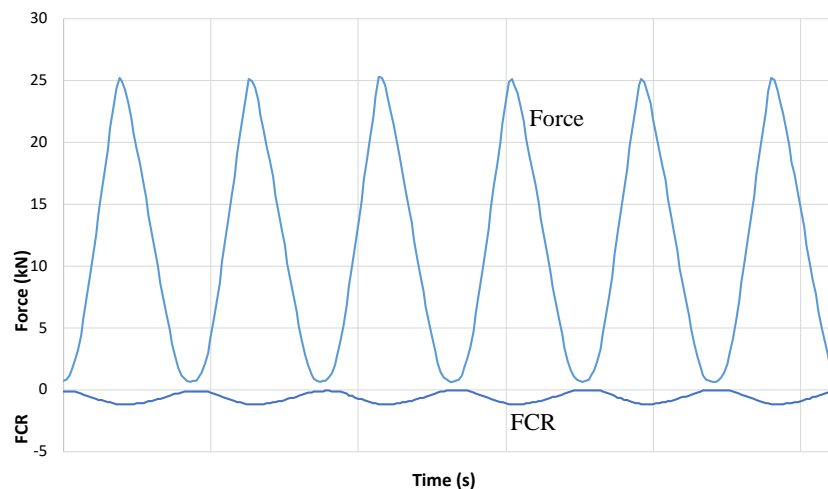


Figure 4: Force *versus* deformation

In Figure 5, the FCR versus deformation plot is shown. It can be observed that an approximately linear relation exists between these two variables. The regression equation, also shown in figure, have a correlation coefficient $R^2 = 0.94$ and a gauge factor in microstrain (ratio between the FCR and the deformation) equal to 0.0513. This means that a variation of 1 in FCR equals a change of approximately 1.7 MPa in compression.

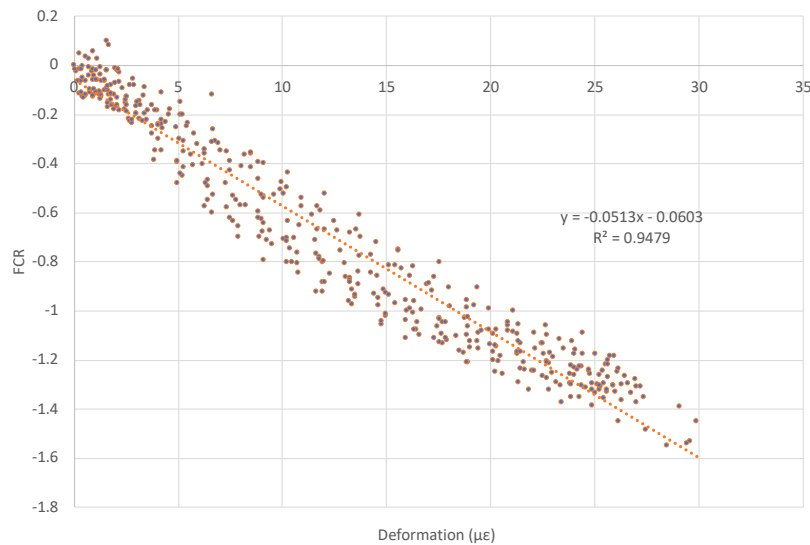


Figure 5: FCR vs deformation and regression

5. CONCLUSIONS

Results on the use of carbon black show that the piezoresistive effect of concrete is improved, allowing the possibility of using this material for traffic sensors. This material is cost effective, due to the low cost of carbon black and quite resistant due to strength and durability of concrete, making it a very good option for building sensors. The results are quite encouraging, but further studies are still needed, but these results are highly encouraging.

ACKNOWLEDGEMENTS

Authors wish to acknowledge FCT – Portuguese Foundation for Science and Technology for the financial support of Research Unit RISCO, FCT/UID/ECI/04450/2013.

REFERENCES

- [1] B. Han, S. Ding, and X. Yu, Intrinsic self-sensing concrete and structures: A review. *Measurement*, 2015. 59: p. 110-128.
- [2] C. Pu-Woei and D.D.L. Chung, Carbon fiber reinforced concrete for smart structures capable of non-destructive flaw detection. *Smart Materials and Structures*, 1993. 2(1): p. 22.
- [3] F. Azhari and N. Banthia, Cement-based sensors with carbon fibers and carbon nanotubes for piezoresistive sensing. *Cement and Concrete Composites*, 2012. 34(7): p. 866-873.
- [4] S. Wen and D.D.L. Chung, Effects of Strain and Damage on Strain-Sensing Ability of Carbon Fiber Cement. *Journal of Materials in Civil Engineering*, 2006. 18(3): p. 355-360.
- [5] M. Chiarello and R. Zinno, Electrical conductivity of self-monitoring CFRC. *Cement and Concrete Composites*, 2005. 27(4): p. 463-469.
- [6] B.W. Ramme, J.J. Noegel, R.H. Setchell, and R.F. Bischke, Electrically conductive concrete and controlled low strength materials having carbon fibers, 2010, Google Patents.
- [7] S. Wen and D.D.L. Chung, Electrical-resistance-based damage self-sensing in carbon fiber reinforced cement. *Carbon*, 2007. 45(4): p. 710-716.
- [8] B. Han, X. Guan, and J. Ou, Electrode design, measuring method and data acquisition system of carbon fiber cement paste piezoresistive sensors. *Sensors and Actuators A: Physical*, 2007. 135(2): p. 360-369.

- [9] Y. Ding, Z. Chen, Z. Han, Y. Zhang, and F. Pacheco-Torgal, Nano-carbon black and carbon fiber as conductive materials for the diagnosing of the damage of concrete beam. *Construction and Building Materials*, 2013. 43: p. 233-241.
- [10] S. Wen and D.D.L. Chung, Self-sensing of flexural damage and strain in carbon fiber reinforced cement and effect of embedded steel reinforcing bars. *Carbon*, 2006. 44(8): p. 1496-1502.
- [11] G.Y. Li, P.M. Wang, and X. Zhao, Pressure-sensitive properties and microstructure of carbon nanotube reinforced cement composites. *Cement and Concrete Composites*, 2007. 29(5): p. 377-382.
- [12] X. Yu and E. Kwon, A carbon nanotube/cement composite with piezoresistive properties. *Smart Materials and Structures*, 2009. 18(5): p. 055010.
- [13] A. D'Alessandro, M. Rallini, F. Ubertini, A.L. Materazzi, and J.M. Kenny, Investigations on scalable fabrication procedures for self-sensing carbon nanotube cement-matrix composites for SHM applications. *Cement and Concrete Composites*, 2016. 65: p. 200-213.
- [14] M.-q. Sun, R.J.Y. Liew, M.-H. Zhang, and W. Li, Development of cement-based strain sensor for health monitoring of ultra high strength concrete. *Construction and Building Materials*, 2014. 65: p. 630-637.
- [15] N. Banthia, S. Djeridane, and M. Pigeon, Electrical resistivity of carbon and steel micro-fiber reinforced cements. *Cement and Concrete Research*, 1992. 22(5): p. 804-814.
- [16] E. Teomete and O.I. Kocyigit, Tensile strain sensitivity of steel fiber reinforced cement matrix composites tested by split tensile test. *Construction and Building Materials*, 2013. 47: p. 962-968.
- [17] H. Li, H.-g. Xiao, and J.-p. Ou, Effect of compressive strain on electrical resistivity of carbon black-filled cement-based composites. *Cement and Concrete Composites*, 2006. 28(9): p. 824-828.
- [18] A.O. Monteiro, P.B. Cachim, and P.M.F.J. Costa, Electrical Properties of Cement-based Composites Containing Carbon Black Particles. *Materials Today: Proceedings*, 2015. 2(1): p. 193-199.
- [19] H. Li, H. Xiao, and J. Ou, Electrical property of cement-based composites filled with carbon black under long-term wet and loading condition. *Composites Science and Technology*, 2008. 68(9): p. 2114-2119.
- [20] V.W.J. Lin, M. Li, J.P. Lynch, and V.C. Li. Mechanical and electrical characterization of self-sensing carbon black ECC. 2011.
- [21] S. Wen and D.D.L. Chung, Partial replacement of carbon fiber by carbon black in multifunctional cement–matrix composites. *Carbon*, 2007. 45(3): p. 505-513.

MODAL IDENTIFICATION OF A DOUBLE-CURVATURE CONCRETE ARCH DAM UNDER NATURAL EXCITATION: ANALYSIS OF THE ACCURACY ACHIEVED WITH DIFFERENT TYPES OF ACCELEROMETERS

Sérgio Pereira (1), Filipe Magalhães (1), Carlos Moutinho (1) and Álvaro Cunha (1)

(1) Construct-ViBest, Faculty of Engineering (FEUP), University of Porto, Portugal

Abstract

At present time, the accurate estimation of modal properties of large civil structures (e.g. buildings, bridges, chimneys, wind turbines) can be easily achieved by applying state of art output-only modal identification methods (e.g. SSI-cov, SSI-Data, p-LSCF) to the data obtained with ambient vibration tests performed with appropriate sensors and data acquisition systems.

However, when dealing with massive structures like concrete dams, the signals are very low (of the order of micro-g) and the signal to noise ratio very challenging in terms of modal identification.

In this context, this paper describes an investigation developed on the Alto Lindoso dam (a double curvature arch dam in the North of Portugal, 110 m high) with the purpose of analysing the level of accuracy achieved, in terms of modal identification with the alternative use of different type of accelerometers (force-balance, piezoelectric, MEMS), developing a complete ambient vibration test along the dam crest.

Keywords: modal identification, accuracy, noise, dams

1. INTRODUCTION

Even though the modal identification of dams is historically associated to forced vibration tests [1] [2], there are already some successful examples of operational modal analysis applied to this type of structures, both through the performance of ambient vibration tests [3] [4] and the installation of vibration-based health monitoring systems [5] [6]. Nevertheless, when compared to forced vibration tests, much lower levels of vibration and much lower signal to noise ratios should be expected under natural excitation [7]. Thus, very sensitive sensors and high-resolution digitizers are required to obtain good results.

However, top quality equipment is generally associated with high costs, so it may not be always available. To overcome this, more economical solutions, with lower capabilities, may arise as an alternative in certain situations. Consequently, it is important to explore the accuracy of the results achieved with different types of accelerometers [8] when performing operational modal analysis.

In this context, the present work presents the ambient vibration test performed on Alto Lindoso arch dam, using force balance accelerometers. Additionally, a comparison between the results obtained from the modal identification of the structure through the analysis of the measured data and through the analysis of data simulating characteristic levels of noise associated to different types of accelerometers, such as piezoelectric and MEMS, is presented as well.

2. TESTED CONCRETE ARCH DAM

The Alto Lindoso hydroelectric power plant, located in the north of Portugal, in the Lima river, started operating in 1992 with an installed capacity of 630 MW, which makes it the most powerful hydroelectric plant in the country to this day. Its 347 million m³ reservoir is assured by a double-curvature concrete arch dam, 110 m high, whose crown develops for 297 m. An ambient vibration test was performed on the dam on 22/02/2017, using 10 three-axial seismographs that were distributed over the dam crest. To guarantee a good characterization of modal shapes in the post processing, 21 measuring points were defined, which were covered by 6 reference sensors and 4 mobile sensors, over 4 measuring setups. Aerial pictures of the dam and its reservoir are presented in Figure 1, along with the representation of the measuring points on the dam scheme, where red dots represent reference measuring points and blue dots represent mobile measuring points.

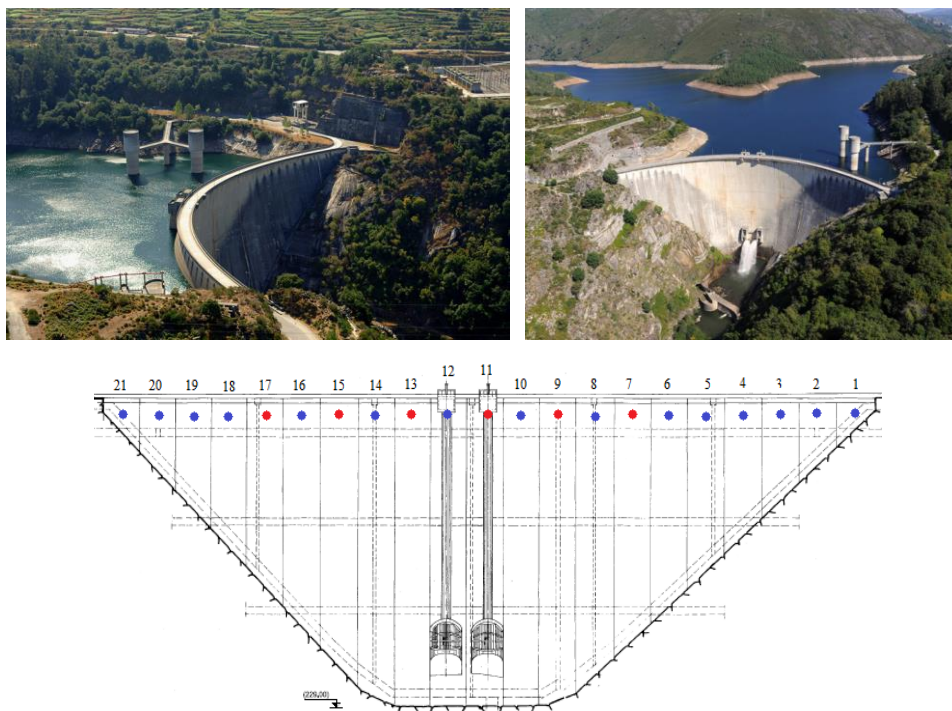


Figure 1 - Alto Lindoso arch dam pictures [9] and test layout

3. METHODOLOGY FOR DATA SIMULATION

To complement the data obtained with force balance sensors (FB) during the ambient vibration test and investigate on the feasibility of sensors with different functioning basic principles, such as Piezoelectric and MicroElectricalMechanical Systems [10] accelerometers, being used to test arch dams, the noise floor expected for regular sensors was ascertained.

Through the performance of laboratory measurements with four different conventional sensors, including two piezoelectric accelerometers (PE1 and PE2) and a medium-quality (MEMS 2) and a high-quality (MEMS1) MicroElectricalMechanical Systems accelerometers, it was possible to assess typical noise levels of these types of sensors. Numerically generated white noise time series were tuned with different amplitudes in order to simulate the spectral noise levels assessed in laboratory for each of the four tested sensors. The four numerically generated noise floors considered as characteristic are presented in Figure 2, and taking into account that the vertical scale is logarithmic, the quality difference between piezoelectric and MEMS accelerometers is clear. While both the considered piezoelectric sensors present a noise floor well below $10^{-11} [(m/s^2)^2 / Hz]$, in the case of MEMS this values are close to 10^{-9} and $10^{-10} [(m/s^2)^2 / Hz]$ respectively.

In Figure 3, the considered noise floors are compared to different auto-spectra obtained from real data measured by two accelerometers positioned in different points during the ambient vibration test. In the case of the considered piezoelectric noise floors, while PE1 is constantly below the peaks of the real spectra, PE2 is below most of the peaks, but eventually crossing one or other peak. In turn, for MEMS the opposite is verified, since MEMS2 is constantly over the top of the peaks and the position of MEMS1 generally lays between going through the peaks and over the top of the peaks.

Finally, the simulated band-limited white noise time series were added to the originally measured acceleration time series. Therefore, it was assumed that the spectral noise is constant in the frequency range under analysis.

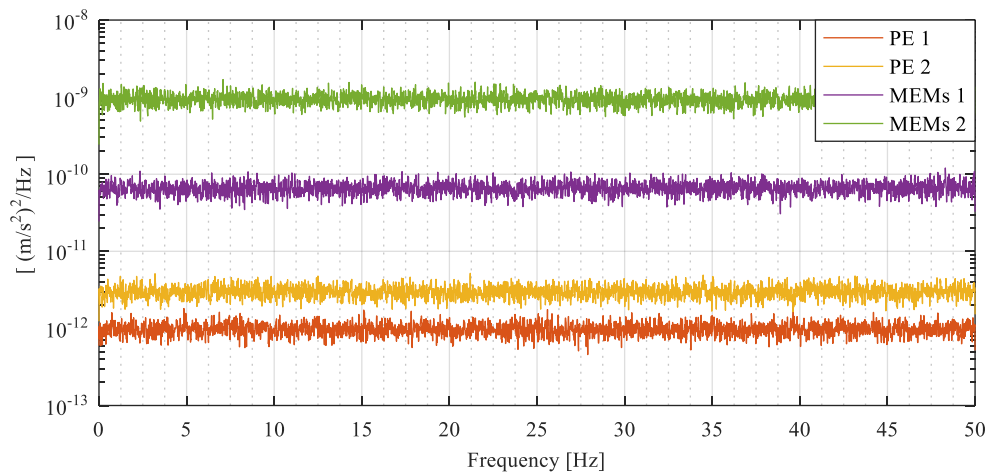


Figure 2 - Numerically generated noise spectra

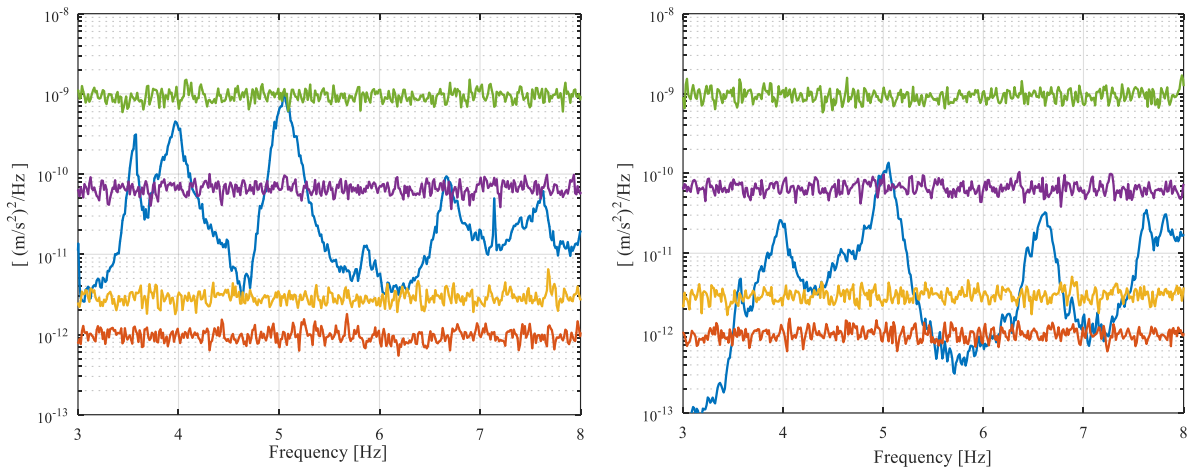


Figure 3 – Auto-spectra from real measuring points (blue) and auto-spectra of numerically generated noise floors

4. RESULTS

Since the noise time series were added to the measured data, new time series were obtained that simulate the data that would have been measured if the piezoelectric or the MEMS accelerometers had been used during the ambient vibration test.

Figure 4 shows the auto-spectra obtained from real data measured by two differently positioned force balance accelerometers and the auto spectra obtained from the piezoelectric and from the MEMS simulated time series.

Whereas most of the peaks in the spectra obtained from the real measured time series (FB) are reproduced in the spectra obtained from simulated piezoelectric time series (PE1 and PE2), the same does not apply to the ‘MEMS’ derived spectra which, depending on the time series used to compute the spectra, may hide the peaks under the noise floor.

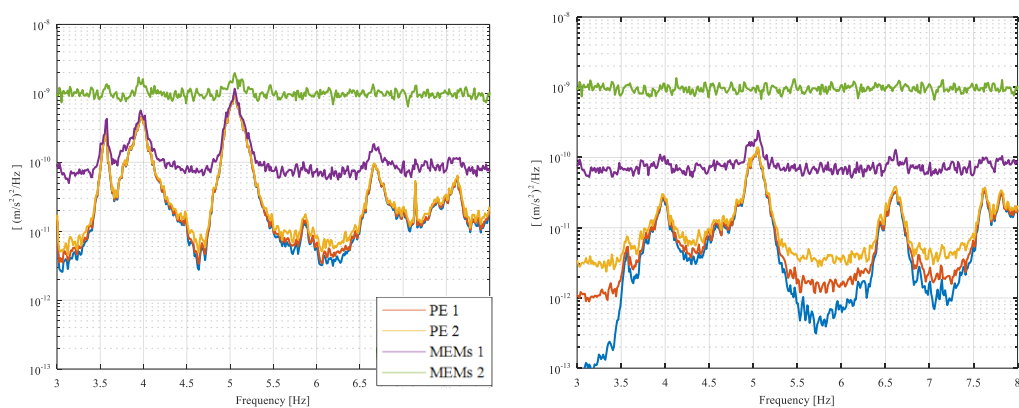


Figure 4 – Force balance, piezoelectric and MEMS auto-spectra

The first four vibration modes were identified for the five scenarios using the peak-picking method. The modes are well separated so the peaks of all four modes were clear for the cases of force balance and piezoelectric sensors. In the cases of the two MEMS sensors the peaks

were not always clear, or not even present at all, and being able or not to identify the four modes depended on the measuring point used as computing reference. The natural frequencies and the description of each mode shape are presented in Table 1.

To quantify the quality of the mode shapes obtained from piezoelectric and MEMS sensors, the mode shapes obtained from measured data were assumed as references and the Modal Assurance Criterion (MAC) between these references and the mode shapes from the other four cases were calculated and presented in Table 2.

Table 1: Identified modal parameters

	Mode 1	Mode 2	Mode 3	Mode 4
Frequency [Hz]	3.54	3.98	5.03	6.69
Description	Antisymmetric	Symmetric	Symmetric	Antisymmetric

Table 2: MAC between mode shapes obtained from measured data and mode shapes obtained from data contaminated with noise

MAC between FB and	PE 1	PE 2	MEMS 1	MEMS 2
Mode 1	0.999	0.993	0.401	0.010
Mode 2	0.988	0.944	0.472	0.249
Mode 3	0.986	0.943	0.773	0.447
Mode 4	0.975	0.784	0.062	0.007

The results presented in Table 2 show the modal configurations obtained with PE 1 and PE 2 are almost identical to the ones that were obtained with force balance sensors, even though a slight loss of quality is associated to PE 2. On the contrary, much lower values for the MAC are obtained with MEMS. In the case of the mode shapes obtained with MEMS 1, the first two modes present a correlation that indicates at least a minimum similarity between the tested configurations and a satisfactory result is achieved for the third mode, but the fourth mode presents a MAC value close to 0. A worse scenario is achieved with MEMS 2. The obtained MAC values are generally close to 0 and only the third mode seems to present a minimum similarity with its reference.

However, even though the MAC values provide important information, they do not replace the usefulness of a visual evaluation. Thus, the modal configurations obtained for the first and third modes in the five studied scenarios are presented in Figure 5 and Figure 6.

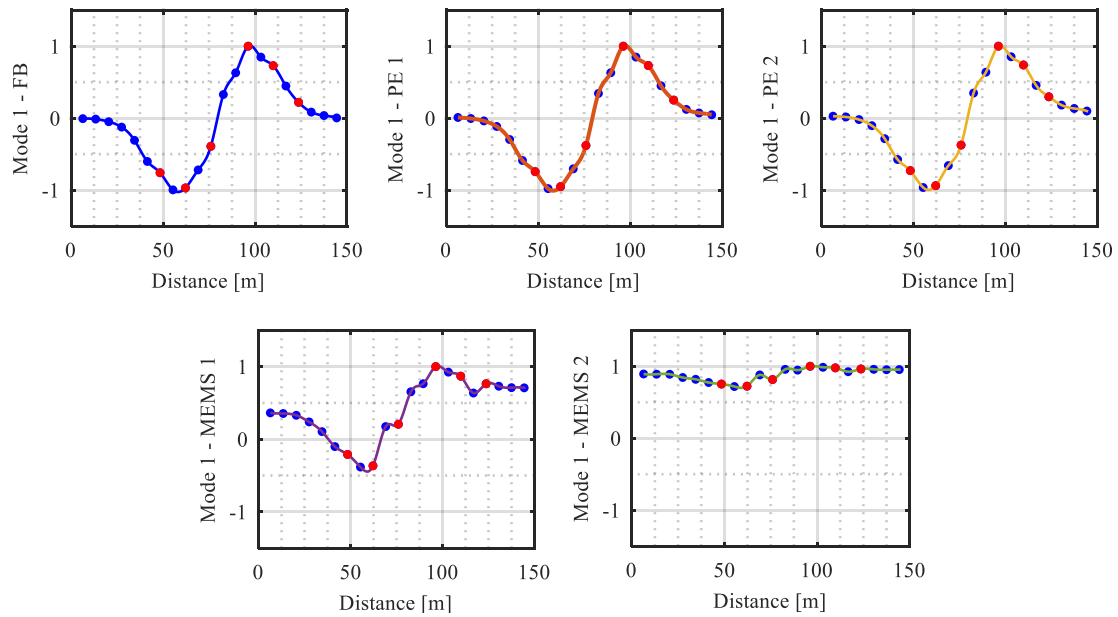


Figure 5 – Mode shapes obtained for the first vibration mode in the five studied scenarios

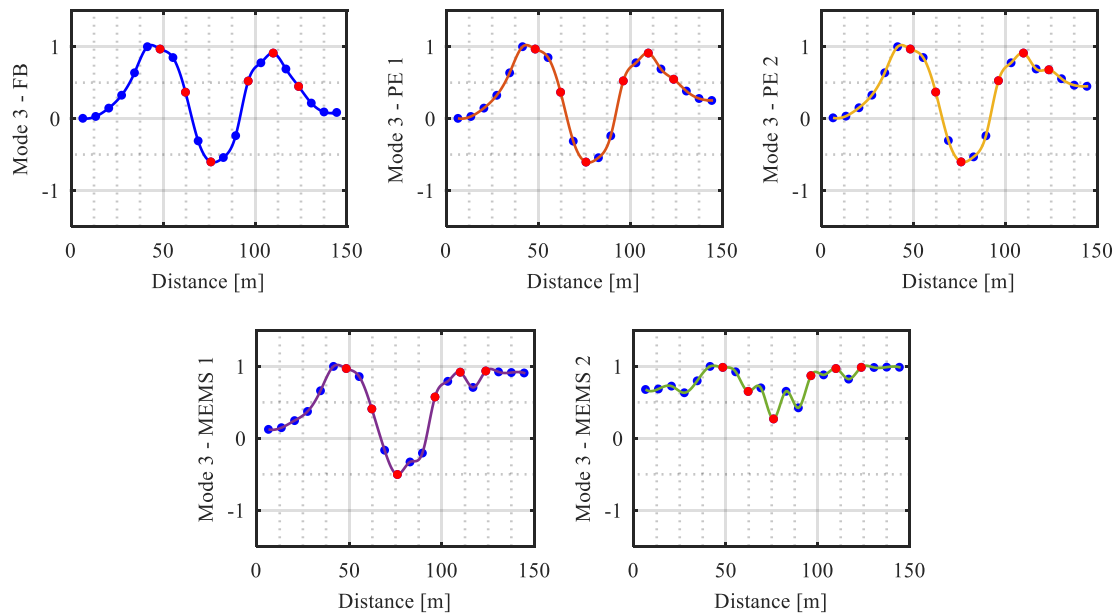


Figure 6 – Mode shapes obtained for the third vibration mode in the five studied scenarios

The mode shapes obtained using the measured data (FB), in blue, are clear and well defined. The same is verified for the mode shapes obtained with piezoelectric sensors, as it was expected after analysing Table 2. In turn, the modal configurations obtained from MEMS 1 time series are not so well defined, but still it is possible to identify the mode shapes

involved. Lastly, the modal configurations obtained using the MEMS 2 data provide almost null information, only slightly suggesting the definition of the mode shapes involved.

It is worth noticing that even though the higher MAC values obtained with both types of MEMS are related to the third mode, the visual evaluation of the mode shapes involved, deprived of clearer information from any other type of sensors, could mistakenly lead to the conclusion that the third mode was antisymmetric, instead of symmetric. Therefore, it is important to consider that the higher the order of the mode, the higher its complexity, thus the identification process becomes harder and associated with increasing levels of uncertainty, especially when dealing with lower quality sensors.

5. CONCLUSIONS

An ambient vibration test was performed on Alto Lindoso arch dam using force balance accelerometers, radially disposed along the dam's crest. The measured time series were then modified using numerically generated noise to simulate the time series that would have been measured if different sensors had been used during the test, including sensors with two levels of noise characteristic of piezoelectric accelerometers, and two other sensors with levels of noise characteristic of high-quality MEMS accelerometers. Natural frequencies and mode shapes were obtained for the five presented scenarios.

The auto-spectra obtained from measured time series were compared to the auto-spectra obtained from the time series corresponding to the four simulated scenarios. In both cases of time series simulated with noise characteristic of piezoelectric sensors (PE1 and PE2), the obtained auto-spectra were identical to the ones obtained from the measured time series (FB) with well-defined peaks that would allow the identification of the first four modes. Moreover, the mode shapes were also clear and when compared with the references generally presented MAC values above 0.9. On the other hand, most of the auto-spectra obtained from time series simulated with noise characteristic of MEMS sensors (MEMS1 and MEMS2) do not present clear peaks, and in some cases no peaks are defined at all. Also, the MAC values between the references and the obtained mode shapes are generally below 0.5. However, a distinction should be made between MEMS1 and MEMS2, since some results may be obtained with the first, while almost no identification could be made with the second.

To conclude, although piezoelectric accelerometers could have been used during the ambient vibration test and good results were likely to be obtained, the same does not apply to MEMS accelerometers. Nevertheless, if high levels of vibration were present, high-quality MEMS could possibly provide acceptable results.

The results obtained in the present work cannot be directly extrapolated to other structures, but can still be used as a reference mark when preparing an ambient vibration test on an arch dam.

ACKNOWLEDGEMENTS

This work was financially supported by: PTDC/ECM-EST/0805/2014/16761 – DAM AGE - Advanced Online Dynamic Structural Health Monitoring of Concrete Dams, funded by FEDER funds through COMPETE2020 - Programa Operacional Competitividade e Internacionalização (POCI) – and by national funds through FCT - Fundação para a Ciência e a Tecnologia; FCT PhD Scholarship SFRH/BD/100587/2014 provided to the first author. The

authors would like also to acknowledge all the collaboration and support provided by EDP Produção.

REFERENCES

- [1] Gomes, J. and E. Carvalho, *Ensaaios de Vibração Forçada para a Caracterização do Comportamento Dinâmico de Barragens de Betão. Aplicação à Barragem de Cahora Bassa*, in *5ª Jornadas Portuguesas de Engenharia de Estruturas*. 2014: Lisbon. (In Portuguese).
- [2] Gomes, J. and J.V. Lemos, *Characterization of the dynamic behavior of an arch dam by means of forced vibration tests*, in *1st Meeting of EWG Dams and Earthquakes*. 2016, Balkema: Saint Malo, France.
- [3] Deinum, P.J., R. Dungar, B.R. Ellis, A.P. Jeary, G.A.L. Reed, and R.T. Severn, *Vibration tests on emosson arch dam, Switzerland*. *Earthquake Engineering & Structural Dynamics*, 1982. **10**(3): p. 447-470.
- [4] Proulx, J., P. Paultre, J. Rheault, and Y. Robert, *An experimental investigation of water level effects on the dynamic behaviour of a large arch dam*. *Earthquake Engineering and Structural Dynamics*, 2001. **30**(8): p. 1147-1166.
- [5] Darbre, G.R. and J. Proulx, *Continuous ambient-vibration monitoring of the arch dam of Mauvoisin*. *Earthquake Engineering and Structural Dynamics*, 2002. **31**(2): p. 475-480.
- [6] Mendes, P., *Observação e Análise do Comportamento Dinâmico de Barragens de Betão*. 2010, Faculdade de Engenharia da Universidade do Porto. (In Portuguese).
- [7] Pereira, S., F. Magalhães, J.P. Gomes, Á. Cunha, and J.V. Lemos, *Dynamic monitoring of a concrete arch dam during the first filling of the reservoir*. *Engineering Structures*, 2018. **174**: p. 548-560.
- [8] Pacheco, J., G. Oliveira, F. Magalhães, C. Moutinho, and Á. Cunha, *Evaluation of low cost vibration based damage detection systems*. *Journal of Physics: Conference Series*, 2018. **1037**(5): p. 052005.
- [9] EDP. *Energias de Portugal*. [cited 2018 21/09/2018]; Available from: http://www.a-nossa-energia.edp.pt/centros_produtores/.
- [10] Evans, J.R., R.M. Allen, A.I. Chung, E.S. Cochran, R. Guy, M. Hellweg, and J.F. Lawrence, *Performance of Several Low-Cost Accelerometers*. *Seismological Research Letters*, 2014. **85**(1): p. 147-158.

DESIGN FOR DURABILITY OF REINFORCED CONCRETE STRUCTURES UNDER THE HOT DESERT CLIMATE OF THE ARABIAN PENINSULA

Sotiris Demis (1) and Vagelis G. Papadakis (2)

(1) Department of Civil Engineering, School of Engineering, University of Patras, Greece

(2) Department of Environmental and Natural Resources Management, School of Engineering, University of Patras, Greece

Abstract

Given the extreme environmental conditions of the Arabian Peninsula, emphasis should be paid on the durability design process of reinforced concrete (RC) structures in this region. In this direction, on the newly imposed Regulation “Guide for the Design of Concrete Structures in the Arabian Peninsula” by the UK Concrete Society, utilization of service life estimation is prescribed. In the current study, after presenting the basic principles of a structured durability design process addressing the particularities of the hot desert climate of the Arabian Peninsula, a comparison between stochastic and physicochemical deterministic (according to performance-related methods) service life estimation, part of the durability design of a newly erected structure, is given. The results show that not only the physicochemically derived values verify the stochastic ones, but additional enhancement of the durability design can be achieved. Hence, an appropriate (for the exposure environment) physicochemical deterministic approach on service life estimation can produce feasible and valid results.

Keywords: durability design, service life estimation, arabian peninsula, carbonation, chlorides

1. INTRODUCTION

In previous studies [1-2] the need for a structured durability design process for RC structures exposed in harsh environments, beyond the limits of the Deemed-to-satisfy method [3-5], has been strongly emphasized and presented. A four-step durability design process of RC structures, according to the principles defined by fib [6-7] has been proposed (Figure 1), in which the service life of the structure is a direct design factor. A crucial part of this process is the estimation of the service life, which although according to fib [6-8] should take place in a stochastic way, “*in most cases there is insufficient amount of data available to fully represent the statistical variability of the input parameters of the deterioration model*” [7]. A simpler approach is to utilize a deterministic approach, based on service life estimation tools developed

based on performance-related methods (PRMs) for durability, in accordance to EN206-1 [5] using data derived from established performance test methods or through proven predictive mathematical models. As fib [7] states “*clearly the validity of the method depends on how appropriate the deterioration model is for the particular hazard*”.

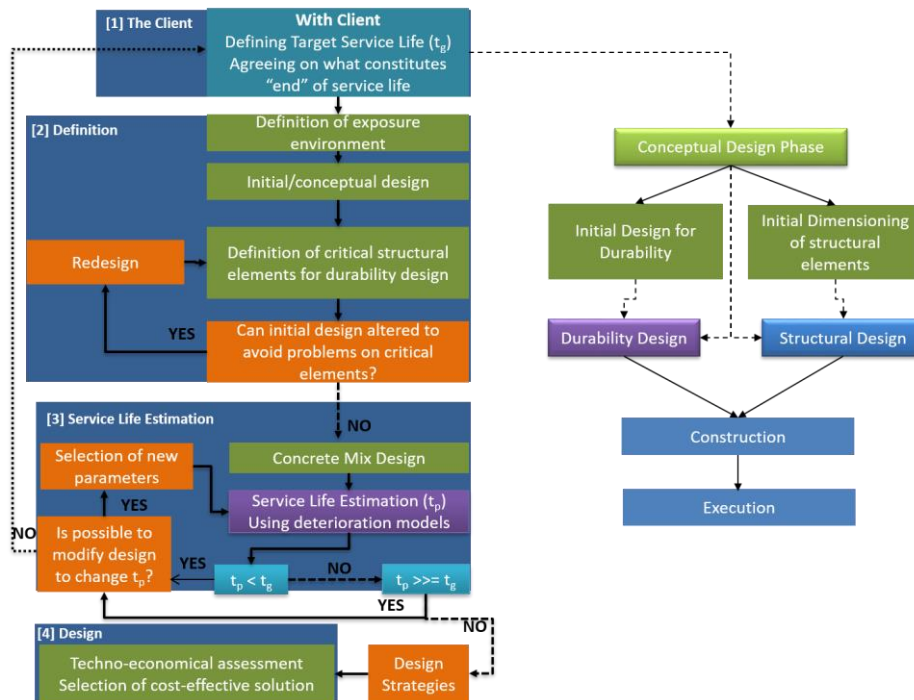


Figure 1: Service life design procedure of an RC structure [1,2]

Such a procedure is of paramount importance in durability design of structural elements exposed in extremely aggressive environments, as in the Arabian Peninsula.

2. DURABILITY OF RC STRUCTURES IN THE ARABIAN PENINSULA

The environmental conditions in the Arabian Gulf (hot desert climate) pose a major challenge for durable concrete structures. Factors such as combinations and fluctuations of high ambient temperatures, high relative humidity (from 2% at night, up to 85% during the day), high levels of chlorides and sulphates in soil and groundwater, wind-blown sand and marine aerosols [9-10], account for increased signs of premature structural deterioration observed, even on structures after as little as 5 to 15 years.

Research efforts [11-12] to overcome these issues, led to the development of the “*Guide for the Design of Concrete Structures in the Arabian Peninsula*” by the Concrete Society [10], in which the design for durability is part of the conceptual design stage of the structure, and the service life as the conditions that constitute the end of it, are direct design factors. Based on the design service life, importance of structure and location, structures are characterized as normal or special. For the former, with shorter design lives (up to 30 years) located in the more benign inland (usually dry) conditions, the deemed-to-satisfy procedure with up-scaled values due to the aggressiveness of the region is usually adequate, while for special structures located in the more aggressive coastal, marine or underground environments (with service lives higher than

30 years) a project-specific durability study should be undertaken [10]. For structures located in inland areas (very dry regions) chlorides are not a problem for above ground elements. Structures located in coastal zones are exposed to airborne chlorides, while their underground elements are exposed to sulfate attack and chlorides. For structures under marine exposure, the high salinity of the sea water and with the high environmental temperatures leads to a quick build-up of salt concentrations in the surface concrete. As a result, corrosion of reinforcement and sulfate attack are by far the greatest causes of premature deterioration of concrete structures in that region. The aggressivity of each exposure class for reinforcement corrosion is further divided based on the presence (or absence) of moisture in the structural element, providing in this way two designation classes (mild, moderate) for carbonation and four (moderate, aggressive, severe, extreme) for the action of chlorides. For each designation class, according to the Deemed-to-satisfy method, minimum cement contents, maximum w/c ratios and nominal covers to reinforcement for an intended working life of 30 years are prescribed. Both the minimum cover value (c_{min}) and the reinforcement fixing tolerance (Δc) are considerably higher than the ones in the Eurocodes for similar exposure classes. In addition a series of measures are suggested, as i) use of CEM II/CEM III cement types with high levels of silica fume, ggbs or fly ash, ii) utilization of triple blend mixes (Portland cement and both silica fume and fly ash or ggbs), and iii) use of additional enhancement techniques as coatings, special types of reinforcement, corrosion-inhibiting admixtures, cathodic protection systems. In terms of sulfate attack, specific instructions are given for the characterization of the sulfate exposure in four classes, based on the soil and groundwater investigation in terms of chloride, sulfate ion concentrations and pH, and durability provisions are prescribed [10].

The regulation prescribes the use of service life estimation modelling, to verify the design parameters of the durability study, especially for chloride exposure in which their ingress is modeled according to Fick's 2nd law of diffusion. Such an approach neglects the chloride interaction with the solid phase, leading to an underestimation of the service life based on the "apparent" chloride diffusivity, and not on the actual "intrinsic" diffusion coefficient, taking under consideration the chloride interaction and binding with the solid phase, which will give more accurate service life estimation.

Based on all the above, implementation of the regulation CS163 [10] took place on the durability design of the concrete elements of the metro railway network of a country in the Arabian Peninsula, which led to certain disputes between the partners involved. The authors of this study provided expert advice on this dispute, by performing durability design on the same structural components, using a physicochemical deterministic approach on service life estimation, according to performance-related methods.

3. EXPERIMENTAL PROCEDURE

The requirement according to the client's demands and the recommendations [10] is that the service life of the concrete elements should be 120 years. Three different cases of structural elements were evaluated (Table 1). The structural elements of Case A (in contact with ground), since their external surface is in contact with groundwater will not suffer from carbonation (due to high surrounding humidity) but will be exposed to chloride attack, since the ground investigation analysis indicated that chlorides are present in the ground and groundwater. The concrete of Cases B and C (internal elements) will not suffer from chloride attack as they are not in contact with ground (or groundwater), but will be exposed to carbonation. Stochastic

estimation of concrete service life of a Case A structural element (concrete wall in contact with groundwater, with a depth of 1.2 m), with the parameters shown in Table 2, showed that based on the concrete mix design and the type of membrane used (Table 1), the reliability factor (β value) remained above 1.3 (hence at an acceptable level) for the design service life of 120 years. Hence, the mix design selected and the cover of 50 mm used in the analysis are adequate.

Table 1: Concrete Mix Design [10, 13]

	External Elements Concrete in contact with ground (Case A)	Internal Elements Concrete not in contact with ground (Case B)	High strength concrete for internal columns (Case C)
Strength Class	C40/50	C40/50	C60/75
Triple blend mix	25% OPC, 70% GGBS, 5% SF		
min C (kg/m ³)	400	400	420
max W/C	0.35	0.35	0.33
d _{max} (mm)	20	20	20
Additional Measures	Fully bonded waterproof membrane	None	None
Aggressive agent	Chlorides	CO ₂	CO ₂
Cover (mm)	75/50	50	50

Table 2: Parameters of stochastic estimation of concrete service life [13]

Parameter	Mean	SD	Value	Distribution
Cl ⁻ concentration in ground water (mg/l)	1477	315	-	Logarithmic
Initial Cl ⁻ concentration in concrete (% wt cement)	-	-	0/0.1	Binary
Critical Cl ⁻ concentration (% wt cement)	0.4	-	-	Constant
Age at first exposure to Cl ⁻ / Age at which tested (weeks)	1040*/8	-	-	Constant
Service life (years)	114	-	-	Constant
Cover / Element thickness (m)	0.04 / 1.2	-	-	Constant
Temperature (K)	306	5	-	Linear
Apparent Cl ⁻ diffusion coefficient (m ² /s)	1.5E-12	3E-12	-	Linear

* the action of the protective membrane is conservatively taken as 20 years.

4. SERVICE LIFE ESTIMATION USING PERFORMANCE-RELATED TOOLS

The deterministic service life estimation tool EUCON, based on proven predictive models according to performance-related methods for the estimation of concrete service life under harsh environments, developed and validated by the authors of this study [14-16], was used to evaluate the service life of the structural elements of the three cases previously identified.

Upon entering the concrete mix design and the oxide analysis of the triple blend mix used in the project (Table 3), emphasis was given on defining the environmental exposure conditions. In terms of carbonation, the highest value for CO₂ content was used (0.08% or 800 ppm, corresponding to urban areas). Based on the values of relative humidity measured in the region (from 68-85%) the range of 70%, 75% and 80% was selected. The chloride concentration on the external surface of the structural elements was calculated based on the analysis of the in-situ boreholes measurements of chloride ions in the groundwater [13]. Although their mean value was found to be 4.35 kg/m³ solution, according to standard practice the geometrical mean of the higher values (8.36 kg/m³ solution) was used in EUCON. Furthermore, the intrinsic effective diffusivity of Cl⁻ in fully saturated concrete was used. Based on the parameters defined

in EUCON the service life of structural element of case A was estimated under chloride exposure, while those of cases B and C for carbonation exposure.

Table 3: Initial parameters of EUCON

<u>Concrete Mix Design and Structure</u>	Cement type: CEM III/B 42.5 R (Clinker 25%, SCM 75% = 70% GGBS + 5% SF) Cement Content 400 kg/m ³ , Cement Density 2820 kg/m ³ , W/C 0.35, d _{max} : 20 mm Portland clinker oxide analysis: Clinker (SiO ₂ 21.2%, Al ₂ O ₃ 5%, Fe ₂ O ₃ 3.1%, CaO 66.8%, SO ₃ 0.5), Additions activity and oxide analysis: 70% GGBS + 5% PFA: (SiO ₂ 36.5%, Al ₂ O ₃ 13.8%, Fe ₂ O ₃ 0.33%, CaO 39%, SO ₃ 0.7), Silica's (SiO ₂) activity ratio, $\gamma_s = 90\%$, Alumina's (Al ₂ O ₃) activity ratio, $\gamma_a = 90\%$, Concrete cover : 50 mm
Carbonation	Exposure Class: XC3 (moderate humidity), CO ₂ concentration : 0.08%, RH: 70%, 75%, 80%
Chlorides	Exposure Class: XD2 (wet, rarely dry) Cl ⁻ concentration at external concrete surface: 8.36 kg/m ³ solution / 4.35 kg/m ³ solution, Exposure degree: 1 (no protection) / 0.833 (protection), Efficiency factor of SCM regarding Cl ⁻ penetration: 2.2, Initial Cl ⁻ concentration: 0 kg/m ³ concrete, Critical Cl ⁻ concentration for corrosion initiation: 1.48 kg/m ³ concrete
Time factor	Service life (years): 120

5. RESULTS AND DISCUSSION

5.1 Carbonation Exposure

The service life (corrosion initiation and corrosion propagation period) of the structural elements exposed in carbonation (cases B and C; with 50 mm concrete cover) is above 120 years (Table 4). Marginally for the case B structural element for 70% RH, with an estimated service life of 115 years, the adequate concrete cover was found to be 50.9 mm. For the most expected value of relative humidity (75%), covers of 42 mm for Case B and 37.2 mm for Case C are estimated, for 120 years.

Table 4: Adequate concrete cover c (mm) and service life t (years) for carbonation exposure

Relative Humidity (RH)		70%		75%		80%	
		c (mm)	t (years)	c (mm)	t (years)	c (mm)	t (years)
Case B		50.9	115.2	45	168.8	32.9	>200
Case C		45,3	146	37,2	>200	29,1	>200
Case B - Control (OPC 25%, 400 kg/m ³)		50.9					
↓↑ Binder Content	↓C (OPC 25%, 380 kg/m ³)	52.9					
	↑C (OPC 25%, 450 kg/m ³)	48.3					
↓↑ OPC (%)	↓OPC (OPC 20% , 400 kg/m ³)	64.6					
	↑OPC (OPC 30% , 400 kg/m ³)	36.2					
↓↑ Binder & OPC (%)	↑OPC/↓C (OPC 30% , 380 kg/m ³)	40.1					
	↑OPC/↓C (OPC 35% , 380 kg/m ³)	30.8					

By changing the binder content (from 400 kg/m³ to 380 – 450 kg/m³, and keeping all other compositional parameters constant), the carbonation resistance is slightly affected (Figure 2). Decreasing the binder content from 400 to 380 kg/m³, the service life was reduced to 108 years, while the adequate cover was increased to 52.9 mm. Considerable changes in carbonation resistance were noticed when the proportion of OPC in the triple blend mix was altered. Increasing the relative proportion of OPC to 30% from 25% (hence to 30% OPC-65% GGBS-5% SF), gave significant reduction of carbonation depth, thus lower adequate concrete cover is required (36.2 mm). Furthermore, increasing of the OPC percentage to 35% and reducing the

binder content to 380 kg/m³ proved to be the most effective in terms of adequate concrete cover needed (30.8 mm) to sustain a corrosion free structure for 120 years.

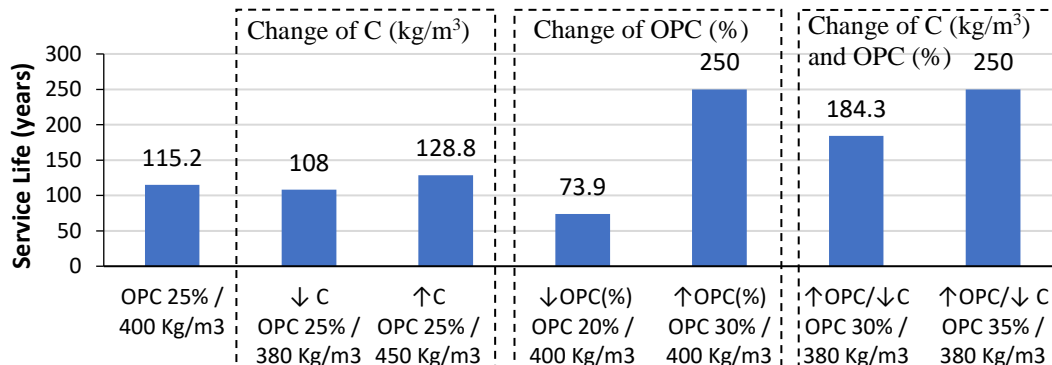


Figure 2. Service life values for carbonation exposure

5.2 Chloride Exposure

Estimation of Cl⁻ profiles of case A elements, revealed that application of the membrane reduced the adequate concrete cover needed to 35 mm, instead of 55mm when the membrane is not applicable (Figure 3). Although the chloride resistance is not affected when the binder content is changed, it changes considerably when the proportion of OPC in the triple mix is altered (Table 5). For 20% OPC (from 25%), the concrete cover for 120 years is increased to 77 mm, even with the action of the protective membrane. Increasing the OPC percentage to 30%, a lower concrete cover of 11 mm is required. As in the case of carbonation exposure, increasing of the OPC percentage to 30% or 35% and, at the same time reducing the binder content to 380 kg/m³ proved to be most effective in terms of adequate concrete cover (15 mm and 13mm, for membrane use, or no membrane, respectively) to sustain a corrosion free structure for 120 years.

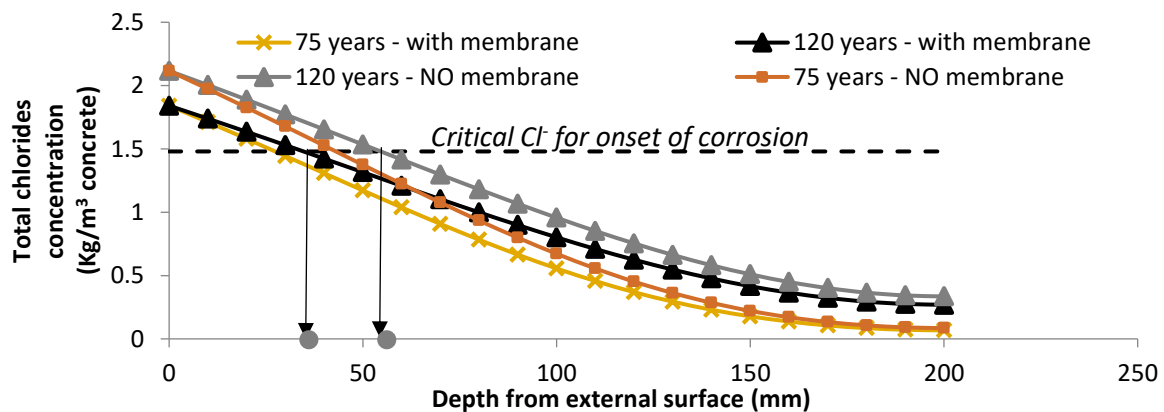


Figure 3. Chloride profiles Service life values for chloride exposure

Table 5: Adequate concrete cover (mm) for chloride exposure for 120 years

		With membrane	Without membrane
	Case A - Control (OPC 25% - C 400 Kg/m ³)	35	55
↓↑ Binder Content	↓C (OPC 25% - C 380 Kg/m ³)	35	-
	↑C (OPC 25% - C 450 Kg/m ³)	33	-
↓↑ OPC (%)	↓ OPC (OPC 20% - C 400 Kg/m ³)	77	-
	↑ OPC (OPC 30% - C 400 Kg/m ³)	11	-
↓↑ Binder & OPC (%)	↑ OPC /↓C (OPC 30% - C 380 Kg/m ³)	15	-
	↑ OPC /↓C (OPC 30% - C 380 Kg/m ³)	-	29
	↑ OPC /↓C (OPC 35% - C 380 Kg/m ³)	-	13

Overall, deterministic service life estimation of the cut and cover in-situ permanent concrete works part of the metro rail network of a country in the Arabian Peninsula, verified the stochastic durability design performed by the partners of the project. For the investigated environmental conditions and the suggested concrete composition, a concrete cover of 50 mm is fully sufficient to ensure a service life of 120 years. However, modifications can be performed on binder and concrete compositional parameters that could further enhance the durability of the structural elements (Table 6). Increasing the proportion of OPC against GGBS & SF in the triple mix, a lower concrete cover is required for a service life of 120 years, without the need for a protective membrane, for both deterioration mechanisms.

Table 6: Suggested concrete mix design

	Concrete elements in contact with ground (Case A)		Concrete elements not in contact with ground (Case B)		High strength concrete for internal columns (Case C)	
	Initial	Suggested	Initial	Suggested	Initial	Suggested
Strength Class	C40/50	C40/50	C40/50	C40/50	C60/75	C60/75
Triple blend mix	25% OPC 70% GGBS 5% SF	30-35% OPC 60-65% GGBS 5% SF	25% OPC 70% GGBS 5% SF	30-35% OPC 60-65% GGBS 5% SF	25% OPC 70% GGBS 5% SF	30-35% OPC 60-65% GGBS 5% SF
min C (kg/m ³)	400	380	400	380	420	380
max W/C	0.35	0.35	0.35	0.35	0.33	0.33
d _{max} (mm)	20	20	20	20	20	20
Prot. measures	Membrane	None	None		None	
cover (mm)	70	50	50	50	50	50
Exposure	Chlorides		CO ₂		CO ₂	

6. CONCLUSIONS

The aggressivity of the Arabian Peninsula on the durability of reinforced concrete structures necessitates the need for a structured durability design process. In the Regulation “Guide for the Design of Concrete Structures in the Arabian Peninsula” by the Concrete Society [10], such a process is prescribed, in which the service life of the structure is a direct design parameter and its estimation is encouraged for special types of structures. On this note, comparison and verification of stochastically driven service life values, part of the durability design of the concrete works of the metro rail network of a country in the Arabian Peninsula, with physicochemical deterministic (according to performance-related methods) service life values took place. The results of the deterministic approach, verified the stochastic durability design

performed. In addition, modifications in terms of mix design and protective measures were proposed to enhance the durability of the structural elements, for the demanded service life of 120 years. Overall, taking under consideration the effectiveness of the deterministic approach in service life estimation, as presented in this study, for a considerable highly aggressive environment on concrete structures as that of the Arabian Peninsula, it can be said, that despite concerns which have been raised [2] on the precision of particular models in connection to the real behavior of the structure in the actual service environment, a valid (for the exposure environment) physicochemical verified deterministic approach on service life estimation can produce accurate estimates. Furthermore, if such a tool is reinforced with specific safety factors taking under account the probabilistic nature of the problem (e.g. scatter in material resistance properties and environmental load parameters), a semi-probabilistic method as has been suggested by the *fib* for the action of carbon dioxide, should be the way forward as well for chloride induced corrosion.

REFERENCES

- [1] Demis, S. and Papadakis, V.G., ‘Durability design process of reinforced concrete structures from a practical point of view’, in ‘17th Greek Concrete Conference’, Proceedings, Thessaloniki, November, 2016 (Technical Chamber of Greece, 2016).
- [2] Demis, S. and Papadakis, V.G., ‘Durability design process of reinforced concrete structures-Service life estimation, problems and perspectives’, *J. Build. Eng.* (submitted) (2018).
- [3] EN 1992-1-1, ‘Eurocode 2: Design of concrete structures - part 1-1: General rules and rules for buildings’, European Committee for Standardization, Brussels, (2004).
- [4] EN 1990:2002+A1, ‘Eurocode – Basis of structural design’, European Committee for Standardization, Brussels, (2005).
- [5] EN 206:2013, ‘Concrete - Specification, Performance, Production and Conformity’, European Committee for Standardization, Brussels, (2014).
- [6] *fib* Bulletin 34, ‘Model Code for Service Life Design’, International Federation for Structural Concrete (*fib*), (2006).
- [7] *fib* Bulletin 53, ‘Structural Concrete – Textbook on behavior, design and performance Volume 3’, International Federation for Structural Concrete (*fib*), (2010).
- [8] *fib* Model Code, ‘Model Code 2010 Final Draft’, International Federation for Structural Concrete (*fib*), (2012).
- [9] CIRIA, ‘Guide to the Construction of Reinforced Concrete in the Arabian Peninsula’, Construction Industry Research and Information Association C577-02 (2002).
- [10] CS163, ‘Guide for the Design of Concrete Structures in the Arabian Peninsula’, Concrete Society (2008)
- [11] Song, H.W., Lee, C.H. and Ann, K.Y. “Factors influencing chloride transport in concrete structures exposed to marine environments” *Cem. Concr. Comp.* **30** (2008) 113–121.
- [12] Tamini, A.K., Abdalla, J.A. and Sakka, Z.I., ‘Prediction of long term chloride diffusion of concrete in harsh environment’ *Const. Build. Mat.* **22** (2008) 829–836.
- [13] ALYSJ, ‘Doha Metro: Gold Line- Structural Concrete Durability Assessment M006-GDB-STR-RTP-00016’ (2014).
- [14] Papadakis, V.G., ‘Effect of supplementary cementing materials on concrete resistance against carbonation and chloride ingress’ *Cem. Concr. Res.* **30** (2000) 291-299.
- [15] Papadakis, V.G., ‘Service life prediction of a reinforced concrete bridge exposed to chloride induced deterioration’ *Adv. in Concr. Constr.*, **1** (2013) 201-213.
- [16] Demis, S., Efstathiou, M.P. & Papadakis, V.G., ‘Computer-aided modeling of concrete service life’ *Cem. Concr. Comp.* **47** (2014) 9-18.

EVALUATION OF SERVICE LIFE OF REINFORCED CONCRETE IN THE MIDDLE EAST - EIGHT YEARS OF TESTING

Mohamad Nagi (1), Jessi Meyer (2), Nizar Marjaba (3)

(1) American University in Dubai, Dubai, UAE

(2) Cortec Corporation, St. Paul, MN, USA

(3) Cortec Middle East, Dubai, UAE

Abstract

A comprehensive long-term study managed by the Middle East Durability Research Consortium (MEDRC) was initiated in March of 2010 to evaluate the service life of reinforced concrete structures in the unique environments of the Middle East, and to correlate these findings to standard testing methodology and service life prediction modeling. It is known that chloride-induced corrosion of reinforcing steel in concrete is the main durability factor controlling the performance and service life of concrete structures in the Middle East, which is considered one of the most corrosive places in the world. Structural design of major structures currently include the durability design required to achieve the specified service life of the structures. Developers and Authorities are demanding 100 years or more for their structures with minimum life cycle cost.

Seventeen concrete mix designs currently used in the region were included in the study. The mixes included different levels of supplementary cementing materials (ground granulated blast furnace slag, fly ash and silica fume) with and without corrosion inhibitor (MCI).

The study consisted of laboratory testing and service life prediction. ASTM G 109 is the main laboratory test considered in the study. Three specimens were prepared in accordance with ASTM G 109 for each of the 17 selected mixes and being monitored at the American University in Dubai Laboratory. This paper presents data on corrosion rates, corrosion potentials and chloride transport levels for the different mixes. It also compares actual results with predictions using available service-life prediction models. In addition, for each mix, the chloride migration and diffusion coefficients were measured at three different ages (28, 56 and 90 days). These parameters are used to verify the service life of each concrete mix using the currently available models. Also these data are used to establish correlation between the rapid migration test and the effective chloride diffusion coefficient. At the end of five year testing, Sulfate resistant cement (SRC) and Ordinary Portland Cement (OPC) specimens with and without MCI were broken open and evaluated.

Keywords: Service life, diffusion coefficient, corrosion, concrete durability

1. INTRODUCTION

During the first construction boom in the Gulf and Arabian Peninsula in the early 1970's, many concrete structures were built based on foreign codes without paying attention to the unique environment in the region. As a result, the high temperature and harsh environment have led to a major durability-related deterioration in some of the structures within 10 to 15 years (1, 2).

Currently, the Gulf and Arabian Peninsula region is on the top of the world's list in concrete construction and the daily consumption of concrete is one of the highest rates in the world. From super tall towers to marine, industrial, and highway structures, reinforced concrete (RC) stands as the material of choice used in construction in the region.

In the last decade, Supplementary Cementing Materials (SCM) such as fly ash, silica fume, and ground granulated blast furnace slag (GGBFS) made their way to the Gulf and are commonly used to produce high strength and high performance concrete.

Considering the high initial construction cost, developers and authorities are demanding much longer service life for their structures (75 to 100 years or more) with minimum maintenance and life cycle cost. Due to the harsh and severe environment in the Gulf region, durability characteristics of concrete control its service life. Production of durable and quality concrete is the key to extending the service life of the structures. Designers are now looking into durability modeling to assess the service life of the designed facilities.

In general, service life is the period of time during which a structure meets or exceeds the minimum requirements set for it. The requirements limiting the service life can be technical, functional or economical (3). The technical service life is the time in service until a defined unacceptable state is reached, such as cracking, spalling of concrete or failure of elements. Service life methodologies have application in the design phase of a structure and in the operation phase where inspection and maintenance strategies can be developed in support of life-cycle cost analysis (4).

The main deterioration factors affecting the service life of concrete structures are durability related ones. Durability by definition is the ability of concrete to resist weathering action, chemical attack, and abrasion while maintaining its desired engineering properties. Concrete ingredients and their proportions, and interaction among ingredients, curing and placing of concrete control its ultimate durability (5). Alkali-aggregate reaction, sulfate attack, and corrosion are the main factors affecting the performance of concrete structures. In the Gulf region, while other factors exist, corrosion of reinforcing steel is the main factor controlling the service life of RC structures. The corrosion mechanism is well covered and understood. Steel reinforcement is usually protected in concrete as long as the passive layer (protective iron oxide film) is formed in the high-alkali concrete environment (6, 7). Whenever this layer is damaged, either due to carbonation (reduction in concrete alkalinity) or due to the presence of chloride ions, and in the presence of oxygen, corrosion will start. The chloride-induced corrosion is the common form of corrosion in the region. The Gulf area is predominantly ex-seabed sand. There is a very high chloride content in the soil and ground water. Salt content of the soil can be several times that of the seawater, and when combined with the high ambient temperature and high humidity, the Gulf becomes one of the most corrosive locations in the world.

A long-term study managed by the Middle East Durability Research Consortium (MEDRC) was initiated to evaluate the service life of R/C structures in the unique

environments of the Middle East. The objectives of the program, description of the experimental program, and the updated results collected so far are the focus of this paper.

2. EXPERIMENTAL PROGRAM

The experimental program presented in this paper focuses on assessing the concrete technology in the Middle East and developing guidelines for consultants and concrete designers to select the optimum mixtures, which achieve the designed service life of reinforced concrete structures.

The program was developed by the Middle East Durability Research Consortium (MEDRC), a group of experts representing government authorities, consultants, industry, and academic centers in the region. Based on the experience of MEDRC members, a series of typical concrete mix designs currently used in the Middle East, mainly in the Gulf region were selected. The mixes were carefully selected to represent the majority of the concrete mixes used in all construction sectors in the region.

The selected mixes (Table 1) contain a control mix using Ordinary Portland Cement (OPC) with 0.4 water-to-cement ratio. Other mixes contain Fly ash, Micro silica, GGBFS and sulfate resistance cement (SRC). In addition to the mixes shown in Table 1, similar mixes were prepared using an organic-based corrosion inhibitor.

Table 1. Typical concrete mix designs used in the study (kg/m³)

	OPC	OPC + GGBS	SRC	OPC + PFA	OPC + MS	OPC + GGBS + MS	OPC + PFA + MS	OPC + PFA + GGBS
Date	5/8/201	5/12/201	5/17/201	5/19/201	5/22/201	5/25/201	6/1/2010	6/3/2010
OPC	400	136		280	368	116	260	140
SRC			400					
GGBS		264				20		180
MS					32	264	20	
Fly Ash				120			120	80
Total Cement	400	400	400	400	400	400	400	400
Water	160	160	160	160	160	160	160	160
w/c (Free)	0.40	0.40	0.40	0.40	0.40	0.40	0.40	0.40

As indicated above, chloride induced corrosion is the key durability parameter controlling the service life of concrete structures in the Middle East. Therefore, the experimental program focused on assessing the corrosion preventing characteristics of the selected mixes. Slightly modified ASTM G109 test (8) was used in the study. ASTM G109 is a reliable laboratory test used to assess the corrosion resistance of concrete system based on macroscopic corrosion cell. In the test, two reinforcing steel layers are placed in a concrete prism. One bar is placed at the top near the surface and two bars at the bottom of the prism (Figure 1). The top surface of the prism is subjected to wetting and drying cycles using salt water (3% NaCl). As the chloride ions reach the top bar and exceed the corrosion threshold, the passivated layer around the bar will be destroyed (depasivated) and becomes anodic (9). A corrosion cell is formed, and produce an electrical potential

difference between the top bar and the bottom bars, which remain cathodic (chloride free concrete). This potential difference produces a flow of an electrical (corrosion) current. The top and bottom bars are externally connected through a 100-ohm resistor used to measure the macrocell corrosion current. The measured current is related to the corrosion activity at the top bar. The modification in the test from the ASTM G109 is the use of variety of mixes and reduction of the concrete cover from 25 mm to 20 mm.

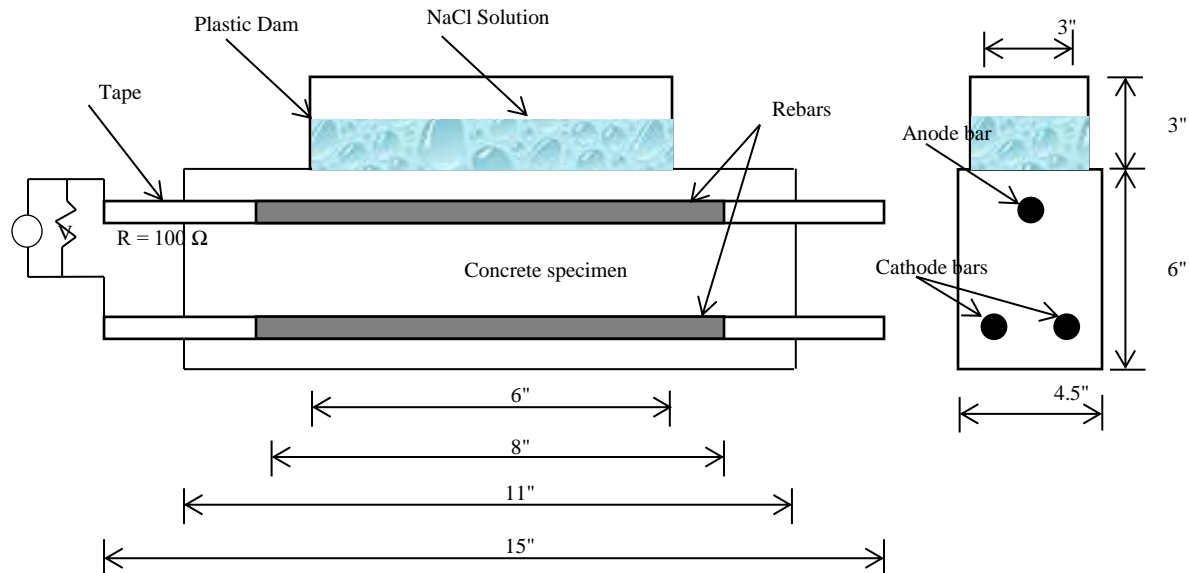


Figure 1. Corrosion test setup

For each concrete mix selected, including the corrosion inhibiting mixes, three specimens were prepared and currently being tested. For each mix, the main durability parameters are measured. Water absorption (BS 1881 Part 122), effective water permeability (BS EN 12390, DIN 1048), and rapid chloride permeability test (ASTM C 1202) were conducted on specimens cured for 28, 56 and 90 days. One of the objectives of the study is to evaluate the current service life models used in the literature and to correlate the findings with the experimental study. The rapid chloride migration coefficient (NT BUILD 492) and the chloride diffusion coefficient (Effective Chloride Transport Coefficient-NT BUILD 443) were measured at the age of approximately 28, 56 and 90 days. The reason behind conducting the diffusion and the migration coefficient tests is to establish a correlation between the two values. One benefit of this correlation is to use the rapid migration test results at the trial stage of mix development to assess the service life of a given mix, based on the preliminary design concrete cover.

The main criteria for selecting the optimum mixture will be based on G109 findings. For each mix, the chloride content at the level of the top steel bar will be measured (corrosion threshold) for the first specimen which reaches a macrocell current of $10 \mu A$. The other two specimens in the set will remain under testing until cracking. The mixes will be evaluated based on threshold values and time of cracking. The measured corrosion threshold values will be utilized in the service life computer models for predicting the service life of a given mix.

In order to correlate the laboratory findings with field performance, field-testing station was established. Relatively large-scale reinforced concrete specimens using selected mixes from the laboratory study program are placed in the field-testing station. Performance of these specimens will be monitored and compared with lab findings.

3. RESULTS

For each mix, workability of the concrete was assessed using the slump test immediately after mixing and after 30 minutes (Table 2). Forty six standard cubes were prepared for each mix. The cubes were used for compressive strength and durability testing. Compressive strength was measured at 1, 3, 7, 28, 56 and 90 days. The range of strength at 28-day age was 46 to 68.8 MPa and 55 to 78 MPa at the age of 90 days. The data shows clearly the difference in strength development between the control mixes and mixes with fly ash and GGBFS, as the hydration of the SCM's such as fly ash is slower than that of Portland cement.

Water absorption, water permeability, and rapid chloride permeability (RCP) test results showed that for all SCM mixes the RCP values were less than 1000 coulombs indicating low permeability. Correlation between the two tests for the SCM mixes at 28, 56 and 90 days were established. Typical comparison between the Chloride migration coefficient (NTB 492) and diffusion coefficient (NTB 443) data tests at 90 days is shown in Figure 2. Tang, L. and Sorensen indicated in their paper published in 2001 (10) that both tests are fairly, comparable.

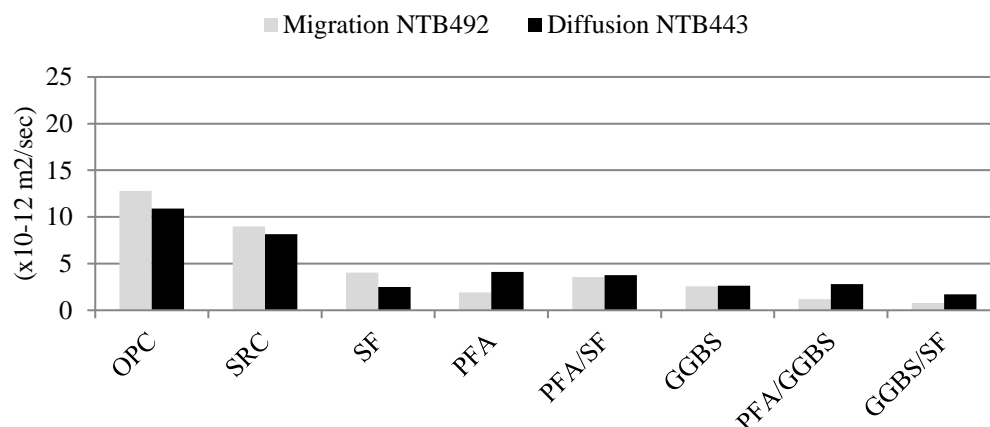


Figure 2. Comparison between chloride diffusion and migration coefficients at 90 days

The up-to-date measured corrosion currents (108-cycle) of the on-going experimental corrosion study were low for the SCM mixes (integrated current less than 50 Coulombs) indicating that no corrosion activity in the top bars has initiated yet in all of the specimens. However, mix (OPC+ PFA + MS) showed higher current started at Cycle 17 as shown in Figure 3.

Powder samples were collected from one specimen of each set of specimens at the level of the steel bars. Samples were collected at the end of the 36th cycle and acid soluble chloride content was measured. Average chloride content of all SCM specimens was 0.03 to 0.06% by weight of concrete, close to corrosion threshold of normal concrete. One cycle

after collecting the samples for chloride analysis and core holes in the specimens were grouted, misleading results were obtained on some of the specimens, most likely due to damage occurred in the specimens, therefore, such specimens readings were removed from data analysis of the program.

The relatively high readings in the (OPC+PFA + MS) mix is most likely due to the properties of concrete of such specific mix. However, the macrocell current readings are still less than 10 μ A. The half-cell potentials measured on the top surface of all ASTM G 109 specimens in accordance with ASTM C 886 were more positive than -150 mV indicating that corrosion has not been initiated yet.

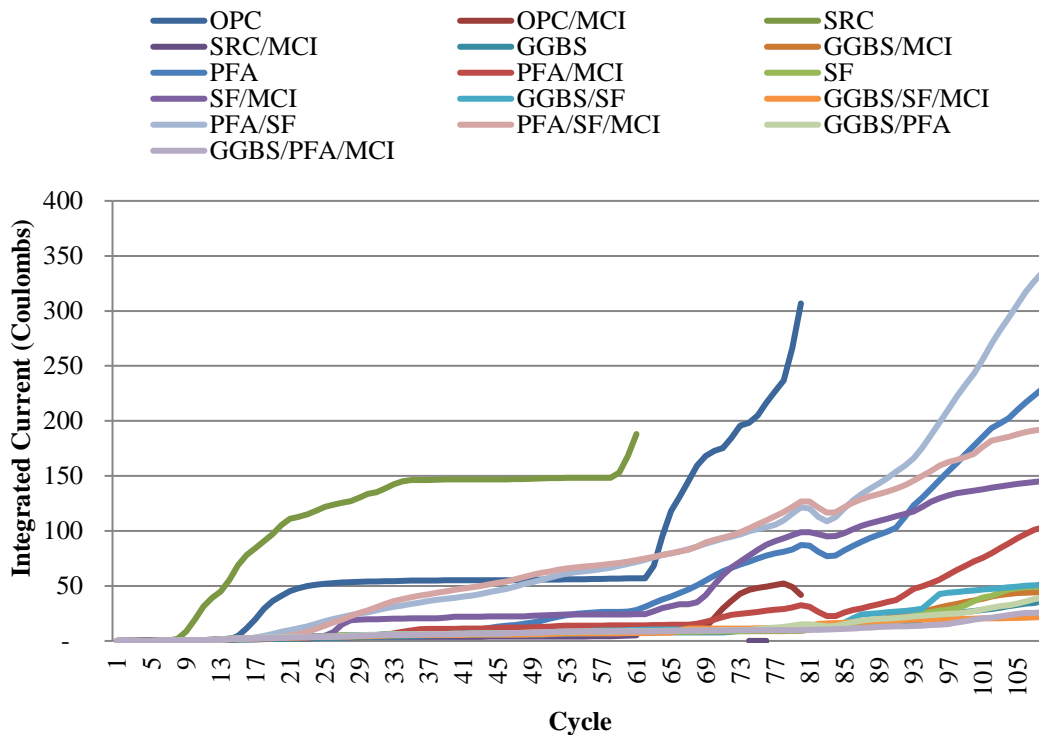


Figure 3 Integrated current (Coulombs) v. number of cycles for all mixes

3.1 Interim corrosion test

The control mix containing SRC and OPC showed relatively high corrosion current starting at cycles 11 and cycle 17, respectively.

At cycle 63, the integrated current of SRC control mix reached 150 Coulombs. Figures 4 shows total integrated macrocell current (Coulombs) vs. number of cycles for the control mixes with and without corrosion inhibitor (MCI).

At cycle 70, the integrated current of OPC control mix exceeded the 150 Coulombs as well. Figure 4 shows total integrated macrocell current (Coulombs) vs. number of cycles for the control mixes with and without corrosion inhibitor (MCI).

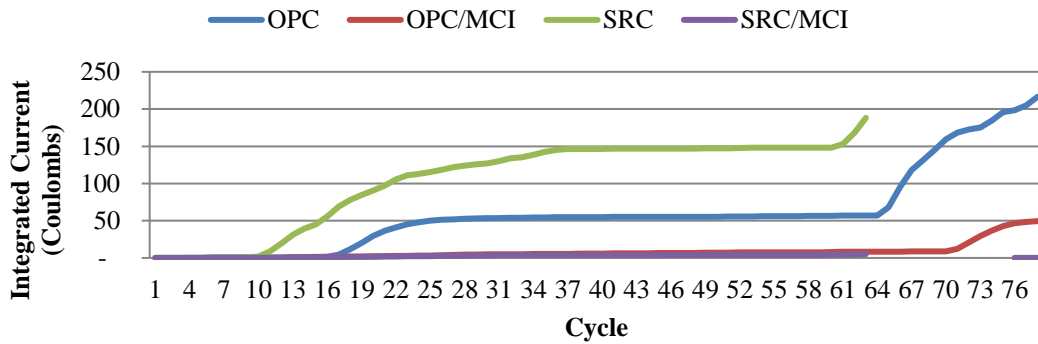


Figure 4 Integrated current (Coulombs) vs. number of cycles for SRC and OPC mixes

When the integrated current reached 150 Coulombs or higher, specimens should be broken and reinforcing steel bars examined in accordance with ASTM G 33 and ASTM G 46. SRC and OPC (control) and SRC and OPC with MCI mixes specimens were broken and reinforcing steel specimens. Typical Photos of the reinforcing steel bars of SRC and OPC specimens are shown in Figures 5 and 6. As shown in the figures, steel bars of control specimens were subjected to uniform corrosion and pitting as well, while the bars of SRC and OPC with MCI specimens were in a good shape with no pitting or uniform corrosion observed. The mass loss of control bar was close to 1% and the pitting is rated 3 in accordance of ASTM G 46. Average soluble chloride contents measured in the vicinity of the bars were 0.16% by weight of concrete of MCI specimens and 0.11 % for the control specimens.



SRC Control



SRC with MCI

Figure 5 Reinforced steel removed from of SRC and SRC with MCI



OPC Control



OPC with MCI

Figure 6 Reinforced steel removed from OPC and OPC with MCI specimens

4. SUMMARY AND CONCLUSIONS

- A comprehensive research study is currently being conducted under the supervision of MEDRC in order to evaluate the effectiveness of the majority of concrete mixes used in the Middle East in reducing corrosion of reinforcing steel.
- Up-to-date results of G109 test indicated that there is no corrosion activity in the main SCM mixes.
- Corrosion activities were observed in the Control mixes specimens prepared with SRC and OPC. Laboratory inspection of such mixes showed that the use of MCI enhance the service life of such mixes compared to control ones. While the SRC and OPC mixes showed corrosion activities exceeding the ASTM G 109 criteria, no sign of corrosion was observed in the SRC+ MCI and OPC + MCI specimens.

REFERENCES

- [1] Concrete Society, "Guide to the Maintenance and Repair of Reinforced Concrete Structures in the Arabian Peninsula", presented at the Bahrain 6th International Conference, November 2000.
- [2] Rasheeduzzafar et al., "Deterioration of Concrete Structures in the Environment of the Middle East," ACI Journal proceedings, Vol. 81, No. 1, pp. 13-20, 1984.
- [3] Vesikari, E, "Service Life of Concrete Structures with regard to Corrosion of Reinforcement," Technical Research Centre of Finland, ESPOO 1988.
- [4] American Concrete Institute, ACI 365 "Service-Life Prediction," ACI, Detroit, MI, USA.
- [5] Kosmatka et.al, "Design and Control of Concrete Mixtures," Fourteenth Edition, Portland Cement Association, Skokie, IL, U.S.A.
- [6] Nagi, M. and Whiting, D, "Corrosion of Prestressed Reinforcing Steel in Concrete Bridges, State-of-the-Art," Concrete Bridges Aggressive Environments Symposium, SP 151, 1994 American Concrete Institute, Detroit, Michigan, U.S.A.
- [7] Broomfield, J., "Corrosion of Steel in Concrete," 1997 E & FNSpon, U.K.
- [8] American Standard and Testing Materials, ASTM G109 "Standard Test Method for Determining Effects of Chemical Admixtures on Corrosion of Embedded Reinforcement in Concrete Exposed to Chloride Environment." West Conshohocken, PA, U.S.A.
- [9] Virmani, Y.P, "Time-to-Corrosion of Reinforcing Steel in Concrete Slabs, Vol. VI, Federal Highway Administration, FHWA-RD-88-165, 1980-1987.
- [10] Tang, L and Sorensen, H.E. "Precision of the Nordic Test Methods for Measuring the Chloride Diffusion/Migration coefficients of Concrete." Materials and Structures, Vol. 34, October 2001, pp 479-485.

8-YEAR PERFORMANCE OF CATHODIC PROTECTION SYSTEMS IN REINFORCED CONCRETE SLABS AND LIFE-CYCLE COST BENEFITS

Deepak K. Kamde (1), Naveen Krishnan (1), Radhakrishna G. Pillai (1), George Sergi (2), Dhruvesh Shah (2), and Rajendran Velayudham (3)

(1) Department of Civil Engineering, Indian Institute of Technology Madras, India

(2) Vector Corrosion Technologies Ltd., UK & India

(3) Trade winds, Chennai, India

Abstract

NACE impact report (2016) states that nearly 50% of reinforced concrete (RC) structures experience major repair in about 10 years. The existing approach of conventional patch repair does not usually address the root cause and may not be durable – resulting in re-repairs in short period (say, 5 to 10 years) and substantial economic loss. Clients and practitioners do not adapt to cathodic protection technique as their preference, due to limited long-term performance data. Besides, clients wrongly believe that the installation of the anode can significantly increase the cost of repair. This paper presents data disproving these two wrong beliefs. For this, two slab specimens of (1 × 1 × 0.25) m were cast with chloride contaminated concretes (2% Cl⁻ by weight of cement) and subjected to natural exposure for eight years. Protection current and corrosion potential were recorded at various instances during this period. It was found that the sacrificial anode systems could mitigate the corrosion of steel reinforcement in RC structures for long term. In addition, a case study was conducted on a coastal finger jetty repaired using a sacrificial anode cathodic protection (SACP) system. Depolarized steel potential was monitored for 4.5 years. For the same structure, life-cycle cost analysis was performed and compared with other service life extension techniques; such as cathodic prevention using sacrificial anode and the conventional patch repair using micro-concrete. It was found that the life-cycle cost of repair with sacrificial anode cathodic prevention and protection systems were significantly lower than the total cost of repair using conventional patch repair.

Keywords: Reinforced concrete, chlorides, corrosion, repair, cathodic protection, cathodic prevention, sacrificial anodes, life-cycle cost.

1 INTRODUCTION

Corrosion of reinforcement is one of the major deterioration mechanisms in reinforced concrete (RC) structures. The poor quality of material and construction practices can lead to premature corrosion of rebars in concrete structures. NACE (2016) reported that 50% of structures experience a major repair in about 10 years of service. Generally, conventional repair techniques (say, patch repair, partial replacement of concrete, microconcrete, etc.) are used to repair these concrete structures. However, due to the differential pH of the new and parent concrete, the probability of formation of localized corrosion cells at the interface between the new and parent concretes is high [1] – resulting in repeated repair. If we continue the repair with conventional repair methods, soon, a large number of infrastructures will need major repair. In the Netherlands, it is expected that there will be about 670 to 1220 bridges that require repair by 2020 [2]. However, if regular maintenance and cathodic protection (CP) systems are adopted, this number can be reduced significantly to about 50 bridges (about 85 to 95% reduction). Similarly, a study by the Indian bridge management system found that at least 6000 bridges are structurally distressed and would need immediate repair. If repaired without considering the durability of the repair, then the future repair costs would be very high. Similar is the case with many countries and there is a need to sensitize the stakeholders on the life-cycle cost benefits of cathodic prevention/protection (CP/P) systems.

CP/P is widely used in protecting corrosion in metallic structures. The principle is to force the steel (metal to be protected) to become cathode by supplying the additional electrons from the anode. Recently, this application is extended to concrete structures. Sacrificial anode cathodic protection (SACP) systems are used for CP/P of reinforced concrete structures (BS 12696 2012). Cathodic prevention (CPrev) is meant for delaying the initiation of corrosion and can be achieved by installing the anodes during the construction stage or when the rebars are not in active state of corrosion. On the other hand, the cathodic protection (CP) is a technique, where sacrificial anodes are installed for mitigating the ongoing corrosion.

In most cases, CP/P technique is not adapted while repairing RC structures. This may be due to the lack of experience and evidence on the long-term performance of sacrificial anodes. There are many literature available to validate the working of CP/P for RC systems in laboratory studies [3-5]. Though, a very few literature are available to substantiate the long-term performance of sacrificial anodes in RC structures [6-9]. Also, many clients wrongly believe that the cost of the anodes can significantly increase the cost of repair. Therefore, there is a dire need to generate the database on working of SACP systems for long-term performance. Byrne et al. (2016) reported that the cost of anode for CPrev was around 2-3% of the total project cost [11]. The cost may vary based on the corrosion rate, steel density, resistivity of base and repair concretes, exposure conditions etc.. For better comparison of these techniques, a detailed life-cycle cost analysis of structures with conventional patch and CP/P techniques is necessary. This paper presents data from an 8-year long laboratory experiment on the performance of CP in concrete slab specimens. Also, 4-year data on the performance of CP in a marine structure and the cost benefits of various repair options (say, conventional repair and CP/P techniques) are presented.

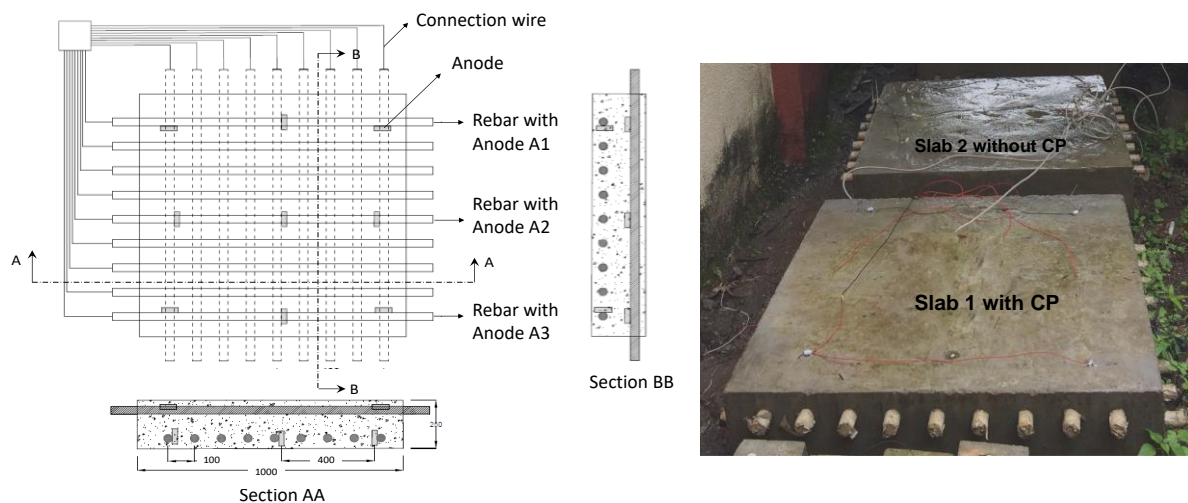
2 EXPERIMENTAL PROGRAM

To investigate the performance of SACP anodes, this study is divided into three parts: i) 8-year long exposure of RC slabs and ii) cathodic protection of finger jetty using sacrificial anodes,

and iii) life-cycle cost analysis of the cathodic prevention technique and the repairs using conventional patch repair with and without cathodic protection.

2.1 8-year long natural exposure of RC slabs in laboratory

Figure 1 shows the schematic and photograph of the slab specimens with a dimension of (1×1×0.25) m with 32 mm diameter transverse and longitudinal rebars at 100 mm c/c distance. This makes ratio between the steel surface area to the concrete surface area to 1.45. The concrete was prepared with 360 kg/m³ of Ordinary Portland Cement (53 Grade) and a water-to-cement ratio of 0.55. Also, it was premixed with 2% chlorides by weight of cement. One slab each with and without sacrificial anodes (Slab 1 and Slab 2, respectively) were cast. The number of anodes was decided based on the corrosive environment of concrete and steel surface area. Three sacrificial anodes (A1, A2, and A3) with surface areas of 4000, 8000, 16000 mm², respectively, were installed in the Slab 1. The slab specimens were cast and cured for 7 days. Later, these slabs were placed in a natural marine environment (within 10 km distance from the seashore) with relative humidity ranging from 65 to 85 % throughout the year. This creates a highly corrosive environment. Protection current output from each type of anodes and corrosion potentials of depolarized steels were measured frequently during the 1st and then at the end of 7th and 8th year of exposure. In addition, corrosion potential of Slab 2 without sacrificial anodes (say, control specimen) was also measured.



a) Schematic of anode locations in Slab 1

b) Photograph of Slab1 and Slab 2

Figure 1: Schematic and photograph of the concrete slabs with and without sacrificial anodes

2.2 4-year long natural exposure of RC piers in marine environment

Figure 2 shows the photographs from a 20-year old finger jetty located in the East coast of South India, was considered for this study. The finger jetty is expected to have the service life of 100+ years. These piers experience cyclic wetting and drying condition in the splash zone – leading to accelerated chloride ingress. After about 20 years of service, significant corrosion was observed on the splash zone of the piers (see Figure 2(a)). It was also found that the chloride concentration at rebar level was significantly higher than the chloride threshold of the

steel rebars. Concrete jacketing with additional rebars was done to enhance the strength of the piers. For this, a total of 9200 kg of additional reinforcing steel and 10 m³ micro concrete were used. Considering the high chloride concentration at the rebar level, a total of 1390 sacrificial anodes were installed in various structural elements (pier, pier cap, longitudinal beams, and slabs). Figure 2(b) shows the additional reinforcement and sacrificial anodes installed on a typical pier. A monitoring box was installed so that the sacrificial anodes can be disconnected to measure the depolarized potentials. Figure 2(c) shows the piers after repair using CP technique. Later, the depolarized steel potentials were monitored for about 4.5 years.



Figure 2 Finger jetty in the coastal region

2.3 Life-cycle cost analysis

Life-cycle-cost of any structure involves repair cost, which is the sum of the direct and indirect costs. The direct cost includes the cost of concrete removal, surface preparation of steel and concrete, repair material, anodes, manpower, monitoring box, etc.; whereas the indirect cost includes the cost of change/interruption in functionality of the facility, etc.. Also, the life-cycle cost is dependent on the number of repairs and corresponding costs. For this study

jetty structure with one repair, the direct cost was obtained from the project consultant. To obtain the cost of repeated repairs, the inflation rate was assumed to be 5% and the indirect cost was ignored during this cost analysis. Then, the life-cycle cost was estimated for the aforementioned scenarios with the following strategies: (i) CR - conventional patch repair using microconcrete and without CP, (ii) CP - conventional patch repair using microconcrete and with CP (iii) CPrev - cathodic prevention. Considering the steel density, corrosion rate, chloride concentration at rebar level, and the number of anodes provided, the service life of this repair was determined using Faraday's law. It was found that the provided anodes can mitigate/control the corrosion of rebar in the structure for about 15 years. For this, the cost of repair was calculated. In addition, cost for conventional patch repair and CPrev was estimated for the same structure. For conventional repair, the cost of direct repair was calculated by eliminating the cost of sacrificial anodes from the adopted strategy (repair using SACP). For cathodic prevention, the required protection current was assumed to be 0.6 mA/m^2 . The spacing between anodes was assumed to be the same as that for cathodic protection (i.e., 500 mm). Considering the assumed spacing of anodes and the current density, the expected service life of these anodes was found to be about 100 years. In the present analysis, it was assumed that the life of conventional repair is about 5 years.

3 RESULTS AND DISCUSSIONS

3.1 Long-term performance of sacrificial anodes – Laboratory experiments

Figure 3(a) shows the average current output from Slab 1 with A1, A2, and A3 type sacrificial anodes. For the entire exposure period, the instantaneous current output ratio was found to be 1:2:4, which is proportional to the ratio of surface area of these anodes. The output current reduced significantly during the initial exposure time (say, upto about 2 months) beyond which the rate of change was negligible – indicating a reduction in the corrosion rate of the rebars. Note that at the end of 8 years, the output current from the anodes A1, A2, and A3 were 0.3, 0.6, and 1.8 mA, respectively. Sum of these are more than 2 mA, which is usually required to maintain a passive state for steel exposed to aggressive conditions. This also indicate that the anodes are able to supply the required current even after 8 years. Figure 3(b) shows the average depolarized corrosion potential of individual rebars of the slab with and without sacrificial anodes, measured at the end of 8 years of exposure – also indicating that the anodes A1, A2, and A3 may perform for longer period.

3.2 Long-term performance of sacrificial anodes – Field experience & cost benefits

Figure 4 shows the half-cell potential of the steel reinforcement before and after the repair of the piers of finger jetty. The depolarized steel potentials were monitored for 48 months, and they were found to be more positive than -270 mV versus CSE. As per ASTM C876, this indicate that the probability of corrosion is less than 10% at the end of 4 years after installation. The anodes were installed in 2008 and the structure (after 10 years) is still not in need of a major repair. Figure 5 shows the comparison of the estimated cost of CPrev, CR, and CP as defined earlier. CR1 and CP1 represent the point of the first repair using the conventional patch repair with and without sacrificial anode systems, respectively. The total cost of the sacrificial anodes

used during this repair was about 2.5 % of the total cost of repair. Once these anodes are consumed, a replacement of anodes may be required to mitigate the further corrosion process.

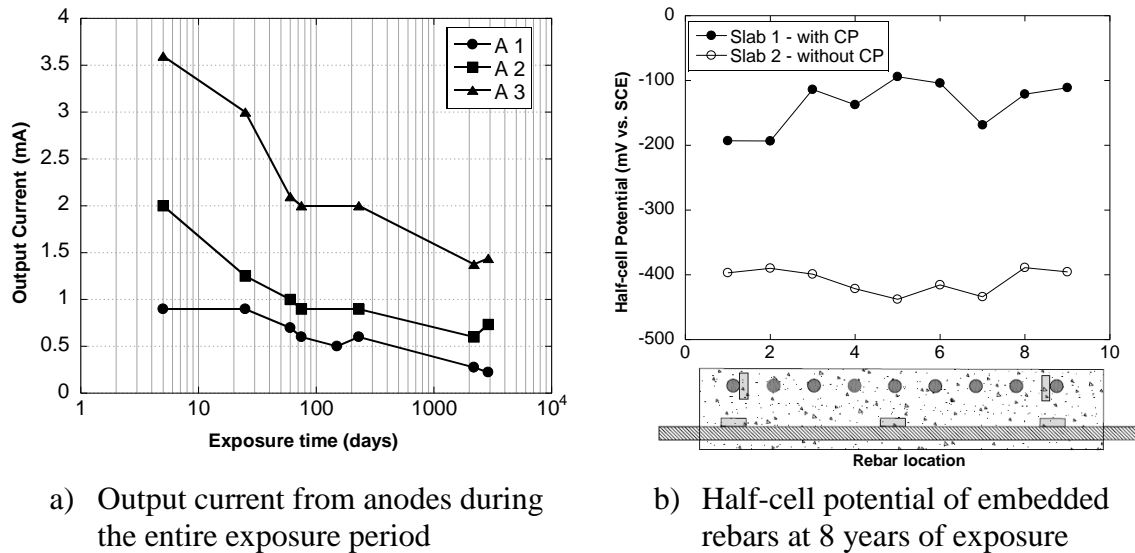


Figure 3 Long-term performance of anodes in protecting the embedded steel reinforcement

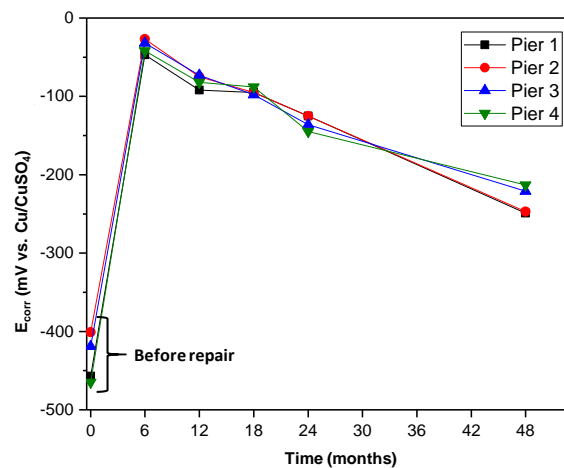


Figure 4 Corrosion potentials of pier elements

As exhibited in Figure 4 and corresponding discussions, the time between the 1st and 2nd repair could be about 10 to 15 years. Assuming this to be 15 years, the anodes may need to be replaced for three times (mentioned as, CP2, CP3, and CP4) to meet the service life of 80 years. The cost of each repair was calculated by assuming the inflation rate at 5%. It was also assumed that after the failure of 4th repair, the structure will approach its end of service life (EOL).

A similar cost analysis was performed for other two service life extension techniques (say, CR and CPrev). In Figure 5, CR1 represents the point of first conventional repair using microconcrete. The total cost of consecutive conventional repairs (say, CR1 + CR2 + CR3) was estimated to be significantly higher than the total cost of repair using CP approach

(CP1 +...+CP4). In the case of CR approach, the corrosion could initiate in the regions adjacent to the repaired regions (due to halo effect) and at other regions (due to chloride attack) leading to deterioration of repaired and other regions. Therefore, the EOL was assumed to approach after two repeated repairs of CR2 and CR3 (i.e., a total service life of 35 years). In the case of CPrev approach, sacrificial anode systems could be designed such that no repair would be required for long period of time (say, several decades). This is possible because the output current required is much less in the case of CPrev because the system does not allow the steel to depassivate. Further studies are required in these areas. However, CPrev technique can be considered as the most economical strategy for the prevention of corrosion and extension of the service life – a very good preventive maintenance strategy.

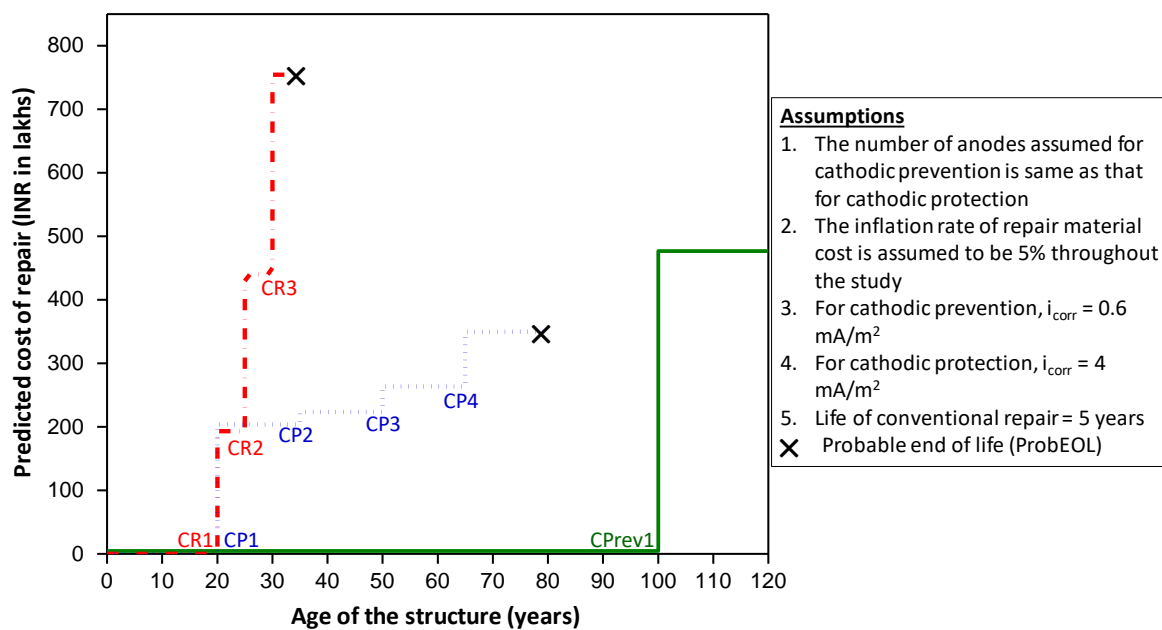


Figure 5: Life-cycle cost of repair for finger jetty

4 CONCLUSIONS

Sacrificial anodes were installed in slab specimens (for laboratory study) and in piers in marine environment (for field study). Depolarized corrosion potential measurements of the rebars indicated that the sacrificial anodes could passivate the steel reinforcement even in highly aggressive environment. With adequate design and intact electrical connections, the cathodic protection approach is expected to mitigate the corrosion for about 10 to 15 years. Also, the life-cycle cost analysis for the case study showed that the cathodic prevention is the most economical repair technique [i.e., among cathodic prevention (CPrev) and the conventional repairs with and without sacrificial anodes (CR and CP)].

ACKNOWLEDGEMENTS

The authors acknowledge the financial support from the Ministry of Human Resource and Development, Govt. of India through the Department of Civil Engineering, Indian Institute of

Technology (IIT) Madras, Chennai, India. Also, the support from the Vector Corrosion Technologies – India and Canada in preparing the test specimens and early age data and the support from Dr. Prakash Nanthagopalan in the Department of Civil Engineering, IIT Bombay, Mumbai, India in storing the test specimens for continued natural exposure is acknowledged.

REFERENCES

- [1] M. Raupach, 'Patch repairs on reinforced concrete structures - model investigations on the required size and practical consequences', *Cem. Concr. Compos.* 28 (8) (2006) 679–684.
- [2] R. Polder, G. Leegwater, and D. Worm, 'Service life and life cycle cost modelling of cathodic protection systems for concrete structures', *Cem. Concr.* 47 (2014) 69-74.
- [3] L. Bertolini and E. Redaelli, 'Throwing power of cathodic prevention applied by means of sacrificial anodes to partially submerged marine reinforced concrete piles: results of numerical simulations', *Corros. Sci.* 51 (9) (2009) 2218 – 2230.
- [4] M. J. Dugarte and A. A. Sagüés, 'Sacrificial point anodes for cathodic prevention of reinforcing steel in concrete repairs: Part 1-polarization behavior', *Corrosion* 70 (3) (2014) 303–317.
- [5] Sagues, A. A., and M. J. Dugarte, 'Galvanic point anodes for extending the service life of patched areas upon reinforced concrete bridge', (2009) Department of Civil and Environmental Engineering, University of South Florida, Tempa.
- [6] G. Sergi, 'Ten-year results of galvanic sacrificial anodes in steel reinforced concrete', *Mater. Corros.* 62(2), (2011) 98–104.
- [7] R. B. Polder and W. H. A. Peelen, '25 Years of Experience with Cathodic Protection of Steel in Concrete in the Netherlands', *Durability of Reinforced Concrete from Composition to Protection.* (2014) 69–75.
- [8] M. Walsh and A. Sagues, 'Steel Corrosion in Submerged Concrete Structures - Part 1: Field observations and corrosion distribution modeling', *Corro. Jour.* 72(4) (2016) 518 - 533.
- [9] NACE, 'SP0290-2007 Standard Practice Impressed Current Cathodic Protection of Reinforcing Steel in Atmospherically Exposed Concrete Structures', NACE International Impact Report, 2007.
- [10] A. Byrne, N. Holmes, and B. Norton, 'State-of-the-art review of cathodic protection for reinforced concrete structures', *Mag. Concr. Res.* 68(13) (2016) 664–677.

ORGANIC CORROSION INHIBITORS – BIO BASED TECHNOLOGY TO EXTEND DURABILITY OF CONCRETE FOR NEW BUILD AND EXISTING STRUCTURES PERFORMANCE

Ivana Lipošćak(1) ,Jessi Meyer(2) , Boris Mikšić(3)

(1) Cortec Corporation, Croatia

(2) Cortec Corporation, SAD

(3) Cortec Corporation, SAD

Abstract

Corrosion of embedded steel is a leading cause of deterioration in reinforced concrete structures. While concrete mix designs have become more durable, the possibility of cracking due to shrinkage, movement, or other forces is a consideration when designing for long service life. In addition, preserving integrity and extending the useful service life of existing structures is of paramount importance. Migrating, organic corrosion inhibitors have been used for more than 30 years in construction applications as an economical method of corrosion mitigation. Migrating corrosion inhibitors, based on organic amines have become available with the claimed advantage that, as well as being capable of application as admixtures, they may be applied as remedial agents to the surface of the concrete. This paper will give details on the chemistry of organic corrosion inhibitors, test methods used to assess the efficacy of migrating corrosion inhibitors in concrete and their performance in new construction, repair and specialty applications.

Keywords: Organic Migratory Corrosion Inhibitor, Test methods, Concrete, New Construction, Repair Speciality

1. INTRODUCTION

High performance mix designs have significantly improved the quality of today's concrete. Unfortunately, cracking, whether due to shrinkage, settlement or other forces, is a reality that is never eliminated no matter how good concrete is. The need for a corrosion inhibitor that can provide protection in the presence of minor cracks is very real. In addition, with aging infrastructure, preserving the integrity of structures and extending useful service life is of paramount importance. Surface corrosion inhibitor treatments must be capable of penetrating to the depth of embedded reinforcing steel. Migrating organic corrosion inhibitors meet these challenges in a cost-effective manner. They are available in many different forms for all types of construction – admixtures for new concrete; repair mortars and grouts; topical treatments; injectable products; and many specialty formats.

Organic corrosion inhibitors (OCI) are effective against chloride induced corrosion, as well as carbonation and other corrosive elements (H₂S, SO₂, etc.). Organic corrosion inhibitors (OCI) are amine-based chemicals that possess saturated vapour pressure under atmospheric conditions, thus allowing vapour transport of the inhibitive substance [1]. Concrete and other cementitious materials have pore structures that allow for liquid and vapour diffusion of these chemicals throughout the substrate. When organic inhibitors encounter embedded reinforcing, they have an attraction to it, adsorbing onto the metal surface forming a protective molecular layer.

OCI are a mixed (anodic/cathodic) inhibitor system. The inhibition of the cathodic process is achieved by the incorporation of one or more oxidising radicals in an organic molecule. Inhibitor molecules are hydrolysed in the electrolyte and then adsorbed on the metal surface. The nitrogen of the amine group can enter a coordinate bond with metal (including steel reinforcement) thus enhancing the adsorption process. Adsorption of amines and carboxylates increases the resistivity of metal to corrosion. This molecular layer serves as a buffer to hold the pH at the interface in the basic regime (above pH 9) [2].

Organic corrosion inhibitors migrate through the concrete depending on the OCI type and application method. OCI admixtures are readily dispersed in the mixing process and can also migrate to reinforcement by diffusion as both a liquid and a vapour. OCI surface treatments penetrate first as a liquid through capillary suction and then by diffusion [3].

The first generation of OCI was based on amine alcohol technology. The latest generation is based on amine carboxylates. The amine carboxylate technology includes by-products of corn – a renewable resource.

Amine carboxylate based OCI can delay setting time of concrete 3-4 hours at 20°C. This delay is less pronounced at warmer temperatures. Set delay is a desired side effect in warm weather as less retarder will need to be added to the concrete mix when using OCI. Combining amine carboxylate based organic corrosion inhibitors with some set retarding materials (admixtures) may create increased setting times, but generally no other concrete properties are affected. In cases where set delay is not desired, normal set (NS) versions of OCI have been developed, or non-chloride accelerators can be used.

2. CHEMISTRY OF ORGANIC CORROSION INHIBITORS

Corrosion inhibitors are classified based upon the part of the corrosion cell that they affect. Organic corrosion inhibitors are classified as mixed inhibitors, meaning they affect both anodic and cathodic portions of the corrosion cell. These inhibitors adsorb onto metal, forming a protective molecular layer on steel surfaces. This film prevents corrosive elements from further reacting with embedded reinforcement and reduces existing corrosion rates. Adsorption of the inhibitor takes place via its polar functional group anchored to the metal while the non-polar or hydrophobic chain is oriented perpendicularly to the metal surface. The hydrophobic chains not only repel aqueous corrosive fluids but interact with each other to form aggregates thereby forming a tight film on the metal surface [2]. Figures 1 and 2 illustrate adsorption of amine alcohol and amine carboxylate organic inhibitors respectively.

Organic migrating corrosion inhibitors reach embedded reinforcement in several ways. First, the inhibitor is dispersed through the concrete with adequate mixing. The transportation of OCI within concrete then occurs via infiltration through concrete pore capillary networks. Thirdly, due to their relatively high vapour pressures, OCI move via diffusion in a gaseous state through the pore network and minor cracks. Finally, when the molecules meet embedded metals, they have a specific attraction (as described above) to it. The molecules move randomly from areas of high concentration to areas of low concentration until equilibrium is reached (Fick's 2nd

Law of Diffusion). Because of the final adsorption of OCI on embedded metal, the concentration gradient drives OCI to move towards the metal. X-Ray Photoelectron Spectroscopy (XPS) analysis has demonstrated the nitrogen rich layer (from amine moiety in OCI molecules) formed on rebar surfaces embedded in concrete that received a topical treatment of OCI. This protective, monomolecular layer also reduces the corrosion rate [4,5].

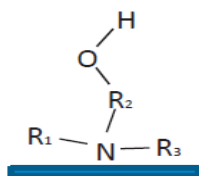


Figure 1. Illustration of Amine Alcohol Inhibitor, where R1,2,3 is H or alkyl group, OH tail end group

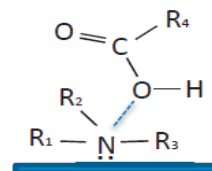


Figure 2. Illustration of Amine Carboxylate Inhibitor, where R1,2,3 is H or alkyl group, OH tail end group

Amine alcohols differ from amine carboxylates in their tail end group. As can be seen in Figures 1 and 2 above, the amine alcohols contain an OH terminal group at the tail end, whereas amine carboxylates have no such hydrophilic terminal group. The exposed OH group on amine alcohols makes it available to interact with water-based electrolyte near the rebar. This means that the amine alcohol film could more easily desorb from the metal surface compared to the amine carboxylate film and allow corrosive species (such as chlorides) to attack the metal. As a result, the amine carboxylate based OCI by nature have a more tenacious bond to the metal surface [2]. The strength of the bond between the OCI molecule and the rebar is what delays the onset of corrosion and reduces corrosion rates compared to a control once initiated. With amine alcohols, we typically see a slight extension in time to corrosion initiation, and corrosion currents cut in half compared to a control following corrosion initiation. With amine carboxylates, we typically see a double to tripling in time to corrosion initiation, and once corrosion starts, rates are reduced by 5-15 times compared to a control [6]. Another small effect amine carboxylates have is that as they migrate through the concrete, some of them will react with calcium hydroxide to form calcium carboxylate/ $\text{Ca}(\text{COO})_2$, an insoluble salt, which effectively blocks some of the pores, making future ingress of chlorides and other contaminants more tortuous [7].

There are many test methods used to assess the efficacy of migrating corrosion inhibitors in concrete. It is important to note that these tests are described by category – corrosion protection, migrating ability, film forming ability, and compatibility with other materials.

2.1 Assessment of Corrosion Protection

The most widely used test method for evaluating concrete corrosion inhibiting admixtures is ASTM C1582 / C1582M – Standard Specification for Admixtures to Inhibit Chloride-Induced Corrosion of Reinforcing Steel in Concrete [8]. This standard consists of two components. The first is an evaluation of how the corrosion inhibitor affects concrete properties such as setting time, air entrainment, compressive and flexural strengths, freeze thaw resistance, and length change. The second component involves corrosion testing according to ASTM G109 – Standard Test Method for Determining Effects of Chemical Admixtures on Corrosion of Embedded Steel Reinforcement in Concrete Exposed to Chloride Environments [9] or ASTM G180 – 13, Standard Test Method for Corrosion Inhibiting Admixtures for Steel in Concrete by Polarization Resistance in Cementitious Slurries [10].

ASTM G109 test samples can be seen in Figure 3 below. The test consists of casting concrete blocks containing a triangular arrangement of rebar embedded within them – one bar on top and two on the bottom. These samples are then exposed to cyclic wetting and drying cycles with salt water, and the macrocell current between the top bar and bottom two bars is monitored and recorded every 4 weeks (4 weeks = one cycle). The testing stops once the total integrated macrocell current reaches 150 Coulombs.



Figure 3. Example of ASTM G109 Test Blocks

The ASTM G180 – 13 [10] test method provides a means for assessing corrosion-inhibiting concrete admixtures in a filtered cementitious liquid. Compared with a testing period of up to a few years required by ASTM G 109, this test method provides results within a few days. In this test, the polarization resistance of a steel sample is measured by applying a current through the test solution while varying the voltage. According to ASTM C1582, an admixture is behaving as a corrosion inhibitor when using the G180 Test Method (using 0.5 M NaCl with four control and four test specimens) if the mean $1/R_p$ value is less than or equal to $1/8$ the control average. Poor performance in G180 requires additional testing to determine if the admixture improves corrosion resistance.

Electrochemical Impedance Spectroscopy (EIS) is a powerful, rapid and accurate non-destructive method for the evaluation of a wide range of materials including coatings, anodised films and organic corrosion inhibitors on metal surfaces [11]. During EIS experiments, a small amplitude AC signal is applied to the metal system being studied. Data from EIS can provide detailed information on corrosion rate, electrochemical mechanisms, reaction kinetics, and detection of localised corrosion in a system.

In addition to the above standard tests, ASTM G109 is frequently modified to make it more aggressive so results can be seen faster. These tests are generally referred to as a Modified ASTM G109 or a cracked beam test. In a cracked beam test, test samples are created in the same manner as the ASTM G109 standard shown above, but the beams are cracked in a controlled way (saw cut and application of flexural stress) prior to salt water cycling to make the test more aggressive. Other modifications include changing the NaCl (salt) concentration (increasing from 3.5% to 6%) as well as the cycle times (adjusting from 4 weeks down to as little as 1-week cycles). Another variation on ASTM G109 is permanent immersion of concrete beams in salt water instead of using ponding cycles.

The most recent test for evaluating organic corrosion inhibitors in repair applications is the U.S. Bureau of Reclamation M-82 - *Standard Protocol to Evaluate the Performance of Corrosion Mitigation Technologies in Concrete Repairs* (USBR M-82) [12]. The protocol covers two methods for measuring and differentiating the performance of reinforcing steel corrosion mitigating techniques for concrete repairs caused by damage due to chloride ingress. This protocol doesn't differentiate between active and passive corrosion, but it has all of the positive aspects of impedance testing (described in EIS above) but on a larger scale which is more representative of slabs in the field [13].

2.2 Assessment of Migrating Ability

Migration of OCI materials into concrete can be evaluated using UV Spectroscopy. This method allows us to detect OCI presence at various depths of concrete by analysing sliced core samples. OCIs are visible in the UV range. By extracting powdered concrete in deionised water, and measuring the extract using UV spectroscopy, the presence of OCI in concrete can be detected. This is done by comparing the absorbance values from treated concrete against the absorbance values of untreated concrete at specific wavelengths. While initial results are only qualitative, if a calibration curve is created with known doses of OCI, the actual concentration can be more accurately determined.

2.3 Assessment of Film Forming Ability

The film forming ability of OCIs can be measured using Scanning Electron Microscopy (SEM) and X-ray Photoelectron Spectroscopy (XPS). SEM is microscopy that produces images of a sample by scanning it with a focused beam of electrons. The electrons interact with atoms in the sample, producing various signals that can be detected and contain information about the sample's surface composition and topology. The presence of OCI, or the lack of it, on metal surfaces can thus be detected.

XPS is a spectroscopic technique in which a beam of x-rays is focused onto the surface of a material and as the beam bounces off the surface it is received by an electron collection device. The data received is then analysed to determine the elemental composition of the material which reflected the x-ray beam.

In terms of organic, migrating corrosion inhibitors XPS detection can be used to analyse a sample of rebar to determine if there is inhibitor on the surface. Both amine alcohols and amine carboxylates are nitrogen containing compounds which is not found in abundance in the concrete matrix. Therefore, nitrogen levels (relative concentration when comparing two plots, i.e. control vs. treated) recorded on the XPS spectrogram can be used to determine if corrosion inhibitor has migrated to the depth of the rebar. XPS also has the capability to look at the depth at which an element is from the surface of the steel, so the spectrogram can be used to determine depth at which the corrosion inhibitor adsorbed into the rebar in comparison to other elements like chloride.

3. REFERENCES

3.1 New construction applications

In new construction, OCI are incorporated into concrete as an admixture, either by adding to the mix water at a ready mix plant, or by adding on the jobsite to the ready mix truck prior to pouring. Their dosage rate is independent of the expected chloride levels. The recommended dosage rate is a sufficient concentration of inhibitor to form a monomolecular film on embedded metals and is independent of chloride concentrations. Unlike anodic inhibitors such as calcium nitrite, OCI do not have a “dangerous” concentration level – situations where a lower than required dosage rate relative to chloride content concentration would promote pitting corrosion. The latest generation of OCI admixtures, based on amine carboxylates, are certified to meet NSF/ANSI 61 – 2016 *Drinking Water System Components -Health Effects* requirements, meaning they are safe for use at their recommended dosage rates in structures containing potable water. These corrosion inhibitors also contain renewable resources as raw materials – one of the corrosion inhibiting materials in the amine carboxylate admixtures is derived from corn. They have been tested to ASTM C1582 / C1582M – *Standard Specification for Admixtures to*

Inhibit Chloride-Induced Corrosion of Reinforcing Steel in Concrete and pass the requirements for both physical property effects on concrete as well as for corrosion inhibition capability.

3.1.1 Randolph Avenue Bridge

One of the oldest applications of OCI admixtures was a bridge deck overlay done 32 years ago on the Randolph Avenue Bridge which spans Interstate 35E in St. Paul, MN. The bridge is located in an area where winters are severe and de-icing salts are heavily used to combat icy road conditions. Originally built in 1963, the deck underwent repair in 1986 to mitigate chloride induced corrosion of the reinforcing steel and spalling that was occurring. Repair involved removing deteriorated concrete and milling to within 13 mm of embedded reinforcement. The deck was then replaced with a low slump, dense concrete (LSDC) overlay. Depth of the overlay varied from 58 to 107 mm, with the top layer of reinforcing steel located at 76 mm depth. Mix design parameters for the overlay were: Type I Cement, W/C Ratio 0.32, with Water-Reducing admixtures, Air-Entraining Agent and OCI. An amine alcohol based OCI admixture was added to the overlay for the two westbound traffic lanes at a rate of 0.6 l/m³. The two eastbound traffic lanes used the same mix design without the corrosion inhibitor, to act as a control.

Chloride contents readings indicate that the chloride levels in the control side were higher than the treated side and that they have continued to rise at the depth of the steel over time.

Corrosion current readings, Figure 4, have increased on both sides of the bridge over time. Readings taken in July of 2011 showed that the control side had entered into active corrosion levels (corrosion rate readings above 0.5 $\mu\text{A}/\text{cm}^2$). All three sections tested indicated readings in the active corrosion range with the highest rate of corrosion recorded in the centre section of the control side, with an average reading of 1.27 $\mu\text{A}/\text{cm}^2$. In comparison, all three sections of the control side had readings in the passive range (corrosion rate readings less than 0.5 $\mu\text{A}/\text{cm}^2$), with the highest being the centre section with an average reading of 0.42 $\mu\text{A}/\text{cm}^2$, indicating the treated side had roughly 67% lower rates than the untreated areas.

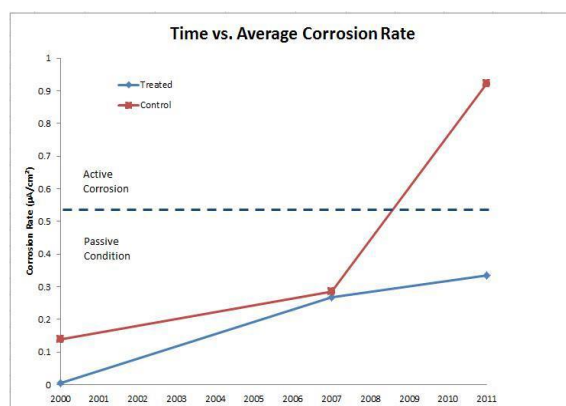


Figure 4. Randolph Avenue Bridge Average Corrosion Rates

3.2 Specialty and repair applications

OCI inhibitors have also been developed to help with corrosion issues in unique construction environments. Use of powder based OCI inhibitors on post tensioned structures has been occurring for more than 10 years to provide temporary protection to PT cables prior to grouting. Some researchers confirmed that the powder based OCI fogged into PT cable construction provided a significant reduction in corrosion compared to control samples in long term laboratory-based corrosion studies (one year of saltwater exposure) and that the OCI did not significantly affect the bond of grout injected after their application. Based on this data and

additional research, a novel use of OCI was created for the Severn Bridge Structure in the United Kingdom.

3.2.1 Severn Bridge, United Kingdom

The Severn Bridge is a 988 m span suspension bridge over the Severn River between Bristol and South Wales [37]. Inspections found that the PT cables were corroded and had reduced structural strength. Following this investigation, an acoustic monitoring system and dry air injection system were installed on both main suspension cables to control the deterioration. The purpose of the dry air injection system was to reduce the relative humidity (RH) within the cables to <40%, an accepted percentage to prevent corrosion of metals [14].

To provide additional corrosion protection to the PT cable wires during the initial period of moisture reduction—when corrosion rates could increase as oxygen became more available—and to provide a back-up if the dehumidification system went out of service (i.e. for maintenance), an organic corrosion inhibitor system was developed for introduction into the dry air stream. Concerns over fogged OCI powders blocking air voids in the cables, water-based systems being unsuitable when looking for moisture reduction to reduce corrosion rate, and solvent based systems being incompatible with the cable wrap and RH probes, meant a different approach had to be used in development of the OCI.

For these reasons, a powder version OCI, contained in a vapour permeable pouch, was developed to introduce pure inhibitor vapour into the system using the dehumidification air stream as the carrier. This ensured a sufficient level of inhibitor would be present within the air voids to protect exposed metal surfaces while avoiding the risks of blockage by solid or liquid material. Because the protective inhibitor layer is at a molecular level, it has no influence on clearances and had only a minimal effect on other physical properties. Testing showed that use of the inhibitor caused a small increase in wire-to-wire friction at low contact pressure and no significant frictional effect at higher loads. Further testing was carried out to confirm the inhibitor would not adversely affect other components in the system; including; cable wraps, sealants, and probes.

The OCI system manufacturer also developed an inhibitor detection kit. This detection method is used in ongoing field inspections to ensure presence of the inhibitor.

The consulting engineers for the project also developed monitoring criteria and systems for future management of the bridge to comply with the principals in the British BD79/13 Standard - The Management of Sub-standard Highway Structures. This involves visual inspections by bridge operators who record any observations that may be relevant to the condition of the cables.

4. CONCLUSIONS

Organic corrosion inhibitors (OCI) have been used in the construction industry for more than 30 years. OCI are made from a renewable raw material and its effectiveness has been demonstrated on many types and ages of construction. OCI Admixtures have been tested to meet the requirements of ASTM C1582 Standard Specification for Admixtures to Inhibit Corrosion in Chloride Exposed Environments and have demonstrated their ability to significantly increase expected service life of structures with a single application during construction.

OCI surface treatments used for repair have also been tested extensively and shown to reduce corrosion rates significantly even in the presence of existing chlorides and carbonation. Long term study on repair projects has demonstrated their ability to extend the useful life of existing structures.

Finally, use of OCI is not limited to concrete admixtures or surface treatments, but can also be done in applications as seen on the post tensioned tendons and cable ducts of the post tensioned and suspension structures.

Sustainable construction has become a goal for owners across the globe. Often overlooked aspect is the durability and service life of the final structure. However, OCI are undoubtedly one of the main future factors influencing structural sustainability.

REFERENCES

- [1] Miksic B.A., Use of vapor phase inhibitors for corrosion protection of metal products, Corrosion, 83, Paper No. 308, NACE, Houston, 1983.
- [2] Miksic B.A., Improving the durability of infrastructure with migratory corrosion inhibitors (MCI) handbook, Cortec Corporation, St Paul, 2014.
- [3] Bjegovic D., Sipos L., Ukrainczyk V., et.al., Diffusion of the MCI 2020 and 2000 corrosion inhibitors into concrete, In:Swamy R N Ed, Proceedings of Steel in Concrete, Sheffield, Academic Press, 865-877, 1994.
- [4] Bavarian B. and Reiner L., Current progress in corrosion inhibition of reinforcing steel in concrete using migrating corrosion inhibitors, Corrosion 2006, Paper No. 06347, San Diego, NACE, 2006.
- [5] Zarenin V.A. and Ostrovski A.B., MCI-2000 Diffusion Rate Testing Report, Moscow, Institute for Corrosion Protection Russian Federation, 1993.
- [6] Suess T. and Stehly R., Report of Corrosion Inhibitor Testing AET Job No. 05-00021, St. Paul, American Engineering and Testing, 2002.
- [7] Rudy A. and Wachowski L., ASTM E96 (2005) - Standard Test Methods for Water Vapor Transmission of Materials. TCG Project No. 09146, Kalamazoo, Tourney Consulting Group, 2010.
- [8] ASTM International, ASTM C1582 / C1582M-11, Standard Specification for Admixtures to Inhibit Chloride-Induced Corrosion of Reinforcing Steel in Concrete [Internet]. West Conshohocken, PA: ASTM International; 2011 [updated 2011 July 1; cited 2017 June 26]. Available from: www.astm.org
- [9] ASTM International, ASTM G109-07(2013), Standard Test Method for Determining Effects of Chemical Admixtures on Corrosion of Embedded Steel Reinforcement in Concrete Exposed to Chloride Environments [Internet]. West Conshohocken, ASTM International; 2011 [updated 2013 May 1; cited 2017 June 26]. Available from: www.astm.org
- [10] ASTM International. ASTM G180-13, Standard Test Method for Corrosion Inhibiting Admixtures for Steel in Concrete by Polarization Resistance in Cementitious Slurries [Internet]. West Conshohocken, ASTM International; 2011 [updated 2013 May 1; cited 2017 June 26]. Available from: www.astm.org
- [11] Furman, A, Austin, L. Measurement of Electrochemical Impedance of Concrete Samples. Cortec Test Method CC-022. St. Paul, Cortec Corporation, 2016.
- [12] United States Department of the Interior Bureau of Reclamation, M-82 (M0820000.714), Standard Protocol to Evaluate the Performance of Corrosion Mitigation Technologies in Concrete Repairs. Denver, July 2014. [cited 2017 June 26]. Available from: www.usbr.gov/tsc/techreferences/mands/mands-pdfs/StandardCorrosionProtocol_07-2014rev08-2016_508.pdf
- [13] Shen M., Heurung C., et. al., Mitigating corrosion of concrete steel reinforcement with surface treatments containing migrating corrosion inhibitors, Concrete Service Life Extension Conference, Paper No. W15, Orlando, NACE; 2016.
- [14] Lambert P. and Fisher J., Corrosion control of the Severn Bridge main suspension cables, Materials Performance, 53, 11, 2-7, 2014.

**International Conference on Sustainable
Materials, Systems and Structures
(SMSS 2019)**
Durability, Monitoring and Repair of Structures

Lime-based historic repair

TESTING PROPERTIES GOVERNING THE DURABILITY OF LIME-BASED REPAIR MORTARS

Members of RILEM TC 277 LHS Members: I. Papayianni, J. Válek, J. Alvarez, V. Bokan Bosiljkov, P. Faria, L. Ferrara, C. Groot, D. Gulotta, L. Toniolo, H. Gunozu, R. van Hees, J. Hughes, I. Ioannou, C. L. Nunes, A. Padovnik, N. P. Maravelaki, V. Pacht, S. Pavia, U. Peter, D. Rani, M. Secco, M. Stefanidou, C. Tedeschi, M. Theodoridou, R. Veiga, A. Velosa, S. Martínez Ramírez, M. Ramesh, C. Passian, A. Torok, P. Stukovnik

Corresponding author: Ioanna Papayianni⁽¹⁾

(1) Laboratory of Building Materials, School of Civil Engineering, Aristotle University of Thessaloniki, Greece

Abstract

Lime-based mortars seem to be preferred in repairing historical structures. The long-term performance of lime-based repair mortars is closely related to durability issues concerning the old structure substrate, the new repair mortars and the interface between the two aforementioned materials, which is also much influenced by the technique of mortars application. It is well known that durability is a multifunctional property affected by a number of parameters, including local environmental conditions. However, experience (based on research and survey of real case studies) showed that some of the parameters concerning the characteristics of materials play a dominant role in assessing the durability of repair lime-based mortars and have a direct impact on longevity of the repaired structure.

This paper presents comments of review papers concerning research publications or case studies, as well as Master or PhD theses supervised or carried out by the members of RILEM TC 277 LHS. Through the review and evaluation of research and common practice concerning durability challenges, we anticipate to find answers to questions arising in assessing the durability of repair lime-based mortars, such as: the most often encountered failures due to mortar durability inadequacy, the mortar properties/characteristics that seem to be influential on durability, the test methods used for testing the durability of lime-based mortars and comments related to their applicability and performance and the importance of quality control and on site execution practices.

Keywords: lime-based mortar, durability, properties, test methods, quality control, execution practices

This work was invited for publication in the open access journal *RILEM Technical Letters*. You can visit the journal and benefit from the full open access to the published articles at: letters.rilem.net.

DURABILITY OF LIME BASED RENDERS: A REVIEW OF SOME DEGRADATION MECHANISMS AND ASSESSMENT TEST METHODS

Rosário Veiga (1), Maria Stefanidou (2), Kristin Balksten (3), José I. Alvarez (4), Cristiana Nunes (5), Magdalini Theodoridou (6), Paulina Faria (7), Ioanna Papayianni (2), Rob van Hees (8)

(1) National Laboratory for Civil Engineering, Lisbon, Portugal

(2) Laboratory of Building Materials, School of Civil Engineering, AUTH, Hellas

(3) Uppsala University, Visby, Sweden

(4) Department of Chemistry, Universidad de Navarra

(5) Institute of Theoretical and Applied Mechanics, Czech Academy of Sciences

(6) Cardiff School of Engineering, Cardiff University, Wales, UK

(7) CERIS and Faculty of Science and Technology, NOVA University of Lisbon, Portugal

(8) TU Delft, Faculty of Architecture and the Built Environment Heritage & Technology, Netherlands

Abstract

Lime based mortars used for the repair and renovation of old lime renders have important functions in historic buildings, such as the protection of the masonry and aesthetics of the surfaces. Hence, they have a significant contribution to the durability of the walls, which often are structural elements.

Cracking and loss of adherence are two of the most severe defects for renders, as they drastically affect their functional capacity. Cracking is related to shrinkage, elastic characteristics, and kinetics of the gain of strength as well as to water transport properties of the render. Most of these aspects are governed by the porous structure of the mortar, which is a function of the composition of the mix and application issues. Loss of adherence is related to the compatibility of the render with the substrate, concerning mechanical, thermal and hygric aspects. Loss of cohesion, due to leakage of the binder, freeze-thaw, salts crystallization or other causes, results in significant damage, difficult to repair. The appearance of stains either by pollutants deposition or by biocolonization is also a concern related to durability of renders.

In the present paper the degradation mechanisms leading to cracking, loss of adhesion or cohesion and stains formation are analysed based on literature, and a review of assessment test methods are carried out. Finally, the need for test improvement in this area is highlighted.

Keywords: Lime render; Degradation mechanism; Cracking; Loss of adhesion; Test method

1. INTRODUCTION

Lime based mortars used for the repair and renovation of old lime renders have essential functions in historic buildings. In particular, they are meant to protect the masonry, hence they have a significant contribution to the durability of the walls, which are often structural elements. Repair lime renders are mainly intended to increase the durability of the masonry. However, their durability is also an important issue. They are directly exposed to weathering agents and to all external actions and their main anomalies are: cracking, loss of adherence, loss of cohesion, chemical reactions related to pollution and soluble salts and biological colonization.

Cracking is due to shrinkage and thermal, hygric and salt-related dimensional variations [1]. It depends on the elastic characteristics of the mortar and their evolution in time, as well as with the kinetics of the gain of strength [2]. The water transport properties of the render are also significant factors, as they condition shrinkage. Most of these aspects are governed by the porous structure of the mortar, which is a function of the composition of the mix and application issues. Loss of adherence is related to the compatibility of the render with the substrate, concerning mechanical, thermal and hygric aspects [3,4]. Differences in the modulus of elasticity and in thermal and hygric dilation coefficients of the materials generate stresses in their interface; variations in water transport produce water vapour pressure and accumulation of soluble salts between layers; these mechanisms are important causes of loss of adherence. The appearance of stains due to pollution emissions also affect the state of conservation of renders and their durability [5,6]. Atmospheric pollutants are also very aggressive for calcitic materials, which are the main constituents of lime renders. The aesthetic quality of renders can also be seriously affected by biological stains caused by the growth of microorganisms [7] which may even reduce the durability of the renders by biodeterioration [8].

2. SYNTHESIS OF MAIN ANOMALIES AND CAUSES

Anomalies of renders may be caused by inappropriate composition or application of the render or by particularly aggressive unforeseen external factors. For historical materials, natural weathering is also a cause of degradation. The main anomalies that affect the functionality and durability of renders are summarized in table 1 along with their respective causes.

Table 1 – Main anomalies of renders, consequences, and causes

Main anomalies	Functions affected xxx (maximum) to – (doesn't affect)				Causes
	Protection of masonry	Aesthetics of the façade	Durability of the masonry	Durability of the render	
Cracking	XXX	XXX	XXX	XXX	<ul style="list-style-type: none"> • High shrinkage + stiff mortar <ul style="list-style-type: none"> • Mixing ratio between lime and sand • Sand curve • Fat or lean lime, crystal structure of lime • Thickness of render in comparison to suction of substrate • Unfavourable curing conditions • Movements of the substrate (structural or due to thermal and hygric variations)

					<ul style="list-style-type: none"> • Formation of expansive compounds in the substrate • Weak adhesion to the substrate, promoting stress concentration • Freeze-thaw cycles • Salts crystallization
Loss of adherence	XXX	XXX	XX	XXX	<ul style="list-style-type: none"> • Incompatibility with the substrate: Physical; Chemical; Mechanical • Lack of adequate pressure in application • Surface film of lime of each layer of render • Freeze-thaw between layers • Salts crystallization between layers
Loss of cohesion	X	X	-	XXX	<ul style="list-style-type: none"> • Crystallization of soluble salts inside porous network <ul style="list-style-type: none"> • Dissolution and leaching of the lime binder, caused by frequent or severe water circulation
Stains	-	XXX	-	X	<ul style="list-style-type: none"> • Pollution • Biological colonization • Leakage of soluble salts and other products from bricks and stones

3. CRACKING – CAUSES AND ASSESSMENT METHODS

Cracking produces complete loss of the renders' protective function against water and aggressive solutions, hence reducing the durability of the masonry and damaging its aesthetic appearance. It is caused by stress, usually tensile stress, induced by: a) drying shrinkage of the mortar restrained by the adhesion to a stiffer substrate; b) movements of the substrate that are transmitted to the render; c) volume increase of products inside the porous structure, such as water (freeze-thaw), soluble salts (dissolution-crystallization and hygroscopic volume changes) and expansive compounds formed.

The ability of the render to accommodate stress without cracking depends of: a) the magnitude of the stress; b) the ductility of the mortar and in general of its ability to deform without cracking during the stress application period; c) the tensile strength of the mortar in the period of stress development. Stress is often not instantaneously induced in mortars, on the contrary, it is slowly developed: shrinkage occurs for several days or months after application, with increasing values; thermal and hygric variations follow the rhythm of weather changes. This slow process allows for relaxation and creep phenomena to contribute to the cracking susceptibility [9,10,11,12]; creep is higher (more favourable) for lime mortars than for cement ones [13]. In most cases, tensile stress is transmitted through the substrate, hence the bond between the substrate and the render as well as its uniformity are important parameters. Poor adhesion causes stress concentration in some areas, which is a cause of cracking. Many factors are involved and their interrelation is complex. The definition, improvement and validation of a reliable test for the assessment of the cracking behaviour of rendering mortars, taking into account all the most significant factors, is then needed.

The methods found in literature to assess the cracking susceptibility of mortars may be grouped into several types:

– **Determination of ductility using flexural strength tests**

Cracking susceptibility has been related to ductility since long time ago [9]. Recent studies have used three-point bending test and analysis of the force-displacement curve [14] sometimes with a crack artificially produced at middle span [15]. These methodologies are easy to perform, do not require special equipment and give quantitative information, however, the values obtained are comparative and cannot be directly related to in-service stresses.

– **Ring tests**

Ring tests are among the oldest quantitative tests developed with the aim to determine stress due to restrained shrinkage [9,16,17,18]. Different variations of the test are still used by many researchers [19,20]. They are based on molding the mortar inside two concentric metallic rings, measurement of the rings deformations and calculation of stress induced in the mortar. They are both quantitative and qualitative methods, allowing to obtain stress, deformations, and patterns of cracks, due to restrained shrinkage. The drawbacks are: for low modulus mortars, like renderings, very large rings are needed in order to have restrained shrinkage stress high enough to produce cracks; very specific equipment is needed; the stress measured is difficult to relate with real stress installed in-service, due to the shape of the specimens.

– **Uniaxial linear restrained shrinkage tests**

These tests are based on moulding a uniaxial specimen inside a device that allows blocking the deformation, and measurement of the force induced by restrained shrinkage [11,21,22,10,2] (Figure 1 a). Free shrinkage can be measured simultaneously in similar specimens. Some advantages of this type of method are: curves force-displacement and force-time can be drawn; restrained shrinkage can be compared with free shrinkage; parameters such as energy of fracture and maximum elongation at rupture load may be determined; due to the simple geometry of the device, the values obtained can be simply related to stress and strain to be obtained in-service. A drawback is that a very specific equipment is needed.



Figure 1 – Restrained shrinkage tests: a) Uniaxial test; b) Slab test

– **Bidimensional restrained shrinkage tests (slab tests)**

These methods [23,24,25] are based on the application of a mortar on a stiff substrate, such as a concrete slab, which simulates the wall that restrains shrinkage (Figure 1 b); the cracks formed are observed and several parameters are measured: time of opening of the first crack; pattern and area of cracking; number of cracks; maximum crack width, etc. These are the tests that better simulate the in-service conditions and they are easy to perform and do not need

complex equipment. They allow comparison between different materials, however, they are mainly qualitative, not permitting stress measurement.

Simplified analytical models for predicting the age at cracking, based on elastic modulus, tensile relaxation, shrinkage strain and tensile strength, have also been developed [12].

Nevertheless, studies on cracking have been mainly performed on cement-based mortars. Thus, some of the referred methods may be inadequate for low strength lime mortars.

4. LOSS OF ADHERENCE – CAUSES AND ASSESSMENT METHODS

The adhesion resistance between substrate and mortar is an important mechanical property affected by many parameters such as the roughness of the substrate, the penetration of water and binder into the pores of the substrate, depending on the suction conditions and the porosity of the base. Other parameters such as compaction, curing conditions and design of the mortar are also important. The influence of substrate texture and rheological characteristics of the mortar on the shear and tensile bond strength of mortars on concrete slabs were tested by researchers concluding that the rheology of the mortar is the main factor controlling their bonding capacity [3]. In the case of mortar-brick system, the parameter of the firing conditions of the brick and its role in the adhesion was tested leading to the conclusion that the firing temperature and its microstructure is an important variable influencing the adhesion [26]. Application techniques were also found to be a key factor for good adhesion [27]

A method for determining the adhesion strength between mortar and substrate is described in EN1015-12 and is defined as the maximum tensile strength applied by a direct load perpendicular to the surface of the mortar on a substrate. The adhesive strength obtained is the quotient between the failure load and the test area. It is commonly known as pull-off method and is performed with a pull-off dynamometer specified also in several standards and Guides [28,29,30]. Pull-off is a widespread method (Figure 2 a), easy to perform. However, it has some drawbacks concerning air lime mortars: their tensile strength is very low, and as the test is based on the application of a tensile load, the obtained adhesion values are in the range 0.01-0.10 MPa [31,32], corresponding to applied forces of 20-100 N, which significantly reduce the precision of the method. In fact, pull-off devices commonly available with the best accuracy have capacity until 5000-6000 N, and low sensitivity to small variations of load. Additionally, the load application control is limited. Hence, the accuracy of results for low strength mortars is insufficient. A method based on a tensile load applied on a composite specimen substrate-mortar by a mechanical machine of higher precision and allowing adequate control of load application has been tested and results obtained proved to be more sensitive [31,32] (Figure 2 b). However, this method is not applicable on site.



Figure 2 Adhesion with a) pull-off apparatus and b) tensile machine

5. LOSS OF COHESION – CAUSES AND ASSESSMENT METHODS

The cohesion of lime mortar is obtained by the bond between the binder matrix and the aggregates. Several factors may affect that bond, such as cracking, salts attack, and leaching of the binder. Loss of cohesion can be assessed by different methods such as Shore hardness [33] and peeling method [34, 35] which can be applied in laboratory and *in situ*.

6. STAINS – CAUSES AND ASSESSMENT METHODS

The main responsible for stains on renders surfaces are the deposition of airborne particulate matter, aerosol dry deposition and, sometimes, the irreversible formation of black crusts. Some of the pollutant gases that produce stains present an acidic character (sulfur and nitrogen oxides), so that their interaction with calcium carbonate of the lime-based renders and later formation of soluble salts (mainly sulfates and nitrates) leads to calcium leaching of the renders and a loss of cohesion.

The assessment of the black soiling on surfaces has been carried out by either monitoring the colour changes using a colorimeter [36], or by quantifying the elemental and organic carbon deposited. A method based on combustion/chromatographic determination of CO₂ combined with dissolution after different chemical attacks have been also proposed [37] and tested [38].

Regarding the biological colonization, algae and cyanobacteria are considered as pioneering inhabitants of outdoor exposed surfaces, being able to adapt to a large variety of substrates (stones, mortars, plasters...). For renders, chemical composition and pore structure affect water retention on external surfaces. This allows the growth of algae and cyanobacteria, and subsequently of lichens and moss, thus accumulating large amounts of biological matter.

To assess the biocolonization, Tiano [39] suggests, on one hand, the investigation of biological markers as indicators of the presence of viable micro-organisms. Bioluminescence methods to determine ATP have been proved on stone surfaces [40]. The non-invasive portable fluorescence remote Lidar sensing has been successfully applied to monitor the biodeteriogens on outdoor surfaces [41].

7. CONCLUSIONS

Besides their proved durability along time, lime renders suffer different kinds of anomalies, such as cracking, loss of adherence, loss of cohesion and different kinds of stains due to biocolonization and pollution. Cracks occur in mortars in the fresh state due to plastic shrinkage and in the hardened state due to restrained shrinkage, stress by displacement, freeze-thaw or salt crystallisation. There are methods to measure stress induced by restrained shrinkage and to analyse and identify cracks, both by quantitative and qualitative methods. Loss of adherence is related to the hygric properties of the mortar and is currently assessed by the pull-off test frequently using equipment with low sensibility for the strength of lime-based mortars. Therefore, the tensile load applied on a composite specimen substrate-mortar by a mechanical equipment with higher precision and allowing adequate control of load application seems to be a more suited method. Loss of cohesion of lime renders and plasters can be indirectly assessed by several methods such as the Shore hardness test or directly by the peeling test. Stains have very different causes and different degrees of damaging potential. The assessment can be based on the origin of the stains, with resource to diversified methods, or more simply by measurement of colour changes, when there is no need of evaluating the causes. This review identified needs of research to define and validate adequate methods for assessment of

susceptibility to different kinds of degradation mechanisms of lime-based repair mortars for historical renders and plasters, in order to contribute to the selection of durable repair materials.

ACKNOWLEDGEMENTS

This review was developed within RILEM TC 277 LHS - Specifications for testing and evaluation of lime-based repair materials for Historic Structures.

REFERENCES

- [1] van Hees, R. and Lubelli, B., 'Analysis of transport of salts in restoration plasters, European Research on Cultural Heritage – State of the Art Studies 5, (ITAM, Prague, 2006) 315-327.
- [2] Veiga, M.R., Velosa, A.L. and Magalhães, A.C., 'Evaluation of mechanical compatibility of renders to apply on old walls based on a restrained shrinkage test', Mater. Struct. 40 (2007) 1115-1126.
- [3] Stolz, C., Pagnussat, D.T., Masuero, A.B. and Kirchheim, A.P., 'Influence of substrate texture on the tensile and shear bond strength of rendering mortar', Const. Build. Mater. 128 (2016) 298-307.
- [4] Botas, S., Veiga, M.R. and Velosa, A., 'Air lime mortars for conservation of historic tiles: bond strength of new mortars to old tiles', Const. Build. Mater. 145 (2017) 426-434.
- [5] Brimblecombe, P., and Grossi, C.M., 'Aesthetic thresholds and blackening of stone buildings', Sci Total Environ 349 (2005) 175-89.
- [6] Camuffo, D., 'Dry deposition of airborne particulate matter: mechanisms and effects', Microclimate for Cultural Heritage (Elsevier, Boston, 2014) 283-346.
- [7] Barberousse, H., 'Factors involved in the colonisation of building façades by algae and cyanobacteria in France', Biofouling 22 (2006) 69-77
- [8] Warscheid, T., Oelting, M. and Krumbein, W.E., 'Physico-chemical aspects of biodeterioration processes on rocks with special regard to organic pollutants', Int. Biodeter. 28 (1991) 37-48.
- [9] Sousa Coutinho, A., 'A fissurabilidade dos cimentos, argamassas e betões, por efeito da sua contracção', Memória 57 (1954), LNEC, Lisboa.
- [10] Veiga, M.R., 'Influence of application conditions on the cracking susceptibility of renderings', Concrete Science and Eng. 2 (2000) 134-140.
- [11] Tamin et al., 'Plastic shrinkage cracking of normal and high strength concrete: a comparative study', ACI Mater. J. January-February (1996) 36-40.
- [12] Beushausen, H. and Arito, P., 'The influence of mix composition, w/b ratio and curing on restrained shrinkage cracking of cementitious mortars', Const. Build. Mater. 174 (2018) 38-46.
- [13] Papayianni, I., 'Creep and shrinkage deformations of lime-based mortars', in '13th IB2MAC', Proceedings of an International Conference, Amsterdam (2004).
- [14] Lee, K.-J., Lee, J.-H., Jung, C.-Y. and Choi, E., 'Crack-closing performance of NiTi and NiTiNb fibers in cement mortar beams using shape memory effects', Comp. Struct. 202 (2018) 710-718.
- [15] Huang, Y., Guan, Y., Wang, L., Zhou, J., Ge, Z. and Hou, Y., 'Characterization of mortar fracture based on three point bending test and XFEM', Int. J. Pavement Res, Techn. 11 (2018) 339-344.
- [16] L'Hermite, R., 'Expériences et théories sur la technologie du béton. Deuxième partie. Déformation du béton sans charge (retrait et gonflement)', Annales de l'ITBTP 375 (1979).
- [17] Shah, S. P., Karaguler, M.E. and Sarigaphuti, M., 'Effects of shrinkage-reducing admixtures on restrained shrinkage cracking of concrete', ACI Materials Journal May-June (1992) 289-295.
- [18] Bentur, A. and Mindess, S., 'Fibre reinforced cementitious composites' (Elsevier Applied Science, London and New York, 1990).
- [19] Sadati, S. and Khayat, K.H., 'Restrained shrinkage cracking of recycled aggregate concrete', Mater. Struct. 50 (2017) 206.
- [20] Zou D. and Weiss, J., 'Early age cracking behavior of internally cured mortar restrained by dual rings with different thickness', Const. Build. Mater. 66 (2014) 146-153.

- [21] Penev, D. and Kawamura, M., 'A laboratory device for restrained shrinkage fracture of soil-cement mixtures', *Mater. Struct.* 25 (1992) 115-120.
- [22] Dupin, I. and Détriché, C. H., 'Analyse expérimentale des effets du retrait empêché sur des couches minces de mortier', *Revue Technique du Bâtiment et des Const. Industrielles* 124 (1988) 37-43.
- [23] Kheder, G.F., Al-Rawi, R.S. and Al-Dhahi, J. K., 'A study of the behaviour of volume change cracking in base restrained walls', *Mater. Struct.* 27 (1994) 383-392.
- [24] Siviero, E. and Forin, M., 'Use of acrylic fibers to reduce plastic shrinkage in concrete structures', in RILEM, Barcelona, 1993.
- [25] Wang, Z., Wu, J., Zhao, P., Dai, N., Zhai, Z. and Ai, T., 'Improving cracking resistance of cement mortar by thermo-sensitive poly N-isopropyl acrylamide (PNIPAM) gels', *J. Cleaner Prod.* 176 (1) (2018) 1292-1303.
- [26] Azevedo, A.R.G., Franca, B.R., Alexandre, J., Marvila, M.T., Zanelato, E.B. and Xavier, G.C., 'Influence of sintering temperature of a ceramic substrate in mortar adhesion for civil construction', *J. Build. Eng.* 19 (2018) 342-348.
- [27] Pachta, V., Marinou, P. and Stefanidou, M. 'Development and testing of repair mortars for floor mosaic substrates', *J. Build. Eng.* 20 (2018) 501-509.
- [28] EN 1015-12:2000, Methods of test for mortar for masonry, Part 12: Determination of adhesive strength of hardened rendering and plastering mortars on substrates. CEN, Brussels.
- [29] EOTA, ETAG 004, Guideline for European Technical Approval of External Thermal Insulation Composite Systems (ETICS) with Rendering. Brussels, 2013.
- [30] EN 12618-2:2004, Products and systems for the protection and repair of concrete structures, Test methods, Part 2: Determination of the adhesion of injection products, with or without thermal cycling, Adhesion by tensile bond strength. CEN, Brussels.
- [31] Botas, S., Veiga, R. and Velosa, A., 'Bond strength in mortar/ceramic tile interface - testing procedure and adequacy evaluation', *Mater. Struct.* 50 (2017) 211.
- [32] Veiga, M.R., Santos, A.R., Marques, A. and Santos, D., 'Non-standard testing of mechanical characterization to support the conservation of old renderings', in 'Prohitec17', Proc. 3rd Int. Conf. on Protection of Historical Constructions, Lisbon, July, 2017, paper 54.
- [33] Borsoi, G., Tavares, M., Veiga, M. R. and Santos Silva, A. 'Microstructural and physical-mechanical analysis of the performance of nanostructured and other compatible consolidation products for historical renders', *Mater. Techn. Magazine* 46 (2012), 93-97.
- [34] Drdácý, M., Lesák, J., Niedoba, K., and Valach, J., 'Peeling tests for assessing the cohesion and consolidation characteristics of mortar and render surfaces', *Mater. Struct.* 45(6) (2014) 1947–1963.
- [35] Faria, P., Santos, T. and Aubert, J.-E., 'Experimental characterization of an earth eco-efficient plastering mortar', *J. Mater. Civil Eng.* 28(1) (2016) 04015085.
- [36] Grossi, C.M., Esbert, R.M., Díaz-Pache, F. and Alonso, F.J., 'Soiling of building stones in urban environments', *Build. Environ.* 38 (2003) 147–159.
- [37] Ghedini, N., Gobbi, G., Sabbioni, C. and Zappia, G., 'Determination of elemental and organic carbon on damaged stone monuments', *Atmospheric Environment* 34 (25) (2000) 4383-4391.
- [38] Bonazza, A., Sabbioni, C. and Ghedini, N., 'Quantitative data on carbon fractions in interpretation of black crusts and soiling on European built heritage', *Atm. Environ.* 39 (14) (2005) 2607-2618.
- [39] Tiano, P., 'Biodeterioration of Stone Monuments a Worldwide Issue', *The Open Conference Proceedings J.* 7 (suppl 1: M3) (2006) 29-38.
- [40] Tiano, P., Tomaselli, L., Orlando, C., 'The ATP-Bioluminescence method for a rapid evaluation of the microbial activity in the stone materials of monuments', *J. Biolumin. Chemil.* 3 (1989) 213-216.
- [41] Raimondi, V., Cecchi, G., Lognoli, D., Palombi, L., Grönlund, R., Johansson, A., Svanberg, S., Barup, K. and Hällström, J., 'The fluorescence lidar technique for the remote sensing of photoautotrophic biodeteriogens in the outdoor cultural heritage: A decade of in situ experiments', *Int. Biodet. Biodegr.* 63, (7) (2009) 823-835.

MICROSTRUCTURE ASPECTS RELATED TO DURABLE LIME MORTARS

Maria Stefanidou (1)

(1) Associate Professor, School of Civil Engineering, Aristotle University of Thessaloniki, HELLAS

Abstract

The durability of old lime-based mortars was for many years a research subject and many techniques have been employed in order to understand the influence of the microstructure on macro properties that those mortars present. Under a wide range of magnification, important information can be revealed and enlighten their behavior. Particularly for the “soft” nature of lime mortars, information concerning the proportion of empty spaces (porosity) in relation to solid material, their shape, geometry and position as well as the composition of the crystal matrix and the aggregate characteristics has a detrimental role to the remarkable durability that old lime mortars present. The binder- aggregate transition zone was recorded strong in some cases while in others a loose bond was recorded. The proportion of aggregates in relation to the binder, the maximum size used, and their gradation seems to affect the volume stability and the form of discontinuities.

Microstructure analysis performed in historic mortars reveals that the most durable mortars combine natural and brick aggregates with smooth granulometry, in combination with strong binders. The blending of good quality lime with reactive natural pozzolan formed a strong binding system consisting of micro-grained, well-connected crystals.

Keywords: old lime mortars; microstructure; durability

1. INTRODUCTION

Old mortars are composite materials consisting of binder and aggregates. Those of the old mortars characterized by durability continue to play their role in the structure despite the fact that they were subjected to many wetting-drying cycles and to extreme conditions for a long period of time.

They are generally of low strength in comparison with modern cement-based mortars and they have been manufactured by using soft, low potential binders such as mud, lime and local pozzolans. Old mortars despite their homogeneous macroscopic appearance present a rather heterogeneous structure. Moreover, they contain a net of pores and cracks by which their

mechanical strength and durability are strongly influenced. The study of an old mortar, taken from a monument or historic building, is usually a “black box” as no data can be obtained from any source (except the rare cases where information can be taken from the archaeological work). Approaching the physical, mechanical, chemical and mineralogical properties of old mortar, aiming to decode its behavior into the structure, requires combined techniques. To understand the role of the components into the mortar mixture is a key factor in order to understand the behavior of old mortars [1][2]. Microscopic analysis of material’s structure is valuable for many applications, such as the material’s understanding, development and improvement, quality control and evaluation of performance. The analysis and understanding of microstructure has played a vital role in understanding the complex structure of old lime-based mortars. The role of binders in old mortars is of paramount importance for the quality and durability of the mortar. From the analysis performed so far, it has been proved that old mortars were based on lime and when it was necessary, different binders were combined [3][4]. The use of natural pozzolan and brick dust with lime was a common technique, in cases where special needs were covered, such as high strength and water tightness [5].

2. MORTAR CONSTITUENTS

2.1 Binders

The role of binders in old mortars is of paramount importance for the quality and durability of the mortar. From the analysis performed so far, it has been proved that old mortars were based on lime and when it was necessary, different binders were combined [3][4]. The use of natural pozzolan and brick dust with lime was a common technique, in cases where special needs were covered, such as high strength and water tightness [5].

An important parameter of the quality of old mortars is the size, the chemical composition and the way the crystals of the binder are bound together. Good quality, reactive binders form a continuous matrix with well-connected micro-crystals (Fig.1).

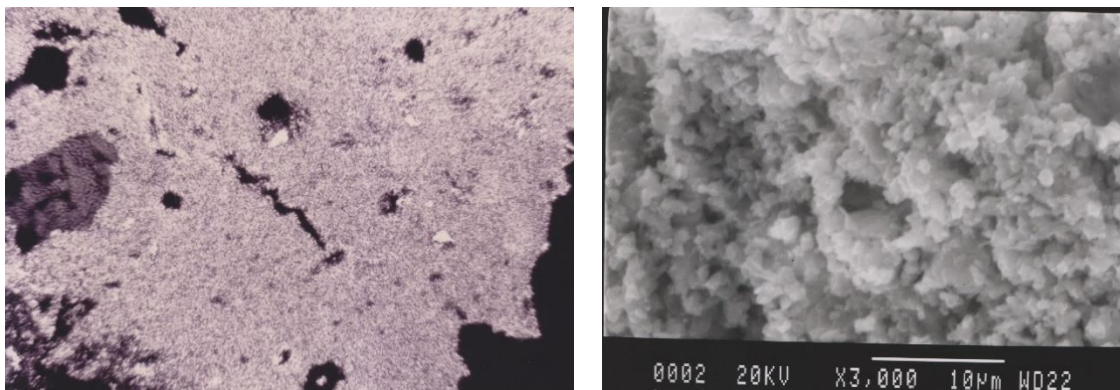


Figure 1: Fine grained binder in roman mortar under polarized microscope (x5-left) and under SEM (right)

A stable connective fine-crystallized tissue is created that contributes to coherent binder. Secondary cracks, attributed to different reasons, disrupt the binding net. The presence of the aggregates seems to play an important role to the crack propagation (Fig2).

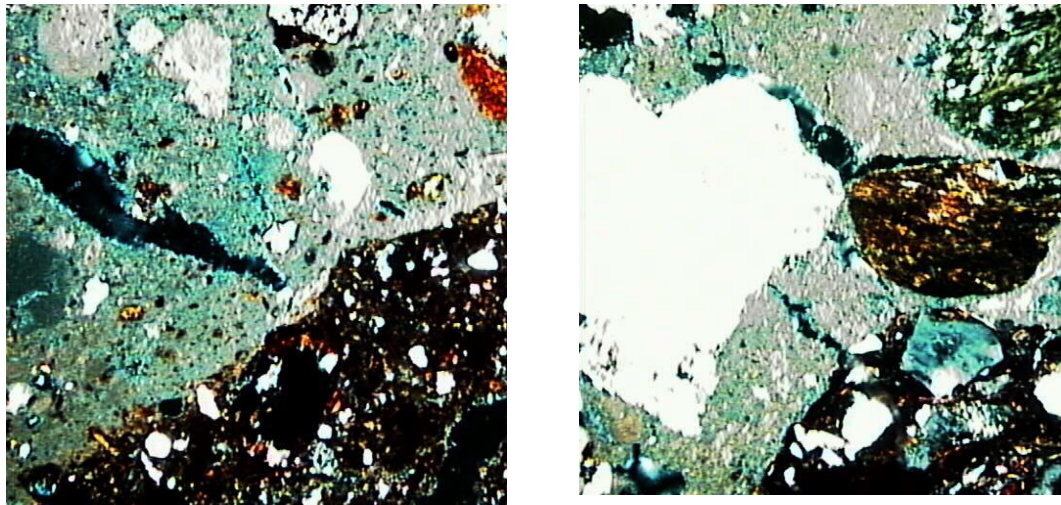


Figure 2: Cracks into the matrix under polarized microscope (X10)

2.2 Aggregates

In durable old mortars, aggregates act as barrier to crack propagation. That means that their nature, size and proportion should be the proper one. The size of the aggregates seems to be related to the binder type. Pure lime mortars perform better when the maximum size of the aggregates does not exceed 8mm while strong binders can contain larger aggregates and present high mechanical properties [7]. The aggregates used in old mortars were usually natural in origin, while crushed ceramic or limestone pebbles in various granulometries with even distribution were also used in some cases [6] [7]. The binder- aggregate transition zone was recorded strong in some cases where brick aggregates were recorded in combination with pozzolanic binder while in cases of natural aggregates a loose mechanical bond was recorded. (Fig.3). The proportion of aggregates in relation to the binder, the maximum size used and their gradation seem to directly affect the volume stability and the form of discontinuities such as pores and cracks [8].

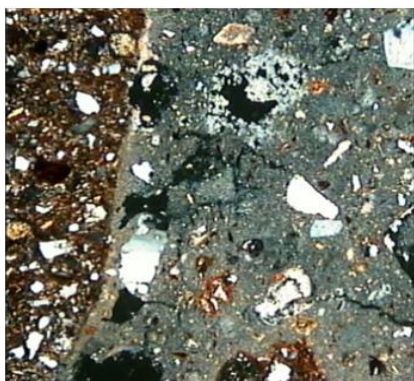


Figure 3a: Interface zones under polarized microscope x150 in brick-mortar interface

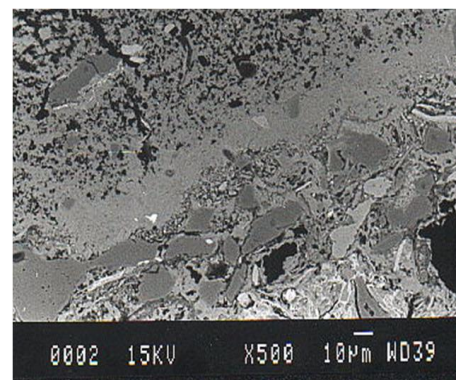


Figure 3b: SEM micrograph of contact zone of 30µm thickness between brick fragment and binder

2.3 Additives

The microscopic study of ancient mortars, reveals, that apart from the main ingredients, binders and aggregates, there are other materials as well, in small percentages in the mass, such as shells, charcoal particles, lime lumps, chips of wood or straw. These enclosures are met in structural mortars as well as in renders and they are observed in different historical periods (from the mud mortars of archaic period to strong pozzolanic mortars of Roman and Byzantine era and even in the mortars of 19th century or pre-cement period) [13]. Their role in the behavior of ancient mortars, as well as their origin, is not always clear, but their morphologic characteristics (shape, size and distribution), their percentage (not more than 2wt %) and their cohesion with the binder (usually strong) gives useful information about the older technology of building construction. Additives such as fibres, act as reinforcement and they have been widely used either knitted into the matrix or added as a net between mortar layers (Fig4).



Figure 4a: Straw in the structure of old lime mortar

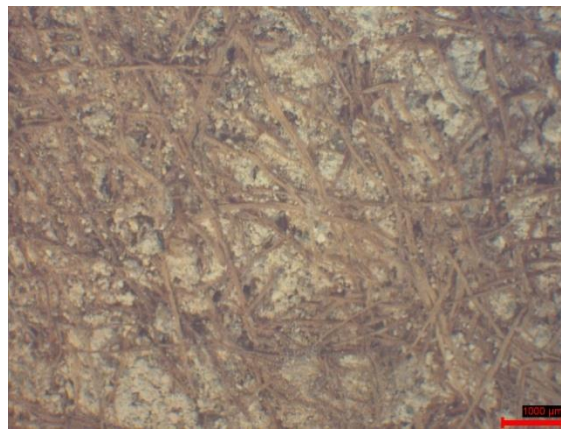


Figure 4b: A net of fibers for the cohesion between two layers

2.4 Porosity

Also, the porosity influences the macroscopic properties of the mortars and it is strongly correlated with the material's decay process. The pore distribution recorded in old mortars, allows some flow of water inside the structure without being held there. The porosity that characterizes old mortars (20-40%) is mainly due to micro-pores of 0.1-1 μ m (Fig6) while large pores of >100 μ m are also present but they are limited in well compacted mortars [9]. Cracks have also been observed usually in the binder-aggregate transition zone, because of the poor co-operation between the two phases or within the binder due to shrinkage phenomena. The co-existence of pores and cracks, which is the most common case, makes the structure vulnerable, especially when cracks join the pores, forming "interconnecting phases" within the structure. This is more critical when these openings have access to the surface, consisting paths through which deteriorating agents penetrate inside the material's structure. The geometric characteristics, the position, the way of communication and the crack orientation, are factors affecting the strength [10]. Pores may be isolated or filled with secondary crystals (salts, calcite).

Because of long exposure, old mortars develop different pathology symptoms such as cracks, crumbling, erosion and color alteration [11]. To study the ageing of various materials as they

degrade with time, it is important to analyse the microstructure changes supplemented with measurement of the area of damages in the form of micro-voids (Fig5).

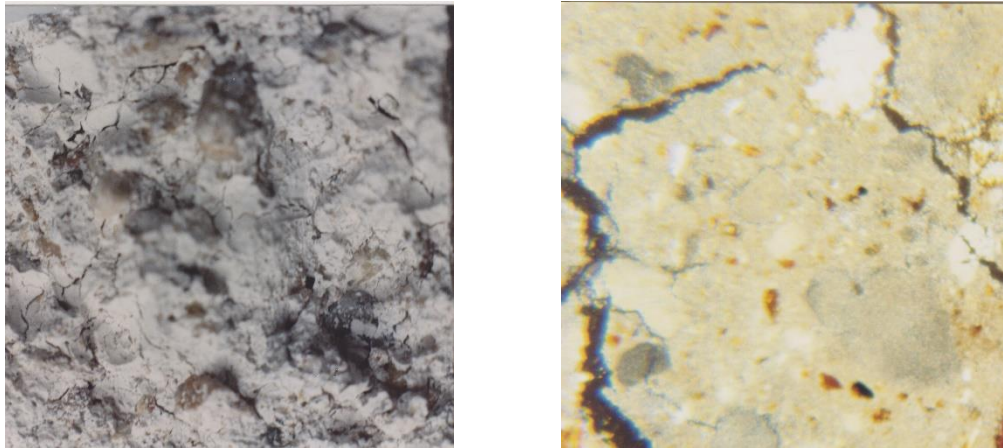


Figure 5: Loosening of the structure due to microcracks as seen macroscopically (left) and under polarized microscope (x10- right)

Secondary re-crystallization phases are often observed in the structure of ancient lime-based mortars (Fig6). They are mainly situated in previously formed cracks, in spherical pores and in the loose transition zone. The composition of these phases depends mainly on the type of binders used and the hydro thermal conditions to which the mortar was subjected during its service life. The secondary crystals reduce the porosity, as they fully or partly cover pores and cracks [12].



Figure 6a: Secondary crystallization in pores

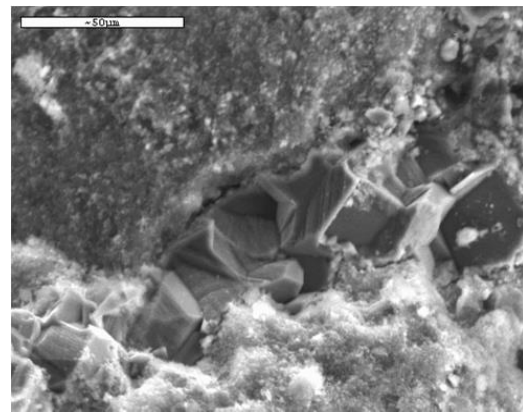


Figure 6b: Re-crystallization of calcite in the contact zone of binder-aggregate filling the crack in Bezesteni 16th century Thessaloniki)

3. CONCLUSIONS

The detrimental role of microstructure on the macroscopic properties of building materials and in mortars, in particular, is well-known. To fully benefit from microstructure control, it is

important to properly apply the full range of available microscopic techniques working under different magnification. Microstructure analysis performed in historic mortars reveals that the most durable mortars combine natural and brick aggregates with smooth granulometry, in the presence of few coarse grains and low proportion of fines ($<75\mu\text{m}$) in combination with strong binders. In the old mortars, the high proportion of aggregates is not always a quality criterion. Application of different aggregate / binder ratio, depending on the functional role of the mortar in the structure, the type of binder and the environment, seems to influence the durability and quality of mortars. The combination of good quality lime with reactive natural pozzolan, formed a strong binding system consisting of micro-grained, well-connected crystals.

Microscopes have been proven valuable tools to researchers, in order to detect damages, identify phases, understand the behaviour and develop improved materials used in the construction field. A number of analytical techniques are needed to be combined for the complete characterization of historic mortar. The ability to penetrate and have a direct observation of the structure in the scale of micro or nano allows the detection of inherent defects as well as ageing or deterioration effects which determine the behavior of the material. The study of building materials has benefited greatly from the study of microstructure. The evolution and specialization of building materials in order to cover different construction needs was in a significant extent based on it.

REFERENCES

- [1] Riccardi M., Lezzerini M., Caro F., Franzini M. and Messoga B., 'Microtextural and microchemical studies of hydraulic ancient mortars: Two analytical approaches to understand pre-industrial technology processes', *Journal of Cultural Heritage* **8** (2007) 350-360.
- [2] Papayianni I., 'Design and manufacture of repair mortars for interventions on monuments and historical building' Book title: Workshop Repair Mortars for Historic Masonry, Editor(s): C. Groot, e-ISBN: 978-2-35158-083-7, Publisher: RILEM Publications SARL, (2009) 292 – 304.
- [3] Papayianni I. and Stefanidou M., 'Durability Aspects of ancient mortars of the archaeological site of Olynthos', *Journal of Cultural Heritage* **8** (2007) 193-196.
- [4] Johansson S. and Lindqvist L.E., 'Historic mortars with Burned Alum Shale as an Artificial Pozzolan', Historic Mortars Characterization, Assessment and Repair, Springer RILEM Bookseries, Editors: J. Valek, J. Hughes, C.J.W.P. Groot, (2012) 77-88.
- [5] Weber J., Bayer K. and Pinter F., 'Nineteenth Century “Novel” Building Materials: Examples of various historic mortars under the Microscope', Historic Mortars Characterization, Assessment and Repair, Springer RILEM Bookseries, Editors: J. Valek, J. Hughes, C.J.W.P. Groot (2012) 89-103.
- [6] Scannell S., Lawrence M. and Walker P., 'Impact of aggregate type on air lime mortar properties' *Energy Procedia* **62** (2014) 81 – 90.
- [7] Stefanidou M. and Papayianni I., 'The role of aggregates on the structure and properties of lime mortars', *Cement and Concrete Composites*, **27** (9-10) (October- November 2006) 914-919.
- [8] Lawrence S.J. and Cao H.T., 'Microstructure of the Interface between brick and Mortar', Proc. 8th International Brick/Block masonry conference, Dublin Ed. J.W. DeCourcy vol.1, (1987) 194-204.
- [9] Stefanidou M., 'Methods for measuring porosity of lime-based mortars', *Construction and Building Materials* **24** (2010) 2572-2578.
- [10] Larbi J.A., 'Microscopy applied to the diagnosis of the deterioration of brick masonry', *Construction and Building Materials* **18** (2004) 299–307.
- [11] Stefanidou M. and Papayianni I., 'Salt accumulation in historic and repair mortars', Heritage, Weathering and Conservation, Editor R. Fort, M. Alvarez de Buergo, Gomez-Heras & Vazquez-Calco, Taylor & Francis, (2006) 269-272.

- [12] De Nardi C., Cecchi A., Ferrara L., Benedetti A., Cristofori D., 'Effect of age and level of damage on the autogenous healing of lime mortars', *Composites Part B* **124** (2017) 144-157.
- [13] Stefanidou M. and Papayianni I., 'Inclusions in selected mortars of ancient technology', 10th Euroseminar on Microscopy Applied to Building Materials (2005) University of Paisley

DURABILITY ASPECTS RELATED TO REPOINTING OF HISTORIC MORTARS WITH LIME BASED MORTARS

Caspar Groot (1), Rob van Hees (2) and Ioanna Papayianni (3)

- (1) Faculty of Civil Engineering and Geosciences, TU Delft, The Netherlands
- (2) TNO, Netherlands Organisation for Applied Scientific Research, Delft, The Netherlands;
Presently, R-Kwadraat MonumentenAdvies, Zoetermeer, The Netherlands
- (3) Department of Civil Engineering, Aristotle University of Thessaloniki, Greece.

Abstract

The durability of repointing repair in historic masonry is, apart from general parameters such as, environmental exposure, materials properties, design and maintenance, technically in particular determined by compatibility of the chosen repair material with the existing masonry and adequate on-site practices.

First, the paper discusses basic technical requirements stemming from the need of hygric and mechanical compatibility; these are placed in the context of durability of repointing in historic masonry. Further on, the effects of in-adequate on-site practices are discussed.

Most of the mortars applied in historic masonry are traditionally lime-based, with or without hydraulic components. For repair often lime, lime+pozzolans or natural hydraulic lime (NHL) are the most appropriate binders to be applied.

The durability of repair mortars using these binders is not always satisfying. In the paper some reasons for this unsatisfying behaviour and suggestions on how to deal with this are given.

Keywords: repointing, durability, lime-based mortars, risks

1. INTRODUCTION

The durability of repointing is determined by a series of factors such as materials properties, environmental exposure, on-site practices, maintenance and design.

For historic buildings, requirements to repointing mortars should fit in a general framework, which ranges from a general approach, which includes authenticity questions, over conceptual requirements like compatibility (with the existing masonry and with the environment) to functional and technical requirements.

However, in this paper we will primarily focus on technical requirements.

Choosing the composition of a repointing repair especially materials properties of the repair mortar, compatible with the surrounding masonry, taking into account the environmental exposure conditions are important selection components.

For durability in terms of service life not only the materials choice is important but as well the quality of on-site practices, i.e. the how-to-execute the repointing, is playing a decisive role [1]. Practice learns that more than half of premature failure of repointing is caused by inadequate on-site practices.

2. BASIC TECHNICAL REQUIREMENTS ASSURING COMPATIBILITY

The technical properties for a repair repointing mortar stem in the first place from the requirement that the new material is compatible to the surrounding existing material. This means that the repointing should not increase the risk of damage to the existing masonry. Moreover, the pointing mortar should be sacrificial: should be the weakest part of the masonry. So that failure occurs in the repointing (easy to replace) and not in the bricks or bedding mortar. Hygric and mechanical compatibility are basic requirements for durable repointing in historic masonry.

2.1 Hygric compatibility

The effects of lacking compatibility between new repointing mortar and existing masonry have been observed in various damage cases. In particular the application of dense (low porosity) repointing mortars on traditional high-porous lime-based bedding mortars may result in a significant decrease of drying of the masonry causing frost-damage in sometimes centuries old bedding mortars (figure 1, right picture).

This example stresses the relevance of hygric compatibility between new and existing material, enabling the easy transport of moisture in the masonry through the mortar joints: the repointing should promote the drying of the masonry.

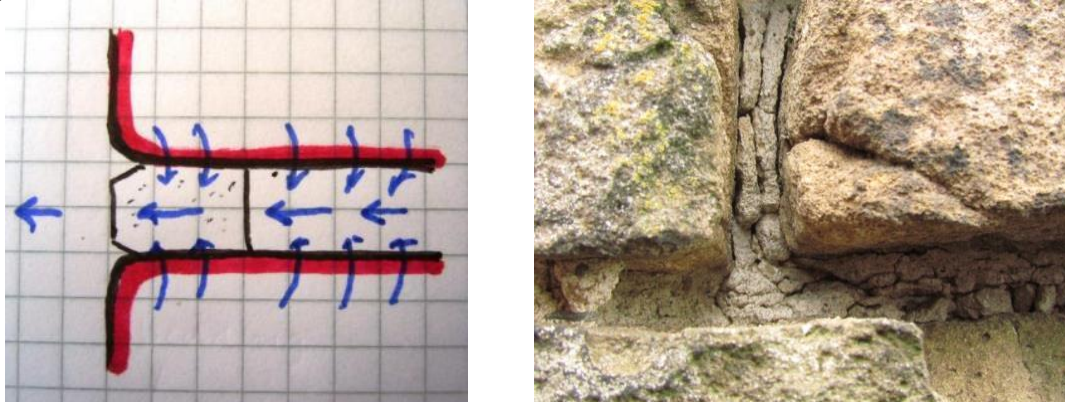


Figure 1: Left: Preferred moisture movement: from coarser porosity towards finer porosity.
Right: Frost damage in a bedding mortar

The ingress of rain water in masonry may be considerable. The bricks are often highly absorptive, causing a major source of moisture ingress. Little moisture is absorbed by the mortar itself, however interface cracks strongly contribute to rainwater absorption. It can be understood that interface cracks in repointing are hardly to avoid as the repointing mortar is applied between two fixed parallel surfaces (the bricks) while most of the mortars shrink after

application. Applying a lime based mortar, with transport and deposition of lime in the interface over time (self-healing effect) may sometimes fill up the crack.

Minimising cracking may be pursued by adequate material choice such as sand type, correct binder-aggregate ratio type and competent execution: compaction and slow evaporation of moisture.

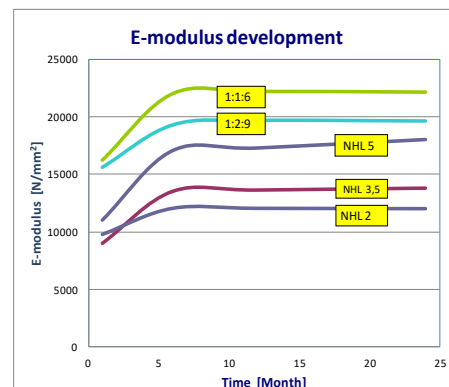
Good mortar-brick bond is an important means to resist rainwater ingress. The bond should not necessarily be strong but the interface should show a dense structure with good mortar-brick contact.

Assuring good bond is mostly determined by adequate on-site practices such as square joint-space (no V-form), properly cleaned, pre-wetted, fully filled and cured under appropriate conditions (depending on binder type)

For more detailed info on mortar shrinkage and mortar-brick bond (see [1], Chapter 5)

2.2 Mechanical compatibility

The application of a repair repointing mortar should not lead to stress concentrations. This will happen if the deformation behaviour of the new material differs significantly from the existing masonry. Differences in E-modulus and thermal/moisture deformation determine to a high degree the possible occurrence of stress concentrations.



<http://www.stastier.co.uk/nhl/info/hydraul.htm> [3]

Figure 2: Left: Push out of joints by thermal deformation cycling; Right: graph with E-modulus development of various mortar compositions (NHL mortars, 1:2,5 (vol. parts NHL3,5:sand); cement lime mortars e.g.1:1:6 (vol. parts cement:lime:sand)); (curing conditions 20°C and RH 90%: favourable hydration conditions!)

Lime-based mortars of historic masonry often are highly deformable: low E-modulus. Furthermore, the thermal expansion coefficient [α] is low: lime-based mortars 4-6 ($\text{m/m}10^{-6}/^{\circ}\text{K}$) (cement-based mortar 10-14 ($\text{m/m}10^{-6}/^{\circ}\text{K}$)). This means that thermal stresses under increasing temperature are rather low (under constrained conditions) [2].

Lime-based mortars used in Historic Masonry

Air lime, pozzolan (+lime) and natural hydraulic lime (NHL) are binders used traditionally and also often in repair in historic masonry.

Table 1: Basic differences of the lime-based binders

Air lime (air-hardening)

Non-hydraulic lime. It does not harden under water. When incorporated into a mortar mix, it slowly hardens in air by reacting with atmospheric carbon dioxide (carbonation). It may be either quicklime or hydrated lime.

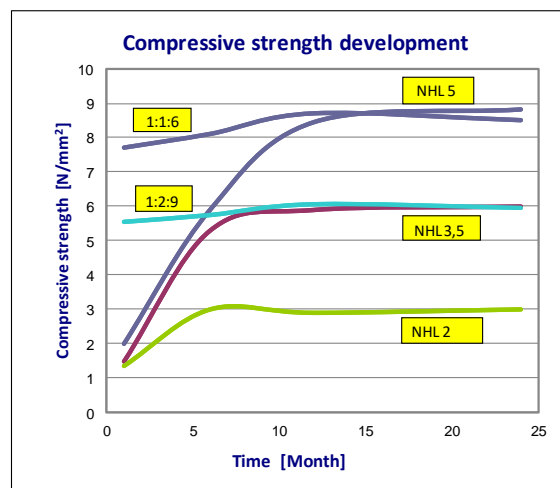
Pozzolans +calcium hydroxide (hydraulic)

A pozzolan is defined as a siliceous or siliceous and aluminous material which in itself possesses little or no hydraulic property but will, in a finely divided form and in the presence of moisture, chemically react with calcium hydroxide at ordinary temperatures to form compounds possessing hydraulic properties. So, basically pozzolanic materials are latent-hydraulic (well known pozzolans: volcanic ashes, metakaolin, trass, crushed bricks and by-products of industrial processes). Pozzolanic materials differ in strength depending on their nature (mineralogical composition) and fineness.

Natural Hydraulic Lime (NHL) (hydraulic and air-hardening)

A binder which shows hydraulic as well as air-hardening properties. It is obtained from limestone containing clay materials (e.g. silica and alumina), or a mixture of similar composition, and fired at temperatures up to 1250°C. Natural Hydraulic Lime contains a mix of air lime, calcium silicates (in particular belite) and calcium aluminates. Hardening occurs through direct reaction with water and by carbonation.

Characteristic for the binders mentioned above, compared to the modern cement-lime mortars, is the slow strength development (see figure 3). This means in practice that the curing conditions over a long(er) period of time should be favourable to the hardening process. Given the slow strength development pointing should be done well before or after freezing weather.



<http://www.stastier.co.uk/nhl/info/hydraul.htm> [3]

Figure 3: Slow strength development for the HNL mortars and quick hardening of the cement-lime mortars; for composition mortars and curing conditions: see caption figure 2.

3. DURABILITY RISKS FOR LIME-BASED MORTARS IN REPOINTING

Generally, lime-based mortars applied in restoration show good hygric and mechanical compatibility with the existing masonry. However, it is also observed that there are certain

durability risks in applying these mortars. These risks are partly related to their material characteristics and partly related to inadequate on-site practices (especially for repointing).

3.1 Pure lime mortar in repointing

The application of pure air lime mortars in repointing asks for serious consideration.

Especially for parts of the masonry exposed to rain substantial loss of mortar material may occur during the first months after application: when uncarbonated, air lime ($\text{Ca}(\text{OH})_2$) is still highly soluble. However, as soon as the calcium hydroxide is carbonated the solubility of the formed compound (CaCO_3) is more than hundred times lower (solubility of $\text{Ca}(\text{OH})_2$ is ~0,185 g/100ml; solubility of CaCO_3 is 0,0014-15 g/100 ml).

The carbonation process is very slow. Measurements in a render (exterior plaster exposed to the weather) have shown penetration depths of 8 mm in 2 months [5] and 5 mm in 4 weeks [5]; obviously, the carbonation rate will decrease with depth. Hence, dissolution and leaching of air lime are real risks in the first months after application.

It should be noted as well that uncarbonated air lime is susceptible to frost.

3.2 Incomplete hydration of lime-pozzolan repointing

As for the reaction between pozzolan and hydrated lime ($\text{Ca}(\text{OH})_2$) water/moisture is needed, wetting of the mortar directly and over a longer period of time after application is essential to the formation of hydraulic compounds. If the mortar dries out too quickly (no proper and long enough period of wetting of the slow-reacting pozzolan) this will lead to the carbonation of the hydrated lime (formation of chemically inert CaCO_3). Consequently, not enough calcium hydroxide will be left for the pozzolanic reaction. The result will be a mortar with a strongly reduced strength.



Figure 4: Damage in a trass-lime repointing caused by incomplete hydration of the binding system.

Figure 4 shows an example of incomplete hydration of a lime-pozzolan mortar. The composition in volume parts is: 1 trass-lime : $\frac{1}{4}$ blast furnace cement : $3\frac{1}{2}$ river sand. The object is a 35 m high tower of fired clay brick masonry. The site is close to the sea. Incomplete hydration of the mortar resulted into a low strength so that rain and wind erosion could cause damage.

3.3 Strength decrease of lime-pozzolan mortars over time

In practice as well as in research it was observed that lime-pozzolan mortars may lose strength over time, especially if the environmental conditions are dry.

In their research Cizer et al. [6] detected a strength reduction at the very early stage for rice hull ash cement lime (RHA-cement-lime) mortars containing 10%-wt cement. Initially hydrated cement phases appeared to be destructed by calcium carbonate phases and subsequently to carbonate, causing negative effects on the mechanical properties.

They concluded that a form of competition between hydration and carbonation reactions had taken place.

Decrease of strength over time was as well noted in lime-metakaolin pastes. During investigations by Santos Silva et al. [7] it was found that, dependent of the lime/MK ratio and the curing conditions, the mechanical properties decreased after 180 days of curing. In this study compounds like Stratlingite (C_2ASH_8), contributing to the mechanical strength of the paste, appeared to be unstable.

These results underline that lime-pozzolan mortars perform better over time under wet ambient conditions: a reason why the application of lime-pozzolan mortars appears to be more appropriate in hydraulic structures.

It should also be noted that much on the phenomenon and effects of competition between hydration and carbonation in lime-pozzolan mortars is still unknown.

3.4 Risks in the application of Natural Hydraulic Lime (NHL)

Since also natural hydraulic lime is a slow-developing strength mortar, especially the control of the curing conditions over a period of time is basic for a good start of the hydration.

Subsequently, as NHL contains calcium silicates (belite) and hydrated lime ($Ca(OH)_2$) hydraulic reaction and air-hardening will alternately take place depending on the ambient weather conditions. In contrast to lime-pozzolan mortars the risk of under-hydration as a results of carbonated calcium hydroxide does not exist: after all, the calcium in the binder is incorporated in the calcium silicate compound of the NHL.

In practice it is shown that the degree of hydration of NHL, and with that the mechanical strength of the mortar, is depending on the orientation of the facade, as rain is the driving ingredient for further hydraulic hardening.

It is curious to note that the hydraulic hardening process of NHL is in fact a process of 'hydraulic penetration' in the (depth of) the wall: this in contrast to modern cement binders where the hydraulic hardening is an overall process in the mix; while this 'hydraulic penetration' is analogue in terms of penetration, to the carbonation process of air-hardening.

3.5 Salt damage

In this section some examples are shown of salt damage in lime-pozzolan and natural hydraulic lime repointing mortars. Possible future damage by salts should be detected during the preliminary studies on site, so that the repair mortar composition can be adapted to existing masonry conditions.

Salt damage of lime-pozzolan mortar

Repair mortars based on lime-natural pozzolan binders are of high porosity and the problems of salt damages are commonly appearing in the bricks or at brick-mortar interfaces.

The total open porosity of these mortars ranges from 22-30% and about 45-55% of the pores are of the size 250-650 μ m. In most cases (apart from the monuments exposed to sea spray such

as the fortress Hagios Nikolaos in Rhodes) the salt types determined are sulfates or salts coming from the salt contaminated old masonry.

In the pictures taken from repaired masonry (figure 5) of the Galerius Palace (4th century BC) after the earthquake of 1978, the salt damages are obvious.

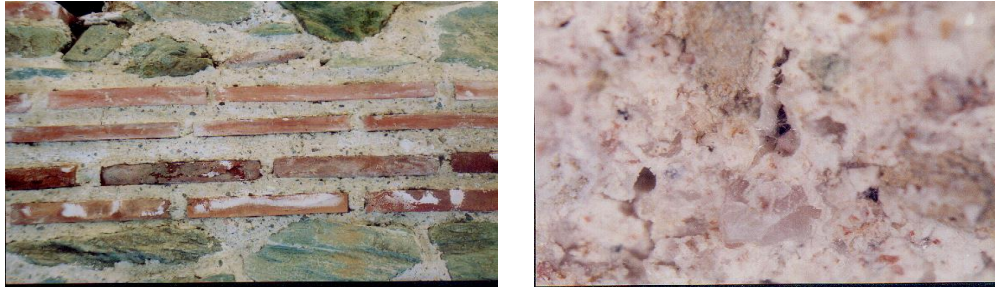


Figure 5: Left: Galerius palace (4th century BC). Detail of the repaired masonry. Right: Repair mortar from salt damage area of masonry of Galerius Palace. Content in soluble salts which are mostly accumulated into the pores ($\text{Cl}^- = 0.28\%$, $\text{NO}_3^- = 0.83\%$, $\text{SO}_4^{2-} = 1.14\%$)

Sulfate damage of NHL mortar

Salts, such as sulfates present in the masonry may induce damage to a repointing. Crystallisation of for example sodium sulfate at the interface between two different pore systems like the bedding mortar and the repointing, could result in push out of the repointing.

A situation which is even worse than the above occurs when a reaction can take place between the salt and components of the mortar. For example, in case of hydraulic lime or trass lime mortars in the presence of sulfate, mainly thaumasite may be formed [8], [9]. The sulfate may derive from the atmosphere (SO_2) or from the brick (due to low firing of sulfate containing clays).



Figure 6: Mortar prisms after 15 weeks in sulfate solution. Natural Hydraulic Lime based (HL) specimens with clear expansion and deformation. Hydrated lime based (L) not any expansion, [10]

Thaumasite ($\text{CaCO}_3 \cdot \text{CaSiO}_3 \cdot \text{CaSO}_4 \cdot 15\text{H}_2\text{O}$) is a swelling compound that can be formed due to a reaction of mortar components with calcium sulfate and water. The conditions for this reaction are a high sulfate content together with high moisture content. The mortar needs to contain calcium carbonate and calcium (mono)silicate. Sulfate is necessary in the form of calcium sulfate (gypsum). High water content is necessary to allow the reaction to take place and also serves for the transport of sulfate from the brick to the mortar.

In practice it is therefore advisable to first try to take the essential conditions, in this case the sources away (moisture and sulfate). When this appears impossible, in order to come to an

adequate choice of repair mortar, it is suggested to first make trial mixes and follow a test procedure like described in [10].

4. CONCLUSIONS

Generally, lime-based mortars applied in restoration show good hygric and mechanical compatibility with the existing relatively low-strength historic masonry. However, it is also observed that there are certain durability risks in applying these mortars. These risks may be related to their material characteristics and/or to inadequate on-site practices (esp. repointing)

Regarding the materials-related durability risks treated in this paper, the phenomenon of loss of strength over time of lime-pozzolan mortars, is for repointing (and renders) a risk with many unknowns. More research is needed to understand the mechanisms and effects of this phenomenon on durability.

Durability risks related to on-site practices are manifold, especially for slow hardening lime based historic repointing. For optimal durability special attention should be paid to scheduling of the works (seasonal conditions), preparation, mixing and installation of the joint, and adequate curing conditions and period.

REFERENCES

- [1] Maurenbrecher, P. and Groot, C. (Editors), 'Repair Mortars for Historic Masonry, State of the Art Report of RILEM TC 203-RHM. RILEM Report 45. (2016), Paris
- [2] Groot, C., 'Repair mortars for historic masonry; Effects of the binder choice on durability'. HERON Vol. 61 (2016) No. 1, pp 33-56
- [3] Hydraulicity and properties of St Astier NH. <http://www.stastier.co.uk/nhl/info/hydraul.htm>
- [4] Waldum A.M., 'Historic Materials and Their Diagnostic, State of the Art for Masonry Monuments in Norway'. Norwegian Building Research Institute. Ariadne 9 Workshop on Historic Materials and their Diagnostics. (2002) See www.arcchip.cz
- [5] Ratcliffe T. and Orton J. Success with lime renders. Interim discussion article of the Society Protection Ancient Buildings (SPAB), (1998), UK
- [6] Cizer, O., Van Balen, K., Van Gemert, D., 'Competition between hydration and carbonation in hydraulic lime and lime-pozzolana mortars'. *Advanced Materials Research* (2010) Vol. 133-134, pp 241-246
- [7] Santos Silva, A., Gameiro, A., Grilo, J., Veiga, R., Velosa, A., 'Long-term behavior of lime–metakaolin pastes at ambient temperature and humid curing condition. *Applied Clay Science* (2014) Vol. 88–89, pp 49–55
- [8] Hartshorn, S.: Thaumasite, A brief guide for engineers; Concrete September (1998) p. 24-27
- [9] Van Balen, K., Toumbakari, E. E., Blanco-Varela, M. T., Aguilera, J. Puertas, F., Paloma, A., Sabbioni, C., Riontini, C., and Zappia, G. 'Environmental Deterioration of Ancient and Modern Hydraulic Mortar (EDAMM)'. Protection and Conservation of European Cultural Heritage, Research Report European Commission, N°15, Luxemburg: Office for Official Publications of the European Communities, EUR 19863, (2003), 202 p., ISBN 62-894-3169-5.
- [10] Van Hees, R.P.J., Wijffels, T.J., van der Klugt, L.J.A.R., 'Thaumasite swelling in historic mortars. Field observations and laboratory research', *Cement & Concrete Composites* 25 (2003), pp. 1165-1171

SELF-HEALING LIME MORTARS: OVERVIEW OF AN EXPERIMENTAL INVESTIGATION FROM MATERIAL TO SUBASSEMBLY SCALE

Cristina De Nardi (1), Claudia Brito de Carvalho Bello (2), Liberato Ferrara (3) and Antonella Cecchi (2)

(1) Università IUAV di Venezia, Italy; now at Cardiff University, School of Civil Engineering, Cardiff, UK

(2) Università IUAV di Venezia, Italy

(3) Politecnico di Milano, Italy

Abstract

Natural hydraulic lime-based mortars are recommended for retrofitting operations in historical buildings, primarily because of their high chemical, physical and mechanical compatibility with the existing mortars; moreover, their autogenous and engineered self-healing capacities make them a suitable material for the aforementioned interventions.

The authors' group has undertaken a comprehensive investigation on the topic, developing tailored methodologies for the assessment and characterization of the healing capacity of lime based mortars at the material and structure subassembly level, and have addressed a constitutive modelling approach which incorporates the effects of healing scenario on the response of lime based mortars. At the material level the methodology was based on pre-damaging specimens, at different ages and levels of damage (70% of the compression strength in pre-peak regime; 90% of the compression strength in post-peak regime), curing them under different exposure conditions for the healing to occur, and retesting them after scheduled "healing period" to evaluate the recovery of physical and mechanical properties. At the sub-assembly level the same concept was applied to brick-mortar specimens, to evaluate the effects of healing on the brick-mortar bond, meant a crucial to the structural behaviour of the masonry render.

The paper summarizes the main results obtained with a focus on the scalability of the healing results from the material to the subassembly to the structural level, as required for engineering applications.

Keywords: self-healing, lime-mortars, brick-mortar subassemblies, architectural heritage.

1. INTRODUCTION

Lime-based mortars—consisting of lime as a binder, fine aggregates (generally river or quarry sand) and water—have been used since ancient times in stone and brick masonry buildings, dating back to as early as 12.000 BC in Palestine and Turkey [1] and, through ancient Greek and the Roman Empire [2], have been continuously used almost without interruption so far. Several reasons can be called to justify this long-time use of lime as binder, including availability, relatively easy production, good workability and adhesion to different subgrades, as well as the ability of accommodating movements, such as settlements, and avoiding the resulting stress concentrations that can cause failure in brick masonry wall. In recent years, the use of lime-based mortars in restoration of cultural heritage has increased, also because of their chemical-physical and mechanical compatibility with old renders. Several studies can be found in the literature investigating the composition and properties of mortars for repairs, with an increasing interest in the use of pure lime and hydraulic lime mortars [3,4]. As a matter of fact, cement based mortars are not compatible with ancient masonry, not only because of their higher mechanical strength and stiffness and because they may introduce soluble salts, [5], whereas lime mortars, due to their high chemical purity, hardly can act as efflorescence promoters.

As a matter of fact, due to dissolution, transport and re-precipitation of calcium compounds, it can also have autogenous self-healing properties, as firstly recognized by Anderegg [6], in 1942. He attributed this capacity, in mortars with high lime content, to the deposition of calcite in cracks and also noticed that mortar made from hydrated dolomitic lime had a better performance than one high-calcium quicklime. Lubelli et al. [7], through microscopy analysis, highlighted that the presence of water, even in form of air moisture, is the necessary condition for the occurrence of self-healing. They observed that, in case of a relevant amount of free lime, water could be responsible of its dissolution and transport to the damaged area. Therefore, autogenous-healing is possible if atoms or molecules can move from their initial position to the micro-crack surfaces, and there can re-crystallize to form calcium compounds. These processes of transport and re-precipitation observed for both CaCO_3 and Ca(OH)_2 into voids and micro-cracks, are responsible for the reconstruction of the matrix trough-crack continuity and build-up of an enhanced load bearing capacity. The same authors also developed a test procedure to reproduce the self-healing of lime-based mortars (both pure calcium and magnesium-calcium) in laboratory conditions. The main conclusion of these studies is an interesting relationship between the healing capacity and the precipitation of magnesium phases.

So far, several studies have regarded to self-healing capacity of lime-based mortars as a sort of bonus, mainly in old masonry constructions [3], but these properties have seldom been sought through an appropriate material design. The possibility of engineering this process with the addition of innovative constituents in traditional lime mortars, is therefore of the utmost interest. The aim is to obtain advanced “smart” lime mortars, which are able to enhance the durability of the whole building, while maintaining the authenticity of structural brick elements.

In this paper the results of a comprehensive investigation are presented which focused on the development and calibration of an experimental methodology to ascertain and quantify the self-healing capacity of lime mortars through the recovery of physical (ultrasonic pulse velocity UPV) and mechanical (compressive strength) properties. Autogenous self-healing was investigated together with stimulated/engineered one, via both commercial crystalline additives and tailor-made capsules containing different “active” compounds. The effects on brick masonry subassemblies have been also preliminary assessed.

2. EXPERIMENTAL CAMPAIGN: MATERIALS AND TEST METHODS

With the aim of reproducing the composition and performance of mortars found in existing historical building, a reference lime mortar was produced, consisting of natural hydraulic lime (NHL5) with the addition of calcium hydroxide ($\text{Ca}(\text{OH})_2$), in equal mass proportion, and with dolomitic sand (lime to sand weight ratio equal to 1/3). A water to lime mass ratio equal to 0.22 was employed. The composition of the lime is listed in Table 1. 50 mm side cubes were cast with the mortar, which were demoulded 96 hours after casting (during which time they stayed in a lab environment) and then stored in a room at $(23 \pm 2)^\circ\text{C}$ and $(50 \pm 4\%)$ RH until testing..

The mortar compressive strength was first determined at 14, 28, 56 and 84 days. Before testing, UPV tests were performed on each specimen, according to three directions. At the same ages, other specimens were pre-damaged by loading them respectively at 70% of the compressive strength in the pre-peak regime and at 90% of the same strength in the post-peak regime. Three specimens per each level of pre-loading and age were pre-damaged. Before and after pre-damaging, UPV measurements were taken for these specimens as well. Six damaged pre-loaded specimens per level, together with six further undamaged specimens per each pre-cracking age, were then cured in water for 14 and 28 days respectively.

At the end of the curing periods as above, all specimens were re-analysed by means of UPV test end re-tested up to the maximum compressive strength and then re-cured in water for further 14 days. At the end of this second curing period, specimens were finally tested to failure (UPV measurements were taken once again before this first test). Tests were performed on a Galdabini Sun 20 testing machine under displacement control, at a displacement rate equal to 0.2 mm/min

The recovery, in case, of compressive strength along the cracking/healing cycles and the comparison with the strength evolution of undamaged specimens will allow the effects of healing to be quantified and connected to the recovery of the damage as through UPV tests.

For stimulated/engineered healing a simpler version of the programme was implemented, consisting of the following phases (per each type of mix/healing stimulating agent):

- after 28 days of curing, one specimen was tested for evaluating compressive strength;
- four specimens were pre-damaged at 70% of the compressive strength as above;
- two out of these four specimens were immediately retested after pre-damaging;
- the remaining two pre-damaged specimens were tested to failure after 14 days in water.

A commercial crystalline admixture (Penetron Admix[®]), dosed at 3% by weight of lime, was used as healing stimulator, already widely employed in concrete [8-11]. The admixture consists of proprietary active chemicals, highly hydrophilic, able to react with the calcium hydroxide.

As for the encapsulated agents, four types of coated granules were produced and tested:

- hydraulic lime-based, with an inorganic shell (NHL5_NaF – sodium fluoride), with organic shell (NHL5_AM_AF maleic/phtalic anhydride) and with shellac shell;
- cement based, with two different types of organic shell (CEM_AM; CEM_AF) or shellac;
- calcium hydroxide $\text{Ca}(\text{OH})_2$ with maleic/phtalic(AM/AF) anhydride or shellac shell.

Capsules were dosed from 3 to 6% by mass of the lime. Further details can be found in [12]. The whole experimental campaign is summarized in the Gantt chart in Figure 1.

Table 1. Chemical analysis of the main constituents of lime.

CaO	MgO	Al ₂ O ₃	K ₂ O	Na ₂ O	Fe ₂ O ₃	SiO ₂
62%	1%	5%	0,7%	0,3%	3,5%	21%

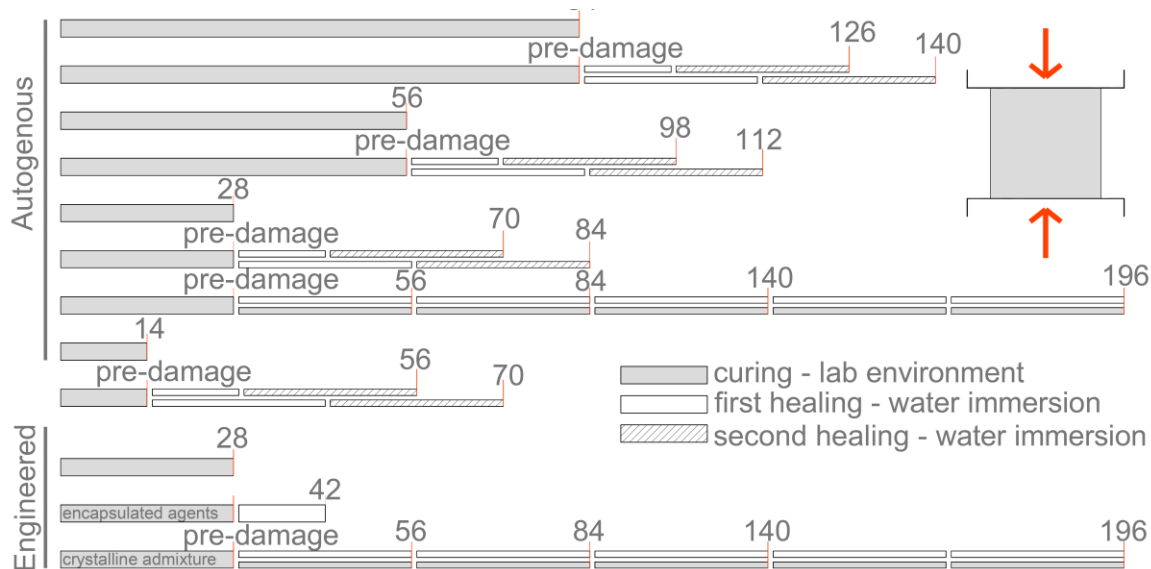


Figure 1: summary of the experimental campaign

In order to evaluate the influence of the self-healing capacity of the mortar on brick-mortar masonry subassemblies, shear tests were performed on masonry triplets consisting of three clay bricks and two 10 mm thick mortar layers, tested as per EN 1052 -3. Bricks 250x120x60 mm³ were used, with free water absorption equal to 10% by mass, dry density 1660 kg/m³, compressive strength 18 MPa and splitting strength ± 2.2 MPa. Bricks were conditioned by submerging them in water for 200 seconds. A first series of triplets, cured at 23°C $\pm 2^\circ$ and 50% $\pm 4\%$ RH for 28 days, was tested with and without transverse normal stress equal to 0.6 MPa, to determine the shear bond strength. Then, a second series of samples was pre-loaded up to 70% of the shear bond strength, determined as above, immersed in water for 3 months and re-tested to failure. Reference undamaged samples undergoing the same curing history as the damaged ones were tested as well. All tests were performed with and without a transverse normal stress equal to 0.6 MPa and using a Galdabini Sun 20 testing machine under displacement control at a displacement rate equal to 0.2 mm/min. The transverse pre-compression force, was applied through four transversal threaded rods by a torque wrench, held constant during the whole test, and measured before and after the tests.

3. EXPERIMENTAL AND NUMERICAL RESULTS

3.1 Autogenous healing: material level

Figure 2 shows the results of compressive strength tests performed on undamaged and damaged specimens, for both levels of damage, at different ages and for the different scheduled post-damage curing periods. It can be first of all observed that the compressive strength of the mortar decreases over time, a phenomenon attributable to the dry lab environment in which the specimens were kept, which may have promoted the formation of microcracks. The strength increase after curing in water, even for virgin specimens, is likely to confirm this assumption, since water, penetrating through crevices, may reactivate hydration reactions.

The effects of healing are also evident. Specimens cured in water continuously undergo a recovery of the strength, up to level comparable to virgin ones. Moreover, even if tested up to

the maximum stress and recured in water, specimens did exhibit the capacity of gaining back the original load bearing capacity, if not higher. This phenomenon progressively decreases with the age of the first damage, being due to the reactions which involve potentially reactive material, which is progressively consumed along the aging of the specimens.

From the results of the UPV tests, shown in Figure 3 in terms of damage (grey bars) and healing ratios (blueish bars), a damage and healing ratios were defined as follows :

$$\text{Damage ratio } D = 1 - v_d/v_o \quad (1a)$$

$$\text{Healing ratio } H = v_h/v_o - I \quad (1b)$$

where v is the UPV, subscripts o, d, h refer respectively to the virgin, damaged and healed state.

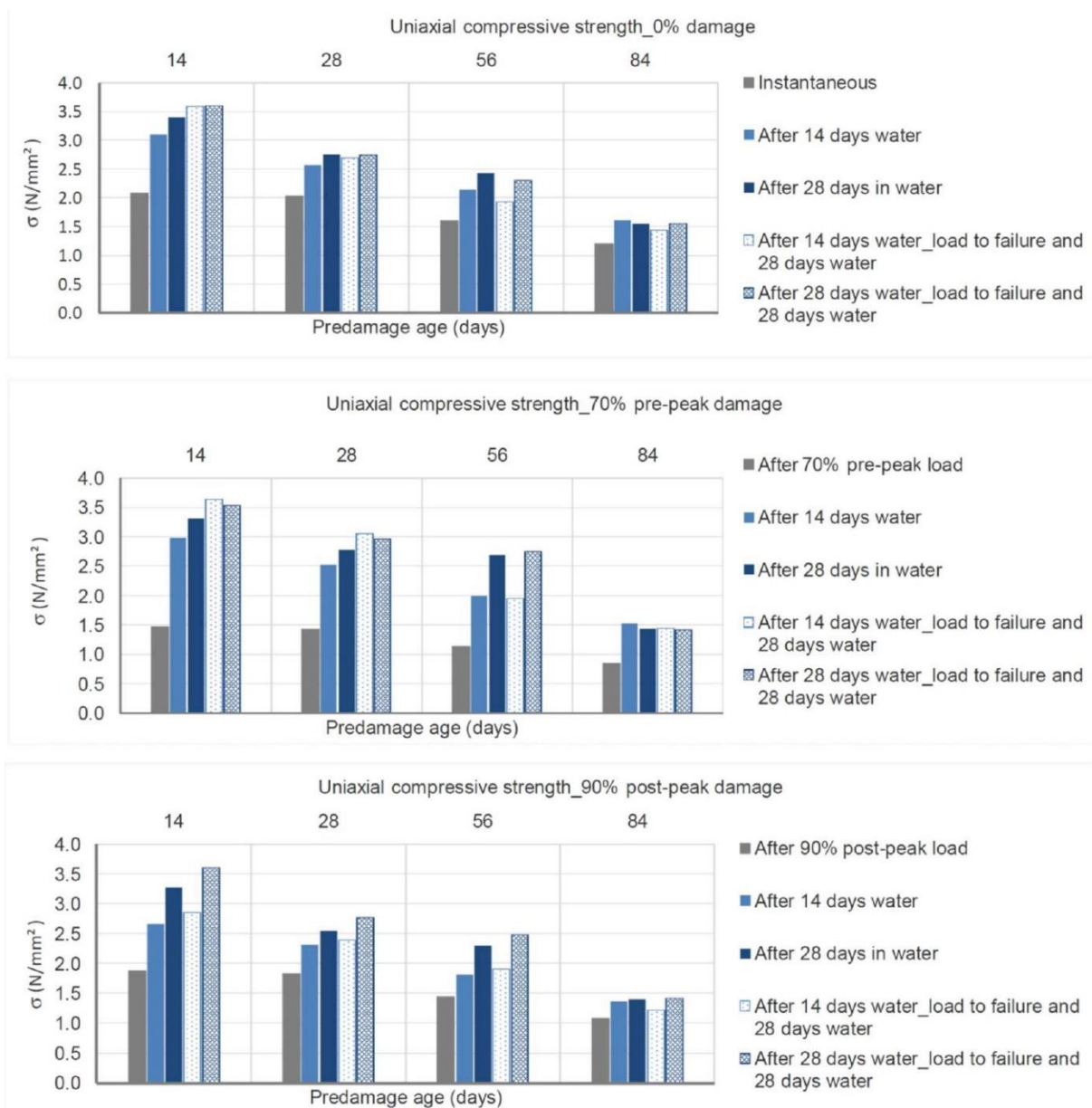


Figure 2: effect of loading level/age and of curing regime on mortar compressive strength

The healing capacity decreases with the age of predamage, most significantly for longer ages, whereas it increases with the duration of the curing. The level of damage also affects the healing capacity, the latter being far less significant for specimens damaged in the post-peak regime. Significantly, a prolonged curing in water (28 days) can promote a healing sufficient to gain back the pristine level of performance even for heavily damaged specimens, preloaded up to 90% of the compressive strength in the post-peak regime.

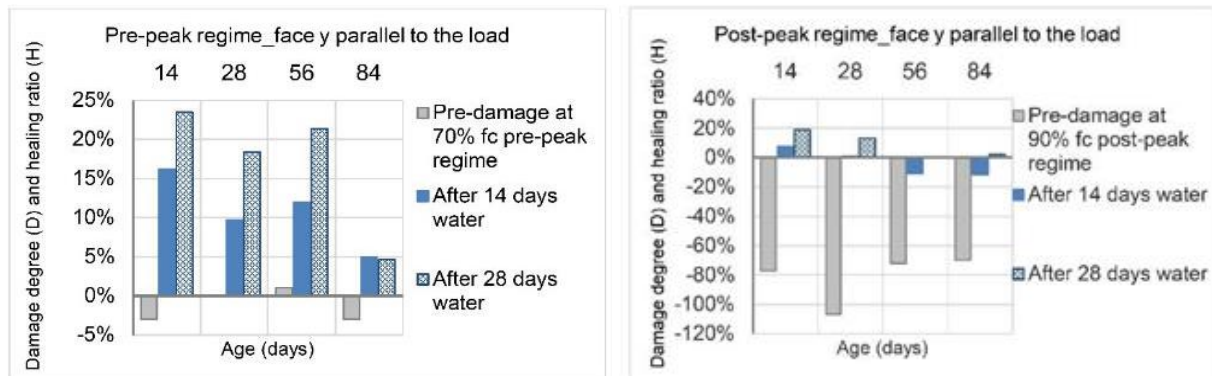


Figure 3: damage and healing degree as function of pre-loading level, age and curing regime.

3.2 Stimulated/engineered healing: material level

Figure 4 shows the healing ratio for the different types of encapsulated agents. As expectable, capsules containing cement provide the highest healing, whereas for other encapsulated materials the results are quite comparable, if not sometimes worse, with those of the reference mortar. It is worth remarking that these results may have also been affected by the actual compressive strength of the mortars with encapsulated additions, which in some case was significantly lower than for the reference mortar, since capsules may act as defects.

In order to quantify the stimulating effect of the crystalline admixture on the healing capacity an index of healing (Index of Load Recovery ILR) was calculated as follows:

$$ILR = \frac{f_{m,after\ healing} - 0.7 f_{m,28d}}{f_{m,28d}} \quad (2)$$

where f_m denotes the compressive strength of the mortar, pedices specifying at which stage it was measured. The beneficial effects of the crystalline admixture are clearly evident (Figure5), for both specimens immersed in water and cured in air. It can be hypothesized that the admixture reacts with water even in the form of air moisture, sealing the cracks and fostering the recovery. As time goes by, the sealing proceeds and water can pass through the matrix to a lesser and lesser extent, slowing the rate of performance recovery, which stabilizes after six months.

3.3 Autogenous and stimulated healing: subassembly level

All masonry triplet specimens failed in sliding shear, which allowed to process the results in terms of Mohr-Coulomb criterion:

$$f_v = f_{v0} + \mu \sigma \quad (3)$$

where f_v is the shear strength; f_{v0} , is the shear strength with zero normal stress applied (which can be regarded as a “cohesion” parameter; μ , the friction coefficient. Results are summarized in Table 2 (in brackets the scattering). The effect of healing on pre-damaged subassemblies is likely to bring a significant recovery of the performance, up to about 85% of the capacity of

virgin specimens in terms of cohesion, and even better in terms of friction. The effect of the admixture as well appears to be significant in terms of friction and quite negligible in terms of cohesion. This may be due to an increase in the roughness of the interface surfaces, which, while counteracting with the shear strength under no confinement, can significantly benefit from the presence of normal stress, as occurs in real masonry assemblies.

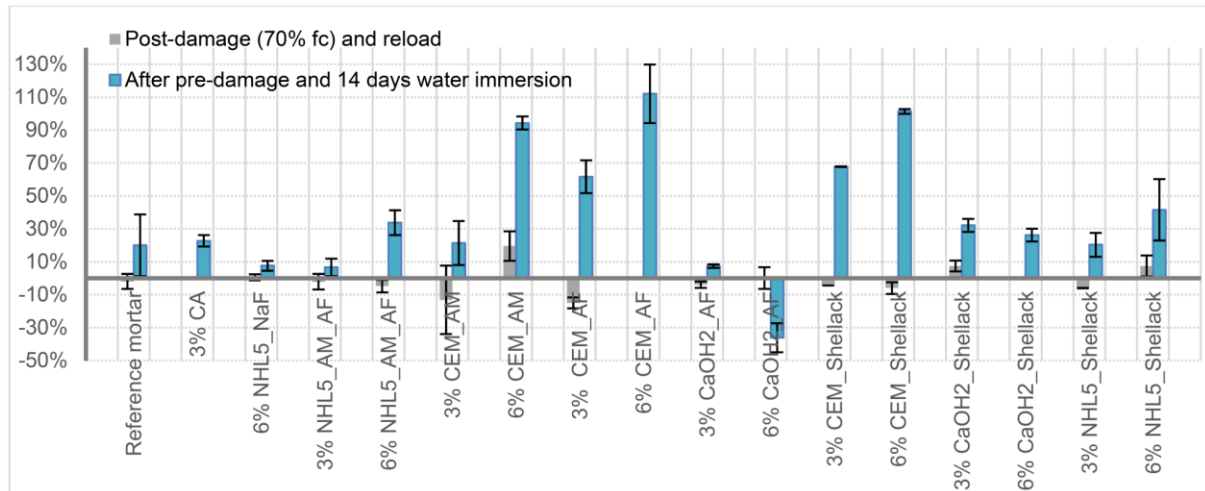


Figure 4: influence of different investigated capsules on load recovery – water healed mortars.

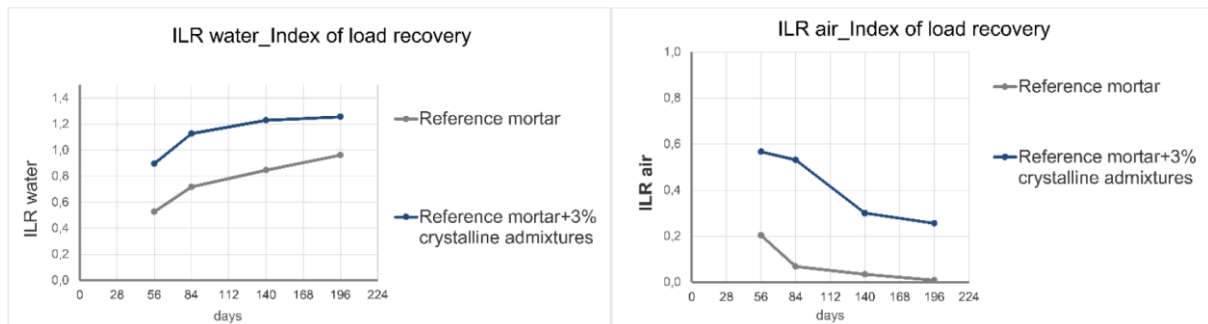


Figure 5: influence of crystalline admixture on load recovery - mortars healed in water/air.

Table 2. Effects of pre-damage and healing on subassembly behaviour parameter

	Reference mortar		With crystalline adm.	
	f_{v0} [MPa]	μ	f_{v0} [MPa]	μ
Undamaged - instantaneous test	0,19 (0,07)	0,29 (0,14)	0,16 (0,04)	0,43 (0,11)
Undamaged - 3 months in water	0,41 (0,08)	0,20 (0,13)	0,18 (0,05)	0,31 (0,13)
Pre-damaged - 3 months in water	0,35 (0,12)	0,57 (0,16)	0,21 (0,13)	0,51 (0,16)
Pre-damaged - 6 months in water			0,20 (0,09)	0,47

4. CONCLUSIONS

The results of the experimental investigation summarized in this paper have shown that lime mortars possess an inherently autogenous healing capacity, depending on the level on age of damage. Being the self-healing dependent of dissolution, transport and re-precipitation of

calcium compounds, its effectiveness depends on the available amount of the latter, the degree of carbonation of the mortar and the presence of phases affecting the solubility of calcium bearing compounds, besides the curing environment conditions. The presence of crystalline admixtures enhances the aforementioned self-healing capacity and speeds up the sealing of the cracks and the recovery of the mechanical properties. Coated granules, in case containing the same mortar as an active principle, also may interestingly enhance the healing, the scalability of their production to an industrially feasible level being the major hindrance to their use in real scale applications. Effects of the healing on the mechanical performance of subassemblies are likely to suggest that further healing of the mortar addition may not increase the cohesion value, though positively affecting the friction coefficient.

ACKNOWLEDGEMENTS

The authors thank the technicians of the Construction/Materials Science Laboratory (Labsco), Università Iuav di Venezia, for their support in performing the experimental tests.

The kind availability is also acknowledged of Penetron Italia, and of its CEO, MArch. Enrico Maria Gastaldo Brac, for providing the crystalline admixture; of dr. Lucio Ronchin and Andrea Vavasori, Ca' Foscari University, Venice, for supplying the capsule also employed in this study.

REFERENCES

- [1] von Landsberg D., 'The history of lime production and use from early times to the industrial revolution', *Zement-Kalk-Gips* 45 (1992) 199–203
- [2] Maravelaki-Kalaitzaki P., Bakolas A. and Moropoulou A., 'Physico-chemical study of Cretan ancient mortars', *Cem. Concr. Res.* 33 (2003) 651–661.
- [3] Lanas J. and Alvarez G., 'Masonry repair lime-based mortars: factors affecting the mechanical behaviour', *Cem. Concr. Res.*, 33 (2003) 1867–1876.
- [4] Moropoulou A., Bakolas A., Moundoulas P., Aggelakopoulou E. and Anagnostopoulou S., 'Strength development and lime reaction in mortars for repairing historic masonries', *Cem. Concr. Comp.* 27 (2005) 289–294.
- [5] Moropoulou A., Polikreti, K., Ruf V. and Deodatis G. 'San Francisco Monastery, Quito, Ecuador: characterisation of building materials, damage assessment and conservation considerations', *J. Cult. Her.*, 4 (2003) 101–108.
- [6] Anderegg, F.O. 'Autogeneous healing in mortars containing lime', *ASTM Bulletin*, 16 (1942) 22pp.
- [7] B. Lubelli, T.G. Nijland, R.P.J. van Hees, 'Simulation of the self-healing of dolomitic lime mortar', *Materials and Technology* 46 (2012) 3, 291–296.
- [8] Ferrara, L., Krelani, V. and Carsana, M., 'A fracture testing based approach to assess crack healing of concrete with and without crystalline admixtures', *Constr. Bldg. Mats.*, 68 (2014) 515–531.
- [9] Ferrara, L., Krelani, V. and Moretti, F., 'On the use of crystalline admixtures in cement based construction materials: from porosity reducers to promoters of self-healing', *Smart Mats. & Struct.* 25 (2016) paper 084002.
- [10] Borg, R.P., Cuenca, E., Gastaldo Brac, E.M. and Ferrara, L., 'Crack sealing capacity in chloride rich environments of mortars containing different cement substitutes and crystalline admixtures', *J. Sust. Cem. Based Mats.*, 7(3) (2018) 141–159.
- [11] Cuenca, E., Tejedor, A. and Ferrara, L., 'A methodology to assess crack sealing effectiveness of crystalline admixtures under repeated cracking-healing cycles', *Constr. Bldg. Mats.*, 179 (2018) 619–632.
- [12] De Nardi, C., Bullo, S., Ferrara, L., Ronchin, L. and Vavasori, A., 'Effectiveness of crystalline admixtures and lime/cement microcapsules in engineered self-healing capacity of lime mortars', *Mats. & Struct.* ,50 (4) (2017) 191.1–191.12.

EVALUATION OF LIME-BASED MORTARS FOR REPAIRING THE GALERIUS PALACE (4TH CENT. BC) DURING RESTORATION PROJECT (1994-2014)

I. Papayianni (1), M. Stefanidou (1), V. Pachta (1), S. Konopisi (1), F. Athanasiou (2) and M. Sarantidou (2)

(1) Laboratory of Building Materials, School of Civil Engineering, Aristotle University of Thessaloniki, Greece

(2) Ministry of Culture, Ephorate of Antiquities of the town of Thessaloniki, Greece

Abstract

The restoration of the Galerius Palace in Thessaloniki was carried out from 1994 up to 2006, including removal of eroded mortars and replacement by compatible mortars, reconstruction of brickworks, restoration of floor mosaics. A significant number of compatible repair mortars was used, based on the systematic study and analysis of the existing ones. Written instructions were given for the in situ preparation and application of the different type of repair mortars, which could be characterized as lime-based mortars. An archive of all works was also kept by the supervisors. In this paper a detailed survey of repair with lime-based is presented, including macro and micro scale photos, description of damages and other relevant remarks. Furthermore, analysis of mortar samples, showed volume stability and strength of them. Local environmental conditions and other accidental reasons were taken into account for interpreting the results. Generally, it could be said that the respond of the applied repair mortars to the functional requirements of their position in the ancient structure was very good.

Keywords: Galerius Palace, repair materials, durability, lime-based mortars

1. INTRODUCTION

The complex of Galerius Palace, is one of the most impressive monuments of the Late Antiquity in South Eastern Europe. It is situated in the center of the city of Thessaloniki, covering an area of 9000m², including six ancient structures, decorated area of 1682m² and plasters of 308m². Many historical and constructional phases were recognized by restorers who decided to respect the monument's original structural system, preserve the constructional phases of the structures, limit interventions to the actions absolutely necessary (in order to

protect and make the monumental complex statically safe and recognizable by the public). They also decided the repair materials to be compatible with the authentic ones.

The whole restoration project was executed in three periods (1994-2000, 2002-2006, 2011-2012), under the supervision of the 16th Ephorate of Prehistoric and Classical Antiquities [1]. The Lab. of Building Materials of AUTH undertook the systematic study of the old materials and the proposal of compatible repair materials, taking into account the local environmental conditions, followed by technical instructions about the raw materials and the appliance on site [1,2]. An excellent co-operation among the scientists of the Laboratory, restorers/supervisors and technicians/conservators was achieved after the first two-three years. An archive of all works was kept by the supervisors.

The pathology symptoms of the monumental Complex of Galerius were severe, since after the excavation of 1971, the ruins remained without any protection and were exposed to weathering. Previous (fortunately at limited extend) interventions of the 70's, based on cement had worsened the pathology of the masonry units [1]. The following photos (Fig. 1-4) are representative of the state of the monumental complex of Galerius before restoration.



Fig. 1-4 Preservation state of the Galerius Palace after the intervention of the 70's [1]

The restoration works included [1]:

- removal of eroded mortars of the masonry joints and their replacement by compatible mortars, following the characteristics of the existing building phases.
- reconstruction and integration of brickworks with new hand-made bricks and mortars. It must be mentioned that bricks used for the repair work were of traditional type (manufactured by order) and they were immersed in water for 3-4 minutes before their use, while care was taken to remove water from lime when mortars were applied.
- application of a protective layer on the masonries' top
- construction of plaster chiefly in the baths and Octagon
- restoration of floor mosaics by resetting of the mosaics and completion of geometric motifs with compatible colored mortars for unification of the old pavements.

From the great number of the analyzed samples (more than 60) and the proposed repair materials, the behavior of bedding/deep pointing repair mortars and plasters, which had been applied 15-20 years ago, was studied by comparing data from archives and analysis of samples taken from the site this year, 2018.

2. THE PATHOLOGY OF THE OLD MASONRY

The old masonries, consisting of alternate courses of stone and brick connected with thick mortar joints, had suffered deterioration (particularly bricks), up to a depth of 0.15-0.3m (in the structures of Octagon) and up to 0.60m (in Basilica) from the surface of the masonry. Concentrations of salts in the mortars and more in the bricks were visible, as well as

discolorations, due to pollutants and biological attack. Destruction and demolition the masonry parts made the morphological unity of the building 'complexes' no recognizable. Plasters in many places were detached, while mortar joints were eroded (Fig.5). Uncontrolled natural growth of plants created additional problems (Fig.6).



Figures 5-6 Deterioration problems of the masonries before the intervention works.

3. METHODOLOGY FOLLOWED FOR ACCEPTANCE OF A PROPOSED RECIPE OF REPAIR MORTAR

The methodology followed focused on the following aspects [1-3]:

- Take into account, during the evaluation of the analysis results, the information given by the archaeological, historical and architectural study of the complex.
 - Inform the restorers and technicians that they were engaged with the project requirements, which should be followed during the selection of raw materials and the application techniques
- The accomplishment of this multi-disciplinary collaboration was feasible, under the holistic methodology developed in the lab. of building materials (1993-1998), comprising of [2-4]:
- analysis and documentation of the ancient materials
 - comparative evaluation of the analysis results, taking into account the principles of compatibility between the old and repair materials and the problems associated with the resistance of the new materials to weathering
 - design of compatible repair materials
 - laboratory preparation and testing of multiple trial mixes
 - on site small scale application of the proposed repair materials, in collaboration with the restorers, in order to make adaptations (i.e. color hue harmonization, workability)
 - technical instructions related to the characteristics of the repair materials and their application. The limitations and requirements of raw materials were identified (i.e. aggregates, binders), as well as the standards according to which all tests were performed.

The analysis of the historic mortars included : on site study of the masonries and mapping of the pathology symptoms and the morphological characteristics of the building materials, photographic documentation, on site non destructive techniques, sampling and sampling area historical phase identification, samples' description, color hue identification, stereoscopic analysis (structure stability, cracks, aggregates origin, proportion, inclusions), determination of the physico-mechanical characteristics, application of analytical chemical techniques for the determination of the type and proportion of the binding system, determination of soluble salts concentration, granulometric analysis of the aggregates.

4. STUDY OF MASONRIES AND CHARACTERISTICS OF OLD MORTARS

Masonries were of mixed type with unshaped local green stone pieces (gneiss, found in many monuments in Thessaloniki) and series of bricks with thick joints (4-5cm).

Regarding the results of analysis of the bedding mortars, taken from different parts of the building complex of Galerius, it could be said that there was a specific type of mortar of pale white color (A), with coarse aggregates that prevailed, with small scale variations, in the W. wall of the central complex, in the W wall of Octagon, as well as in the masonries of Basilica, Baths and the N colonnade. This type of mortar was based on lime and clayish material with pozzolanic properties and the proportion of the binders ranged from place to place.

A second type of mortar, with white-reddish hue (B), was found at few locations (i.e. the NW plaster of the Octagon and the N wall of the colonnade); in this mortar brick dust and crushed brick were also added in the structure. The binding system concerned of lime, clayish material with pozzolanic properties and brick dust, while the aggregates' gradation varied from 0-8 to 0-16mm, consisting of natural, siliceous aggregates and crushed brick.

The plasters and renders of the complex had a different composition, compared to the bedding mortars. They consisted of two layers (internal 4-4.5cm thick, external: 1.5-2cm) of white-reddish color. The internal layer had coarse aggregates of 0-8 to 0-16mm gradation, consisting mainly of crushed brick, while the binding system of both layers consisted of lime, clayish material with pozzolanic properties and brick dust.

The sampling area of all samples is presented in Figure 7. The characteristics of the old bedding mortars and the proposed repair mortars for the interventions are given in Tables 1-4.

Table 1. Physico-mechanical and chemical characteristics of the old bedding mortars

Mortar type	Color	Aggregates max. size (mm)	Compr. Strength (MPa)	Porosity (%)	Ap. Spec. gravity	Ca(OH) ₂ (%w/w)	SiO ₂ +Al ₂ O ₃ +Fe ₂ O ₃ (%w/w)
A	Very pale brown	8-16	2.5-4.0	29-38	1.2-1.5	25-55	19-60
B	White-reddish	8-16	1-5	15-22	1.6-1.8	30-45	35-43

The soluble salt content of the analyzed mortars was (w/w %): Cl⁻: 0-0.1, NO₃⁻: 0-0.2, SO₄⁻: 0-0.07

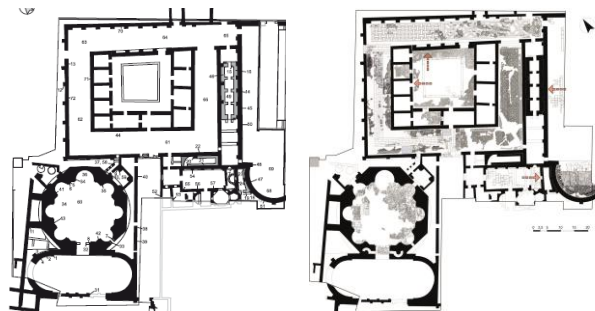


Figure 7 Sampling area of the analyzed historic (1999, left) and repair mortars (2018, right)

5. SAMPLING LIME BASED REPAIR MORTARS

A number of nine samples of repair mortars applied in the monumental complex during the restoration works of 1997 and 2000 have been taken and analyzed, as presented in Table 3 [4]. The sampling area of the analyzed repair mortars is given in Fig.7.

Table 2. Composition/properties of repair bedding mortars before and after on-site adaptations

Raw materials	Proportions by weight			
	A	A (after on site adaptations)	B	B (after on site adaptations)
Lime putty	1	2.125	1	1.35
Pozzolan (Santorine earth)	0.625	1	1	1
Clay of brownish color	0.25	-	-	0.5
Brick dust	-	-	-	0.5
White cement	0.25	0.5	0.5	-
River sand (0-4mm)	3	4.5	3	3
Coarse natural aggregates (4-8mm)	1.5	1.5	2	2
Coarse natural aggregates (8-16mm)	0.5	1.5		-
Crushed brick (4-8mm)	-	-	2	2
Crushed brick (8-16mm)	-	-	2	2
Compressive strength (28d) (MPa)		3.8		2.8
Porosity (28d) (%)		17.9		22.5
Water for expansion 15±1cm (according to EN 1015-3)				
Superplasticizer 1% w/w of binders				

Table 3. Type and characteristics of the analyzed samples

Code Nr	Restoration work (year)	Mortar type	Category	Damage rate	Sampling type
1	1997	bedding	A (very pale brown)	sound	drilling
2	1997	bedding (protective layer)	A (very pale brown)	Sound (black crust)	chisel
3	1997	Bedding	A (very pale brown)	sound	drilling
4	1997	Bedding / black crust	A (very pale brown)	loose	chisel
5	1997	Bedding	B (white-reddish)	sound	drilling
6	1997	Bedding	A (very pale brown)	sound	drilling
7	2000	plaster	A (very pale brown)	sound	chisel
9	2000	Bedding	A (very pale brown)	sound	drilling
10	2000	plaster	B (white-reddish)	sound	chisel

6. EVALUATION OF THE REPAIRED AREAS

The repaired masonries were generally in a very good state. Repair mortars were adjusted to the historic ones and presented similar colour hue and texture, as well as aggregates' type and proportion in the matrix (Fig.8). Limited deterioration phenomena were encountered, in specific places (probably due to the microclimate of each area), such as:

- Micro-cracking in the mortar joints, especially near the vertical joints (Fig.9a)
- Black crust on protective mortar layer, on the top of the masonries (Fig.9b)
- Loosening of material due to alveolization
- Discoloration of the masonry elements due to oxidation products from the gneiss (Fig.9c)

- Biological growth (Fig.9d)



Figure 8 Preservation state of the complex's masonries 20 years after repair



Figure 9 Deterioration phenomena of the repaired structures. a. microcracking, b. black crust, c. oxidation products, d. biological growth

7. ANALYSIS OF THE MORTAR SAMPLES TAKEN 20 YEARS AFTER RESTORATION

The analysis concerned [4]: determination of porosity and pore size distribution, DTA-TG analysis, determination of soluble salt content, stereoscopic and thin section analysis, compressive strength by crushing a sample around 4x4x4cm. The results are presented in Table 4 and Diagrams 1-2. The stereoscopic observation of the samples is synoptically presented in Table 5.

Table 4 Physico-mechanical and chemical properties of the analyzed samples

Code Nr	Binding system L: lime P: Pozzolan C: cement	Porosity (%)	Absorption (%)	Ap. Spec. gravity	Compr. Strength (MPa)	Soluble salt content (%w/w)		
						Cl ⁻	NO ₃ ⁻	SO ₄ ²⁻
2	L:P:C	29.85	17.04	1.752	3.84	0.05	0.01	0.03
3	L:P:C	25.87	14.25	1.816	1.88	-	-	-
4	black crust	-	-	-	-	3.23	9.38	0.39
5	L:P	28.99	16.49	1.758	5.40	-	-	-
7	L:P	26.69	14.79	1.804	2.01	-	-	-
9	L:P	26.47	14.88	1.780	2.61	-	-	-
10	L:P	34.90	22.17	1.574	3.01	0.24	0.60	2.35

The DTA-TG analysis (Diagram 1) showed that in all cases of lime-pozzolan mortars there was no available portlandite, while hydrates and carbonates were detected. The pore size distribution was performed in samples 5 and 9, in the upper (surface) and lower (in contact

with the brick) side of the samples, using Image Analysis system under Stereoscope Leica M10 (x8) (Diagram 2). Differences were recorded between the two samples. In sample 5, with coarse brick fragments, pores of 350-600 μ m prevailed in the structure. The lower part of the sample (in contact with the bricks) showed larger pores (84% of the pores were above 350 μ m), while in the upper part of the sample pores of less than 600 μ m prevailed.

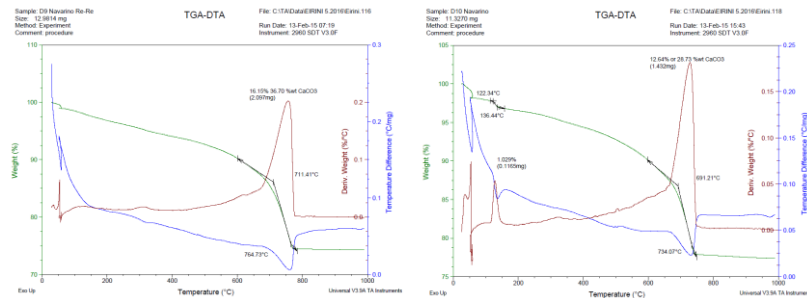


Diagram 1. DTA-TG diagram of sample nr 9 (left) and 10 (right)

Table 5. Stereoscopic photos and observation of the analyzed samples

Code nr	Stereoscopic photo		Stereoscopic observation
1 / 2			1. Good cohesion of the brick-mortar interface without indications of chemical reaction (left) 2. Detachment of large aggregates. The surface in contact with bricks is smooth while the upper surface is rough. Fine cracks due to shrinkage in the binder (right)
3			Upper surface similar with the lower as they were both in contact with bricks. Fine microcracks in contact with the large aggregates are present probably due to shrinkage. Compact structure Lower surface similar with the upper
5 (top)			Upper Surface with smooth texture Upper part of structure is compact with strong interfaces small cracks in the binder and pores
5 (bottom)			Lower surface present high roughness Lower part of the structure with open cracks which are blocked by the brick aggregates and pores
7 / 8			7. Biological alteration on the surface with color alterations Smooth surfaces, compact structure (left) 8. Strong cohesion of brick-mortar interface with chemical reaction and formation of a compact transition zone of 80 μ m thickness (right)
9			Upper surface with smooth structure and few openings Strong binder- aggregate cohesion (left) Lower surface with smooth structure and few openings. Small pores prevail (right)

In sample 9 pores of 250-350 μ m prevailed. A difference between the upper and lower part of the samples was also recorded, as the lower part of the samples presented larger pores in relation to the upper part. The 82% of the pores of the upper layer was below 350 μ m.

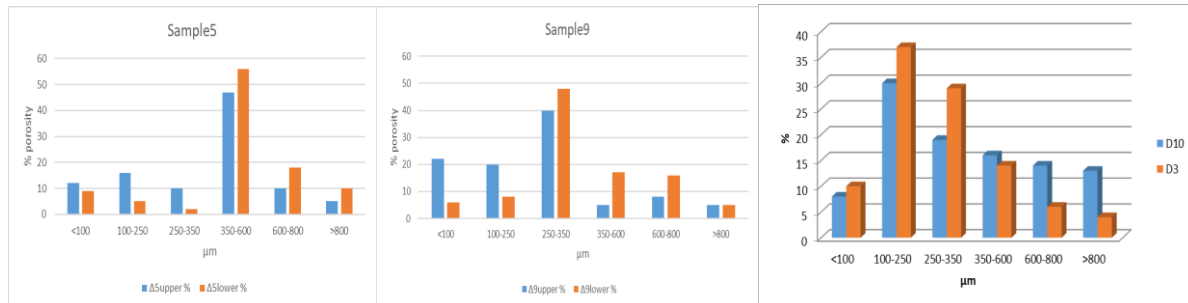


Diagram 2 Pore size distribution of samples 5 (left), 9 (middle) and 3, 10 (right)

8. CONCLUSIONS

The study of the repair materials applied in the Galerius building complex during 1994-2012, showed that 20 years after the restoration works the repair mortars remained sound and cracking was limited. The defects recorded were more localized in the western and north-western masonry, where the application of repair mortars firstly started. Salt appearance was relatively limited, mostly in bricks coarses that were near to the ground. Taking into account the salt contamination in the old masonry, the ground as well as the pollutant deposition, the behaviour of the bedding and repointing repair mortars was considered to be quite good. Salt content in general was reduced but in some areas when mortars covered the external parts of the masonry, the salt concentrations was higher. It is supposed that pollutants deposition made the difference since specific local climate was created at the low level archaeological site surrounded by multistory buildings.

The assessment of repair mortars after 15-20 years of service-ability under local environmental conditions is an actual validation of the criteria used for designing the repair mortars and proposing the applying techniques. The limited inadequacies detected, were mainly due to the weathering action of the microclimate of specific areas, as well as due to the time needed in order for the technicians to get familiar with the application techniques.

REFERENCES

- [1] Ministry of Culture, Ephorate of Antiquities of the town of Thessaloniki, The Restoration of the remnants of the Galerius complex in Thessaloniki (1994-2014), Volume B', The restoration works (Thessaloniki, 2015).
- [2] Papayianni, I., Pachta, V., Stefanidou, M., 'Analysis of ancient mortars and design of compatible repair mortars: the case study of Odeion of the Archaeological site of Dion', *Construction and Building Materials* **40** (2013) 84-92.
- [3] Stefanidou, M., Papayianni, I., Pachta, V., 'Analysis and Characterization of Roman and Byzantine fired bricks from Greece', *Materials and Structures* **48** (7) (2015) 2251-2260.
- [4] Papayianni, I., Stefanidou, M., Pachta, V., 'Survey of Repaired and Artificial Stone at Archaeological Site of Pella Five Years after Restoration Works', Proceedings of an International Conference, Milan, November 2013 (Built Heritage 2013 Monitoring Conservation Management, Milan, 2013).

MATERIAL PROPERTIES OF HERITAGE MASONRY BUILDINGS FROM 19TH CENTURY

Davor Grandić, Paulo Šćulac and Natalija Bede

Faculty of Civil Engineering, University of Rijeka, Croatia

Abstract

In this work we present in situ and laboratory testing campaign carried out on the brick masonry heritage buildings of the Stud Farm Lipik consisting of: (i) laboratory testing of brick and mortar material properties, and (ii) in situ shear tests performed by displacing an element of the masonry wall with a hydraulic piston. Obtained results will be very valuable for complementing the existing material properties database of historic masonry buildings.

Keywords: heritage masonry buildings, material testing, compressive strength, shear strength

1. INTRODUCTION

While assessing the safety of old masonry structures structural engineers often encounter difficulties related to unknown material properties. Testing of masonry strength are difficult to conduct since undisturbed samples have to be taken from the structures. That is why masonry compressive strength is usually obtained on the basis of compressive strength test results of both masonry units and mortar, rather than testing a whole masonry sample.

Experimentally measured mechanical properties of historical masonry made of clay units using lime mortars are relatively rare. Testing is mostly conducted on masonry specimens made in the laboratory [1]. In [2] strength results of clay brick masonry using lime mortar of both in situ tests and tests on samples taken from the structures built from the end of 19th and beginning of the 20th century are presented. Despite the small number of available test results the authors have tried to establish several relations: flexural bond strength of masonry-compressive strength of masonry, initial shear strength of masonry-compressive strength of mortar and flexural bond strength of masonry-compressive strength of mortar.

Conducting a larger number of shear tests on historical buildings in situ is often very impractical and therefore there is a constant need for expressions to predict masonry shear strength in relation to other masonry properties that are easier to determine like masonry compressive strength and mortar compressive strength. In order to establish such an expression there should exist a representative database of material properties for different types of historical masonry, which is still not the case.

2. GENERAL ABOUT THE BUILDINGS

The Stud Farm Lipik was established by count Izidor Janković who built this complex in 1843. The subject of this research are the following buildings (figure 1): horse stable (1), workers' houses (6a, 6b and 6c) and manager's building (7). All the buildings are predominantly made of clay brick with a small part of natural stone masonry units using lime mortar. The horse stable is quite impressive: 170 m long and 10.5 m wide without dilatation. It has been partially reconstructed in 2007 and is still in use for its original purpose: breeding Lipizzaner horses. Other buildings are in ruins, without roof and partially inaccessible.



Figure 1: Ground plan of the Stud Farm complex in Lipik

3. LABORATORY AND IN SITU TESTING AND ASSESMENT OF MECHANICAL PROPERTIES OF MASONRY

3.1 Compressive strength of mortar

Mortar testing has been conducted on samples taken from bed joints, which were then formed in specimens by hand cutting in order not to disturb the specimen strength. Specimens had the shape of a prism with approximately rectangular base and height equal to the bed joint thickness which was about 18.9-29.6 mm. Mortar specimen dimensions are given in table 1: samples 6A, 6B and Z1 are taken from buildings 6a, 6b and 1, respectively. Based on a visual inspection of the masonry quality it was estimated that samples taken from buildings 6a and 6b are also representative for buildings 7 and 6c, respectively. Before testing upper and lower base have been levelled with a thin layer of gypsum (figure 2). Testing (figure 3) has been conducted according to EN 1015-11 [3].



Figure 2: Mortar samples (left) and specimens prepared for testing (right)



Figure 3: Compressive test of mortar specimens: before (left) and after testing (right)

Table 1: Mortar specimen dimensions

Specimen	Mass (g)	Length (mm)	Width (mm)	Height (mm)
6A U1	32	35.5	30	22.8
6A U2	12.8	21.4	21.4	21
6A U4	60.2	42	39.1	25
6A U5	15.3	24.7	21.5	19.3
6A U6	50.3	35.7	32.4	29.6
6A U7	22.1	31.4	23.5	20
6B U1	54.3	32	42.3	29.5
6B U2	16.1	23.5	23.6	22.3
6B U3	30.8	30.3	33.8	25.9
6B U4	30.5	30.7	39.6	22.2
6B U5	59.7	34.2	43.9	31.1
6B U6	24.4	26.4	33.8	21.2
Z1 U1	49.7	30.8	31.9	25.7
Z1 U2	32.1	27.6	28.5	20.8
Z1 U3	30.2	28	29.6	26.9
Z1 U4	27.2	25	28.2	19.1
Z1 U5	41.1	30.3	30.4	23.7
Z1 U6	15.4	19.8	30.2	18.9
Z1 U7	21.6	26.6	26.4	21.5

Considering that the dimensions of mortar specimens considerably vary from standardised dimensions the measured compressive strengths have to be converted to the standardised compressive strengths. For lime mortars Drdácý [4] proposed the following expression:

$$f_{m,i} = f_{e,i} / (h/a)^{-1,9114} \quad (1)$$

where $f_{m,i}$ denotes the computed standard compressive strength of each specimen, $f_{e,i}$ is the experimentally measured compressive strength, h denotes the height and a the length of the tested specimen. Table 2 summarises experimentally measured and corresponding computed standard strengths according to expression (1).

Table 2: Experimentally measured and standard compressive strengths of mortar specimens

Specimen	Area (mm ²)	Load (kN)	Experimentally measured compressive strength $f_{e,i}$ (MPa)	Standard compressive strength $f_{m,i}$ (MPa)	Mean standard compressive strength (MPa)
6A U1	1065	2.69	2.52	1.08	1.21
6A U2	458	0.59	1.28	1.48	
6A U4	1642.2	6.81	4.15	1.49	
6A U5	531	1.26	2.38	1.47	
6A U6	1156.7	1.44	1.25	0.77	
6A U7	738	1.71	2.32	0.99	
6B U1	1354	1.19	0.88	0.45	0.49
6B U2	554.6	0.56	1.02	0.83	
6B U3	1024	0.49	0.48	0.30	
6B U4	1215	1.71	1.41	0.23	
6B U5	1501.4	1.36	0.91	0.47	
6B U6	892	1.39	1.56	0.63	
Z1 U1	982.52	13.26	13.49	9.04	3.90
Z1 U2	786.6	5.41	6.88	3.78	
Z1 U3	828.8	0.89	1.07	0.90	
Z1 U4	705	13.05	18.51	8.88	
Z1 U5	921.12	12.49	13.56	8.41	
Z1 U6	597.96	6.23	10.42	4.27	
Z1 U7	702.24	1.03	1.46	0.98	

It may be noticed that specimens Z1 U1, Z1 U2, Z1 U4, Z1 U5 and Z1 U6 taken from building 1 indicate relatively high compressive strength and high toughness for a lime mortar. This mortar was light brown and had larger grains of black aggregate of eruptive origin. Binder (lime) content in the observed specimens was high and we assume that the original binder has hydraulic properties due to usage of local limestone with additions of clay or marl in lime production. Other samples taken from the same masonry wall (specimens Z1 U3 and Z1 U7), which were of poor quality, had a lighter colour, a less filled structure and significantly lower strengths. It is possible that this is the same mortar but with degraded properties due to atmospheric actions. The mean compressive strength of mortar from building 1 is due to heterogeneous properties determined as arithmetic mean of mean values of aforementioned two types of mortar ($f_m = 3.90$ MPa).

3.2 Compressive strength of brick units

Compressive strength of clay brick units was determined on a total of 19 specimens according to HRN EN 772-1 [5]. Prior to testing the surface of specimens was treated by

grinding in order to satisfy the planeness and parallelism requirements and the specimens have been dried according to [5]. In figure 4 a specimen is shown before and after testing.



Figure 4: Clay brick specimen before (left) and after testing (right)

Normalised compressive strengths have been determined using expression [5]:

$$f_{b,i} = d \cdot f_i \quad (2)$$

where d denotes the shape factor while f_i is the compressive strength of the unit.

Dimensions of the clay brick units before treatment were approximately 300×150×75 mm, except for some specimens taken from newer parts of worker's houses (built around 1910) whose approximate dimensions were 250×120×65 mm. Shape factors have been determined for the measured dimensions after the surface treatment by grinding. Normalised mean compressive strengths f_b of clay units are given in table 3.

Samples from building 1 have not been taken to avoid unnecessary wall damage since the building is still in use. By visual inspection it has been noticed that all clay units of old format (300×150×75 mm) have the same marking and that were produced at the same time in the same brickyard. It is estimated that the normalised compressive strength of building 1 is approximately equal to the mean value of normalised compressive strengths of buildings 6a and 7 and equals to 21.33 MPa.

Table 3: Normalised mean compressive strength of clay brick units

Building	Normalised mean compressive strength f_b (MPa)
6a	23.13
6b	17.86
6c	7.15
7	19.52

3.3 Compressive strength of masonry

Characteristic compressive strength of the clay brick masonry f_k given in table 4 have been determined using normalised mean compressive strength of the clay units f_b and compressive strength of the mortar f_m according to the expression given in EN 1996-1-1 [7]:

$$f_k = K \cdot f_b^{0.7} \cdot f_m^{0.3} \text{ (MPa)} \quad (3)$$

where K denotes a coefficient depending on type of the masonry unit.

For clay brick masonry where there is a mortar joint parallel to the face of the wall coefficient K equals to $K = 0.55 \cdot 0.8 = 0.44$. Expression (3) was derived from the general formulation of the relation between the characteristic compressive strength of masonry and strength of its components (i.e. clay units and mortar):

$$f_k = K \cdot f_b^\alpha \cdot f_m^\beta \text{ (MPa)} \quad (4)$$

Coefficient K and exponents α and β are calibrated based on the test results. In [8] it was shown that by applying the values proposed in EN 1996-1-1 [7] the calculated results are quite close to experimentally obtained values.

Table 4: Characteristic compressive strength of clay masonry

Building	Characteristic compressive strength of masonry f_k (MPa)
1	5.64
6a	4.20
6b	2.67
6c	1.85
7	3.72

3.4 Shear and tensile masonry strength

Shear masonry strength has been carried out according to the recommendations given in TC 127-MS [9]: „MS-D6 – In situ measurement of masonry bed joint shear strength, method B“. The following equipment has been used: digital indicator with a resolution of 0.01 mm, digital pressure gauge and a hydraulic jack (figure 5). Shear test was performed by applying a horizontal force on a masonry unit using a hydraulic jack and recording the applied force and horizontal displacement of the masonry unit (previously a masonry unit was removed from opposite sides of the test masonry unit). Shear strength is then determined [9] using the force for which in the load-displacement curve there is a significant change in the slope (force of 14.5 kN on figure 6).

Shear masonry strength f_v may be determined using expression:

$$f_v = H / (A_u + A_o) \quad (5)$$

where H denotes the horizontal force at the point of change of slope of the load-displacement curve, while A_u and A_o are the lower and upper masonry unit areas, respectively.

Initial shear masonry strength f_{v0} is determined using expression [7]:

$$f_{v0} = f_v - 0.4 \cdot \sigma_d \quad (6)$$

where σ_d denotes the estimated vertical compressive stress in the test masonry unit. In table 5 determined initial shear strength f_{v0} are given together with characteristic tensile strength of masonry subjected to in plane loading obtained from the test results of both masonry units and mortar and literature [10, 11]. Obtained values for initial shear strength f_{v0} given in table 5 are in the range of expected values for lime mortar clay brick masonry [2, 7].



Figure 5: Shear test, building 7 – outside wall

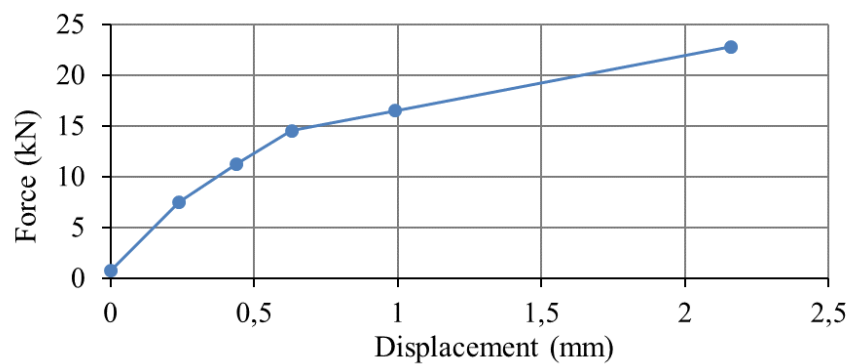


Figure 6: Horizontal load-displacement diagram (building 7 – outside wall)

Table 5: Shear strength of masonry

Building	Initial shear strength determined by testing f_{v0} (MPa)	Estimated characteristic tensile strength of masonry f_{tk} (MPa)
1	0.113	0.180
6a	0.133	0.090
6b (1843)	0.153	0.090
6b (1913)	0.096	0.040
6c	0.153	0.090
7	0.119*	0.090

*...mean shear strength determined on the basis of test results on an outside and an inner wall

4. CONCLUSIONS

Rational decisions for strengthening and restoration of heritage masonry structures may be made only based on known material parameters of masonry. Therefore it is necessary to carry out laboratory and in situ tests of masonry elements, mortar and masonry. Test results may not always correspond to expected values with regard to the age and appearance of the masonry. To be specific, quality of the presented masonry from the Stud Farm Lipik considering their age and exposure to degradation processes is very good. Despite being a

historical structure the measured masonry unit strengths were very high: normalised mean compressive strength were in range from 7.15 to 23.13 MPa. Mean standard compressive strengths of mortar are in accordance with the expected values for lime mortars for the period of construction (0.49 – 1.21 MPa); however the mortar compressive strength for the building 1 is considerably higher and equals to 3.9 MPa.

Reliability assessment of masonry properties may be increased based on the analysis of relations between masonry strength and strength of both masonry units and mortar, shear and tensile masonry strength considering also expected values from literature. A large number of in situ test results is often very difficult or impractical to conduct. Hence, expressions to predict masonry shear and tensile strength in relation to other masonry properties have to be established, and therefore a representative database is needed. Test results presented in this work may be very valuable for complementing the existing database of historic lime mortar masonry buildings.

ACKNOWLEDGEMENTS

This work has been supported in part by Ministry of Science, Education and Sports of the Republic of Croatia under the project Research Infrastructure for Campus-based Laboratories at the University of Rijeka, number RC.2.2.06-0001. Project has been co-funded from the European Fund for Regional Development (ERDF). The authors thank the University of Rijeka for supporting this paper through grant No. 13.05.1.1.01. and No. uniri-tehnic-18-127.

REFERENCES

- [1] Costigan A., Pavía S., 'Influence of the mechanical properties of lime mortar on the strength of brick masonry', in: Válek J., Hughes J., Groot C. (eds) 'Historic Mortars', RILEM Bookseries, vol 7. (Springer, Dordrecht, 2012) 359-372.
- [2] Biggs, D. and Ingham, J., 'Compressive, flexural bond, and shear strengths of in situ New Zealand unreinforced clay brick masonry constructed using lime mortar between the 1880s and 1940s', *Journal of Materials in Civil Engineering*, **26** (4) (2014) 559-566.
- [3] EN 1015-11:1999, 'Methods of test for masonry - Part 11: Determination of flexural and compressive strength of hardened mortar' (CEN, Brussels, 1999).
- [4] Drdácý, M., 'Non-standard testing of mechanical characteristics of historic mortars', *International Journal of Architectural Heritage*, **5** (4-5) (2011) 383-394.
- [5] EN 772-1:2015+A1, 'Methods of test for masonry units - Part 1: Determination of compressive strength' (CEN, Brussels, 2015).
- [6] ASTM D5731 - 95: 'Standard Test Method for Determination of the Point Load Strength Index of Rock' (American Society for Testing and Materials, 1995).
- [7] EN 1996-1-1:2005, 'Eurocode 6 - Design of masonry structures - Part 1-1: General rules for reinforced and unreinforced masonry structures' (CEN, Brussels, 2005).
- [8] Liberatore, D., Marotta, A. and Sorrentino, L., 'Estimation of clay-brick unreinforced masonry compressive strength based on mortar and unit mechanical parameters', in '9th International Masonry Conference', Proceedings of an International Conference, Guimarães, July, 2014 (International Masonry Society, 2014) 1-12.
- [9] Rilem TC 127-MS, 'Tests for masonry materials and structures', *Materials and Structures*, **29** (1996) 459-475.
- [10] Tomažević, M., 'Earthquake-resistant design of masonry buildings', (Imperial College Press, London, 2009).
- [11] Sorić, Z., 'Zidane konstrukcije', (Zagreb, Croatia, 2016).

STRUCTURAL AND MATERIAL DIAGNOSTICS OF HISTORIC INDUSTRIAL BUILDINGS

P. Berkowski (1), G. Dmochowski (1)

(1) Faculty of Civil Engineering, Wrocław University of Science and Technology, Poland

Abstract

Many old industrial buildings that come from the turn of the 19th and 20th centuries still exist in the city of Wrocław, as well as in the Lower Silesia region (Poland). Some of them have been used in recent years, but due to deterioration caused by the flow of time have become ruins, causing them to be closed because of not meeting structural and technological requirements. The lucky ones, which are recognized as industrial monuments, are currently undergoing the process of refurbishment in order to adapt them to new utility functions or to keep them functioning in an industrial manner with new types of production. Issues related to the processes of ensuring the continuous serviceability of such heritage buildings are closely linked with the processes of their technical state assessment, repair and strengthening procedures. Architectural and structural historic surveys, which are extremely important elements for a proper diagnosis of the technical condition of such buildings, are related to the following aspects of a structure's history: structural modelling, methods of structural analysis and dimensioning of structural components, properties of building materials, technologies of their production, and also the technology of construction. These studies, supported by the use of modern material examination techniques and computational simulations, allow for a more complete understanding of analysed historic structures, which in turn supports their proper refurbishment. Based on several existing historic industrial buildings, the process of the evaluation of their technical state is presented in this paper.

Keywords: historic industrial buildings, structural and material diagnostics, construction history, revitalization

1. INTRODUCTION

As a result of the urban development of cities, areas with different types of industrial plants, which during construction (mainly at the turn of the 19th and 20th century) and subsequent exploitation were located on the outskirts of these cities, were suddenly found to be situated in city centre areas and began to be, for many years, disruptive to the surrounding environment [1, 2]. Deindustrialization and the industrial overhaul in Poland in the post-1990

period, natural structural and technological degradation of old industrial facilities, as well as the need to move factories and plants to the outskirts of agglomerations resulted in the appearance of large, degraded post-industrial areas in city centres. Some of these industrial facilities, due to their undeniable architectural and constructional qualities that testify the engineering skills of their builders, have been included as post-industrial monuments. Their renewal (revitalization) has thus become one of the basic conditions for sustainable urban development. This revitalization of post-industrial sites covers two basic issues:

- demolition of parts of buildings not suitable for reconstruction and adaptation to new purposes due to structural or production problems harmful to the environment;
- structural and functional reconstruction of buildings recognized as historic ones with adaptation to new utility functions.

In the article, using the example of four bakery and brewery plant objects that are recognized as post-industrial monuments, selected elements of the assessment of their technical condition are shown. This technical condition significantly affects the process of their revitalization.

2. PROCEDURE OF THE TECHNICAL STATE ASSESSMENT OF HISTORIC BUILDINGS

The execution of architectural and structural historic analysis of such objects can be seen as an extremely important element when conducting a proper diagnosis of the technical condition of historic buildings. It is also crucial for the adequate design of their refurbishment, which aims to prolong the time of their use, as well as the preparation of a process associated with their maintenance. This analysis must be related to the following aspects applied during the design and construction of these buildings: design solutions, calculation methods of structural analysis, methods of the dimensioning of structural components, properties of building materials and the technologies of their production, and also the technology of construction, including the quality of workmanship. There are recommendations, defined by ICOMOS [3], for the reconstruction process of monumental buildings of historic value that consist of a set of principles and guidelines and define the three main phases in the study of historic constructions. They are essential when defining the durability related maintenance plan for heritage structures [4]:

- diagnosis:
 - analysis of archival documentation,
 - an architectural and structural survey,
 - the opinion of a conservator,
 - a geotechnical study,
 - the examination of materials,
 - definition of the level of technical deterioration,
 - cause of damage;
- safety evaluation:
 - structural expertise (structural and strength calculations, etc.);
- design of structural and architectural intervention:
 - definition of repair technologies,
 - definition of structural safety during repair,
 - monitoring of a structure during repair.

3. TECHNICAL STATE ASSESSMENT OF THE SELECTED HISTORIC INDUSTRIAL BUILDINGS – CASE STUDIES

Based on the procedures briefly described in the previous chapter, selected elements of the structural assessment of buildings that form an essential part of two post-industrial complexes form the beginning of the 20th century, situated in the central part of the city of Wroclaw (Poland), are presented: a bakery called “Mamut” and a brewery called “Piastowski”. In the case of both these historic industrial complexes, the design works being carried out (preceded by conservation studies and structural assessment) aim to revitalize both areas and re-integrate them into the urban fabric, while at the same time taking into account the principles of sustainable development.

3.1 General description of the bakery complex

The bakery complex was built in stages at the turn of the 19th and 20th centuries. In addition to being the largest bakery in the city, and even in Europe, the objects built in it were examples of modern architectural and structural solutions at that time. The bakery functioned until 2007, and in 2008 it was enlisted in the register of industrial heritage monuments. The two main buildings: the flour warehouse made of reinforced concrete with a brick façade (Figs. 1 & 2), and the main production building (bakery) made from a steel, skeletal structure (Figs. 5 & 6), are the most interesting from a structural engineering point of view [5].

3.1.1. The flour warehouse

The bearing structure of the flour warehouse (Fig. 1) is made of reinforced concrete, its load-bearing longitudinal walls are made of brick and it has two rows of reinforced concrete pillars that define a central communication passage (Fig. 2). The floors are massive, made of reinforced concrete, slab-ribbed, and based on the central pillars and external walls (Fig. 3). The structure of the two floors of the attic is also reinforced concrete, with an oblique frame determining the slanted roof in the form of a thin reinforced concrete slab. The floors are based on longitudinal beams and transverse frames, which transfer loads to the external walls and central pillars. All the load-bearing structural elements, due to the complex geotechnical conditions, are placed on wells.



Figure 1: Current view of the flour warehouse

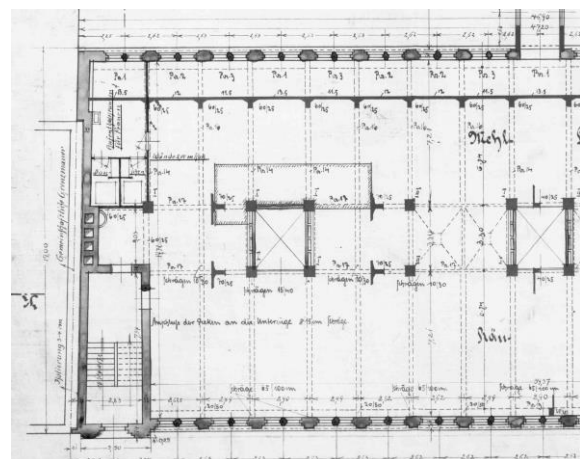


Figure 2: Archival structural plan



Figure 3: RC structure of the flour warehouse



Figure 4: Reinforcement identification

In the case of this object, due to its intended use for lofts and apartments, the main problem concerned the proper detection and assessment of steel rebars in the RC elements (Fig. 4).

3.1.2. The bakery building

The structure of the bakery building (Fig. 5) is of the hall type. It is mainly steel, made of beams and columns, with sectional floors on steel beams on the first three older floors. At the end of the 1920s, the building was reconstructed – two floors of the attic of the main building were pulled down and 5 new storeys were built (Fig. 6). The new storeys had a decreasing construction area with Ackerman floors based on steel beams. In addition, due to the significant increase of loads, all the foundations of the building were strengthened.



Figure 5: Current view of the bakery building

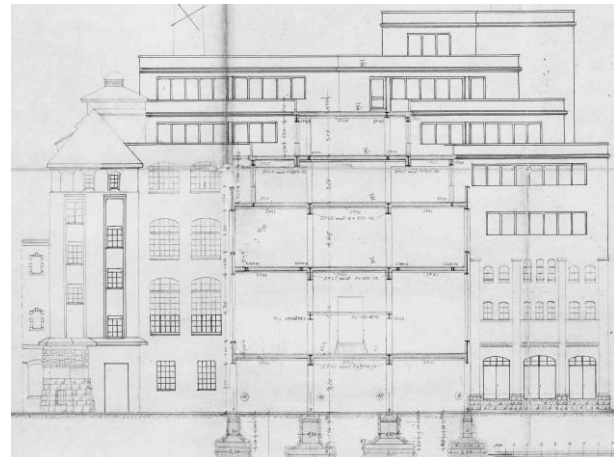


Figure 6: Archival section plan

In the case of this building - its degraded Ackerman (Fig. 7) and Klein floors were the main structural problem, the bad condition of which meant that they could not be used as bearing elements. Additionally, the vast majority of the steel beams of the floors over the ground on the 1st and 2nd levels showed deep corrosion. It was decided to replace them all with new RC floors. However, all floors with very decorative ceramic claddings on parts of the ceilings (as well as on walls) were preserved and restored (Fig. 8).



Figure 7: Destruction on Ackerman floors



Figure 8: Ceramic tiles in social rooms

3.2 General description of the brewery complex

The first brewery buildings were built in the early '90s of the 19th century and subsequent buildings were built until the end of the 1930s. The brewery produced beer until 2004. The current owner of the complex forecast the implementation of a comprehensive urban plan in the local area, including the construction of apartments, lofts, shops and offices. Some of the old buildings, such as the lagering cellar (Figs 9 & 10) and former stables (Figs 13 & 14), are among objects that would be reconstructed and adapted to new functions [6].

3.2.1. The lagering cellar

The structure of the building (Fig. 9) is very diverse, depending on the period of construction and technological purpose of its individual parts: from a typical brick masonry construction to skeletal cast iron and steel, as well as reinforced concrete elements. The most spectacular structure is the roof steel truss over one of the main production rooms, which has a span of about 24 m (Fig. 10). The majority of floors were made as arch brick masonry ones and based on steel beams. However, in one of the halls there was a slab carrying RC reservoir, based on cast iron columns, with a masonry floor over it (Fig. 11).



Figure 9: Lagering building current view

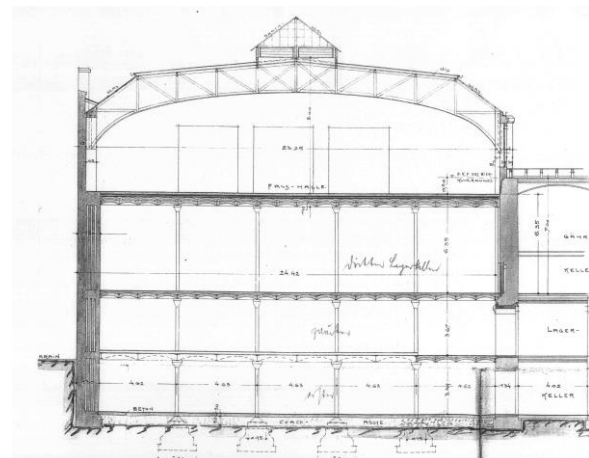


Figure 10: Archival section plan



Figure 11: RC reservoirs with cast iron columns



Figure 12: Destruction of brick masonry floors

Most of the masonry floor slabs were strongly damped and there was also locally strong corrosion degradation of steel beams, binders and columns (Fig. 12). Some of the floors are designed to be replaced with new, composite ones.

3.2.2. The stables building

The main bearing structure of the stables building (Fig. 13) constitutes a system of steel columns (part of them covered with concrete or brick and mortar), situated in two internal longitudinal axis, as well as on the bearing external and internal walls. Transversal steel binders are located on columns and longitudinal walls, while steel slab beams are arranged on both them and the external walls. The floors are brick masonry arch ones on steel beams over a cellar, and its Klein type floors are on steel beams over the remaining stories. The thickness of the floors is diverse - 30 cm, 40÷45 cm and 50 cm; full brick was used in the masonry arc slabs, and hollow bricks in the Klein ones. In the central part of the building there is an inclined ramp (Fig. 14) that was used for the transportation of horses to stables on the ground and 1st floors (Fig. 15). The building is designed to be an apartment house.



Figure 13: Stables building current view

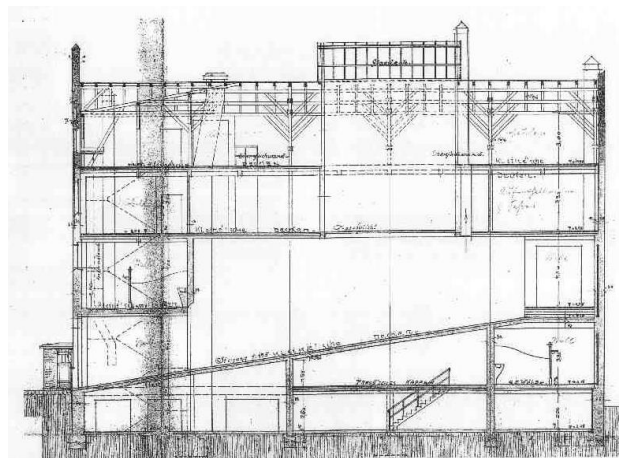


Figure 14: Archival section plan with ramp



Figure 15: View of stables room



Figure 16: Drilling core of stables floor

The main constructional problem to be solved involved the object's very thick slabs – the bearing capacity of the slabs and steel beams was almost at the limit state. Moreover, the bricks and pavement layers were extremely chemically polluted (Fig. 16). There was a necessity to remove a 10 cm layer of concrete by milling or hand-made demolition, and also a need to construct new floor layers with acoustic insulation and to decontaminate all the floors.

4. CONCLUSIONS

Revitalization of old post-industrial areas, which are very often located in central parts of cities, and transforming and adapting them for new functional duties is an extremely demanding and responsible task. The guidelines resulting from the adopted visions of the urban transformation of cities, including the requirements of their sustainable development, as well as aspects of conservation, architectural and construction issues, must be taken into account.



Figure 17: View of the revitalized bakery building (courtesy of GRUPA 5 Architekci Ltd., Warsaw, Poland)



Figure 18: View of the revitalized lagering cellar building (courtesy of GRUPA 5 Architekci Ltd., Warsaw, Poland)

Therefore, it is necessary to create a combination of knowledge, new technologies and a wide cooperation of specialists from various fields related to the broadly understood process of designing revitalization processes.

This paper presents, based on examples of four objects belonging to two historic dilapidated industrial plants (a bakery and a brewery), selected elements of the assessment of their technical condition. The paper also presents the very different construction problems encountered, as well as ways to solve these problems in order to achieve the best design solutions (Fig 17 & 18).

ACKNOWLEDGEMENTS

The authors would like to thank GRUPA 5 Architekci Ltd., Warsaw, Poland for permission to include in the article their visualization of revitalization designs of the former bakery (Fig. 17) and former brewery area (Fig. 18). They would also like to thank ST Wrocław Sienkiewicza Ltd., Poland for permission to include revitalization designs of the former bakery (Fig. 17).

REFERENCES

- [1] Loures, L., 'Industrial Heritage: the past in the future of the city', WSEAS Transactions on Environment and Development, 2008, **4(9)** 784-793.
- [2] Loures, L., 'Post-industrial landscapes as drivers for urban redevelopment: public versus expert perspectives towards the benefits and barriers of the reuse of post-industrial sites in urban areas', *Habitat Int.*, **45** (Part 2) (2015), 72-81.
- [3] ICOMOS International Council on Monuments and Sites. 2003. ISCARSAH – Recommendations for the analysis, conservation and structural restoration of architectural heritage.
- [4] Berkowski, P., Kosior-Kazberuk, M., 'Historical and structural aspects of the durability and maintenance of a reinforced concrete market hall building from the early 20th century', in 'Concrete Solutions', Proceedings of the 6th International Conference on Concrete Repair, Thessaloniki, Greece, June, 2016 (CRC Press/Balkema, Leiden, 2016) 335-343.
- [5] Berkowski, P., Dmochowski, G., Barański, J., Szołomicki, J., 'The construction history and assessment of two heritage industrial buildings in Wrocław', in 'ECCE 2018', Proceedings of the 3rd Scientific Conference Environmental Challenges in Civil Engineering, Opole, Poland, April 2018 (EDP Sciences, Les Ulis, 2018) 1-10, <https://doi.org/10.1051/mateconf/201817403008>.
- [6] Berkowski, P., Dmochowski, G., Minch, M., Szołomicki, J., 'Selected constructional problems related to renovation of historic industrial buildings from 19th century in Lower Silesia (Poland)', in 'SAHC 2014', Proceedings of the 9th International Conference on Structural Analysis of Historical Constructions, Mexico City, Mexico, October, 2014 1-11.

OPTIMISING IN-SITU TESTING FOR HISTORIC MASONRY STRUCTURES: A CASE STUDY

Miroslav Sýkora (1), Dimitris Diamantidis (2), Jana Markova (1), Maria G. Masciotta (3)

(1) Klokner Institute, Czech Technical University in Prague, Czech Republic

(2) Faculty of Civil Engineering, Ostbayerische Technische Hochschule, Germany

(3) Institute for Sustainability and Innovation in Structural Engineering, University of Minho, Portugal

Abstract

Masonry structures were built by means of various techniques, using materials whose properties exhibit a considerable scatter depending on the period of construction, region-specific soil resources and manufacturing procedures. Significant spatial variability within the structural system is often observed due to diverse deterioration mechanisms. Therefore, it is important to obtain case-specific information on the mechanical properties of existing masonry structures.

The case study of a historic building illustrates how the number of destructive tests (DTs) used to calibrate non-destructive tests (NDTs) can be optimised for the reliability assessment. Calibrated NDTs are used to establish the probabilistic model for compressive masonry strength. The specific focus is on compressive strength of masonry units; tests of mortar strength are only briefly discussed.

The preliminary assessment is based on non-calibrated NDTs. The number of DTs for calibration is then optimised by means of probabilistic cost optimisation, considering also possible subsequent actions – ‘do nothing’ or ‘strengthen the structure’. It appears that the estimates of masonry unit strength based on NDTs are associated with large dispersion and may be significantly biased. Consequently, it is often beneficial to conduct at least one DT. A practical tool is provided to determine optimum number of DTs for different outcomes of a NDT survey and different failure consequences.

Keywords: compressive strength, destructive test, historic masonry, masonry unit characterization, non-destructive test

1. INTRODUCTION

Due to the diversity and complexity of the masonry material, historic masonry structures inherently feature a high degree of uncertainty, especially in what concerns their mechanical behaviour. The removal of these uncertainties plays a crucial role for improving the estimates of masonry unit strength and accurately assessing the structural reliability. However, when dealing with heritage assets, the range of applicable techniques for the system characterization is rather limited, given the need to respect the heritage value of the construction [1] and be as less invasive as possible. For this reason, non-destructive tests (NDTs) are typically carried out, whereas the application of destructive tests (DTs) is minimized. As NDTs are subject to uncertainties – according to ISO 13822:2010 for assessment of existing structures, DTs may be necessary to calibrate NDTs. Indeed, this is the common practice in reliability verifications.

While calibrating NDTs by DTs allows reducing uncertainty and improving reliability estimates, i.e. reliability index β , the invasiveness of destructive testing can be in conflict with heritage preservation principles. Therefore, it is fundamental to optimize the number of DTs to support reliability verifications of built cultural heritage and minimize test intrusiveness.

The principal aim of this study is to illustrate how to consistently make use of all the information available considering uncertainties related to tests and rank preferences amongst different actions. The challenges for further investigations are outlined. This contribution is an outcome of the international cooperation that has been initiated with COST Action TU1402 focused on quantifying the value of structural health monitoring; cost-tu1402.eu.

2. DATABASE OF NDT AND DT RESULTS

The study encompasses a database of 15 historic masonry constructions built in the Czech Republic between 17th-20th centuries [2]. In each building, two types of NDTs – rebound hammer and modified drill – were performed for estimating the strength of masonry units and the results were verified through DTs. In this contribution, only the results from the rebound hammer are analysed for the sake of brevity. Detailed information on the type of testing procedures, number of measurements, tested materials and use of the investigated buildings are provided in [2]. Figure 1 illustrates the variation of the ratio between DT and NDT masonry unit strengths, $f_{b,DT}/f_{b,NDT}$, with $f_{b,DT}$. Based on the evidence of the information collected in the database, it is inferred that NDTs tend to overestimate the masonry strength in 78% of the cases. Structure-specific NDT re-calibration seems to be imperative considering the previous studies indicating that a universal law between compressive strengths based on NDTs and DTs hardly exists – see ISO 18265:2013 for metallic materials, [3] for concrete, and [4] for historic masonry.

As information regarding the material properties of historic masonry is always scarce and degradation effects cannot be assessed without measurements, NDTs are considered the *sine qua non* of reliability assessment. Thus, their results are used here as given information for preliminary reliability assessment and optimisation of the number of subsequent DTs, n_{DT} .

3. RELIABILITY ANALYSIS

It is assumed that the assessment of the heritage masonry structure under investigation aims to satisfy the reliability condition based on the partial factor method. The example of a historic masonry wall illustrates the principles of decision making.

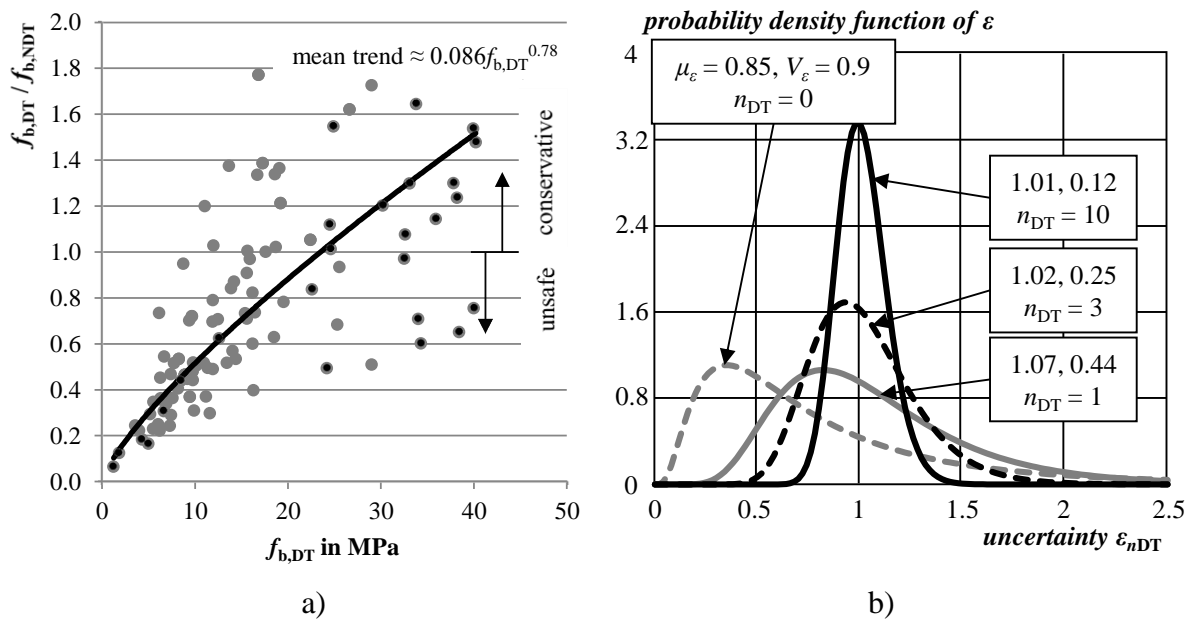


Figure 1: a) Variation of measurement uncertainty $f_{b,DT} / f_{b,NDT}$ with $f_{b,DT}$ (grey dots – clay bricks; black dots – stones); b) Probability density function of uncertainty ε_{nDT}

Table 1: Models of basic variables

Basic variable	Dist.	Mean	CoV	Note
Coefficient K for determination of compressive strength of masonry	LN	$1.2K_{nom}$	0.3	Sykora et al. [6], CoV accounts for higher variability for historic masonry compared to modern structures. Includes resistance model uncertainty. $K_{nom} = 0.44$ according to CSN 73 0038 :2014 – the Czech standard for assessment of existing structures including heritage structures.
Standardised strength of masonry units assessed from tests, f_b	det.	~ 12.5 MPa	-	The mean value obtained from NDTs calibrated by DTs. True value, $f_{b,true}$, assumed to be 12.5 MPa – representative value for historic bricks [2].
Uncertainty in f_b for NDTs calibrated by DTs, ε_{nDT}	LN	~ 1	Dependent on n_{DT} .	Uncertainty related to the estimate of $f_{b,true}$. Based on the analysis of a large database of NDT/ DT results. See the following text.
Strength of mortar, f_m	LN	1 MPa	0.1	Needs to be estimated on the basis of NDTs. CoV expresses the uncertainty in mean mortar strength on the basis of a large number NDTs. Representative model selected on the basis of the authors' experience with surveys of historic masonry structures.
Standardised axial stress due to permanent action, G	N	1 MPa	0.15 MPa	CoV accounts for load effect model uncertainty and implicitly also for a small contribution of a variable load with a larger CoV.

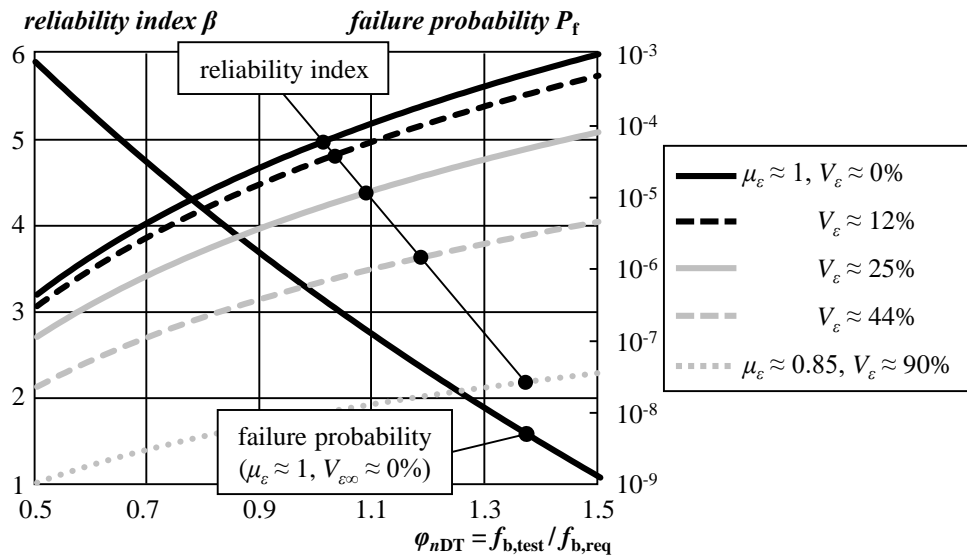


Figure 2: Reliability index β and failure probability P_f as a function of φ_{nDT}

While numerous simplifying assumptions are adopted in the probabilistic reliability analysis and optimisation, the attempt is made to capture all the key steps that need to be undertaken in practice. Reliability analysis is based on the following assumptions and steps:

1. The failure mode is compression with a small eccentricity of the acting axial force.
2. The limit state function is given as:

$$Z(\mathbf{X}) = K (\varepsilon_{nDT} f_{b,test})^{0.73} f_m^{0.16} - G \quad (1)$$

and failure probability is $P_f = Z(\mathbf{X}) < 0$. The wall is predominantly exposed to permanent actions (seismic situations are beyond the scope of this study). The probabilistic models of the basic variables are given in Table 1. The exponents in Eq. (1) are taken from the JCSS PMC [5] for full clay bricks and a general purpose mortar. The probabilistic model of uncertainty ε_{nDT} is based on a previous study [2] and the additional numerical analyses of the NDT/ DT database – Figure 1b) shows the probability density function of ε_{nDT} :

$$f_{b,true} \approx \varepsilon_{nDT} f_{b,test} \quad (2)$$

3. The strength of masonry units required by the partial factor method is obtained by:

$$K_{nom} f_{b,req}^{0.73} f_m^{0.16} / \gamma_M - \gamma_G G = 0 \quad (3)$$

$$f_{b,req} = [\gamma_M \gamma_G G / (K_{nom} f_m^{0.16})]^{1/0.73} = 20.0 \text{ MPa}$$

where $\gamma_M = 2.9$ and $\gamma_G = 1.35$ according to CSN 73 0038. When $f_{b,test} < f_{b,req}$ the wall is upgraded.

Figure 2 displays reliability index β and failure probability P_f as a function of the ratio $\varphi_{nDT} = f_{b,test}(nDT) / f_{b,req}$, taking into account the uncertainty ε_{nDT} . n_{DT} is a study parameter varied in the range of practical relevance – from 0 to 10. The low reliability indices for $n_{DT} = 0$ are attributable not only to a large CoV, but also to a negative bias – NDTs tend to overestimate f_b by about 15% in the case of no calibration. It is interesting to note that for a perfect survey, $n_{DT} \rightarrow \infty$, reliability index is $\beta(\varphi_{nDT} = 1) = 4.9$ for the case when the reliability condition based

on the partial factor method is exactly satisfied. Reliability index approaches 3.8 for $\varphi_{nDT} = 0.625$, revealing an extra-capacity of around 40%.

4. OPTIMISATION OF NUMBER OF DESTRUCTIVE TESTS

The optimal decision should be identified as the decision that minimizes the expected costs, which is then equivalent to maximizing the expected utility. It is assumed that the estimate of masonry unit strength based on a sufficient amount of NDTs ($n_{NDT} \geq 25$) is always available and $\varphi_0 = f_{b,test}(0) / f_{b,req}$ is known. The only decision to be made and optimised is the number of DTs to carry out to calibrate NDTs. The decision tree is shown in Figure 3. Initially, $f_{b,true}$ is assumed as known. $n_{opt}|f_{b,true}$ is then optimised as follows:

1. For φ_0 resulting from a NDT survey, the total cost $C_{tot}(n_{DT}|\varphi_0, f_{b,true})$ is evaluated for all n_{DT} -values under consideration and n_{opt} is selected on the basis of cost minimisation.
2. In accordance with current engineering practice, it is assumed that the wall is always upgraded when $f_{b,test} < f_{b,req}$ (and thus $\varphi_{nDT} < 1$). In the absence of DTs, $n_{DT} = 0$, the wall is upgraded when $\varphi_0 < 1$ while no intervention takes place otherwise. Note that the decision to upgrade only on the basis of NDTs is unrealistic. In principle, a second decision could be made (upgrade/ maintain) – the effect of this decision will be investigated in a future study. When several DTs are conducted, the distribution of $f_{b,test}|f_{b,true}$ is approximated as $f_{b,true} / \varepsilon_{nDT}$ according to Eq. (2) using a *preposterior analysis* [7, 8]. Probability of two complementary random events (no decision here) – upgrade Up and no upgrade NUp – is then obtained as follows:

$$n_{DT} \geq 1: P(Up) = P[f_{b,true} / \varepsilon_{nDT} < f_{b,req}] \quad (4)$$

$$P(NUp) = 1 - P(Up)$$

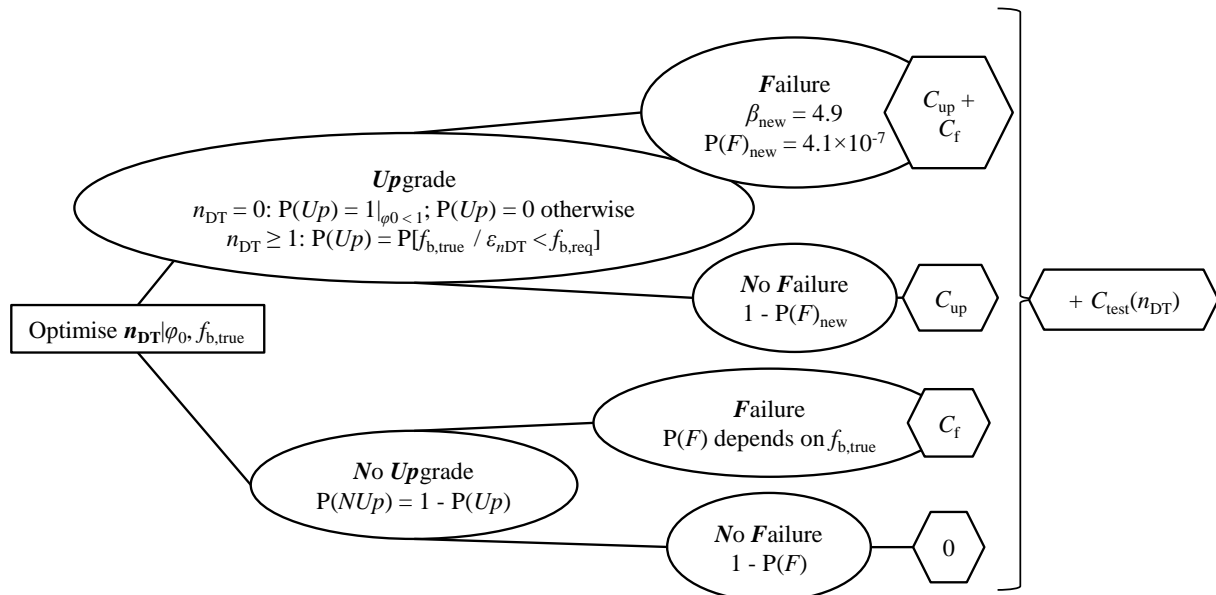


Figure 3: Decision tree for a given $f_{b,true}$

3. The wall is assumed to be upgraded to reach $\beta(f_{b,req}) = 4.9$. In the case of no upgrade, the estimate of real failure probability is obtained from the limit state function (1) by replacing $\varepsilon_{nDT} f_{b,test}$ by $f_{b,true}$; the latter is associated with no variability (keeping in mind that f_b – characteristic of the existing wall – is a mean value that can be exactly estimated on the basis of a large number of DTs (Figure 2).
4. Each scenario is associated with costs, the estimates of which are provided in Table 2.
5. For any $n_{DT} = 0, 1, \dots, 10$, total cost $C_{tot}(n_{DT}|\varphi_0, f_{b,true})$ are determined.

The decision on n_{DT} needs to be made on the basis of φ_0 only – $f_{b,true}$ is unknown. Considering Eqs. (2) and (3) and Figure 1b), a *prior* distribution of the latter can be estimated as $f_{b,true}(\varphi_0) \approx \varepsilon_0 f_{b,test} = \varepsilon_0 \varphi_0 f_{b,req}$ where only ε_0 is a random variable.

Table 2: Costs – illustrative examples (25 NDTs, area of the wall – 100 m²)

Type of cost	Estimate	Explanation
Cost of upgrade (C_{up})	150 € per m ²	Based on experience and on the study [9]. Includes costs of scaffolding, injections and other simple strengthening, treatment of mortar joints, colouring, planning (consulting) costs. Strengthening by reinforcement, ties etc. not covered.
Cost of testing (C_{test})	40 € per one location for NDT	Based on experience. Hardness tests of masonry unit and mortar. Includes repair of surface after tests. Dependent on accessibility of the location. To be increased for surfaces with heritage value.
	160 € per one DT	Masonry units only, similar costs for bricks and stones. Includes repair after tests. To be increased for surfaces with heritage value [10].
	200 € + 25% of test cost	Analysis of results and report.
Cost of failure (C_f)	C_f / C_{up} as a study parameter.	Failure cost should cover all expected economic, societal and environmental consequences (ISO 2394 and [11]) as well as the damage to the cultural heritage value [10].

For any n_{DT} , the total cost $C_{tot}(n_{DT}|\varphi_0)$ is obtained from $C_{tot}(n_{DT}|\varphi_0, f_{b,true})$ by integrating over $f_{b,true}(\varphi_0)$ (Figure 4a for *low failure cost* $C_f / C_{up} = 10$). No DTs seem to be needed when a positive result is obtained from a NDT survey ($\varphi_0 \geq 1$) while the optimum number of DTs is $n_{opt} = 1$ for a negative result $\varphi_0 = 0.5$ that would lead to upgrade.

This result is confirmed by Figure 4b) displaying n_{opt} as a function of φ_0 and C_f / C_{up} . As a first approximation, it can be considered that:

- No DTs are needed for $\varphi_0 < 0.2$
- Otherwise:
 - For low relative failure consequences: $n_{opt} = 1$ for $\varphi_0 < 1$ and $n_{opt} = 0$ for $\varphi_0 \geq 1$
 - For medium consequences: $n_{opt} = 1$ for $\varphi_0 < 2$ and $n_{opt} = 0$ for larger φ_0
 - For high consequences: $n_{opt} = 1$ for $\varphi_0 < 2.5$ and $n_{opt} = 2$ for larger φ_0

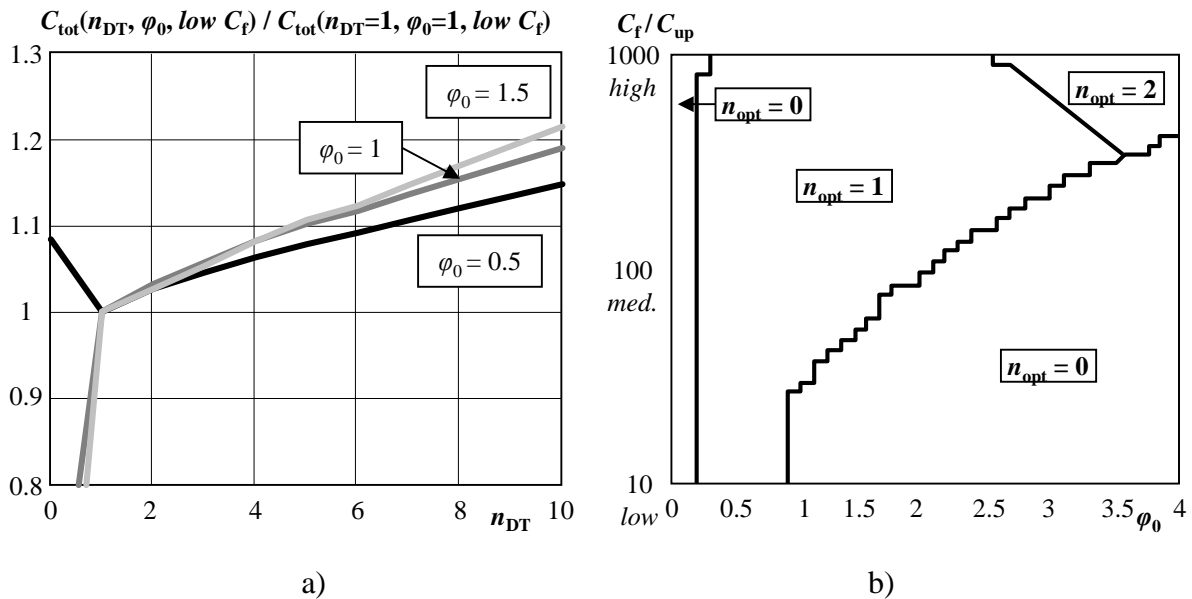


Figure 4: a) Variation of total cost with n_{DT} for $\varphi_0 = 0.5, 1$ and 1.5 , and low failure cost, relative to $C_{tot}(n_{DT} = 1; \varphi_0 = 1; \text{low failure cost})$; b) n_{opt} versus φ_0 for C_f / C_{up}

5. CONCLUDING REMARKS

- The estimates of masonry unit strength based on hardness tests (NDTs) are associated with large dispersion and may be significantly biased. Therefore, it is often beneficial to conduct at least one destructive test (DT). Figure 4b) can be used to estimate an optimum number of DTs given the outcome of a NDT survey and specified failure consequences.
- The recommendations provided here for optimum survey strategy assume that the requirements based on the partial factor method are strictly followed. These recommendations might be updated when target levels for masonry structures are revised considering realistic estimates of failure consequence and large uncertainties associated with resistance of historic masonry structures and applied resistance models.

ACKNOWLEDGEMENTS

This work was supported by the Ministry of Culture of the Czech Republic under Grant DG16P02M050 “Optimisation of Observations and Assessment of Heritage Structures”.

REFERENCES

- [1] Masciotta, M., Ramos, L.F. and Lourenço, P.B., 'The importance of structural monitoring as a diagnosis and control tool in the restoration process of heritage structures: A case study in Portugal', *J Cult Herit* **27** (Supplement C) (2017) 36-47.
- [2] Sykora, M., Diamantidis, D., Holicky, M., Markova, J. and Rozsas, A., 'Assessment of Compressive Strength of Historic Masonry Using Non-Destructive and Destructive Techniques (under review)', *Constr.Build.Mater.* (2018)
- [3] Breyse, D., 'Nondestructive evaluation of concrete strength: An historical review and a new perspective by combining NDT methods', *Constr.Build.Mater.* **33** (-) (2012) 139-163.

- [4] Sykora, M., Holicky, M., Markova, J. and Diamantidis, D., '*Assessment of Compressive Strength of Historic Masonry Using In-Situ Measurements*', in Proc. 15th International Probabilistic Workshop, Dresden, 27-29 September 2017 (TUDpress, Dresden, 2017) 161-172.
- [5] JCSS, 'JCSS Probabilistic Model Code (periodically updated, online publication)', (Joint Committee on Structural Safety, 2018).
- [6] Sykora, M., Cejka, T., Holicky, M. and Witzany, J., '*Probabilistic Model for Compressive Strength of Historic Masonry*', in Proc. ESREL 2013, Amsterdam, 29 September – 2 October 2013 (CRC Press/Balkema, Leiden, 2013) 2645-2652.
- [7] Bismut, E., Schneider, R., Sousa, H. and Straub, D., Framework and Categorization for Value of Information Analysis (fact sheet of COST TU1402 WG3, cost-tu1402.eu), pp. 8, 2018.
- [8] Diamantidis, D. and Sykora, M., 'Optimizing monitoring – implementation of draft guideline and case study of roof exposed to snow loads (accepted for publication)', in Proc. 40th IABSE Symp. Nantes, 19-21 September 2018 2018) 8.
- [9] Dan, M.B., Penelis, G. and Bourlotos, G., 'Retrofit of Stone Masonry Buildings in Greece. II. Determination of Costs', · *Bulletin of the Polytechnic Institute of Jassy, CONSTRUCTIONS. ARCHITECTURE Section LIX* (3) (2013) 193-209.
- [10] Eberhardt, S. and Pospíšil, M., 'Assessing Cultural Monuments: Identifying and Evaluating Heritage Values of Masonry and Cast-Iron Structures (under review)', *Int. J. Archit. Herit.* (2018)
- [11] Diamantidis, D., Holicky, M. and Sykora, M., '*Target Reliability Levels Based on Societal, Economic and Environmental Consequences of Structural Failure*', in Proc. ICOSSAR 2017, Vienna, 6-10 August 2017 (TU-MV Media Verlag GmbH, Wien, 2017) 644-653.
- [12] Sykora, M., Holicky, M., Jung, K. and Diamantidis, D., 'Target Reliability for Existing Structures Considering Economic and Societal Aspects', *Struct Infrastruct E* **13** (1) (2016) 181-194.
- [13] Steenbergen, R.D.J.M., Sykora, M., Diamantidis, D., Holicky, M. and Vrouwenvelder, A.C.W.M., 'Economic and Human Safety Reliability levels for Existing Structures', *Struct Concrete* **16** (September 2015) (2015) 323-332.
- [14] Caspeele, R., Sykora, M., Allaix, D.L. and Steenbergen, R., 'The Design Value Method and Adjusted Partial Factor Approach for Existing Structures', *Struct.Eng.Int.* **23** (4) (2013) 386-393.

THERMAL BEHAVIOR OF RIGID AND FLEXIBLE COMPOSITE-TO-SUBSTRATE STRENGTHENING

Bogusław Zajac (1) and Arkadiusz Kwiecień (1)

(1) Faculty of Civil Engineering, Cracow University of Technology, Poland

Abstract

This paper presents influence of elevated temperatures as well as of a thermal stress factor and glass transition temperature of stiff and flexible adhesives on strain distribution of composite-to-substrate strengthening. Various substrates as concrete, brick and timber were also considered. Single lap shear test was taken for analysis with constant load of 5 kN. Specimens consisted of a composite CFRP laminate were bonded to concrete, brick and timber substrates using stiff epoxy Sikadur 30 and 330 (S30 and S330) and highly deformable polyurethane Sika®PS (PS) adhesives. They were tested under 4 levels of temperature: 20, 40, 60 and 80 Celsius degrees. Changes of strain distributions at the composite surface were measured by strain gauges and compared graphically, indicating changes in strain distribution behaviour under thermal influences and constant load. Obtained results are presented in relation to temperature changes, substrate changes and adhesive changes. Comparison of them indicates that flexible polyurethane adhesive works stable in elevated temperatures, stiff epoxy adhesives work unstable in elevated temperatures when their glass transition temperature is reached or exceed. These results help understand durability aspects of composite-to-substrate strengthening when it works under load in elevated temperatures.

Keywords: composites, durability, elevated temperatures, stiff and flexible adhesives

1. INTRODUCTION

Mechanical compatibility between various structural substrates (concrete, masonry or timber) and repair or strengthening materials is crucial issue in case of intervention techniques durability [1]. Thermal behaviour of adhesives used in structural strengthening is of great importance [2], because of different mechanical and thermal properties of materials joined together. Thermal movements of structural elements are observed in regions where they are exposed to seasonally variable temperatures. Their surface temperature can easily increase up to 70°C during sunny days and rapidly cool to 0°C at night. These changes generate significant bond stress when materials of different coefficients of thermal expansion (CTE) are joined together and significantly change adhesive mechanical properties of those with the

glass transition temperature T_g in the considered temperature range. Degradation of repair bonds by thermal influences is a complex problem of natural weathering (solar radiation, impact of oxygen, rain, hail, variable temperature etc.) of structural materials [3]. In composite-to-substrate strengthening mainly stiff epoxy (FRP, SRP) and mineral (FRCM, SRG, TRM) adhesives are used but also highly deformable adhesives are introduced, made of flexible polyurethanes (FRPU, SRPU) [1, 4]. Testing of composite-to-substrate strengthening should be carried out under constant load (as in real conditions), because most of epoxy adhesives heated above their T_g recover properties after cooling below the T_g , thus results obtained during tests in normal thermal condition [5], carried out on earlier thermally aged specimens (with temperature above T_g), do not differ so much from reference specimens tested up to damage in normal laboratory conditions. Significantly different results are obtained when highly elevated temperature (also above T_g) acts during a loading test [6, 7], due to loss of epoxy adhesive strength and consequent change in the stiff adhesive behaviour or even failure of specimens at lower loads. In this approach comparison between loaded specimens with various substrates working under 4 levels of temperature is presented.

2. INFLUENCE OF GLASS TRANSITION TEMPERATURE AND THERMAL STRESS FACTOR

Various epoxy resins lose their mechanical properties (start to be soft) in their glass transition temperature T_g (ranging between +40 and +80°C) and change their behavior in the bond when load is carried (e.g. S30 and S330). On the other hand, flexible polyurethane adhesives (e.g. PS) work in the stable plateau beyond their characteristic T_g (about -40°C) in the environmental temperature range (-25 to +70°C or even up to +100°C), therefore are more predictable and safe in practical applications when thermal loads are considered – Figure 1a.

Mechanical compatibility of joined materials from the thermal point of view is dependent on a thermal stress factor $E\alpha$ [MPa/°C], which characterize the increase of stress $\Delta\sigma$, generated by the considered material during thermal expansion, under temperature increase of $\Delta T = 1^\circ\text{C}$. The thermal stress factor is defined by Eq. (1), where α is the coefficient of thermal expansion (CTE) and the E is the Young's modulus. The calculated thermal stress factors $E\alpha$ for structural materials are presented in Figure 1b (in logarithmic scale).

$$E\alpha = \frac{\Delta\sigma}{\Delta T} \quad (1)$$

Only adhesives of low $E\alpha$ and of high deformability (e.g. Sika®PS) are able to reduce shear stress in a bond caused by thermal influences, whereas adhesives of high $E\alpha$ and of low deformability (e.g. epoxy resin) generate high shear stress.

3. CHANGES IN STRAIN DISTRIBUTION IN ELEVATED TEMPERATURES

Setup of tested specimens is presented in Figure 2. Composite carbon laminates S512 ($E = 165.0$ GPa) were bonded to concrete (C), brick (B) and timber (T) substrates using epoxy resins S30 ($E = 12.8$ GPa), S330 ($E = 4.5$ GPa) and polyurethane PS ($E = 0.016$ GPa) – more detailed properties are in [8]. Specimens were loaded in a Single Lap Shear Test (SLST) [8] with constant force of 5 kN and strain distributions on the composite were determined using strain gauges in 4 levels of temperature: 20, 40, 60 and 80 Celsius degrees. Obtained strain profiles for tested adhesives, substrates and temperatures are presented for comparison.

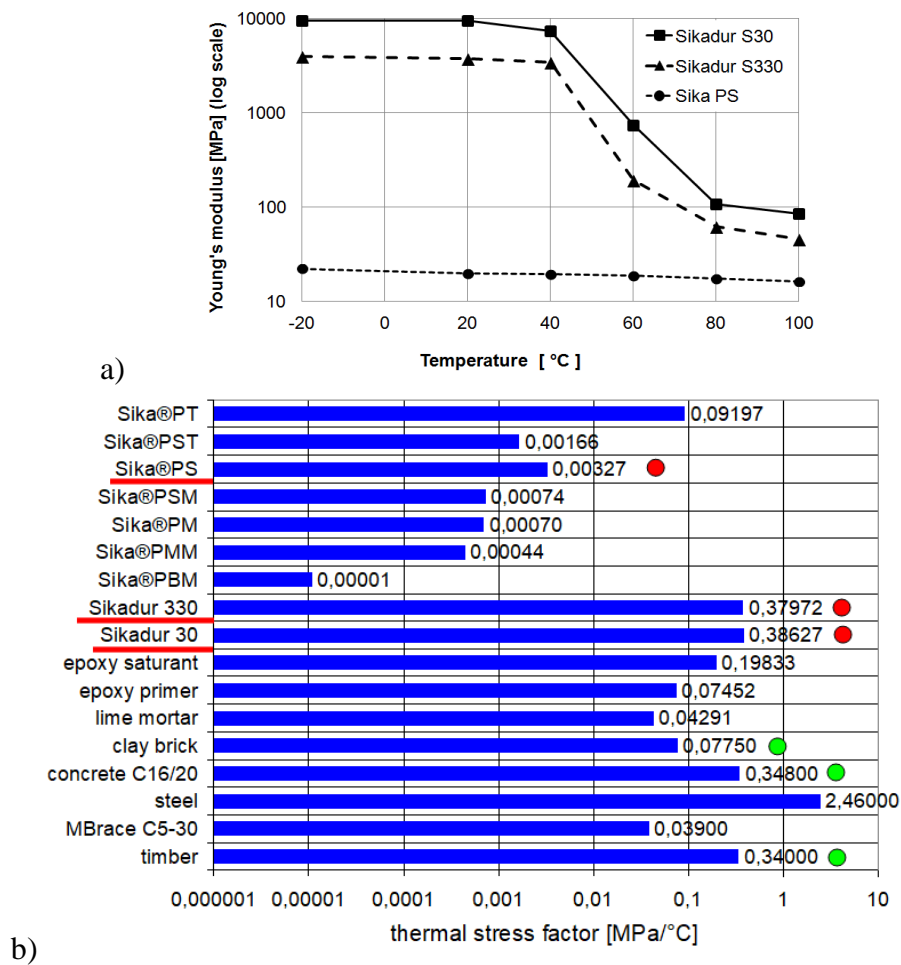


Figure 1: (a) Changes in stiffness of epoxy (S30, S330) and polyurethane (PS) adhesives with temperature and (b) values of thermal stress factors of structural materials

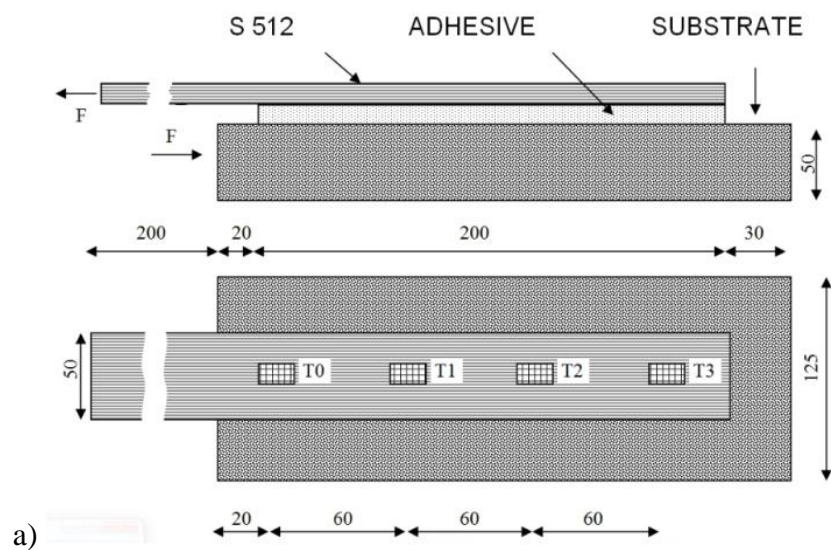


Figure 2: Setup of SLST with location of strain gauges on carbon laminate S512 – see [4]

3.1 Concrete substrate

For the concrete substrate of high stiffness ($E = 32.0$ GPa), significant change in strain profile (caused by softening – loss of properties) is observed for epoxies after exceeding their T_g (between $+40$ and $+60^\circ\text{C}$), whereas polyurethane Sika®PS adhesive assures stable work of the S512 laminate in the whole tested range of temperatures (Figure 3).

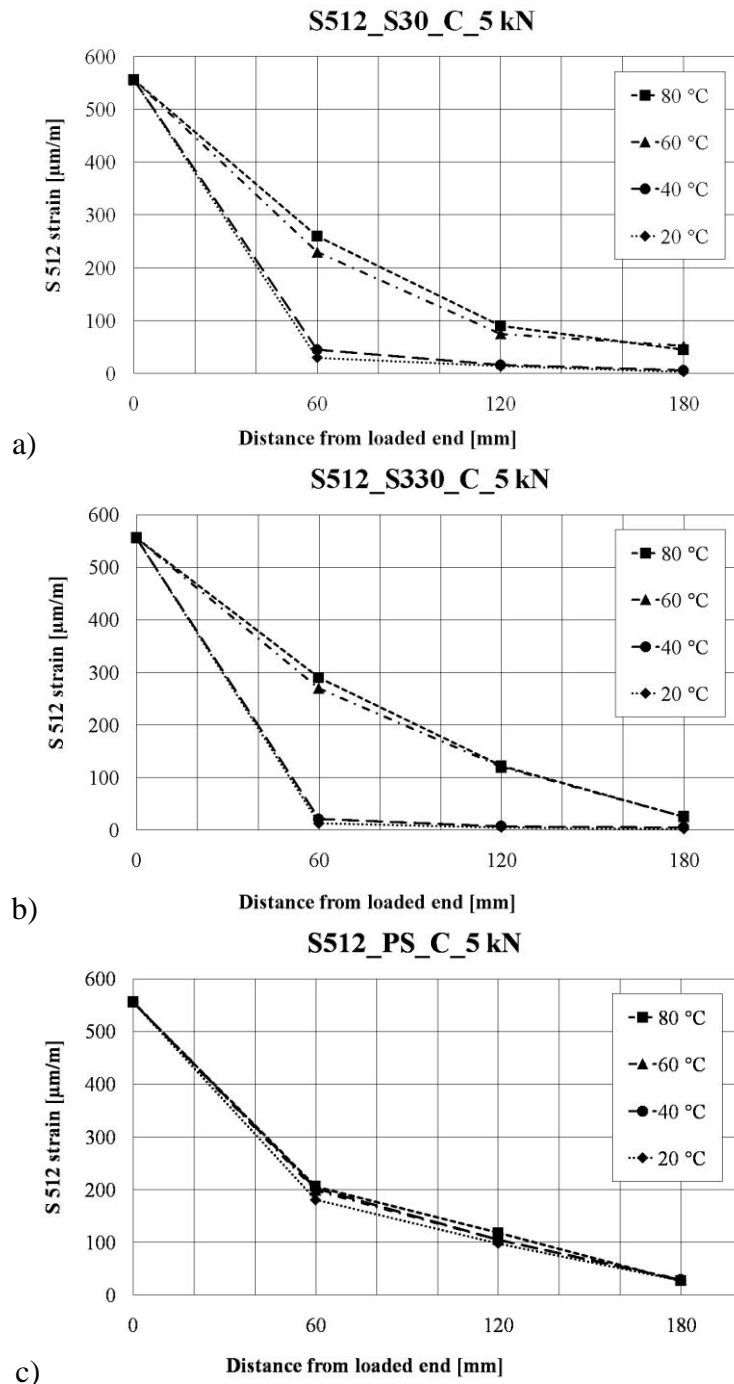


Figure 3: Strain distribution at S512 bonded to concrete substrate on epoxy S30 (a), S330 (b) and polyurethane Sika®PS (c), tested under load of 5 kN in temperatures: 20, 40, 60 and 80°C

3.2 Brick substrate

For the brick substrate of medium stiffness ($E = 5.7$ GPa), changes in strain profile are of lower gradient for epoxies after exceeding their T_g (influenced by substrate stiffness), whereas as previously polyurethane Sika®PS adhesive assures stable work of the S512 laminate in the whole tested range of temperatures (Figure 4).

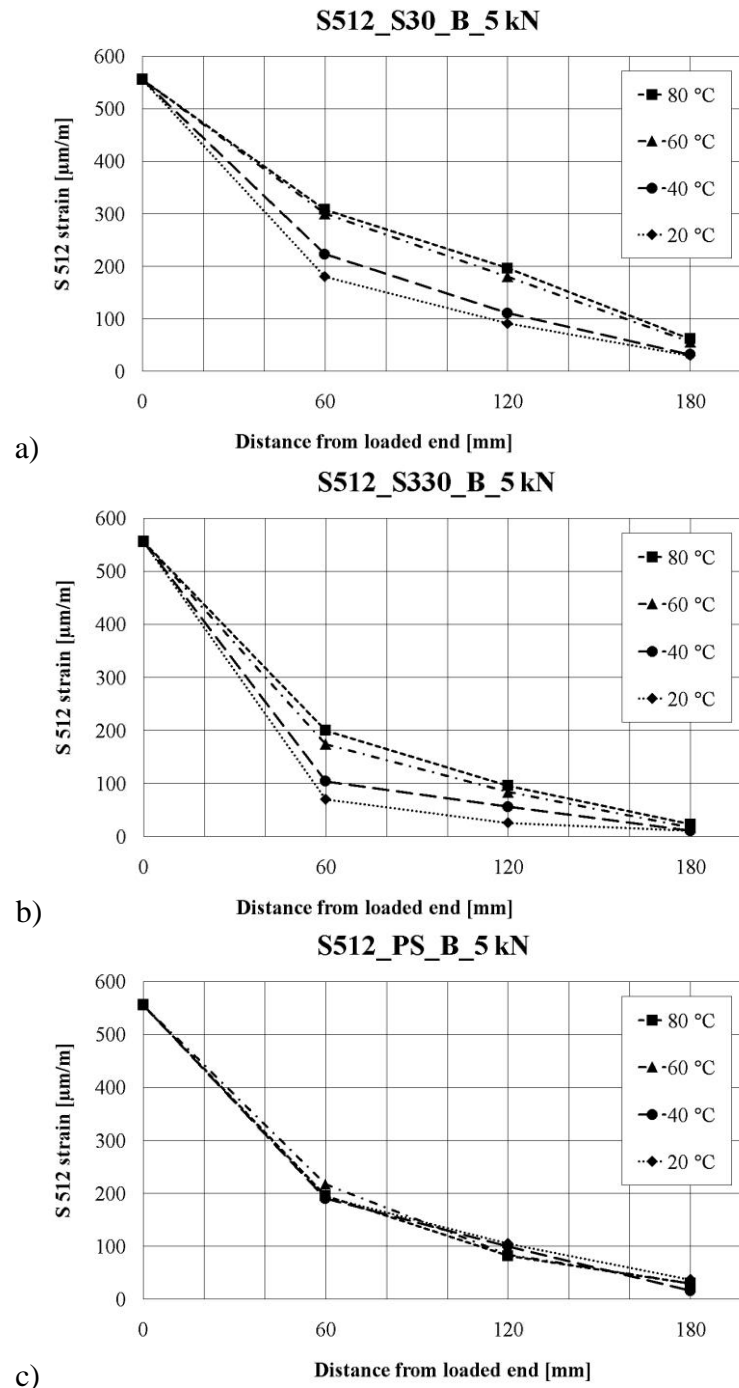


Figure 4: Strain distribution at S512 bonded to brick substrate on epoxy S30 (a), S330 (b) and polyurethane Sika®PS (c), tested under load of 5 kN in temperatures: 20, 40, 60 and 80°C

3.3 Timber substrate

For the timber substrate of low stiffness ($E = 3.3$ GPa), changes in strain profile are of the lowest gradient for epoxies after exceeding their T_g (influenced by substrate stiffness), whereas as in the case of stiffer substrates polyurethane PS adhesive assures stable work of the S512 laminate in the whole tested range of temperatures of the same character (Figure 5).

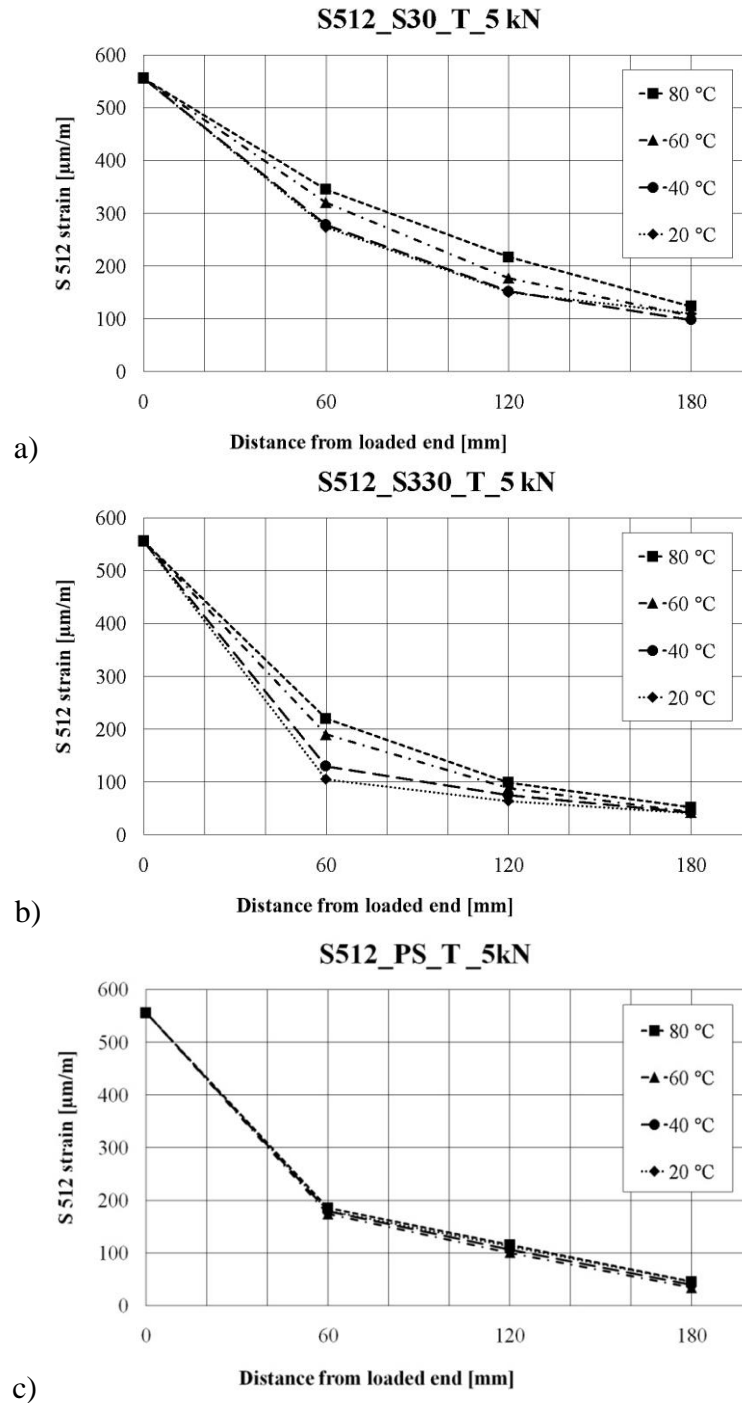


Figure 5: Strain distribution at S512 bonded to timber substrate on epoxy S30 (a), S330 (b) and polyurethane Sika®PS (c), tested under load of 5 kN in temperatures: 20, 40, 60 and 80°C

3.4 Influence of substrate and adhesive stiffness in room temperature

Comparison of graphs in Figure 6 indicates that strain profiles of the S512 laminate in the temperature 20°C change the most with the change of substrates stiffness when epoxy adhesive is the stiffest (Figure 4). Flexible polyurethane PS assures the most stable working conditions.

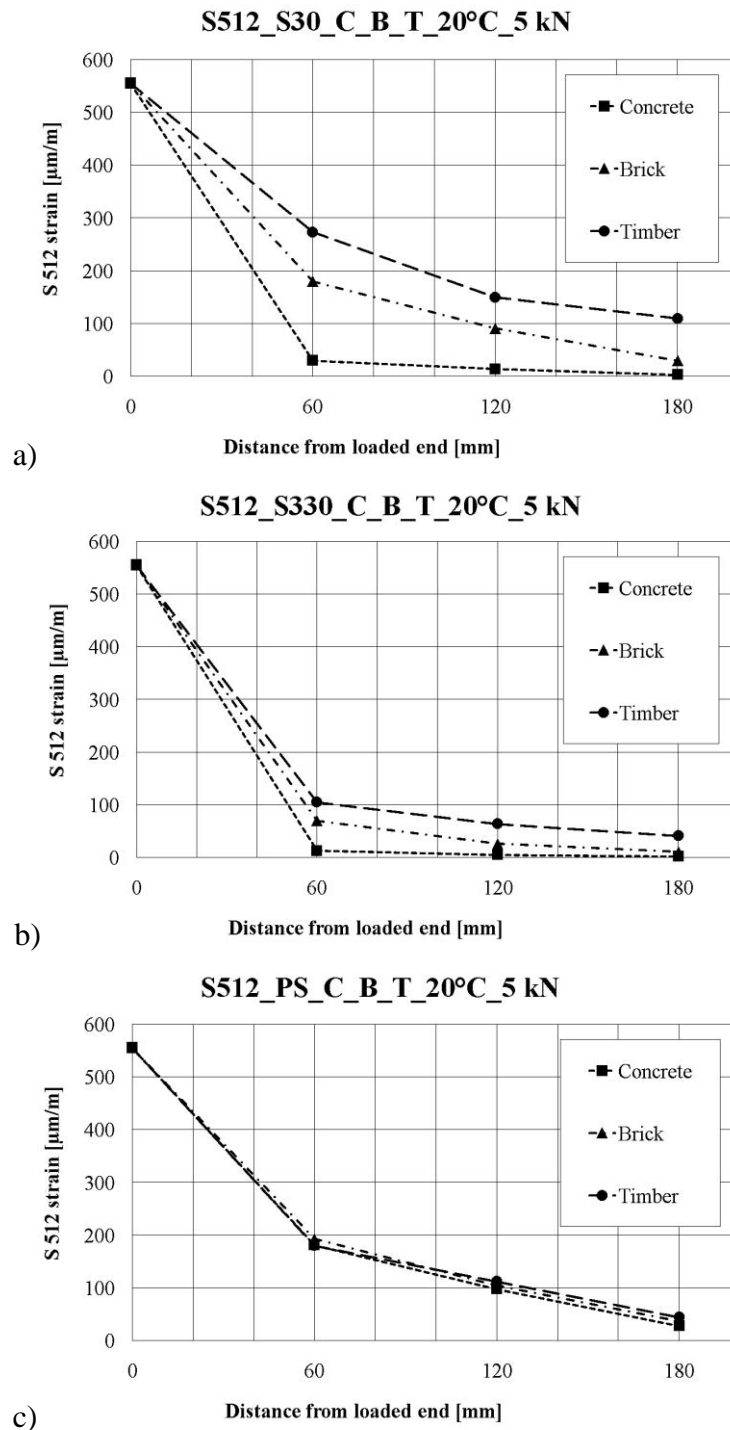


Figure 6: Strain distribution at S512 bonded to concrete, brick and timber substrates on epoxy S30 (a), S330 (b) and polyurethane PS (c), tested under load of 5 kN in temperature 20°C

4. CONCLUSIONS

It was presented that a thermal stress factor influences thermo-mechanical compatibility of composite-to-substrate strengthening components and thus should be taken into consideration when adhesives of high stiffness and low deformability (epoxy resin) are used. On the other hand, flexible adhesives of high deformability (polyurethane Sika®PS) can reduce high shear stress, protecting the bond against damage.

Glass transition temperature of adhesives plays role of great importance if it is present within the range of exploitation temperatures. Changes in mechanical properties of such adhesives (epoxy resins) are significant, causing work of composite-to-substrate strengthening systems unpredictable, thus less safe. Flexible adhesives without this drawback (polyurethane Sika®PS) assures stable work in elevated temperatures, does not matter what level of temperature is applied.

The tests results indicates that the stiffer substrate and the used stiff adhesive (epoxy), the larger changes in strain distribution are under high gradient temperature changes during exploitation (day/night or summer/winter). It influences durability aspects of composite-to-substrate strengthening when it works under load in the range of elevated temperatures, because of substrate degradation (especially weak and brittle – in historical masonries). On the other hand, tested flexible adhesive polyurethane Sika®PS does not manifest any unfavourable behaviour according to temperature changes or substrate stiffness. Thus, this kind of adhesives is more stable and predictable in the use, making composite-to-substrate strengthening systems more safer and durable. Nevertheless, future tests are required.

REFERENCES

- [1] De Santis, S., Stryzewska, T., Bandini, S., de Felice, G., Hojdys, Ł., Krajewski, P., Kwiecień, A., Roscini, F., Zajac, B., 'Durability of steel reinforced polyurethane-to-substrate bond', *Composites Part B*, **153** (2018), 194-204.
- [2] Valluzzi, M.R., Garbin, E., Panizza, M., Binda, L., Tedeschi, C., 'Moisture and Temperature Influence on FRP Masonry Bonding', In: Proc. XII Int. Conference on Durability of Building Materials and Components, 12-15 April (Porto, 2011).
- [3] RILEM TC 139-DBS: 'DURABILITY OF BUILDING SEALANTS, Durability test method - Determination of changes in adhesion, cohesion and appearance of elastic weatherproofing sealants for high movement façade joints after exposure to artificial weathering', *Materials and Structures*, **34** (2001), 579-588.
- [4] Kwiecień, A., 'Shear bond of composites-to-brick applied with highly deformable, in relation to resin epoxy interface materials', *Materials and Structures* **47** (2014), 2005-2020.
- [5] Zajac, B., Kwiecień, A., 'Thermal stress generated in masonries by stiff and flexible bonding materials', Proceedings of the 9th Int. Masonry Conference in (Guimarães 2014), ID_1629.
- [6] Klammer, E.L., 'Influence of temperature on concrete beams strengthened in flexure with CFRP'. Eindhoven, the Netherlands: PhD Thesis. (Eindhoven 2009): Technische Universiteit.
- [7] Calvet, V., Valcuende, M., Benlloch, J., Cánoves, J., 'Influence of moderate temperatures on the bond between carbon fibre reinforced polymer bars (CFRP) and concrete', *Construction and Building Materials* **94** (2015), 589–604.
- [8] Kwiecień, A., Krajewski, P., Hojdys, Ł., Tekieli, M., Słowski, M., 'Flexible Adhesive in Composite-to-Brick Strengthening—Experimental and Numerical Study', *Polymers* 2018, **10**, 356; doi:10.3390/polym10040356.

A PROBABILISTIC APPROACH TO INVESTIGATE THE PHYSICAL COMPATIBILITY BETWEEN BEDDING AND RE-POINTING MORTARS

C. Tedeschi (1), E. Garavaglia (1)

(1) Politecnico di Milano, Department of Civil and Environmental Engineering, Milan, Italy

Abstract

The decay due to salts can seriously compromise the conservation of the exposed surface of the cultural heritage. This attack, at first, compromises the mortar joints.

When choosing a mortar for re-pointing the existing masonry, an on-site survey must be carried out on the causes of the damage and their effects on the masonry, and perform laboratory characterization tests of the most representative materials (mortars, bricks, stones) present in the masonry. At the end of the investigation the results could help in the choice of the most appropriate intervention and of the materials for re-pointing.

The research has pointed out the great importance of the compositional and microstructural features of porous material on their salt-decay attitude and the need for experimental work taking into account the masonry substrate. Salt-decay attitude is investigated through laboratory salt crystallization and porosimetry tests.

The damage parameter assumed are: the loss of material from the surface measured through a laser profilometer device, and the pore distribution obtained by MIP test.

The aim of this research is to correlate the damage and its evolution with the different size and distribution of the pores into the repointing mortars. This correlation will be investigated using a probabilistic approach.

Keywords: repointing, crystallization test, MIP test, damage, probabilistic approach.

1. INTRODUCTION

One of the major causes of degradation affecting building materials, especially in Mediterranean countries, is the crystallization of soluble salts (sulfates, nitrates, chlorides, etc.) present in the pores of the material. Degradation mechanisms caused by salt crystallization have been discussed in several studies. [1] [2].

Often the degradation due to salt crystallization can seriously compromise above all the conservation of surfaces, which is why repointing of mortar joints is used as intervention. The improper use of re-pointing mortar may cause serious damages not only to the same re-pointing,

but also to the original components of the masonry. The laboratory experimentation involved a series of tests aimed at verifying the physical compatibility of pointing mortar and bedding mortar with respect to the other components of the masonry. To evaluate the salt resistance to the sulphates of different mortars, crystallization tests and porosity tests according to RILEM recommendations were carried out [3] on masonry samples packed with the same type of brick and mortar bed, and with different types of re-pointing mortar. Re-pointing was characterised by porosity analysis while the evolution of the damage of wallettes was monitored, after several cycles of salt crystallisation, by visual observation and through the quantification of the loss of materials from surfaces. From the data obtained from the experimental investigation, a correlation between porosity, damage level and degradation rate was sought, while to interpret the extent of degradation an appropriate parameter of damage was chosen to describe the process of deterioration of the studied material. The parameter assumed is the loss of surface material in each measurement. Measurements were carried out with a laser device along the profile chosen on the surface of the mortar joint and the loss was quantified as the variation of the depth of the profile over time. The randomness present in the mortar conglomerate suggests treating the process of deterioration as a stochastic of the random variable a (where a is the loss of surface material) and modelling it, cycle by cycle, with a Log-Normal distribution. The temporal evolution of this process has been, instead, interpreted through the construction of fragility curves [4],[5].

The research, that was carried out, highlighted the great importance of the study of the physical and microstructural characteristics of porous materials on their ability to degrade due to the presence of salt and the need for an experimental work which takes into account the substrate of the masonry [6].

2. EXPERIMENTAL PROGRAM

2.1 Mortar characterisation

The wallettes subject to resistance test to sulphates, were carried-out with three bricks and two mortar beds. The bricks used were “thumbed”, much used in Lombardy, and mortar from bedding of slaked lime.

The specimens were initially carried out not pointed but made with tooled bedding and then pointed with different types of pointing mortars: a) hydrated lime mortar ; b) putty lime (air lime and white cement - 2:1); c) mortar with hydrated lime; d) mortar with only white cement. The composition of mortars used for the construction of masonry prisms is shown in Table 1. Moreover, a specimen with only bedding mortar was used as a reference. On hardened mortar samples, to obtain further microstructural information, porosity was carried out using a mercury porosimeter. Table 2 shows the total porosity and the median pore radius in volume.

2.2 Test procedure

The test was carried out following the RILEM MS A.1 Recommendation by making some changes to the standard procedure, such as the increase of salts concentration in the solution, to accelerate the test. For the packing of the specimens prismatic plexiglass containers with approximative dimensions of 326x326x170mm were used, and with a height greater than that of the specimens of at least 50mm. Specimens were placed inside the boxes, in contact with a Na_2SO_4 at 12.5% saline solution (by weight), taking care to leave the test surface upwards (pointing). The test started by pouring 200mm of saline solution in the boxes, in one minute,

after four hours the topping up was carried out in order to bring the level back to 20mm of solution, and after eight hours the box was filled with the saline solution up to 5mm away from the upper edge of the box. All these operations were carried out, without the test side coming into contact with the solution. The specimens were placed in an air-conditioned room with 20°C of temperature and 50% of relative humidity, and just after four weeks the first signs of deterioration were observed, that is the first appearance of salt efflorescences.

Table 1: Schematization of the types of masonry prisms used for the test

Units	Bedding mortar	Pointing mortar
Softmud red bricks	Putty lime and siliceous + calcareous aggregate (binder/sand ratio 1:3)	L3: hydrated lime and siliceous + calcareous aggregate (binder/sand ratio 1:3)
		Cp: White cement +calcareous aggregate (binder/sand ratio 1:3)
		LC: hydrated lime + white cement (2:1) and siliceous + calcareous aggregate (binder/sand ratio 1:3)
		LAp: Hydraulic lime +calcareous aggregate (binder/sand ratio 1:3)

Table 2: Porosity and Median Pore Radius (Volume)

Type of mortar	Porosity [%]	Median Pore Radius Volume [μm]
B	30.28	4.79
LAp	15.28	0.09
LC	23.60	0.43
L3	27.55	0.46
Cp	15.08	0.40

A first visual analysis was followed by a photographic campaign, aimed at monitoring the formation of crystals on the surface. After the photographic documentation had been completed, the crystalline formations were removed, and once the cleaning operation was completed, the reading was carried out through a laser profilograph.

The monitoring was carried out monthly, taking care to add distilled water in sealed boxes every four weeks, up to the height of half a wall. This device made it possible to continue the solubilization of salts still contained in the sample, since as analysed by previous research, after one month, the water absorbed during the packing phase was almost completely evaporated; in this way, the continuation of the test was assured, thus reactivation the process of the transport of the salts on the surface. A laser profilometer was used to monitor the damage (Fig. 1a, 1b,) [7]. The use of the laser profilometer allows to measure, with an excellent resolution, the loss of material from the exposed surface calculated in subsequent moments.

Profiles recorded at the end of each 4-week cycle show how the surface is changing over time due to the degradation process [5]. Figure 3 shows an example of measurements made using the laser profilometer.

3. COMMENTS TO THE RESULTS OF THE EXPERIMENTAL TESTS

The crystallization of the salt began immediately after the addition of salt, due to the high amount of saline solution used in the test and the porosity of the materials. In all the wallettes with bedding mortar, the damage to the bricks occurred in the first two months and showed

itself by a detachment of thin layers of 1 mm thick. Upon visual investigation, the wallettes appeared completely covered with soft consistency salts, especially in the brick/mortar interface. The damage on the bricks started from the edges with efflorescences directed towards the centre of the wall causing damage by exfoliation. This is due to the fact that the mortar joint has a much higher absorption compared to bricks (Figure 2).

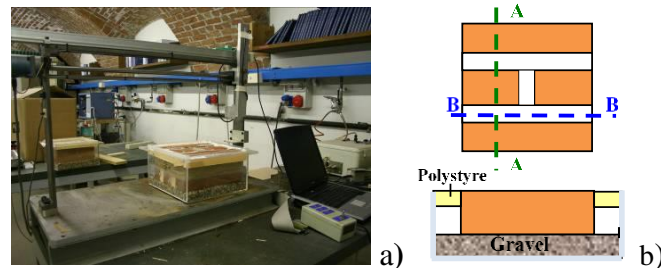


Figure 1: a) wallettes in the boxes and laser profilometer, b) measurement scheme.

After 6 months, the deterioration due to crystallization was clearer and differentiated according to the type of reconstruction. In masonry with bedding mortar (B), the deterioration has increased regularly over time, and there was a greater deterioration in the vicinity of the leaks of the bed joints. In the walls with re-pointing made with hydrated lime mortar (LC and L3), the damage became more regular over time, but of a thickness lower than that of the walls with only lime and cement mortar, and after 4 months was visibly higher in the mortar than in bricks.

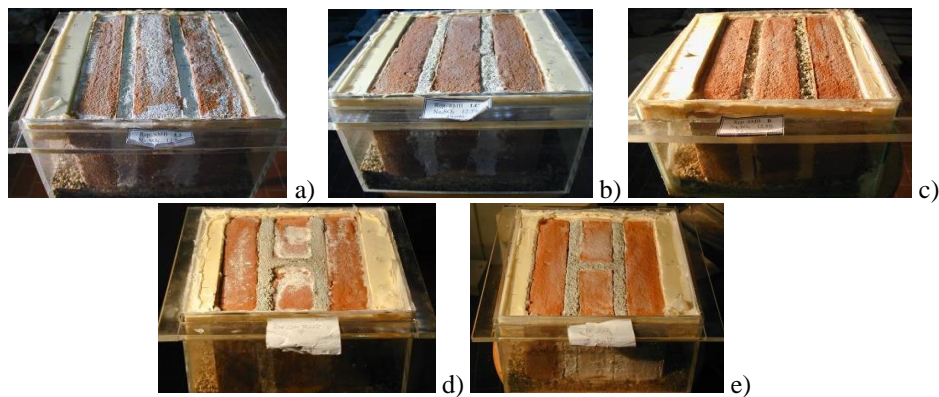


Figure 2: Surface of wallette after 11 four week cycles: (a) L3, (b) LC, (c) B, (d) Cp, (e) Lap

In the walls with re-pointing using cement (Cp) and lime (LAp), the degradation is evenly distributed. The presence of only cement (Cp) in re-pointing seemed to increase the damage of the bricks over the same period of time. Normally the degradation begins where the highest capillary flow occurs, that is at the brick/mortar interface and where the most porous material is found, in the event where only the mortar is present, the degradation process is very fast and after a month the whole surface of the bricks is equally damaged. The presence of re-pointing with this type of mortar reduces this phenomenon, but without avoiding it, and only slowing the release of salts. If the re-pointing mortar is instead of reduced porosity (LAp), the salts

outflow is slowed down and the accumulation takes place in the surrounding bricks with subsequent and more rapid degradation of the latter, rather than the re-pointed joint.

3.1 A significant parameter to quantify the damage

After the collection of the experimental results, we proceeded to quantify the damage over time. The methodology used to measure damage over time refers to what was developed in [4] and subsequent studies [5]. The parameter of damage taken as a measure of damage is the area between two successive detection profiles obtained with laser reading. Therefore, for each profile i and at each cycle k , it is assumed that the area a_{ik} (expressed as a percentage) between the two profiles quantifies the damage occurred in the time span between the two surveys/detections:

$$a_{ik} = \frac{\text{area, } A_i, \text{ lost}}{\text{area transversal section}} * 100 \quad (1)$$

The percentages of loss a_{ik} calculated at the end of each reading cycle collected in a graph allow already to understand the behaviour over time of the loss of material due to salt attacks (Figure 4).

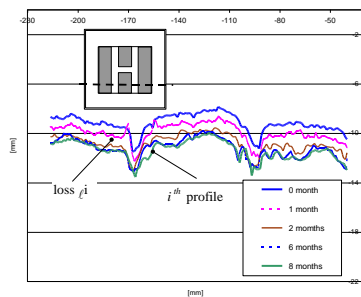


Figure 3: example of the measurements made with the laser profilometer on a wall.

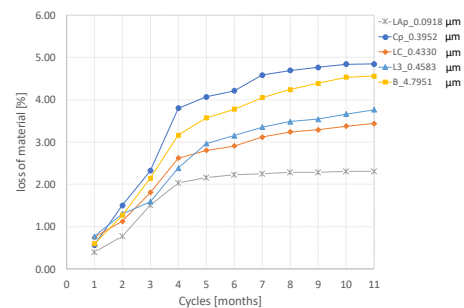


Figure 4: Deterioration (mean values) vs. cycles for the six mortar types (Model MB).

Figure 4 highlights how the degradation of the re-pointing mortars has a speed of evolution depending on their porosity. The LAp mortar, very compact and with low porosity ($0.0918\mu\text{m}$) has a degradation that stabilises after the 4th cycle, it remains constant and however much lower than the degradation recorded for other mortars. The joints made with bedding mortar (B) which has a much more open porosity ($4.7951\mu\text{m}$) shows a higher loss of material, justified by the fact that the salts outflow is abundant and their crystallization quite destructive for the material; the damage seems to stabilise after the 10th cycle. The two LC and L3 mortars have a porosity of the same order of magnitude, and the damage, although slowed down, still seems to be evolving. A different behaviour is instead shown by the mortar Cp mortar which, although having a reduced porosity, shows a damage superior to all those recorded.

To better represent the ratio that binds the porosity of the material to the entity of the degradation and its evolution, the 3D representation shown in Figure 5 has been adopted.

In Figure 5 it is evident that the 4° cycle is significant for all types of mortar, in fact the degradation seems to accelerate between the 2° and the 4° cycles, while for the subsequent cycles there seems to be a slowing down up to tend in some cases, to an almost asymptotic

degradation rate around the 11^o cycle.

In Figure 6, the ratio between maximum loss of material and porosity is highlighted. As expected, the trend curve shows a propensity of damage to increase as the porosity increases, even if the behaviour is certainly altered by the data relating to the damage recorded for the cement mortar Cp. This behaviour is due to another very important aspect regarding the microstructure of the material.

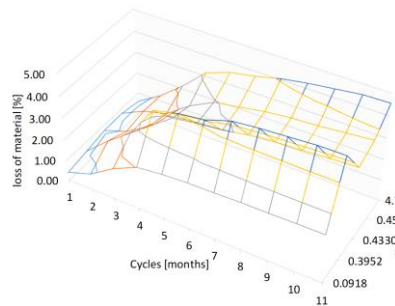


Figure 5: 3D representation of deterioration vs. cycles in function of median pore diameter

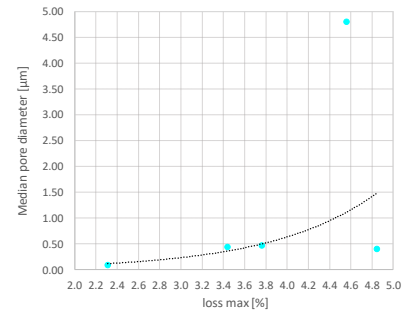


Figure 6: Pores dimension vs maximum percentage of material loss

In Figure 7, the porosimetric distribution and the total porosity of the sample (B) and of the sample (Cp) are shown, as can be clearly seen, that even if the value of the porosity varies a lot, the porosimetric distribution, a factor which affects the evaporation of water, is very similar.

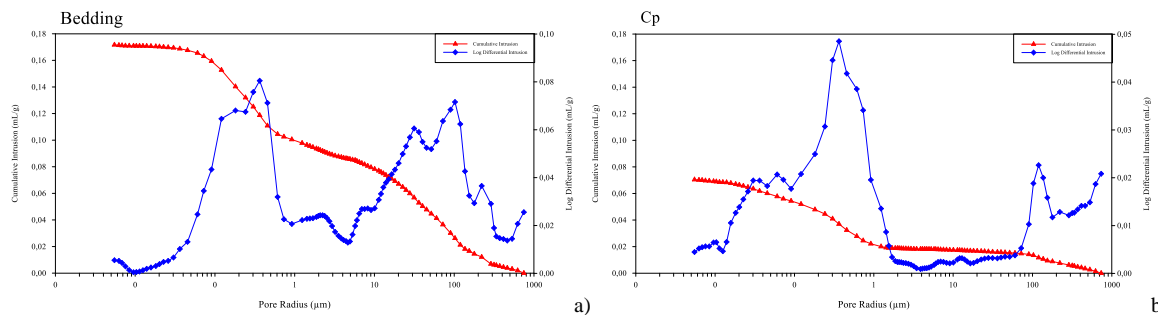


Figure 7: Porosimetric distribution of: a) cement mortar sample (Cp) and b) bedding mortar (B).

4 THE DETERIORATION PROCESS AS A STOCHASTIC PROCESS IN THE RANDOM VARIABLE a

The degradation process is a process that requires a probabilistic interpretation of its evolution. It can be considered as a stochastic process in the random variable a . In fact, the loss a is due to uncertainties which are related both to the variability of the attacks, and in the case of repeated tests, to epistemic uncertainties linked to the reproduction of the test itself which, even if controlled, could still remain. The measurements made at each cycle k on different portions of wallettes return values that can show a consistent dispersion around the mean value. Therefore, an appropriate probability density is used to model this behaviour. This choice is not simple, it must be based on the physical knowledge of the modeled phenomenon and on the knowledge of the mathematical framework that governs the behaviour of the tails of distribution. In [4],[5] this topic is widely explained and the conclusion is that a plausible probability density function (PDF) capable of interpreting the dispersion in the loss of material,

cycle by cycle, is the Log-Normal distribution (Figure 8). Figure 9 shows the experimental fragility curves (symbols) and their probabilistic modeling with Weibull-type cumulative distributions (lines) [5].

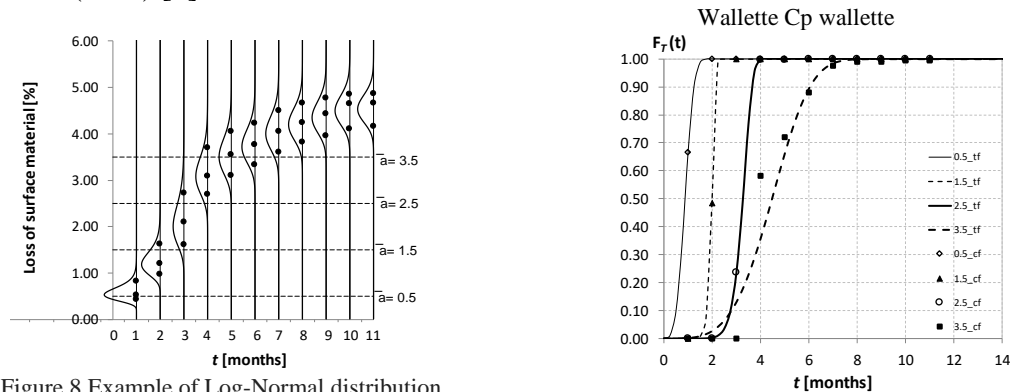


Figure 8 Example of Log-Normal distribution modelling applied on Bedding data (B)

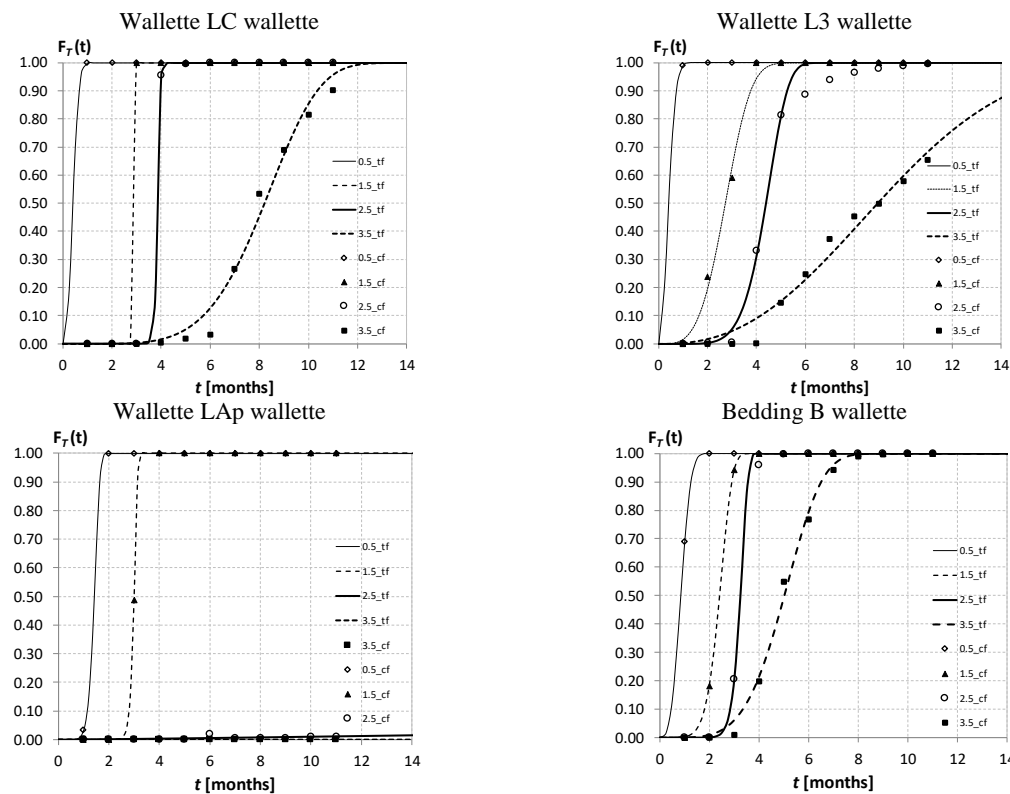


Figure 9. Fragility curves for different thresholds \bar{a}

It is evident that for the mortar characterized by a higher median pore radius (B) the probability of exceeding the thresholds of damage taken as significant is quite high already from the first test cycles. Vice versa, the low-porosity LAP mortar shows a behaviour very similar to the others for the first two cycles (high probability of exceeding the first two thresholds of damage) while the subsequent ones are not reached during the 11 months trial. For LC and L3 mortars the behavior is similar, while Figure 4 shows a greater loss for L3 compared to LC. The probabilistic modeling shows a probability of greater damage to LC than

to L3, this could be related to the speed of achievement of the faster degradation for LC compared to L3. With regard to the cement mortar (Cp) also the modeling shows a probability of evolution of the degradation very similar to that of bedding (B) even if the two porosities are significantly different, but as we have seen in Figure 8, they are similar with regard to the distribution of the pore. However, from Figure 9, it emerges that the probability of first and second damage is high already from the first cycles for all types of mortar, while the porosity seems to have a greater influence on the higher damage thresholds.

5 CONCLUSIONS

Crystallization tests have highlighted some different behaviours of the mortar. This different behaviour seems to be related to the size and distribution of pores of the material.

An important data is the ratio between the median radiant pore and the damage: for the first damage it can be seen that the lower the median pore and the higher the probability of damage. For higher damage thresholds, instead, the probability that this damage is recorded is higher for high porosity, whereas medium-low porosities seem to slow down this effect.

The results obtained certainly show a relationship between the level of damage, the speed of achievement of the same and the degree of porosity of the material. Having worked on repointed composite walls, this relationship may in some cases be unclear or contradictory, but we think it should be compared to what occurs on the re-pointed material, because a poor damage in repointing mortar may be a problem for the material adjacent to the re-pointed joint, for example it could be such material to suffer damage and effect of the high compactness of repointing mortar. Research is continuing on this topic.

REFERENCES

- [1] Binda, L., Charola, A.E., Baronio, G., 'Deterioration of porous materials due to salt crystallization under different thermohygrometric conditions', in 5th Int. Conf. on Deterioration and Conservation of Stone, Losanna1985, 279-288,
- [2] Cardani G, Tedeschi C, Binda L, Baronio G., 'Laboratory Crystallisation Tests for Damage Evaluation' in Maintenance of Pointing in Historic Building: Decay and Replacement, Contract EV-CT98-0706, Final Report 2001.
- [3] RILEM MS-A1, 'Determination of the resistance of wallettes against sulphates and chlorides',1998.
- [4] Garavaglia E, Lubelli B, Binda L., 'Two Different Stochastic Approaches Modelling the Deterioration Process of Masonry Wall over Time'. *Materials and Structures, Springer Ed.*, **35**(248), (2002) 246-256.
- [5] Garavaglia E., Anzani A., Binda L., Cardani G., 'Fragility curve probabilistic model applied to durability and long term mechanical damages of masonry' *Materials and Structures, Springer Ed.*, **41**(4), (2008) 733-749.
- [6] Tedeschi C., Binda L., Garavaglia E., Probabilistic evolution of durability of ready mix mortar, XII DBMC, 12th Int internationale Conference on Durability of Building Materials and Components, Porto, Portugal, April 12th-15th, 2011. Peixoto de Freitas, H. Corvacho & M. Lacasse Editors, U.Porto, Faculdade de Engenharia, FEUP Edições, Porto, Vol I, pp.1403-1412, ISBN 978-972-752-132-6.
- [7] Binda, L., Cardani, G., Tedeschi, C., 'The evaluation of damage due to salt crystallisation of different re-pointing mortars studied in laboratory, 10DBMC International Conference On Durability of Building Materials and Components LYON, France, 17-20 April 2005, CD-ROM, TT1-214, pp. 1-8, 2005.

SEISMIC RETROFITTING OF MASONRY WALLS WITH TEXTILE REINFORCED MORTAR COMPOSITES

Gianmarco de Felice, Stefano De Santis

⁽¹⁾ Roma Tre University, Department of Engineering, Rome, Italy

Abstract

Stone masonry walls are particularly vulnerable against out-of-plane seismic actions as a consequence of bending, leaf separation or disaggregation. Textile Reinforced Mortar (TRM) composites could be used to contrast these failure modes, but the knowledge on the seismic behaviour of TRM reinforced masonry structures is still insufficient. This work describes a shake table test carried out on two full-scale walls, one made of two leaves of rubble stones and one of regular tuff blocks. The walls were provided with a reinforced brickwork top beam, whose horizontal displacement was constrained to avoid overturning and induce out-of-plane vertical bending. Natural accelerograms were applied in horizontal and vertical directions with increasing scale factor up to collapse. The walls were tested unreinforced, retrofitted with TRMs and tested again. A bidirectional basalt mesh was applied over the entire surface of the stone wall, whereas a unidirectional steel textile was used on the tuff wall. The response of the specimens before and after retrofitting are compared to contribute to the development of a deeper understanding of the effectiveness of TRM composites for the seismic retrofitting of the building stock.

Keywords: Basalt Textile Reinforced Mortar (BTRM); Shake Table Tests; Steel Reinforced Grout (SRG); Strengthening.

1. INTRODUCTION

Due to the limited tensile strength and the inherent discrete nature of the material, stone masonry walls may exhibit a high vulnerability against out-of-plane seismic actions. Traditional retrofitting solutions, such as steel tie-bars or restraining top beams, can effectively prevent, or at least delay, the onset of overturning mechanisms [1,2]. Nevertheless, collapse may still occur under either vertical or horizontal bending, leaf separation or disaggregation, especially in historic structures [3]. With specific respect to flexural failure modes, a deep understanding of the seismic response of existing masonry structures and on the most appropriate retrofitting technologies still needs to be gained. To this end, Textile Reinforced Mortar (TRM) composites, comprising high strength textiles externally bonded to

the structural members by means of an inorganic matrix, appear particularly promising, thanks to their high strength-to-weight ratio, versatility and ease of installation. In addition to TRM, other names and acronyms are used in the literature, including Fabric Reinforced Cementitious Matrix (FRCM), Fabric Reinforced Mortar (FRM) and, when comprising steel textiles, Steel Reinforced Grout (SRG). Experimental evidence exists which proves the effectiveness of TRM composites for enhancing the ultimate flexural strength of masonry walls [4-8]. Nonetheless, these studies have been carried out under static loads, and, in view of applying TRMs for the retrofitting of existing masonry structures in earthquake prone areas, a deeper understanding of the seismic behaviour of TRM-reinforced structural members should still be developed.

This work describes a shake table test carried out on two full-scale wall specimens, one of regular tuff blocks and one made of two leaves of rubble stone masonry. The walls were tested unreinforced, then repaired and retrofitted with TRM composites and tested again. The seismic behaviour of the specimens was recorded using accelerometers and a non-conventional high-resolution 3D motion capture system. The dynamic behaviour of the walls before and after retrofitting is discussed to derive information on the effectiveness of TRMs for seismic retrofitting.

2. TESTING SETUP AND SEISMIC RECORDS

Two full-scale wall specimens were tested on the shake table (Figure 1a). One wall was built in regular tuff masonry and one was in rubble stone masonry. Each specimen each had 3.48m height, 1.53m width and 0.25m thickness. The walls were built on a single reinforced concrete foundation with 0.35m×0.35m cross section, anchored to the shake table, to make it possible to test them together under the same input signal. On top of each wall, a reinforced brickwork top beam was built, in which strips of steel textile were embedded in the bed joints. To prevent overturning, the horizontal displacement of the top beams was constrained, whereas vertical displacement and rotation were free. In order to apply such constrain condition, two steel frames were placed on the shake table and connected to each other on top by two I girders; eight rubber cylinders were fixed to the I girders and put in contrast with the top beams. An additional load of 600kN was placed on top of each wall (Figure 1b).

Tests were carried out on a 4m×4m shake table with six degrees of freedom. Piezoelectric accelerometers were used to record accelerations on the reinforced concrete foundation and on the walls along their height. A high-resolution 3D motion capture system, named 3DVision [9, 10], was used to measure displacements. A total of 53 spherical wireless retro-reflecting markers were glued on the wall specimens, on the top beams, on the foundation and on the shake table. Nine near infrared digital cameras were placed around the shake table to record the spatial displacements of the markers. 3DVision made it possible to monitor a large number of measurement points with the additional advantage that it is not affected by the range and encumbrance limitations typical of the traditional displacement sensors and it does not require the building of any stiff frame as a reference for the out-of-plane displacements. Finally, thanks to the use of cheap passive wireless markers, no relevant instrumentation damage is risked during collapse.

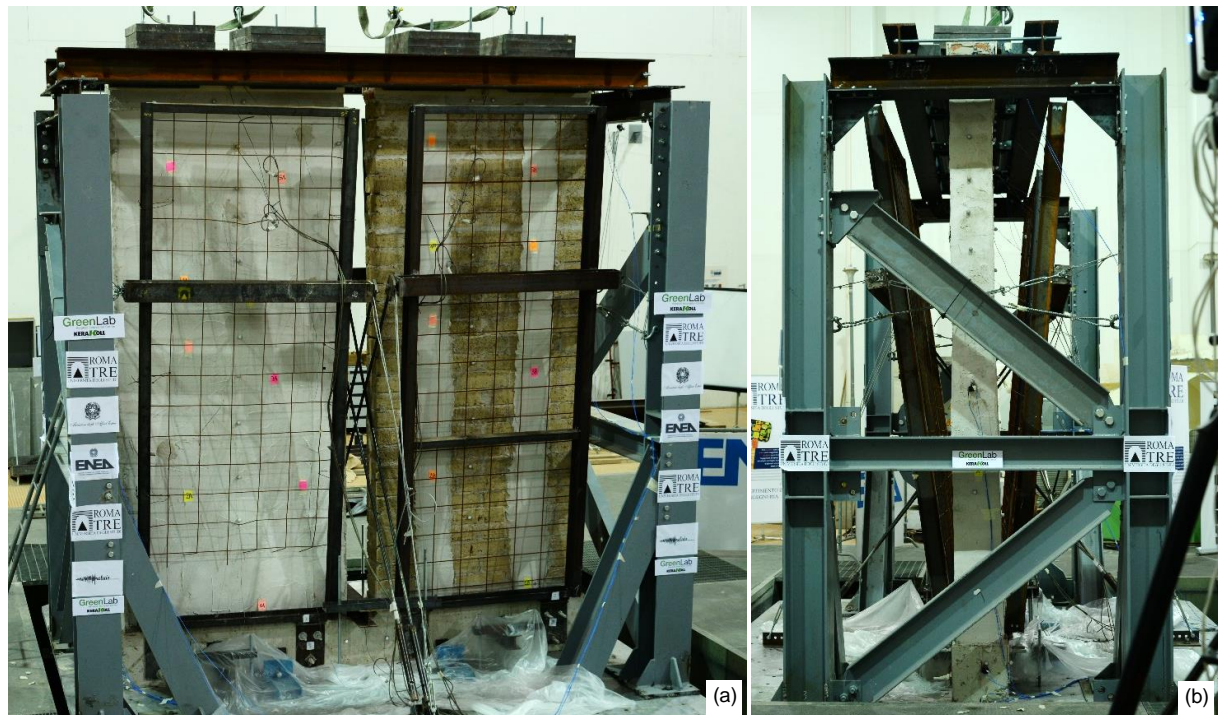


Figure 1: Front (a) and side (b) views of the experimental setup

Five input signals were selected from the European Strong Motion Database and applied in both the out-of-plane horizontal direction and in the vertical direction, with increasing scale factor (SF) up to collapse, starting from SF=0.25. Table 1 lists the selected records including the year and the magnitude of the event (M_w), the record station, and the peak ground acceleration (PGA) in horizontal and vertical directions. The inputs are listed in the table in the chronological order used in the tests, which was based on the horizontal PGA to obtain a sequence with increasing intensity.

Table 1: Records selected as seismic inputs

Event and year	M_w	Record station	Horizontal PGA	Vertical PGA
Irpinia, 1980	6.9	Bagnoli, BGI	0.18 g	0.10 g
Emilia, 2012	6.1	Mirandola, MRN	0.27 g	0.29 g
Amatrice, 2016	6.0	Amatrice, AMT	0.38 g	0.40 g
Umbria-Marche, 1997	6.0	Nocera Umbra, NCR	0.49 g	0.39 g
L'Aquila, 2009	6.1	L'Aquila, AQP	0.64 g	0.48 g

4. RESULTS OF THE TESTS ON THE UNREINFORCED WALLS

The shake table tests on the unreinforced stone wall were performed with SF from 0.25 to 0.75, for a total of 20 tests. The dynamic behaviour of the specimen was governed by a hinge developed in the mortar joint at 2.54m height (z), which crushed at the end of the series with SF=0.25 (after the first 5 tests). From this moment on, the wall behaved as a two-block mechanism. In the last test, performed under AQP signal with SF=0.75, the maximum horizontal acceleration measured at the base was $a_{h,max}=0.53g$, whereas the maximum

displacement of the marker at $z=2.31\text{m}$ (near the hinge) was $\delta=134.4\text{mm}$. After this test, the wall was considered collapsed.

In total, 31 seismic tests were carried out on the unreinforced tuff wall, starting with $SF=0.25$ up to $SF=1.25$. In this case, two hinges formed, one at $z=2.60\text{m}$ (appeared after AQV, $SF=0.50$, $a_{h,\max}=0.31\text{g}$) and one at $z=3.09\text{m}$, surveyed after the last test. The maximum acceleration of the entire test session was $a_{h,\max}=0.86\text{g}$ and the maximum out-of-plane displacement (recorded by the marker at $z=2.46\text{m}$, near the hinge) was $\delta_{\max}=112.8\text{mm}$. The final survey revealed that despite the mortar joints of the two hinges were crushed, the tuff blocks were not badly cracked.

5. RETROFITTING WITH MORTAR BASED COMPOSITES

After the tests, the stone wall was repaired by repointing the crushed joints with lime-based grout and replacing the stones that had fallen down. Then, it was reinforced on both sides with a BTRM system, including a bidirectional basalt fabric [11] and lime-based mortar (Figure 2a). The fabric had $18\text{mm}\times 18\text{mm}$ grid spacing, 881N/mm^2 tensile strength and 51.9kN/mm^2 Young's modulus. Given the irregular arrangement of the stone masonry, the BTRM system was installed onto the whole surface of the wall, to prevent disaggregation. Moreover, since the wall had two leaves, transversal steel connectors (with density of $2/\text{m}^2$) were also installed to prevent leaf separation.

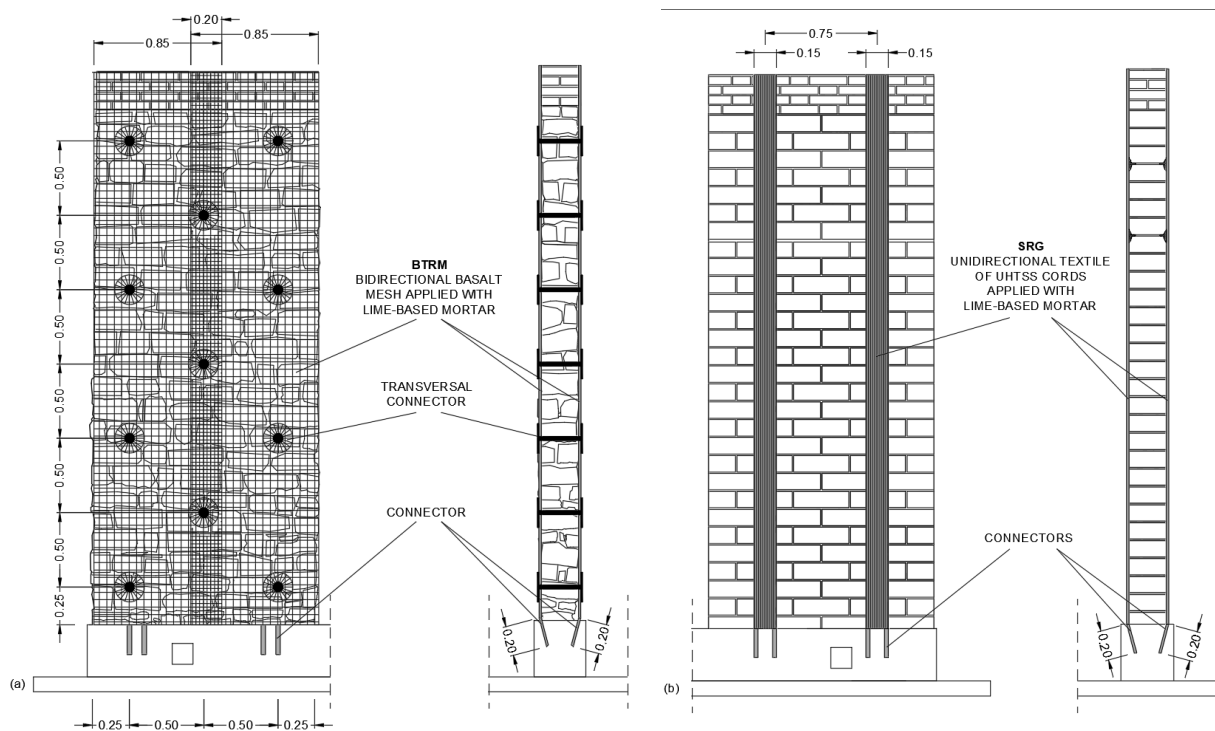


Figure 2: Retrofitting design for the stone (a) and tuff (b) walls

The tuff wall was retrofitted with Steel Reinforced Grout (SRG), comprising a unidirectional textile of Ultra High Tensile Strength Steel (UHTSS) cords [12] and lime-based mortar. The textile had 6.35mm cord spacing, 3191N/mm^2 tensile strength and 186kN/mm^2 Young's modulus. Two 150mm wide SRG strips were installed onto each side of the wall at

750mm spacing (Figure 2b). After the retrofiting works, the specimens were kept wet for the first 24 hours and then stored in the laboratory for 5 weeks before testing.

6. RESULTS OF THE TESTS ON THE RETROFITTED WALLS

After repair and retrofiting, the specimens were tested again on the shake table, under the same input signals applied in the first session. As for the stone wall a maximum SF of 1.75 was attained. The BTRM reinforcement entailed a gain in seismic capacity of 113%, as the maximum (absolute) acceleration recorded on the foundation was $a_{h,max}=1.13g$, measured during a test performed under NCR signal amplified by a SF=1.50.

Collapse occurred during a test performed under AMT signal, with SF=1.75 and $a_{h,max}=0.67g$. Thanks to the tensile strength provided by the reinforcement, the development of a hinge was avoided and the onset of a mechanism was not observed. The basalt mesh detached locally from the substrate during the set of tests with SF=1.0; damage progressively developed and, at failure, a large surface of the reinforcement was debonded, but the steel connectors did not pull out. Therefore, they effectively avoided leaf separation and ensured the bond performance of the TRM overlay. The gain in strength is clearly visible in the acceleration vs. displacement curves shown in Figure 3a and 3b for NCR and AQV records (the most severe ones), respectively.

Finally, BTRM reduced the deflection of the wall under nominally identical base inputs, as shown by the response in time plotted in Figure 4 (referred, as sake of example, to a test with AQV record, SF=0.75). In the graph, a_h and a_v are the horizontal and vertical components of the acceleration measured on the reinforced concrete foundation at the base of the wall and δ is the out-of-plane displacement of the marker at $z=2.31m$.

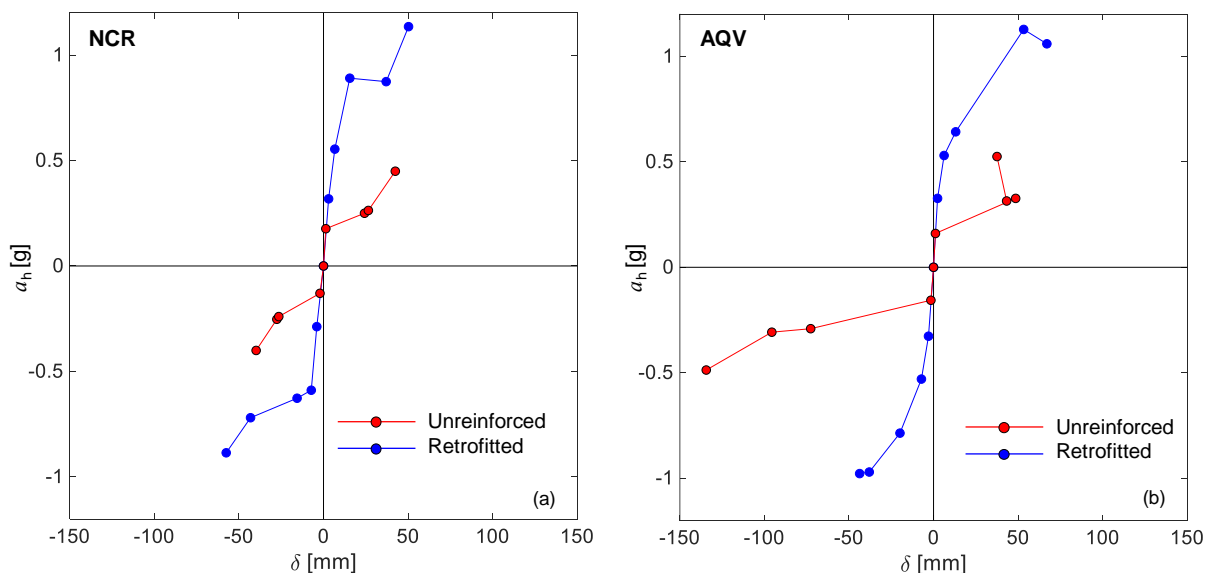


Figure 3: Maximum base acceleration vs maximum out-of-plane displacement of the stone wall before and after retrofitting with BTRM under NCR (a) and AQV (b) input signals

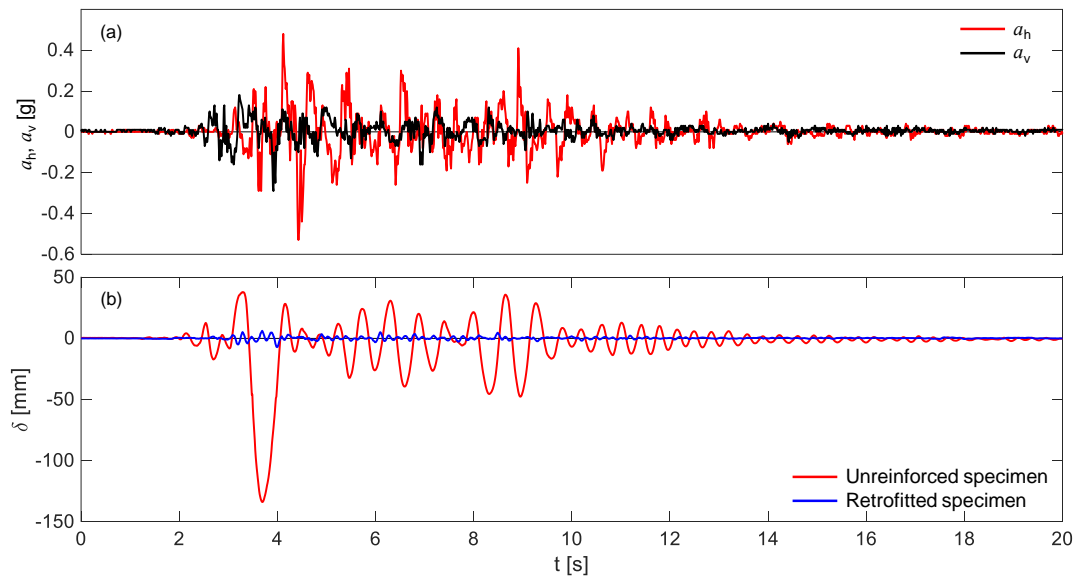


Figure 4: Seismic behaviour of the stone wall before and after retrofitting (AQV, SF=0.75)

The seismic tests carried out on the tuff wall retrofitted with SRG had SF ranging from 0.50 to 2.50. As in the stone wall, the tensile strength of the steel textile prevented the development of hinges and the dynamic response was more similar to that of an elastic beam rather than to that of a two-block mechanism. Collapse occurred by crushing of the tuff blocks in the same joints where the hinges had formed in the previous tests, but no SRG debonding took place. The maximum (absolute) value of a_h was 2.05g, which is 238% that of the unreinforced wall (Figure 5). SRG also limited the out-of-plane deflection of the wall under medium-high intensity signals, as shown in Figure 6, in which the response in time under the (nominally) same input signal (AQV, SF=1.25) is represented.

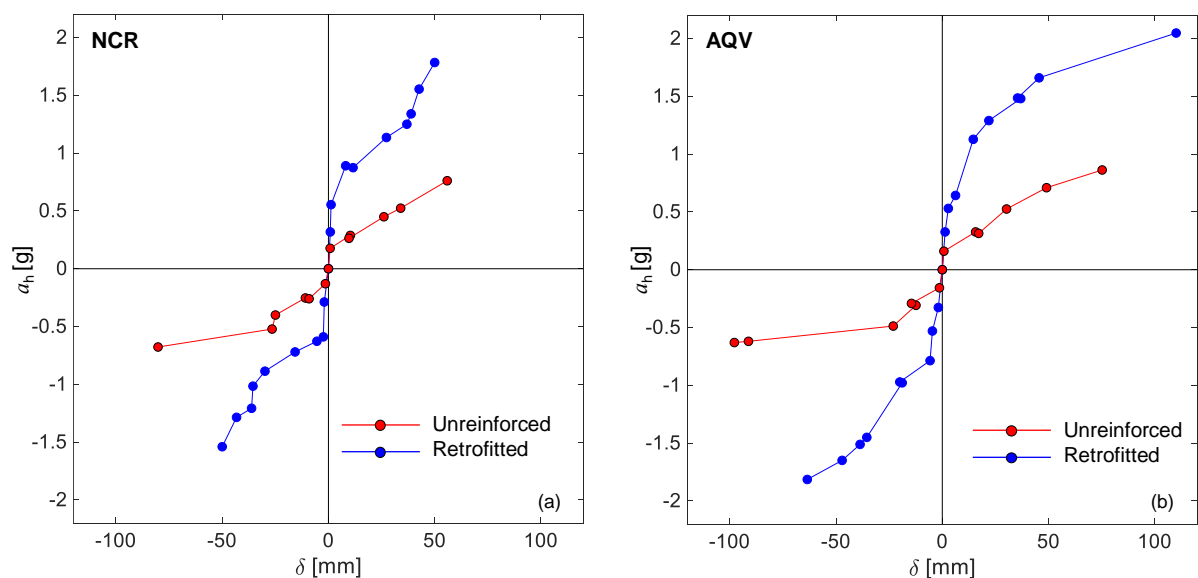


Figure 5: Maximum base acceleration vs maximum out-of-plane displacement of the tuff wall before and after retrofitting with SRG under NCR (a) and AQV (b) input signals

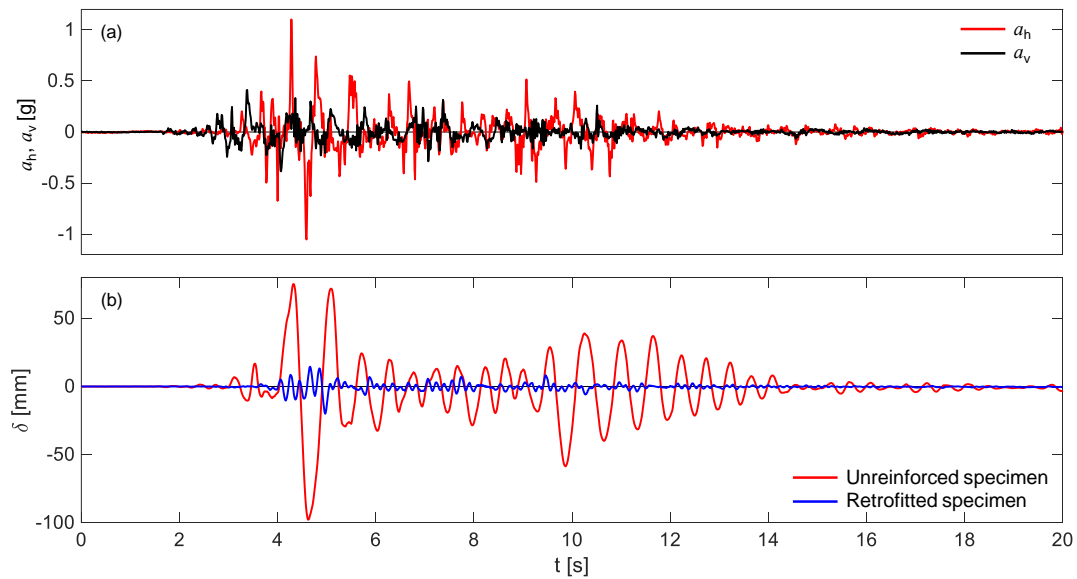


Figure 6: Seismic behaviour of the tuff wall before and after retrofitting (AQV, SF=1.25)

7. CONCLUSIONS

The shake table tests performed in this investigation provided information on the dynamic behaviour of masonry walls retrofitted with textile reinforced mortar composites and on the effectiveness of mortar-based composites for enhancing their flexural strength.

- A basalt textile reinforced mortar (BTRM) system was installed on a two-leaves rubble stone masonry wall. The composite was bonded onto the entire surface of the specimen in order to prevent disaggregation, together with transversal steel connectors which were used to avoid leaf separation. The reinforcement entailed an increase of resistance of 113% (from 0.53g to 1.13g of maximum base acceleration).
- Steel reinforced grout (SRG) strips were applied onto a single-leaf wall made of squared tuff blocks, without the need of covering its entire surface nor of installing connectors. The SRG retrofitting system led to an increase of the maximum base acceleration of 138% (from 0.86g to 2.05g).
- In both cases, the deflections under nominally identical seismic base inputs of medium-high intensity were significantly reduced by the reinforcement.
- Thanks to the tensile strength provided by the high-strength fabrics embedded in the TRM overlays, the development of cracks was delayed. Accordingly, the dynamic response of the walls subjected to out-of-plane seismic loads was more similar to that of a nearly-elastic simply supported beam rather than to that of a two-block mechanism, as in the case of unreinforced walls.

This study indicates that mortar-based composites can be successfully employed to safeguard existing structures in earthquake prone areas. Their reduced thickness makes it possible to embed the fabrics within the plaster layer of the façades. A deeper understanding should still be gained with other experimental tests in order to develop design guidelines. This would foster the full exploitation of research outcomes in structural rehabilitation activities through a proper knowledge transfer from academia to engineering practice.

ACKNOWLEDGEMENTS

This work was carried out within the Research Projects “Composites with inorganic matrix for sustainable strengthening of architectural heritage” funded by the Italian Ministry for Foreign Affairs (Years 2017-2018, Grant N. PGR00234) and “ReLUIS-DPC 2017, Thematic Area Innovative materials for interventions in seismic areas”, funded by the Italian Department of Civil Protection. The shake table testing was conducted at the ENEA, SSPT-USER-SITEC Laboratory, Rome, Italy, thanks to the active participation of Dr. Gerardo De Canio and Dr. Ivan Roselli, within the Project “CO.B.RA” funded by Lazio Region. Kerakoll SpA (Sassuolo, Italy) is acknowledged for cofounding the research and for providing reinforcement materials.

REFERENCES

- [1] D’Ayala, D.F., Paganoni, S., ‘Assessment and analysis of damage in L’Aquila historic city centre after 6th April 2009’, *Bull. Earthq. Eng.* **9** (1) (2011) 81-104.
- [2] Sorrentino, L., Cattari, S., da Porto, F., ‘Seismic behaviour of ordinary masonry buildings during the 2016 central Italy earthquakes’, *Bull. Earthq. Eng.* Doi: 10.1007/s10518-018-0370-4.
- [3] de Felice, G., De Santis, S., Lourenço, P.B., Mendes, N., ‘Methods and challenges for the seismic assessment of historic masonry structures’, *Int. J. Archit. Herit.* **11** (1) (2017) 143-160.
- [4] Babaeidarabad, S., De Caso, F., Nanni A., ‘Out-of-Plane Behavior of URM Walls Strengthened with Fabric-Reinforced Cementitious Matrix Composite’, *J. Compos. Constr.* **18** (4) (2014) 04013057.
- [5] Bellini, A., Incerti, A., Bovo, M., Mazzotti, C., ‘Effectiveness of FRCM reinforcement applied to masonry walls subject to axial force and out-of-plane loads evaluated by experimental and numerical studies’, *Int. J. Archit. Herit.* **12** (3) (2017) 376-394.
- [6] Giaretton, M., Valluzzi, M.R., Mazzon, N., Modena, C., ‘Out-of-plane shake-table tests of strengthened multi-leaf stone masonry walls’, *Bull. Earthq. Eng.* **15** (10) (2017) 4299-4317.
- [7] Gattesco, N., Boem, I., ‘Out-of-plane behavior of reinforced masonry walls: Experimental and numerical study’, *Compos. Part B Eng.* **128** (2017) 39-52.
- [8] Papanicolaou, C.G., Triantafillou, T.C., Lekka, M., ‘Externally bonded grids as strengthening and seismic retrofitting materials of masonry panels’, *Constr. Build. Mater.* **25** (2) (2011) 504-515.
- [9] De Canio, G., de Felice, G., De Santis, S., Giocoli, A., Mongelli, M., Paolacci, F., Roselli, I., ‘Passive 3D motion optical data in shaking table tests of a SRG-reinforced masonry wall’, *Earthq. Struct.* **10** (1) (2016) 53-71.
- [10] De Santis, S., Casadei, P., De Canio, G., de Felice, G., Malena, M., Mongelli, M., Roselli, I., ‘Seismic performance of masonry walls retrofitted with steel reinforced grout’, *Earthq. Eng. Struct. Dyn.* **54** (2) (2016) 229-251.
- [11] Lignola, G.P., Caggegi, C., Ceroni, F., De Santis, S., Krajewski, P., Lourenço, P.B., Morganti, M., Papanicolaou, C.G., Pellegrino, C., Prota, A., Zuccarino, L., ‘Performance assessment of basalt FRCM for retrofit applications on masonry’, *Compos. Part B Eng.* **128** (2017) 1-18.
- [12] De Santis, S., Ceroni, F., de Felice, G., Fagone, M., Ghiassi, B., Kwiecień, A., Lignola, G.P., Morganti, M., Santandrea, M., Valluzzi, M.R., Viskovic, A., ‘Round Robin Test on tensile and bond behaviour of Steel Reinforced Grout systems’, *Compos. Part B Eng.* **127** (2017) 100-120.

**International Conference on Sustainable
Materials, Systems and Structures
(SMSS 2019)**
Durability, Monitoring and Repair of Structures

High-performance repair

EXPERIMENTAL INVESTIGATION ON RC BEAMS STRENGTHENED WITH BOTTOM OR SIDE NSM FRP BARS

Thanongsak Imjai (1), Monthian Setkit (1), Navapadol Khumthong (2), Kornrit Keeratithanikkul (3) and Reyes Garcia (4)

(1) School of Engineering and Resources, Walailak University, Thailand

(2) Faculty of Civil Engineering, Kasetsart University, Thailand

(3) Faculty of Engineering, Rajamangala University of Technology Tawan-Ok, Thailand

(4) School of Engineering, University of Warwick, UK

Abstract

This paper investigates the use of Near Surface Mounted Fibre Reinforced Polymers (NSM FRP) to strengthen reinforced concrete (RC) beams. Three RC beams were tested in flexure with different configurations: one control, one strengthened with one NSM FRP bar at the soffit, and one strengthened with two NSM FRP bars on the beam sides. This paper discusses the main experimental results. It is shown that results predicted by existing analytical models match well the test results, thus confirming the effectiveness of adding bars to the sides of the beams as a potential strengthening solution.

Keywords: NSM, Side NSM, Bottom NSM, reinforced concrete, Sectional analysis

1. 1. INTRODUCTION

Near Surface Mounted Fibre Reinforced Polymers (NSM FRP) are extensively used to strengthen existing reinforced concrete (RC) structures. NSM systems involve the insertion of FRP strips or bars into pre-cut grooves filled with epoxy adhesive [1-3]. Previous research has proven the effectiveness of RC beams strengthened in flexure using NSM FRP [1, 4-7]. The results from these studies indicate that the flexural capacity of NSM FRP-strengthened specimens increases between 30-70% over control specimens, thus making NSM a very attractive strengthening solution.

NSM systems are usually applied at the soffit of RC beams or slabs. This implies that such elements should be wide enough to accommodate the necessary edge clearance and clear spacing between adjacent NSM grooves [3]. However, in many structures, beams and slabs hold suspended ceilings, air ducts, extractors and electrical wiring at their soffit [7], which reduces

the area in which the NSM FRP system can be installed. Consequently, it is necessary to explore alternative strengthening locations (other than the soffit) so as to make NSM FRP systems more versatile.

This study investigates experimentally the use of side and bottom NSM FRP reinforcement in the flexural strengthening of beams. Side NSM (SNSM) is used to overcome the limitation of bottom NSM (BNSM). The experimental results are discussed in terms of observed damage, load capacity and deflection. The effectiveness of sectional analysis at predicting the behaviour of the beams is also briefly discussed.

2. 2. CRACKED SECTIONAL ANALYSIS OF RC NSM-STRENGTHENED BEAMS

The capacity of NSM FRP-strengthened beams can be calculated using cracked sectional analysis. Force equilibrium and strain compatibility requirements [8] are used to calculate the ultimate load of original and strengthened beams.

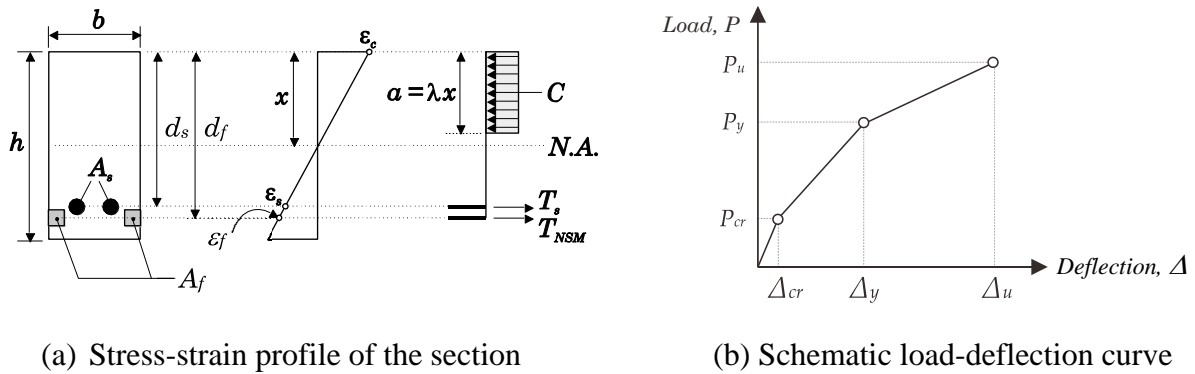


Figure 1: Sectional analysis of strengthened beam

For force equilibrium, the forces C , T_s , and T_{NSM} can be expressed in the following manner:

$$C = \lambda x \cdot b \cdot f'_c \quad (1)$$

$$T_s = A_s \cdot f_y \quad (2)$$

$$T_{NSM} = A_f \cdot E_f \cdot \epsilon_f \quad (3)$$

The moment-curvature distribution of the beam can be divided into three stages [8,9] as follows:

2.1 Pre-cracked stage: $0 \leq M_a \leq M_{cr}$

The cracking moment of the strengthened concrete beam, M_{cr} , is considered as similar to that of a non-strengthened beam by taking the tensile concrete into an account:

$$M_a = \frac{f_t I_0}{h - x_0} \quad (4)$$

The moment of inertia of the uncracked section, I_0 , can be expressed as:

$$I_0 = \frac{bx_0^3}{3} + \frac{b(h-x_0)^3}{3} + nA_s(d_s - x_0)^2 + n_f A_f (d_f - x_0)^2 \quad (5)$$

and

$$x_0 = \frac{\frac{bh^2}{2} + nA_s d_s + n_f A_f d_f}{bh + nA_s + n_f A_f} \quad (6)$$

where $n = E_s/E_c$ and $n_f = E_f/E_c$. In the above equations, b =beam width; h =beam height, A_s =steel cross-sectional area; d_s and d_f are the distances between the most compressed concrete fibre and the centre of gravity of the steel bars and the CFRP rods/strips, respectively; x_0 = distance between the most compressed concrete fibre and the neutral axis before concrete cracking; E_c , E_s , E_f are the elastic modulus of concrete, steel bars and CFRP rods, respectively; and f_t is the concrete tensile strength at 28 days.

2.2 Pre-yielded stage: $M_{cr} \leq M_a \leq M_y$

The bending moment of the strengthened section at the steel yielding level, M_y , is calculated by considering that the strain of the steel reinforcement has reached the yielding strain, according to the following equation:

$$M_y = \frac{n f_y I_c}{d_s - x_0} \quad (7)$$

The moment of inertia of the cracked section, I_c , can be expressed as:

$$I_c = \frac{bx_0^3}{3} + nA_s(d_s - x_0)^2 + n_f A_f (d_f - x_0)^2 \quad (8)$$

and

$$x_0 = \frac{-(nA_s + n_f A_f) + \sqrt{(nA_s + n_f A_f)^2 + 2b(nA_s d_s + n_f A_f d_f)}}{b} \quad (9)$$

where x_0 is the distance between the most compressed concrete fibre and the neutral axis after concrete cracking

2.3 Post-yielded stage: $M_y \leq M_a \leq M_u$

From Figure 1, the strain developed in the FRP rod/strip (ε_{NSM}) can be calculated as:

$$\varepsilon_f = \varepsilon_c \cdot \frac{d_f - x}{x} \leq \varepsilon_{fu} \quad (10)$$

where ε_f is the strain in the NSM reinforcement; ε_c is the strain of the top fibre of concrete; x is the neutral axis depth; and ε_{fu} is the ultimate strain in the NSM FRP rod/strips. The neutral axis (x) can be obtained by substituting Eq. (10) into Eq. (3), and the ultimate moment of the section (M_u) can be computed as follows:

$$M_u = A_s f_y (d_s - 0.4x) + A_{NSM} E_{NSM} \varepsilon_c \cdot \left[\frac{d_{NSM} - x}{x} \right] \cdot (d_f - 0.4x) \quad (11)$$

3. EXPERIMENTAL PROGRAMME

3.1 Details of beam specimens

Three reinforced concrete beams were tested in four-point bending. All beams had a cross section of 150×250 mm and an effective span length of 2300 mm. The bottom reinforcement consisted of two $\phi 12$ mm steel bars ($f_y = 392$ MPa). The top reinforcement in the compression zone (outside the midspan) consisted of two $\phi 9$ mm bars ($f_y = 235$ MPa), which also held vertical shear stirrups. Shear failure was prevented by adding steel stirrups (two legs) of $\phi 9$ mm at a spacing of 100 mm ($\rho_w = 0.84\%$). Beam TB1 was used as a control specimen. Specimen TB2 was strengthened using a NSM system by adding 1 CFRP rod into the pre-cut groove at the beam soffit (BNSM). Beam TB3 was strengthened using 2 CFRP bars embedded on the beam's sides (SNSM). Figure 2 shows the geometry of the beams tested in this study.

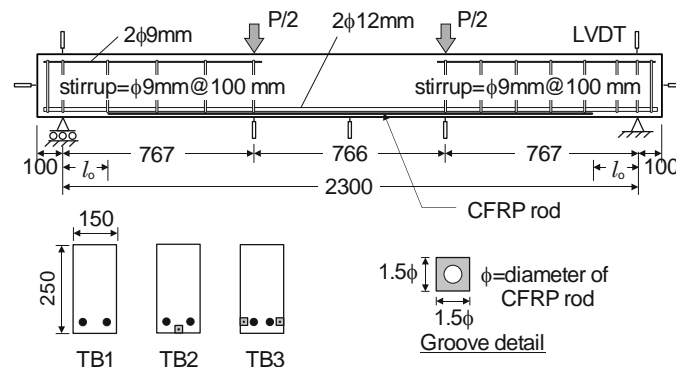


Figure 2: Typical test setup

3.2 Material properties and test setup

The beams were cast using a single batch of ready-mix concrete. The compressive strength of concrete ($f'_c = 30$ MPa) was obtained from 150 mm cubes. The indirect tensile splitting strength ($f_t = 3.1$ MPa) was determined from tests on six 150×300 mm cylinders. The flexural strength ($f_b = 4.1$ MPa) was obtained from three prisms of 100×100×500 mm tested in four-point bending. The bars used to strengthen beams TB2 and TB3 were sand coated Carbon FRP (CFRP) bars of $\phi 8$ mm. The tensile strength of the bars was 2400 MPa, and the modulus of elasticity (E_{NSM}) was 200 GPa, with an elongation at rupture (ϵ_{fu}) of 1.5%. To bond the CFRP bars to the concrete, a commercially available epoxy adhesive (Sikadur 30) was used.

The beams were tested in four-point bending to produce a constant moment at the midspan. The beams were simply supported on steel plates and rollers. The tests were performed using a UTM with a maximum capacity of 100 t in displacement control at a loading rate of 1 mm/min. Overall beam deflections were measured using Linear Variable Displacement Transducers (LVDTs), as shown in Figure 2.

4. TEST RESULTS AND DISCUSSION

Table 1 summarises the experimental results for the beam specimens strengthened by bottom (BNSM) and side (SNSM) CFRP bars. The moment, load, and deflection are reported for three stages: i) prior to cracking, ii) steel rebar yielding, and iii) maximum load. The effectiveness of the strengthening interventions is expressed as the ratio of load capacities of the strengthened

specimen over the original specimen (P/P_{TB1}). To compare the strengthening effect over the overall member cross-section, the strength effect per axial rigidity (i.e. P_u/EA) is adopted. The results in Table 1 are further discussed in the following sections.

4.1 Observed damage and capacity

As expected, the initial load produced flexural cracks at the beams' midspan. Further flexural cracks developed as the load increased, but the NSM CFRP bars limited the crack width in specimens TB2 and TB3. Failure was dominated by yielding of the tensile steel, followed by concrete crushing at the compression zone. The capacity of the NSM CFRP-strengthened specimens TB2 and TB3 was 143% and 194% higher over the control beam TB1, respectively. Only minor FRP debonding was observed in beam TB2. Figure 3 shows a typical failure of the beams.

Table 1: Summary of experimental results

Stage	Parameters	unit	TB1 (Control)	TB2 (1-BNSM)	TB3 (2-SNSM)
(i) Cracking	M_{cr}	N.mm x10 ³	6442.8	7152.3	7673.8
	P_{cr}	kN	16.80	18.65	20.01
	Δ_{cr}	mm	1.62	1.55	1.78
	$P_{cr} / P_{cr,TB1}$	-	1.00	1.11	1.19
(ii) Yielding	M_y	N.mm x10 ³	22151.0	26365.6	28532.4
	P_y	kN	57.8	68.8	74.4
	Δ_y	mm	11.4	14.2	13.3
	$P_y / P_{y,TB1}$	-	1.00	1.19	1.29
(iii) Ultimate	M_u	N.mm x10 ³	22818.3	32712.6	44275.1
	P_u	kN	59.5	85.3	115.5
	Δ_u	mm	22.4	34.5	51.9
	$P_u / P_{u,TB1}$	-	1.00	1.43	1.94
Strength effect per axial rigidity	$P_u / EA \times 10^3$	-	2.08	2.45	3.91



Figure 3: Failure of NSM FRP-strengthened beam TB2

The load-deflection curves for the tested beams are shown in Figure 4. The results show that the load-deflection curves have three slopes that characterise three stages: (i) cracking of concrete to reinforcement yielding, (ii) yielding to ultimate and (iii) ultimate to failure. Initially, the curves are linear since the beams have their full flexural rigidity. As it is shown in Table 2 and Figure 4, the first cracking loads of TB2 and TB3 were 11% and 19% higher than that of

TB1, respectively. Likewise, TB3 enhanced the first cracking load over TB2 by up to 8%. After yielding, the NSM FRP bars controlled the number and width of cracks, as the maximum tensile stress of concrete exceeded the flexural strength of concrete. Damage reduced the beams' stiffness as the load increases. The loads at yielding of beams TB2 and TB3 were 19% and 29% higher than that of TB1, respectively. The use of side NSM FRP bars (SNSM in TB3) enhanced the yield load by 8% over the beams with bottom NSM FRP bars (BNSM in TB2). At ultimate load near failure, the load gradually dropped while the deflection increased rapidly. The ultimate load of the strengthened beams was 43% (TB2) and 94% (TB3) higher over TB1, respectively. The ultimate load of TB3 was 35% higher than that of TB2. It is also evident that TB3 sustain more deflection than TB2 at failure (51.9 vs 34.5 mm, respectively). The comparison of strengthening effects per axial rigidity proved that specimen TB2 is smaller than TB3 specimen (60% greater than TB2) because the NSM reinforcement is higher than that of TB2 specimen.

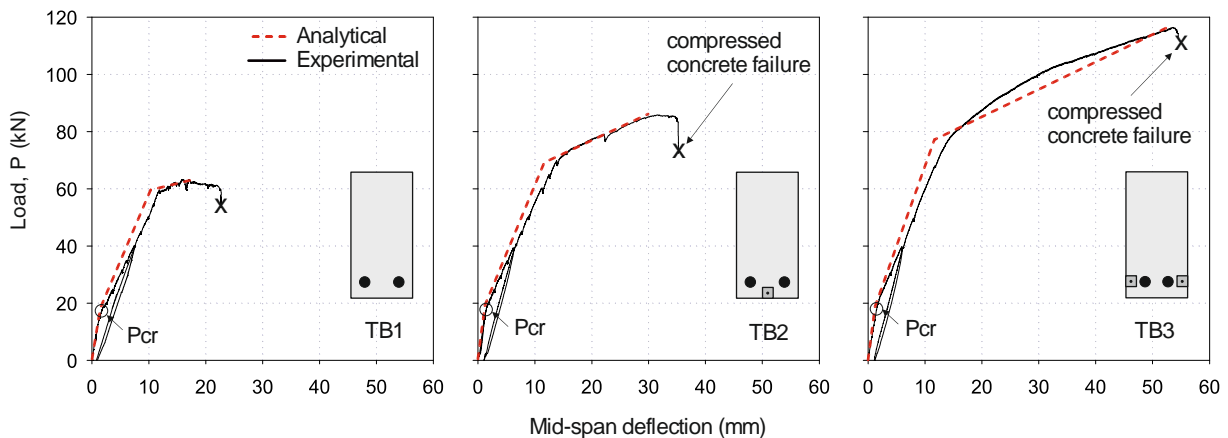


Figure 4: Comparison between experimental and analytical load-deflection curves

4.2 Comparison of experimental data and analytical analysis

Figure 4 also compares the analytical predictions given by cracked sectional analysis (CSA in section 2) with the test results. The curves predicted by CSA match well the experimental results of all beams up to a serviceability deflection $L/480=4.79$ mm [10], or about 40 kN. After such service load level, the deflections predicted by CSA for TB2 and TB3 can be underestimated by up to 15%. Such inconsistencies are due to the formation of shear cracks at higher load levels, which result in an additional component of deformation ('shear crack-induced deformations'), as reported recently by Imjai et al. [11] using results from FRP RC beams. Ongoing work by the authors focuses on improving deflection predictions (including shear) of NSM FRP-strengthened beams.

5. CONCLUDING REMARKS

It is concluded that side NSM CFRP bars can be effectively used to strengthen RC beams. The capacity of such a beam tested in this study was enhanced by 94% over a control specimen. The deflection of the beam specimens can be adequately predicted by cracked section analysis (CSA), but only up to service load. At higher load levels, CSA can significantly underestimate deflections by up to 15% due to shear crack-induced deflections.

ACKNOWLEDGEMENTS

T. Imjai thankfully acknowledges the grant support from the National Research Council of Thailand (Contract No. 560265/2560).

REFERENCES

- [1] Tang, W.C., Balendran, R.V., Nadeem, A. and Leung, H.Y. 'Flexural strengthening of reinforced lightweight polystyrene aggregate concrete beams with near surface mounted GFRP bars', *Build Environ* **41**(10) (2006) 1381–93.
- [2] Parretti, R. and Nanni, A. 'Strengthening of RC members using near-surface mounted FRP composites: design overview', *Advances in Structural Engineering* **7**(6) (2004). 469-483.
- [3] Lorenzis, De L. and Teng, J.G. 'Near-surface mounted FRP reinforcement: an emerging technique for strengthening structure', *Composites: Part B*, **38**(2) (2007).119–143.
- [4] Jung, W.T., Park, Y.H., Park, J.S., Kang, J.Y. and You, Y.J. 'Experimental investigation on flexural behaviour of RC beams strengthened by NSM CFRP reinforcements', *ACI special publication*, (2005) 230 pp.
- [5] Mahmoud, F., Castel, Francois, A. R. and Tourneur, C. 'Strengthening of RC members with near-surface mounted CFRP rods', *Composite Structures*, **91**(2) (2009) 138–47.
- [6] Housen, M.D.A., Jumaat, M.Z. and Saiful Islan, A.B.M. 'Side near surface mounted (SNSM) technique for flexural enhancement of RC beams', *Material & Design*, **83** (2015) 587-597.
- [7] Imjai, T., Chaisakulkiet, U. and Garcia, R. 'flexural strengthening of pre-cracked RC beams using side nsm cfrp bars: an experimental investigation', in 9th International Conference on Fibre-Reinforced Polymer (FRP) Composites in Civil Engineering (CICE 2018), Paris 17-19 July 2018
- [8] Bischoff, P.H. 'Re-evaluation of deflection prediction for concrete beams reinforced with steel and FRP bars', *Journal of Structural Engineering, ASCE*, **131** (2005) 363–374.
- [9] Al-Mahmoud, F., Castel, A., François, R. and Tourneur, C. 'Strengthening of RC members with near-surface mounted CFRP rods', *Composite Structures* **91** (2009) 138–147.
- [10] ACI 318-15. 'Building Code Requirements for Structural concrete and Commentary', B.M Johnson and A.H. Wilson, Terminology of Building Conservation Industry, Division of Building Research, NRC Canada, 2015.
- [11] Imjai, T., Guadagnini, M., Garcia, R. and Pilakoutas, K. 'A practical method for determining shear crack induced deformation in FRP RC members', *Engineering Structures*, 126 (2016), 253-364.

USE OF NSM FRP FOR THE STRENGTHENING OF A BRIDGE DECK – A CASE STUDY

Alejandro Pérez Caldentey (1) (2)

(1) Technical University of Madrid (UPM), Madrid

(2) FHECOR North America, USA

Abstract

The Park Central Drive Bridge is part of the LBJ Expressway located North of the city of Dallas. During the second widening of the structure, in 2013, it was decided to reinforce the existing 1960's bridge with an overlay to account for the increase in traffic loads. A bonding agent was used to help bond the new overlay with the existing concrete. However, this bonding agent did not work properly and created a discontinuity surface which has resulted in the progressive destruction of the overlay due to the intense traffic on the bridge and the need to execute emergency repairs.

To solve the problem FHECOR Consulting Engineers first made a diagnosis of the problem and proposed an innovative repair procedure based on reinforcing the overlay with carbon fibre strips inserted into vertical grooves sawed on the deck. This solution has been partially implemented and has allowed to minimize traffic disruption and environmental impact when compared with other more traditional repair possibilities.

Keywords: bridge repair, FRP, bridge maintenance, high traffic, sustainability

1. INTRODUCTION

Park Central Dr. Bridge, a typical slab and beam bridge built in the 1960's and belonging to the Lyndon B. Johnson Expressway (I-635), located in Dallas, was reported to be affected in 2016 by a pathology consisting in the appearance of large longitudinal cracks, sensibly coinciding with the plan position of the longitudinal precast girders. Additionally, some transverse cracks with small crack openings were also detected.

The current structure is the result of the widening of an existing structure. The original structure was built in the 1960's and was first widened in 2001, and then again in 2013. When the second widening was undertaken it was decided to increase the capacity of the deck to conform to the newer standards. For this, an overlay of lightweight concrete of variable depth (from 3-7/8" to 0") was designed over the existing structures. For its construction, and to have

good bond conditions with the existing slab, the 50 mm cover of the existing slab was demolished, and a bonding agent was applied between layers. The total height of the overlay concrete, considering the demolition of the cover varied from 50 to 143 mm. The longitudinal reinforcement of the overlay was placed directly on the surface of the existing structure after demolishing the cover.

In 2016, it came to the attention of the infrastructure managers that large cracks were occurring in the overlay. The cracking and ensuing deterioration of the overlay was so severe that it led to the need to execute local emergency repairs (see Figure 1). These emergency repairs were however, very ineffective and were themselves heavily damaged within a short period of time.



Figure 1: – Observed cracking and deterioration of the overlay requiring emergency repair procedures

Figure 2 shows a mapping of the cracks on the West-bound and East-bound Bridges taken in February 2016. At that point, the West-bound deck was more cracked than the East-bound one. It was also observed that cracking was evolving and affecting new girders over time.

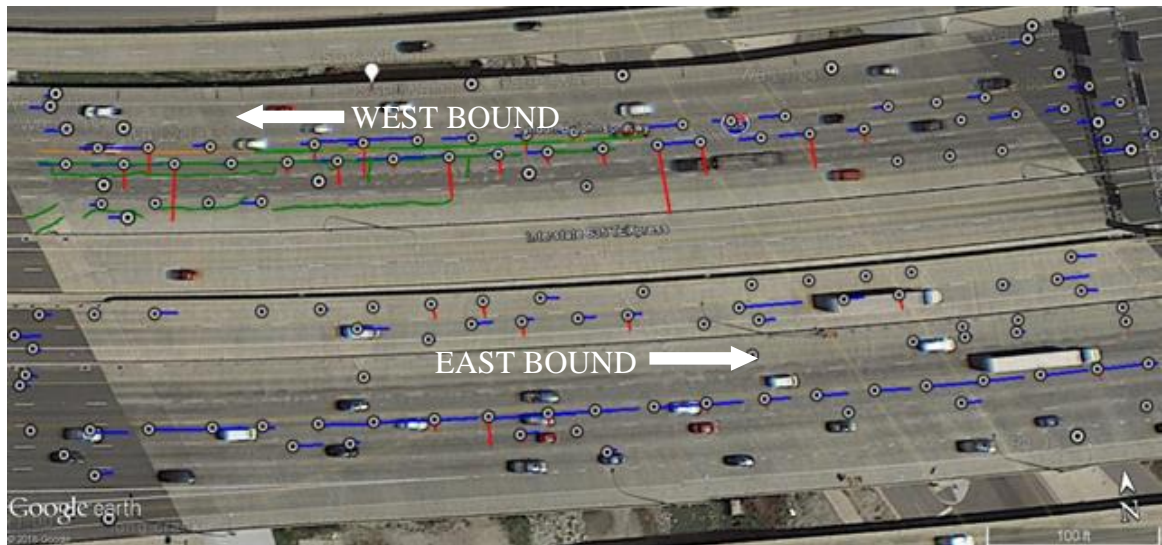


Figure 2: Comparison of cracks detected in February, in blue, and cracks mapped in the following months (in green and red).

In October 2016, FHECOR North America was contacted to help analyse and propose a solution to the observed problem.

2. ANALYSIS AND REPAIR PROPOSAL

The problem was identified as a lack of bonding between the original 1960's concrete slab and the overlay, which resulted in both elements functioning independently from each other instead of conjointly leaving the overlay virtually without negative bending capacity explaining the large longitudinal cracks along the longitudinal axis on either side of the longitudinal girders.

The lack of bonding was confirmed by cores extracted from the slab, where the two concretes, the original one from the 1960's (whiter) and the light weight concrete overlay (much darker) could clearly be distinguished and were easily separated by the interface. This feature was also observed during repair works. Because of the lack of bonding between the overlay and the original slab, instead of a thicker monolithic element the deck was performing as two separate slabs, one on top of the other. Furthermore, since the reinforcement of the overlay is placed near the bottom, this slab has virtually no resistance to negative bending, which explains why large uncontrolled longitudinal cracks appear on either side of the girders.



Figure 3: Core extraction

It is thought that the process of deterioration is as follows:

- First, longitudinal cracks form, marking the edges of the top flange of the beams, which are stiff points. These cracks form due to negative bending from traffic loads and are too large due to the lack of reinforcement near the top surface of the overlay, as explained above. Essentially the overlay is failing in negative bending at these points.
- The formation of the longitudinal cracks leaves a transversally unsupported concrete strip, on which truck wheel loads will generate longitudinal bending whose value will be increased by the possible gaps between the original slab and the overlay. It is likely that this strip will try to support itself on the transversal reinforcement bars which are placed over longitudinal bars placed directly on the original slab, forming, again, stiff points. Since the overlay lacks longitudinal reinforcement near its top fibre, uncontrolled cracks will form transversally where negative bending occurs. Most likely, this would be over the points where there is transversal reinforcement. This seemed to be what was currently occurring on the East-Bound lanes, where cracks seem to mirror the reinforcement spacing, as can be seen in the photograph of Figure 4.



Figure 4: Cracking pattern in one of the East-bound lanes

- As a result, the concrete overlay is divided into rectangular chunks, essentially broken at their edges. The fact that the crack widths are very large due to the lack of reinforcement makes them vulnerable to deterioration from passing traffic. Their width increases due to repeated loading and impact, forming even more cracks and eventually destroying the concrete.

Due to the large problem of interrupting traffic on a major congested highway for repair, FHECOR North America proposed to limit the reconstruction of the overlay using traditional repair procedures (reconstruction) to the more damaged areas and to reinforce the overlay where damage was still minor using Near Surface Mounted (NSM) Fibre Reinforced Polymer (FRP) strips placed in the transversal direction in order to provide the overlay with negative bending capacity, thereby stopping the deterioration process (see Figure 5). This type of technique has been studied since the late 1990's [1] and has been demonstrated in several real bridge applications [2], [3].

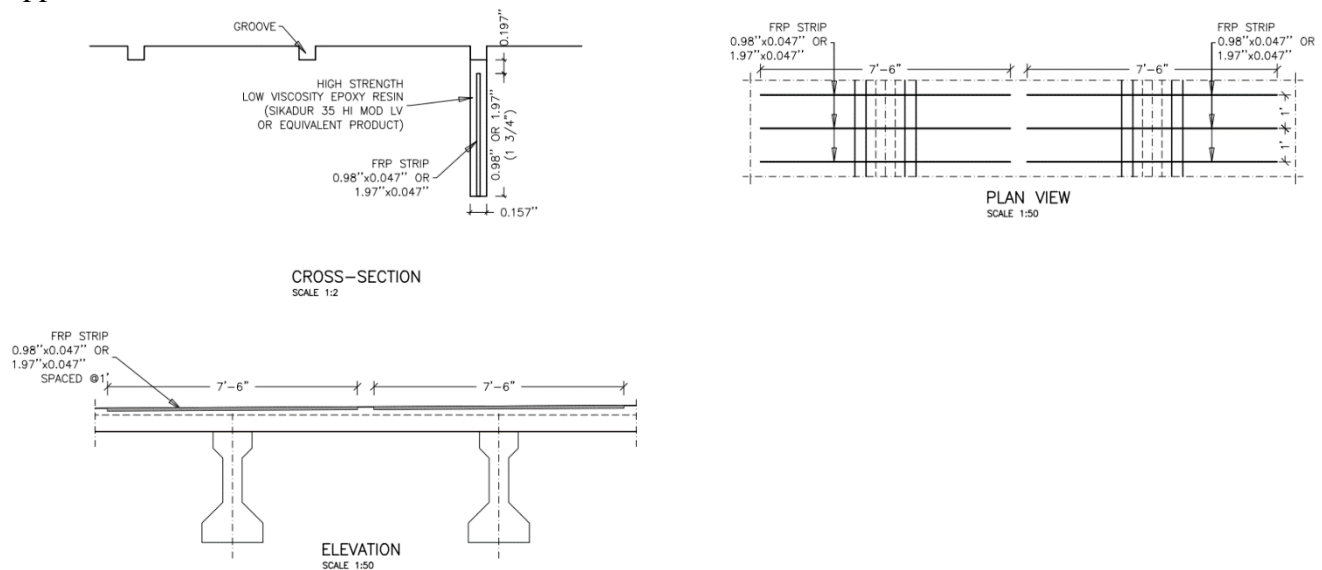


Figure 5: Reinforcement using NSM FRP strips

3. EXECUTION OF REPAIR WORKS

Due to the continuation of the deterioration process, the area to be repaired by traditional means increased with time. Finally, about 40% of the overlay area had to be rebuilt in 14 different weekend operations spanning from September 2017 to July 2018, with a forced break in winter due to low temperatures not allowing to open traffic in time.

For each operation, the reconstruction process began at 21:00 hours on Friday morning and had to be completed, achieving a minimum concrete resistance of 19.3 MPa, by 6:00 on Monday morning, with 24-hour shifts, and involved the following phases (see Figure 6):

- Marking of the area to be demolished.
- Saw cutting of the perimeter.
- Milling of the concrete to a depth of about 3”.
- Hydrodemolition of the rest of the overlay, until full removal of the defective bonding agent. The remaining interface surface was roughened using pneumatic hammers where the roughness obtained from hydrodemolition was insufficient.
- Replacement of the overlay reinforcement.
- Concreting and curing.



Figure 6: Demolition and reconstruction of overlay – from left to right, top to bottom: Saw cutting of demolition perimeter, milling machine, result of milling, hydrodemolition machine, aspirator truck helping clear debris, left-over rough surface showing original slab, new reinforcement mat in place, and concreting.

Installation of FRP strips was much less disruptive and could be done in overnight operations during the week. It involved the following steps:

- Using a saw disk, execution of vertical slots having 2.3 m in length, centred over the beams and having a width of 4 mm and a height of 55 mm, if the thickness of the overlay is more than 100 mm and 30 mm if the thickness of the overlay is less than 100 mm.
- Proper cleaning of the slots using oil-free compressed air
- Filling of the slots with a low-viscosity, high strength epoxy resin, such as Sikadur 35 HI MOD LV, or an equivalent product.
- Insertion of the FRP strips (either $25 \times 1.2 \text{ mm}^2$ or $50 \times 1.2 \text{ mm}^2$), having a characteristic strength greater than 2800 MPa, and a modulus of elasticity of 165000 MPa.
- Curing of the epoxy resin. There was some concern regarding the possible negative effect that vibrations due to traffic could have on the curing of the epoxy resin. However, experience has shown this not to be a problem.

For the connection between the rebuilt overlay and the FRP reinforced remaining overlay, FRP strips having a section of $25 \times 1.2 \text{ mm}^2$ and a length of 1000 mm, were placed perpendicular to the interface between repaired and remaining overlays every 300 mm.

Figure 7 shows the tests that were carried out to demonstrate the procedure before implementation on the bridge, and Figure 8 shows a saw cut of the test slab, where the FRP strip is well placed and fully monolithic with the slab.



Figure 7: Test installation – from left to right: saw cuts, mixing of epoxy resin, FRP strip introduced and maintained in place using wires, filling of the slot with epoxy resin and result

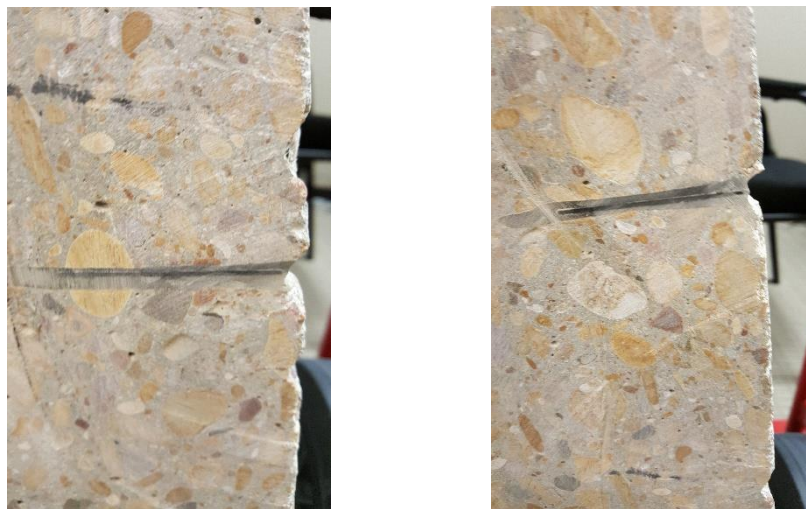


Figure 8: Saw cut of test slab showing the FRP strip well positioned with respect to the slot and excellent bonding with the base concrete

Due to the innovative character of the repair proposed, the area reinforced with NSM FRP strips will be monitored every 6 months. The outlook is good as the engineering team had a chance to supervise the behaviour of an area that was reinforced 6 months previously when supervising one of the overlay reconstruction operations and there was no observable deterioration since the installation of the FRP strips (see Figure 9).



Figure 9: Area repaired after 6 months or traffic. On the two pictures on the left one of the large longitudinal cracks along the beam can be observed being crossed by the FRP strips. No further deterioration was observed since the installation of the NSM FRP strips.

4. CONCLUSIONS

From the above discussion the following considerations can be made:

- Strengthening of the wear surface of bridge deck slabs with NSM FRP strips to solve a problem such as that described in this paper has many advantages: it is an innovative technique which is clearly superior to rebuilding in terms of traffic disruption, especially in a congested highway, and, also very importantly, in terms of sustainability.
- The non-traditional character of the proposed solution, however, has sparked resistance from the infrastructure managers, which, despite all, have accepted the solution given its clear advantages. However, in agreement with FHECOR an inspection program has been set up to monitor the proper functioning of the reinforced slab in the long term.
- Such experiences should help provide confidence in the good behaviour this type of solutions and should help make them part of tomorrow's standard practices.

REFERENCES

- [1] De Lorenzis, L., and Nanni, A., 'Strengthening of Reinforced Concrete Beams with Near-Surface Mounted Fiber-Reinforced Polymer Bars', Structural Journal, ACI, V. 98, No. 1, pp. 60-68, 2001.
- [2] Soliman, S.M., El-Salakawy, E. and Benmokrane, B. 'Bond performance of Near Surface Mounted FRP bars', ASCE J. of Composites for Construction, Vol. 15, Issue 1 (February 2011).
- [3] Alkhrdaji, T., Nanni, A., Chen, G., and Barker, M. 'Upgrading the transportation infrastructure: Solid RC Decks Strengthened with FRP', Concrete International: Design and Construction, Vol. 21, No.10, Oct. 1999, pp. 37-41.

EFFECT OF CORNER RADIUS ON THE AXIAL BEHAVIOR OF FRCM-CONFINED MEMBERS

Jaime Gonzalez-Libreros (1), Flora Faleschini (1,2), Mariano A. Zanini (1), and Carlo Pellegrino (1)

(1) Department of Civil, Environmental and Architectural Engineering, University of Padua, Italy

(2) Department of Civil, Environmental and Architectural Engineering, University of Padua, Italy

Abstract

Recent research has shown that an increase in the axial strength of concrete compression members can be achieved with the confinement of such members by means of fibre reinforced cementitious matrix (FRCM) composites. Unfortunately, the available experimental evidence on the topic is still scarce, and a significant research effort is needed in order to fully understand the behaviour of FRCM-confined members.

For instance, for the case of fibre reinforced polymer (FRP) composites it has been shown that the gain in strength is directly proportional to the corner radius of the elements. However, the influence of this parameter on the effectiveness of the FRCM-confinement has not been deeply investigated.

Based on this need, the results of an experimental campaign on FRCM-confined concrete members with four different radius corners (i.e., four different cross-sections) tested under monotonic compression are presented in this paper. Values of axial strength of the confined members are compared to that of unconfined control specimens and the influence of the confinement and the corner radius in the gain in axial strength is discussed. In addition, the behaviour of the confined members is analysed in terms of type of failure mode attained depending on the corner radius of each specimen.

Keywords: FRCM composites, confinement, corner radius, concrete, strengthening

1. INTRODUCTION

The effectiveness of fibre reinforced polymer (FRP) composites for the confinement of existing reinforced concrete (RC) structures has been the focus of extensive research in the previous decades [1]–[3]. Results have shown that the use of such composites is able to provide

adequate gain in axial strength and a significant increase in the element ductility [4]. The reason is that when an element is wrapped with FRP composites with the fibres aligned transversely to the longitudinal direction of the element, the transverse or hoop fibres provide an effect similar to that of conventional spiral or tie reinforcing steel [5], restraining the concrete from dilating laterally.

When compared to more traditional strengthening techniques used for the confinement of RC elements such as concrete and steel jacketing, FRP composites show extremely high strength-to-weight ratio, good corrosion behaviour, electromagnetic neutrality, high tailorability and are easier to apply [2]. However, some drawbacks of the technique such as poor behaviour at temperatures near or above the glass transition temperature, poor compatibility with the substrate, inability to apply onto wet surfaces or at low temperatures, and difficulty in carrying out post-earthquake assessment of damaged structures have been pointed out [6]. These disadvantages have been linked mainly to the use of organic resins and therefore in recent years there has been a growing interest in developing new strengthening techniques that overcome these drawbacks guarantying an adequate structural performance of the strengthened elements. Among these new techniques, fibre reinforced cementitious matrix (FRCM) composites, in which the organic resins are replaced by cementitious ones, have shown promising results [7]–[9].

When the behaviour of FRP and FRCM confined specimens is compared, the limited available experimental research has shown that FRCM wraps provide a lower increase in the in strength and ductility but present a less abrupt failure mode [10]. However, an important research effort is still required to understand the behaviour of FRCM-confined specimens. For instance, for the case of FRP composites, it has been shown that the effectiveness of the system is strongly related to the section corner radius, with a higher increase for specimens with circular sections, i.e., corner radius equal to the section radius, or square sections with larger corner radius [1], [11]. However, the influence of this variable for the case of FRCM-confined specimens has not been deeply studied.

In this paper, the results of an on-going experimental campaign carried out on FRCM-confined specimens are presented. Considering the influence of the section geometry on the performance of FRP-confined specimens, variables studied included the cross-section shape and the section corner radius. To this aim, cylindrical, and square concrete specimens with three different corner radii (evaluated before strengthening procedure) were casted, confined using Carbon FRCM composites and then tested under axial compression. Results are discussed in terms of gain in strength with respect to the unconfined specimens and witnessed failure modes.

2. EXPERIMENTAL PROGRAM

A total of 24 specimens were included in the experimental campaign presented in this paper and were divided in four different series (S3, S4, S5, S6) depending on the cross-section geometry. In each series, three specimens were confined using two layers of carbon FRCM composites while the remaining three worked as control specimens, i.e., were not confined. Series S3 is comprised of concrete cylinders of 150 mm diameter and 300 mm height. Series S4, S5, and S6 had a square section with side equal to 150 mm, height of 300 mm, and corner radius, r_c , equal to 0, 22, and 38 mm, respectively. The corner radius ratio, defined as the ratio of the corner radius to the half breadth of the column ($2r_c/b$) are equal to 1.0 for series S3, 0.0 for series S4, 0.29 for series S5, and 0.51 for series S6. For all the specimens, the specimen

breadth (b) is equal to 150 mm. The specimens were designated according to the convention: XC-Sa-D0-#, where XC indicates if confinement was provided to the specimen (NC= Not confined, C= confined using carbon fibres), Sa indicates the series (S3, S4, S5, S6), D0 indicates that the specimens were not pre-damaged before testing, and # is the specimen number.

2.1 Materials

The specimens were casted using Portland cement type I 32.5N with a maximum aggregate size of 12.5mm. The concrete mixture was designed to produce specimens with low unconfined concrete strength, typical of many existing RC structures, thus for this reason a relatively high w/c ratio and low cement dosage were used. Average concrete strength was equal to 16.8 MPa, obtained from the unconfined cylinder specimens (Series S3) according to the specifications given in EN-12390-3 [12].

The FRCM composite was comprised of balanced bidirectional carbon sheets embedded in a fibre-reinforced cementitious matrix. The overall area weight (W), elastic modulus (E_f), tensile strength (f_u), ultimate strain, ($\varepsilon_{f,u}$) and equivalent nominal thickness (t) of the fibres as reported by the manufacturer were 2200 g/m², 240 GPa, 4700 MPa, 1.8%, and 0.047 mm, respectively [13]. The mechanical characteristics of the cementitious matrix were obtained using 40x40x160 mm prisms according to standards EN-12390-3 [12] and EN-12390-5 [14]. The prisms were casted and tested within four days from the confinement and testing of the concrete specimens. Average values of flexural strength (f_{fm}) and compressive strength (r_{cm}) were 5.23 MPa (COV=0.103) and 22.8 MPa (COV=0.117) respectively.

2.2 Confinement procedure

The first layer of the cementitious matrix was applied on the surface of the specimens after it was superficially damped, as shown in Figure 1a. The first layer of carbon fibres was then applied directly on the matrix while this was still fresh (see Figure 1b), and slightly pressed and then covered by a second layer of cementitious matrix. The procedure was then repeated for the second fibres layer and last cementitious matrix layer (see Figure 1c). The surface of the FRCM composite was then superficially wetted and the specimens were covered by a wet cloth that was removed seven days after the confinement procedure took place. The overlapping length of the fibres was set equal to 150 mm.

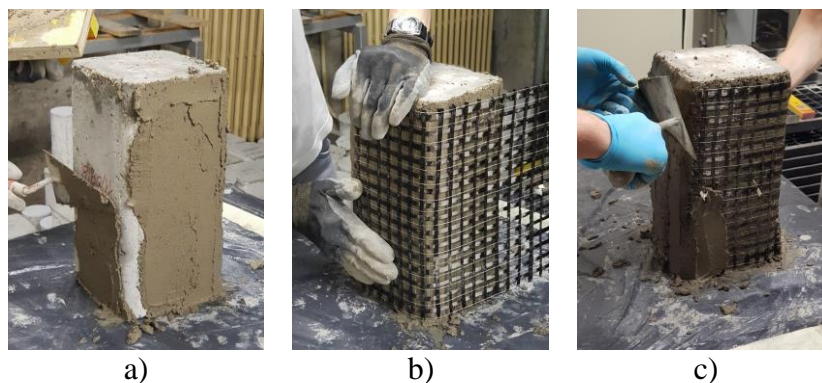


Figure 1: Confinement procedure: a) placement of the first layer of matrix, b) placement of carbon fibres; c) placement of matrix on top of the carbon fibres

2.3 Test set-up

All specimens were tested monotonically under uni-axial loading by means of a hydraulic press with a total capacity of 600 kN. The load was applied using a constant displacement rate of 0.01 mm/s. Axial strains until peak load were measured by means of three strain transducers, named “ST” in Figure 2a, applied directly onto the concrete or FRCM surfaces. After peak load, it was observed that for the confined specimens, measurements obtained from ST instrumentation were highly affected by the cracking of the FRCM confinement. Consequently, two linear voltage displacement transducers (LVDTs), shown as well in Figure 2b, were placed between the two pressing plates and were used to measure axial strains from peak load until the end of the test.

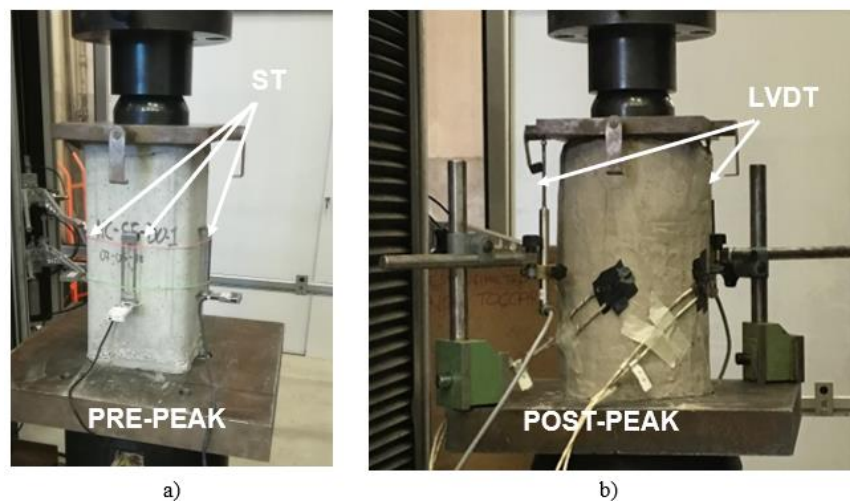


Figure 2: Test set-up: a) strain transducers disposition, b) LVDTs disposition.

3. RESULTS AND DISCUSSION

3.1 Failure mode

Figure 3 presents the cracking pattern observed on the FRCM surface after testing for specimens C-S3-D0-3 and C-S5-D0-1. In all confined specimens, cracks run mainly vertically along the specimen height and were formed before peak load was reached. This behaviour is in agreement with the available experimental evidence regarding carbon FRCM confined elements [7]. After forming, cracks start to wide slowly with the increase in the axial deformation of the specimens. Detachment between the FRCM and the concrete substrate was not observed for any of the specimens, even though the surface was not prepared, i.e., grinded, before the composite was applied.

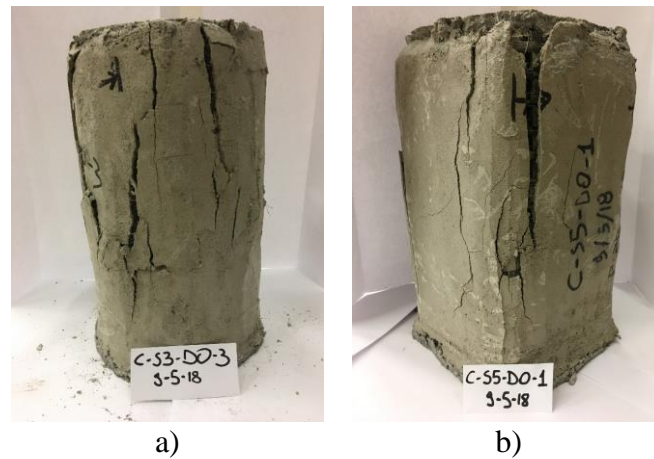


Figure 3: Failure mode for specimens: a) C-S3-D0-3, b) C-S5-D0-1

For specimens in Series S3, cracks were distributed along the element perimeter, but start forming on or around the end of the fibre overlapping area. For square cross-section specimens, indistinctly of the corner radius, cracks started forming over the specimen edges and were mainly located in this area, which might be related with a stress concentration in this region.

3.2 Axial strength gain

Table 1 summarizes the values of unconfined (f_{c0}) and confined (f_{cc}) average compressive strengths for specimens in Series S3, S4, S5, and S6. Average confined/unconfined compressive strength ratios, f_{cc}/f_{c0} , are also shown in Table 1. Axial stress vs. Axial strains responses of the tested specimens are presented in Figure 4.

Table 1: Average values of f_{c0} , f_{cc} , and f_{cc}/f_{c0} for S1, S2, S3, and S4

SPECIMEN	f_{c0} (MPa)	COV	SPECIMEN	f_{cc} (MPa)	COV	f_{cc}/f_{c0}
NC-S3-D0-1	16.8	0.018	C-S3-D0-1	22.3	0.055	1.32
NC-S3-D0-2			C-S3-D0-2			
NC-S3-D0-3			C-S3-D0-3			
NC-S4-D0-1	13.3	0.040	C-S4-D0-1	15.7	0.065	1.18
NC-S4-D0-2			C-S4-D0-2			
NC-S4-D0-3			C-S4-D0-3			
NC-S5-D0-1	13.7	0.041	C-S5-D0-1	17.2	0.106	1.25
NC-S5-D0-2			C-S5-D0-2			
NC-S5-D0-3			C-S5-D0-3			
NC-S6-D0-1	14.0	0.067	C-S6-D0-1	18.3	0.156	1.31
NC-S6-D0-2			C-S6-D0-2			
NC-S6-D0-3			C-S6-D0-3			

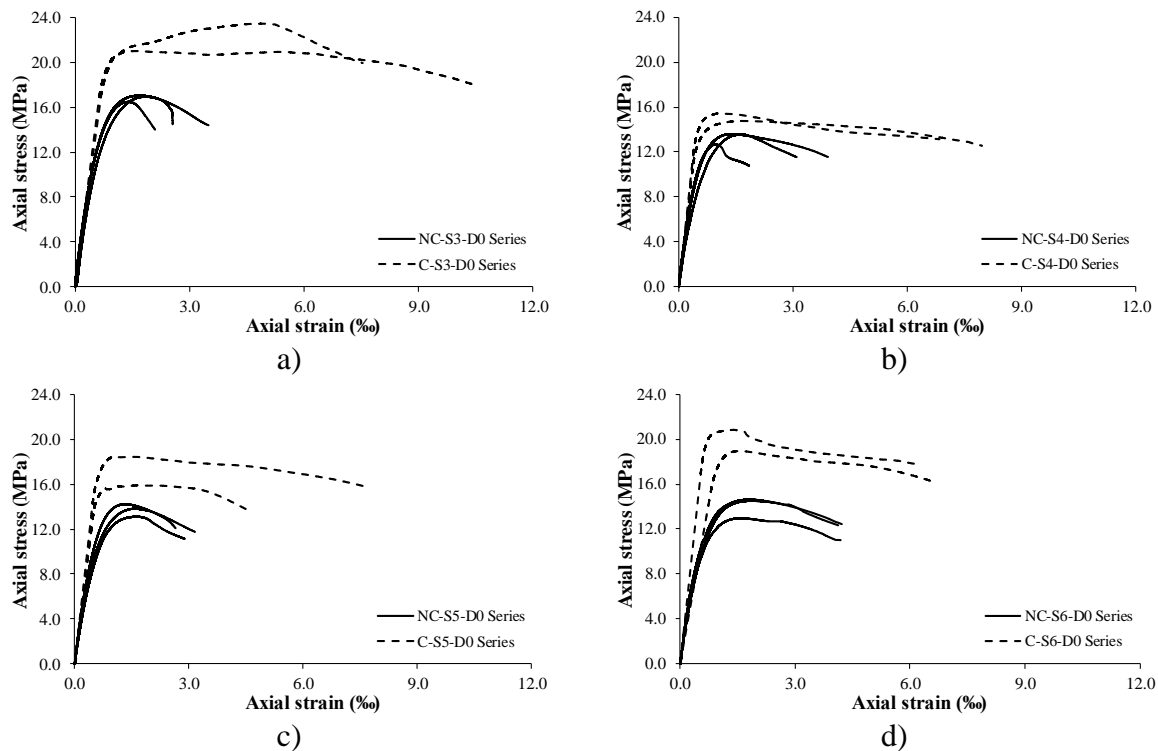


Figure 4: Axial stress vs. Axial strain curves for series: a) S3; b) S4; c) S5; d) S6

Results in Table 1 and Figure 4 show that the FRCM confinement provides an increase in the axial strength for all confined specimens. This result is observed regardless of the cross-section shape but the higher increase, i.e., the higher value of f_{cc}/f_{c0} ratio, is observed for the cylindrical specimens (see section 3.3). Figure 4 also shows that the confinement can increase significantly the ultimate axial strains at failure.

3.3 Corner radius effect

Figure 5 presents the f_{cc}/f_{c0} ratio vs. corner radius ratio curve. According to Figure 5, the influence of the corner radius ratio in the strength gain is important up to a value of corner radius ratio of 0.50, with higher values of f_{cc}/f_{c0} ratios obtained when the corner radius ratio is increased. After this point, the influence of this variable on the FRCM system effectiveness seems to be negligible, as values of f_{cc}/f_{c0} ratios for series S3 and S6 are almost the same (1.32 and 1.31, respectively). It should be noted, however, that only a 11% difference on the f_{cc}/f_{c0} ratios was found for specimens in series S3 ($r_c=75$ mm) and S4 ($r_c=0$ mm).

When these results are compared to those reported for FRP-confined specimens, important differences are found. For instance, Wang and Wu [11] showed that values of f_{cc}/f_{c0} are also directly proportional to the corner radius ratio but do not have a defined point after which the influence of this variable can be neglected. In addition, they did not witness a gain in axial strength for specimens with sharp corners ($2r_c/b=0$), while for specimens of series S4 in this paper, the average f_{cc}/f_{c0} ratio was equal to 1.18.

This is explained because the stress concentration around the corners in FRP-confined elements causes the premature fracture of the fibres, reducing the effectiveness of the confinement, being this effect more pronounced for specimens with smaller corner radius. For

the case of FRCM-confined specimens studied in this paper, even though there is still a significant stress concentration in this area, as proved by the development of cracks in the matrix around the corner regions (see Figure 3b), fibre rupture is not attained. Instead, failure of the FRCM system is achieved by progressive slippage of the fibres in the matrix-fibre interface as the cracks widen, irrespectively of the corner radius of the section.

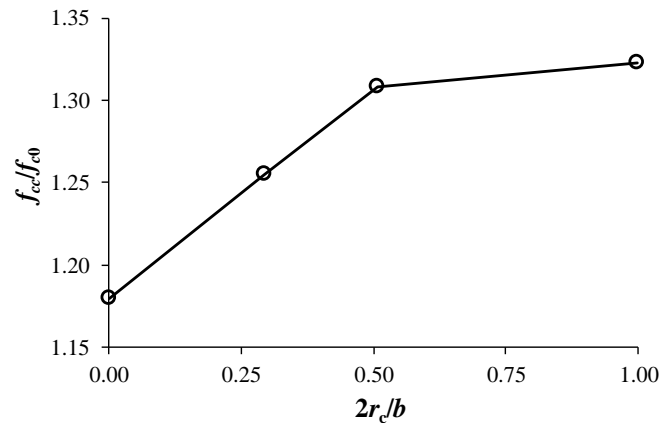


Figure 5: Effect of corner radius ratio on the confinement: f_{cc}/f_{c0} vs. corner radius ratio curve

4. CONCLUSIONS

- Results show that the FRCM confinement can provide an increase in the axial strength of concrete specimens, irrespectively of the section corner radius. Maximum and minimum values of confined to unconfined compressive strengths were equal to 1.32, obtained for cylindrical specimens, and 1.18, found for square specimens with sharp corners.
- In addition to the gain in axial strength, FRCM-confined specimens showed an increase in axial strains at ultimate load when compared to their unconfined counterparts.
- For both cylindrical and square sections shapes, the cracking pattern of the FRCM-confined specimens at failure was characterized by vertical cracks visible on the cementitious matrix surface that run vertically along the height of the specimens. For cylinders, these cracks were located mainly around the end of the fibre overlapping area, while for square elements, cracks were concentrated on the section corners.
- According to the results presented in this paper, higher increases on the axial strength of confined specimens are obtained when the corner radius ratio is increased. However, for larger corner radius ratios (0.50 in this paper), the influence of the cross-section corner radius on the confinement effectiveness might be neglected.

ACKNOWLEDGEMENTS

The authors wish to thank master students Filippo Andreose and Piervittorio Facco for their assistance in the experimental program. G&P Intech of Altavilla Vicentina (Italy) is gratefully acknowledged for providing the FRCM composite materials.

REFERENCES

- [1] C. Pellegrino and C. Modena, “Analytical Model for FRP Confinement of Concrete Columns with and without Internal Steel Reinforcement,” *J. Compos. Constr.*, vol. 14, no. 6, pp. 693–705, 2010.

- [2] L. De Lorenzis and R. Tepfers, "Comparative study of models on confinement of concrete cylinders with fiber reinforced polymer composites," *J Comp Constr*, vol. 7, no. 3, pp. 219–237, 2003.
- [3] R. Realfonzo and A. Napoli, "Concrete confined by FRP systems: Confinement efficiency and design strength models," *Compos. Part B Eng.*, vol. 42, no. 4, pp. 736–755, 2011.
- [4] S. Pantazopoulou *et al.*, "Confinement of RC elements by Means of EBR FRP systems," in *Design Procedures for the Use of Composites in Strengthening of Reinforced Concrete Structures: State-of-the-Art Report of the RILEM Technical Committee 234-DUC*, C. Pellegrino and J. Sena-Cruz, Eds. Springer, 2016, pp. 131–194.
- [5] ACI Committee 440, *Guide for the design and construction of externally bonded FRP systems for strengthening concrete structures*, ACI 440.2R. Farmington Hills, MI., 2008.
- [6] T. C. Triantafillou and C. G. Papanicolaou, "Shear strengthening of reinforced concrete members with textile reinforced mortar (TRM) jackets," *Mater. Struct. Constr.*, vol. 39, no. 285, pp. 93–103, 2006.
- [7] J. Gonzalez-Libreros, C. Sabau, L. H. Sneed, and C. Pellegrino, "Effect of Confinement with FRCM Composites on Damaged Concrete Cylinders," in *RILEM Bookseries*, vol. 15, V. Mechtcherine and P. Kabele, Eds. Springer, Dordrecht, 2018.
- [8] J. H. Gonzalez-Libreros, L. H. Sneed, T. D'Antino, and C. Pellegrino, "Behavior of RC beams strengthened in shear with FRP and FRCM composites," in *RILEM Bookseries*, vol. 15, Elsevier Ltd, 2017.
- [9] F. Faleschini, J. H. Gonzalez-Libreros, M.A. Zanini, L. Hofer, L. H. Sneed, C. Pellegrino, "Repair of severely-damaged rc exterior beam-column joints with FRP and FRCM composites", *Comp. Struct.* doi:10.1016/j.compstruct.2018.09.059, 2018.
- [10] P. Colajanni, M. Fossetti, and G. Macaluso, "Effects of confinement level, cross-section shape and corner radius on the cyclic behavior of CFRM confined concrete columns," *Constr. Build. Mater.*, vol. 55, pp. 379–389, 2014.
- [11] L. M. Wang and Y. F. Wu, "Effect of corner radius on the performance of CFRP-confined square concrete columns: Test," *Eng. Struct.*, vol. 30, no. 2, pp. 493–505, 2008.
- [12] EN-12390-3, *Testing hardened concrete-Part 3: Compressive strength of test specimens*. Brussels, Belgium: EUROPEAN COMMITTEE FOR STANDARDIZATION, 2009.
- [13] G&PIntech, "Technical datasheets," 2017. [Online]. Available: <http://www.gpintech.com/>. [Accessed: 19-Jan-2017].
- [14] EN-12390-5, *Testing hardened concrete - Part 5: Flexural strength of test specimens*. Brussels, Belgium: EUROPEAN COMMITTEE FOR STANDARDIZATION, 2009.

REHABILITATION OF AN OLD STEEL RAILWAY BRIDGE USING UHPFRC – MATERIAL CHARACTERISTICS AND CASTING TECHNOLOGY

Aljoša Šajna (1), Irina Stipanović Oslaković (2, 3), Henar Martín-Sanz (4), Domagoj Damjanovic (5)

(1) Slovenian National Building and Civil Engineering Institute, Ljubljana, Slovenia

(2) Infra Plan Consulting, Zagreb, Croatia

(3) University of Twente, Faculty of Engineering Technology, Enschede, Netherlands,

(4) Department of Civil, Environmental and Geomatic Engineering (IBK), ETH Zurich, Switzerland

(5) University of Zagreb Faculty of Civil Engineering, Zagreb, Croatia

Abstract

The variety of UHPFRCs (Ultra High Performance Fibre Reinforced Concretes) represents a powerful family of modern cementitious materials, which have proven their superior characteristics over the past 20 years, especially when fast, durable and sustainable rehabilitation of infrastructure is required.

Recently, an in house UHPFRC mix was used for strengthening an existing 9 m long steel railway bridge by casting a thin slab over the main steel girders. The bridge was brought from the railway track to the laboratory where it was meticulously inspected as well as dynamically and statically tested. Based on these observations, a strengthening slab was designed, according Swiss and European technical specifications. Next the UHPFRC formula was designed, taking into consideration the design requirements and the technological limitations, such as mixing, transporting and casting. After the rehabilitation, the bridge was thoroughly inspected and tested again, to evaluate the design model and the efficiency of the rehabilitation.

In this paper the UHPFRC design, mixing, transporting and casting procedures and the material characteristics are presented. Furthermore, the most relevant outcomes of the bridge structural assessment after the addition of UHPFRC deck are described.

Keywords: steel bridge, UHPFRC, concrete-steel composite structure, strengthening, concrete works

1. INTRODUCTION

Nowadays, the current European railway network consists a high percentage of bridges built more than 50 years ago, which were not designed for current loads and high speed trains. These are mainly bridges made of hot rolled steel or cast iron, mainly connected by means of rivets. Due to economic and environmental reasons, extending the service life of these structures proves beneficial, in opposite to demolishing or reconstructing them. A well established idea when strengthening existing steel bridges relies on adding a bearing deck connecting the main girders without replacing them. [1-4]

The family of Ultra-High Performance Fibre Reinforced Concrete (UHPFRC) materials has been increasingly applied for rehabilitation projects over the past two decades, proving itself as a reliable, cost efficient and sustainable alternative against conventional methods, but mostly for strengthening and rehabilitation of concrete structures [5-7]. In this work, the UHPFRC strengthening of a real-world case steel bridge is presented. The initial research work has been done within the EU 7th Framework Programme call SST.2011.5.2-6 Cost-effective improvement of rail transport infrastructure research project SMART RAIL. [8, 9] The concept of strengthening steel bridge sections by transforming them into a composite section has been developed earlier [1, 2], while the innovation of this research lies in the use of UHPFRC for the construction of a composite deck.

The reason for using an UHPFRC for the strengthening of a steel railway bridge, apart from its demonstrated mechanical properties, is the fact that the deck is not reinforced with a standard reinforcement net, and it is expected that the procedure related to the execution of deck cast in situ will be shorter in relation to the standard reinforced-concrete deck. Therefore, the railway line will be closed to traffic for a shorter period of time, rendering not only economical but further advantages for the users. And probably most important, the UHPFRC deck height is less than the standard reinforced-concrete deck height, which minimizes problems related to adjustment of the track substructure geometry to the new height of the bridge. The described strengthening concept has been tested in the laboratory on the 60 years old bridge superstructure which has been removed from its original location on the railway route in Croatia (Figure 1a and b).

The old steel railway bridge superstructure, originally built in 1953, composed of 2 main steel girders of “I” shape, was newly thoroughly assessed and the rehabilitation intervention redesigned. The results of the assessment and the re-design procedure are presented in [10].

In this paper the rehabilitation procedure of the steel railway bridge starting from UHPFRC design, welding of studs, mixing, transporting and casting of concrete, and the UHPFRC characteristics are presented. Furthermore, the most relevant information about the rehabilitation effect on the bridge performance is described.



Figure 1: Original bridge on site (a, b) and in the lab (right)

Although all rehabilitation works were performed in the lab, they were carried out as they would be on-site, in order to a) check and prove the feasibility of the proposed rehabilitation method, b) enable the evaluation of the railway closure time and c) deliver valuable data for LCC and LCA assessments.

2. PRELIMINARY WORKS ON THE BRIDGE

The preliminary works conducted before casting of the UHPFRC deck, consisted on several phases. Firstly two rows of steel studs were welded on the upper flange of the steel girders. Secondly, a formwork was built up and finally, secondary minimum reinforcement in transverse direction was deployed. Before casting the UHPFRC, sensors were embedded inside the slab, to determine temperature and shrinkage during the drying and strengthening process.

The preparation procedure consisted of

- cleaning and painting of the steel structure, and welding of studs,
- building-up the formwork,
- fixing secondary reinforcement in transverse direction and
- instrumentation of the bridge for static and dynamic testing.

After the bridge has been transported to the laboratory of Institute IGH, Zagreb, Croatia, where first structural assessments had been performed [9], the steel structure was sandblasted and painted, see Figure 2a.

Once the initial assessment was completed, the bridge was moved to the laboratory of Slovenian National Building and Civil Engineering Institute (Figure 1c).

For improving the load transfer between the steel girders and the concrete slab, steel studs have been welded on the upper flange of the girders. The commercially available studs were shortened to a length of 55 mm, to fit into the concrete slab of designed thickness of 70 mm. Two rows of studs with an axial distance of 100 mm were welded on each girder using standard welding procedure (Figure 2b).

The formwork for the slab was set-up as it would be done on-site, i.e. the formwork was supported by the steel girders only (Figure 2c).

The concrete slab was in the transverse direction reinforced with re-bars of $\phi 12$ mm at a spacing of 250 mm. The reinforcement was placed 2 cm under the designed upper surface of the slab.



Figure 2: a) Bridge cleaned and painted, b) Welded studs, c) Secondary reinforcement and the formwork

3. UHPFRC MATERIAL

3.1 Raw materials and mix design

The UHPFRC designed within the SMART RAIL project was adapted to the requirements of the new design, following the recommendations from the ARCHES project [12].

As the thickness of the slab was designed to be 70 mm, locally available dolomite aggregate of maximum size of 4 mm was selected. In order to minimize the environmental impact of the concrete (CO₂ footprint), locally available raw materials (cement, limestone filler, superplasticizer) were selected.

Due to the refinement of the design, a lower amount of reinforcement was needed in comparison with more traditional concrete constructions. This in turn provides an undemanding slab geometry from the concrete workability point of view, allowing to eliminate this factor as a critical design item. The pumpability of the concrete was not an issue, as the casting was planned to be performed by concrete bucket.

The selected concrete mix is presented in Table 1. Fresh concrete properties were determined as follows: the slump (acc. EN 12350-2), the air content (acc. EN 13950-7) and the density. The concrete had a slump of 190 mm, air content of 3.3 % and density of 2620 kg/m³.

Table 1: Selected concrete mix proportion

Raw material	Supplier	Type	kg/m ³
Cement	Salonit Anhovo	CEM I 52,5	536
Silica fume	Kema Puconci	Mikrosilica	107
Limestone filler	Apnenec d.o.o.	Kalcevita	697
Sand	Trgograd d.o.o.	Dolomite, 0/4 mm	610
Steel fibres	Baumbach Metall E.S. GmbH	10 mm / 0.2 mm	306
Steel wool	Gervois	GV2	102
Superplasticizer	TKK	Cementol Hiperplast 463	49
Water added	/	tap water	177

3.2 Hardened concrete characteristics

The hardened concrete characteristics were determined both on the samples cast in the preliminary concrete mix design phase and on the samples cast during the casting of the slab. As the concrete of the preliminary phase was mixed under laboratory conditions in a 30 l laboratory size mixer, while the slab concrete was prepared in a concrete plant by a 2 m³ mixer and transported to the casting place in approximately a quarter of an hour, some differences in hardened concrete characteristics were inevitable.

In all cases the samples were demoulded one day after casting and till the day of testing stored in a 20°C, 97 % RH chamber, according EN 12390-2. The compressive strength was determined on 40x40x160 mm prisms according EN 196-1, and on 100 mm cubes according EN 12390-3. The bending strength was determined on 40x40x160 prisms according EN 196-1, as well as E-modulus according EN 13412.

Results of strength development over time are presented in Figure 3, and the remaining hardened concrete characteristics are presented in Table 2.

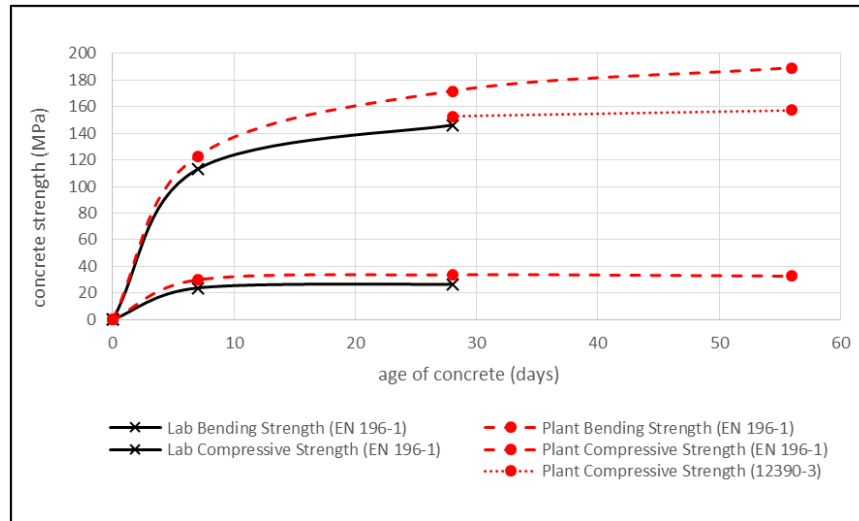


Figure 3: Bending and compressive strength test results of UHPFRC specimens from laboratory and plant produced concrete

As the design of the composite structure was performed acc. SIA 2052, the tensile stress-strain curve of the UHPFRC was determined acc. SIA 2052, Annex E. Instead of cut-out plates of 500 x 100 x 30 mm, cast plates dimension 500 x 200 x 30 mm were used. Load – deflection diagrams are presented in. Figure 4. Samples No. 1 to 6 were tested at 35 days, while plates No. 7 to 12 were tested at the age of 58 days. Samples 1 to 3 and 7 to 9 were tested without 3 load-unloading cycles at the beginning of the test, the rest were subjected to 3 load-unloading cycles up to 3.13 kN (plates No. 7 to 12 up to 2.59 kN). The deflection rate (i.e. the piston movement rate) was 0.5 mm/min up to the maximum load, and 5 mm/min after the maximum load was reached.

To evaluate the durability of the concrete the air permeability was determined on the bending plates before the bending test acc. SIA 262A, Annex E and the capillary water absorption was determined on 100 x 30 mm cylinder acc. EN 13507.

Table 2: Hardened concrete characteristics

Mix	Material characteristics	Test method	Concrete age [days]	Value
Plant	E modulus	EN 13412	28	41.6 GPa
Plant	E modulus	EN 13412	56	42.1 GPa
Plant	Capillary water absorption	EN 13507	28	0.08 kg/m ² x h ^{0.5}
Plant	Air permeability	SIA 262A	28	0.018 x 10 ⁻¹⁶ m ²
Plant	Air permeability	SIA 262A	56	0.089 x 10 ⁻¹⁶ m ²

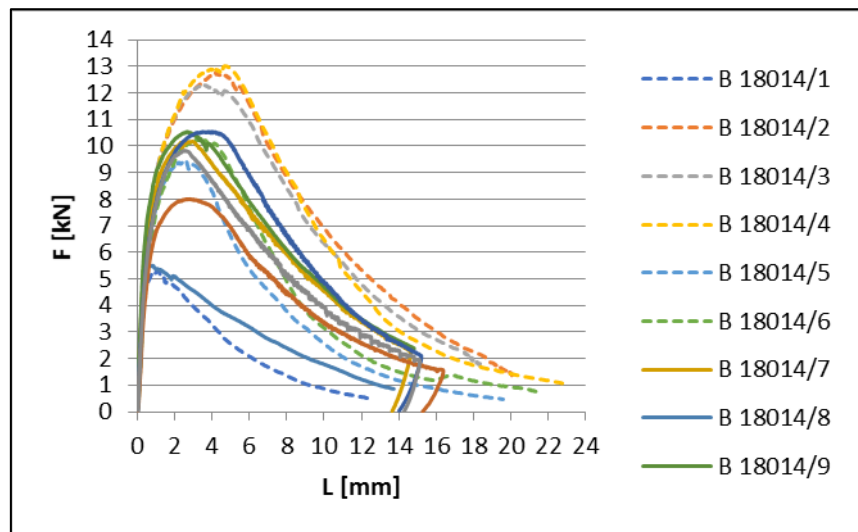


Figure 4: Load – deflection graph determined on plates

4. MIXING, TRANSPORTATION AND CASTING

4.1 Concrete mixing

Mixing of concrete was performed by an ORU ROME CZ 5P 50N horizontal twinshaft mixer with a nominal capacity of 2 m³, owned by Trgograd d.o.o., Litija, located in a suburb of Ljubljana. Sand and water were added automatically, where else the other raw materials manually. The total amount of app. 2 m³ was cast in 6 batches. The mixing time was app. 6 minutes.

4.2 Concrete transportation, casting and curing

From the concrete plant to the lab of Slovenian Building and Civil Engineering Institute, where casting was performed, the concrete was transported in one batch using a conventional concrete truck mixer. Distance between initial and final point was circa 10 km and the transport last for app. 15 minutes.

The concrete was transported from the truck mixer to the placing position via small bucket and levelled using rakes and lath. Subsequently, the slab was gently moistened and covered by a plastic sheet. As the bridge was located indoor, no measure was undertaken to protect the concrete from cold temperatures. The slab was covered by the sheet for 5 days.

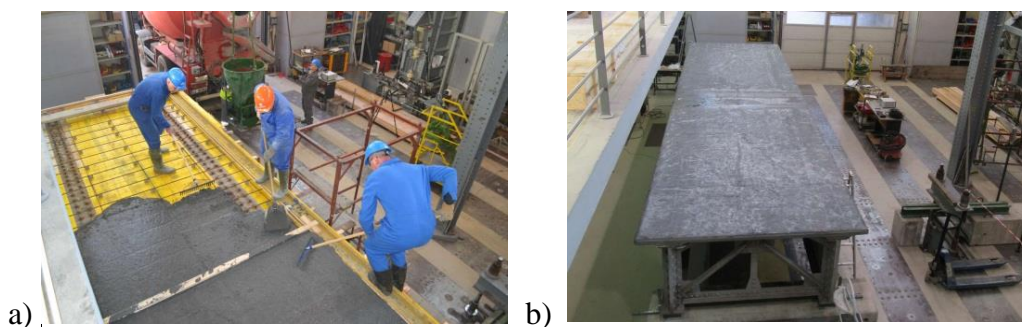


Figure 5: Placing of concrete (a) and the bridge with the slab (b)

5. ASSESMENT OF THE REHABILITATION

The assessment of the strengthened bridge included static and dynamic tests in order to determine the bridge behaviour after rehabilitation. This information was used also to update the FE model, and to reveal the genuine strength of the system and determine the fatigue strength. [10] The results of static tests are described in detail in paper Skaric Palic et al. [11], also compared to the original static tests performed in 2013 [9]. Dynamic and static test results were employed to create an updated physical Finite Element model, which allows simulating different loading scenarios, such as fatigue under several types of trains and velocities. It is demonstrated that, for the worst case scenario, the rehabilitated case presents a 60 % reduction in stresses amplitudes. Such a reduction can be readily attributed to the additional compressive zone offered by the UHPFRC, which in essence assumes the greatest part of compressive stresses and therefore alleviates the steel structure. Apart from the significant vibration mitigation though, this amplitude reduction allows to extend the fatigue life of the structure, which often constitutes the design driven parameter for steel bridges. The UHPFRC slab introduces thus a stress redistribution in the bridge, elevating the neutral axis and reducing the tensile stress on the lower flange, zone prone to fatigue issues. [10]

6. CONCLUSIONS

In this work, a case study of strengthening a steel bridge by applying a slab of UHPFRC is presented. The main emphasis of the paper is on the UHPFRC mix proportion, its fresh and hardened characteristics and on the execution of concrete works.

Although the old steel railway bridge superstructure was moved from the track to the lab, all works including formwork, classic reinforcement, concrete mixing at the plant and transporting to the lab, have been performed as if the bridge was still on site. In this way it has been shown and proven that utilising UHPFRC materials for strengthening bridges on-site is feasible, by using standard concrete technology and tools, as long as special requirements for UHPFRCs are taken into account and experts' recommendations are respected.

7. ACKNOWLEDGEMENTS

The authors would like to acknowledge and gratefully thank the Slovenian Research Agency for the financial support through the Research Programme P2-0273 and the company Trgograd d.o.o., Litija, for mixing and transporting of concrete. Furthermore, they would like to thank the Swiss National Science Foundation (SNSF) within the context of project 154060 and the COST Action TU1406 for their financial support.

8. REFERENCES

- [1] McCarron, P. Way Beam Replacement and Bridge Deck Strengthening using Concrete Composite Construction, University of Surrey Department of Civil Engineering, 2005.
- [2] Carroll, M. An Investigation into Concrete Composite Strengthening of a Continuous Wrought Iron Railway Bridge using Precast Concrete Deck Slabs, Dissertation, 2010, University of Surrey Department of Civil Engineering.
- [3] Network Rail, Railway Bridges Today and Tomorrow, Proceedings of the conference, UK, 2006.
- [4] Olofsson, I., Elfgren, L., Bell, B., Paulsson, B., Niederleithinger, E., Sandager, J., Jensen, Feltrin G., Täljsten, B., Cremona, C., Kiviluoma, R., Bien, J.: Assessment of European railway bridges for

- future traffic demands and longer lives – EC project “Sustainable Bridges”, Structure and Infrastructure Engineering, Vol. 1, No. 2, June 2005, pp. 93 – 100.
- [5] Brühwiler E, Denarié E. Rehabilitation and Strengthening of Concrete Structures Using Ultra-High Performance Fibre Reinforced Concrete. *Structural Engineering International*. 2013; 23(4): 450-7.
- [6] Franssen, R., Guner, S., Courard, L., Mihaylov, B., A study on the numerical modelling of UHPFRC-strengthened members, MATEC Web of Conferences 199, 09001 (2018) <https://doi.org/10.1051/mateconf/201819909001>, ICCRRR 2018.
- [7] Sakr, M.A., Sleemah, A.A., Khalifa, T.M., Mansour, W.N. Behavior of RC beams strengthened in shear with ultra-high performance fiber reinforced concrete (UHPFRC) MATEC Web of Conferences 199, 09002 (2018) <https://doi.org/10.1051/mateconf/201819909002>, ICCRRR 2018
- [8] SMART RAIL FP7 Project, Deliverable 3.3 Rehabilitation of Bridges and Tunnels, Recommendations for the rehabilitation of engineering structures (bridges and tunnels), <http://smartrail.fehrl.org/>, 2013.
- [9] Dzajic, I., Stipanovic Oslakovic, I., Sajna, A. Rehabilitation of steel railway bridges by implementation of UHPFRC deck. *Proceedings of the International Conference on Road and Rail Infrastructure CETRA*, 2014, Publisher: University of Zagreb, ISSN: 1848-9850.
- [10] Martín-Sanz, H., Tatsis, K., Chatzi, E., Brühwiler, E., Stipanovic, I., Mandic, A., Damjanovic, D. & Sajna, A. Towards the use of UHPFRC in railway bridges: the rehabilitation of Buna Bridge, *Life-Cycle Analysis and Assessment in Civil Engineering: Towards an Integrated Vision – Caspeele, Taerwe & Frangopol (Eds) © 2019 Taylor & Francis Group, London, ISBN 978-1-138-62633-1*, pp. 203-209.
- [11] Škarić Palić, S., Damjanovic, D., Stipanović Oslaković, I., Martín-Sanz, H., Koščak, J., Duvnjak, I., Šajna, A. Experimental Investigation of a Steel Railway Bridge Strengthened with UHPFRC Deck Slab, *Proceedings of RILEM Conference “Spring Convention and Sustainable Materials, Systems and Structures Conference”*, Rovinj, Croatia, 2019.
- [12] ARCHES FP6 Project, Assessment and Rehabilitation of Central European Highway Structures, Deliverable D06 Recommendations for the tailoring of UHPFRC recipes for rehabilitation, <http://arches.fehrl.org/>, 2009.

EXPERIMENTAL INVESTIGATION OF A STEEL RAILWAY BRIDGE STRENGTHENED WITH UHPFRC DECK SLAB

Domagoj Damjanovic (1), Sandra Škarić Palić (2), Irina Stipanović Oslaković (2, 3), Henar Martín-Sanz (4), Janko Koščak (1), Ivan Duvnjak (1), Uroš Bohinc (5)

(1) University of Zagreb Faculty of Civil Engineering, Zagreb, Croatia

(2) Infra Plan Consulting, Zagreb, Croatia

(3) University of Twente, Faculty of Engineering Technology, Enschede, Netherlands,

(4) Department of Civil, Environmental and Geomatic Engineering (IBK), ETH Zurich, Switzerland

(5) Slovenian National Building and Civil Engineering Institute, Ljubljana, Slovenia

Abstract

Growing number of aging, structurally deficient and obsolete railway bridges are facing infrastructure managers, owners and operators with decision making dilemmas about constant repair and maintenance activities and decommissioning choices. New sustainable materials are being developed during past decades which deliver novel possibilities in infrastructure asset management.

Ultra High Performance Fibre Reinforced Concrete is a material that has been used as a strengthening solution for concrete bridges for some time now. The difference between UHPFRC and conventional concrete regarding mixture is in the amount of binder, the size of the aggregate and the presence of fibres. Compared to a conventional concrete, the matrix of the UHPFRC is much denser which influences its durability due to additional impermeability protection. Superior material characteristics and its workability have already been proven in practice. This paper describes a case study dealing with a UHPFRC-steel composite structure which is a solution which has much less been analysed and investigated.

The case study presents results of experimental investigations performed on an actual steel bridge, the Buna bridge, which was decommissioned and transported into the laboratory. Static and dynamic testing was performed on the bridge before and after casting of a UHPFRC deck slab on the steel superstructure in the laboratory.

Keywords: steel bridge, UHPFRC, static testing, dynamic testing

1. INTRODUCTION

Ageing of the transport networks has large financial and environmental consequences on infrastructure owners and the whole society on many different levels. Replacement costs for civil engineering infrastructure assets such as rail bridges are prohibitive. Given constant economic constraints and the numerous challenges, such as the need for increase of traffic loads or higher load capacity, it is vital to maintain safety level and develop optimal ways to manage rail network and maximise the use of all resources. The key to effective infrastructure and an efficient society lies in combining and optimising development of new infrastructure but also efficient and sustainable management of existing assets.

New materials are being developed in the context of sustainability and ease of application as strengthening solutions for existing structures in the last decades. Ultra High Performance Fibre Reinforced Cement-based Concrete (UHPFRC) is a cementitious material characterized by extremely low permeability, high strength and deformation capacity (Dzajic et al., 2014). [1] In this paper static and dynamic testing of a composite steel -UHPFRC railway bridge is presented and analysed. Buna bridge was originally built in 1893 with the first reconstruction in 1953. The length of the bridge is 8,87 m, it consists of two 0,9 m high I shaped main girders placed at 1,8 m distance, connected by L shape profiles over the supports and in each quarter of the span. Steel superstructure of the bridge was removed from its original location on a railway line near Zagreb and transported into laboratory where it was cleaned, recoated and finally strengthened with a designed 7 cm (actual thickness achieved after casting was measured app 8 cm in the lab) UHPFRC bridge deck. Material characteristics and casting technology applied on this bridge are described in detail in paper Sajna et al. [2]



Figure 1: Bridge before deck casting with welded studs on the upper girder flange (a) and bridge with UHPFRC deck, sleepers and tracks mounted with sensors and testing equipment in the lab (b)

Short overview of exploitation of the Buna bridge for investigation purposes in the laboratory:

- decommissioning of the Buna bridge by Croatian Rails and transportation of the bridge into the laboratory where first static testing of the steel superstructure was performed in 2013
- 2016 dynamic testing of the steel superstructure
- 2018 casting of UHPFRC deck slab and static and dynamic testing of composite steel-UHPFRC structure

2. BRIDGE STRENGTHENING – OBJECTIVES

Ultra-High-Performance Fibre-Reinforced Concrete (UHPFRC) is a composite material which tends to exhibit superior properties such as advanced strength, durability, and long-term stability compared to conventional concrete. Mechanical properties like compressive and tensile strengths are much higher and this enables slender constructions due to increased capacity of transferring forces. Very dense matrix causes outstanding durability properties and it is shown that the concrete is very resistant to chloride and other chemical attacks and has a high abrasion and fire resistance. [3]

When a decision was made to replace the steel superstructure of a railway bridge near Zagreb the opportunity came up for experimental investigations on a real characteristic example of a steel bridge connected with rivets. It was decided to use the enhanced performance in strength and durability of UHPFRC and cast a deck slab upon the existing steel superstructure of a bridge in the lab. The original steel structure was transported and tested within a laboratory setting prior to the implementation of a cast in-situ UHPFRC deck. Results of these tests can be found in Dzajic et. al 2014 and Martin-Sanz et. al 2016. [1, 4]

The main objective of strengthening the Buna bridge was converting the existing steel cross section to composite cross-section. This caused rising of the neutral axis, increase of the bearing capacity and finally enables the composite cross section to carry additional loads. In addition, the concrete deck stiffens the upper steel flange and thus reduces or even eliminates the problem of stability of the cross-section. The advantages of UHPFRC particularly valuable for rehabilitation of railway bridges are high strength and ductility, low added dead load, low added thicknesses, i.e. change in the track vertical alignment, extreme durability. [1, 4]

3. PERFORMED INVESTIGATIONS

Investigations performed on the bridge strengthened with UHPFRC deck slab are a repetition of experimental investigations performed on a steel bridge, static testing which was conducted in 2013 and modal analysis which was done 2016.

3.1 Static testing

Loading was applied using 4 hydraulic pistons in order to simulate Load model 71 specified in Eurocode (Figure 1b), consisting of four 250 kN axle loads at 1,6 m distance. When multiplied by dynamic factor the total loading reaches approx. 1530 kN. During the static test loading was controlled by load cells placed under each support.

Static testing was performed using the same elastomeric bearings as the supports, the same loading distribution, with rails and sleepers mounted on the slab, as it was the case during the testing prior to casting of the slab. This was done in order to ensure the same conditions as on the original bridge which will enable more realistic assessment and comparison of testing results.

In the scope of static testing performed after the casting of the slab a large number of sensors were installed on the bridge for measuring different parameters like concrete temperature and shrinkage during strengthening, as well as for measuring strains, stresses and displacements during static loading. Eight fiber optic sensors were embedded in deck slab for strain measurement of the UHPFRC slab as shown in figure 2. Prior to static testing 10 LVDT sensors were installed on the slab in each quarter of span (section A, B and C). LVDT's

measured the strains on the top and bottom face of the slab in longitudinal and transverse direction, at the initial length of 100 mm or 200 mm (L_0). Strains of the steel girders were measured using strain gauges, a total of 20 strain gauges were installed in sections, 6 in sections A and C, while 8 sensors were installed in mid span section B. Disposition of LVDT's and strain gauges is presented in figure 3.

Displacements were measured in the middle of the span and on the supports at both steel girders, using 6 LVDT sensors.

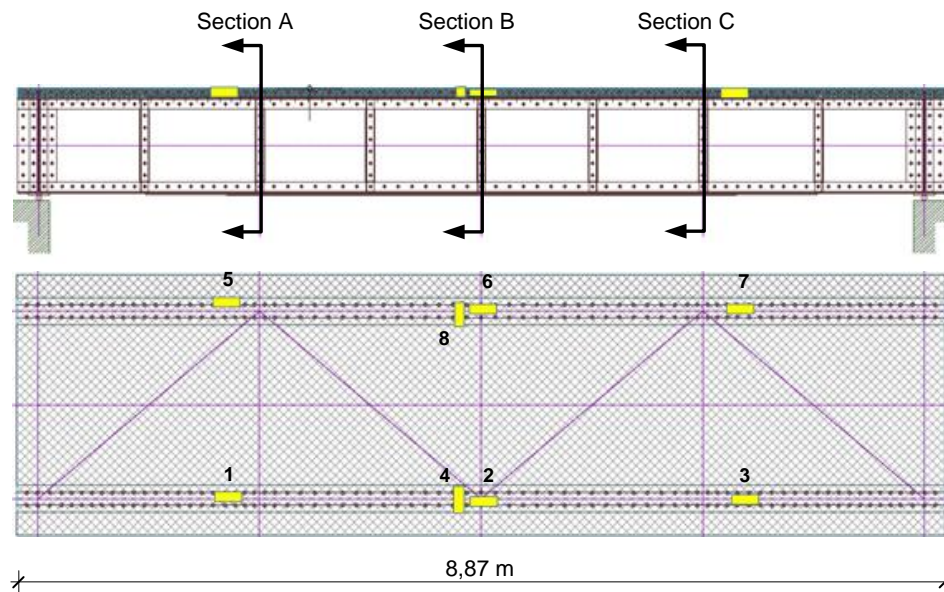


Figure 2: Fibre optic sensors embedded in UHPFRC deck slab for strain measurement

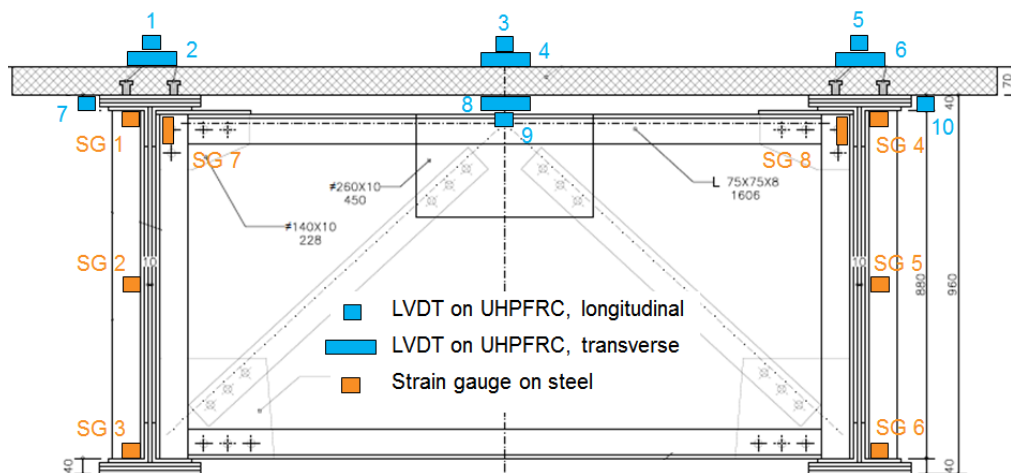


Figure 3: Static tests – LVDTs and strain gauges on steel and concrete placed in sections A, B and C (SG 7 & SG 8 were placed only in cross section B)

3D Digital Image Correlation (DIC) was implemented on one quarter of the bridge, primarily to determine if there are any changes in the bond between the UHPFRC slab and the steel girder. DIC is no-contact optical technique for measuring displacements and strains which is based on comparison of digital photographs at various loading stages [5, 6].

8 Acoustic Emission (AE) sensors were also installed on the bottom face of the UHPFRC deck slab. AE measurements are not presented in this paper as they are going to be used in next phase of this research in which damage will be inflicted to the bridge and damage detection will be performed.

3.2 Dynamic testing

In the scope of dynamic testing determination of modal parameters using PULSE Operational Modal Analysis (OMA) software was performed. When using OMA, the dynamic parameters are determined only from the response functions of the structure measured under operational conditions. Identification of modal parameters was conducted using methods of frequency domain decomposition (FDD) [7, 8]. FDD technique estimates the modes using a Singular Value Decomposition (SVD) of the Spectral Density matrices.

The initial testing of the steel superstructure was performed in 2016 and the testing of bridge with UHPFRC slab in 2018. During both of these testing campaigns the bridge was supported on same elastomeric bearings, while the sleepers and the rails were removed from the bridge. Ambient vibration was simulated with impact excitation using two hammers, providing suitable excitation for OMA. Response of the structure was measured by 5 Brüel & Kjær 4508 accelerometers.

The initial dynamic measurement consisted of total of 119 measuring points, in each measuring point response was measured in vertical and transverse direction, giving the total of 238 measured DOF's. On the strengthened bridge the number of measuring points increased by additional 61, on the UHPFRC slab, resulting in total of 180 measuring points and 360 measured DOF's.

4. TESTING RESULTS

4.1 Static testing

During the static testing of strengthened bridge strains were measured in 3 sections (A, B and C) by 18 SG's on the steel girders, 30 LVDT's on the top and bottom face of the deck slab and 8 FBG sensors embedded in the slab. Static testing was performed in 3 phases, 20 %, 50 % and 100 % of maximum load which was 1530 kN.

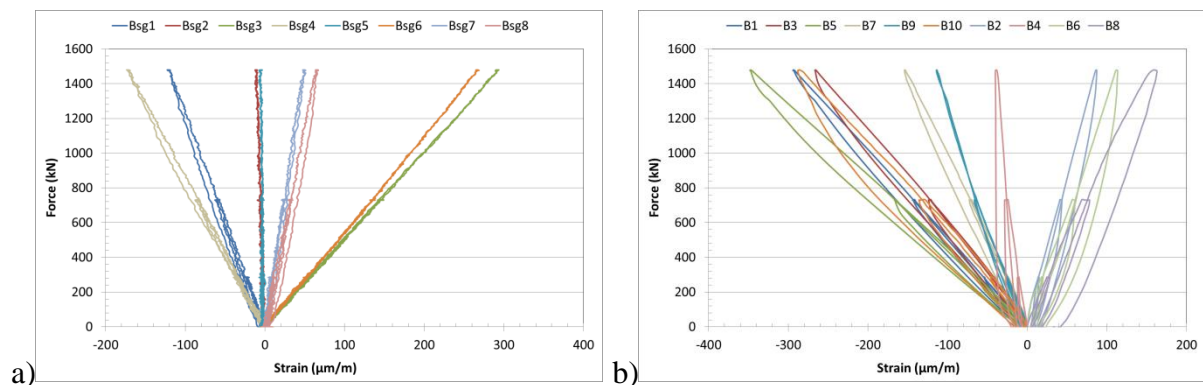


Figure 4: Force - strain diagram a) 8 SG's on steel girders section B, b) 10 LVDT's on UHPFRC deck slab section B

Figure 4 presents the results of strains measurements in cross section B (middle of the span), while in figure 5 average values of strain distribution in cross section B and C for 50 % and 100 % of loading are shown. Figure 6 presents graphical image of longitudinal displacements determined by 3D Digital Image Correlation method at 100 % of loading and diagrams of displacements for points P3 (on the UHPFRC) and point P7 (on the top of the steel girder).

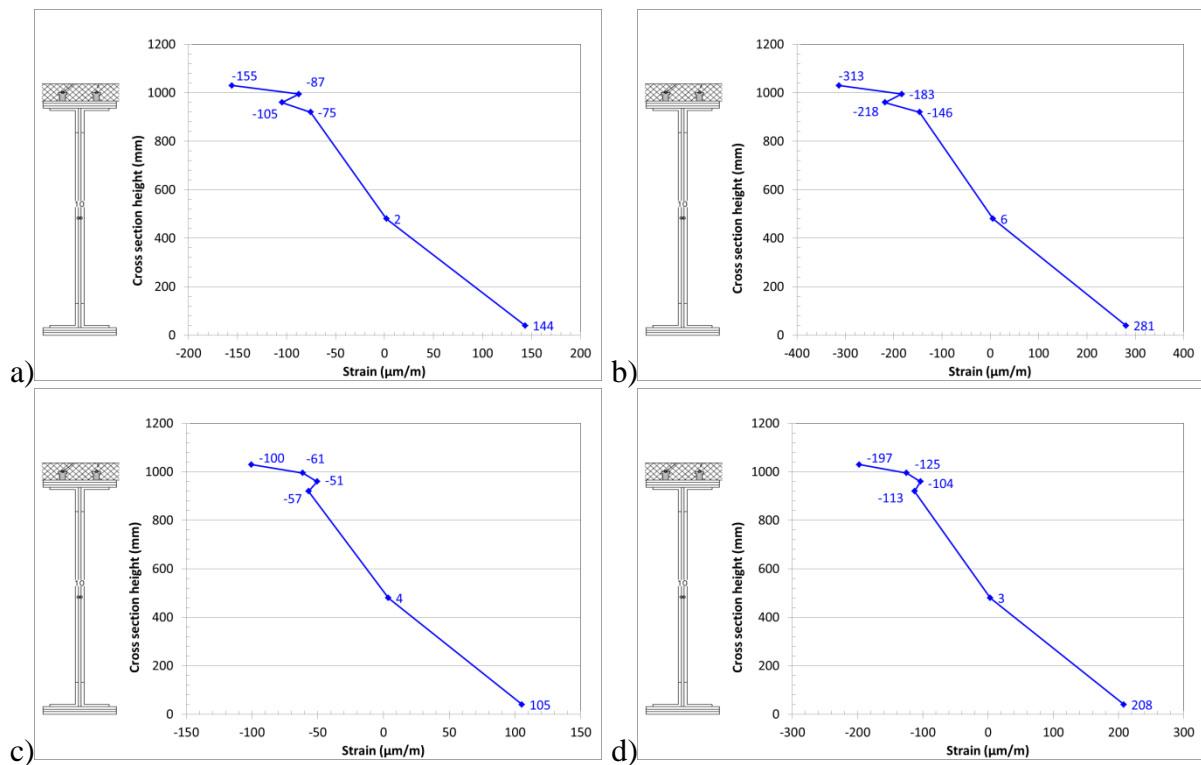


Figure 5: Strain distribution a) cross section B at 50 % of loading, b) cross section B at 100 % of loading, c) cross section C at 50 % of loading, d) cross section C at 100 % of loading

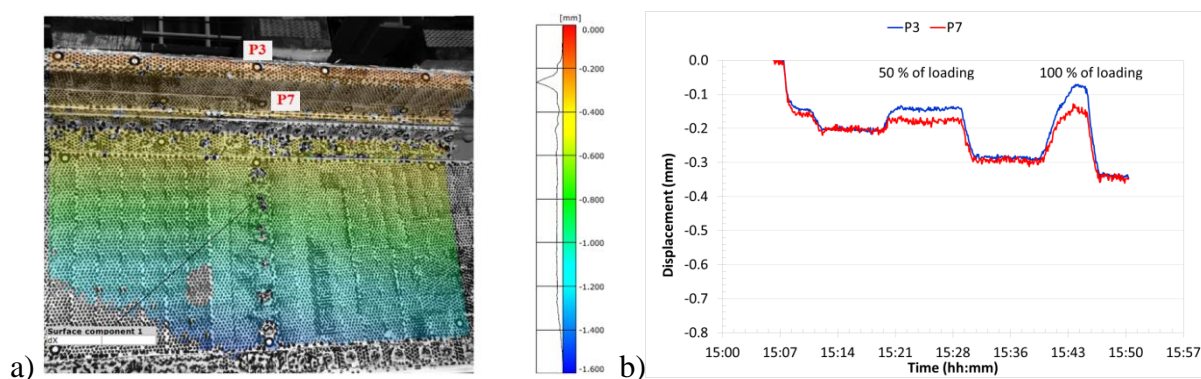


Figure 6: a) Graphical image of longitudinal displacements determined by 3D DIC at 100 % of loading, b) displacements in longitudinal directions for points P3 and P7

Some inconsistencies in the strain distribution in cross section, which can be seen in figure 5, can be attributed to the position of the LVDT sensors on the bottom face of the UHPFRC

slab which is dislocated from the axis of the steel girders in which all other sensors are positioned. This is confirmed with the graphical image of longitudinal displacements determined by 3D DIC and displacements in longitudinal directions for points P3 and P7, presented in figure 6. Comparison of displacements and strains measured during initial testing on the steel superstructure [1] and those measured after the bridge was strengthened with UHPFRC deck slab is shown in table 1.

Table 1: Comparison of displacements and strains at 100 % of loading

	Displacement in L/2 (mm)		Strain – lower flange ($\mu\text{m/m}$)	
	Girder 1	Girder 2	Girder 1	Girder 2
Initial measurement	8,64	8,28	481	467
Strengthened bridge	6,68	6,42	275	297

4.2 Dynamic testing

The frequencies determined during the initial testing and the testing of the strengthened bridge together with the corresponding mode shapes are presented in Figure 7.

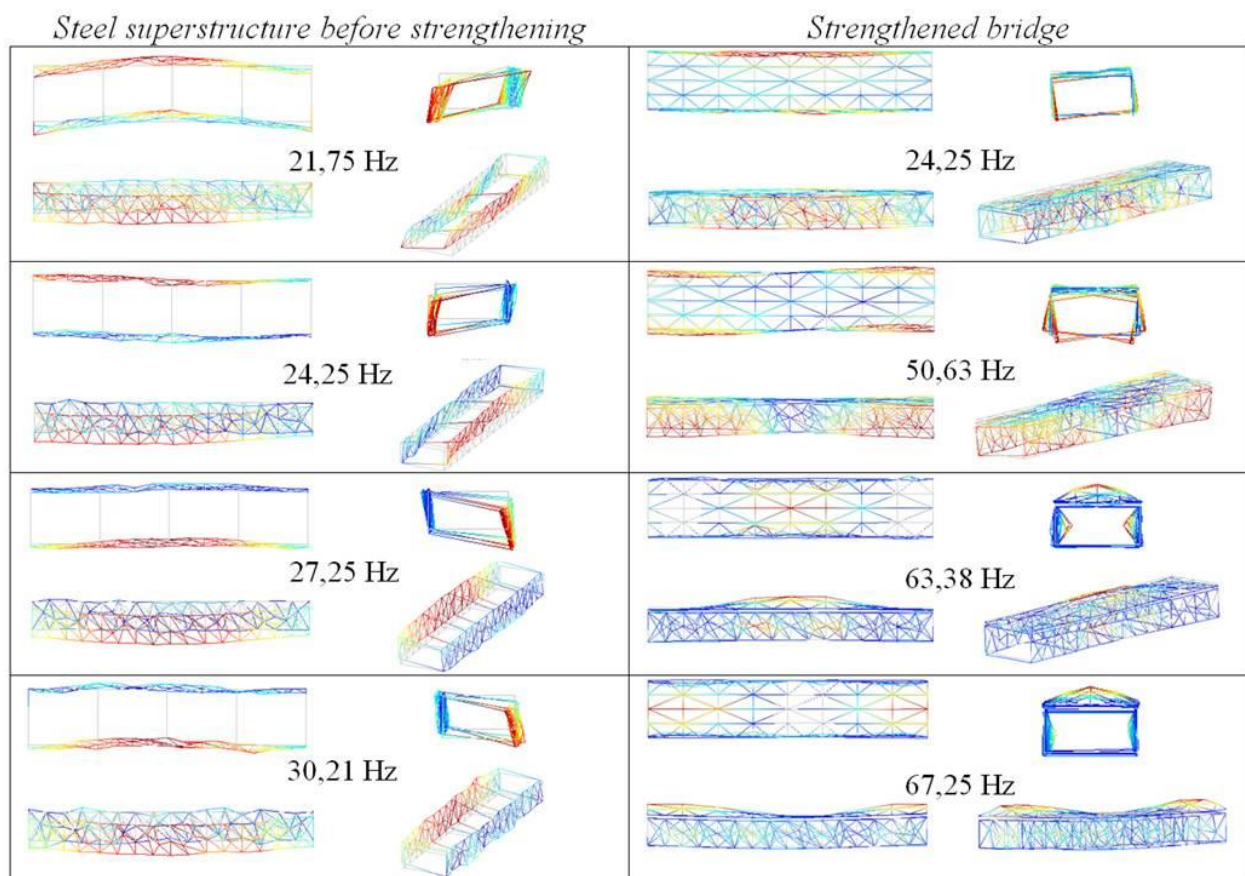


Figure 7: Experimentally determined modal shapes and corresponding natural frequencies

5. CONCLUSION AND DISCUSSION

Based on the testing performed on original steel riveted bridge which was strengthened by a 7 cm UHPFRC bridge deck and extensively tested in the same laboratory conditions following conclusions are made:

- After the strengthening a 22 % reduction in deflection was observed, the reduction of strains/stresses was 43 % for girder no. 1 and 36 % for girder no. 2.
- Results of experimentally determined modal parameters show the increase of natural frequencies.
- All experimental results show substantial increase of stiffness which was achieved by strengthening of the bridge with UHPFRC deck slab.
- Results of extensive testing campaign can be used for further analysis which can include updating of FE model and fatigue analysis.
- Experimental results can also be utilized for future assessment of health state and damage detection of the structure.

ACKNOWLEDGEMENTS

The authors would like to acknowledge the ZAG institute in Ljubljana for the support in the execution of the experimental testing and the company Trgograd d.o.o., Litija, for mixing and transporting of concrete. Furthermore, they would like to thank the Slovenian Research Agency (Research Programme P2-0273), the Swiss National Science Foundation (SNSF - project 154060) and the COST Action TU1406 for their financial support.

REFERENCES

- [1] Dzajic I., Sajna A., Stipanovic Oslakovic I., 'Rehabilitation of steel railway bridge by implementation of UHPFRC deck, CETRA 2014 3rd International Conference on Road and Rail Infrastructure, Split, Croatia.
- [2] Sajna A., Stipanovic I., Martin-Sanz H., Damjanovic D., 'Rehabilitation of an old steel railway bridge using UHPFRC – material characteristics and casting technology', RILEM International Conference on Sustainable Materials, Systems and Structures, 20 – 22 March 2019, Rovinj, Croatia.
- [3] Bøhnsdalen Eide M., Hisdal J.M., SINTEF Building and Infrastructure, Ultra High Performance Fibre Reinforced Concrete (UHPFRC) – State of the art, COIN Project report 44 – 2012
- [4] Martín-Sanz H., Tatsis K., Chatzi E., Brühwiler E., Stipanovic I., Mandic A., Damjanovic D., Sajna A., 'Towards the use of UHPFRC in railway bridges: the rehabilitation of Buna Bridge', IALCCE, Ghent, Belgium, October, 2018, The Sixth International Symposium on Life-Cycle Civil Engineering.
- [5] Frančić Smrkić M., Koščak J., Damjanović D., 'Application of 2D digital image correlation for displacement and crack width measurement on RC elements', GRAĐEVINAR 70 (2018) 9, 771-781.
- [6] McCormick, N., Lord, J.: Digital Image Correlation, Materials Today, 13 (2010) 12, pp. 52–54, [https://doi.org/10.1016/S1369-7021\(10\)70235-2](https://doi.org/10.1016/S1369-7021(10)70235-2).
- [7] Herlufsen H., Andersen P., Gade S., Møller N., Identification techniques for operational modal analysis an overview and practical experiences Proceedings of 1st IOMAC Conference, Copenhagen, Denmark, April 26-27, 2005.
- [8] Jacobsen N. J., Andersen P., Brincker R.: Applications of Frequency Domain Curve-fitting in the EFDD Technique , Proceedings of the 26th IMAC, Orlando, USA, 2008.

EXPERIMENTAL INVESTIGATIONS OF UHPC, STEEL FIBRES AND EMBEDDED STEEL FIBRES UNDER CYCLIC TENSILE LOADING

Martin Empelmann (1), Vincent Oettel (1), Jan-Paul Lanwer (1)

(1) iBMB, Division of Concrete Construction, Technische Universität Braunschweig, Germany

Abstract

Modern high performance concretes, like ultra-high performance fibre-reinforced concrete (UHPFRC), need for avoidance of brittle failure modes a relatively high fibre content, which leads to an overcritical tensile load-bearing behaviour and a high post-cracking tensile strength. Additionally, UHPFRC can preferably been used for lean and thin-walled structures due to its very high compressive strength. The combination of weight reduction and high slenderness make UHPFRC-structures susceptible to cyclic loading, e.g. in case of bridge girders or masts and towers.

Currently, the effect of cyclic loading on UHPFRC, in particular the tensile bearing behaviour and post cracking tensile strength is not quite clear. Therefore, the degradation processes of UHPFRC under cyclic tensile loading have to be investigated fundamentally. This is done in experimental investigations by iBMB, Division of Concrete Constructions of TU Braunschweig, on small-sized specimens, like fibre tests and tensile tests on plain ultra-high performance concrete and as well as fibre pull-out tests. Within this test program, the number of cycles and amplitudes are varied to examine the mechanical properties and to display the degradation processes. Imaging techniques like digital microscopy, x-ray scans (CT) and scanning electron microscopy (SEM) are used to obtain the degradation of the fibre, the UHPC and the interfacial transition zone (ITZ) between fibre and UHPC. The following paper contains a current state of the research project “Degradation Processes of UHPFRC under cyclic tensile Loading” as part of the priority program SPP 2020 “Cyclic deterioration of High-Performance Concrete in an experimental-virtual lab” founded by the German Research Foundation (Ger. DFG).

Keywords: UHPFRC, cyclic tensile loading, degradation processes, imaging techniques

1. INTRODUCTION

Currently ultra-high performance fibre-reinforced concrete (UHPFRC) usually contains high ratios of fibres up to 2.0 Vol.-% (200 kg/m³). This high content of fibres leads to an overcritical tensile load-bearing behaviour and a high post-cracking tensile strength (see figure 1). The tensile load-bearing behaviour of UHPFRC can be divided into three phases according to [7]:

- Phase I: Linear-elastic behaviour of concrete matrix
- Phase II: Failure of concrete matrix and activation of steel fibres
- Phase III: Steel fibres are pulled out of the concrete matrix

At phase I, the steel fibres have no influence on the load-bearing behaviour of the specimen. It is mainly determined by the concrete matrix. In Phase II, the concrete fails at its weakest point and the steel fibres are activated. The load can be increased until the fibres are pulled out of the concrete matrix. This is where phase III starts. The crack width rises and the steel fibres slip out of the concrete matrix. A load enhancement is not possible anymore. The characteristics of all three phases are shown in figure 1.

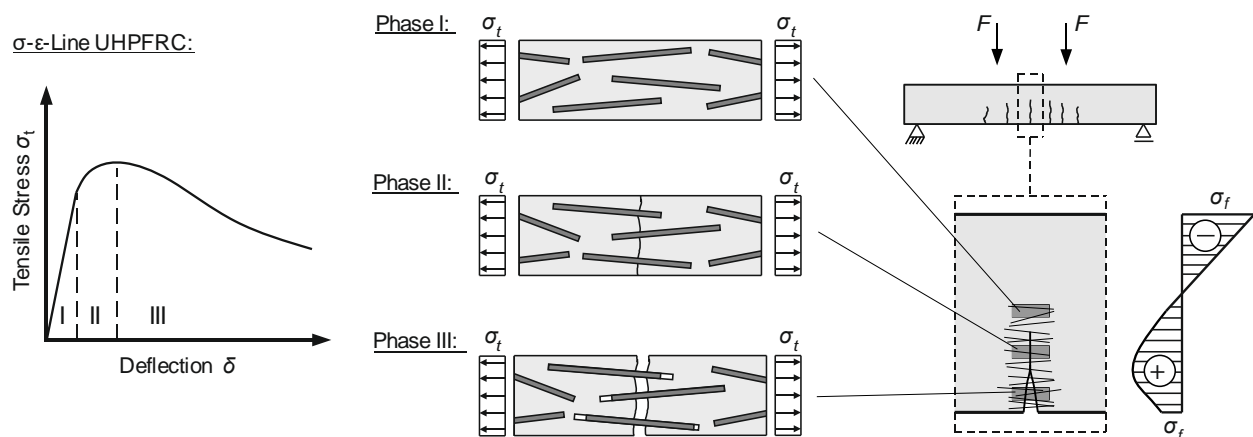


Figure 1: Load-bearing behaviour of fibre reinforced concrete with high fibre content under tensile loading

To describe and understand the fatigue behaviour of UHPFRC, the degradation processes have to be clear. By reviewing literature, some degradation processes of UHPFRC under cyclic tensile loading are observed and mentioned ([1], [3], [4] and [5]):

- Continuous fibre pull-out
- Abrasion of fibre surface and concrete canal
- Fibre rupture
- Spalling and pulverisation of concrete matrix

Nevertheless, fundamental and systematic investigations to analyse the degradation behaviour of UHPFRC are still missing. Within the Priority Program SPP 2020 “Cyclic deterioration of High-Performance Concrete in an experimental-virtual lab” funded by the German Research Foundation (Ger. DFG), the degradation behaviour of UHPFRC under cyclic tensile loading is fundamentally studied at iBMB, Division of Concrete Construction of TU Braunschweig. The main goal of the research project is to capture, describe and model the degradation processes of UHPFRC under cyclic tensile loading.

2. EXPERIMENTAL INVESTIGATIONS

2.1 Steel fibre and ultra-high performance concrete properties

The experimental investigations are divided into three different investigations units. First, the plain UHPC and the steel fibre are investigated separately in direct tensile tests. Then, UHPC and steel fibre are put together for fibre pull-out tests. All tests contain monotonic and cyclic loaded test set-ups. The UHPC mixture has been predefined by SPP2020 and the composition is given in table 1.

Table 1: UHPC-mixture (kg/m³)

Components	SPP2020-UHPC1017
Cement: CEM I 52.5 R (Holcim Sulfo 5R)	795.0
Microsilica: Sika Sillicol P	168.6
Superplasticizer: BASF MasterGlenium ACE 394	24.1
Quartz Powder: Quarzwerke W12	198.4
Quartz Sand: Quarzwerke H33	971.0
Water	189.9

Due to the high bond stress, UHPFRC usually requires high-strength micro steel fibres. The dimensions of the steel fibres (length and diameter) are aligned to UHPC's strength properties to avoid sudden failure. The properties of the steel fibre are given in table 2 (manufacturer's information).

Table 2: Steel fibre properties

Type	Weidacon FM 0.19/13.0
Coating	Brass
Shape	Round, Straight
Dimensions Ø/l	0.19/13.0 [mm]
Tensile Stress	> 2,000 N/mm ²
Young's modulus	200,000 N/mm ²

2.2 Plain ultra-high performance concrete

For investigations on plain ultra-high performance concrete, a dumbbell shaped specimen is used for monotonic and cyclic loading. The dimensions of the specimen has been chosen according to [1] with a flexible bearing, though. On top of the specimen a steel plate with four hanger bolts are used for load applications. That load applications has been developed at iBMB/MPA for centric tensile testing of concrete cylinders [6]. One strain gauge on each side of the specimen measures the strain. The dimensions, formwork and test set-up of the test specimens are shown in figure 2.

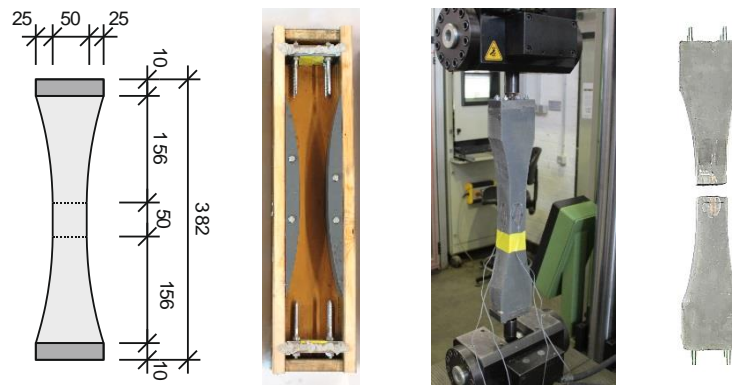


Figure 2: Formwork, test set-up of dumbbell UHPC specimens and after testing

The test series contained six specimens of which three are tested under monotonic and cyclic loading, respectively. The cyclic loaded specimens were tested for 10,000 load changes and a following monotonic loading. The fatigue stress amplitude was set to:

$$\frac{\sigma_o}{\sigma_u} = \frac{0.7 \cdot f_{ctm}}{0.1 \cdot f_{ctm}} \quad (1)$$

where:

σ_o : Maximum fatigue load

σ_u : Minimum fatigue load

f_{ctm} : Ultimate tensile stress of UHPC matrix

Afterwards, the fractured surface was examined by digital microscopy. Figure 3 shows the tensile stress-strain curve of monotonic (black lines) and cyclic (red lines) loaded UHPC specimens as well as digital microscopic images of two cut off fractured surfaces, respectively.

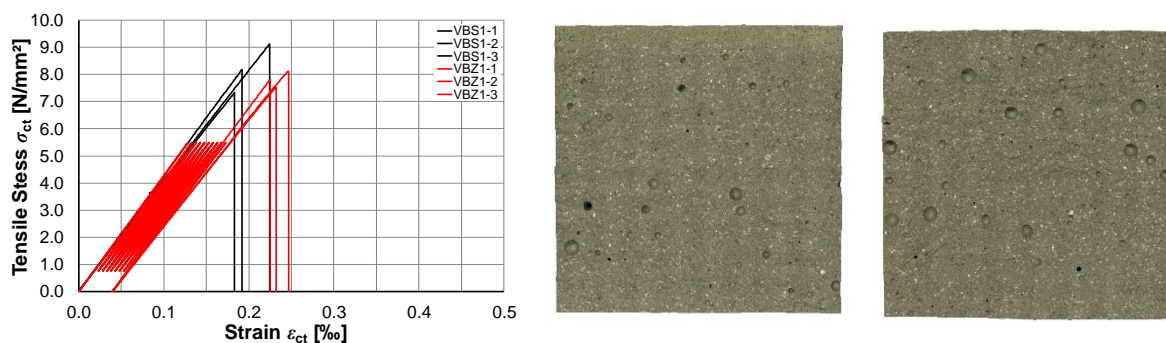


Figure 3: Tensile stress-strain behaviour (left) and digital microscopy images of fractured surfaces of monotonic (centre) and cyclic loaded of dumbbell UHPC specimen (right)

The tensile stress-strain curves of the monotonic loaded tests show linear behaviour until the UHPC specimen reaches its ultimate tensile stress and fails brittle. The ultimate tensile stress varies between $f_{ct} = 7.00$ and 9.00 N/mm² at an ultimate strain of approximately $\epsilon = 0.20$ ‰. Regarding the cyclic loaded test specimens, the strain increases to $\epsilon = 0.05$ ‰ within 10,000 load changes and $\epsilon = 0.25$ ‰ after monotonic loading. The ultimate limit stress remains nearly unchanged compared to the monotonic loaded specimens. This means, cyclic tensile loading

causes an increased plastic strain but nearly no alteration in tensile stresses (for less or equal 10,000 load changes). The slight differences in ultimate tensile stresses might be result of material scattering.

The digital microscopy images of monotonic and cyclic loaded fractured areas show in the first instance no differences in degradation matters. These fractured areas are currently investigated by scanning electronic microscopy (SEM) for more detailed information.

2.3 High-strength micro steel fibre

Due to the high tensile stress and the low diameter of the steel fibre (see table 2), it is not possible to fix the steel fibre straight into the clamping jaws of the testing machine. Therefore, both ends of the steel fibre were glued into steel cannulas with a diameter of 2.1 mm and a length of 80.0 mm. The test length between the two cannulas was set to 100.0 mm (see figure 4).

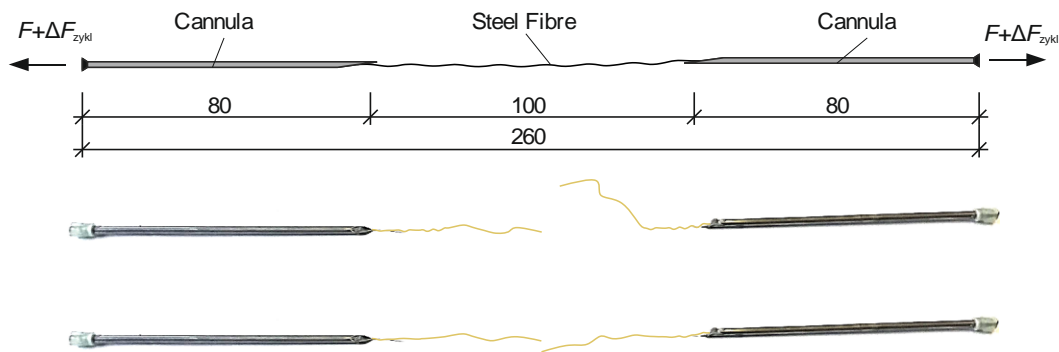


Figure 4: Dimensions of steel fibre test specimen for monotonic and cyclic loading (on top and centre) and failed steel fibre specimen under monotonic loading (bottom)

Fourteen steel fibres, of which nine fibres were tested under monotonic tensile loading, three under cyclic loading for 1,000 load changes with following monotonic loading and two steel fibres until fatigue. The stress amplitude was chosen to:

$$\frac{\sigma_o}{\sigma_u} = \frac{0.7 \cdot \sigma_t}{0.1 \cdot \sigma_t} \quad (2)$$

where:

σ_o : Maximum fatigue load

σ_u : Minimum fatigue load

σ_{tm} : Tensile stress of steel fibre

Afterwards, the surface of fibres was examined by SEM images. SEM images were prepared of fibres in condition as supplied, monotonic loaded, cyclic and following monotonic loaded as well as only cyclic loaded. The tensile stress-strain curves are shown in figure 5 and SEM images in figure 6.

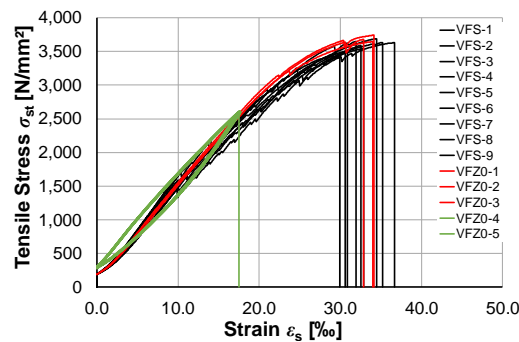


Figure 5: Tensile stress-strain behaviour of steel fibres under monotonic and cyclic tensile loading

The tensile stresses of the steel fibres that was determined by monotonic tensile tests, are at least 50 % higher compared to the manufacturer's information (black lines in figure 5). The young's modulus of the monotonic loaded steel fibres remains nearly the same compared to the cyclic loaded steel fibres. The stress-strain curves show no degradation of the cyclic loaded steel fibres for 1,000 load changes at all (red lines in figure 5). Steel fibres that were tested to fatigue failed after about 1,300 load changes (green lines in figure 5).

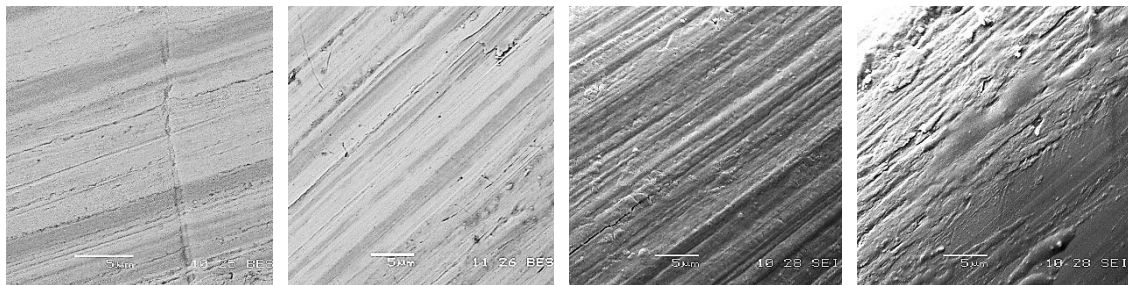


Figure 6: SEM images of steel fibres in condition as supplied (left), monotonic loaded (centre left), cyclic and following monotonic loaded (centre right) and cyclic loaded (right)

Regarding the SEM images in figure 6, the layer of brass, that is covering the steel fibre, shows some gouges longitudinal on the fibre's surface (figure 5, left). These gouges have been flattened in case of monotonic loading (figure 5, centre left) and the layer of brass becomes crumbly at some spots. The cyclic and monotonic loaded caused a longitudinal crack at the surface of the steel fibre (lower left-hand corner in figure 6, left). The brazen layer is almost undamaged. The steel fibre that failed under cyclic loading shows a completely destroyed surface in figure 6 (right hand side). Although no degradation of the steel fibre is recognized in the stress-strain relationships in figure 5, the SEM images show that the surface of the steel fibres has been changed depending on the type of loading. SEM images of the fractured surface are currently under investigation to get more information of the degradation processes of steel fibres under cyclic tensile loading.

2.4 Multiple steel fibre pull-out tests

The specimens for multiple fibre pull-out tests contain two rectangular prisms of UHPC. A plastic film separated both prisms from each other to avoid adhesive forces. Forty-nine steel fibres have been aligned between those two prisms. The specimens were stored in air-

conditioned room at 23 °C and 65 % relative humidity. Steel plates for load transmission were glued to the front face of the specimen for flexible bearing as shown in figure 7. This specimen has also been used by [2] for monotonic loading.

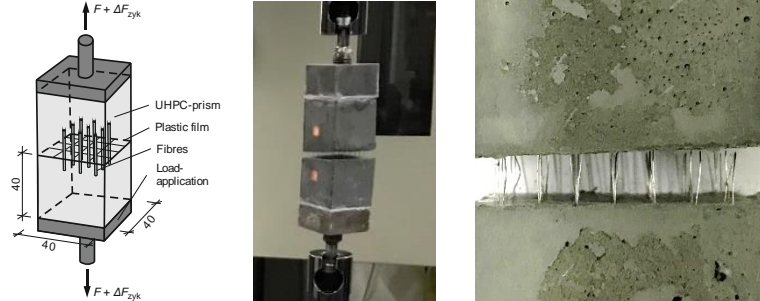


Figure 7: Multiple steel fibre pull-out test specimen (left, centre left), test set-up (centre right) and pulled-out steel fibres (right)

First, three specimens were tested under monotonic loading. For cyclic loaded specimen, the stress amplitude was set to:

$$\frac{\sigma_o}{\sigma_u} = \frac{0.7 \cdot \sigma_{ctm}^f}{0.1 \cdot \sigma_{ctm}^f} \quad (3)$$

where:

σ_o : Maximum fatigue load

σ_u : Minimum fatigue load

σ_{ctm}^f : Maximum pull-out stress

After cyclic tensile loading of 1,000 load changes, the specimen was tested under monotonic tensile loading until the steel fibres were completely pulled out of the concrete matrix. No fibre rupture has been occurred. The stress-slip curves of monotonic and cyclic loaded specimens as well as the SEM images of pulled-out fibres are shown in figure 8.

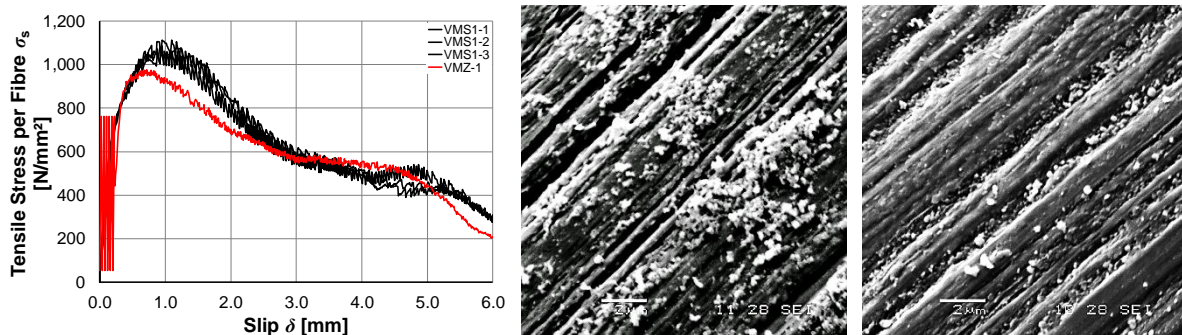


Figure 8: Tensile stress-slip behaviour of multiple steel fibre pull-out tests (left) and SEM images of monotonic (centre) and cyclic (right) loaded pulled-out fibres

Compared to the stress-slip curves of the monotonic loaded specimens (black lines), the cyclic loading causes a slip of approximately $\delta = 0.20$ mm. The tensile stress-slip curve reaches its maximum at about 1,000 N/mm², which is approximately 10 % lower than the ultimate stress

of the monotonic loaded specimens (red lines in figure 8). SEM images of the monotonic loaded fibre show many concrete particles that are located beside the gouges (figure 8 centre). By looking at the cyclic loaded steel fibre, most UHPC particles are located inside the gouges of the steel fibre (figure 8, right). This means that the cyclic loading initiated a shearing off and moving of UHPC particles into the gouges of the steel fibre. Due to the filled up gouges with concrete particles the contact surface of the steel fibre to the UHPC could become larger and the steel fibre transfers more friction forces into the UHPC. This might be the reason why the stress-slip curve of the cyclic loaded pull-out tests rises above the monotonic pull-out tests in figure 8.

3. CONCLUSIONS AND OUTLOOK

The fatigue behaviour of UHPC, fibres and embedded fibres have been investigated in monotonic and cyclic tensile test to understand the degradation process of UHPFRC. Due to the results and microscopy images following conclusions can be drawn:

- Strain of UHPC rises in case of cyclic loading
- No change of ultimate tensile stress of UHPC and fibres in terms of cyclic loading
- Steel fibres are pulled out of the UHPC matrix
- Gouges are located on the steel fibre's surface
- Layer of brass on fibre is destroyed by cyclic loading
- UHPC particles fill up gouges in case of cyclic loading

Further investigations of UHPC, fibres and embedded fibres with different amplitudes and numbers of load changes are currently conducted at iBMB, Department of Concrete Construction of TU Braunschweig. The angle, number and embedded length of fibres in UHPC's matrix will also be changed within these investigations. X-Ray scans and SEM images will give more information of the degradation processes of UHPFRC.

ACKNOWLEDGEMENT

This research project is part of the priority program SPP 2020 which is founded by the DFG (German Research Foundation). The authors acknowledge the financial support.

REFERENCES

- [1] Fitik, B.: Ermüdungsverhalten von ultrahochfestem Beton (UHPC) bei zyklischen Beanspruchungen im Druck-Zug-Wechselbereich. Dissertation, (Munich 2012).
- [2] Stürwand, S.: Versuche zum Biegetragverhalten von UHPC mit kombinierter Bewehrung. Research Paper, (Kassel, 2011).
- [3] Lappa, E. S.: High Strength Fibre Reinforced Concrete Static and fatigue behaviour in bending. Dissertation, (Delft, 2007).
- [4] Graybeal, B. A., Hartmann J. L.: Ultra-High Performance Concrete Material properties. 2003 Transportation Research Board Conference, (2002).
- [5] Makita, T., Brühwiler E.: Tensile fatigue behavior of ultra-high performance fibre reinforced concrete (UHPFRC). *Materials and Structures*, Vol. **47**, Issue 3, (2014). 475-491.
- [6] Gutsch, A.-W.: Stoffeigenschaften jungen Betons – Versuche und Modelle. Dissertation, (Braunschweig, 1998).
- [7] Visalvanich, K., Naaman, A. E.: Fracture Model for Fiber Reinforced Concrete. *ACI Journal* **80**, No. 2, (1983), 128-138.

UPGRADING THE CONCEPT OF UHPFRC FOR HIGH DURABILITY IN THE CRACKED STATE: THE CONCEPT OF ULTRA HIGH DURABILITY CONCRETE (UHDC) IN THE APPROACH OF THE H2020 PROJECT RESHEALIENCE

Pedro Serna (1), Francesco Lo Monte (2), Eduardo J. Mezquida-Alcaraz (1), Estefania Cuenca (2), Viktor Mechtcherine (3), Michaela Reichardt (3), Alva Peled (4), Oren Regev (4), Ruben P. Borg (5), Alexej Tretjakov (6), Dennis Lizunov (6), Konstantin Sobolev (7), Stamatina Sideri (8), Kim Nelson (9), Enrico Maria Gastaldo Brac (10) and Liberato Ferrara (2)

(1) Universitat Politècnica de Valencia, Spain

(2) Politecnico di Milano, Italy

(3) Technische Universität Dresden, Germany

(4) Ben Gurion University of the Negev, Israel

(5) University of Malta, Malta

(6) ANF Development OU, Estonia

(7) University of Wisconsin at Milwaukee, USA

(8) API Europe, Greece

(9) American Process, USA

(10) Penetron Italia, Italy

Abstract

Current solutions for new concrete constructions in Extremely Aggressive Exposures, as recommended and enforced by design codes, are not taking into account new cement-based construction materials, such as Ultra High Performance Fibre Reinforced Concrete, neither new constituents specifically conceived to improve the concrete durability, because of the lack of standards and technical awareness by most designers and contractors. The H2020 ReSHEALience project will upgrade to the concept of Ultra High Durability Concrete (UHDC), combining nano-scale constituents (nano-cellulose, alumina nanofibers) and self-healing promoters (crystalline admixtures). The paper will present the approach pursued in the project together with a synopsis of the results of ongoing research.

Keywords: Ultra High Durability Concrete, (micro)cracked state, nanoparticles, self-healing.

1. INTRODUCTION

Reinforced Concrete structures exposed to Extremely Aggressive Environments (EAE) experience several durability time-dependent problems, including ageing and corrosion of reinforcement, which may result into the need of early and often continuous repairs. A recent case history analysis [1], showed that 50% of the repaired concrete structures failed once again, 25% of which in the first 5 years, 75% within 10 years and 95% within 25 years. This highlights the urgent need of a profound rethinking of the concept and design processes for new and repaired R/C structures in EAE in view of cost-effectiveness demands. Current solutions as recommended and enforced by design codes, are not taking into account new cement-based construction materials, such as Ultra High Performance (Fibre Reinforced) Concrete - UHP(FR)C, neither new constituents specifically conceived to improve the concrete durability, because of the lack of standards and technical awareness by most designers and contractors.

UHPFRC can be regarded among the most significant innovations in concrete technology introduced in the last twenty years or so. The material concept relies upon a micro-mechanical design of the mix composition, based on the balance between crack-tip toughness and fibre pull-out work [2-4]. Once the first crack is formed, the crack bridging action of the fibres is activated. This results into signature tensile behaviour, characterized by stable multiple cracking process and strain-hardening response, up to the onset of the unstable localization of one single crack [5]. The mix-composition that enables the material to achieve this signature tensile behaviour is characterized by a high binder content and a low water/binder ration, compensated by a high dosage of superplasticizer and results into:

- a superior performance in the fresh state, highly conducive to self-compacting consistency, which may also result into the possibility of tailoring the fibre alignment along the direction of the casting flow and optimize the “in-structure” material performance [6-8];
- a superior durability in the un-cracked state, because of the high compactness of the matrix, as due to the high content of fibres as well as to the use of small aggregates;
- a superior durability in the cracked state, due to the highly effective crack-width control, the penetration of aggressive agents being governed by the width of the single crack [9-10].

Moreover, the synergy between crack tightness and material composition also results into a high conduciveness to autogenous self-healing, with synergetic effects on the enhancement of the material and structural durability [11-24]. Healing products reconstruct the through-crack continuity and also improve the fibre-matrix bond, which may result, when reloading a healed specimen, into the formation of new cracks instead of the re-opening of the healed one [17].

Despite the widely predicated and lab-scale demonstrated benefits that the UHPC/UHPFRC technology is able to bring to the construction sector, its market penetration is still limited. This is due, on the one hand, to the higher inertia of the construction sector in implementing innovation, as compared to other industry sectors, as also due to the “safety of people concerns” embedded in the design and building of each and all building/civil engineering feats as well as to the “uniqueness” of each feat. On the other hand, though some national guidelines are going to be published, UHPFRC still suffers from the lack of internationally recognized testing and design standards, which would provide engineers the required confidence to exploit its multiple benefits in the design and construction of high-end engineering applications. Information is also scant with reference to the durability in the cracked state, which is the true service condition directly affecting the service life of the structure. The methodology proposed by the H2020 project ReSHEALience in order to fill the aforementioned gap will be addressed in this paper.

2. ULTRA HIGH DURABILITY CONCRETE (UHDC): TOWARDS A METAMATERIAL CONCEPT AND A HOLISTIC DESIGN METHODOLOGY.

Improving the durability and extending the service life of structures exposed to EAEs, at the same time reducing their maintenance needs, is an extremely challenging goal which the civil engineering community has to face in the current social and economic framework. The H2020 project ReSHEALience is proposing to upgrade the concept of UHPFRC through the incorporation of tailored functionalities to a “metamaterial” concept, named Ultra High Durability Concretes (UHDCs), which will share the signature tensile “strain hardening” behaviour of UHPFRC.

The ReSHEALience consortium has agreed upon the following definition of UHDC: “strain-hardening (fibre reinforced) cementitious material with functionalizing micro- and nano-scale constituents (alumina nanofibers, cellulose nanofibers/crystals, crystalline admixtures, especially added to obtain a high durability in the cracked state”. It is understood that UHDC contains fibres to obtain the strain-hardening response (so it is a FRC, and also a HPFRCC) and it has a special selection of solid particles to achieve the required durability as well as a self-compacting consistency, also instrumental to obtain a homogeneous fibre distribution.

3. TAILORED FUNCTIONALIZATION OF UHDC MIXES: LITERATURE SURVEY AND PRELIMINARY RESULTS

The implemented metamaterial approach to the UHDC concept and design aims to transform the material from a passive provider of protection against degradation into an active player able to govern degradation processes through multi-scale manipulation of the material structure. In order to achieve this goal, three main strategies will be followed, including:

- **Densification of the matrix:** nano-cellulose fibrils and crystals will be used to improve the density of the Interfacial Transition Zones (ITZs) and compensate autogenous shrinkage.
- **Crack growth control:** alumina nano-fibres will be used to control the crack initiation phase and different types of micro- and macro-fibres for the propagation phase.
- **Self-healing:** self-healing admixtures (crystalline admixtures) will be employed to seal small cracks and defects, in case also guaranteeing recovery of material properties.

3.1 Nano-cellulose products

Different nano-cellulose products, including fibrils and crystals, obtained by refining pulps from different sources have been reportedly used in cementitious composites [25], in percentages not higher than 1% by volume. Reported obtained benefits range from increase of compressive and flexural strength [26-29] to reduction of autogenous shrinkage [30].

Microstructural analyses have shown that the obtained improvements are due to two concurrent mechanisms. The first mechanism is the steric stabilization, as confirmed by rheological and heat flow rate measurements and microscopic imaging. The second proposed mechanism, which is likely to be dominant, is referred to as short circuit diffusion, which appears to increase cement hydration by increasing the transport of water from outside the hydration product shell on a cement grain to the unhydrated cement cores. [27].

The ReSHEALience project consortium will employ BioPlus® Cellulose Nanofibrils (CNF), with dimensions ranging from 5-20 nm in diameter and 500-2,000+ nm in length, and BioPlus® Cellulose Nanocrystals (CNC), with dimensions ranging from 5 nm in diameter and 50-500 nm in length (Figure 1) supplied in sonicated suspension at 10% solid content.

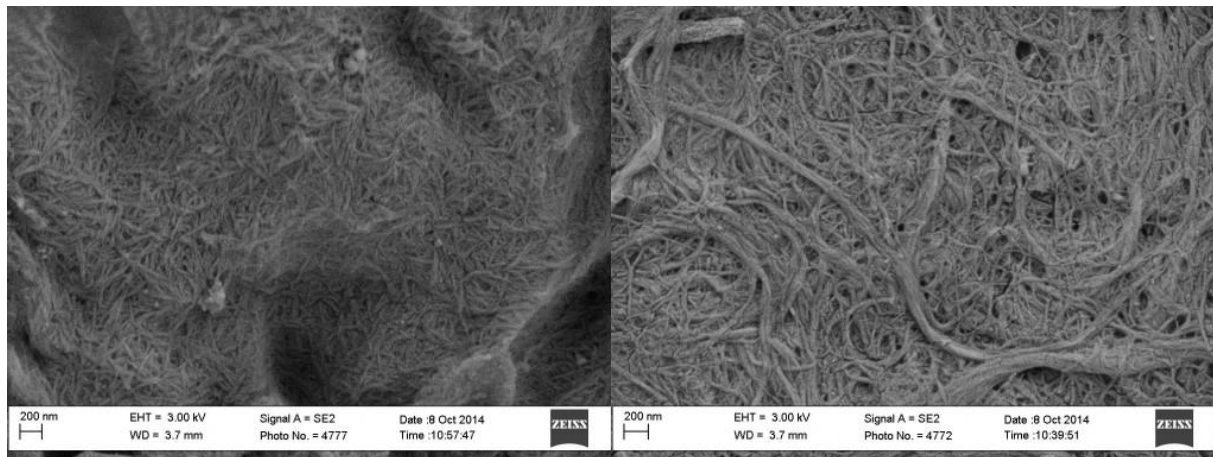


Figure 1: Bioplus ® cellulose nanocrystals (left) and nanofibrils (right).

3.2 Alumina nanofibers

In the literature, the use of alumina Al_2O_3 nano-particles, employed at dosages varying from 0.5% to 1%, is reported to improved strength and reduced setting time, as a results of more compact microstructure. A lower strength decay after exposure to high temperature was also reported [31] as well as an improvement in freeze-thaw resistance [32].

The aluminium oxide nanofibers branded as NAFENTM, which will be employed in the current project, have been so far applied into a broad range of industrial products (aerospace, automotive, energy), resulting into a confirmed 20-50% improvements in mechanical properties of polymer and composite end products. The fibres are 4 to 11 nm in diameter and from 100 to 900 nm long, with a specific surface equal to $155 \text{ m}^2/\text{g}$ [Figure 2]. In order to be employed into a cementitious composite mix featuring low w/b ratios they need to be supplied into a sonicated suspension at a solid concentration ratio equal to 10%, much higher than for other applications.

Preliminary investigation has been performed at University of Wisconsin at Milwaukee, with reference to a typical UHPC matrix, with NAFEN fibres dosed at 0.25% by weight of cement, and in case with 1% addition of either meta-kaolin or silica-fume. The results have shown a roughly 30% increase of both 7 and 28 days compressive strength. The same improvements are confirmed also when different fibres (12 mm long) have been added (Figure 3).

3.3 Crystalline admixtures

Though Crystalline Admixtures, are well known and widely used in modern concrete technology, being classified as a special type of permeability reducing admixture, they have only recently started receiving special attention as self-healing promoters. Significant amount of work in this respect has been done [33-38]. Moreover, an interesting synergy with the dispersed fibre reinforcement has been observed [39 – Figure 4a-b], in the case of a UHPFRC mix (w/b ratio 0.18) containing 0.8% by cement weight of Penetron Admix ® and 100 kg/m^3 straight short steel fibres ($l_f/d_f = 13/0.16$). The filling of the cracks by crystalline healing products is likely to activate a sort of chemical pre-stressing throughout the cracked material, from which the healing induced recovery of the performance is likely to benefit to a greater extent than in the case of ordinary FRC and plain concrete. A contribution in this sense may also come from the light shrinkage-reducing effect that the admixtures may provide, as from preliminary results shown in Figure 5.

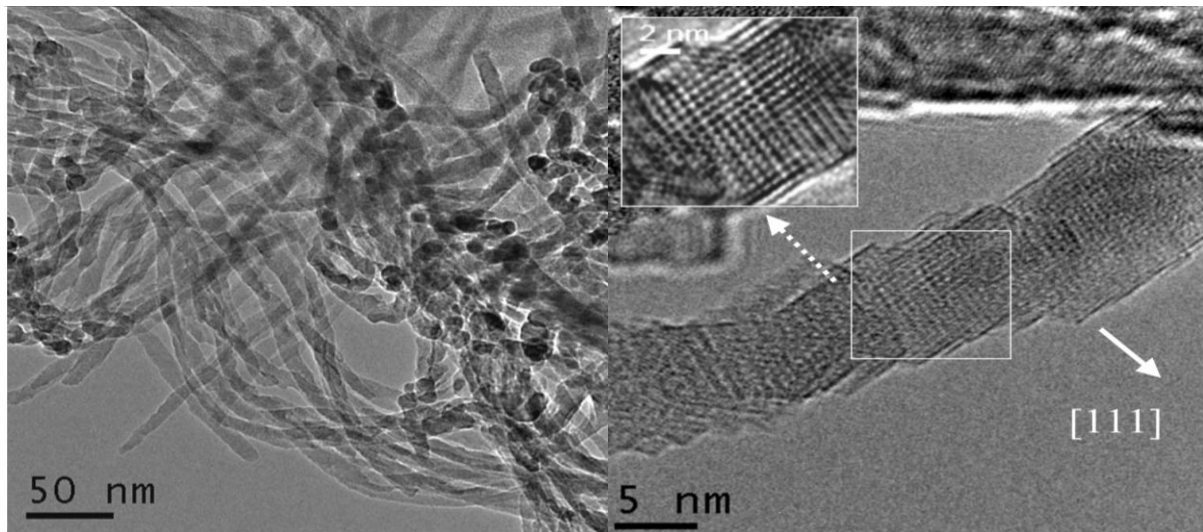


Figure 2. NAFEN® aluminium oxide nano-fibres at different magnification scale.

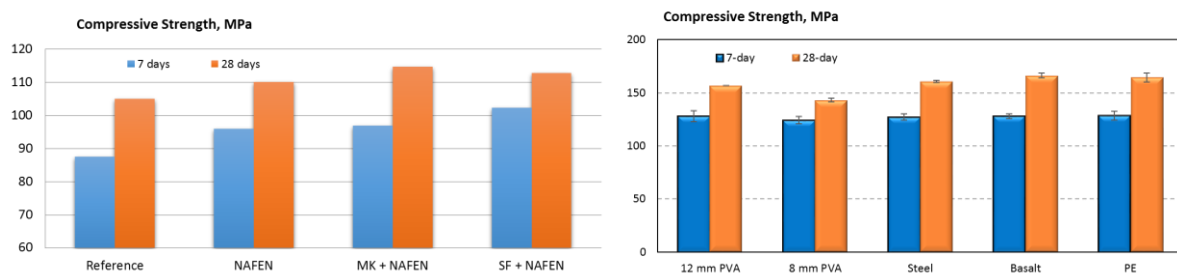


Figure 3. Effect of NAFEN™ fibres on the compressive strength of UHPC mortars (left) and effect of fibres on compressive strength of UHPC mortars with NAFEN™ fibres (right).

The research activity performed in the framework of the project is going to further investigate this issue, so far limited to the results of a tailored experimental campaign, also with reference to the EAE of interest as well as to the synergy between the employed crystalline admixture and the selected nano-scale constituents detailed above.

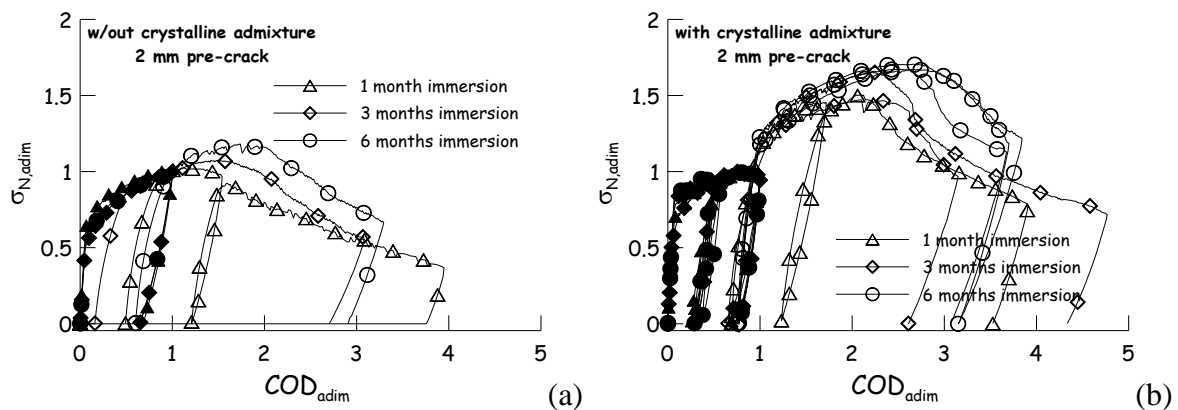


Figure 4. Crack-healing induced recovery of mechanical properties (4point bending) in UHPC specimens without (a) and with (b) crystalline admixture cured in water after cracking [52].

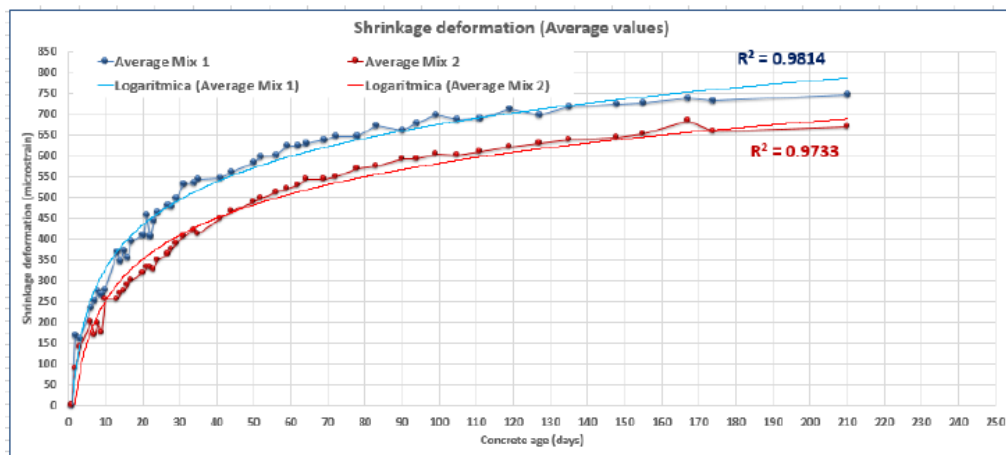


Figure 5. Effect of crystalline admixture (0.8% by cem weight Penetron Admix ®) on free drying shrinkage in FRC mix (0.45 w/c ratio)

4. CONCLUSIONS

The main objective of H2020 project ReSHEALience is to upgrade the concept of UHPC to Ultra High Durability Concrete (UHDC). The underlying key idea is to transform, through the incorporation of self-healing stimulators and nano-constituents, the material from a passive provider of protection into an active player, able to respond to degradation processes as a function of the durability requirements. The self-healing functionalization, with continuous tailored recovery of performance achievable on demand, will reduce the need of repair actions and the global cost, which will compensate the higher initial material cost (Figure 6). This will result into a breakthrough metamaterial concept in which durability is not a bonus but becomes the governing objective, able to “convert” cement-based construction materials from “durability passive” spectators with structural functions, into active players, using value-added synergy-acting functionalities “tailored” to an as broad as possible range of applications.

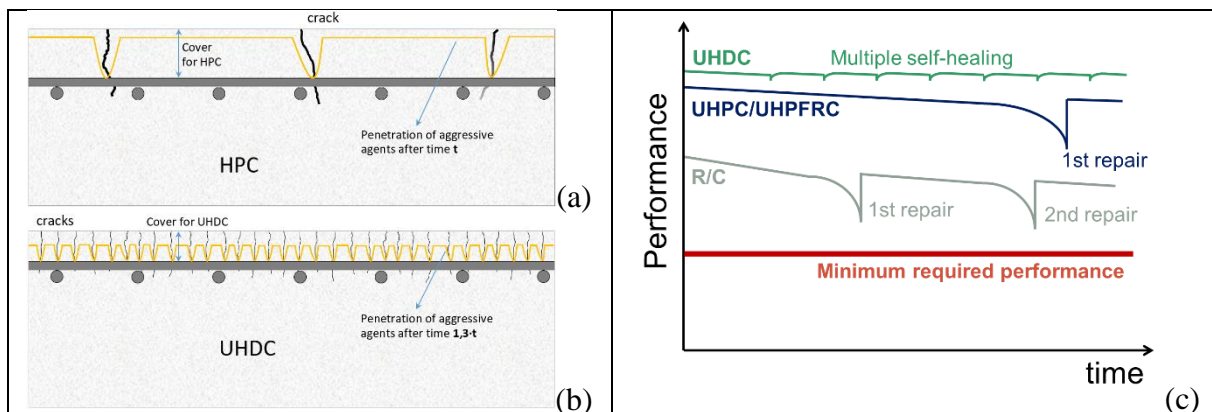


Figure 6. Concept of HPC and UHDC (a-b) durability in performance/repair/time frame (c).

Acknowledgements

This project has received funding from the European Union’s Horizon 2020 research and innovation programme under grant agreement No 760824.

REFERENCES

- [1] Matthews, S., 'Conrepnet: Performance-based approach to the remediation of reinforced concrete structures: Achieving durable repaired concrete structures', *J. Bldng. Appr.* 3(1) (1997) 6-20.
- [2] Li, V.C. and Wu, H.C., 'Conditions for pseudo strain-hardening in fiber reinforced brittle matrix composites', *Appl. Mech. Rev.*, 45 (8) (1992) 390-398.
- [3] Li, V.C., Stang, H. and Krenchel, H., 'Micromechanics of crack bridging in fibre-reinforced concrete', *Mats. & Structs.*, 26 (8) (1993) 486-494.
- [4] Li, V.C., 'On engineered cementitious composites. A review of the material and its applications' *J. Adv. Concr. Tech.*, 1 (3) (2003) 215-230.
- [5] Naaman, A.E. and Reinhardt, H.W., 'Proposed classification of HPFRC composites based on their tensile response', *Mats. & Structs.* 39 (5) (2006) 547-555.
- [6] di Prisco, M., Ferrara, L. and Lamperti, M.G.L., 'Double Edge Wedge Splitting (DEWS): an indirect tension test to identify post-cracking behaviour of fibre reinforced cementitious composites', *Mats. & Structs.* 46(11) (2013) 1893-1918.
- [7] Ferrara, L., Ozyurt, N. and di Prisco, M. 'High mechanical performance of fiber reinforced cementitious composites: the role of "casting-flow" induced fiber orientation', *Mats. & Structs.* 44(1) (2011) 109-128.
- [8] Ferrara, L., Faifer, M., Muhaxheri, M. and Toscani, S., 'A magnetic method for non destructive monitoring of fiber dispersion and orientation in Steel Fiber Reinforced Cementitious Composites – part 2: correlation to tensile fracture toughness', *Mats. & Structs.* 45 (4) (2012) 591-598.
- [9] Lepech, M.D. and Li, V. 'Water permeability of Engineered Cementitious Composites', *Cem. Concr. Comp.* 31 (2009) 744-753.
- [10] Plagué, T., Desmettre, C. & Charron, J.P., 'Influence of fiber type and fiber orientation on cracking and permeability of reinforced concrete under tensile loading', *Cem. Concr. Res.*, 94 (2017) 59-70.
- [11] Li, V., Lim, Y., and Chan, Y., 'Feasibility of a passive smart self-healing cementitious composite. *Comp. B: Engrg.*, 29 (1998) 819-827.
- [12] Yang, Y., Lepech, M., Yang, E., and Li, V., 'Autogenous healing of engineered cementitious composites under wet-dry cycles', *Cem. Concr. Res.* 39 (2009) 382-390.
- [13] Yang, Y., Yang, E.-H. and Li, V.C., 'Autogenous healing of engineered cementitious composites at early age', *Cem. Concr. Res.* 41 (2011) 176-183.
- [14] Li, M., and Li, V., 'Cracking and healing of Engineered Cementitious Composites under chloride environment', *ACI Mats. J.* 108(3) (2011) 333-340.
- [15] Özbay, E., Şahmaran, M., Lachemi, M., and Yücel, H., 'Self-healing of microcracks in high volume fly ash incorporated engineered cementitious composites', *ACI Mat. J.*, 110 (2013) 33-44.
- [16] Zhang, Z., Qian, S. and Ma, S., 'Investigating mechanical properties and self-healing behavior of micro-cracked ECC with different volume of fly ash', *Constr. Build. Mats.* 52 (2014) 17-23.
- [17] Ferrara, L., Ferreira, S.R., Krelani, V., Della Torre, M., Silva, F. and Toledo, R., 'Natural fibers as promoters of autogenous healing in HPFRCCs: Results from on-going Brazil-Italy cooperation', In M.A. Chiorino et al., eds., ACI SP-305. Proc. DSCS, Bologna, Italy, Oct. 1-3 2015, 11.1-11.10.
- [18] Ferrara, L., Krelani, V. and Moretti, F., 'Autogenous healing on the recovery of mechanical performance of HPFRCCs: part 2 – correlation between healing of mechanical performance and crack sealing. *Cem. Concr. Comp.*, 73 (2016) 299-315.
- [19] Ferrara, L., Krelani, V., Moretti, F., Roig Flores, M. and Serna Ros, P., 'Effects of autogenous healing on the recovery of mechanical performance of HPFRCCs: part 1'. *Cem. Concr. Comp.*, 83 (2017) 76-100.
- [20] Şahmaran, M., Yildirim, G., Noori, R., Ozbay, E. and Lachemi, M., 'Repeatability and pervasiveness of Self-Healing in Engineered Cementitious Composites', *ACI Mats. J.*, 112(4) (2015) 513-522.
- [21] Yildirim, G., Kasap Keskin, Ö., Bahadır Keskin, S., Şahmaran, S. and Lachemi, M. 'A review of

- intrinsic self-healing capability of engineered cementitious composites: recovery of transport and mechanical properties', *Constr. Bldg. Mats.* 101 (2015) 10-21.
- [22] Yildirim, G., Alyousif, A., Şahmaran, M., and Lachemi, M., 'Assessing the self-healing capability of cementitious composites under increasing sustained loading'. *Adv. Cem. Res.*, 27(10) (2015) 581-592.
- [23] Yildirim, G., Şahmaran, M., Balcikanlib, M., Ozbay, E. and Lachemi, M., 'Influence of cracking and healing on the gas permeability of cementitious composites', *Constr. Bldg. Mats.*, 85 (2015) 217-226.
- [24] Snoeck, D. and De Belie, N., 'Repeated autogenous healing in strain-hardening cementitious composites by using superabsorbent polymers', *ASCE J. Mats. Civ. Engrg.*, 28(1) (2016) 1-11.
- [25] Fu, T., Moon, R., Zavaterri, P., Youngblood, J. and Weiss, J., 'Cellulose nanomaterials as additives for cementitious materials', In *Cellulose-Reinforced Nanofibre Composites*, Jawaid, M. et al. eds., Woodhead Publishing Series in Composites Science and Engineering, 455-482.
- [26] Ardanuy, M., Claramunt, J., Arevalo, R., Pares, F., Aracri, E. and Vidal, T., 'Nanofibrillated cellulose (NFC) as a potential reinforcement for high-performance cement mortar composites'. *Bioresources*, 7 (3) (2012) 3883-3894.
- [27] Cao, Y., Zavaterri, P., Youngblood, J., Moon, R. and Weiss, J., 'The influence of cellulose nanocrystal additions on the performance of cement paste', *Cem. Concr. Comp.*, 56 (2015) 73-83.
- [28] Cao, Y., Zavaterri, P., Youngblood, J., Moon, R. and Weiss, J., 'The relationship between cellulose nanocrystal dispersion and strength', *Constr. Bldg. Mats.*, 119 (2016) 71-79.
- [29] Mejdoub, R., Hammi, H., Sunol, J.J., Khitouni, M., M'nif, A. and Boufi, S., 'Nanofibrillated cellulose as nano reinforcement in Portland cement: thermal, mechanical and microstructural properties', *J. Comp. Mats.*, 51 (1) (2016) 2491-2503.
- [30] Ferrara, L., Ferreira, S.R., Della Torre, M., Krelani, V., Silva, F. and Toledo Filho, R.D., 'Effect of cellulose nanopulp on autogenous and drying shrinkage of cement based composites', In K. Sobolev and S.P. Shah, eds., *Proc. Nicom 5*, Springer, Chicago, 26-28 May 2015, 325-330.
- [31] Gowda, R., Narendra, H., Rangappa, D. and Prabhakar, R., 'Effect of nano-alumina on workability, compressive strength and residual strength at an elevated temperature of Cement Mortar', *Materials Today: Proceedings*, 4(11) (2017) 12152-12156.
- [32] Behfarnia, K. and Salemi, N. The effects of nano-silica and nano-alumina on frost resistance of normal concrete. *Constr. Bldg. Mats.* 48 (2013) 580-584.
- [33] Ferrara, L., Krelani, V. and Carsana, M., 'A fracture testing based approach to assess crack healing of concrete with and without crystalline admixtures', *Constr. Bldg. Mats.*, 68 (2014) 515-531.
- [34] Roig-Flores, M., Moscato, S., Serna, P. and Ferrara, L., 'Self-healing capability of concrete with crystalline admixtures in different environments', *Constr. Bldg. Mats.*, 86 (2015) 1-11.
- [35] Roig Flores, M., Pirritano, F., Serna Ros, P. and Ferrara, L., 'Effect of crystalline admixtures on the self-healing capability of early-age concrete studied by means of permeability and crack closing tests', *Constr. Bldg. Mats.*, 114 (2016) 447-457.
- [36] Borg, R.P., Cuenca, E., Gastaldo Brac, E.M. and Ferrara, L., 'Crack sealing capacity in chloride rich environments of mortars containing different cement substitutes and crystalline admixtures', *J. Sust. Cem. Based Mats.*, 7(3) (2018) 141-159.
- [37] Cuenca, E., Tejedor, A. and Ferrara, L., 'A methodology to assess crack sealing effectiveness of crystalline admixtures under repeated cracking-healing cycles', *Constr. Bldg. Mats.*, 179 (2018) 619-632.
- [38] Escoffres, P., Desmettre, C. and Charron, J.P., 'Effect of a crystalline admixture on the self-healing capability of high-performance fiber reinforced concretes in service conditions', *Constr. Bldg. Mats.* 173 (2018) 763-774.
- [39] Ferrara, L., Krelani, V. and Moretti, F., 'On the use of crystalline admixtures in cement based construction materials: from porosity reducers to promoters of self-healing', *Smart Mats. & Struct.* 25 (2016) paper 084002.

HIGH-PERFORMANCE AND DURABLE FIBER CONCRETE MADE OF RECYCLED CARBON FIBERS

Magdalena Kimm (1), Thomas Gries (1)

(1) Institut für Textiltechnik of RWTH Aachen University, Germany

Abstract

The controversial issue of the reuse of carbon fibre waste from high-performance parts is still unsolved. Especially in the construction industry, the use of carbon-textile reinforced concrete is increasing. Current waste masses of carbon fibres lie around 4.000 t per year in Europe which shall rise up to 30.000 t per year within the next 10 years. However, recycled carbon fibres are up to 5 times cheaper than new fibres - and offer almost identical performance. Only the shortening of the fibre length currently prevents the material from returning to its original application. Therefore, a new application for recycled carbon fibres in fibre concrete is currently developed.

Tests on carbon fibre concrete specimen show an increase in bending strength of approx. 14 % compared to the benchmark of glass fibre concrete, while the required fibre mass could be reduced by 75 mass-%. Therefore, material efficiency of the carbon fibre reinforcement is increased and the long-term durability of the novel composite material is significantly improved. First estimations show, that a recycling rate of 22 % of the current carbon fibre waste in Europe can be achieved by replacing 20 % of steel fibres for fibre concrete applications in Germany only.

Keywords: Recycling, carbon fibre, fibre reinforced concrete, mortar, cement

1. INTRODUCTION

The diversity of materials and the proportion of fibre-reinforced composites in the material cycle has been increasing for years in the aviation, automotive, construction and sports sectors. The current demand for carbon fibres is expected to increase by >10 % annually by 2022 up to 117.000 t carbon fibres (CF) and 194.000 t carbon fibre-reinforced plastics (CFRP) [1]. Simultaneously, legal recycling rates, e.g. 95 % in the automotive industry and 70 % for construction and demolition waste (Waste Framework Directive 2008/98/EG, [2]), raise urgent questions about recycling and the environmental impact of CF and CFRP waste. According to the current European CFK recycling industry 4.000 t of CF and CFRP are annually produced in Europe today. Around 30.000 t per year are a realistic value in the next 10 years containing dry and pre-impregnated waste from production and cured waste from End-of-Life CFRP

components. Especially the share End-of-Life components will rise – and therefore the share of recycled CF (rCF) treated by mechanical, thermal or chemical processing, e.g. pyrolysis or solvolysis [3].

With the current state of the art, it is not possible to recycle carbon fibres without loss in their length [3]. In contrast, rCF from cut waste retain 100 % and treated rCF retain 80-90 % of the mechanical properties of virgin fibres and are significantly more cost-effective as investigations at Institut für Textiltechnik of RWTH Aachen University have shown [4]. Current products made with recycled CF (rCF) focus on new fibre reinforced plastics e.g. made of nonwovens, yarns, bulk/sheet moulding compounds [5–9]. Often these products target the original markets, automotive & aerospace industry. Those industries mostly show a demand for “virgin” cut fibre by directly reusing their own waste in a closed-loop-production. Currently, there is a lack of a high-quality recycling concept for treated rCF. This work therefore focusses on the material development of rCF-reinforced concrete.

2. STATE OF THE ART

The usage of high performance fibres in concrete is popular since the 1970ies (steel fibres) and 1980ies (AR-glass fibres) [10]. Several testing and processing standards for short fibre reinforced concrete (FRC) already exist on international, European and German level.

A comparison of rCF with established fibres for concrete including virgin CF is shown in Table 2. As polymer fibres have significantly lower tensile strength than all other fibre types (as polypropylene for example) and therefore are not used for reinforcement purposes, they will not be discussed here.

Table 1: Fibre types and their material properties for application in FRC

Fibre	Costs [€/kg]	Tensile strength [MPa]	E-Modulus [MPa]	Dosage [kg/m ³]	Fibre length [mm]
Steel [11]	1	1,000-2,400	210,000	25-30	6,13, 20, 25, 30, 35, 45, 50, 60 ¹
AR-Glass [12]	6.50 - 9	1,000-1,700 ²	70,000-90,000	0.75-3 (anticrack) 50-90 (reinfor.)	6, 12, 18, 24, 36 ²
Polypropy- lene	6 - 9	250-590	4,900-11,000	2-9	3, 6, 12, 18 (Micro) ¹ 48, 54 (Macro) ¹
rCF ³	6-12	2,500-3,600	200,000	?	3-10, 10-30, 30-60, 60- 90 ⁴
Virgin CF (HT/ST)[13]	20-30	3,500-4,600	239,000	17-70 [14, 15]	6, 12 ⁵

¹ Steel and polymer fibres, Krampe Harex GmbH & Co. KG. <https://www.krampeharex.com/de/fasern/produkte/> (visited on 15.08.2018)

² Cem-Fil®, OCV Reinforcements. <http://www.ocvreinforcements.com/CemFIL/ab-properties.aspx?lg=en>.
https://durapact.de/index.php?de_kurzfasern (visited on 15.08.2018)

³ From material tests performed at ITA of RWTH Aachen University and ITA Augsburg gGmbH

⁴ carbiso C, ELG CF Ltd., www.elgcf.com/products/chopped-carbon-fibre (visited at 27.09.2018)

⁵ carbiso CT, ELG CF Ltd., <http://www.elgcf.com/products/chopped-tow> (visited at 27.09.2018)

In the 1970ies carbon fibres for reinforcing mortar were investigated for the first time [15, 16]. In the late 1980ies and 1990ies cement-based composites reinforced with short new CF based on pitch and polyacrylonitrile (PAN) were studied as part of extensive research in Japan and the Unites States. There are several US patents [17, 18] from that period. Current investigations on virgin CF for use in heatable floors and in 3D-printable cement pastes [19] provide the following results: 0, 1, 2 and 4 vol.% with a length of virgin CF of 0.2, 1, 3 and 10 mm are tested. The maximum flexural and compressive strengths were found at 1 vol.-% with 3 mm fibres [14].

However, up to date, virgin CFs have not been extensively used for concrete applications, mainly due to economic reasons as their cost is considerably high. However, rCF might be attractive for concrete applications as their cost is much lower (see Table 2). First results for reuse of rCF from cut, un-impregnated CF-sheets (YC-N200, no producer provided, tensile strength of 3550 MPa) in concrete have been achieved [20, 21]. These CF are, regarding their mechanical performance, comparable with virgin, short carbon fibres.

OGI et al. have used shredded CFRP pieces of three sizes as crack bridging devices in concrete. The improvement of flexural strength rises with decreasing CFRP piece size. An improving effect by volume content cannot be evaluated clearly. But it can be stated that CFRP pieces in concrete enable a constant, gradually decrease of load after the maximum stress (instead of a rough de-crease), resulting in large displacement values of work of fracture compared to plain concrete. [22]

3. MATERIALS AND METHODS

In this work, flexural tests – according to EN 1170-5 (see Fig. 1) – were carried out on fibre-reinforced fine concrete with AR-Glass fibres, virgin carbon fibres and recycled carbon fibres (see also Fig. 2 a, b).

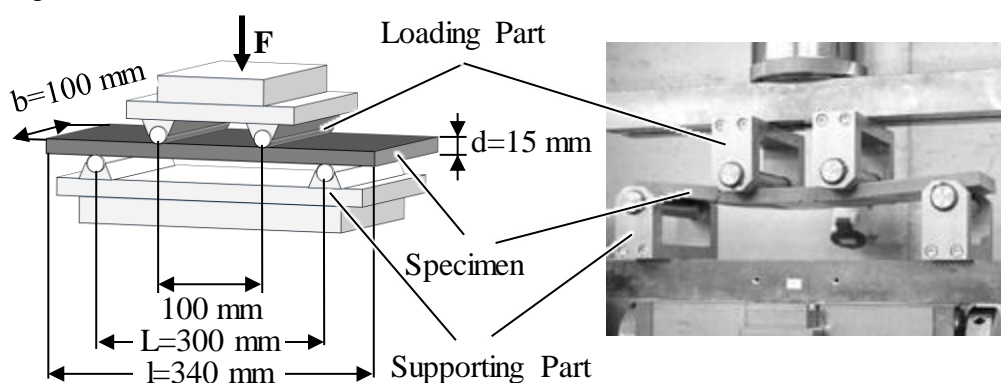


Figure 1: Test setup according to EN 1170-5

The rCF were recovered by pyrolysis. All fibres were manually cut at a length of 12 mm. The following table summarizes the product data.

Table 2: Properties of used fibre types (properties of rCF fibres were measured at ITA's textile laboratory)

	AR-glass fibre	Carbon fibre
Fibre type	CEM-FIL® 5325, 1200 tex, OCV Reinforcements	Tenax® HTS 40 12k, 800 tex, Toho Tenax Europe GmbH
Density	$2,68 \frac{\text{g}}{\text{cm}^3}$	$1,77 \frac{\text{g}}{\text{cm}^3}$
E-Modulus	$72.000 \frac{\text{N}}{\text{mm}^2}$	$239.000 \frac{\text{N}}{\text{mm}^2}$
Tensile strength	$1.700 \frac{\text{N}}{\text{mm}^2}$	$4.620 \frac{\text{N}}{\text{mm}^2}$

The tests were performed with 0.2 Vol.-% (3.75 kg/m³) of virgin CF and rCF. Due to the higher density and lower tensile strength AR-Glass fibres the equivalent fibre volume of glass fibres was increased in accordance with these property relations:

$$\text{Density-factor } \frac{\rho_{\text{virgin Carbon}}}{\rho_{\text{ARGlass}}} = \frac{2.68 \frac{\text{g}}{\text{cm}^3}}{1.77 \frac{\text{g}}{\text{cm}^3}} \approx 1.51 \quad (1)$$

$$\text{Tensile-Strength-factor } \frac{R_{m_ARGlass}}{R_{m_virgin Carbon}} = \frac{1700 \frac{\text{N}}{\text{mm}^2}}{4620 \frac{\text{N}}{\text{mm}^2}} \approx 2.72 \quad (2)$$

$$\text{Total factor} = 1.51 \cdot 2.72 \approx 4.1 \quad (3)$$

$$\text{Equivalent AR-Glass-fibre mass} = 3.75 \frac{\text{kg}}{\text{m}^3} \cdot 4.1 = 15.4 \frac{\text{kg}}{\text{m}^3} \quad (4)$$

Moulds with the dimensions 61 × 34 × 1,5 cm³ were used to produce the test specimens. The mould is made in such a way that the specimens are marked by slots on the surface. Six specimens were cut out per plate. The concrete matrix is composed from cement CEM I 52.2 N (147,0 g), fly ash (52,5 g), silica powder (EMSAC 500 SE, Ha-Be Betonchemie, 21,0 g), quartz flour (Silverbond® M4, Sibelco, Benelux, 150,0 g), sand 0,2 - 0,6 mm (213,9 g), water (73,5 g) and PCE-based plasticizer (MasterGlenium® 51, BASF, 2,10 g).

The solid and liquid components were pre-mixed individually and then mixed with a collo mixer. During this final mixing process, the cut fibres were added. For this purpose, small quantities were continuously put into the concrete by hand, see Fig. 2 c. A significant increase in the workability of the concrete were noticeable during mixing. Especially the concrete with the CF and rCF needed a higher power effort compared to the AR-GF. However, the consistency of the fresh concrete became more viscous and stiff with all fibres. For compacting, the moulds were placed on a vibrating plate for approx. 10 minutes (see Fig. 2 d).

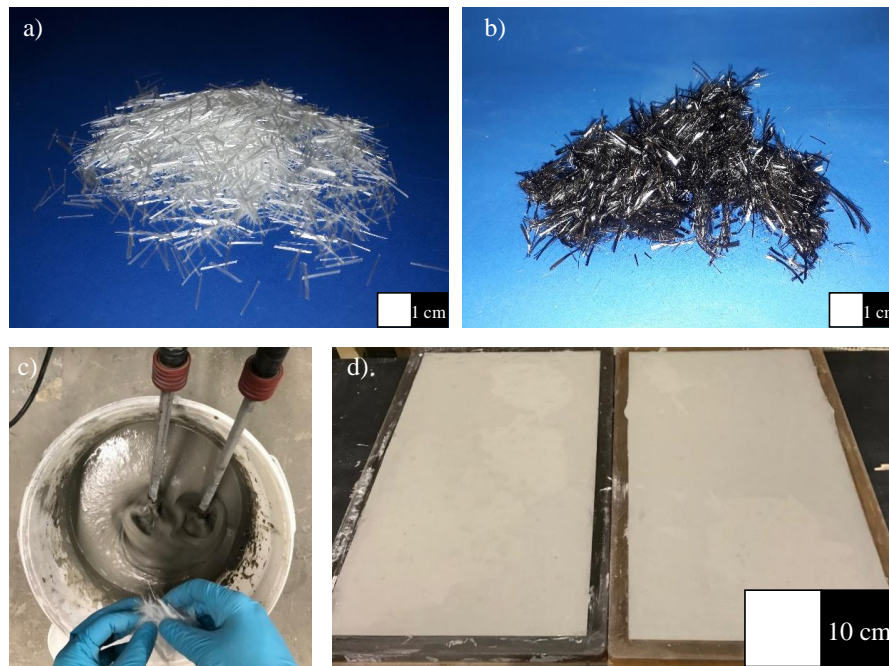


Figure 2: a) AR glass fibres, b) recycled carbon fibres by pyrolysis before cutting down to 12 mm, c) adding of fibres into fresh concrete, d) fresh specimen plates in mould during vibration

After the fresh concrete had been stored for 24 hours, the plates were de-moulded. The finished but not yet cut test plates were then placed in a container with water, where they are stored for approx. 6 days. After 6 days, the specimens were removed from the water bath and stored for a further 21 days in a room climate of 20 ± 3 °C. 24 hours before the test, the specimens were again placed in a water bath.

4. RESULTS

In Fig. 3 the force-displacement curves of the test series with AR GF, rCF and virgin CF are shown. From these, the bending strength σ at the point of maximum stress and the associated elongation ε were determined using the following formulae according to EN 1170-5 (variables see Fig. 1):

$$\sigma = \frac{F \times 1000 \times L}{b \times d^2} \quad \varepsilon = \frac{\left[\frac{108}{23} \times \frac{\Delta l}{L^2} \times d \right]}{100} \quad (5)$$

Flexural strength could be increased by 14 % from 5,66 MPa to 6,46 MPa with rCF-reinforced specimens compared to the state of the art (AR-GF), although the theoretical AR-glass fibre-equivalent mass for carbon fibres was already reduced according to the calculations in (4). The average elongation of rCF concrete (0,00132 %) is equal to AR-GF concrete. Virgin CF reinforced concrete shows even higher bending strength of 7,73 MPa (+ 37 %) but a lower elongation at point of rupture (0,00118 %). The percentage difference in elongation between AR GF/rCF and virgin CF lies around 11 %.

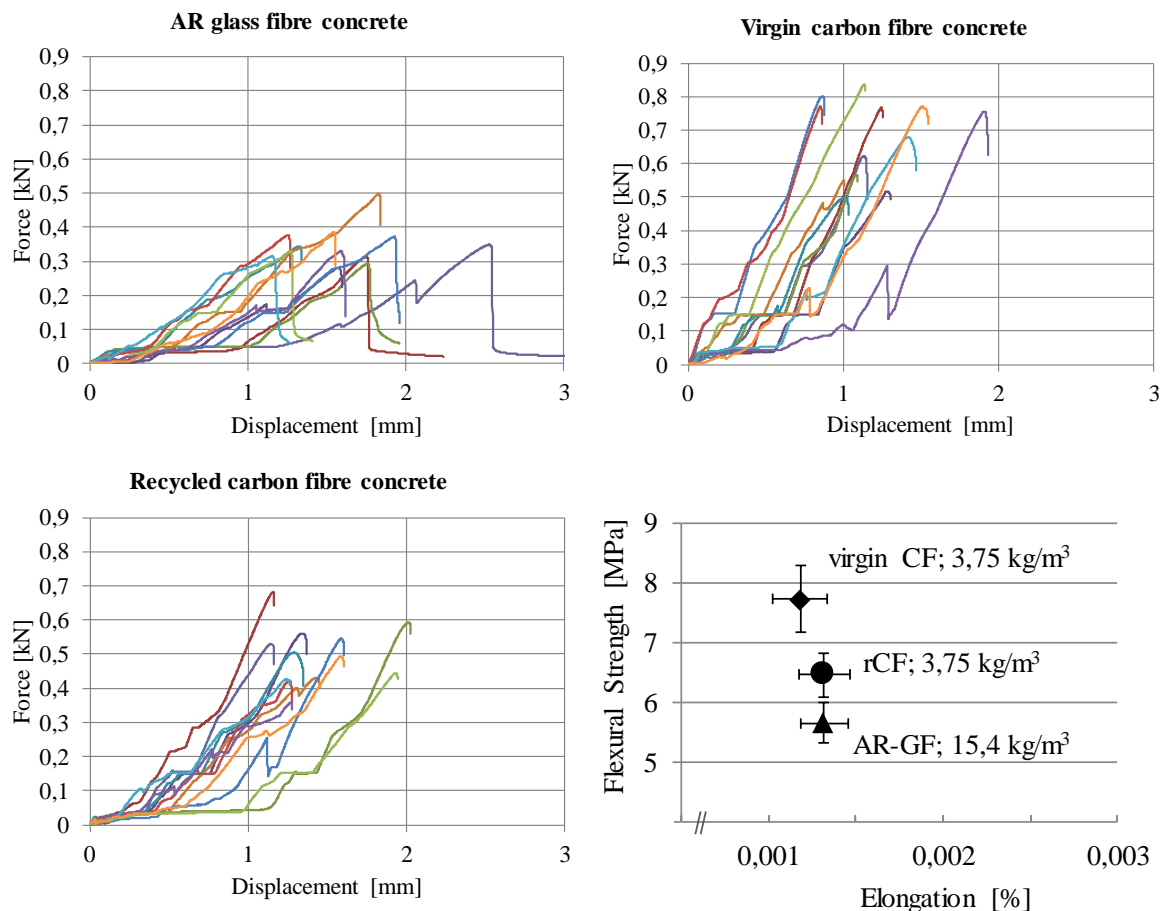


Figure 3: Force-displacement curves of the test series (each with 12 specimen) as measured.
 Comparison of flexural strength and elongation (calculation according to EN 1170-5).

5. CONCLUSIONS AND OUTLOOK

Concrete specimen, reinforced with pyrolyzed rCF based on PAN, showed an increase of 14 % in flexural strength compared to a reinforcement of AR GF, although only $3,75 \text{ kg/m}^3$ of rCF instead of $15,4 \text{ kg/m}^3$ of AR GF had been used. This is an increase of material efficiency of more than 400 %. The mean elongation at point of rupture stayed the same.

The used fibres had not been modified before integration into concrete. rCF generally show an inert surface which usually does not react with concrete, therefore it might be expediently to investigate methods for surface modification to achieve a stronger bond between fibre and concrete which could directly improve the flexural and tensile strength.

The current market size for steel fibres in steel fibre concrete is 50.000 t per year in Germany (according to German association of steel fibre concrete producers, status on 24.11.2017). In addition to AR glass fibres, steel accounts for over 95 mass-% of all reinforcement fibres used in concrete (Currently approx. 500 t AR-GF used for fibre concrete in Germany per year/a; according to expert interview with Dr. Ulrich Pachow, DuraPact Gesellschaft für Faserbetontechnologie mbH, Haan, Germany in 11.2017). More than two thirds of all fibre concretes are cast into industrial floors, the remainder being mainly precast concrete elements and tunnel construction elements. If only 20 % of the steel fibres currently used would be

replaced by recycled carbon fibres, this results in an annual application potential of 870 t rCF in Germany alone, leading into a high-quality reuse:

$$50.000 \text{ t} \cdot 20 \% = 10.000 \text{ t} \text{ (quantity of steel fibres of 20 \% market share)} \quad (6)$$

Then, the equivalent quantity of rCF, due to a lower density and higher tensile strength, accounts for:

$$10.000 \text{ t} \cdot \frac{1,7 \frac{\text{g}}{\text{cm}^3}}{7,8 \frac{\text{g}}{\text{cm}^3}} \cdot \frac{1200 \text{ MPa}}{3000 \text{ MPa}} = 5.000 \text{ t} \cdot 8,7 \% = 870 \text{ t} \quad (7)$$

This corresponds to a potential recycling rate of 22 % of the current carbon fibre waste in Europe of approx. 4.000 t per year (see chapter 1). Even from an economic point of view, the first estimate shows at least equivalent cost characteristics. The cost/m³ of steel fibre concrete amount to:

$$30 \text{ kg/m}^3 \cdot 1 \text{ €/kg} = 30 \text{ €/m}^3 \quad (8)$$

Then, the cost/m³ of rCF fibre concrete amount to:

$$30 \text{ kg/m}^3 \cdot 8,7 \% \cdot 10 \text{ €/kg} = 26 \text{ €/m}^3 \quad (9)$$

Studies on the health effects of carbon fibre fragments and dusts caused by mechanical processing, such as sawing and drilling, have shown no dangerous effects as known from WHO fibres [23]. Accordingly, when using the new fibre concrete based on recycled carbon fibres, e.g. in industrial floors with increased abrasion, no restrictions on operation are to be expected.

The investigations have shown, that recycled carbon fibres have a very high potential for reuse as short fibre reinforcement in concrete – from a technical as well as from an economical point of view.

ACKNOWLEDGEMENTS

The work was carried out under the aegis of the PhD-programme “Verbund.NRW”, supported by the North-Rhine-Westphalian funding scheme “Forschungskolleg” of the ministry of culture and science.

6. REFERENCES

- [1] Witten, E., Sauer, M., and Kühnel, M., 2017, 'Composites-Marktbericht 2017. (Composites market report 2017)'.
- [2] European Parliament & Council, 2008, 'Waste Framework Directive (2008/98/EG)'.
- [3] Oliveux, G., Dandy, L. O., and Leeke, G. A., 'Current status of recycling of fibre reinforced polymers Review of technologies, reuse and resulting properties', *Progress in Materials Science* **72** (2015), 61–99.
- [4] Lütke, C., Niebel, V., Gries, T., Endres, A., and Teufl, D., 'Hybrid-process development for efficient carbon fibre waste processing, Chania, Crete, Greece, 2016).
- [5] Lütke, C., 'Hybrid staple fibre nonwoven process for the production of organo sheets' (Dissertation, RWTH Aachen University, 2017).
- [6] Möbitz, C., Lütke, C., Niebel, V., and Gries, T., 'Recycled carbon fibre nonwovens for electromagnetic shielding applications', in 'Proceedings of the 8th Aachen-Dresden International Textile Conference, Dresden, November 27-28, 2014, Dresden, 27. - 28. November 2014.
- [7] Lütke, C., Löhner, M., Gloy, Y.-S., Gries, T., Rotheut, M., Quicker, P., Rüßmann, D., Feil, A., and Pretz, T., 'Innovative recycling processes for carbon fibre based materials to provide

- innovative and cost competitive composites', in 'Eren, Recep (Ed.): AUTEX 2014 : 14th World Textile Conference, May 26th - 28th, 2014, Bursa, Turkey'.
- [8] Hengsternann, M., Hasan, M. M. B., Abdkader A., and Cherif, C., 'Industrial manufacturing of hybrid yarns made of recycled carbon fibres for thermoplastic composites. In:', in 'Proceedings of SAMPE Europe Conference 2017, Stuttgart, 14.-16.11.2017.
- [9] Goergen, C., Baz, S., Mitschang, P., and Gresser, G. T., 'Recycled Carbon Fibers in Complex Structural Parts - Organic Sheets Made of rCF Staple Fiber Yarns', *KEM* **742** (2017), 602–609.
- [10] Wietek, B., 'Faserbeton im Bauwesen. (Fibre concrete in construction sector)' (Springer Vieweg, Wiesbaden, 2015).
- [11] Wietek, B., 'Stahlfaserbeton. (Steel fibre concrete)' (Springer Fachmedien, Wiesbaden, 2010).
- [12] Teschner, R., 'Glasfasern. (Glass fibres)' (Springer-Verlag, Berlin, Heidelberg, 2013).
- [13] Schürmann, H., 'Konstruieren mit Faser-Kunststoff-Verbunden. (Designing with fibre reinforced polymer composites)', (Springer-Verlag, Berlin, Heidelberg, 2007).
- [14] Hambach, M., 'Hochfeste multifunktionale Verbundwerkstoffe auf Basis von Portlandzement und Kohlenstoffkurzfasern. (High-strength multifunctional composites based on Portland cement and short carbon fibres.)' (Dissertation, Universität Augsburg, 2016).
- [15] Ali, M. A., Majumdar, A. J., and Rayment, D. L., 'Carbon fibre reinforcement of cement', *Cement and Concrete Research* **2** (2 (1972), 201–212.
- [16] Briggs, A., 'Carbon fibre-reinforced cement', *J Mater Sci* **12** (2 (1977), 384–404.
- [17] Matsushashi, T., Suzuki, K., Saito, K., Ogawa, H., Aga, M., Yamamiya, T., Sugimoto, K., and Tsuruta, Y., 1991, 'Carbon fiber-reinforced cementitious composite and method for producing the composite. US (5030282A).
- [18] Tezuka, M., Awata, M., and Shiraki, A., 1997, 'Carbon fiber-reinforced concrete and method for preparing the same. US (5685902A).
- [19] Hambach, M., Möller, H., Neumann, T., and Volkmer, D., 'Portland cement paste with aligned carbon fibers exhibiting exceptionally high flexural strength (> 100 MPa)', *Cement and Concrete Research* **89** (2016), 80–86.
- [20] Mastali, M. and Dalvand, A., 'The impact resistance and mechanical properties of self-compacting concrete reinforced with recycled CFRP pieces', *Composites Part B: Engineering* **92** (2016), 360–376.
- [21] Mastali, M., Dalvand, A., and Sattarifard, A., 'The impact resistance and mechanical properties of the reinforced self-compacting concrete incorporating recycled CFRP fiber with different lengths and dosages', *Composites Part B: Engineering* **112** (2017), 74–92.
- [22] Ogi, K., Shinoda, T., and Mizui, M., 'Strength in concrete reinforced with recycled CFRP pieces', *Composites Part A: Applied Science and Manufacturing* **36** (7 (2005), 893–902.
- [23] Bienkowski, N., Hillemann, I., Streibel, T., Kortmann, J., Kopf, F., Zimmermann, R., and Jehle, P., 'Bearbeitung von Carbonbeton - eine bauverfahrenstechnische und medizinische Betrachtung. (Processing of carbon concrete - a study considering construction process engineering and healthcare)', *Bauingenieur* (2017/2018 (2017), 110–118.

SHEAR BEHAVIOR OF FIBER REINFORCED CONCRETE BEAMS

Marta Kosior-Kazberuk (1), Julita Krassowska (1) and Piotr Berkowski (2)

(1) Bialystok University of Technology, Poland

(2) Wroclaw University of Science and Technology, Poland

Abstract

The failure mode of reinforced concrete elements due to transverse forces results from a complicated mechanism, related to the value and type of load, dimensions and geometric shape of the cross-section and material properties of concrete and reinforcement. The fibers can be used to improve the behavior of structure at the ultimate limit state, or to improve service conditions at the serviceability limit state. In the ultimate limit state, the addition of fibers can partially or completely replace the traditional reinforcement for tensile or shear. However, the full potential of fiber reinforced concrete is still not fully exploited in practice. Considering potential applicability of basalt fibers further experimental studies should be conducted on the use of this type of fibers in concrete for reinforced structures. The recognition of the failure mode of concrete elements with fibers is crucial for the development of design methods that take the presence of dispersed reinforcement in concrete into account. Experimental research was focused on observing the behavior of the tested elements depending on the amount of shear reinforcement and the content of fibers. The two-span beams with a length of 4500 mm were tested. The beams had a varied stirrup spacing. The amount of basalt fibers in concrete were 5.0 kg/m^3 . The reference concrete beams without fibers were also examined. The beams were loaded in a five-point bending test. Shear or tension capacity of the element was determined. Fiber reinforced concrete beams were not destroyed rapidly. Failure mode of beams varied in dependence on the amount of shear reinforcement and fiber presence in concrete. Basalt fibers revealed the ability to transfer significant shear stress after cracking in comparison to plain concrete.

Keywords: reinforced concrete beam, basalt fiber, shear failure

1. INTRODUCTION

The failure mode of reinforced concrete elements due to transverse forces results from a complicated mechanism, related to the value and type of load, dimensions and geometric shape of the cross-section and material properties of concrete and reinforcement [1]. The main

purpose of the fibers application in concrete is to provide control of cracking and to increase the fracture toughness of the brittle matrix through bridging action during both micro and macrocracking of the matrix. Debonding, sliding and pulling-out of the fibers are the local mechanisms that control the bridging action [2-4]. The resultant composite concrete can have considerable ductility, often termed “toughness”. However, the ductility characteristic is dependent on the fiber type and dosage, tensile strength and anchorage mechanism.

Basalt fibers are relatively new material. The basalt fiber has inherited the basalt ore structure and performance characteristics, such as outstanding thermal stability, anti-corrosive performance, ideal heat insulation, sound absorption, and low moisture absorption. In addition, this fiber exhibits high strength and high module performance [5, 6]. The basalt fibers do not need any other additives, which make additional advantage in cost. According to Sim et al. [7] the fibers have better tensile strength than the E-glass fibers, greater failure strain than the carbon fibers as well as good resistance to chemical attack, impact load and fire. These features, combined with lower cost, could make basalt fibers a suitable replacement for steel, glass, and carbon fibers in many applications [8, 9]. However, previous studies on the use of basalt fibers in concrete are limited. Kabay [5] reported that the addition of short basalt fibers resulted in decrease in compressive strength and at the same time the enhancement of fracture energy and reduction of abrasive wear of concrete. The discussion of basalt fibers influence on the fracture mechanics parameters can be found in [10].

The fibers can be used to improve the behavior of structure at the ultimate limit state, or to improve service conditions at the serviceability limit state. In the ultimate limit state, the addition of fibers can partially or completely replace the traditional reinforcement for tensile or shear. However, the full potential of fiber reinforced concrete is still not fully exploited in practice. This is mainly due to a lack of specific rules for this type of concrete in building codes. Considering potential applicability of basalt fibers [11-13] further experimental studies should be conducted on the use of this type of fibers in concrete for reinforced structures.

In order to assess the nature of the failure process of reinforced concrete elements with dispersed basalt fiber reinforcement, experimental studies were carried out, in which the emphasis was placed on the identification and analysis of the behavior of tested members depending on the amount of shear reinforcement (steel stirrups) and basalt fibers. In order to obtain more test results, including tests of shear zones at both external and mid-range supports, taking into account different ratio of bending moment to shear force, as well as to reduce the scatter of measurement results, two-span natural scale beams were used in the research.

2. EXPERIMENTAL PROGRAMME

2.1 Concrete mix composition and specimen preparation

The geometry and properties of basalt fibers were presented in Table 1. The fibers were added at the content of 5.0 kg/m^3 , which gave volume fraction 0.19%. The content of fibers was determined on the basis of the fiber manufacturers' recommendations. The concrete without fibers was also tested.

The Portland cement CEM I 42.5R (300 kg/m^3) was used to make concrete for tested members. The water to cement ratio was equal to 0.5. The mixture of sand with a grain diameter up to 2 mm and coarse aggregate with a grain diameter up to 8 mm was used. The fibers were introduced as a replacement of the adequate portion of aggregate by volume. The modified polycarboxylate and phosphonate based super-plasticizer (1% c.m.) was used.

Table 1. Properties of basalt fibers

Property	Basalt fibers
Fiber shape	straight
Length (mm)	50
Diameter (mm)	0.02
Tensile strength (MPa)	1680
Elastic modulus (GPa)	89
Density (kg/m ³)	2660

The dry aggregate was mixed with steel or basalt fibers respectively, followed by cement. The materials were dry mixed for 2 min before adding water with super-plasticizer. Mixing continued for a further 4 min. The time of mixing was considered sufficient for the proper dispersion of the fibers in the mix without causing a “balling” effect. The specimens were vibrated in molds and then stored under polyethylene cover for one day. After demolding, all specimens were cured in water at the temperature of 18 ± 2 °C until they were tested.

The strength properties of concretes were tested. The test of compressive strength was carried out in accordance with PN-EN 12390-3 [14]. The flexural strength was determined according to PN-EN 12390-5 [15]. The elastic modulus was tested in accordance with PN-EN 12390-13 [16] and the splitting tensile strength - according to PN-EN 12390-6 [17].

2.2 Two-span beams' test

In the research program, three series of beams differing in the spacing of transversal reinforcement (Fig. 1) were used. Each series consisted of 3 beams with dimensions 120×300×4150 mm. The change in the spacing of stirrups in particular series was aimed at demonstrating the possibility of limiting the number of stirrups, whose task will partially be taken over by the fiber reinforced concrete. The amount of main longitudinal reinforcement and shear reinforcement were calculated in accordance with PN-EN 1992-1-1 [18]. Series A-I beams were reinforced with shear stirrups spacing determined according to [18]. In series A-II, the stirrups had a spacing twice as large as determined according to [18]. The shear span/effective depth ratio of the tested beams a_v/d was equal to 3.5. A description of the series of beam specimens was shown in Table 2.

Table 2. Designation of beam specimens

Stirrup spacing [cm]	Reference beams (no fibers)	Beams of concrete with basalt fibers
10/20	A-I-W0	A-I-WB
15/30	A-II-W0	A-II-WB
No stirrups	A-III-W0	A-III-WB

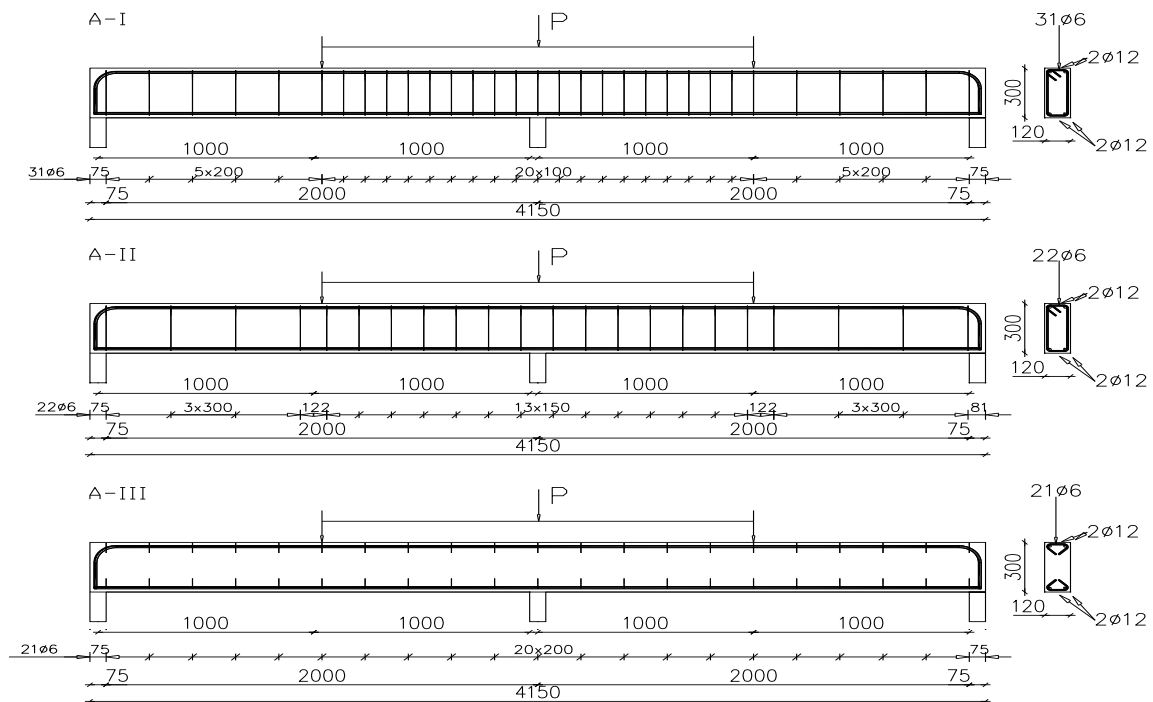


Figure 1: Steel reinforcement of beams tested ($f_{yk}=500$ MPa)

During the test the shear and/or bending capacity of the member was determined. The deformation in the compression and tension zone at the level of longitudinal reinforcement were also measured. Fig. 2 shows the test stand with equipment.



Figure 2: Test setup with beam specimen

The beams were loaded in a five-point system using a force increase every 10 kN, until break. The beams have been loaded three times with a preload to 30 kN. The load increase was 10 kN every 30 sec. The load was applied using a hydraulic HYSDOZOK loading system with a capacity of 500 kN.

3. ANALYSIS OF TEST RESULTS

3.1 Strength properties of concretes

Table 3 presents the results of strength properties test: compressive strength f_{cm} , flexural strength f_{cfm} , splitting tensile strength f_{ct} and modulus of elasticity E_s in relation to the fiber content in concrete (V_f).

Table 3. Strength properties of concretes (average values and range of accuracy).

Fiber	V_f [kg/m ³]	f_{cm} [MPa]	f_{cfm} [MPa]	f_{ct} [MPa]	E_s [GPa]
no fiber	-	52.96 (± 6.36)	5.14 (± 0.33)	3.22 (± 0.39)	33.29 (± 1.28)
basalt	5.0 (0.19%)	46.24 (± 5.35)	6.72 (± 1.22)	4.49 (± 0.24)	32.86 (± 2.33)

Concrete with the addition of basalt fibers was characterized by compressive strength f_{cm} lower by approx. 10% in comparison to the reference one. The increase in flexural strength was about 30% in the case of concrete with basalt fibers. The failure mode of basalt fiber reinforced concrete specimens was brittle as in the concrete without fiber, however, the value of destructive force was much higher. The increase in splitting tensile strength was as high as 40% for basalt fibers in comparison to reference concrete.

3.2 Analysis of failure mode of two-span beams

Table 4 shows the values of ultimate load P_{ult} and their increase ΔP_{ult} in comparison to the values of destructive loads for the reference beams (without fibers).

Table 4. Ultimate load P_{ult} and its increase ΔP_{ult} in comparison to series without fibers

Series	No fibers (W0)		Basalt fibers (WB)		
	P_{ult} [kN]	Failure mode	P_{ult} [kN]	ΔP_{ult} [%]	Failure mode
A-I	222	F	229	3	F
A-II	193	F+S	228	19	F+S
A-III	109	S	134	23	S

F - failure due to flexural tension, S - failure due to shear

The influence of the dispersed reinforcement on the shear capacity can be determined by comparing the value of ultimate loads in individual series. Series A-I beams have been damaged due to flexure, and the value of ultimate force increased slightly for concrete beams with fibers. In series A-II-WB the value of ultimate force was comparable to the value of the force recorded for A-I-W0 series. The basalt fibers caused an increase in the ultimate load, despite the use of only half number of stirrups. The shear failure model was obtained in A-III series beams. The beams were not reinforced with stirrups, the role of stirrups was taken over by the dispersed reinforcement. In the case of beams made of concrete with basalt fibers, the increase in ultimate force was 23% compared to reference concrete beams.

3.3 Shear stress analysis

The value of shear stress was determined at three supports. The plots in Fig. 3 show the influence of fibers on shear stresses, determined on the basis of the values of support reactions measured during test.

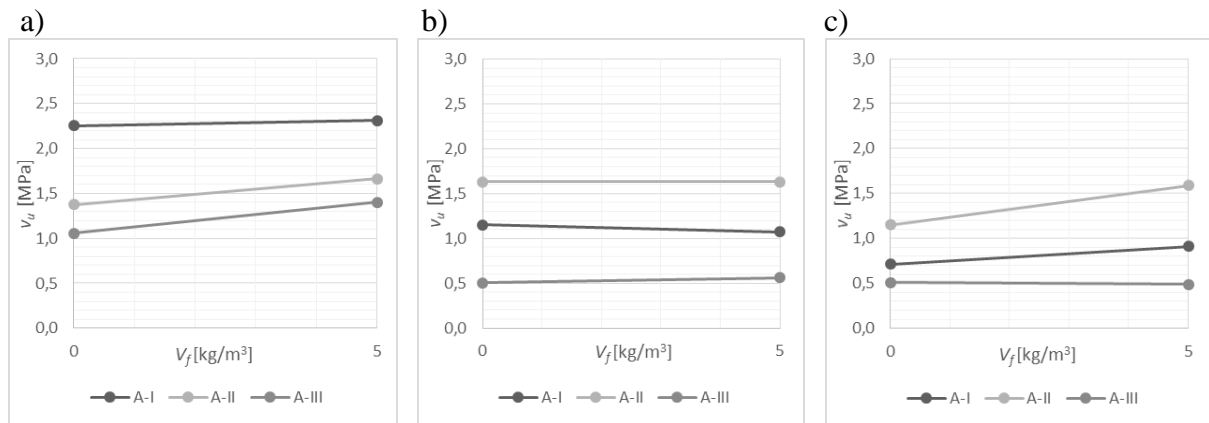


Figure 3: Shear stress v_u in beams made of basalt fiber reinforced concrete at the supports: a) mid-range b) left c) right

Analyzing the A-I series in Fig. 3, one can observe an increase in stresses on the right support, while in the case of the left and middle supports, the stress value is constant. The beams in this series were destroyed by flexural tension in one of the spans, and the other one (less damaged) was still able to transfer stresses to the support. In series A-II and A-III, where the failure occurred due to shear, the main shear stresses were transferred to the central support. The increase in shear stress at the central support, due to the use of concrete with basalt fibers, was respectively 20% for A-II series and 30% for A-III series.

3.4 Analysis of strains in concrete

The Figs 4-6 present the P - ε relationship for concrete in beams. The P - ε relationship is generally non-linear in compression and tension zones. The elastic deformations of the concrete occur only for a short segment of the plot.

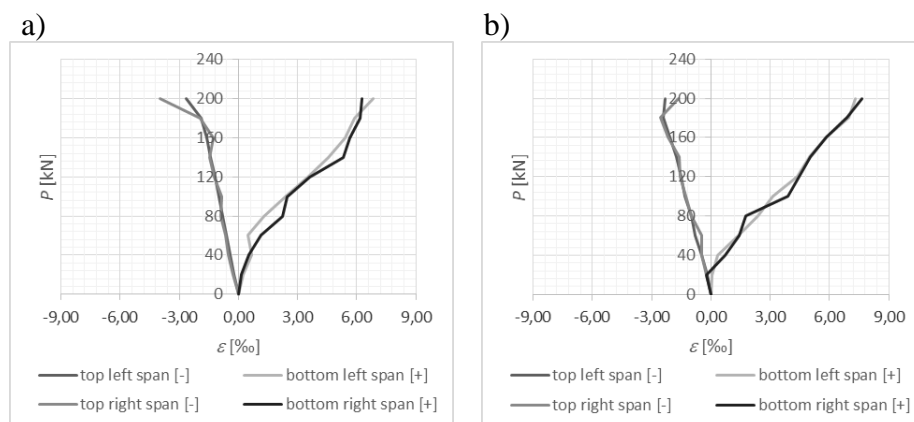


Figure 4: Comparison of strain development in concrete in beam series a) A-I-W0 b) A-I-WB

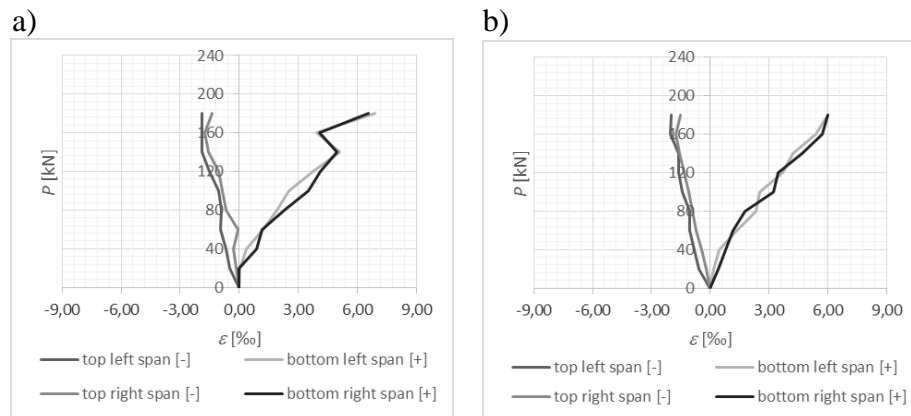


Figure 5: Comparison of strain development in concrete in beam series a) A-II-W0 b) A-II-WB

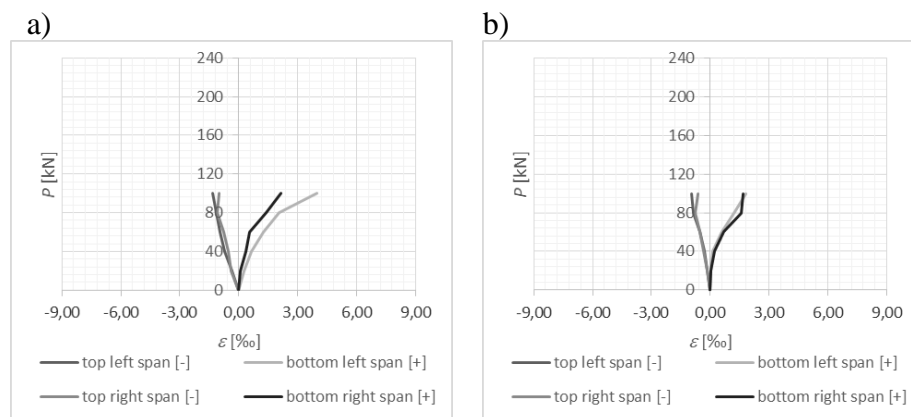


Figure 6: Comparison of strain development in concrete in beam series a) A-III-W0 b) A-III-WB

In the tensile zone of A-I series beams, the largest deformations at the same load level were recorded for beams of concrete with basalt fibers. In the compression zone, the largest deformations were recorded for the reference beams. The A-II-W0 and A-II-WB series beams were characterized by the comparable increase in strains development. A similar distribution of strains can be observed in the A-III series, where the strains of concrete in the compressive zone of the reference beam have reached the greatest values. In the tensile zone, the strains at the same load level were comparable for structural members made of both type of concrete.

4. CONCLUSIONS

Incorporation of basalt fibers into concrete did not change the failure mode dramatically, but it had an effect on the course of destruction. The results of two-span beams' tests revealed that the basalt fibers had a positive effect on the value of destructive force. The fibers directly influenced the shear capacity of concrete beams. They do so by basically delaying the occurrence of the shear failure mechanism and, eventually, by altering the collapse from shear to flexure with enhanced load capacity and ductility. The moment of first crack appearance in the fiber reinforced beams occurred later than in the beam without fibers. The influence of

basalt fibers was fully revealed during the analysis of A-II series beams with half-reduced shear reinforcement. This was confirmed by the results of the analysis of deformation of concrete in the tensile zone. The obtained results confirm the potential possibility of using fibers to partially replace the stirrups. The combination of stirrups and basalt fibers can improve both the ultimate and serviceability limit states.

REFERENCES

- [1] Imam, M., Vandewalle, L., Mortelmans, F. and Van Gemert, D., 'Shear domain of fiber-reinforced high-strength concrete beams', *Engineering Structures* **9** (1997) 738-747.
- [2] ACI 544. IR-96. State-of-the-art report on fiber reinforced concrete. Manual of concrete practice. (Farmington Hills, 1998).
- [3] Model Code 2010, Comité Euro-International du Béton fib (CEB-FIP) (2012).
- [4] Soutsos, M.N., Le, T.T. and Lampropoulos, A.P., 'Flexural performance of fiber reinforced concrete made with steel and synthetic fibers', *Construction and Building Materials* **36** (2012) 704-710.
- [5] Kabay, N., 'Abrasion resistance and fracture energy of concretes with basalt fibre', *Construction and Building Materials* **50** (2014), 95-101.
- [6] Wei, B., Cao, H. and Song, S., 'Tensile behavior contrast of basalt and glass fibers after chemical treatment', *Materials & Design* **31** (2010) 4244-4250.
- [7] Sim, J., Park, C. and Moon, D.Y., 'Characteristics of basalt fibre as a strengthening material for concrete structures', *Composites Part B* **36** (2005) 504-512.
- [8] Borhan, T.M., 'Properties of glass concrete reinforced with short basalt fiber', *Materials and Design* **42** (2012) 265-271.
- [9] Branston, J., Das, S., Kenno, S. Y. and Taylor, C., 'Mechanical behaviour of basalt fibre reinforced concrete', *Construction and Building Materials* **124** (2016) 878–886.
- [10] Kosior-Kazberuk, M. and Krassowska, J., 'Post-cracking behaviour of basalt fibre reinforced concrete', in: *Recent advances in mechanics and materials in design M2D2015*, Proceedings of the 6th International Conference on Mechanics and Materials in Design, Ponta Delgada, July 26-30, 2015, 673-682.
- [11] Dinh, H.H., Parra-Montesinos, G.J. and Wight, J.K., 'Shear behavior of steel fibre-reinforced concrete beams without stirrup reinforcement', *ACI Structural Journal* **107** (2010) 597-606.
- [12] High, C., Seliem, H. M., El-Safty, A.S. and Rizkalla, H., 'Use of basalt fibers for concrete structures', *Construction and Building Materials* **96** (2015) 37 – 46.
- [13] Jiang, C., Fan, K., Wu, F. and Chen, D., 'Experimental study on the mechanical properties and microstructure of chopped basalt fibre reinforced concrete', *Materials & Design* **58** (2014) 187-193.
- [14] EN 12390-3:2009 Concrete tests - Part 3: Compressive strength of test specimens.
- [15] EN 12390-5:2009 Concrete testing - Part 5: Bending strength of test specimens.
- [16] EN 12390-13:2014-02 Concrete tests - Part 13: Determination of the secant elastic modulus under compression.
- [17] EN 12390-6:2010 Concrete tests - Part 6: Tensile splitting strength of test specimens
- [18] EN 1992-1-1 Eurocode 2:2004+A1:2014 - Designing concrete structures - Part 1-1: General rules and rules for buildings.

ANALYSIS OF STEEL FIBERS DISTRIBUTION AND ORIENTATION IN HYBRID-FIBERS REINFORCED HIGH-PERFORMANCE CONCRETE COLUMN USING MICRO-COMPUTED TOMOGRAPHY

Taehoon Park (1), Heongwon Suh (1), Jaeyeon Park (1), Bumyeon Cho (2), Seyoon Yoon (3) and Sungchul Bae (1)

(1) Department of Architectural Engineering, Hanyang University, Republic of Korea

(2) Korea Institute of Civil Engineering and Building Technology, Republic of Korea

(3) Department of Civil Engineering, Kyonggi University, Republic of Korea

Abstract

High-performance concrete (HPC) offers better structural engineering properties such as higher compressive and tensile strength, enhanced durability, and better stiffness, compared to conventional normal concrete. However, a marked increase in the use of HPC has led to concerns regarding its brittle fracture characteristics and spalling under high temperature. Reinforcing HPC using hybrid-fibers (steel fibers + polypropylene fibers) is a popular method for reducing explosive fracture due to spalling and improving the mechanical properties of HPC. The performance of hybrid-fiber reinforced HPC concrete (HFRHPC) is determined by the fibers' distribution and orientation within the concrete, which has been analyzed by optical and tomographic methods in previous studies. However, most of analyses were conducted on specimens that were produced in a laboratory. In this study, the distribution and orientation of the internal steel fibers of specimens extracted from an actual HFRHPC column were analyzed by micro-computed tomography (micro-CT). A total of nine core specimens were extracted according to the column's height and distance from the mold. By using micro-CT, we visualized the distribution of steel fibers in the HFRHPC specimen. Moreover, the direction vector, scale, center position, volume, and surface area of the steel fibers in HFRHPC were successfully calculated.

Keywords: HFRHPC, Micro-CT, fiber distribution, fiber orientation, image analysis

1. INTRODUCTION

Nowadays, high-performance concrete (HPC) is commonly used to improve the properties of normal concrete, such as compressive and tensile strength, and toughness [1]. Owing to these properties, the size, span, and height of concrete structures are increasing. However, because

HPC is highly brittle, even if it is minutely damaged, there is a high probability that it will crack and eventually fail. Furthermore, when it is exposed to high temperature, there is a risk of spalling. Unlike normal concrete, HPC requires particular care and maintenance to preserve its stability.

To supplement the above conditions, HPC is reinforced with hybrid-fibers (steel fibers + polypropylene (PP) fibers) to prevent failure from spalling and to enhance the mechanical properties of HPC. The key factors that determine the performance of hybrid-fiber reinforced HPC concrete (HFRHPC) are the fiber properties (elastic modulus, strength) and fiber distribution and orientation inside the concrete [2]. Fiber distribution and orientation are influenced by many factors, such as fiber and matrix properties, and placing methods [3-5]. In addition, the mechanical properties of cementitious composites improve when fibers are oriented in a parallel direction and distributed evenly [6, 7].

Previously, in many studies, steel fiber distribution and orientation were analyzed by optical and tomographic methods [8, 9]. In the optical method, the distribution and orientation of steel fibers are found by cutting the model horizontally and vertically, and then counting the fibers on the cut section. However, this method does not allow for examining the fibers within the model. On the other hand, in the tomographic method, an entire fiber can be examined by two-dimensional (2D) and three-dimensional (3D) views. The CT technique is a novel, non-destructive, and accurate method for analyzing materials inside cementitious composites. Until now, most of the analyses have been conducted on specimens with specific size that were created in a laboratory. Therefore, investigating the distribution and orientation of fibers in an actual building structural member is needed.

In this study, we aim to determine the characterization of fiber distribution and orientation of an HFRHPC column in 3D images by micro-CT image reconstruction. An analysis software was used to attain the direction vector, scale, center position, volume, and surface area of steel fibers. The results can be used as a standard to complement the weak sections in HFRHPC buildings.

2. EXPERIMENTAL PROCEDURE

2.1 Materials and mix proportions

Ordinary Portland cement, a blast furnace slag, fly ash, sand, gravel, a PP fiber, and a steel fiber were used as the raw materials for HFRHPC. 6 mm and 12 mm PP fibers (SSQ Teq, Republic of Korea) were used in the ratio of 7 (1.05 kg/m³):3 (0.45 kg/m³). The steel fibers (Kosteel, Republic of Korea) were hooked end steel fibers with a length of 30 mm. The slump flow of HFRHPC was designed to be more than 600 mm because of the possibility of lowering the workability when steel fibers with 30 mm length are mixed. The target air content was 3.0% and the strength at 28 days aimed to be more than 60 MPa. The mix proportions and physical properties of HFRHPC are shown in Table 1 and Table 2, respectively.

Table 1: Mix proportions of the HFRHPC (kg/m³)

W/B	Unit Weight of Material						Fiber	
	W	C	BS	FA	S	G	PP	Steel
0.2	165	572	163	82	639	759	1.5	40

Table 2: Physical properties of the HFRHPC

Type	Flow (mm)		Air Content (%)	Strength at 28 Days (MPa)
60MPa	630	620	3.5	75.5

2.2 Sample preparation

HFRHPC was cast in a column mold with the dimensions $400 \times 500 \times 3000 \text{ mm}^3$. After casting, it was cured for 28 days and then demolded. As the column was exposed to the exterior environment, its temperature and humidity varied. After demolding, a total of nine specimens were extracted according to two parameters: the height of the column (bottom (A), middle (B), and top (C)) and distance from the mold (far (1), between (2), and near (3)) (Figure 1(a)). A boring machine extracted specimens with a length of 300 mm and diameter 70 mm (seen in Figure 1(b)). For the experiment, the sample ($70 \text{ mm} \times 70 \text{ mm}$) that was inside the column was cut (seen in Figure 1(c)).

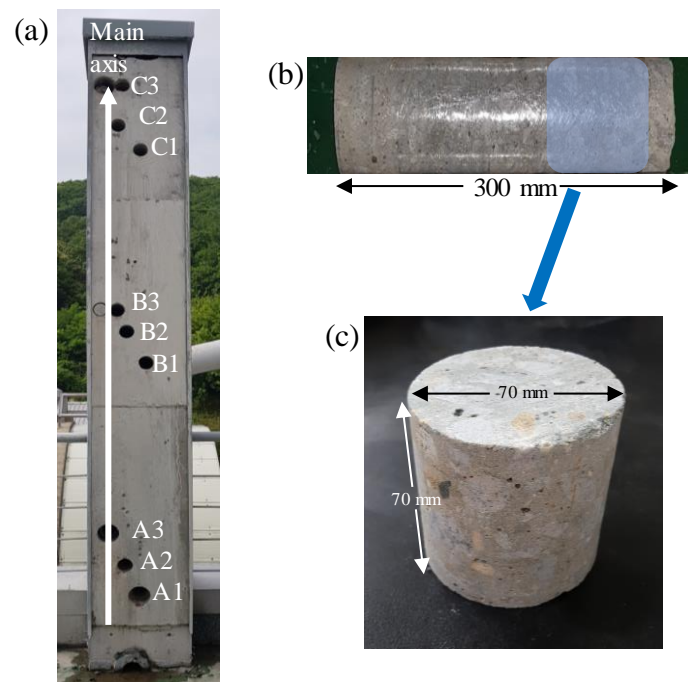


Figure 1: Extraction point and specimens: (a) location of extracted specimens, (b) initial extracted specimen, and (c) actual sample

3. IMAGE ANALYSIS

3.1 Image acquisition and reconstruction

A total of nine specimens were analyzed using a micro-CT system (SkyScan 1173, Bruker-CT, Belgium), and the software used was SkyScan 1173 control software (Ver 1.6, Bruker-CT). The source voltage was 130 kV and the source current was $60 \mu\text{A}$. The device captured approximately 2200 high resolution images with 2240×2240 pixels, whereby the pixel size was $33.03 \mu\text{m}$.

The brightness of a CT image depends on the density of the materials that are inside the sample. As the brightness of the CT image increases when the density of the materials is high, it is easy to recognize steel fibers because steel has the highest density among all the materials within the sample, as seen in Figure 2(a). To achieve better visualization of the fibers, 2D reconstruction was conducted by a reconstruction program (NRecon, Bruker) that darkened all the materials except the fibers, as seen in Figure 2(b).

3.2 Image binarization

Image binarization is needed to attain only the region of interest. After establishing the appropriate threshold, contrast enhancement was used to obtain the fiber only images. Following contrast enhancement, the fibers appeared white against a black background. In this way, analysis of the fibers became possible (see Figure 2 (c)).

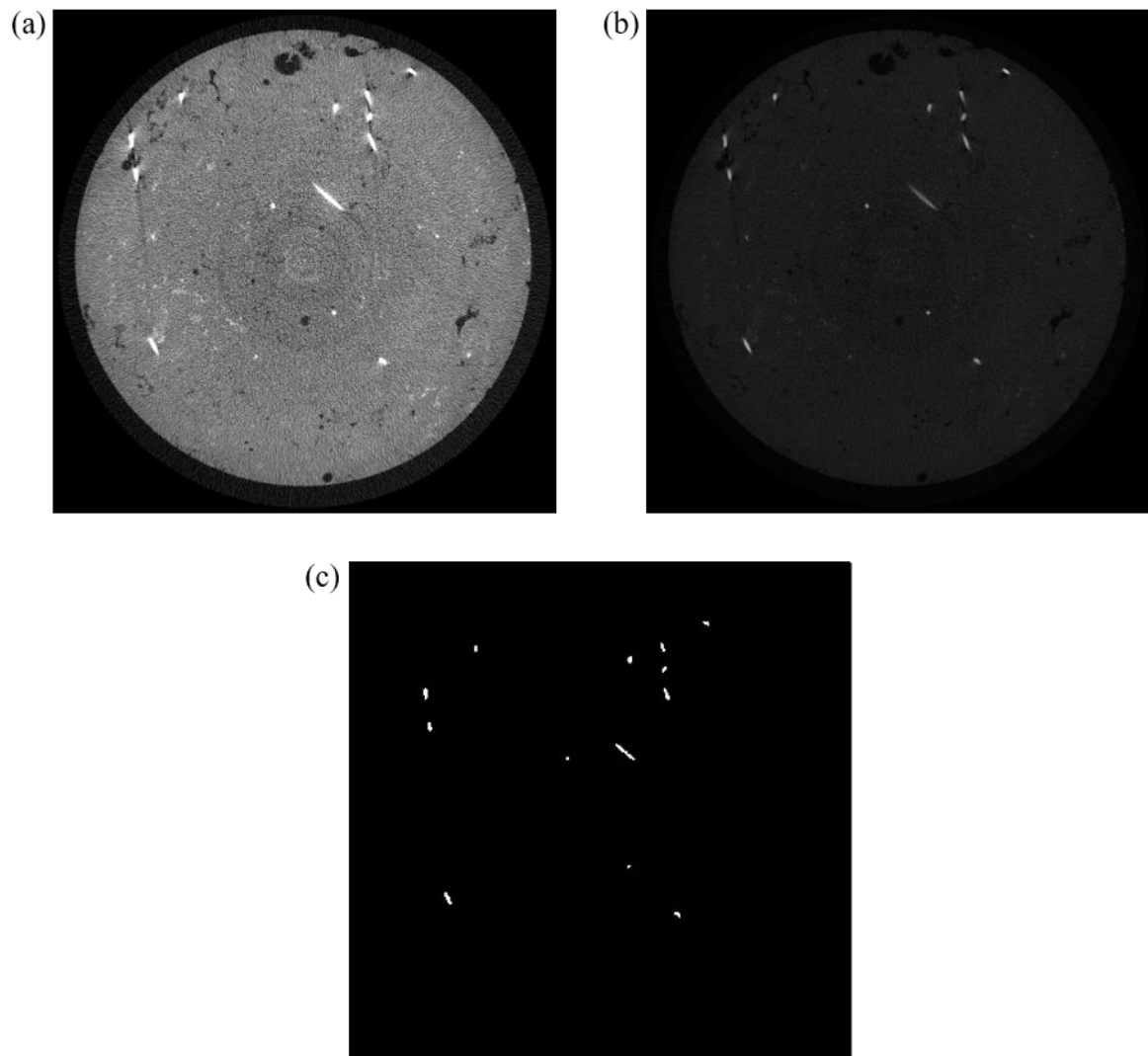


Figure 2: Image acquisition and binarization: (a) original acquired CT image, (b) 2D image reconstruction, and (c) image binarization

3.3 3D image reconstruction

After acquiring 2D images from micro-CT, reconstruction and visualization were performed using a computer software (MATLAB, MathWorks, USA) [10]. All the 2D images were stacked to create an entire 3D image. As noise had been removed, only the fibers appeared in the image (Figure 3). Furthermore, as specimens were extracted from the column, many fibers that were on the side of the sample could be detected.

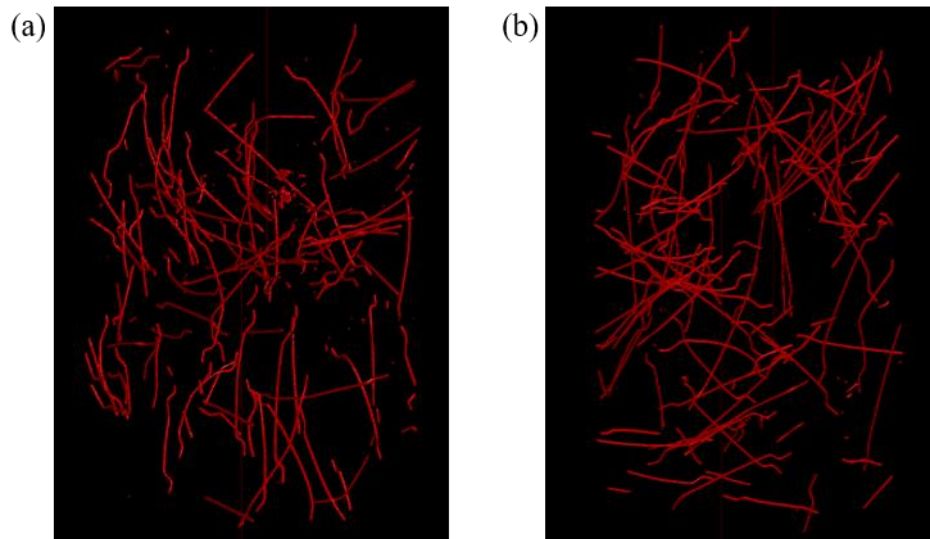


Figure 3: Examples of 3D fiber image reconstruction: (a) A1 specimen and (b) B1 specimen

3.4 Fiber characterization

To attain the direction vector, scale, center position, volume, and surface area of each steel fiber, fiber analysis was conducted using MATLAB. In the previous studies, pore within carbon/carbon composites was characterized by calculating each principal moment of inertia [11]. To obtain the fiber's characteristics, the previous method was applied in our study to calculate the principal moment of inertia of each fiber. However, measuring and classifying each fiber was difficult as many fibers touch each other. Although studies on the extraction of a single fiber have been reported, the ability of the utilized methods to extract a fiber without disturbing the original image has been limited [12-14]. In this study, we determined an optimum method for separating each fiber without disturbing the original image; however, classifying each fiber is still challenging.

4. RESULTS

4.1 Fiber orientation

When determining fiber orientations expressed as an angle, the main axis direction was the direction which is parallel to reinforcement steel bar within the HFRHPC column (Figure 1(a)). The main axis is also the direction in which HFRHPC column is cast and the load direction when it is a part of a building. The fiber orientation was calculated based on each fiber's direction vector.

When classified according to the column's height, the average percentage of the A, B, and C specimens with greater than 45° of orientation is 79%, 85%, and 85% respectively (Figure

4(a)). This means that the fibers that are located in the middle and top sections of the column have a greater tendency to lie horizontally, and the fibers that are located at the lower part of the column have a tendency to lie vertically. However, it can be seen that the fibers in all parts of the column tend to lie horizontally, overall.

According to the distance from the mold, the average percentage of the 1, 2, and 3 specimens with greater than 45° of orientation is 81%, 76%, and 92% respectively (Figure 4(b)). Fibers that are far from the mold and also in the middle section of the column exhibit the maximum tendency to lie horizontally. Fibers that are located near the mold, which is also near the main reinforcement, also have a tendency to lie horizontally. Among them, fibers that are between the mold and middle part of the column have the lowest probability to lie horizontal to the main axis.

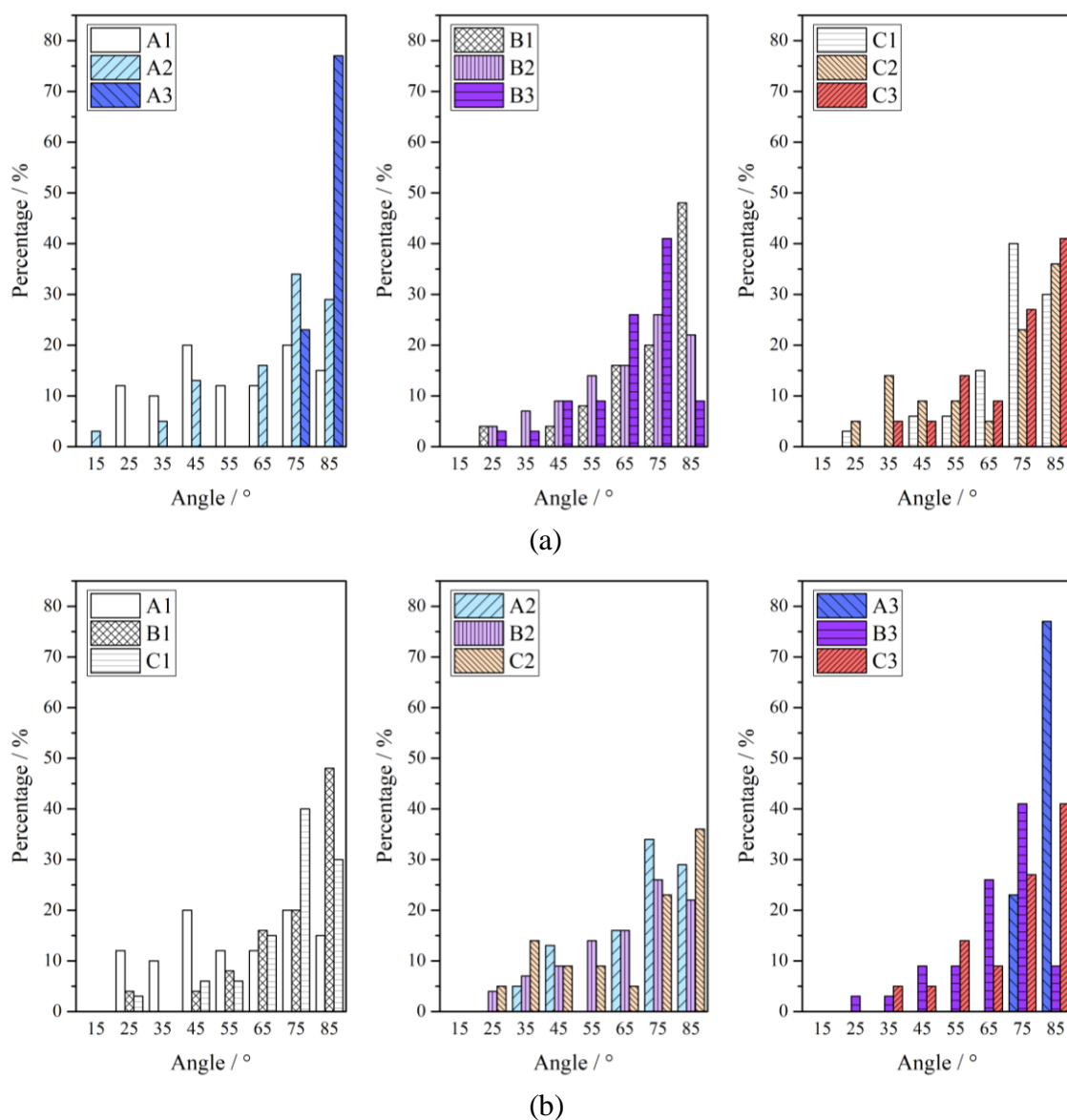


Figure 4: Fiber orientation based on location of the HFRHPC column: (a) column's height and (b) distance from the mold

4.2 Fiber distribution

The volume of each fiber was used to determine the fiber distribution. The voxels from 3D images were stacked to measure the fiber volume. In addition, the surface area of each fiber was calculated to verify the achieved values.

From the perspective of the column's height, 959850 voxels, 847452 voxels, and 563290 voxels were achieved for A, B, and C, respectively. The lower part of the column had the highest fiber volume followed by the middle part of the column. However, the fiber volume at the upper part of the column decreased significantly. It can be seen that fibers settled at the bottom of the column as HFRHPC was poured at the upper part of the column.

From the perspective of the distance from the mold, 924090 voxels, 779137 voxels, and 667365 voxels were achieved for 1, 2, and 3, respectively. Fibers that were the farthest from the mold appeared to have the highest fiber volume, and fibers near the mold had the lowest fiber volume.

5. CONCLUSION

Steel fiber analysis was conducted by micro-CT to visualize fibers inside an HFRHPC column. A total of nine specimens were extracted from the column according to the column's height and distance from the mold. 2D images of the region of interest were reconstructed to achieve 3D images of the fibers. The direction vector, scale, center position, volume, and surface area of each fiber were measured, and the values were used to determine the fiber orientation and distribution of the fibers in the specimens. The conclusions are as follows.

- By 3D reconstruction of steel fibers within the HFRHPC column, clear 3D images were obtained in a non-destructive manner. Furthermore, the orientation and distribution of the fibers could be measured quantitatively.
- Characterization of each fiber was successfully determined by techniques that were performed on the pores. However, extracting single fibers from tangled fibers is still challenging.
- Fibers at the upper and middle parts of the column, and those that were far from the mold tended to be oriented horizontally to the main reinforcement. Overall, in all locations, the orientation was horizontal. As the concrete contains aggregate, the fibers could not orient themselves randomly.
- Most of the fibers appeared at the bottom of the column and at the location farthest from the mold. HFRHPC was cast from the top of the mold; therefore, fibers settled at the bottom of the column with the passage of time.

ACKNOWLEDGEMENTS

This research was supported by the Ministry of Land, Infrastructure and Transport, Korea (16TBIP-C111710-01)

REFERENCES

- [1] Wu, Z., Shi, C., He, W., Wang, D. J. C. and Composites, C., 'Static and dynamic compressive properties of ultra-high performance concrete (UHPC) with hybrid steel fiber reinforcements.' **79** (2017) 148-157.

- [2] Liu, J., Li, C., Liu, J., Cui, G., Yang, Z. J. C. and Materials, B., 'Study on 3D spatial distribution of steel fibers in fiber reinforced cementitious composites through micro-CT technique.' **48** (2013) 656-661.
- [3] Ozyurt, N., Mason, T. O., Shah, S. P. J. C. and Composites, C., 'Correlation of fiber dispersion, rheology and mechanical performance of FRCs.' **29**(2) (2007) 70-79.
- [4] Park, S.-S. J. G. and Geomembranes, 'Effect of fiber reinforcement and distribution on unconfined compressive strength of fiber-reinforced cemented sand.' **27**(2) (2009) 162-166.
- [5] Zhou, J., Qian, S., Ye, G., Copuroglu, O., van Breugel, K., Li, V. C. J. C. and Composites, C., 'Improved fiber distribution and mechanical properties of engineered cementitious composites by adjusting the mixing sequence.' **34**(3) (2012) 342-348.
- [6] Akkaya, Y., Shah, S. P. and Ankenman, B. J. J. o. E. M., 'Effect of fiber dispersion on multiple cracking of cement composites.' **127**(4) (2001) 311-316.
- [7] Kang, S.-T., Kim, J.-K. J. C. and Research, C., 'The relation between fiber orientation and tensile behavior in an Ultra High Performance Fiber Reinforced Cementitious Composites (UHPFRCC).' **41**(10) (2011) 1001-1014.
- [8] Gettu, R., Gardner, D., Saldivar, H., Barragán, B. J. M. and Structures, 'Study of the distribution and orientation of fibers in SFRC specimens.' **38**(1) (2005) 31-37.
- [9] Pinter, P., Dietrich, S., Bertram, B., Kehrer, L., Elsner, P., Weidenmann, K. J. N. and International, E., 'Comparison and error estimation of 3D fibre orientation analysis of computed tomography image data for fibre reinforced composites.' **95** (2018) 26-35.
- [10] Yoon, S., Galan, I., Celik, K., Glasser, F. P. and Imbabi, M. S., 'Characterization of micro-pore structure in novel cement matrices'. in 'Materials Research Society Symposium Proceedings', Materials Research Society.
- [11] Drach, B., Drach, A., Tsukrov, I. J. Z. J. o. A. M. and Mechanik, M. Z. f. A. M. u., 'Characterization and statistical modeling of irregular porosity in carbon/carbon composites based on X-ray microtomography data.' **93**(5) (2013) 346-366.
- [12] Griesser, A., Westerteiger, R., Wagner, C., Hagen, H. and Wiegmann, A., 'Machine Learning-based Single Fiber Extraction from Micro-CT Scans with GeoDict.'
- [13] Gaiselmann, G., Manke, I., Lehnert, W. and Schmidt, V., 'Extraction of curved fibers from 3D data'. in 'Forum Bildverarbeitung'.
- [14] Zauner, H., Salaberger, D., Heinzl, C. and Kastner, J. J. A. S., '3D image processing for single fibre characterization by means of XCT.' (2015).

TOWARDS THE DEVELOPMENT OF DAMAGE TOLERANT ENGINEERED CEMENTITIOUS COMPOSITES WITH SUPER-ELASTIC REINFORCEMENT

Dario Mirza (1), Eduardo Pereira (1), João A.P.P. Almeida (1), Vítor Cunha (1)

(1) ISISE, Department of Civil Engineering, School of Engineering, University of Minho, Azurém, 4810-058 Guimarães, Portugal

Abstract

Certain types of dynamic or extreme loading, such as seismic loading, are extremely damaging to structures in general, and in particular to reinforced concrete. In this regard, great efforts have been dedicated to the development of engineering solutions that lead to increased safety of structures in seismic scenarios and under extreme loading cases. The main goal is to increase the capacity of the structures to deform and to accommodate damage without excessive degradation of their integrity or stability.

Recently, the application of shape memory alloys (SMA), either as reinforcement or at certain parts of the structure, has been studied as a means to reach the aforementioned goal. Additionally, Engineered Cementitious Composites (ECC), due to their ability to develop multiple cracks in tension at steadily increasing tensile stresses and the very high ultimate tensile strains that they typically reach, seem to present the ideal characteristics to accommodate the level of damage that is expected in these cases without suffering critical degradation of integrity. Therefore, in the present work the combination of ECC with SMA in a composite system was studied. Considering that the most critical aspect of such composite should reside at the level of the interface between both materials, two types of arrangement of the reinforcement have been studied, in order to assess the importance of the interfacial properties.

The results showed that there is great potential in the ECC-SMA composite systems. However, the adhesion of the SMA to the ECC matrix is low. In order to fully explore the potential of both materials, the interface properties of the typically smooth SMA should be redesigned in order to increase the adhesion between both materials and enhance the composite effect.

Keywords: Shape memory alloys, ductility, Engineered Cementitious Composites, seismic behavior, pull-out, micromechanics.

1. INTRODUCTION

Shape memory Alloys (SMA), such as Nitinol, exhibit peculiar mechanical characteristics that are related to the cristaline structure of this special category of alloys. If stabilized in the austenite phase, the martensitic transformations cannot be induced by an applied load [1, 2],

therefore the tensile stress-strain diagram shows only the Super-Elastic Effect. This characteristic is particularly interesting for structures which need to withstand significant deformations, or for cases where the full recovery to the initial geometry after undergoing severe deformation is desired, such as self-centering structural systems.

To demonstrate the efficacy of SMAs as diagonal braces in frame structures, some studies have been conducted by various researchers [1]. Gilbert and Rasmussen in 2012 [3] tested Drive-In Steel Storage Racks subjected to horizontal loads with different spine and plan bracing configurations. The numerical studies demonstrated that the use of these materials can reduce the inter-story drift and can limit the residual drift in steel buildings. SMA dampers can be used to mitigate the wind induced vibrations in cable-stayed bridges. Casciati in 2008 [1] studied the feasibility of an SMA wire-steel cable system that consists of a steel cable with SMA super-elastic wire wrapped several times around the cable. The tests have shown that this smart system increases the fundamental frequencies and the damping coefficient while decreasing the amplitude of the vibrations. Faravelli in 2010 [1] developed a hybrid control system that combined SMA wrapped wires and an open loop control strategy to further improve the behaviour of stay-cables when they are subjected to strongly non-linear vibrations.

On the other hand, ECC materials have been recently used in structures that also need to undergo large deformations and must remain in service under extraordinary load events or imposed deformations. Therefore, in addition to its superior tensile strength and ductility, ECC must show high durability under extreme environmental conditions, such as long term tensile loading, freezing and thawing cycles, exposition to chloride and to alkali-silicate reactions. The most important mechanical characteristic of the ECC is its tensile ductility. In 2004 Li and Lepech [4] investigated the long-term tensile capacity of ECC. Formulations including hybrid fibre reinforcement have also been developed and characterized for special applications [5,6].

This research has as main purpose to investigate the combination of both a Superelastic material (Nitinol) and ECC, combined in a composite fashion, by studying the tensile behaviour of this combination. Due to the outstanding mechanical properties of both materials, unconventional mechanical behaviours are expected, which could result in interesting alternative solutions for structural elements or nodes that need to withstand severe stresses and deformations.

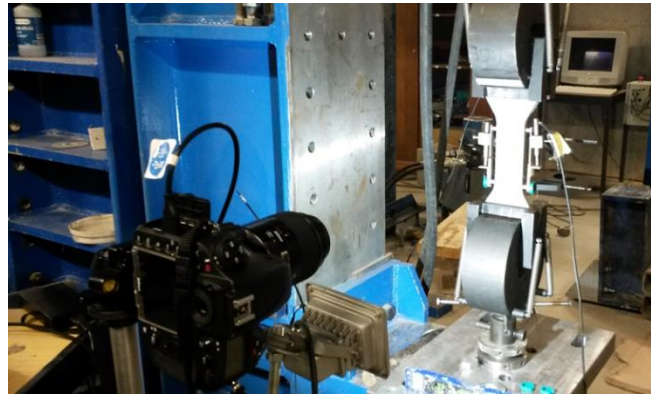
2. MATERIALS AND METHODS

In order to prepare and test hybrid specimens of ECC-Nitinol, first one mixture of ECC was tested. The composition of this mixture is presented in Figure 1.

With the purpose of evaluating the hardened properties of the ECC mixture, four specimens were prepared using dogbone shaped acrylic moulds. All specimens were kept for 28 days in a climatic chamber at approximately 20°C and 60% of relative humidity. The specimens were tested in tension using two clamps: one clamp was connected to the actuator with a 200 KN load cell and the other fixed to the reaction frame, as shown in Figure 1. The fixed part of the specimens on each edge was about 4 cm deep. During the tests the specimens were subjected to an imposed increasing tensile displacement at a constant rate of 0,010 mm/s. The axial force, the displacement between the two clamps and the displacement between two fixed points in the specimen at a distance of 10 cm, were measured. To measure the displacements three LVDT's sensors were used, which were positioned at the lateral faces of the dogbone specimen, with a

spacing of approximately 100 mm between measuring points. The width of the dogbone was approximately 50 mm and the thickness was approximately 15 mm.

Material	Mass [Kg]
Cement 42.5R	438
Fly Ash	876.5
Sand	153.5
Limestone Filler	153.5
Water	290
SP Sika 2002HE	16.5
VMA	1
Fiber PVA	26



a)

b)

Figure 1: a) Composition of the ECC mixture tested, per m³, and b) test setup for tensile testing of hardened ECC.

The responses obtained with the third mixture are presented in Figure 1. Before the appearance of the first micro-crack, approximately at 0,20% of tensile strain and an applied stresses between 3,2 MPa and 3,8 MPa, the behaviour was approximately linear elastic with a slope of 16000 MPa. The plastic stage of the response was characterized by the formation of a large number of micro cracks, as shown in Figure 2, where one representative specimen is presented. This large increment of the tensile strains occurred at a slow but constant increment of the tensile stress.



Figure 2: Close-up of the cracked surface of the ECC dogbone specimen after tensile testing. The longitudinal distance between pins is 110 mm and the transverse is 50 mm.

The ultimate tensile stress was reached at 3,8 MPa and 4,5 MPa, for tensile strains between 2,9% to 4,3%. The range of tensile strains reached in the plastic stage of the tensile responses are 14,5 to 21,5 larger than the elastic stage, resulting in very high ductility indexes. The main

tensile characteristics, such as the ultimate stress and strain, are in close agreement to the ones found in the literature.

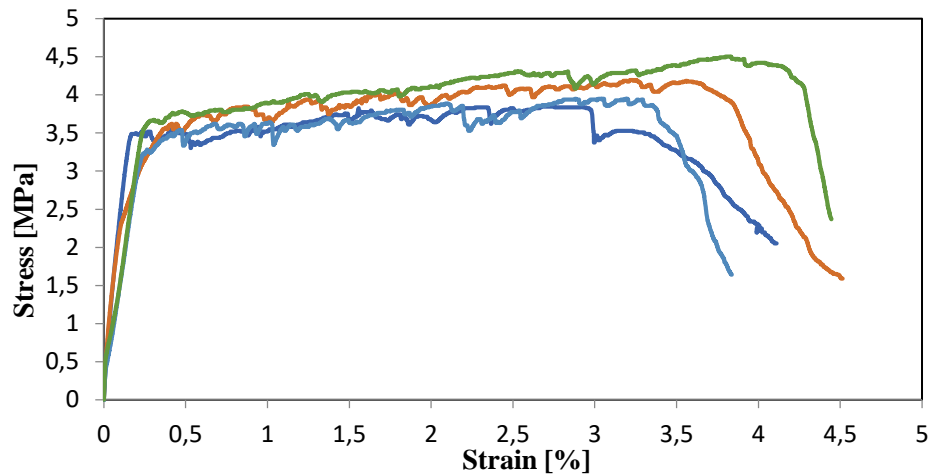


Figure 3: Tensile stress-strain response of the ECC dogbone specimens tested.

With regards to the reinforcement material, among all the available materials showing Super-Elastic and Shape-Memory effect, Nitinol was selected because of its characteristic temperature range. It is especially interesting for civil engineering applications where both the Super-Elastic and the Shape-Memory effects can be exploited. Nitinol wires with a diameter of 0,71 mm, produced by “Furukawa Electric Group”, were used.

Tensile testing was carried out following the international ASTM standard F2516-07 [7], which suggests that the Nitinol wire should be pulled up to a tensile strain of 6%, then unloaded until a stress lower than 7 MPa is reached, and then finally pulled up to failure. The recommended velocity for the test depends on the wire thickness, as shown in Table 1.

Table 1: Testing parameters of Nitinol wires depending on their diameter according to ASTM F2516-07 [7].

d , diameter or thickness (mm) ^A	Maximum crosshead speed in mm/min per mm† of initial length of reduced section (or initial distance between grips for specimens not having reduced sections)	
	First Cycle (load to 6 % strain and unload)	Second Cycle (load to failure)
$d \leq 0.2$	0.08	0.8
$0.2 < d \leq 0.5$	0.04	0.4
$0.5 < d \leq 2.5$	0.02	0.2
$d > 2.5$	0.01	0.1

The Nitinol wire samples, with 0.71 mm of diameter and 150 mm long, were subjected to a first cycle of imposed tensile elongation at a constant rate of 0.05 mm/s and a second cycle at a constant rate of 0.5 mm/s. The wire specimens were tested in tension using two clamps to fix

both edges of the specimen. One of the edges was connected to a load cell and the actuator, and the other was fixed to the reaction frame. The embedded length into the grips of the specimens edges was 50 mm. Different types of sandpaper and epoxy glue were tried to increase the friction between the grips and the wire during tensile testing. The sandpaper with the finest grain size and the epoxy glue resulted in the best conditions for tensile testing without the occurrence of slippage at the grips. The tensile stress – strain responses obtained for the three Nitinol wire specimens are shown in Figure 4. The main tensile characteristics of the Nitinol obtained according to ASTM F2516-07 [7] are presented in Figure 5.

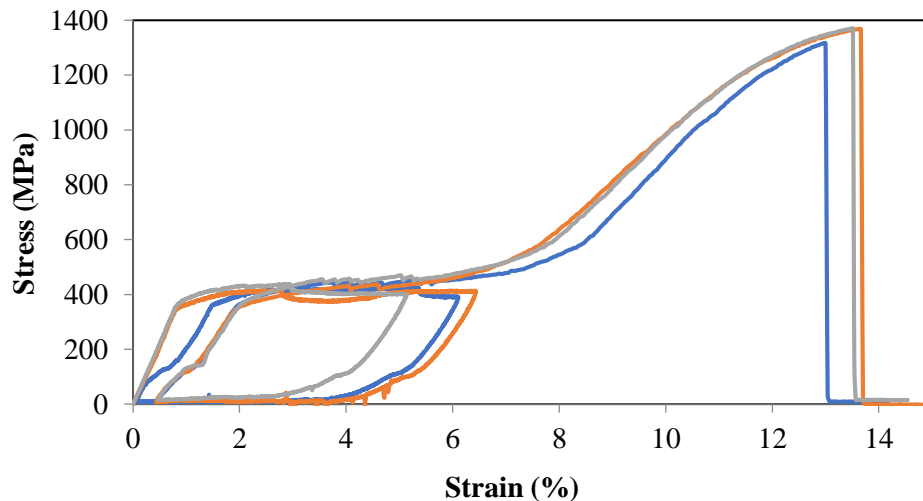


Figure 4: Tensile Stress-Strain response of the three Nitinol wires tested.

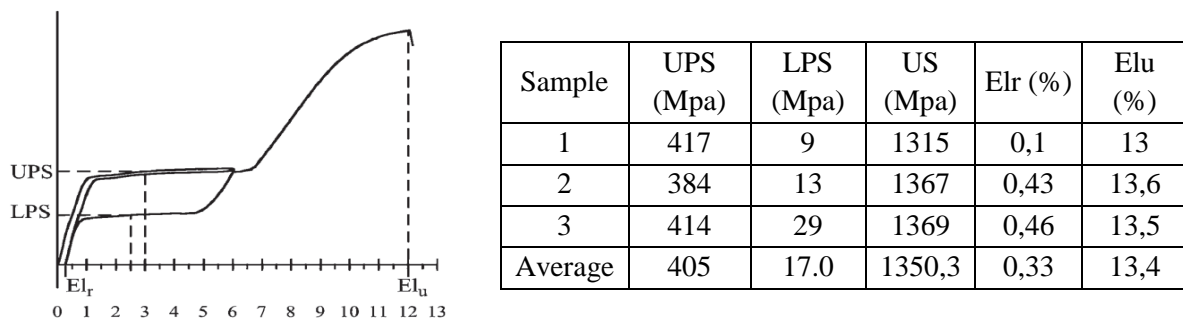


Figure 5: Main tensile characteristics of the Nitinol tested according to ASTM F2516-07 [7].

In order to prepare the hybrid specimens of ECC reinforced with NiTinol for direct tension, the ECC fresh mixture was poured into the acrylic moulds previously used for casting the dogbone-shaped tensile specimens. Four dogbone-shaped specimens reinforced with 6 NiTinol wires, which represent 0,47% of the cross-section area of the cementitious composite, were casted. The procedure followed to fix the 6 wires in the mould was carefully developed in order to avoid the entanglement of the wires and assure their correct placement in the section during casting and vibration, which was particularly difficult due to the super-elastic effect. First the wires were placed in a wood plate and fixed with 12 connectors, located at the edges of the plate as shown in Figure 6.

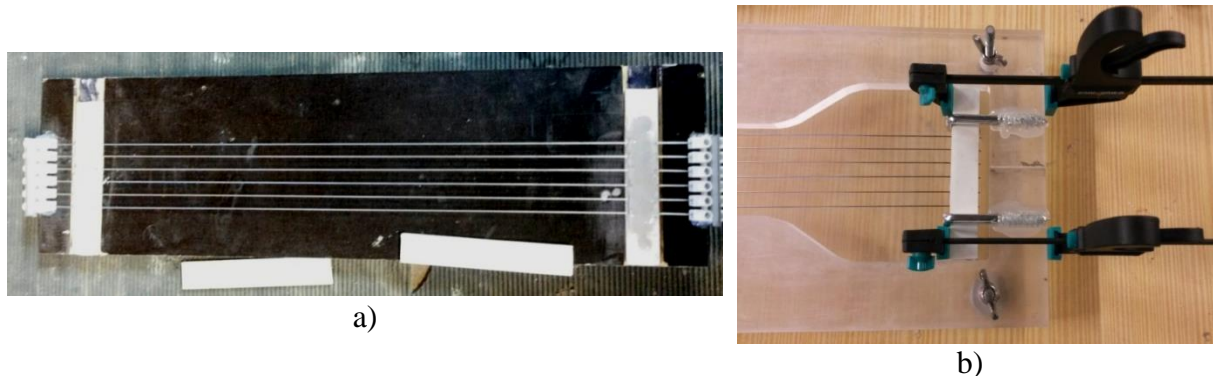


Figure 6: a) Wood plate with the connectors fixed at the edges, and b) plastic plate fixed at the edge of the mould using mechanical devices to stretch and hold it, while the “L” screws were fixed to the mould.

The stretched wires were then glued between two plastic plates using hot glue and epoxy glue, in order to assure the correct position of the wires in the final section. After 48 hours of curing the wires were removed from the wood plate and placed in the casting acrylic mould using a temporary mechanical device to avoid the entanglement of the wires.

The mechanical devices were removed and the ECC composite was poured into the moulds. The air bubbles were removed from the composite by subjecting it to vibration using a shaking table for 2 minutes. The specimens were then placed in a 20°C and 60% RH ventilated room for 28 days. After one day of curing the “L” screws were removed.

In order to assess the effect of the adherence mechanisms between the ECC matrix and the Nitinol wires on the tensile behaviour of the composite, three dogbone-shaped specimens containing 6 twisted wires, which represent 0.94% of the cross-section of the cementitious composite, were also casted. The procedure to fix the twisted wires in the mould was practically identical to the one previously reported for the case of the 6 single wires, but it was necessary to proceed with more precaution in order to avoid the wire entanglement and the damage of the specimens and the equipment. The procedure included the twisting of the wires, which were twisted 10 times on each edge, and the removal of the wires from the wood-plate using a device that kept immobilized the stretched wires between the two plastic plates due to the increased rotational force and the risk of entanglement of the wires.

The hybrid ECC dogbone specimens were tested adopting the same set-up as before, for the case of the tensile tests on ECC dogbone specimens. All tests were carried out under displacement control, subjecting the specimens to displacement increments at a constant rate of ± 0.015 mm/s.

3. RESULTS AND DISCUSSION

The results obtained in terms of tensile stress-strain responses are represented in Figure 7:

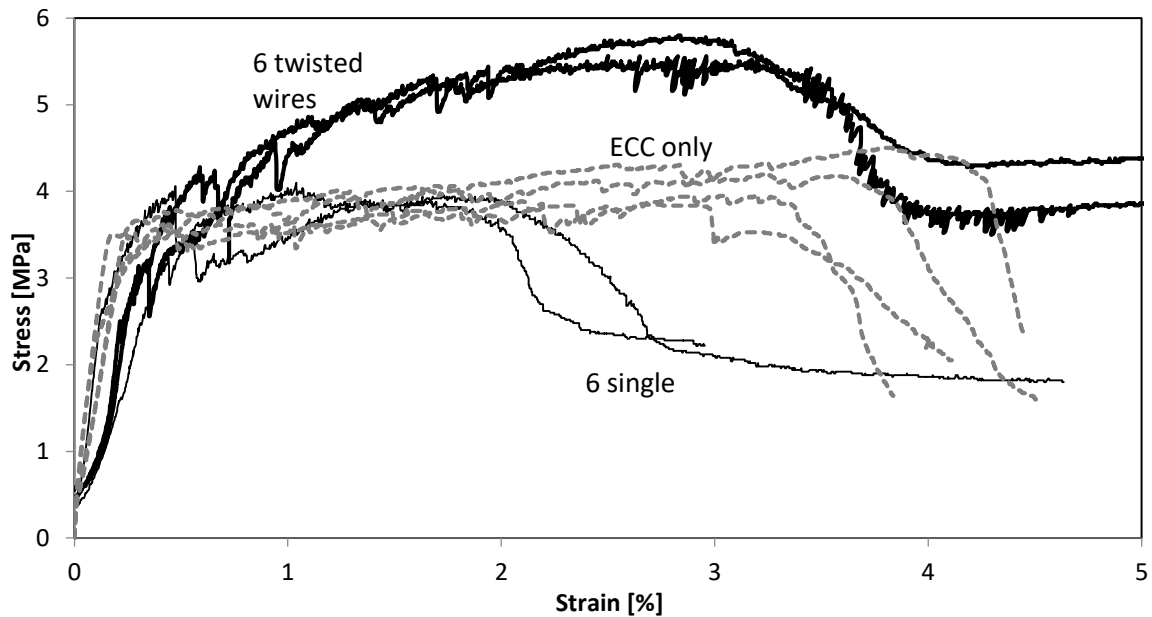


Figure 7: Tensile stress – strain responses of the ECC-Nitinol composites tested with single and twisted wires.

As shown, the addition of the 6 single wires did not result in significant improvement of the tensile properties of the ECC in tension. As a matter of fact, by comparing the tensile results obtained with or without the 6 Nitinol single wires, the tensile responses obtained reveal the same maximum tensile stress at the tensile plateau and a significantly lower tensile strain deformation at peak stress. By looking at the surface of the dogbone specimens after testing in tension, a poorer cracking distribution and cracking control was clearly visible, as shown in Figure 8, especially when comparing to the cracking patterns obtained with ECC only.

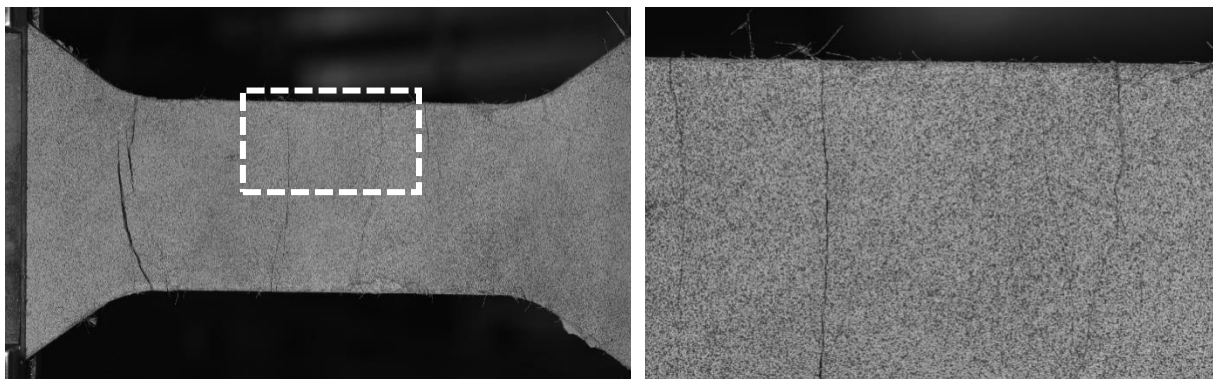


Figure 8: General view and detail of the dogbone surface of a ECC-Nitinol specimen after testing.

In contrast, the use of the 6 twisted wires resulted in a substantial improvement of the tensile performance of the composites tested, when compared to the previous ones. As a result, pull-out tests are recommended to further characterise the Nitinol wire - ECC matrix interaction.

5. CONCLUSIONS

This study has contributed to assess the tensile behaviour of a novel composite material made of ECC and superelastic Nitinol, which involves the use of low percentages of Nitinol in the form of thin wires. As shown, the manipulation of the wires is difficult and needs to be carried out very carefully, in order to guarantee its correct placement inside the composite.

The composite did not reveal a substantial benefit as a result of the addition of the Nitinol wires. However, considering that the Nitinol ultimate tensile stress and strain are very high, it was possible to confirm that the wire-ECC interfacial interaction needs to be significantly enhanced, in order to take full advantage of Nitinol tensile characteristics and its supreme superelastic performance.

The twisting of the wires has led to an increment of the mechanical interlocking and adhesion of the wires to the surface, and this has resulted in a significant enhancement of the composite behaviour in tension. However, the tensile cracking behaviour and the typical cracking control ability of ECC was not improved, it was actually less exuberant than in the case where no reinforcement was used. Therefore, the main conclusion is that the wire-ECC interaction properties need to be carefully studied and improved, in order to take full advantage of the composite action and accomplish outstanding levels of tensile performance with this hybrid composite concept.

ACKNOWLEDGEMENTS

The third author wish to acknowledge the grant SFRH/BD/115090/2016, provided by FCT. As well as the support by project. This work was co-financed by Programa Operacional Regional do Norte (NORTE2020), through Fundo Europeu de Desenvolvimento Regional (FEDER), Project NORTE-01-0145-FEDER-000032 – NextSea.

REFERENCES

- [1] O. E. Ozbulut, S. Hurlbaeus and R. Desroches (2011) ; Seismic Response Control Using Shape Memory Alloys: A Review; *Journal of Intelligent Material Systems and Structures*, pages 2-16.
- [2] Federica Daghia (2008); Active fibre-reinforced composites with embedded shape memory alloys; University of Bologna.
- [3] Gilbert and Rasmussen (2012); Drive-In Steel Storage Racks: Stiffness Tests and 3D Load-Transfer Mechanisms; American Society of Civil Engineers.
- [4] Victor C. Li (2007); Engineered Cementitious Composites (ECC) – Material, Structural, and Durability Performance; University of Michigan, MI 48109, pages 1-78.
- [5] E. B. Pereira, G. Fischer, and J. A. O. Barros, “Effect of hybrid fiber reinforcement on the cracking process in fiber reinforced cementitious composites,” *Cem. Concr. Compos.*, vol. 34, no. 10, pp. 1114–1123, 2012.
- [6] E. B. Pereira, G. Fischer, and J. A. O. Barros, “Hybrid fiber reinforcement and crack formation in cementitious composite materials,” *RILEM Bookseries*, vol. 2. ISISE, University of Minho, Guimaraes, Portugal, pp. 535–542, 2012.
- [7] ASTM International (2008); “ASTM F2516-07: Standard Test Method for Tension Testing of Nickel-Titanium Superelastic Materials”.

TESTS ON STRENGTHENING FASTENERS IN RIVETED STEEL STRUCTURES – FIT BOLTS AND WELD STUDS

Bernard Wichtowski (1), Janusz Holowaty (1)

(1) West Pomeranian University of Technology Szczecin, Poland

Abstract

Issues associated with the renovation of two truss semi-gantry cranes located on a port wharf are discussed. The axial spacing of the structures is $L = 71.47$ m and mass $m = 405$ t. The cranes move on tracks at a speed of 10 m/min. A grab crane with a stable cantilever jib of capacity $Q = 7.5$ t and mass 63 t is installed on each structure. The top flanges of the bridge girders under the rails had cracked structural members that required replacement together with an under rail plate of section 550×12 mm and length 40 m. Replacement of all the rivets with fit bolts was impossible due to the enclosed location of the bolt nuts. Therefore, the vertical rivets on the vertical axis were replaced in the two structures by weld studs numbering in total 2428 units.

The lack of a broad basis for calculating the resistance of such fasteners was the inspiration for an attempt to assess their static and fatigue strength via experimental tests. The test methodology and the results obtained are given in the paper.

Keywords: structural strengthening; fit bolts; weld studs; fatigue

1. CHARACTERISTICS OF SEMI-GANTRY CRANES

One of Szczecin's sea port wharves is served by two semi-gantry cranes of a truss structure, with overall dimensions given in Fig. 1. Travelling transporters called bridge cranes have span length $L = 71.47$ m and mass 405 t. Installed on each crane is a grab crane with a stable cantilever jib of capacity $Q = 7.5$ t and mass 63 t. The bridge cranes move at a speed of 10 m/min.

After 49 years in service, and taking into account the poor technical condition of the trackage structures (Fig. 2a), the decision was taken to commence repairs [1]. Existing damage was associated with loose rivets in the top chords of the bridge truss girders in addition to cracks in the angles under the rails and fatigue cracks in the truss girder joints.

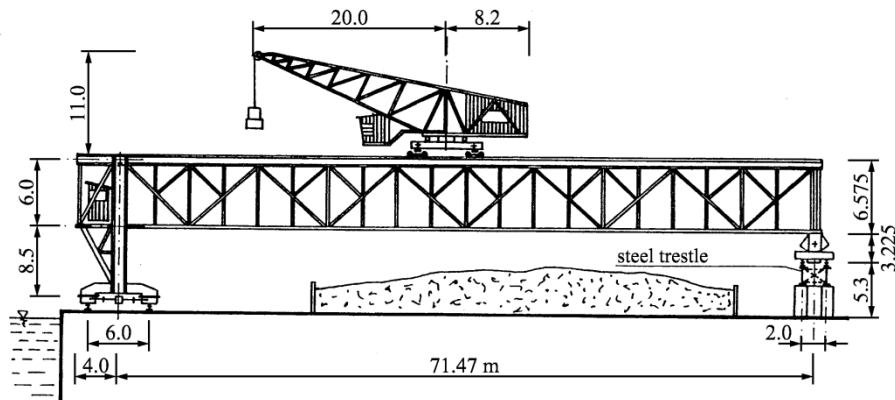


Figure 1: Semi-gantry cranes on the port wharf: a) general view, b) structure scheme

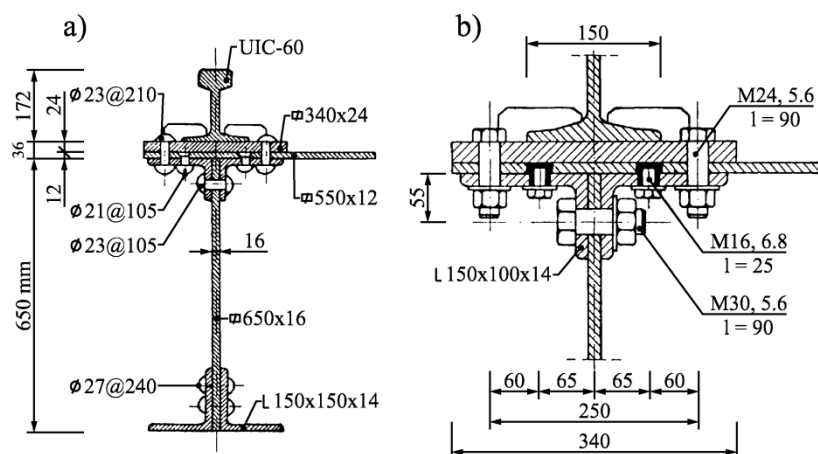


Figure 2: Top chord structure of the semi-gantry cranes: a) as existing, b) upper part of repaired structure (under the rail)

The damage discovered was as follows:

- Loose rivets: vertical rivets of 23 mm diameter at spacing 210 mm and vertical rivets of 21 mm diameter at spacing 105 mm, with horizontal rivets of 23 mm diameter at spacing 105 mm
- Cracks of maximum continuous length 17.3 m and 26.32 m for the particular gantry crane in the top unequal angles 150×100×14 mm (under the rails)
- Fatigue cracks of length from 45 mm to 240 mm located in the gantry joints, 7 and 8 cracks respectively for gantry crane No. 1 and 2

2. REPAIR WORK TECHNOLOGY

Fracture gusset plates and external angles with total lengths of 36.0 m for bridge No. 1 and 39.6 m for bridge No. 2 were designated for replacement. It was also necessary to replace the under-rail steel plates with 550×12 mm sections. The use of fit bolts was planned for joining the new sections and for replacement of the loose rivets. However, such a simple replacement proved to be impossible due to the overly-tight location of the bolt nuts. It was therefore decided to replace the rivets on the vertical axis and the rivets with one flat head by weld studs. The total number of rivets for replacement was 1532 and 896 units for bridges No. 1 and 2 respectively.

Finally, repair of the under-rail parts for each girder included the connectors shown in Fig. 2b. In the first stage, after removal of the rivets and re-boring of the holes, M30 class 5.6 fit bolts were fixed on the horizontal axis. Next, a horizontal plate of 12 mm thickness was put in and the holes were re-bored in shape as shown in Fig. 3a. M16, class 6.8 bolts (studs) with washers of 18 mm diameter fitted in these holes, and welded using rutile electrodes of 3.25 mm diameter. After welding the studs (Fig. 3b), the excess weld metals were ground and top plates of 24 mm thickness were fixed in place. The top plates were connected to the bottom plates and angles by M24 class 5.6 fit bolts. The finished structure is shown in Fig. 4. In the last stage of the repair works, the broken gusset plates were strengthened using new overlap plates of 200×24 mm sections and 1.1 m length welded from the inter-track side.

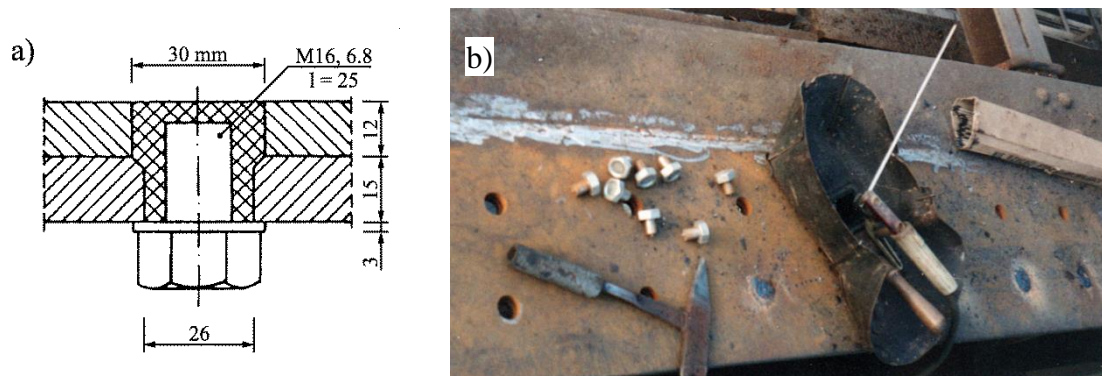


Figure 3: Weld studs: a) hole geometry, b) installation view

3. MATERIAL TESTING AND STATIC TESTS FOR CONNECTORS

A paucity of complex information on the fatigue shear resistance of fit bolts combined with a total lack of such knowledge for weld studs were the inspiration to undertake attempts to assess their static and fatigue strengths.



Figure 4: Top chord of semi-gantry crane girder after repair

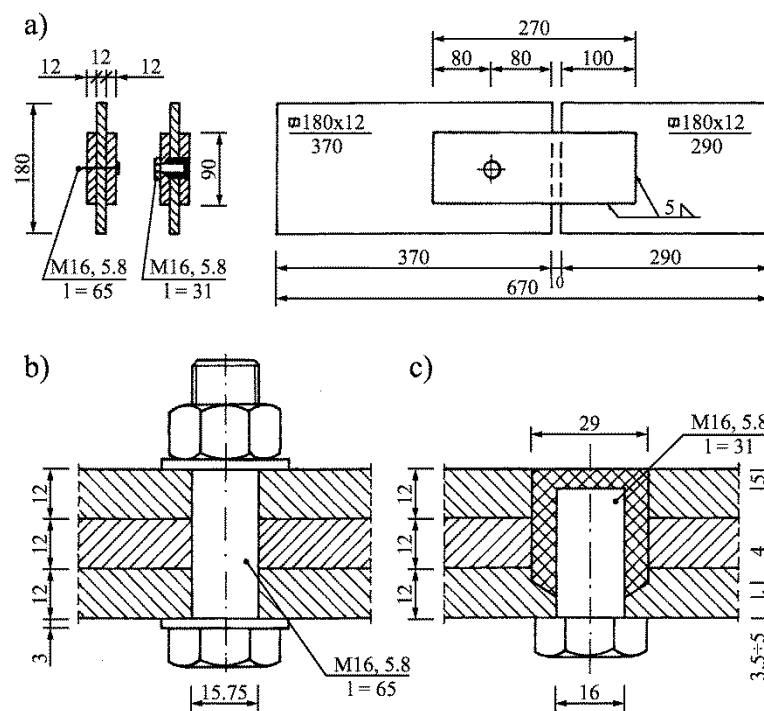


Figure 5: Geometry of specimens for joint testing: a) general alignment, b) fit bolt joint, c) weld stud joint

The geometry of the specimens for joint testing is given in Fig. 5. For the M16 class 5.8 fit bolts, holes with 15.75 mm diameter were used. The nuts were tight, with 100 Nm moments. This value is 10 % higher than the recommended standard value. Studs of 31 mm length were made by cutting M16 class 5.8 bolts. Welding was made in the PA flat position using a semi-automatic arc welding machine in CO₂ shielding with 160 A and 28 V current. The wire was of SpG35 type with 1.2 mm diameter.

Before the endurance tests, the chemical compositions of the steel plates, bolt shanks and weld material were assessed – see Tables 1 and 2. For comparison, standard values for the particular elements are also given. The mechanical properties were also satisfactory. The values given in Table 2 are the average test values from three specimens. Fracture surfaces of three specimens of 10 mm diameter for weld metal showed slag inclusion and gas pores which lower the section by 17.3 % on average. It may be assumed that the ultimate strength of the weld metal is $f_u = 370 \cdot 1.173 = 434$ MPa [5].

Deviations from typical values were found in the toughness tests. All the tested specimens showed low toughness values in the test temperature range from -20 °C to +20 °C. Charpy KV toughness values at temperature -20 °C for steel and bolts were 11 J and 13 J respectively. These values are 41 % and 47 % of the required minimum standard values for new structures (27 J). The transition temperature for these steels is -5 °C and -2.5 °C.

Table 1. Chemical composition for tested specimens, weld studs and weld metal

Tested specimen Standard value	Chemical composition [%]				
	C	Mn	Si	P	S
1	2	3	4	5	6
Steel	0.19	0.66	0.15	0.020	0.024
Shank (bolt M16)	0.09	0.57	0.18	0.012	0.016
Weld metal	0.057	0.34	0.007	0.015	0.024
Steel St3M	max 0.20	min 0.40	0.12 ÷ 0.30	max 0.05	max 0.05
Bolt class 5.8	max 0.55	-	-	max 0.05	max 0.06
Wire SpG3S	max 0.10	0.35 ÷ 0.65	max 0.30	max 0.03	max 0.03

Table 2. Mechanical properties of tested specimens, weld studs and weld metal
 (acc. to EN ISO 6892-1:2016-09, EN ISO 148: 2017-2)

Specimen	Specimen dimension [mm]	Mechanical properties								
		f_y	f_u	A_5	Z	KV [J]				
		[MPa]	[MPa]	[%]	[%]	-20°C	-10°C	0°C	+10°C	+20°C
1	2	3	4	5	6	7	8	9	10	11
Steel	φ10 (10×10)	317.3	464.9	32	38	11.3	18.7	37.3	40.8	53.5
Shank	φ5 (10×10)	458.0	606.3	13	40	13.0	16.8	31.4	22.8	36.9
Weld met.	φ10 (10×10)	296.8	370.1	11	11	4.8	4.9	5.6	7.6	11.9

Static shear tests were carried out on four types of joints, obtaining an average value of shear strength τ from three specimens:

- Type I: M16, 5.8 fit bolts, $\tau = 441$ MPa
- Type II: weld studs by an automatic machine in CO₂ shielding with MAG method, $\tau = 238$ MPa
- Type III: weld studs using rutile electrode BES 1.460R of 3.25 mm diameter, $\tau = 263$ MPa
- Type IV: weld metal in 29 mm holes using SpG3S wire, $\tau = 232$ MPa

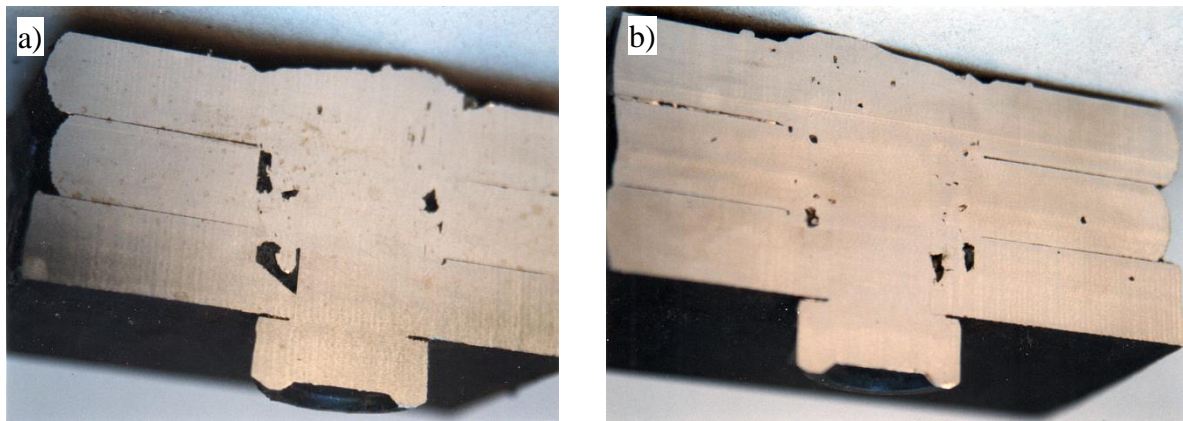


Figure 6: Macrography of non-etched cross sections of weld stud joints: a) type II, b) type III

Fracture of the type II and III studs was noted for average forces $N = 314$ and 347 kN which differ in only about 10 %. For the type III joint, using rutile electrodes, a surprisingly good penetration of weld material was obtained (Fig. 6b).

4. FATIGUE TESTS

Fatigue tests were planned according to the Polish code. In the fatigue tests, pulsing tension with stress ratio $R = 0.1$ was assumed. Tests on $16+15 = 31$ specimens were carried out on a pulsator using working frequency 6.0 Hz. Five values of loading forces were assumed: from 80 to 120 kN for bolt testing and from 75 to 200 kN for stud testing. The forces induced shear stress, shown in Fig. 7. The specimens, depending on the stress, fracture at the number of cycle loading from $11\,500$ to $2.557 \cdot 10^6$ [3-5].

On the basis of the test results, adopting the least square method, straight regression equations were elaborated in a logarithmic scale in the form (1) for fit bolts (Fig. 7a) and for weld studs (Fig. 7b):

$$y = 3.04946 - 0.11364x \quad (1)$$

$$y = 3.05633 - 0.19437x \quad (2)$$

where

$x = \lg N_i$ and $y = \lg \tau$

N_i is the number of cycles when the specimen is broken

τ is the cyclic shear stress in MPa

Simultaneously, the linear correlation coefficient was calculated as $r = -0.94$ for bolts and $r = -0.93$ for studs. The high values of the coefficients provide confirmation of the low scatter of the results. From Eqs. (1) and (2) for $\bar{x} = N_i = 2 \cdot 10^6$, the values of an average infinitive fatigue strength for shear are obtained as $Z_{\tau j} = 215$ MPa and 68 MPa respectively.

The structure stress spectrum caused by loading is characterised by the number of load cycles N_i as well as the appropriate difference between the extreme values of characteristic stresses (range of stress) $\Delta\tau$. According to [6], to ensure the safety of bolt and stud shear connectors, the stress range $\Delta\tau$ should not exceed the fatigue strength assessed for the given number of load cycles and notch type:

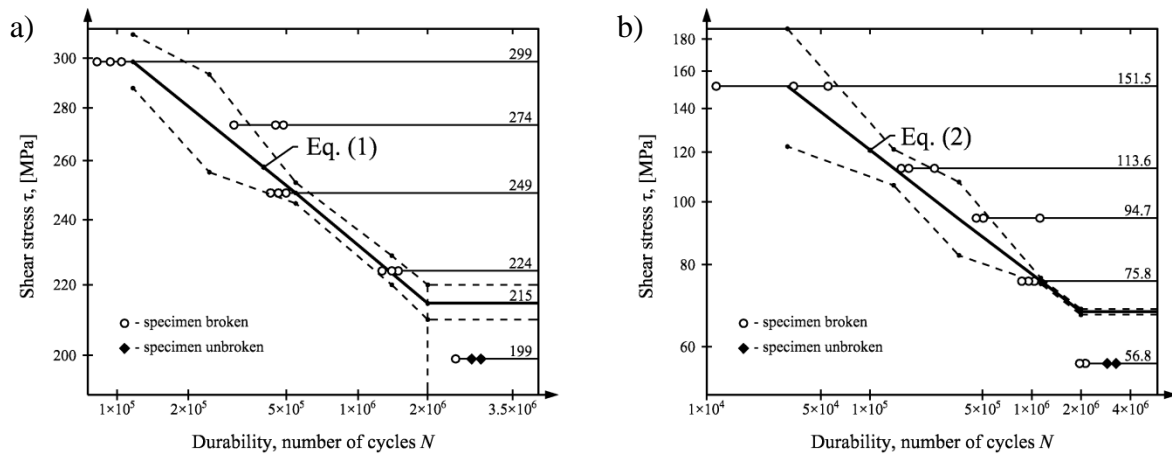


Figure 7: Linear regression of tested joints: a) for fit bolts, b) for weld studs

$$\Delta\tau_k \leq \Delta\tau / \gamma_s \quad (3)$$

where:

$\Delta\tau_k = \tau_{kmax} - \tau_{kmin}$ is the load stress range of characteristic loads for number of load cycles N_i

$\Delta\tau = \tau_{max} - \tau_{min}$ is the fatigue strength for number of load cycles N_i

$\gamma_s = 1.14$ material factor for bolts and studs acc. [6]

EN 1993-1-9 introduced partial factor $\gamma_{Mf} = 1.15$ for tolerable damage method and high consequence of damage and $\gamma_{Mf} = 1.0$ for low consequence.

Fig. 8 shows the results of 16 specimen tests on weld studs, along with the relation between the number of loading cycles N_i and fatigue strength for shear $\Delta\tau$ divided by material factor γ_s (the lower line). The strength was obtained from Eq. (4). At the same time the fatigue strength was obtained for fit bolts $\Delta\tau/\gamma_s$ as a function of loading cycles N_i from Eq. (5) – the upper line.

$$\lg(\Delta\tau/\gamma_s) = 2.95508 - 0.29464 \cdot \lg N_i \quad (4)$$

$$\lg(\Delta\tau/\gamma_s) = 2.94674 - 0.11364 \cdot \lg N_i \quad (5)$$

For comparison purposes, the regression line for the fit bolts fatigue strength for shear $\Delta\tau/\gamma_s$ according to EN 1993-1-9 and Polish standard PN-90/B-03200 (the middle line) is given. The detail category was taken as $\Delta\tau_c = 100$ MPa for $m = 5$ (EN) and the standard equation (PN) was used according to annex No. 3 – Eq. (6).

$$\Delta\tau = \Delta\tau_c (2 \cdot 10^6 / N_i)^{1/5} \geq \Delta\tau_L = 45.7 \text{ MPa} \quad (6)$$

9. CONCLUSIONS

The development of weld studs changed the net section resulting from existing rivet holes into gross section, and the basic function of a shear joint was also maintained. Literature research [1, 5] has shown that the fatigue strength of solid bars at stress range $R = 0.1$ is approximately 30 % higher than the fatigue strength of riveted bars.

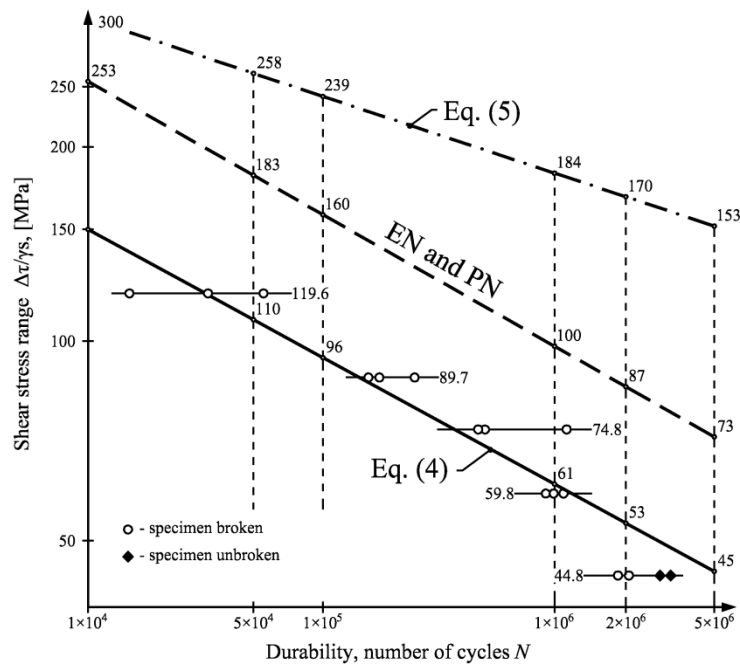


Figure 8: Weld studs and fit bolts fatigue strength for shear

Fatigue shear stress $Z_{rj,b}$ on fit bolts makes 49 % of the shear stress at static loading. In the case of weld studs this is only 26 % and 28 %.

During replacement of defective rivets due to ovalisation of the sections and the possibility for stud welding, re-boring of the holes was carried out, and in the same way the section for shear was enlarged. This resulted in weld stud resistance according to (2) being not smaller than the dismantled rivet resistance after $2 \cdot 10^6$ load cycles (4). In the retrofitted top flanges of the crane girders (Fig. 2) the fatigue strength of these connectors is:

$$N_{rf} = 0.25(3.14 \cdot 2.1^2)10.0 = 34.6 \text{ kN for rivets, and}$$

$$N_{sf} = 0.25(3.14 \cdot 3.0^2)6.79 = 48.0 \text{ kN for studs} \geq 34.6 \text{ kN}$$

Following the retrofit, the semi-gantry cranes with weld studs have been in service for many years. Their heavy use confirms the usability of weld studs in the strengthening of dynamically loaded riveted structures. So far, no loose or cut connectors have been found.

REFERENCES

- [1] Wichtowski, B., 'Untypical reconstruction of semi-gantry truss cranes', *Inż. i Bud.* **59** (5) (2003) 246-249 (in Polish).
- [2] Kulak, G.L., Fisher, J.W. and Struik, J.H., 'Guide to design criteria for bolted and riveted joints' (John Wiley & Sons, New York, 1987).
- [3] Wichtowski, B., 'Investigation of fit bolt fatigue strength', *Inż. i Bud.* **56** (10) (2000) 571-574 (in Polish).
- [4] Wichtowski B., 'Untersuchungen zur Ermüdungsfestigkeit von Paßschrauben beim Abscheren', *Stahlbau* **76** (4) (2007) 235-240
- [5] Wichtowski, B., 'Weld stud capacity for shear', *Inż. i Bud.* **57** (5) (2001) 294-298 (in Polish).
- [6] Łaguna, J., and Łypacewicz, K., 'Bolted and riveted joints' (Arkady, Warszawa, 1986 in Polish).

METHODOLOGY OF NUMERICALLY AIDED OPTIMISATION OF CONSOLIDANTS FOR SURFACE TREATMENTS OF MORTARS

Janez Perko (1), Li Yu (1), Diederik Jacques (1), Eddie.A.B. Koenders (2), Neven Ukrainczyk (2), Anna Varzina (1), Pagona-Noni Maravelaki (3), Ioannis Arabatzis (4)

- (1) Belgian Nuclear Research Centre SCK•CEN, Institute for Environment, Health and Safety, Boeretang 200, Mol Belgium B-2400
- (2) Technische Universität Darmstadt (TUDa), Franziska-Braun-Straße 3, Darmstadt, Germany D- 64287
- (3) University of Crete (TUC), School of Architecture, Chania, Greece GR-73100
- (4) NANOPHOS, Lavrio technological & Science park, Lavrio, Greece GR-19500

Abstract

Tetraethoxysilanes (TEOS), an alkoxyasilane, are widely used consolidants which form the basis of most existing commercial strengthening agents for protecting porous building materials against deterioration. These products can provide consolidation and water repellent behaviour simultaneously. TEOS are polymerized inside the pores of porous materials in the presence of water. It is necessary to achieve a sufficient penetration depth of TEOS into the porous building material before polymerization to achieve a good performance

Alkoxyasilanes are immiscible with water and alcohol is often used as the mutual solvent. Alcohol assures not only miscibility but also influences the reaction kinetics and rheology of the consolidants. Moreover, properties of the water-alcohol-TEOS mixture are time dependent. For example, initial viscosity, which is one of the factors influencing the penetration depth, is lower when more alcohol is added. On the other hand, higher concentration of alcohol in a mixture causes faster gelation and evaporation which would decrease the penetration depth. Reaction kinetics also depends on a pore size which is the function of (aged) material. Since cementitious structures are not fully saturated when consolidants are applied, the main mechanism of consolidants penetration in a porous material, such as concrete, is by capillary forces. Studies on cementitious materials indicate that the capillary sorption of fluid in concrete exhibits a complex time dependence, and depends on several parameters, such as surface tension and contact angle between consolidants and the material. The process is additionally complicated because sol-gel behaves initially as a Newtonian fluid, but later as a thixotropic fluid where viscosity is time dependent and increases during gelation. Obviously, defining an optimised mixture of water and alcohol which defines the penetration depth and consequently assures good performance of consolidants is a complex process.

As a part of EC project InnovaConcrete, an ambitious plan is developed to combine experimental observations with numerical capabilities in order to facilitate the development of

optimized consolidants. This methodology includes numerical developed degraded matrix, experimental rheological properties of consolidants and pore-scale model to determine the penetration depth.

In this presentation we describe the methodology and first steps taken forward to combine experimental and numerical means of the optimisation of consolidants for surface treatments of mortars.

Keywords: surface treatments, mortars, concrete structures, alkoxysilane, InnovaConcrete

**International Conference on Sustainable
Materials, Systems and Structures
(SMSS 2019)**
Durability, Monitoring and Repair of Structures

Sponsors and support

UNIVERSITY OF ZAGREB FACULTY OF CIVIL ENGINEERING



100
Years

1919-2019



Mision, Vision and Strategy

Mission

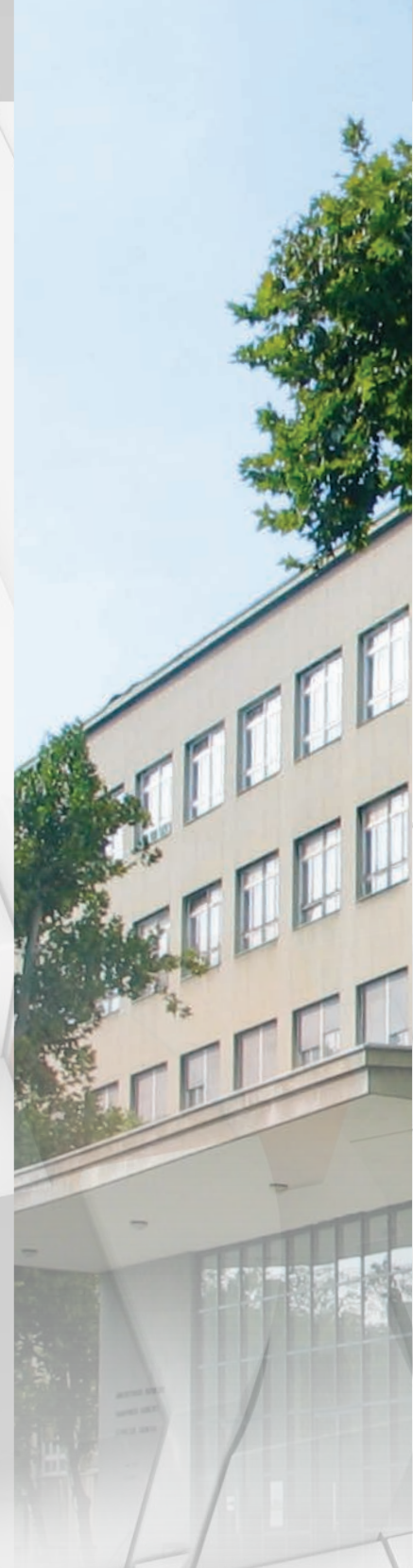
The Faculty of Civil Engineering of the University of Zagreb is the oldest civil engineering faculty in Croatia conducting university education at an undergraduate, graduate and postgraduate level in all branches of civil engineering. It is continually developing and advancing higher education, scientific research activities and overall education, and actively participates in the development of the profession and implementation of new technologies.

Vision

- to retain and strengthen the leading position as a university and scientific-research centre in the country, which covers all branches of civil engineering
- to achieve international recognisability by developing a culture of quality higher education and research work by implementing the best European and world practices, promoting the mobility of students and researchers, and by becoming one of the regional centres of excellence in individual disciplines, as well as a "cooperation bridge" for countries of the European Union and the region
- to retain and strengthen cooperation with the business sector in high-expertise tasks and developmental projects, specialised life-long higher education, and the development of an alumni network for mutual support and progress

Objectives

- further harmonisation of the outcome of learning with the demands of the profession and market, with continual modernisation of the teaching process and content
- connecting and expanding cooperation with related university institutions and scientific institutions, primarily in the European Union, along with promoting the international mobility of students and researchers
- participation in joint research projects and joint studies with partners from EU countries and the region
- founding individual study programmes in the English language, and organising life-long learning and non-formal education in the English language
- development and modernisation, and certification of laboratories
- increasing spatial and personnel capacities for teaching and research needs
- further ties with the business sector and searching for adequate organisational forms



ENABLING BETTER CONSTRUCTION AND REPAIR

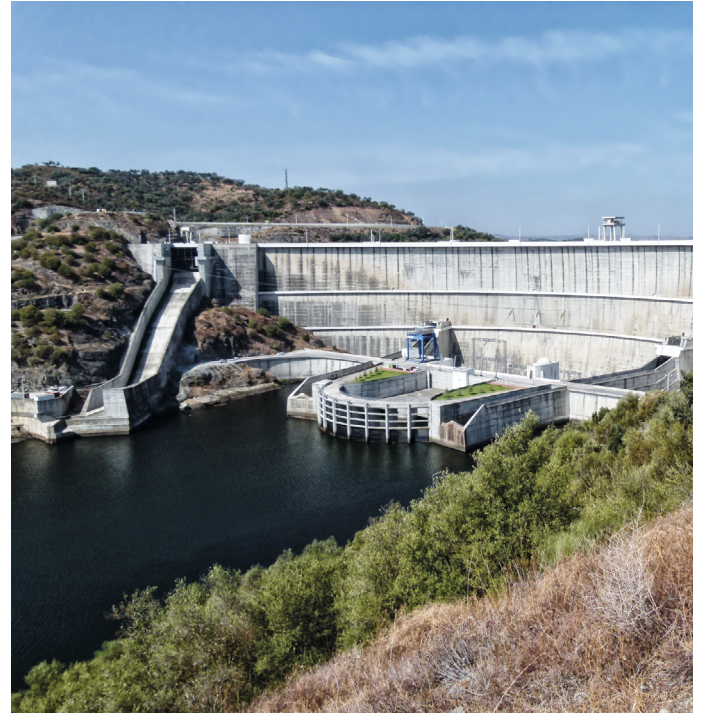
Each individual product can have a critical effect on an entire structure or its repair. Choosing the wrong solutions or applying them incorrectly can lead to component and structural damage and, in extreme cases, even endanger life.

Planners, engineers and applicators therefore have a significant responsibility to bear, of which we are only too aware.

It is not only your own good name that is at stake; businesses and people also have to be protected.

Hence – through reliable and sound technical advice and product solutions – we dedicate our fullest efforts, care and attention to ensuring that each project performed by our customers is executed to their enduring satisfaction and peace of mind. Because part of being MC really does mean accepting responsibility for lives and reputations.

We take building seriously.
BE SURE. BUILD SURE.



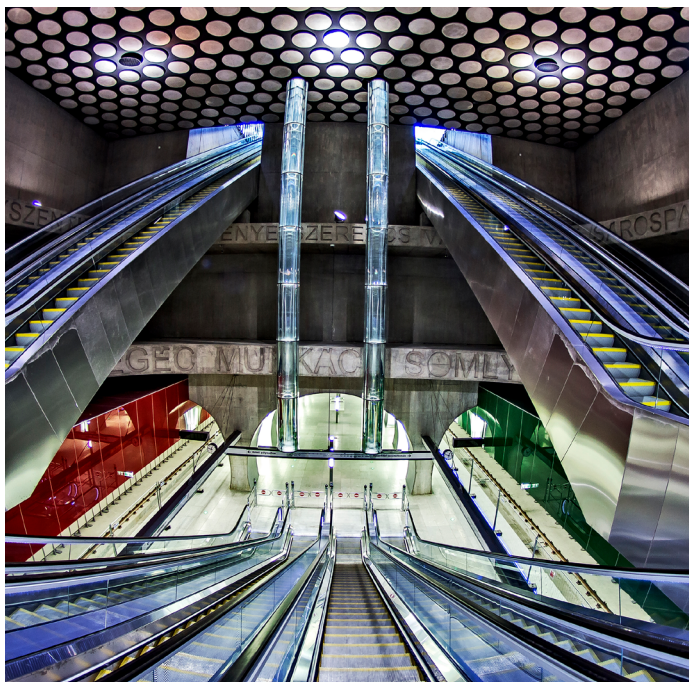
Injection systems



Admixtures for precast concrete



Admixtures
Concrete cosmetics
Grouting mortar



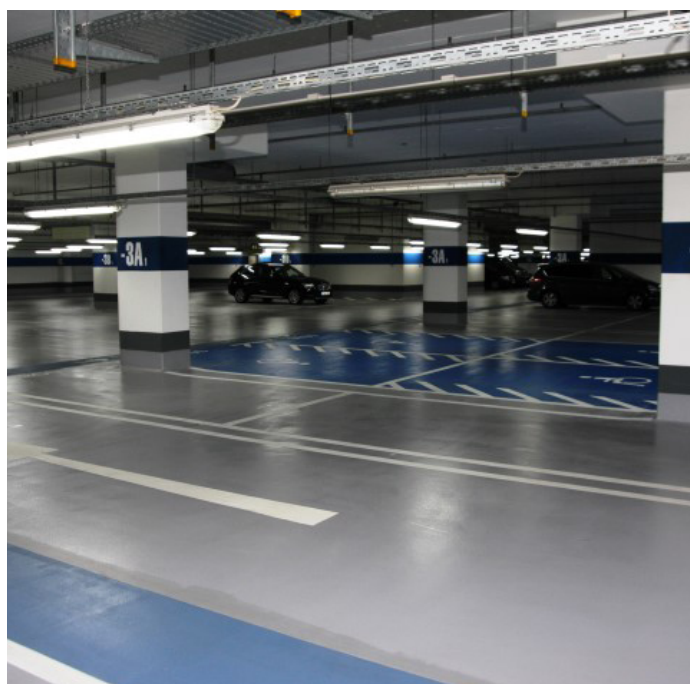
Admixtures
Concrete cosmetics



Floor coatings
Epoxy, Polyurethane



Injection systems
Concrete repair



Floor coatings
Waterproofing
Surface protection

MC solutions in demand throughout the world

MC solutions have been used in major construction and repair projects around the world for more than 50 years now. Developers, promoters, architects, planning engineers and applicators know they can rely both on the advice of our experienced consultants and on the high quality of our product systems.

MC – Building Chemicals d.o.o.
Kovinska 4a, 10090 Zagreb
Tel. +385 (1) 5587 797

www.mc-bauchemie.hr
infocro@mc-bauchemie.com



I WANT TO GET THE MOST OUT OF MY QUARRY

MasterSuna SBS: The solution for fine aggregates containing clay



35 %
Reduction
in sand costs*

25-ton
Reduction
in CO₂ emissions
per year*

Zero
Sand transportation*



QUANTIFIED SUSTAINABLE BENEFITS – REDUCE YOUR FOOTPRINT AND BOOST YOUR BOTTOM LINE

Clay containing fine aggregates were once regarded as unsuitable for the production of high-quality concrete. But this is no longer the case. With the new MasterSuna SBS sand blocker from BASF, it is even possible to convert difficult sands into a valuable resource. Thanks to MasterSuna SBS, the concrete producer BRONZO PERASSO in Marseille, France, no longer needs to transport sand from remote sites. That reduces sand and transportation costs, and saves up to 25 tons of CO₂ per year.

Discover more about this success story:

sustainability.master-builders-solutions.basf.com

 **BASF**
We create chemistry

Cast off for non-metallic reinforcements

Textile concrete with AR glass or carbon reinforcements is economically and functionally far superior to standard steel concrete. The non-metallic reinforcements are alkali-resistant, non-corrosive and light. This is your introduction to modern concrete construction. Textile concrete is superbly suited to extreme conditions in a maritime environment where the wind and water are a permanent challenge.

Permanently and sustainably superior

- Six times stronger than steel
- Resistant to the effect of chloride
- Non-corrosive:
 - > Reduced concrete coverings
 - > Thin, streamlined and light components
- Lower transport costs for components
- Easy to handle during installation
- No renovation and maintenance costs



solidian®

Leading in construction with non-metallic reinforcement

📍 Dr. Slavka Rozgaja 3
47000 Karlovac, Croatia

✉ info@solidian.hr
🌐 www.solidian.hr

☎ P +385 47 693 300
☎ F +385 47 434 203



CONFERENCE EXHIBITORS



KNAUF INSULATION



GRAĐEVINAR

Journal of the Croatian Association of Civil Engineers

Scientific and Professional Papers
Professional news items

Indexed in:
Science Citation Index Expanded

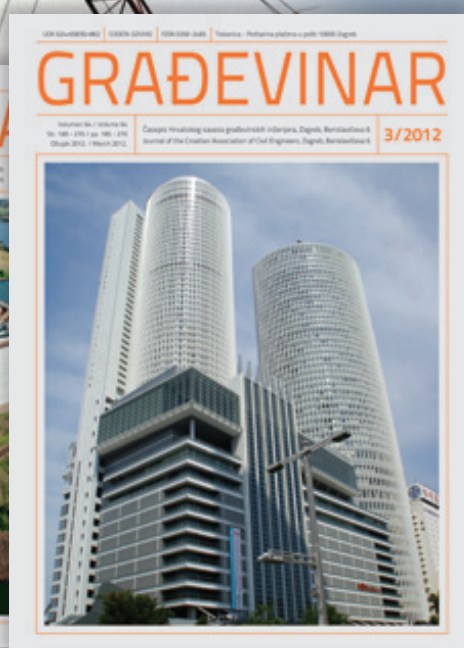
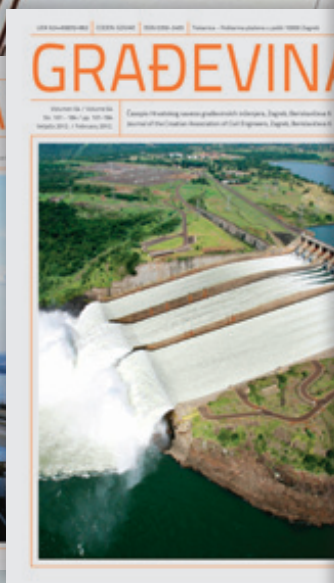
The journal is published regularly
12 times a year since 1949.

Papers are published in Croatian
language and, all papers in the
online edition are entirely in
Croatian and English

The biggest scientific & professional
journal of civil engineering in Croatia

Journal published monthly
(12 issues/year)

Circulation: 3500 copies



GRADEVINAR

Journal of the Croatian Association of Civil Engineers

Editor-in-Chief

Prof. **Stjepan Lakusic**
University of Zagreb
Faculty of Civil Engineering

stjepan.lakusic@grad.hr

Journal GRADEVINAR (eng. CIVIL ENGINEER)
is a scientific/professional journal with a strong
focus on all aspects of Civil Engineering

12 issues/year
3500 copies/issue

The journal GRADEVINAR is a monthly publication that has been regularly appearing **12 times a year** without interruption for three decades now. As the journal is published each month, the publication process of reviewed and accepted papers is relatively fast. The Journal uses the **double blind review** process for evaluation of papers. All papers are printed in Croatian language, but the online edition of the journal features full versions of all papers in English language as well.

The journal GRADEVINAR encourages submission of good papers, not only to help disseminate technical information useful in the field of civil engineering, but also to provide authors with the opportunity to have their paper reviewed by peers and, when published, receive proper recognition for their efforts. The scientific/professional papers are grouped into four categories, depending on their contribution to the advancement of research or professional work.

According to its circulation (3,500 copies), GRADEVINAR is the biggest scientific/professional journal in the field of technical engineering in Croatia and wider region, and is **Indexed in Science Citation Index Expanded**.

On the homepage of Journal GRADEVINAR you can:

- Find all information about the journal
- Acquire information about the journal's most read papers
- Read all papers free of charge
- Find submission information

For more information and for submission guidelines, please visit us at
www.casopis-gradjevinar.hr

International Conference on Sustainable Materials, Systems and Structures (SMSS2019) – 20-22 March 2019 – Rovinj, Croatia

Durability, Monitoring and Repair of Structures

Edited by Ana Baričević, Marija Jelčić Rukavina, Domagoj Damjanović and Maurizio Guadagnini

RILEM Proceedings PRO 128

ISBN: 978-2-35158-217-6

VOL 3. ISBN: 978-2-35158-225-1

e-ISBN: 978-2-35158-218-3

2019 Edition

As part of the RILEM International Conference on Sustainable Materials, Systems and Structures (SMSS 2019), segment DURABILITY, MONITORING AND REPAIR OF STRUCTURES has consisted of 107 scientific papers which cover durability aspects of construction material in a variety of structures and harsh environments, maintenance and management of civil infrastructure and sustainable repair, rehabilitation and retrofitting. Among the others, the topics addressed are characterization of innovative and traditional durable materials, diagnosis of structures including service life design, seismic safety assessment, fire resistance, repair and conservation of heritage structures, advanced materials for structural rehabilitation, strengthening methods and case studies.

RILEM Publications S.a.r.l.

4 avenue du Recteur Poincaré

75016 Paris - FRANCE

Tel: + 33 1 42 24 64 46 Fax: + 33 9 70 29 51 20

E-mail : dg@rilem.net